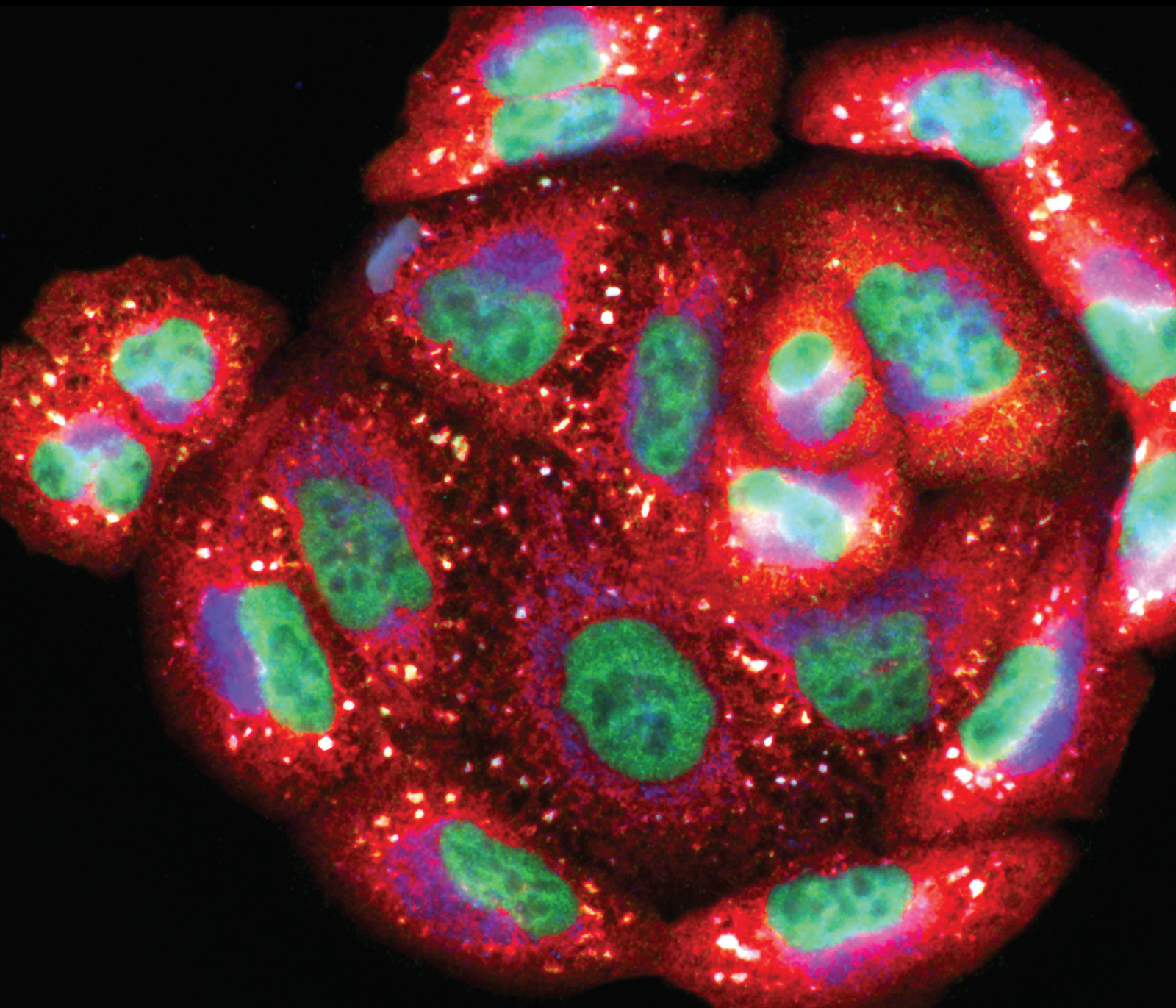


Molecular Mechanisms and Health Implications of Ferroptosis

Lead Guest Editor: Lianxiang Luo

Guest Editors: Xiang Xue and Yanqing Liu





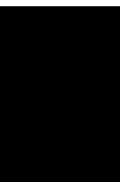
Molecular Mechanisms and Health Implications of Ferroptosis

Oxidative Medicine and Cellular Longevity

**Molecular Mechanisms and Health
Implications of Ferroptosis**

Lead Guest Editor: Lianxiang Luo

Guest Editors: Xiang Xue and Yanqing Liu



Copyright © 2023 Hindawi Limited. All rights reserved.

This is a special issue published in "Oxidative Medicine and Cellular Longevity" All articles are open access articles distributed under the Creative Commons Attribution License, which permits unrestricted use, distribution, and reproduction in any medium, provided the original work is properly cited.

Chief Editor

Jeannette Vasquez-Vivar, USA

Associate Editors

Amjad Islam Aqib, Pakistan
Angel Catalá , Argentina
Cinzia Domenicotti , Italy
Janusz Gebicki , Australia
Aldrin V. Gomes , USA
Vladimir Jakovljevic , Serbia
Thomas Kietzmann , Finland
Juan C. Mayo , Spain
Ryuichi Morishita , Japan
Claudia Penna , Italy
Sachchida Nand Rai , India
Paola Rizzo , Italy
Mithun Sinha , USA
Daniele Vergara , Italy
Victor M. Victor , Spain

Academic Editors

Ammar AL-Farga , Saudi Arabia
Mohd Adnan , Saudi Arabia
Ivanov Alexander , Russia
Fabio Altieri , Italy
Daniel Dias Rufino Arcanjo , Brazil
Peter Backx, Canada
Amira Badr , Egypt
Damian Bailey, United Kingdom
Rengasamy Balakrishnan , Republic of Korea
Jiaolin Bao, China
Ji C. Bihl , USA
Hareram Birla, India
Abdelhakim Bouyahya, Morocco
Ralf Braun , Austria
Laura Bravo , Spain
Matt Brody , USA
Amadou Camara , USA
Marcio Carcho , Portugal
Peter Celec , Slovakia
Giselle Cerchiaro , Brazil
Arpita Chatterjee , USA
Shao-Yu Chen , USA
Yujie Chen, China
Deepak Chhangani , USA
Ferdinando Chiaradonna , Italy

Zhao Zhong Chong, USA
Fabio Ciccarone, Italy
Alin Ciobica , Romania
Ana Cipak Gasparovic , Croatia
Giuseppe Cirillo , Italy
Maria R. Ciriolo , Italy
Massimo Collino , Italy
Manuela Corte-Real , Portugal
Manuela Curcio, Italy
Domenico D'Arca , Italy
Francesca Danesi , Italy
Claudio De Lucia , USA
Damião De Sousa , Brazil
Enrico Desideri, Italy
Francesca Diomede , Italy
Raul Dominguez-Perles, Spain
Joël R. Drevet , France
Grégory Durand , France
Alessandra Durazzo , Italy
Javier Egea , Spain
Pablo A. Evelson , Argentina
Mohd Farhan, USA
Ioannis G. Fatouros , Greece
Gianna Ferretti , Italy
Swaran J. S. Flora , India
Maurizio Forte , Italy
Teresa I. Fortoul, Mexico
Anna Fracassi , USA
Rodrigo Franco , USA
Juan Gambini , Spain
Gerardo García-Rivas , Mexico
Husam Ghanim, USA
Jayeeta Ghose , USA
Rajeshwary Ghosh , USA
Lucia Gimeno-Mallench, Spain
Anna M. Giudetti , Italy
Daniela Giustarini , Italy
José Rodrigo Godoy, USA
Saeid Golbidi , Canada
Guohua Gong , China
Tilman Grune, Germany
Solomon Habtemariam , United Kingdom
Eva-Maria Hanschmann , Germany
Md Saquib Hasnain , India
Md Hassan , India


Tim Hofer , Norway
John D. Horowitz, Australia
Silvana Hrelia , Italy
Dragan Hrnčić, Serbia
Zebo Huang , China
Zhao Huang , China
Tarique Hussain , Pakistan
Stephan Immenschuh , Germany
Norsharina Ismail, Malaysia
Franco J. L. , Brazil
Sedat Kacar , USA
Andleeb Khan , Saudi Arabia
Kum Kum Khanna, Australia
Neelam Khaper , Canada
Ramoji Kosuru , USA
Demetrios Kouretas , Greece
Andrey V. Kozlov , Austria
Chan-Yen Kuo, Taiwan
Gaocai Li , China
Guoping Li , USA
Jin-Long Li , China
Qiangqiang Li , China
Xin-Feng Li , China
Jialiang Liang , China
Adam Lightfoot, United Kingdom
Christopher Horst Lillig , Germany
Paloma B. Liton , USA
Ana Lloret , Spain
Lorenzo Loffredo , Italy
Camilo López-Alarcón , Chile
Daniel Lopez-Malo , Spain
Massimo Lucarini , Italy
Hai-Chun Ma, China
Nageswara Madamanchi , USA
Kenneth Maiese , USA
Marco Malaguti , Italy
Steven McAnulty, USA
Antonio Desmond McCarthy , Argentina
Sonia Medina-Escudero , Spain
Pedro Mena , Italy
V́ctor M. Mendoza-Núñez , Mexico
Lidija Milkovic , Croatia
Alexandra Miller, USA
Sara Missaglia , Italy

Premysl Mladenka , Czech Republic
Sandra Moreno , Italy
Trevor A. Mori , Australia
Fabiana Morroni , Italy
Ange Mouithys-Mickalad, Belgium
Iordanis Mourouzis , Greece
Ryoji Nagai , Japan
Amit Kumar Nayak , India
Abderrahim Nemmar , United Arab Emirates
Xing Niu , China
Cristina Nocella, Italy
Susana Novella , Spain
Hassan Obied , Australia
Pál Pacher, USA
Pasquale Pagliaro , Italy
Dilipkumar Pal , India
Valentina Pallottini , Italy
Swapnil Pandey , USA
Mayur Parmar , USA
Vassilis Paschalis , Greece
Keshav Raj Paudel, Australia
Ilaria Peluso , Italy
Tiziana Persichini , Italy
Shazib Pervaiz , Singapore
Abdul Rehman Phull, Republic of Korea
Vincent Pialoux , France
Alessandro Poggi , Italy
Zsolt Radak , Hungary
Dario C. Ramirez , Argentina
Erika Ramos-Tovar , Mexico
Sid D. Ray , USA
Muneeb Rehman , Saudi Arabia
Hamid Reza Rezvani , France
Alessandra Ricelli, Italy
Francisco J. Romero , Spain
Joan Roselló-Catafau, Spain
Subhadeep Roy , India
Josep V. Rubert , The Netherlands
Sumbal Saba , Brazil
Kunihiro Sakuma, Japan
Gabriele Saretzki , United Kingdom
Luciano Saso , Italy
Nadja Schroder , Brazil



Anwen Shao , China
Iman Sherif, Egypt
Salah A Sheweita, Saudi Arabia
Xiaolei Shi, China
Manjari Singh, India
Giulia Sita , Italy
Ramachandran Srinivasan , India
Adrian Sturza , Romania
Kuo-hui Su , United Kingdom
Eisa Tahmasbpour Marzouni , Iran
Hailiang Tang, China
Carla Tatone , Italy
Shane Thomas , Australia
Carlo Gabriele Tocchetti , Italy
Angela Trovato Salinaro, Italy
Rosa Tundis , Italy
Kai Wang , China
Min-qi Wang , China
Natalie Ward , Australia
Grzegorz Wegrzyn, Poland
Philip Wenzel , Germany
Guangzhen Wu , China
Jianbo Xiao , Spain
Qiongming Xu , China
Liang-Jun Yan , USA
Guillermo Zalba , Spain
Jia Zhang , China
Junmin Zhang , China
Junli Zhao , USA
Chen-he Zhou , China
Yong Zhou , China
Mario Zoratti , Italy

Contents






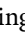
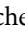



Ferroptosis-Related lncRNAs Act as Novel Prognostic Biomarkers in the Gastric Adenocarcinoma Microenvironment, Immunotherapy, and Chemotherapy

Yushi Zheng, Shanshan Wu, Xueshan Huang, and Lianxiang Luo 
Research Article (28 pages), Article ID 9598783, Volume 2023 (2023)






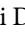





Inhibition of TRF2 Leads to Ferroptosis, Autophagic Death, and Apoptosis by Causing Telomere Dysfunction

Qihui Yang, Ziyang Nie, Yukun Zhu, Mingying Hao, Siqi Liu, Xuelu Ding, Feng Wang, Fei Wang , and Xin Geng 
Research Article (13 pages), Article ID 6897268, Volume 2023 (2023)



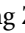
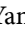



Long Noncoding RNA LINC00578 Inhibits Ferroptosis in Pancreatic Cancer via Regulating SLC7A11 Ubiquitination

Haoran Li , Yijun Wei , Jie Wang , Jun Yao , Chen Zhang , Chengqing Yu , Yuchen Tang , Dongming Zhu , Jian Yang , and Jian Zhou 
Research Article (17 pages), Article ID 1744102, Volume 2023 (2023)





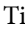

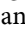

Ferroptosis in Rat Lung Tissue during Severe Acute Pancreatitis-Associated Acute Lung Injury: Protection of Qingyi Decoction

Peng Ge , Yalan Luo , Qi Yang , Haiyun Wen , Jin Liu , Yibo Zhang , Xuanchi Dong , Guixin Zhang , Caiming Xu , Jing Liu , Zheyi Liu , and Hailong Chen 
Research Article (22 pages), Article ID 5827613, Volume 2023 (2023)


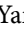
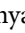

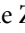

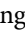
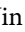

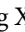
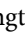


Enriched Environment Attenuates Ferroptosis after Cerebral Ischemia/Reperfusion Injury via the HIF-1 α -ACSL4 Pathway

Jingying Liu , Qihang Luo , Jie Ke , Dongdong Zhang , Yang Xu , Weijing Liao , Xiuping Chen , and Xin Zhang 
Research Article (14 pages), Article ID 5157417, Volume 2023 (2023)




Carbonic Anhydrase IX Controls Vulnerability to Ferroptosis in Gefitinib-Resistant Lung Cancer

Chen Zhang , Xiyi Lu , Xinyin Liu , Jiali Xu , Jun Li , Tianyu Qu , Jiali Dai , and Renhua Guo 
Research Article (21 pages), Article ID 1367938, Volume 2023 (2023)

Modulation of the p38 MAPK Pathway by Anisomycin Promotes Ferroptosis of Hepatocellular Carcinoma through Phosphorylation of H3S10

Wei Chen , Wenjing Yang , Chunyan Zhang , Te Liu , Jie Zhu , Hao Wang , Tong Li , Anli Jin , Lin Ding , Jingrong Xian , Tongtong Tian , Baishen Pan, Wei Guo , and Beili Wang 
Research Article (20 pages), Article ID 6986445, Volume 2022 (2022)

Hypoxia Enhances Glioma Resistance to Sulfasalazine-Induced Ferroptosis by Upregulating SLC7A11 via PI3K/AKT/HIF-1 α Axis

Shicheng Sun, Changfa Guo, Taihong Gao, Dengzhen Ma, Xiangsheng Su , Qi Pang , and Rui Zhang 
Research Article (22 pages), Article ID 7862430, Volume 2022 (2022)

Attenuation by Time-Restricted Feeding of High-Fat and High-Fructose Diet-Induced NASH in Mice Is Related to Per2 and Ferroptosis

Yan-yun Shu , Wen-kang Gao , Hui-kuan Chu , Ling Yang , Xiao-li Pan , and Jin Ye 


Research Article (20 pages), Article ID 8063897, Volume 2022 (2022)

Energy-Stress-Mediated AMPK Activation Promotes GPX4-Dependent Ferroptosis through the JAK2/STAT3/P53 Axis in Renal Cancer

Yanze Li , Ye Zhang , Qiangmin Qiu , Lei Wang , Hu Mao , Juncheng Hu , Zhiyuan Chen , Yang Du , and Xiuheng Liu 




Research Article (17 pages), Article ID 2353115, Volume 2022 (2022)

Mesenchymal Stem Cell-Derived Exosomes Ameliorate Delayed Neurocognitive Recovery in Aged Mice by Inhibiting Hippocampus Ferroptosis via Activating SIRT1/Nrf2/HO-1 Signaling Pathway

Jie Liu , Jingyao Huang, Zhenjiang Zhang, Rui Zhang , Qijuan Sun, Zhihao Zhang, Yongxin Liu, and Baoyu Ma 









Research Article (22 pages), Article ID 3593294, Volume 2022 (2022)

The Regulatory Effects of Traditional Chinese Medicine on Ferroptosis

Qian Gao , Xue-dong Yin, Fan Zhang, Yi-Zhun Zhu , and Zhi-ling Li 







Review Article (11 pages), Article ID 4578381, Volume 2022 (2022)

lncRNA ZFAS1 Positively Facilitates Endothelial Ferroptosis via miR-7-5p/ACSL4 Axis in Diabetic Retinopathy

Yu Liu , Zhengyu Zhang , Jing Yang , Jingfan Wang , Yan Wu , Rongrong Zhu , Qinghuai Liu , and Ping Xie 







Research Article (17 pages), Article ID 9004738, Volume 2022 (2022)

Ferroptosis-Related Long Noncoding RNAs Have Excellent Predictive Ability for Multiomic Characteristics of Bladder Cancer

Jingchao Liu , Jingyi Cui , Shuangyi Zhao , Meng Wu , Jiawen Wang, Yaoguang Zhang , Bin Jin , and Jianye Wang 



Research Article (30 pages), Article ID 9316847, Volume 2022 (2022)

MITD1 Deficiency Suppresses Clear Cell Renal Cell Carcinoma Growth and Migration by Inducing Ferroptosis through the TAZ/SLC7A11 Pathway

Ye Zhang , Yanze Li , Qiangmin Qiu , Zhiyuan Chen , Yang Du , and Xiuheng Liu 

Research Article (14 pages), Article ID 7560569, Volume 2022 (2022)

Dapagliflozin Ameliorates Renal Tubular Ferroptosis in Diabetes via SLC40A1 Stabilization

Bin Huang , Wenjie Wen, and Shandong Ye 

Research Article (17 pages), Article ID 9735555, Volume 2022 (2022)

Contents

From Iron Metabolism to Ferroptosis: Pathologic Changes in Coronary Heart Disease

Xinbiao Fan , Aolin Li , Zhipeng Yan , Xiaofei Geng , Lu Lian , Hao Lv , Dongjie Gao , and Junping Zhang 









Review Article (14 pages), Article ID 6291889, Volume 2022 (2022)

Lysionotin Induces Ferroptosis to Suppress Development of Colorectal Cancer via Promoting Nrf2 Degradation

Zhuo Gao , Junnan Jiang , Lijian Hou , and Fujian Ji 

Research Article (18 pages), Article ID 1366957, Volume 2022 (2022)

Emerging Potential Therapeutic Targets of Ferroptosis in Skeletal Diseases

Xin Liu , Tianhao Wang , Wei Wang , Xiaolong Liang , Yating Mu , Yaozeng Xu , Jiexiang Bai , and Dechun Geng 

Review Article (19 pages), Article ID 3112388, Volume 2022 (2022)

Research Article

Ferroptosis-Related lncRNAs Act as Novel Prognostic Biomarkers in the Gastric Adenocarcinoma Microenvironment, Immunotherapy, and Chemotherapy

Yushi Zheng,¹ Shanshan Wu,² Xueshan Huang,² and Lianxiang Luo ^{3,4}

¹The First Clinical College, Guangdong Medical University, Zhanjiang, Guangdong 524023, China

²Department of Biology, School of Basic Medical Science, Guangdong Medical University, Zhanjiang, Guangdong 524023, China

³The Marine Biomedical Research Institute, Guangdong Medical University, Zhanjiang, Guangdong 524023, China

⁴The Marine Biomedical Research Institute of Guangdong Zhanjiang, Zhanjiang, Guangdong 524023, China

Correspondence should be addressed to Lianxiang Luo; luolianxiang321@gdmu.edu.cn

Received 11 August 2022; Revised 1 March 2023; Accepted 21 April 2023; Published 19 May 2023

Academic Editor: Xiao-Jie Lu

Copyright © 2023 Yushi Zheng et al. This is an open access article distributed under the Creative Commons Attribution License, which permits unrestricted use, distribution, and reproduction in any medium, provided the original work is properly cited.

Ferroptosis, a form of programmed cell death akin to necrosis, is managed by iron and is distinguished by lipid peroxidation. Gastric cancer is a highly aggressive form of cancer, responsible for the third highest number of cancer-related deaths globally. Despite this, the potential of ferroptosis to predict the occurrence of this cancer is yet to be determined. In this research, a comprehensive examination was conducted to explore the link between long noncoding RNAs (lncRNAs) and ferroptosis, in order to uncover an lncRNA signature that can predict drug susceptibility and tumor mutational burden (TMB) in gastric adenocarcinoma. We conducted an in-depth analysis of the GC immune microenvironment and immunotherapy, with a particular focus on ferroptosis-related lncRNA prognostic biomarkers, and further explored the correlation between these factors and prognosis, immune infiltration, single nucleotide variation (SNV), and drug sensitivity for gastric adenocarcinoma patients. Through our investigations, we have discovered five lncRNA signatures related to ferroptosis that can accurately forecast the prognosis of gastric adenocarcinoma patients and also regulate the proliferation, migration, and occurrence of ferroptosis in gastric adenocarcinoma cells. In conclusion, this lncRNA signature associated with ferroptosis may be employed as a prognostic indicator for gastric adenocarcinoma, thus presenting a potential solution.

1. Introduction

Gastric cancer (GC) is one of the five most commonly diagnosed diseases and the third leading cause of cancer-related fatalities across the globe, making it a major challenge for oncology [1]. Gastric adenocarcinomas (STAD) account for approximately 95% of all GC cases [2]. Most of the early symptoms of cancer are not evident, owing to the fact that the majority of patients are diagnosed at an advanced stage when the prognosis is poor, and the treatment options are limited [3]. Regrettably, the tumor markers most commonly used for the initial clinical diagnosis of GC have a low level of sensitivity and specificity [4, 5]. Consequently, more accurate biomarkers are urgently needed to reflect an individual's cancer risk and to develop new therapeutic strategies.

Generally, GC is a multifaceted condition, which involves a variety of genetic mutations, epigenetic modifications, chromosomal translocations, deletions, and amplifications. These can all be contributory to the genesis of the disorder. In contrast to mutations in or abnormal expression of protein-coding genes, epigenetic modifications, such as the overexpression or downregulation of long noncoding RNA (lncRNA), not only play a role in cancer initiation and progression [6]. Simultaneously, they can also display tumor-suppressive or oncogenic effects. Owing to the genome-wide expression patterns of lncRNAs in diverse tissues, they may be used as biomarkers and therapeutic targets for cancer [7]. Uncovering the key lncRNAs participating in GC progression is essential for comprehending the mechanisms at work.

Ferroptosis, a recently identified form of cell death, is caused by a massive lipid peroxidation process that requires iron, leading to damage of the cell membrane [8]. Ferroptosis, initially induced by the small molecule erastin, is primarily defined by the decrease of a cell's volume and the intensification of mitochondrial membrane density, without the usual signs of apoptosis and necrosis [9]. It has been established in prior research that lncRNAs are connected to a range of PCD phenomena, including apoptosis, autophagy, necroptosis, and ferroptosis. It has been observed that certain lncRNAs can function as competing endogenous RNA, thereby hindering oxidation and thus, ferroptosis; in contrast, some lncRNAs are known to induce autophagy. Research has indicated that examining the correlation between lncRNA and ferroptosis in various cancers, including GC and non-small cell lung cancer, has significant implications [10]. In order to explore the connections between ferroptosis, ferroptosis-related lncRNA, and gastric adenocarcinoma, a comprehensive evaluation is necessary.

The TME consists of several stromal cells that are necessary for cancer cells to flourish and propagate [11]. Accumulating evidence has indicated that gastric adenocarcinoma has a particular microenvironment that facilitates tumor progression and metastasis [12]. It is essential to conduct further research into the connection between the TME and gastric adenocarcinoma, as the exact mechanism of interaction is still unknown. Precision medicine and targeted therapies have been incorporated into medical oncology, leading to a transformation of the way cancer is treated [13]. Precision medicine has exposed significant heterogeneity in cancer pathways gone awry, and the employment of novel targeted therapies, especially immune checkpoint inhibitor therapies whose responsiveness is evaluated using a TIDE score, has been especially effective [14] and has shown even broader prospects in various cancer types [15]. Recently, immune checkpoint inhibitors (ICIs) have been put forward as a possible treatment option for gastric adenocarcinoma. Cytotoxic T lymphocyte-associated antigen-4 (CTLA-4) and programmed cell death protein 1 (PD-1), two immune checkpoints that control lymphocyte activation and balance immune responses, can shield tumor cells from the immune system [16].

Our study makes use of prognostic biomarkers of ferroptosis-related lncRNA to analyze the tumor-immune microenvironment and immunotherapy in a comprehensive manner. Five lncRNA signatures linked to ferroptosis were established, as well as a relevant nomogram. lncRNA signatures associated with ferroptosis have proved to be a reliable predictor of the prognosis of gastric adenocarcinoma patients. We have successfully created a prognostic model to examine the connection between prognosis, immune infiltration, SNV, and drug sensitivity of STAD patients.

2. Materials and Methods

2.1. Data Acquisition and Preprocess. The Cancer Genome Atlas (TCGA) database (<https://portal.gdc.cancer.gov/repository>) provided access to the RNA sequencing (HTSeq-Counts), simple nucleotide variation data, and clin-

ical information of 380 TCGA-STAD patients. Afterward, we transformed the count data into FPKM (fragments per kilobase of transcript sequence per millions of base pairs sequenced) in order to carry out the following analysis. The study encompassed 224 samples with comprehensive clinical information (Table 1). The FerrDb database was used to assemble a gene list comprising 291 ferroptosis-related genes (<http://www.zhounan.org/ferrdb>) [17] and the human gene database (Gene Cards) using the keyword “ferroptosis” (<https://www.genecards.org/>) [18]. Applying the “edgeR” package, a differential analysis was conducted, which yielded 18 ferroptosis-related differentially expressed genes (DEGs) in TCGA-STAD [19, 20]. False discovery rate (FDR) < 0.05 and $|\log_2 \text{fold change (FC)}| \geq 1$ are the statistical parameters for significance. Subsequently, the STRING database (<https://string-db.org/>) [21] was used to generate a protein-protein interaction network (PPI) of 18 ferroptosis-related genes and ran a Cytoscape plugin, CytoHubba [22], to accurately determine which genes served as hubs in the PPI network. Pearson's correlation analysis (with $|\text{Pearson } R| > 0.5$ and $p < 0.001$) was utilized to identify strong interactions between TCGA-STAD lncRNAs and ferroptosis-related genes, thus allowing the selection of ferroptosis-related lncRNAs. Through differential analysis, we identified 142 upregulated and 121 downregulated ferroptosis-related lncRNAs.

2.2. Establishment and Evaluation of a Ferroptosis-Related lncRNA Signature Prognosis Model. Utilizing the criteria stated above, we conducted an analysis of 200 patients with complete clinical information. A total of 200 patients were randomly divided into two groups: a training group of 100 and a test cohort of 100. The clinical characteristics of the training cohort and the test cohort were identical. Through the utilization of univariate and multivariate Cox regression analysis and the “survival” R package, lncRNA signatures pertinent to ferroptosis were determined [23] relevant to the prognosis of gastric adenocarcinoma patients. A prognostic risk model that is based on five ferroptosis-related lncRNAs was developed through multivariate Cox regression analysis, allowing the prediction of the prognosis of individuals suffering from gastric adenocarcinoma. The risk score was obtained by the following equation: Risk score = (exprgene1 × coefficientgene1) + ... + (exprgene5 × coefficientgene5). In order to validate the risk characteristic model in the data set, we computed the risk score for each patient with gastric adenocarcinoma in both the training and test sets. By taking into consideration the median value of the risk score, all samples were split into two categories—a high-risk group and a low-risk group—for the purpose of examining the prognosis of individuals suffering from gastric adenocarcinoma. To evaluate the overall survival (OS) of the two patient cohorts, a Kaplan-Meier analysis was performed. We selected the “survminer” R package to calculate the optimal cutoff expression. To evaluate the risk assessment model's independence from other clinical features, a multivariate Cox regression analysis was employed. The AUC analysis evaluated the effectiveness of the ferroptosis-related lncRNA

TABLE 1: The clinical characteristics of TCGA-STAD.

	Alive ($n = 173$)	Dead with tumor ($n = 47$)	Dead tumor free ($n = 4$)	Total ($n = 224$)	p value
Gender*					
Female	72 (41.6%)	9 (19.1%)	1 (25.0%)	82 (36.6%)	0.016
Male	101 (58.4%)	38 (80.9%)	3 (75.0%)	142 (63.4%)	
Age***					
>65	89 (51.4%)	33 (70.2%)	4 (100.0%)	126 (56.2%)	4.9e-20
≤65	84 (48.6%)	14 (29.8%)		98 (43.8%)	
AJCC stage**					
Stage I	33 (19.1%)	8 (17.0%)	1 (25.0%)	42 (18.8%)	0.002
Stage II	86 (49.7%)	7 (14.9%)	1 (25.0%)	94 (42.0%)	
Stage III	39 (22.5%)	19 (40.4%)	2 (50.0%)	60 (26.8%)	
Stage IV	15 (8.7%)	13 (27.7%)		28 (12.5%)	
T (tumor)					
T1	15 (8.7%)	1 (2.1%)		16 (7.1%)	0.151
T2	50 (28.9%)	11 (23.4%)	3 (75.0%)	64 (28.6%)	
T3	94 (54.3%)	29 (61.7%)	1 (25.0%)	124 (55.4%)	
T4	14 (8.1%)	6 (12.8%)		20 (8.9%)	
M (metastasis)***					
M0	164 (94.8%)	40 (85.1%)	4 (100.0%)	208 (92.9%)	7.4e-45
M1	9 (5.2%)	7 (14.9%)		16 (7.1%)	
N (lymph node)					
N1	74 (42.8%)	12 (25.5%)	1 (25.0%)	87 (38.8%)	0.249
N2	56 (32.4%)	11 (23.4%)	1 (25.0%)	68 (30.4%)	
N3	37 (21.4%)	14 (29.8%)	2 (50.0%)	53 (23.7%)	
N4	6 (3.5%)	10 (21.3%)		16 (7.1%)	

* $p < 0.05$, ** $p < 0.01$, *** $p < 0.001$.

and the validity of this risk model. The Kaplan–Meier analysis was employed to individually assess the five ferroptosis-related lncRNAs, in order to investigate the correlation between their expression and patient survival. Utilizing the “rms” R package, a nomogram was constructed based on risk score and independent clinical information, with calibration curves established for 3, 5, and 7 years.

2.3. Comprehensive Immunoassay. A comparison of immune cells between TCGA-STAD groups with high and low risk was conducted with the help of seven algorithms [TIMER [24], CIBERSORT [25, 26], CIBERSORT-ABS, QUANTISEQ [27], MCPOUNTER, XCELL [28], and EPIC [29]], and the results were visualized by “limma” and “heat map” R package. Applying the “GSVA” R package, single-sample gene set enrichment analysis (ssGSEA) was carried out to assess immune-related cells and pathways in each TCGA-STAD sample [30]. The sample’s immune infiltration result was found to be trustworthy, as the p value was below 0.05. Samples from the TCGA-STAD were assigned a stromal score, an immunological score, and an ESTIMATE score using the “estimate” R tool [31]. Furthermore, CIBERSORT was employed to illustrate the ratio of 22 different types of immune cells in the sample.

Using the TIDE algorithm (<http://tide.dfci.harvard.edu/>), to predict the response of each sample in the TCGA-STAD

cohort to anti-PD-1 and anti-CTLA4 immunotherapy, we calculated the TIDE scores for each sample. According to the official definition, immune checkpoint inhibitor therapy is considered to be nonresponsive if the TIDE score is higher than 0, while a TIDE score lower than 0 is indicative of a responsive therapy.

Subsequently, we formulated the immunotherapy score (IPS) by detecting the presence of immunosuppressive transmembrane proteins, PD-1 and CTLA4, on the surface of T cells in GC patients. The TCGA-STAD immunotherapy scoring file can be accessed from the TCIA website (<https://tcia.at/>). By dividing the expression of PD-1 and CTLA4 into four groups (PD-1 positive/CTLA4 negative, PD-1 negative/CTLA4 positive, PD-1 positive/CTLA4 positive, and PD-1 negative/CTLA4 negative), we aimed to investigate the immune prognostic signatures (IPS) in gastric adenocarcinoma between high- and low-risk groups. We further investigated the differences in PD-1, PD-L1, and CTLA4 levels between gastric adenocarcinoma and normal patients using the “ggpubr” and “ggplot2” R packages.

2.4. Gene Enrichment and Function Analysis Gene Set Enrichment Analysis (GSEA). An analysis of Gene Ontology (GO) and Kyoto Encyclopedia of Genes and Genomes (KEGG) pathways was conducted on mRNAs related to ferroptosis, which exhibited varying expression levels, in order

to gain insight into the mechanism that distinguishes between high- and low-risk groups of gastric adenocarcinomas. A potential gene set pathway was identified, with an FDR of less than 0.05. GSEA (version 4.0.3) was employed to assess the enrichment degree and statistical significance of a ferroptosis-related gene set between two groups [32]. This algorithm was used to explore the potential functions and pathways of the signature genes. It was determined that a 25% FDR and a nominal p value of less than 0.05 would be the threshold for significance.

2.5. Consensus Clustering Analysis and GSVA (Gene Set Variation Analysis) Analysis. Utilizing the “ConsensusClusterPlus” R package, we clustered the TCGA-STAD cohort into four groups based on the consensus expression of the lncRNAs associated with ferroptosis [33]. To achieve consensus clustering, 1000 k-means iterations were conducted, and 80% of the genes or samples were bootstrapped. Subsequently, the Kaplan–Meier statistics were applied to analyze the differences in OS across clusters. GSVA analysis revealed the activation status of genes related to ferroptosis and the associated biological pathways [34]. We graphically represented these biological processes using heatmaps, with red representing activation and blue representing inhibition.

2.6. The Ferroptosis Potential Index (FPI) Model. The functional profile index (FPI) is a metric for assessing the level of ferroptosis and its significance. ssGSEA was employed to calculate the gene set enrichment scores (ES) which either stimulate or inhibit ferroptosis. Analyses of gastric adenocarcinoma samples showed that a higher FPI score is usually associated with metastasis, medical characteristics, and drug responsiveness [35]. This model enabled us to evaluate the FPI value in each gastric adenocarcinoma sample, thereby uncovering the ferroptosis level of each patient.

2.7. Drug IC_{50} Prediction and Secondary Structure Prediction. We established the score of related immune cells by comparing the immune cells of high- and low-risk groups. The Genomics of Drug Sensitivity in Cancer (GDSC) database provides an extensive list of drugs (<https://www.cancerrxgene.org/>) [36]. Utilizing the PRRophetic algorithm, we established a ridge regression model. The “PRRophetic” R package was utilized to forecast the IC_{50} values of high- and low-risk groups in TCGA-STAD [37]. Twelve antitumor drugs were evaluated, and the IC_{50} values between the two groups varied significantly. A drug with a lower IC_{50} was found to be more effective in inhibiting cancer cells. Additionally, we investigated the steadiness of lncRNA structure on the lncAR database (<https://lncar.renlab.org/website>), acquiring the secondary structure of LINC00460 and miR205HG [38]. The stability of the lncRNA secondary structure is indicative of the structure and purpose of RNA. LINC00460 and miR205HG were acquired showing a comparatively consistent secondary structure.

2.8. Gene Mutation and m6A RNA Methylation Regulator. A comprehensive analysis of gene mutation was conducted using the maftools R package, and gastric adenocarcinomas

were divided into high- and low-risk groups. Additionally, mutations of ferroptosis-related mRNAs were also evaluated. We conducted a Pearson analysis to investigate the correlation between CDKN2A and the five related lncRNAs, given that the mutation pathway of cyclin-dependent kinase inhibitor 2A (CDKN2A) in gastric adenocarcinoma was the most significant. We obtained the mutation maf file of each gastric adenocarcinoma patient from the TCGA database, which enabled us to calculate the TMB score of each patient. By analyzing the mutations of gastric adenocarcinoma and based on the median score, we divided the samples into high- and low-mutation groups. We employed the “reshape2” and “limma” R packages to analyze the expression of m6A RNA methylation regulators between the high- and low-risk groups.

2.9. Statistical Analysis. The data processing for this study was done using R software (version 4.0.3; <https://www.R-project.org>). The decision curve analysis (DCA) and operating characteristic curve (ROC) were employed to investigate the sensitivity, specificity, and accuracy of the prognostic features of STAD by leveraging “timeROC” and “ggDCA” packages, respectively. This was done in comparison to other clinicopathological characteristics. Utilizing the Kaplan–Meier survival analysis, the overall survival of STAD patients was evaluated in terms of the ferroptosis-related lncRNA signatures. All analyses yielded a p value of less than 0.05, indicating a statistically significant difference.

3. Results

3.1. Identification of Ferroptosis-Related Differentially Expressed mRNAs and lncRNAs and Construction of a PPI Network. As depicted in Figure 1, we combined data from TCGA, FerrDb, and Gene Card databases to construct gene matrices associated with ferroptosis. We utilized the “edgR” package to conduct a differential analysis of 18 ferroptosis-related genes with significant differential expression in gastric adenocarcinoma, resulting in 12 upregulated genes (ALB, ALOX15, GDF15, CDKN2A, HELLS, MIOX, TRIB3, AURKA, NOX1, CP, NOS2, and MYB) and 6 downregulated genes (ANGPTL7, PLIN4, ALOX12, TP63, HBA1, and AKR1C1) (Figures 2(a) and 2(b)). To identify lncRNAs associated with ferroptosis, a Pearson correlation analysis (with Pearson $R > 0.5$ and $p < 0.001$) was performed, resulting in 142 upregulated and 121 downregulated ferroptosis-related lncRNAs (Figures 2(c) and 2(d)). The correlation between ferroptosis genes and lncRNAs was depicted in Figure 2(e), and a PPI network in the STRING database showed the relationship between 18 nodes and 11 edges (Figure 2(f)). In addition, 12 hub genes were further pinpointed by the CytoHubba application (Figure 2(g)).

3.2. Establishment of Ferroptosis-Related lncRNA Prognostic Signature. We conducted a screening of 200 TCGA-STAD samples with complete clinical information and randomly allocated them into two groups, with 100 samples in each group for training and testing purposes (as depicted in Figures 3(a) and 3(b)). The samples were divided into two

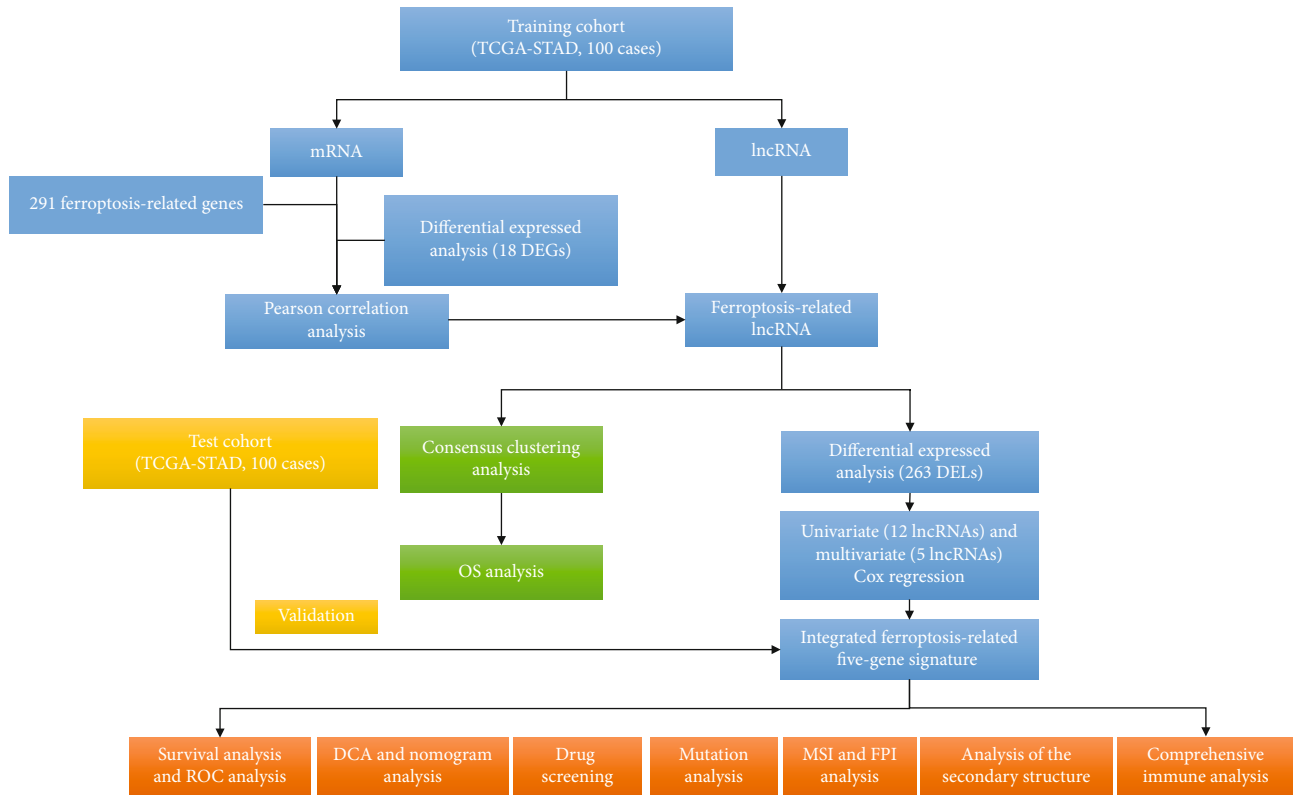


FIGURE 1: A flow chart of overall study design.

groups, a high-risk group and a low-risk group, based on the median value of the risk score, in order to assess the prognosis of gastric adenocarcinoma patients. The risk score and survival status distribution are illustrated in Figures 3(c)–3(f). Survival analysis revealed that the high-risk group had a worse survival rate in the training set ($p = 0.003$) and test set ($p = 0.002$) (Figures 3(g) and 3(h)). To gauge whether the ferroptosis-related lncRNA signature acted as an independent prognostic factor in STAD patients, univariate and multivariate Cox regression analyses were employed, taking into account TIDE, TNM, stage, risk score, gender, age, and FPI (Figures 3(i)–3(l)). The results of the study confirmed that the risk score was a significant prognostic factor ($p < 0.001$). Univariate Cox regression analysis identified 12 ferroptosis-related lncRNAs (RP11-186F10.2, RP4-781 K5.5, LINC01537, LINC00601, AC103563.8, AC103563.9, RP11-1143G9.5, LINC00460, RP11-64B16.4, LINC00454, KB-68A7.1, and miR205HG) as having a strong association with the prognosis of gastric adenocarcinoma patients, as determined by the “survival” R package. Multivariate Cox regression analysis was used to screen for biomarkers in relation to the prognosis of patients, and 5 ferroptosis-related lncRNAs (RP11-1143G9.5, AC103563.8, LINC00460, RP11-186F10.2, and miR205HG) were selected (Figures 4(a) and 4(b), Supplementary Table 1 and Supplementary Table 2). Additionally, a ferroptosis-related lncRNA signature and the clinical features associated with this signature were evaluated and constructed, including TMB, TIDE, FPI, TNM stage, stage, age, gender, immune score, cluster, and risk (Figure 4(c)). A prognostic model of gastric

adenocarcinoma was established with these five ferroptosis-related lncRNAs. We then established a prognostic risk score for the 5 ferroptosis-related lncRNAs, and the risk score was equal to the following: (expression value of RP11-1143G9.5 $\times (-0.423917081201679)$) + (expression value of AC103563.8 $\times 1.2071928010986$) + (expression value of LINC00460 $\times 0.40956647259787$) + (expression value of RP11-186F10.2 $\times 1.07891999972853$) + (expression value of miR205HG $\times (-0.366418490206812)$).

3.3. Validation of the Ferroptosis-Related lncRNA Signature. A nomogram was created to assess the precision and dependability of the prognostic model, incorporating clinical characteristics such as age, tumor (T) status, metastasis (M) status, risk score, stage, and risk, as well as 1-, 3-, and 5-year calibration curves (see Figures S1A and S1B). Results from the examination of the relationship between microsatellite instability and risk score demonstrated that microsatellite stability (MSS) had a more significant influence on the high-score group (70%) than on the low-score group (62%), as shown in Figure S1C and S1D. Figure S1E–G displays the DCA curves of 3, 5, and 7 years. The DCA curves demonstrated that the features associated with the ferroptosis-related lncRNA signature had a superior predictive value. The Kaplan–Meier curves of the five ferroptosis-related lncRNAs (AC103563.8, LINC00460, miR205HG, RP11-186F10.2, and RP11-1143G9.5) between the high- and low-risk groups are shown in Figure S2A–E. Except for RP11-1143G9.5, the OS of the other four genes (AC103563.8, LINC00460, miR205HG, and RP11-186F10.2) in the high-risk group was significantly

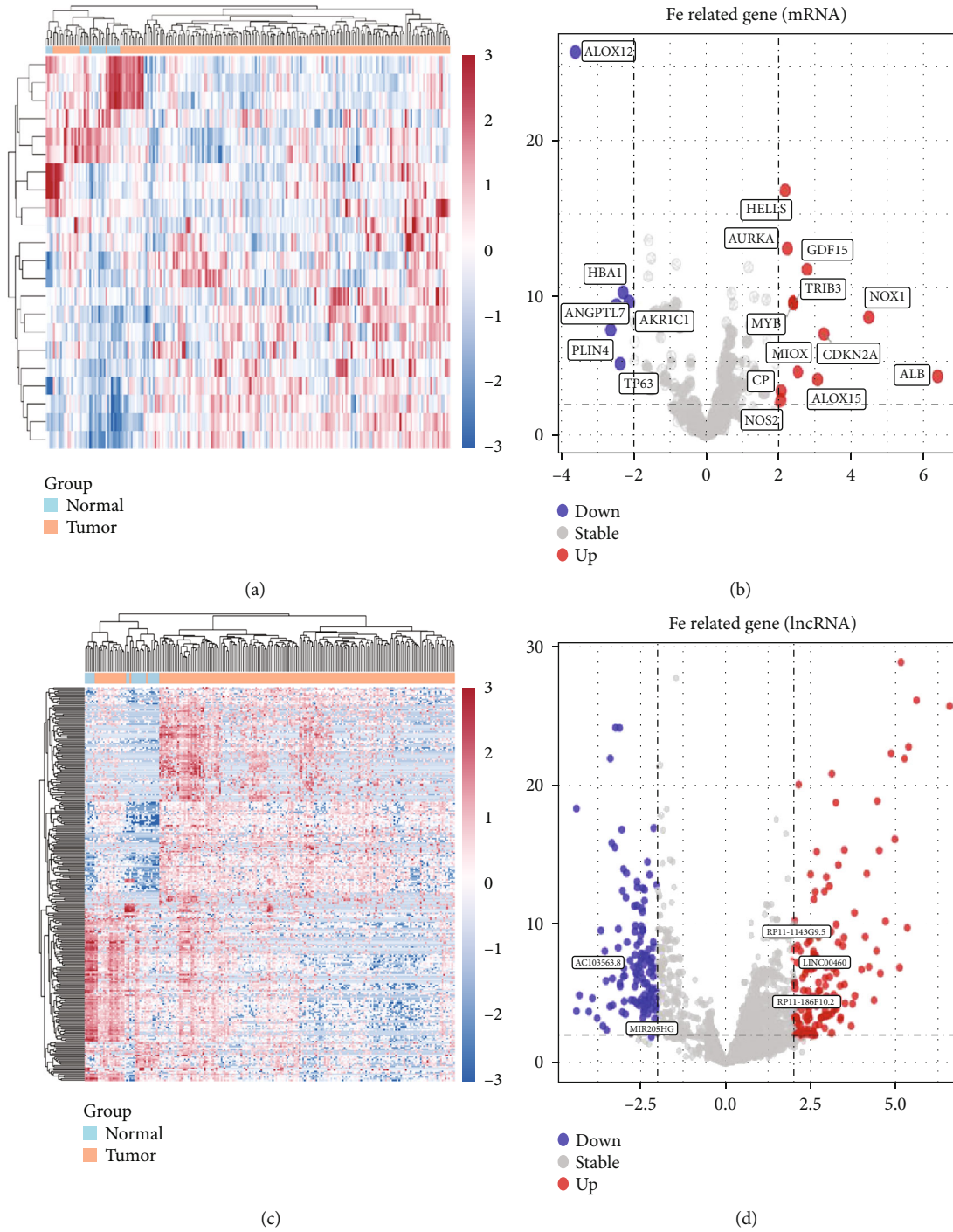


FIGURE 2: Continued.

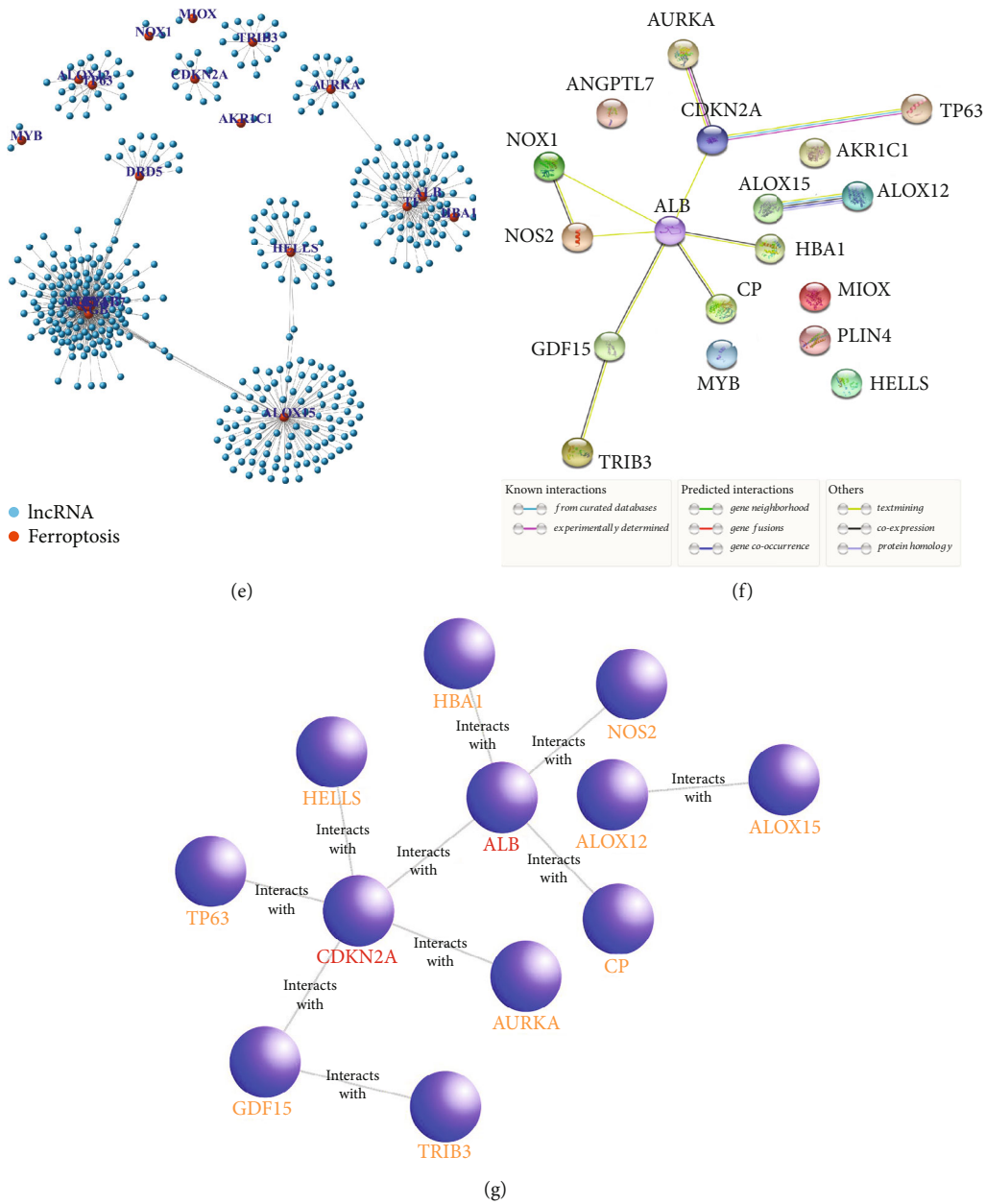


FIGURE 2: Screening of differentially expressed ferroptosis-related lncRNAs in gastric adenocarcinoma. (a) Heatmap of ferroptosis-related mRNA expression in gastric adenocarcinoma and normal tissues. (b) Volcano plot manifesting differentially expressed genes (DEGs) in ferroptosis-related mRNAs. (c) Heatmap of ferroptosis-related lncRNA expression in gastric adenocarcinoma and normal tissues. (d) Volcano plot manifesting DEGs in ferroptosis-related lncRNA. (e) The correlated network between 263 ferroptosis-related lncRNAs and 18 mRNAs. (f) Differentially expressed ferroptosis-related genes in PPI. (g) The selected 12 hub genes of ferroptosis-related genes via Cytoscape.

lower than that in the low-risk group. Additionally, we explored the expression of these five ferroptosis-related lncRNAs in various tissues and organs (Figure S3A–E). Among them, RP11-1143G9.5, RP11-186F10.2, and AC103563.8 were expressed in gastric tissues. It is worth mentioning that AC103563.8 and RP11-1143G9.5 were highly expressed in gastric tissues compared with other tissues and organs. The ROC curves of 3, 5, and 7 years reflected the advantage of the model, which included all sets (3 years, $AUC = 0.754$; 5 years, $AUC = 0.707$; 7 years, $AUC = 0.797$), training set (3 years,

$AUC = 0.874$; 5 years, $AUC = 0.786$; 7 years, $AUC = 0.786$) and test set (3 years, $AUC = 0.753$; 5 years, $AUC = 0.682$; 7 years, $AUC = 0.737$) (Figure S4A–I).

3.4. Gene Enrichment and Function Analysis. We further investigated the biological functions of DEGs by utilizing the “clusterProfiler,” “org.Hs.eg.db,” and “enrichplot” R packages for GO annotation and KEGG pathway analysis. The p filter and p adjust filter had a value of less than 0.05, respectively. This study conducted GO pathway and process

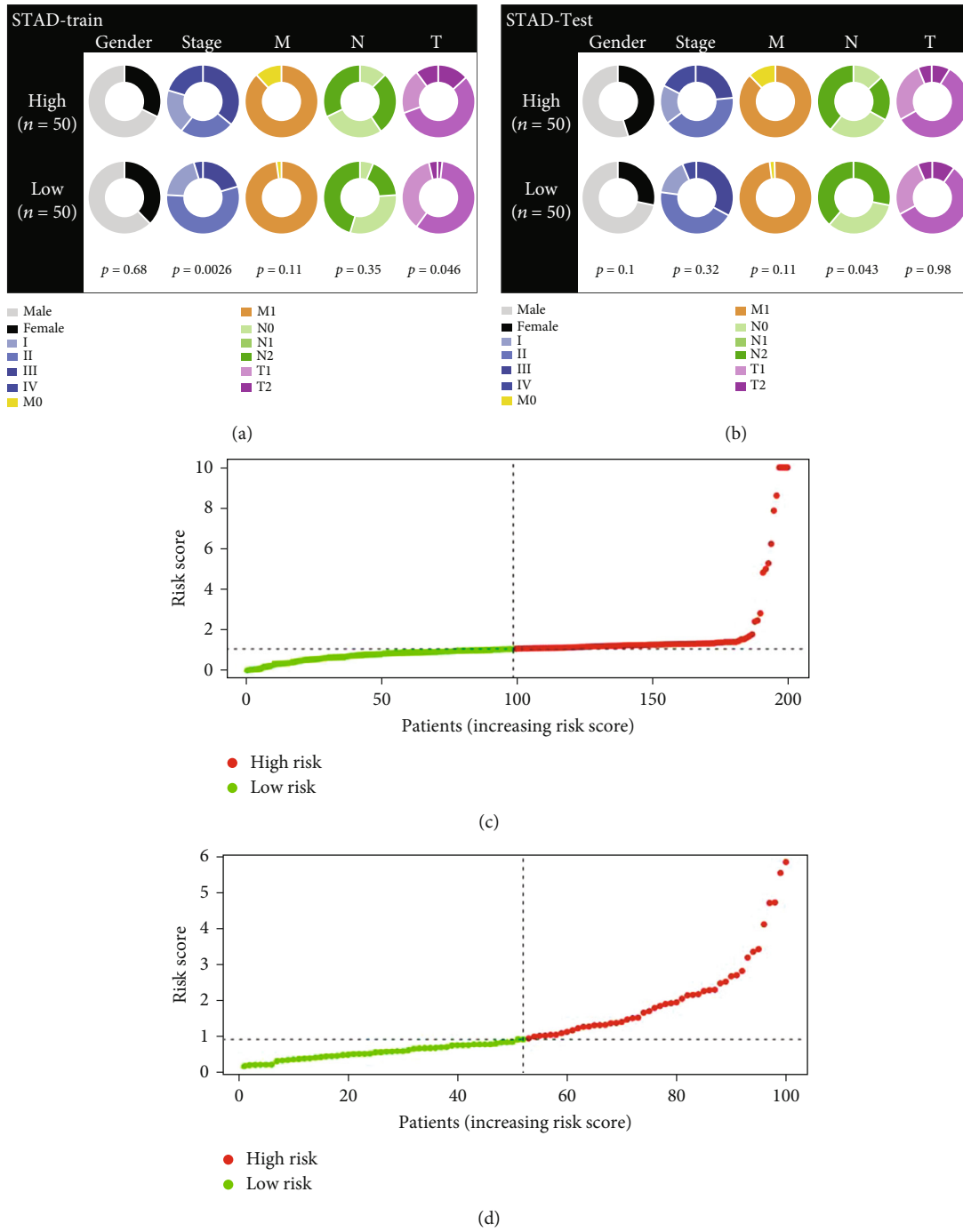


FIGURE 3: Continued.

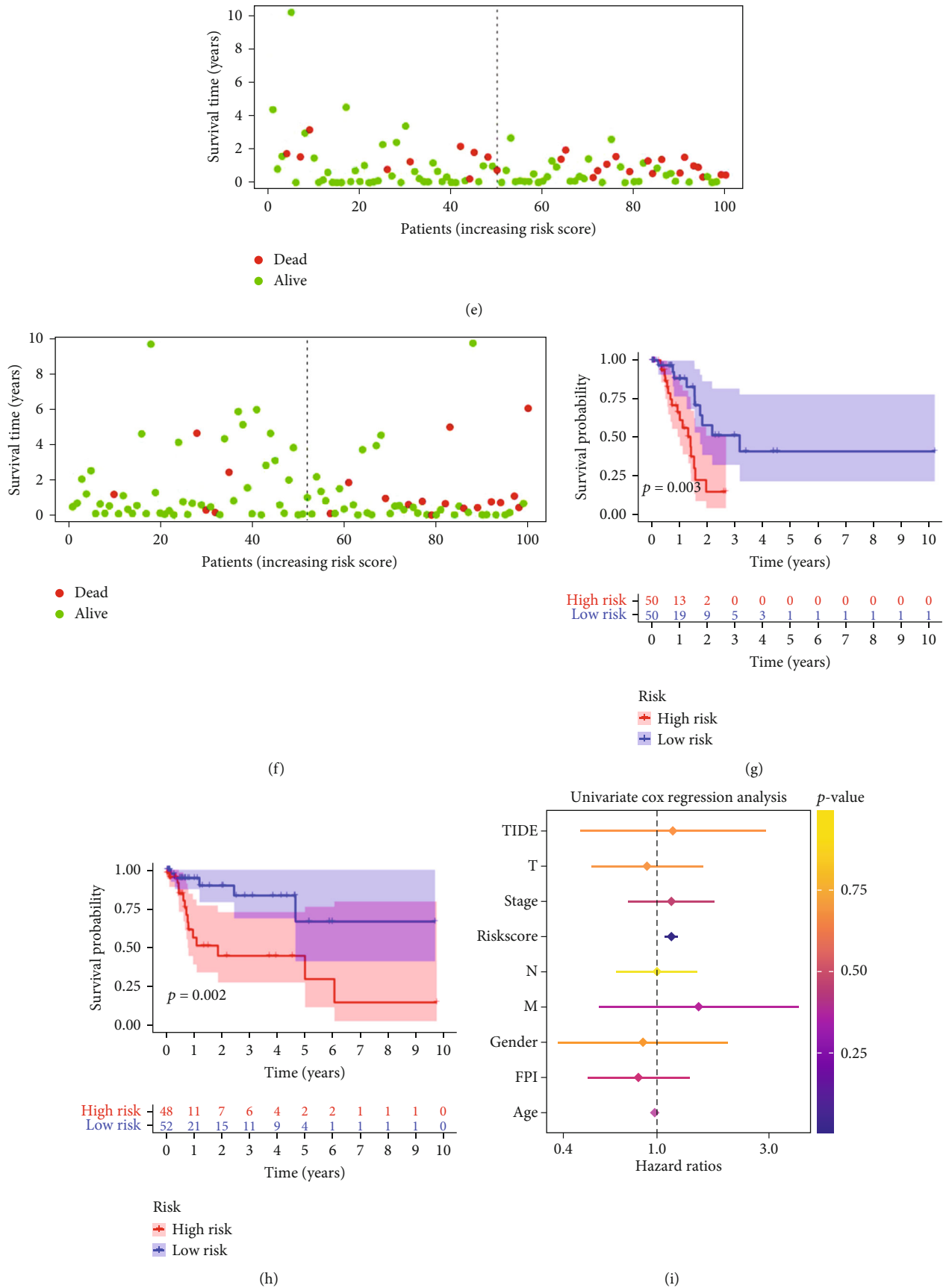


FIGURE 3: Continued.

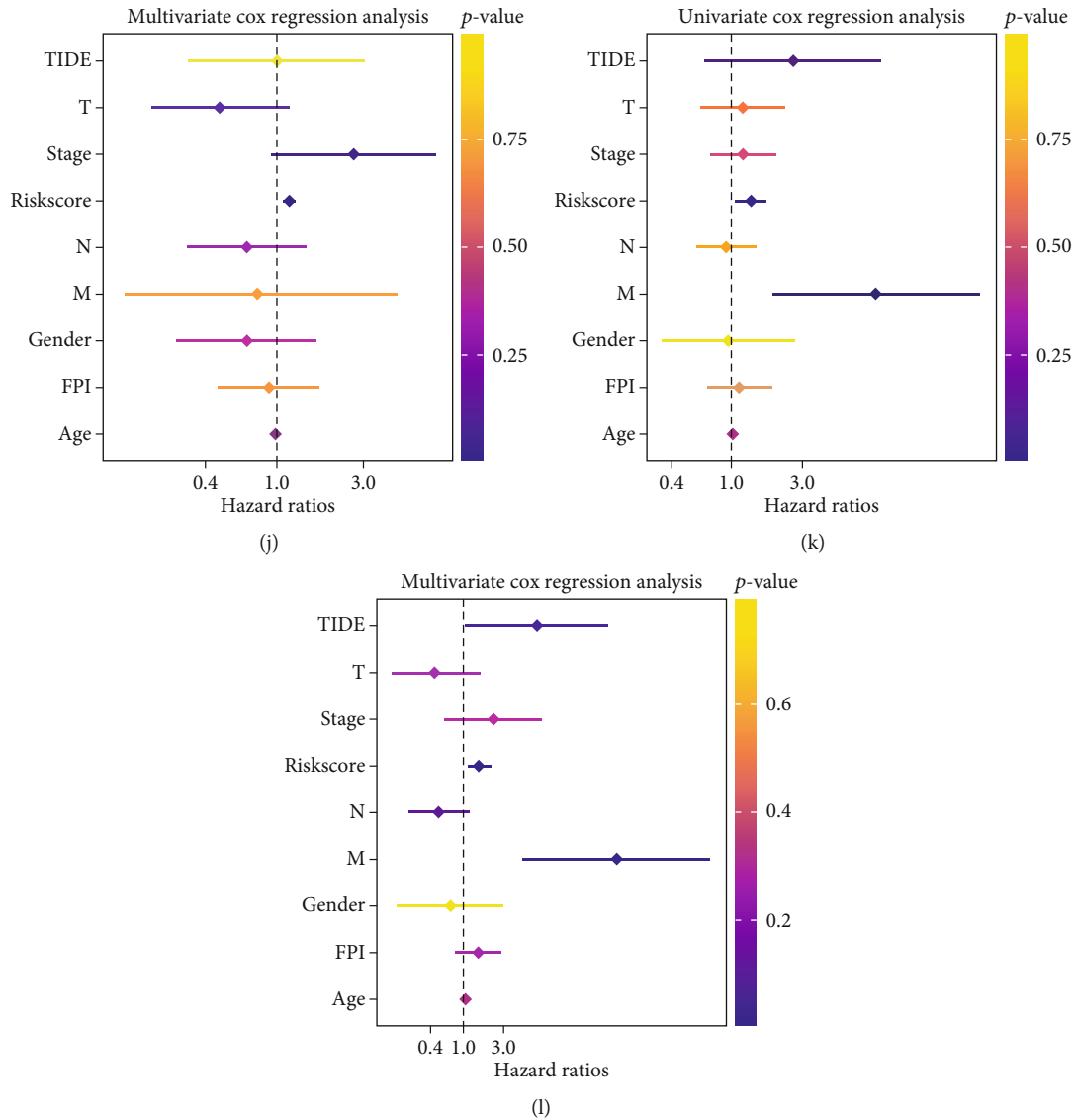
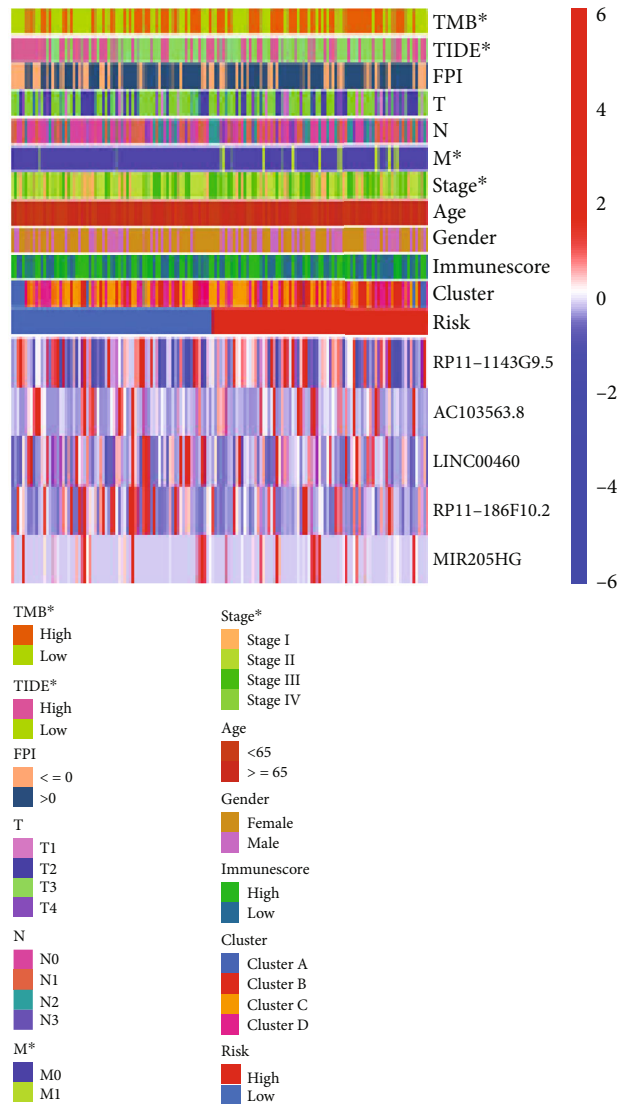
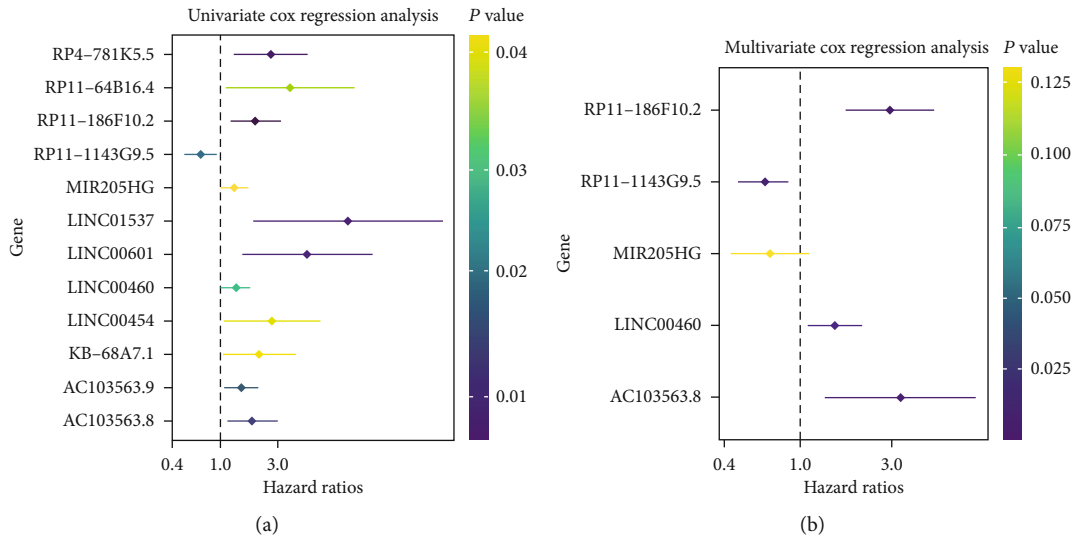


FIGURE 3: Construction and evaluation of a ferroptosis-related lncRNA prognostic signature in training and test sets. (a, b) Clinical characteristics of gastric adenocarcinoma patients in TCGA training and test sets. (c–f) Distribution of risk score, survival status, and (g–h) OS Kaplan–Meier curves (training cohort: $p = 0.003$, test cohort: $p = 0.002$) of STAD patients in TCGA training and test cohorts. (i–l) The independence of the ferroptosis-related lncRNA signature in OS was verified by univariate and multivariate Cox regression analysis in TCGA training cohort.

enrichment analysis, which included molecular function (functional set), biological process (pathway), and cellular component (structural complex). The top 21 clusters and their representative enrichment terms are shown in Figures 4(d) and 4(e). The consequence of GO functional annotation demonstrated that the biological processes related to oxygen metabolism were significantly correlated with the differential expression of ferroptosis-related genes, including GO:0006801 (superoxide metabolic process), GO:0019372 (lipoxygenase pathway), GO:0072593 (reactive oxygen species metabolic process), GO:0016701 (oxidoreductase activity, acting on single donors with incorporation of molecular oxygen), GO:0016651 (oxidoreductase activity, acting on NAD(P)H), GO:0016702 (oxidoreductase activity,

acting on single donors with incorporation of molecular oxygen, incorporation of two atoms of oxygen), GO:0019825 (oxygen-binding activity), and GO:0016709 (oxidoreductase activity, acting on paired donors, with incorporation or reduction of molecular oxygen, NAD(P)H as one donor, and incorporation of one atom of oxygen). In addition, the ferroptosis-related genes were also related to cell proliferation, such as GO:0048661 (positive regulation of smooth muscle cell proliferation). KEGG pathway enrichment analysis showed that the ferroptosis pathway was significantly enriched (Figure 4(f)), which mechanism and regulation of intracellular Fe^{2+} as shown in Figure S5A and S5B. GSEA for the ferroptosis-associated lncRNA signature demonstrated that gene silencing, negative regulation of gene expression, and



(c)

FIGURE 4: Continued.

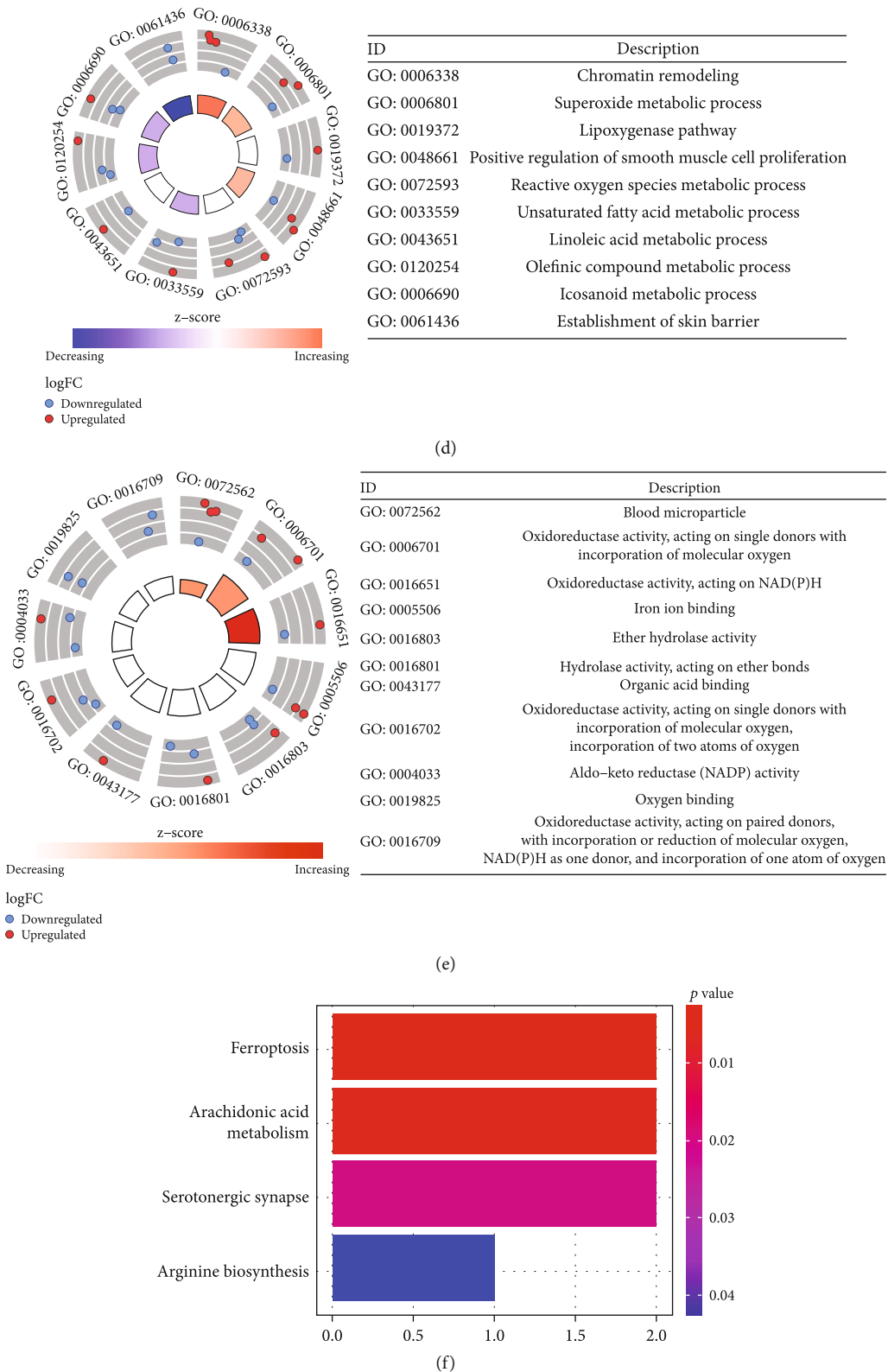


FIGURE 4: Screening of candidate genes and functional enrichment analysis. (a) Selection of ferroptosis-related lncRNAs related to prognosis by univariate Cox regression analysis. (b) Five ferroptosis-related lncRNAs correlated to the prognosis of gastric adenocarcinoma were obtained by multivariate Cox regression analysis. (c) Expression in different clinical characteristics (including TMB, TIDE, FPI, TNM stage, stage, age, gender, immune score, cluster, and risk) of five ferroptosis-related lncRNAs in gastric adenocarcinoma. (d, e) Gene Ontology (GO) analysis. (f) Kyoto Encyclopedia of Genes and Genomes (KEGG) pathway analysis.

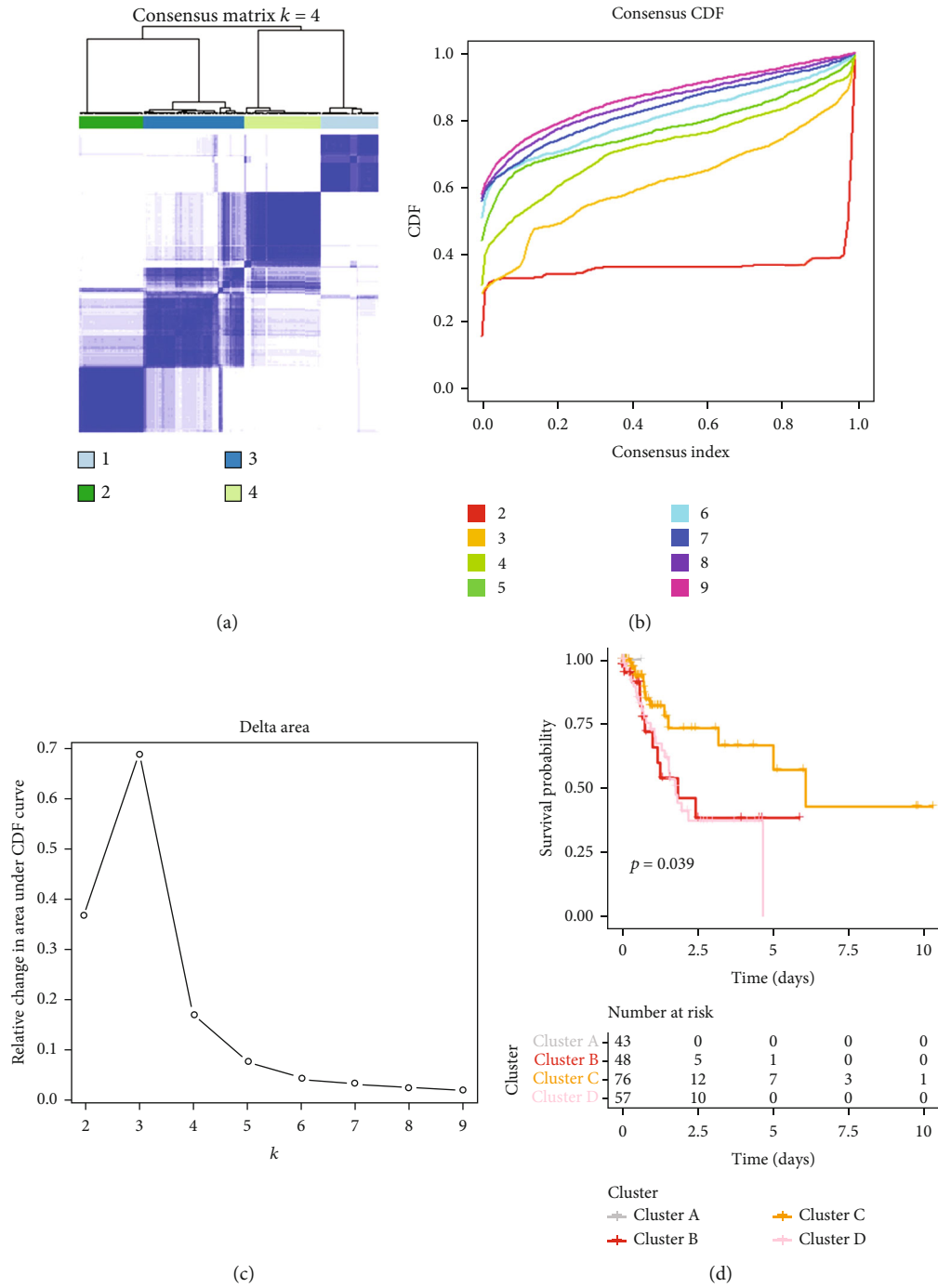


FIGURE 5: Continued.

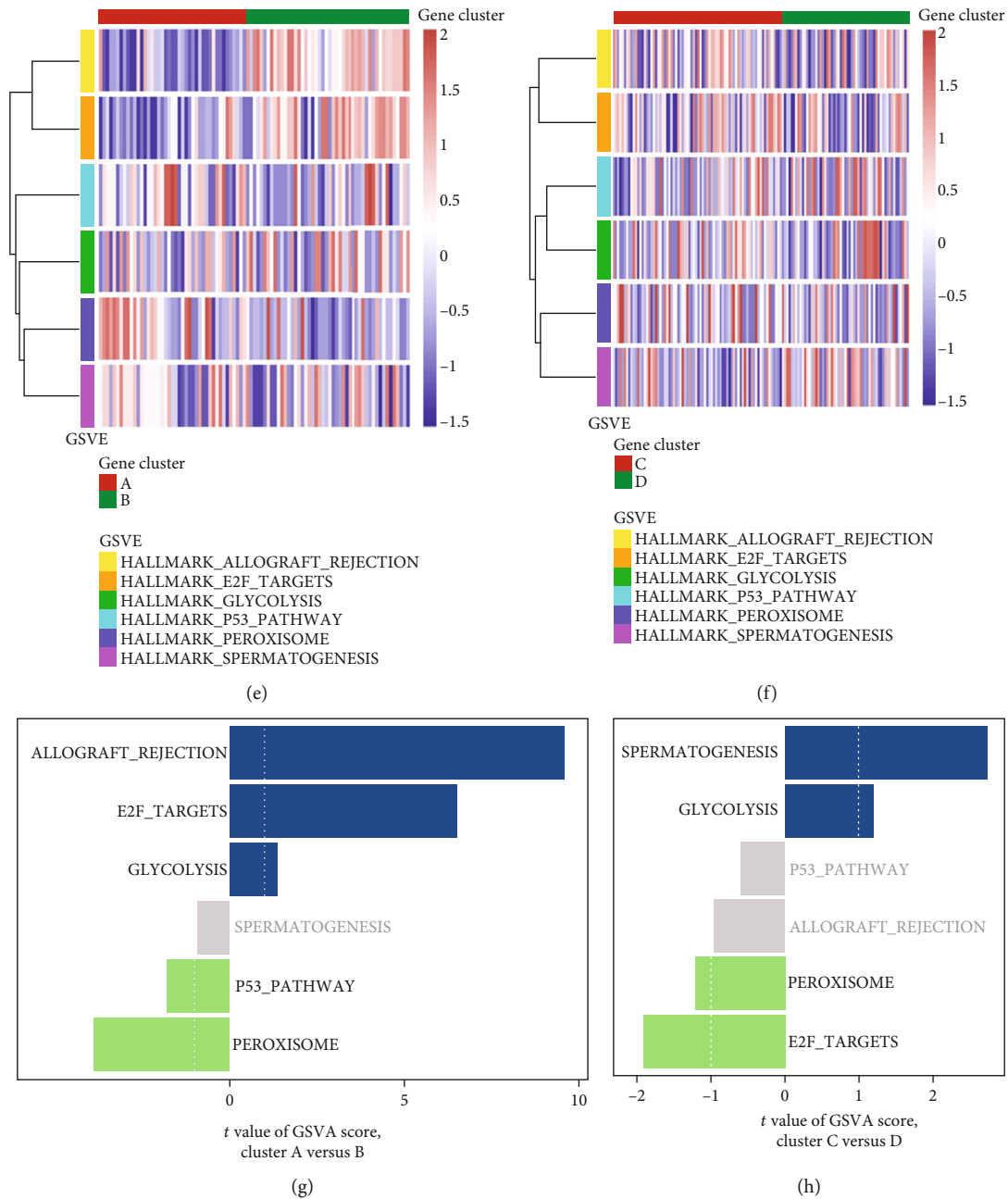


FIGURE 5: The OS of STAD in the cluster A/B/C/D subgroups and GSVA enrichment analysis. (a) Consensus clustering matrix for $k=4$. (b, c) When $k=2-9$, the consensus clustering cumulative distribution function (CDF) and relative change of the area under the CDF curve. (d) Kaplan-Meier curves of the overall survival for patients with STAD in four clusters (cluster A/B/C/D). (e-h) GSVA enrichment analysis showed the activation status of ferroptosis-related genes and related biological pathways. Heatmaps are used to visualize these biological processes, with red indicating activation pathways and blue indicating inhibition pathways. The GC cohort was annotated as a sample. (e, g) Cluster A vs. cluster B. (f, h) Cluster C vs. cluster D.

posttranscriptional regulation of gene expression were significantly enriched in high-risk groups of gastric adenocarcinoma samples (Figure S5C-G).

3.5. Consensus Clustering Analysis of Ferroptosis-Related lncRNAs and GSVA Analysis. The “ConsensusClusterPlus” R package was used to cluster the ferroptosis-related lncRNAs into four clusters, and the crossover between STAD samples was found to be the lowest in this case (Figures 5(a)-

5(c)). Consequently, we divided the samples into four clusters (A/B/C/D). Compared with other clusters, the Kaplan-Meier algorithm found that the patients in cluster C had a better OS than the patients in cluster A (Figure 5(d)). GSVA enrichment analysis showed the activation status of ferroptosis-related genes and related biological pathways. As shown in Figures 5(e) and 5(f), ferroptosis-related genes were enriched in allograft rejection, E2F targets, glycolysis, p53 pathway, peroxisome, and spermatogenesis. Comparing

the enrichment of cluster A and cluster B, the results demonstrated allograft rejection and 8E2F significant enrichment in cluster A, and cluster A was negatively regulated relative to cluster B in the p53 pathway (Figure 5(g)). A comparison between cluster C and cluster D revealed that cluster C had a higher presence of peroxisome and E2F target, as illustrated in Figure 5(h).

3.6. Comprehensive Immunoassay of Immune Infiltration, Immune Checkpoints, and Immunotherapy Response. To gain a better comprehension of the relationship between risk scores and immune cells, we conducted an analysis of immune cells between the high- and low-risk groups of TCGA-STAD, utilizing seven algorithms. The heatmap plot presented the expression of immune cells in both the high- and low-risk groups, as well as various clinical features (Figure 6(a)). Cancer-associated fibroblasts, hematopoietic stem cells, stroma score, B cells, T cell CD4+ memory, T cell CD4+ effector memory, CD8+ T cells, and T cell CD8+ central memory were all significantly expressed in the high-risk group, with p values of less than 0.01, 0.001, 0.05, 0.05, 0.05, 0.05, and 0.01, respectively. Tumor tissues exhibited a notable rise in the expression of T follicular helper cells, resting NK cells, and resting mast cells (Figure 6(b)). Correlation analysis was used to show the interaction among immune cells, risk score, and TMB. The results demonstrated that T cells, endothelial cells, and myeloid dendritic cells had positive and negative regulatory relationships with a risk score and TMB. As depicted in Figure 6(c), red was indicative of a positive correlation, whereas green was indicative of a negative correlation. The ESTIMATE score displayed an inverse correlation with tumor purity, as demonstrated in Figure S6A. In addition, we analyzed the score of connected immune cells and immune-related pathways in the high- and low-risk groups (Figure S6B). The proportion of 22 immune cells in gastric adenocarcinoma samples was manifested by heatmap and box plot based on the CIBERSORT algorithm (Figure S6C and 6E). We analyzed the expression levels of 23 regulatory factors linked to m6A between high- and low-risk groups. It was noteworthy that the expression of FTO (alpha-ketoglutarate dependent dioxygenase) ($p < 0.01$), IGFBP3 (insulin-like growth factor-binding protein 3) ($p < 0.05$), and VIRMA ($p < 0.05$) in the high-risk group was higher than that in low-risk group (Figure S6D). Immunotherapy scores were constructed by the expression of PD-1 and CTLA4 in T cells of patients with gastric adenocarcinoma. IPS was evaluated with four groups, including PD-1 negative CTLA4 negative (Figure 7(a)), PD-1 positive CTLA4 negative (Figure 7(b)), PD-1 negative CTLA4 positive (Figure 7(c)), and PD-1 positive CTLA4 positive (Figure 7(d)). The data revealed that the high-risk group had poorer scores than the low-risk group, signifying that their immunotherapy was not as effective. The scoring file of TCGA-STAD immunotherapy was downloaded from the TCIA database. The expression of PD-1, PD-L1, and CTLA4 between tumor tissue and normal tissue was also explored via the “limma” R package. The box plot indicated that expression of PD-1 (Figure 7(e)), PD-L1 (Figure 7(f)), and CTLA4 (Figure 7(g)) in tumor tissues was notably higher

than in normal tissues. PD-1 inhibited T cell activation and induced T cell death by binding with PD-L1 (or PD-L2), playing a paramount role in tumor immunotherapy. It demonstrated that the tumor immune escape ability of the high-risk group was stronger than that of the low-risk group. The high-risk group was more likely to respond to anti-CTLA4 immunotherapy, as indicated by a nominal p value of 0.007, and its Bonferroni-corrected p value was lower than that in other cases (Figure 8(a)). The data from Figure 8(b) indicates that the ICIs connected to the research were expressed in greater amounts in the high-risk group than in the low-risk group.

3.7. Prediction of Antitumor Drug and Secondary Structure, Immunotherapy Scores (IPS), Ferroptosis Potential Index (FPI), and Mutation Analysis. As shown in Figures 8(c) and 8(e), LINC00460 (MFE = -273.3 kcal/mol) and miR205HG (MFE = -1109.3 kcal/mol) both showed stable secondary structure, reflecting the function of RNA transcription. We established a Ridge regression model for forecasting the IC_{50} of drugs. The p value of all 12 drugs (ABT.263, AMG.706 (motesanib), AP.24534, CCT007093, DMOG, imatinib, JNJ.26854165, JNK inhibitor VIII, KIN001.135 (benzimidazole-thiophene carbonitrile), lenalidomide, and nilotinib, AKT inhibitor VIII.) were less than 0.05 (Supplementary Table 3). Figure 8(d) demonstrated that the IC_{50} value for the high-risk group was greater than that for the low-risk group, demonstrating enhanced antitumor effectiveness. To gain a better understanding of the role of ferroptosis-related lncRNAs in gastric adenocarcinoma, the secondary structure of the five lncRNA biomarkers was determined using the lncCAR database. We defined an FPI less than or equal to 0 as the low-score group and an FPI greater than 0 as the high-score group. After removing meaningless samples, we included 198 gastric adenocarcinoma samples and divided them into four groups, including (A) “FPI < 0 high-risk” group, (B) “FPI < 0 low-risk” group, (C) “FPI > 0 high-risk” group, and (D) “FPI > 0 low-risk” group (Figure S7A). The Kaplan–Meier analysis concluded that the (D) “FPI > 0 low-risk” group had the best OS, and “FPI < 0 low-risk” (B) had the worst OS. The findings of the study suggested that a high FPI score can reduce the risk of gastric cancer. A total of 198 cases of gastric adenocarcinoma were studied, out of which 122 had an FPI score greater than 0 (Figure S7B), and 76 had an FPI score less than 0 (Figure S7C). The Kaplan–Meier analysis showed that the patients with an FPI score greater than 0 had a worse survival rate in the high-risk group ($p = 0.0328$). Moreover, the high and low FPI scores were evaluated in the context of MSI (microsatellite instability) analysis. Figures S7D and S7E illustrate that the high-risk group, as determined by their FPI score, had a greater prevalence of MSI-H (17%) than the low-risk group (15%). Tumor tissues had a considerably greater FPI than normal tissues ($p = 8.3e - 17$), as illustrated in Figure S7F. In order to explore the mutations of ferroptosis-related genes in STAD, a mutation panorama of STAD genes was analyzed between the high-risk group and low-risk group (Figures 9(a) and 9(b)). TTN, TP53, MUC16, SYNE1, and



(a)

FIGURE 6: Continued.

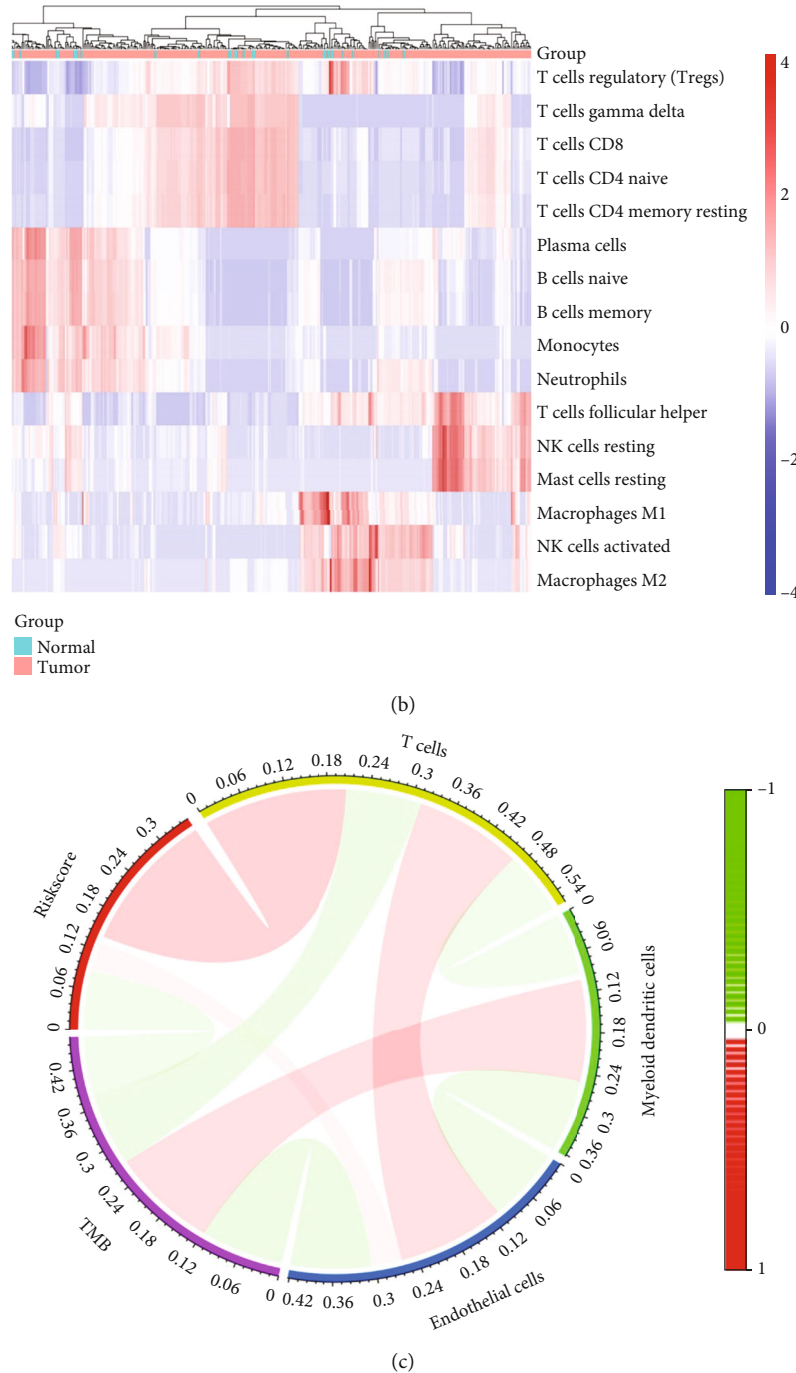


FIGURE 6: The results of immune cell infiltration were verified based on seven different algorithms. (a) A heatmap based on seven different algorithms (TIMER, CIBERSORT, CIBERSORT-ABS, QUANTISEQ, MCPOUNTER, XCELL, and EPIC) of the immune infiltration of gastric adenocarcinoma patients with different clinical characteristics in TCGA. (b) The heatmap shows the expression of 16 types of immune cells in tumor and normal tissues. (c) Correlation of T cells, endothelial cells, and myeloid dendritic cells with TMB and risk score. Red represents positive correlation, and green represents negative correlation.

LRP1B were found to be highly mutated in both the high-risk and low-risk groups. The highest mutation rate of ferroptosis-related genes in gastric adenocarcinoma samples was CDKN2A (Figure 9(c)). The results demonstrated that there was a significant correlation between CDKN2A and LINC0046 ($R > 0.1$, $p < 0.05$). The $C > T$ occurred frequently in single nucleotide variation (SNV) (Figures 9(d)

and 9(e)). The Pearson analysis was performed between CDKN2A and five ferroptosis-related lncRNA biomarkers (Figure 9(f)). RTK-RAS, Hippo, and TP53 pathways were vulnerable to STAD gene mutations (Figure S8A). The erb-b2 receptor tyrosine kinase 4 (ERBB4) showed a high mutation state in the RTK-RAS pathway (Figure S8B). Notably, CUL3 was the most highly mutated gene in the

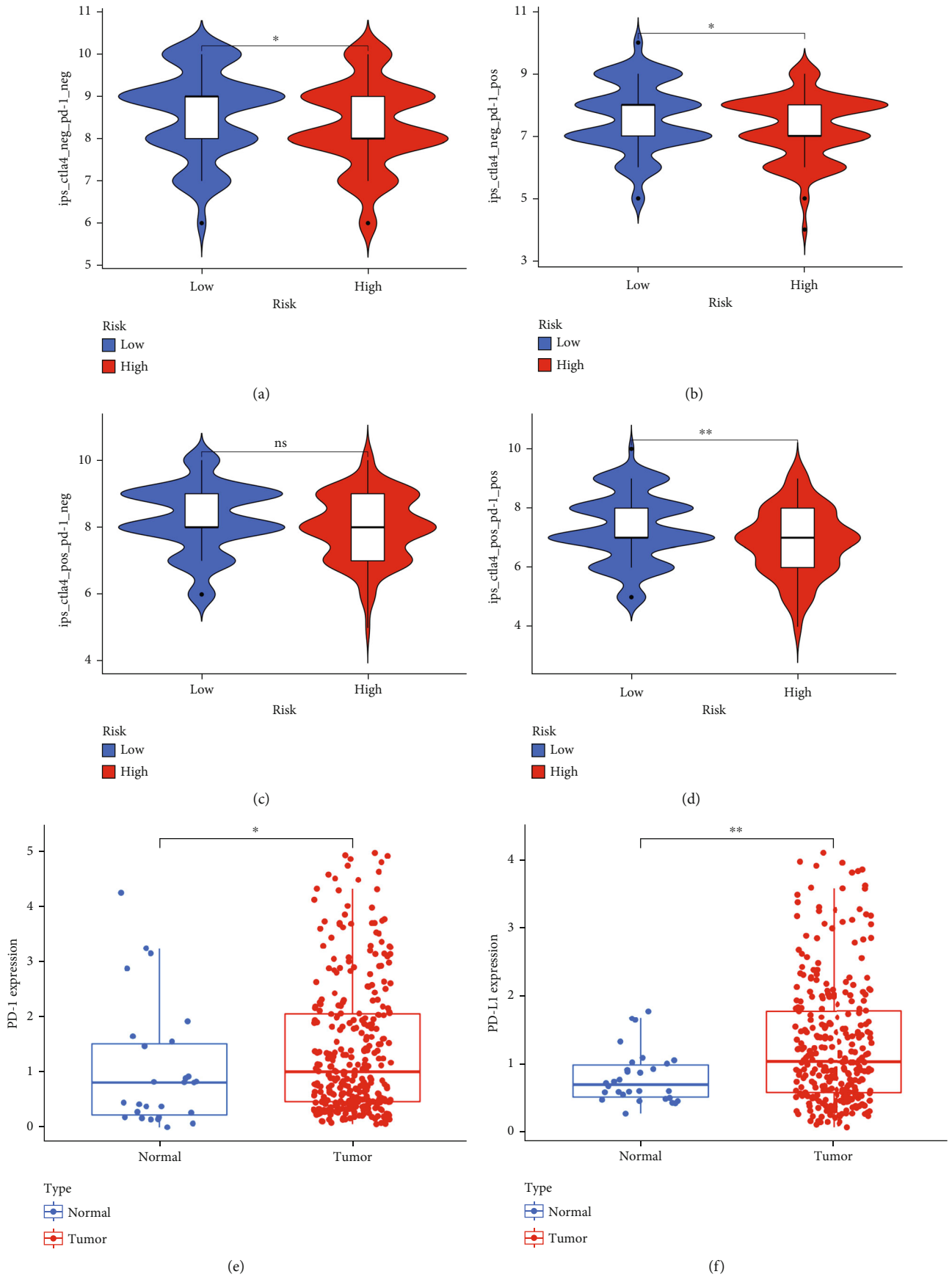


FIGURE 7: Continued.

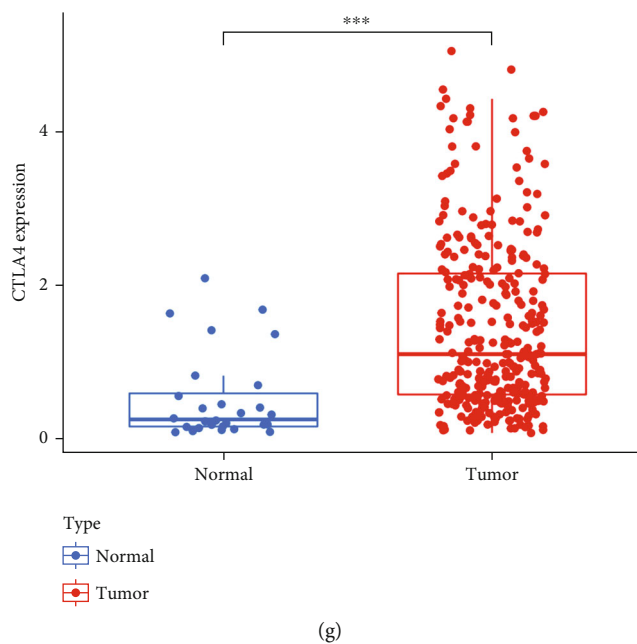


FIGURE 7: Immunotherapy scores (IPS) and gene expression analysis of immune checkpoints. (a) IPS of CTLA4-negative and PD-1-negative cells in high- and low-risk groups. (b) IPS of CTLA4-negative and PD-1-positive cells in high- and low-risk groups. (c) IPS of CTLA4-positive and PD-1-negative cells in high- and low-risk groups. (d) IPS of CTLA4-positive and PD-1-positive cells in high- and low-risk groups. (e–g) Expression of PD-1, PD-L1, and CTLA4 in the gastric adenocarcinoma and normal groups. The expressions of PD-1, PD-L1, and CTLA4 in tumor tissues were significantly higher than those in normal tissues. * $p < 0.05$; ** $p < 0.01$; *** $p < 0.001$.

NRF2 pathway (Figure S8C). The mutation rate of serine/threonine kinase (ATM) was higher in the TP53 pathway (Figure S8D). In the NOTCH pathway, the mutation rate of contactin 6 (CNTN6) was the highest (Figure S8E), and in the PI3K pathway, PIK3CA was the most highly mutated gene. (Figure S8F). In the Hippo pathway, both FAT atypical cadherin 3 (FAT3) and FAT atypical cadherin 4 (FAT4) showed high mutation rates (Figure S8G). Interestingly, the highest mutated gene in the cell cycle pathway was CDKN2A, which was consistent with our previous research conclusions (Figure S8H). ACVR2A and APC were observed to have high mutation rates in the TGF- β and WNT pathways, respectively, as depicted in Figure S8I–J.

4. Discussion

As a novel modality of iron-dependent cell death characterized by the accumulation of lipid peroxides and reactive oxygen species, ferroptosis presents an innovative viewpoint on the treatment of cancer and provides the possibility of developing new strategies for the treatment of gastric adenocarcinoma [8, 9]. Increased ferroptosis has been shown to aid in the anticancer effectiveness of immunotherapy, according to a recent research [39], which suggests a strong association between ferroptosis and immunotherapy. Despite the lack of research on the role of ferroptosis-related lncRNAs in gastric adenocarcinoma, particularly the mechanism connecting it to the immune microenvironment, our study seeks to address this issue. We conducted a thorough investigation of ferroptosis-related lncRNAs in gastric adenocarcinoma,

which included evaluating immunotherapy response, immune infiltration, IPS scores, predicting somatic mutations, analyzing tumor immune microenvironment, and assessing tumor drug sensitivity, as well as analyzing the stability of the secondary structure of lncRNAs in RNA transcription.

In this study, we conducted a comprehensive analysis of the TCGA database to identify ferroptosis-related lncRNAs and assess their potential predictive value. After differential analysis, 18 mRNAs and 263 lncRNAs were found to be differentially expressed between gastric adenocarcinoma and normal tissues. Subsequently, a univariate Cox regression analysis was employed to identify lncRNA signatures associated with prognosis. Through multivariate Cox regression analysis, we identified five lncRNAs (LINC00460, miR205HG, AC103563.8, RP11-186F10.2, and RP11-1143G9.5) that were associated with overall survival and used them to construct a risk model. In the following analysis, the outcome of the Kaplan–Meier analysis suggested that the high expression of LINC00460, miR205HG, AC103563, and RP11-186F10.2 was strongly associated with poor prognosis in gastric adenocarcinoma tissues, and in turn, RP11-1143G9.5 high expression was closely related to a good prognosis. In addition, we found that the survival rate of patients in the low-risk group was significantly improved, indicating that the low-risk score was closely related to longer survival. In addition, the ROC graph showed that high AUC values amongst the TCGA training set, TCGA training test set, and TCGA entire set for 3, 5, and 7 years were all greater than 0.65, indicating good prediction performance of our model.

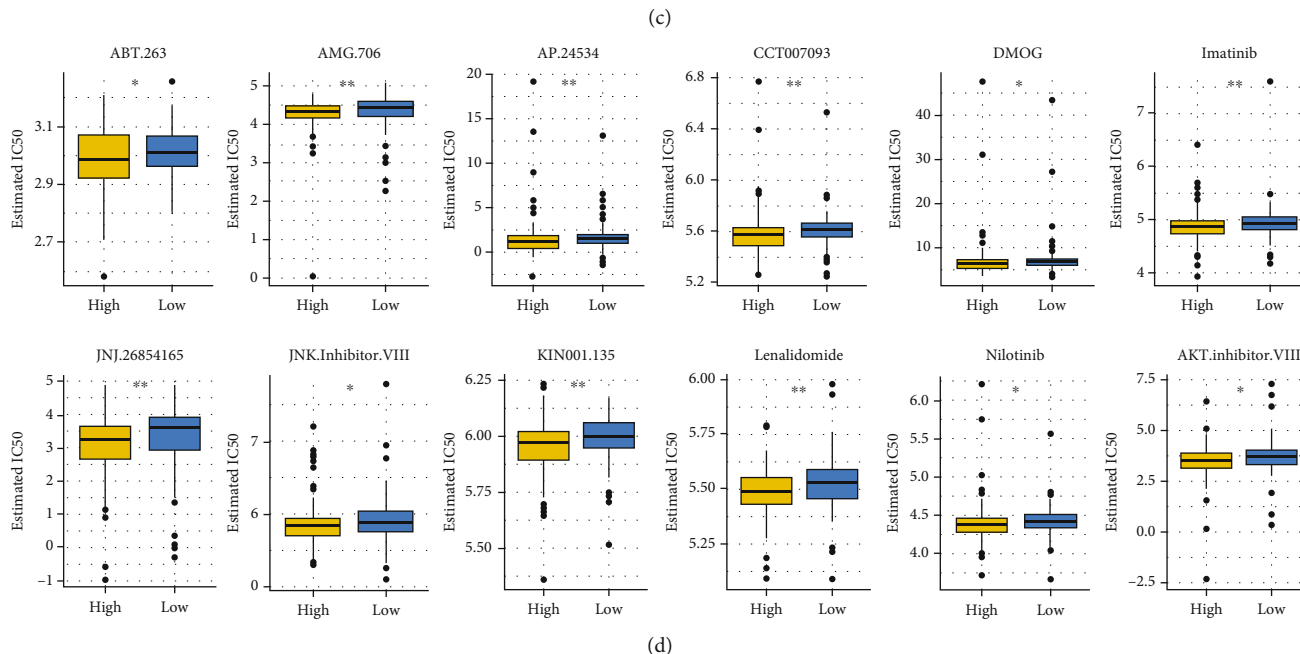
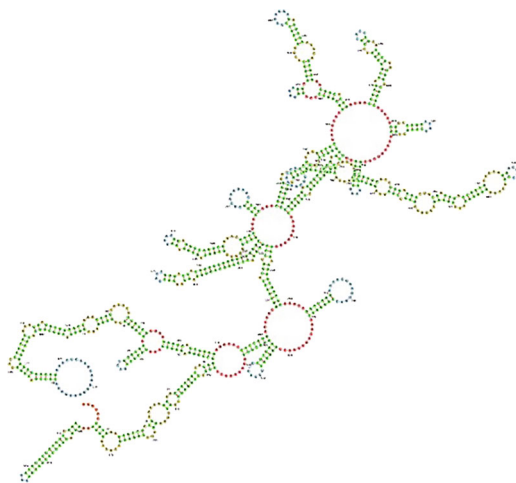
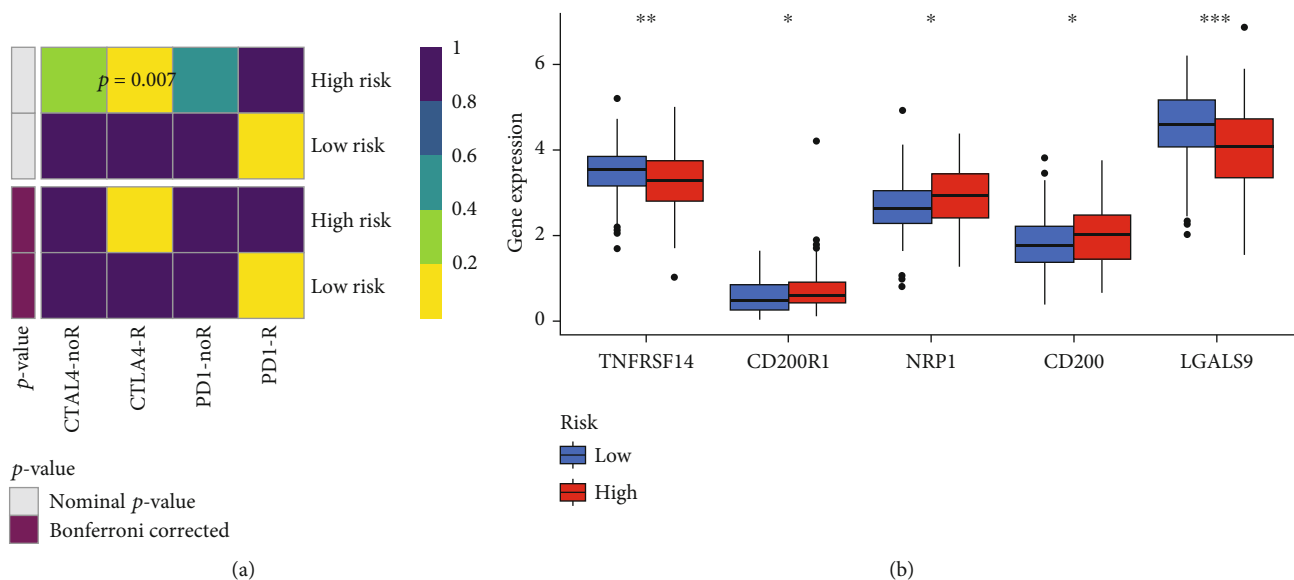


FIGURE 8: Continued.

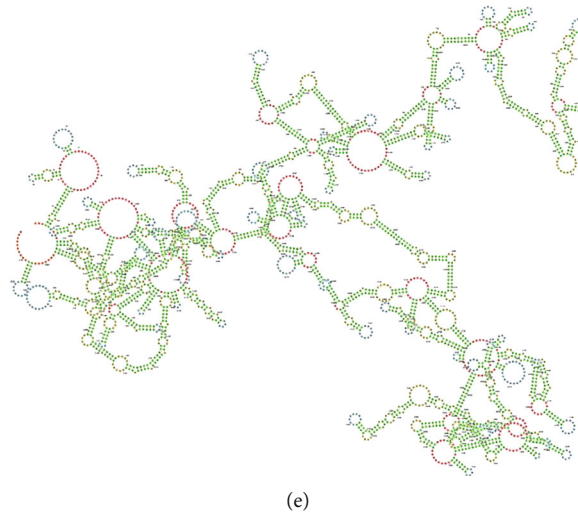


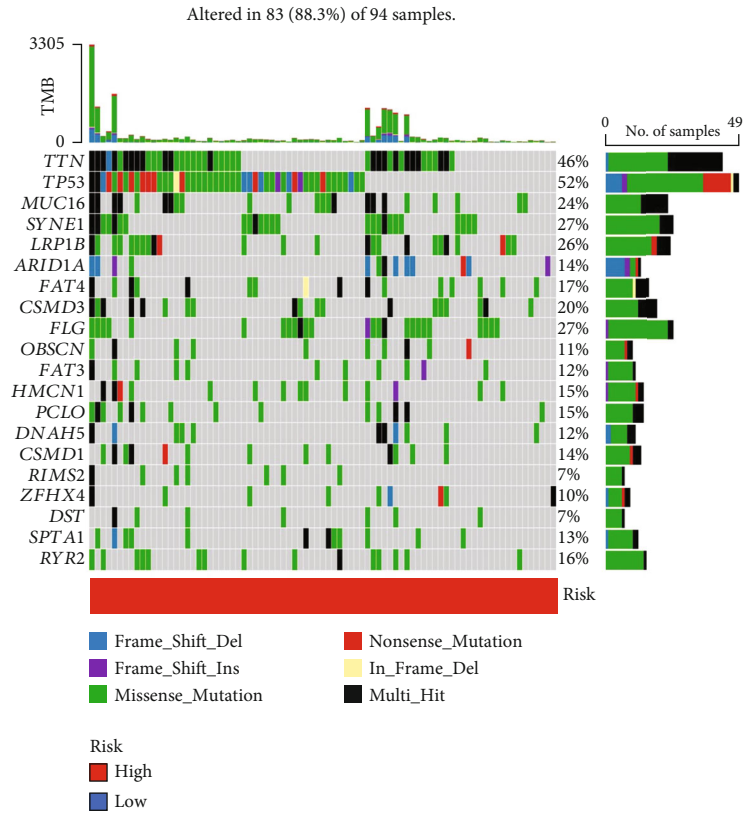
FIGURE 8: Anti-CTLA4, anti-PD-1 immunotherapy, construction of secondary structure, and drug IC_{50} prediction. (a) The heatmap shows the response of anti-CTLA4 and anti-PD-1 immunotherapy for gastric adenocarcinoma in the high-risk and low-risk groups. In terms of a nominal p value, anti-CTLA4 immunotherapy was more likely to lead to a response in the high-risk group ($p = 0.007$), and the Bonferroni corrected p value was less than that in other cases. (b) Expression of the five immune checkpoint inhibitors in the high- and low-risk groups. (c) The secondary structure of LINC00460. (d) The IC_{50} values of 12 drugs expressed in the high-risk and low-risk groups were used to screen drugs with substantial differences between the two groups. (e) The secondary structure of miR205HG. IC_{50} , half-maximal inhibitory concentration. * $p < 0.05$; ** $p < 0.01$; *** $p < 0.001$.

We also evaluated the clinical characteristics of ferroptosis-related lncRNAs in gastric adenocarcinoma patients in TCGA training and test sets.

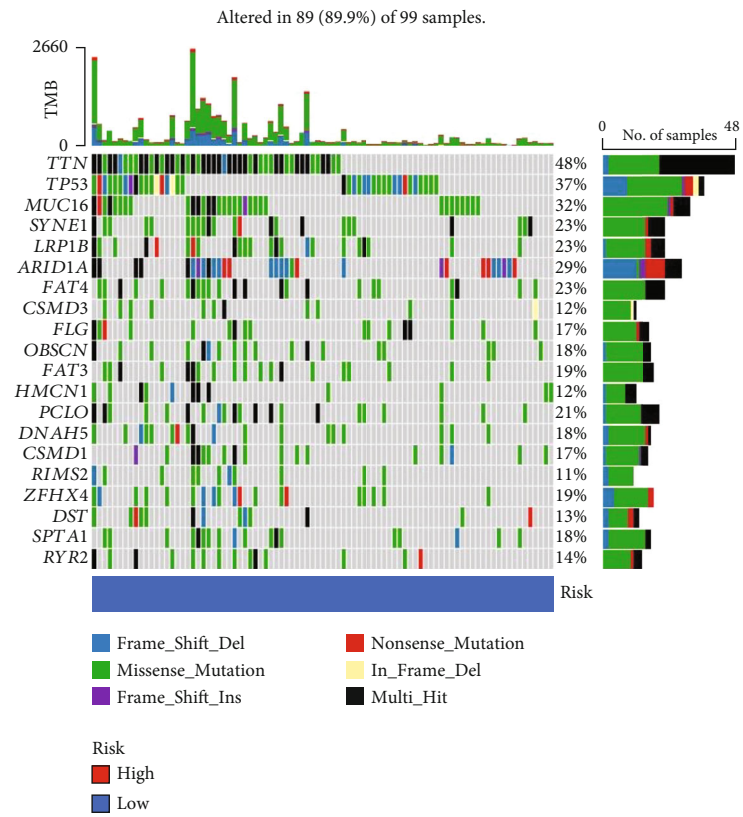
The findings of the GO analysis indicated a tight relationship with the principal molecular function of ferroptosis regulation, such as the superoxide metabolic process and iron ion binding. KEGG pathway analysis showed the four important pathways—ferroptosis, arachidonic acid metabolism, serotonergic synapse, and arginine biosynthesis. To assess the correlation of genes related to ferroptosis, we amalgamated the STRING online database and Cytoscape software to create a PPI network comprising 18 nodes and 11 edges. The 10 most important hub genes were identified by the Cytoscape plugin CytoHubba, including ALB, CDKN2A, NOS2, GDF15, NOX1, HBA1, ALOX12, ALOX15, AURKA, and CP. The CDKN2A gene showed an important position in the network. We also summarized genetic aberrations, including the incidence of somatic mutations and copy number variations (CNVs) of 18 ferroptosis regulators in gastric adenocarcinoma. We discover that CDKN2A exhibited the highest mutation frequency, which may improve our understanding of the genetic heterogeneity in GC. Among single nucleotide variations, $C > T$ was the most commonly encountered. The cell cycle was affected by gene mutations in CDKN2A. CDKN2A was shown previously to be a novel ferroptosis driver [40] and encodes the ARF (alternative reading frame) protein [41]. It has been previously demonstrated that cyclin-dependent kinase inhibitor 2A (CDKN2A/ARF) causes cancer cells to be sensitive to ferroptosis by inhibiting the ability of NRF2 and its transcriptional target SLC7A11 [42] through pathways dependent or independent of p53 tumor suppression gene in the cancerous cells [43, 44]. Therefore, we examined the

correlation between CDKN2A, the five lncRNAs, and overall survival (LINC00460, miR205HG, AC103563.8, RP11-186F10.2, and RP11-1143G9.5). Data analysis revealed a substantial correlation between LINC00460 and CDKN2A, implying that these two elements may be related to the survival and prognosis of patients with gastric adenocarcinoma.

LINC00460 is a novel lncRNA with 935 nucleotides located on chromosome 13q33.2. Growing research indicates that the lncRNA LINC00460 has an oncogenic function in the advancement of many malignancies. It has been confirmed that LINC00460 functioned as an oncogene regulating prostate cancer progression through the promotion of cell proliferation and a reduction in apoptosis [45]. Wang et al. demonstrated that LINC00460 can promote the proliferation and repress the apoptosis of non-small cell lung cancer cells by targeting miR-539 [46]. By sponging miR-4443, LINC00460 promotes cell progression in squamous cell carcinoma of the head and neck [47]. By competitively binding miR-489-5p to elevate FGF7 expression and enhancing downstream AKT signaling, LINC00460 promotes breast cancer progression [48]. LINC00460 can also function as a molecular sponge to adsorb miR-1224-5p, thereby promoting esophageal cancer (ESCA) metastasis and progression [49]. Yuan et al. reported that the downregulation of LINC00460 inhibits colorectal cancer metastasis via WWC2 [50]. miR205HG, also known as LINC00510, is a novel lncRNA with 4173 bp located at chromosome location 1q32.2. According to many studies, miR205HG was affirmed as important in its oncogenic role in cancer progression. It has been shown that lncRNA miR205HG drives the advancement of esophageal squamous cell carcinoma through the miR-214/SOX4 axis. [51]. Liu et al. concluded that miR205HG expedited the cell proliferation and

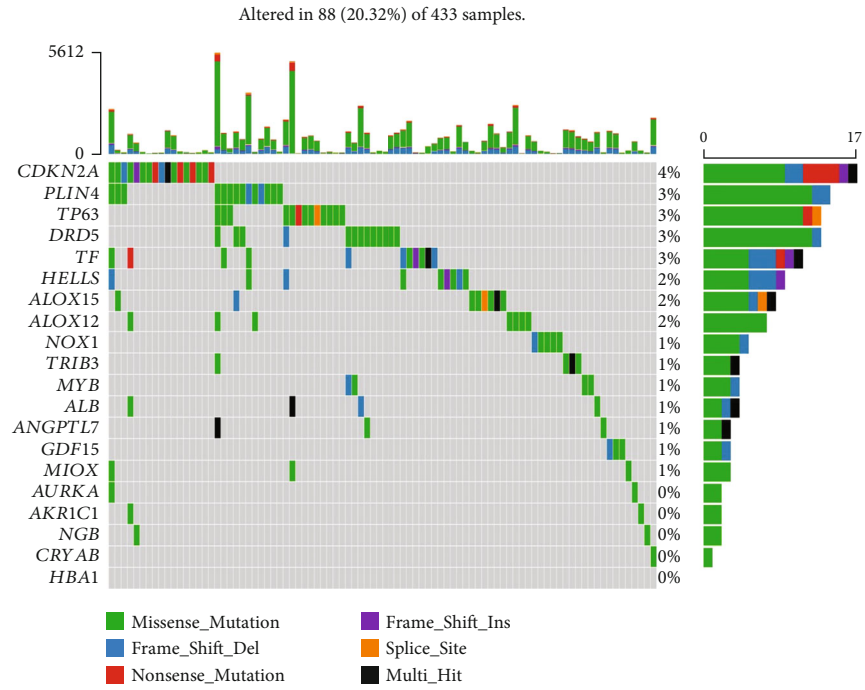


(a)

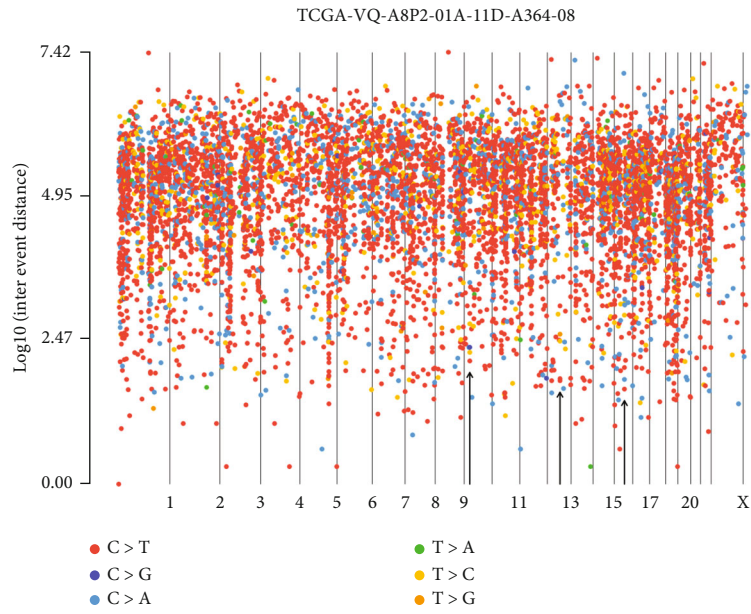


(b)

FIGURE 9: Continued.

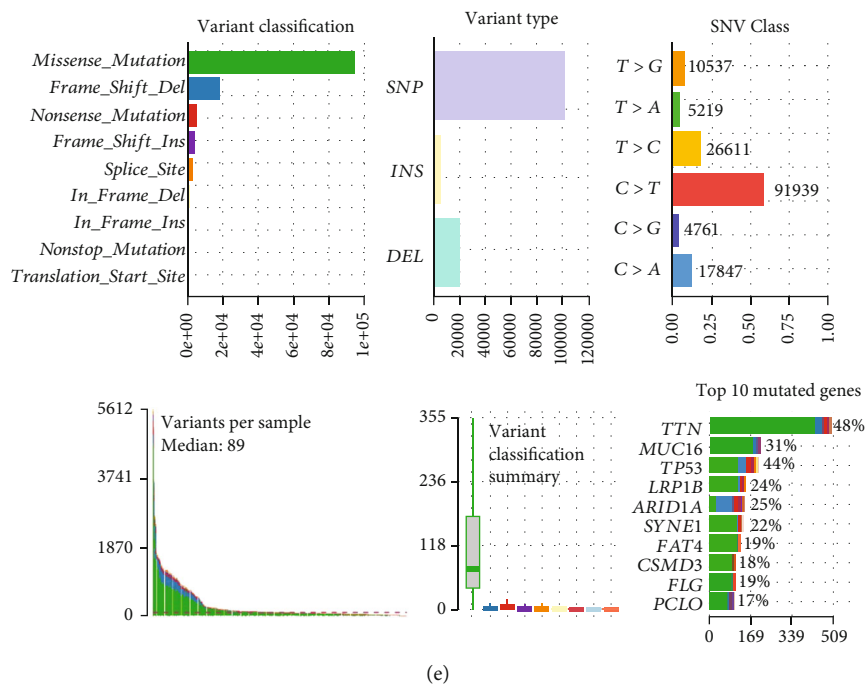


(c)

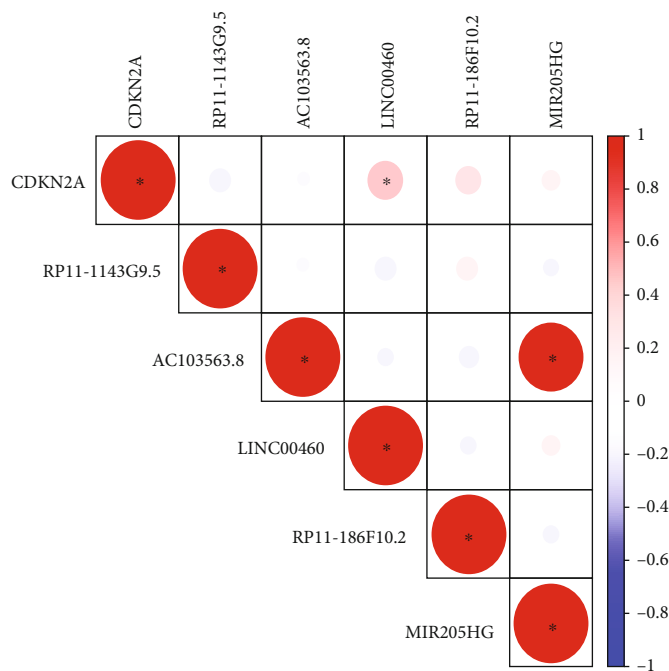


(d)

FIGURE 9: Continued.



(e)



(f)

FIGURE 9: Landscape of TMB in STAD. (a, b) The top 20 mutant genes with the highest mutation rate in the high- and low-risk groups. (c) Mutations of ferroptosis-related genes in STAD patients. (d) Chromosome mutation in gastric adenocarcinoma samples. (e) A comprehensive plot of genetic alterations in STAD. $C > T$ occurred frequently in single nucleotide variation (SNV). (f) The relevance between highly mutated gene CDKN2A and a five ferroptosis-related lncRNA signatures ($R > 0.1$, $p < 0.05$). * $p < 0.05$; ** $p < 0.01$; *** $p < 0.001$.

progression of lung squamous cell carcinoma via targeting miR-299-3p [52]. miR205HG also functions as a competing endogenous RNA (ceRNA) to accelerate tumor growth and progression via sponging miR-122e5p in cervical cancer [53]. The results demonstrate that expression of lncRNA LINC00460 is higher in tumors, and those with a decrease in LINC00460 expression had a prolonged survival time. In

comparison to lncRNA LINC00460, the expression of lncRNA miR205HG was lower in tumor samples than in normal stomach tissue, and those with a decrease in miR205HG had a poorer prognosis. Additionally, the strong association between lncRNA LINC00460 with CDKN2A ferroptosis drivers suggested the potential that LINC00460 affected patient survival via CDKN2A.

It is widely accepted that epithelial–mesenchymal transition is a fundamental mechanism in the progression of cancer cells to invasion and metastasis [54]. lncRNAs can be employed to forecast the clinical course, aggressiveness, invasion, and metastasis potential of GC, in addition to providing a model for investigating ways to inhibit or reverse metastatic potential. lncRNAs can be considered crucial elements of epigenetic regulation of gene expression in tumorigenesis and carcinogenesis, and their impact on the EMT can be achieved by either directly regulating the vimentin and E-cadherin function or by controlling the transcription of these genes through various factors [55]. To further explore the biological nature of the different ferroptosis subtypes, we conducted a gene set variation analysis (GSVA) enrichment. The results showed that four ferroptosis clusters were enriched in the pathway related to immune (allograft rejection), activation of cancer-related pathways (p53 pathway, e2f targets, and peroxisome), cell proliferation-related metabolic (glycolysis), and spermatogenesis, which suggested an important role in tumor progression and a tight association with the tumor microenvironment. An evaluation of immune cell infiltration was conducted using seven distinct algorithms, and it was determined that T cells and macrophages had significantly infiltrated the gastric microenvironment. Previous mouse models of gastritis and GC revealed that a notable quantity of macrophages migrates to the GC microenvironment, which influences angiogenesis or tumor immunity [56–61]. Tumor-infiltrating lymphocytes (TILs) composed of T cells, natural killer (NK) cells, B cells, and T-cell-mediated adaptive immunity are usually considered the manifestation of the host antitumor immune response. The upregulation of PD-L1 or CTLA-4 expression can mediate the escape of tumor cells from the host immune response, lead to an immunosuppressive state, and inhibit the antitumor immune response in some tumor microenvironments [62]. Therefore, IPS and gene expression analysis of immune checkpoints were also performed. We examined the expression levels of PD-1 (PDCD1), PD-L1, and CTLA4 (cytotoxic T-lymphocyte associated protein 4) in tumor and normal groups. The expression of PD-1, PD-L1, and CTLA4 in gastric adenocarcinoma was all higher than in the normal group, with the expression levels of three common immune checkpoints distinctly upregulated in high-risk cohorts. Additionally, the high-risk group was more likely to respond to anti-CTLA4 immunotherapy ($p = 0.007$). Interestingly, in our immunotherapy analysis, the low-risk group achieved higher CTLA4-negative/PD-1-negative, CTLA4-negative/PD-1-positive, and CTLA4-positive/PD-1-positive scores, indicating that patients with a low-risk score are better candidates for immunotherapy. It may be that high-risk patients had a very serious gastric adenocarcinoma or that lncRNAs were highly expressed, reducing immunotherapy effectiveness. To explore immunotherapy responses, the TIDE algorithm was used to identify significant differences in immunotherapy responses between the high- and low-risk groups (better responses in the low-risk group). The TIDE score will help us better select patients who are more suitable for immune checkpoint suppression therapy, and it will be of interest to test the clinical efficacy of TIDE scores in

immune checkpoint suppression treatment decision-making in prospective clinical trials. In addition, 12 antigastric adenocarcinoma drugs were screened according to lncRNA signals associated with iron drop: ABT.263, AMG.706 (Motesanib), AP.24534, CCT007093, DMOG, imatinib, JNJ.26854165, JNK inhibitor VIII, KIN001.135 (benzimidazole-thiophene carbonitrile), lenalidomide, nilotinib, and AKT inhibitor VIII. All of the above drugs have different degrees of antitumor effects and vital clinical significance [63–73].

In conclusion, our study identified five ferroptosis-related lncRNAs (LINC00460, miR205HG, AC103563.8, RP11-186F10.2, and RP11-1143G9.5) involved in gastric adenocarcinoma that are of great value in predicting OS in gastric adenocarcinoma patients. It was discovered that five ferroptosis-related lncRNAs could be used as significant prognostic biomarkers to forecast long-term survival in gastric adenocarcinoma patients and regulate the proliferation and migration of gastric adenocarcinoma cells and the development of ferroptosis. In addition, we evaluated the clinical signs of FPI, TMB, and tide and completed a thorough examination of immunotherapy and drug prediction. It has been noted that immunotherapy, particularly anti-CTLA4 immunotherapy and 12 antigastric adenocarcinoma drugs, has resulted in a higher survival rate for patients with gastric adenocarcinoma. Therefore, lncRNAs (LINC00460, miR205HG, AC103563.8, RP11-186F10.2, and RP11-1143G9.5) may serve as potential biomarkers of prognostic value in gastric adenocarcinoma. This study had certain limitations, such as the use of public databases for mining and analysis. To improve the dependability of our results and eliminate selection bias, larger population and multicenter clinical trials are required. In order to gain insight into the potential functions of the five ferroptosis-related lncRNAs in gastric cancer, since all the mechanical studies in our work were descriptive, further laboratory experiments were necessary.

Data Availability

The original contributions presented in the study are included in the article/Supplementary Material. Further inquiries can be directed to the corresponding author.

Conflicts of Interest

The authors declare that they have no known competing financial interests or personal relationships that could have appeared to influence the work reported in this paper.

Authors' Contributions

L.X. Luo conceived and designed the study, reviewed the paper, and provided comments. L.X. Luo, S.S. Wu, Y.S. Zheng, and X.S. Huang performed data mining and analysis and wrote the manuscript. All authors contributed to the article and approved the submitted version. Yushi Zheng and Shanshan Wu contributed equally to this work.

Acknowledgments

This project was supported by the Science and Technology Program of Guangdong Province (no. 2023A1515010850); funds for PhD researchers of the Guangdong Medical University in 2020 (no. GDMU2020018); the Medical Scientific Research Foundation of Guangdong Province (no. A2020633); the Medical Scientific Research Foundation of Guangdong Province of China (A2021243). We thank the Public Service Platform of South China Sea for R&D Marine Biomedicine Resources for the support.

Supplementary Materials

Please see the supplementary material section of the author guidelines for details on the different file types accepted. (*Supplementary Materials*)

References

- [1] F. Bray, J. Ferlay, I. Soerjomataram, R. L. Siegel, L. A. Torre, and A. Jemal, "Global cancer statistics 2018: GLOBOCAN estimates of incidence and mortality worldwide for 36 cancers in 185 countries," *CA: a Cancer Journal for Clinicians*, vol. 68, no. 6, pp. 394–424, 2018.
- [2] F. A. Rima, M. Hussain, R. K. Dewan et al., "Clinicopathologic features of gastric and Gastroesophageal junction adenocarcinoma," *Mymensingh Medical Journal*, vol. 29, no. 1, pp. 195–201, 2020.
- [3] L. Necula, L. Matei, D. Dragu et al., "Recent advances in gastric cancer early diagnosis," *World Journal of Gastroenterology*, vol. 25, no. 17, pp. 2029–2044, 2019.
- [4] M.-M. Tsai, C.-S. Wang, C.-Y. Tsai et al., "Potential diagnostic, prognostic and therapeutic targets of MicroRNAs in human gastric cancer," *International Journal of Molecular Sciences*, vol. 17, no. 6, p. 945, 2016.
- [5] D. Wu, P. Zhang, J. Ma et al., "Serum biomarker panels for the diagnosis of gastric cancer," *Cancer Medicine*, vol. 8, no. 4, pp. 1576–1583, 2019.
- [6] T. N. Patel, S. Roy, and R. Ravi, "Gastric cancer and related epigenetic alterations," *Ecancermedicalscience*, vol. 11, p. 714, 2017.
- [7] A. Bhan, M. Soleimani, and S. S. Mandal, "Long noncoding RNA and cancer: a new paradigm," *Cancer Research*, vol. 77, no. 15, pp. 3965–3981, 2017.
- [8] B. R. Stockwell, J. P. Friedmann Angeli, H. Bayir et al., "Ferroptosis: a regulated cell death nexus linking metabolism, redox biology, and disease," *Cell*, vol. 171, no. 2, pp. 273–285, 2017.
- [9] S. J. Dixon, K. M. Lemberg, M. R. Lamprecht et al., "Ferroptosis: an iron-dependent form of nonapoptotic cell death," *Cell*, vol. 149, no. 5, pp. 1060–1072, 2012.
- [10] N. Jiang, X. Zhang, X. Gu, X. Li, and L. Shang, "Progress in understanding the role of lncRNA in programmed cell death," *Cell Death Discovery*, vol. 7, no. 1, p. 30, 2021.
- [11] R. Derynck, S. J. Turley, and R. J. Akhurst, "TGF β biology in cancer progression and immunotherapy," *Clinical Oncology*, vol. 18, no. 1, pp. 9–34, 2021.
- [12] A. Rojas, P. Araya, I. Gonzalez, and E. Morales, "Gastric tumor microenvironment," *Advances in Experimental Medicine and Biology*, vol. 1226, pp. 23–35, 2020.
- [13] L. S. Lamb, H.-W. Sim, and A. I. McCormack, "Exploring the role of novel medical therapies for aggressive pituitary tumors: a review of the literature-are we there yet?," *Cancers*, vol. 12, no. 2, p. 308, 2020.
- [14] P. Jiang, S. Gu, D. Pan et al., "Signatures of T cell dysfunction and exclusion predict cancer immunotherapy response," *Nature Medicine*, vol. 24, no. 10, pp. 1550–1558, 2018.
- [15] A. Re, C. Nardella, A. Quattrone, and A. Lunardi, "Editorial: precision medicine in oncology," *Frontiers in Oncology*, vol. 8, p. 479, 2018.
- [16] Y. Zhong, X. Li, H. Yao, and K. Lin, "The Characteristics of PD-L1 Inhibitors, from Peptides to Small Molecules," *Molecules*, vol. 24, no. 10, p. 1940, 2019.
- [17] N. Zhou and J. Bao, "FerrDb: a manually curated resource for regulators and markers of ferroptosis and ferroptosis-disease associations," *Database*, vol. 2020, article baaa021, 2020.
- [18] G. Stelzer, N. Rosen, I. Plaschkes et al., "The GeneCards suite: from gene data mining to disease genome sequence analyses," *Current Protocols in Bioinformatics*, vol. 54, no. 1, 2016.
- [19] M. D. Robinson, D. J. McCarthy, and G. K. Smyth, "edgeR: a bioconductor package for differential expression analysis of digital gene expression data," *Bioinformatics*, vol. 26, no. 1, pp. 139–140, 2010.
- [20] D. J. McCarthy, Y. Chen, and G. K. Smyth, "Differential expression analysis of multifactor RNA-Seq experiments with respect to biological variation," *Nucleic Acids Research*, vol. 40, no. 10, pp. 4288–4297, 2012.
- [21] D. Szklarczyk, A. Franceschini, S. Wyder et al., "STRING v10: protein-protein interaction networks, integrated over the tree of life," *Nucleic Acids Research*, vol. 43, no. D1, pp. D447–D452, 2015.
- [22] H. Zhang, J. Zhong, Y. Tu et al., "Integrated bioinformatics analysis identifies hub genes associated with the pathogenesis and prognosis of esophageal squamous cell carcinoma," *BioMed Research International*, vol. 2019, Article ID 2615921, 9 pages, 2019.
- [23] T. M. Therneau and P. M. Grambsch, "The Cox Model," in *Modeling Survival Data: Extending the Cox Model*, T. M. Therneau and P. M. Grambsch, Eds., pp. 39–77, Springer New York, New York, NY, 2000.
- [24] T. Li, J. Fan, B. Wang et al., "TIMER: a web server for comprehensive analysis of tumor-infiltrating immune cells," *Cancer Research*, vol. 77, no. 21, pp. e108–e110, 2017.
- [25] F. Petitprez, Y. A. Vano, E. Becht et al., "Transcriptomic analysis of the tumor microenvironment to guide prognosis and immunotherapies," *Cancer Immunology, Immunotherapy*, vol. 67, no. 6, pp. 981–988, 2018.
- [26] B. Chen, M. S. Khodadoust, C. L. Liu, A. M. Newman, and A. A. Alizadeh, "Profiling Tumor Infiltrating Immune Cells with CIBERSORT," *Methods in Molecular Biology*, vol. 1711, pp. 243–259, 2018.
- [27] F. Finotello, C. Mayer, C. Plattner et al., "Molecular and pharmacological modulators of the tumor immune contexture revealed by deconvolution of RNA-seq data," *Genome Medicine*, vol. 11, no. 1, p. 34, 2019.
- [28] D. Aran, Z. Hu, and A. J. Butte, "xCell: digitally portraying the tissue cellular heterogeneity landscape," *Genome Biology*, vol. 18, no. 1, p. 220, 2017.
- [29] J. Racle and D. Gfeller, "EPIC: A Tool to Estimate the Proportions of Different Cell Types from Bulk Gene Expression

- Data,” *Methods in Molecular Biology*, vol. 2120, pp. 233–248, 2020.
- [30] S. Hänzelmann, R. Castelo, and J. Guinney, “GSVA: gene set variation analysis for microarray and RNA-seq data,” *BMC Bioinformatics*, vol. 14, no. 1, p. 7, 2013.
 - [31] K. Yoshihara, M. Shahmoradgoli, E. Martínez et al., “Inferring tumour purity and stromal and immune cell admixture from expression data,” *Nature Communications*, vol. 4, no. 1, p. 2612, 2013.
 - [32] S. M. Lin, P. Du, W. Huber, and W. A. Kibbe, “Model-based variance-stabilizing transformation for Illumina microarray data,” *Nucleic Acids Research*, vol. 36, no. 2, article e11, 2008.
 - [33] M. Seiler, C. C. Huang, S. Szalma, and G. Bhanot, “ConsensusCluster: a software tool for unsupervised cluster discovery in numerical data,” *OMICS: a Journal of Integrative Biology*, vol. 14, no. 1, pp. 109–113, 2010.
 - [34] Y. Tao, C. Tian, N. Verma et al., “Recovering intrinsic fragmental vibrations using the generalized subsystem vibrational analysis,” *Journal of Chemical Theory and Computation*, vol. 14, no. 5, pp. 2558–2569, 2018.
 - [35] Z. Liu, Q. Zhao, Z.-X. Zuo et al., “Systematic analysis of the aberrances and functional implications of ferroptosis in cancer,” *iScience*, vol. 23, no. 7, article 101302, 2020.
 - [36] W. Yang, J. Soares, P. Greninger et al., “Genomics of drug sensitivity in cancer (GDSC): a resource for therapeutic biomarker discovery in cancer cells,” *Nucleic Acids Research*, vol. 41, no. Database issue, pp. D955–D961, 2013.
 - [37] P. Geeleher, N. Cox, and R. S. Huang, “pRRophetic: an R package for prediction of clinical chemotherapeutic response from tumor gene expression levels,” *PLoS One*, vol. 9, no. 9, article e107468, 2014.
 - [38] Y. Zheng, Q. Xu, M. Liu et al., “lncCAR: a comprehensive resource for lncRNAs from cancer arrays,” *Cancer Research*, vol. 79, no. 8, pp. 2076–2083, 2019.
 - [39] W. Wang, M. Green, J. E. Choi et al., “CD8⁺ T cells regulate tumour ferroptosis during cancer immunotherapy,” *Nature*, vol. 569, no. 7755, pp. 270–274, 2019.
 - [40] Z.-W. Hu, Y.-H. Wen, R.-Q. Ma et al., “Ferroptosis driver SOCS1 and suppressor FTH1 independently correlate with M1 and M2 macrophage infiltration in head and neck squamous cell carcinoma,” *Frontiers in Cell and Developmental Biology*, vol. 9, article 727762, 2021.
 - [41] R. Fontana, M. Ranieri, G. La Mantia, and M. Vivo, “Dual role of the alternative reading frame ARF protein in cancer,” *Bio-molecules*, vol. 9, no. 3, p. 87, 2019.
 - [42] Z.-Z. Shi, Z.-W. Fan, Y.-X. Chen et al., “Ferroptosis in carcinoma: regulatory mechanisms and new method for cancer therapy,” *Oncotargets and Therapy*, vol. Volume 12, pp. 11291–11304, 2019.
 - [43] D. Chen, O. Tavana, B. Chu et al., “NRF2 is a major target of ARF in p53-independent tumor suppression,” *Molecular Cell*, vol. 68, no. 1, pp. 224–232.e4, 2017.
 - [44] J.-Y. Duan, X. Lin, F. Xu et al., “Ferroptosis and its potential role in metabolic diseases: a curse or revitalization?,” *Frontiers in Cell and Developmental Biology*, vol. 9, article 701788, 2021.
 - [45] Y. Dong and H. Y. Quan, “Downregulated LINC00460 inhibits cell proliferation and promotes cell apoptosis in prostate cancer,” *European Review for Medical and Pharmacological Sciences*, vol. 23, no. 14, pp. 6070–6078, 2019.
 - [46] H. X. Wang, L. J. Kang, X. Qin, J. Xu, and J. W. Fei, “LINC00460 promotes proliferation and inhibits apoptosis of non-small cell lung cancer cells through targeted regulation of miR-539,” *European Review for Medical and Pharmacological Sciences*, vol. 24, no. 12, pp. 6752–6758, 2020.
 - [47] M. Li, X. Zhang, X. Ding et al., “Long noncoding RNA LINC00460 promotes cell progression by sponging miR-4443 in head and neck squamous cell carcinoma,” *Cell Transplantation*, vol. 29, 2020.
 - [48] Y. Zhu, L. Yang, Q.-Y. Chong et al., “Long noncoding RNA LINC00460 promotes breast cancer progression by regulating the miR-489-5p/FGF7/AKT axis,” *Cancer Management and Research*, vol. 11, pp. 5983–6001, 2019.
 - [49] Y. Cui, C. Zhang, H. Lian et al., “lncRNA linc00460 sponges miR-1224-5p to promote esophageal cancer metastatic potential and epithelial-mesenchymal transition,” *Pathology, Research and Practice*, vol. 216, no. 7, article 153026, 2020.
 - [50] B. Yuan, J. Yang, H. Gu, and C. Ma, “Down-regulation of LINC00460 represses metastasis of colorectal cancer via WWC2,” *Digestive Diseases and Sciences*, vol. 65, no. 2, pp. 442–456, 2020.
 - [51] H. Li, J. Jia, L. Yang et al., “lncRNA miR205HG drives esophageal squamous cell carcinoma progression by regulating miR-214/SOX4 axis,” *Oncotargets and Therapy*, vol. 13, pp. 13097–13109, 2020.
 - [52] L. Liu, Y. Li, R. Zhang, C. Li, J. Xiong, and Y. Wei, “miR205HG acts as a ceRNA to expedite cell proliferation and progression in lung squamous cell carcinoma via targeting miR-299-3p/MAP3K2 axis,” *BMC Pulmonary Medicine*, vol. 20, no. 1, p. 163, 2020.
 - [53] Y. Li, H. Wang, and H. Huang, “Long non-coding RNA miR205HG function as a ceRNA to accelerate tumor growth and progression via sponging miR-122-5p in cervical cancer,” *Biochemical and Biophysical Research Communications*, vol. 514, no. 1, pp. 78–85, 2019.
 - [54] M. A. Nieto, R. Y.-J. Huang, R. A. Jackson, and J. P. Thiery, “EMT: 2016,” *Cell*, vol. 166, no. 1, pp. 21–45, 2016.
 - [55] I. V. Bure, M. V. Nemtsova, and D. V. Zaletaev, “Roles of E-cadherin and noncoding RNAs in the epithelial-mesenchymal transition and progression in gastric cancer,” *International Journal of Molecular Sciences*, vol. 20, no. 12, p. 2870, 2019.
 - [56] H. Kinoshita, Y. Hayakawa, M. Konishi et al., “Three types of metaplasia model through KRAS activation, PTEN deletion, or CDH1 deletion in the gastric epithelium,” *The Journal of Pathology*, vol. 247, no. 1, pp. 35–47, 2019.
 - [57] H. Oshima, M. Oshima, K. Inaba, and M. M. Taketo, “Hyperplastic gastric tumors induced by activated macrophages in COX-2/mPGES-1 transgenic mice,” *The EMBO Journal*, vol. 23, no. 7, pp. 1669–1678, 2004.
 - [58] M. Kaparakis, A. K. Walduck, J. D. Price et al., “Macrophages are mediators of gastritis in acute *Helicobacter pylori* infection in C57BL/6 mice,” *Infection and Immunity*, vol. 76, no. 5, pp. 2235–2239, 2008.
 - [59] H. Oshima, K. Hioki, B. K. Popivanova et al., “Prostaglandin E₂ signaling and bacterial infection recruit tumor-promoting macrophages to mouse gastric tumors,” *Gastroenterology*, vol. 140, no. 2, pp. 596–607.e7, 2011.
 - [60] C. P. Petersen, V. G. Weis, K. T. Nam, J. F. Sousa, B. Fingleton, and J. R. Goldenring, “Macrophages promote progression of spasmodic polypeptide-expressing metaplasia after acute loss of parietal cells,” *Gastroenterology*, vol. 146, no. 7, pp. 1727–1738.e8, 2014.

- [61] T. Okumura, R. E. Ericksen, S. Takaishi et al., “K-ras mutation targeted to gastric tissue progenitor cells results in chronic inflammation, an altered microenvironment, and progression to intraepithelial neoplasia,” *Cancer Research*, vol. 70, no. 21, pp. 8435–8445, 2010.
- [62] Y. Oya, Y. Hayakawa, and K. Koike, “Tumor microenvironment in gastric cancers,” *Cancer Science*, vol. 111, no. 8, pp. 2696–2707, 2020.
- [63] A. J. Souers, J. D. Levenson, E. R. Boghaert et al., “ABT-199, a potent and selective BCL-2 inhibitor, achieves antitumor activity while sparing platelets,” *Nature Medicine*, vol. 19, no. 2, pp. 202–208, 2013.
- [64] S. Caenepeel, L. Renshaw-Gegg, A. Baher et al., “Motesanib inhibits kit mutations associated with gastrointestinal stromal tumors,” *Journal of Experimental & Clinical Cancer Research*, vol. 29, no. 1, p. 96, 2010.
- [65] S. Rayter, R. Elliott, J. Travers et al., “A chemical inhibitor of PPM1D that selectively kills cells overexpressing PPM1D,” *Oncogene*, vol. 27, no. 8, pp. 1036–1044, 2008.
- [66] W.-S. Wang, H.-Y. Liang, Y.-J. Cai, and H. Yang, “DMOG ameliorates IFN- γ -induced intestinal barrier dysfunction by suppressing PHD2-dependent HIF-1 α degradation,” *Journal of Interferon & Cytokine Research*, vol. 34, no. 1, pp. 60–69, 2014.
- [67] M. Kumar, R. Kulshrestha, N. Singh, and A. S. Jaggi, “Expanding spectrum of anticancer drug, imatinib, in the disorders affecting brain and spinal cord,” *Pharmacological Research*, vol. 143, pp. 86–96, 2019.
- [68] R. J. Jones, D. Gu, C. C. Bjorklund et al., “The novel anticancer agent JNJ-26854165 induces cell death through inhibition of cholesterol transport and degradation of ABCA1,” *The Journal of Pharmacology and Experimental Therapeutics*, vol. 346, no. 3, pp. 381–392, 2013.
- [69] K. A. Heslop, A. Rovini, E. G. Hunt et al., “JNK activation and translocation to mitochondria mediates mitochondrial dysfunction and cell death induced by VDAC opening and sorafenib in hepatocarcinoma cells,” *Biochemical Pharmacology*, vol. 171, article 113728, 2020.
- [70] P. Bamborough, J. A. Christopher, G. J. Cutler et al., “5-(1H-benzimidazol-1-yl)-3-alkoxy-2-thiophenecarbonitriles as potent, selective, inhibitors of IKK- ϵ kinase,” *Bioorganic & Medicinal Chemistry Letters*, vol. 16, no. 24, pp. 6236–6240, 2006.
- [71] Z. Wang, G. Zhou, N. Risu et al., “Lenalidomide enhances CAR-T cell activity against solid tumor cells,” *Cell Transplantation*, vol. 29, 2020.
- [72] B. N. Ostendorf, P. le Coutre, T. D. Kim, and A. Quintás-Cardama, “Nilotinib,” *Recent Results in Cancer Research*, vol. 201, pp. 67–80, 2014.
- [73] C. Liu, K. Chen, H. Wang et al., “Gastrin attenuates renal ischemia/reperfusion injury by a PI3K/Akt/bad-mediated anti-apoptosis signaling,” *Frontiers in Pharmacology*, vol. 11, article 540479, 2020.

Research Article

Inhibition of TRF2 Leads to Ferroptosis, Autophagic Death, and Apoptosis by Causing Telomere Dysfunction

Qihui Yang,^{1,2} Ziyang Nie,^{1,2,3} Yukun Zhu,^{1,2,4} Mingying Hao,^{1,2} Siqi Liu,^{1,2} Xuelu Ding,^{1,2,5} Feng Wang,⁶ Fei Wang^{ID},⁷ and Xin Geng^{ID}^{1,2}

¹Department of Biochemistry and Molecular Biology, School of Basic Medical Sciences, Tianjin Medical University, Tianjin 300070, China

²Key Laboratory of Immune Microenvironment and Disease (Ministry of Education), Tianjin Medical University, Tianjin 300070, China

³School of Life Sciences, Central China Normal University, Hubei Province, China

⁴Fuyang Hospital Affiliated to Anhui Medical University, Anhui Province 236000, China

⁵Department of Neurology, Tianjin Neurological Institute, Tianjin Medical University, General Hospital, Tianjin 300052, China

⁶Department of Genetics, School of Basic Medical Sciences, Tianjin Medical University, Tianjin 300070, China

⁷Department of Neurology, General Hospital, Tianjin Medical University, Tianjin 300052, China

Correspondence should be addressed to Fei Wang; feiwang@tmu.edu.cn and Xin Geng; gengx@tmu.edu.cn

Qihui Yang, Ziyang Nie, and Yukun Zhu contributed equally to this work.

Received 25 September 2022; Revised 23 October 2022; Accepted 4 February 2023; Published 18 April 2023

Academic Editor: Lianxiang Luo

Copyright © 2023 Qihui Yang et al. This is an open access article distributed under the Creative Commons Attribution License, which permits unrestricted use, distribution, and reproduction in any medium, provided the original work is properly cited.

Background. Gastric cancer (GC) is an aggressive malignancy with a high mortality rate and poor prognosis. Telomeric repeat-binding factor 2 (TRF2) is a critical telomere protection protein. Emerging evidence indicates that TRF2 may be an essential treatment option for GC; however, the exact mechanism remains largely unknown. **Objective.** We aimed to explore the role of TRF2 in GC cells. The function and molecular mechanisms of TRF2 in the pathogenesis of GC were mainly discussed in this study. **Methods.** Relevant data from GEPIA and TCGA databases regarding TRF2 gene expression and its prognostic significance in GC samples were analyzed. Analysis of 53BP1 foci at telomeres by immunofluorescence, metaphase spreads, and telomere-specific FISH analysis was carried out to explore telomere damage and dysfunction after TRF2 depletion. CCK8 cell proliferation, trypan blue staining, and colony formation assay were performed to evaluate cell survival. Apoptosis and cell migration were determined with flow cytometry and scratch-wound healing assay, respectively. qRT-PCR and Western blotting were carried out to analyze the mRNA and protein expression levels after TRF2 depletion on apoptosis, autophagic death, and ferroptosis. **Results.** By searching with GEPIA and TCGA databases, the results showed that the expression levels of TRF2 were obviously elevated in the samples of GC patients, which was associated with adverse prognosis. Knockdown of TRF2 suppressed the cell growth, proliferation, and migration in GC cells, causing significant telomere dysfunction. Apoptosis, autophagic death, and ferroptosis were also triggered in this process. The pretreatment of chloroquine (autophagy inhibitor) and ferrostatin-1 (ferroptosis inhibitor) improved the survival phenotypes of GC cells. **Conclusion.** Our data suggest that TRF2 depletion can inhibit cell growth, proliferation, and migration through the combined action of ferroptosis, autophagic death, and apoptosis in GC cells. The results indicate that TRF2 might be used as a potential target to develop therapeutic strategies for treating GC.

1. Introduction

Gastric cancer remains a significant clinical problem worldwide. With over 1 million estimated new cases in 2018, gastric cancer is the fifth most common cancer. Gastric cancer is estimated about 783,000 people deaths globally in 2018, making it the third leading cause of cancer-related death [1]. It is a molecularly and phenotypically highly heterogeneous disease [2]. Gastric cancer represents a major burden of society, and treatment of this disease needs to be improved [3]. For early-stage gastric cancer, there is a greater emphasis placed on the tumour resection. A comprehensive treatment approach including traditional radiotherapy and chemotherapy, targeted therapy, and immunotherapy was adopted for intermediate-stage gastric cancer. Targeted therapy combined with chemotherapy has become the first-line treatment guideline for advanced gastric cancer. The choice of targeted drugs for gastric cancer is relatively limited. Trastuzumab, a recombinant humanized IgG1 monoclonal antibody directed against the extracellular domain of HER2, is the only first-line targeted therapy drug. However, only 20% or less of gastric cancer patients are HER-2 positive [4, 5]. Although significant efforts have been made to treat gastric cancer effectively, the incidence and mortality of gastric cancer remain high. Individualized treatment strategies and deeper molecular mechanisms need to be explored [6, 7].

Telomeres, regions of repetitive DNA sequences at the ends of chromosomes, are composed of tandem DNA repeats and shelterin complexes [8]. Shelterin specifically binds to telomeric DNA and is composed of six proteins: TRF1, TRF2, RAP1, POT1, TIN2, and TPP1 [9]. The shelterin complex protects the ends of chromosomes from the DNA damage response (DDR) and maintains genome stability [10]. Maintaining the normal structure and function of telomeres plays a vital role in the stability of the genome. Telomere dysfunction can lead to genome disorders, which in turn lead to cell apoptosis. Researchers have paid increasing attention to the role of telomeres in tumours [11, 12]. The primary function of TRF2, one of the core proteins of shelterin, is to prevent telomeres from being recognized as double-strand breaks (DSBs) by promoting the formation of telomere terminal T loops, thereby maintaining the stable function of telomeres [13, 14]. It has been reported that inhibition of TRF2 leads to chromosome end fusion, growth arrest, and apoptosis [15, 16]. Apoptosis is a kind of programmed cell death that plays a key role in the physiology and pathophysiology of multicellular organisms [17]. TRF2 not only has telomere protection-related functions but also acts as a DNA damage repair factor to promote the survival of cancer cells. Hence, TRF2 has been considered a potential oncogene [18, 19]. A comprehensive and mechanistic understanding of the cellular impact of TRF2 is necessary for further exploration.

Ferroptosis is an iron-dependent form of regulated cell death characterized by mitochondrial shrinkage, iron accumulation, and excess lipid peroxidation [20]. Several studies have implicated the contribution of ferroptosis in the progression of multiple diseases [21], including gastric cancer [22]. Cystine uptake by the cystine/glutamate transporter

system xc⁻ represents the upstream event of ferroptosis under extracellular oxidative conditions [23]. p53 can enhance ferroptosis by inhibiting the expression of the cystine/glutamate antiporter SLC7A11 (also commonly known as xCT) or by enhancing the expression of SAT1 and GLS2 [24]. Tanshinone IIA was also found to upregulate p53 expression and downregulate xCT expression, thereby suppressing the proliferation of gastric cancer via inducing p53 upregulation-mediated ferroptosis [25]. TRF2 deletion provokes the induction of an acute DDR at telomeres, leading to the activation of p53 signalling pathways and programmed cell death [19]. However, whether TRF2 depletion causes ferroptosis in gastric cancer cells remains unclear.

Autophagy is a catabolic process in which cytoplasmic components are delivered to vacuoles or lysosomes for degradation and nutrient cycling [26]. This degradation process is critical to maintaining cellular homeostasis, as it rids the cell of either excess or damaged organelles, aggregated proteins, or pathogens [27]. However, excessive autophagy can inhibit the growth and proliferation of cells. The loss of autophagy function is necessary for cancer cell proliferation [28, 29]. Telomere dysfunction can cause cell autophagy through the cyclic GMP-AMP synthase-stimulator of interferon genes (cGAS-STING) signalling pathway. The G-quadruplex ligand SYUIQ-5 triggered potent telomere damage through TRF2 delocalization from telomeres and eventually induced autophagic cell death in cancer cells [30]. In our present study, we explored whether inhibiting the expression level of TRF2 in gastric cancer could limit the growth, proliferation, and migration of gastric cancer cells by inducing autophagic death.

Overall, we aimed to explore whether TRF2 depletion in gastric cancer cells could inhibit cell growth, proliferation, and migration through the combined action of ferroptosis, autophagic death, and apoptosis and whether inhibition of ferroptosis or autophagy would augment the recovery of cell growth, proliferation, and migration. These data will provide new targets and avenues for treating of gastric cancer.

2. Materials and Methods

2.1. Bioinformatics Analysis. The mRNA expression levels of TRF2 in normal tissues and gastric cancer tissues were searched in the GEPIA (<http://gepia.cancer-pku.cn/>) and TCGA (<http://portal.gdc.cancer.gov>) databases, respectively. The relationship between the expression level of TRF2 mRNA and the survival time of patients from which gastric cancer samples and normal samples were collected was determined using the cBioPortal database (<http://www.cbioportal.org/>), and the statistical significance was analyzed by GraphPad Prism 5 software. The STRING database (<http://string-db.org/>) was used to query the network of proteins interacting with TRF2, p53, SLC7A11, and glutathione peroxidase 4 (GPX4). The STRING database can be used to annotate the structure, function, and evolutionary properties of proteins. It can also explore and predict interacting protein networks and provide new research directions for future experiments.

2.2. Cell Culture and Plasmid Amplification. The human gastric cancer cell line BGC-823 was from ATCC. Cells were cultured in Dulbecco's modified Eagle's medium (DMEM; 06-1055-57-1ACS Biological Industries) supplemented with 10% foetal bovine serum (FBS; 04-001-1ACS, Biological Industries) in a humidified chamber with 5% CO₂ at 37°C. To establish a stable TRF2 knockdown cell line, lentiviruses carrying TRF2-targeting shRNA (GenePharma) were transduced into BGC-823 cells along with 5 µg/mL polybrene (H8761, Solarbio), and cells were selected for with 1 µg/mL puromycin (A1113803, Thermo Fisher). Plasmid transfection was carried out using PEI (919012-100MG, Sigma-Aldrich), as recommended by the manufacturer. TRF2 shRNA sequences were as follows: shRNATRF2-1 sense, 5'-CCGGGCGCATG ACAATAAGCAGATTCTCGAGAATCTGCTTATTGTCAT GCGCTTTTT-3', antisense, 5'-AATTA AAAAGCGCATG ACAATAAGCAGATTCTCGAG AATCTGCTTATTGTCATGCGC-3'; and shRNATRF2-2 sense, 5'-CCGGCATTGGA ATGATGACTCTGAACTCGAGTTCAGAGTCATCATTCC AATGTTTTT-3', antisense 5'-AA TTA AAAACATTGGAAT GATGACTCTGAACTCGAGTTCAGAGTCATCATTCCAA TG-3'. The TRF2 gene was amplified by PCR from the cDNA of BGC-823 cells. The PCR products were purified with a gel extraction kit (DP209-03, TIANGEN). Then, the restriction endonucleases EcoRI and AgeI were used to digest the purified products and the pLKO.1-TRC cloning vector. After purification, the products and vector were ligated using T4 DNA ligase (e0879, Takara). Finally, the plasmids were amplified in DH5α *E. coli* cells and identified by sequencing.

2.3. Quantitative Real-Time PCR (qRT-PCR). Total RNA was isolated using a total RNA extraction kit (DP419, TIANGEN) according to the manufacturer's instructions. One microgram of RNA was used as a template to synthesize cDNA using the GoScript Reverse Transcription System (PRA5000, Promega). All qPCRs were carried out using the Roche LightCycler System. The primers used in this study are from GenBank (<https://pga.mgh.harvard.edu/primerbank/index.html>) and are as follows: GAPDH, 5'-GTCTCCTCT GACTTCAACAGCG-3' and 5'-ACCACCCTGTTGCTGT AGCCAA-3'; TRF2, 5'-GTGGAAAAGCCACCCAGAGA AC-3' and 5'-TGCAAAGGCTGCCTCAGAATCC-3'; GPX4, 5'-ACAAGAACGGCTGCGTGTTGAA-3' and 5'-GCCACA CACTTGTGGAGCTAGA-3'; SLC7A11, 5'-TCCTGCTTT GGCTCCATGAACG-3' and 5'-AGAGGAGTGTGCTTGC GGACAT-3'; p62, 5'-ACGCAGAACAGAGTTACGAAGG C-3' and 5'-CCAGTCATCTTGTCCGTAGGCTTC-3'; and ATG5, 5'-GCAAGCCAAGGAGGAGAAGATTCC-3' and 5'-GTGTCTCAGCGAAGCAGTGTTG-3'. Each sample was assayed in triplicate.

Relative mRNA levels were determined using the 2^{-ΔΔCt} method.

2.4. Western Blotting. Cells were lysed in RIPA lysis buffer (R0020, Solarbio) supplemented with phosphatase inhibitor cocktail (4906837001, Roche) and protease inhibitor cocktail (11836170001, Roche). Protein contents were measured with

the BCA Protein Assay (23227, Thermo Fisher Scientific). Equal amounts of protein extracts were separated on an SDS-PAGE gel, followed by electrotransfer onto a PVDF membrane (EZWB05-ISEQ00010-1, Millipore). The blots were subsequently incubated for 2 h in a blocking buffer. The membranes were incubated at 4°C overnight with monoclonal antibodies, followed by corresponding secondary anti-rabbit or anti-mouse antibodies for 2 h. The antibodies used for Western blotting were as follows: SLC7A11 (A2413, ABclonal), GPX4 (A1933, ABclonal), ATG5 (10181-2-AP, Proteintech), LC3 (14600-1-AP, Proteintech), β-actin (81115-1-RR, Proteintech), GAPDH (10494-1-AP, Proteintech), TRF2 (22020-1-AP, Proteintech), secondary anti-rabbit antibody (SA00001-2, Proteintech), and anti-mouse antibodies (SA00001-1, Proteintech). The proteins were detected with ECL Blotting Detection Reagents (32106, Thermo Fisher Scientific).

2.5. Trypan Blue Staining. Cell activity was detected with trypan blue staining. In brief, the medium in six-well plates was discarded. Trypsin was added to digest the cells for 90 sec, and then, the trypsin was discarded. A total of 900 µL of complete medium and 100 µL of 0.4% trypan blue dye were added to the six-well plates; they were shaken well and then incubated for 3 minutes. Finally, 10 µL of the trypan blue cell suspension (C0040, Solarbio) was dropped onto a special cell counting plate, and the cells were counted under an ordinary light microscope (MARIENFELD). Cell viability was expressed as a percentage of the DMSO-treated control.

2.6. Cell Proliferation Assay with Cell Counting Kit-8 (CCK-8). A CCK-8 assay was used to evaluate cell proliferation. Cells were counted and seeded into 96-well plates. The Cell Counting Kit-8 (CCK-8; C3007, Beyotime Institute of Biotechnology) was used to determine the cell proliferation rate according to the manufacturer's instructions. Briefly, after 0, 24, 48, and 72 h of growth, the cells were incubated in CCK-8 reagent at 37°C for 2 h. Then, absorbance at 450 nm was measured using a microplate reader. Each test was repeated in triplicate under the same conditions.

2.7. Scratch-Wound Healing Assay. Three parallel lines were drawn across the bottom of the wells in a six-well plate, and the cells were spread onto the plates. The cells were scratched in the direction perpendicular to the drawn parallel lines using a 200 µL pipette tip. The old medium was discarded, and 1 mL PBS was added for washing. A total of 2 mL of serum-free medium was added, and then, the cells were observed and photographed with a fluorescence microscope. The scratch width was measured 48 h after the first scratch was made, and the healing percentage and scratch width recovery percentage between cells in each well were compared. The wound surface area was quantified by ImageJ software.

2.8. Colony Formation Analysis. BGC-823 cells were slowly washed twice with deionized water, then 4% tissue cell fixative (BL539A, Biosharp) was added, and the cell culture dish was allowed to stand for 20 min. The cells were washed with deionized water three times, a 0.5% crystal violet dye

solution (E607309-0100, Sangon Biotech) was added to completely infiltrate the cells, and the cells were allowed to stand at room temperature for 30 min. Deionized water was added, and the cell culture dish was slowly washed three times on a shaker for 2 min each time. Finally, the cell culture dish was placed upside down on filter paper, the water was drained, and the results were analyzed with ImageJ. Each experiment was repeated in triplicate under the same conditions.

2.9. Analysis of 53BP1 Foci at Telomeres by Immunofluorescence. BGC-823 cells were fixed with paraformaldehyde (E672002-0500, Sangon), washed, and permeabilized in 0.5% Triton X-100 (T8787-100ML, Sigma). After blocking, the cells were immunostained with 53BP1 antibody (1:1000; ab175933, Abcam) and then immunostained with Alexa Fluor 555-labeled anti-rabbit IgG fluorescent antibody (1:2000, ab150078, Abcam). Prepared PBST solution was added for washing, followed by dehydration with ethanol. Finally, 4',6-diamidino-2-phenylindole (DAPI; H-1200-10, Vectorlabs) was added and sealed, and the results were observed under a fluorescence microscope.

2.10. Metaphase Spreads and Telomere Fluorescence In Situ Hybridization (FISH) Analysis. Telomere dysfunction-induced foci (TIFs) were assessed by metaphase spreads and telomere-specific FISH to detect telomere dysfunction. Cy3-labeled telomere-specific peptide nucleic acid (PNA) was applied to the sample, denatured by incubation for 4 min at 83°C, and hybridized in the dark at room temperature for 2 hours. Slides were then rinsed in PBST, followed by the application of fluorescent secondary antibody conjugated to Alexa Fluor 488 (diluted 1:100; A11034, Life Technologies, Grand Island, NY) and incubation at room temperature for 30 min. Slides were then counterstained with DAPI, and the results were observed under a fluorescence microscope.

2.11. Cell Apoptosis Assay. An Annexin V-FITC and PI apoptosis detection kit (556547, BD Biosciences) was used according to the manufacturer's directions. Briefly, cells were resuspended at 1×10^5 cells/mL in 100 μ L of binding buffer. Annexin V-FITC (5 μ L) and PI (5 μ L and 20 μ g/mL) were added to the cell suspension, followed by incubation at room temperature for 10 minutes in the dark and then mixing with 1 mL of binding buffer. A total of 1×10^6 cells/sample was analyzed on a FACSCalibur.

2.12. Statistical Analysis. Each test in this study was repeated in triplicate under the same conditions. Quantitative data are expressed as means \pm SD of three independent experiments. Statistical significance was determined using one-way ANOVA and two-tailed Student's *t*-test. Data analysis was carried out using GraphPad Prism 7.0 (GraphPad Software). *P* values of < 0.05 were considered statistically significant.

3. Results

3.1. TRF2 Is an Oncogene in Gastric Cancer, and TRF2 Depletion Inhibits the Growth, Proliferation, and Migration of Gastric Cancer Cells. We used a bioinformatic method to

predict whether TRF2 could be used as an oncogene in gastric cancer. First, we compared the expression level of TRF2 mRNA between gastric cancer tissues and corresponding normal gastric mucosa tissues by searching the GEPIA and TCGA databases. As shown in Figures 1(a) and 1(b), TRF2 mRNA in gastric cancer tissues was significantly higher than in normal tissues. This finding indicates that TRF2 is overexpressed in gastric cancer. To predict whether TRF2 affects the survival and prognosis of patients with gastric cancer, we used the clinical information obtained from the cBioPortal database for survival analysis. As shown in Figure 1(c), the survival time of gastric cancer patients with low TRF2 mRNA expression was significantly longer than that of patients with high TRF2 expression.

Because we have demonstrated that TRF2 may be an important oncogene of gastric cancer using bioinformatic databases, we next explored the effects of TRF2 on the growth, proliferation, and migration of gastric cancer cells. We designed two plasmids containing different sequences of TRF2-shRNA and infected BGC-823 cells with these lentiviral vectors. To verify the efficiency of TRF2 knockdown by two plasmids, we conducted qRT-PCR and Western blot experiments. As shown in Figures 1(d) and 1(e), the expression levels of TRF2 mRNA and protein in the experimental group were significantly lower than those in the control group, which indicated that both plasmids could be used in subsequent molecular biology experiments. We compared the proliferation, survival, and migration of gastric cancer cells between the control group and the stable knockdown TRF2 group by CCK-8, colony formation, trypan blue staining, and scratch-wound healing assays. As shown in Figures 2(a) and 2(b), knockdown of TRF2 significantly inhibited the migration level of gastric cancer cells. The results in Figures 2(c)–2(e) show that knockdown of TRF2 could evidently restrict the growth and proliferation of gastric cancer cells. The results of the trypan blue staining assay (Figure 2(f)) showed that reducing the expression level of TRF2 in gastric cancers could obviously inhibit the viability of the cells. The above results suggest that specific knockdown of TRF2 has a remarkable inhibitory effect on the growth, proliferation, and migration of gastric cancer cells, and TRF2 may play an important role in the occurrence and development of gastric cancer.

3.2. TRF2 Knockdown in Gastric Cancer Cells Causes Telomere Dysfunction. TRF2 is one of the key telomere protection proteins. Telomere dysfunction caused by TRF2 inhibition in various types of cancer cells will activate the DDR, which will lead to abnormal telomere end signals [10, 11]. To determine whether knockdown of TRF2 leads to the same outcome in gastric cancer cells, we detected telomere dysfunction-induced foci (TIFs) in gastric cancer cells by immunofluorescence of 53BP1 foci at telomeres and telomere FISH assays. The results showed that knockdown of TRF2 significantly upregulated the colocalization of the DNA damage marker 53BP1 with telomeres (Figures 3(a) and 3(b)). The results of telomere-specific FISH (Figures 3(c) and 3(d)) showed that knockdown of TRF2 in gastric cancer cells could induce obvious abnormal signals at telomere ends,

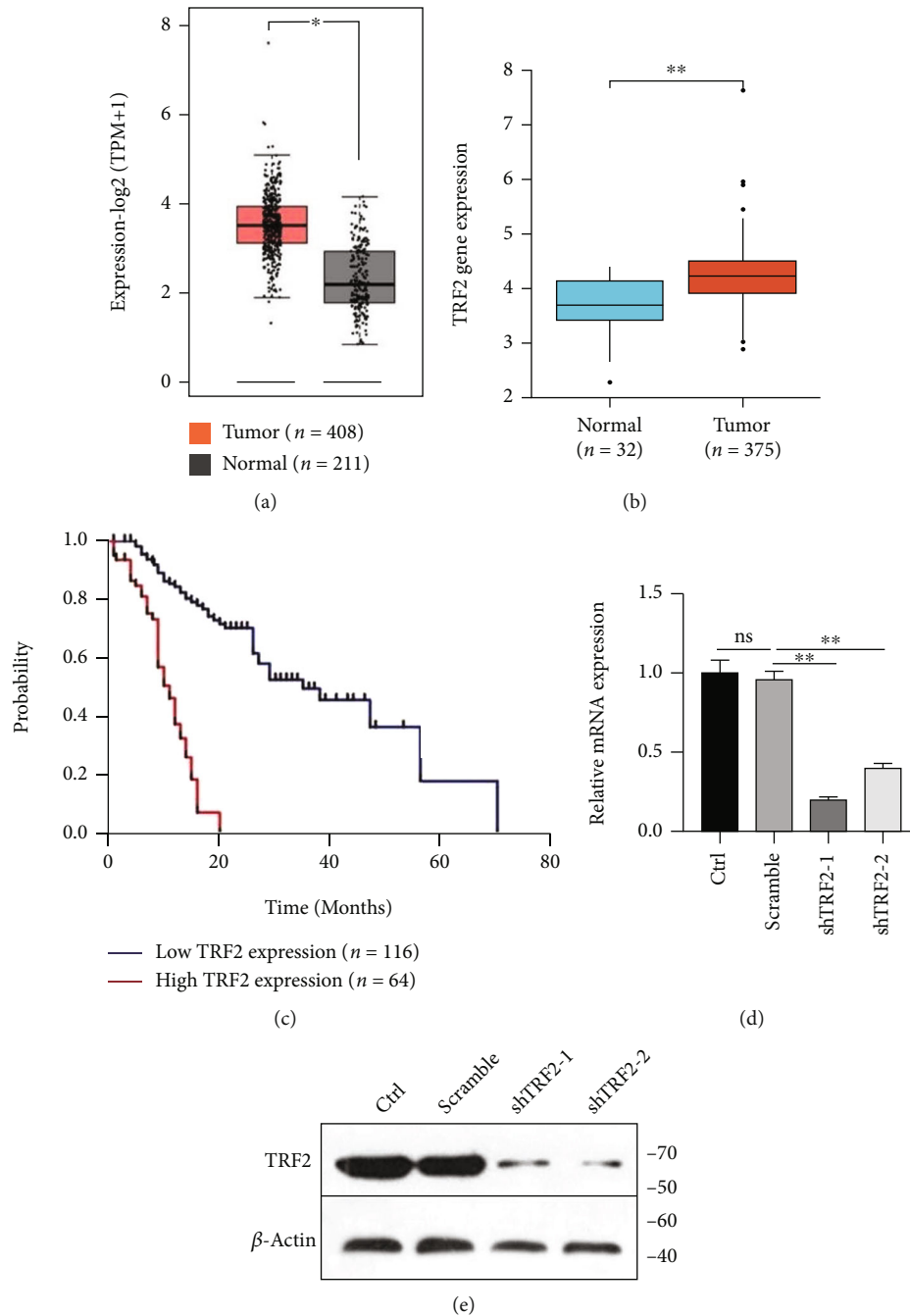


FIGURE 1: Analysis of TRF2 mRNA expression levels in gastric cancer using bioinformatic databases and TRF2 shRNA knockdown. (a, b) Box plots of the TRF2 mRNA expression levels in gastric cancer tissues and corresponding normal tissues obtained by searching the GEPIA database (a) and TCGA database (b). (c) Survival analysis of gastric cancer patients with high levels of TRF2 mRNA expression and with low levels of TRF2 mRNA expression. (d, e) TRF2 mRNA expression levels and protein expression levels in TRF2 shRNA-transfected cells and scramble shRNA control cells. Each test was repeated in triplicate under the same conditions, and representative data are shown. Comparisons were performed using Student's *t*-test and one-way ANOVA. ns: not significant. **P* < 0.05 and ***P* < 0.01.

including telomere signal free ends (SFEs) and multiple telomere signals (MTSs). Furthermore, the frequency of chromosome end-to-end fusions significantly increased was observed in depletion of TRF2. These results suggest that specific inhibition of TRF2 in gastric cancer cells can cause significant telomere dysfunction and chromosome end-to-end fusions.

3.3. Knockdown of TRF2 Promotes Autophagic Death and Apoptosis. It has been reported that telomere dysfunction can lead to autophagic death, apoptosis, and other forms of death. To further verify whether the telomere dysfunction caused by TRF2 knockdown in gastric cancer cells can induce autophagic death and apoptosis, we compared the

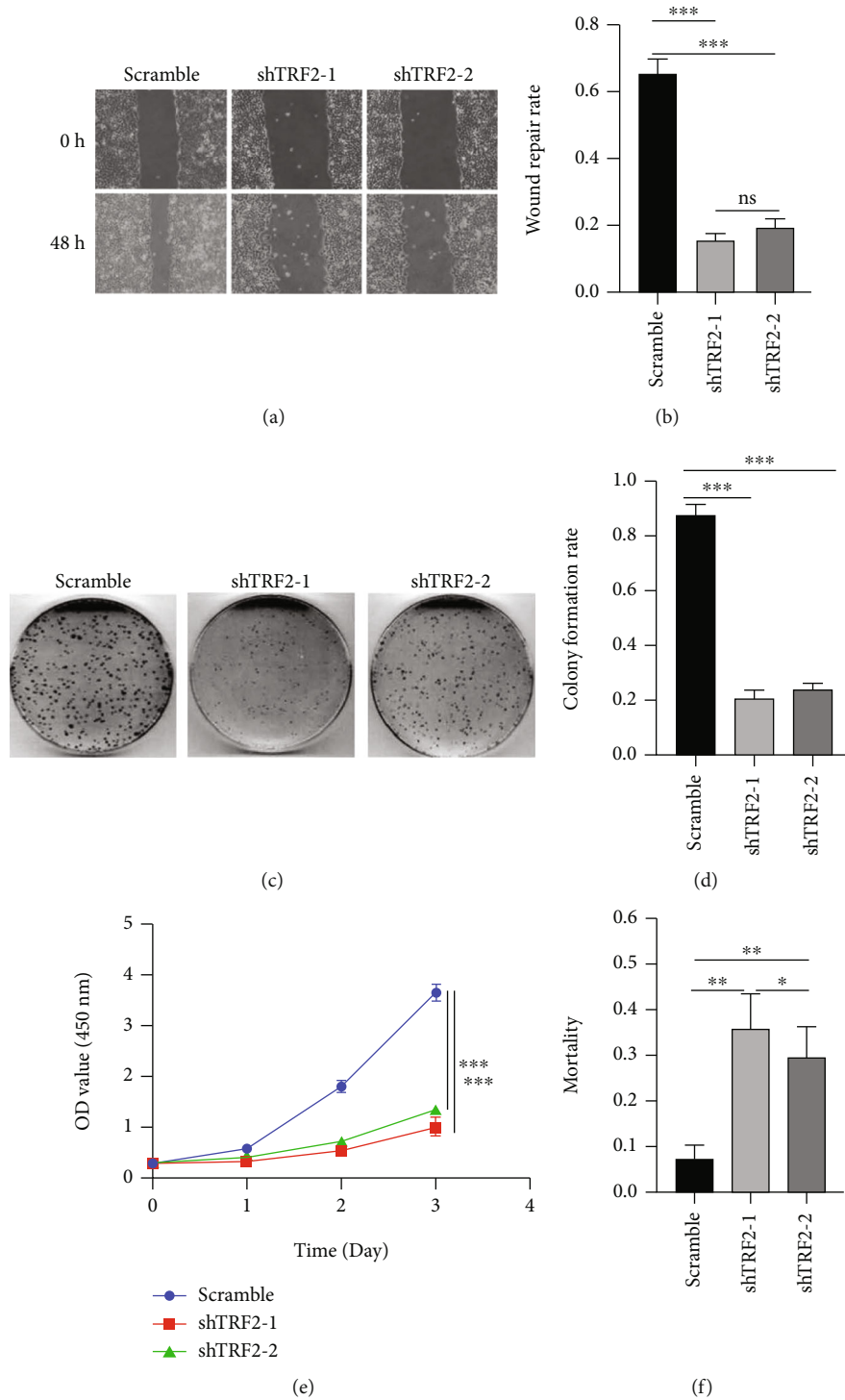


FIGURE 2: Effects of TRF2 knockdown on the growth, proliferation, and migration of gastric cancer cells. (a, b) The cell migration ability was detected by scratch-wound healing assays. (c, d) Cell proliferation was detected by colony formation assays. (e) CCK-8 assay growth curves of TRF2 knockdown cells and control cells. (f) Cell viability determined by the trypan blue staining assay. Each test was repeated in triplicate under the same conditions, and representative data are shown. Comparisons were performed using Student's *t*-test and one-way ANOVA. ns: not significant. * $P < 0.05$, ** $P < 0.01$, and *** $P < 0.001$.

levels of autophagy and apoptosis between control and TRF2 knockdown gastric cancer cells by qRT-PCR, Western blotting, and flow cytometry. The mRNA level of autophagy-related 5 (ATG5) was significantly increased, and p62 was

significantly decreased (Figure 4(a)) in the TRF2 knockdown cells. ATG5 is a molecule involved in the activated autophagy machinery, while decreased levels of p62, an autophagic flux marker, can be observed when autophagy is induced.

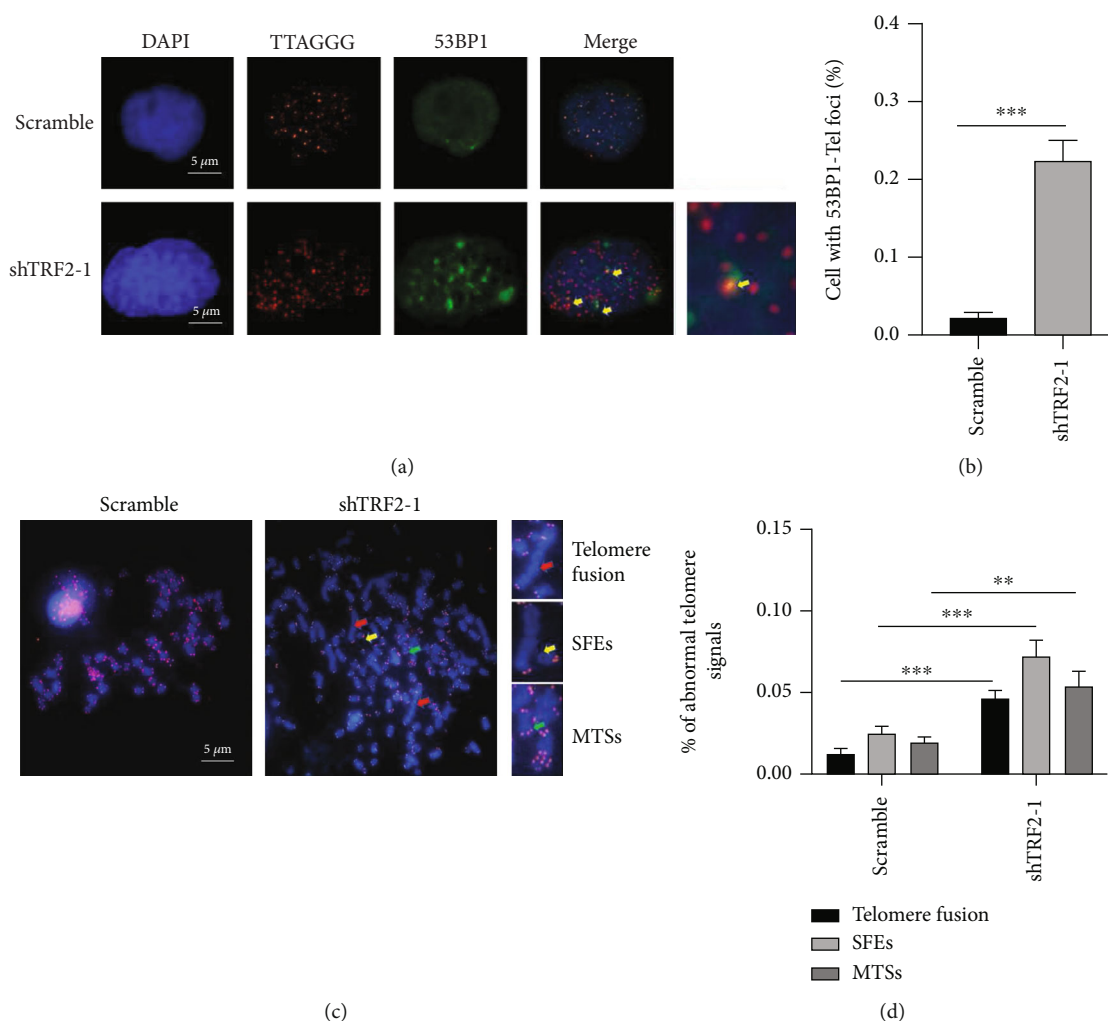


FIGURE 3: Effect of TRF2 knockdown on telomere dysfunction in gastric cancer cells. (a, b) Analysis of 53BP1 foci at telomeres by immunofluorescence. The red dots represent telomere signals, and the green dots represent 53BP1 signals. The yellow arrows represent 53BP1 foci at the telomeres. Scale bars, 5 μm . (c, d) The results of metaphase spreads and telomere fluorescence in situ hybridization (FISH) analyses. At least 10 mitotic phases were counted in each group, and the total number of chromosomes was more than 300. SFES: telomere signal free ends; MTSs: multiple telomere signals. Scale bars, 5 μm . Comparisons were performed using Student's *t*-test and one-way ANOVA. ns: not significant. ** $P < 0.01$ and *** $P < 0.001$.

The protein levels of LC3-II (phosphatidylethanolamine-conjugated form of MAP1LC3B) and ATG5 were significantly increased (Figure 4(b)) in the TRF2 knockdown cells. The quantitative analysis results showed that the expression of LC3 and ATG5 protein increased by more than 50% compared with the scramble group. Figures 4(c) and 4(d) show that TRF2 knockdown can also induce apoptosis. Therefore, these results show that telomere dysfunction caused by TRF2 inhibition can promote autophagic death and apoptosis in gastric cancer cells.

3.4. Inhibition of TRF2 Simultaneously Boosts Ferroptosis.

Ferroptosis is a new type of programmed cell death that is iron-dependent and different from apoptosis and autophagic death. The main sign of ferroptosis is the decreased expression of SLC7A11 and GPX4. A large number of studies have shown that p53 inhibits the expression of SLC7A11 and promotes ferroptosis. It is well known that telomere DNA dam-

age can activate p53 pathway. Therefore, to understand the relationship between TRF2, p53, and ferroptosis-related proteins (SLC7A11 and GPX4), the STRING database was used to analyze their protein interaction network. Some important proteins may play roles, including AURKA, BARD1, CDK2, CREBBP, DDX5, EP300, MDM2, RPA1, SIRT1, and UBE3A, which were found to be a part of the TRF2, p53, and ferroptosis-related protein network (Figure 5(a) and Table 1). To further clarify the effect of TRF2 knockdown on ferroptosis in gastric cancer cells, we measured the expression levels of ferroptosis-related markers in TRF2 knockdown gastric cancer cells at the mRNA and protein levels. As shown in Figures 5(b) and 5(c), knockdown of TRF2 significantly decreased the expression levels of SLC7A11 and GPX4 in gastric cancer cells. The quantitative analysis results showed that the expression of SLC7A11 and GPX4 protein decreased by more than 50% compared with the scramble group. These results suggest that depletion of TRF2 can facilitate ferroptosis in gastric cancer cells.

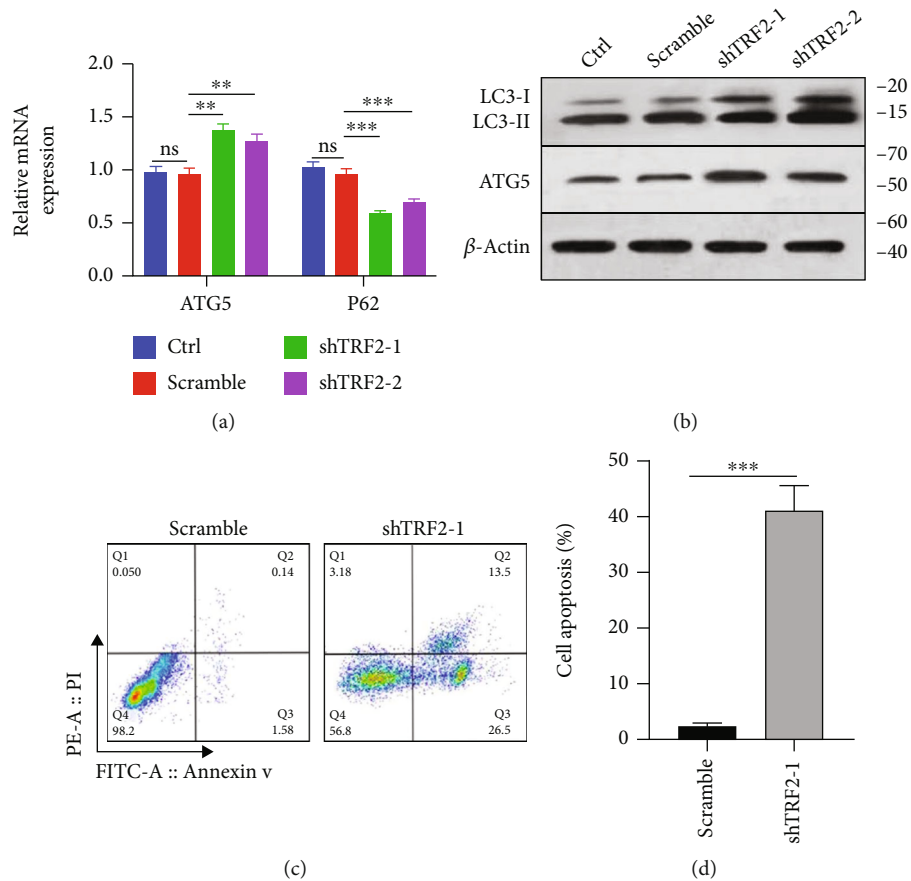


FIGURE 4: Effects of TRF2 knockdown on autophagy and apoptosis in gastric cancer cells. (a, b) The mRNA and protein expression levels of autophagy markers were measured by qRT-PCR and Western blotting, respectively. (c, d) The level of apoptosis was detected by flow cytometry. Each test was repeated in triplicate under the same conditions, and representative data are shown. Comparisons were performed using Student's *t*-test and one-way ANOVA. ns: not significant. ** $P < 0.01$ and *** $P < 0.001$.

3.5. Autophagic Death and Ferroptosis Inhibitors Restore the Inhibition of Cell Growth, Proliferation, and Migration Caused by TRF2 Depletion. To further prove that the decline in the growth, proliferation, and migration ability of gastric cancer cells caused by knockdown of TRF2 is related to autophagy and ferroptosis, we used chloroquine (CQ), an autophagy inhibitor, and ferrostatin-1 (Fer-1), a ferroptosis inhibitor, to pretreat TRF2 knockdown gastric cancer cells. The growth, proliferation, and migration of gastric cancer cells were detected by CCK-8, colony formation, and trypan blue staining assays. The results are shown in Figures 6(a)–6(f). Pretreatment with the autophagy inhibitor CQ and the ferroptosis inhibitor Fer-1 obviously reversed the inhibited growth, proliferation, and migration ability of gastric cancer cells induced by the knockdown of TRF2. Therefore, telomere dysfunction caused by knockdown of TRF2 can indeed inhibit gastric cancer cell growth and survival through the autophagic death and ferroptosis pathways.

4. Discussion

Gastric cancer is the most common malignant tumour of the digestive system, and gastric cancer mortality ranks among the top of all tumour types in China [31, 32]. To date, the

annual number of patients diagnosed with and dying of gastric cancer is still increasing, especially in patients with *Helicobacter pylori* infection [33]. Thus, there is an urgent need to develop effective therapies for gastric cancer. The role of telomeres in tumours has attracted increasing attention from researchers. The telomere protective protein shelterin maintains telomere stability and plays an important role in the occurrence and development of tumours. TRF2, one of the core components of shelterin, can protect telomeres and prevent telomere terminal fusion and the DDR. Inhibition of TRF2 can lead to apoptosis mediated by p53 and ATM [34]. The small molecules, curcucione C and quindoline derivative CK1-14, could induce telomeric DNA-damage response in cancer cells through inhibition of TRF2. These small molecules could inhibit tumour cell proliferation and cause cell cycle arrest, resulting in cell apoptosis [35, 36]. Lentiviral vectors and RNA interference technology determine the impact of targeted depletion of TRF2 on the proliferation and tumour-generating activity of human glioblastoma stem cells (GSCs). Targeting TRF2 significantly increased the survival of mouse bearing GSC xenografts [37]. In this regard, we explored the expression levels of TRF2 mRNA in gastric cancer by bioinformatic methods. Our results showed that the mRNA expression

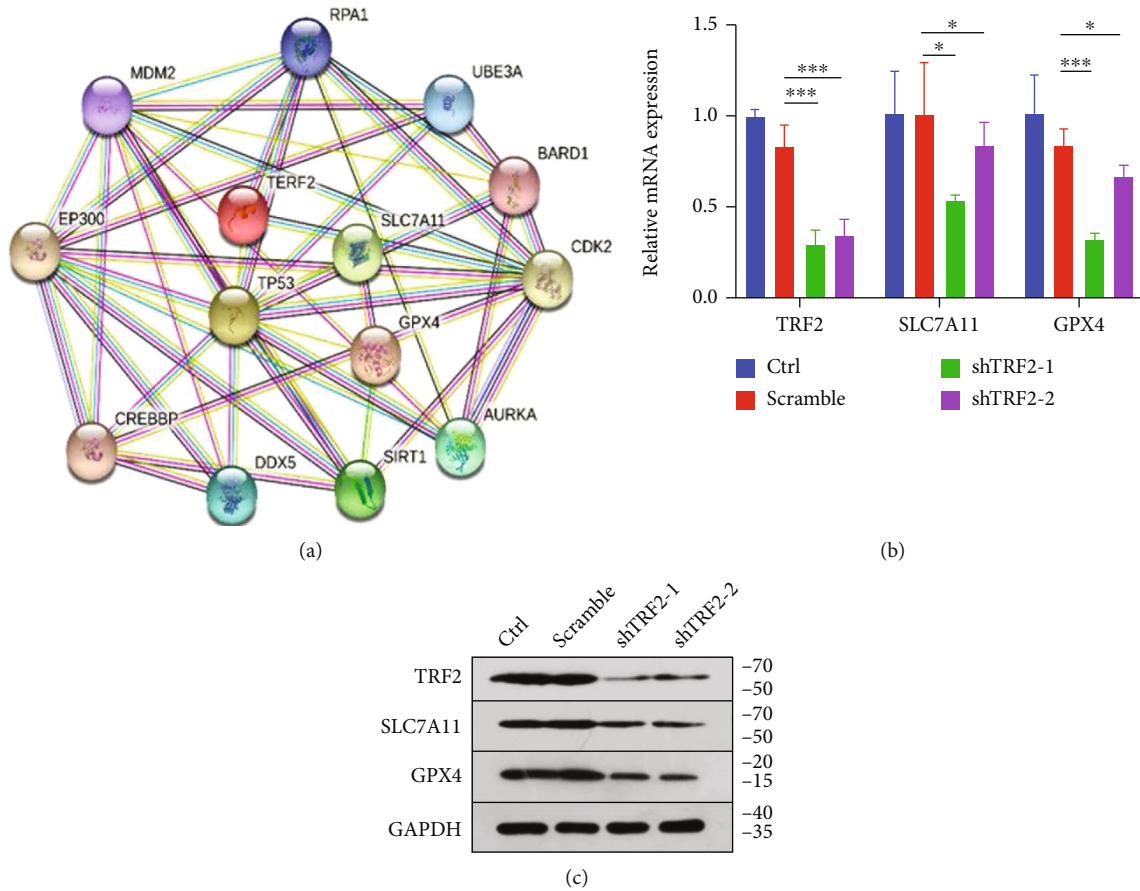


FIGURE 5: Effects of TRF2 knockdown on ferroptosis in gastric cancer cells. (a) The TRF2, p53, and ferroptosis-related protein interaction network was determined using the STRING database. (b, c) The mRNA and protein expression levels of ferroptosis markers were measured by qRT-PCR and Western blotting, respectively. Each test was repeated in triplicate under the same conditions, and representative data are shown. Comparisons were performed using Student's *t*-test and one-way ANOVA. ns: not significant. * $P < 0.05$ and *** $P < 0.001$.

TABLE 1: List of proteins in TRF2-p53-SLC7A11-GPX4 interaction network.

Abbreviation of gene	Full name of gene*
AURKA	Aurora kinase A
BARD1	BRCA1-associated RING domain protein 1
CDK2	Cyclin-dependent kinase 2
CREBBP	CREB-binding protein
DDX5	DEAD-box helicase 5
EP300	E1A-binding protein P300
GPX4	Glutathione peroxidase 4
MDM2	MDM2 protooncogene
RPA1	Replication protein A1
SIRT1	NAD-dependent protein deacetylase sirtuin-1
SLC7A11	Solute carrier family 7 (Xc-system), member 11
TERF2	Telomeric repeat-binding factor 2
TP53	Tumour protein P53
UBE3A	Ubiquitin-protein ligase E3A

*The full names of genes are from the GeneCards database (<http://www.genecards.org>).

levels of TRF2 in gastric cancer samples were higher than those in healthy controls. The survival time of patients with high TRF2 expression was shorter than that of patients with low TRF2 expression. We found that knockdown of TRF2 could inhibit gastric cancer cell growth, proliferation, and migration. These data suggest that TRF2 might promote the progression of gastric cancer.

Apoptosis is a type of programmed cell death that plays key roles in the physiology and pathophysiology of multiple cellular organisms [17]. Knockdown of TRF2 in healthy T cells increased in telomeric DNA damage and T cell apoptosis. In contrast, overexpression of TRF2 in HCV T cells alleviated telomeric DNA damage and T cell apoptosis [38]. Our present research found that knockdown of TRF2 significantly exacerbated apoptosis in gastric cancer cells.

Autophagy is usually described as a double-edged sword in different states of cancer. Cytoprotective autophagy can provide cancer cells with the ability to resist injury. Conversely, cytotoxic autophagy is considered an independent mechanism of cell death [39], and that excessive stimulation of autophagy through overexpression of beclin1 suppresses tumorigenesis [40]. The activation of autophagy is critical for cell death, as its suppression promotes bypass of crisis, continued proliferation, and accumulation of genome

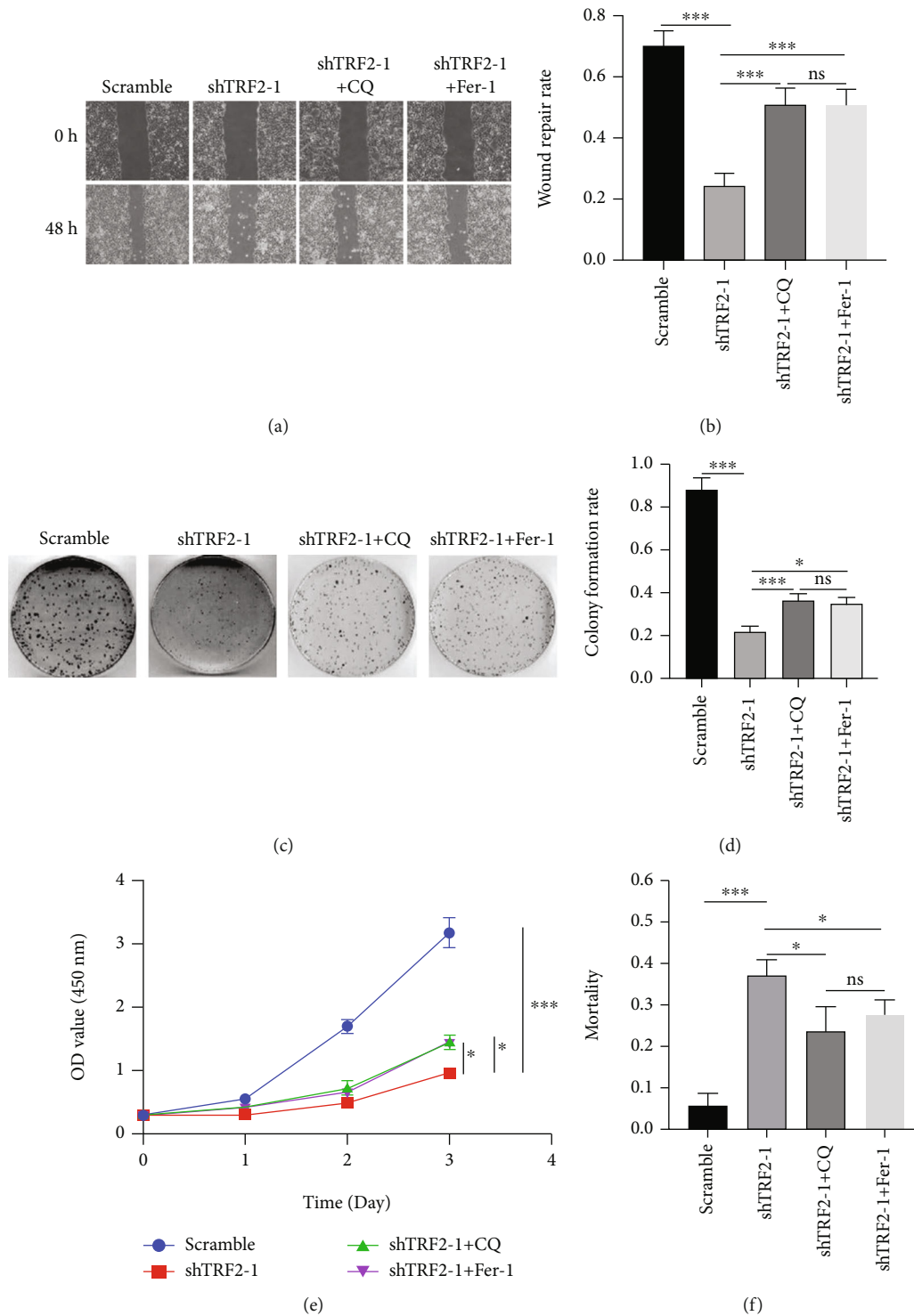


FIGURE 6: Effects of pretreatment with autophagy and ferroptosis inhibitors on the growth, proliferation, and migration of TRF2 knockdown gastric cancer cells. (a, b) The cell migration ability was detected by scratch-wound healing assays. (c, d) Cell proliferation was detected by colony formation assays. (e) CCK-8 assay growth curves of TRF2 knockdown cells and control cells. (f) Cell viability determined by the trypan blue staining assay. Each test was repeated in triplicate under the same conditions, and representative data are shown. CQ: chloroquine; Fer-1: ferrostatin-1. Comparisons were performed using Student's *t*-test and one-way ANOVA. ns: not significant; * $P < 0.05$ and *** $P < 0.001$.

instability. Prolonged stress and progressive autophagy can also eventually lead to cell death [41]. Telomere dysfunction specifically triggers autophagy, indicating that the telomere-

driven autophagy pathway is not induced by intrachromosomal breaks. Telomeric DNA damage generates cytosolic DNA species with fragile nuclear envelopes. The cytosolic

chromatin fragments activate the cGAS-STING pathway and engage the autophagy machinery [42]. Telomere deprotection by TRF2 depletion was sufficient to activate autophagy independently of replicative crisis [43]. Our present research found that inhibition of TRF2 in gastric cancer cells could significantly increase the expression of autophagy markers (ATG5 and LC3-II) and decrease the expression of the autophagic flux marker p62, indicating that TRF2 deficiency facilitated the process of autophagy in gastric cancer cells. Additionally, pretreatment with chloroquine significantly reversed the inhibition of cell growth, proliferation, and migration caused by the knockdown of TRF2, which helped us to confirm that autophagy was occurring. Our study also found that knockdown of TRF2 could induce significant telomere dysfunction. Therefore, we speculated that TRF2 deficiency-induced telomere dysfunction might trigger autophagic death, which depends on the activation of the cGAS-STING pathway. However, a more detailed connection between autophagic death and TRF2 still needs further investigation.

Ferroptosis is a novel form of cell death discovered in recent years. An increasing number of studies have shown that promoting ferroptosis is a new way to inhibit the growth of cancer cells [44]. Activation of p53 signalling pathway can promote ferroptosis by repressing the expression of SLC7A11 [45], and telomere dysfunction inevitably activates the p53 signalling pathway [46]. However, it is unclear whether telomere damage in cancer cells promotes ferroptosis through the p53 signalling pathway. Therefore, we used gastric cancer cells as a model to investigate this; we inhibited the expression of TRF2 and then measured the mRNA and protein expression levels of the ferroptosis biomarkers. Our results showed that knockdown of TRF2 in gastric cancer cells resulted in the downregulation of SLC7A11 and GPX4 expressions at the mRNA and protein levels, while the expression of SLC7A11 and GPX4 recovered after pretreatment with the ferroptosis inhibitor ferrostatin-1. Therefore, we believe that inhibition of TRF2 in gastric cancer cells can induce ferroptosis. Additionally, pretreatment with the ferroptosis inhibitor Fer-1 significantly reversed the inhibition of cell growth, proliferation, and migration caused by the knockdown of TRF2, which helped us confirm that ferroptosis was occurring. Next, we wanted to determine whether p53 signalling pathway-mediated ferroptosis was caused by the inhibition of TRF2 in gastric cancer cells. To further study the interaction relationship between TRF2, p53, and SLC7A11, the STRING database was used to analyze their protein interaction network. We found twelve proteins (MDM2, RPA1, UBE3A, EP300, TERF2, BARD1, TP53, GPX4, CREBBP, CDK2, DDX5, and SIRT1) involved in the TRF2, p53, and SLC7A11 protein networks. Based on these results, we speculated that p53-dependent telomere dysfunction might be the bridge mediating the regulation of ferroptosis by TRF2 depletion. The specific mechanism between them needs further investigation in future research.

5. Conclusions

In conclusion, we found that TRF2 depletion in gastric cancer cells can inhibit cell growth, proliferation, and migration

through the combined action of ferroptosis, autophagic death, and apoptosis, and inhibition of ferroptosis or autophagic death would augment the recovery of cell growth, proliferation, and migration. Our study provides new ideas for the role of telomere protective protein TRF2 in gastric cancer cells, deepens our understanding of the molecular mechanisms underlying the occurrence and development of gastric cancer, and provides new strategies for the treatment of gastric cancer.

Data Availability

The data used to support the findings of this study are available from the corresponding authors upon request.

Conflicts of Interest

The authors declare that there is no conflict of interest regarding the publication of this paper.

Authors' Contributions

Qihui Yang, Ziyang Nie, and Yukun Zhu contributed equally to this work.

Acknowledgments

This work was supported by the Chinese National Natural Science Foundation Grants (nos. 82271265 and 81771135), Research Project of Tianjin Education Commission (2021ZD037), Tianjin Natural Science Grant (no. 19JCQJC63500), Training Program for Young and Middle-Aged Key Innovative Personnel (no. 303078100407), Tianjin Key Medical Discipline (Specialty) Construction Project, and Scientific Research Project of Higher Education in Anhui Province (no. 2022AH050753).

References

- [1] F. Bray, J. Ferlay, I. Soerjomataram, R. L. Siegel, L. A. Torre, and A. Jemal, "Global Cancer Statistics 2018: GLOBOCAN estimates of incidence and mortality worldwide for 36 cancers in 185 countries," *CA: a Cancer Journal for Clinicians*, vol. 68, no. 6, pp. 394–424, 2018.
- [2] E. C. Smyth, M. Nilsson, H. I. Grabsch, N. C. T. van Grieken, and F. Lordick, "Gastric cancer," *The Lancet*, vol. 396, no. 10251, pp. 635–648, 2020.
- [3] F. M. Johnston and M. Beckman, "Updates on management of gastric cancer," *Current Oncology Reports*, vol. 21, no. 8, p. 67, 2019.
- [4] E. Bollschweiler, F. Berlth, C. Baltin, S. Mönig, and A. H. Hölscher, "Treatment of early gastric cancer in the Western World," *World Journal of Gastroenterology*, vol. 20, no. 19, pp. 5672–5678, 2014.
- [5] Y. Wang, L. Zhang, Y. Yang, S. Lu, and H. Chen, "Progress of gastric cancer surgery in the era of precision medicine," *International Journal of Biological Sciences*, vol. 17, no. 4, pp. 1041–1049, 2021.
- [6] Y. Wang, J. H. Lu, F. Wang et al., "Inhibition of fatty acid catabolism augments the efficacy of oxaliplatin-based chemotherapy in gastrointestinal cancers," *Cancer Letters*, vol. 473, pp. 74–89, 2020.

- [7] M. Mare, L. Memeo, C. Colarossi, and D. Giuffrida, "Third- and late line treatments of metastatic gastric cancer: still more to be done," *Current Oncology*, vol. 29, no. 9, pp. 6433–6444, 2022.
- [8] T. de Lange, "Shelterin: the protein complex that shapes and safeguards human telomeres," *Genes & Development*, vol. 19, no. 18, pp. 2100–2110, 2005.
- [9] E. Lazzarini-Denchi and A. Sfeir, "Stop pulling my strings – what telomeres taught us about the DNA damage response," *Nature Reviews. Molecular Cell Biology*, vol. 17, no. 6, pp. 364–378, 2016.
- [10] L. Xu, S. Li, and B. A. Stohr, "The role of telomere biology in cancer," *Annual Review of Pathology*, vol. 8, no. 1, pp. 49–78, 2013.
- [11] P. Martinez, M. Thanasoula, A. R. Carlos et al., "Mammalian Rap1 controls telomere function and gene expression through binding to telomeric and extratelomeric sites," *Nature Cell Biology*, vol. 12, no. 8, pp. 768–780, 2010.
- [12] S. Kabir, A. Sfeir, and T. de Lange, "Taking apart Rap1: an adaptor protein with telomeric and non-telomeric functions," *Cell Cycle*, vol. 9, no. 20, pp. 4061–4067, 2010.
- [13] N. Huda, S. Abe, L. Gu, M. S. Mendonca, S. Mohanty, and D. Gilley, "Recruitment of TRF2 to laser-induced DNA damage sites," *Free Radical Biology & Medicine*, vol. 53, no. 5, pp. 1192–1197, 2012.
- [14] P. S. Bradshaw, D. J. Stavropoulos, and M. S. Meyn, "Human telomeric protein TRF2 associates with genomic double-strand breaks as an early response to DNA damage," *Nature Genetics*, vol. 37, no. 2, pp. 193–197, 2005.
- [15] A. Smogorzewska and T. de Lange, "Different telomere damage signaling pathways in human and mouse cells," *The EMBO Journal*, vol. 21, no. 16, pp. 4338–4348, 2002.
- [16] E. L. Denchi and T. de Lange, "Protection of telomeres through independent control of ATM and ATR by TRF2 and POT1," *Nature*, vol. 448, no. 7157, pp. 1068–1071, 2007.
- [17] V. Shahin, "Strategic disruption of nuclear pores structure, integrity and barrier for nuclear apoptosis," *Seminars in Cell & Developmental Biology*, vol. 68, pp. 85–90, 2017.
- [18] S. A. M. Imran, M. D. Yazid, W. Cui, and Y. Lokanathan, "The intra- and extra-telomeric role of TRF2 in the DNA damage response," *International Journal of Molecular Sciences*, vol. 22, no. 18, p. 9900, 2021.
- [19] M. Bellon, A. Datta, M. Brown et al., "Increased expression of telomere length regulating factors TRF1, TRF2 and TIN2 in patients with adult T-cell leukemia," *International Journal of Cancer*, vol. 119, no. 9, pp. 2090–2097, 2006.
- [20] J. Luoqian, W. Yang, X. Ding et al., "Ferroptosis promotes T-cell activation-induced neurodegeneration in multiple sclerosis," *Cellular & Molecular Immunology*, vol. 19, no. 8, pp. 913–924, 2022.
- [21] B. R. Stockwell, X. Jiang, and W. Gu, "Emerging mechanisms and disease relevance of ferroptosis," *Trends in Cell Biology*, vol. 30, no. 6, pp. 478–490, 2020.
- [22] X. Jiang, Q. Yan, L. Xie et al., "Construction and validation of a ferroptosis-related prognostic model for gastric cancer," *Journal of Oncology*, vol. 2021, Article ID 6635526, 14 pages, 2021.
- [23] C. Liang, X. Zhang, M. Yang, and X. Dong, "Recent progress in ferroptosis inducers for cancer therapy," *Advanced Materials*, vol. 31, no. 51, article e1904197, 2019.
- [24] Y. Su, B. Zhao, L. Zhou et al., "Ferroptosis, a novel pharmacological mechanism of anti-cancer drugs," *Cancer Letters*, vol. 483, pp. 127–136, 2020.
- [25] Z. Guan, J. Chen, X. Li, and N. Dong, "Tanshinone IIA induces ferroptosis in gastric cancer cells through p53-mediated SLC7A11 down-regulation," *Bioscience Reports*, vol. 40, no. 8, 2020.
- [26] C. Xu and J. Fan, "Links between autophagy and lipid droplet dynamics," *Journal of Experimental Botany*, vol. 73, pp. 2848–2858, 2022.
- [27] A. L. Anding and E. H. Baehrecke, "Cleaning house: selective autophagy of organelles," *Developmental Cell*, vol. 41, no. 1, pp. 10–22, 2017.
- [28] E. White and R. S. DiPaola, "The double-edged sword of autophagy modulation in cancer," *Clinical Cancer Research*, vol. 15, no. 17, pp. 5308–5316, 2009.
- [29] G. Kroemer and B. Levine, "Autophagic cell death: the story of a misnomer," *Nature Reviews. Molecular Cell Biology*, vol. 9, no. 12, pp. 1004–1010, 2008.
- [30] W. J. Zhou, R. Deng, X. Y. Zhang, G. K. Feng, L. Q. Gu, and X. F. Zhu, "G-quadruplex ligand SYUIQ-5 induces autophagy by telomere damage and TRF2 delocalization in cancer cells," *Molecular Cancer Therapeutics*, vol. 8, no. 12, pp. 3203–3213, 2009.
- [31] A. Ferro, B. Peleteiro, M. Malvezzi et al., "Worldwide trends in gastric cancer mortality (1980–2011), with predictions to 2015, and incidence by subtype," *European Journal of Cancer*, vol. 50, no. 7, pp. 1330–1344, 2014.
- [32] M. Arnold, S. P. Moore, S. Hassler, L. Ellison-Loschmann, D. Forman, and F. Bray, "The burden of stomach cancer in indigenous populations: a systematic review and global assessment," *Gut*, vol. 63, no. 1, pp. 64–71, 2014.
- [33] S. N. Thibodeau, A. J. French, P. C. Roche et al., "Altered expression of hMSH2 and hMLH1 in tumors with microsatellite instability and genetic alterations in mismatch repair genes," *Cancer Research*, vol. 56, no. 21, pp. 4836–4840, 1996.
- [34] J. Karlseder, D. Broccoli, Y. Dai, S. Hardy, and T. de Lange, "p53- and ATM-dependent apoptosis induced by telomeres lacking TRF2," *Science*, vol. 283, no. 5406, pp. 1321–1325, 1999.
- [35] M. Wang, J. Cao, J. Y. Zhu et al., "Curcucione C induces telomeric DNA-damage response in cancer cells through inhibition of telomeric repeat factor 2," *Biochim Biophys Acta Proteins Proteom*, vol. 1865, no. 11, pp. 1372–1382, 2017.
- [36] Y. Zhang, D. Zeng, J. Cao et al., "Interaction of quindoline derivative with telomeric repeat-containing RNA induces telomeric DNA-damage response in cancer cells through inhibition of telomeric repeat factor 2," *Biochimica et Biophysica Acta - General Subjects*, vol. 1861, no. 12, pp. 3246–3256, 2017.
- [37] Y. Bai, J. D. Lathia, P. Zhang, W. Flavahan, J. N. Rich, and M. P. Mattson, "Molecular targeting of TRF2 suppresses the growth and tumorigenesis of glioblastoma stem cells," *Glia*, vol. 62, no. 10, pp. 1687–1698, 2014.
- [38] P. Solek, N. Shemedyuk, A. Shemedyuk, E. Dudzinska, and M. Koziorowski, "Risk of wild fungi treatment failure: *Phallus impudicus* -induced telomere damage triggers p21/p53 and p16-dependent cell cycle arrest and may contribute to male fertility reduction in vitro," *Ecotoxicology and Environmental Safety*, vol. 209, article 111782, 2021.
- [39] I. Ulasov, J. Fares, P. Timashev, and M. S. Lesniak, "Editing cytoprotective autophagy in glioma: an unfulfilled potential for therapy," *Trends in Molecular Medicine*, vol. 26, no. 3, pp. 252–262, 2020.
- [40] X. H. Liang, S. Jackson, M. Seaman et al., "Induction of autophagy and inhibition of tumorigenesis by beclin 1," *Nature*, vol. 402, no. 6762, pp. 672–676, 1999.

- [41] R. Mathew, V. Karantza-Wadsworth, and E. White, "Role of autophagy in cancer," *Nature Reviews. Cancer*, vol. 7, no. 12, pp. 961–967, 2007.
- [42] J. Nassour, R. Radford, A. Correia et al., "Autophagic cell death restricts chromosomal instability during replicative crisis," *Nature*, vol. 565, no. 7741, pp. 659–663, 2019.
- [43] E. Zlotorynski, "Telomere crisis activates autophagic death," *Nature Reviews. Molecular Cell Biology*, vol. 20, no. 3, p. 133, 2019.
- [44] J. Yang, Y. Zhou, S. Xie et al., "Metformin induces ferroptosis by inhibiting UFMylation of SLC7A11 in breast cancer," *Journal of Experimental & Clinical Cancer Research*, vol. 40, no. 1, p. 206, 2021.
- [45] L. Jiang, N. Kon, T. Li et al., "Ferroptosis as a p53-mediated activity during tumour suppression," *Nature*, vol. 520, no. 7545, pp. 57–62, 2015.
- [46] E. Sahin, S. Colla, M. Liesa et al., "Telomere dysfunction induces metabolic and mitochondrial compromise," *Nature*, vol. 470, no. 7334, pp. 359–365, 2011.

Research Article

Long Noncoding RNA LINC00578 Inhibits Ferroptosis in Pancreatic Cancer via Regulating SLC7A11 Ubiquitination

Haoran Li ¹, Yijun Wei ², Jie Wang ¹, Jun Yao ², Chen Zhang ¹, Chengqing Yu ¹,
Yuchen Tang ¹, Dongming Zhu ¹, Jian Yang ¹ and Jian Zhou ¹

¹Department of General Surgery, The First Affiliated Hospital of Soochow University, Suzhou, Jiangsu 215006, China

²Department of General Surgery, The Dushu Lake Hospital Affiliated to Soochow University, Suzhou, Jiangsu 215006, China

Correspondence should be addressed to Jian Yang; yangjian38850@suda.edu.cn and Jian Zhou; zhoujian06@suda.edu.cn

Received 30 August 2022; Revised 27 September 2022; Accepted 28 January 2023; Published 14 February 2023

Academic Editor: Lianxiang Luo

Copyright © 2023 Haoran Li et al. This is an open access article distributed under the Creative Commons Attribution License, which permits unrestricted use, distribution, and reproduction in any medium, provided the original work is properly cited.

Background. Pancreatic cancer is a highly aggressive malignancy worldwide with rapid development and an exceedingly poor prognosis. lncRNAs play crucial roles in regulating the biological behaviors of tumor cells. In this study, we discovered that LINC00578 acted as a regulator of ferroptosis in pancreatic cancer. **Methods.** A series of loss- and gain-of-function experiments in vitro and in vivo were performed to explore the oncogenic role of LINC00578 in pancreatic cancer development and progression. Label-free proteomic analysis was performed to select LINC00578-related differentially expressed proteins. Pull-down and RNA immunoprecipitation assays were carried out to determine and validate the binding protein of LINC00578. Coimmunoprecipitation assays were used to investigate the association of LINC00578 with SLC7A11 in ubiquitination and to confirm the interaction between ubiquitin-conjugating enzyme E2 K (UBE2K) and SLC7A11. An immunohistochemical assay was used to confirm the correlation between LINC00578 and SLC7A11 in the clinic. **Results.** LINC00578 positively regulated cell proliferation and invasion in vitro and tumorigenesis in vivo in pancreatic cancer. LINC00578 can obviously inhibit ferroptosis events, including cell proliferation, reactive oxygen species (ROS) generation, and mitochondrial membrane potential (MMP) depolarization. In addition, the LINC00578-induced inhibitory effect on ferroptosis events was rescued by SLC7A11 knockdown. Mechanistically, LINC00578 directly binds UBE2K to decrease the ubiquitination of SLC7A11, thus accelerating SLC7A11 expression. In the clinic, LINC00578 is closely associated with clinicopathologic factors and poor prognosis and correlated with SLC7A11 expression in pancreatic cancer. **Conclusions.** This study elucidated that LINC00578 acts as an oncogene to promote pancreatic cancer cell progression and suppress ferroptosis by directly combining with UBE2K to inhibit the ubiquitination of SLC7A11, which provides a promising option for the diagnosis and treatment of pancreatic cancer.

1. Introduction

Pancreatic cancer is a highly aggressive malignancy worldwide with rapid development and an extremely poor prognosis. It is currently regarded as the fourth leading cause of cancer mortality and is expected to be the second leading cause in 2030 [1]. The high mortality of pancreatic cancer is predominantly due to a lack of screening and diagnosis methods, low resection rates, and insensitivity to chemotherapy and radiotherapy [2]. Therefore, further exploration and understanding of the underlying specific molecular mechanisms of pancreatic cancer progression are of great necessity.

Long noncoding RNAs (lncRNAs) are RNA molecules with transcript lengths longer than 200 nucleotides that are generally considered to be without the potential to encode proteins. Many studies have proven the crucial roles of lncRNAs in modulating biological activities in cancer cells, including cell proliferation, invasion, ferroptosis, and apoptosis [3–5]. Recently, the mechanisms by which lncRNAs fulfill their tumor-suppressing and tumor-driving functions in pancreatic cancer have attracted considerable attention. LINC00578, a newly identified lncRNA, was found to be associated with prognosis in lung cancer and breast cancer [6, 7]. In addition, another study indicated that LINC00578

is upregulated and could be a prognostic signature in pancreatic cancer [8]. Nevertheless, the concrete mechanisms of LINC00578 in pancreatic cancer development and metastasis remain to be elucidated.

Ferroptosis is a novel cell death modality that is triggered by intracellular iron-dependent phospholipid peroxidation. To date, ferroptosis has been found in a variety of cancer cells, including hepatocellular cancer cells, breast cancer cells, and pancreatic cancer cells. Solute carrier family 7 member 11 (SLC7A11), a critical regulator of ferroptosis, functions to import cystine for glutathione biosynthesis and antioxidant defense, thus inhibiting ferroptosis. SLC7A11 overexpression promotes phospholipid peroxidation, which inhibits ferroptosis events in various tumor cells [9–11]. Mounting studies have illustrated that lncRNAs are involved in cancer progression by regulating ferroptosis events. For example, the lncRNA OIP5-AS1-induced inhibitory effect on ferroptosis promotes prostate cancer progression through the miR-128-3p/SLC7A11 pathway [12]. lncRNA MT1DP promotes erastin-induced ferroptosis in lung cancer cells via MT1DP/miR-365a-3p/NRF2 signaling [13]. Intriguingly, chemotherapy-resistant cancer cells, especially those prone to metastasis, are very susceptible to ferroptosis [14]. Notably, although ferroptosis-related lncRNAs have been indicated as prognostic markers in pancreatic cancer, no studies have reported on the role of ferroptosis in the regulation of pancreatic cancer cell progression by lncRNAs.

In our study, the effect of LINC00578 on the development and metastasis of pancreatic cancer was determined. We also explored the role of ferroptosis in regulating pancreatic cancer cell development and invasion by LINC00578. Furthermore, we mechanistically explored whether LINC00578 inhibits ferroptosis in pancreatic cancer cells by reducing ubiquitin-conjugating enzyme 2K- (UBE2K-) mediated SLC7A11 degradation. To conclude, our study will provide vital theoretical evidence for explaining the mechanisms by which LINC00578 inhibits ferroptosis in pancreatic cancer and will provide a novel target for the diagnosis and treatment of pancreatic cancer.

2. Materials and Methods

2.1. Cell Culture and Treatment. The human pancreatic cancer cell lines PL45 and PATU8988 were delivered from the Chinese Academy of Sciences (Shanghai, China). The PL45 and PATU8988 cell lines were cultured in Dulbecco's modified Eagle's medium (DMEM; HyClone) supplemented with 10% fetal bovine serum (FBS; GIBCO) under a humidified atmosphere of 5% CO₂ at 37°C. LINC00578 shRNA plasmids, LINC00578 Sh-NC plasmids, LINC00578 overexpression plasmids, LINC00578 vector plasmids, and Si-SLC7A11 plasmids were purchased from GenePharma (Shanghai, China). We treated PL45 cells with lentivirus and selected puromycin. For transient silencing, INTERFERin Reagent was used to transfect siRNA into PATU988 cells. Regarding stable LINC00578 silencing and transient SLC7A11 silencing, the target sequences are listed in Table S1. For the cell death assay, LINC00578-overexpressing cells and vector cells were treated with different stimuli, including erastin

(Beyotime, China), ferrostatin-1 (Fer-1) (Beyotime, China), erastin+Fer-1, and DMSO.

2.2. Human Tissue Samples. Pancreatic cancer and adjacent nontumor tissue samples in the Su cohort and IHC samples were collected from the Department of General Surgery, the First Affiliated Hospital of Soochow University. Before surgery, none of the patients received preoperative chemotherapy or radiotherapy. The excised samples were rapidly stored in -80°C liquid nitrogen or formalin. The research was approved by the First Affiliated Hospital of Soochow University. All patients signed informed consent forms.

2.3. RNA Isolation and Quantitative Real-Time PCR (qRT-PCR). TRIzol reagent (Invitrogen, USA) was used to extract total RNA. The RNA concentration was then detected. Subsequently, 1 µg of total RNA was reverse transcribed with random primers using the RevertAid™ First Strand cDNA Synthesis Kit and oligo (dT) (GENMED Scientific, Inc., USA). PCR was conducted in a 20 µL PCR containing 1 µL of diluted cDNA. qRT-PCR was performed with a LightCycler 480 II Real-Time PCR system using the SYBR Green method. The PCR primers are listed in Table S2. All qRT-PCR experiments were repeated at least three times.

2.4. CCK-8 and Colony Formation Assays. A total of 5000 cells in 100 µL of complete medium were seeded into each well of 96-well culture plates to detect PATU8988 and PL45 cell viability. Next, 10 µL of the Cell Counting Kit-8 (CCK8) was added to each well at 0, 24, and 48 h, and after that, the plates were cultured for 2 h under a humidified atmosphere of 5% CO₂ at 37°C. The absorbance at 450 nm was measured on a 96-well plate reader (Thermo Fisher Scientific).

For colony formation assays, PATU8988 and PL45 cells (a gradient density of 50 cells/well) were seeded in plates and then incubated for 2–3 weeks until the appearance of colonies. Methanol was used to fix cell colonies, which were then stained with Giemsa. Rate of colony formation = (number of clones/number of cells inoculated) × 100%. The experiment was repeated three times.

2.5. Wound-Healing Assay. The invasive ability of the pancreatic cancer cells was tested via wound-healing assay. A 10 µL pipette tube was used to create an acellular area, and the distance of cells migrating to the wounded area was observed after 0 and 48 h via photography. The invasive ability was detected by counting the number of cells that migrated to the original wound. The experiment was repeated three times.

2.6. Construction of the Tumor Xenograft Model. In this research, all animal studies were approved by the Institutional Animal Care and Use Committee (IACUC) of Soochow University. Nude mice (female, 6 weeks old, and 18 ± 2 g) were delivered from the Shanghai Experimental Animal Centre (Shanghai, China). A total of 5 × 10⁶ PATU8988 cells transfected with LINC00578 overexpression or control vector were slowly injected into the subcutaneous area of the bilateral flanks of the nude mice (n = 6 per group). Body weights and tumor volumes were measured every 3 days. The nude mice

were euthanized on day 30 or when they were moribund. Then, the tumors were isolated carefully. Each mouse's tumor was measured through length and width and weighed on the scales. Tumor volume = length \times width² \times 1/2.

2.7. Label-Free Proteomics, GO Terms, and KEGG Pathway Analysis. Cells of the Sh-LINC00578 group and Sh-NC group were collected and then sonicated using an ultrasonic processor (Scientz) in a lysis buffer on ice three times. The samples were centrifuged (12,000 g, 4°C) for 10 min to remove the remaining debris. The supernatant was collected, and then, a BCA kit was used to determine the protein concentration of the Sh-LINC00578 group and Sh-NC group. Dithiothreitol (5 mM, 56°C, and 30 min) was used to reduce the protein solution, and the reduced protein was then alkylated by iodoacetamide (11 mM, in darkness, and 15 min) to obtain the postdigested product.

Triethylammonium bicarbonate (TEAB, 100 mM) was added to the protein samples to keep the urea concentration less than 2 M. Next, the mass ratio of trypsin to protein was maintained at 1:50 by adding trypsin to the protein. It was digested overnight. Then, a second 4 h digestion was performed at a 1:100 trypsin to protein ratio. Label-free LC-MS/MS analysis was used to analyze collected protein samples from the Sh-LINC00578 group and the Sh-NC group. Tandem mass spectrometry (MS/MS) was performed in Q Exactive™ Plus (Thermo) on peptides previously subjected to an NSI source. The MaxQuant search engine (v.1.5.2.8) was used to further process the MS/MS data. Then, the tandem mass spectra were searched using the human UniProt database, which was concatenated with the reverse decoy database.

Then, GO terms were used to classify the proteins of the Sh-LINC00578 group and the Sh-NC group into three categories: cellular compartment, molecular function, and biological process. For enrichment of the differentially expressed proteins, the evaluation was conducted via Fisher's exact test. A *P* value < 0.05 was considered statistically significant.

The enriched pathways were identified via Kyoto Encyclopedia of Genes and Genomes (KEGG) pathway analysis. For enrichment of the differentially expressed proteins, evaluation was conducted via Fisher's exact test. A *P* value < 0.05 was considered statistically significant.

2.8. Western Blot Analysis. The RIPA lysis buffer (Beyotime Biotechnology, Shanghai, China) was used to extract total proteins, which were then quantified by the bicinchoninic acid (BCA) quantitative protein assay according to the manufacturer's instructions. Then, 10% SDS-PAGE was used to separate protein lysates. Proteins were transferred to PVDF membranes. The membrane was blocked with 5% nonfat milk. Primary antibodies were added and incubated at 4°C overnight. Next, the membranes were incubated with horseradish peroxidase-conjugated anti-rabbit IgG or anti-mouse IgG for 1 h, and then, the blots were detected using an enhanced chemiluminescence (ECL) detection system (FDBio, Shanghai, China). GAPDH was chosen as an internal loading control. All primary and secondary antibodies

are presented in Table S3. All western blot assays were repeated at least three times.

2.9. Measurement of Ferrous Iron (Fe²⁺) and Malondialdehyde (MDA). Cells were treated according to the corresponding procedures. An Iron Assay Kit (AB83366, Abcam) was used to detect the Fe²⁺ content in PATU8988 and PL45 cells. First, the cells were added to an iron assay buffer, which was then homogenized on ice. Then, the samples were centrifuged at 13,000 \times g and 4°C for 10 min. Next, the supernatant was collected. Fifty microliters of supernatant were incubated with 50 μ L of assay buffer at room temperature for 30 min. Subsequently, 50 μ L of the assay buffer with 200 μ L of reagent mix was incubated at room temperature in the dark for 30 min. The absorbance was measured at 593 nm using a microplate reader.

PATU8988 and PL45 cells were plated in 6-well cell culture plates (Corning). After cell homogenization, a BCA protein assay kit (Beyotime) was used to measure protein concentrations, and then, intracellular MDA levels were detected using a lipid peroxidation MDA assay kit (Beyotime). This experiment was repeated at least three times.

2.10. Measurement of Reactive Oxygen Species (ROS) and Mitochondrial Membrane Potential (MMP). To determine ROS levels, vector and OE-LINC00578 group cells were seeded in a 6-well plate. Then, the culture media was replaced with serum-free media containing 10 μ mol/L of 2',7'-dichlorodihydrofluorescein diacetate (Sigma). The samples were then placed in the dark for 20 min and shaken gently every 5 min. The cells were resuspended in PBS and then subjected to flow cytometry to detect changes in ROS expression levels. The experiment was repeated three times.

Tetraethylbenzimidazolylcarbocyanine iodide (JC-1) staining was used to measure MMP in PATU8988 and PL45 cells. Cells were treated with NaAsO₂ and stained with 5 μ M JC-1 (Beyotime, China) at 37°C in the dark for 20 min. The cells were washed twice with PBS and observed using a fluorescence microscope. The ratio of red/green fluorescence intensity was analyzed via Image-Pro Plus 6.0 software.

2.11. RNA Pull-Down and Mass Spectrometry. A DNA fragment containing LINC00578 full-length sequence or a negative control sequence was PCR amplified using SP6 (for antisense)/T7 (for sense) polymerase. Biotin RNA Labeling Mix (Roche) and T7 RNA polymerase were used for the reverse transcription of biotin-labeled RNA. Then, the products were treated with RNase-free DNase I (Roche) and an RNeasy Mini Kit (Qiagen, MD, USA) for purification. Four micrograms of RNA were denatured in a PA buffer. The mixture was then cooled to room temperature. Subsequently, the folded RNA was incubated with streptavidin Dynabeads (Invitrogen) for 1 h at 4°C with 2 U/mL RNasin (Promega). The cells were washed to clear the protein lysate from 1 \times 10⁷ PL45 cells, which were then incubated with the folded RNA-bead complex with 20 μ g/mL yeast tRNA. The beads were boiled with 40 μ L of 1x SDS loading buffer after washing. Sodium dodecyl sulfate-polyacrylamide gel electrophoresis can further separate lncRNA-interacting proteins.

The gel was stained with silver. Next, the specific bands of LINC00578 were subjected to Q Exactive mass spectrometry.

For each sample, 1/2 peptides were alienated and explored using Q Exactive mass spectrometry (Thermo). Then, the peptides were separated. H₂O with 0.1% FA, 2% ACN (phase A) and 80% ACN, and 0.1% FA (phase B) were the mobile phases. A 120 min gradient at a 300 nL/min flow rate was performed to separate the samples. The gradient was comprised of an increase of solvent B from 0% to 3% in 8 min, 3% to 8% in 3 min, 8% to 20% in 77 min, 20% to 40% in 10 min, and 40% to 90% in 4 min, then holding at 90% for 6 min, and a subsequent decrease of solvent B from 90% to 3% in 4 min and 3% to 0% in 8 min.

Data-dependent acquisition was accomplished in profile as well as in positive mode with an Orbitrap analyzer at a resolution of 70,000 FWHM and a *m/z* range of 300–1400 for MS1. For dd-MS2, the resolution was fixed to 17,500 FWHM. The automatic gain control (AGC) target for MS1 was 3.0 e⁶ with a max IT of 60 ms and was 5.0 e⁴ for dd-MS2 with a max IT of 80 ms. HCD with a normalized collision energy (NCE) of 27% was used to disintegrate the top 10 strongest ions.

Then, we investigated the raw MS files with Proteome Discoverer. The protein sequence database (UniProt_Human_2020_08.13) was acquired from UniProt. All the additional parameters were kept as default.

2.12. RNA Immunoprecipitation (RIP) Assay. A RIP RNA-Binding Protein Immunoprecipitation Kit (Millipore, MA) was used to perform RIP. In brief, 2×10^7 PL45 cell lysates were incubated with beads conjugated with anti-UBE2K or negative control (normal mouse IgG). The immunoprecipitated RNAs were extracted. Then, qRT-PCR was performed to verify binding target enrichment. Finally, the products were subjected to agarose gel electrophoresis. The primers for LINC00578 are listed in Table S2. The RIP assay was repeated three times.

2.13. Immunoprecipitation Assay. The cells were washed with PBS and lysed with a protein extraction reagent buffer on ice for 1 h. The samples were centrifuged at $15,000 \times g$ at 4°C for 10 min, and then, the supernatant was collected. The supernatant was incubated with a primary antibody against GAPDH (1 : 2000; 60004-1-Ig, Proteintech) or mouse immunoglobulin G control at 4°C for 4 h with gentle agitation. Regarding the coimmunoprecipitations (IPs), 20 μ L of prewashed protein A/G agarose beads was incubated with 400 μ g of samples at 4°C overnight with gentle agitation. After incubation, the immune complexes were washed three times with a lysis buffer. Then, the proteins were collected after centrifugation and boiled with the SDS loading buffer. Finally, western blotting was performed. The experiment was repeated three times.

2.14. Immunohistochemical (IHC) Assay. Tissues were fixed with formalin and embedded in paraffin. Four-micrometer-thick sections were cut and mounted on glass slides according to the specifications of the S-P (streptavidin peroxidase) kit. They were incubated with anti-SLC7A11 (1 : 200; 26864-

1-AP, Proteintech) antibodies overnight at 4°C. Subsequently, the membranes were incubated with the secondary antibody and ExtrAvidin-conjugated horseradish peroxidase. Sections were evaluated via light microscopy.

2.15. Bioinformatics. Bioinformatic analysis was carried out with pancancer and pancreatic cancer data, which were from The Cancer Genome Atlas (TCGA). The data were analyzed by the R package (Version 4.2.0). Kaplan–Meier analysis was conducted to construct overall survival curves.

2.16. Statistical Analysis. SPSS 21.0 software (IBM, Armonk, NY, USA) was used for statistical analysis. All continuous data are presented as the mean \pm standard deviation for multiple (SD). GraphPad Prism 9 software was used for statistical analysis. For cellular assays in vitro and animal experiments in vivo, a two-sided Student's *t* test was performed to analyze the difference between two groups. One-way ANOVA was performed for comparisons among multiple groups. The correlation between LINC00578 expression and clinical characteristics was validated by Fisher's exact test. In this study, a *P* value < 0.05 was defined as significantly different.

3. Results

3.1. The Expression of LINC00578 Is Closely Correlated with Clinicopathologic Factors and Associated with Poor Prognosis in Pancreatic Cancer. To grasp the role of LINC00578 in cancer progression, pancancer analysis was first performed in a TCGA cohort, and the results showed that the expression of LINC00578 was dramatically decreased in 15 kinds of cancers, including colon adenocarcinoma and esophageal carcinoma, and increased in 16 kinds of cancers, including pancreatic adenocarcinoma and liver hepatocellular carcinoma (Figure 1(a)). Subsequently, we analyzed LINC00578 expression levels in a PAAD cohort from the TCGA database. As expected, the expression level of LINC00578 was increased in pancreatic cancer compared with normal tissues (Figure 1(b)). Therefore, we focused on investigating the role of LINC00578 in pancreatic cancer. Subsequently, the expression of LINC00578 in the Su cohort of 50 paired cases was examined to validate the increased level of LINC00578 in pancreatic cancer, and the results showed that the expression level of LINC00578 was significantly higher in pancreatic cancer tissues than in benign tissues (Figure 1(c)). The expression ratio of LINC00578 between tumors and adjacent normal tissues showed that the ratio of T/NT of 38% of cases ranged from 2 to 5, and the ratio of 28% of cases exceeded 5 (Figure 1(d)). Then, to determine whether LINC00578 expression is associated with pancreatic cancer progression, the relationship between LINC00578 expression and clinicopathologic factors was analyzed, and we discovered that a higher LINC00578 expression level was positively associated with advanced T stage (*P* = 0.0106), N stage (*P* = 0.0001), and TNM stage (*P* < 0.0001) (Figures 1(e)–1(g), Table 1). Kaplan–Meier analysis of PAAD cohorts in TCGA showed that a high LINC00578 expression level predicted poor overall survival of patients with pancreatic cancer (Figure 1(h), Figure S1).

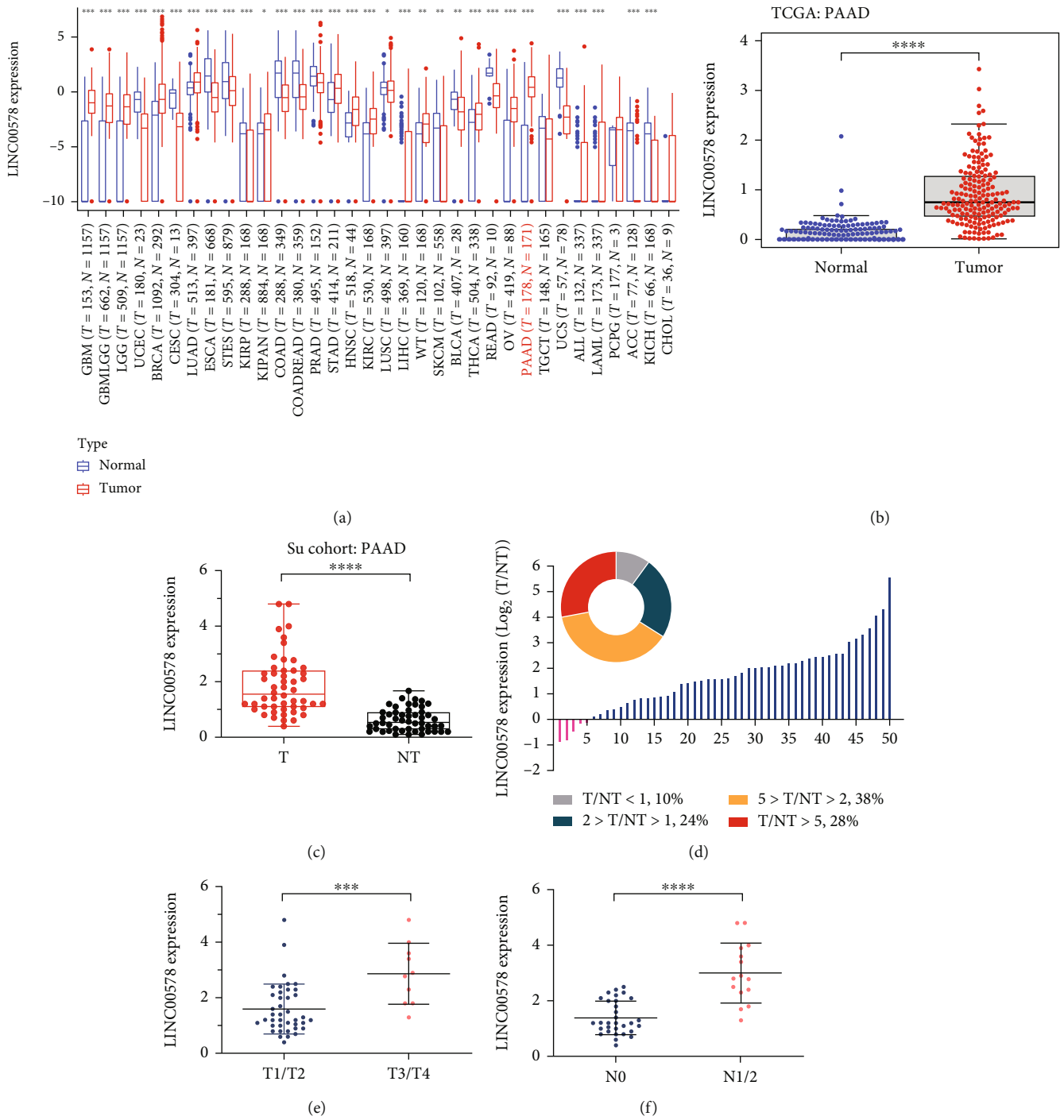


FIGURE 1: Continued.

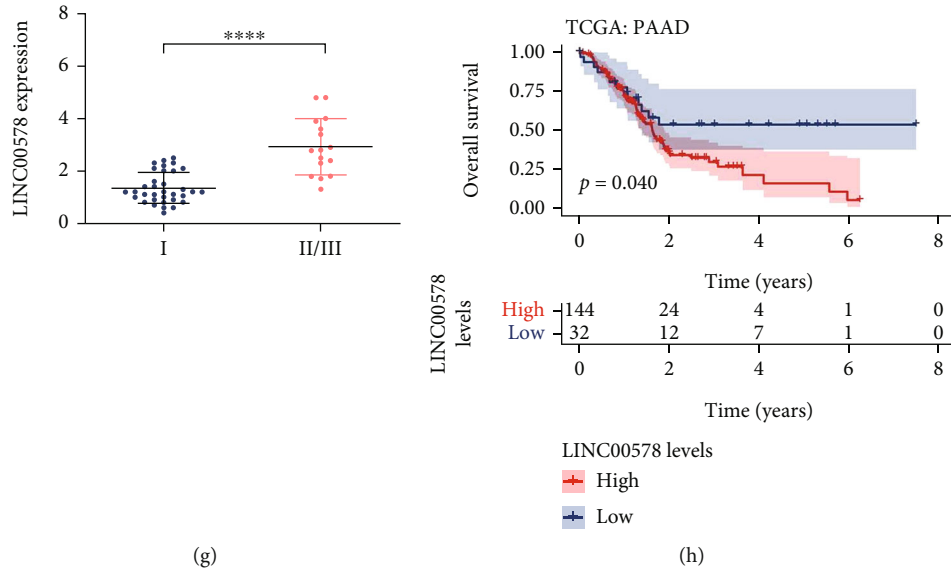


FIGURE 1: LINC00578 is upregulated in pancreatic cancer and correlated with clinicopathological factors. (a) Box plot of LINC00578 expression in 34 kinds of cancers from the TCGA (PANCAN, $N = 19131$, $T = 60499$) cohort. (b) Box plot of LINC00578 expression in both pancreatic cancer tissues ($n = 177$) and normal tissues ($n = 171$) from the TCGA-GTEx cohort. (c) Box plot of LINC00578 expression in pancreatic cancer tissues ($n = 50$) and adjacent normal tissues ($n = 50$) from the Su cohort. (d) The expression ratio of LINC00578 between tumors and adjacent normal tissues from the Su cohort. (e) The expression of LINC00578 between T1/T2 and T3/T4 stages from the Su cohort. (f) The expression of LINC00578 between N0 and N1/N2 stages from the Su cohort. (g) The expression of LINC00578 between Grade I and Grade II from the Su cohort. (h) Kaplan–Meier curve showing the correlation of the LINC00578 expression with overall survival (OS) ($P = 0.04$) in the TCGA cohort. $*P < 0.05$; $**P < 0.01$; $***P < 0.001$; $****P < 0.0001$. Abbreviations: ACC: adrenocortical carcinoma; ALL: acute lymphoblastic leukemia; BLCA: bladder urothelial carcinoma; CESC: cervical squamous cell carcinoma and endocervical adenocarcinoma; COAD: colon adenocarcinoma; COADREAD: colon adenocarcinoma/rectum adenocarcinoma; CHOL: cholangiocarcinoma; ESCA: esophageal carcinoma; GBM: glioblastoma multiforme; GBMLGG: glioma; HNSC: head and neck squamous cell carcinoma; KICH: kidney chromophobe; KIRC: kidney renal clear cell carcinoma; KIRP: kidney renal papillary cell carcinoma; KIPAN: pankidney cohort (KICH+KIRC+KIRP); LAML: acute myeloid leukemia; LGG: brain lower grade glioma; LIHC: liver hepatocellular carcinoma; LUAD: lung adenocarcinoma; LUSC: lung squamous cell carcinoma; OV: ovarian serous cystadenocarcinoma; PAAD: pancreatic adenocarcinoma; PCPG: pheochromocytoma and paraganglioma; PRAD: prostate adenocarcinoma; READ: rectum adenocarcinoma; STAD: stomach adenocarcinoma; STES: stomach and esophageal carcinoma; SKCM: skin cutaneous melanoma; THCA: thyroid carcinoma; TGCT: testicular germ cell tumors; UCEC: uterine corpus endometrial carcinoma; UCS: uterine carcinosarcoma; WT: high-risk Wilms tumor.

TABLE 1: Relationship between LINC00578 expression level and clinicopathologic factors in pancreatic cancer patients.

Clinicopathologic factors	Cases	LINC00578		P value
		Low expression	High expression	
Gender	Male	11	15	0.3961
	Female	14	10	
Age	≥ 65	13	10	0.5709
	< 65	12	15	
T stage	T1+T2	24	16	0.0106*
	T3+T4	1	9	
N stage	N0	24	11	0.0001***
	N1/2	1	14	
TNM stage	I	24	10	$< 0.0001****$
	II/III	1	15	
Tumor location	Head and neck	11	14	0.5721
	Body and tail	14	11	

* $P < 0.05$; *** $P < 0.001$; **** $P < 0.0001$.

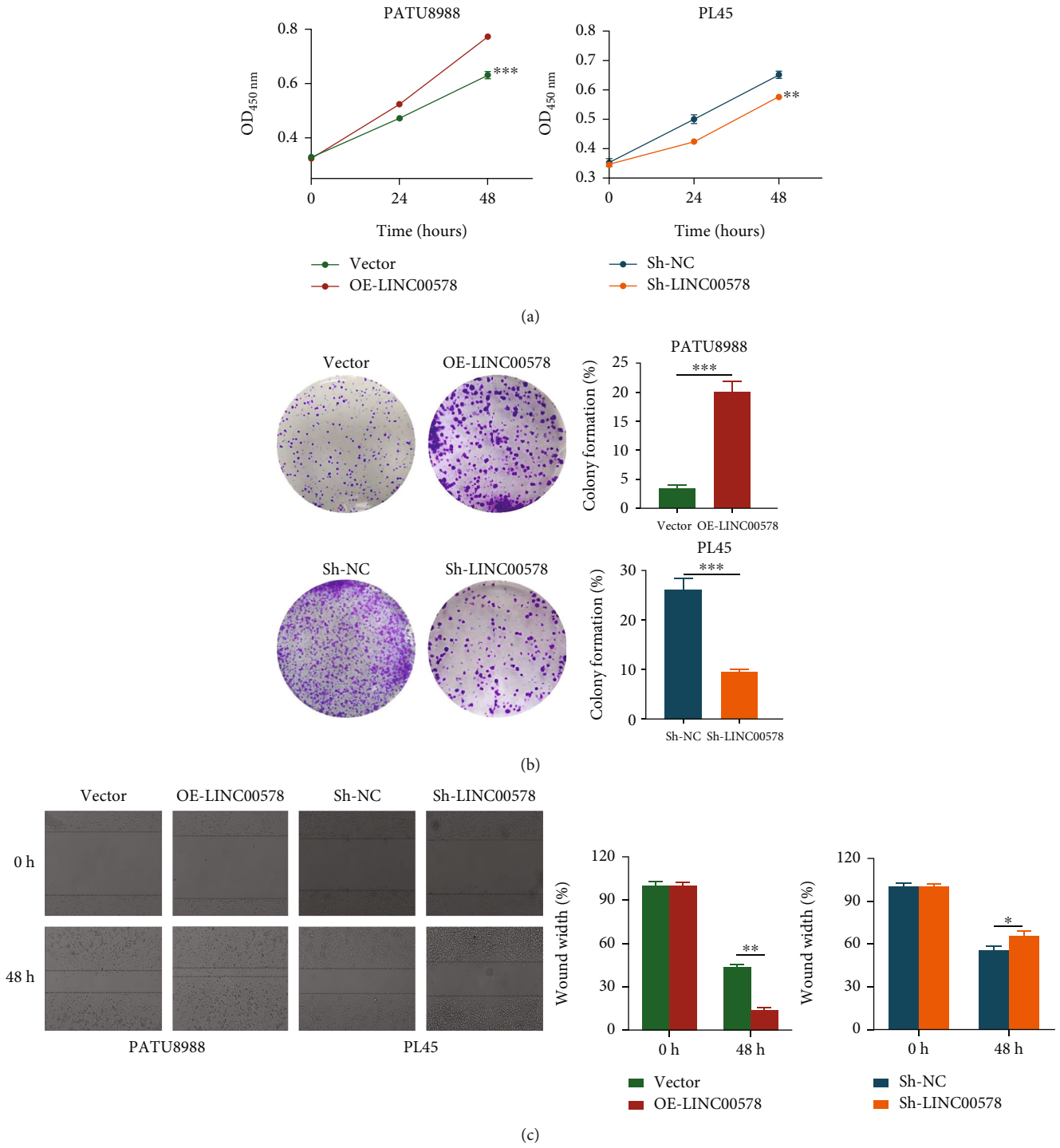


FIGURE 2: Continued.

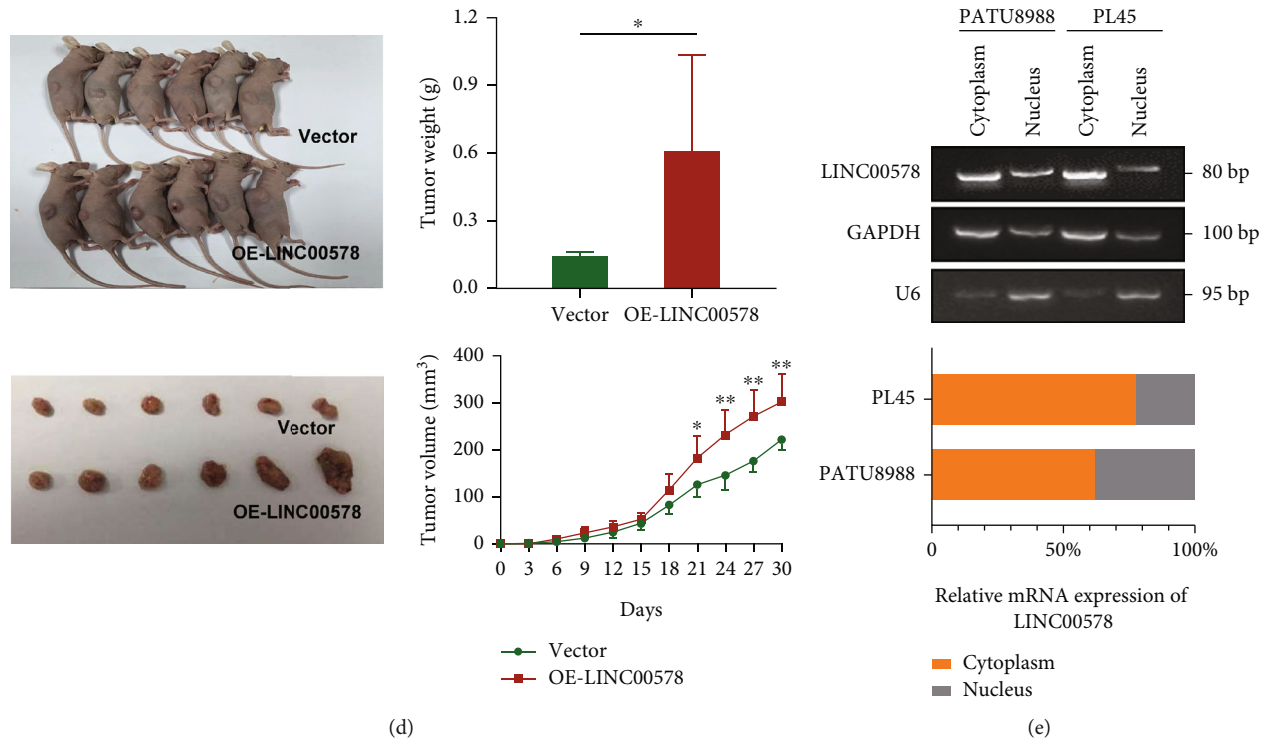


FIGURE 2: LINC00578 promotes pancreatic cancer cell proliferation and invasion in vitro and tumor growth in vivo. (a) CCK-8 assays were applied to detect cell viability at the indicated time points in PATU8988 cells transfected with LINC00578 (OE-LINC00578) versus empty vector-transfected PATU8988 cells (Vector) and LINC00578 knockdown PL45 cells (Sh-LINC00578) versus empty vector knockdown PL45 cells (Sh-NC). (b) Colony formation assays were applied to detect cell proliferation in PATU8988 cells (OE-LINC00578 group versus vector group) and PL45 cells (Sh-LINC00578 group versus Sh-NC group). (c) Wound-healing assay indicating LINC00578-induced increased migration in PATU8988 and PL45 cells. (d) Tumor size, volume, and weight at day 30 after subcutaneous injection of LINC00578-overexpressing PATU8988 cells ($n = 6$) compared with the vector group ($n = 6$). (e) A nucleocytoplasmic separation assay was used to determine the intracellular location of LINC00578 in PATU8988 cells and PL45 cells. * $P < 0.05$; ** $P < 0.01$; *** $P < 0.001$.

3.2. LINC00578 Promotes Pancreatic Cancer Cell Proliferation and Invasion In Vitro and Tumor Growth In Vivo. To identify the biological role of LINC00578 in pancreatic cancer, we first upregulated the expression of LINC00578 in the PATU8988 cell line and downregulated the expression of LINC00578 in the PL45 cell line using lentivirus stable transfection. The overexpression and knockdown efficiency of OE-LINC00578 and Sh-LINC00578 are shown in Figure S2. Next, the possible role of LINC00578 in regulating pancreatic cancer cell growth and invasion was evaluated by CCK-8, colony formation, and wound-healing assays. LINC00578-overexpressing cells (OE-LINC00578) showed significantly increased proliferation, colony formation, and invasion ability compared with empty vector-transfected cells (Vector) and, as expected, compared with the Sh-NC group; notably, decreased proliferation, colony formation, and invasion ability were observed in LINC00578 knockdown cells (Sh-LINC00578) (Figures 2(a)–2(c)). Then, to investigate whether LINC00578 can regulate pancreatic cancer growth in vivo, LINC00578-overexpressing cells or empty vector-transfected cells were injected subcutaneously into nude mice. The results showed that the tumor weight and volume were greater in the OE-LINC00578 group than in the vector group (Figure 2(d)). Furthermore, a nucleocytoplasmic

separation experiment revealed the cytoplasmic distribution of LINC00578, indicating posttranslational regulation pathways (Figure 2(e)). Collectively, our data demonstrate that LINC00578 can promote the proliferative and invasive abilities of pancreatic cancer cells.

3.3. LINC00578 Represses Ferroptosis in Pancreatic Cancer. To further investigate the effect of LINC00578 expression on related proteins, label-free proteomic analysis was performed. Compared with the Sh-NC group, there were 43 upregulated proteins and 32 downregulated proteins in the Sh-LINC00578 group (Figure S3). Gene Ontology analysis revealed that LINC00578 was correlated with voltage-gated anion channel activity and transmembrane receptor proteins in molecular function and associated with cell chemotaxis and regulation of anion transport in biological processes (Figure 3(a)). The results of KEGG analysis of these proteins indicated that proteins with a trend of change when LINC00578 was knocked down were significantly correlated with ferroptosis (Figure 3(b)). We hypothesized that LINC00578 is associated with ferroptosis in pancreatic cancer. Ferroptosis is characterized by the accumulation of iron-dependent lipid peroxidative products and increasing levels of ROS. To verify our hypothesis, we first detected the

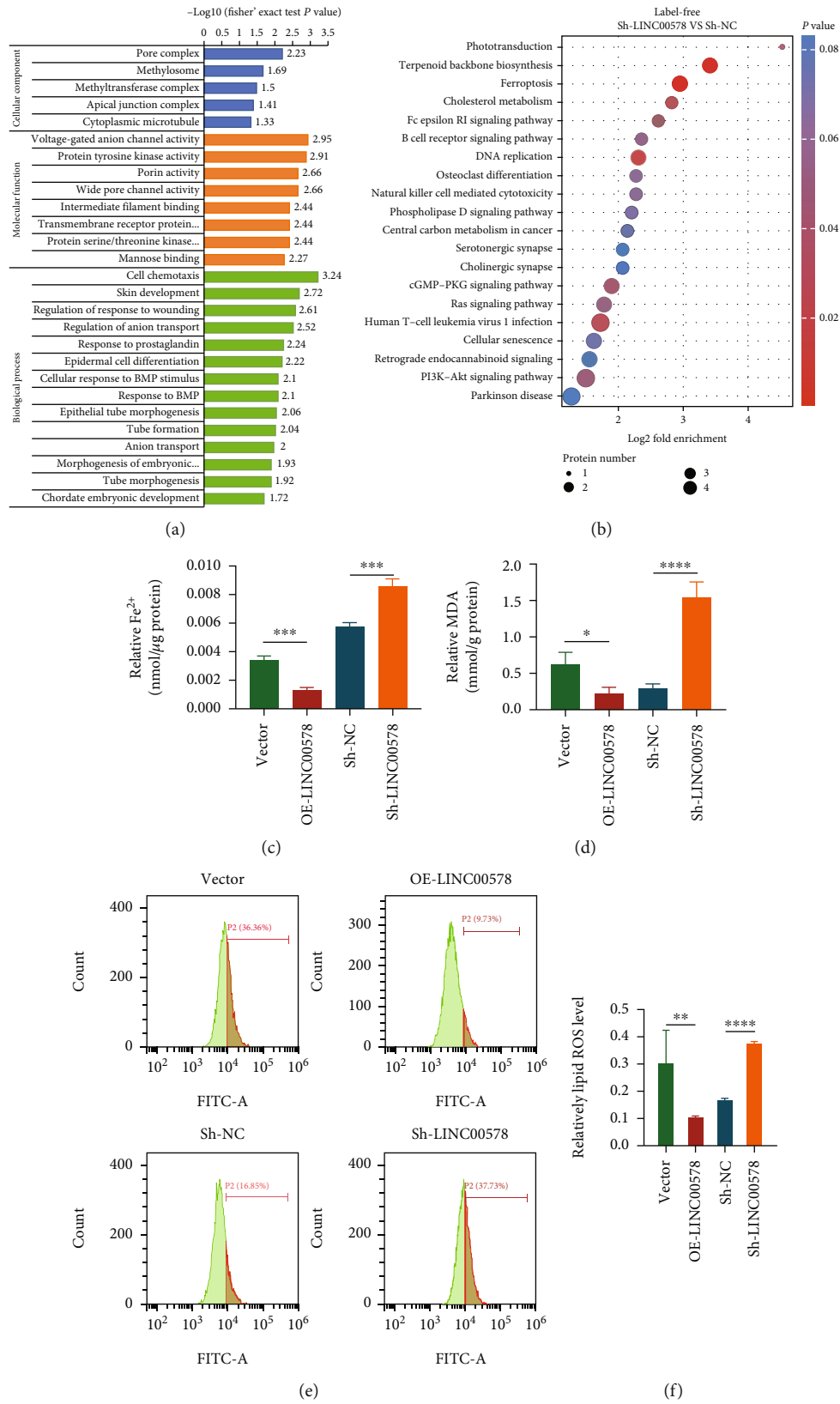


FIGURE 3: Continued.

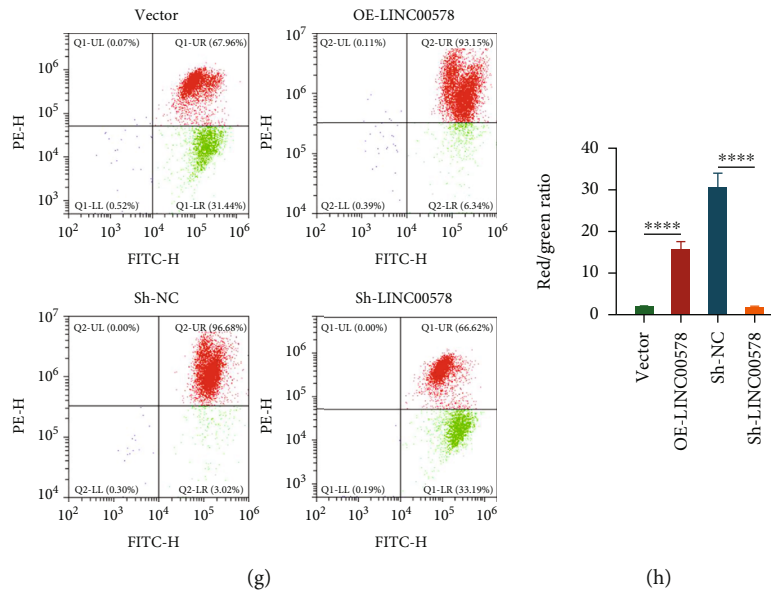


FIGURE 3: LINC00578 acts as a ferroptosis repressor in pancreatic cancer. (a) Statistical distribution of differentially expressed proteins in GO secondary classification. Blue represents cellular components. Yellow represents molecular function. Green represents biological processes. (b) Bubble map showing the distribution of differentially expressed proteins (Sh-LINC00578 group versus Sh-NC group, selected by label-free proteomics) enriched in the KEGG pathway. (c) Quantitative analysis of intracellular Fe^{2+} . (d) Quantitative analysis of intracellular malondialdehyde (MDA). (e) OE-LINC00578, vector, Sh-LINC00578, and Sh-NC cells were stained with DCFH-DA to measure intracellular ROS levels via flow cytometry. (f) Quantitative analysis of ROS generation. (g) OE-LINC00578, vector, Sh-LINC00578, and Sh-NC cells were stained with JC-1 to measure MMP levels via flow cytometry. Green represents the depolarized state of cells. Red represents the normal state of cells. (h) Quantitative analysis of MMP. Red/green ratio showing the effect of LINC00578 on inhibiting MMP depolarization. * $P < 0.05$; ** $P < 0.01$; *** $P < 0.001$; **** $P < 0.0001$.

Fe^{2+} content in PATU8988 cells and PL45 cells, and the results showed that the Fe^{2+} content was significantly decreased in the OE-LINC00578 group compared to the vector group and increased in the Sh-LINC00578 group compared to the Sh-NC group (Figure 3(c)). Meanwhile, MDA, the end product of lipid peroxidation, was markedly decreased in the LINC00578-overexpressing group and increased in the LINC00578 knockdown group (Figure 3(d)). Next, we detected the ROS level through flow cytometry. As expected, LINC00578-overexpressing cells showed decreased ROS levels compared with the vector group, while LINC00578 knockdown cells showed increased ROS levels compared with the Sh-NC group (Figures 3(e) and 3(f)). Given that cysteine deprivation-induced ferroptosis leads to MMP depolarization, MMP assays were then performed. As shown in Figures 3(g) and 3(h), MMP was increased in the LINC00578-overexpressing group and decreased in the LINC00578 knockdown group.

To verify the repressor actor of LINC00578 in ferroptosis, we observed the cell number changes of LINC00578-overexpressing and vector groups induced by erastin and Fer-1. The results showed that LINC00578 overexpression significantly weakened erastin-induced decreased viability. In addition, the ferroptosis inhibitor Fer-1 rescued the erastin-induced decrease in viability in the vector group, which was not obvious in the OE-LINC00578 group (Figures 4(a) and 4(b)). These findings indicated that the ferroptosis activator erastin could inhibit the viability of PATU8988 cells and that LINC00578 overexpression inhibited erastin-induced decreased viability in PATU8988 cells.

3.4. LINC00578 Negatively Modulates Ferroptosis by Targeting SLC7A11. To understand the mechanism by which LINC00578 modulates ferroptosis, the expression levels of ferroptosis-related proteins in response to overexpression or knockdown of LINC00578 were detected. Compared to the vector group, the protein levels of SLC7A11, Survivin, C-MYC, and GPX4 increased, while the protein levels of P53 decreased in the LINC00578-overexpressing group. Meanwhile, compared with the Sh-control group, the protein levels of SLC7A11, Survivin, C-MYC, and GPX4 decreased, while the protein levels of P53 increased in response to Sh-LINC00578 (Figures 4(c) and 4(d)). Subsequently, we detected whether the protein levels of SLC7A11 changed after the addition of erastin. As shown in Figures 4(e) and 4(f), LINC00578 promoted the protein levels of SLC7A11, and as expected, erastin repressed the protein levels of SLC7A11 in both the LINC00578-overexpressing and vector groups. To further validate whether LINC00578 modulates ferroptosis via SLC7A11, several rescue experiments were performed. SLC7A11 was knocked down through siRNA. Compared to the OE-LINC00578+Si-NC group, the protein levels of SLC7A11, Survivin, C-MYC, and GPX4 decreased, while P53 increased in the OE-LINC00578+Si-SLC7A11 group in response to the knockdown of SLC7A11 (Figures 4(g) and 4(h)). Colony formation assays showed that LINC00578 overexpression enhanced the proliferative ability of PATU8988 cells and that Si-SLC7A11 reversed this effect (Figures 5(a) and 5(b)). In the MMP experiment, Si-SLC7A11 successfully rescued the inhibition of mitochondrial membrane potential depolarization mediated by OE-LINC00578 in the PATU8988 cell line (Figures 5(c) and 5(d)). These findings illustrate that

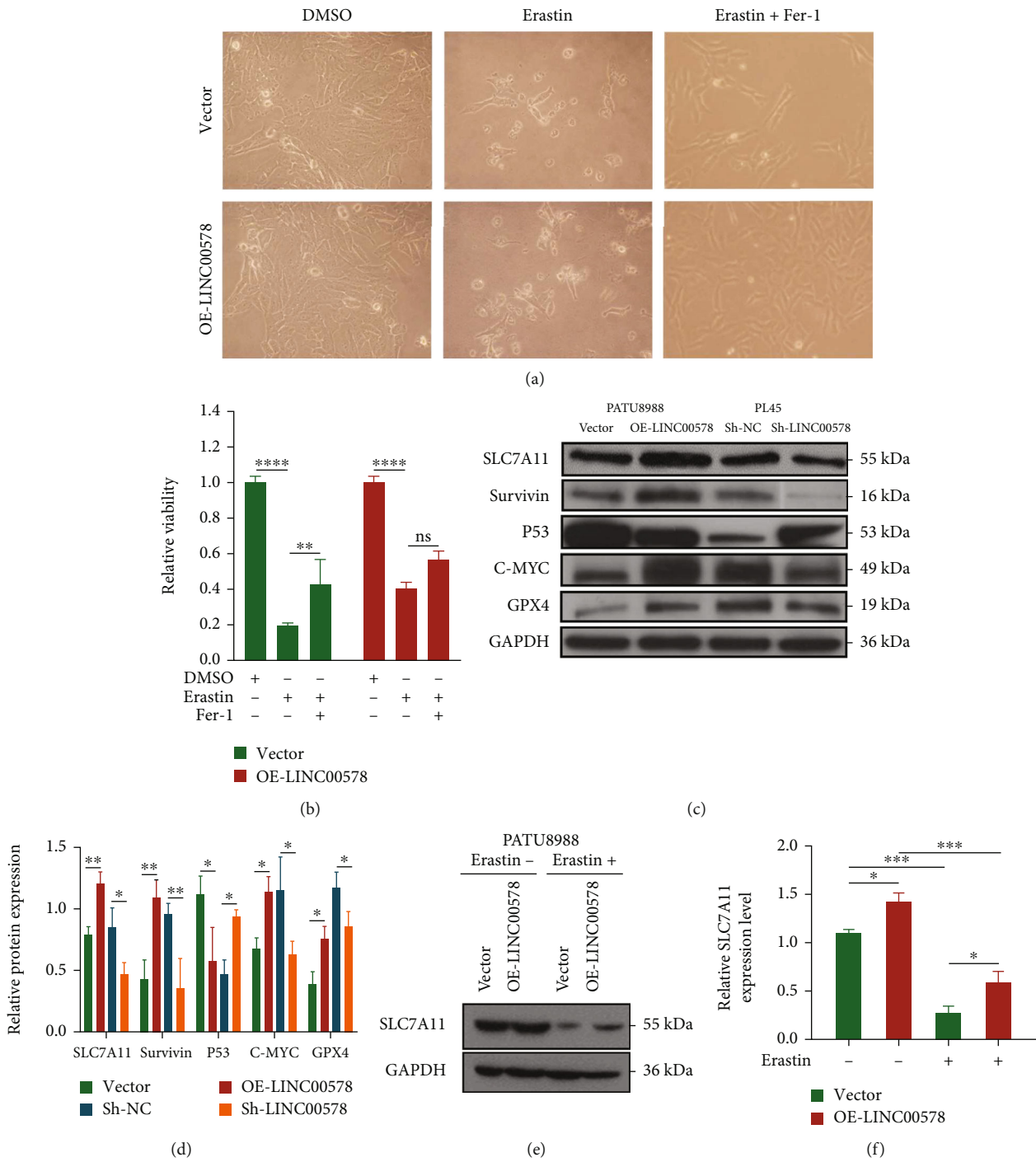


FIGURE 4: Continued.

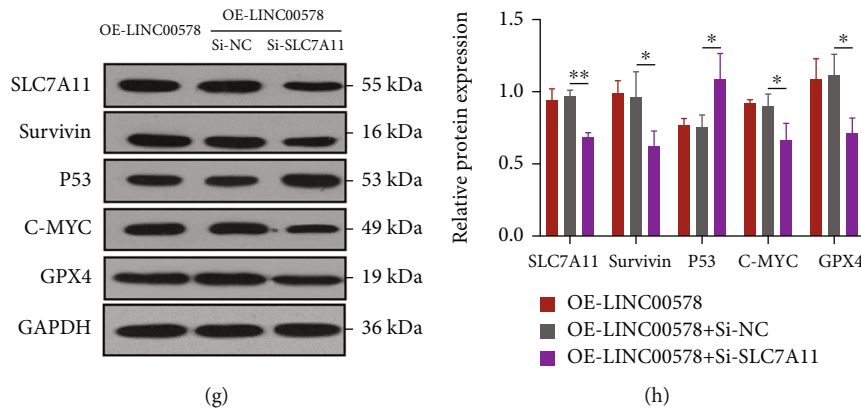


FIGURE 4: LINC00578 negatively modulates ferroptosis by targeting SLC7A11. (a) Observation of cell number changes in the OE-LINC00578 group versus the vector group under the induction of DMSO, erastin, and erastin+Fer-1. (b) CCK-8 assay showing the relative cell viability in the OE-LINC00578 group versus the vector group after induction with DMSO, erastin, and erastin+Fer-1. (c) Western blot results showing the levels of ferroptosis-related proteins (SLC7A11, P53, GPX4, Survivin, and GPX4) in pancreatic cancer cells. (d) Quantitative analysis of the levels of ferroptosis-related proteins. (e) Western blotting to measure the protein level of SLC7A11 in PATU8988 cells with or without erastin induction. (f) Quantitative analysis of the protein level of SLC7A11. (g) SLC7A11 silencing inhibited LINC00578-induced ferroptosis-related protein (SLC7A11, P53, GPX4, Survivin, and GPX4) expression. (h) Quantitative analysis of the protein level of LINC00578-induced ferroptosis-related proteins (SLC7A11, P53, GPX4, Survivin, and GPX4) reversed by SLC7A11 silencing. * $P < 0.05$; ** $P < 0.01$; *** $P < 0.001$ and **** $P < 0.0001$.

LINC00578 suppresses ferroptosis in pancreatic cancer cells primarily through SLC7A11.

3.5. LINC00578 Inhibits SLC7A11 Ubiquitination by Interacting with UBE2K. Then, we wondered how LINC00578 promotes SLC7A11 expression to inhibit ferroptosis in pancreatic cancer. First, an RNA pull-down assay was conducted. There were 5 differentially expressed proteins in the LINC00578-antisense group and 18 differentially expressed proteins in the LINC00578-sense group, among which UBE2K is a ubiquitin-conjugating enzyme and was selected as a candidate target of LINC00578 (Figure 6(a)). Subsequently, we performed a western blot assay to confirm that UBE2K was a specific binding protein for LINC00578 (Figure 6(b)). RIP assays were performed to further verify the specific interaction between LINC00578 and SLC7A11 (Figure 6(c)). The RNA levels of SLC7A11 in the OE-LINC00578/Sh-LINC00578 and vector groups were detected, and there was no significant difference in the RNA levels between the OE-LINC00578/Sh-LINC00578 group and the vector group, indicating that LINC00578 may regulate SLC7A11 through posttranslational pathways (Figure 6(d)).

To validate whether LINC00578 can affect the protein degradation rate of SLC7A11, the stability of SLC7A11 in response to knockdown of LINC00578 was detected with MG132 (proteasome inhibitor) and cycloheximide (protein synthesis inhibitor). As shown in Figure 6(e), treatment with MG132 in the LINC00578 knockdown group increased the expression of SLC7A11. Moreover, LINC00578 knockdown accelerated the protein degradation of SLC7A11 in PL45 cell lines (Figure 6(f)). Then, the SLC7A11 protein was immunoprecipitated in the Sh-LINC00578 and Sh-control groups to investigate the status of SLC7A11 ubiquitination. The results showed a significant increase in ubiquitinated proteins in response to knockdown of LINC00578 (Figure 6(g) and

Figure S4). Therefore, we deduced that LINC00578 impeded the ubiquitination of SLC7A11, which inhibits ferroptosis in pancreatic cancer. Next, coimmunoprecipitation (Co-IP) was used to validate the interaction between UBE2K and SLC7A11. The Co-IP results indicated that compared with the Sh-NC group, SLC7A11 was more enriched in the immunoprecipitated products of UBE2K in the Sh-LINC00578 group, proving that LINC00578 knockdown facilitated the interaction between UBE2K and SLC7A11 (Figure 6(h)). Collectively, LINC00578 directly binds UBE2K and affects the interaction between UBE2K and SLC7A11, thereby inhibiting ubiquitination of SLC7A11.

To investigate whether LINC00578 and SLC7A11 are clinically relevant, IHC for SLC7A11 was performed on 50 pancreatic cancer tissues. Figure 6(i) illustrates that SLC7A11 expression positively correlates with that of LINC00578 ($P = 0.0484$). Collectively, these findings illustrate that LINC00578 binds UBE2K to inhibit ubiquitination of SLC7A11, thus inhibiting ferroptosis in pancreatic cancer, which renders tumor cells highly invasive and aggressive (Figure 6(j)).

4. Discussion

Pancreatic cancer is one of the leading causes of cancer-related death worldwide. Moreover, the mortality and incidence of pancreatic cancer are increasing rapidly [15]. Although enormous efforts have been made to investigate early diagnosis and treatment methods, early diagnosis and efficient therapy of pancreatic cancer remain a formidable challenge. More than 90% of the genome is transcribed into ncRNAs, among which lncRNAs constitute the primary elements [16]. lncRNAs have been found to be correlated with various biological activities, including tumorigenesis, inflammation, and cell differentiation, through transcriptional regulation or posttranslational regulation [17–19]. In the

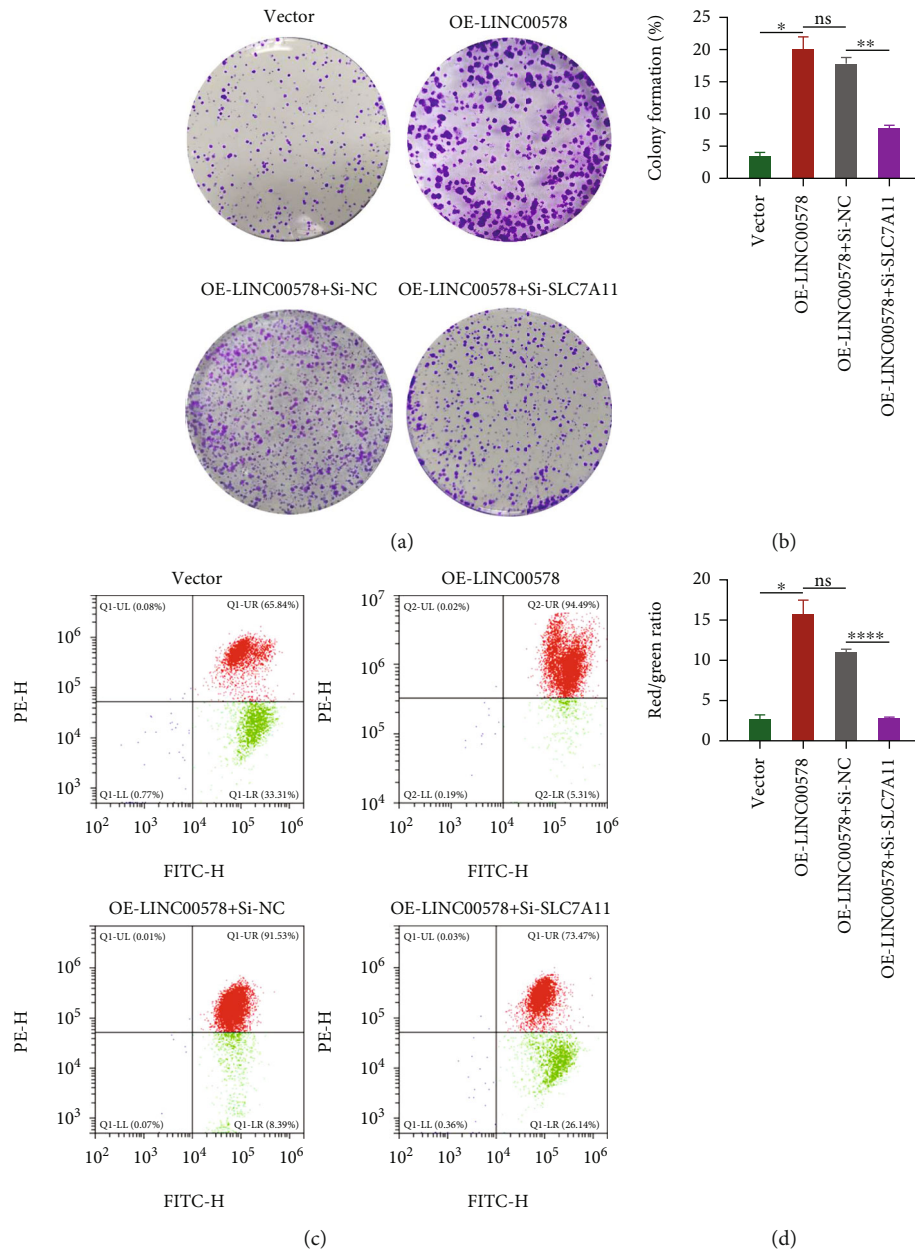
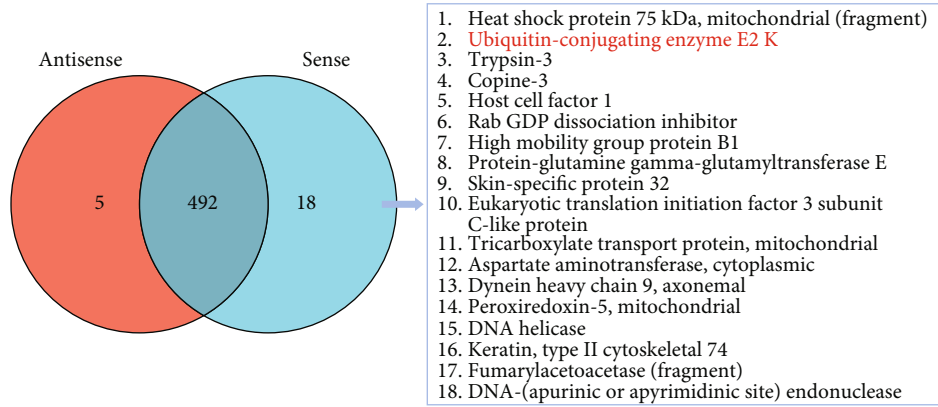


FIGURE 5: SLC7A11 knockdown reversed the effects of OE-LINC00578 on ferroptosis. (a) Colony formation assay showed that cell proliferation promotion in PATU8988 cells by OE-LINC00578 introduction was reversed by Si-SLC7A11. (b) Quantitative analysis showed that the promotion of cell proliferation in PATU8988 cells by OE-LINC00578 introduction was reversed by Si-SLC7A11 by the colony formation assay. (c) Si-LINC00578 significantly reversed the inhibition of MMP depolarization in PATU8988 cells by OE-LINC00578 introduction. (d) Quantitative analysis of MMP. Red/green ratio showing the effect of Si-SLC7A11 in the reverse of OE-LINC00578 on inhibiting MMP depolarization. * $P < 0.05$; ** $P < 0.01$; **** $P < 0.0001$.

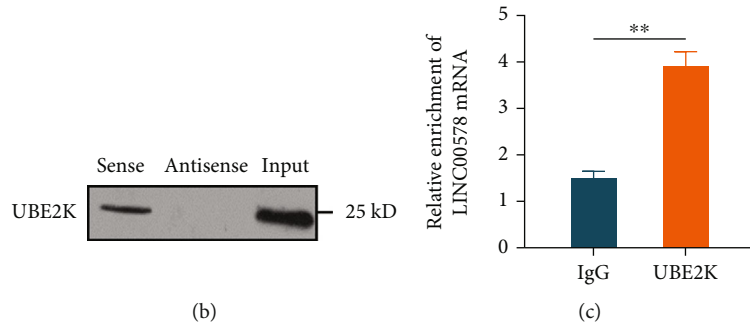
nucleus, lncRNAs participate in alternative splicing and transcriptional regulation and control the epigenetic state of genes. In the cytoplasm, the regulatory effect of lncRNAs on gene expression is mostly at the posttranslational level, including stabilizing mRNAs and competing for microRNA-mediated inhibition [20, 21]. In this study, we investigated a novel lncRNA named LINC00578 in pancreatic cancer, which was upregulated in pancreatic cancer cell lines and tissues and correlated with poor patient survival. In addition, LINC00578 was found to be related to the

advanced clinical stage in pancreatic cancer patients. These findings indicate that LINC00578 might be involved in pancreatic cancer progression. As expected, we demonstrated that LINC00578 is positively regulated in cell proliferation and invasion in vitro and tumorigenesis in vivo in pancreatic cancer. Therefore, LINC00578 plays a positive regulatory role in pancreatic cancer progression.

Ferroptosis, a novel form of iron-dependent cell death due to phospholipid peroxidation, has attracted enormous attention worldwide [22, 23]. Extensive studies have

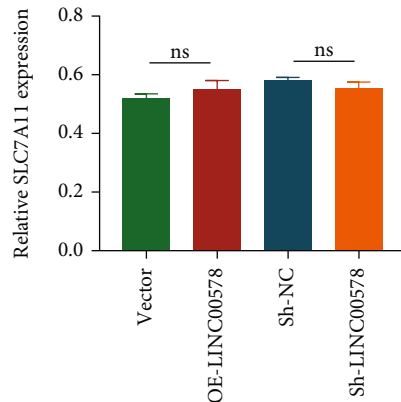


(a)

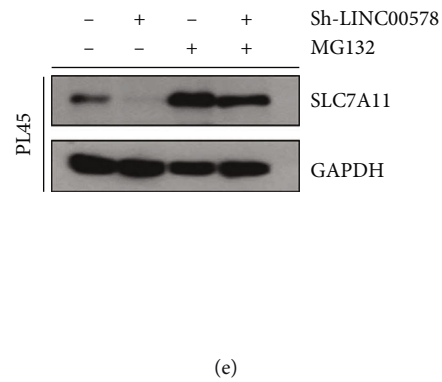


(b)

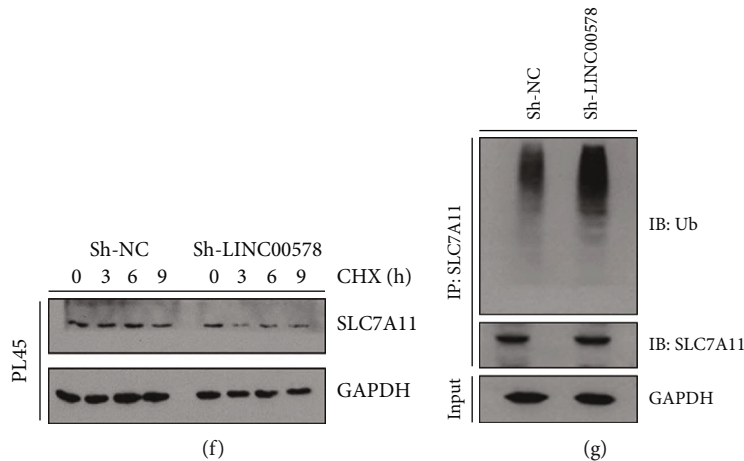
(c)



(d)



(e)



(f)

(g)

FIGURE 6: Continued.

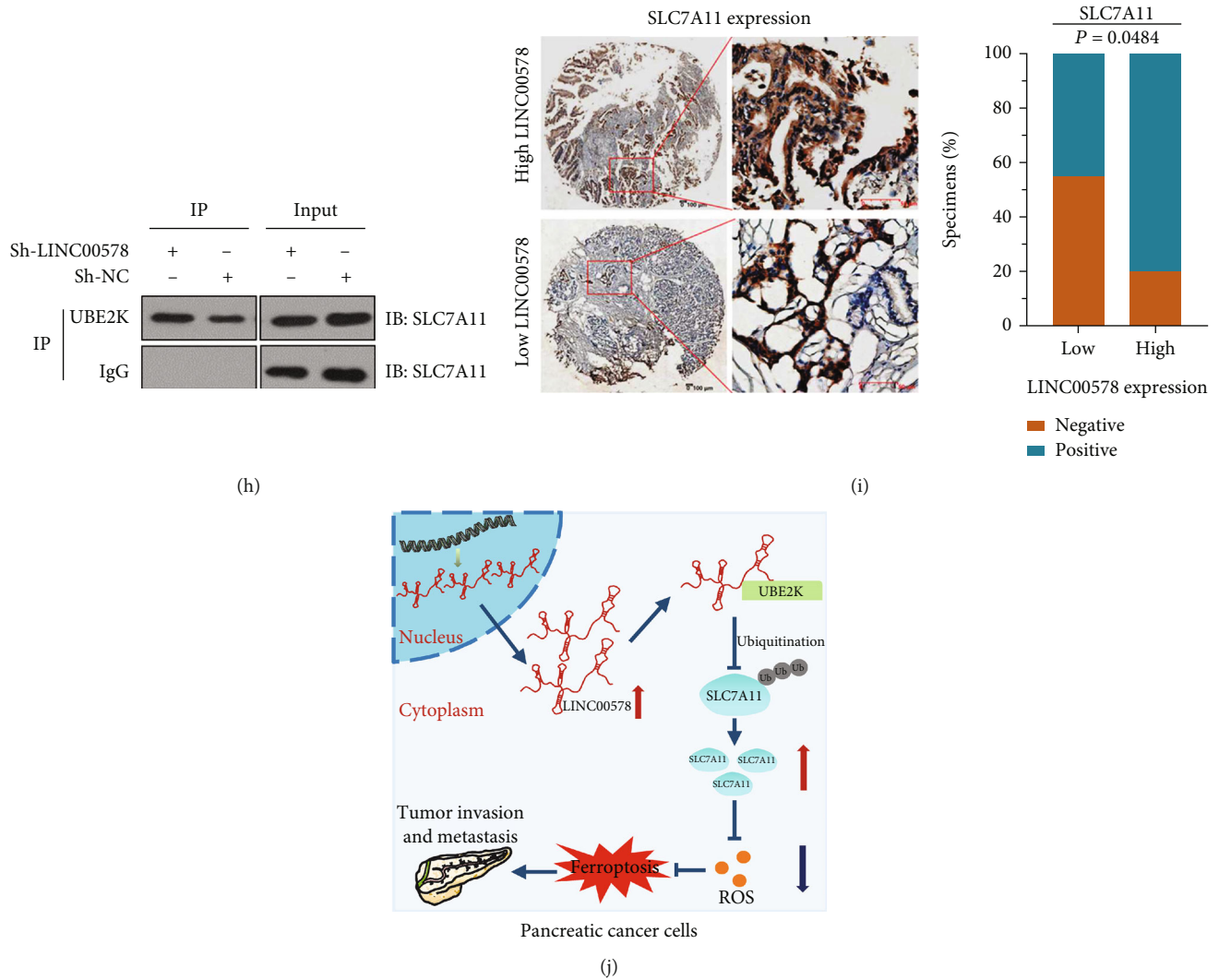


FIGURE 6: LINC00578 inhibits the ubiquitination of SLC7A11 by directly interacting with UBE2K. (a) Venn diagram showing 5 LINC00578 antisense proteins and 18 LINC00578 sense proteins by pull-down assay of PL45 cells. (b) Western blotting showing that LINC00578 interacts with UBE2K in pancreatic cancer cells. (c) qRT-PCR showing LINC00578 enrichment in UBE2K-immunoprecipitated RNAs in PL45 cells. An antibody against human IgG was used as a negative control for RIP. (d) qRT-PCR analysis showing the RNA level of SLC7A11 in the OE-LINC00578 group versus the vector group and the Sh-LINC00578 group versus the Sh-NC group. (e) Western blot assay revealing the reverse effect of MG132 on the protein degradation of SLC7A11 by Sh-LINC00578 introduction. (f) Western blot assay showing the promotion of CHX on the protein degradation rate of SLC7A11 by Sh-LINC00578 introduction. (g) Cells stably expressing Sh-NC or Sh-LINC00578 were subjected to a deubiquitination assay, and polyubiquitylated proteins were detected with an anti-Ub antibody. (h) Co-IP assay showing the interaction between UBE2K and SLC7A11. (i) IHC for SLC7A11 was applied between the LINC00578 high-expression group (above panel) and the low-expression group (below panel) in 50 paired pancreatic cancer tissue samples. The correlation analysis showed a positive correlation between LINC00578 and SLC7A11 ($P = 0.0484$, Fisher's exact test) expression. (j) Diagram illustrating how LINC00578 promotes SLC7A11 to inhibit ferroptosis. $**P < 0.01$.

identified that ferroptosis plays a crucial role in regulating tumor progression and maintains promising prospects for cancer therapy [24, 25]. Ferroptosis can be regulated by multiple essential factors, including SLC7A11, GPX4, and P53 [26, 27]. SLC7A11, as a key repressor of ferroptosis, is upregulated in tumors and can interact with ALOX12 to promote tumor progression [28]. He et al. found that as the core target of ferroptosis regulation, SLC7A11 is upregulated in most pancreatic cancer cell lines [29]. However, until now, no study has reported specific regulatory mechanisms between lncRNAs and ferroptosis in pancreatic cancer. Interestingly,

our study found that activated LINC00578 can obviously inhibit ferroptosis events, including erastin-induced cell proliferation inhibition, ROS generation, and MMP depolarization. The inhibitory effect of LINC00578 on ferroptosis events can be rescued by SLC7A11 knockdown. Importantly, we first demonstrated that LINC00578 overexpression can inhibit ferroptosis by targeting SLC7A11 in pancreatic cancer, suggesting that LINC00578 regulates pancreatic cancer progression by inhibiting SLC7A11-dependent ferroptosis.

The ubiquitin-proteasome pathway is a prevalent form of endogenous protein degradation, where ubiquitination

is mediated by linking ubiquitin to target proteins through an enzymatic reaction. Mounting studies illustrate that cytoplasmic-located lncRNAs are suitable for translational regulation, including ubiquitin-mediated protein stability control and translational efficiency regulation [30–32]. For example, LINC00673 enhances the interaction of PTPN11 with the ubiquitin ligase PRPF19 and promotes PTPN11 degradation through ubiquitination in pancreatic cancer [33]. LINC00669, which is located in the cytoplasm of nasopharyngeal carcinoma cells, can bind to SOC1 and block its ubiquitination of STATA1 [34]. In agreement with these findings, in our study, the direct interaction between cytoplasmic LINC00578 and the ubiquitin regulatory enzyme UBE2K was investigated by a pull-down assay and validated by subsequent western blotting and RIP, revealing that LINC0578 can directly bind UBE2K to control downstream protein stability. SLC7A11 can be regulated at multiple levels, in which posttranslational regulation plays a critical role. For example, Liu et al. identified that OTUB1 (an ovarian tumor family member deubiquitylase) can interact with SLC7A11 to prevent its degradation [35]. Additionally, Chen's study revealed that fascin directly interacts with SLC7A11 and decreases its stability via ubiquitin-mediated degradation [36]. In concert with these findings, we demonstrated that LINC00578 knockdown can promote ubiquitination of SLC7A11. In addition, for the first time to our knowledge, the interaction between UBE2K and SLC7A11 was validated via Co-IP in our study. Considering the direct interaction between LINC00578 and UBE2K that was proven previously, we demonstrated that LINC00578 can directly bind UBE2K, thus reducing UBE2K-mediated ubiquitination of SLC7A11.

Taken together, this study revealed that LINC00578 promoted pancreatic cancer progression and inhibited ferroptosis by directly binding UBE2K to suppress SLC7A11 ubiquitination. However, it is elusive whether LINC00578 participates in pancreatic cancer progression through SLC7A11-independent ferroptosis. Another limitation of this research lies in the cohort sample size, which will be improved in further studies.

5. Conclusions

This study illustrates that LINC00578 promotes pancreatic cancer cell progression and suppresses ferroptosis by directly binding UBE2K to inhibit the ubiquitination of SLC7A11. These findings demonstrate that LINC00578 might be a crucial biomarker for pancreatic cancer progression and may provide a promising option for the diagnosis and treatment of pancreatic cancer.

Data Availability

The data are presented within the paper. The raw data supporting the conclusions of this article will be made available on request from the corresponding authors, without undue reservation.

Conflicts of Interest

The authors declare no conflict of interest to the publication of this article.

Authors' Contributions

(I) Conception and design were handled by J Zhou, HR Li, and YJ Wei; (II) administrative support was provided by J Zhou and J Yang; (III) provision of study materials or patients was handled by J Zhou and HR Li; (IV) collection and assembly of data were handled by J Wang and J Yao; (V) data analysis and interpretation were provided by C Zhang, CQ Yu, and YC Tang; (VI) manuscript writing was handled by all authors; and (VII) final approval of the manuscript was given by all authors. Haoran Li and Yijun Wei have contributed equally to this work

Acknowledgments

This study was supported by the Project of National Natural Science Foundation of China (grant number: 81902385), the Natural Science Foundation of Jiangsu Province (grant number: BK20201173), the Project of Medical Research of Jiangsu Province (grant number: Y2018094), and the Project of Extracurricular Academic Research of Soochow University (KY2022132A).

Supplementary Materials

Supplementary 1. Figure S1: Kaplan-Meier analysis of the correlation of LINC00578 expression with disease-free survival (DFS) ($P = 0.002$), from the cBioPortal (TCGA Firehose Legacy) cohort. Figure S2: relative expression levels of LINC00578 in PATU8988 cells with LINC00578 overexpression and PL45 cells with LINC00578 knockdown. Figure S3: differential expressed proteins between Sh-LINC00578 and Sh-NC groups selected by label-free proteomics. Figure S4: relative ubiquitinated protein levels between Sh-LINC00578 and Sh-NC groups by coimmunoprecipitation.

Supplementary 2. Table S1: shRNA/siRNA sequence.

Supplementary 3. Table S2: PCR primers used in this study.

Supplementary 4. Table S3: antibody list.

References

- [1] W. Park, A. Chawla, and E. M. O'Reilly, "Pancreatic cancer: a review," *JAMA*, vol. 326, no. 9, pp. 851–862, 2021.
- [2] J. Cai, H. Chen, M. Lu et al., "Advances in the epidemiology of pancreatic cancer: trends, risk factors, screening, and prognosis," *Cancer Letters*, vol. 520, pp. 1–11, 2021.
- [3] W. X. Peng, P. Koirala, and Y. Y. Mo, "lncRNA-mediated regulation of cell signaling in cancer," *Oncogene*, vol. 36, no. 41, pp. 5661–5667, 2017.
- [4] A. Bhan, M. Soleimani, and S. S. Mandal, "Long noncoding RNA and cancer: a new paradigm," *Cancer Research*, vol. 77, no. 15, pp. 3965–3981, 2017.
- [5] C. Mao, X. Wang, Y. Liu et al., "A G3BP1-interacting lncRNA promotes ferroptosis and apoptosis in cancer via nuclear

- sequestration of p53," *Cancer Research*, vol. 78, no. 13, pp. 3484–3496, 2018.
- [6] L. Wang, H. Zhao, Y. Xu et al., "Systematic identification of lincRNA-based prognostic biomarkers by integrating lincRNA expression and copy number variation in lung adenocarcinoma," *International Journal of Cancer*, vol. 144, no. 7, pp. 1723–1734, 2019.
- [7] X. Li, Y. Li, X. Yu, and F. Jin, "Identification and validation of stemness-related lincRNA prognostic signature for breast cancer," *Journal of Translational Medicine*, vol. 18, no. 1, p. 331, 2020.
- [8] B. Zhang, C. Li, and Z. Sun, "Long non-coding RNA LINC00346, LINC00578, LINC00673, LINC00671, LINC00261, and SNHG9 are novel prognostic markers for pancreatic cancer," *American Journal of Translational Research*, vol. 10, no. 8, pp. 2648–2658, 2018.
- [9] P. Koppula, L. Zhuang, and B. Gan, "Cystine transporter SLC7A11/xCT in cancer: ferroptosis, nutrient dependency, and cancer therapy," *Protein & Cell*, vol. 12, no. 8, pp. 599–620, 2021.
- [10] X. Lang, M. D. Green, W. Wang et al., "Radiotherapy and immunotherapy promote tumoral lipid oxidation and ferroptosis via synergistic repression of SLC7A11," *Cancer Discovery*, vol. 9, no. 12, pp. 1673–1685, 2019.
- [11] W. Lin, C. Wang, G. Liu et al., "SLC7A11/xCT in cancer: biological functions and therapeutic implications," *American Journal of Cancer Research*, vol. 10, no. 10, pp. 3106–3126, 2020.
- [12] Y. Zhang, S. Guo, S. Wang et al., "lncRNA OIP5-AS1 inhibits ferroptosis in prostate cancer with long-term cadmium exposure through miR-128-3p/SLC7A11 signaling," *Ecotoxicology and Environmental Safety*, vol. 220, article 112376, 2021.
- [13] C. Gai, C. Liu, X. Wu et al., "_MT1DP_ loaded by folate-modified liposomes sensitizes erastin-induced ferroptosis via regulating miR-365a-3p/NRF2 axis in non-small cell lung cancer cells," *Cell Death & Disease*, vol. 11, no. 9, p. 751, 2020.
- [14] X. Jiang, B. R. Stockwell, and M. Conrad, "Ferroptosis: mechanisms, biology and role in disease," *Nature Reviews Molecular Cell Biology*, vol. 22, no. 4, pp. 266–282, 2021.
- [15] H. Zhu, T. Li, Y. Du, and M. Li, "Pancreatic cancer: challenges and opportunities," *BMC Medicine*, vol. 16, no. 1, p. 214, 2018.
- [16] W. Lin, Q. Zhou, C. Q. Wang et al., "lncRNAs regulate metabolism in cancer," *International Journal of Biological Sciences*, vol. 16, no. 7, pp. 1194–1206, 2020.
- [17] M. C. Bridges, A. C. Daulagala, and A. Kourtidis, "LNCcation: lncRNA localization and function," *The Journal of Cell Biology*, vol. 220, no. 2, 2021.
- [18] S. U. Schmitz, P. Grote, and B. G. Herrmann, "Mechanisms of long noncoding RNA function in development and disease," *Cellular and molecular life sciences : CMLS*, vol. 73, no. 13, pp. 2491–2509, 2016.
- [19] F. X. Guo, Q. Wu, P. Li et al., "The role of the lncRNA-FA2H-2-MLKL pathway in atherosclerosis by regulation of autophagy flux and inflammation through mTOR-dependent signaling," *Cell Death and Differentiation*, vol. 26, no. 9, pp. 1670–1687, 2019.
- [20] K. Zhang, Z. M. Shi, Y. N. Chang, Z. M. Hu, H. X. Qi, and W. Hong, "The ways of action of long non-coding RNAs in cytoplasm and nucleus," *Gene*, vol. 547, no. 1, pp. 1–9, 2014.
- [21] X. Wei, X. Yi, X. H. Zhu, and D. S. Jiang, "Posttranslational modifications in ferroptosis," *Oxidative Medicine and Cellular Longevity*, vol. 2020, Article ID 8832043, 12 pages, 2020.
- [22] X. Chen, J. Li, R. Kang, D. J. Klionsky, and D. Tang, "Ferroptosis: machinery and regulation," *Autophagy*, vol. 17, no. 9, pp. 2054–2081, 2021.
- [23] X. Chen, R. Kang, G. Kroemer, and D. Tang, "Broadening horizons: the role of ferroptosis in cancer," *Nature reviews Clinical oncology*, vol. 18, no. 5, pp. 280–296, 2021.
- [24] G. Lei, L. Zhuang, and B. Gan, "Targeting ferroptosis as a vulnerability in cancer," *Nature Reviews Cancer*, vol. 22, no. 7, pp. 381–396, 2022.
- [25] C. Liang, X. Zhang, M. Yang, and X. Dong, "Recent progress in ferroptosis inducers for cancer therapy," *Advanced materials*, vol. 31, no. 51, article e1904197, 2019.
- [26] L. Jiang, N. Kon, T. Li et al., "Ferroptosis as a p53-mediated activity during tumour suppression," *Nature*, vol. 520, no. 7545, pp. 57–62, 2015.
- [27] B. R. Stockwell, X. Jiang, and W. Gu, "Emerging mechanisms and disease relevance of ferroptosis," *Trends in Cell Biology*, vol. 30, no. 6, pp. 478–490, 2020.
- [28] H. Zhang, Y. Zhuo, D. Li et al., "Dihydroartemisinin inhibits the growth of pancreatic cells by inducing ferroptosis and activating antitumor immunity," *European Journal of Pharmacology*, vol. 926, article 175028, 2022.
- [29] J. He, H. Ding, H. Li, Z. Pan, and Q. Chen, "Intra-tumoral expression of SLC7A11 is associated with immune microenvironment, drug resistance, and prognosis in cancers: a pan-cancer analysis," *Frontiers in Genetics*, vol. 12, article 770857, 2021.
- [30] C. Carrieri, L. Cimatti, M. Biagioli et al., "Long non-coding antisense RNA controls *Uchl1* translation through an embedded SINEB2 repeat," *Nature*, vol. 491, no. 7424, pp. 454–457, 2012.
- [31] Y. T. Tan, J. F. Lin, T. Li, J. J. Li, R. H. Xu, and H. Q. Ju, "lncRNA-mediated posttranslational modifications and reprogramming of energy metabolism in cancer," *Cancer communications (London, England)*, vol. 41, no. 2, pp. 109–120, 2021.
- [32] J. Zhu, H. Fu, Y. Wu, and X. Zheng, "Function of lncRNAs and approaches to lncRNA-protein interactions," *Science China Life sciences*, vol. 56, no. 10, pp. 876–885, 2013.
- [33] J. Zheng, X. Huang, W. Tan et al., "Pancreatic cancer risk variant in *_LINC00673_* creates a miR-1231 binding site and interferes with PTPN11 degradation," *Nature Genetics*, vol. 48, no. 7, pp. 747–757, 2016.
- [34] X. Qing, G. L. Tan, H. W. Liu et al., "LINC00669 insulates the JAK/STAT suppressor SOCS1 to promote nasopharyngeal cancer cell proliferation and invasion," *Journal of experimental & clinical cancer research : CR*, vol. 39, no. 1, p. 166, 2020.
- [35] T. Liu, L. Jiang, O. Tavana, and W. Gu, "The deubiquitylase OTUB1 mediates ferroptosis via stabilization of SLC7A11," *Cancer Research*, vol. 79, no. 8, pp. 1913–1924, 2019.
- [36] C. Chen, B. Xie, Z. Li et al., "Fascin enhances the vulnerability of breast cancer to erastin-induced ferroptosis," *Cell Death & Disease*, vol. 13, no. 2, p. 150, 2022.

Research Article

Ferroptosis in Rat Lung Tissue during Severe Acute Pancreatitis-Associated Acute Lung Injury: Protection of Qingyi Decoction

Peng Ge ^{1,2,3}, Yalan Luo ^{1,2,3}, Qi Yang ⁴, Haiyun Wen ^{1,2,3}, Jin Liu ^{1,3},
Yibo Zhang ^{1,2,3}, Xuanchi Dong ^{1,3}, Guixin Zhang ^{1,2,3}, Caiming Xu ^{1,5}, Jing Liu ^{2,6},
Zheyi Liu ⁶, and Hailong Chen ^{1,2,3}

¹Department of General Surgery, The First Affiliated Hospital of Dalian Medical University, Dalian, Liaoning, China

²Institute (College) of Integrative Medicine, Dalian Medical University, Dalian, Liaoning, China

³Laboratory of Integrative Medicine, The First Affiliated Hospital of Dalian Medical University, Dalian, Liaoning, China

⁴Department of Traditional Chinese Medicine, The Second Affiliated Hospital of Dalian Medical University, Dalian, Liaoning, China

⁵Department of Molecular Diagnostics and Experimental Therapeutics, Beckman Research Institute of City of Hope, Biomedical Research Center, Comprehensive Cancer Center, CA, USA

⁶CAS Key Laboratory of Separation Sciences for Analytical Chemistry, Dalian Institute of Chemical Physics, Chinese Academy of Sciences, Dalian, Liaoning, China

Correspondence should be addressed to Zheyi Liu; zy_liu@dicp.ac.cn and Hailong Chen; chen hailong@dmu.edu.cn

Received 20 September 2022; Revised 6 November 2022; Accepted 25 November 2022; Published 11 February 2023

Academic Editor: Lianxiang Luo

Copyright © 2023 Peng Ge et al. This is an open access article distributed under the Creative Commons Attribution License, which permits unrestricted use, distribution, and reproduction in any medium, provided the original work is properly cited.

Qingyi decoction (QYD) has anti-inflammatory pharmacological properties and substantial therapeutic benefits on severe acute pancreatitis (SAP) in clinical practice. However, its protective mechanism against SAP-associated acute lung injury (ALI) remains unclear. In this study, we screened the active ingredients of QYD from the perspective of network pharmacology to identify its core targets and signaling pathways against SAP-associated ALI. Rescue experiments were used to determine the relationship between QYD and ferroptosis. Then, metabolomics and 16s rDNA sequencing were used to identify differential metabolites and microbes in lung tissue. Correlation analysis was utilized to explore the relationship between core targets, signaling pathways, metabolic phenotypes, and microbial flora, sorting out the potential molecular network of QYD against SAP-associated lung ALI. Inflammatory damage was caused by SAP in the rat lung. QYD could effectively alleviate lung injury, improve respiratory function, and significantly reduce serum inflammatory factor levels in SAP rats. Network pharmacology and molecular docking identified three key targets: ALDH2, AnxA1, and ICAM-1. Mechanistically, QYD may inhibit ferroptosis by promoting the ALDH2 expression and suppress neutrophil infiltration by blocking the cleavage of intact AnxA1 and downregulating ICAM-1 expression. Ferroptosis activator counteracts the pulmonary protective effect of QYD in SAP rats. In addition, seven significant differential metabolites were identified in lung tissues. QYD relatively improved the lung microbiome's abundance in SAP rats. Further correlation analysis determined the correlation between ferroptosis, differential metabolites, and differential microbes. In this work, the network pharmacology, metabolomics, and 16s rDNA sequencing were integrated to uncover the mechanism of QYD against SAP-associated ALI. This novel integrated method may play an important role in future research on traditional Chinese medicine.

1. Introduction

Acute pancreatitis (AP) is a common inflammatory disease of the pancreas, which places a significant financial burden on patients and public health systems due to its rising inci-

dence and hospitalization rates [1]. Mild AP patients have a better prognosis, with a death rate of less than 3%. However, severe acute pancreatitis (SAP) with pancreatic hemorrhage and necrosis could induce systemic inflammatory response syndrome (SIRS) and potentially multiple organ

dysfunction syndrome (MODS), causing a mortality rate of 15–35% [1]. Acute lung injury (ALI)/acute respiratory distress syndrome (ARDS) is a frequent SAP consequence and cause of mortality. Elucidation of the mechanism of SAP-associated ALI and the development of effective medications to arrest the disease's malignant progression are urgently needed [2, 3].

Qingyi decoction (QYD) is derived from the traditional Chinese medicine (TCM) formula Da Chai Hu decoction and Da Cheng Qi decoction in “Shanghan Lun.” This TCM formula is often used to treat people with AP because it induces purgation and clears heat and toxic materials [4]. QYD is a robust anti-inflammatory agent that can improve the intestinal barrier damage caused by SAP, microcirculatory disorders, and pulmonary inflammatory response. A recent meta-analysis of 38 clinical trials involving 2254 patients confirmed that QYD dramatically lowered levels of proinflammatory factors, including interleukin- (IL-) 6, tumor necrosis factor- α (TNF- α), and IL-1 β while increasing levels of the anti-inflammatory factor IL-10 in patients with AP [5]. However, the fundamental mechanism of QYD for SAP and associated organ injury is yet unknown.

An emerging discipline called network pharmacology (NP) is frequently utilized to reveal the molecular mechanisms of herbal formulas for treating diseases. NP could anticipate the active ingredients and targets of herbal formulas for treating conditions and build ingredient-target networks [6]. Through a thorough investigation of metabolite alterations before and after illness onset, metabolomics directly reflects the disease phenotype at the functional level. Currently, metabolomic methods are frequently used in the research of ALI/ARDS and are crucial for identifying biomarkers and assessing medication effectiveness [7]. Moreover, the alterations of the lung microbiome before and after illness have been reported recently and have gained increasing attention. Several studies have found that the lung microbiome is not only influenced by host illness but also plays a role in disease progression and severity via eliciting host immune responses [8, 9]. However, changes in the lung microbiota of SAP-associated ALI have not been discovered.

Through a comprehensive investigation, the molecular mechanisms by which QYD intervenes in SAP-associated ALI have been determined in this work. We first used a network pharmacology approach to screen potential targets of QYD, which determined the central role of ferroptosis in SAP-associated ALI. In exploring the effect of QYD on ferroptosis, we further combined metabolomics and 16s rDNA sequencing to analyze the correlation of ferroptosis-related markers with differential metabolites and microbes. To sum up, we have presented a new paradigm and provided a novel idea for research into TCM.

2. Materials and Methods

2.1. Preparation of Qingyi Decoction. The herbal material of QYD is resourced from the First Affiliated Hospital of Dalian Medical University (Dalian, Liaoning, China). QYD consists of *Bupleurum chinense* DC (Chai Hu in Chinese, 15 g), *Corydalis yanhusuo* (Yan Hu Suo in Chinese, 15 g),

Scutellaria baicalensis Georgi (Huang Qin in Chinese, 12 g), *Gardenia jasminoides* J. Ellis (Zhi Zi in Chinese, 15 g), *Paeonia lactiflora* Pall. (Bai Shao in Chinese, 15 g), *Rheum officinale* Baill. (Da Huang in Chinese, 20 g), *Aucklandia costus* Falc. (Mu Xiang in Chinese, 15 g), and $\text{Na}_2\text{SO}_4 \cdot 10 \text{H}_2\text{O}$ (Mang Xiao in Chinese, 10 g). Professor Aijing Leng certified the authenticity of all the herbs. The QYD extract (1 g crude herb/ml) was made according to the reported methods. Briefly, the herbs are weighed, combined with 10 times their weight in water, steeped for 0.5 h, boiled for 1 h, and filtered while still hot. The residue is boiled again in 8 times the quantity of water used for the herbs and decocted for 0.5 h, and then, the *Rheum officinale* Baill. is added and simmered for an additional 0.5 h. Filter when hot, add $\text{Na}_2\text{SO}_4 \cdot 10 \text{H}_2\text{O}$, blend the two filtrates, concentrate to 1 g/ml, sterile package, and store at 4°C for future use. The chemical profiles of QYD mapped using ultraperformance liquid chromatography coupled with quadrupole time-of-flight mass spectrometry are presented in the previous study [10].

2.2. Reagents. Antibodies against ALDH2 (A11500), AnxA1 (A1118), ICAM-1 (A5597), GPX4 (A11243), nuclear factor- κB p65 (p65, A16271), β -actin (AC026), and horseradish peroxidase- (HRP-) conjugated anti-rabbit IgG antibody (AS014) were purchased from ABclonal, Inc. (Wuhan, China). Antibodies against phosphorylated p65 (Ser 536, p-p65, bs-0982R) and 8-hydroxy-2'-deoxyguanosine (8-OHdG, bs-1278R) were purchased from Bioss (Beijing, China). Antibodies against SLC7A11 (DF12509), NCOA4 (DF4255), and FTH1 (DF6278) were purchased from Affinity (Liyang, China). Rat tumor necrosis factor- α (TNF- α , E-EL-R2856c) and interleukin-6 (IL-6, E-EL-R0015c) ELISA kits were obtained from Elabscience Biotechnology Co., Ltd. (Wuhan, China). Glutathione (GSH) assay kit (A006-2-1), amylase assay kit (C016-1-1), myeloperoxidase (MPO) assay kit (A044-1-1), malondialdehyde (MDA) assay kit (A003-1-2), and tissue Fe^{2+} assay kit (A039-2-1) were obtained from Nanjing Jiancheng Bioengineering Institute (Nanjing, China).

2.3. Animals and Treatment. All animal experiments were conducted by the People's Republic of China Legislation Regarding the Use and Care of Laboratory Animals and approved by the Committee for Research and Animal Ethics of Dalian Medical University, Dalian, China (approved number: AEE19003). Sprague-Dawley (SD) male rats weighing 180–220 g (6–8 weeks old) were provided by the Experimental Animal Center of Dalian Medical University. All animals were kept in ventilated caging systems at $22.0 \pm 2.0^\circ\text{C}$, with a 12 h light-dark cycle, allowed free access to standard rat chow and water *ad libitum*. Rats were acclimated to the housing condition for one week before experiments. Firstly, 60 rats were randomly assigned to four groups ($n = 15$): a blank control group (the CON group), a severe acute pancreatitis model group (the SAP group), a severe acute pancreatitis model +Qingyi decoction-treated group (the SAP+QYD group), and a blank control+Qingyi decoction-treated group (the CON+QYD group). Rats in the SAP group were retrograde-injected into the biliopancreatic duct with 5.0% sodium

taurocholate (STC, 50 mg/kg) as reported previously [11], and the same volume of sterile saline was used in the CON group. Rats in the SAP+QYD and CON+QYD groups were administered Qingyi decoction (10 g/kg, crude drug volume: 1 g/ml) via gastric perfusion 0.5 h before and 12 h after administration of STC and sterile saline. Secondly, 30 SD male rats were then separated into four groups: CON ($n = 6$), SAP ($n = 8$), SAP+QYD ($n = 8$), and SAP+QYD+erastin ($n = 8$). The CON, SAP, and SAP+QYD groups were handled as previously stated. In the SAP+QYD+erastin (Era, ferroptosis activator, MCE) group, QYD was administered by gavage 0.5 h before and 12 h after STC administration, while Era (10 μ mol/kg [12]) was administered intraperitoneally 0.5 h after STC administration. Rats were sacrificed after 24 h of STC administration. The pancreas, lung tissues, and blood from each rat were collected and stored at -80°C for subsequent experiments.

2.4. Network Pharmacology Analysis. The TCMSP (<https://tcmsp-e.com/>), TCMIP (<http://www.tcmip.cn/>), and previous chemical profiles were used to screen the active ingredients of QYD (no active ingredient was detected for $\text{Na}_2\text{SO}_4 \cdot 10 \text{H}_2\text{O}$), and the screening conditions were referenced to the rules proposed by Lipinski [13]. The 2D and 3D structures of the candidate ingredients were queried using the PubChem (<https://pubchem.ncbi.nlm.nih.gov/>) database and compared with the data obtained by TCMSP and TCMIP to confirm the final molecular structures. The TCMSP, TCMIP, DrugBank (<https://go.drugbank.com/>), and SwissTargetPrediction (<http://www.swisstargetprediction.ch/>) databases were then used to predict the targets of action of the candidate ingredients. Target names were corrected using the UniProt database (<https://www.uniprot.org/>). In summary, 225 ingredients and 514 potential targets for QYD were identified (Supplementary File S1).

Fold change (FC) > 1.2 or FC < 0.83 with P value < 0.05 was used as the primary criterion for differentially expressed proteins (DEPs) [14]. Converting DEPs' names to gene names using the UniProt database. Volcano plots were drawn to show the screening results. The DAVID database (<https://david.ncifcrf.gov/>) was utilized for the Gene Ontology (GO) and KEGG pathway enrichment analyses. Target names were corrected using the UniProt database, and 3D structures of target proteins were obtained from the AlphaFold database (<https://alphafold.ebi.ac.uk/>). Cytoscape 3.8.2 software was used to construct the ingredient-target network. The operation procedure was as follows: (1) preprocess the data to generate two original files, network, and type, respectively; (2) import the original data into the software and adjust the edges, nodes, and colors according to the type classification; (3) set the size of each node according to the degree value to highlight the targets and ingredients.

2.5. Molecular Docking. The ingredients and targets were imported into Discovery Studio (DS) software and then pretreated with dehydration and hydrogenation and selected as receptor and ligand, respectively. Precise docking was performed using the CDocker module of DS software, and the ligand-receptor binding mode was analyzed. CDocker is a semiflexible docking program based on the CHARMM force

field and determines the binding activity by calculating the ligand-receptor interaction energy [15]. In general, lower ligand-receptor interaction energies in CDocker docking represent better binding of ingredients and targets during docking.

2.6. Histopathological Analysis. Isolated pancreatic and pulmonary specimens were fixed in 4% paraformaldehyde for 24 h, paraffin-embedded, and sectioned (4 μ m). The sections were stained with hematoxylin and eosin (HE). The pathological score of stained sections was conducted in a blinded fashion referred to previous reports [16, 17]. Three parameters (inflammatory cell infiltration, vacuolization, and acinar necrosis) were utilized to determine the pancreatic histological score. The pulmonary histological score was based on three parameters: inflammatory cell infiltration, hemorrhage, and alveolar septal thickening. Each of the individual parameter was graded from 0 to 3. The total score for the three parameters was calculated. The specimens of at least three rats from each group were evaluated.

2.7. Measurement of Serum Amylase. Serum was extracted from rat blood by centrifuging at 3000 rpm for 10 min. Serum amylase activity was measured using a commercial amylase assay kit. Briefly, the serum sample was added with a known concentration and excess substrate (amylum). The amylase in the sample hydrolyzed the amyllum, and then, iodine was added to react with the unhydrolyzed amyllum, generating some blue compounds. The amount of hydrolyzed amyllum could be deduced from the absorbance of blue compounds at 660 nm, and thus, the amylase activity could be calculated. The unit was expressed as U/l.

2.8. Assessment of Serum Levels of Inflammatory Factors. Concentrations of inflammatory cytokines (IL-6 and TNF- α) in rat serum were measured by commercial ELISA kits following to manufacturer's instructions.

2.9. Lung Wet/Dry Weight Ratio. The lung wet/dry weight (W/D) ratio reflects pulmonary edema and congestion. The inferior lobe of the rat's right lung was cut out, and the fluid on the lung surface was wiped using filter paper. Lung tissue was weighed immediately for its wet weight and again after drying at 80°C for 48 h to determine its dry weight. The wet weight was divided by the dry weight to obtain the lung W/D ratio.

2.10. MPO Activity. MPO activity in lung tissue homogenate was measured as an indication of pulmonary neutrophil infiltration via a commercial assay kit provided by Nanjing Jiancheng Bioengineering Institute (Nanjing, China). The unit was expressed as U/g.

2.11. Fe^{2+} , GSH, and MDA Measurements. The concentration of Fe^{2+} , GSH, and MDA in lung tissue represents pulmonary ferroptosis to some extent. The Fe^{2+} assay kit, GSH assay kit, and MDA assay kit, purchased from Nanjing Jiancheng Bioengineering Institute, were used to detect Fe^{2+} , GSH, and MDA levels in lung tissues strictly with the manufacturer's instructions.

2.12. Quantitative Real-Time PCR. RNA extraction from rat lung tissue in each group was performed with *RNAex Pro* Reagent (AG21102, Accurate Biology, Changsha, China). The obtained single-stranded mRNA was reverse transcribed into cDNA using the *Evo M-MLV* Reverse Transcription Mix Kit (AG11728, Accurate Biology). Synthesized cDNA was amplified by SYBR® Green Premix *Pro Taq HS* qPCR Kit II (AG11702, Accurate Biology). All primers used are listed in Supplementary File S2. The expression of the target gene relative to the house-keeping gene GAPDH was quantified by the $2^{-\Delta\Delta CT}$ method [18]. Three independent samples were analyzed in each group.

2.13. Western Blotting. The Protein Extraction Kit and the BCA Protein Quantitation Kit (KGP10100, KGP903, Key-Gen Biotech, Nanjing, China) were used to achieve protein extraction and quantification of rat lung tissue. Protein samples were separated via 10%-12% sodium dodecyl sulfate-polyacrylamide gel electrophoresis and electrotransferred onto 0.22 μm polyvinylidene fluoride membranes. The membranes were blocked with 5% bovine serum albumin solution for 2 h at room temperature and then incubated overnight at 4°C with the following primary antibodies: ALDH2 (1:1000), GPX4 (1:1000), p65 (1:1000), p-p65 (1:500), AnxA1 (1:1000), ICAM-1 (1:1000), and β -actin (1:50 000). After TBST solution rinsing, the membranes were incubated with HRP-conjugated secondary antibodies for 2 h at room temperature. Protein levels were visualized and quantified using a chemiluminescence system (Tanon-4800, Shanghai, China) and ImageJ software.

2.14. TdT-Mediated dUTP Nick End Labeling (TUNEL) Assay. Sections of lung tissue were stained using a TUNEL kit (Roche, Basel, Switzerland). Follow the directions provided by the supplier of the reagent to the letter. Briefly, paraffin-embedded lung tissue was sectioned at a 5 μm thickness for dewaxing and hydration and subsequent antigen repair. Sections were blocked using the serum for 30 minutes, and then, appropriate amounts of TdT and dUTP (1:10 mix) were added and incubated overnight at 4°C in a moist box. 4',6-Diamidino-2-phenylindole (DAPI) was used to restrain cell nuclei and micrographs were taken. TUNEL – positive cell rate = (number of TUNEL – positive cells/total number of cells) \times 100%.

2.15. Immunofluorescence. Paraffin-embedded lung tissue was sectioned at a 5 μm thickness for dewaxing, hydration, and repair. Sections were blocked using 10% goat serum and incubated at 37°C for 0.5 h. The sections were sequentially incubated with diluted primary antibody (incubated at 4°C overnight) and secondary antibody (incubated at 37°C for 1 h). DAPI working solution was added dropwise to the tissue sections and incubated for 5 min at room temperature before washing 3 times with PBS. The liquid on the sections was shaken off, an antifluorescent agent was added, and the sections were sealed and kept at 4°C and out of the light. The sections were observed using a fluorescent microscope.

2.16. Metabolomic Analysis. An aliquot of 10 mg lung tissue was placed into a centrifuge tube, added with 1 ml of extraction reagent containing internal standard [19], vortexed, and homogenized thoroughly. The homogenate was sonicated in an ice-water bath for 10 min and incubated at -20°C for 1 h to fully precipitate the proteins. The mixture was dispensed by centrifugation at 14000 g for 10 min at 4°C. Take 50 μl of supernatant from each tube and mix to obtain quality control (QC) samples. Lyophilize all samples to be tested. The lyophilized powder was redissolved in 100 μl of methanol/water (4/1) and then vortex-mixing for 2 min. The supernatant was obtained by centrifugation at 14000 g for 10 min at 4°C. 60 μl of supernatant was taken from each tube for analysis. Chromatographic-mass spectrometry conditions were referenced to previously reported methods [20]. Samples were separated using an Acquity UPLC system and a Waters Acquity BEH C8 column (100 mm \times 2.1 mm and 1.7 μm). Details of the analytical conditions and data preprocessing are provided in Supplementary File S3. Metabolites were identified and annotated using the mzCloud (<https://www.mzcloud.org/>), the KEGG (<https://www.genome.jp/kegg/>), and the HMDB (<https://hmdb.ca/>) databases. Metabolites with variable importance in the projection (VIP) > 1, FC > 1.2 or FC < 0.83, and *P* value < 0.05 were considered significant. MetaboAnalyst 5.0 database (<http://www.metaboanalyst.ca/>) was used for partial least squares discriminant analysis (PLS-DA), orthogonal partial least squares discriminant analysis (OPLS-DA), and metabolic pathway analysis.

2.17. 5S 16S rDNA Sequencing Analysis. Samples were collected, processed, and sequenced, referring to previous articles. 50 mg of lung tissue samples was extracted using the CTAB method. 16S rRNA gene amplification and sequencing were done by amplifying 5 regions on the 16S rRNA gene in the multiplex. The libraries were sequenced on Illumina NovaSeq 6000 system. Reads were demultiplexed per sample, filtered, and aligned to each of the five amplified regions based on the primers' sequences. The Short Multiple Regions Framework (SMURF) method was applied to combine read counts from the five regions into coherent profiling results solving a maximum likelihood problem. For this purpose, we referred to the GreenGenes database (updated version from May 2013). Differences in microbial communities were analyzed using an online website (<https://www.omicstudio.cn/>). Alpha diversity was performed using the Chao1, Shannon, and Simpson indices. Differences in lung microbiota composition between the CON and SAP groups and between the SAP and QYD groups were uncovered using the linear discriminant analysis effect size (LEfSe). Taxa having an LDA score of >3.0 were deemed to be significant. We utilized PICRUSt2, which stands for Phylogenetic Investigation of Communities by Reconstruction of Unobserved States 2, to infer metabolic function from 16S rDNA sequences.

2.18. Statistical Analysis. All experimental data were presented as mean \pm standard deviation (SD). One-way analysis of variance (ANOVA) was performed for comparisons

among multiple groups. The post hoc test was estimated using Fisher's least square difference (LSD, if homogeneity of variance was satisfied) or Tamhane (if homogeneity of variance was not satisfied). Correlation analysis of ferroptosis-related indicators, differentially metabolites, and microbiota was performed using the Spearman rank correlation analysis. P value < 0.05 indicates statistical significance ($*P < 0.05$, $**P < 0.01$, and $***P < 0.001$). Statistical analysis and visualization were performed using SPSS 24.0 and GraphPad Prism 8.2.

3. Results

3.1. QYD Alleviated SAP-Associated ALI. Rats injected with STC showed histopathological characteristics of SAP, including diffuse necrosis of acinar cells, vacuolization, inflammatory cell infiltration, and hemorrhage. Meanwhile, secondary ALI was observed in rats with SAP induced by STC. Lung tissue destruction was evident in rats in the SAP group, such as alveolar and interstitial infiltration of inflammatory cells, congestion, and alveolar septal thickening (Figure 1(a)). After the gavage of QYD, the histopathological damage to rat pancreas and lung was significantly improved, and the pathological score was reduced compared with the SAP group (Figures 1(b) and 1(c)). Serum amylase is a biomarker with high accuracy, specificity, and sensitivity in the early diagnosis of acute pancreatitis. The lung wet/dry weight ratio is an indicator to evaluate pulmonary edema and congestion. Consistent with histological findings, QYD significantly inhibited the increase of serum amylase (Figure 1(d)) and lung wet/dry weight ratio (Figure 1(e)) in SAP rats. The accumulation of circulating inflammatory mediators is an essential bridge in the progression of the pancreas from local inflammation to SIRS and distal organ damage. Serum levels of TNF- α and IL-6 were higher in the SAP group than in the CON group, as shown in Figures 1(f) and 1(g), and QYD considerably reduced these inflammatory factor levels in the SAP group. These results suggest that QYD could improve pancreatic inflammation and associated ALI during SAP.

3.2. Target and Mechanism Analysis of QYD against SAP-Associated ALI. Previous proteomic data were used to preliminarily screen possible targets for QYD intervention in SAP-associated ALI [14]. As shown in Figures 2(a) and 2(b), 731 differential expression proteins (DEPs) occurred between the SAP and CON groups based on the screening criteria stated in Materials and Methods, while 382 DEPs existed between the QYD and SAP groups. Among these, 202 differentially expressed genes (DEGs) (Supplementary File S1) with overlap were discovered and used for functional enrichment analysis. The GO biological process terms of the overlapped DEGs were mainly involved in DNA replication-dependent nucleosome assembly, negative regulation of megakaryocyte differentiation, nucleosome assembly, cellular response to interferon-gamma, cell-matrix adhesion, fatty acid metabolic process, adaptive immune response, and response to ethanol (Figure 2(c)). KEGG enrichment analysis revealed that the overlapped DEGs were

more enriched in signaling pathways such as ferroptosis, pyruvate metabolism, and neutrophil extracellular trap (NET) formation (Figure 2(d)). According to these data, QYD may exert a protective effect by regulating the expression patterns of genes related to lipid metabolism, ferroptosis, and neutrophil function.

3.3. Ingredient-Target Network Construction and Molecular Docking. To further certain the core targets of QYD against SAP-associated ALI, we searched the drug targets of QYD using network pharmacology and performed a secondary screening in combination with proteomics data. As depicted in Figure 2(e), network pharmacology identified 514 drug targets (Supplementary File S1) of QYD intersected with 202 DEGs to generate three core targets of QYD in the treatment of SAP-associated ALI: acetaldehyde dehydrogenase 2 (ALDH2), annexin A1 (AnxA1), and intercellular cell adhesion molecule-1 (ICAM-1). Based on these three intersecting targets, the active ingredient was identified in reverse, and the drug-active ingredient-target network was established (Figure 2(f)). Next, the structures of core targets and corresponding active ingredients were imported into the DS software for CDOCKER docking. Figure 3(a) shows the binding pattern of ALDH2 to several ingredients, such as pulmatin, chrysophanein, and 8-methoxy-5-O-glucoside flavone. Figure 3(b) shows the binding pattern of AnxA1 to ingredients such as palbinone and gardenolic acid B. Figure 3(c) shows the binding pattern between ICAM-1 and ingredients such as kaempferol and quercetin. The CDOCKER interaction energy of all ingredients and proteins during molecular docking is shown in Supplementary File S4. According to the findings, each active ingredient formed several strong hydrogen bonds with its core target and had low binding energies. In a word, QYD may be able to directly target and affect the activity of the core target since its active ingredients have been shown to have a high affinity for the core target in the study.

3.4. QYD Inhibits Ferroptosis and Apoptosis by Activating ALDH2. To validate the core targets acquired from the integrative analysis of proteomics and network pharmacology, qRT-PCR and western blotting were first performed to detect the expression levels of ALDH2 in rat lung tissues. ALDH2, a mitochondrial aldehyde dehydrogenase, has recently been reported to play a protective role in various inflammatory diseases by regulating lipid peroxidation and ferroptosis [21, 22]. As shown in Figures 4(a) and 4(b), lung tissue of rats in the SAP group exhibited lower levels of ALDH2 mRNA and protein than those in the CON group, while QYD significantly promoted the transcription and translation of ALDH2. In addition, the apoptotic rate was much higher in the lung tissues of SAP rats than in normal rats. Still, apoptosis induced by SAP was significantly decreased by QYD therapy (Supplementary File S5). Glutathione peroxidase 4 (GPX4) is a key regulator of ferroptosis, preventing cellular ferroptosis by eliminating peroxides, reducing reactive oxygen species (ROS) accumulation, and inhibiting NF- κ B activation [23]. As indicated in Figures 4(c)–4(f), GPX4 was decreased, and p-p65 increased

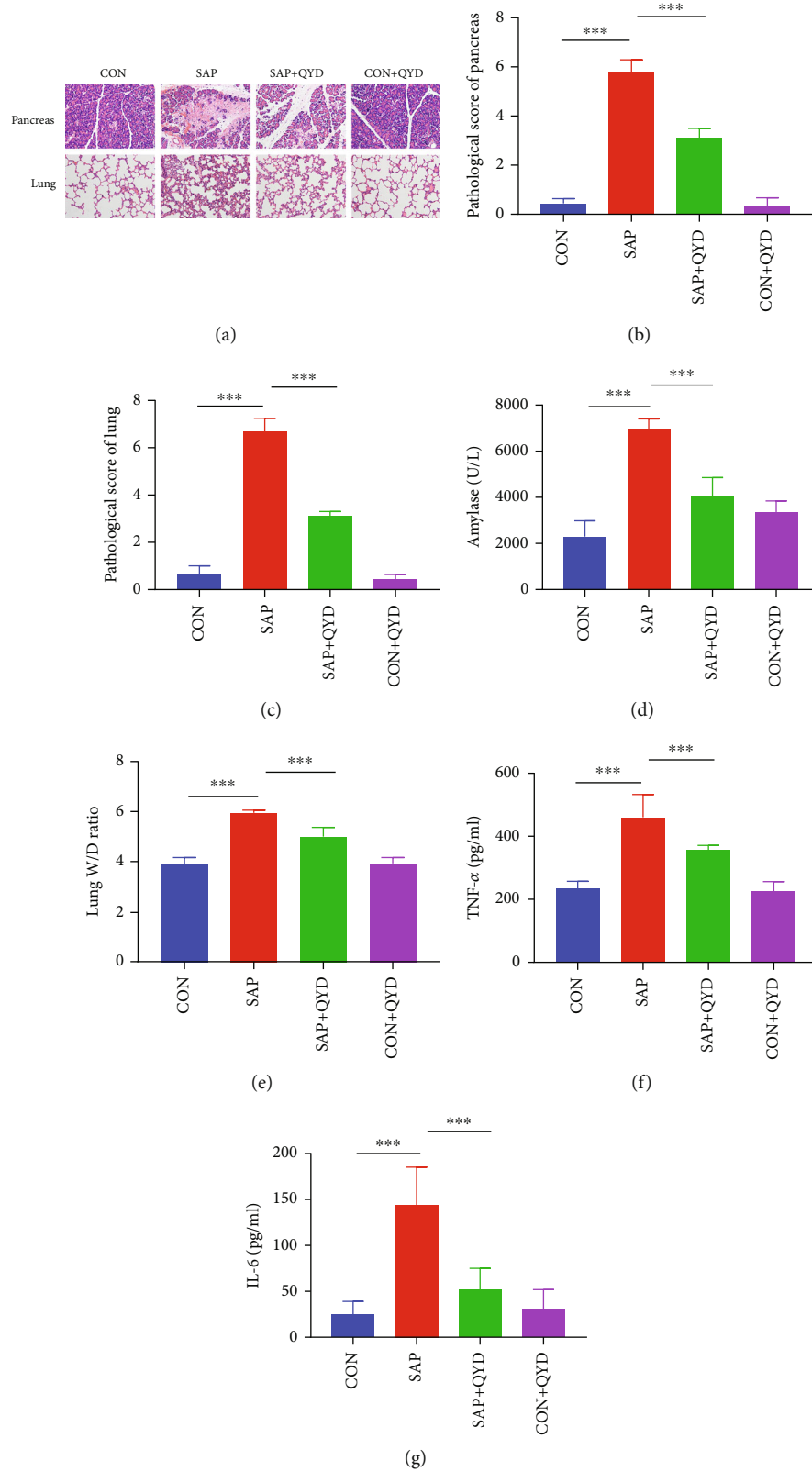


FIGURE 1: Protective effect of QYD on pancreatic and pulmonary tissue injury in rats with SAP. (a) Representative images of HE staining of the pancreas (upper) and lung tissues (lower) of rats in each group (scale bar, 100 μ m). (b, c) Histopathological scores of pancreas and lung tissues of rats in each group. (d) Serum amylase levels of rats in each group. (e) The lung W/D ratio was used to evaluate pulmonary edema in each group of rats. (f, g) Serum levels of inflammatory factors TNF- α and IL-6 of rats in each group. Data are presented as representative images or as the mean \pm SD of each group of rats ($n = 6$ per group) from at least three separate experiments. *** $P < 0.001$.

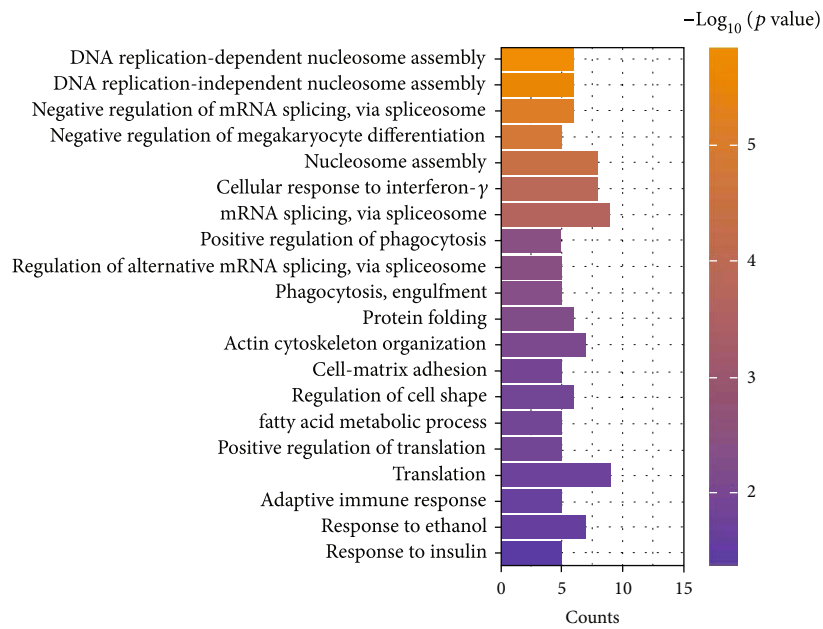
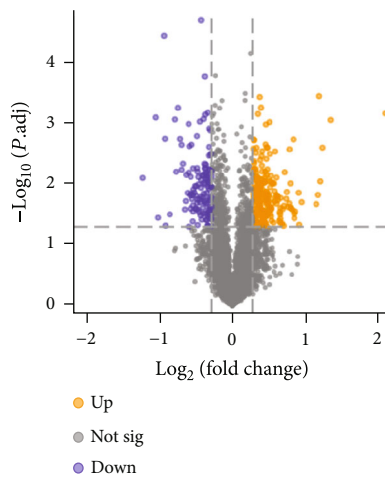
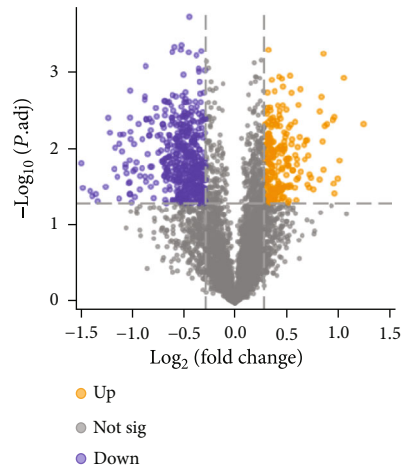


FIGURE 2: Continued.

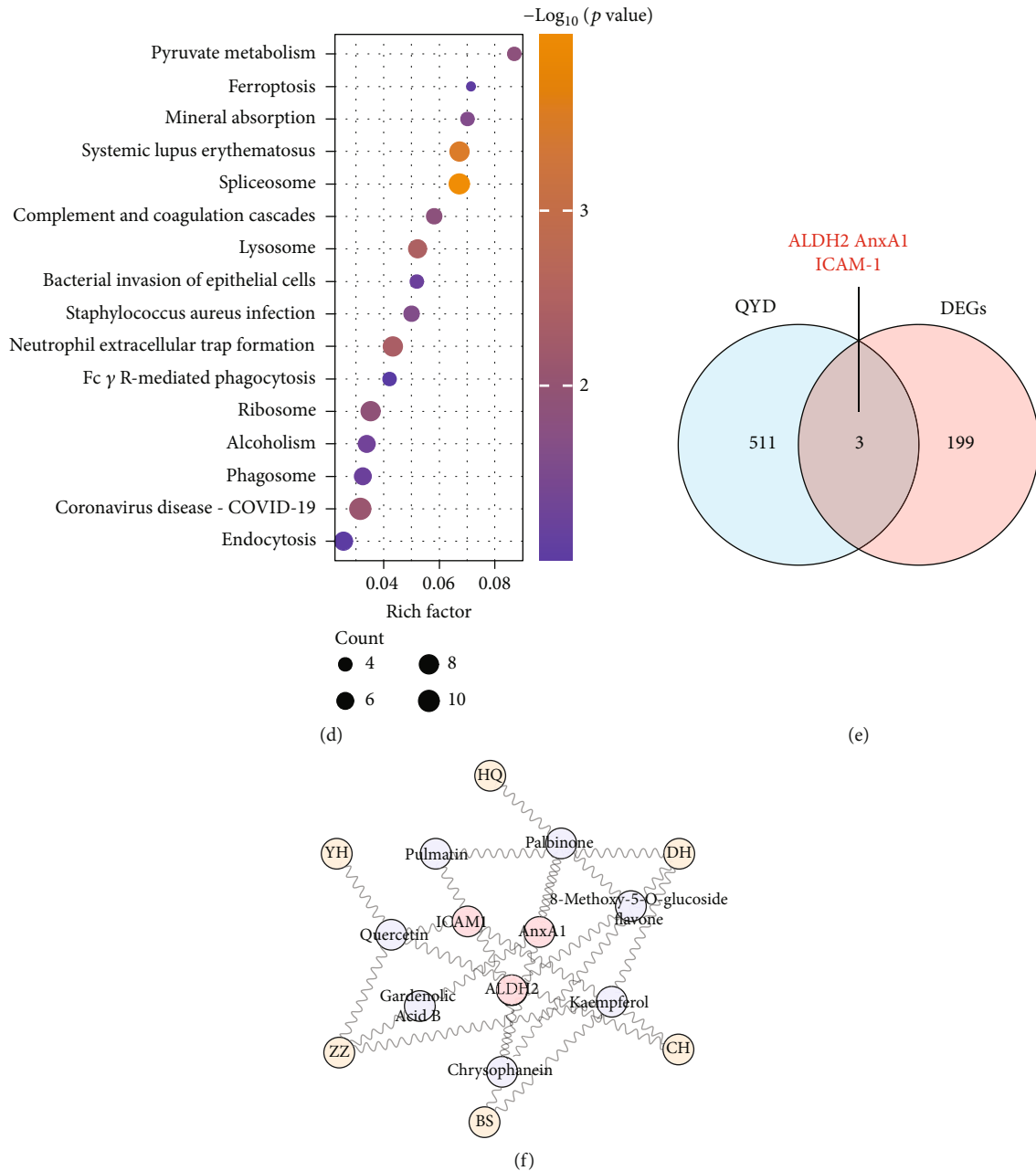


FIGURE 2: Determination of core targets of QYD against SAP-associated ALI. (a) Volcano plot showing DEPs between the SAP and CON groups. (b) Volcano plot showing DEPs between the QYD and SAP groups. (c) GO enrichment analysis of 202 overlapped DEGs in the term of biological process. (d) Pathway annotation of 202 overlapped DEGs by KEGG terms. (e) Venn diagram between the 202 overlapped DEGs and the 514 drug targets of QYD. The integrated analysis of proteomic data and network pharmacology results yielded three core targets of QYD for SAP-associated ALI: ALDH2, AnxA1, and ICAM-1. (f) Construction of a drug-active ingredient-target network based on the three core targets obtained. Yellow dots represented each herb of QYD; purple dots represented the active ingredients of QYD; red dots represented the target proteins.

in lung tissues of rats in the SAP group compared to those in the CON group. However, GPX4 protein expression was elevated compared with that of the SAP group following the administration of QYD. In contrast, the level of p-p65 protein expression could be reduced by QYD administration. In addition, solute carrier family 7 member 11 (SLC7A11), ferritin heavy chain 1 (FTH1), and nuclear receptor coactivator 4 (NCOA4) were ferroptosis marker genes. SLC7A11 and FTH1 protein expressions were dramatically downregu-

lated, and NCOA4 protein expression was significantly upregulated in the lung tissue of SAP rats relative to the CON group, whereas QYD partly reversed these alterations (Supplementary File S6). Our data further demonstrated that QYD countered SAP-induced upregulation of Fe^{2+} (Figure 4(g)), MDA (Figure 4(h)), and 8-OHdG (Supplementary File S7) and downregulation of GSH (Figure 4(i)) in lung tissue, which are characteristic indicators of ferroptosis. In addition, rescue experiments confirm that Era

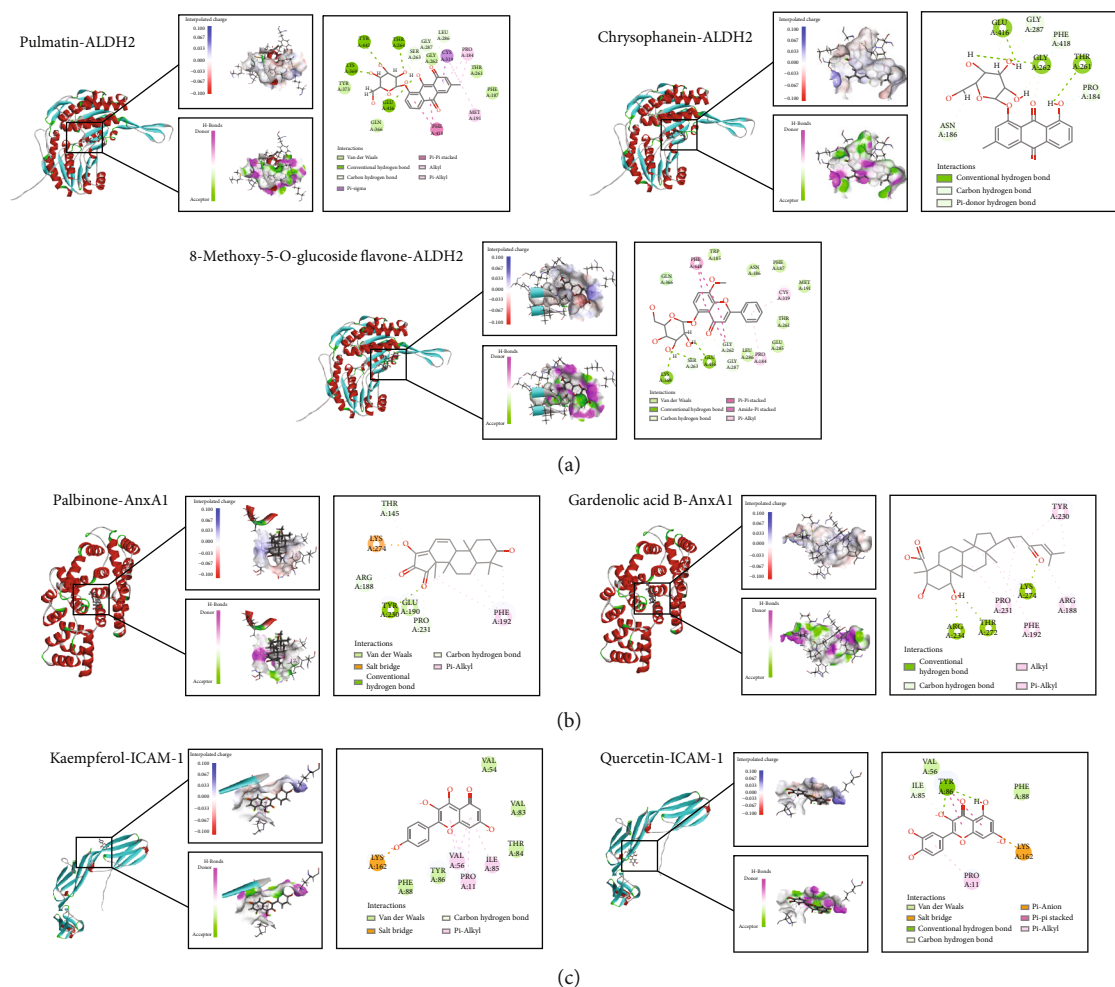


FIGURE 3: Interactions between ingredients and targets. (a) Molecular docking interaction of pulmatin, chrysophanein, and 8-methoxy-5-O-glucoside flavone with ALDH2. **(b)** Molecular docking interaction of palbinone and gardenolic acid B with AnxA1. **(c)** Molecular docking interaction of quercetin and kaempferol with ICAM-1. The left part of each molecular docking result showed the structure of the ingredient-target complex after docking; the middle part showed the interaction space of interpolated charge and hydrogen bonds (acceptor in green and donor in pink) between the ingredient and the target; and the right part showed the two-dimensional diagram of interaction sites between the ingredient and the target.

eliminated the protective effect of QYD against pathological damage in lung tissue. Similarly, serum levels of TNF- α and IL-6 were elevated in SAP rats, and QYD could partly inhibit the production of inflammatory factors. Era, in contrast, prevented the downregulation of QYD (Supplementary File S8). These findings support the potential therapeutic effect of QYD on SAP-associated lung injury by enhancing ALDH2 activity to inhibit ferroptosis and apoptosis.

3.5. QYD Limits Neutrophil Infiltration by Increasing Active Form of AnxA1. Besides ALDH2, AnxA1 and ICAM-1 are also predicted core targets of QYD intervention in SAP-associated ALL. AnxA1 is a calcium-dependent phospholipid-binding protein, existing in two primary forms, a 33-kDa inactive form and a 37-kDa bioactive, which inhibits neutrophil tissue accumulation by reducing leukocyte infiltration and activating neutrophil apoptosis, with anti-inflammatory and tissue-protective properties.

ICAM-1 is one of the essential leukocyte-endothelial cell adhesion molecules, and its elevated expression in ALI has become a marker of inflammatory cell migration and endothelial barrier injury. As shown in Figure 5(a), the mRNA expression of AnxA1 was elevated in the SAP group compared to the CON group and decreased after QYD treatment. Western blotting, as we expected, revealed that AnxA1 displayed two distinct bands. The expression of AnxA1 with a molecular weight of 37 kDa was reduced, whereas that of 33 kDa was raised in the SAP group compared to the CON group. After QYD gavage, we noticed an increase in intact AnxA1 (Figures 5(b) and 5(c)). Meanwhile, we found that ICAM-1 expression level was elevated in the SAP group, while QYD greatly reduced the mRNA and protein expression levels of ICAM-1 (Figures 5(d) and 5(e)). In addition, MPO activity, a marker of neutrophil infiltration, was elevated in the SAP rats, whereas QYD dramatically decreased MPO activity (Figure 5(f)). These

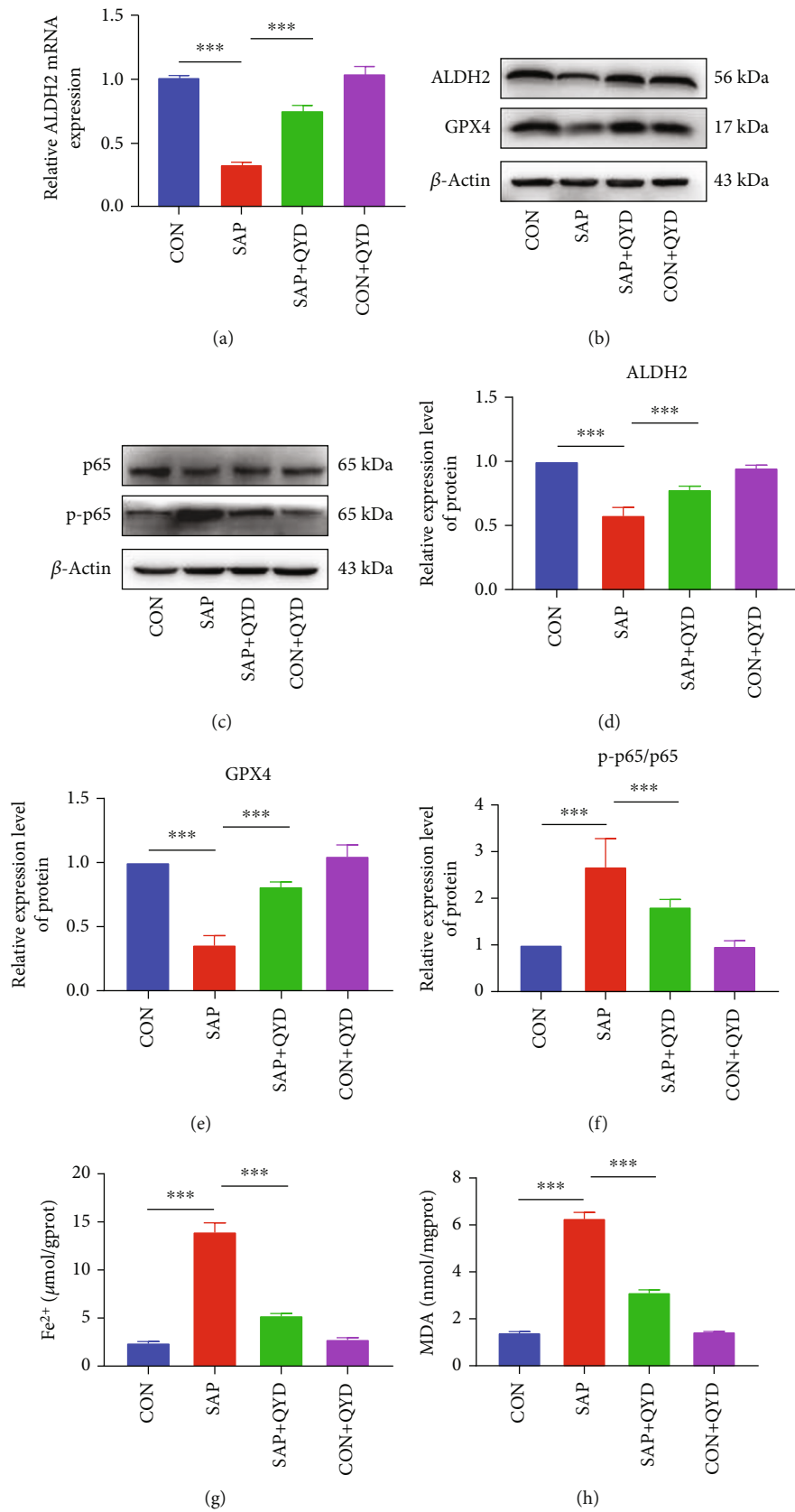


FIGURE 4: Continued.

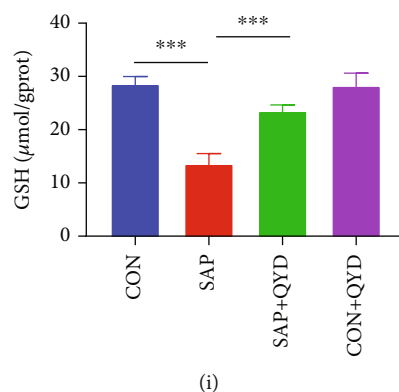


FIGURE 4: QYD enhancing ALDH2 activity protects against ferroptosis in SAP-associated ALI. (a) qRT-PCR was performed to assess the mRNA expression level of ALDH2 in the rat lung tissue of each group. GAPDH was used as the reference gene. (b, c) Western blotting was conducted to evaluate the protein expression levels of ALDH2, GPX4, p65, and p-p65 in the lung tissue of rats. β -Actin was used as a loading control. (d–f) Semiquantification of protein expression of ALDH2, GPX4, and p-p65 using histograms. (g) Measurement of Fe^{2+} in rat lung tissue of each group served as an iron metabolism indicator. (h) MDA concentration in the rat lung tissue of each group was measured as an indicator of lipid peroxidation. (i) GSH levels in rat lung tissue of each group were monitored to reflect antioxidant capacity. Data are presented as representative images or as the mean \pm SD of each group of rats ($n = 6$ per group) from at least three separate experiments. *** $P < 0.001$.

findings imply that QYD may contribute to the inhibition of neutrophil infiltration and restoration of lung inflammation by posttranslationally regulating AnxA1 protein levels.

3.6. Effects of QYD on Lung Metabolism. PLS-DA is a supervised data analysis approach that overlooks intragroup and random errors in favor of focusing on sample variability between groups. The samples from the CON group were substantially separated from the SAP group in the PLS-DA model of this study, demonstrating the metabolic phenotype of lung tissue is significantly altered in STC-induced SAP rats. The QYD group was closer to the CON group, indicating that QYD may modulate those metabolites changed during SAP to return to normal levels. Furthermore, the overlap in the PLS-DA plot between the CON+QYD group and the CON group indicated that QYD had no significant effects on the metabolic phenotype of normal rats (Figure 6(a)).

The OPLS-DA method was adopted to investigate the effect of QYD on the regulation of metabolites in lung tissue. Differentiation between CON and SAP samples showed an altered metabolic profile of lung tissue in rats during STC-induced SAP (Figure 6(b)). Similarly, a significant trend of separation was also seen between SAP and QYD samples (Figure 6(c)). The VIP, FC, and P values were then used to screen the samples from each group for differential metabolites; the screening conditions are detailed in Materials and Methods. Compared to the CON group, SAP affected the relative intensities of 41 metabolites in the lungs (4 from the negative ion model and 37 from the positive ion model). In comparison to the SAP group, the QYD group changed 29 metabolites. Among these, seven intersecting differential metabolites were extracted by the Venn diagram, including choline glycerophosphate, hippuric acid, hypoxanthine, indole-3-carbinol, isoleucine, trichloroacetic acid, and tryptophan, and their changes in the relative intensities could be seen in Figure 6(d). Heat maps were used to visualize each group's relative abundance of differential metabolites

(Figure 6(e)). The functional enrichment analysis results of the differential metabolites between the QYD and SAP groups indicated that potential pathways were related to aminoacyl-tRNA biosynthesis, phenylalanine metabolism, phenylalanine, tyrosine and tryptophan biosynthesis, purine metabolism, glyoxylate and dicarboxylate metabolism, and glycine, serine, and threonine metabolism (Figure 6(f)).

3.7. Effects of QYD on Lung Microbes. Alpha diversity was used to analyze the microbial diversity within the samples. Although there was no statistically significant difference between the SAP and CON groups, the data revealed that all three indices were reduced in the SAP group. When comparing the QYD group to the SAP group, the microbiome abundance did increase, albeit only a little. Please refer to Supplementary File S9. Differential microbe composition between the study groups was determined using LEfSe. On a phylum level, the relative abundance of Cyanobacteria increased in the SAP group than in the CON group. On a genus level, the SAP group had a higher relative abundance of Sphingomonas, Serratia, Pelomonas, and Methylobacterium and a lower relative abundance of Bacteroides than the CON group (Figure 7(a)). It is worth noting that in the QYD group, Bacteroides and Bradyrhizobium increased at the genus level compared to the SAP group (Figure 7(b)). The pulmonary microbiome's metabolic function was predicted using PICRUSt2. The pathways selected from the KEGG database were shown off. Significant differences were observed between the SAP and QYD groups in 23 level 2 pathways, including cell growth and death, cellular processes and signaling, digestive system, energy metabolism, excretory system, genetic information processing, immune system, and lipid metabolism (Figure 7(c)).

3.8. Integrative Analysis of the Ferroptosis, Metabolites, and Microbes. Next, a complete investigation was conducted to determine the link between ferroptosis indicators,

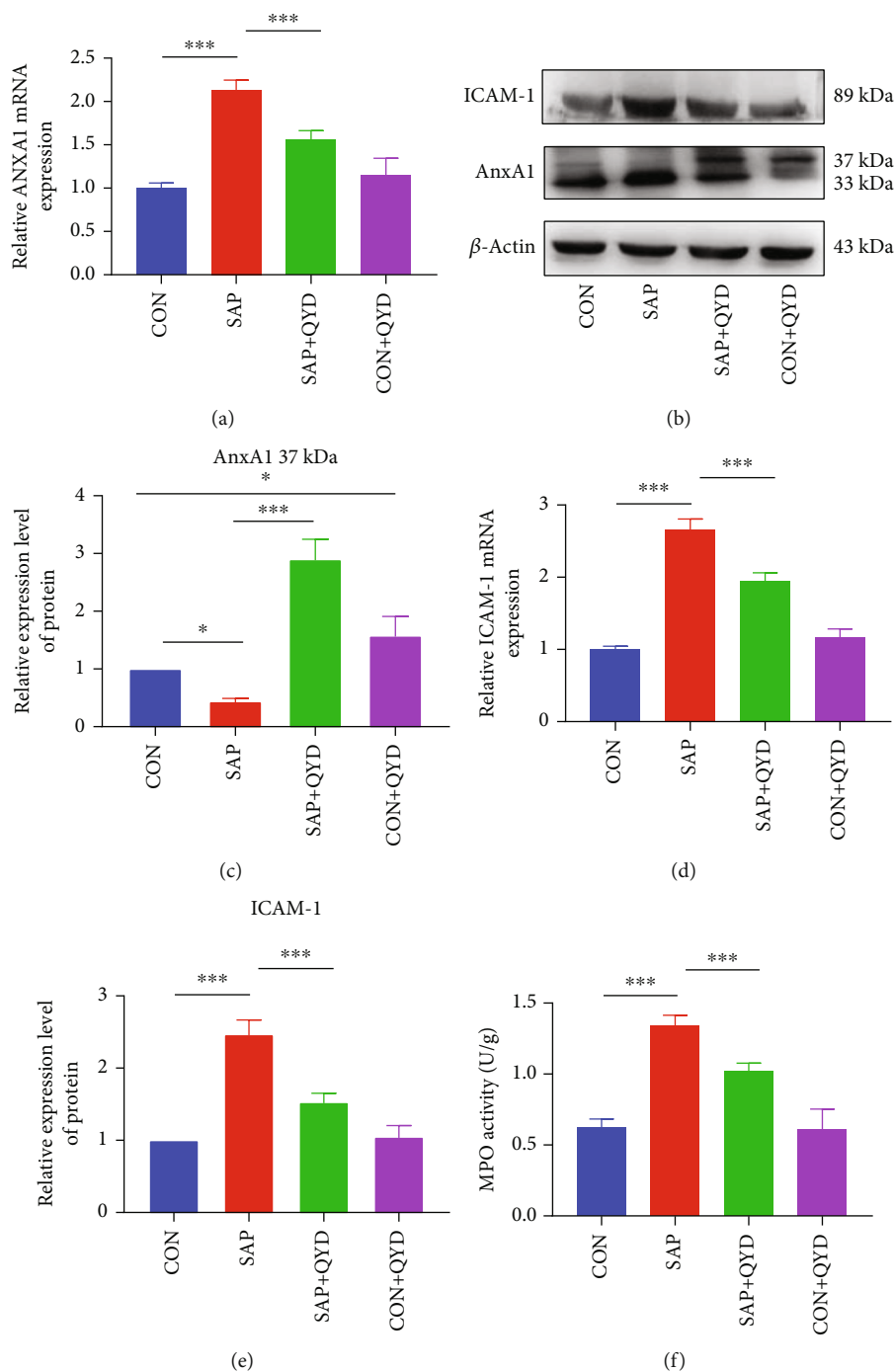


FIGURE 5: QYD decreases neutrophil infiltration via upregulating active AnxA1. (a) Analysis of the relative levels of AnxA1 mRNA in lung tissues using quantitative RT-PCR. (b, c) Western blotting analysis of the protein expression levels of AnxA1 in the lung tissues. (d, e) Analysis of the relative levels of ICAM-1 mRNA and protein in lung tissues. (f) MPO activity in the lung tissues. Data are presented as representative images or as the mean \pm SD of each group of rats ($n = 6$ per group) from at least three separate experiments. * $P < 0.05$ and *** $P < 0.001$.

differential metabolites, and differential bacterial genera in rats. First, the connection between differential metabolites and ferroptosis markers was investigated. Specifically, hippuric acid was negatively connected with Fe^{2+} , MDA, and inflammatory markers (IL-6, TNF- α , and MPO) and positively correlated with GSH levels. The concentration of Fe^{2+} was positively associated with that of indole-3-

carbinol. See Figure 8(a). Also, we linked ferroptosis markers to differential bacterial genera (Figure 8(b)). The following combinations of ferroptosis and bacterial genera showed a significant correlation: Serratia- Fe^{2+} (positive), Serratia-MDA (positive), Serratia-GSH (negative), Pelomonas- Fe^{2+} (positive), Pelomonas-MDA (positive), Methylobacterium- Fe^{2+} (positive), Massilia- Fe^{2+} (negative),

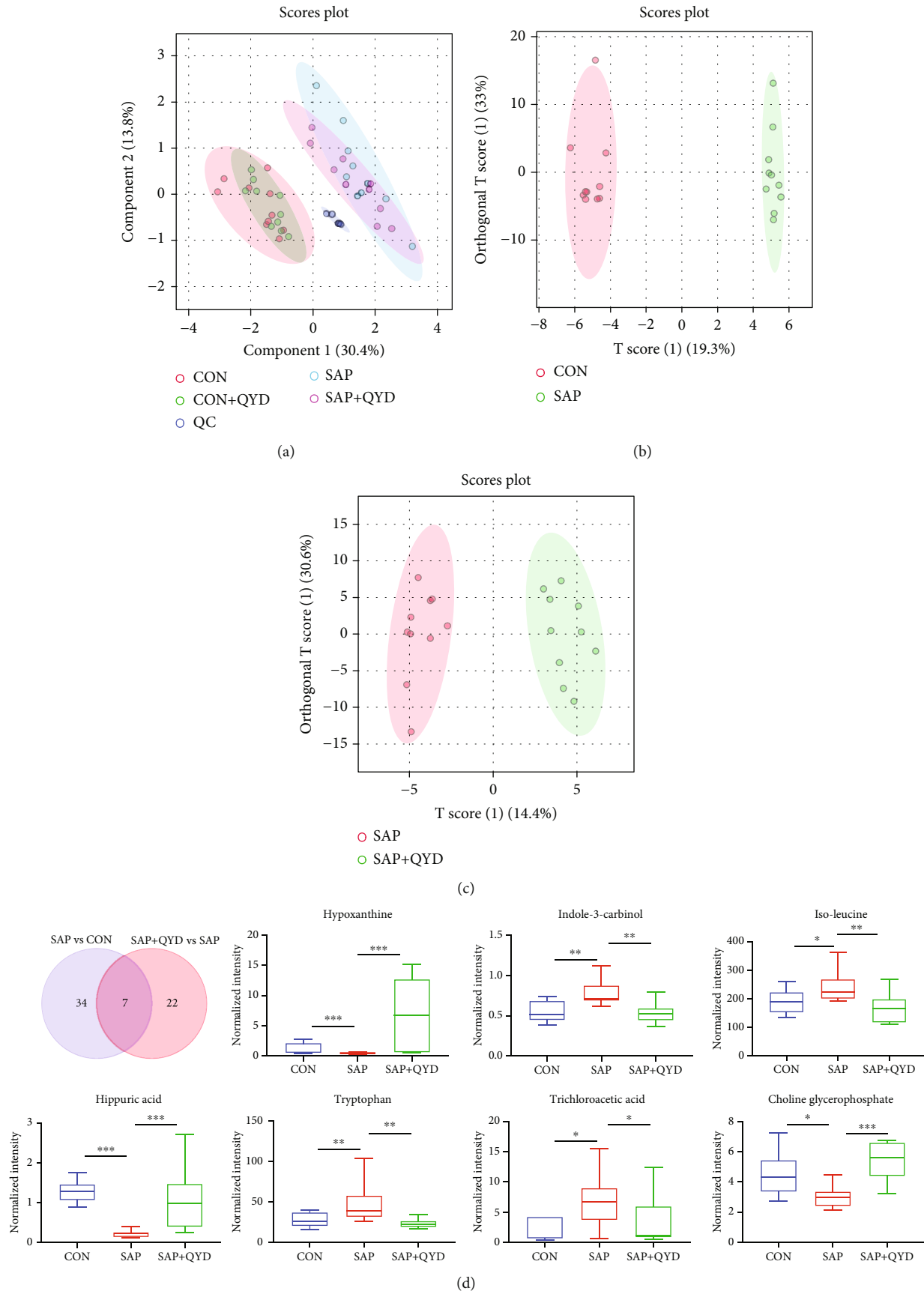


FIGURE 6: Continued.

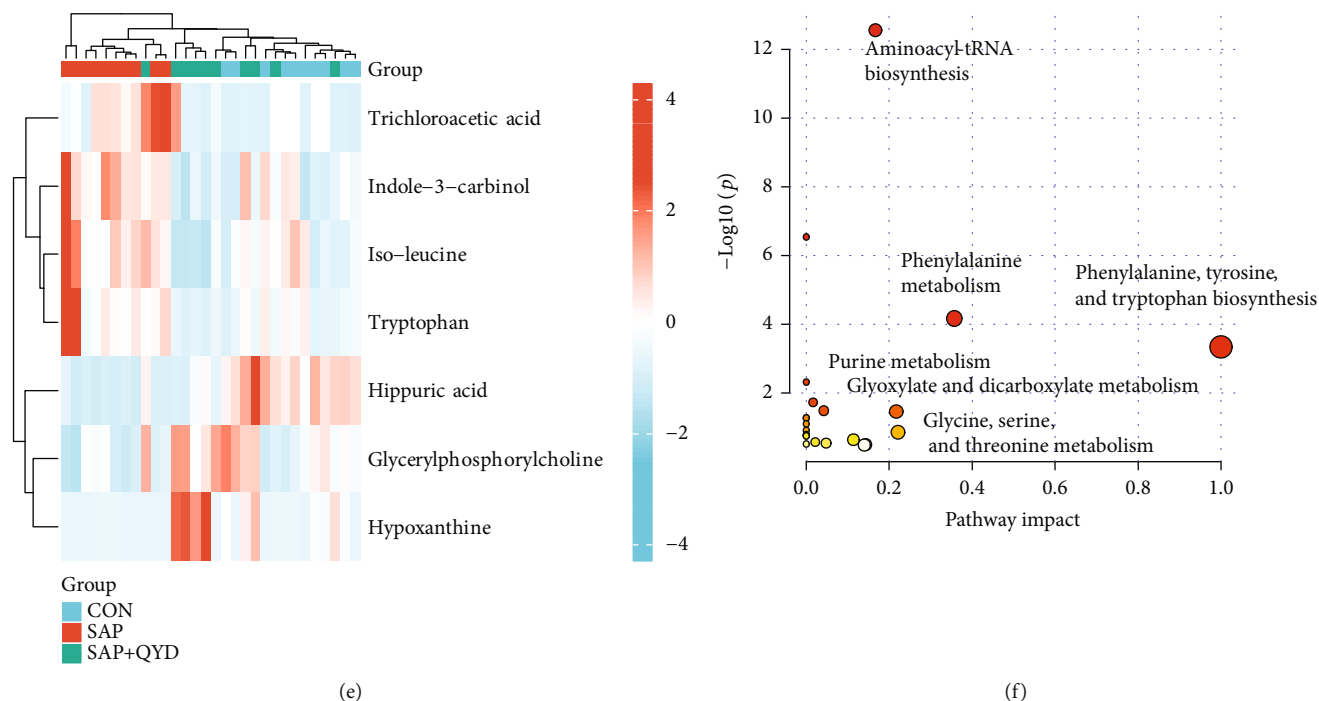


FIGURE 6: Effect of QYD on the lung metabolites of SAP rats. (a) PLS-DA score plots of the CON group, SAP group, SAP+QYD group, and CON+QYD group. (b) OPLS-DA score plots of the SAP vs. CON groups. (c) OPLS-DA score plots of the SAP+QYD vs. SAP groups. (d) Venn diagram of differential metabolites between SAP vs. CON groups and SAP+QYD vs. SAP groups. Effects of QYD on 7 differential metabolites levels in rats. (e) Heat map of 7 metabolites in each sample. (f) Analysis of metabolic pathway of differential metabolites between the QYD and SAP groups. Data are presented as the mean \pm SD. $n = 10$ per group. * $P < 0.05$, ** $P < 0.01$, and *** $P < 0.001$.

Massilia-MDA (negative), and Massilia-GSH (positive). Figure 8(b) also depicts the results of an investigation of the relationships between the bacterial genera and inflammatory markers. Lastly, we linked differential metabolites in lung tissue with bacterial genera. *Methylobacterium-hippuric acid* was the metabolite-microbe combination with the strongest connection among those studied (Figure 8(c)).

4. Discussion

QYD for treating SAP patients has demonstrated distinct advantages in suppressing the inflammatory response, enhancing gastrointestinal function, lowering infection rates, and facilitating quick recovery [24–26]. Several basic investigations have shown the molecular mechanisms of QYD in the treatment of SAP and associated distant organ damage. Wei et al.'s network pharmacology study demonstrated that QYD might attenuate pancreatic injury during SAP by inhibiting NF- κ B-mediated inflammatory response [10]. By suppressing intestinal sPLA2 expression, QYD dramatically reduced AP-induced intestinal barrier damage [27]. Furthermore, QYD prevented SAP-induced myocardial injury [28]. However, there have been fewer investigations on QYD's effectiveness against SAP-associated ALI. In our work, 5% of STC injected retrogradely into the biliopancreatic duct resulted in severe pancreatic and pulmonary histopathological injury. This method of establishing a rat model of SAP-associated ALI is stable and repeatable. QYD effectively ameliorated pancreatic and lung tissue injury in SAP, inhib-

ited the release of inflammatory cytokines, alleviated pulmonary edema, and restored respiratory function.

SAP-associated ALI is an indirect secondary lung injury, the mechanism of which remains incompletely understood. It has been proposed that the pulmonary air-blood barrier is disrupted by inflammatory mediators from the circulation [2]. Many activated immune cells enter the lung and produce excess inflammatory factors, ROS, and damage-associated molecular patterns, causing damage and death of lung parenchymal cells. In our study, ALDH2, AnxA1, and ICAM-1 were identified to play an important role in the pathogenesis of lung injury followed by SAP and are potential core targets of QYD against SAP-associated ALI. This antagonistic mechanism may depend on the regulation of ferroptosis and neutrophil infiltration by QYD.

ALDH2 is a member of the acetaldehyde dehydrogenase family, and its gene polymorphisms are related to alcoholic pancreatitis susceptibility, particularly in Asian populations [29]. Previously, Cao et al. found that Alda-1 (an activator of ALDH2) decreased pancreatic enzyme, MDA, and 4-hydroxy nonanoic acid levels in mice with cerulein-induced mild AP and delayed apoptosis of acinar cells via the Bax/Bcl-2 pathway [30]. Many investigations have demonstrated that Alda-1 protects against hyperoxia- or heatstroke-induced ALI. Alda-1 has lung-protective effects by inhibiting ROS generation and endothelial inflammation in the blood vessels [31, 32]. Our work showed that mRNA and protein expressions of ALDH2 were considerably decreased in SAP-associated ALI rats' lung tissue. QYD enhanced the transcription and translation of the *aldh2*

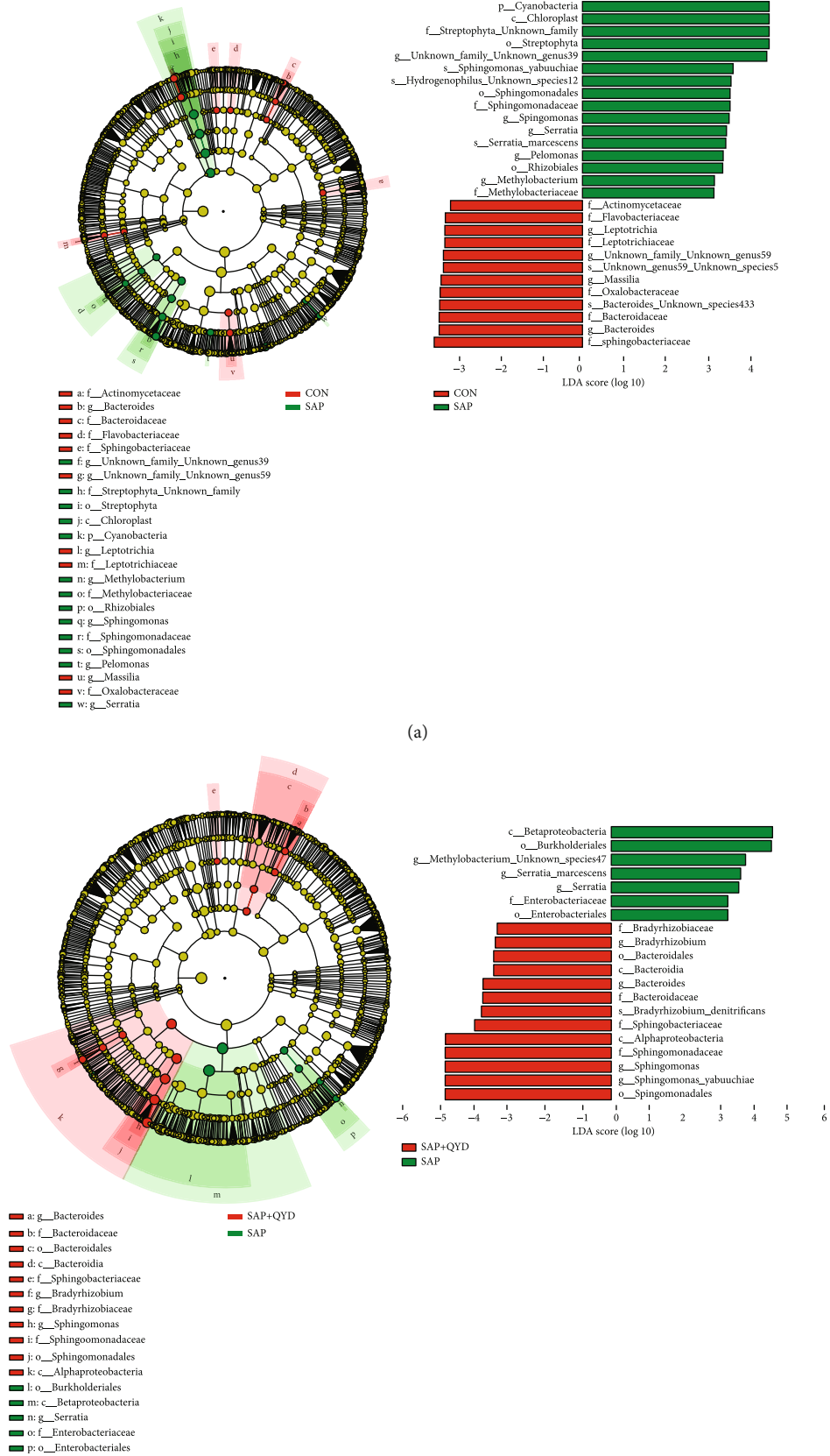


FIGURE 7: Continued.

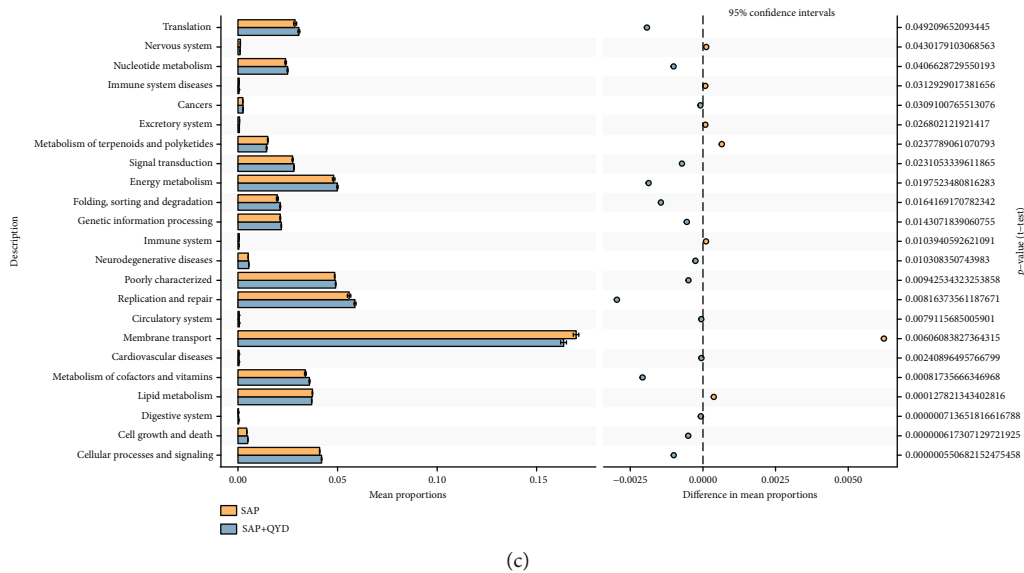


FIGURE 7: Effect of QYD on the lung microbiota composition of SAP rats. (a) Linear discriminant analysis between the SAP and CON groups (LDA score ≥ 3 , $P < 0.05$). (b) Linear discriminant analysis between the QYD and SAP groups (LDA score ≥ 3 , $P < 0.05$). (c) Metabolic pathways predicted by PICRUST analysis that were statistically different between the QYD and SAP groups. Data are presented as the mean \pm SD. $n = 10$ per group.

gene, which was consistent with the NP analysis. In addition, mitochondria-mediated apoptosis is intrinsically linked to the mitochondrial oxidoreductase ALDH2, which scavenges reactive aldehydes and reduces cellular oxidative damage. Multiple studies have indicated that increasing ALDH2 expression alleviates AP [30], myocardial infarction [33], atherosclerosis [34], heart failure [35], and ALI [32] by inhibiting apoptosis. Our study showed that QYD significantly reduced apoptosis in lung parenchymal cells caused by SAP, suggesting that QYD may alleviate lung damage by decreasing apoptosis via elevation of ALDH2 expression. Ferroptosis is a novel form of programmed cell death caused by the accumulation of iron-dependent lipid peroxides. The significance of ferroptosis in the development of SAP is crucial. The premature activation of trypsin is the first trigger for the onset of AP, and there is evidence that trypsin enhances the sensitivity of pancreatic acinar cells to ferroptosis, which significantly exacerbates pancreatic damage during AP [36]. Inhibiting ferroptosis reduced intestinal injury, bacterial translocation, and renal injury induced by AP [37, 38]. Ferroptosis of lung tissue, especially in alveolar epithelial cells, has been linked to ALI [39, 40]. Lung tissue GPX4 activity was dramatically suppressed in SAP-associated ALI, and ferroptosis aggravated lung damage [41]. Inhibiting the occurrence of ferroptosis is a potential strategy to combat SAP-associated ALI [42, 43]. Recently, ferroptosis has shown to be regulated by ALDH2. Researchers found that ALDH2 inhibits Alzheimer's disease-induced myocardial injury by regulating lipid peroxidation and ACSL4-dependent ferroptosis [44]. As a result, we performed downstream functional experiments. In rats with SAP-associated ALI, ferrous ions, 8-OHdG, MDA, and NCOA4 were expressed at higher levels, whereas GSH activity, SLC7A11, FTH1, and GPX4 proteins were expressed at lower levels. QYD therapy improved SAP-

induced ferroptosis in lung tissues, as predicted. As shown by our rescue experiment (Supplementary File S8), Era counteracted the protective effect of QYD on lung damage and inflammatory response in SAP-associated ALI rats. In a word, our data shows that QYD may protect against SAP-induced pulmonary ferroptosis and apoptosis by promoting the ALDH2 expression.

The other two targets are linked to neutrophil infiltration. Neutrophils are widely recognized for being among the first immune cells to rush to the site of damage following the initiation of inflammation [45]. Similarly, one of the features of SAP-associated lung damage is significant neutrophil infiltration. Elastase, ROS, and neutrophil extracellular traps are the main culprits in SAP-associated SIRS [46, 47]. AnxA1 is a glucocorticoid downstream mediator with anti-inflammatory and tissue-healing properties. AnxA1 and its mimetic peptide (Ac2-26) inhibit NF- κ B and eNOS signaling to minimize neutrophil infiltration and improve oxidative damage in lung tissue [48]. Our findings show that SAP increased AnxA1 mRNA expression in rat lung tissues, indicating that a robust inflammatory response encouraged *anxa1* transcription. AnxA1 protein, which has anti-inflammatory action, did not show increased expression after the occurrence of SAP. During severe inflammation, elastase released from neutrophils promotes the cleavage of the 37 kDa fragment form of AnxA1, which has anti-inflammatory activity, to the 33 kDa fragment, which has no anti-inflammatory action [49]. Similarly, upon rapid migration of neutrophils to injury sites after SAP induction, intact AnxA1 (37 kDa) is cleaved by elastase and proteinase-3 to the inactive form (33 kDa), losing its inhibitory effect on neutrophil recruitment and leading to a stormy accumulation of neutrophils in lung tissues. Following QYD treatment, when the number of neutrophils infiltrating the lung is gradually reduced, the 37 kDa form

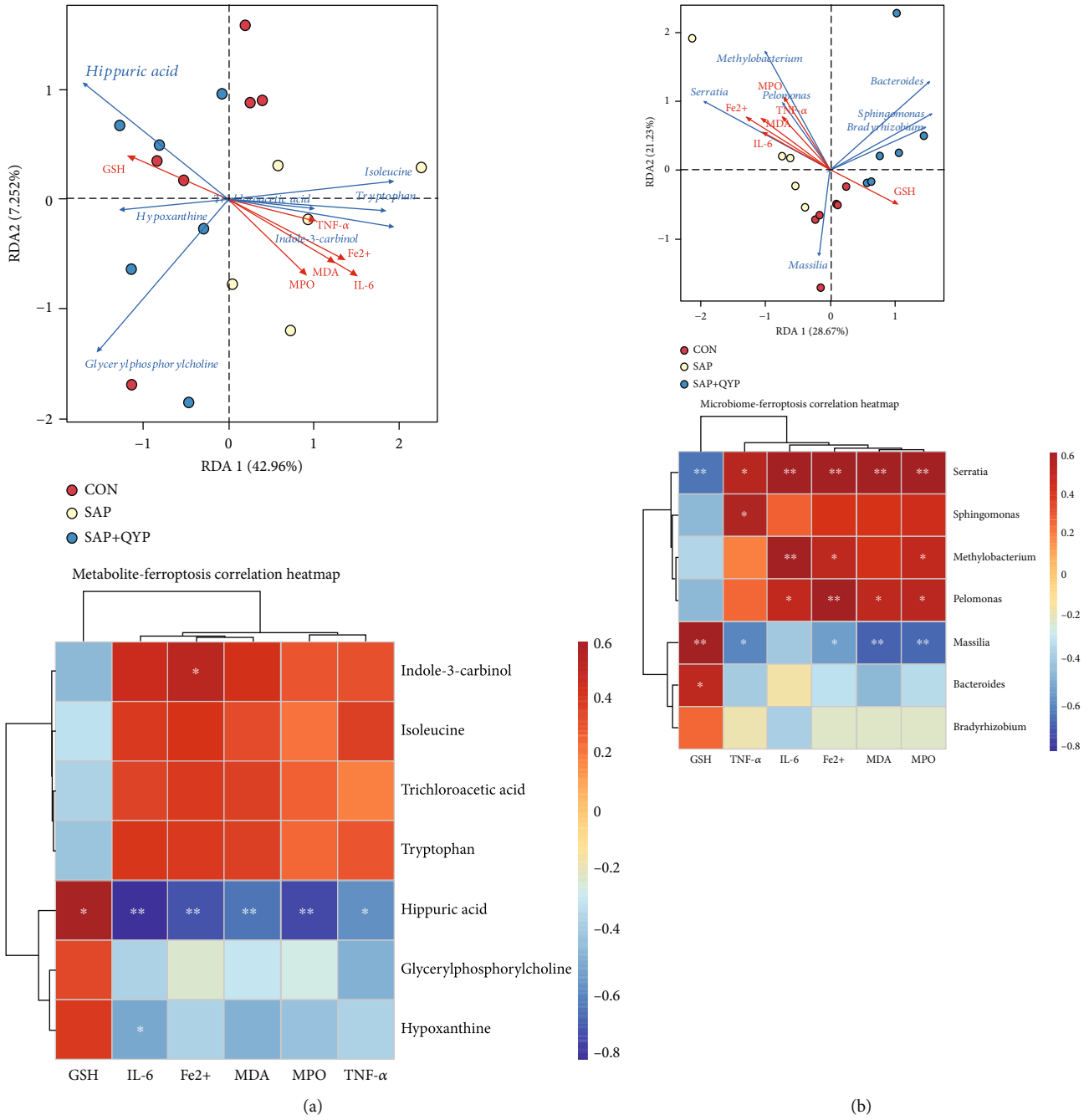


FIGURE 8: Continued.

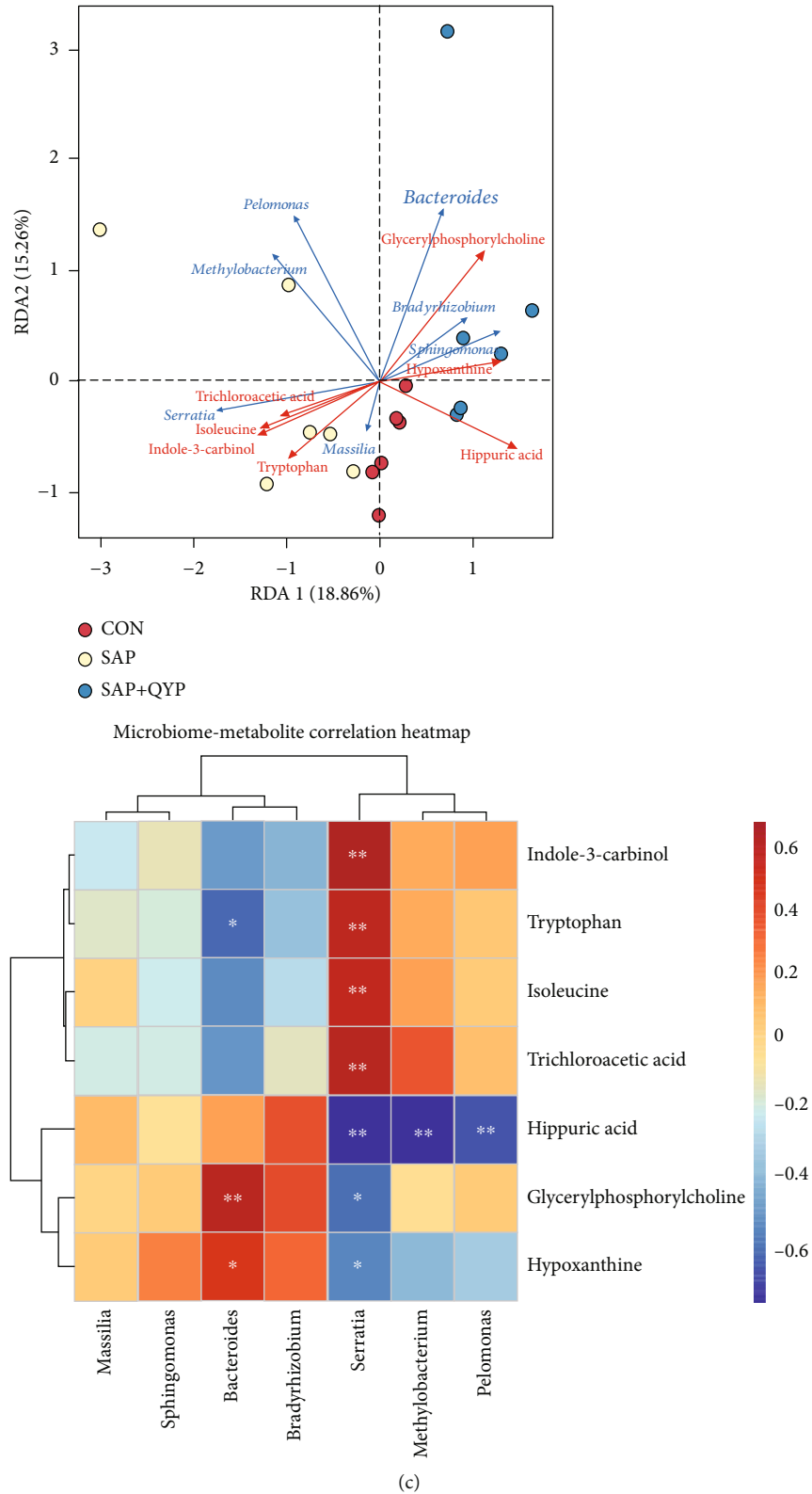


FIGURE 8: Correlation analysis of ferroptosis, metabolites, and microbiota. (a) Ferroptosis and metabolites. (b) Ferroptosis and microbiota. (c) Microbiota and metabolites. Each point in the RDA plot represents a sample, and the connecting arrows' length indicates the correlation's magnitude. The angle between the connecting arrows indicates the correlation, with acute angles indicating positive correlations and obtuse angles indicating negative correlations. The smaller the angle, the higher the correlation. The red color in the heat map indicates a positive correlation, while the blue indicates a negative one. * $P < 0.05$ and ** $P < 0.01$.

of AnxA1 with anti-inflammatory activity rises, further limiting neutrophil recruitment and the production of pro-inflammatory mediators and promoting the subsidence of inflammation. This suggests that QYD blocks the neutrophil-amplified inflammatory cascade by inhibiting the cleavage of active AnxA1. ICAM-1 is a key adhesion molecule that recruits neutrophils, and its expression is one of the markers of neutrophil infiltration. Knockdown of ICAM-1 inhibits the development of ALI [50]. ICAM-1 expression was increased in the SAP-associated ALI model, whereas QYD therapy decreased ICAM-1 expression. In conclusion, our findings show that QYD may have lung-protective effects by increasing AnxA1 expression, inhibiting neutrophil infiltration and excessive inflammatory response.

Metabolomics is one of the applied approaches used for describing, at the metabolite level, the molecular processes of QYD against SAP-associated ALI. Hippuric acid is a significantly differentially expressed metabolite in our study. Hippuric acid is converted from phenolic compounds in the diet and is a normal component of urine. The relationship between hippuric acid and energy metabolism is tight. Any factor that affects mitochondrial oxidative phosphorylation may impact hippuric acid production [51]. Compared with the CON group, the expression of hippuric acid was down-regulated in lung tissue during SAP, which may be associated with impaired energy metabolism in the lung during ALI. QYD upregulated the expression of hippuric acid, suggesting its ability to counteract mitochondrial dysfunction. In the correlation analysis, hippuric acid was negatively correlated with Fe^{2+} and MDA and positively correlated with GSH levels. This finding further suggests that improving energy metabolism and counteracting ferroptosis may be one of the mechanisms by which QYD intervenes SAP and improves ALI. In addition, this study found that aminoacyl-tRNA biosynthesis, phenylalanine metabolism, phenylalanine, tyrosine and tryptophan biosynthesis, purine metabolism, glyoxylate and dicarboxylate metabolism, and glycine, serine, and threonine metabolism are the primary metabolic pathways involved in QYD to improve SAP-associated ALI. The clearance of acetaldehyde and reactive oxygen species is tightly connected with glyoxylate and dicarboxylic acid metabolism. Intriguingly, our NP analysis revealed that QYD regulates critical targets, including ALDH2, in rats with SAP-associated ALI. In addition, two recent studies revealed that the glyoxylate and dicarboxylic acid metabolism are significantly altered in the lung tissue of mice with fine particle-associated lung injury and the serum of rats with radiation-associated lung injury [52, 53]. Tryptophan is an essential amino acid consumed only through the diet and produces active metabolites via the kynurenine or serotonin pathway. Tryptophan expression was significantly elevated in SAP-associated ALI, consistent with previous reports showing that kynurenine pathways are significantly increased during the AP-induced SIRS. Inhibition of kynurenine prevents extrapancreatic organ damage [54]. These findings confirm that QYD exerts anti-inflammatory effects by affecting the metabolic phenotype and ferroptosis.

Numerous studies demonstrate that the lung microbiome influences the development of illness by regulating immune responses. Before this study, Kyo et al. discovered a substantial decrease in alpha diversity of lung microbiome in the bronchoalveolar lavage fluid (BALF) from ARDS patients [55]. This parallels our results. SAP partially influenced the structure of the lung microbiome. After QYD intervention, the abundance of the lung microbiome partially increased. Kyo et al. identified a distinct microbial community structure represented by Betaproteobacteria, linked with elevated serum IL-6 levels and hospital mortality in patients with ARDS [55]. Our analysis found strong correlations between *Sphingomonas*, *Serratia*, *Pelomonas*, *Methylobacterium*, and *Massilia* and serum inflammatory markers (TNF- α , IL-6, and MPO) in rats. The difference in the bacterial genus may be associated with the variation in samples (BALF vs. lung tissue). Interestingly, we also discovered relationships between bacterial genera and ferroptosis in rats. Simultaneously, the connection between *Methylobacterium* and differential metabolites was discovered. Clearly, further research is required to understand the exact processes. The investigation of the lung microbiome composition at the phylum level indicated that the abundance of Firmicutes was dramatically reduced in the SAP group relative to the CON group. The Firmicutes maintain the homeostasis of the immune system, and their lower abundance was directly linked to inflammatory reactions. The degree of dysbiosis was closely related to the abundance of Firmicutes [56]. The increased abundance of Firmicutes in the QYD group compared to the SAP group indicated that dysbiosis was obtained. Finally, we conclude that QYD reduces SAP-induced lung injury by partly influencing the lung microbiome.

This research performed a multidimensional analysis to parse the potential mechanism of QYD against SAP-associated ALI from the perspective of systems biology, but there are still several limitations. First, we hypothesized that QYD exerts a pulmonary protective effect via promoting the ALDH2 expression and, by extension, suppressing ferroptosis. However, it is not yet known whether inhibition of ALDH2 expression can reverse the inhibitory effect of QYD on ferroptosis. The mechanism by which ALDH2 regulates signaling molecules associated with ferroptosis requires additional exploration. Inhibiting neutrophil infiltration and NET formation, QYD has anti-inflammatory actions. We solely investigated MPO activity in lung tissue. Indeed, the inhibitory effect of QYD on NET formation should be determined in the future as soon as feasible. Secondly, in the study of metabolites and microorganisms, we identified some differential metabolites and microbes associated with ferroptosis and inflammation. However, the substantial link between differential metabolites and microbes and ferroptosis remains poorly characterized. Further research is required to determine if QYD suppresses inflammatory responses by modulating microbe-metabolite-ferroptosis, such as applying metabolites and microbes during SAP therapy. Furthermore, the molecular mechanisms behind the involvement of QYD-related active components, such as palbinone and pulmatin, in SAP rats and the

regulation of ferroptosis remain unknown. Our future endeavors will center on this.

5. Conclusion

In conclusion, network pharmacology, metabolomics, and 16s rDNA sequencing were used to evaluate the molecular mechanisms of QYD against SAP-associated ALI. Functional enrichment and correlation analysis revealed the importance of ferroptosis, metabolic, and microbial function in QYD's lung protective effects. This integrated analysis method is suitable for the study of TCM and offers a fresh paradigm for future research on the therapeutic mechanisms of TCM.

Abbreviations

AP:	Acute pancreatitis
SAP:	Severe acute pancreatitis
SIRS:	Systemic inflammatory response syndrome
MODS:	Multiple organ dysfunction syndromes
ALI:	Acute lung injury
ARDS:	Acute respiratory distress syndrome
QYD:	Qingyi decoction
NP:	Network pharmacology
GSH:	Glutathione
MDA:	Malondialdehyde
MPO:	Myeloperoxidase
Era:	Erastin
TUNEL:	TdT-mediated dUTP nick end labeling
DEPs:	Differential expression proteins
DEGs:	Differentially expressed genes
ALDH2:	Acetaldehyde dehydrogenase 2
AnxA1:	Annexin A1
FTH1:	Ferritin heavy chain 1
NCOA4:	Nuclear receptor coactivator 4
SLC7A11:	Solute carrier family 7 member 11
8-OHdG:	8-Hydroxy-2'-deoxyguanosine
ICAM-1:	Intercellular cell adhesion molecule-1
STC:	Sodium taurocholate
ROS:	Reactive oxygen species
GPX4:	Glutathione peroxidase 4
NET:	Neutrophil extracellular trap
TCM:	Traditional Chinese medicine.

Data Availability

The data used to support the findings of this study are available from the corresponding authors.

Ethical Approval

All animal experiments were approved by the Committee for Research and Animal Ethics of Dalian Medical University.

Conflicts of Interest

The authors declare no conflict of interest.

Authors' Contributions

Hailong Chen and Zheyi Liu conceived the study. Peng Ge and Yalan Luo conducted the experiments and wrote the draft, contributing equally to this work. Zheyi Liu and Jing Liu conducted the metabolomic analysis. Qi Yang evaluated the results. Haiyun Wen, Jin Liu, Yibo Zhang, and Xuanchi Dong participated in data discussions. Caiming Xu, Guixin Zhang, and Zheyi Liu revised and formatted the manuscript. Peng Ge, Yalan Luo, and Qi Yang contributed equally to this work.

Acknowledgments

This study was supported by the National Key R&D Program of China (No. 2019YFE0119300) and National Natural Science Foundation of China (No. 82074158, 82274311, and 82104594).

Supplementary Materials

Supplementary File S1: 225 ingredients and 514 potential targets for QYD. Supplementary File S2: the sequences of the primers for qRT-PCR. Supplementary File S3: details of the analytical conditions and data preprocessing for mass spectrum. Supplementary File S4: the CDocker interaction energy of all ingredients and proteins. Supplementary File S5: apoptosis in the lung tissue of each group of rats. Supplementary File S6: expression of ferroptosis-related proteins in lung tissue of rats in each group. Supplementary File S7: expression of 8-OHdG in lung tissue of rats in each group. Supplementary File S8: effects of QYD and/or erastin on lung tissue damage and inflammation in SAP rats. Supplementary File S9: effect of QYD on the Shannon index, Simpson index, and Chao1 index of SAP rats. Graphical abstract: protective mechanism of QYD in SAP-associated ALI rat model. (*Supplementary Materials*)

References

- [1] J. P. Iannuzzi, J. A. King, J. H. Leong et al., "Global incidence of acute pancreatitis is increasing over time: a systematic review and meta-analysis," *Gastroenterology*, vol. 162, no. 1, pp. 122–134, 2022.
- [2] P. Ge, Y. Luo, C. S. Okoye et al., "Intestinal barrier damage, systemic inflammatory response syndrome, and acute lung injury: a troublesome trio for acute pancreatitis," *Biomedicine & Pharmacotherapy*, vol. 132, article 110770, 2020.
- [3] C. J. Shields, D. C. Winter, and H. P. Redmond, "Lung injury in acute pancreatitis: mechanisms, prevention, and therapy," *Current Opinion in Critical Care*, vol. 8, no. 2, pp. 158–163, 2002.
- [4] C. Yang, T. Wang, J. Chen et al., "Traditional Chinese medicine formulas alleviate acute pancreatitis," *Pancreas*, vol. 50, no. 10, pp. 1348–1356, 2021.
- [5] G. Wang, D. Shang, G. Zhang et al., "Effects of QingYi decoction on inflammatory markers in patients with acute pancreatitis: a meta-analysis," *Phytomedicine*, vol. 95, article 153738, 2022.

- [6] F. Noor, M. Tahir ul Qamar, U. A. Ashfaq, A. Albutti, A. S. Alwashmi, and M. A. Aljasir, "Network pharmacology approach for medicinal plants: *Review and Assessment*," *Pharmaceuticals*, vol. 15, no. 5, p. 572, 2022.
- [7] C. Keskinidou, A. G. Vassiliou, I. Dimopoulou, A. Kotanidou, and S. E. Orfanos, "Mechanistic understanding of lung inflammation: recent advances and emerging techniques," *Journal of Inflammation Research*, vol. 15, pp. 3501–3546, 2022.
- [8] D. Lu, Z. Wang, Z. Chen et al., "Olmesartan attenuates single-lung ventilation induced lung injury via regulating pulmonary microbiota," *Frontiers in Pharmacology*, vol. 13, article 822615, 2022.
- [9] Z. Tian, E. Wu, J. You et al., "Dynamic alterations in the lung microbiota in a rat model of lipopolysaccharide-induced acute lung injury," *Scientific Reports*, vol. 12, no. 1, p. 4791, 2022.
- [10] T. F. Wei, L. Zhao, P. Huang et al., "Qing-Yi decoction in the treatment of acute pancreatitis: an integrated approach based on chemical profile, network pharmacology, molecular docking and experimental evaluation," *Frontiers in Pharmacology*, vol. 12, article 590994, 2021.
- [11] Q. Xu, M. Wang, H. Guo et al., "Emodin alleviates severe acute pancreatitis-associated acute lung injury by inhibiting the cold-inducible RNA-binding protein (CIRP)-mediated activation of the NLRP3/IL-1 β /CXCL1 signaling," *Frontiers in Pharmacology*, vol. 12, article 655372, 2021.
- [12] B. Zhou, J. Zhang, Y. Chen et al., "Puerarin protects against sepsis-induced myocardial injury through AMPK-mediated ferroptosis signaling," *Aging*, vol. 14, no. 8, pp. 3617–3632, 2022.
- [13] C. A. Lipinski, "Rule of five in 2015 and beyond: target and ligand structural limitations, ligand chemistry structure and drug discovery project decisions," *Advanced Drug Delivery Reviews*, vol. 101, pp. 34–41, 2016.
- [14] Z. Sun, L. Li, J. Qu, H. Li, and H. Chen, "Proteomic analysis of therapeutic effects of Qingyi pellet on rodent severe acute pancreatitis-associated lung injury," *Biomedicine & Pharmacotherapy*, vol. 118, article 109300, 2019.
- [15] B. R. Brooks, C. L. Brooks, A. D. Mackerell Jr. et al., "CHARMM: the biomolecular simulation program," *Journal of Computational Chemistry*, vol. 30, no. 10, pp. 1545–1614, 2009.
- [16] G. Matute-Bello, G. Downey, B. B. Moore et al., "An official American Thoracic Society workshop report: features and measurements of experimental acute lung injury in animals," *American Journal of Respiratory Cell and Molecular Biology*, vol. 44, no. 5, pp. 725–738, 2011.
- [17] S. Lee, Y. K. Jeong, J. W. Lim, and H. Kim, "Docosahexaenoic acid inhibits expression of fibrotic mediators in mice with chronic pancreatitis," *European Journal of Cancer Prevention*, vol. 24, no. 4, pp. 233–239, 2019.
- [18] M. W. Pfaffl, "A new mathematical model for relative quantification in real-time RT-PCR," *Nucleic Acids Research*, vol. 29, no. 9, article e45, pp. 45e–445, 2001.
- [19] X. Zhao, Z. Zeng, A. Chen et al., "Comprehensive strategy to construct in-house database for accurate and batch identification of small molecular metabolites," *Analytical Chemistry*, vol. 90, no. 12, pp. 7635–7643, 2018.
- [20] N. Geng, X. Song, R. Cao et al., "The effect of toxic components on metabolomic response of male SD rats exposed to fine particulate matter," *Environmental Pollution*, vol. 272, article 115922, 2021.
- [21] Z. Cao, H. Qin, Y. Huang et al., "Crosstalk of pyroptosis, ferroptosis, and mitochondrial aldehyde dehydrogenase 2-related mechanisms in sepsis-induced lung injury in a mouse model," *Bioengineered*, vol. 13, no. 3, pp. 4810–4820, 2022.
- [22] Q. Yu, J. Gao, X. Shao, W. Lu, L. Chen, and L. Jin, "The effects of Alda-1 treatment on renal and intestinal injuries after cardiopulmonary resuscitation in pigs," *Frontiers in Medicine*, vol. 9, article 892472, 2022.
- [23] Y. Cheng, Y. Song, H. Chen et al., "Ferroptosis mediated by lipid reactive oxygen species: a possible causal link of neuroinflammation to neurological disorders," *Oxidative Medicine and Cellular Longevity*, vol. 2021, Article ID 5005136, 13 pages, 2021.
- [24] W. Chen, X. Yang, L. Huang et al., "Qing-Yi decoction in participants with severe acute pancreatitis: a randomized controlled trial," *Chinese Medicine*, vol. 10, no. 1, p. 11, 2015.
- [25] C. H. Ji, C. W. Tang, W. M. Feng, Y. Bao, and L. Q. Yao, "A Chinese herbal decoction, Huoxue Qingyi decoction, promotes rehabilitation of patients with severe acute pancreatitis: a retrospective study," *Evidence-based Complementary and Alternative Medicine*, vol. 2016, Article ID 3456510, 5 pages, 2016.
- [26] X. J. Guo and W. B. Guo, "A clinical study of Qingyi decoction in the treatment of acute pancreatitis," *Journal of Biological Regulators and Homeostatic Agents*, vol. 33, no. 4, pp. 1197–1200, 2019.
- [27] J. W. Zhang, G. X. Zhang, H. L. Chen et al., "Therapeutic effect of Qingyi decoction in severe acute pancreatitis-induced intestinal barrier injury," *World Journal of Gastroenterology*, vol. 21, no. 12, pp. 3537–3546, 2015.
- [28] L. Li, Y. Q. Li, Z. W. Sun et al., "Qingyi decoction protects against myocardial injuries induced by severe acute pancreatitis," *World Journal of Gastroenterology*, vol. 26, no. 12, pp. 1317–1328, 2020.
- [29] Y. Zhong, J. Cao, R. Zou, and M. Peng, "Polimorfismos genéticos de la alcohol deshidrogenasa, aldehído deshidrogenasa y susceptibilidad a la pancreatitis crónica alcohólica: un meta-análisis," *Gastroenterología y Hepatología*, vol. 38, no. 7, pp. 417–425, 2015.
- [30] S. Cao, Y. Bian, X. Zhou et al., "A small-molecule activator of mitochondrial aldehyde dehydrogenase 2 reduces the severity of cerulein-induced acute pancreatitis," *Biochemical and Biophysical Research Communications*, vol. 522, no. 2, pp. 518–524, 2020.
- [31] S. Sidramagowda Patil, H. Hernández-Cuervo, J. Fukumoto et al., "Alda-1 attenuates hyperoxia-induced acute lung injury in mice," *Frontiers in Pharmacology*, vol. 11, article 597942, 2021.
- [32] H. Y. Tsai, Y. J. Hsu, C. Y. Lu et al., "Pharmacological activation of aldehyde dehydrogenase 2 protects against heatstroke-induced acute lung injury by modulating oxidative stress and endothelial dysfunction," *Frontiers in Immunology*, vol. 12, article 740562, 2021.
- [33] Y. Gao, Y. Xu, S. Hua, S. Zhou, and K. Wang, "ALDH2 attenuates Dox-induced cardiotoxicity by inhibiting cardiac apoptosis and oxidative stress," *International Journal of Clinical and Experimental Medicine*, vol. 8, no. 5, pp. 6794–6803, 2015.
- [34] M. Y. Yang, Y. B. Wang, B. Han et al., "Activation of aldehyde dehydrogenase 2 slows down the progression of atherosclerosis via attenuation of ER stress and apoptosis in smooth muscle cells," *Acta Pharmacologica Sinica*, vol. 39, no. 1, pp. 48–58, 2018.

- [35] A. Sun, Y. Zou, P. Wang et al., “Mitochondrial aldehyde dehydrogenase 2 plays protective roles in heart failure after myocardial infarction via suppression of the cytosolic JNK/p 53 pathway in mice,” *Journal of the American Heart Association*, vol. 3, no. 5, article e000779, 2014.
- [36] K. Liu, J. Liu, B. Zou et al., “Trypsin-mediated sensitization to ferroptosis increases the severity of pancreatitis in mice,” *Cellular and Molecular Gastroenterology and Hepatology*, vol. 13, no. 2, pp. 483–500, 2022.
- [37] D. Ma, P. Jiang, Y. Jiang, H. Li, and D. Zhang, “Effects of lipid peroxidation-mediated ferroptosis on severe acute pancreatitis-induced intestinal barrier injury and bacterial translocation,” *Oxidative Medicine and Cellular Longevity*, vol. 2021, Article ID 6644576, 12 pages, 2021.
- [38] D. Ma, C. Li, P. Jiang, Y. Jiang, J. Wang, and D. Zhang, “Inhibition of ferroptosis attenuates acute kidney injury in rats with severe acute pancreatitis,” *Digestive Diseases and Sciences*, vol. 66, no. 2, pp. 483–492, 2021.
- [39] H. Zhang, J. Liu, Y. Zhou et al., “Neutrophil extracellular traps mediate m6A modification and regulates sepsis-associated acute lung injury by activating ferroptosis in alveolar epithelial cells,” *International Journal of Biological Sciences*, vol. 18, no. 8, pp. 3337–3357, 2022.
- [40] Y. Wang, D. Chen, H. Xie et al., “AUF1 protects against ferroptosis to alleviate sepsis-induced acute lung injury by regulating NRF2 and ATF3,” *Cellular and Molecular Life Sciences*, vol. 79, no. 5, p. 228, 2022.
- [41] R. Fan, J. Sui, X. Dong, B. Jing, and Z. Gao, “Wedelolactone alleviates acute pancreatitis and associated lung injury via GPX4 mediated suppression of pyroptosis and ferroptosis,” *Free Radical Biology & Medicine*, vol. 173, pp. 29–40, 2021.
- [42] J. Li, S. H. Deng, J. Li et al., “Obacunone alleviates ferroptosis during lipopolysaccharide-induced acute lung injury by upregulating Nrf2-dependent antioxidant responses,” *Cellular & Molecular Biology Letters*, vol. 27, no. 1, p. 29, 2022.
- [43] J. Li, M. Li, L. Li, J. Ma, C. Yao, and S. Yao, “Hydrogen sulfide attenuates ferroptosis and stimulates autophagy by blocking mTOR signaling in sepsis-induced acute lung injury,” *Molecular Immunology*, vol. 141, pp. 318–327, 2022.
- [44] S. Wang, L. Wang, X. Qin et al., “ALDH2 contributes to melatonin-induced protection against APP/PS1 mutation-prompted cardiac anomalies through cGAS-STING-TBK1-mediated regulation of mitophagy,” *Signal Transduction and Targeted Therapy*, vol. 5, no. 1, p. 119, 2020.
- [45] J. G. Filep, “Targeting neutrophils for promoting the resolution of inflammation,” *Frontiers in Immunology*, vol. 13, article 866747, 2022.
- [46] Y. Lei, L. Tang, S. Liu et al., “Parabacteroides produces acetate to alleviate heparanase-exacerbated acute pancreatitis through reducing neutrophil infiltration,” *Microbiome*, vol. 9, no. 1, p. 115, 2021.
- [47] B. Pan, Y. Li, Y. Liu, W. Wang, G. Huang, and Y. Ouyang, “Circulating CitH3 is a reliable diagnostic and prognostic biomarker of septic patients in acute pancreatitis,” *Frontiers in Immunology*, vol. 12, article 766391, 2021.
- [48] W. I. Liao, S. Y. Wu, G. C. Wu et al., “Ac2-26, an annexin A1 peptide, attenuates ischemia-reperfusion-induced acute lung injury,” *International Journal of Molecular Sciences*, vol. 18, no. 8, p. 1771, 2017.
- [49] J. P. Vago, L. P. Tavares, M. A. Sugimoto et al., “Proresolving actions of synthetic and natural protease inhibitors are mediated by annexin A1,” *Journal of Immunology*, vol. 196, no. 4, pp. 1922–1932, 2016.
- [50] C. S. Calfee, M. D. Eisner, P. E. Parsons et al., “Soluble intercellular adhesion molecule-1 and clinical outcomes in patients with acute lung injury,” *Intensive Care Medicine*, vol. 35, no. 2, pp. 248–257, 2009.
- [51] G. De Simone, C. Balducci, G. Forloni, R. Pastorelli, and L. Brunelli, “Hippuric acid: could become a barometer for frailty and geriatric syndromes?,” *Ageing Research Reviews*, vol. 72, article 101466, 2021.
- [52] Y. Feng, Y. Gao, W. Tu, Y. Feng, J. Cao, and S. Zhang, “Serum metabolomic analysis of radiation-induced lung injury in rats,” *Dose Response*, vol. 20, no. 1, p. 155932582110670, 2022.
- [53] J. Li, Y. Hu, L. Liu, Q. Wang, J. Zeng, and C. Chen, “PM2.5 exposure perturbs lung microbiome and its metabolic profile in mice,” *Science of the Total Environment*, vol. 721, article 137432, 2020.
- [54] J. P. Hutchinson, P. Rowland, M. Taylor et al., “Structural and mechanistic basis of differentiated inhibitors of the acute pancreatitis target kynurenine-3-monooxygenase,” *Nature Communications*, vol. 8, no. 1, p. 15827, 2017.
- [55] M. Kyo, K. Nishioka, T. Nakaya et al., “Unique patterns of lower respiratory tract microbiota are associated with inflammation and hospital mortality in acute respiratory distress syndrome,” *Respiratory Research*, vol. 20, no. 1, p. 246, 2019.
- [56] R. Prasad, M. J. Patton, J. L. Floyd et al., “Plasma microbiome in COVID-19 subjects: an indicator of gut barrier defects and dysbiosis,” *International Journal of Molecular Sciences*, vol. 23, no. 16, p. 9141, 2022.

Research Article

Enriched Environment Attenuates Ferroptosis after Cerebral Ischemia/Reperfusion Injury via the HIF-1 α -ACSL4 Pathway

Jingying Liu ¹, Qihang Luo ¹, Jie Ke ¹, DongDong Zhang ¹, Yang Xu ²,
Weijing Liao ¹, Xiuping Chen ³, and Xin Zhang ¹

¹Department of Rehabilitation Medicine, Zhongnan Hospital of Wuhan University, Wuhan, China

²Department of Neurosurgery, Renmin Hospital of Wuhan University, Wuhan, China

³Department of Rehabilitation Medicine, The First Affiliated Hospital of Nanchang University, Jiangxi, China

Correspondence should be addressed to Xiuping Chen; ndyfy05061@ncu.edu.cn and Xin Zhang; zhangxin0439@whu.edu.cn

Received 25 August 2022; Revised 2 November 2022; Accepted 25 November 2022; Published 8 February 2023

Academic Editor: Lianxiang Luo

Copyright © 2023 Jingying Liu et al. This is an open access article distributed under the Creative Commons Attribution License, which permits unrestricted use, distribution, and reproduction in any medium, provided the original work is properly cited.

Enriched environment (EE) has been proven to be an effective intervention strategy which can improve neurofunctional recovery following cerebral ischemia/reperfusion (I/R) injury. However, it still needs further investigation for the underlying mechanisms. Recently, it has been shown that ferroptosis played an essential role in the pathophysiological development of ischemic stroke (IS). This study is aimed at investigating whether EE plays a neuroprotective role by attenuating ferroptosis after cerebral I/R injury. We used middle cerebral artery occlusion/reperfusion (MCAO/R) to build a model of cerebral I/R injury. To evaluate the effect of EE on neurological recovery, we used the modified neurological severity score (mNSS) and the Morris water maze (MWM). We used the western blot to detect the protein levels of glutathione peroxidase 4 (GPX4), hypoxia-inducible factor-1 α (HIF-1 α), and acyl-CoA synthetase long-chain family member 4 (ACSL4). We used the quantitative real-time PCR (qRT-PCR) to measure the mRNA levels of ACSL4 and inflammatory cytokines including tumor necrosis factor alpha (TNF α), interleukin-6 (IL-6), and interleukin 1 beta (IL-1 β). The occurrence of ferroptosis was detected by TdT-mediated dUTP nick-end labeling (TUNEL) assay, diaminobenzidine- (DAB-) enhanced Perls' staining, iron level assays, and malondialdehyde (MDA) level assays. The results verified that EE enhanced functional recovery and attenuated ferroptosis and neuroinflammation after cerebral I/R injury. EE increased the expression of HIF-1 α while inhibited the expression of ACSL4. Our research indicated that EE improved functional recovery after cerebral I/R injury through attenuating ferroptosis, and this might be related to its regulation of the neuroinflammation and HIF-1 α -ACSL4 pathway.

1. Introduction

Stroke is the second leading cause of death which also acts as one of the diseases with the highest disability rates worldwide [1, 2]. Ischemic stroke (IS) is the predominant type of stroke, but the treatment options for IS are very limited [3]. To alleviate the neurological deficits caused by IS, intensive poststroke rehabilitation is one of the few valid options. Rehabilitation after stroke has been shown to diminish the risks of stroke recurrence and improve functional recovery [4]. Therefore, it

is vital to explore more rehabilitative strategies to alleviate the neurological deficits caused by IS.

Enriched environment (EE) is a stimulus complex. By providing the housing animals with larger space, novel play props, and more social partners, the animals housed in the EE have more sensory, cognitive, motor, and social stimulation than in the standard conditions (SC) [5, 6]. It has been proven that EE could be a bright strategy to improve cognitive-behavioral performance and functional recovery after IS [7–11]. In animal experiments, EE has been shown

to reduce brain infarct volumes and enhance angiogenesis in I/R rats [9, 11]. EE also influenced cell death following IS. It promoted autophagy while inhibited pyroptosis and apoptosis of neurons in the penumbra which eventually facilitate functional recovery [10, 12, 13]. Despite the fact that multiple pathophysiological processes are involved in cerebral I/R injury and its recovery, research is needed to clarify how EE improves functional recovery after IS with the aim of clinical transformation in the future [14–16].

Ferroptosis is a recently discovered form of cell death that is distinguished from apoptosis, pyroptosis, and autophagy, characterized by the iron-dependent accumulation of lipid hydroperoxides [17]. Recent studies have shown that I/R injury can induce reactive oxygen species (ROS) and lipid peroxidation to trigger ferroptosis [18]. Following the stroke, ferroptosis occurred and the iron levels in the brain increased [19]. The inhibition of ferroptosis effectively reduced poststroke injury [20]. Inhibition of ferroptosis and promotion of the levels of glutathione peroxidase 4 (GPX4) by selenium significantly protect neurons after stroke [21]. GPX4 plays an important role in ferroptosis by inhibiting lipid peroxidation and thus regulating ferroptosis [22]. When the activity of GPX4 is inhibited, ferroptosis will be triggered as the lethal amount of lipid peroxidation accumulation [23]. Postischemic neuroinflammation might play a crucial role in ferroptosis. Inflammatory cytokines (e.g., TNF α , IL-1 β , and IL-6) have been demonstrated to directly affect GPX4 levels, implying that these cytokines may regulate ferroptosis [24]. Although there is growing evidence that ferroptosis is involved in cerebral I/R injury, the relationship between ferroptosis and the neuroprotective effects of EE after IS remains unknown.

Acyl-CoA synthetase long-chain family member 4 (ACSL4) is an enzyme involved in the metabolism of polyunsaturated fatty acids (PUFA) [25]. ACSL4 could facilitate free PUFAs to synthesize PUFA-phosphatidylethanolamines, which are unstable and prone to lipid peroxidation [18]. Lipids are important components of the brain, and increased ACSL4 expression makes lipids more susceptible to peroxidation, which exacerbates the occurrence of ferroptosis [26]. Studies have shown that ACSL4 makes cells more susceptible to ferroptosis [27]. Recently, ACSL4-modulated ferroptosis has been demonstrated in cerebral and intestinal I/R injury, indicating that ACSL4 is a novel regulator of ferroptosis [27, 28]. Hypoxia-inducible factor-1 α (HIF-1 α) is a critical regulator in cerebral I/R injury. It modulates the expression of a set of genes involved in cellular adaptation to hypoxia [29–31]. According to recent research, HIF-1 α , as a transcriptional factor, may bond to the ACSL4 promoter region to suppress its transcription [32]. In addition, HIF-1 α has been shown to inhibit ACSL4 transcription in cerebral I/R injury [28]. The inhibition of HIF-1 α could increase ROS levels, implying that HIF-1 α may be an important target in the regulation of ferroptosis [33].

We hypothesized that EE treatment could improve neurological outcomes after cerebral I/R injury by attenuating ferroptosis. In this study, we investigated how EE affected the expression of inflammatory cytokines, ACSL4, and HIF-1 α and the potential link between them. We also looked

into whether EE attenuated ferroptosis after cerebral I/R injury, as well as the underlying molecular mechanism.

2. Materials and Methods

2.1. Animal and Subject. All animal experiments were authorized by the Animal Care and Use Committee at Wuhan University (WP2020-08052). Animal welfare was valued during the experiments, and every effort was made to mitigate the pain of experimental animals. During the experimental process, every effort was made to keep animal mortality and suffering to a minimum. Specific pathogen-free male SD rats (6–7 weeks old, 210–220 g) were purchased from Beijing Vital River Laboratory Animal Technology Company. Rats were housed in an artificially controlled environment (55 \pm 5% relative humidity, 20 \pm 2°C, and photoperiod from 8:00 to 20:00) and had unrestricted access to food and water. Figures 1(a) and 1(b) illustrate the setting of EE and the experimental timeline. After three days of adaption training, the rats were marked and randomized into four groups as follows: (1) SSC group: the sham+standard condition group, (2) SEE group: the sham+enriched environment group, (3) ISC group: the ischemia/reperfusion+standard condition group, and (4) IEE group: the ischemia/reperfusion+enriched environment group.

2.2. Rat Middle Cerebral Artery Occlusion and Reperfusion (MCAO/R) Model. As previously reported, middle cerebral artery occlusion and reperfusion (MCAO/R) was used to build the cerebral I/R injury model in rats [13, 34]. Briefly, isoflurane was used to anesthetize rats with a face mask (induction concentration: 3%, maintenance concentration: 1.5%, in 2:1 N₂O: O₂). A midline incision of approximately 2 cm is made in the neck and the left common carotid artery (CCA), and the left external carotid artery and left internal carotid artery (ICA) are separated. A small incision was made in the CCA, and a 5-0 nylon monofilament (Beijing Xinong Biotech, China) was passed through the incision into the ICA approximately 20 \pm 2 mm. The nylon monofilament wire was carefully removed 90 minutes later to ensure the reperfusion [35]. The sham-operated rats were operated on the same as the surgical group except that the nylon monofilament was not inserted. After surgery, the rats were scored on a five-point neurological deficit using a blinded method (only scores 1-3 were retained and excluded scores 0 and 4) [36].

2.3. Housing Conditions. The rats were placed in the respective environment 24 hours following MCAO/R according to the groupings. The following are the specifics of standard condition (SC): three rats were housed in a cage (40 cm \times 30 cm \times 20 cm) with bedding, food, and water. The specifics of the enriched environment (EE) are as follows: six rats were kept in a special cage (90 cm \times 75 cm \times 50 cm) with stairways, stages, swing boards, tunnels, and running wheels. To ensure novelty and exploration, the cage settings were changed every three days (Figure 1(b)).

2.4. Behavioral Tests. The modified neurological severity score (mNSS) was used to evaluate sensorimotor deficits

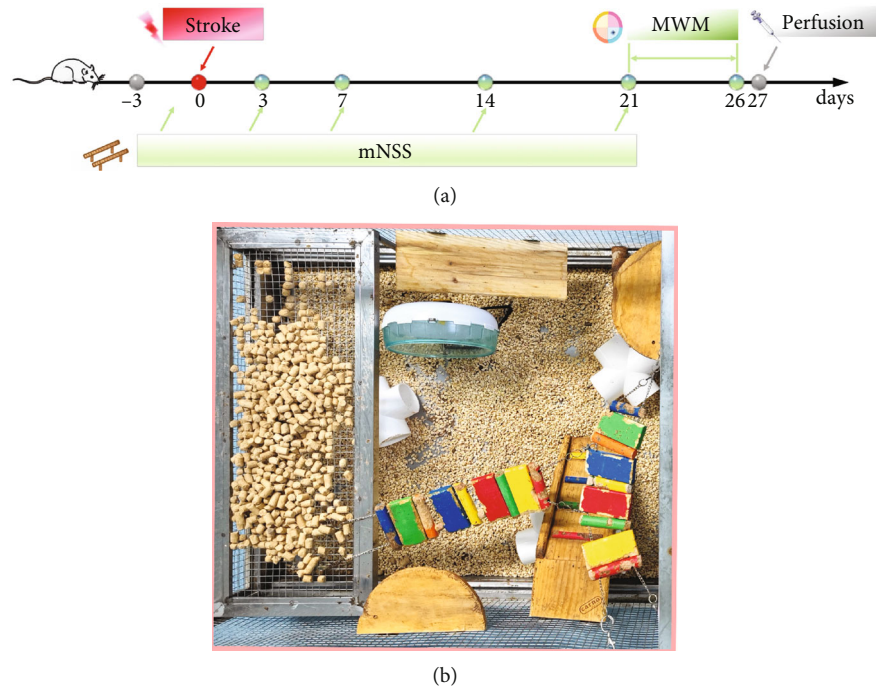


FIGURE 1: Experimental flow and enriched environment setting. (a) Timeline of the experimental procedure for this experiment. Rats were tested on day 3, 7, 14, and 21 by using the modified neurological severity score (mNSS) to assess sensorimotor deficits. On day 21 to 26, rats were tested using the Morris water maze (MWM) to assess spatial learning and memory. (b) The setting of an enriched environment in this experiment.

(including motor, sensory, reflex, and balance assessments), and higher scores indicated more severe neurological damage ($n = 6/\text{group}$) [12]. The Morris water maze (MWM) test was used to assess the spatial learning and memory abilities of rats ($n = 6/\text{group}$) [37]. For the first five days, the platform position was fixed and each animal was trained 4 times a day, each time the rats were placed in the water from four different quadrants, and their movement trajectory and time were recorded. The rats were permitted to rest on the platform for 15 seconds after reaching it in less than 60 seconds. If it took more than 60 seconds to reach the platform, the tester would lead it to stay at the platform for 15 seconds. We recorded the escape latency of each animal. On day 6, the platform was withdrawn and rats were permitted to swim freely for 1 min. An Animal Video Tracking Analysis System was used to record swimming trajectories, time in correct quadrant, and platform crossovers to make a reasonable judgment on the learning memory ability of the spatial location (Anilab Scientific Instruments Co., Ltd., China).

2.5. Western Blot. Protein sample tissues were collected from the peri-infarct cortex. Proteins were separated on SDS/PAGE gels (10%) and electroblotted into a PVDF membrane. The PVDF membranes were then incubated in 5% nonfat milk at room temperature for 1 h and then incubated with primary antibodies overnight at 4°C. The membrane was washed three times with phosphate-buffered saline (PBS) containing 0.1% Tween-20 and incubated in the secondary antibodies (ABclonal, China) for 1 h at room temperature. We used the Bio-Rad system to scan the proteins ($n = 3/\text{group}$). The primary antibodies used in this experiment were listed as follows: GAPDH

(Proteintech, China), GPX4 (Abmart, China), HIF-1 α (Zen-Bio, China), and ACSL4 (Abcam, UK).

2.6. Quantitative Real-Time PCR (qRT-PCR) Analysis. According to the manufacturer's instructions, total RNA was extracted from peri-infarct cortex tissues using TRIzol reagent (Invitrogen, USA). We performed qRT-PCR to detect mRNA levels by using SYBR Premix Ex Taq II (Takara, Japan) in a 2.1 Real-Time PCR System (Bio-Rad, USA) according to the manufacturer's protocol. The relative Ct method was used for data comparison, and GAPDH was set as an internal control ($n = 3/\text{group}$). The primer sequences are given below.

IL-1 β (F): TGACTTCACCATGGAACCCG
 IL-1 β (R): TCCTGGGGAAGGCATTAGGA
 IL-6 (F): TCCTACCCCAACTTCCAATGCTC
 IL-6 (R): TTGGATGGTCTTGGTCCTTAGCC
 TNF- α (F): TTGCTTCTCCCTGTTCC
 TNF- α (R): CTGGGCAGCGTTTATTCT
 ACSL4 (F): TATGGGCTGACAGAATCATG
 ACSL4 (R): CAACTCTTCCAGTAGTG TAG
 GAPDH (F): CGCTAACATCAAATGGGGTG
 GAPDH (R): TTGCTGACAATCTTGAGGGAG

2.7. Immunofluorescence Assays. Paraffin sections were obtained from brain specimens of different groups. They were hydrated and antigen retrieval was performed using a buffered solution with sodium citrate. Sections were blocked with 5% bovine serum albumin for 1 h. And the sections were then incubated with primary antibody for 12 h at 4°C. PBS buffer was used to wash sections 3 times (5 min each), and sections were incubated with fluorescent secondary

antibody for 1 h at room temperature. Nuclei were stained with DAPI (Antgene, China). The images were observed and taken by a BX53 microscope (Olympus, Japan). The number of positive cells was calculated using ImageJ ($n = 3$ /group).

2.8. TdT-Mediated dUTP Nick-End Labeling (TUNEL) Assay. TUNEL assay is a well-established, fast, and simple technique to detect and quantify neurons undergoing regulated cell death [38]. TUNEL staining was performed according to the method described by the manufacturer. Briefly, paraffin sections were pretreated as previously described. The sections were then reacted with proteinase K for 30 min at room temperature. PBS buffer was used for sections' washing (5 min each for 5 times) followed by incubating with the TUNEL assay solution. Then, the reaction was stopped and the slides were washed three times with PBS. Nuclei were stained with DAPI (Antgene, China). The images of the peri-infarct cortex were observed and taken by a BX53 microscope (Olympus, Japan), and the number of positive cells was calculated using ImageJ ($n = 3$ /group).

2.9. Diaminobenzidine- (DAB-) Enhanced Perls' Staining. Prussian Blue Iron Stain Kit (Solarbio, China) was used to detect iron deposits in rat brain tissue ($n = 3$ /group). Paraffin sections were pretreated as previously described and washed with distilled water. 3% hydrogen peroxide was used to block paraffin sections for 10 minutes. Perls' staining solution was configured according to the instructions. Then, the sections were put into the Perls' staining solution and incubated at 37°C for 12 hours. After washing 3 times (5 min each) with PBS, sections were stained with DAB Horseradish Peroxidase Color Development Kit (Beyotime, China). The images were observed and taken by a BX53 microscope (Olympus, Japan).

2.10. Iron and Malondialdehyde (MDA) Level Assays. The level of iron in rat brains was measured using the tissue iron assay kit (Nanjing Jiancheng Bio, China) according to the manufacturer's instructions. The concentration of lipid peroxidation product malonaldehyde (MDA) in rat brains was measured by an MDA assay kit (Beyotime, China) following the manufacturer's instructions ($n = 3$ /group).

2.11. Statistical Analysis. The nonparametric Kruskal-Wallis test was used to analyze the mNSS data. MWM data were analyzed by Tukey's *post hoc* test and two-way repeated measures ANOVA. One-way ANOVA and Tukey's *post hoc* test were used to compare differences between groups. We used SPSS 23 software and GraphPad Prism 8 for statistical analysis. All data were expressed as mean \pm standard deviation (SD). Statistical significance was established as $p < 0.05$.

3. Results

3.1. Enriched Environment Attenuated Neurological Deficits Caused by Cerebral I/R Injury. Cerebral I/R injury caused significant behavioral dysfunction. Various behavioral tests were performed to determine whether EE could attenuate

neurological deficits caused by cerebral I/R injury. Neurological deficits were assessed in rats using mNSS at 3, 7, 14, and 21 days after cerebral I/R injury. EE significantly reduced neurological deficits despite the persistence of sensorimotor impairment because of cerebral I/R injury (Figure 2(a); $p < 0.01$). At 21-26 days after cerebral I/R injury, the MWM was used to assess the spatial learning and memory ability of rats. During the spatial learning phase, the escape latency was decreasing with the increasing training time. During the first five days of training, rats in the I/R groups (ISC and IEE) took more time to reach the platform compared with the sham-operated groups (SSC and SEE). However, rats in the IEE group exhibited shorter escape latency compared with the ISC group (Figure 2(b); $p < 0.001$). At the end of the five-day spatial learning training, probe trials were conducted. In the I/R groups, the IEE group performed better than the ISC group, as they stayed longer in the correct quadrant and revealed more crossovers (Figures 2(c)–2(e); $p < 0.01$ and $p < 0.05$). These results demonstrated that neurological deficits could be reduced by EE following I/R injury.

3.2. Enriched Environment Reduced Ferroptosis after Cerebral I/R Injury. To investigate whether EE enhanced functional recovery by inhibiting ferroptosis after cerebral I/R injury, we used TUNEL staining, DAB-enhanced Perls' staining, iron assay kit, and MDA assay kit to detect ferroptosis-related features. We used TUNEL staining to detect whether EE reduced the occurrence of regulated cell death in the peri-infarct cortex. Massive positive cells were observed in the I/R groups, whereas few positive cells were detected in the sham-operated groups. EE significantly reduced the number of positive cells, and the proportion of positive cells in the IEE group was obviously lower than in the ISC group (Figures 3(a) and 3(b); $p < 0.01$). These results demonstrated that EE inhibited regulated cell death. The western blot results of GPX4 showed that I/R injury significantly decreased the expression level of GPX4, while EE significantly improved the level of GPX4 after I/R injury (Figures 4(a) and 4(b); $p < 0.01$ and $p < 0.001$). In the I/R groups, Perls' staining showed that the number of iron depositions in the peri-infarct cortex was significantly increased in comparison with the sham-operated groups (Figure 4(c)). The iron assay kit was used to further explore iron alterations, and the results showed that iron levels elevated following I/R injury. However, EE could reduce the iron deposition caused by cerebral I/R injury (Figure 4(d); $p < 0.01$). Significant accumulation of lipid peroxides is a typical feature that distinguishes ferroptosis from other types of regulated cell death [39]. Therefore, we applied the MDA assay to assess lipid peroxidation alterations in the peri-infarct cortex. The results showed that I/R injury significantly elevated MDA levels, while the IEE group showed a significant decrease in MDA levels compared to the ISC group (Figure 4(e); $p < 0.001$). Collectively, all of these data implicated that ferroptosis after cerebral I/R injury was suppressed by EE.

3.3. Enriched Environment Reduced the Expression of the Inflammatory Cytokines. Considering that ferroptosis might be regulated by inflammatory cytokines. The expression levels of inflammatory factors (TNF- α , IL-1 β , and IL-6) were

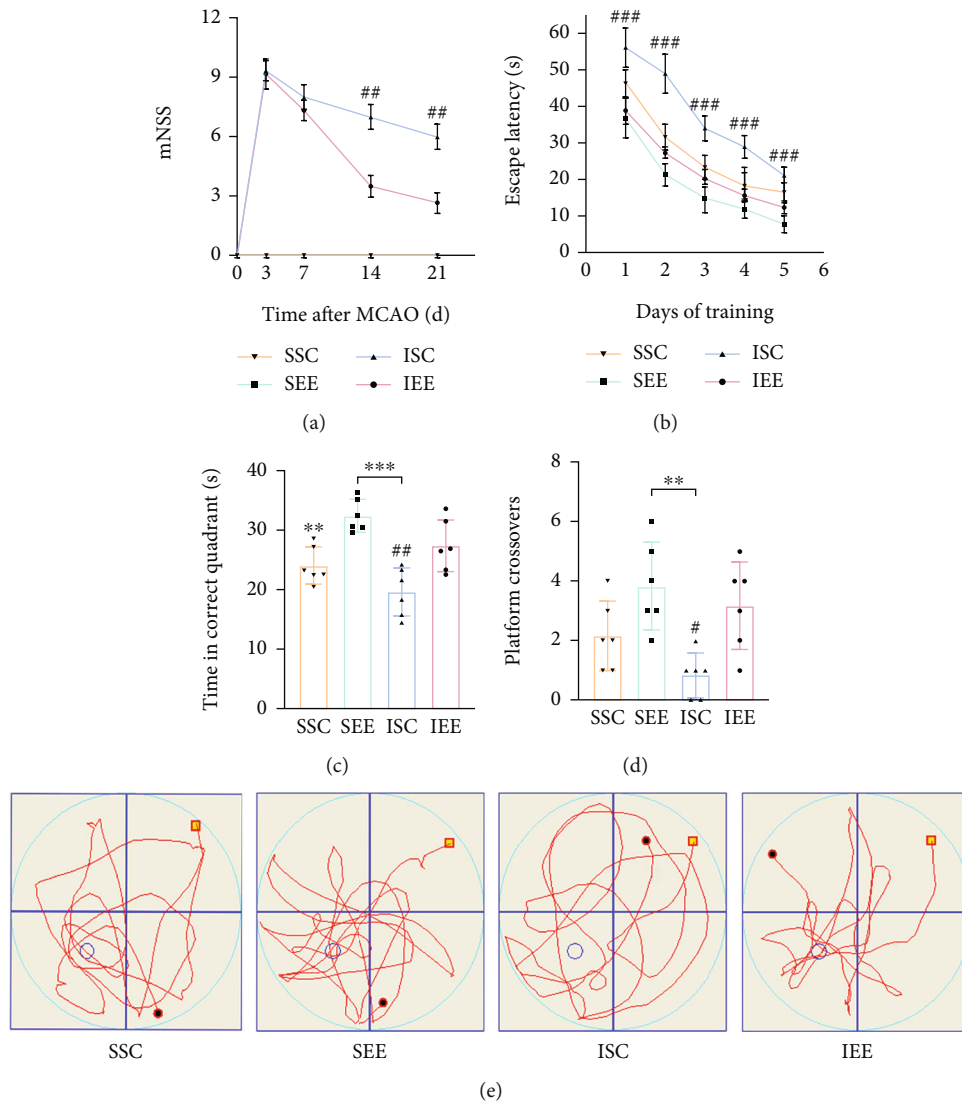


FIGURE 2: Enriched environment attenuated neurological deficits caused by I/R injury. (a) Changes in mNSS for different groups on day 3, 7, and 21. Rats were trained preoperatively to avoid errors. (b) The escape latency in the spatial learning phase. (c, d) Time in the correct quadrant and the crossovers in the target quadrant was recorded and analyzed. (e) Representative swimming trajectories of SSC, SEE, ISC, and IEE groups in the probe trials. $n = 6$. Data are expressed as mean \pm SD. ** $p < 0.01$ and *** $p < 0.001$ vs. SEE group; # $p < 0.05$ and ## $p < 0.01$ vs. IEE group.

measured by qRT-PCR. The results revealed that the mRNA levels of inflammatory factors were increased in the I/R groups compared with the sham-operated groups. However, the mRNA levels of inflammatory factors were obviously less in the IEE group in comparison with the ISC group (Figures 5(a)–5(c); $p < 0.05$, $p < 0.001$, and $p < 0.05$).

3.4. Enriched Environment Reduced the Expression of ACSL4 after Cerebral I/R Injury. ACSL4 expression was positively associated with the occurrence of ferroptosis [40], and exploring the effect of EE on ACSL4 expression would help to investigate the role of EE on ferroptosis. As shown in the western blot results, the expression of ACSL4 was obviously increased following cerebral I/R injury. However, EE reduced the expression of ACSL4 (Figures 6(b) and 6(c); $p < 0.01$). The immunofluorescence results showed that the

ACSL4 was increased in neurons after I/R injury and the proportion of ACSL4/Neun-positive cells in the ISC group was obviously higher compared with the IEE group (Figures 6(a) and 6(d); $p < 0.01$). These results suggested that EE attenuated ferroptosis by inhibiting the ACSL4 expression.

3.5. Enriched Environment Increased the Expression of HIF-1 α after Cerebral I/R Injury. As HIF-1 α was reported as the transcriptional regulator of ACSL4, we further investigated whether EE attenuated ferroptosis via the HIF-1 α -ACSL4 pathway. Western blot results revealed that the HIF-1 α expression level of the I/R groups obviously increased versus the sham-operated groups. Moreover, HIF-1 α expression levels were uplifted in the IEE group versus the ISC group (Figures 7(b) and 7(c); $p < 0.05$). These

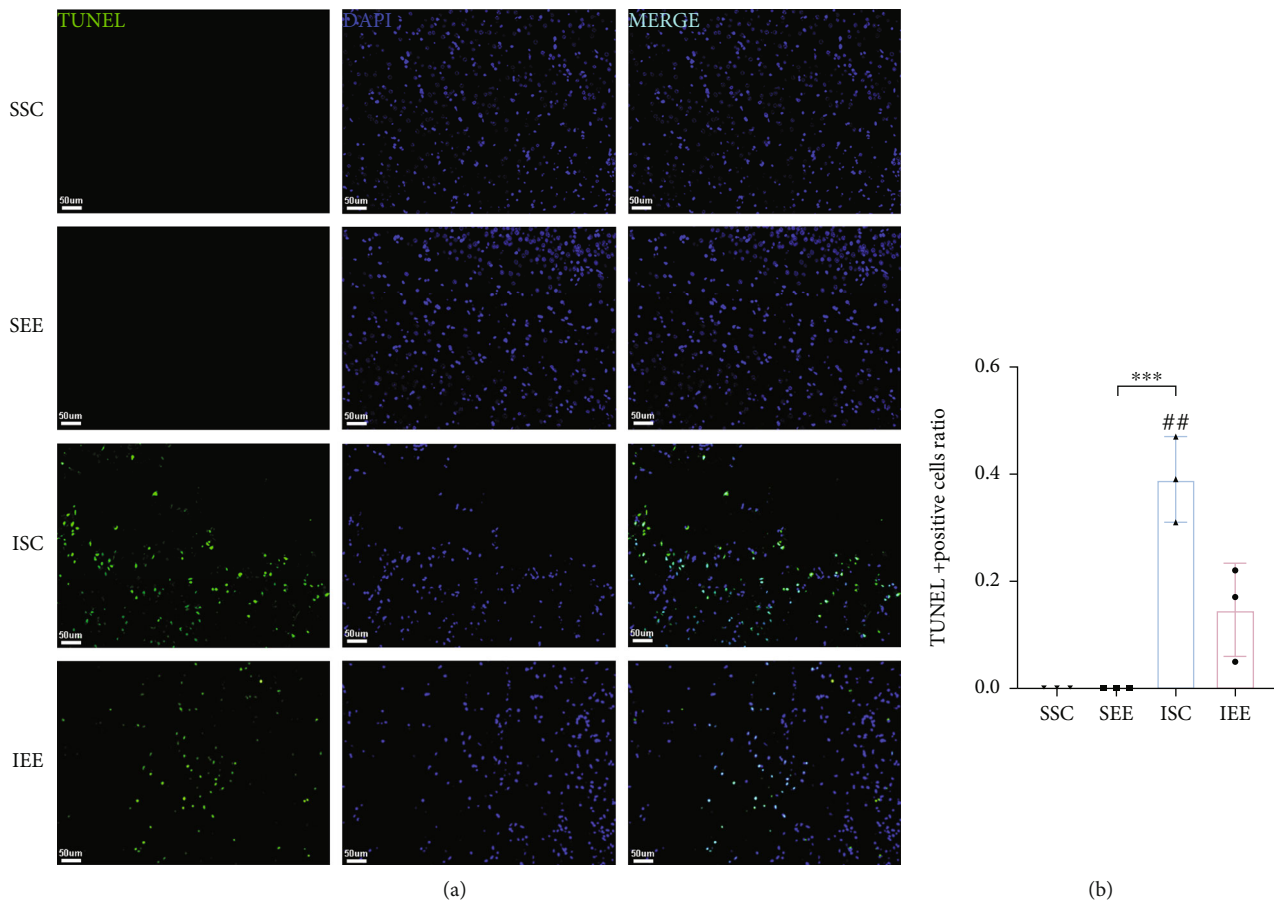


FIGURE 3: Enriched environment reduced regulated cell death in the peri-infarct cortex. (a) TUNEL staining for evaluation of the regulated cell death in the peri-infarct cortex. (b) Quantitative analysis for the number of TUNEL-positive cells. Scale bars, 50 μm . $n = 3$. Data are expressed as mean \pm SD. *** $p < 0.001$ vs. SEE group; ## $p < 0.01$ vs. IEE group.

results were further supported by immunofluorescence results. In addition, HIF-1 α was mostly expressed in the nucleus as it was colocalized with DAPI, which indicated that HIF-1 α might act as a transcription factor (Figures 7(a) and 7(d); $p < 0.001$). To clarify the underlying mechanism of how HIF-1 α negatively regulated ACSL4 expression, we further used qRT-PCR to examine the ACSL4 mRNA level. The outcomes demonstrated that the ACSL4 mRNA level of the IEE group was considerably less than the ISC group, which suggested that HIF-1 α might inhibit ACSL4 expression at the transcriptional level (Figure 6(e); $p < 0.05$).

4. Discussion

While stroke mortality is declining because of advances in thrombectomy and thrombolytic therapies, disability caused by IS remains high [41, 42]. Disability or functional impairment after IS severely affects the life quality of survivors and imposes a heavy burden on their families [12]. It is a top priority to find ways to reduce functional deficits after IS. Growing evidence in animal models has shown that EE can promote functional recovery after IS [43, 44]. Exploring

the mechanisms underlying EE will help to optimize EE setting, potentially benefiting clinical practice in the future.

To test the effect of EE on neurological function, a series of behavioral experiments were conducted. The results of mNSS suggested that neurological function was impaired in I/R rats. The mNSS included motor, sensory, reflex, and balance assessments. In this study, the results of mNSS indicated that EE could reverse motor dysfunction, sensory abnormalities, and balance disorders caused by I/R injury, thereby improving neurobehavioral function [45]. The results of MWM indicated that EE improved long-term spatial learning and memory functions after stroke. Previous studies have also shown that EE can reduce neurological deficits after I/R injuries, thereby reducing mNSS scores [10, 46]. These results were consistent with our study.

Ferroptosis was closely associated with neurological diseases. The accumulation of excess iron in intracerebral hemorrhage (ICH) could lead to oxidative stress and neuronal damage. Inhibiting ferroptosis by regulating the miR-124/ferroportin signaling pathway could ameliorate neuronal cell death after ICH [47]. In ischemic stroke, lipid peroxidation increased while GSH expression decreased in the injured region, and inhibiting this change mediated a neuroprotective

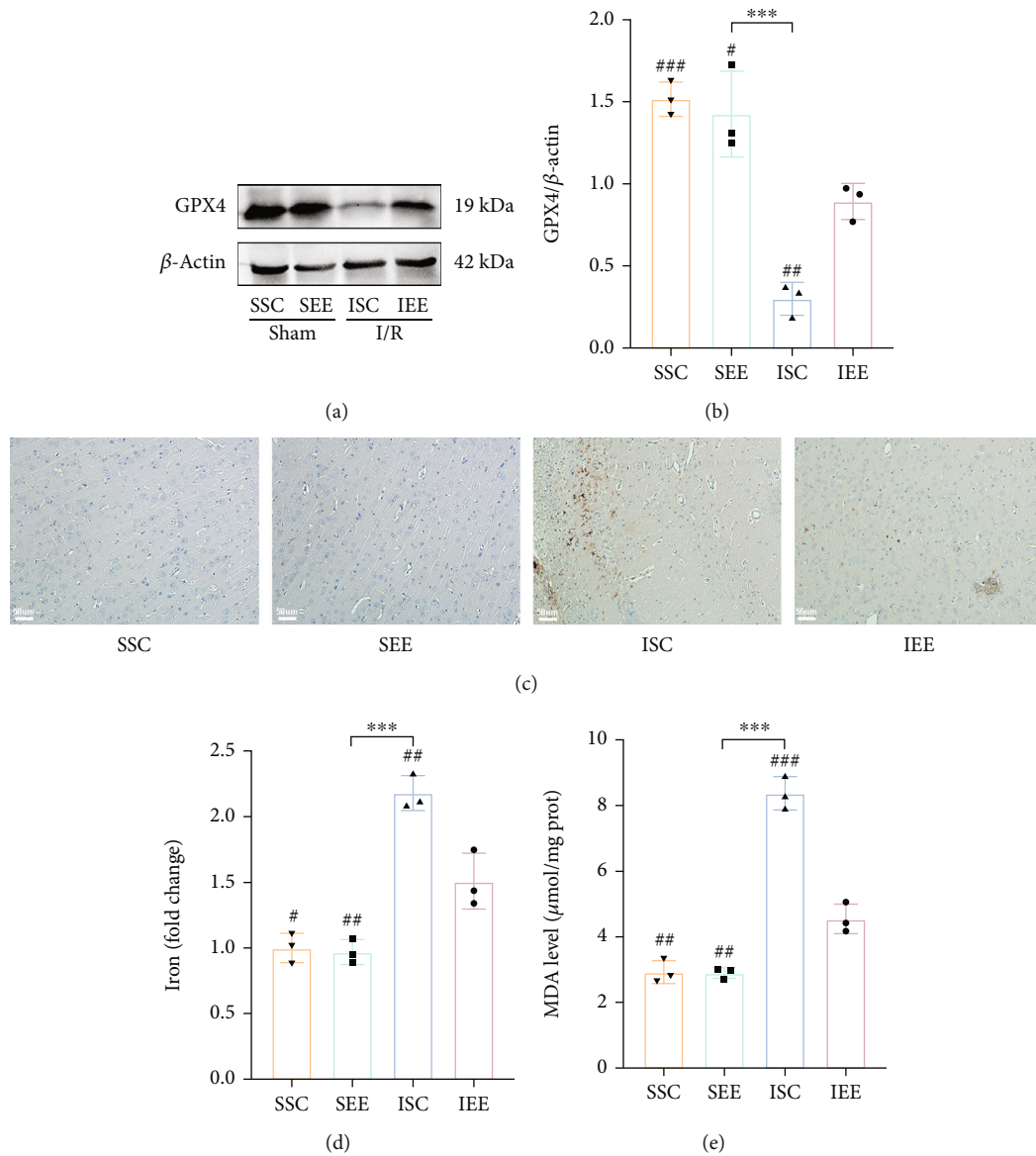


FIGURE 4: Enriched environment reduced iron deposition and ferroptosis. (a, b) Western blots and quantification of GPX4 in the peri-infarct cortex. (c) Perls' staining of iron in the peri-infarct cortex. (d) Quantitative analysis of iron levels in the peri-infarct cortex. (e) Quantitative analysis of MDA levels in the peri-infarct cortex. Scale bars, 50 μ m. $n = 3$. Data are expressed as mean \pm SD. *** $p < 0.001$ vs. SEE group; # $p < 0.05$, ## $p < 0.01$, and ### $p < 0.001$ vs. IEE group.

effect [48]. Iron chelators, such as ferrostatin-1 (Fer-1) and liproxstatin-1 (Lip-1) that act as ferroptosis inhibitors, could protect the neurovascular unit in acute stroke [49]. However, the precise mechanism by which ferroptosis was involved in the pathophysiological process of stroke is unclear. Previous studies have shown that exercise training could improve functional recovery after stroke by inhibiting ferroptosis [50]. However, there was still no evidence whether EE-mediated neurological recovery was associated with ferroptosis. We examined key indicators of ferroptosis to investigate whether EE-mediated neuroprotection was mediated by modulating ferroptosis. The TUNEL assay can detect and quantify cells undergoing regulated cell death, including ferroptosis, by labeling indicative of endonucleolytic cleavage of DNA [51]. According to the TUNEL assay results, EE significantly

inhibited regulated cell death. GPX4 scavenges lipid hydroperoxides to prevent ferroptosis [52]. The GPX4 expression was then examined in different groups, and EE significantly improved the level of GPX4 after I/R injury. One feature of ferroptosis is iron accumulation [53]. To investigate the changes in iron after cerebral I/R injury and whether EE could alter iron content, we used Perls' staining and iron assay kit to detect iron alterations. The results showed that cerebral I/R injury obviously increased the iron level, whereas EE could decrease the iron level. Another feature of ferroptosis is lipid peroxidation due to iron accumulation [54]. Lipid peroxidation generates a variety of oxidation products, MDA being one of the most common [55]. The MDA assay results revealed that changes in MDA were consistent with the changes in iron content. We hypothesize that EE may reduce

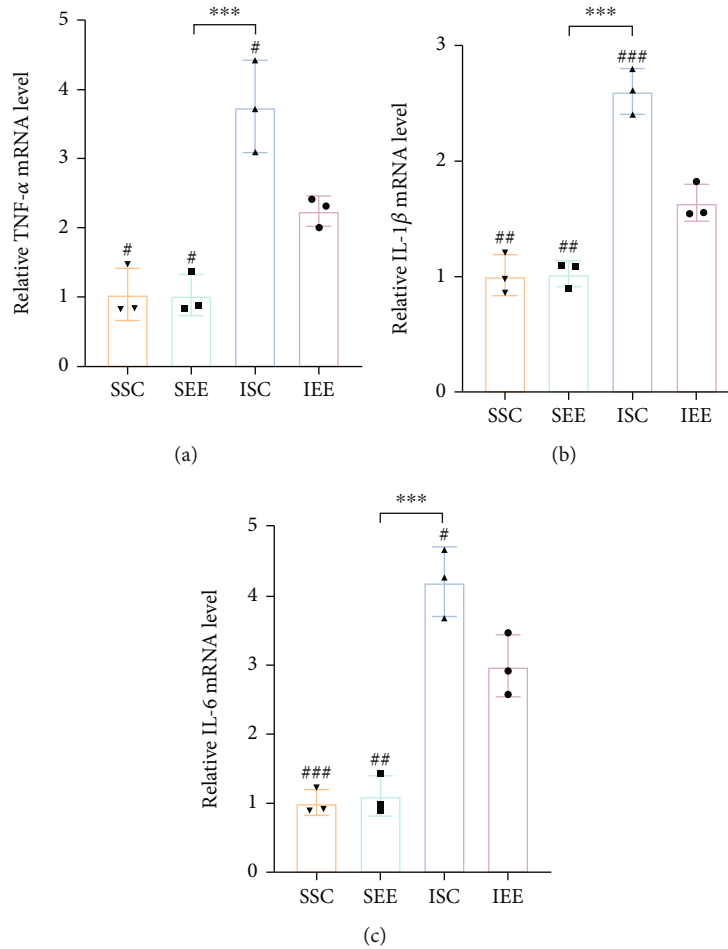


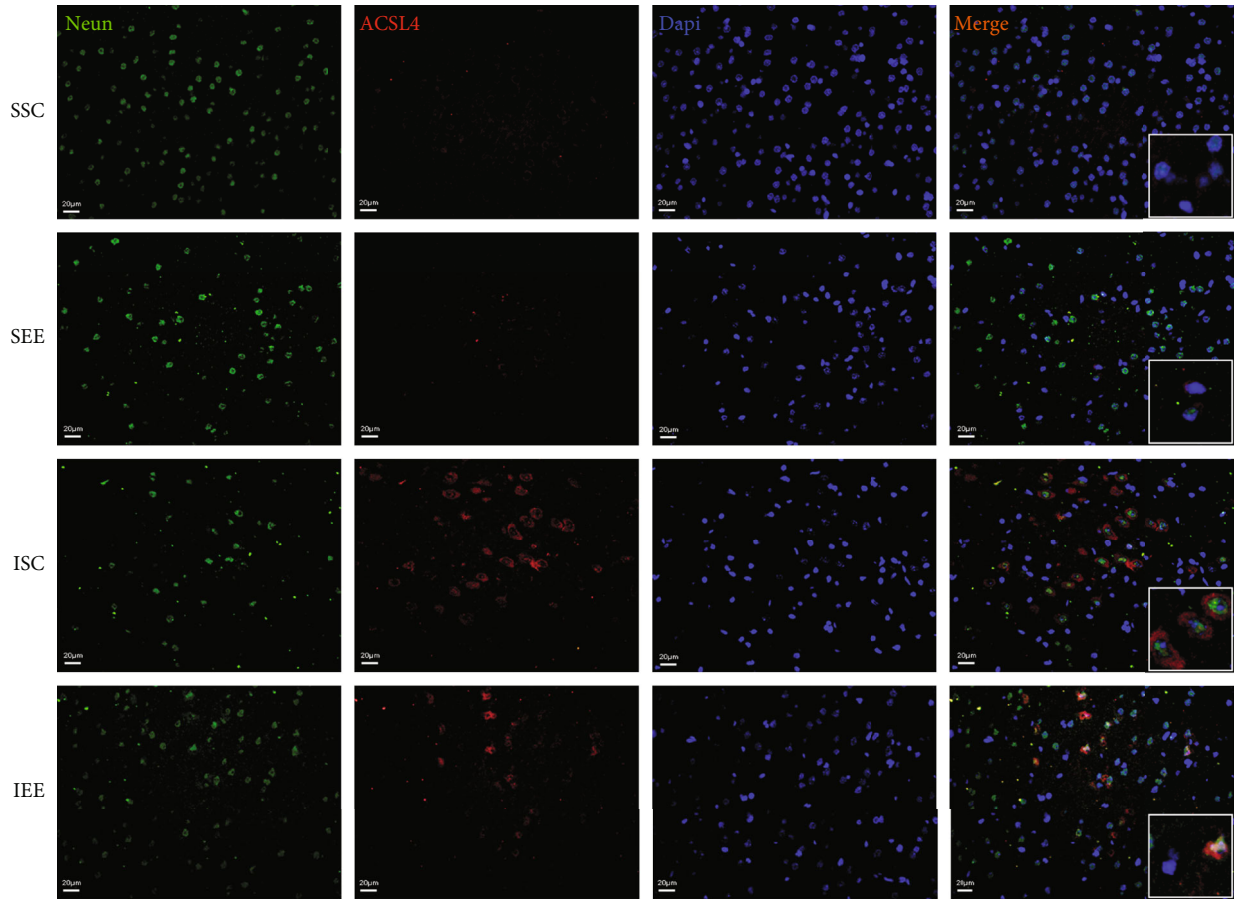
FIGURE 5: Enriched environment reduced the expression of the inflammatory cytokines. (a) Quantitative analysis of TNF- α mRNA levels in the peri-infarct cortex. (b) Quantitative analysis of IL-1 β mRNA levels in the peri-infarct cortex. (c) Quantitative analysis of IL-6 mRNA levels in the peri-infarct cortex. $n = 3$. Data are expressed as mean \pm SD. *** $p < 0.001$ vs. SEE group; # $p < 0.05$, ## $p < 0.01$, and ### $p < 0.001$ vs. IEE group.

ferroptosis and thus promote recovery after cerebral I/R injury based on these alterations in ferroptosis-related factors.

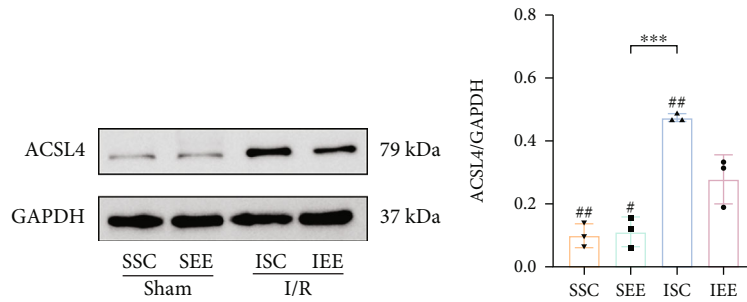
Given that ferroptosis may be regulated by inflammatory cytokines, the inflammatory cytokines (TNF α , IL-6, and IL-1 β) and mRNA expression levels were measured using qRT-PCR. The results showed that EE reduced the mRNA expression levels of inflammatory cytokines after I/R injury indicating that EE may attenuate ferroptosis by inhibiting neuroinflammation. Our findings were supported by several studies. An earlier study has demonstrated that the increased expression of IL-1 β made cells more susceptible to ferroptosis [56]. Additionally, IL-6 may potentially interfere with iron homeostasis and induce ferroptosis [57]. Most importantly, these inflammatory cytokines have been proven to directly affect the GPX4 expression level, indicating that inflammatory cytokines may be able to regulate ferroptosis [58]. However, numerous studies have shown that the presence of ferroptosis could also affect the expression of inflammatory factors [58, 59]. Ferroptosis played an important role in the model of non-alcoholic steatohepatitis, since it served as the trigger for inflammation [60]. In the model of psoriatic, inhibition of ferroptosis reduced the production of cytokines including TNF α ,

IL-6, and IL-1 β [61]. In the model of diabetes, ferroptosis induced inflammation in the diabetic wound, and the application of ferroptosis inhibitors reduced the expression of inflammation markers [62]. More research is required to determine how inflammation and ferroptosis are related. Further research is needed to determine the precise involvement of EE in the interplay between ferroptosis and the inflammatory response following stroke.

Our previous studies have identified some mechanisms of EE on functional recovery after cerebral I/R injury, including the promotion of vascular regeneration and inhibition of neuronal apoptosis and pyroptosis [9, 13, 34]. This study also showed that EE could promote the expression of HIF-1 α . HIF-1 α could regulate many target genes as a transcription factor [29, 63]. Vascular endothelial growth factor (VEGF) is one of the downstream target genes of HIF-1 α , which is extensively involved in the pathological process of ischemic stroke [64, 65]. HIF-1 α plays a neuroprotective role by regulating VEGF-mediated angiogenesis and neuroregeneration [66]. In addition, HIF-1 α has a neuroprotective effect by increasing erythropoietin expression, which can enhance oxygen transport and increase cerebral blood flow [67, 68]. However, several studies have also

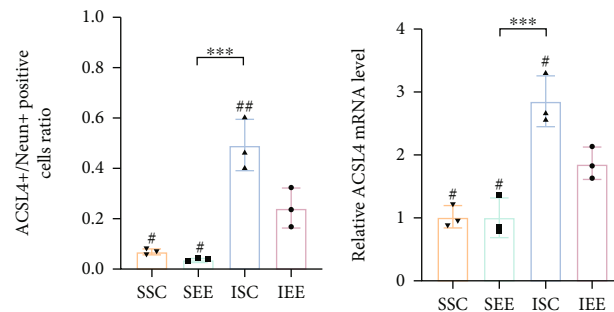


(a)



(b)

(c)



(d)

(e)

FIGURE 6: Enriched environment reduced the expression of ACSL4 after I/R injury. (a, d) Double immunostaining of Neun and ACSL4. Statistical analysis of the positive rate was shown. (b, c) Western blots and quantification of ACSL4 in the peri-infarct cortex. (e) Quantitative analysis of ACSL4 mRNA levels in the peri-infarct cortex. Scale bars, 20 µm. $n = 3$. Data are expressed as mean ± SD. *** $p < 0.001$ vs. SEE group; # $p < 0.05$ and ## $p < 0.01$ vs. IEE group.

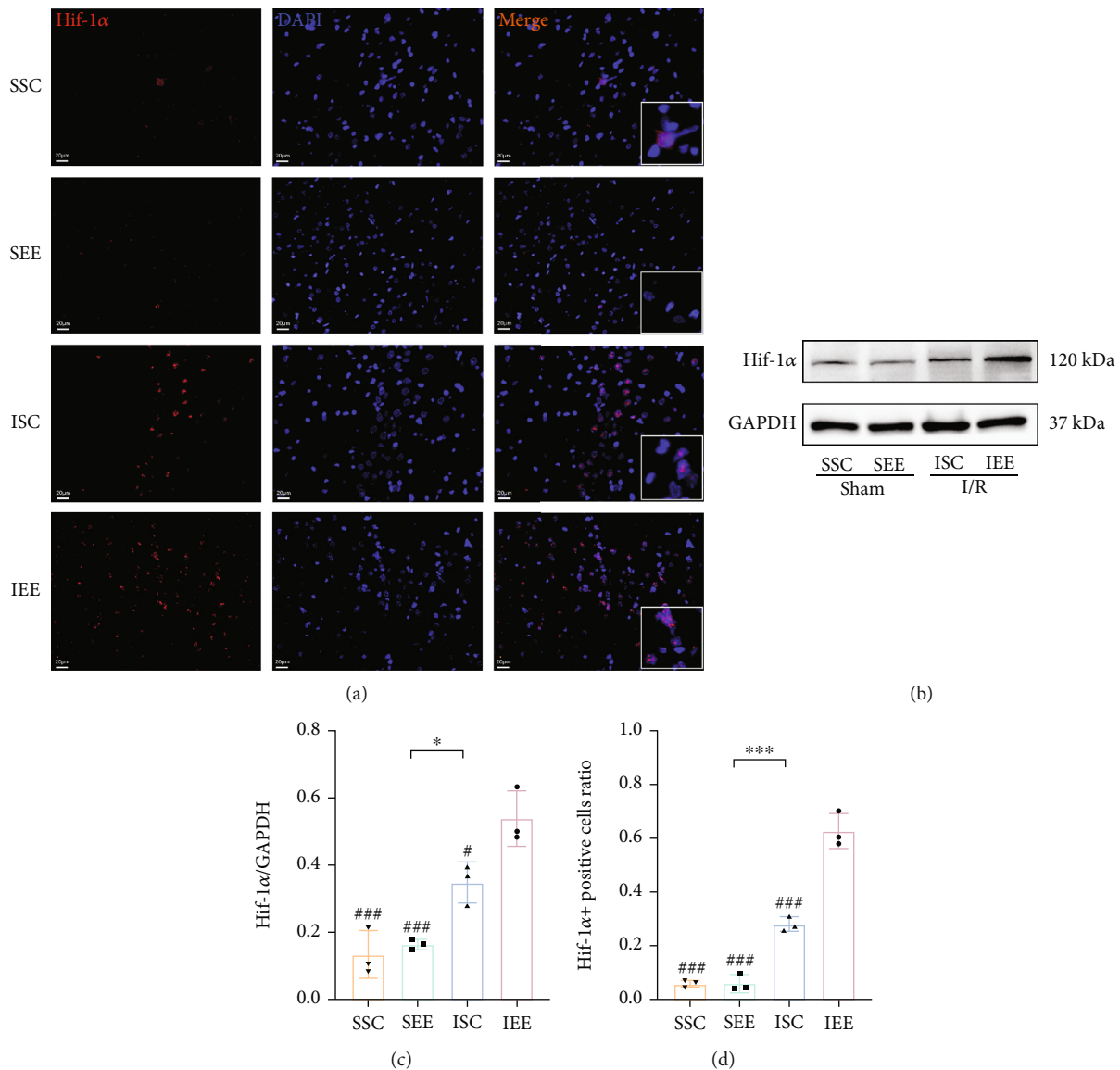


FIGURE 7: Enriched environment increased the expression of HIF-1α after I/R injury. (a, d) Immunofluorescence images of HIF-1α and statistical analysis of the positive rate. (b, c) Western blots and quantification of HIF-1α in the peri-infarct cortex. Scale bars, 20 μm. $n = 3$. Data are expressed as mean \pm SD. * $p < 0.05$ and *** $p < 0.001$ vs. SEE group; # $p < 0.05$ and ### $p < 0.001$ vs. IEE group.

pointed out that in the early stages of ischemic stroke, HIF-1α aggravates neurological damage by exacerbating the permeability of the blood-brain barrier and mediating the expression of proinflammatory factors and inflammatory responses [69–71]. The same molecule may play very different roles at various stages of the disease pathology. Therefore, it is necessary to further investigate the complex and significant role that HIF-1α plays in ischemic stroke. According to the western blot results, cerebral I/R injury markedly increased the expression level of HIF-1α, while EE could further increase the HIF-1α expression. Immunofluorescence results also showed that EE increased the expression of HIF-1α mainly in the nucleus which further supported the idea that HIF-1α might act as a transcription factor. These results implied that HIF-1α played a fundamental role in the neuroprotective effect of EE after cerebral I/R injury.

Increased expression of ACSL4 exacerbates brain injury by making cells more susceptible to ROS-induced ferroptosis [26, 27, 28, 72]. In our study, western blot results showed that cerebral I/R injury remarkably elevated the expression of ACSL4, while EE reduced the expression of ACSL4. Double immunofluorescence staining showed that ACSL4 was predominantly expressed in neurons after cerebral I/R injury, and EE reduced the proportion of ACSL4/Neun-positive cells. We hypothesized that EE could enhance neuronal tolerance to ROS caused by cerebral I/R injury by decreasing ACSL4 expression. As a lipid metabolism enzyme, ACSL4 is necessary for ferroptosis, which results in increased lipid peroxidation and ferroptosis [73]. Recently, ACSL4 has already been regarded as a ferroptosis modulators [23]. Numerous studies have demonstrated that increased ACSL4 expression can promote ferroptosis and the inhibition

of ACSL4 expression could reduce ferroptosis [74]. Decreased ferroptosis is inextricably linked to decreased ACSL4 expression, and when ferroptosis inducers are applied, ACSL4 expression is elevated [75]. In future studies, we should involve overexpressing ACSL4 to further determine the relationship between EE-suppressed ferroptosis and ACSL4. Besides, the qRT-PCR results indicated that the ACSL4 reduction occurred at the transcriptional level. Recent studies showed that HIF-1 α was bound to the ACSL4 promoter region to repress its transcription [28, 32]. Our study further verified that the increase in HIF-1 α expression level induced by EE might also affect the transcription of ACSL4 after cerebral I/R injury. Previous studies confirmed that the ischemia-induced increase in HIF-1 α expression could suppress ACSL4 expression after oxygen and glucose deprivation (OGD). Knockdown of HIF-1 α in SH-SY5Y enhanced the expression of ACSL4 following OGD. After OGD treatment, HIF-1 α binds to the conserved noncoding sequences 1 and 2 promoter regions of ACSL4 thereby suppressing the expression of ACSL4 [28]. It was further established that HIF-1 α negatively regulates the expression of ACSL4 in vitro. In HK-2 cells, ACSL4 expression increased after the knockdown of HIF-1 α . The application of HIF-1 α inhibitors could enhance the mRNA level of ACSL4 [32]. Our experimental results are consistent with previous studies. Less perfection of our study was the lack of HIF-1 α knockdown experiments to verify the deterministic effect of EE on the expression of HIF-1 α . Further studies should be conducted on this aspect in the future.

As an important environmental intervention, EE inhibits ferroptosis and improves functional recovery after I/R injury. Our findings showed new light on the potential therapeutic mechanisms of EE as well as the pathophysiological development of stroke recovery. This also provides us with novel insight for poststroke rehabilitation in clinical transformation. For example, clinical patients can be treated in an integrated EE-like environment that includes appropriate intensity physical activity, active social interaction, a mindful natural environment, and appropriate challenging tasks to accelerate recovery after stroke. Also, treatments that target ferroptosis and its related molecules may be a new option for the rehabilitation of stroke. However, there are still some limitations in our study. We only explored the effect of EE on ferroptosis after stroke. The effect of EE on other forms of cell death and their relevance remain to be explored. Also, we only investigated the effect of a specific duration of EE intervention on stroke recovery. The effect of different duration of EE intervention on stroke recovery remains to be investigated. We will work to optimize our experimental protocols and designs in future studies.

5. Conclusions

In this study, we confirmed the effectiveness of EE in promoting functional recovery after cerebral I/R injury by attenuating ferroptosis. And this process might be activated by the HIF-1 α -ACSL4 pathway. EE also inhibited the expression levels of inflammatory cytokines including TNF α , IL-6, and IL-1 β , which might facilitate functional recovery after stroke. This study provides more theoretical evidence that EE is a promising rehabilitation strategy for stroke.

Data Availability

The article contains the original contributions discussed in the study; further questions should be addressed to the relevant author(s).

Ethical Approval

The animal study was reviewed and approved by the experimental animal Ethics Committee of Wuhan University (WP2020-08052).

Conflicts of Interest

The authors declare that there are no conflicts of interest.

Authors' Contributions

Jingying Liu, Qihang Luo, and Jie Ke have contributed equally to this work.

Acknowledgments

The authors thank the personnel in the Department of Rehabilitation Medicine at the Zhongnan Hospital of Wuhan University. Thanks are due to all those who helped in the experiment. This work was supported by grants from the National Natural Science Foundation of China (No. 81902304 to XZ and No. 82002401 to XP C) and Zhongnan Hospital of Wuhan University Science, Technology and Innovation Seed Fund (Project: znp2019113).

References

- [1] R. L. Sacco, S. E. Kasner, J. P. Broderick et al., "An updated definition of stroke for the 21st century: a statement for healthcare professionals from the American Heart Association/American Stroke Association," *Stroke*, vol. 44, no. 7, pp. 2064–2089, 2013.
- [2] F. Z. Caprio and F. A. Sorond, "Cerebrovascular disease: primary and secondary stroke prevention," *The Medical Clinics of North America*, vol. 103, no. 2, pp. 295–308, 2019.
- [3] Stroke Unit Trialists' Collaboration, "Organised inpatient (stroke unit) care for stroke," *Cochrane Database of Systematic Reviews*, vol. 2013, no. 9, article CD000197, 2013.
- [4] C. Ayala, J. Fang, C. Luncheon et al., "Use of outpatient rehabilitation among adult stroke survivors — 20 states and the District of Columbia, 2013, and four states, 2015," *MMWR. Morbidity and Mortality Weekly Report*, vol. 67, no. 20, pp. 575–578, 2018.
- [5] L. V. Gonçalves, A. L. Herlinger, T. A. A. Ferreira, J. B. Coitinho, R. G. W. Pires, and C. Martins-Silva, "Environmental enrichment cognitive neuroprotection in an experimental model of cerebral ischemia: biochemical and molecular aspects," *Behavioural Brain Research*, vol. 348, pp. 171–183, 2018.
- [6] R. Farrell, S. Evans, and D. Corbett, "Environmental enrichment enhances recovery of function but exacerbates ischemic cell death," *Neuroscience*, vol. 107, no. 4, pp. 585–592, 2001.
- [7] P. Langhorne, O. Wu, H. Rodgers, A. Ashburn, and J. Bernhardt, "A very early rehabilitation trial after stroke

- (AVERT): a phase III, multicentre, randomised controlled trial," *Health Technology Assessment*, vol. 21, no. 54, pp. 1–120, 2017.
- [8] X. Chen, X. Zhang, W. Liao, and Q. Wan, "Effect of physical and social components of enriched environment on astrocytes proliferation in rats after cerebral ischemia/reperfusion injury," *Neurochemical Research*, vol. 42, no. 5, pp. 1308–1316, 2017.
- [9] X. Zhang, X. P. Chen, J. B. Lin, Y. Xiong, W. J. Liao, and Q. Wan, "Effect of enriched environment on angiogenesis and neurological functions in rats with focal cerebral ischemia," *Brain Research*, vol. 1655, pp. 176–185, 2017.
- [10] Y. H. Deng, L. L. Dong, Y. J. Zhang, X. M. Zhao, and H. Y. He, "Enriched environment boosts the post-stroke recovery of neurological function by promoting autophagy," *Neural Regeneration Research*, vol. 16, no. 5, pp. 813–819, 2021.
- [11] Y. Zhang, D. Xu, H. Qi et al., "Enriched environment promotes post-stroke neurogenesis through NF- κ B-mediated secretion of IL-17A from astrocytes," *Brain Research*, vol. 1687, pp. 20–31, 2018.
- [12] D. Young, P. A. Lawlor, P. Leone, M. Dragunow, and M. J. During, "Environmental enrichment inhibits spontaneous apoptosis, prevents seizures and is neuroprotective," *Nature Medicine*, vol. 5, no. 4, pp. 448–453, 1999.
- [13] J. Liu, J. Zheng, Y. Xu et al., "Enriched environment attenuates pyroptosis to improve functional recovery after cerebral ischemia/reperfusion injury," *Frontiers in Aging Neuroscience*, vol. 13, article 717644, 2021.
- [14] A. Liesz, A. Dalpke, E. Mracsko et al., "DAMP signaling is a key pathway inducing immune modulation after brain injury," *The Journal of Neuroscience*, vol. 35, no. 2, pp. 583–598, 2015.
- [15] R. M. L'e Orme, N. M. McGrath, R. J. Rankin, and R. W. Frith, "Extracranial vertebral artery dissection presenting as neurogenic pulmonary oedema," *Australian and New Zealand Journal of Medicine*, vol. 29, no. 6, pp. 824–825, 1999.
- [16] Q. Li, Y. Cao, C. Dang et al., "Inhibition of double-strand DNA-sensing cGAS ameliorates brain injury after ischemic stroke," *EMBO Molecular Medicine*, vol. 12, no. 4, p. e11002, 2020.
- [17] S. J. Dixon, K. M. Lemberg, M. R. Lamprecht et al., "Ferroptosis: an iron-dependent form of nonapoptotic cell death," *Cell*, vol. 149, no. 5, pp. 1060–1072, 2012.
- [18] X. Jiang, B. R. Stockwell, and M. Conrad, "Ferroptosis: mechanisms, biology and role in disease," *Nature Reviews Molecular Cell Biology*, vol. 22, no. 4, pp. 266–282, 2021.
- [19] Q. Z. Tuo, P. Lei, K. A. Jackman et al., "Tau-mediated iron export prevents ferroptotic damage after ischemic stroke," *Molecular Psychiatry*, vol. 22, no. 11, pp. 1520–1530, 2017.
- [20] D. C. Fuhrmann, A. Mondorf, J. Beifuß, M. Jung, and B. Brüne, "Hypoxia inhibits ferritinophagy, increases mitochondrial ferritin, and protects from ferroptosis," *Redox Biology*, vol. 36, article 101670, 2020.
- [21] I. Alim, J. T. Caulfield, Y. Chen et al., "Selenium drives a transcriptional adaptive program to block ferroptosis and treat stroke," *Cell*, vol. 177, no. 5, pp. 1262–1279.e25, 2019.
- [22] G. C. Forcina and S. J. Dixon, "GPX4 at the crossroads of lipid homeostasis and ferroptosis," *Proteomics*, vol. 19, no. 18, p. 1800311, 2019.
- [23] J. Wu, A. M. Minikes, M. Gao et al., "Intercellular interaction dictates cancer cell ferroptosis via NF2-YAP signalling," *Nature*, vol. 572, no. 7769, pp. 402–406, 2019.
- [24] H. Mao, Y. Zhao, H. Li, and L. Lei, "Ferroptosis as an emerging target in inflammatory diseases," *Progress in Biophysics and Molecular Biology*, vol. 155, pp. 20–28, 2020.
- [25] X. L. Fang, S. Y. Ding, X. Z. Du, J. H. Wang, and X. L. Li, "Ferroptosis—a novel mechanism with multifaceted actions on stroke," *Frontiers in Neurology*, vol. 13, article 881809, 2022.
- [26] Z. Fan, L. Cai, S. Wang, J. Wang, and B. Chen, "Baicalin prevents myocardial ischemia/reperfusion injury through inhibiting ACSL4 mediated ferroptosis," *Frontiers in Pharmacology*, vol. 12, article 628988, 2021.
- [27] Y. Li, D. Feng, Z. Wang et al., "Ischemia-induced ACSL4 activation contributes to ferroptosis-mediated tissue injury in intestinal ischemia/reperfusion," *Cell Death & Differentiation*, vol. 26, no. 11, pp. 2284–2299, 2019.
- [28] Y. Cui, Y. Zhang, X. Zhao et al., "ACSL4 exacerbates ischemic stroke by promoting ferroptosis-induced brain injury and neuroinflammation," *Brain, Behavior, and Immunity*, vol. 93, pp. 312–321, 2021.
- [29] G. L. Semenza, "HIF-1 and mechanisms of hypoxia sensing," *Current Opinion in Cell Biology*, vol. 13, no. 2, pp. 167–171, 2001.
- [30] A. Rattner, J. Williams, and J. Nathans, "Roles of HIFs and VEGF in angiogenesis in the retina and brain," *Journal of Clinical Investigation*, vol. 129, no. 9, pp. 3807–3820, 2019.
- [31] H. Shi, "Hypoxia inducible factor 1 as a therapeutic target in ischemic stroke," *Current Medicinal Chemistry*, vol. 16, no. 34, pp. 4593–4600, 2009.
- [32] Y. Wang, M. Zhang, R. Bi et al., "ACSL4 deficiency confers protection against ferroptosis-mediated acute kidney injury," *Redox Biology*, vol. 51, article 102262, 2022.
- [33] S. Guo, M. Miyake, K. J. Liu, and H. Shi, "Specific inhibition of hypoxia inducible factor 1 exaggerates cell injury induced by *in vitro* ischemia through deteriorating cellular redox environment," *Journal of Neurochemistry*, vol. 108, no. 5, pp. 1309–1321, 2009.
- [34] X. Chen, X. Zhang, L. Xue, C. Hao, W. Liao, and Q. Wan, "Treatment with enriched environment reduces neuronal apoptosis in the periinfarct cortex after cerebral ischemia/reperfusion injury," *Cellular Physiology and Biochemistry*, vol. 41, no. 4, pp. 1445–1456, 2017.
- [35] E. Z. Longa, P. R. Weinstein, S. Carlson, and R. Cummins, "Reversible middle cerebral artery occlusion without craniectomy in rats," *Stroke*, vol. 20, no. 1, pp. 84–91, 1989.
- [36] D. Barthels and H. Das, "Current advances in ischemic stroke research and therapies," *Biochimica et Biophysica Acta (BBA) - Molecular Basis of Disease*, vol. 1866, no. 4, article 165260, 2020.
- [37] R. Morris, "Developments of a water-maze procedure for studying spatial learning in the rat," *Journal of Neuroscience Methods*, vol. 11, no. 1, pp. 47–60, 1984.
- [38] S. Bedoui, M. J. Herold, and A. Strasser, "Emerging connectivity of programmed cell death pathways and its physiological implications," *Nature Reviews Molecular Cell Biology*, vol. 21, no. 11, pp. 678–695, 2020.
- [39] S. S. Karuppagounder, L. Alin, Y. Chen et al., "N-acetylcysteine targets 5 lipoxygenase-derived, toxic lipids and can synergize with prostaglandin E₂ to inhibit ferroptosis and improve outcomes following hemorrhagic stroke in mice," *Annals of Neurology*, vol. 84, no. 6, pp. 854–872, 2018.
- [40] I. Ingold, C. Berndt, S. Schmitt et al., "Selenium utilization by GPX4 is required to prevent hydroperoxide-induced ferroptosis," *Cell*, vol. 172, no. 3, pp. 409–422.e21, 2018.

- [41] T. G. Jovin, A. Chamorro, E. Cobo et al., “Thrombectomy within 8 hours after symptom onset in ischemic stroke,” *The New England Journal of Medicine*, vol. 372, no. 24, pp. 2296–2306, 2015.
- [42] N. Wahlgren, N. Ahmed, A. Dávalos et al., “Thrombolysis with alteplase for acute ischaemic stroke in the safe implementation of thrombolysis in stroke-monitoring study (SITS-MOST): an observational study,” *The Lancet*, vol. 369, no. 9558, pp. 275–282, 2007.
- [43] G. Kempermann, “Environmental enrichment, new neurons and the neurobiology of individuality,” *Nature Reviews Neuroscience*, vol. 20, no. 4, pp. 235–245, 2019.
- [44] J. Nithianantharajah and A. J. Hannan, “Enriched environments, experience-dependent plasticity and disorders of the nervous system,” *Nature Reviews Neuroscience*, vol. 7, no. 9, pp. 697–709, 2006.
- [45] X. Xu, W. Gao, S. Cheng et al., “Anti-inflammatory and immunomodulatory mechanisms of atorvastatin in a murine model of traumatic brain injury,” *Journal of Neuroinflammation*, vol. 14, no. 1, p. 167, 2017.
- [46] P. Dahlqvist, A. Rönnebeck, S.-A. Bergström, I. Söderström, and T. Olsson, “Environmental enrichment reverses learning impairment in the Morris water maze after focal cerebral ischemia in rats,” *The European Journal of Neuroscience*, vol. 19, no. 8, pp. 2288–2298, 2004.
- [47] W. D. Bao, X. T. Zhou, L. T. Zhou et al., “Targeting miR-124/Ferroptin signaling ameliorated neuronal cell death through inhibiting apoptosis and ferroptosis in aged intracerebral hemorrhage murine model,” *Aging Cell*, vol. 19, no. 11, article e13235, 2020.
- [48] S. Ahmad, N. M. Elsherbiny, R. Haque et al., “Sesamin attenuates neurotoxicity in mouse model of ischemic brain stroke,” *Neurotoxicology*, vol. 45, pp. 100–110, 2014.
- [49] K. Yang, L. Zeng, X. Yuan et al., “The mechanism of ferroptosis regulating oxidative stress in ischemic stroke and the regulation mechanism of natural pharmacological active components,” *Biomedicine & Pharmacotherapy*, vol. 154, article 113611, 2022.
- [50] T. Liu, Y. Cui, S. Dong et al., “Treadmill training reduces cerebral ischemia-reperfusion injury by inhibiting ferroptosis through activation of SLC7A11/GPX4,” *Oxidative Medicine and Cellular Longevity*, vol. 2022, Article ID 8693664, 11 pages, 2022.
- [51] J. P. Friedmann Angeli, M. Schneider, B. Proneth et al., “Inactivation of the ferroptosis regulator Gpx4 triggers acute renal failure in mice,” *Nature Cell Biology*, vol. 16, no. 12, pp. 1180–1191, 2014.
- [52] K. Bersuker, J. M. Hendricks, Z. Li et al., “The CoQ oxidoreductase FSP1 acts parallel to GPX4 to inhibit ferroptosis,” *Nature*, vol. 575, no. 7784, pp. 688–692, 2019.
- [53] J. Zheng and M. Conrad, “The metabolic underpinnings of ferroptosis,” *Cell Metabolism*, vol. 32, no. 6, pp. 920–937, 2020.
- [54] X. Chen, C. Yu, R. Kang, and D. Tang, “Iron metabolism in ferroptosis,” *Frontiers in Cell and Development Biology*, vol. 8, article 590226, 2020.
- [55] A. Ayala, M. F. Muñoz, and S. Argüelles, “Lipid peroxidation: production, metabolism, and signaling mechanisms of malondialdehyde and 4-hydroxy-2-nonenal,” *Oxidative Medicine and Cellular Longevity*, vol. 2014, Article ID 360438, 31 pages, 2014.
- [56] X. Yao, K. Sun, S. Yu et al., “Chondrocyte ferroptosis contribute to the progression of osteoarthritis,” *Journal of Orthopaedic Translation*, vol. 27, pp. 33–43, 2021.
- [57] S. Bin, L. Xin, Z. Lin, Z. Jinhua, G. Rui, and Z. Xiang, “Targeting miR-10a-5p/IL-6R axis for reducing IL-6-induced cartilage cell ferroptosis,” *Experimental and Molecular Pathology*, vol. 118, article 104570, 2021.
- [58] Z. Gu, T. Liu, C. Liu et al., “Ferroptosis-strengthened metabolic and inflammatory regulation of tumor-associated macrophages provokes potent tumoricidal activities,” *Nano Letters*, vol. 21, no. 15, pp. 6471–6479, 2021.
- [59] Y. Sun, P. Chen, B. Zhai et al., “The emerging role of ferroptosis in inflammation,” *Biomedicine & Pharmacotherapy*, vol. 127, article 110108, 2020.
- [60] S. Tsurusaki, Y. Tsuchiya, T. Koumura et al., “Hepatic ferroptosis plays an important role as the trigger for initiating inflammation in nonalcoholic steatohepatitis,” *Cell Death & Disease*, vol. 10, no. 6, p. 449, 2019.
- [61] Y. Shou, L. Yang, Y. Yang, and J. Xu, “Inhibition of keratinocyte ferroptosis suppresses psoriatic inflammation,” *Cell Death & Disease*, vol. 12, no. 11, p. 1009, 2021.
- [62] S. Li, Y. Li, Z. Wu, Z. Wu, and H. Fang, “Diabetic ferroptosis plays an important role in triggering on inflammation in diabetic wound,” *American Journal of Physiology-Endocrinology and Metabolism*, vol. 321, no. 4, pp. E509–E520, 2021.
- [63] L. Kong, Y. Ma, Z. Wang et al., “Inhibition of hypoxia inducible factor 1 by YC-1 attenuates tissue plasminogen activator induced hemorrhagic transformation by suppressing HMGB1/TLR4/NF- κ B mediated neutrophil infiltration in thromboembolic stroke rats,” *International Immunopharmacology*, vol. 94, article 107507, 2021.
- [64] M. Khan, T. Dhammu, F. Matsuda et al., “Promoting endothelial function by S-nitrosoglutathione through the HIF-1 α /VEGF pathway stimulates neurorepair and functional recovery following experimental stroke in rats,” *Drug Design, Development and Therapy*, vol. 9, pp. 2233–2247, 2015.
- [65] X. Wu, S. Liu, Z. Hu, G. Zhu, G. Zheng, and G. Wang, “Enriched housing promotes post-stroke neurogenesis through calpain 1-STAT3/HIF-1 α /VEGF signaling,” *Brain Research Bulletin*, vol. 139, pp. 133–143, 2018.
- [66] R. G. Abdel-Latif, R. A. Rifaai, and E. F. Amin, “Empagliflozin alleviates neuronal apoptosis induced by cerebral ischemia/reperfusion injury through HIF-1 α /VEGF signaling pathway,” *Archives of Pharmacal Research*, vol. 43, no. 5, pp. 514–525, 2020.
- [67] Y. X. Li, S. J. Ding, L. Xiao, W. Guo, and Q. Zhan, “Desferoxamine preconditioning protects against cerebral ischemia in rats by inducing expressions of hypoxia inducible factor 1 alpha and erythropoietin,” *Neuroscience Bulletin*, vol. 24, no. 2, pp. 89–95, 2008.
- [68] M. G. Ryou, R. Liu, M. Ren, J. Sun, R. T. Mallet, and S. H. Yang, “Pyruvate protects the brain against ischemia-reperfusion injury by activating the erythropoietin signaling pathway,” *Stroke*, vol. 43, no. 4, pp. 1101–1107, 2012.
- [69] Z. G. Zhang, L. Zhang, Q. Jiang et al., “VEGF enhances angiogenesis and promotes blood-brain barrier leakage in the ischemic brain,” *The Journal of Clinical Investigation*, vol. 106, no. 7, pp. 829–838, 2000.
- [70] C. Chen, Q. Hu, J. Yan et al., “Early inhibition of HIF-1 α with small interfering RNA reduces ischemic-reperfused brain injury in rats,” *Neurobiology of Disease*, vol. 33, no. 3, pp. 509–517, 2009.
- [71] S.-H. Yeh, L.-C. Ou, P.-W. Gean, J.-J. Hung, and W.-C. Chang, “Selective inhibition of early—but not late—expressed HIF-1 α

- is neuroprotective in rats after focal ischemic brain damage,” *Brain Pathology*, vol. 21, no. 3, pp. 249–262, 2011.
- [72] J. Chen, L. Yang, L. Geng et al., “Inhibition of acyl-CoA synthetase long-chain family member 4 facilitates neurological recovery after stroke by regulation ferroptosis,” *Frontiers in Cellular Neuroscience*, vol. 15, article 632354, 2021.
- [73] G. Lei, Y. Zhang, P. Koppula et al., “The role of ferroptosis in ionizing radiation-induced cell death and tumor suppression,” *Cell Research*, vol. 30, no. 2, pp. 146–162, 2020.
- [74] J. Liu, F. Kuang, G. Kroemer, D. J. Klionsky, R. Kang, and D. Tang, “Autophagy-dependent ferroptosis: machinery and regulation,” *Cell Chemical Biology*, vol. 27, no. 4, pp. 420–435, 2020.
- [75] C. Chen, D. Wang, Y. Yu et al., “Legumain promotes tubular ferroptosis by facilitating chaperone-mediated autophagy of GPX4 in AKI,” *Cell Death & Disease*, vol. 12, no. 1, p. 65, 2021.

Research Article

Carbonic Anhydrase IX Controls Vulnerability to Ferroptosis in Gefitinib-Resistant Lung Cancer

Chen Zhang , Xiyi Lu , Xinyin Liu , Jiali Xu , Jun Li , Tianyu Qu , Jiali Dai ,
and Renhua Guo 

Jiangsu Province Hospital and Nanjing Medical University First Affiliated Hospital, Nanjing, Jiangsu, China

Correspondence should be addressed to Renhua Guo; rhguo@njmu.edu.cn

Received 6 August 2022; Revised 13 October 2022; Accepted 24 November 2022; Published 31 January 2023

Academic Editor: Lianxiang Luo

Copyright © 2023 Chen Zhang et al. This is an open access article distributed under the Creative Commons Attribution License, which permits unrestricted use, distribution, and reproduction in any medium, provided the original work is properly cited.

Acquired resistance to epidermal growth factor receptor tyrosine kinase inhibitors (EGFR-TKI, such as gefitinib) in lung cancer continues to be a major problem. Recent studies have shown the promise of ferroptosis-inducing therapy in EGFR-TKI resistant cancer, but have not been translated into clinical benefits. Here, we identified carbonic anhydrase IX (CA9) was upregulated in gefitinib-resistant lung cancer. Then we measured the cell viability, intracellular reactive oxygen species (ROS) levels, and labile iron levels after the treatment of ferroptosis inducer erastin. We found that CA9 confers resistance to ferroptosis-inducing drugs. Mechanistically, CA9 is involved in the inhibition of transferrin endocytosis and the stabilization of ferritin, leading to resistance to ferroptosis. Targeting CA9 promotes iron uptake and release, thus triggering gefitinib-resistant cell ferroptosis. Notably, CA9 inhibitor enhances the ferroptosis-inducing effect of cisplatin on gefitinib-resistant cells, thus eliminating resistant cells in heterogeneous tumor tissues. Taken together, CA9-targeting therapy is a promising approach to improve the therapeutic effect of gefitinib-resistant lung cancer by inducing ferroptosis.

1. Introduction

Non-small cell lung cancer (NSCLC) is one of the most common cancers worldwide with high mortality rate [1]. With the advent of molecular targeted therapies, survival in NSCLC continues to improve. Epidermal growth factor receptor (EGFR) is a critical molecular target in NSCLC patients. Although EGFR-tyrosine kinase inhibitors (EGFR-TKI, such as gefitinib or erlotinib) have resulted in significant clinical benefit in patients with EGFR-mutant NSCLC [2, 3], acquired resistance inevitably develops [4]. Multiple mechanisms of gefitinib resistance have been reported, including the EGFR T790M mutation, MET amplification, ERBB2 amplification, and cancer phenotypic transformation [5–7]. Therapeutic options could be developed according to the resistance mechanisms, such as adopting osimertinib or combining with MET inhibitors. However, the resistance mechanisms of gefitinib have yet to be discovered in approximately 20% of NSCLC patients [8]. Therapeutic options are limited in these patients.

Ferroptosis is a nonapoptotic form of cell death that is iron-dependent. Ferroptosis was first found to be triggered by erastin, a RAS inhibitor, which is characterized by intracellular redox imbalance and increased levels of reactive oxygen species (ROS) [9]. Recently, the therapy-resistant cell state in cancer cells has been reported to be vulnerable to ferroptosis [10]. You et al. reported that erlotinib-tolerant persister head and neck cancer cells are vulnerable to ferroptosis by GPX4 or xCT inhibition [11]. Zhang et al. found that the histone deacetylase inhibitor vorinostat combined with erastin could suppress the viability of EGFR-TKI-resistant lung cancer cells by inducing ferroptosis [12]. These results show the promise of ferroptosis-inducing therapy in EGFR-TKI resistant cancer cells.

However, there are outstanding questions that remain to be addressed before the practical application of ferroptosis-inducing therapy. For example, most of the ferroptosis-inducing agents were only examined in cultured cell lines, which have not been translated into clinical benefits [13]. As a common inducer of ferroptosis, cisplatin is the most

frequently used agent for lung cancer in clinical practice [14]. Cisplatin-based chemotherapy shows certain efficacy for NSCLC patients after EGFR-TKI resistance. In addition, cisplatin-based chemotherapy has been reported to eliminate EGFR-TKI resistant cells, thus creating beneficial conditions for the retreatment of EGFR-TKI [15]. We speculated that cisplatin could play a role in eliminating drug-resistant cells by inducing ferroptosis. However, the long-term benefits of EGFR-TKI retreatment after cisplatin-based chemotherapy are still limited [15]. It is important to identify what genetic alterations in EGFR-TKI resistant cells may contribute to the vulnerability to ferroptosis. Thus, we can find ways to induce ferroptosis in resistant cancers more effectively.

Carbonic dehydratase IX (CA9), a ferroptosis-related gene, was found to be upregulated in gefitinib-resistant cells in our study. CA9 is a member of the carbonic anhydrase family, which catalyzes the reversible hydration of carbon dioxide to maintain intracellular pH homeostasis [16]. A recent study showed that the upregulation of CA9 significantly inhibits tumor cell ferroptosis under hypoxia [17]. The abnormal expression of CA9 has been reported to affect the treatment efficacy in NSCLC [18–20]. In addition, elevated CA9 expression is closely related to poor prognosis in EGFR-mutant lung cancer [21]. Although CA9 is highly expressed in EGFR-TKI resistant NSCLC cells, as a marker of hypoxia [22, 23]. The role of CA9 in regulating ferroptosis remains unknown.

In the present study, we suggest that CA9 confers resistance to ferroptosis in gefitinib-resistant lung cancer cells by regulating iron metabolism. Inhibiting CA9 is a promising approach to improve lung cancer treatment by targeting ferroptosis.

2. Materials and Methods

2.1. Cell Culture. The human non-small-cell lung cancer cell lines PC9 (EGFR exon 19 deletion) and HCC827 (EGFR exon 19 deletion), and the normal human bronchial epithelial cell lines (Beas2B and HBE) were purchased from Shanghai Institute of Biochemistry and Cell Biology, Chinese Academy of Sciences (Shanghai, China). The gefitinib-resistant cell lines PC9/GR and HCC827/GR were established by exposing PC9 and HCC827 cells to increasing concentrations of gefitinib (HY-50895, MCE, China) as previously described [24]. The parental cells were cultured in the medium containing 0.3 μM gefitinib until they could survive in the medium containing 1.0 μM gefitinib. During this process, the drug-containing medium was replaced twice per week. Then the resistant cells were maintained in 1.0 μM gefitinib. All cells were cultured in RPMI-1640 medium supplemented with 10% fetal bovine serum.

2.2. Clinical Samples Collection. Clinical tissues and peripheral blood were acquired from the First Affiliated Hospital of Nanjing Medical University. Collection of samples and clinical information was undertaken with ethical review board approval (No. 2019-SRFA-226).

2.3. Cell Counting Kit-8 (CCK8) Assay. The CCK8 assay was performed according to the manufacturer's instructions for the CCK8 kit (HY-K0301, MCE, China). Briefly, cells were plated in 96-well plates and treated with various concentrations of gefitinib, erastin (HY-15763, MCE, China), U104 (HY-13513, MCE, China), z-VAD (HY-16658B, MCE, China), ferrostatin-1 (Fer-1, HY-100579, MCE, China) and desferrioxamine mesylate (DFO, HY-B0988, MCE, China) for 48 h. Ten microliters of CCK8 reagent was added to each well and incubated for 1 h at 37°C. Then, the plates were measured by a microplate reader at 450 nm.

2.4. Colony Formation Assay. Cells were plated in 6-well plates at a density of 3000 cells/well and incubated overnight. Then, the medium was replaced twice a week for approximately 10 days. The colonies were stained with a 0.1% crystal violet solution (C0121, Beyotime, China). Visible colonies that were larger than 0.5 mm were counted.

2.5. Measurement of ROS. The level of intracellular ROS was measured according to the manufacturer's instructions for the ROS assay kit (S0033S, Beyotime, China). Briefly, cells were plated into 6-well plates and stained with DCFH-DA (10 μM) for 20 min at 37°C. Then, the cells were harvested, and the fluorescence was detected by flow cytometry (FITC channel) to measure the intracellular ROS.

2.6. Measurement of Labile Iron. The level of intracellular labile iron was measured according to the manufacturer's instructions of the FerroFarRed kit (GC903-01, Goryo Chemical, Japan). Cells were plated on confocal dishes. After treatment, the live cells were stained with SiRhoNox-1 (5 μM) for 1 h at 37°C. The medium was replaced with observation buffer, followed by observation with a confocal microscope (LSM710, Carl Zeiss, Germany). The excitation/emission used for SiRhoNox-1 was 635/660 nm.

2.7. Transferrin Endocytosis Assay. Cells were plated on confocal dishes. After treatment, the live cells were placed on ice for 10 min and then stained with pHrodo™ Red transferrin conjugate (P35376, Thermo Fisher Scientific, USA) for 20 min at 37°C. The medium was replaced with observation buffer, followed by observation with a confocal microscope (LSM710, Carl Zeiss, Germany). The excitation/emission used for pHrodo™ Red was 560/585 nm.

2.8. Western Blot Analysis. The total cellular protein lysates were separated by 12% SDS-PAGE and transferred to polyvinylidene fluoride membranes (Millipore, USA). The membranes were incubated with specific antibodies against CA9 (1:1000), transferrin receptor (TrfR) (1:1000), and ferritin heavy chain (FTH1) (1:1000) at 4°C. GAPDH (1:5000) was used as an internal control. Anti-CA9 antibody was obtained from Proteintech (Wuhan, China). The other antibodies were purchased from Cell Signaling Technology (Beverly, MA, USA).

2.9. Enzyme-Linked Immunosorbent Assay (ELISA). Quantification of plasma CA9 in the clinical samples was performed by ELISA. Peripheral blood was collected and

plasma was isolated by centrifugation at 4°C (2000 × g, 10 min). The isolated plasma was stored at −20°C until the assay. The plasma samples were diluted (1:20) with ELISA buffer and analyzed by using CA9 Human ELISA Kit (EHCA9, Thermo Fisher Scientific, USA) according to the manufacturer instructions. The absorbance was measured at 450 nm.

2.10. RNA Isolation and Quantitative Real-Time PCR Analysis. Total RNA was extracted from tissues or cells with TRIzol reagent (Invitrogen, USA). The isolated RNA (1.0 μg) was reverse-transcribed into cDNA using random primers with a reverse transcription kit (R047A, Takara, Japan) according to the manufacturer's instructions. Real-time PCR analyses were performed with SYBR Green (R420A, Takara, Japan). For paired samples, the results were normalized to the expression of GAPDH (as an internal reference) and calculated according to the $2^{-\Delta\Delta CT}$ method [25]. For unpaired samples, the relative expression was compared by ΔCT . Specific primer sequences were as follows: human CA9, forward, 5'-CAGCACAGAAGGGGAACCAA-3'; reverse, 5'-GAGCAGGACAGGACAGTTACC-3'; human PTGS2, forward, 5'-CGGTGAACTCTGGCTAGACAG-3'; reverse, 5'-GCAAACCGTAGATGCTCAGGGA-3'; human GAPDH, forward, 5'-AGCCACATCGCTCAGACAC-3'; reverse, 5'-GCCCAATACGACCAAATCC-3'.

2.11. Transfection of Cell Lines and In Vitro Lentivirus Infection. Full length of CA9 gene was inserted into the EX-Z5727-M02 vector (GenePharma, China) to construct the CA9 overexpression plasmid. The empty EX-NEG-M02 vector was used as the control (GenePharma, China). To knock down CA9, specific short hairpin RNA (shRNA) sequences were inserted into the pGPU6/GFP/Neo vector (GenePharma, China), and the sh-CA9#1 and sh-CA9#2 plasmids were generated. The shRNA target sequences were as follows: sh-CA9#1, 5'-GCCTATGAGCAGTTGCTGT-3'; sh-CA9#2, 5'-TCGCGTTCCTTGTGCAGAT-3'; sh-NC, 5'-TTCTCCGAACGTGTCACGT-3'. pGPU6/GFP/Neo-shNC (sh-NC) was used as the control (GenePharma, China). The plasmids were transfected with X-treme GENE HP DNA transfection reagent (Roche, Switzerland). Typically, cells were seeded into 6-well plates and transfected the next day with 2 μg/well of specific plasmids. 48 h posttransfection, the cells were harvested and processed for the following experiments.

To label gefitinib-resistant cells, cells were transduced with lentiviral vectors encoding eGFP (LPP-NEG-Ly201-025-C, GeneCopoeia, China) at a multiplicity of infection of 20. Cells were subjected to puromycin (2 μg/mL) selection after 48 h of transduction. EGFP fluorescence was detected by flow cytometry with the FITC channel.

2.12. Xenograft Mouse Model Assay. Five-week-old male BALB/c mice were maintained under specific pathogen-free conditions and manipulated according to protocols approved by the Institutional Animal Care and Use Committee (IACUC). PC9/GR cells and PC9 cells were

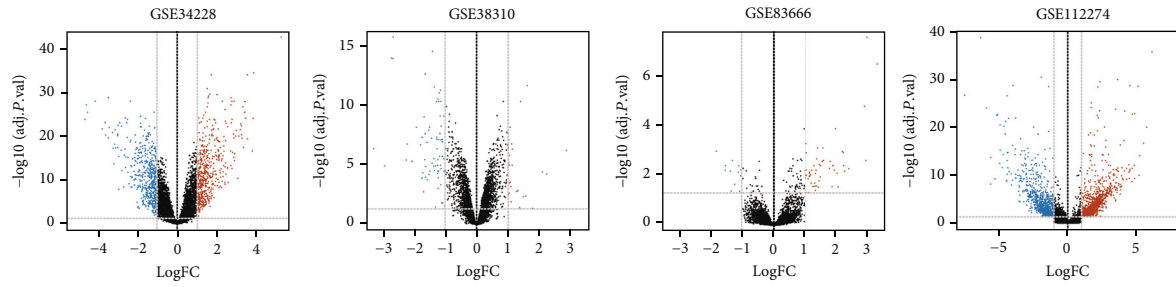
mixed at a ratio of 9:1 and subcutaneously injected into mice in a 100 μL volume. Tumor growth was examined every 3 days. When the tumor volumes ($0.5 \times \text{length} \times \text{width}^2$) reached an average of 100 mm³, mice were treated as follows: (a) saline by oral gavage; (b) gefitinib (25 mg/kg) daily by oral gavage; (c) U104 (19 mg/kg) daily by intraperitoneal injection; (d) cisplatin (4 mg/kg) on days 1, 7, 14, and 21 by intraperitoneal injection; (e) U104 (19 mg/kg) daily combined with cisplatin (4 mg/kg) on days 1, 7, 14, and 21 by intraperitoneal injection. The tumors were resected after 28 days. Tumor weights were measured, and tumor tissues were stained with haematoxylin-eosin (HE) and immunohistochemistry (IHC).

2.13. Bioinformatics Analysis and Statistical Analysis. The publicly available gefitinib-resistant and parental cell line RNA sequencing (RNA-seq) datasets (GSE34228, GSE38310, GSE83666, and GSE112274) were obtained from the GEO database (<https://www.ncbi.nlm.nih.gov/geo>). Ferroptosis-related genes were obtained from the FerrDb database (<http://www.zhounan.org/ferrdb>) [26]. RNA-seq, mutation, methylation, copy number (GISTIC output), and clinical data from 574 patients with lung adenocarcinoma were derived from The Cancer Genome Atlas (TCGA) portal (<https://portal.gdc.cancer.gov>). RNA-seq and clinical data from 305 patients with lung adenocarcinoma were accessed from cBioPortal (<http://www.cBioPortal.org/>). Protein expression data of TCGA was accessed from Clinical Proteomic Tumor Analysis Consortium (CPTAC) portal (<https://proteomics.cancer.gov/programs/cptac>). All R-based analyses were conducted using R v4.1.0. R packages were used as follows: “Limma,” “UpSetR,” “VennDiagram,” “Survival,” and “Survminer”. Protein-protein interaction analysis was performed via the STRING tool (<http://string-db.org/>).

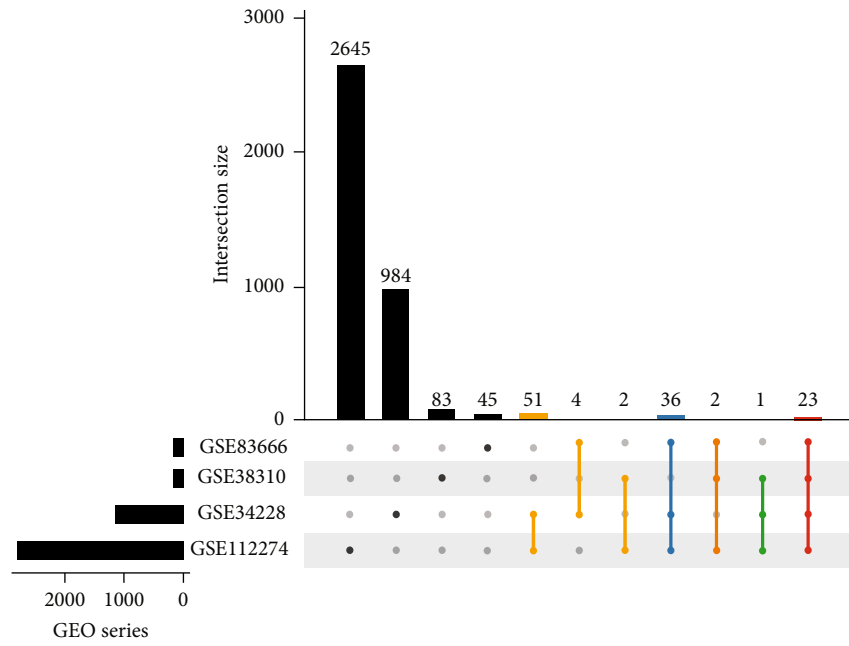
Statistical analysis was performed with GraphPad Prism 8.3.0 (GraphPad Software, USA). For parametric data, *t*-test (two-sided) or one-way ANOVA was performed. For comparison of multiple groups with repeated measures, two-way ANOVA with Bonferroni correction was performed. The mean values and the standard deviation (SD) are presented. Statistically significant differences are designated as follows: **P* < 0.05, ***P* < 0.01, and ****P* < 0.001. All experiments were repeated at least three times.

3. Results

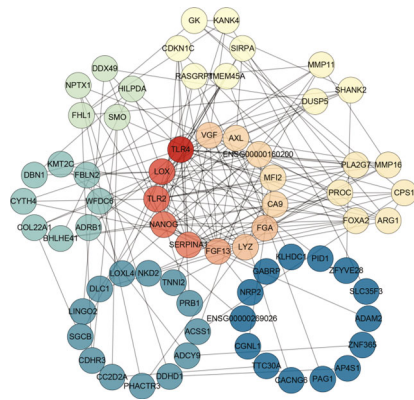
3.1. CA9 Is Upregulated in Gefitinib-Resistant Lung Cancer. To explore the genetic alterations in gefitinib-resistant cancer cells, which may contribute to the vulnerability to ferroptosis, we performed a systematic bioinformatics analysis. As shown in Figure 1(a), differential expression analysis was performed in four RNA-seq datasets between gefitinib-sensitive and gefitinib-resistant cell lines (log₂ fold change (log₂FC) > 1, *P* < 0.05). Coupregulated or codownregulated genes were screened in two or more datasets (Figure 1(b)). Protein-protein interaction networks were constructed to analyze protein interactions between the dysregulated protein-coding genes, and 68 differentially expressed genes (DEGs) were identified (Figure 1(c) and Supplementary



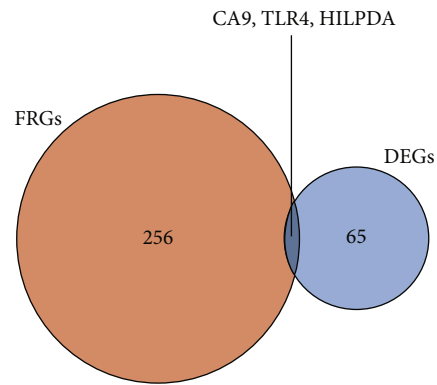
(a)



(b)



(c)



(d)

FIGURE 1: Continued.

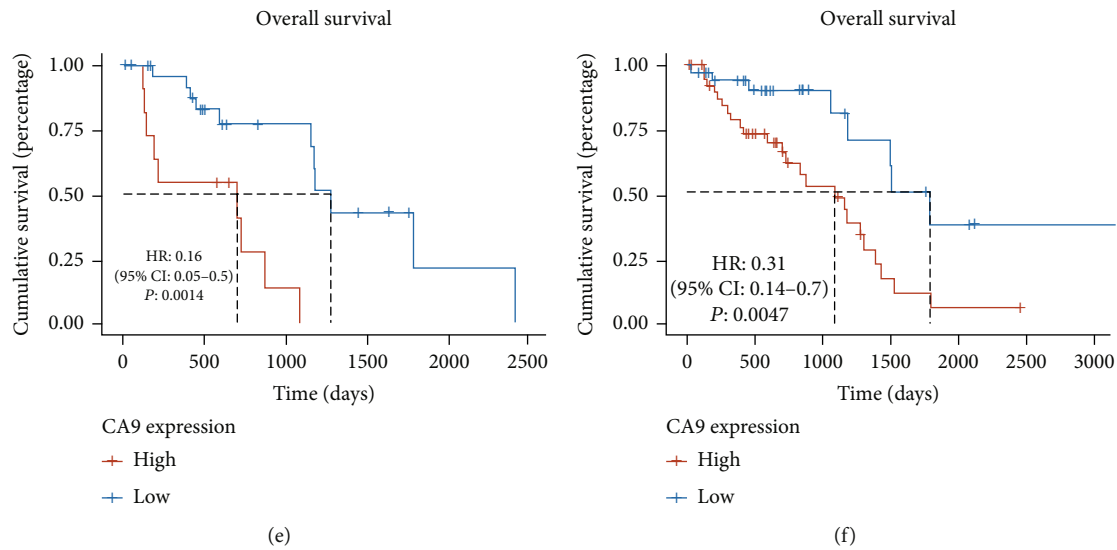


FIGURE 1: Systematic bioinformatics analysis identifies CA9 is upregulated in gefitinib-resistant lung cancer. (a) Differential expression analysis was performed in four RNA-seq datasets between gefitinib-sensitive and gefitinib-resistant cell lines ($\log_{2}FC > 1$, $P < 0.05$) from the GEO database. (b) Coupregulated or codownregulated genes were screened in two or more datasets. (c) Protein–protein interaction analysis was performed via the STRING tool to summarize the protein interactions between the dysregulated protein-coding genes. (d) Wayne figure showing the intersection of the differentially expressed genes (DEGs) and ferroptosis-related genes (FRGs). (e, f) Survival analysis was performed in EGFR-mutant lung adenocarcinoma patients in the training set ((e), $n = 39$) and the testing set ((f), $n = 76$) from the TCGA database.

Table S1). Finally, three genes were obtained by taking the intersection of the DEGs and the ferroptosis-related genes (FRGs) from the FerrDb database [26] (Figure 1(d) and Supplementary Table S2).

Then, we performed survival analysis to explore the effect of these dysregulated genes on prognosis. Only the ferroptosis suppressor gene CA9 was identified to be upregulated in gefitinib-resistant cells and predicted poor prognosis in 39 EGFR-mutant lung adenocarcinoma patients (the training set) from the TCGA database (Figure 1(e) and Supplementary Figure S1 (a, b)). We further confirmed that the upregulated gene CA9 was related to poor prognosis in 76 EGFR-mutant lung adenocarcinoma patients (the testing set) from the TCGA database (Figure 1(f)). We analyzed the relationship between CA9 mRNA expression level and tumor stage or histological grade in 305 lung adenocarcinoma patient samples [27]. The results showed that CA9 expression was not associated with tumor stage or histological grade (Supplementary Figures S1 (c, d)), which indicates that high CA9 expression is a poor prognostic factor in lung cancer patients independent of tumor stage or grade. We also performed multiomic analysis using the TCGA data to figure out the mechanism underlying CA9 upregulation. As shown in Supplementary Figure S1(e) and Supplementary Table S3, no correlations were observed between CA9 expression and mutations. Despite the positive relationship between CA9 expression and copy number, the correlation is weak (Supplementary Figure S1(e), correlation coefficient (r) = 0.115, $P < 0.01$). Then, we compared the correlations between CA9 expression and DNA methylation status. CA9 expression showed a strong negative correlation

with methylation level of the CpG site cg20610181 (Supplementary Figure S1(e), $r = -0.658$, $P < 0.001$). Therefore, we inferred that DNA demethylation could be the underlying mechanism of CA9 upregulation.

Compared to the nontumor tissues, we demonstrated significantly higher CA9 mRNA expression using the TCGA database ($P < 0.001$; Figure 2(a)) and higher CA9 protein expression using the CPTAC database ($P < 0.001$; Figure 2(b)) in lung cancer tissues. Then, we measured CA9 expression in lung cancer tissues biopsied from patients who benefitted from gefitinib and patients who acquired gefitinib resistance. The clinical characteristics of patients are summarized in Supplementary Table S4. The results suggest that CA9 mRNA levels were commonly upregulated in gefitinib-resistant lung cancer tissues compared with sensitive tissues (Figure 2(c)). Also, the CA9 protein levels were higher in the plasma collected from patients who acquired gefitinib resistance (Figure 2(d)). We established gefitinib-resistant cells (PC9/GR and HCC827/GR) by exposing EGFR-mutant PC9 and HCC827 human lung cancer cells to increasing concentrations of gefitinib. In the CCK8 assay, PC9/GR and HCC827/GR cells survived in the presence of high-dose gefitinib (Figure 2(e)), whereas parental PC9 and HCC827 cells were sensitive to gefitinib (Figure 2(f)). Then, CA9 expression was evaluated in the gefitinib-resistant and parental cell lines as well as normal human bronchial epithelial cell lines (Beas2B and HBE). The expression levels of CA9 were higher in parental cell lines than in normal human bronchial epithelial cell lines. Furthermore, the gefitinib-resistant cell lines showed much higher CA9 mRNA and protein expression (Figures 2(g) and 2(h)). We challenged these

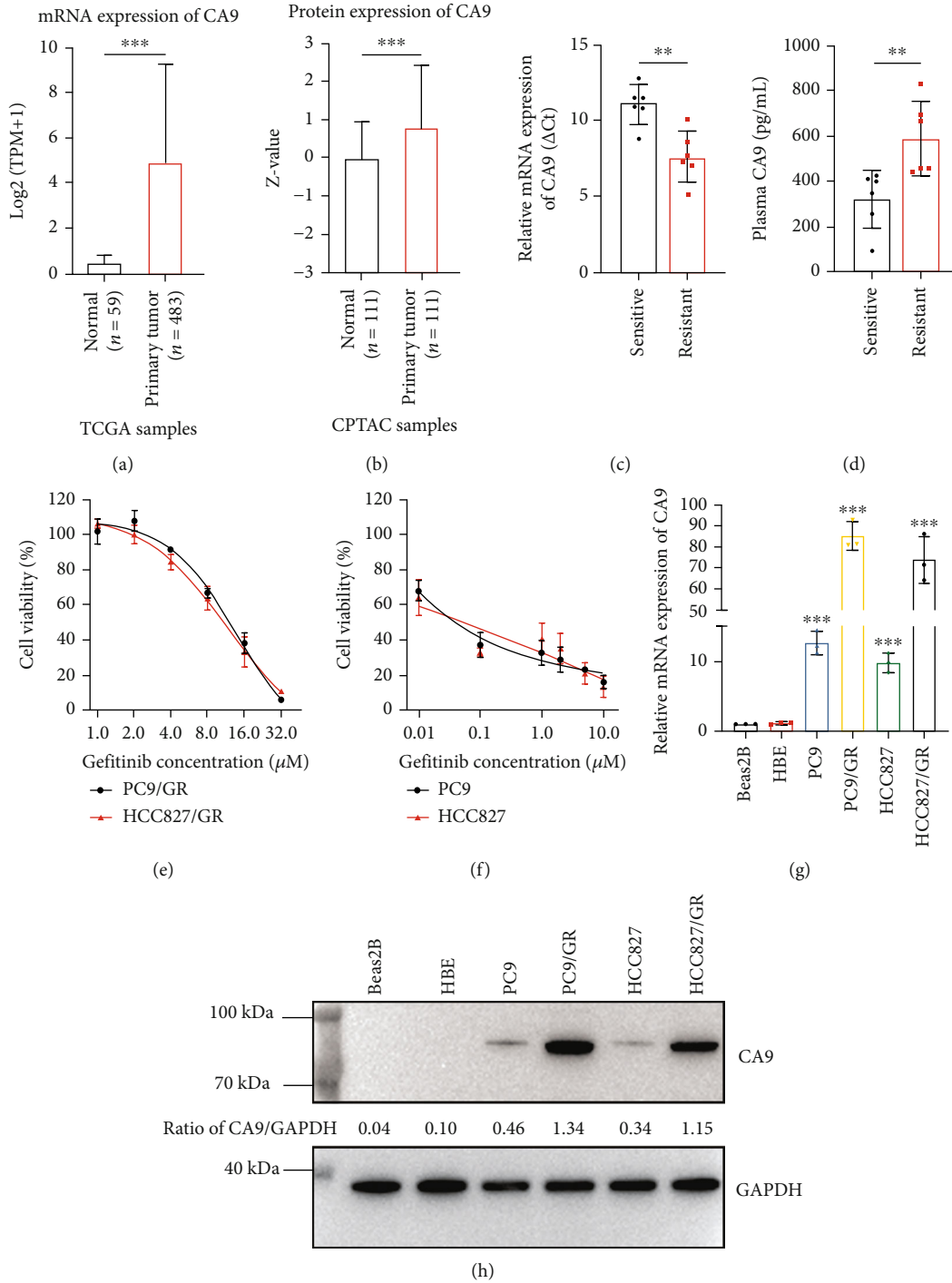


FIGURE 2: CA9 is upregulated in gefitinib-resistant cell lines and clinical samples. CA9 mRNA and protein expression levels were compared between nontumor tissues and lung cancer tissues in the TCGA database (a) and the CPTAC database (b). qPCR and ELISA were performed to investigate CA9 expression in lung cancer tissues (c) and plasma (d) from patients who benefitted from gefitinib ($n = 6$) and patients who acquired gefitinib resistance ($n = 6$). Smaller ΔCt values indicate higher mRNA levels. (e, f) Gefitinib sensitivity in parental (PC9 and HCC827) and gefitinib-resistant (PC9/GR and HCC827/GR) cells were analyzed by CCK8 assay. Expression of CA9 mRNA (g) and protein (h) in normal human bronchial epithelial cells (Beas2B and HBE), parental, and gefitinib-resistant cells was assessed by qPCR and western blot. Data shown are the Mean \pm SDs of three independent experiments unless specified. (** $P < 0.01$, *** $P < 0.001$, Student's t -test).

cells with gefitinib and measured mRNA expression levels of CA9. As we speculated, the expression of CA9 in resistant cells gradually increased in time- and dose-dependent

manner (Supplementary Figures S2 (a, b)). However, the CA9 expression in normal human bronchial epithelial cell lines (Supplementary Figures S2 (c, d)) and parental cell

lines remained unaffected by gefitinib (Supplementary Figures S2 (e, f)).

3.2. CA9 Confers Resistance to Ferroptosis in Gefitinib-Resistant Cells. A recent study reported that CA9 was involved in malignant mesothelioma resistance to ferroptosis under hypoxia [17]. Whether CA9 regulates ferroptosis sensitivity in gefitinib-resistant cells remains unknown. We challenged the parental and gefitinib-resistant cells with the widely used ferroptosis inducer, erastin. The parental cells were sensitive to erastin, in contrast, gefitinib-resistant cells were resistant to ferroptosis induction (Figure 3(a)). Knockdown of CA9 by shRNAs sensitized resistant cells to erastin (Figures 3(b) and 3(c) and Supplementary Figures S3 (a, b)), while overexpression of CA9 decreased the sensitivity of erastin in the parental cells (Figure 3(d) and Supplementary Figure S3(c)). In addition, the long-term colony formation assay indicated that the proliferation inhibition effect of erastin in parental cells was reduced by CA9 overexpression (Figure 3(e)). Previous study reported that CA9 is involved in erastin-induced ferroptosis [17]. However, erastin treatment did not affect the mRNA expression of CA9 in the resistant cells PC9/GR and HCC827/GR (Supplementary Figures S3(d)).

It is well known that ferroptosis is a form of cell death characterized by intracellular redox state imbalance and ROS elevation [9]. Thus, we measured ROS levels after erastin treatment. In parental cells, erastin induced ROS accumulation. Whereas, the erastin induced ROS elevation was markedly attenuated by CA9 overexpression in parental cells (Figure 3(f)). Since ferroptosis is a form of cell death that is iron-dependent [9], an increased intracellular labile iron pool is a hallmark of ferroptosis. Thus, we measured intracellular labile iron by immunofluorescence staining. As shown in Figures 3(g) and 3(h), elevated labile iron was detected after erastin treatment, while this effect was abolished by overexpression of CA9.

We also examined whether CA9 was involved in gefitinib resistance. We challenged the parental cells PC9 with gefitinib as well as Fer-1 (a specific ferroptosis inhibitor), DFO (an iron chelator), and z-VAD (an apoptosis inhibitor). Z-VAD rescued cell death induced by gefitinib in parental cells, but Fer-1 and DFO failed (Supplementary Figure S3(e)). Moreover, overexpression of CA9 did not affect gefitinib sensitivity in parental cells (Supplementary Figure S3 (f, g)). Collectively, these data suggest that CA9 confers resistance to erastin-induced ferroptosis rather than resistance to gefitinib.

3.3. CA9 Inhibition Triggers Ferroptosis in Gefitinib-Resistant Cells. To further investigate CA9's effect on ferroptosis regulation, we challenged the gefitinib-resistant cells PC9/GR with CA9 inhibitor, U104. U104 treatment triggered substantial cell death in PC9/GR cells. To confirm the ferroptotic cell death triggered by CA9 inhibition, Fer-1, DFO and z-VAD were cotreated with U104 in PC9/GR cells. Fer-1 and DFO rescued cell death induced by U104, while z-VAD only partially protected against U104-induced cell death (Figure 4(a)).

Then, we evaluated whether CA9 inhibition either by genetic or pharmacological approaches could affect the ROS levels in gefitinib-resistant cells. The results showed that the ROS levels were elevated after CA9 inhibition (Figures 4(b)–4(e)). Then, the levels of intracellular labile iron were detected after CA9 inhibition by immunofluorescence staining. Inhibiting CA9, whether by U104 treatment or CA9 knockdown, increased the labile iron levels in resistant cells (Figures 4(f) and 4(g)). Overall, inhibiting CA9 could trigger ferroptosis in gefitinib-resistant cells.

3.4. CA9 Controls Vulnerability to Ferroptosis through Regulation of Iron Metabolism. As an iron-dependent form of cell death, iron metabolism plays an essential role in ferroptosis regulation [28]. We found elevated intracellular labile iron after CA9 inhibition (Figures 4(f) and 4(g)), which indicates that iron metabolism might be involved in ferroptosis regulation by targeting CA9. The transmembrane protein CA9 has a similar property as heat shock proteins (HSPs) in cytoskeletal networks of tumor cells by regulating cytosolic filaments [29]. HSPs have been reported to affect the endocytosis of transferrin by regulating the cytoskeleton, thus affecting iron uptake and inhibiting ferroptosis [30]. CA9 may potentially affect the endocytosis of transferrin [31], thus affecting iron uptake by cancer cells [32]. Next, we tried to determine the effect of CA9 on transferrin endocytosis by live-cell microscopy experiments with pH-sensitive pHrodo™ Red. Once internalized within endocytic vesicles, the labelled transferrin will be fluorescent and detectable in acidic environments. As speculated, the endocytosis of transferrin was enhanced by CA9 inhibition (Figure 5(a) and Supplementary Figure 4(a)). Then, we overexpressed CA9 in parental cells and found that the endocytosis of transferrin was suppressed as expected (Figure 5(b)).

Ferritin is the major iron storage protein in all living organisms [33]. A previous study showed that the stability of ferritin is pH-dependent [34]. CA9 has been reported to exert important functions in stabilizing the intracellular pH of cancer cells [16]. Therefore, we hypothesized that CA9 may be involved in the stabilization of intracellular ferritin. To test this hypothesis, we detected ferritin levels in gefitinib-resistant cells after genetic or pharmacological inhibition of CA9. As CA9 was inhibited, the FTH1 (the subunit of ferritin) protein level gradually decreased (Figures 5(c) and 5(e) and Supplementary Figures S4 (b, c)). Meanwhile, the TrfR protein level was increased after CA9 inhibition, which confirmed the ability of CA9 to suppress iron uptake (Figures 5(c) and 5(e) and Supplementary Figures S4 (b, c)). In keeping with our hypothesis, the protein levels of TrfR were downregulated but the levels of FTH1 were upregulated after CA9 overexpression in parental cells (Figures 5(d) and 5(f)).

These results suggest that CA9 is involved in the inhibition of transferrin endocytosis and the stabilization of ferritin. Targeting CA9 promotes iron uptake and release, thus triggering gefitinib-resistant cell ferroptosis.

3.5. Targeting CA9 Enhances the Ferroptosis-Inducing Effect of Cisplatin on Gefitinib-Resistant Cells. Previous studies

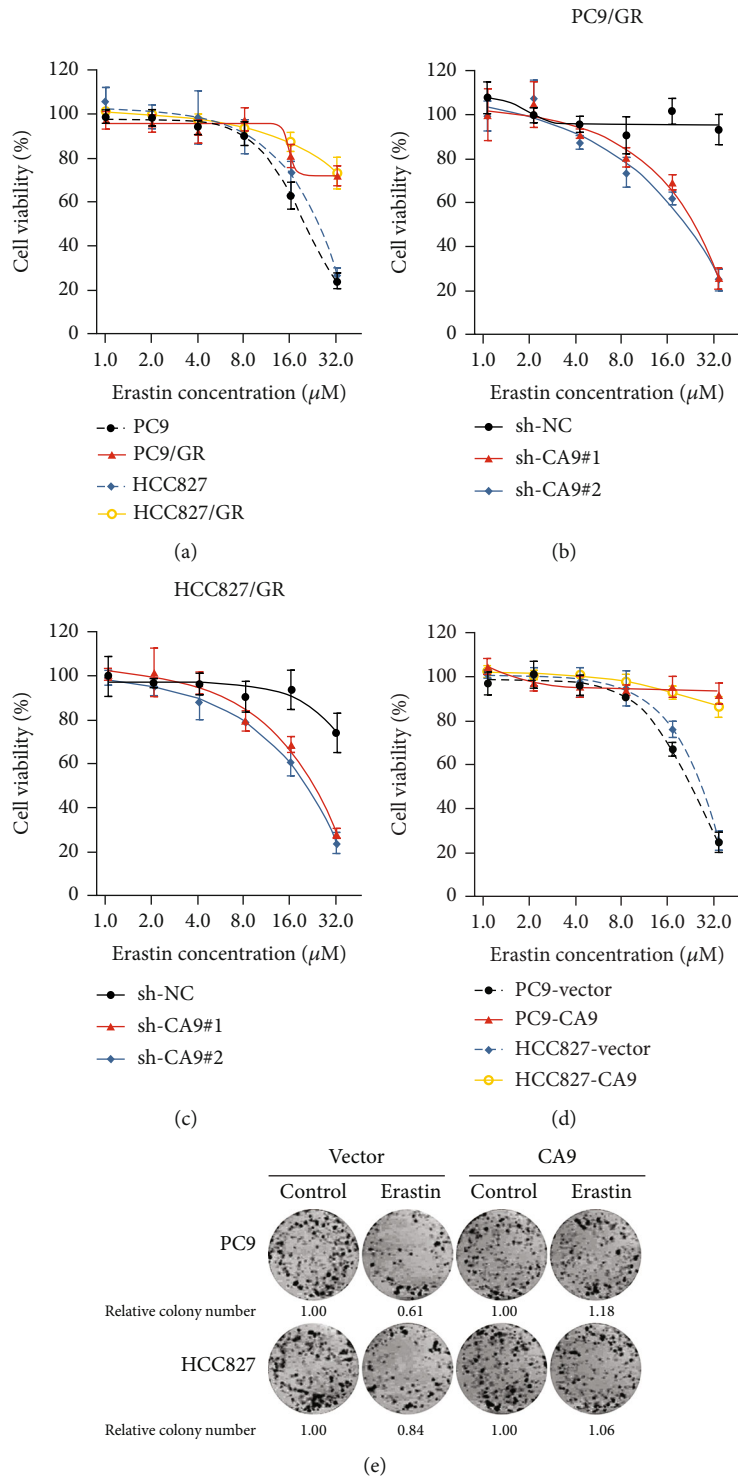


FIGURE 3: Continued.

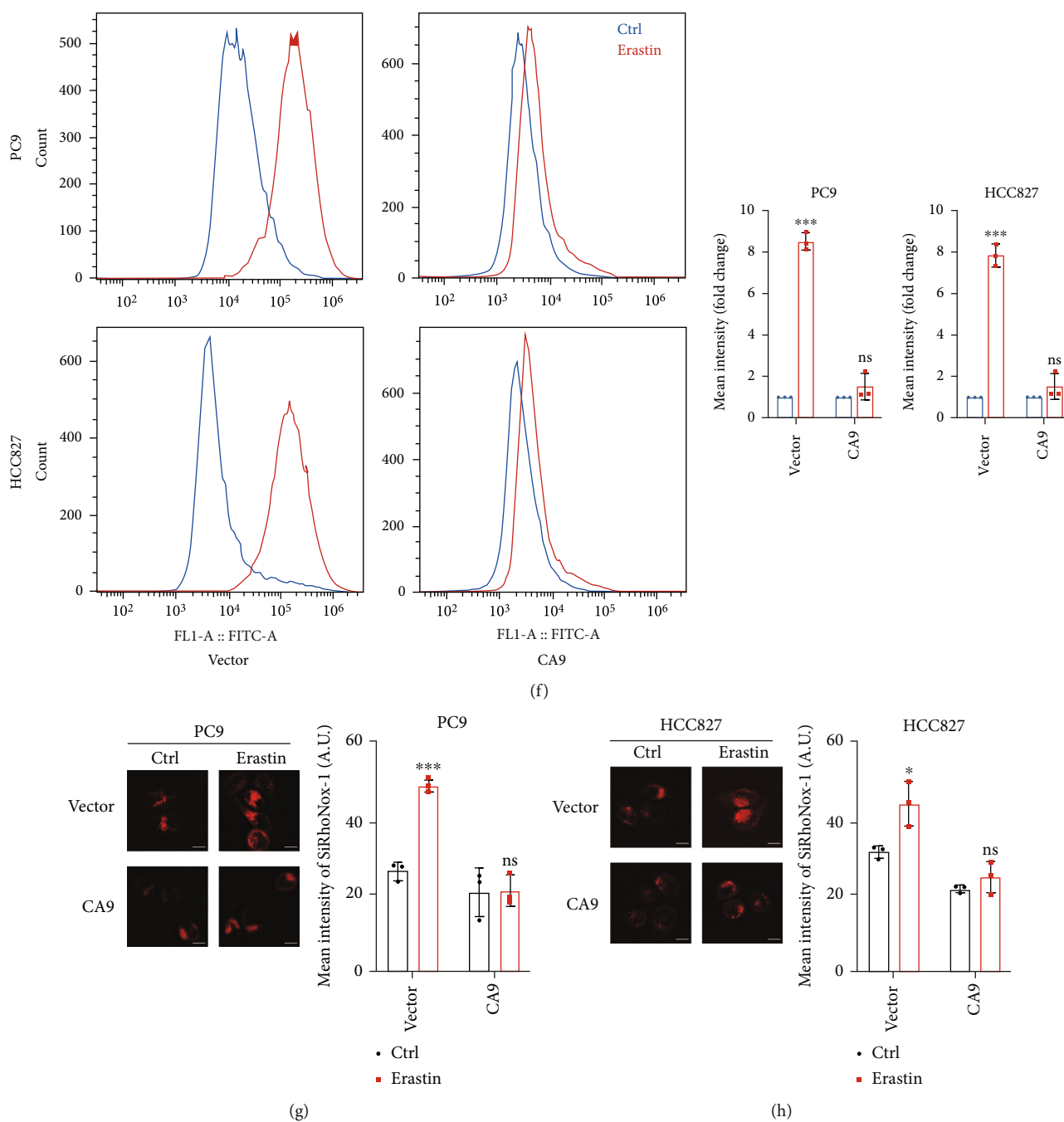


FIGURE 3: CA9 confers resistance to ferroptosis in gefitinib-resistant cells. (a) Erastin sensitivity in parental (PC9 and HCC827) and gefitinib-resistant (PC9/GR and HCC827/GR) cells were analyzed by CCK8 assay to reflect ferroptosis sensitivity. CA9-knockdown resistant cells (b, c) and CA9-overexpressing parental cells (d) were treated with erastin; cell viability was measured by CCK8 assay. (e) Long-term colony formation of CA9-overexpressing parental cells in the treatment of erastin ($10\ \mu\text{M}$). (f) Intracellular ROS were measured by flow cytometry (FITC channel) in CA9-overexpressing parental cells after erastin ($10\ \mu\text{M}$) treatment for 48 h. (g, h) Intracellular labile iron were measured by immunofluorescence staining in CA9-overexpressing parental cells after erastin ($10\ \mu\text{M}$) treatment for 48 h. The Mean \pm SDs of three independent experiments are shown. (ns indicates not significant, $*P < 0.05$, $***P < 0.001$, Student's *t*-test).

have reported that NSCLC patients who respond well to treatment with initial EGFR-TKI and later experience therapy failure, demonstrate a second response to EGFR-TKI retreatment after drug withdrawal, known as the drug holiday effect [35, 36]. This effect can be explained, at least in

part, by the elimination of drug-resistant cells in the heterogeneous tumor cell populations [37]. Compared to the drug holiday, cisplatin-based chemotherapy appeared to be more efficient in eliminating resistant cells [15]. As a widely used ferroptosis inducer, cisplatin may play a role in eliminating

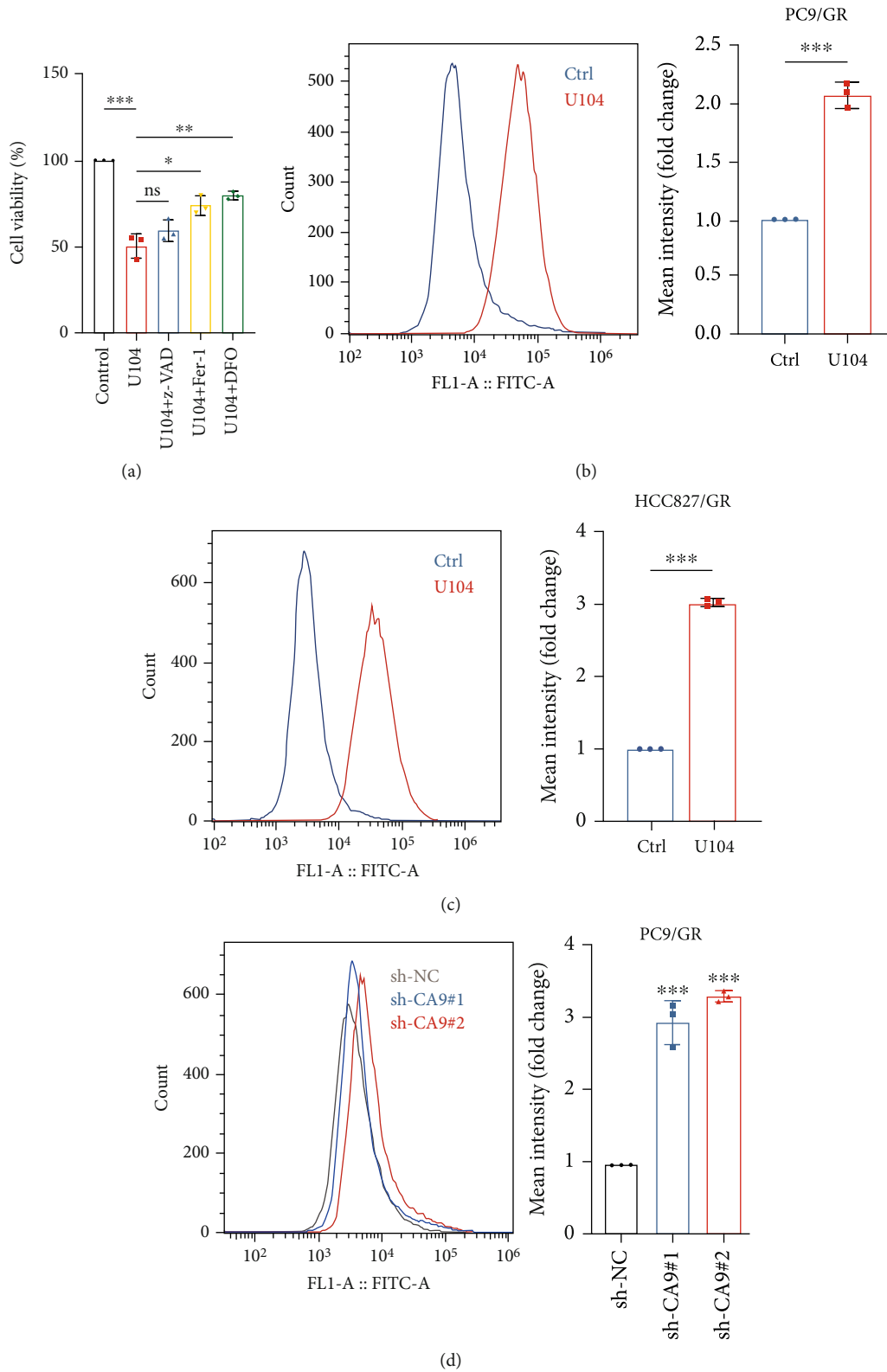
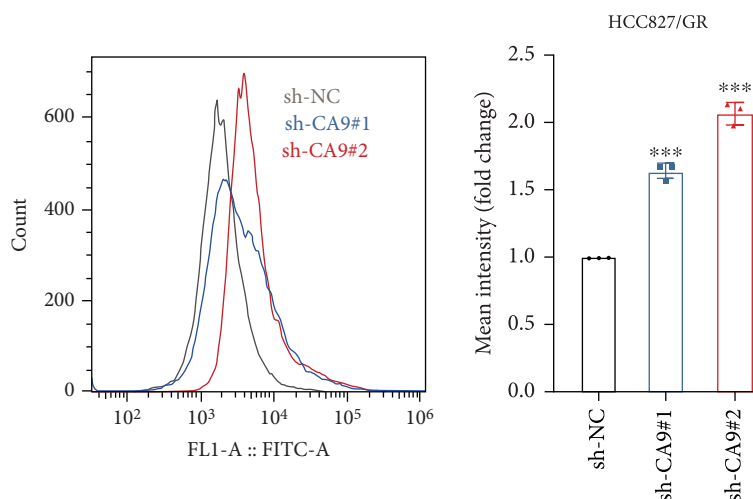
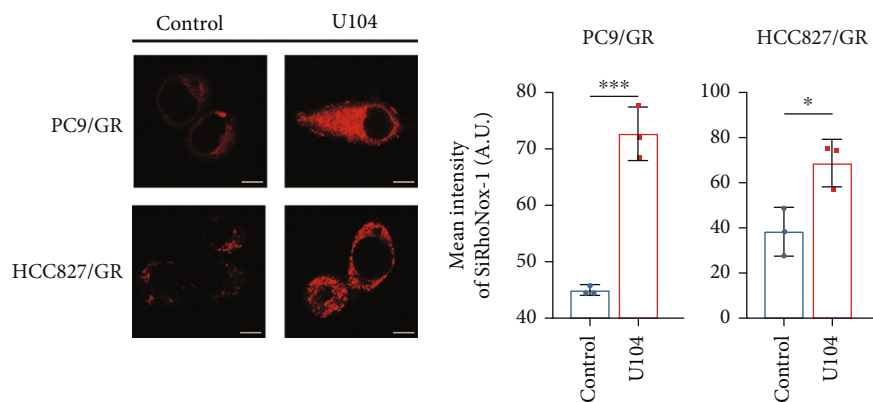


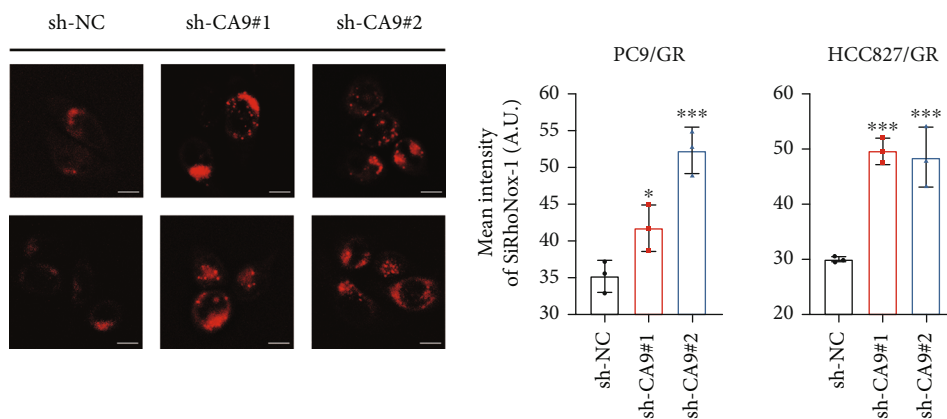
FIGURE 4: Continued.



(e)



(f)



(g)

FIGURE 4: CA9 inhibition triggers ferroptosis in gefitinib-resistant cells. (a) Gefitinib-resistant PC9/GR cells were treated with CA9 inhibitor U104 (80 μ M) alone or combined with apoptosis inhibitor z-VAD (50 μ M), ferroptosis inhibitor Fer-1 (3 μ M), or iron chelator DFO (0.5 μ M) for 48 h. CCK8 assay was performed to measure cell viability. Intracellular ROS in gefitinib-resistant PC9/GR (b) and HCC827/GR (c) cells were measured by flow cytometry (FITC channel) after U104 (80 μ M) treatment for 48 h. Intracellular ROS in gefitinib-resistant PC9/GR (d) and HCC827/GR (e) cells were measured by flow cytometry (FITC channel) after CA9 knockdown. Intracellular labile iron in gefitinib-resistant cells was measured by immunofluorescence staining after U104 treatment for 48 h (f) or CA9 knockdown (g). The Mean \pm SDs of three independent experiments are shown. (ns indicates not significant, * P < 0.05, ** P < 0.01, *** P < 0.001, Student's t -test).

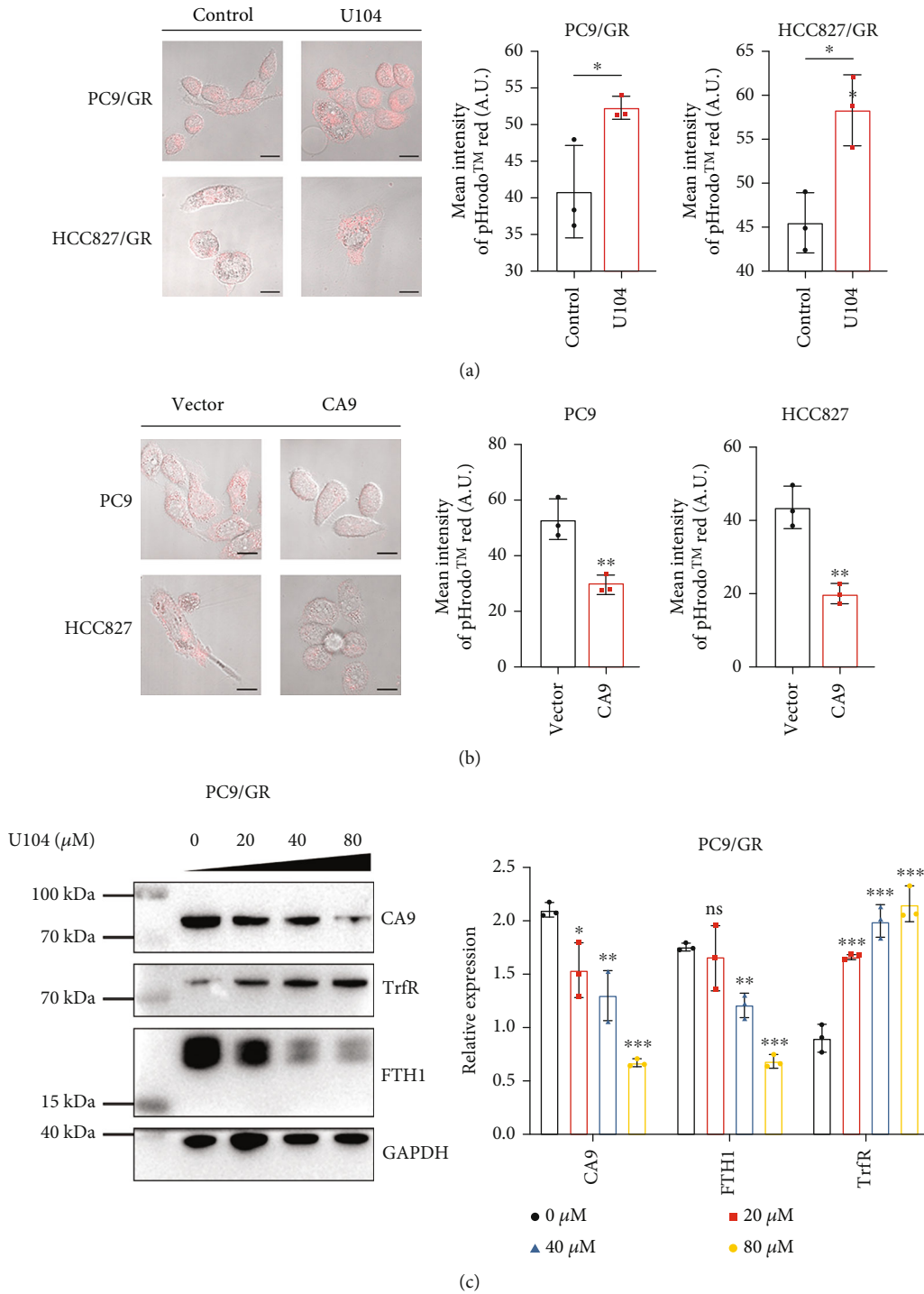


FIGURE 5: Continued.

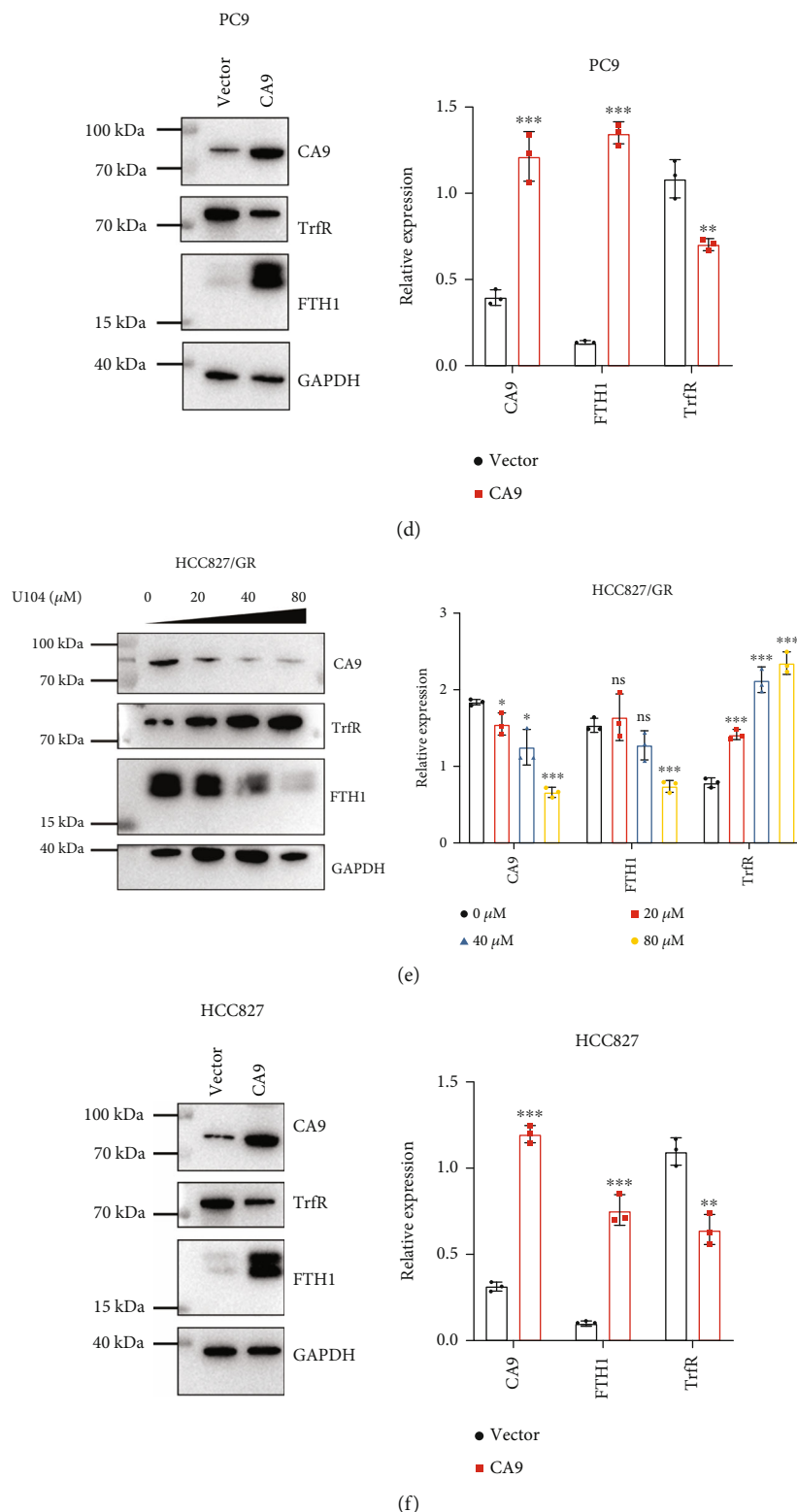


FIGURE 5: CA9 controls vulnerability to ferroptosis through regulation of iron metabolism. Transferrin endocytosis was detected by live-cell microscopy experiments with pH-sensitive pHrodo™ Red in gefitinib-resistant cells (PC9/GR and HCC827/GR) after U104 (80 μ M) treatment for 48 h (a) and in parental cells (PC9 and HCC827) after CA9 overexpression (b). Once internalized within endocytic vesicles, the labelled transferrin will be fluorescent (pink) and detectable in acidic environments. Protein lysates were harvested from gefitinib-resistant cells after U104 (80 μ M) treatment for 48 h (c, e) and parental cells after CA9 overexpression (d, f). Western blot analysis was performed for transferrin receptor (TrfR) as an iron uptake marker and ferritin heavy chain (FTH1) as an iron storage marker. The Mean \pm SDs of three independent experiments are shown. (*ns* indicates not significant, **P* < 0.05, ***P* < 0.01, ****P* < 0.001, Student's *t*-test).

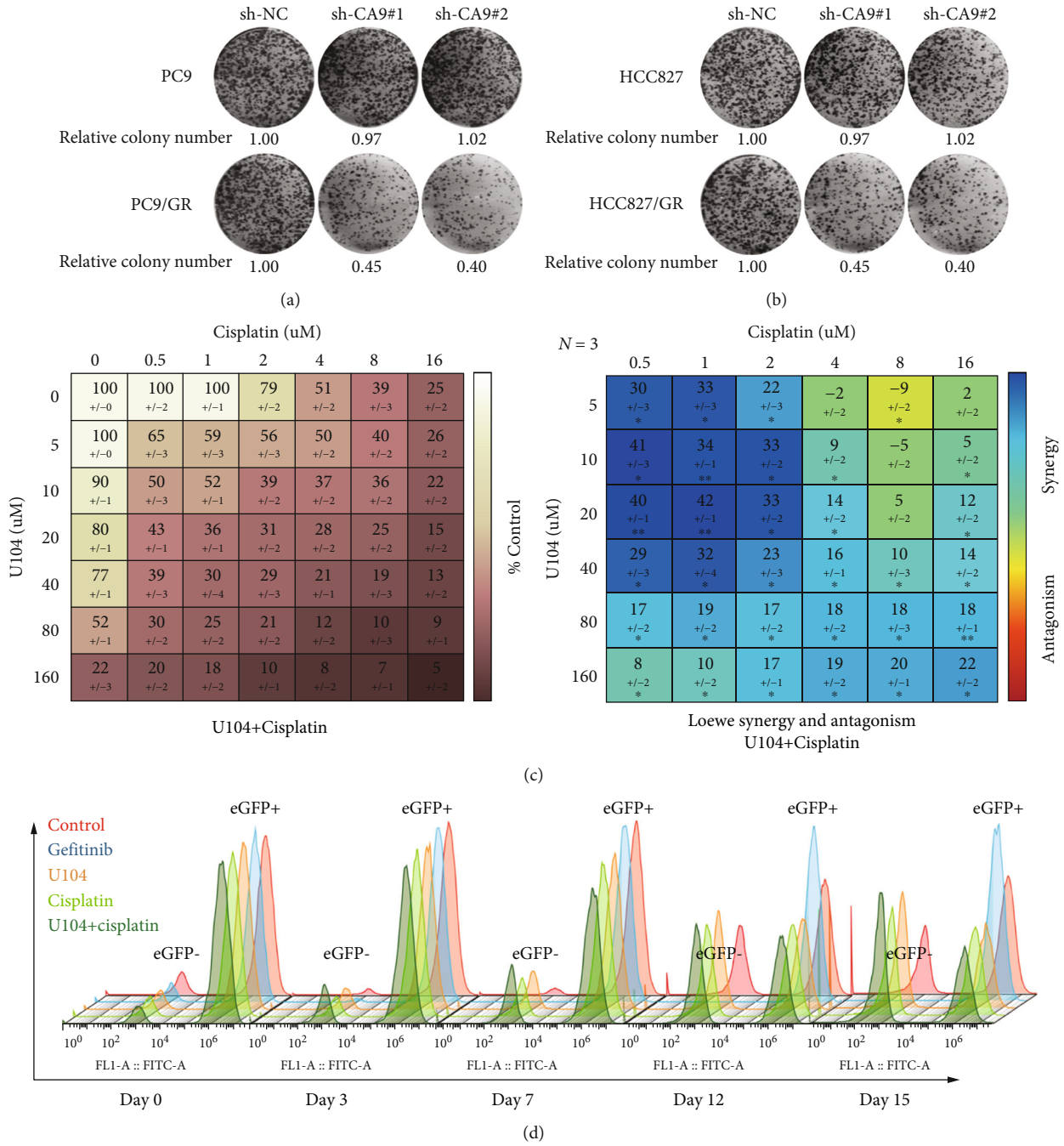


FIGURE 6: Continued.

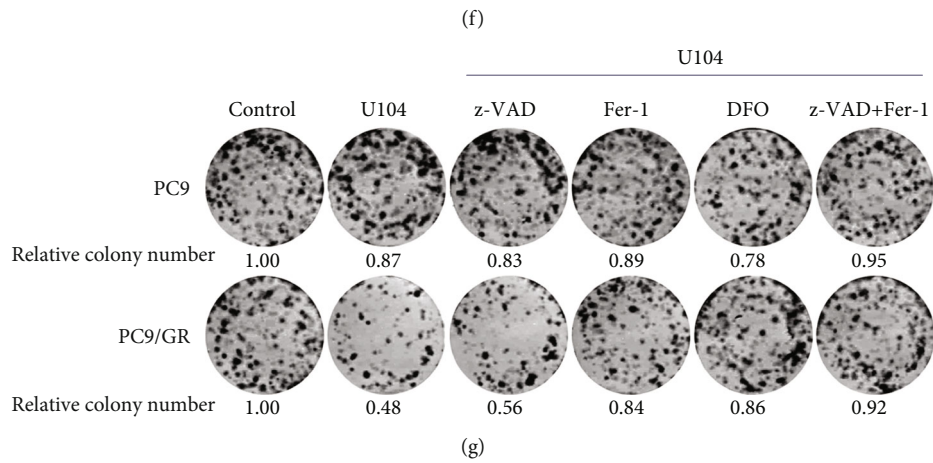
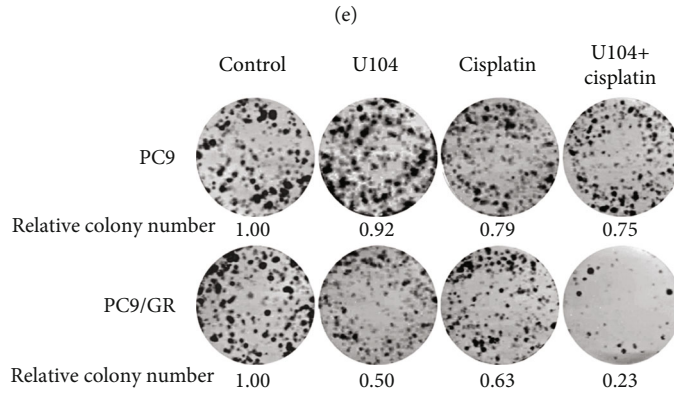
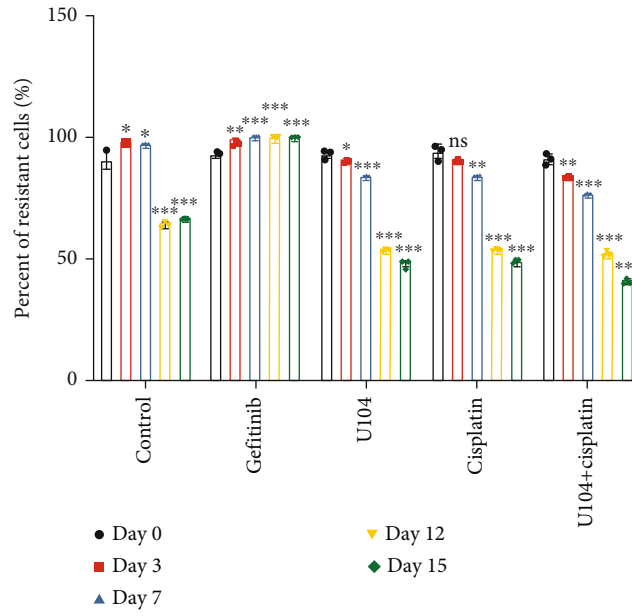


FIGURE 6: Continued.

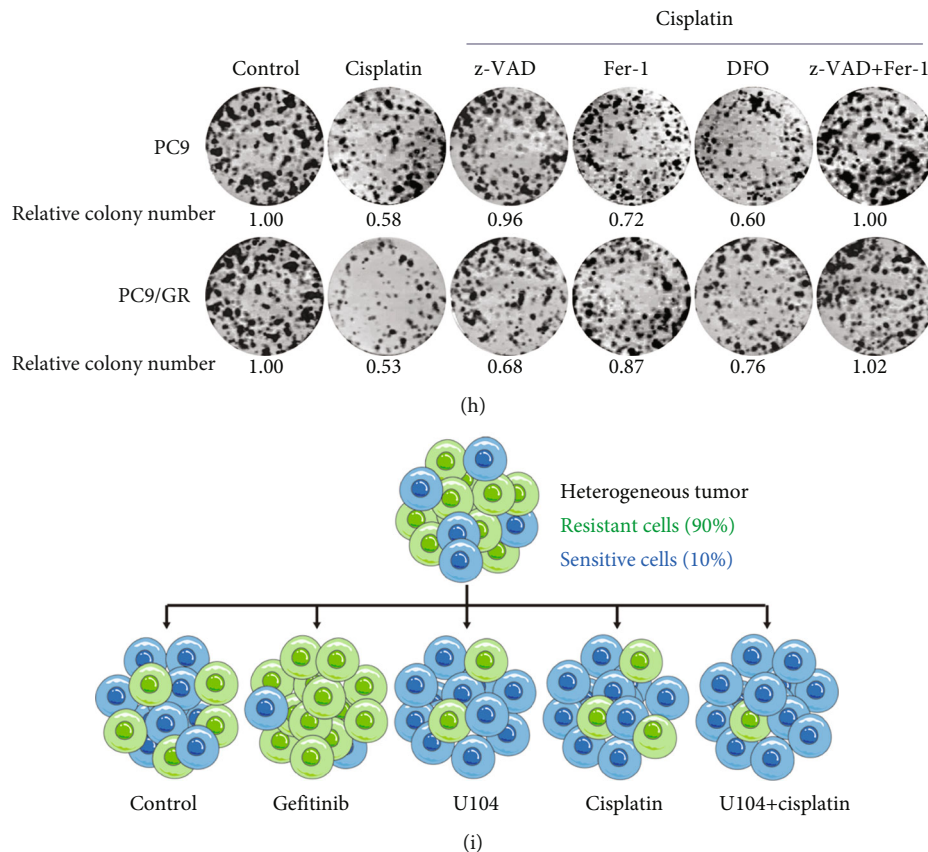


FIGURE 6: Targeting CA9 enhances the anticancer effect of cisplatin on gefitinib-resistant cells. (a, b) Long-term colony formation of CA9-knockdown parental and gefitinib-resistant cells. (c) Gefitinib-resistant PC9/GR cells were treated with different concentrations of CA9 inhibitor U104 and cisplatin for 48 h. A CCK8 assay was performed to measure cell viability. Shown is the heatmap of cell viability (%) at different combinations (left panel). A synergistic effect was measured by the Combeneft tool. Shown is the heatmap of synergy scores based on the Loewe excess additivity model (right panel). (d, e) Gefitinib-resistant PC9/GR cells were labelled with green by transduction with lentiviral vectors encoding eGFP. Then, gefitinib-resistant PC9/GR and parental PC9 cells were mixed at a ratio of 9:1 and treated with no drug, gefitinib (1 μ M), U104 (10 μ M), cisplatin (0.5 μ M), or U104 (10 μ M) + cisplatin (0.5 μ M) for 15 days. The relative abundance of the two populations was measured by flow cytometry (FITC channel). (f) PC9 parental and PC9/GR resistant cells were treated with U104 (10 μ M), cisplatin (0.5 μ M), or U104 (10 μ M) + cisplatin (0.5 μ M) in a long-term colony formation assay. (g, h) PC9 parental and PC9/GR resistant cells were treated with U104 (10 μ M), cisplatin (0.5 μ M) alone, or in combination with z-VAD (50 μ M), Fer-1 (3 μ M), DFO (0.5 μ M), or z-VAD (50 μ M) + Fer-1 (3 μ M) in the long-term colony formation assay. (i) Schematic of the in vitro competition assay to study the effect of CA9 inhibition in a heterogeneous tumor containing both gefitinib-resistant and gefitinib-sensitive cells. The Mean \pm SDs of three independent experiments are shown. (*ns* indicates not significant, * P < 0.05, ** P < 0.01, *** P < 0.001, Student's *t*-test).

drug-resistant cells by inducing ferroptosis [14]. Yet, the efficacy of cisplatin-based chemotherapy between initial EGFR-TKI and TKI retreatment remains poor. We suppose that targeting CA9 could enhance the ferroptosis-inducing effect of cisplatin in gefitinib-resistant cells.

We first performed genetic silencing of CA9 using shRNAs in parental and gefitinib-resistant cells. In long-term proliferation assays, these shRNAs suppressed proliferation in gefitinib-resistant cells, but not in parental cells (Figures 6(a) and 6(b)). Our present data indicate that targeting CA9 is more efficient in gefitinib-resistant than in sensitive cells.

Then, we determined the synergistic effects of the CA9 inhibitor U104 and cisplatin in gefitinib-resistant cells. Drug-resistant cells were treated with different concentrations of U104 or cisplatin, and the synergistic scores were

measured by the Combeneft software using data from the cell viability assays [38]. The results showed that U104 and cisplatin had significant synergistic effects in gefitinib-resistant cells (Figure 6(c)). The combination of 10 μ M U104 and 0.5 μ M cisplatin was selected for the next in vitro competition assay. Gefitinib-resistant cells were labelled with green by transduction with eGFP-encoding lentiviral vectors. Then, gefitinib-resistant and gefitinib-sensitive cells were mixed in a 9:1 ratio of resistant cells to sensitive cells. The mixed cells were treated with no drug, gefitinib, U104, cisplatin, or U104 + cisplatin. Over the following 15 days, the relative proportion of the two populations was tracked by flow cytometry (Figures 6(d) and 6(e)). The results showed that gefitinib enriched eGFP-positive gefitinib-resistant cells, while U104 or cisplatin efficiently depleted gefitinib-resistant cells. The tendency of the relative

proportion changes in the U104 + cisplatin combination group was the same as in U104 or cisplatin single group. However, these changes were significant and started earlier.

Furthermore, we performed colony formation assay on parental and resistant cells under treatment of U104 or cisplatin. As shown in Figure 6(f), treatment of U104 inhibited the proliferation of resistant cells without affecting the parental cells. Cisplatin treatment showed stronger suppressive effects in resistant cells. The U104 + cisplatin combination showed significant synergistic effects in resistant cells rather than in parental cells. To determine the mode of cell death, we cotreated the parental and resistant cells with z-VAD, Fer-1, DFO as well as U104 and cisplatin. As expected, Fer-1 and DFO significantly rescued U104-mediated proliferation inhibition in resistant cells, while z-VAD could not (Figure 6(g)). Under cisplatin treatment, z-VAD showed stronger protective effects in parental cells but could only partially rescue the proliferation defect in resistant cells. Conversely, Fer-1 and DFO showed stronger protective effects in resistant cells (Figure 6(h)).

Collectively, these results indicate that targeting CA9 cooperates with cisplatin to eliminate gefitinib-resistant cells in the heterogeneous tumor cell populations by inducing ferroptosis, as shown in Figure 6(i).

3.6. Targeting CA9 Improves the Therapeutic Efficacy of Cisplatin in Gefitinib-Resistant Lung Cancer. To model the therapeutic targeting of heterogeneous tumor cell populations in vivo, we mixed gefitinib-resistant PC9/GR cells together with gefitinib-sensitive PC9 cells and injected the admixture (PC9/GR: PC9, 9:1) subcutaneously in mice (Figure 7(a)) [39]. The mice were randomly divided into five groups and treated with saline, gefitinib, U104, cisplatin, or U104 + cisplatin to explore whether CA9 inhibition could improve the treatment effect of cisplatin. The results suggested that tumor growth was significantly inhibited in the U104 + cisplatin group (Figures 7(b)–7(d)) than that in the control group. No significant weight loss was observed in the combination group, indicating good tolerance to the combination therapy (Figure 7(e)). We further evaluated the mRNA expression of PTGS2, a marker for assessment of ferroptosis in vivo [40], finding that U104 combined with cisplatin significantly increased the PTGS2 expression in isolated tumor tissues (Figure 7(f)). CA9 staining indicated that CA9 expression was significantly suppressed in the combination group (Figures 7(g) and 7(h)). Ki67 staining demonstrated significantly reduced proliferative activity in the combination group (Figures 7(g) and 7(i)). Collectively, these findings indicate that the CA9 inhibitor, U104, reinforced the treatment effect of cisplatin by inducing ferroptosis on gefitinib-resistant xenograft tumors.

4. Discussion

Acquired resistance to EGFR-TKI in lung cancer remains a major problem to be solved in clinical practice. The subsequent treatment options after acquired resistance could be adopted depending on the resistance mechanisms [5–7]. However, for patients with acquired resistance mediated

by an unknown mechanism, the therapeutic options remain limited. Recent studies have shown the promise of ferroptosis-inducing therapy in EGFR-TKI resistant cancer cells [10–12]. Even though several agents have been reported to induce ferroptosis, these ferroptosis inducers have not been translated into clinical benefits [13]. Here, we show that CA9 is upregulated in gefitinib-resistant lung cancer and confers resistance to ferroptosis-inducing drugs. Mechanistically, CA9 is involved in the inhibition of transferrin endocytosis and the stabilization of ferritin, leading to resistance to ferroptosis through regulation of iron metabolism. Targeting CA9 has been demonstrated to induce ferroptosis in gefitinib-resistant lung cancer.

Multiple studies have hinted that drug-resistant and sensitive clones coexist in heterogeneous tumor tissues. After EGFR-TKI treatment, the drug-sensitive cells are eliminated. Once the drug-resistant cells achieve dominant status in the heterogeneous tumor cell populations, clinical resistance develops. In the second-line of treatment, cisplatin-based chemotherapy targets these drug-resistant cells while sparing the sensitive cells. This means that subsequent rechallenge with EGFR-TKI could theoretically provide clinical benefit as the left cells still retain sensitivity to EGFR-TKI [41–43]. As the widely used ferroptosis inducer, cisplatin may play a role in eliminating drug-resistant cells by inducing ferroptosis [14]. A prospective, multicenter phase II study (RECHALLENGE, CTONG1304) has reported that patients who received first-line gefitinib treatment could still benefit from gefitinib retreatment after the second-line cisplatin-based chemotherapy. Median progression-free survival of these patients receiving third-line gefitinib treatment was 4.4 months and median overall survival was 10.3 months [15]. Despite the favorable efficacy data shown in this study, the long-term benefit remains poor. Exploring more effective therapeutic strategies to eliminate more gefitinib-resistant cells and to gain a longer drug holiday period is important.

Our present data indicate that CA9-targeting treatment is more efficient in gefitinib-resistant cells than in sensitive cells. Therefore, we explored the role of targeting CA9 in combination with cisplatin in inducing ferroptosis in gefitinib-resistant cells. Our study found that targeting CA9 has a significant synergistic effect with cisplatin in inhibiting the viability of gefitinib-resistant cells. The synergistic effect of targeting CA9 and cisplatin on the elimination of gefitinib-resistant cells was further verified through an in vitro competition assay. Moreover, the combined treatment with cisplatin and CA9 inhibitor U104 was much more effective than cisplatin alone in the xenograft model containing heterogeneous tumor cell populations. In our study, inhibiting CA9 triggers ferroptosis through regulation of iron metabolism. Cisplatin was reported to induce ferroptosis predominantly through the depletion of reduced glutathione and the inactivation of glutathione peroxidase [14]. Consistent with our study, CA9 regulation was not involved in cisplatin-induced ferroptosis. Of note, the U104 + cisplatin combination treatment promoted ferroptosis via two distinct pathways in tumor tissues. These findings indicate that CA9 is an actionable target for enhancing cisplatin efficacy in gefitinib-resistant lung cancer by inducing ferroptosis.

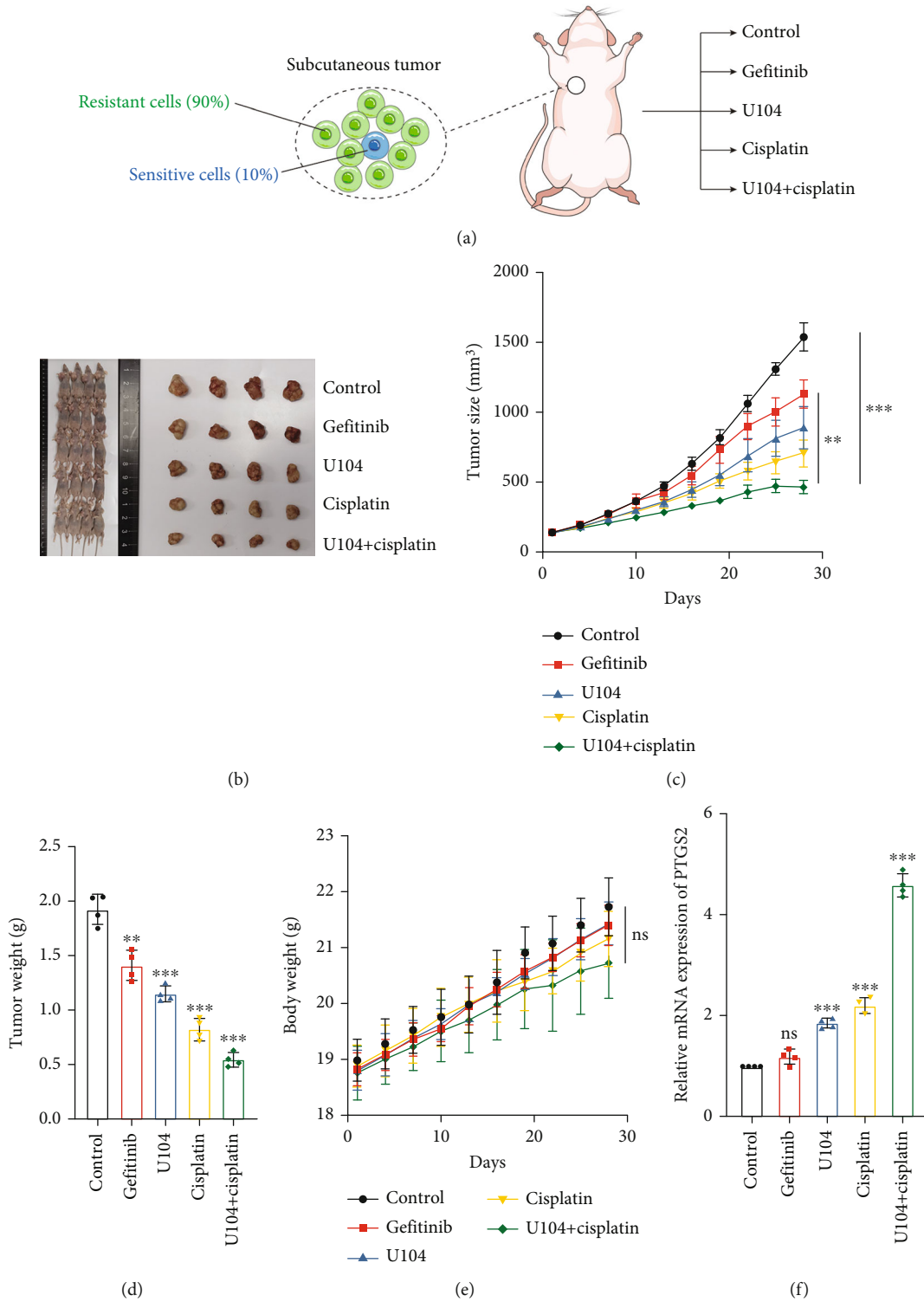


FIGURE 7: Continued.

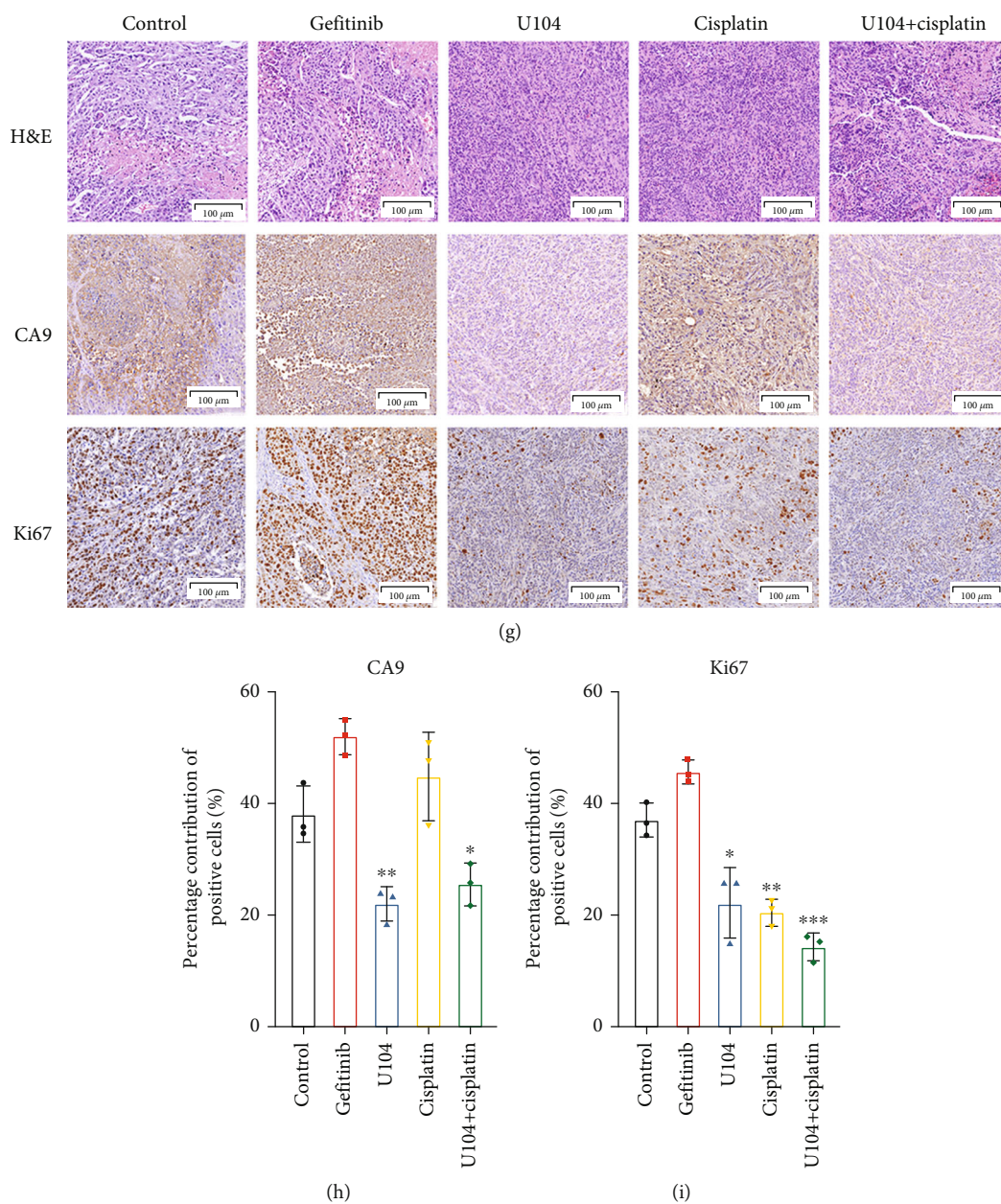


FIGURE 7: Targeting CA9 improves the therapeutic efficacy of cisplatin in gefitinib-resistant lung cancer. (a) A mixture of gefitinib-resistant PC9/GR and parental PC9 cells (PC9/GR: PC9, 9: 1) were subcutaneously injected into BALB/c nude mice to model therapeutic targeting of heterogeneous tumor cell populations in vivo. (b) Mice were treated as follows: saline daily, gefitinib (25 mg/kg) daily, U104 (19 mg/kg) daily, cisplatin (4 mg/kg) on days 1, 7, 14, and 21, and U104 (19 mg/kg) daily combined with cisplatin (4 mg/kg) on days 1, 7, 14, and 21. Endpoint tumor images of the mice are shown. (c) Growth curves of tumors after different treatments. (** $P < 0.01$, *** $P < 0.001$, two-way ANOVA-RM with Bonferroni post hoc correction). (d) Tumor weights were compared at the endpoint. (** $P < 0.01$, *** $P < 0.001$, Student's t -test). (e) Body weights of mice were measured during treatments. (ns indicates not significant, two-way ANOVA-RM with Bonferroni correction). (f) qPCR analysis was performed for PTGS2 as a marker of ferroptosis in vivo. (g) Haematoxylin-eosin (HE) and immunohistochemical (IHC) staining were performed to evaluate the proliferative activity of tumors. (h) Quantification of CA9-positive cells. (i) Quantification of Ki67-positive cells. The data shown are the Mean \pm SDs of four independent experiments. (* $P < 0.05$, ** $P < 0.01$, *** $P < 0.001$, Student's t -test).

There are several limitations in this study. First, considering the heterogeneity of gefitinib resistance mechanisms, we performed our experiments in two types of gefitinib-resistant cell lines PC9/GR and HCC827/GR. However, it is still controversial whether the two resistant cell lines could faithfully recapitulate clinical drug resistance. Second, we

injected the admixture of resistant and sensitive cells subcutaneously in mice to model the heterogeneous tumor cell populations. But, we were not able to evaluate the relative abundance of the two populations in vivo. At last, we only demonstrated that CA9-targeting therapy improved gefitinib-resistant lung cancer treatment. We also

identified CA9 upregulation in osimertinib-resistant cell lines HCC827/OR (data not shown). Thus, further studies on whether CA9-targeting therapy improves osimertinib-resistant lung cancer treatment would be beneficial.

Altogether, this study found that CA9 is upregulated in gefitinib-resistant lung cancer and confers resistance to ferroptosis-inducing drugs. CA9-targeting therapy is a promising approach to improve the therapeutic effect of gefitinib-resistant lung cancer by inducing ferroptosis.

Data Availability

All data and materials supporting the conclusions were included in the main paper.

Conflicts of Interest

We state here that none of our authors has financial or other conflicts of interest that might be constructed as influencing the results or interpretation of our study.

Authors' Contributions

Zhang C, Lu XY, and Liu XY designed and performed the experiments, analyzed the data, and wrote the manuscript. Xu JL and Li J revised the manuscript. Qu TY and Dai JL performed the statistical analysis and prepared the figures. Guo RH provided material support and contributed in the design of experiments. Chen Zhang, Xiyi Lu, and Xinyin Liu contributed equally to this work.

Acknowledgments

This work was supported by the National Natural Science Foundation of China (81972188 and 82103133), the Natural Science Foundation of Jiangsu Province (BK20210973), and the China Postdoctoral Science Foundation (2020M671395).

Supplementary Materials

Figure S1: TCGA analysis of dysregulated genes. Figure S2: qPCR analysis of CA9 expression after gefitinib treatment. Figure S3: CA9 expression does not affect gefitinib sensitivity in lung cancer cells. Figure S4: CA9 inhibition affects cellular iron metabolism. Table S1: 68 differential expressed genes (DEGs) identified by protein-protein interaction analysis. Table S2: 259 ferroptosis-related genes (FRGs) obtained from FerrDb database. Table S3: mutations in CA9 in the TCGA cohort. Table S4: the clinical characteristics of 12 NSCLC patients. (*Supplementary Materials*)

References

- [1] R. L. Siegel, K. D. Miller, H. E. Fuchs, and A. Jemal, "Cancer statistics, 2021," *CA: a Cancer Journal for Clinicians*, vol. 71, no. 1, pp. 7–33, 2021.
- [2] T. S. Mok, Y. L. Wu, S. Thongprasert et al., "Gefitinib or carboplatin-paclitaxel in pulmonary adenocarcinoma," *New England Journal of Medicine*, vol. 361, no. 10, pp. 947–957, 2009.
- [3] C. Zhou, Y. L. Wu, G. Chen et al., "Erlotinib versus chemotherapy as first-line treatment for patients with advanced EGFR mutation-positive non-small-cell lung cancer (OPTIMAL, CTONG-0802): a multicentre, open-label, randomised, phase 3 study," *Lancet Oncology*, vol. 12, no. 8, pp. 735–742, 2011.
- [4] P. S. Hammerman, P. A. Jänne, and B. E. Johnson, "Resistance to epidermal growth factor receptor tyrosine kinase inhibitors in non-small cell lung cancer," *Clinical Cancer Research*, vol. 15, no. 24, pp. 7502–7509, 2009.
- [5] D. B. Costa, S. T. Schumer, D. G. Tenen, and S. Kobayashi, "Differential responses to erlotinib in epidermal growth factor receptor (EGFR)-mutated lung cancers with acquired resistance to gefitinib carrying the L747S or T790M secondary mutations," *Journal of Clinical Oncology*, vol. 26, no. 7, pp. 1182–1184, 2008.
- [6] J. A. Engelman, K. Zejnullahu, T. Mitsudomi et al., "MET amplification leads to gefitinib resistance in lung cancer by activating ERBB3 signaling," *Science*, vol. 316, no. 5827, pp. 1039–1043, 2007.
- [7] L. V. Sequist, B. A. Waltman, D. Dias-Santagata et al., "Genotypic and histological evolution of lung cancers acquiring resistance to EGFR inhibitors," *Science Translational Medicine*, vol. 3, no. 75, p. 75ra26, 2011.
- [8] J. Rotow and T. G. Bivona, "Understanding and targeting resistance mechanisms in NSCLC," *Nature Reviews: Cancer*, vol. 17, no. 11, pp. 637–658, 2017.
- [9] S. J. Dixon, K. M. Lemberg, M. R. Lamprecht et al., "Ferroptosis: an iron-dependent form of nonapoptotic cell death," *Cell*, vol. 149, no. 5, pp. 1060–1072, 2012.
- [10] M. J. Hangauer, V. S. Viswanathan, M. J. Ryan et al., "Drug-tolerant persister cancer cells are vulnerable to GPX4 inhibition," *Nature*, vol. 551, no. 7679, pp. 247–250, 2017.
- [11] J. H. You, J. Lee, and J. L. Roh, "Mitochondrial pyruvate carrier 1 regulates ferroptosis in drug-tolerant persister head and neck cancer cells via epithelial-mesenchymal transition," *Cancer Letters*, vol. 507, no. 40–54, pp. 40–54, 2021.
- [12] T. Zhang, B. Sun, C. Zhong et al., "Targeting histone deacetylase enhances the therapeutic effect of erastin-induced ferroptosis in EGFR-activating mutant lung adenocarcinoma," *Translational Lung Cancer Research*, vol. 10, no. 4, pp. 1857–1872, 2021.
- [13] F. Yao, Y. Deng, Y. Zhao et al., "A targetable LIFR–NF- κ B–LCN2 axis controls liver tumorigenesis and vulnerability to ferroptosis," *Nature Communications*, vol. 12, no. 1, p. 7333, 2021.
- [14] C. Liang, X. Zhang, M. Yang, and X. Dong, "Recent progress in ferroptosis inducers for cancer therapy," *Advanced Materials*, vol. 31, no. 51, article e1904197, 2019.
- [15] Y. Song, Y. L. Wu, L. J. Cao et al., "Efficacy and safety of Gefitinib as third-line treatment in NSCLC patients with activating EGFR mutations treated with first-line gefitinib followed by second-line chemotherapy: a single-arm, prospective, multicenter phase II study (Re-challenge, CTONG1304)," *American Journal of Clinical Oncology*, vol. 42, no. 5, pp. 432–439, 2019.
- [16] H. J. Shin, S. B. Rho, D. C. Jung, I. O. Han, E. S. Oh, and J. Y. Kim, "Carbonic anhydrase IX (CA9) modulates tumor-associated cell migration and invasion," *Journal of Cell Science*, vol. 124, no. 7, pp. 1077–1087, 2011.
- [17] Z. Li, L. Jiang, S. H. Chew, T. Hirayama, Y. Sekido, and S. Toyokuni, "Carbonic anhydrase 9 confers resistance to

- ferroptosis/apoptosis in malignant mesothelioma under hypoxia,” *Redox Biology*, vol. 26, no. 101297, p. 101297, 2019.
- [18] T. Sowa, T. Menju, T. F. Chen-Yoshikawa et al., “Hypoxia-inducible factor 1 promotes chemoresistance of lung cancer by inducing carbonic anhydrase IX expression,” *Cancer Medicine*, vol. 6, no. 1, pp. 288–297, 2017.
- [19] A. Giatromanolaki, M. I. Koukourakis, E. Sivridis et al., “Expression of hypoxia-inducible carbonic anhydrase-9 relates to angiogenic pathways and independently to poor outcome in non-small cell lung cancer,” *Cancer Research*, vol. 61, no. 21, pp. 7992–7998, 2001.
- [20] A. Giatromanolaki, A. L. Harris, A. H. Banham, C. A. Contrafouris, and M. I. Koukourakis, “Carbonic anhydrase 9 (CA9) expression in non-small-cell lung cancer: correlation with regulatory FOXP3+T-cell tumour stroma infiltration,” *British Journal of Cancer*, vol. 122, no. 8, pp. 1205–1210, 2020.
- [21] D. E. Swinson, G. Cox, and K. J. O’Byrne, “Coexpression of epidermal growth factor receptor with related factors is associated with a poor prognosis in non-small-cell lung cancer,” *British Journal of Cancer*, vol. 91, no. 7, pp. 1301–1307, 2004.
- [22] W. C. Zhang, J. M. Wells, K. H. Chow et al., “miR-147b-mediated TCA cycle dysfunction and pseudohypoxia initiate drug tolerance to EGFR inhibitors in lung adenocarcinoma,” *Nature Metabolism*, vol. 1, no. 4, pp. 460–474, 2019.
- [23] M. B. Nilsson, J. Robichaux, M. H. Herynk et al., “Altered regulation of HIF-1 α in naive- and drug-resistant EGFR-mutant NSCLC: implications for a vascular endothelial growth factor-dependent phenotype,” *Journal of Thoracic Oncology*, vol. 16, no. 3, pp. 439–451, 2021.
- [24] A. N. Hata, M. J. Niederst, H. L. Archibald et al., “Tumor cells can follow distinct evolutionary paths to become resistant to epidermal growth factor receptor inhibition,” *Nature Medicine*, vol. 22, no. 3, pp. 262–269, 2016.
- [25] X. Rao, X. Huang, Z. Zhou, and X. Lin, “An improvement of the 2^{-delta delta CT} method for quantitative real-time polymerase chain reaction data analysis,” *Biostatistics, Bioinformatics and Biomathematics*, vol. 3, no. 3, pp. 71–85, 2013.
- [26] N. Zhou and J. Bao, “FerrDb: a manually curated resource for regulators and markers of ferroptosis and ferroptosis-disease associations,” *Database: The Journal of Biological Databases and Curation*, vol. 2020, article baaa021, 2020.
- [27] J. Chen, H. Yang, A. S. M. Teo et al., “Genomic landscape of lung adenocarcinoma in east Asians,” *Nature Genetics*, vol. 52, no. 2, pp. 177–186, 2020.
- [28] B. R. Stockwell, J. P. Friedmann Angeli, H. Bayir et al., “Ferroptosis: a regulated cell death nexus linking metabolism, redox biology, and disease,” *Cell*, vol. 171, no. 2, pp. 273–285, 2017.
- [29] M. Swayampakula, P. C. McDonald, M. Vallejo et al., “The interactome of metabolic enzyme carbonic anhydrase IX reveals novel roles in tumor cell migration and invadopodia/MMP14-mediated invasion,” *Oncogene*, vol. 36, no. 45, pp. 6244–6261, 2017.
- [30] X. Sun, Z. Ou, M. Xie et al., “HSPB1 as a novel regulator of ferroptotic cancer cell death,” *Oncogene*, vol. 34, no. 45, pp. 5617–5625, 2015.
- [31] Z. Li, L. Jiang, and S. Toyokuni, “Role of carbonic anhydrases in ferroptosis-resistance,” *Archives of Biochemistry and Biophysics*, vol. 689, no. 108440, p. 108440, 2020.
- [32] B. J. Crielaard, T. Lammers, and S. Rivella, “Targeting iron metabolism in drug discovery and delivery,” *Nature Reviews: Drug Discovery*, vol. 16, no. 6, pp. 400–423, 2017.
- [33] J. B. Wish, “Assessing iron status: beyond serum ferritin and transferrin saturation,” *Clinical Journal of the American Society of Nephrology*, vol. 1, Suppl 1, pp. S4–S8, 2006.
- [34] M. Kim, Y. Rho, K. S. Jin et al., “pH-dependent structures of ferritin and apoferritin in solution: disassembly and reassembly,” *Biomacromolecules*, vol. 12, no. 5, pp. 1629–1640, 2011.
- [35] T. Kurata, K. Tamura, H. Kaneda et al., “Effect of re-treatment with gefitinib (Iressa, ZD1839) after acquisition of resistance,” *Annals of Oncology*, vol. 15, no. 1, pp. 173–174, 2004.
- [36] S. Yano, E. Nakataki, S. Ohtsuka et al., “Retreatment of lung adenocarcinoma patients with gefitinib who had experienced favorable results from their initial treatment with this selective epidermal growth factor receptor inhibitor: a report of three cases,” *Oncology Research*, vol. 15, no. 2, pp. 107–111, 2005.
- [37] S. V. Sharma, D. Y. Lee, B. Li et al., “A chromatin-mediated reversible drug-tolerant state in cancer cell subpopulations,” *Cell*, vol. 141, no. 1, pp. 69–80, 2010.
- [38] G. Y. Di Veroli, C. Fornari, D. Wang et al., “Combeneft: an interactive platform for the analysis and visualization of drug combinations,” *Bioinformatics*, vol. 32, no. 18, pp. 2866–2868, 2016.
- [39] A. C. Obenauf, Y. Zou, A. L. Ji et al., “Therapy-induced tumour secretomes promote resistance and tumour progression,” *Nature*, vol. 520, no. 7547, pp. 368–372, 2015.
- [40] W. S. Yang, R. SriRamaratnam, M. E. Welsch et al., “Regulation of ferroptotic cancer cell death by GPX4,” *Cell*, vol. 156, no. 1–2, pp. 317–331, 2014.
- [41] G. R. Oxnard, M. E. Arcila, J. Chmielecki, M. Ladanyi, V. A. Miller, and W. Pao, “New strategies in overcoming acquired resistance to epidermal growth factor receptor tyrosine kinase inhibitors in lung cancer,” *Clinical Cancer Research*, vol. 17, no. 17, pp. 5530–5537, 2011.
- [42] J. E. Chaft, G. R. Oxnard, C. S. Sima, M. G. Kris, V. A. Miller, and G. J. Riely, “Disease flare after tyrosine kinase inhibitor discontinuation in patients with EGFR-mutant lung cancer and acquired resistance to erlotinib or gefitinib: implications for clinical trial design,” *Clinical Cancer Research*, vol. 17, no. 19, pp. 6298–6303, 2011.
- [43] G. J. Riely, M. G. Kris, B. Zhao et al., “Prospective assessment of discontinuation and reinitiation of erlotinib or gefitinib in patients with acquired resistance to erlotinib or gefitinib followed by the addition of everolimus,” *Clinical Cancer Research*, vol. 13, no. 17, pp. 5150–5155, 2007.

Research Article

Modulation of the p38 MAPK Pathway by Anisomycin Promotes Ferroptosis of Hepatocellular Carcinoma through Phosphorylation of H3S10

Wei Chen ¹, Wenjing Yang ¹, Chunyan Zhang ^{1,2}, Te Liu ^{1,3}, Jie Zhu ¹,
Hao Wang ¹, Tong Li ¹, Anli Jin ¹, Lin Ding ¹, Jingrong Xian ¹, Tongtong Tian ¹,
Baishen Pan,^{1,4} Wei Guo ^{1,2,4,5} and Beili Wang ^{1,4,5}

¹Department of Laboratory Medicine, Zhongshan Hospital, Fudan University, Shanghai, China

²Department of Laboratory Medicine, Xiamen Branch, Zhongshan Hospital, Fudan University, Xiamen, China

³Shanghai Geriatric Institute of Chinese Medicine, Shanghai University of Traditional Chinese Medicine, Shanghai, China

⁴Department of Laboratory Medicine, Wusong Branch, Zhongshan Hospital, Fudan University, Shanghai, China

⁵Cancer Center, Shanghai Zhongshan Hospital, Fudan University, Shanghai, China

Correspondence should be addressed to Wei Guo; guo.wei@zs-hospital.sh.cn and Beili Wang; wang.beili@zs-hospital.sh.cn

Received 9 June 2022; Revised 27 September 2022; Accepted 8 October 2022; Published 24 November 2022

Academic Editor: Lianxiang Luo

Copyright © 2022 Wei Chen et al. This is an open access article distributed under the Creative Commons Attribution License, which permits unrestricted use, distribution, and reproduction in any medium, provided the original work is properly cited.

Hepatocellular carcinoma (HCC) is a prevalent malignant tumor worldwide. Ferroptosis is emerging as an effective target for tumor treatment as it has been shown to potentiate cell death in some malignancies. However, it remains unclear whether histone phosphorylation events, an epigenetic mechanism that regulates transcriptional expression, are involved in ferroptosis. Our study found that supplementation with anisomycin, an agonist of p38 mitogen-activated protein kinase (MAPK), induced ferroptosis in HCC cells, and the phosphorylation of histone H3 on serine 10 (p-H3S10) was participated in anisomycin-induced ferroptosis. To investigate the anticancer effects of anisomycin-activated p38 MAPK in HCC, we analyzed cell viability, colony formation, cell death, and cell migration in Hep3B and HCCLM3 cells. The results showed that anisomycin could significantly suppress HCC cell colony formation and migration and induce HCC cell death. The hallmarks of ferroptosis, such as abnormal accumulation of iron and elevated levels of lipid peroxidation and malondialdehyde, were detected to confirm the ability of anisomycin to promote ferroptosis. Furthermore, coinubation with SB203580, an inhibitor of activated p38 MAPK, partially rescued anisomycin-induced ferroptosis. And the levels of p-p38 MAPK and p-H3S10 were successively increased by anisomycin treatment. The relationship between p-H3S10 and ferroptosis was revealed by ChIP sequencing. The reverse transcription PCR and immunofluorescence results showed that NCOA4 was upregulated both in mRNA and protein levels after anisomycin treatment. And by C11-BODIPY staining, we found that anisomycin-induced lipid reactive oxygen species was reduced after NCOA4 knockdown. In conclusion, the anisomycin-activated p38 MAPK promoted ferroptosis of HCC cells through H3S10 phosphorylation.

1. Introduction

Hepatocellular carcinoma (HCC) is the third leading cause of cancer-related deaths worldwide [1]. Numerous drugs have been developed to improve the outcomes of patients with HCC [2]. The targets of these drugs include CRAF, BRAF, EGFR, and VEGFR. However, until now, the overall survival rate of HCC patients is still limited, increasing the

urgent demand for the exploration of additional targets and drugs [3].

The p38 mitogen-activated protein kinase (MAPK) is a stress-activated protein kinase, which could be activated by environmental and intracellular stresses and then stimulate downstream proteins, such as MKK3/6, MSK1/2, or WHIP1 [4]. Some researchers have reported the anticancer effects of p38 MAPK activation, showing its promising potential in

cancer treatment. Yao et al. [5] found that activation of p38 MAPK could promote the phosphorylation of heat shock protein 27 and induce apoptosis in lung squamous cell carcinoma. Furthermore, Zhang et al. [6] found that ferretinide-stimulated p38 MAPK activation could reduce the activation of myosin light chain kinase, thus inhibiting the proliferation and migration of HepG2 cells from human liver cancer. Recently, some studies have found that the p38 MAPK signaling pathway could promote ferroptosis in endometrial stromal cells [7], osteoblasts [8], and cancer cells [9, 10]. More interestingly, noncoding RNAs have also been reported to be involved in the axis of p38-ferroptosis [11, 12]. Moreover, an agonist of p38 MAPK, anisomycin [13], has also shown its potential value in medication, as it could significantly induce cell death in acute lymphoblastic leukemia, melanoma, and glioma [14–18]. Kim et al. [19] described that anisomycin could exert both direct killing effects and immunotherapeutic effects mediated by natural killer cells (NK) in HCC. However, no studies have demonstrated the relationship between anisomycin and ferroptosis.

Histones, known to be part of nucleosomes, undergo multiple types of posttranslational modifications (PTM), such as acetylation, methylation, ubiquitination, phosphorylation, and SUMOylation, and participate in the regulation of chromatin condensation and DNA accessibility [20–22]. Several studies have found that p38 MAPK could promote phosphorylation of histone H3S10/S28 [23–25]. Phosphorylated histone H3 usually modulates chromatin structure to enhance DNA accessibility and subsequently promote transcriptional activation or coordinate another histone PTM [26–28]. In addition, phosphorylation of histone H3 is involved in different biological activities of cancer. For example, H3 phosphorylation through the p38 MAPK signaling pathway has been demonstrated to participate in casticin-induced cytotoxic effects against the human promyelocytic cell line HL-60 [29].

Ferroptosis, an iron-dependent form of nonapoptotic cell death [30], is characterized by iron overload and lipid peroxidation [31, 32]. The canonical ferroptosis induction pathway is activated mainly directly or indirectly by inactivating the main protective mechanism against peroxidation damage, especially glutathione peroxidase 4 (GPX4). Meanwhile, noncanonical ferroptosis induction refers to ferroptosis that is initiated by the accumulation of labile iron pool (LIP), small pools of iron mainly in the form of free ferrous iron (Fe^{2+}) [31, 33]. It is well known that maintaining iron homeostasis is important for cell death and human diseases [34], including noncanonical ferroptosis induction. Increased LIP can directly promote the Fenton reactions and can further increase lipid peroxidation. As one of the inducers of ferroptosis, nuclear receptor coactivator 4 (NCOA4) has been widely reported to regulate ferroptosis mainly by increasing LIP [35–39]. Furthermore, many studies have demonstrated that drug-induced ferroptosis was reduced after NCOA4 knockdown [40–42], and several studies have also demonstrated that drug-induced ferroptosis was increased after NCOA4 overexpression [43]. In human liver cancer cell HepG2, the study by Hattori et al. [44] had found that the activation of the ASK1-p38

pathway was involved in cold stress-induced ferroptosis, although the mechanism has not yet been clarified. To date, the association of phosphorylated H3S10/28 and ferroptosis in HCC and the underlying mechanisms have not been reported.

In this study, we used anisomycin to activate p38 MAPK and investigated whether and how activation of p38 MAPK participates in the killing of HCC cells. Furthermore, we also explored whether histone H3 phosphorylation is involved in ferroptosis promoted by anisomycin-induced activation of p38 MAPK.

2. Materials and Methods

2.1. Cell Culture and Transfection. The HCC cell lines, HCCLM3 and Hep3B, were obtained from Liver Cancer Institute, Zhongshan Hospital, Fudan University (Shanghai, China). All cells were cultured in Dulbecco's Modified Eagle Medium (DMEM, Gibco, USA) supplemented with 10% fetal bovine serum (FBS; BioSun, China) and 1% antibiotics (100 U/mL penicillin G and 100 mg/mL streptomycin, Gibco, USA). Cells were cultured at 37°C in an incubator (Thermo Fisher, USA) with a humidified atmosphere containing 5% CO_2 .

The plasmid or small interfering RNA (siRNA) oligos were transfected into cells by jetPRIME reagent (Polyplus, France) when cells reached 70% confluency. The plasmid of NCOA4 was purchased from GenePharma (Shanghai, China), and they used pEX-6 (pGCMV/MCS/RFP/Neo) as the carrier vector for NCOA4 cDNA. Gene-specific and negative control (NC) siRNAs were synthesized by GenePharma (Shanghai, China). The siRNA sequence for NCOA4#1 was 5'-ACTCTTGTTTATCGAAGTATA-3' and for NCOA4#2 was 5'-CTCTTATTCCAGTCCTATAAT-3' [40]. RT-PCR was used to test NCOA4 knockdown and overexpression in Hep3B and HCCLM3.

2.2. Chemicals and Antibodies. Anisomycin, SB203580 [45], SP600125, and ferrostatin-1 [46] were purchased from MCE (Shanghai, China) and dissolved in dimethyl sulfoxide (DMSO). Cells were treated with anisomycin at the indicated concentration or coincubated with SB203580 (20 μM) or ferrostatin-1 (4 μM). Commercially available antibodies were used in this study. The anti-tubulin antibody was obtained from InTech (Shanghai, China), while anti-c-Myc (#18583), CD133 (#64326), Nanog (#4903), EpCAM (#2929), caspase-3 (#14220), Bcl-2 (#15071), Bax (#5023), N-cadherin (#13116), E-cadherin (#3195), vimentin (#5741), α -smooth muscle actin (α -SMA, #19245), p38 MAPK (#8690), phospho-p38 MAPK (p-p38 MAPK, #9216), histone H3 (#4499), phospho-histone H3 (Ser10) (p-H3S10, #53348), phospho-histone H3 (Ser28) (p-H3S28, #9713), NRF2 (#12721), SLC7A11 (#12691), FTH1 (#4393), and NCOA4 (#66849) antibodies were purchased from Cell Signaling Technology (Boston, USA). Anti-CD24 (ab31622) antibody was provided by Abcam (Cambridge, UK).

2.3. Cell Viability Assay. Cell viability was evaluated using the Cell Counting Kit-8 (CCK-8; Beyotime, China) according to

the manufacturer's instructions. Briefly, cells (1×10^4 cells/well/ $100 \mu\text{L}$) were seeded in a 96-well plate and treated with anisomycin at different concentrations for 24 h. Then, $10 \mu\text{L}$ of CCK-8 solution was added to each well, and the plates were incubated at 37°C for another 2 h. The absorbance values of the samples were evaluated at 450 nm using a microplate reader. Experiments were performed in triplicate.

2.4. Colony Formation Assay. Cells were plated at a density of 4×10^4 cells per well in 6-well plates and allowed to attach. The following day, cells were treated with DMSO, anisomycin, or SB203580 plus anisomycin for 12 h. Then, the medium was replaced with DMEM supplemented with 10% FBS. The medium was changed every 3 days for 2 consecutive weeks. Finally, colonies were stained with crystal violet staining solution (Beyotime, China) for 15 min after fixation with 4% paraformaldehyde for 10 min. The stained colonies were washed with phosphate buffer saline (PBS) and counted using the ImageJ software. Experiments were performed in triplicate.

2.5. Cell Death Detection. Cell death was evaluated using an apoptosis detection kit purchased from BD Biosciences (San Jose, USA). Cells were harvested, stained with annexin V antibody and 7AAD, and then analyzed with a FACSaria™ II flow cytometer (BD Biosciences, USA). The flow cytometry results were further analyzed with the FlowJo 10.1 software (Tree Star, Inc., USA). The calculation of cell death rate was (1, the proportion of viable cells (cells in Q4)). Experiments were performed in triplicate.

2.6. Lipid Reactive Oxygen Species (Lipid-ROS) Levels. The accumulation of lipid-ROS is a major feature of ferroptosis and can be used to infer the degree of ferroptosis [47]. Cells were treated with DMSO, anisomycin, or SB203580 plus anisomycin for 24 h or 12 h. Then, cells were incubated with $3 \mu\text{M}$ C11-BODIPY 581/591 (Invitrogen, USA) in serum-free DMEM medium for 30 min at 37°C in an incubator. Afterwards, cells were washed three times with serum-free medium, trypsinized, and resuspended in PBS before detected by flow cytometry. Lipid-ROS levels were evaluated by the fluorescence intensity of FITC channel, and the mean fluorescence intensities (MFI) of FITC were calculated for each sample. Experiments were performed in triplicate.

2.7. Wound-Healing Assay. When Hep3B and HCCLM3 cells reached 100% confluency in 24-well plates, cells were wounded with a sterile $10 \mu\text{L}$ pipette tip in the cell monolayers and washed with serum-free medium to remove detached cells. Cells were then treated with DMSO, anisomycin, or SB203580 plus anisomycin at the indicated concentration for 12 h. The medium was then replaced with DMEM supplemented with 2% FBS, and cells were cultured for 48 h. The wound gap images were taken using a microscope (Olympus, Japan). Healing areas were calculated using the ImageJ software. Experiments were performed in triplicate.

2.8. Transwell Assay. Cells were treated with DMSO, anisomycin, or SB203580 plus anisomycin for 12 h before seeding

(5×10^4) and cultured in the upper chamber (24-well Transwell chambers, $8 \mu\text{m}$ pore size, Corning, USA) with serum-free DMEM, while serum-containing (10% FBS) DMEM was added to the lower chamber. After 48 h incubation at 37°C , cells were fixed with 4% paraformaldehyde and stained with crystal violet staining solution (Beyotime, China). Cells stained were imaged using a microscope (Olympus, Japan). Experiments were performed in triplicate.

2.9. Western Blotting. Cells were washed with PBS, collected, resuspended in RIPA lysis buffer (Beyotime, China), and kept on ice for 30 min. The suspension was vibrated vigorously every 5 min. Sonication was required. Cell extracts were obtained by centrifugation at $12,000 \times g$ for 10 min at 4°C . The protein concentration was determined using a bicinchoninic acid (BCA) protein assay kit (Thermo Fisher, USA). The denatured proteins were separated by sodium dodecyl sulfate-polyacrylamide gel electrophoresis (SDS-PAGE) and electrotransferred onto polyvinylidene difluoride (PVDF) membranes (Merck Millipore, Germany). The membranes were blocked with QuickBlock blocking buffer (Beyotime, China), incubated with diluted primary antibodies (1:1000) for 12 h at 4°C , and washed three times with TBST for 10 min. The membranes were then incubated with HRP conjugated secondary antibodies (1:2000) for 2 h at room temperature. Hybridization was detected using enhanced chemiluminescence reagents (ECL; Beyotime, China) after three rinses with TBST for 10 min. Image Lab 4.1 software and ImageJ software were used to quantify western blot bands.

2.10. Immunofluorescence Analysis. Cells were fixed in 4% paraformaldehyde for 15 min at room temperature and permeabilized with 0.1% Triton X-100 (Beyotime, China) for 10 min at 4°C . Cells were saturated with TBST containing 2% bovine serum albumin (BSA, Merck Sigma, Germany) for 1 h at room temperature before incubation with primary antibodies against p-p38 MAPK (1:200), p-H3S10 (1:100), or NCOA4 (1:400) overnight at 4°C . Subsequently, cells were incubated with a secondary antibody labeled Alexa Fluor 488 or 594 (Invitrogen, USA) (1:2000). Finally, cells were incubated with DAPI ($5 \mu\text{L}$ DAPI in $200 \mu\text{L}$ TBST) for 10 min. After each antibody incubation step, cells were washed three times for 5 min with TBST. Fluorescence signals were observed using an Olympus Fluoview microscope (Olympus Corp, Japan).

2.11. Chromatin Immunoprecipitation- (ChIP-) Sequencing. ChIP-sequencing was outsourced to Kangcheng Biotechnology (Shanghai, China). Briefly, the p-H3S10 antibody was used for immunoprecipitation. A total of 10 ng of DNA samples were prepared and blunt-ended. Then, a dA base was added to the 3' end of each strand, and genomic adapters were ligated to the DNA fragments. Subsequently, PCR amplification was performed to enrich the ligated fragments, and ~ 200 – 1500 bp fragments < 200 – 1500 bp were selected using AMPure XP beads. The libraries were then sequenced on the Illumina NovaSeq 6000 instrument following the NovaSeq 6000 S4 reagent kit protocol (300 cycles). The reads

were aligned to the human genome (UCSC HG19) using the BOWTIE software (V2.2.7). Aligned reads were used to call the peaks of the ChIP regions using MACS V1.4.2. A P value threshold of 10^{-3} was used to select differentially enriched peaks.

2.12. Bioinformatics. The R packages “clusterProfiler,” “org.Hs.eg.db,” “enrichplot,” and “ggplot2” were used in R 4.0.3 software to perform functional enrichment analyzes of Gene Ontology (GO) and Kyoto Encyclopedia of Genes and Genomes (KEGG). Furthermore, the STRING 11.5 online tool (<https://cn.string-db.org/>) was used to find protein-protein interactions (PPI) between the selected genes with a confidence filter (interaction score > 0.150).

2.13. Iron Assay. Intracellular iron was assessed using an iron colorimetric assay kit (APPLYGEN, China) according to the manufacturer’s instructions. The results were assessed at 550 nm using a microplate reader and normalized to protein concentration. Experiments were performed in triplicate.

2.14. Lipid Peroxidation (LPO) Assay. The Lipid Peroxidation Assay Kit (Nanjing Jiancheng Institute of Bioengineering, China) was used to measure LPO levels in HCC cells. The results were evaluated at 586 nm using a microplate reader and normalized to protein concentration. All procedures were performed in full accordance with the manufacturer’s instructions. Experiments were performed in triplicate.

2.15. Malondialdehyde Assay. The relative concentration of malondialdehyde (MDA) in cell lysates was evaluated using a lipid peroxidation MDA assay kit (Beyotime, China) according to the manufacturer’s instructions. The MDA level was determined by a microplate reader at 532 nm and normalized to protein concentration. Experiments were performed in triplicate.

2.16. Quantitative Reverse Transcription Polymerase Chain Reaction (qRT-PCR). TRIzol reagent (Invitrogen, USA) was used to extract total RNA from HCC cells. RNA was reverse transcribed to cDNA using GoScript™ Reverse Transcription Mix (Promega, USA) according to the manufacturer’s instructions. The cDNA was then detected using the GoTaq® qPCR Master Mix reagent (Promega, USA). The PCR program included denaturation at 94°C for 2 min, followed by 40 cycles of 94°C for 30 s, 56°C for 30 s, 72°C for 30 s, and finally a 5 min elongation at 72°C. The sequences of primers used are listed in Supplementary Table 1. β -Actin was included as the internal control to assess the relative expression of the genes. The relative level of mRNA expression was calculated using $2^{-\Delta\Delta Ct}$. Experiments were performed in triplicate.

2.17. Statistical Analysis. All statistical analyses were performed using the GraphPad Prism software 7.0 (GraphPad Software Inc., USA), and data were displayed as mean \pm standard deviation (SD). The means of the groups were compared using the Student’s t -test for two independent

groups. When the variances were uneven ($P < 0.1$), Welch’s t -test was used. All P values were two-tailed, and $P < 0.05$ was considered statistically significant.

3. Results

3.1. Anisomycin Induced HCC Cell Death through the p38 MAPK Signaling Pathway. Expression levels of p38 MAPK and p-p38 MAPK in different HCC cell lines were evaluated by western blotting (Supplementary Figure 1A). Hep3B and HCCLM3, two cell lines with weak phosphorylation of p38 MAPK, were chosen for subsequent experiments of activation of p38 MAPK. Anisomycin treatment was applied to the two cell lines to investigate the anticancer effects of p38 MAPK activation on HCC cells [14–16]. The results of 24 h anisomycin treatment showed that anisomycin inhibited the proliferation of HCC cells in a dose-dependent manner (Figure 1(a)). When the inhibition rate reached 50%, the anisomycin concentrations for Hep3B and HCCLM3 were approximately 2.5 μ M and 5 μ M, respectively. The indicated concentrations of anisomycin (2.5 μ M for Hep3B and 5 μ M for HCCLM3) were selected for the following experiments. Besides, we performed CCK8 analysis for all 6 cell lines in Supplementary Figure 1A after treatment with different concentrations of anisomycin and integrated all curves. The results showed that low p-p38/p38 ratio cells (Hep3B, HCCLM3, and SK-Hep-1) required lower concentrations of anisomycin than high p-p38/p38 ratio cells (MHCC-97L, MHCC-97H, and HepG2) to reach 50% inhibition rate (Supplementary Figure 1B).

The colony formation assay and cell death detection were performed to further assess the anticancer effects of anisomycin on HCC cells. We shortened the treatment time to 12 h for cell functional assays (colony formation assay, wound-healing assay, and transwell assay) to reduce interference from cell death with experimental results. The number of clones was substantially reduced for cells treated with anisomycin for 12 h, and the cell death rate was substantially increased for cells treated with anisomycin for 24 h. Meanwhile, the anticancer effects of anisomycin were attenuated by SB203580, an inhibitor of activated p38 MAPK (Figures 1(b) and 1(c)), indicating that anisomycin promoted HCC cell death partly through activating the p38 MAPK pathway. Several studies have reported that p38 can inhibit cancer stem cell properties [48] and increase apoptosis [49, 50] in cancer cell. Therefore, the expression levels of the cell stemness-related proteins (c-Myc, CD133, Nanog, CD24, and EpCAM) and the apoptosis-related proteins (cleaved caspase-3, Bcl-2, and Bax) were also analyzed in HCC cells during anisomycin treatment, and the changes in protein expression were consistent with the phenotypic changes above (Supplementary Figures 2A–D). To explore whether activation of the p38 pathway regulates ferroptosis in HCC cells, we used C11-BODIPY staining to examine the accumulation of lipid reactive oxygen species (lipid-ROS) and found that anisomycin significantly increased intracellular lipid-ROS, while SB203580 coinubation almost completely rescued the accumulation of lipid-ROS

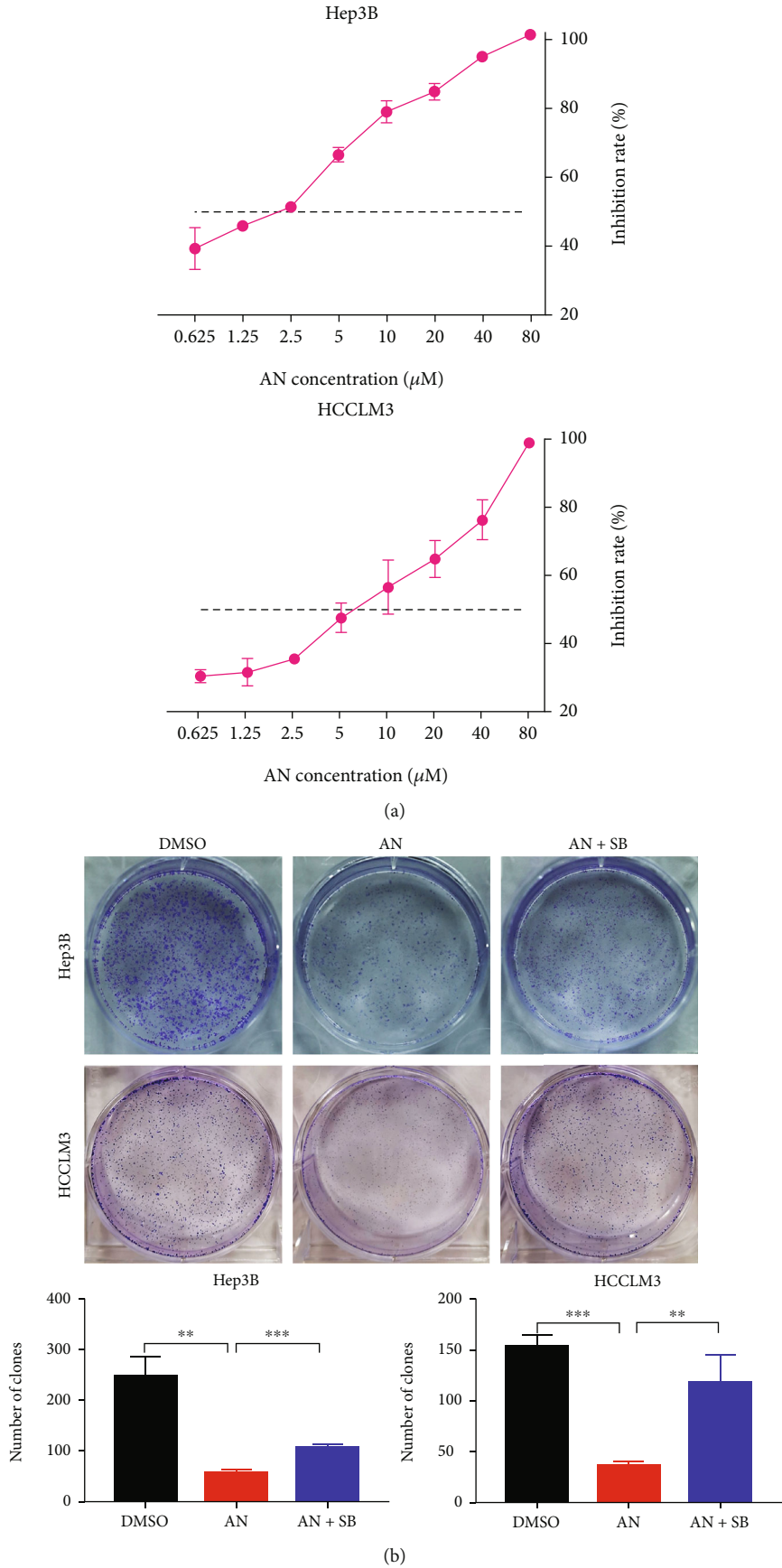


FIGURE 1: Continued.

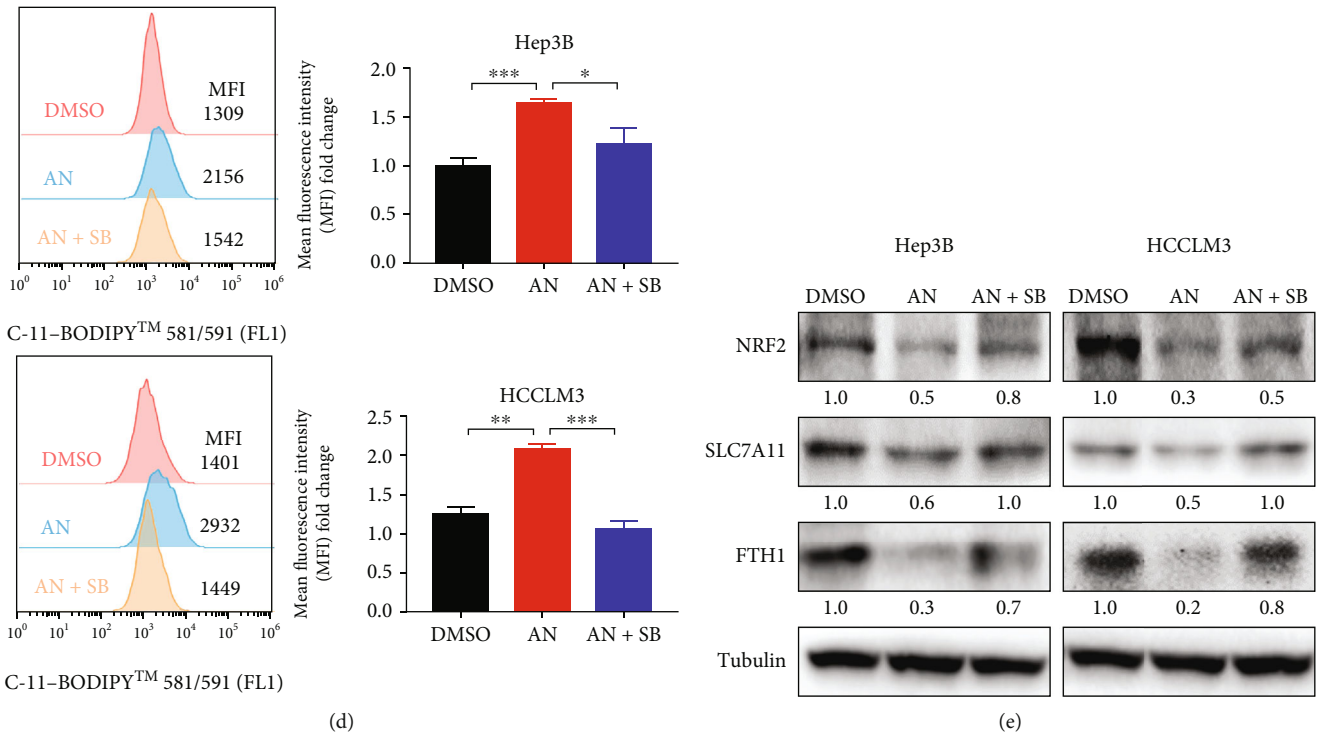
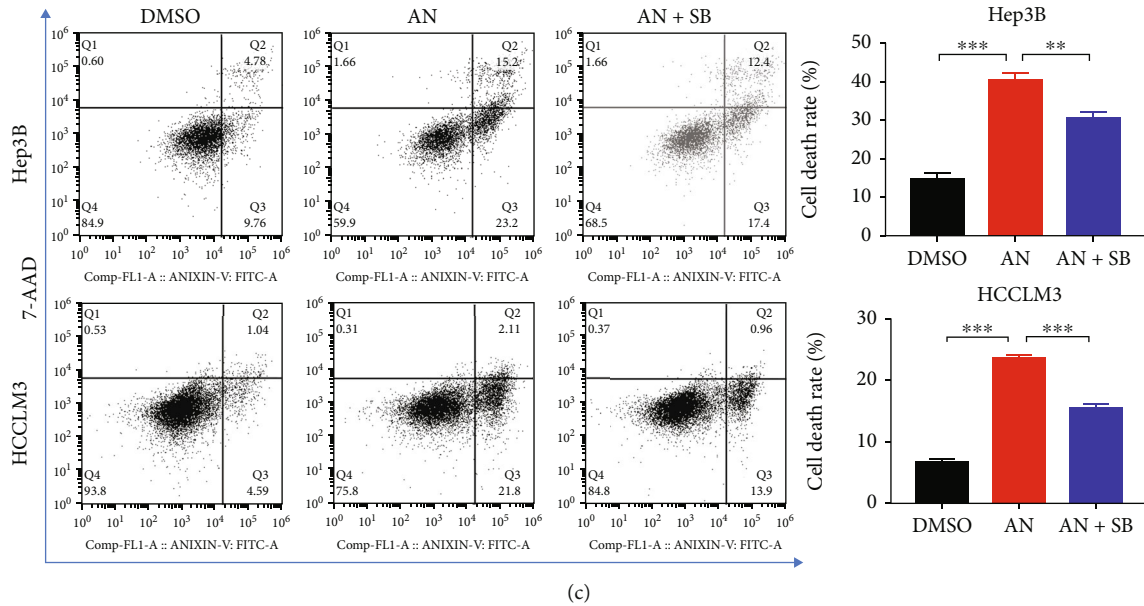


FIGURE 1: Anisomycin (AN) induced HCC cell death through the p38 MAPK pathway. (a) The inhibition rate of Hep3B and HCCLM3 cell proliferation after 24 h treatment with AN. (b) Colony formation of HCC cells under AN treatment. SB203580 (SB), an inhibitor of phosphorylated p38, was used to rescue cells from AN treatment. (c) Cell death rate of HCC cells induced by AN (2.5 μ M for Hep3B or 5 μ M for HCCLM3). (d) The flow cytometry results indicated the accumulation of intracellular lipid reactive oxygen species after 24 h AN treatment. $N = 3$; * $P < 0.05$, ** $P < 0.01$, and *** $P < 0.001$. (e) The expression levels of ferroptosis-related proteins were analyzed by western blotting after 24 h AN treatment.

(Figure 1(d)). Similarly, ferroptosis-related proteins were also analyzed by western blotting. The results showed that the expression levels of nuclear factor erythroid 2-related factor 2 (NRF2), solute carrier family 7 member 11 (SLC7A11), and ferritin heavy chain 1 (FTH1) were downregulated by 24 h anisomycin treatment, and the expression levels of these proteins were recovered by

SB203580 (Figure 1(e)). In general, anisomycin-induced p38 MAPK activation was cytotoxic to HCC cells, and ferroptosis may be involved in this cytotoxic effect.

3.2. Anisomycin Inhibited HCC Cell Migration through the p38 MAPK Signaling Pathway. Cell migration also plays an important role in the steps of tumor progression [51].

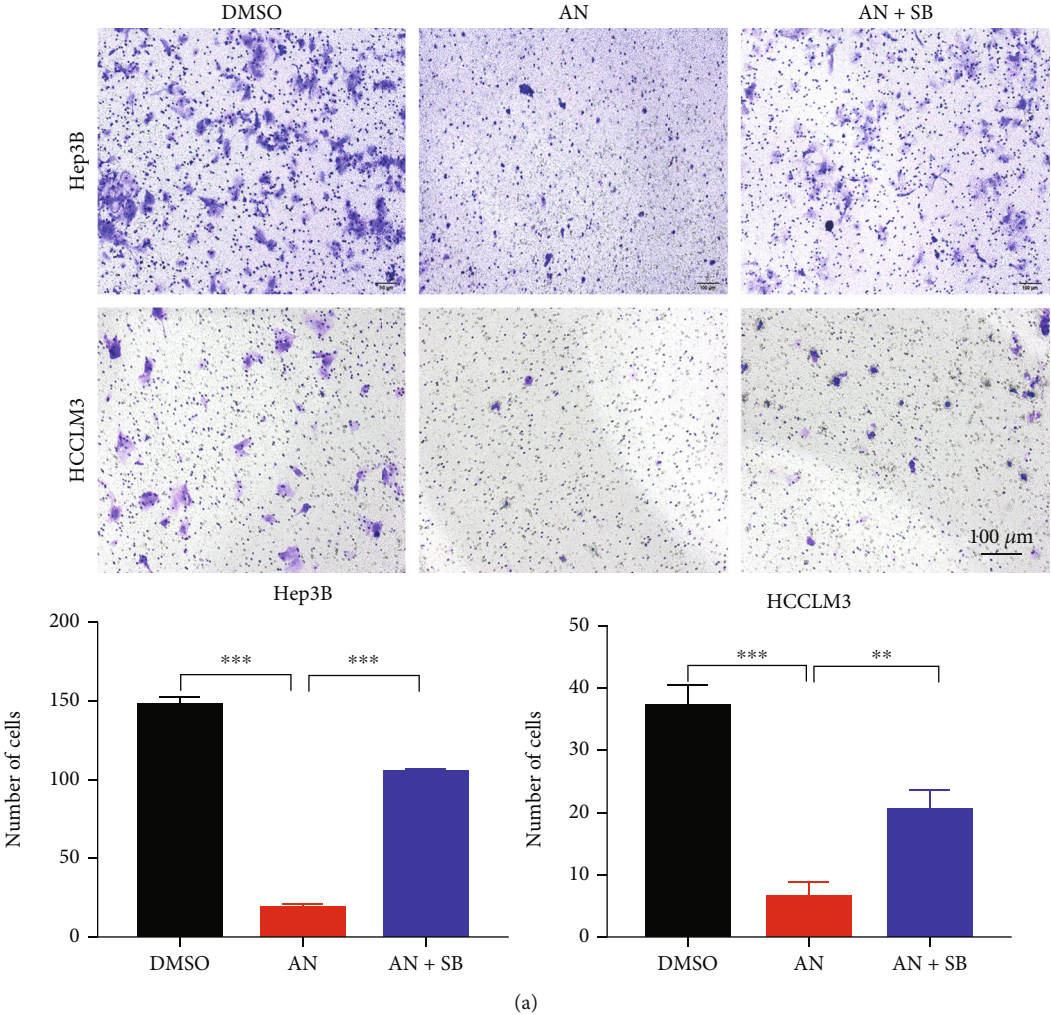


FIGURE 2: Continued.

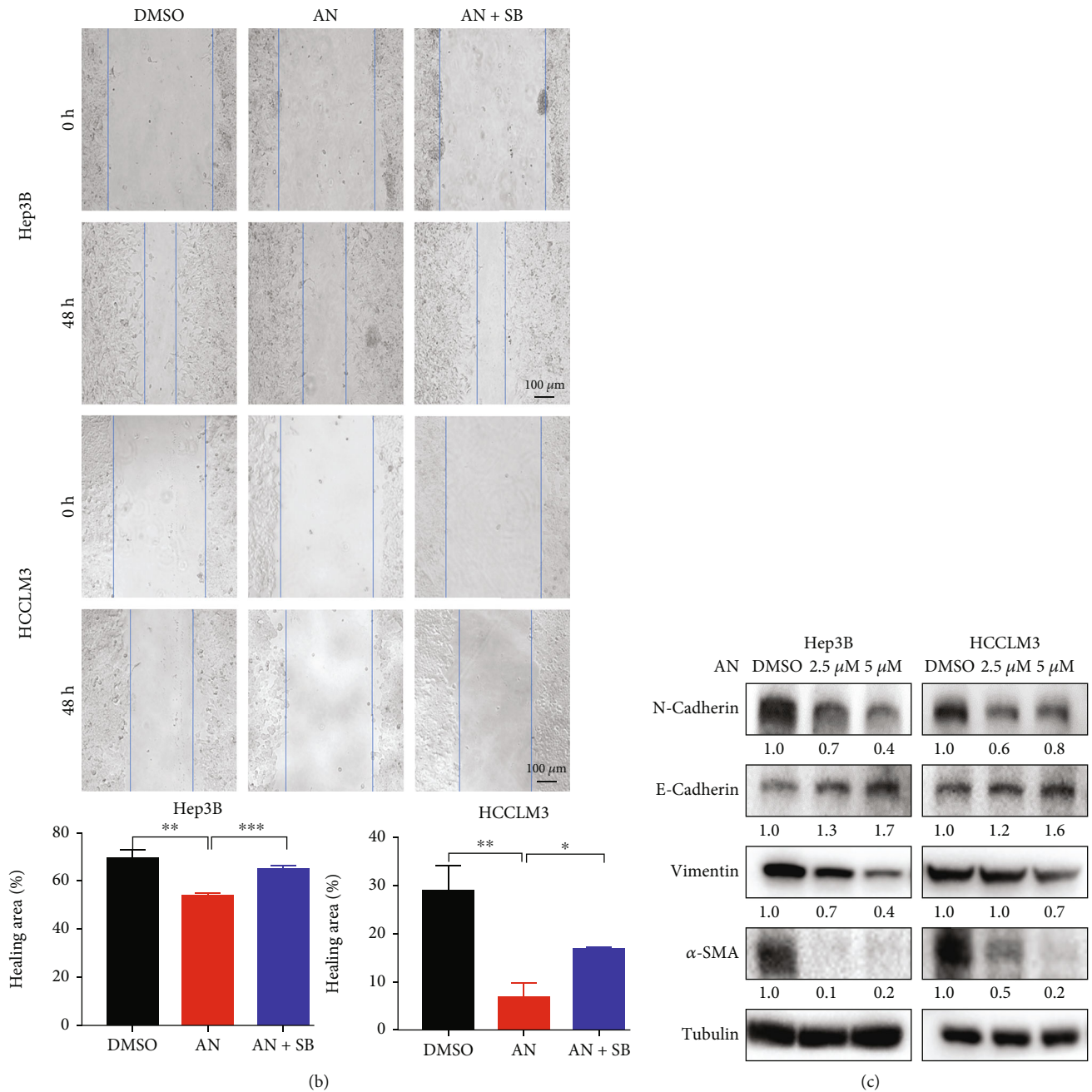


FIGURE 2: Anisomycin (AN) suppressed HCC cell migration through the p38 MAPK pathway. AN suppressed HCC cell migration (a) and healing ability (b). The effect was evaluated by transwell and wound-healing assay. SB203580 (SB) was used to rescue cells from AN treatment. $N = 3$; $*P < 0.05$, $**P < 0.01$, and $***P < 0.001$. (c) The expression levels of epithelial-mesenchymal transition-related proteins in AN treatment (24h).

Transwell and wound-healing assays were performed to assess whether anisomycin could alter the migration ability of HCC cells. The results showed that anisomycin significantly inhibited HCC cell migration, while SB203580 coin-cubation partially alleviated inhibition of HCC cell migration (Figures 2(a) and 2(b)).

The epithelial-mesenchymal transition (EMT) is a process that accelerates HCC cell migration [51]. EMT protein markers (N-cadherin, E-cadherin, vimentin, and α -SMA) were detected during anisomycin treatment by western blot-

ting. After 24h treatment of anisomycin, E-cadherin expression in HCC cells increased, while N-cadherin, vimentin, and α -SMA were decreased (Figure 2(c) and Supplementary Figure 3). The results indicated that anisomycin-activated p38 may inhibit HCC cell migration by inhibiting EMT.

3.3. Anisomycin-Activated p38 MAPK Promoted H3S10 Phosphorylation via Colocalization. Researchers had found that activation of p38 MAPK could promote histone H3 phosphorylation in Ser10 or Ser28 [22–24]. In our study,

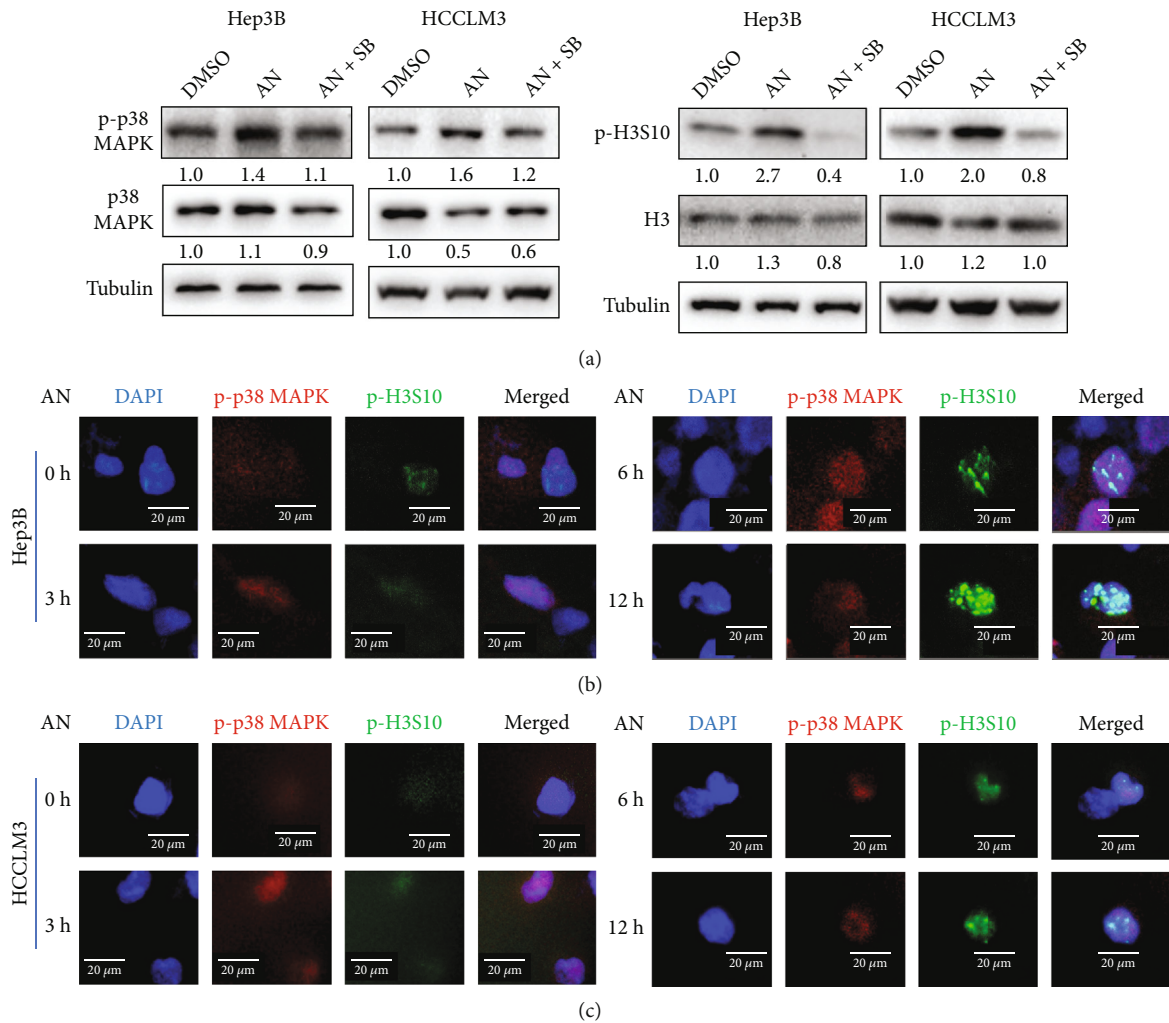
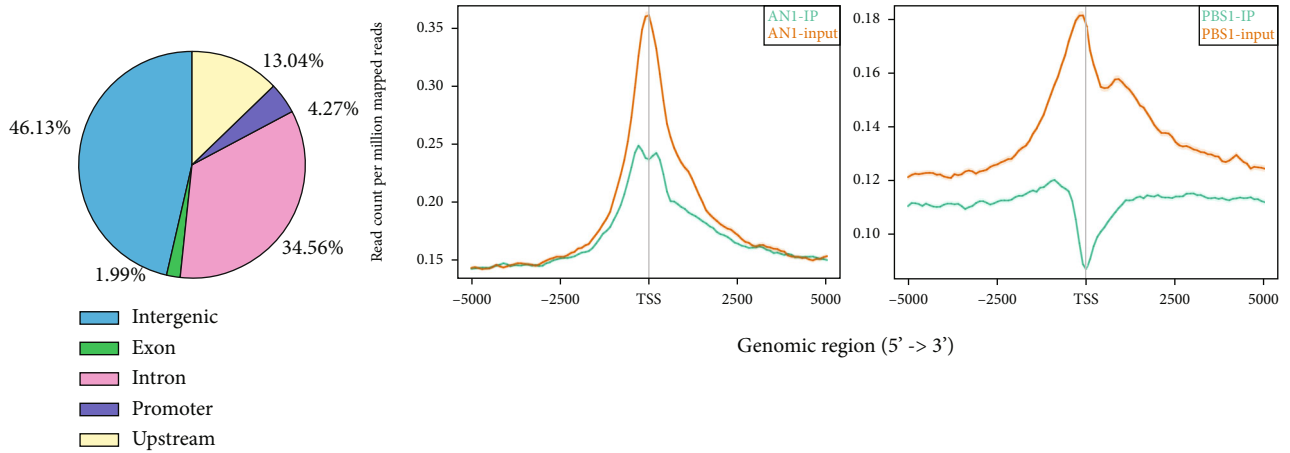


FIGURE 3: Anisomycin (AN) increased phosphorylation of p38 MAPK and H3S10 in HCC cells. (a) Western blotting analysis of p38 MAPK, p-p38 MAPK, H3, and p-H3S10 in HCC cells after a 24 h DMSO, AN, or AN+SB203580 (SB) treatment. Immunofluorescence costained for p-p38 MAPK and p-H3S10 showed their expression levels and cellular localization at different time points of AN treatment in Hep3B (b) and HCCLM3 (c).

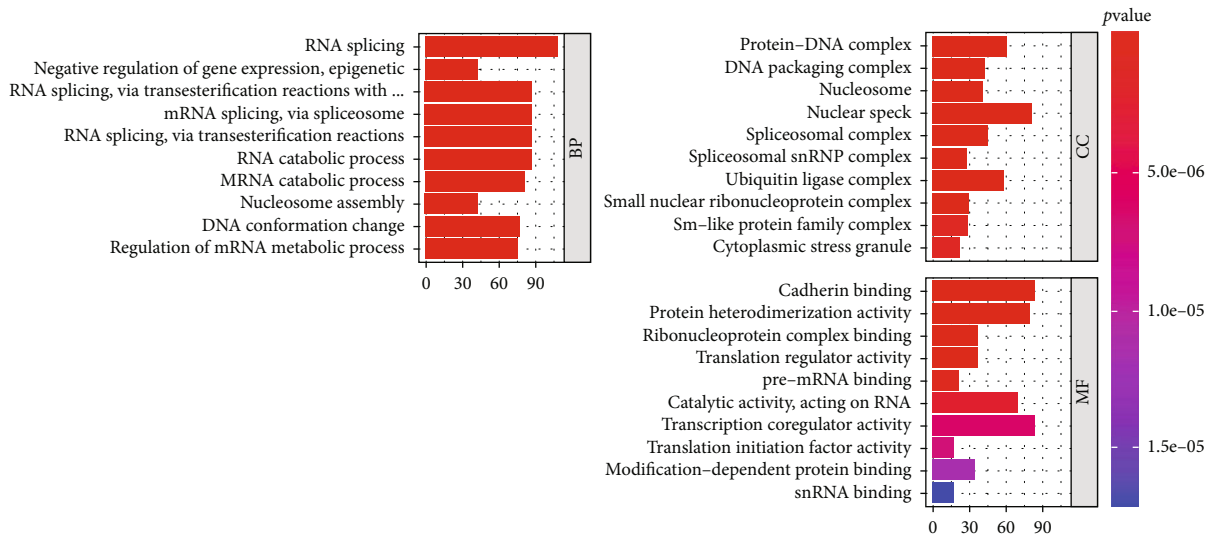
the results of the western blotting showed that p-p38 MAPK and p-H3S10 were upregulated after 24 h anisomycin treatment (Figure 3(a)), while the expression level of p-H3S28 was not obviously upregulated (Supplementary Figure 4), suggesting that anisomycin-activated p38 MAPK induced the phosphorylation of H3S10, rather than of H3S28. In Figure 3(a), we can also see that coincubation of SB203580 reduced the activation of p38 MAPK as well as the phosphorylation of histone H3S10, indicating that anisomycin may induce histone H3S10 phosphorylation in HCC cells through p38 MAPK pathway. Then, we costained p-p38 MAPK and p-H3S10 to show their expression levels and cellular localization in Hep3B and HCCLM3 at different time points of anisomycin treatment. Immunofluorescence results showed that p38 MAPK was activated after anisomycin treatment and subsequently promoted histone H3S10 phosphorylation (Figures 3(b) and 3(c)). After 12 h of anisomycin treatment, histone H3S10 phosphorylation was at a high level, so the

following experiments were mostly performed at 12 h. Furthermore, phosphorylated H3S10 was colocalized with p-p38 MAPK in HCC cells treated with anisomycin, suggesting that anisomycin-induced p-p38 MAPK may phosphorylate histone H3S10 through colocalization.

3.4. Phosphorylated H3S10 Was Enriched in Ferroptosis-Related Gene Promoters. To elucidate the role of phosphorylated H3S10 in anisomycin-induced HCC cell death, ChIP-sequencing was performed in HCCLM3 cells treated with DMSO or anisomycin (Figure 4(a)) for 12 h. Using a P value threshold of 10^{-3} , 2445 differentially enriched regions for peak promoter under anisomycin treatment were identified. GO and KEGG were performed to find the main functions and pathways of the genes corresponding to the differentially enriched promoters. The GO results showed differentially enriched biological processes, cell components, and molecular functions (Figure 4(b)), while the KEGG results revealed the differentially enriched



(a)



(b)

FIGURE 4: Continued.

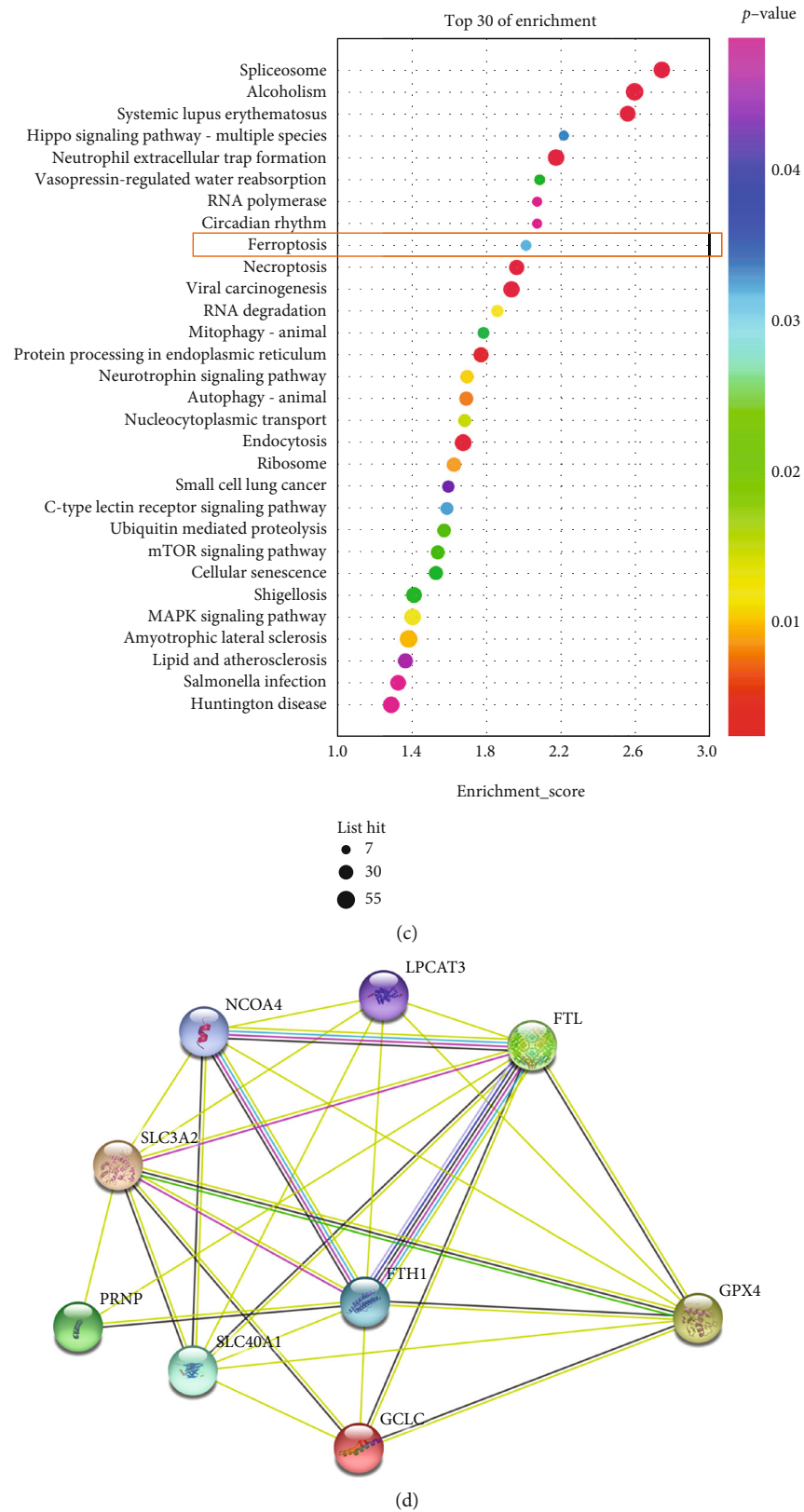


FIGURE 4: Anisomycin-induced phosphorylation of H3S10 was associated with transcriptional activation of ferroptosis-related genes. (a) Representative graphs of chromatin immunoprecipitation- (ChIP-) sequencing results. (b) Gene Ontology (GO) analyses of differentially enriched genes. BP: biological processes; CC: cell components; MF: molecular functions. (c) Kyoto Encyclopedia of Genes and Genomes (KEGG) results ranked by degree of enrichment. (d) Protein-protein interactions of ferroptosis-related genes enriched in the term of ferroptosis in (c) (NCOA4, SLC3A2, LPCAT3, PRNP, FTL, FTH1, SLC40A1, GCLC, and GPX4).

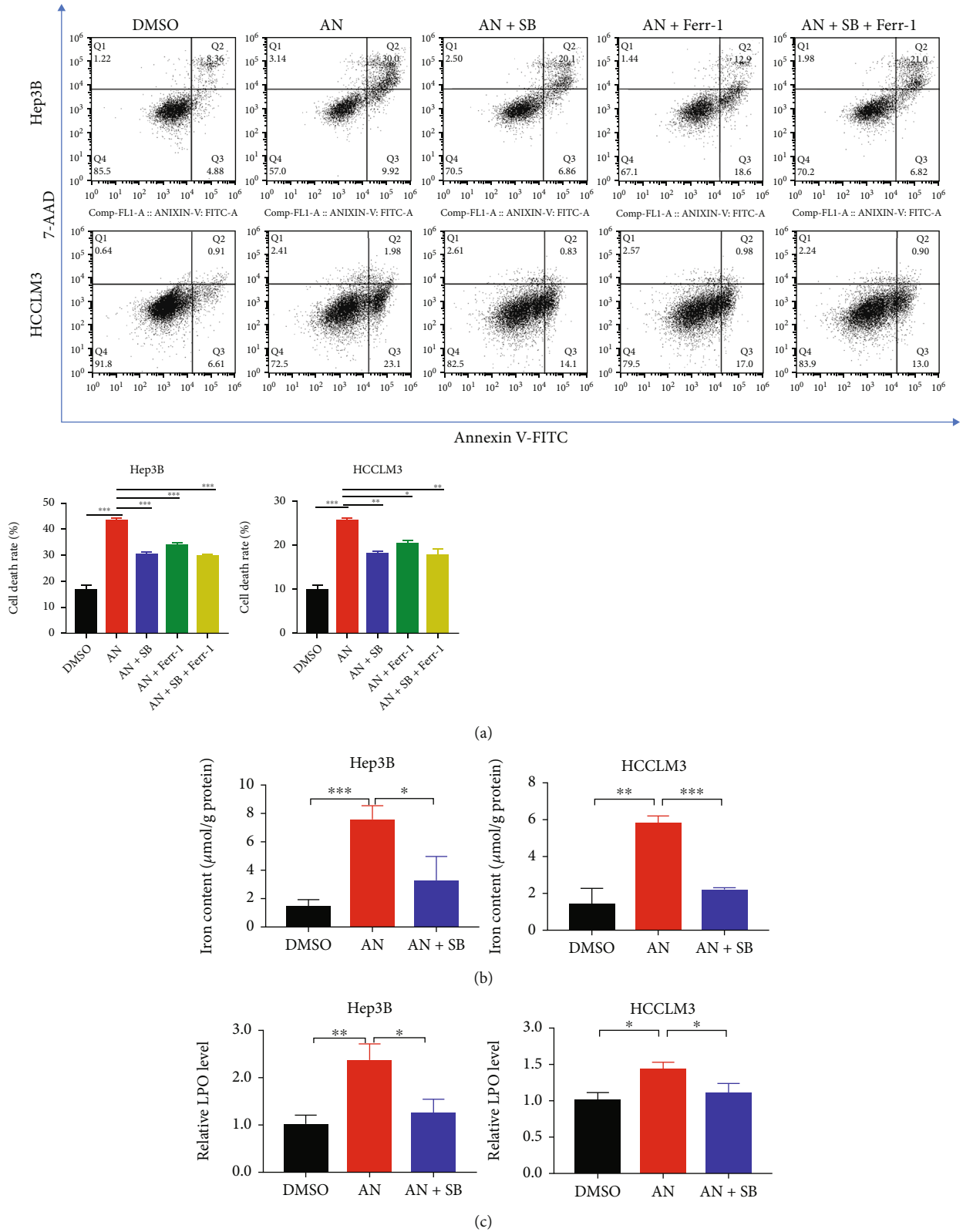


FIGURE 5: Continued.

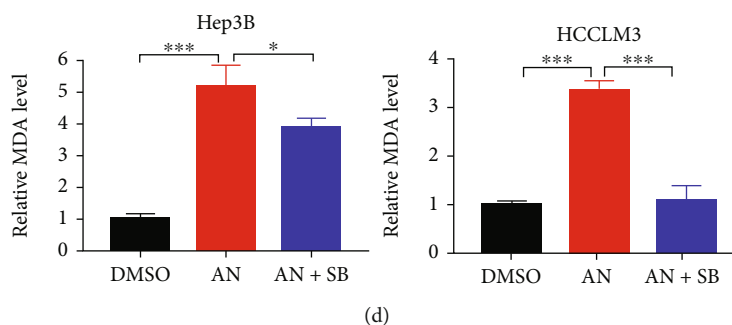


FIGURE 5: Ferroptosis of HCC cells was stimulated by anisomycin (AN) through the p38 MAPK signaling pathway. (a) Cell death was measured by flow cytometry. Ferrostatin-1 (Ferr-1) and SB203580 (SB) were used to inhibit ferroptosis, thus rescuing cells. (b–d) The assays showed that the content of intracellular iron, lipid peroxidation (LPO), and malondialdehyde (MDA) in HCC cells increased after AN treatment (2.5 μ M for Hep3B or 5 μ M for HCCLM3). $N = 3$; * $P < 0.05$, ** $P < 0.01$, and *** $P < 0.001$.

pathways (Figure 4(c)). Since we wanted to know how histone H3S10 is involved in anisomycin-induced HCC cell death, we focused on pathways associated with cell death. The enrichment degree of ferroptosis ranked highest in these cell death-related pathways, leading to the conclusion that p-H3S10 may be involved in the regulation of anisomycin-induced ferroptosis in HCC cells. Nine enriched genes were included in the ferroptosis pathway. The PPI plot showed the connections among the nine proteins (Figure 4(d)).

3.5. Anisomycin Promoted Ferroptosis of HCC Cells through the p38 MAPK Signaling Pathway. To confirm whether anisomycin induces ferroptosis in HCC cells, a series of experiments were conducted. First, a specific ferroptosis inhibitor, ferrostatin-1, was used in cell treatment to see if it could rescue HCC cells from anisomycin-induced cell death. The results showed that anisomycin-induced cell death was partially inhibited by ferrostatin-1 at both 12 h (Supplementary Figure 5) and 24 h (Figure 5(a)), revealing that ferroptosis was involved in anisomycin-induced HCC cell death. In Figure 5(a), anisomycin + SB203580 + ferrostatin-1 is significantly closer to DMSO than anisomycin + ferrostatin-1; it probably means that p38 induced ferroptosis and other forms of cell death together in anisomycin treatment. To further understand anisomycin-induced ferroptosis, we measured major hallmark features of ferroptosis, such as abnormal accumulation of iron and elevation of lipid peroxidation (LPO) and malondialdehyde (MDA). The iron assay showed that iron increased in HCC cells after being treated with anisomycin and that the increase in iron was suppressed by SB203580 (Figure 5(b)). Similar trends were also observed for the content of LPO and MDA (Figures 5(c) and 5(d)). In general, anisomycin could induce ferroptosis through the p38 MAPK signaling pathway in HCC cells.

3.6. NCOA4 Participated in Anisomycin-Induced Ferroptosis in HCC Cells. To further elucidate the potential mechanism of how phosphorylated H3S10 contributed to p38-ferroptosis axis in HCC cells, the mRNA expression levels

of ferroptosis-related genes enriched in ChIP-sequencing were further analyzed by RT-PCR and immunofluorescence. Heatmap shows the stable downregulation of solute carrier family 40 member 1 (SLC40A1), ferritin heavy chain 1 (FTH1) and ferritin light chain (FTL), and stable upregulation of nuclear receptor coactivator 4 (NCOA4) and solute carrier family 3 member 2 (SLC3A2) after anisomycin treatment (Figure 6(a)). The recovery of mRNA expression levels of these five genes was further investigated in the SB203580 coincubation group in Hep3B and HCCLM3 (Figure 6(b)). The expression level of NCOA4 was upregulated in both Hep3B and HCCLM3 cells treated with anisomycin and decreased when SB203580 was coincubated. The SLC40A1 results were exactly the opposite. Many previous studies have shown that phosphorylated histone H3S10 always promotes transcription activation [25, 52, 53]. It was speculated that NCOA4 was the key member, upregulated by the p38 MAPK pathway and phosphorylated H3S10, contributing to anisomycin-induced ferroptosis. The immunofluorescence results confirmed that the protein level of NCOA4 was upregulated in HCC cells soon after anisomycin treatment, and SB203580 alleviated the upregulation of NCOA4 (Figure 6(c) and Supplementary Figure 6A). Our findings suggested that anisomycin-induced activation of p38 MAPK may upregulate NCOA4 by phosphorylating H3S10, thus promoting ferroptosis in HCC cells. To illustrate the important role of NCOA4 in anisomycin-induced ferroptosis, we performed NCOA4 knockdown and overexpression in HCC cells and measured the accumulation of lipid reactive oxygen species by flow cytometry after C11-BODIPY staining to infer the effect of NCOA4 on ferroptosis. We found that anisomycin-induced lipid-ROS in HCC cells was almost completely abolished by NCOA4 knockdown, while NCOA4 overexpression slightly increased anisomycin-induced accumulation of lipid-ROS in HCC cells (Figure 6(d) and Supplementary Figure 6B). RT-PCR was used to test NCOA4 knockdown and overexpression in HCC cells (Supplementary Figure 6C). In conclusion, NCOA4 played an important role in anisomycin-induced ferroptosis in HCC cells.

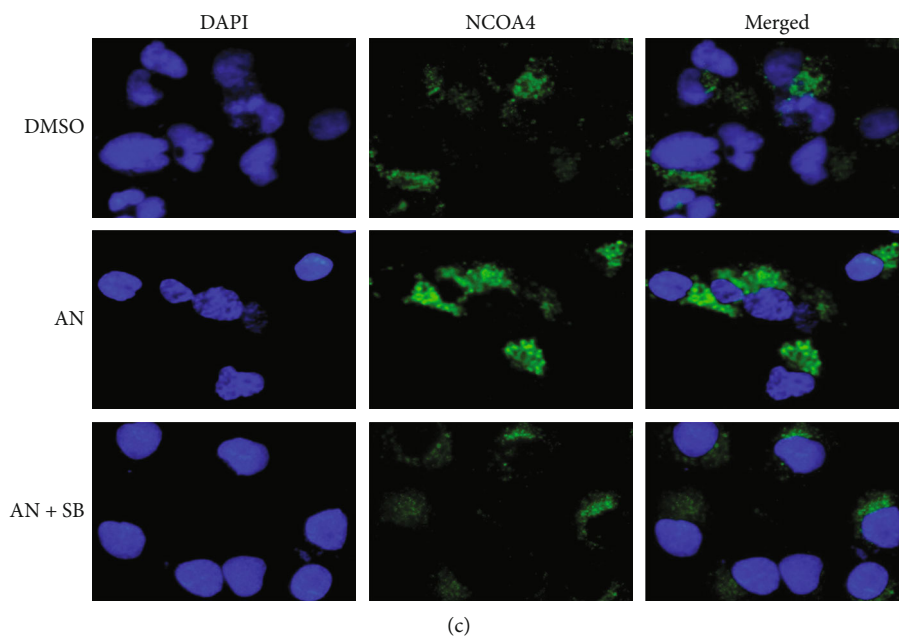
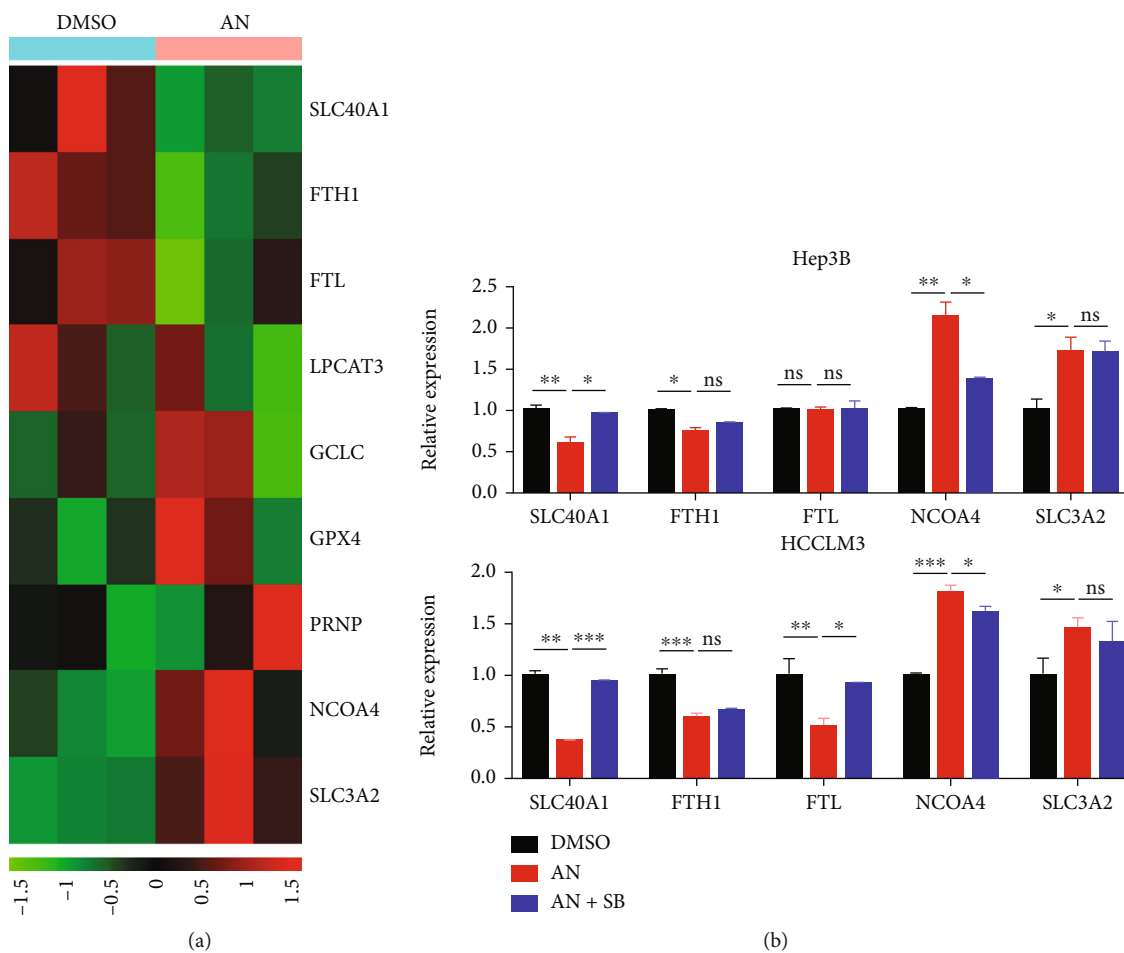
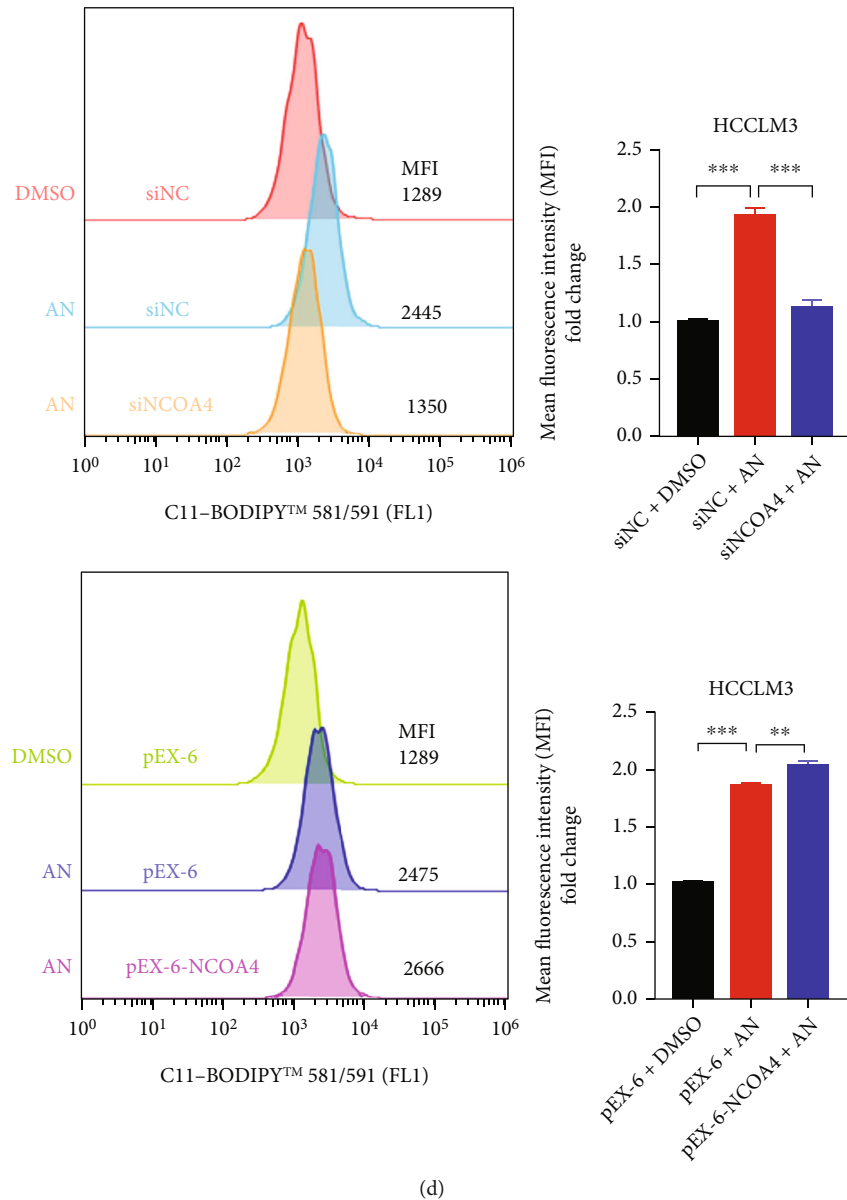


FIGURE 6: Continued.



(d)

FIGURE 6: NCOA4 was upregulated in anisomycin- (AN-) induced ferroptosis. (a) The heatmap based on qRT-PCR indicated changes in ferroptosis-related genes in HCCLM3 after treatment with AN for 12 h. In the inhibitor group, cells were pretreated with SB203580 (SB) for 1 h before being treated with anisomycin ($2.5 \mu\text{M}$ for Hep3B or $5 \mu\text{M}$ for HCCLM3) for 12 h. (b) The qRT-PCR results showed the mRNA expression levels of five ferroptosis-related genes (SLC40A1, FTH1, FTL, NCOA4, and SLC3A2) in different groups of Hep3B and HCCLM3 cells. $N = 3$; $*P < 0.05$, $**P < 0.01$, and $***P < 0.001$. (c) The protein level of NCOA4 was detected in HCC cells after AN treatment by immunofluorescence. (d) The accumulation of lipid-ROS was detected in NCOA4 knockdown or negative control (NC) HCCLM3 after 12 h AN treatment (left). The accumulation of lipid-ROS was detected in NCOA4 cDNA or pEX-6 carrier transfected HCCLM3 after 12 h AN treatment (right).

4. Discussion

Ferroptosis is emerging as a potential mechanism for suppressing tumor growth because it has been shown to accelerate cell death in some malignancies [54, 55]. The studies of Li et al. [56] and Hattori et al. [44] linked the p38 MAPK signaling pathway to ferroptosis; however, the underlying mechanism of how p38 regulates ferroptosis remains unclear. Since the transcriptional expression of various genes

changes during ferroptosis, we speculated that histone modifications may be involved in the regulation of ferroptosis. Many previous studies have shown that activated p38 MAPK could increase the level of p-H3S10 and activate gene transcription by influencing the conformation of chromatin or/and DNA accessibility [27, 28]. Here, we verified the relationship between p38 MAPK and histone H3 modification in HCC and found that anisomycin-activated p38 MAPK was able to activate the level of p-H3S10 by colocalization.

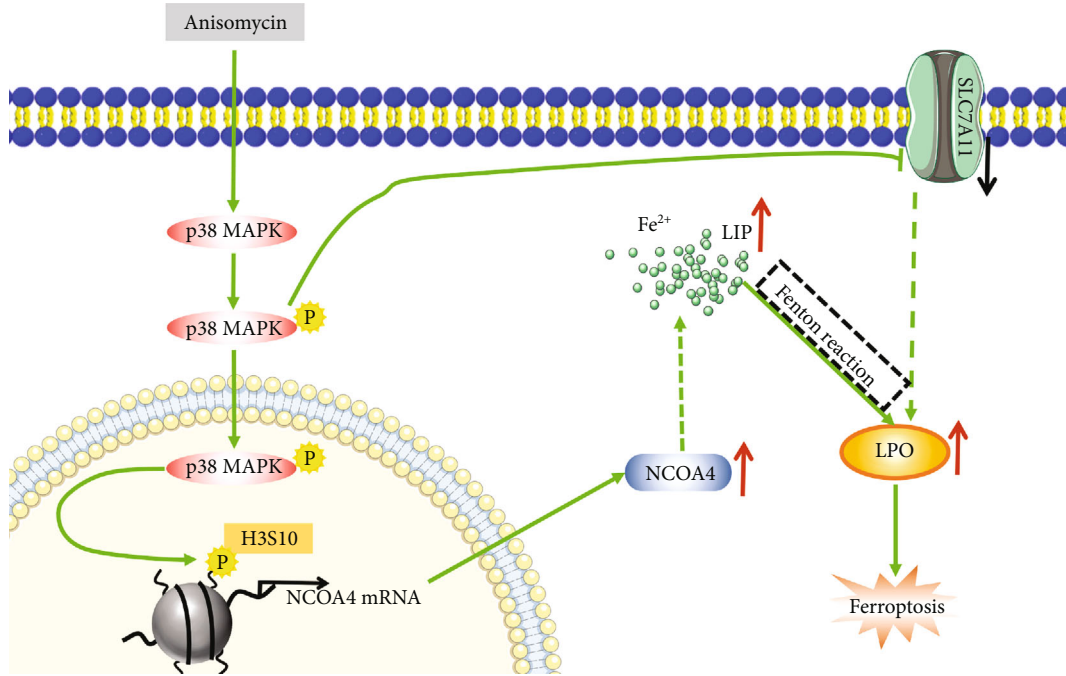


FIGURE 7: Schematic diagram of anisomycin-induced ferroptosis in HCC cells.

The genes regulated by P-H3S10 are involved in a variety of biological processes and pathways. We identified these genes using ChIP-sequencing technology and found that these genes were significantly enriched in ferroptosis by KEGG enrichment analysis. Therefore, anisomycin promoted ferroptosis of HCC cells through the p38 MAPK signaling pathway, as a consequence of being mediated by histone H3S10 phosphorylation.

Our study revealed that anisomycin could induce HCC cell death, which was partially reversed by the p38 MAPK inhibitor (SB203580) and the ferroptosis inhibitor (ferrostatin-1). Anisomycin activated p38 MAPK and then promoted H3S10 phosphorylation by colocalization. Many genes are transcriptionally activated by p-H3S10, including NCOA4, which is one of the drivers of ferroptosis [43, 57]. NCOA4, as a cargo receptor that recruits FTH1 to autophagosomes for lysosomal degradation, could lead to ferritinophagy and iron release and then increases the intracellular labile iron pool (LIP) [58, 59]. The alteration of iron in HCC cells directly increased LPO through the Fenton reaction, leading to ferroptosis of HCC cells [60]. Similarly, Yang et al. [61] reported that p38 activation was involved in upregulation of NCOA4 and downregulation of FTH1 in dental pulp stem cells, which was consistent with our results. In our study, FTH1 was decreased by anisomycin at both protein and RNA level in Figures 1(e) and 6(b). However, coinubation with SB203580 resulted in some recovery of FTH1 protein levels (Figure 1(e)), but no significant recovery in FTH1 RNA levels (Figure 6(b)). We already know that SB203580 coinubation reduced NCOA4, so we believed that the recovery of FTH1 in protein level was mainly caused by the reduction of NCOA4, which in turn reduced its recruitment of FTH1 to autophagosomes [58, 59] and ultimately

lead to reduced FTH1 degradation and reduced iron release [38, 39]. Furthermore, as we can see in Figure 5(e), the solute carrier family 7 member 11 (SLC7A11) was negatively regulated by anisomycin-activated p38 MAPK. However, the protein level of the key molecule of the classical ferroptosis pathway, glutathione peroxidase 4 (GPX4), did not show significant downregulation in HCC cells after anisomycin treatment (Supplementary Figure 7). Therefore, anisomycin-reducing SLC7A11 may be involved in the regulation of ferroptosis through a non-GPX4 inactivation manner. In addition, SLC7A11 functioned to import cystine for glutathione biosynthesis and ferroptosis defense, and NRF2 positively regulated SLC7A11 transcription [62], both of which are ferroptosis suppressors [63, 64]. The study by Wang et al. [65] reported that activation of p38 MAPK could negatively regulate the expression of SLC7A11 in endometrial cancer cells. In summary, anisomycin could induce HCC cell ferroptosis by increasing LPO and LIP (Figure 7).

By detecting intracellular iron, LPO, and MDA, our study demonstrated that anisomycin could induce ferroptosis in HCC cells. The underlying mechanism of how anisomycin induces ferroptosis was also revealed, which identified anisomycin as a novel ferroptosis stimulus distinct from classical ferroptosis inducers, such as erastin, sulfasalazine, and RSL3 [30, 66]. In our study, anisomycin was used to activate p38 MAPK in HCC cells. Nevertheless, anisomycin is also commonly used as an activator of the JNK signaling pathway. Here, we compared the rescue of anisomycin-induced lipid-ROS by SP600125 (an inhibitor of JNK) and SB203580 (Supplementary Figure 8). As we can see, SB203580 almost completely rescued the accumulation of lipid-ROS in HCCLM3. However, the rescue of

anisomycin-induced lipid-ROS by SP600125 was limited. Furthermore, in our study, SB203580, an inhibitor of activated p38 MAPK, partially abrogated the anticancer effects of anisomycin in HCC cells. In conclusion, anisomycin promoted ferroptosis in HCC cells mainly by activating p38 MAPK. Considering the role of p38 MAPK in anisomycin cytotoxicity and the result in supplementary figure 1B, we believed that HCC patients with a low p-p38/p38 ratio may respond better to anisomycin treatment.

It is well known that apoptosis, autophagy, and ferroptosis are different forms of cell death, but they also have some connections to drug treatments [67]. Several studies found that autophagy is a positive regulator of ferroptosis [40, 58, 68]. For example, NCOA4 is one of the key molecules that links autophagy and ferroptosis. Furthermore, iron overload participates not only in the induction of noncanonical ferroptosis but also in endogenous and exogenous apoptosis [34]. Recently, research by Chang et al. [68] revealed that heteronemin could simultaneously induce HCC cell apoptosis and ferroptosis. Besides, HMGB1 has been found to play a vital role in apoptosis, ferroptosis, and autophagy in leukemia cells [32]. From our results, we found that p38 MAPK promoted apoptosis and ferroptosis of HCC cells, making it an ideal target for HCC treatment. Several studies have consistently shown that p38 MAPK was involved in the antiproliferative, apoptotic, and inhibitory effects of EMT in HCC cells [49, 69, 70] and other cancer cells [71–73]. Ras may be involved in the inhibition of HCC cell migration by p38 MAPK pathway, as MAPK provides negative feedback to the Ras activity, which regulates cancer cell migration through PI3K/mTORC2/AKT pathway [74]. Moreover, this mechanism of cell migration is also conserved from 2D culture to 3D organoid [75]. Of course, ferroptosis also has an impact on EMT [76]. The mechanisms involved need to be elucidated by more researchers conducting dedicated studies. In Figure 5(c), there were also necroptosis, autophagy, mitophagy, and cell senescence in the enriched pathways, which suggested that anisomycin-activated p38 MAPK may stimulate HCC cell death through mixed types of cell death. In general, the predominant mode of cell death detected during drug treatment may be related to the concentration of the drug or the duration of treatment [58].

There were also some limitations of our study. First, the function of NCOA4 and FTH1 in ferroptosis was derived from other studies, and no additional experimental validation was performed in our study. Furthermore, how SLC7A11 regulates ferroptosis through a pathway other than GPX4 inactivation in HCC requires further investigation. In addition, the rescue of anisomycin-induced cell death by SB203580 was limited, because anisomycin (AN in figure) is a multifunctional drug that kills cells through multiple targets [77–81]. Moreover, several studies demonstrated that SB203580 could inhibit AKT, and the inhibition of AKT was involved in the induction of ferroptosis and apoptosis [82–84]. We cannot definitively rule out their roles in anisomycin-induced ferroptosis, but we can identify a major role for p38 MAPK. Finally, we will address these limitations to further elucidate the mechanisms of anisomycin-induced HCC cell death in future studies.

In conclusion, anisomycin was confirmed to induce HCC cell ferroptosis through p38 MAPK signaling pathway, and H3S10 phosphorylation may be involved. NCOA4 was revealed to be a key member of p38 MAPK-induced ferroptosis. Furthermore, p38 MAPK may be a worthy target for HCC treatment due to its involvement in various types of cell death.

Data Availability

The data used to support the findings of this study are available from the corresponding authors upon request.

Conflicts of Interest

The authors declare that the research was conducted in the absence of any commercial or financial relationships that could be construed as a potential conflict of interest.

Authors' Contributions

W.C. and T.L. were responsible for the conceptualization. W.C., W.Y., C.Z., and J.Z. were responsible for the methodology. C.W., J.Z., and TL were responsible for the investigation. H.W., T.L., A.J., L.D., J.X., T.T., and B.P. were responsible for the resources. W.C. was responsible for the writing—original draft. W.Y. and H.W. were responsible for the writing—review and editing. W.G. and B.W. were responsible for the supervision. W.G. and B.W. were responsible for the funding acquisition. All authors read and approved the final manuscript. Wei Chen, Wenjing Yang, and Chunyan Zhang contributed equally to this work.

Acknowledgments

Thanks are due to Lihua Lv for her help in the early exploration of this topic. This work was supported by the National Natural Science Foundation of China (81902139, 82102483, 81972000, and 82000275), the Shanghai Medical Key Specialty (ZK2019B28), the Constructing Project of Clinical Key Disciplines in Shanghai (shslczdzk03302), the Specialized Fund for the Clinical Researches of Zhongshan Hospital affiliated Fudan University (2018ZSLC05 and 2020ZSLC54), the Excellent Backbone Plan of Zhongshan Hospital in 2021 (2021ZSGG08), and the Key Medical and Health Projects of Xiamen (YDZX20193502000002).

Supplementary Materials

Supplementary Table 1: the primers used in this study. Supplementary Figure 1: expression levels of p38 MAPK and p-p38 MAPK in 6 HCC cell lines and their inhibition rates at different concentrations of anisomycin for 24 h. Supplementary Figure 2: the expression levels of stemness-related proteins and apoptosis-related proteins. Supplementary Figure 3: the expression levels of epithelial-mesenchymal transition-related proteins in HCC cells after 24 h DMSO, anisomycin (AN), or AN+SB203580 (SB) treatment. Supplementary Figure 4: the protein expression level of p-H3S28 in Hep3B and HCCLM3 after 24 h anisomycin

(AN) treatment. Supplementary Figure 5: cell death rate detection was performed on cells treated with DMSO, anisomycin (AN), or AN+ ferrostatin-1 (AN+Ferr-1) for 12 h by flow cytometry. Supplementary Figure 6: NCOA4 played an important role in the p38-ferroptosis axis. Supplementary Figure 7: the protein expression levels of GPX4 in Hep3B and HCCLM3 cells. SB203580 (SB) was used to rescue cells from anisomycin (AN) treatment. Supplementary Figure 8: the rescue of anisomycin-induced lipid-ROS by SB203580 and SP600125 in HCCLM3 cells after 24 h treatment or cocubation. (*Supplementary Materials*)

References

- [1] H. Tian, S. Zhao, E. C. Nice et al., “A cascaded copper-based nanocatalyst by modulating glutathione and cyclooxygenase-2 for hepatocellular carcinoma therapy,” *Journal of Colloid and Interface Science*, vol. 607, Part 2, pp. 1516–1526, 2022.
- [2] A. Forner, M. Reig, and J. Bruix, “Hepatocellular carcinoma,” *Lancet*, vol. 391, no. 10127, pp. 1301–1314, 2018.
- [3] A. Huang, X. R. Yang, W. Y. Chung, A. R. Dennison, and J. Zhou, “Targeted therapy for hepatocellular carcinoma,” *Signal Transduction and Targeted Therapy*, vol. 5, no. 1, p. 146, 2020.
- [4] A. Martínez-Limón, M. Joaquin, M. Caballero, F. Posas, and E. de Nadal, “The p38 pathway: from biology to cancer therapy,” *International Journal of Molecular Sciences*, vol. 21, no. 6, p. 1913, 2020.
- [5] Y. Yao, L. Cui, J. Ye et al., “Dioscin facilitates ROS-induced apoptosis via the p38-MAPK/HSP27-mediated pathways in lung squamous cell carcinoma,” *International Journal of Biological Sciences*, vol. 16, no. 15, pp. 2883–2894, 2020.
- [6] L. Zhang, D. Huang, D. Shao et al., “Fenretinide inhibits the proliferation and migration of human liver cancer HepG2 cells by downregulating the activation of myosin light chain kinase through the p38-MAPK signaling pathway,” *Oncology Reports*, vol. 40, no. 1, pp. 518–526, 2018.
- [7] G. Li, Y. Lin, Y. Zhang et al., “Endometrial stromal cell ferroptosis promotes angiogenesis in endometriosis,” *Cell Death Discovery*, vol. 8, no. 1, p. 29, 2022.
- [8] Y. Lin, X. Shen, Y. Ke et al., “Activation of osteoblast ferroptosis via the METTL3/ASK1-p38 signaling pathway in high glucose and high fat (HGHF)-induced diabetic bone loss,” *The FASEB Journal*, vol. 36, no. 3, article e22147, 2022.
- [9] J. Yang, J. Mo, J. Dai et al., “Cetuximab promotes RSL3-induced ferroptosis by suppressing the Nrf2/HO-1 signalling pathway in KRAS mutant colorectal cancer,” *Cell Death & Disease*, vol. 12, no. 11, p. 1079, 2021.
- [10] Q. Song, S. Peng, F. Che, and X. Zhu, “Artesunate induces ferroptosis via modulation of p38 and ERK signaling pathway in glioblastoma cells,” *Journal of Pharmacological Sciences*, vol. 148, no. 3, pp. 300–306, 2022.
- [11] X. Qiu, Q. Shi, X. Zhang, X. Shi, H. Jiang, and S. Qin, “LncRNA A2M-AS1 promotes ferroptosis in pancreatic cancer via interacting with PCBP3,” *Molecular Cancer Research*, vol. 20, no. 11, pp. 1636–1645, 2022.
- [12] L. Wang, S. Wu, H. He et al., “CircRNA-ST6GALNAC6 increases the sensitivity of bladder cancer cells to erastin-induced ferroptosis by regulating the HSPB1/P38 axis,” *Laboratory Investigation*, 2022.
- [13] M. Bébien, S. Salinas, C. Becamel, V. Richard, L. Linares, and R. A. Hipskind, “Immediate-early gene induction by the stresses anisomycin and arsenite in human osteosarcoma cells involves MAPK cascade signaling to Elk-1, CREB and SRF,” *Oncogene*, vol. 22, no. 12, pp. 1836–1847, 2003.
- [14] Y. Liu, J. Ge, Q. Li et al., “Low-dose anisomycin sensitizes glucocorticoid-resistant T-acute lymphoblastic leukemia CEM-C1 cells to dexamethasone-induced apoptosis through activation of glucocorticoid receptor and p38-MAPK/JNK,” *Leukemia & Lymphoma*, vol. 55, no. 9, pp. 2179–2188, 2014.
- [15] I. Banik, P. F. Cheng, C. M. Dooley et al., “NRASQ61K melanoma tumor formation is reduced by p38-MAPK14 activation in zebrafish models and NRAS-mutated human melanoma cells,” *Pigment Cell & Melanoma Research*, vol. 34, no. 2, pp. 150–162, 2021.
- [16] V. N. Ivanov, O. Fodstad, and Z. Ronai, “Expression of ring finger-deleted TRAF2 sensitizes metastatic melanoma cells to apoptosis via up-regulation of p38, TNF α and suppression of NF- κ B activities,” *Oncogene*, vol. 20, no. 18, pp. 2243–2253, 2001.
- [17] Y. Chen, F. Gao, R. Jiang et al., “Down-regulation of AQP4 expression via p38 MAPK signaling in temozolomide-induced glioma cells growth inhibition and invasion impairment,” *Journal of Cellular Biochemistry*, vol. 118, no. 12, pp. 4905–4913, 2017.
- [18] Y. Xia, P. You, F. Xu, J. Liu, and F. Xing, “Novel functionalized selenium nanoparticles for enhanced anti-hepatocarcinoma activity in vitro,” *Nanoscale Research Letters*, vol. 10, no. 1, p. 1051, 2015.
- [19] M. Kim, S. J. Lee, S. Shin, K. S. Park, S. Y. Park, and C. H. Lee, “Novel natural killer cell-mediated cancer immunotherapeutic activity of anisomycin against hepatocellular carcinoma cells,” *Scientific Reports*, vol. 8, no. 1, article 10668, 2018.
- [20] Y. Shen, W. Wei, and D. X. Zhou, “Histone acetylation enzymes coordinate metabolism and gene expression,” *Trends in Plant Science*, vol. 20, no. 10, pp. 614–621, 2015.
- [21] P. Tessarz and T. Kouzarides, “Histone core modifications regulating nucleosome structure and dynamics,” *Nature Reviews Molecular Cell Biology*, vol. 15, no. 11, pp. 703–708, 2014.
- [22] W. G. Kaelin and S. L. McKnight, “Influence of metabolism on epigenetics and disease,” *Cell*, vol. 153, no. 1, pp. 56–69, 2013.
- [23] M. H. Dyson, S. Thomson, M. Inagaki et al., “MAP kinase-mediated phosphorylation of distinct pools of histone H3 at S10 or S28 via mitogen- and stress-activated kinase 1/2,” *Journal of Cell Science*, vol. 118, no. 10, pp. 2247–2259, 2005.
- [24] Y. S. Keum, H. G. Kim, A. M. Bode, Y. J. Surh, and Z. Dong, “UVB-induced COX-2 expression requires histone H3 phosphorylation at Ser10 and Ser28,” *Oncogene*, vol. 32, no. 4, pp. 444–452, 2013.
- [25] A. Soloaga, S. Thomson, G. R. Wiggin et al., “MSK2 and MSK1 mediate the mitogen- and stress-induced phosphorylation of histone H3 and HMG-14,” *The EMBO Journal*, vol. 22, no. 11, pp. 2788–2797, 2003.
- [26] T. Jenuwein and C. D. Allis, “Translating the histone code,” *Science*, vol. 293, no. 5532, pp. 1074–1080, 2001.
- [27] K. M. Johansen and J. Johansen, “Regulation of chromatin structure by histone H3S10 phosphorylation,” *Chromosome Research*, vol. 14, no. 4, pp. 393–404, 2006.
- [28] S. J. Nowak and V. G. Corces, “Phosphorylation of histone H3: a balancing act between chromosome condensation and

- transcriptional activation," *Trends in Genetics*, vol. 20, no. 4, pp. 214–220, 2004.
- [29] H. Kikuchi, B. Yuan, E. Yuhara, N. Takagi, and H. Toyoda, "Involvement of histone H3 phosphorylation through p38 MAPK pathway activation in casticin-induced cytotoxic effects against the human promyelocytic cell line HL-60," *International Journal of Oncology*, vol. 43, no. 6, pp. 2046–2056, 2013.
- [30] S. J. Dixon, K. M. Lemberg, M. R. Lamprecht et al., "Ferroptosis: an iron-dependent form of nonapoptotic cell death," *Cell*, vol. 149, no. 5, pp. 1060–1072, 2012.
- [31] B. Hassannia, P. Vandenabeele, and B. T. Vanden, "Targeting ferroptosis to iron out cancer," *Cancer Cell*, vol. 35, no. 6, pp. 830–849, 2019.
- [32] F. Ye, W. Chai, M. Xie et al., "HMGB1 regulates erastin-induced ferroptosis via RAS-JNK/p38 signaling in HL-60/NRAS(Q61L) cells," *American Journal of Cancer Research*, vol. 9, no. 4, pp. 730–739, 2019.
- [33] B. Hassannia, B. Wiernicki, I. Ingold et al., "Nano-targeted induction of dual ferroptotic mechanisms eradicates high-risk neuroblastoma," *The Journal of Clinical Investigation*, vol. 128, no. 8, pp. 3341–3355, 2018.
- [34] T. Nakamura, I. Naguro, and H. Ichijo, "Iron homeostasis and iron-regulated ROS in cell death, senescence and human diseases," *Biochimica et Biophysica Acta - General Subjects*, vol. 1863, no. 9, pp. 1398–1409, 2019.
- [35] Y. Fang, X. Chen, Q. Tan, H. Zhou, J. Xu, and Q. Gu, "Inhibiting ferroptosis through disrupting the NCOA4-FTH1 interaction: a new mechanism of action," *ACS Central Science*, vol. 7, no. 6, pp. 980–989, 2021.
- [36] J. D. Mancias, X. Wang, S. P. Gygi, J. W. Harper, and A. C. Kimmelman, "Quantitative proteomics identifies NCOA4 as the cargo receptor mediating ferritinophagy," *Nature*, vol. 509, no. 7498, pp. 105–109, 2014.
- [37] H. Chen, C. Wang, Z. Liu et al., "Ferroptosis and its multifaceted role in cancer: mechanisms and therapeutic approach," *Antioxidants*, vol. 11, no. 8, p. 1504, 2022.
- [38] S. Ni, Y. Yuan, Z. Qian et al., "Hypoxia inhibits RANKL-induced ferritinophagy and protects osteoclasts from ferroptosis," *Free Radical Biology & Medicine*, vol. 169, pp. 271–282, 2021.
- [39] L. Li, H. Li, Y. Li et al., "Ferritinophagy-mediated ROS production contributed to proliferation inhibition, apoptosis, and ferroptosis induction in action of mechanism of 2-pyridylhydrazone dithiocarbamate acetate," *Oxidative Medicine and Cellular Longevity*, vol. 2021, Article ID 5594059, 17 pages, 2021.
- [40] Y. Zhang, Y. Kong, Y. Ma et al., "Loss of COPZ1 induces NCOA4 mediated autophagy and ferroptosis in glioblastoma cell lines," *Oncogene*, vol. 40, no. 8, pp. 1425–1439, 2021.
- [41] H. Zhou, Y. L. Zhou, J. A. Mao et al., "NCOA4-mediated ferritinophagy is involved in ionizing radiation-induced ferroptosis of intestinal epithelial cells," *Redox Biology*, vol. 55, article 102413, 2022.
- [42] F. Yao, J. Peng, E. Zhang et al., "Pathologically high intraocular pressure disturbs normal iron homeostasis and leads to retinal ganglion cell ferroptosis in glaucoma," *Cell Death & Differentiation*, 2022.
- [43] W. Hou, Y. Xie, X. Song et al., "Autophagy promotes ferroptosis by degradation of ferritin," *Autophagy*, vol. 12, no. 8, pp. 1425–1428, 2016.
- [44] K. Hattori, H. Ishikawa, C. Sakauchi, S. Takayanagi, I. Naguro, and H. Ichijo, "Cold stress-induced ferroptosis involves the ASK1-p38 pathway," *EMBO Reports*, vol. 18, no. 11, pp. 2067–2078, 2017.
- [45] P. Henklova, R. Vrzal, B. Papouskova et al., "SB203580, a pharmacological inhibitor of p38 MAP kinase transduction pathway activates ERK and JNK MAP kinases in primary cultures of human hepatocytes," *European Journal of Pharmacology*, vol. 593, no. 1-3, pp. 16–23, 2008.
- [46] G. Miotto, M. Rossetto, M. L. Di Paolo et al., "Insight into the mechanism of ferroptosis inhibition by ferrostatin-1," *Redox Biology*, vol. 28, article 101328, 2020.
- [47] Z. Ye, Q. Zhuo, Q. Hu et al., "FBW7-NRA41-SCD1 axis synchronously regulates apoptosis and ferroptosis in pancreatic cancer cells," *Redox Biology*, vol. 38, article 101807, 2021.
- [48] K. Deng, L. Liu, X. Tan et al., "WIP1 promotes cancer stem cell properties by inhibiting p38 MAPK in NSCLC," *Signal Transduction and Targeted Therapy*, vol. 5, no. 1, 2020.
- [49] A. L. Jin, C. Y. Zhang, W. J. Zheng et al., "CD155/SRC complex promotes hepatocellular carcinoma progression via inhibiting the p38 MAPK signalling pathway and correlates with poor prognosis," *Clinical and Translational Medicine*, vol. 12, no. 4, article e794, 2022.
- [50] Y. A. Yang, G. M. Zhang, L. Feigenbaum, and Y. E. Zhang, "Smad3 reduces susceptibility to hepatocarcinoma by sensitizing hepatocytes to apoptosis through downregulation of Bcl-2," *Cancer Cell*, vol. 9, no. 6, pp. 445–457, 2006.
- [51] G. Giannelli, P. Koudelkova, F. Daturi, and W. Mikulits, "Role of epithelial to mesenchymal transition in hepatocellular carcinoma," *Journal of Hepatology*, vol. 65, no. 4, pp. 798–808, 2016.
- [52] V. Anest, J. L. Hanson, P. C. Cogswell, K. A. Steinbrecher, B. D. Strahl, and A. S. Baldwin, "A nucleosomal function for I κ B kinase- α in NF- κ B-dependent gene expression," *Nature*, vol. 423, no. 6940, pp. 659–663, 2003.
- [53] W.-S. Lo, L. Duggan, N. C. Tolga et al., "Snf1—a histone kinase that works in concert with the histone acetyltransferase Gcn5 to regulate transcription," *Science*, vol. 293, no. 5532, pp. 1142–1146, 2001.
- [54] C. Liang, X. Zhang, M. Yang, and X. Dong, "Recent progress in ferroptosis inducers for cancer therapy," *Advanced Materials*, vol. 31, no. 51, article e1904197, 2019.
- [55] J. P. Friedmann Angeli, D. V. Krysko, and M. Conrad, "Ferroptosis at the crossroads of cancer-acquired drug resistance and immune evasion," *Nature Reviews Cancer*, vol. 19, no. 7, pp. 405–414, 2019.
- [56] L. Li, Y. Hao, Y. Zhao et al., "Ferroptosis is associated with oxygen-glucose deprivation/reoxygenation-induced Sertoli cell death," *International Journal of Molecular Medicine*, vol. 41, no. 5, pp. 3051–3062, 2018.
- [57] P. L. Lin, H. H. Tang, S. Y. Wu, N. S. Shaw, and C. L. Su, "Saponin formosanin C-induced ferritinophagy and ferroptosis in human hepatocellular carcinoma cells," *Antioxidants*, vol. 9, no. 8, p. 682, 2020.
- [58] M. Gao, P. Monian, Q. Pan, W. Zhang, J. Xiang, and X. Jiang, "Ferroptosis is an autophagic cell death process," *Cell Research*, vol. 26, no. 9, pp. 1021–1032, 2016.
- [59] R. Bellelli, G. Federico, A. Matte et al., "NCOA4 deficiency impairs systemic iron homeostasis," *Cell Reports*, vol. 14, no. 3, pp. 411–421, 2016.

- [60] Z. Shen, T. Liu, Y. Li et al., “Fenton-reaction-acceleratable magnetic nanoparticles for ferroptosis therapy of orthotopic brain tumors,” *ACS Nano*, vol. 12, no. 11, pp. 11355–11365, 2018.
- [61] A. Yang, L. Wang, K. Jiang, L. Lei, and H. Li, “Nuclear receptor coactivator 4-mediated ferritinophagy drives proliferation of dental pulp stem cells in hypoxia,” *Biochemical and Biophysical Research Communications*, vol. 554, pp. 123–130, 2021.
- [62] P. Koppula, L. Zhuang, and B. Gan, “Cystine transporter SLC7A11/xCT in cancer: ferroptosis, nutrient dependency, and cancer therapy,” *Protein & Cell*, vol. 12, no. 8, pp. 599–620, 2021.
- [63] L. Jiang, J. H. Hickman, S. J. Wang, and W. Gu, “Dynamic roles of p53-mediated metabolic activities in ROS-induced stress responses,” *Cell Cycle*, vol. 14, no. 18, pp. 2881–2885, 2015.
- [64] X. Sun, Z. Ou, R. Chen et al., “Activation of the p62-Keap1-NRF2 pathway protects against ferroptosis in hepatocellular carcinoma cells,” *Hepatology*, vol. 63, no. 1, pp. 173–184, 2016.
- [65] H. Wang, S. Peng, J. Cai, and S. Bao, “Silencing of PTPN18 induced ferroptosis in endometrial cancer cells through p-P38-mediated GPX4/xCT down-regulation,” *Cancer Management and Research*, vol. 13, pp. 1757–1765, 2021.
- [66] J. Y. Cao and S. J. Dixon, “Mechanisms of ferroptosis,” *Cellular and Molecular Life Sciences*, vol. 73, no. 11–12, pp. 2195–2209, 2016.
- [67] D. Tang, R. Kang, T. V. Berghe, P. Vandenamee, and G. Kroemer, “The molecular machinery of regulated cell death,” *Cell Research*, vol. 29, no. 5, pp. 347–364, 2019.
- [68] W. T. Chang, Y. D. Bow, P. J. Fu et al., “A marine terpenoid, heteronemin, induces both the apoptosis and ferroptosis of hepatocellular carcinoma cells and involves the ROS and MAPK pathways,” *Oxidative medicine and cellular longevity*, vol. 2021, Article ID 7689045, 12 pages, 2021.
- [69] C. C. Chiu, J. Y. Chen, K. L. Lin et al., “p38 MAPK and NF- κ B pathways are involved in naphtho[1,2-b] furan-4,5-dione induced anti-proliferation and apoptosis of human hepatoma cells,” *Cancer Letters*, vol. 295, no. 1, pp. 92–99, 2010.
- [70] W. P. Zhu, Z. Y. Liu, Y. M. Zhao et al., “Dihydropyrimidine dehydrogenase predicts survival and response to interferon- α in hepatocellular carcinoma,” *Cell Death & Disease*, vol. 9, no. 2, p. 69, 2018.
- [71] X. Sui, N. Kong, L. Ye et al., “p38 and JNK MAPK pathways control the balance of apoptosis and autophagy in response to chemotherapeutic agents,” *Cancer Letters*, vol. 344, no. 2, pp. 174–179, 2014.
- [72] H. J. Kim, J. E. Oh, S. W. Kim, Y. J. Chun, and M. Y. Kim, “Ceramide induces p38 MAPK-dependent apoptosis and Bax translocation via inhibition of Akt in HL-60 cells,” *Cancer Letters*, vol. 260, no. 1–2, pp. 88–95, 2008.
- [73] S. Wen, Y. Hou, L. Fu et al., “Cancer-associated fibroblast (CAF)-derived IL32 promotes breast cancer cell invasion and metastasis via integrin β 3-p38 MAPK signalling,” *Cancer Letters*, vol. 442, pp. 320–332, 2019.
- [74] H. Zhan, S. Bhattacharya, H. Cai, P. A. Iglesias, C. H. Huang, and P. N. Devreotes, “An excitable Ras/PI3K/ERK signaling network controls migration and oncogenic transformation in epithelial cells,” *Developmental Cell*, vol. 54, no. 5, pp. 608–623.e5, 2020.
- [75] N. M. Neumann, M. C. Perrone, J. H. Veldhuis et al., “Coordination of receptor tyrosine kinase signaling and interfacial tension dynamics drives radial intercalation and tube elongation,” *Developmental Cell*, vol. 45, no. 1, pp. 67–82.e6, 2018.
- [76] P. Chen, Q. Wu, J. Feng et al., “Erianin, a novel dibenzyl compound in Dendrobium extract, inhibits lung cancer cell growth and migration via calcium/calmodulin-dependent ferroptosis,” *Signal Transduction and Targeted Therapy*, vol. 5, no. 1, p. 51, 2020.
- [77] M. Nikaido, T. Otani, N. Kitagawa et al., “Anisomycin, a JNK and p38 activator, suppresses cell-cell junction formation in 2D cultures of K38 mouse keratinocyte cells and reduces claudin-7 expression, with an increase of paracellular permeability in 3D cultures,” *Histochemistry and Cell Biology*, vol. 151, no. 5, pp. 369–384, 2019.
- [78] D. Monaghan, E. O’Connell, F. L. Cruickshank et al., “Inhibition of protein synthesis and JNK activation are not required for cell death induced by anisomycin and anisomycin analogues,” *Biochemical and Biophysical Research Communications*, vol. 443, no. 2, pp. 761–767, 2014.
- [79] H. Tan, B. Hu, F. Xie, C. Zhu, and Z. Cheng, “Anisomycin sensitizes non-small-cell lung cancer cells to chemotherapeutic agents and epidermal growth factor receptor inhibitor via suppressing PI3K/Akt/mTOR,” *Fundamental & Clinical Pharmacology*, vol. 35, no. 5, pp. 822–831, 2021.
- [80] Y. Li, J. Hu, H. Song, and T. Wu, “Antibiotic anisomycin selectively targets leukemia cell lines and patient samples through suppressing Wnt/ β -catenin signaling,” *Biochemical and Biophysical Research Communications*, vol. 505, no. 3, pp. 858–864, 2018.
- [81] V. Croons, W. Martinet, A. G. Herman, J. P. Timmermans, and G. R. De Meyer, “The protein synthesis inhibitor anisomycin induces macrophage apoptosis in rabbit atherosclerotic plaques through p38 mitogen-activated protein kinase,” *The Journal of Pharmacology and Experimental Therapeutics*, vol. 329, no. 3, pp. 856–864, 2009.
- [82] F. V. Lali, A. E. Hunt, S. J. Turner, and B. M. Foxwell, “The Pyridinyl Imidazole Inhibitor SB203580 Blocks Phosphoinositide-dependent Protein Kinase Activity, Protein Kinase B Phosphorylation, and Retinoblastoma Hyperphosphorylation in Interleukin-2-stimulated T Cells Independently of p38 Mitogen-activated Protein Kinase,” *The Journal of Biological Chemistry*, vol. 275, no. 10, pp. 7395–7402, 2000.
- [83] D. Tang, X. Chen, R. Kang, and G. Kroemer, “Ferroptosis: molecular mechanisms and health implications,” *Cell Research*, vol. 31, no. 2, pp. 107–125, 2021.
- [84] J. Hao, W. Zhang, and Z. Huang, “Bupivacaine modulates the apoptosis and ferroptosis in bladder cancer via phosphatidylinositol 3-kinase (PI3K)/AKT pathway,” *Bioengineered*, vol. 13, no. 3, pp. 6794–6806, 2022.

Research Article

Hypoxia Enhances Glioma Resistance to Sulfasalazine-Induced Ferroptosis by Upregulating SLC7A11 via PI3K/AKT/HIF-1 α Axis

Shicheng Sun, Changfa Guo, Taihong Gao, Dengzhen Ma, Xiangsheng Su , Qi Pang ,
and Rui Zhang 

Department of Neurosurgery, Shandong Provincial Hospital Affiliated to Shandong First Medical University, Jinan, 250021 Shandong, China

Correspondence should be addressed to Rui Zhang; rui.zhang@sdu.edu.cn

Received 1 July 2022; Revised 19 August 2022; Accepted 4 September 2022; Published 18 November 2022

Academic Editor: Lianxiang Luo

Copyright © 2022 Shicheng Sun et al. This is an open access article distributed under the Creative Commons Attribution License, which permits unrestricted use, distribution, and reproduction in any medium, provided the original work is properly cited.

Glioma is the most common primary brain tumor, with a high rate of recurrence and treatment resistance. Glioblastoma is highly invasive, infiltrating surrounding brain parenchyma, and is known to cause intracranial metastasis resulting in a dismal prognosis. Hypoxia contributes significantly to chemo- and radiotherapy resistance in cancer. Ferroptosis is a nonapoptotic oxidative cell death that has been identified as a potential anticancer mechanism. Sulfasalazine (SAS) activates ferroptosis and plays a potential role in tumor treatment. However, the relationship between hypoxia and SAS resistance has not been elucidated. This study is aimed at investigating the role of hypoxia in SAS-induced ferroptosis and the underlying mechanisms. Here, we found that hypoxia significantly suppressed SAS-induced ferroptosis by upregulating SLC7A11 expression in the U87 and U251 glioma cell lines. Hypoxia promotes SLC7A11 expression by enhancing the PI3K/AKT/HIF-1 α pathway. The AKT inhibitor MK-2206 and HIF-1 α inhibitor PX-478 significantly reversed this effect. In addition, under normoxia, PX-478 induced a higher lipid peroxidation level by decreasing SLC7A11 expression in the U87 and U251 cells but could not induce cell death directly; it could significantly enhance the tumor cell killing effect of SAS. In vivo, the combination of PX-478 and SAS had a coordinated synergistic effect on anticancer activity, as revealed by subcutaneous and orthotopic xenograft mouse models. In conclusion, hypoxia enhanced glioma resistance to SAS-induced ferroptosis by upregulating SLC7A11 via activating the PI3K/AKT/HIF-1 α axis. Combination therapy with PX-478 and SAS may be a potential strategy against glioma.

1. Background

Glioma is the most common primary malignant brain tumor in adults, glioblastoma is its most malignant and aggressive form, and they typically arise from glial or precursor cells and develop into astrocytoma, oligodendroglioma, ependymoma, or oligoastrocytoma [1]. Glioblastoma is an anaplastic, poorly differentiated malignant tumor with a peak incidence between 45 and 70 years [2]. Despite recent advances in diverse therapies for glioma, including surgery, radiotherapy, and chemotherapy, the median survival remains approximately at 15 months [3, 4]. Therefore, developing more efficient therapeutic strategies is imperative.

The tumor microenvironment (TME) refers to the local biological environment in which solid tumors are located [5]. The TME often displays at least some degree of hypoxia

[6]. Coincidentally, gliomas undergo malignant progression under hypoxic conditions [7]. Tumor hypoxia is generated by irregular and tortuous vasculature formed within solid tumors, resulting in poor delivery of oxygen to cells. Hypoxia is associated with malignancy and tumor aggressiveness by increasing tumor cell proliferation and metastasis [8]. In addition, hypoxia has been associated with resistance to radiotherapy and chemotherapy. It also contributes to radioresistance by controlling several cellular processes, including cell cycle, apoptosis and senescence, creation of reactive oxygen species, invasion, and cancer cell stemness [9–12]. Previous studies showed that hypoxia also enhanced the resistance to temozolomide by different mechanisms, such as inducing ferritin light chain, regulating glioma stem cell properties, and mediating ATP-binding cassette proteins [13–15]. Hypoxia-inducible factor (HIF) is upregulated in

the tumor hypoxia microenvironment, in which HIF-1 α and HIF-2 α are considered as the main response regulators [16]. Under hypoxia, HIF-1 α is stabilized and translocated into the nucleus to play a role in transcription [17]. As a selective HIF-1 α inhibitor, PX-478 interferes with HIF-1 α and induces cell cycle arrest in cancer cells [18, 19]. Hypoxia and HIFs play important roles in glioma growth and survival through regulation of several key cell biological process, including glycolytic metabolism, angiogenesis, and drug resistance [20].

Ferroptosis is a nonapoptotic oxidative cell death that plays an essential role in various diseases, including cranial trauma, neuronal diseases, and brain tumors [21]. By analyzing 1,750 gliomas from four independent cohorts, ferroptosis was identified as the most enriched type of programmed cell death in glioma which was widely involved in malignancy progression and drug resistance [22]. Lipid peroxidation underlies the ferroptosis mechanism [23]. SLC7A11-glutathione peroxidase 4 (GPX4) axis, ferroptosis suppressor protein 1 (FSP1)-ubiquinol, and dihydroorotate dehydrogenase (DHODH)-ubiquinol axis constitute three major ferroptosis defense systems through the inhibition of lipid peroxidation. SLC7A11, the cystine/glutamate antiporter to synthesize GSH, neutralizes the oxidative substances in the cell membrane [24]. Sulfasalazine (SAS), a widely recognized antirheumatoid arthritis drug, has been recently found to play an anticancer role in various cancers including malignant gliomas by activating ferroptosis by inhibiting SLC7A11 [25]. SAS had fewer side effects when applied in vivo and better water solubility than other ferroptosis inducers [26, 27]. To date, the relationship between hypoxia and SAS-induced ferroptosis in glioma has not been reported. In the present study, we investigated the role of hypoxia in SAS-induced ferroptosis in glioma cell lines and its underlying molecular mechanisms. Our study not only identified a novel mechanism for SAS resistance but also suggested a novel treatment through a combination of ferroptosis activator and HIF-1 α inhibitor.

2. Material and Methods

2.1. Cell Lines. Human glioma cell lines U87 and U251 were directly purchased from Cell Bank of Type Culture Collection of Chinese Academy of Sciences (Shanghai, China). The U87 and U251 cell lines have been authenticated by STR profiling. These cells were cultured in high glucose Dulbecco's modified Eagle's medium (DMEM, Gibco, USA) with 10% fetal bovine serum (FBS, Biological, Industries) and 1% penicillin-streptomycin (10378016, Invitrogen, USA) at 37°C with 5% CO₂.

2.2. Cell Growth and Cell Viability Assay. Cell growth was determined using a Cell Counting Kit-8 (CCK-8) assay kit (HY-K0301, MCE, Shanghai, China). The U87 and U251 cells were seeded into 96-well plates for 0, 24, 48, and 72 h at a density of 3000 cells per well. Then, 10 μ l CCK-8 solution was added to each well and incubated with the cells for 2 h. Absorbance (Abs) was detected at 450 nm using a microplate reader (Bio-Rad, Hercules, CA, USA).

For cell viability assay, the cells were seeded at 1000 cells per well in 96-well plates with fresh medium and analyzed by using the CCK-8 assay kit according to the above instructions. Reagent used contained SAS (HY-14655, MCE, USA), HIF-2 α -IN-4 (HY-136748, MCE, USA), PX-478 (HY-10231, MCE, USA), and MK-2206 (HY-10358, MCE, USA). Cell viability = (Abs of the experimental group – Abs of the blank group)/(Abs of the control group – Abs of the blank group) \times 100%. The half-maximal inhibitory concentrations (IC₅₀) of SAS was determined using cell viability assay.

2.3. Vector Construction and Transduction. Stable overexpression of SLC7A11 and the control in cells were achieved by transfection with lentivirus synthesized by Genomeditech (Shanghai, China). The cells were infected with Lv-SLC7A11 or negative control lentivirus vectors. SLC7A11 siRNA was used to silence SLC7A11 gene expression. The target sequence of SLC7A11 was 5'-CCAUAUACAUGGCACCAUTT-3'. Scrambled siRNA targeting 5'TTCTCCGAACGTGTACCGT-3' was used as a negative control.

2.4. RNA Extraction and Quantitative Real-Time PCR Array. Total RNA was extracted from cultured cells using a total RNA extraction kit (RC112-01, Vazyme Biotech, Nanjing, China). The concentration and purity of RNA were measured by the absorbance at 260 nm and the ratio of 260/280 nm in NanoDrop ND-1000 (NanoDrop, Wilmington, DE, USA). Total RNA from each sample was reversely transcribed using an all-in-one cDNA synthesis superMix (R333-01, Vazyme Biotech, Nanjing, China). SYBR Green PCR kit (R311-02, Vazyme Biotech, Nanjing, China) was used for real-time PCR. The primers of related genes are listed in Table S1. Quantitative PCR arrays are designed to analyze a panel of ferroptosis-related genes in human glioma cell lines U87 and U251 following the instructions of the manufacturer (Wcgene Biotechnology Corporation, China). The thermocycling conditions used in RT-qPCR were as follows: (1) 95°C for 30 s and (2) 95°C for 5 s and 60°C for 30 s (step 2 requires 45 cycles to be repeated).

2.5. Western Blot Analysis. Protein samples from the cells were lysed in cell lysis buffer (P0013C, Beyotime, Shanghai, China) containing protease/phosphate inhibitors (P1050, Beyotime Biotechnology, Shanghai, China). The concentration of the protein homogenates was determined using the BCA assay Kit (P0012, Beyotime, Shanghai, China). Equal volumes of protein samples were separated by SDS-polyacrylamide gel electrophoresis and electrotransferred to PVDF membranes (Millipore, Billerica, MA, USA). And the percentage of polyacrylamide in SDS-PAGE is 10%. After being blocked with 5% nonfat milk dissolved in TBST (10 mM Tris, 150 mM NaCl, and 0.1% Tween-20; pH 7.6), for 2 h at room temperature, the membranes were incubated with the primary antibodies overnight at 4°C. Thereafter, membranes were incubated with the secondary antibodies coupled to horseradish peroxidase (HRP) for 1 h at room temperature. Protein bands were visualized with a supersensitive electrochemiluminescence (ECL) reagent (WBULS0100, Millipore, USA). The primary antibodies were goat polyclonal

anti-SLC7A11/xCT (ab60171, ab175186, Abcam, USA, 1/1000), rabbit monoclonal anti-STEAP3 (ab151566, Abcam, USA, 1/1000), rabbit monoclonal anti-CA9 (ab108351, Abcam, USA, 1/500), rabbit polyclonal anti- β -actin (ab8227, Abcam, USA, 1/2000), rabbit monoclonal anti-HIF-1 α (ab179483, Abcam, USA, 1/500), rabbit monoclonal anti-PI3K-gamma (ab32089, Abcam, USA, 1/1000), rabbit monoclonal anti-AKT (4691, CST, USA, 1/1000), and rabbit monoclonal anti-p-AKT (4060, CST, USA, 1/2000). The secondary antibody used in western blotting was goat anti-rabbit IgG H&L (HRP) (ab6721, Abcam, USA, 1/5000).

2.6. Immunofluorescence (IF) and Immunohistochemistry (IHC). The U87 and U251 cells were grown on cover slides, fixed, blocked with 3% BSA, and permeabilized with PBS containing 0.1% *w/v* Triton X-100. The mouse brain of the orthotopic intracranial mouse model was cut in the thickness of 20 μ m by a frozen section and blocked with 3% BSA. For protein detection, the primary antibodies used have been already described. For IF, secondary antibodies were donkey anti-goat IgG H&L (ab150129, Abcam, USA). Nuclei were stained by 4,6-diamidino-2-phenylindole (DAPI). Image acquisition was performed on ImageXpress Micro Confocal devices. IHC staining was performed by using Immunofluorescence Two-Step Test Kit (PV-9000, ZSGB-BIO, Beijing China) according to the manufacturer's instructions. Image acquisition was performed on an OLYMPUS BX63 microscope.

2.7. Clone Formation Assay. The U87 and U251 cells (3×10^2 cells/plate) were seeded in 35 mm plates and grew for 2 weeks before being fixed with 4% paraformaldehyde for 15 min at room temperature. The cells were washed twice with PBS and stained with Crystal Violet Staining Solution (C0121, Beyotime Biotechnology, Shanghai, China).

2.8. TUNEL Assay. For the terminal deoxynucleotidyl transferase (TdT) dUTP nick-end labeling (TUNEL) assays, the U87 and U251 cells were seeded into 96-well plates at 1×10^4 cells per well treated with saline, PX-478, SAS, or PX-478 combined with SAS for 24 hours. The cells were then stained with the TMR (red) TUNEL Cell Apoptosis Detection Kit (G1502, Servicebio, China) according to the manufacturer's protocol. Images were acquired with an ImageXpress Micro Confocal (Molecular Devices, USA), and the percentage of TUNEL-positive cells was calculated.

2.9. Cell Apoptosis Analysis by Flow Cytometry. Cell apoptosis was measured by the Annexin V-fluorescein isothiocyanate (FITC)/propidium iodide (PI) kit (BD556547, BD Bioscience, USA). Briefly, the U87 and U251 cells were seeded into 6-well plates treated with saline, PX-478, SAS, or PX-478 combined with SAS for 24 hours, and then, the cells were collected and washed twice with cold PBS. Next, the cells were resuspended in 1x binding buffer at a concentration of 1×10^6 cells per ml and transferred 100 μ l of the solution (1×10^5 cells) to a 5 ml culture tube. Incubate with 5 μ l Annexin V-FITC and 10 μ l PI for 15 min at (RT) 25°C in the dark, and then, add 400 μ l of 1x binding buffer to each

tube. The results were analyzed using a FACS Calibur or an EPICS XL flow cytometer (BD Biosciences).

2.10. TCGA Data Analysis. mRNA expression data from the TCGA database was used to assess correlation between HIF-1 α and SLC7A11 expressions. The analyses were performed using the online analysis software named cBioPortal (<http://www.cbioportal.org>). We used whole-exome and/or whole-genome sequencing of 257 tumor/normal pairs in glioma (TCGA, Cell 2013) study [28].

2.11. Malondialdehyde (MDA) Assay. The relative MDA concentration in cell lysate and tumor tissue was assessed using an MDA Assay kit (BC0025, Servicebio, China) according to the manufacturer's instructions [29]. Measure the absorbance at 532 nm using a microplate reader.

2.12. Subcutaneous Xenograft and Orthotopic Xenograft Mouse Model. All experimental animal procedures were conducted strictly by the Guide for the Care and Use of Laboratory Animals and approved by the Animal Care and Use Committee of the Shandong provincial hospital. The male BALB/c nude mice were randomized and divided into 5 groups in a blinded manner, each group including six 4-week-old nude mice. The animals were anesthetized by intraperitoneal injection of 0.6% pentobarbital sodium, 70 mg/kg, prior to intracranial injection. In the subcutaneous xenograft model, the 1×10^6 U87 cells were subcutaneously implanted in the right flanks of nude mice. At the second week after injection, the control group was intraperitoneally administered with DMSO; meanwhile, orally give saline twice a day; SAS group was intraperitoneally administered with SAS (8 mg in 0.2 ml saline twice daily); meanwhile, orally give saline twice a day for two weeks; PX-478 group was intraperitoneally administered with DMSO; meanwhile, orally give PX-478 (100 mg/kg) twice a day; PX478+SAS group was intraperitoneally administered with SAS; meanwhile, orally give PX-478; PX-478+Lv-SLC7A11+SAS group was subcutaneously implanted 1×10^6 Lv-SLC7A11-transfected U87 cells and was intraperitoneally administered with SAS; meanwhile, orally give PX-478. From the eighth day of the experiment, tumor size was monitored by measuring length (*L*) and width (*W*) with a Vernier caliper every 3 days. The volume of subcutaneous tumor was calculated using the following formula: $V = L \times W^2/2$. In addition, we comprehensively evaluated the state of experimental animals by observing their hair color, abdominal respiration, external genitalia, claw and toe characteristics, etc. At day 23 after implantation, subcutaneous tumors were collected, fixed with 4% paraformaldehyde, and sectioned for measurement. The largest subcutaneous tumor in mice was 9.6 mm in length, 8.7 mm in width, and 363.3 mm³ in volume.

In the orthotopic xenograft mouse model, each mouse was intracranially injected with 1×10^5 luciferase-transfected U87 cells in 10 μ l PBS solution using a stereotactic head frame at a depth of 3 mm through a bur hole placed 2 mm lateral and 2 mm posterior to the bregma. At the second week after injection, mice received SAS and PX-478 treatment the same as subcutaneous xenograft model for 2 weeks. In vivo tumor

growth was monitored with a Xenogen IVIS Spectrum system (PerkinElmer) every week after implantation.

Humane endpoints were established in our study are as follows: (1) significant weight loss for 4 consecutive days; (2) 20% less weight than before the study; (3) Inability to eat or drink; (4) dyspnea: typical symptoms are mouth and nose salivation and/or cyanosis; (5) persistent diarrhea, treatment ineffective; (6) organ failure, respiratory distress; and (7) animals are on the verge of death or unable to move, or do not respond to gentle stimulation. We euthanized the experimental animals by carbon dioxide inhalation asphyxiation.

2.13. Lipid Peroxide Assay. Lipid peroxide level was analyzed by flow cytometry using C11-BODIPY dye. The U87 and U251 cells were seeded into 6-well plates at 3×10^5 cells per well and treated with ferroptosis inducer SAS as well as ferroptosis inhibitor ferrostatin-1 (HY-100579, MCE, Shanghai, China). The culture medium was replaced with 1 ml medium containing $10 \mu\text{M}$ of C11-BODIPY (D3861, Thermo Fisher Scientific, USA), and then, the cells were incubated for 30 min in a humidified incubator (at 37°C , 5% CO_2). The media then were removed and washed cells with PBS three times. For measurement using fluorescence microscope, images were acquired with an ImageXpress Micro Confocal (Molecular Devices, USA). For measurement using flow cytometry, the cells were harvested in 15 ml tubes and resuspended in $500 \mu\text{l}$ of PBS. The cell suspension was filtered through cell strainer ($0.4 \mu\text{m}$ nylon mesh). The results were analyzed using a FACS Calibur or an EPICS XL flow cytometer (BD Biosciences).

2.14. Transmission Electron Microscopy Assay. Transmission electron microscopy analyses were conducted [30]. Briefly, the U87 and U251 cells were seeded into 6-well plates at 3×10^5 cells per well and exposed to saline, PX-478, or Lv-SLC7A11 combined with PX-478 for 24 h. After that, the cells were collected, washed three times with PBS, and fixed with 2.5% glutaraldehyde. The samples were then pretreated according to standard procedures including staining, dehydration, embedding, and slicing to obtain ultrathin sections. During the analysis, images were acquired using a HITACHI-7000 transmission electron microscope (TEM; Hitachi, Tokyo, Japan).

2.15. Statistical Analysis. Data were presented as mean values \pm standard deviation (SD) from at least three experiments. Student's unpaired *t*-test used to analyze the differences between two groups and one-way analysis of variance (ANOVA) used for the comparison among three or more groups were conducted using GraphPad Prism 8 (GraphPad Software, CA, USA) and SPSS (IBM, NY, USA). We used Student-Newman-Keuls (SNK) *q* test ($n < 4$) and least significant difference (LSD) *t*-test ($n > 4$) to perform ANOVA post hoc test. The correlation analysis was conducted using TCGA database by cBioPortal (<http://www.cbioportal.org/>). Statistical analysis contained Spearman's correlation analysis and Pearson's correlation analysis. *P* values less than 0.05 were considered statistically significant (* $P < 0.05$ and ** $P < 0.01$).

3. Results

3.1. Hypoxia Protected Glioma Cells against SAS-Induced Ferroptosis. Hypoxia (1% O_2 , 5% CO_2 , and 94% N_2) is a crucial factor contributing to the aggressive behavior of gliomas [31]. We first explored cell viability at different concentrations of SAS for 24 h. We found that glioma cells in a hypoxic environment became less sensitive to SAS (Figure 1(a)). The half-maximal inhibitory concentrations (IC_{50}) of the hypoxic U87 and U251 cells to SAS were significantly higher than that of normoxic cells (Figure 1(b)). Furthermore, the lipid peroxidation level was measured by flow immunolabeling using a C11-BODIPY probe. The results showed that the high lipid peroxidation level induced by SAS ($500 \mu\text{M}$, 24 h) was decreased under hypoxia condition or by ferroptosis inhibitor Fer-1 (ferrostatin-1, $0.5 \mu\text{M}$, 24 h) incubation (Figure 1(c)). Moreover, we explored the effects of hypoxia and SAS on colony formation. We found that hypoxia and Fer-1 enhanced the colony-forming ability of cells treated with $500 \mu\text{M}$ SAS for 2 weeks (Figure 1(d)). Together, these results suggest that hypoxic environment decreased the sensitivity of glioma cells to SAS.

3.2. SLC7A11 Acted as a Potential Effector Molecule of Hypoxia. To identify potential genes that play vital roles in SAS resistance under hypoxic conditions, a ferroptosis profiling qPCR array was employed by comparing hypoxic cells and normoxic cells. Considering SAS would cause compensatory changes in many ferroptosis-related genes and ferroptosis profiling qPCR array limited the target genes to a small range, we choose to compare the gene changes between hypoxic and normoxic cells. Each group was repeated four times (Figure 2(a)). Heterogeneity of tumor cells resulted in diverse qPCR array results between the U87 and U251 cells. Considering that both cell lines showed decreased SAS sensitivity, we detected genes that changed significantly in both cell lines as potential targets. Three genes were identified as follows: SLC7A11, STEAP3 metalloredutase (STEAP3), and carbonic anhydrase 9 (CA9) (Figure 2(b)). Next, we determined the protein expression levels of the three genes over a series of time points by western blot. We found that the expression of SLC7A11 significantly increased at 6 h, the expression of STEAP3 significantly increased at 24 h, and the expression of CA9 significantly decreased between the 24th and 48th hours (Figure 2(c)).

Meanwhile, we explored the relationship between hypoxia and SAS resistance over a series of time points in the U87 and U251 cells. Durg resistance was measured by the ratio (cells exposed to SAS ($500 \mu\text{M}$, 24 h)/cells exposed to DMSO). We found that hypoxia for 6 hours could induce a strong resistance to SAS (Figure 2(d)). Cell viability plot at the second hour and the sixth hour of hypoxic treatment in Figure S1A could clearly show that hypoxia for 6 hours could induce a strong resistance to SAS. The time course of SLC7A11 protein expression confirmed the trends of enhanced SAS resistance but not the time course of STEAP3 and CA9. To further verify SLC7A11 expression rule, we assessed SLC7A11 protein location and expression level via cellular immunofluorescence. The fluorescence intensity of SLC7A11 protein in cells incubated under

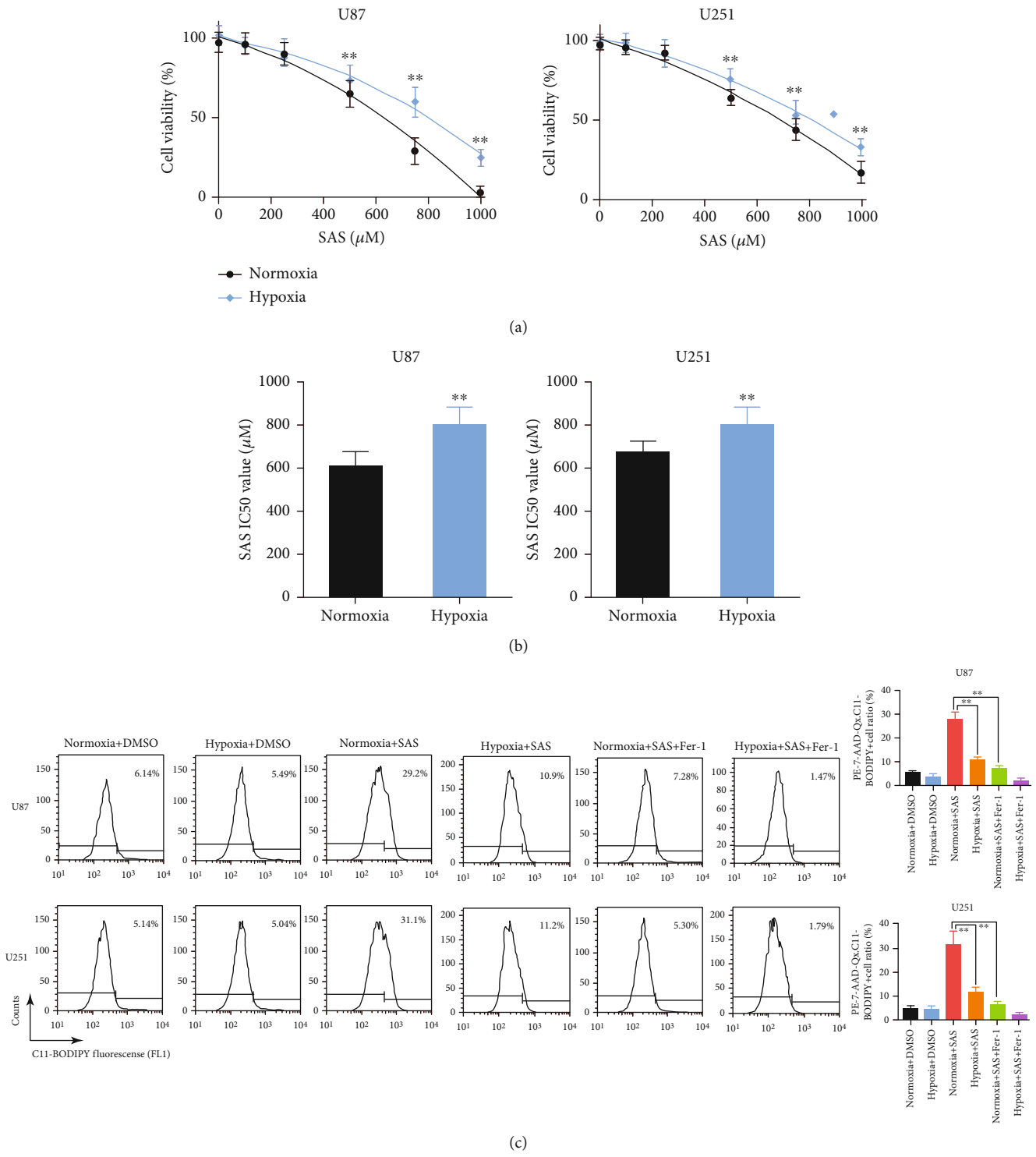


FIGURE 1: Continued.

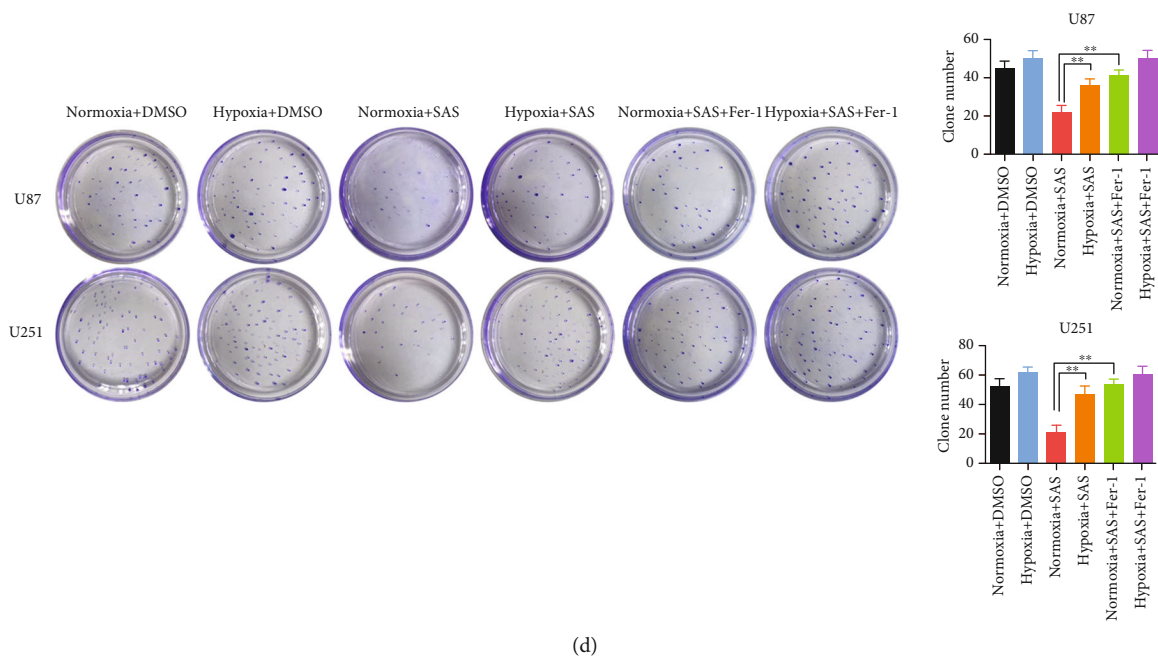


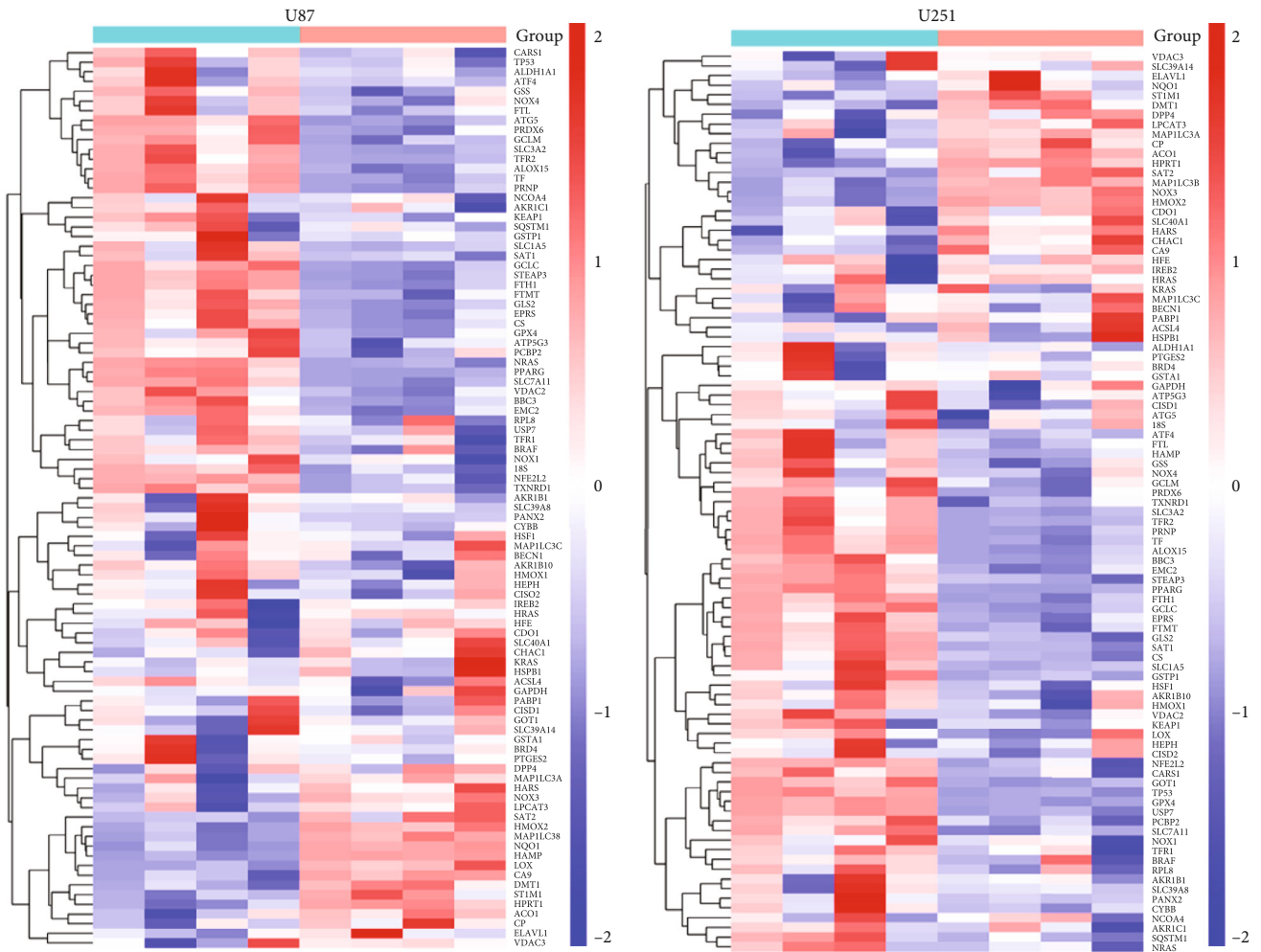
FIGURE 1: Hypoxia enhanced resistance of glioma cells to SAS-induced ferroptosis. (a) Cell viability curves at different concentrations of SAS for 24 h. Glioma cells under hypoxic environment became less sensitive to SAS. (b) Half-maximal inhibitory concentrations (IC_{50}) were calculated in each group. Hypoxic cells had an obvious higher IC_{50} to SAS. (c) Lipid peroxidation assessed in the U87 and U251 cells after exposure to hypoxia, SAS, and Fer-1 by flow cytometry using C11-BODIPY. (d) Clone formation assay of cancer cells in the absence or presence of SAS or Fer-1 under normoxia or hypoxia. The bar graph showed mean \pm SD of 3 independent experiments. * $P < 0.05$ and ** $P < 0.01$.

hypoxia for 6 hours was significantly higher than that in cells incubated under normoxia, and the cell localization of SLC7A11 protein did not change significantly (Figure 2(e)). We conducted experiments to explore the SLC7A11 expression changes in patient samples (Figure S2A) and TCGA database (Figure S2B). Taken together, SLC7A11 acted as a potential effector molecule of hypoxia. Thus, we identified SLC7A11 as the target for further investigation.

3.3. Hypoxia Enhanced the Resistance to SAS via Increasing SLC7A11 Expression. To investigate the role of SLC7A11 in hypoxia-induced SAS resistance, we used SLC7A11 siRNA to inhibit SLC7A11 gene expression in the U87 and U251 cells. Firstly, we analyzed the efficacy of SLC7A11 knockdown (SLC7A11 KD). Western blot showed that siRNA significantly inhibited SLC7A11 protein expression (Figure 3(a)). The quantitative analysis results are shown in Figure S3. The CCK-8 cell viability assay showed that SLC7A11 knockdown could not influence the proliferation rate of glioma cells (Figure 3(b)). Cytotoxicity experiments showed that SLC7A11 knockdown could significantly reverse the enhanced SAS resistance of the U87 and U251 cells induced by hypoxia (Figure 3(c)). The IC_{50} of SLC7A11 knockdown cells was obviously lower than that of scramble cells under hypoxic conditions, which indicated that SLC7A11 knockdown could also reverse the increased IC_{50} of SAS induced by hypoxia (Figure 3(d)). Next, we explored whether SLC7A11 knockdown could influence SAS resistance in colony formation assay. We

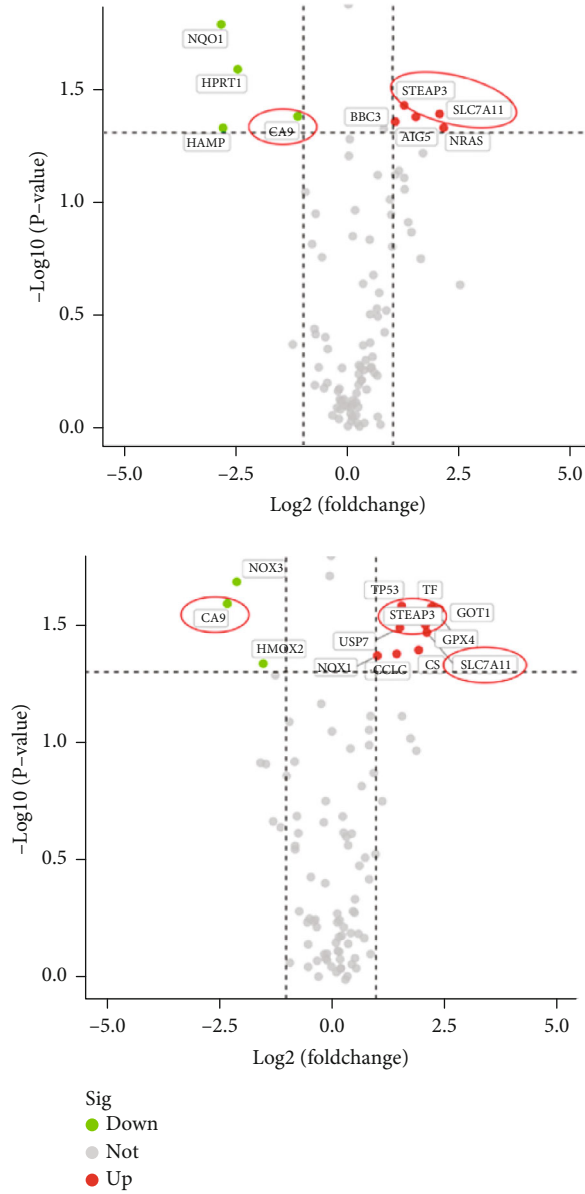
found that SLC7A11 knockdown reversed the enhanced cellular colony formation induced by hypoxia when treated with SAS (Figure 3(e)). In short, we identified SLC7A11 as a vital regulator gene for the ferroptosis defense ability of glioma cells under hypoxic conditions.

3.4. PI3K/AKT/HIF-1 α Pathway Involved in the Upregulation of SLC7A11 Induced by Hypoxia. Next, we would further explore how hypoxia induced SLC7A11 upregulation. Hypoxia-inducible factor (HIF) controlled a wide range of cell response to hypoxia, which included two major HIF- α subunits, HIF-1 α and HIF-2 α [32]. HIF-1 α contributed more to the acute hypoxia-driven transcriptional responses [17], and some researchers had reported that HIF-1 α was related to the SLC7A11 expression [33, 34]. To investigate the mechanism of SLC7A11 upregulation under hypoxia, we employed HIF-1 α inhibitor PX-478 and HIF-2 α inhibitor HIF-2 α -IN-4. We found that treatment glioma cells with PX-478 under hypoxia could significantly reverse the enhanced ferroptosis resistance, but HIF-2 α -IN-4 could not (Figures 4(a) and 4(b)). We explored the effects of PX-478 on the SLC7A11 expression. We found that PX-478 markedly decreased HIF-1 α and SLC7A11 protein levels (Figure 4(c)). The PI3K/AKT pathway was reported to be the upstream of HIF-1 α [35], which had been reported to participate in the malignant progression of glioma and was considered as an important regulator of ferroptosis [36, 37]. Therefore, we hypothesized that the increased SLC7A11 expression might be due to the activation of the



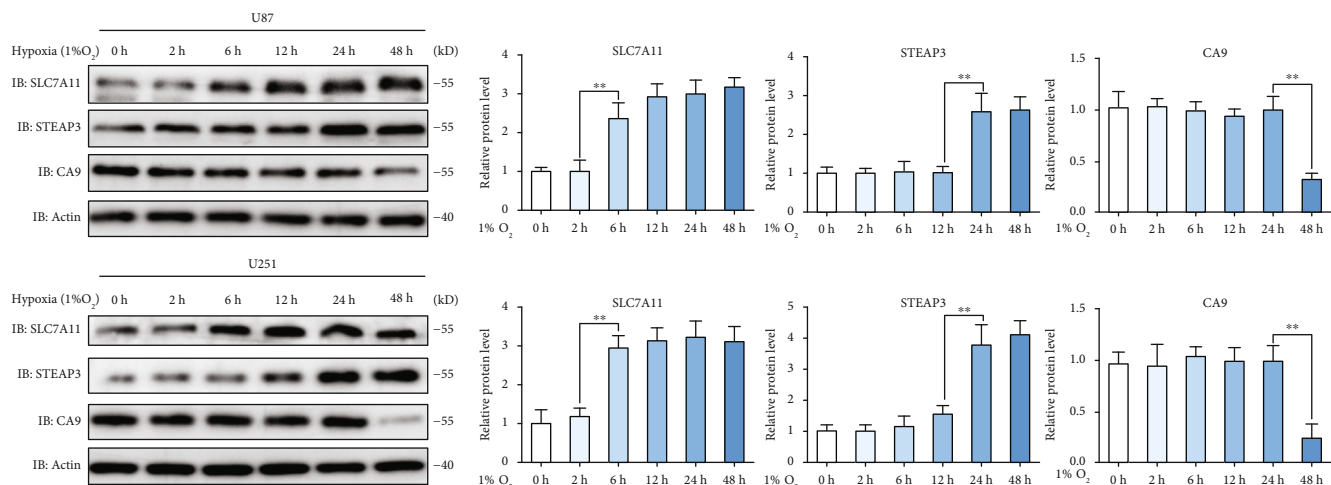
(a)

FIGURE 2: Continued.

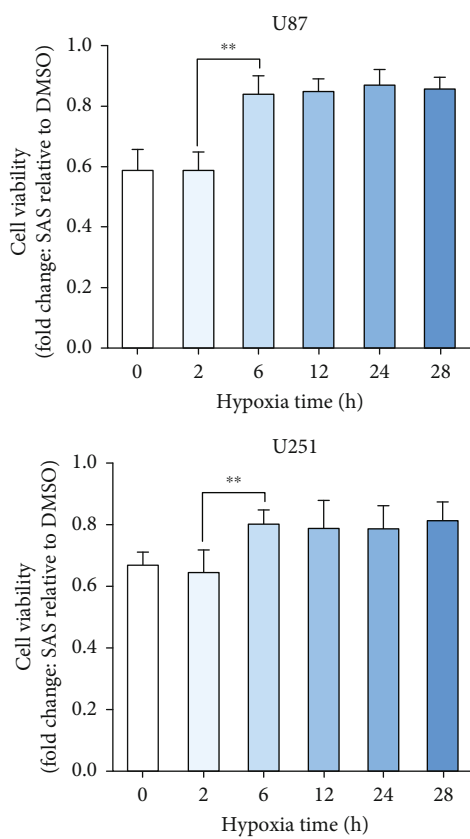


(b)

FIGURE 2: Continued.



(c)



(d)

FIGURE 2: Continued.

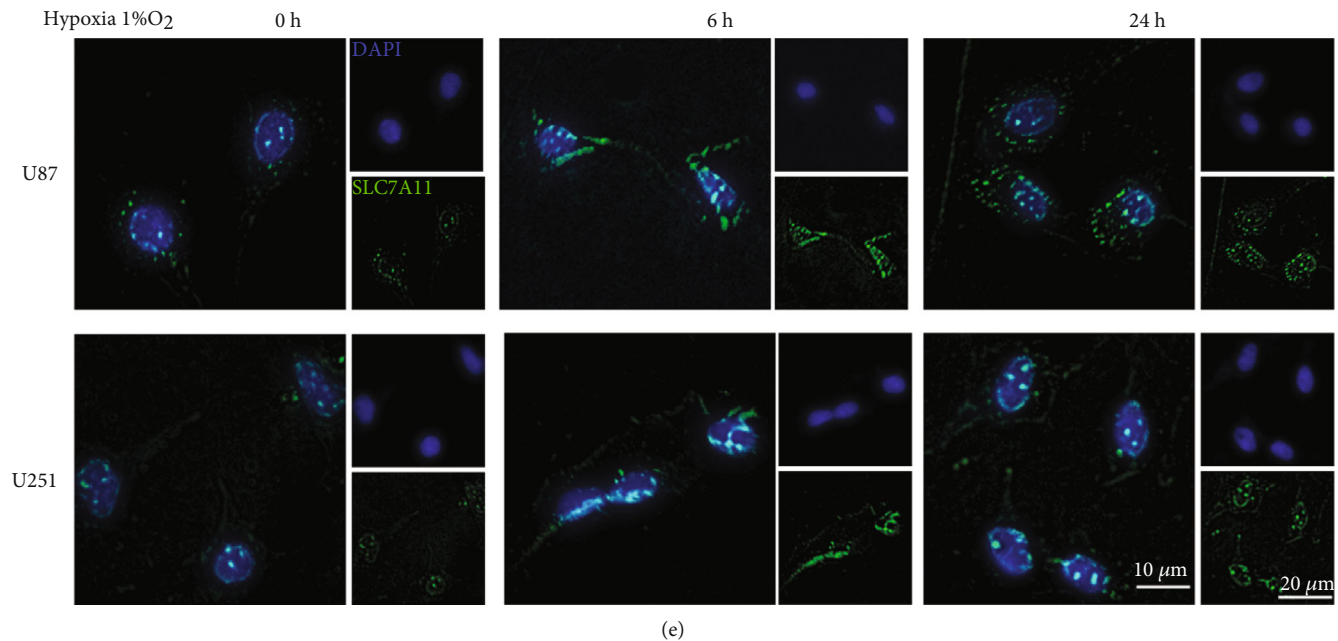


FIGURE 2: SLC7A11 was screened out as a potential effector molecule of hypoxia. (a) Ferroptosis-related qPCR array of normoxia and hypoxia identified several differentially expressed genes in the U87 and U251 cells. (b) The volcano map of differentially expressed genes depicted by difference degree and P value. SLC7A11, STEAP3, and CA9 were picked out. (c) Protein expression level of SLC7A11, STEAP3, and CA9 over a series of time points measured by western blot. SLC7A11 protein expression increased significantly at the sixth hour under hypoxia. (d) SAS resistance was measured by the ratio (cells exposed to SAS (500 μ M, 24 h)/cells exposed to DMSO). Glioma cells under hypoxic environment for at least 6 hours showed stronger SAS resistance. (e) Cell immunofluorescence showed that the fluorescence intensity of SLC7A11 protein in cells incubated under hypoxia for 6 hours was significantly higher than that in cells incubated under normoxia. The bar graph showed mean \pm SD of 3 independent experiments. * $P < 0.05$ and ** $P < 0.01$.

PI3K/AKT/HIF-1 α pathway. To prove our hypothesis, we explored the protein changes in the PI3K/AKT/HIF-1 α pathway by western blotting. The results indicated that hypoxia activated PI3K and phosphorylated AKT, HIF-1 α , and SLC7A11 expressions. Treatment with the AKT inhibitor, MK-2206, significantly attenuated the expressions of p-AKT, HIF-1 α , and SLC7A11 (Figure 4(d)). The quantitative analysis results are shown in Figure S4. We then analyzed the public data and found that the expression of SLC7A11 was positively correlated with HIF-1 α in 257 glioma tumor samples [28] (Figure 4(e)).

3.5. HIF-1 α Inhibitor PX-478 Induced Lipid Peroxidation in Glioma Cells. Ferroptosis resistance can be induced by hypoxia; lipid peroxidation underlies the mechanism of ferroptosis [23]. We were determined to explore whether suppression of HIF-1 α could directly induce lipid peroxidation in glioma cells. We utilized the C11-BODIPY probe and observed that the HIF-1 α inhibitor, PX-478 (20 μ M), significantly increased lipid peroxidation levels in glioma cells. To determine whether SLC7A11, as a downstream effector of HIF-1 α , could reverse the lipid peroxidation induced by PX-478, glioma cells were transfected with lentivirus that overexpresses human SLC7A11 cDNA (PX-478+Lv-SLC7A11 group). As expected, lipid peroxidation levels decreased in the PX-478+Lv-SLC7A11 group (Figure 5(a)). As depicted in Figure 5(b), the ratios of C11-BODIPY+ cells in the PX-478 treatment group were 12.7% and 21.4% in the U87 and

U251 cell lines, respectively; those in the control group were 3.55% and 4.43%, respectively, thereby indicating that the lipid peroxidation level after treatment with PX-478 was significantly increased. Importantly, the combination of PX-478 and Lv-SLC7A11 resulted in a low lipid peroxidation level, with C11-BODIPY+ cell ratios of 4.62% and 5.15% in the U87 and U251 cells, respectively. Furthermore, we confirmed this by measuring malondialdehyde (MDA), a product of lipid-oxidized damage. The results showed that the lipid-oxidized damage level was increased after treatment with PX-478 and reversed in the presence of Lv-SLC7A11 (Figure 5(c)). Transmission electron microscopy revealed that PX-478-treated cancer cells exhibited shrunken mitochondria with enhanced membrane density, which are morphologic features of ferroptosis. The black arrays represent normal mitochondria. White arrays represent shrunken and high membrane density mitochondria. SLC7A11 overexpression reversed this effect (Figure 5(d)). We then studied the potential role of PX-478- in SAS-induced ferroptosis under normoxic condition. We found that treatment with PX-478 alone could not cause cell death, which suggested that a modest degree of lipid peroxidation induced by PX-478 did not directly lead to cell death. We examined the combined effects of SAS and PX-478. The results indicated that the combined medication had a significantly higher cell death rate than SAS alone, as revealed by flow cytometry analysis and TUNEL staining, while SLC7A11 overexpression blocked the cytotoxic effect (Figures 5(e) and 5(f)).

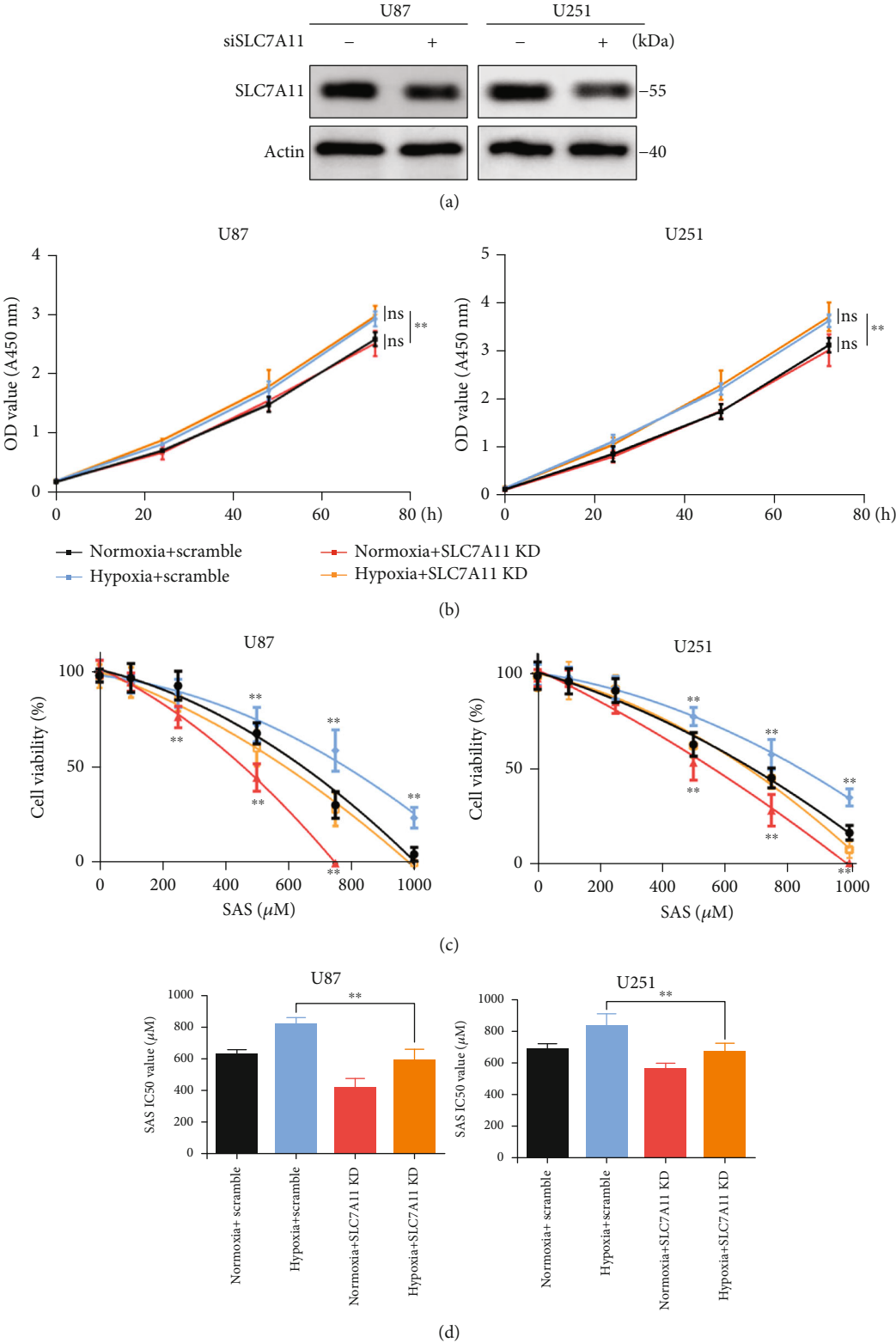


FIGURE 3: Continued.

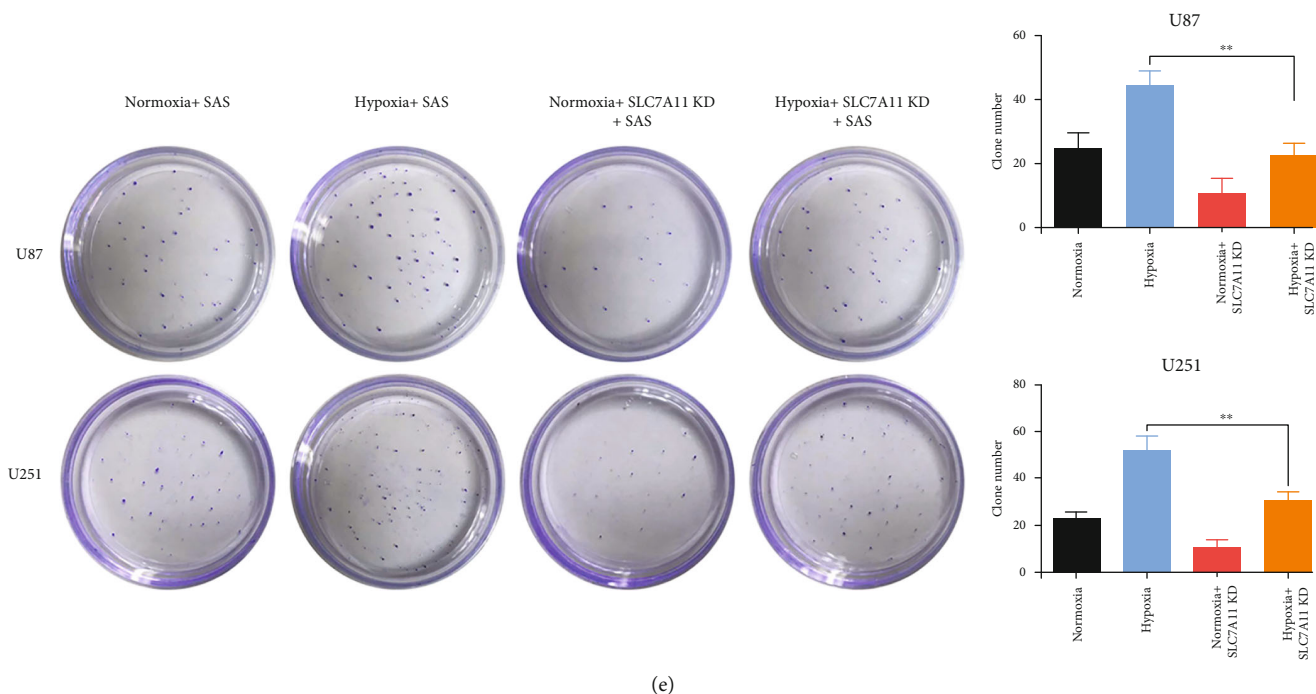


FIGURE 3: Hypoxia promoted SAS resistance via increasing SLC7A11 expression. (a) SLC7A11 protein expression level. SLC7A11 knockdown can significantly inhibit the protein expression level. (b) The growth curves were examined using a CCK-8 assay. SLC7A11 knockdown did not influence the cell proliferation rate of glioma cells. (c) Cell viability curves at different concentrations of SAS for 24 h. SLC7A11 knockdown could reverse the enhanced SAS resistance induced by hypoxia. (d) The IC₅₀ of SAS in SLC7A11 knockdown group was obviously low than that of scramble group under hypoxic or normoxic condition. (e) Clone formation assay of cancer cells in the absence or presence of SAS for 2 weeks. SLC7A11 knockdown could reverse the enhanced cell colony formation ability induced by hypoxia. The bar graph showed mean \pm SD of 3 independent experiments. * $P < 0.05$ and ** $P < 0.01$.

3.6. PX-478 Enhanced the Anticancer Activity of SAS In Vivo. To further investigate the role of PX-478 in promoting SAS sensitivity *in vivo*, we established subcutaneous and orthotopic xenograft mouse models of glioma. In both models, SAS (8 mg in 0.2 ml saline twice daily) was intraperitoneally injected twice a day and PX-478 (100 mg/kg) was orally administered twice a day for 2 weeks. The detailed experimental process is presented in Material and Methods. Compared with the control group (intraperitoneal injection DMSO and oral given saline), the SAS group (intraperitoneal injection SAS and oral given saline) exhibited a certain degree of anticancer effect, but not the PX-478 group (intraperitoneal injection DMSO and oral given PX-478). The combination group (intraperitoneal injection SAS and oral given PX-478) had significantly better anticancer activity than the SAS group. However, the Lv-SLC7A11 group (implant with SLC7A11 overexpression cells, intraperitoneal injection SAS, and oral given PX-478) showed no anticancer effect, as measured by tumor volume, tumor weight, mice body weight, and tumor tissue MDA in the subcutaneous xenograft model (Figures 6(a)–6(e)). Similar results were obtained in the orthotopic xenograft model, as measured by luciferase activity (Figures 6(f) and 6(g)). The overall survival of the combination group was also higher than that of the SAS group (Figure 6(h)). Furthermore, histological analysis indicated that the PX-478 and combination groups exhibited weaker immunoreactivity for SLC7A11; Lv-SLC7A11 could efficiently increase SLC7A11 expression

(Figure 6(i)). Collectively, PX-478 had very little therapeutic effect on glioma; however, it greatly enhanced the anticancer effect of SAS in both subcutaneous and orthotopic xenograft mouse models.

4. Discussion

The global incidence of glioma continues to increase along with the aging of the world's population; glioblastoma remains at a very low 5-year overall survival rate (6.8%) [38]. Tumor cells can develop resistance to various drugs during the therapy process, including ferroptosis-based drugs [39, 40]. In recent years, therapies underlying ferroptosis have attracted much attention with high expectations [41]. Hypoxia is correlated to the drug resistance of solid tumors. Alleviation of hypoxia is expected to sensitize the ferroptosis inducers toward solid tumors [42]. This study shows that hypoxia could enhance glioma resistance to SAS-induced ferroptosis. Therefore, a better understanding of the mechanism underlying SAS resistance may benefit ferroptosis-targeted treatment. We found that one of the most important underlying mechanisms of SAS resistance at the hyperacute phase of hypoxia is the upregulation of SLC7A11. SLC7A11, STEAP3, and CA9 are common genes that have changed significantly in both the U87 and U251 cell lines by PCR array. CA9 and STEAP3 have been reported to be important regulators of ferroptosis under hypoxia [43, 44]. CA9 has an intimate association with

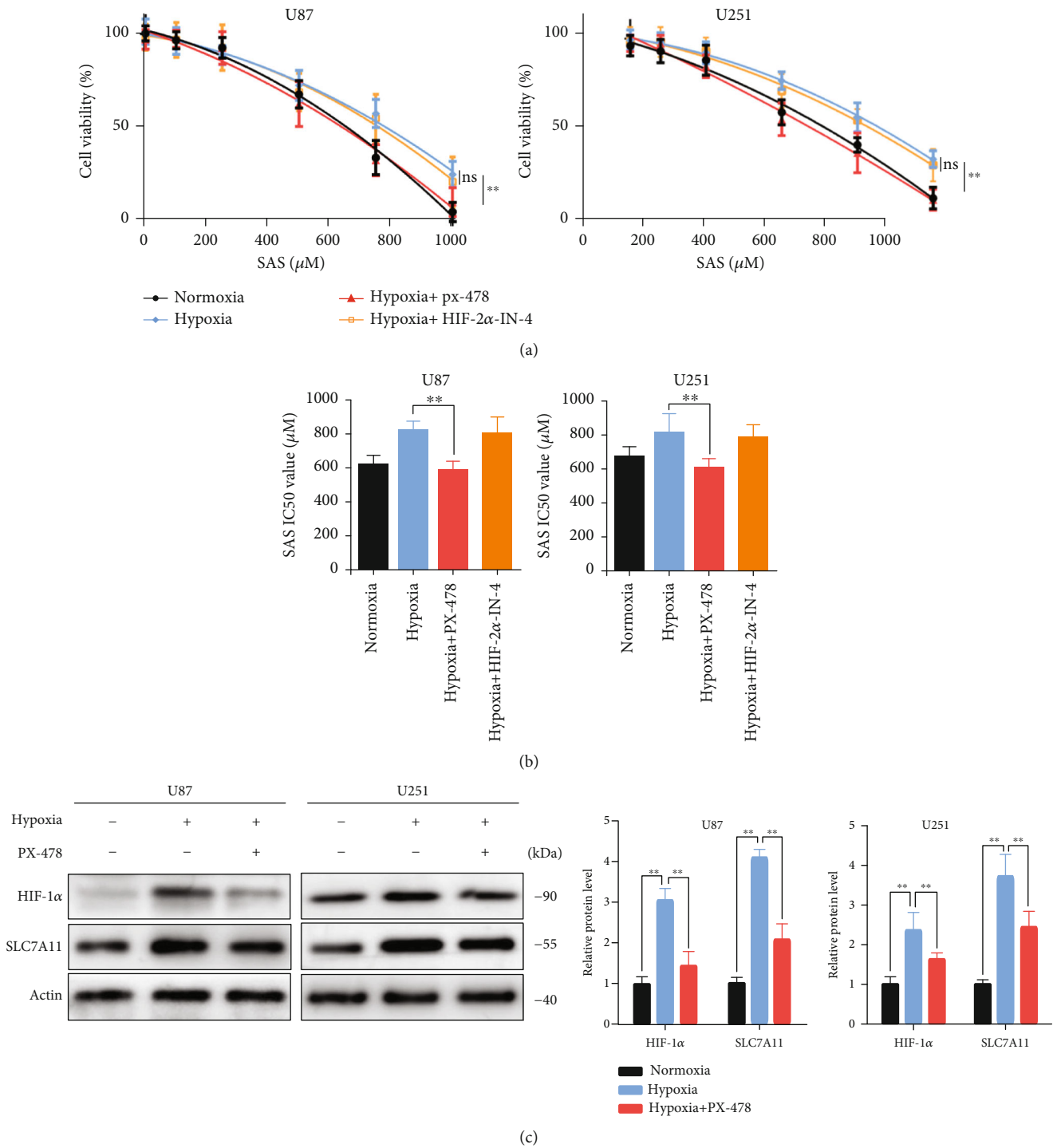


FIGURE 4: Continued.

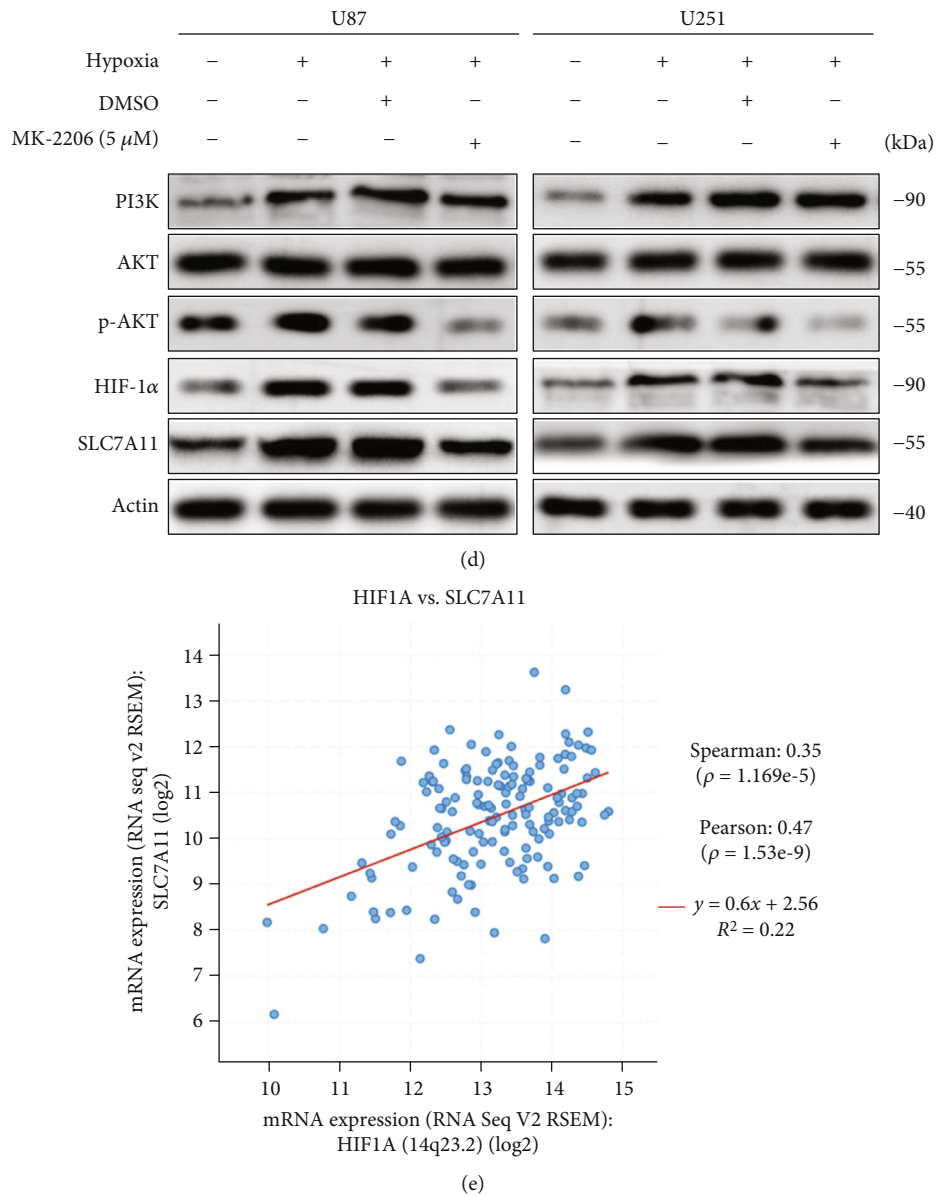


FIGURE 4: Hypoxia promoted SLC7A11 expression via PI3K/AKT/HIF-1 α pathway. (a) Cell viability curves at different concentrations of SAS for 24 h. PX-478 can reverse the enhanced SAS resistance induced by hypoxia. (b) The IC₅₀ of SAS in hypoxia with PX-478 group was obviously low than that of hypoxia group. The bar graph showed mean \pm SD of 3 independent experiments. (c) Protein expression level of HIF-1 α and SLC7A11 influenced by oxygen content and HIF-1 α inhibitor PX-478 measured by western blot. PX-478 markedly decreased HIF-1 α and SLC7A11 protein levels. (d) Protein expression level of PI3K, AKT, p-AKT, HIF-1 α , and SLC7A11 influenced by oxygen content and AKT inhibitor MK-2206 measured by western blot. AKT inhibitor MK-2206 along with hypoxia attenuated the expression level of p-AKT, HIF-1 α , and SLC7A11. (e) The relationship between HIF-1 α and SLC7A11 expression level in TCGA. SLC7A11 was positively correlated with HIF-1 α in 257 glioma tumor samples. * $P < 0.05$ and ** $P < 0.01$.

hypoxia and redox regulation [43]. Through western blot detection, we found that CA9 did not show its function in the hyperacute phase of hypoxia. We speculate that it may play a role in the chronic phase of hypoxia, which is also of great interest to us. STEAP3 increases sensitively to ferroptosis by regulating the p53/SLC7A11 pathway [44]. Namely, SLC7A11 played a central role in the hyperacute phase of hypoxia at least in the U87 and U251 cells, while CA9 and STEAP3 did not; and SLC7A11 was expressed stably in different types of cells and was considered as the most crucial gene at the hypoxia hyperacute phase.

The PI3K/AKT signaling pathway plays a central role in cell survival [37]. The allosteric AKT inhibitor, MK2206, has been reported to decrease tumor growth and enhance the antitumor efficacy of chemotherapeutic agents [45, 46]. We found that hypoxic activation of the PI3K/AKT/HIF-1 α axis was essential for the upregulation of SLC7A11. Both the AKT inhibitor, MK-2206, and HIF-1 α inhibitor PX-478, significantly inhibited SLC7A11 expression under hypoxic conditions. These results suggested that the upregulation of SLC7A11 induced by hypoxia was dependent on the activation of the PI3K/AKT/HIF-1 α axis.

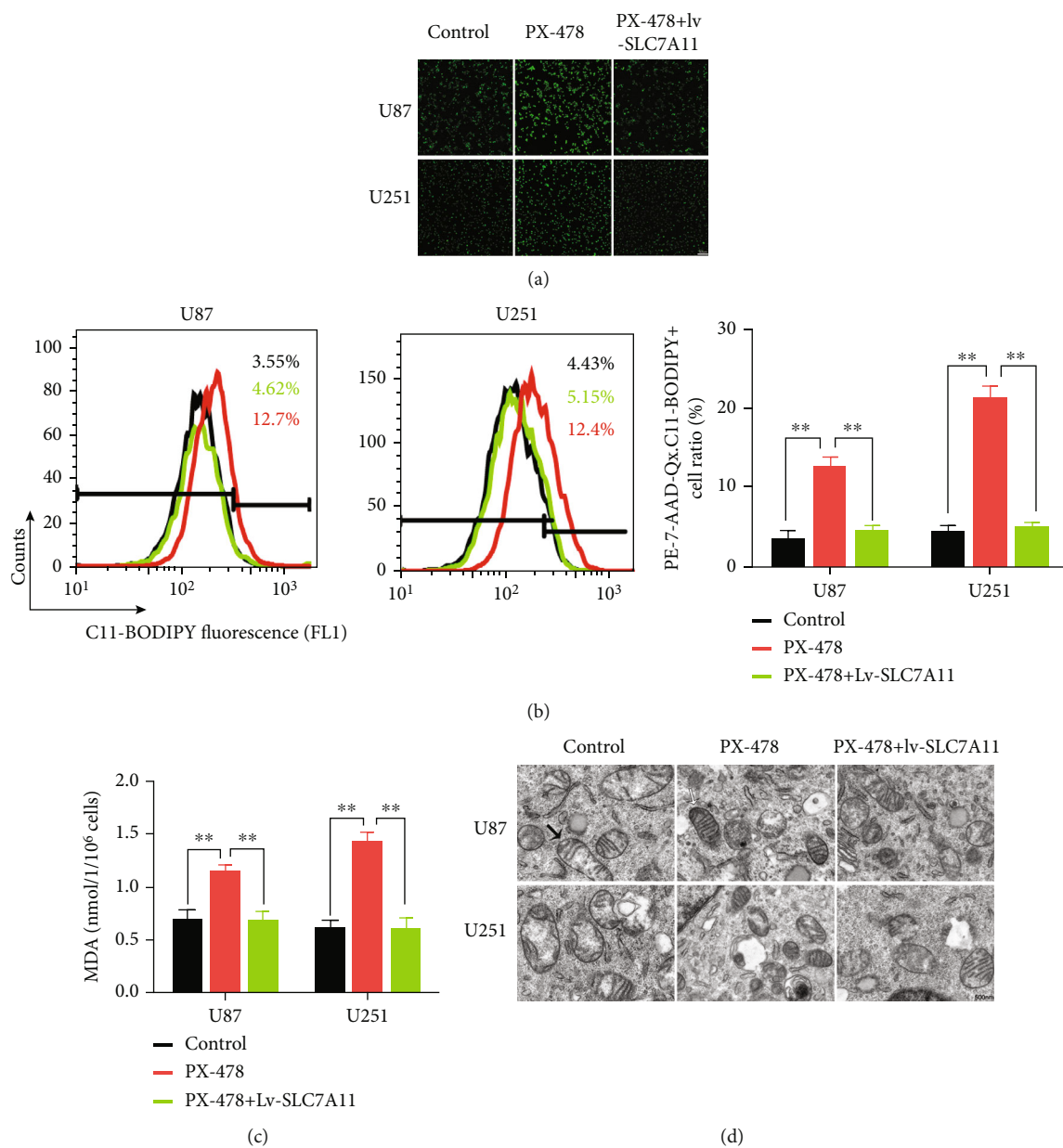


FIGURE 5: Continued.

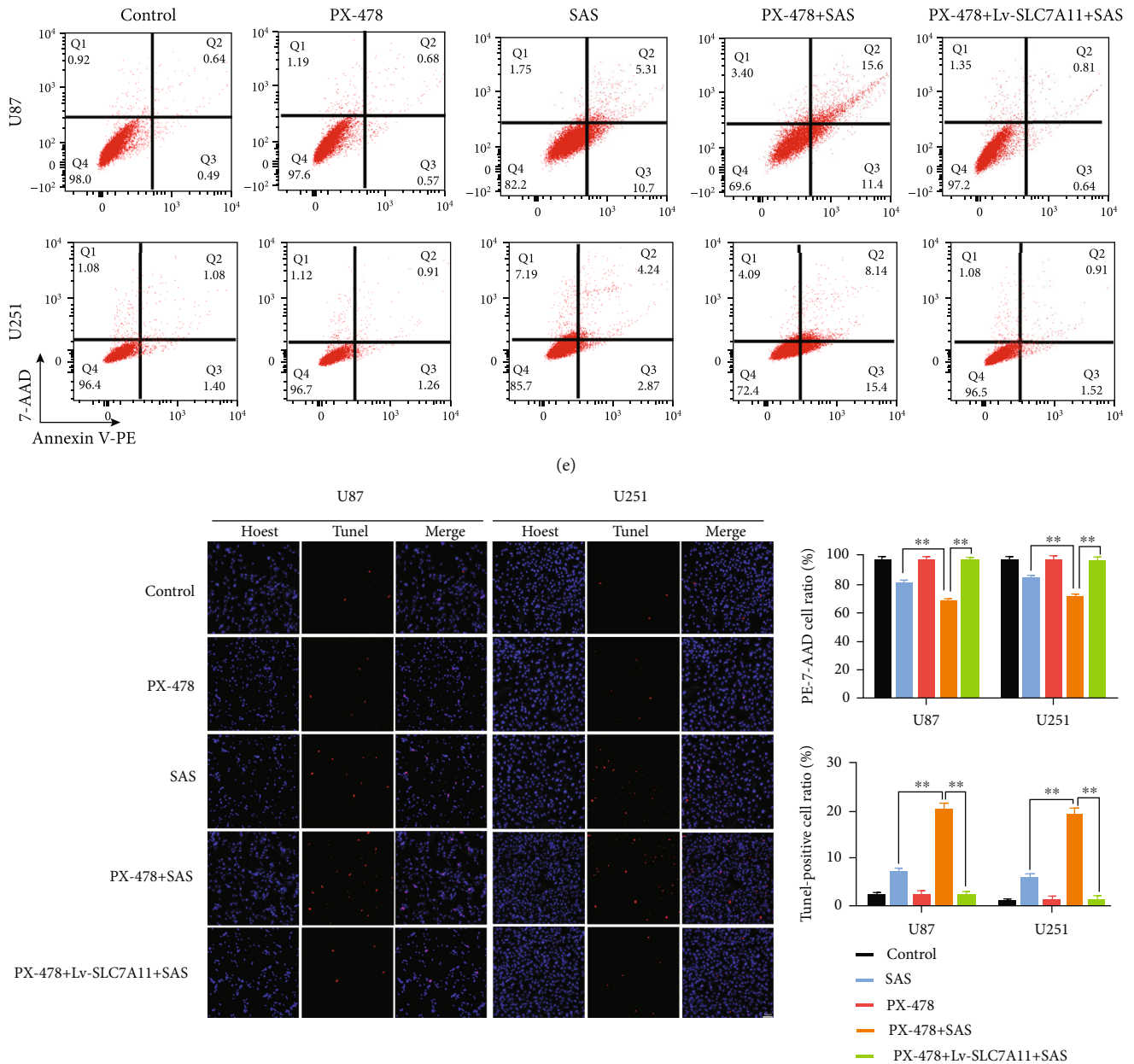


FIGURE 5: PX-478 induced lipid peroxidation in the U87 and U251 cells. (a, b) Lipid peroxidation assessment in U87 and U251 cells after exposure to DMSO, PX-478, or PX-478+Lv-SLC7A11 measured by fluorescence microscope (a) and flow cytometry (b). (c) Quantitative analysis of the expression levels of MDA in the U87 and U251 cells after exposure to DMSO, PX-478, or PX-478+Lv-SLC7A11. MDA increased after treating with PX-478 and reversed in the presence of Lv-SLC7A11. (d) Transmission electron microscopy images of the U87 and U251 cells after exposure to DMSO, PX-478, or PX-478+Lv-SLC7A11. PX-478-treated cancer cells exhibited shrunken mitochondria with enhanced membrane density. Black arrow: normal mitochondria; white arrow: shrunken and high membrane density mitochondria. Quantitative analysis of mitochondrial length was listed on the right. (e, f) Cell apoptosis was detected by flow cytometry (e) and TUNEL fluorescence staining (f) in the U87 and U251 cells after exposure to DMSO, PX-478, SAS, PX-478+SAS, and PX-478+Lv-SLC7A11+SAS. The bar graph showed mean \pm SD of 3 independent experiments. * $P < 0.05$ and ** $P < 0.01$.

Clinical studies have demonstrated that the tumor hypoxic microenvironment is associated with poor prognosis in patients. Especially in advanced metastatic cancer, a hypoxic environment is often established, which plays an important role in cancer evolution [5]. In a hypoxic environment, activated HIF-1 α promotes cancer migration in multiple

ways, such as promoting EMT-related signaling, regulating the alignment of collagen fibers, and mediating the leakage and compression of blood and lymphatic vessels [47–49]. In recent years, the contribution of hypoxia to tumor therapy especially specific targeting of HIFs has been observed in a wide range of neoplastic cells [5]. In this study, we found

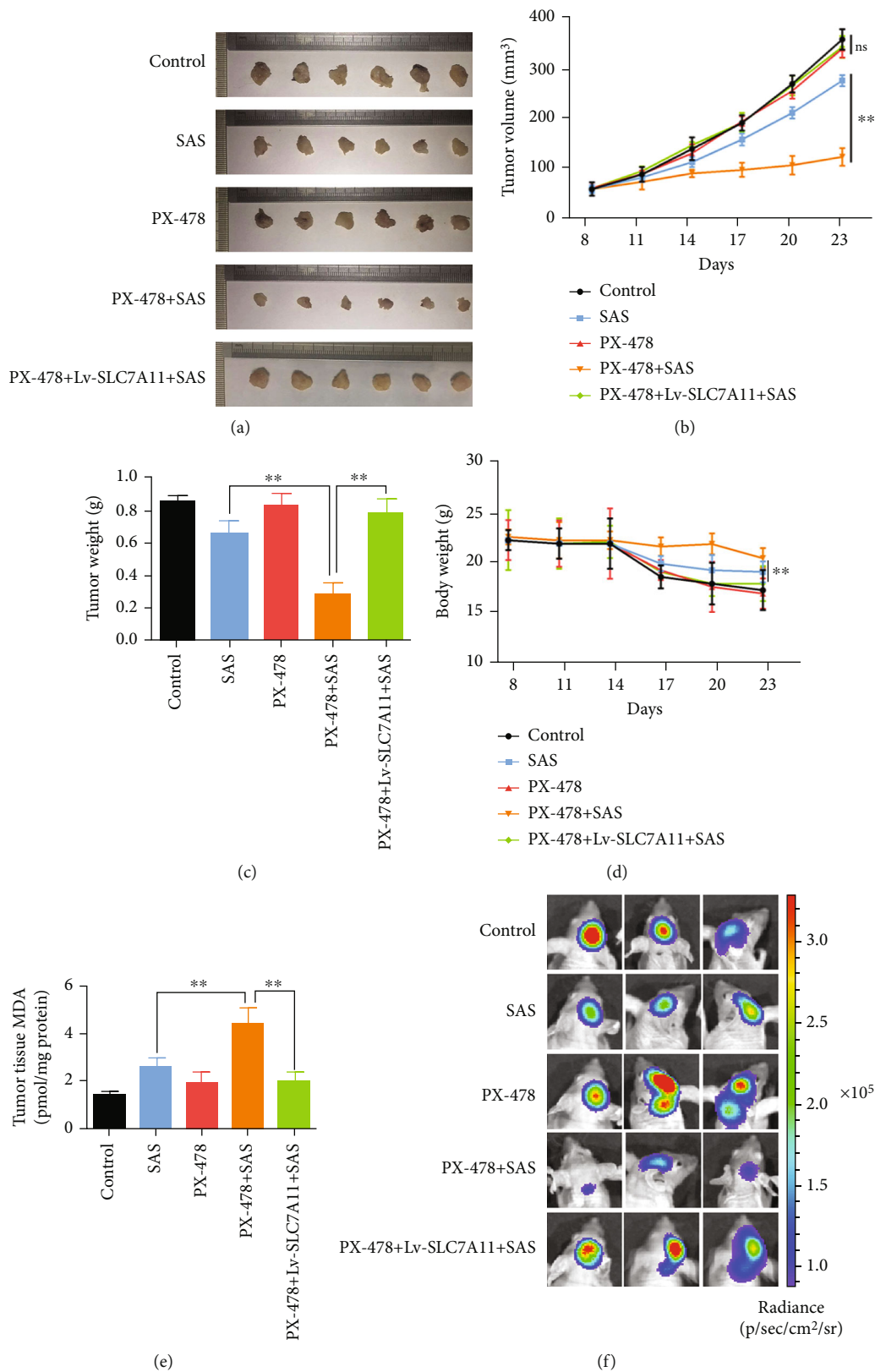


FIGURE 6: Continued.

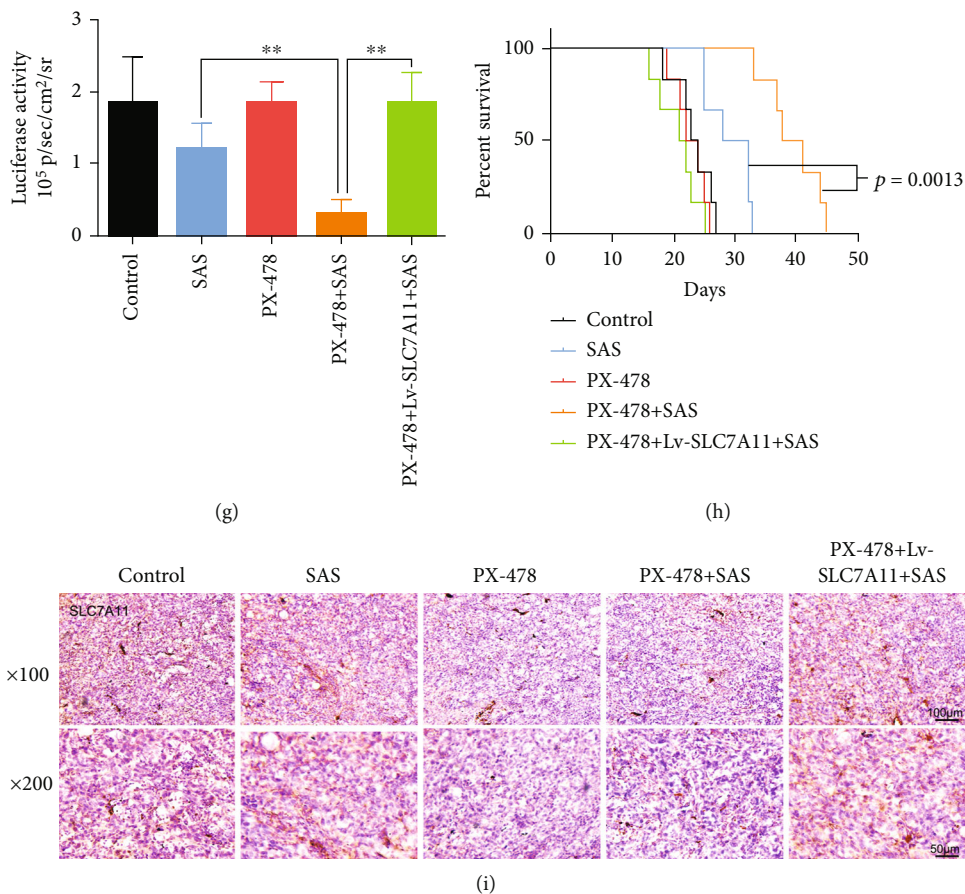


FIGURE 6: PX-478 promoted the anticancer activity of SAS in vivo. (a) Xenografts derived from the U87 or U87/Lv-SLC7A11 cells which were treated with different drugs demonstrated tumor volume (b), tumor weight (c), body weight (d), and tumor tissue MDA (e). (f, g) Luciferase activities verified the decreased and increased tumor growth, respectively, in orthotopic glioma models established by the U87 or U87/Lv-SLC7A11 cells. (h) Survival curves showed the survival rates of the engrafted mice. (i) Immunohistochemical labelling showed that the downregulated expression of SLC7A11 after being treated with PX-478 and Lv-SLC7A11 could efficiently increase SLC7A11 expression in vivo. The bar graph showed mean \pm SD of 3 independent experiments. * $P < 0.05$ and ** $P < 0.01$.

new evidence about the relationship between hypoxia and ferroptosis, which is a potential therapeutic target in cancer therapy. Our research concluded that hypoxia-regulated SLC7A11 expression through PI3K/AKT pathway may provide a theoretical basis for clinical trials to help improve treatment outcomes. PX-478 had an antitumor effect with fewer side effects; it could penetrate the blood-brain barrier; however, its sole effect was limited [50]. As a result, scientists have paid much attention to its synergetic effect, including its combination with radiotherapy or immunotherapy [51, 52]. Radiotherapy and immunotherapy are related to ferroptosis [53, 54]. Given that HIF-1 α regulates the ferroptosis core gene, SLC7A11, we hypothesized that PX-478 played a vital role in promoting ferroptosis by inhibiting SLC7A11 expression. We found that cells treated with PX-478 exhibited higher lipid peroxidation levels following C11-BODIPY staining. We also found deeply stained and shrunken mitochondria on transmission electron microscopy. The TME is characterized by regional hypoxia [55]. Therefore, we hypothesized that regional hypoxia in the TME in vivo would

strengthen HIF-1 α /SLC7A11 axis-regulated SAS resistance. We used subcutaneous and orthotopic xenograft mouse models to test the function of PX-478 in SAS therapy. Ideal experimental results were obtained; data showed that PX-478 can effectively decrease SLC7A11 expression in tumor tissue and promote the anticancer effect of SAS. With respect to how HIF-1 α regulated SLC7A11, we performed ChIP with an anti-HIF-1 α antibody and designed three pairs of primer to test whether HIF-1 α can bind to the SLC7A11 promoter but did not obtain positive result. So, the regulatory mechanism of HIF-1 α on SLC7A11 may be not direct transcriptional regulation, which may be a complicated process. Some researchers found HIF-1 α /SLC7A11 pathway affected liver fibrosis through the mechanism of ferroptosis, but they did not explore the regulatory mechanism [34]. Another team of researchers found that HIF-1 α improved the stability of SLC7A11 mRNA through lncRNA-PMAN, which may be an important mechanism of HIF-1 α regulating SLC7A11 [33]. There may be other regulatory mechanisms which need further research.

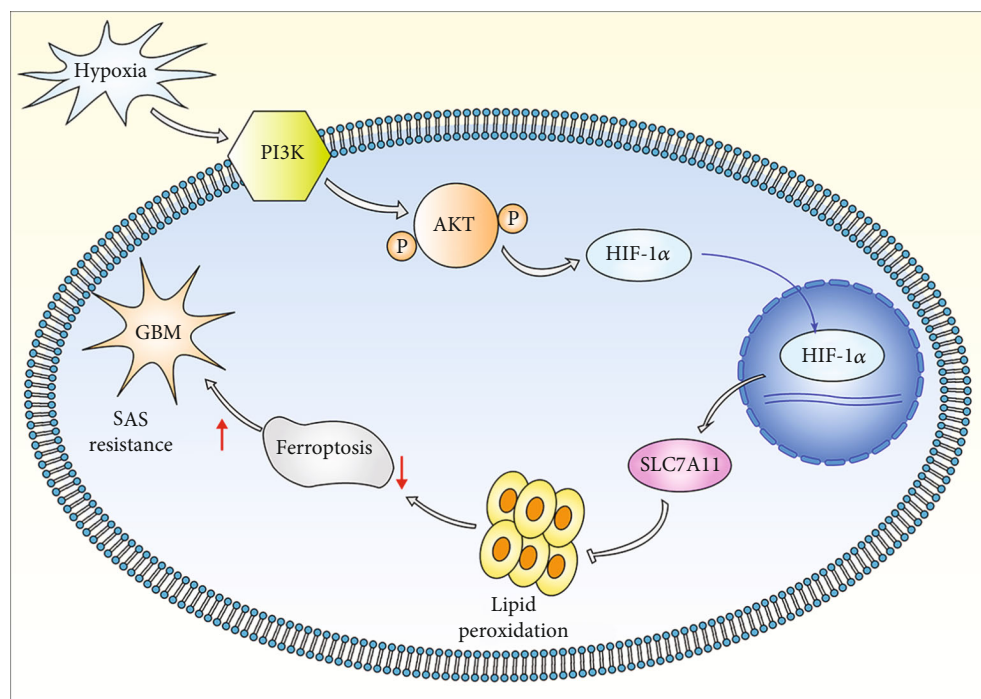


FIGURE 7: Pattern diagram of hypoxia modulation of ferroptosis. Hypoxia activated PI3K/AKT/HIF-1 α pathway to increase SLC7A11 expression in the U87 and U251 cells. SLC7A11 protein neutralized lipid peroxidation to defend SAS-induced ferroptosis.

To the best of our knowledge, we first found that PX-478 could induce increased lipid peroxidation level and promote the anticancer effect of SAS in glioma. As for the mechanism, many factors could influence the activation and translocation of HIF-1 α including growth factors, ROS, and various protein signaling pathways, which suggested that HIF-1 α played vital roles not only under hypoxia [56]. HIF-1 α also regulated SLC7A11 expression under normoxia [33, 34]. We found that the phenotype could be blocked by SLC7A11 overexpression, which indicated that the key effector under normoxia was SLC7A11. Additionally, this is the first study to uncover the relationship between the PI3K/AKT/HIF-1 α pathway and ferroptosis. Beside PI3K/AKT/HIF-1 α pathway, many other pathway also contributed to SLC7A11 expression. However, the pathways related to SLC7A11 expression were not related to hypoxia induction directly in glioma [57]. We first suggested that the combination of SAS and PX-478 had a good anticancer effect. Shortcoming of this study was that we did not test for other ferroptosis-related therapies and other HIF-1 α inhibitory methods. In conclusion, we demonstrated that glioma resistance to SAS-induced ferroptosis was enhanced by hypoxia, owing to the activation of the PI3K/AKT/HIF-1 α pathway and promotion SLC7A11 expression (Figure 7). A preprint has previously been published [58]. We demonstrated that PX-478 and SAS had a coordinated synergistic effect on anticancer activity, both in vitro and in vivo. Future studies should include other kinds of ferroptosis-related therapies to evaluate whether PX-478 not only promotes SAS action but also those of others that are sufficiently effective and safe for the treatment of human tumors.

Abbreviations

TME:	Tumor microenvironment
SLC7A11:	Recombinant solute carrier family 7, member 11
HIF:	Hypoxia-inducible factor
DMEM:	Dulbecco's modified Eagle's medium
FBS:	Fetal bovine serum
CCK-8:	Cell Counting Kit-8
IC ₅₀ :	Half-maximal inhibitory concentration assay
ECL:	Electrochemiluminescence
IF:	Immunofluorescence
IHC:	Immunohistochemistry
MDA:	Malondialdehyde
STEAP3:	STEAP3 metalloredutase
CA9:	Carbonic anhydrase 9.

Data Availability

The datasets used and analyzed during the current study are available from the corresponding author on reasonable request.

Ethical Approval

The protocol of this study was approved by the Ethics and Human Subject Committee of Shandong Provincial Hospital (ID: SZRJJ: NO.2021-055), and all experiments and methods met the standards of the relevant guidelines and regulations.

Conflicts of Interest

The authors declare that they have no competing interests.

Authors' Contributions

SC and CF performed the original draft preparation and revision, created the tables and figures, and were the major contributors in writing the manuscript. TH, DZ, and XS made suggestions to the writing of the manuscript and revisions to tables and figures. RZ participated in the conceptualization and methodology. All authors read and approved the final manuscript. Shicheng Sun, Changfa Guo, and Taihong Gao contributed equally to this work and share first authorship.

Acknowledgments

This work was supported by the National Natural Science Foundation of China (Grant number 81771270), the Shandong Provincial Natural Science Foundation, China (ZR202102230499), the Youth Natural Science Foundation of Shandong Province (ZR2021QH036), and the Clinical Medical Science and Technology Innovation Project of Jinan (202019007).

Supplementary Materials

Table S1: primers used in this study. Figure S1: cell viability plot at the second hour and the sixth hour of hypoxic treatment. Figure S2: the SLC7A11 expression changes in patient samples and TCGA database. Figure S3: quantitative analysis of western blot in Figure 3(a). Figure S4: quantitative analysis of western blot in Figure 4(d). (*Supplementary Materials*)

References

- [1] M. Touat, A. Idhah, M. Sanson, and K. L. Ligon, "Glioblastoma targeted therapy: updated approaches from recent biological insights," *Annals of Oncology*, vol. 28, no. 7, pp. 1457–1472, 2017.
- [2] F. Mudassar, H. Shen, G. O'Neill, and E. Hau, "Targeting tumor hypoxia and mitochondrial metabolism with anti-parasitic drugs to improve radiation response in high-grade gliomas," *Journal of Experimental & Clinical Cancer Research*, vol. 39, no. 1, p. 208, 2020.
- [3] A. C. Tan, D. M. Ashley, G. Y. López, M. Malinzak, H. S. Friedman, and M. Khasraw, "Management of glioblastoma: state of the art and future directions," *CA: a Cancer Journal for Clinicians*, vol. 70, no. 4, pp. 299–312, 2020.
- [4] C. Aliferis and D. T. Trafalis, "Glioblastoma multiforme: pathogenesis and treatment," *Pharmacology & Therapeutics*, vol. 152, pp. 63–82, 2015.
- [5] X. Jing, F. Yang, C. Shao et al., "Role of hypoxia in cancer therapy by regulating the tumor microenvironment," *Molecular Cancer*, vol. 18, no. 1, p. 157, 2019.
- [6] C. Mertens, J. Mora, B. Ören et al., "Macrophage-derived lipocalin-2 transports iron in the tumor microenvironment," *Oncoimmunology*, vol. 7, no. 3, article e1408751, 2018.
- [7] P. Wang, Q. Yan, B. Liao et al., "The HIF1 α /HIF2 α -miR210-3p network regulates glioblastoma cell proliferation, dedifferentiation and chemoresistance through EGF under hypoxic conditions," *Cell Death & Disease*, vol. 11, no. 11, p. 992, 2020.
- [8] S. Cowman, Y. N. Fan, B. Pizer, and V. Sée, "Decrease of Nibrin expression in chronic hypoxia is associated with hypoxia-induced chemoresistance in some brain tumour cells," *BMC Cancer*, vol. 19, no. 1, p. 300, 2019.
- [9] F. Marampon, G. L. Gravina, B. M. Zani et al., "Hypoxia sustains glioblastoma radioresistance through ERKs/DNA-PKcs/HIF-1 α functional interplay," *International Journal of Oncology*, vol. 44, no. 6, pp. 2121–2131, 2014.
- [10] O. Catalina-Rodriguez, V. K. Kolukula, Y. Tomita et al., "The mitochondrial citrate transporter, CIC, is essential for mitochondrial homeostasis," *Oncotarget*, vol. 3, no. 10, pp. 1220–1235, 2012.
- [11] K. Graham and E. Unger, "Overcoming tumor hypoxia as a barrier to radiotherapy, chemotherapy and immunotherapy in cancer treatment," *International Journal of Nanomedicine*, vol. Volume 13, pp. 6049–6058, 2018.
- [12] A. Schulz, F. Meyer, A. Dubrovskaya, and K. Borgmann, "Cancer stem cells and radioresistance. DNA Repair and Beyond," *Cancers (Basel)*, vol. 11, p. 862, 2019.
- [13] J. Liu, L. Gao, N. Zhan et al., "Hypoxia induced ferritin light chain (FTL) promoted epithelia mesenchymal transition and chemoresistance of glioma," *Journal of Experimental & Clinical Cancer Research*, vol. 39, no. 1, p. 137, 2020.
- [14] L. Persano, E. Rampazzo, G. Basso, and G. Viola, "Glioblastoma cancer stem cells: role of the microenvironment and therapeutic targeting," *Biochemical Pharmacology*, vol. 85, no. 5, pp. 612–622, 2013.
- [15] D. Uribe, Á. Torres, J. D. Rocha et al., "Multidrug resistance in glioblastoma stem-like cells: role of the hypoxic microenvironment and adenosine signaling," *Molecular Aspects of Medicine*, vol. 55, pp. 140–151, 2017.
- [16] A. J. Majmundar, W. J. Wong, and M. C. Simon, "Hypoxia-inducible factors and the response to hypoxic stress," *Molecular Cell*, vol. 40, no. 2, pp. 294–309, 2010.
- [17] J. W. Lee, J. Ko, C. Ju, and H. K. Eltzschig, "Intracellular sensing of viral genomes and viral evasion," *Experimental & Molecular Medicine*, vol. 51, no. 12, pp. 1–13, 2019.
- [18] S. T. Palayoor, J. B. Mitchell, D. Cerna, W. Degraff, M. John-Aryankalayil, and C. N. Coleman, "PX-478, an inhibitor of hypoxia-inducible factor-1 α , enhances radiosensitivity of prostate carcinoma cells," *International Journal of Cancer*, vol. 123, no. 10, pp. 2430–2437, 2008.
- [19] M. Lang, X. Wang, H. Wang et al., "Arsenic trioxide plus PX-478 achieves effective treatment in pancreatic ductal adenocarcinoma," *Cancer Letters*, vol. 378, no. 2, pp. 87–96, 2016.
- [20] M. M. Grabowski, E. W. Sankey, K. J. Ryan et al., "Immune suppression in gliomas," *Journal of Neuro-oncology*, vol. 151, no. 1, pp. 3–12, 2021.
- [21] R. Huang, R. Dong, N. Wang et al., "Adaptive changes allow targeting of ferroptosis for glioma treatment," *Cellular and Molecular Neurobiology*, vol. 42, no. 7, pp. 2055–2074, 2021.
- [22] T. Liu, C. Zhu, X. Chen et al., "Ferroptosis, as the most enriched programmed cell death process in glioma, induces immunosuppression and immunotherapy resistance," *Neuro-Oncology*, vol. 24, no. 7, pp. 1113–1125, 2022.
- [23] M. Conrad and D. A. Pratt, "The chemical basis of ferroptosis," *Nature Chemical Biology*, vol. 15, no. 12, pp. 1137–1147, 2019.
- [24] C. Mao, X. Liu, Y. Zhang et al., "DHODH-mediated ferroptosis defence is a targetable vulnerability in cancer," *Nature*, vol. 593, no. 7860, pp. 586–590, 2021.

- [25] H. Sontheimer and R. J. Bridges, "Sulfasalazine for brain cancer fits," *Expert Opinion on Investigational Drugs*, vol. 21, no. 5, pp. 575–578, 2012.
- [26] K. Hu, K. Li, J. Lv et al., "Suppression of the SLC7A11/glutathione axis causes synthetic lethality in KRAS-mutant lung adenocarcinoma," *The Journal of Clinical Investigation*, vol. 130, no. 4, pp. 1752–1766, 2020.
- [27] E. H. Kim, D. Shin, J. Lee, A. R. Jung, and J. L. Roh, "CISD2 inhibition overcomes resistance to sulfasalazine-induced ferroptotic cell death in head and neck cancer," *Cancer Letters*, vol. 432, pp. 180–190, 2018.
- [28] C. W. Brennan, R. G. Verhaak, A. McKenna et al., "The somatic genomic landscape of glioblastoma," *Cell*, vol. 155, no. 2, pp. 462–477, 2013.
- [29] Y. Yang, M. Luo, K. Zhang et al., "Nedd4 ubiquitylates VDAC2/3 to suppress erastin-induced ferroptosis in melanoma," *Nature Communications*, vol. 11, no. 1, p. 433, 2020.
- [30] C. Gai, C. Liu, X. Wu et al., "MT1DP loaded by folate-modified liposomes sensitizes erastin-induced ferroptosis via regulating miR-365a-3p/NRF2 axis in non-small cell lung cancer cells," *Cell Death & Disease*, vol. 11, no. 9, p. 751, 2020.
- [31] F. Torrisi, N. Vicario, F. M. Spitale et al., "The role of hypoxia and SRC tyrosine kinase in glioblastoma invasiveness and radioresistance," *Cancers (Basel)*, vol. 12, no. 10, p. 2860, 2020.
- [32] D. R. Mole, C. Blancher, R. R. Copley et al., "Genome-wide association of hypoxia-inducible factor (HIF)-1 α and HIF-2 α DNA binding with expression profiling of hypoxia-inducible transcripts," *The Journal of Biological Chemistry*, vol. 284, no. 25, pp. 16767–16775, 2009.
- [33] Z. Lin, J. Song, Y. Gao et al., "Hypoxia-induced HIF-1 α /lncRNA-PMAN inhibits ferroptosis by promoting the cytoplasmic translocation of ELAVL1 in peritoneal dissemination from gastric cancer," *Redox Biology*, vol. 52, article 102312, 2022.
- [34] S. Yuan, C. Wei, G. Liu et al., "Sorafenib attenuates liver fibrosis by triggering hepatic stellate cell ferroptosis via HIF-1 α /SLC7A11 pathway," *Cell Proliferation*, vol. 55, article e13158, 2022.
- [35] J. Wei, J. Wu, W. Xu et al., "Salvianolic acid B inhibits glycolysis in oral squamous cell carcinoma via targeting PI3K/AKT/HIF-1 α signaling pathway," *Cell Death & Disease*, vol. 9, no. 6, p. 599, 2018.
- [36] W. Huang, X. Ding, H. Ye, J. Wang, J. Shao, and T. Huang, "Hypoxia enhances the migration and invasion of human glioblastoma U87 cells through PI3K/Akt/mTOR/HIF-1 α pathway," *Neuroreport*, vol. 29, no. 18, pp. 1578–1585, 2018.
- [37] J. Yi, J. Zhu, J. Wu, C. B. Thompson, and X. Jiang, "Oncogenic activation of PI3K-AKT-mTOR signaling suppresses ferroptosis via SREBP-mediated lipogenesis," *Proceedings of the National Academy of Sciences of the United States of America*, vol. 117, no. 49, pp. 31189–31197, 2020.
- [38] P. Y. Wen, M. Weller, E. Q. Lee et al., "Glioblastoma in adults: a Society for Neuro-Oncology (SNO) and European Society of Neuro-Oncology (EANO) consensus review on current management and future directions," *Neuro-Oncology*, vol. 22, no. 8, pp. 1073–1113, 2020.
- [39] E. V. Sazonova, G. S. Kopeina, E. N. Imyanitov, and B. Zhivotovsky, "Platinum drugs and taxanes: can we overcome resistance?," *Cell Death Discovery*, vol. 7, no. 1, p. 155, 2021.
- [40] S. Sun, T. Gao, B. Pang et al., "RNA binding protein NKAP protects glioblastoma cells from ferroptosis by promoting SLC7A11 mRNA splicing in an m(6)A-dependent manner," *Cell Death & Disease*, vol. 13, no. 1, p. 73, 2022.
- [41] Y. Su, B. Zhao, L. Zhou et al., "Ferroptosis, a novel pharmacological mechanism of anti-cancer drugs," *Cancer Letters*, vol. 483, pp. 127–136, 2020.
- [42] J. Fu, T. Li, Y. Yang et al., "Activatable nanomedicine for overcoming hypoxia-induced resistance to chemotherapy and inhibiting tumor growth by inducing collaborative apoptosis and ferroptosis in solid tumors," *Biomaterials*, vol. 268, article 120537, 2021.
- [43] Z. Li, L. Jiang, S. H. Chew, T. Hirayama, Y. Sekido, and S. Toyokuni, "Carbonic anhydrase 9 confers resistance to ferroptosis/apoptosis in malignant mesothelioma under hypoxia," *Redox Biology*, vol. 26, article 101297, 2019.
- [44] C. L. Ye, Y. Du, X. Yu et al., "STEAP3 affects ferroptosis and progression of renal cell carcinoma through the p53/xCT pathway," *Technology in Cancer Research & Treatment*, vol. 21, article 15330338221078728, 2022.
- [45] J. Liu, Z. Duan, W. Guo et al., "Targeting the BRD4/FOXO3a/CDK6 axis sensitizes AKT inhibition in luminal breast cancer," *Nature Communications*, vol. 9, no. 1, p. 5200, 2018.
- [46] H. Hirai, H. Sootome, Y. Nakatsuru et al., "MK-2206, an allosteric Akt inhibitor, enhances antitumor efficacy by standard chemotherapeutic agents or molecular targeted drugs in vitro and in vivo," *Molecular Cancer Therapeutics*, vol. 9, no. 7, pp. 1956–1967, 2010.
- [47] J. P. Thiery, H. Acloque, R. Y. Huang, and M. A. Nieto, "Epithelial-mesenchymal transitions in development and disease," *Cell*, vol. 139, no. 5, pp. 871–890, 2009.
- [48] G. L. Semenza, "Oxygen sensing, hypoxia-inducible factors, and disease pathophysiology," *Annual Review of Pathology*, vol. 9, no. 1, pp. 47–71, 2014.
- [49] J. Pastorek and S. Pastorekova, "Hypoxia-induced carbonic anhydrase IX as a target for cancer therapy: from biology to clinical use," *Seminars in Cancer Biology*, vol. 31, pp. 52–64, 2015.
- [50] K. Lee and H. M. Kim, "A novel approach to cancer therapy using PX-478 as a HIF-1 α inhibitor," *Archives of Pharmacological Research*, vol. 34, no. 10, pp. 1583–1585, 2011.
- [51] H. S. Ban, Y. Uto, and H. Nakamura, "Hypoxia-inducible factor inhibitors: a survey of recent patented compounds (2004 – 2010)," *Expert Opinion on Therapeutic Patents*, vol. 21, no. 2, pp. 131–146, 2011.
- [52] M. Jiang, B. Qin, L. Luo et al., "A clinically acceptable strategy for sensitizing anti-PD-1 treatment by hypoxia relief," *Journal of Controlled Release: official journal of the Controlled Release Society*, vol. 335, pp. 408–419, 2021.
- [53] X. Zhu, Y. Zhou, Y. Ou et al., "Characterization of ferroptosis signature to evaluate the predict prognosis and immunotherapy in glioblastoma," *Aging*, vol. 13, no. 13, pp. 17655–17672, 2021.
- [54] G. Lei, Y. Zhang, T. Hong et al., "Ferroptosis as a mechanism to mediate p53 function in tumor radiosensitivity," *Oncogene*, vol. 40, no. 20, pp. 3533–3547, 2021.
- [55] J. M. Heddleston, M. Hitomi, M. Venere et al., "Glioma stem cell maintenance: the role of the microenvironment," *Current Pharmaceutical Design*, vol. 17, no. 23, pp. 2386–2401, 2011.
- [56] G. L. Semenza, "Targeting HIF-1 for cancer therapy," *Nature Reviews Cancer*, vol. 3, no. 10, pp. 721–732, 2003.

- [57] P. Koppula, L. Zhuang, and B. Gan, "Cystine transporter SLC7A11/xCT in cancer: ferroptosis, nutrient dependency, and cancer therapy," *Protein & Cell*, vol. 12, no. 8, pp. 599–620, 2021.
- [58] <https://www.researchsquare.com/article/rs-1122453/v2>.
<https://assets.researchsquare.com/files/rs-1122453/v1/c78174a7-8579-46d8-a680-d15e4866af68.pdf?c=1642423579>.

Research Article

Attenuation by Time-Restricted Feeding of High-Fat and High-Fructose Diet-Induced NASH in Mice Is Related to Per2 and Ferroptosis

Yan-yun Shu , Wen-kang Gao , Hui-kuan Chu , Ling Yang , Xiao-li Pan ,
and Jin Ye 

Division of Gastroenterology, Union Hospital, Tongji Medical College, Huazhong University of Science and Technology, Wuhan, China 430022

Correspondence should be addressed to Xiao-li Pan; pxiaoli@hotmail.com and Jin Ye; 1977xh0541@hust.edu.cn

Received 7 August 2022; Revised 12 September 2022; Accepted 19 September 2022; Published 15 October 2022

Academic Editor: Lianxiang Luo

Copyright © 2022 Yan-yun Shu et al. This is an open access article distributed under the Creative Commons Attribution License, which permits unrestricted use, distribution, and reproduction in any medium, provided the original work is properly cited.

Nonalcoholic steatohepatitis (NASH) is a chronic and progressive disease whose treatment strategies are limited. Although time-restricted feeding (TRF) is beneficial for metabolic diseases without influencing caloric intake, the underlying mechanisms of TRF action in NASH and its efficacy have not yet been demonstrated. We herein showed that TRF effectively alleviated NASH, producing a reduction in liver enzymes and improvements in liver pathology. Regarding the mechanisms by which TRF mitigates NASH, we ascertained that TRF inhibited ferroptosis and the expression of the circadian gene Per2. By adopting a hepatocyte-specific Per2-knockout (Per2^{Δhep}) mice model, we clarified the critical role of Per2 in exacerbating NASH. According to the results of our RNA-Seq analysis, the knockout of Per2 ameliorated NASH by inhibiting the onset of ferroptosis; this was manifested by diminished lipid peroxidation levels, decreased mRNA and protein levels for ferroptosis-related genes, and alleviated morphologic changes in mitochondria. Furthermore, using a ferroptosis inhibitor, we showed that ferroptosis significantly aggravated NASH and noted that this was likely achieved by regulation of the expression of peroxisome proliferator activated receptor (PPAR) α . Finally, we discerned that TRF and hepatocyte-specific knockout of Per2 promoted the expression of PPAR α . Our results revealed a potential for TRF to effectively alleviate high-fat and high-fructose diet-induced NASH via the inhibition of Per2 and depicted the participation of Per2 in the progression of NASH by promoting ferroptosis, which was ultimately related to the expression of PPAR α .

1. Introduction

Nonalcoholic steatohepatitis (NASH), a progressive form of nonalcoholic fatty liver disease (NAFLD), is a chronic and progressive disease characterized by accumulated liver fat, hepatocyte injury, and inflammatory infiltration [1, 2]. The advent of fast-paced lifestyles and high-calorie diets has enhanced the incidence rate of metabolic diseases [3, 4], contributing to an increased incidence rate of NAFLD. Epidemiologic studies have indicated that the global incidence rate of NAFLD is nearly 25%, and this contributes to the increasing prevalence of NASH [5]. NASH eventually increases the risk of developing end-stage liver disease and

places a great burden on society as a whole [3, 4]. There is therefore an acute need for the elucidation of definitive pathogenesis and effective treatment concerning NASH.

Lifestyle modifications—for example, reducing calorie intake or increasing exercise—constitute the core of NASH therapy; although time-restricted feeding (TRF) is considered to exert some effects on NASH [6, 7], their efficacy and underlying pathophysiologic mechanisms of action remain unclear. TRF refers to regular intermittent calorie control, implying that food intake remains restricted to fixed hours without deliberately reducing calorie intake, while during other hours of the day, food is not made available. Clinical research has shown that intermittent fasting (also

described as TRF) is an effective strategy for weight loss and metabolic-index improvement [8, 9]. While exploring the mechanism of TRF action in metabolic disease, some animal studies showed that TRF protected against weight gain and improved glucose tolerance and lipid metabolism [6, 10]. Furthermore, TRF also protected mice from liver steatosis and damage, without influencing the total calorie intake, when they were fed a high-fat diet [6]. These researchers subsequently ascertained that TRF restored the expression of the circadian genes [6], suggesting the possibility that the effectiveness of TRF was achieved by regulating the expression of such genes.

A pivotal role of the circadian clock in the pathogenesis and progression of NASH has been investigated in recent years [11, 12]. Per2, a member of the circadian gene family, is important in modulating the circadian rhythm and the expression of other circadian genes [13, 14]. Previous studies revealed that mice lacking the Per2 gene or the functional Per2 protein exhibited reductions in body weight, total plasma triacylglycerol, and plasma glucose levels [15, 16]—indicating an important role for Per2 in the metabolism of glucose and fat. Considering that TRF influences the expression of circadian genes [6], we hypothesized that the beneficial effects of TRF were achieved by regulating the Per2 gene. However, whether Per2 participates in NASH and its underlying mechanisms are not clear.

Ferroptosis, a newly uncovered form of cell death, is a type of regulated cell death characterized by iron-dependent accumulation of lipid peroxidation (LPO) [17], which is also related to the pathogenesis and progression of NASH. In addition to its effects on cancer and stroke [18, 19], the ferroptosis is reported to be crucial in triggering inflammation [20, 21] as well as promoting the formation of lipid droplets in NASH [20]. In 2019, researchers demonstrated the promotion of ferroptosis after autophagic degradation of certain circadian genes [22], indicating that ferroptosis might be regulated by such genes.

The family of peroxisome proliferator-activated receptors (PPARs) is significant in regulating body fat and energy metabolism and is reported to occupy a critical position in the progression of NASH [23, 24]. Regarding the subtypes of PPARs, previous investigators reported that PPAR α and PPAR γ were directly or indirectly regulated by the Per2 [15, 25] and that the activity of PPAR α might influence susceptibility to ferroptosis [26]. The aforementioned observations suggested a possible relationship between Per2, ferroptosis, and PPARs in the pathophysiology of NASH.

We therefore herein intended to investigate the efficacy and mechanisms by which TRF alleviated NASH, the relationship between Per2 and ferroptosis, and the mechanism by which Per2 and ferroptosis participated in NASH.

2. Materials and Methods

2.1. Animals and Diets. This animal experiment was approved by the Ethics Committee for Animal Experimentation (IACUC number 2818), and all animals received humane care in accordance with the National Institutes of Health Guide for the Care and Use of Laboratory Animals

(NIH Publications No. 8023, revised, 1978). Male white-type C57BL/6J mice were purchased from Beijing Vital River Laboratory Animal Technology Co., Ltd., and the Per2 double-floxed mice were generated at GemPharmatech Co., Ltd. on a C57BL6J background. An AVV8-TGB-iCre vector (Wuhan Qijing Biotechnology Co., Ltd., China) was injected intravenously (iv) into the tails of Per2 double-floxed mice to generate hepatocyte-specific Per2-knockout (Per2 Δ^{hep}) mice, while the AVV8-TGB-MCS-wpre vector (Wuhan Qijing Biotechnology Co., Ltd., China) was also tail injected into Per2 double-floxed mice to generate the controls (Per2 $^{\text{fl/fl}}$). After acclimating to their experimental environment with a normal chow diet for one week, the aforementioned mice (age 8 weeks) were raised for 16 weeks in a 12 h light/12 h dark cycle on a high-fat and high-fructose diet (HFHFD) (Research Diets Inc., USA) or a normal chow diet, in which lights-on was referred to as ZT0/24 and lights-off as ZT12. RT-qPCR and western immunoblotting analyses were executed to identify the genotypes of the animals.

Some of the C57BL/6J mice were randomly allocated to four groups: ad libitum access to HFHFD (FA) ($n = 8$), access from ZT13 to ZT23 to an HFHFD (FT) ($n = 10$), ad libitum access to a chow diet (NA) ($n = 10$), and access from ZT13 to ZT23 to a chow diet (NT) ($n = 10$). Another group of C57BL/6J mice was used to identify the role of ferroptosis and was randomized into two subgroups: ad libitum access to HFHFD accompanied by liproxstatin-1 (Lip-1) (MedChemExpress, USA) injection (FA+Lip-1) and mice provided the appropriate vehicle (FA+Veh) for the last four weeks. Lip-1 was dissolved in PBS with a small amount of DMSO and administered via intraperitoneal (ip) injection to mice at a dosage of 10 mg per kg per day [27, 28]. The Per2 Δ^{hep} and Per2 $^{\text{fl/fl}}$ mice were fed an HFHFD ad libitum from the beginning of the experiment.

2.2. Sample Collection. After 16 weeks of HFHFD or normal chow diet feeding, the mice were fasted from ZT0 and sacrificed at ZT8 to ZT10, and blood and liver tissue were collected. The blood was stored in a refrigerator at 4°C for 12 h. After centrifugation at 3000 rpm for 10–15 min, the serum was collected and stored at –80°C for further analyses. The liver tissues obtained from the mice were cut into small pieces and immediately frozen in liquid nitrogen and stored at –80°C for further analyses.

2.3. Glucose Tolerance Testing. For mice in the FA+Lip-1 and FA+Veh groups, we adopted an ip glucose tolerance test (IPGTT) [29, 30] the day before the mice were sacrificed to fully reflect the influence of Lip-1 on glucose metabolism. For the other mice, the IPGTT was performed at week 12 of the experiment. All mice were fasted for 10 h (from ZT23 to ZT9), and the IPGTT was conducted as follows according to a previous study [30]. We retrieved a second drop of blood from the tails, measured glucose concentrations (0 min) with a Portable Blood Glucose Meter (Johnson & Johnson, USA), and simultaneously injected a glucose solution (20%, 2 g per kg) ip into the mice. We then measured glucose concentrations using the same method as above at 30, 60, 90, and 120 min after glucose injection.

The mice were fasted during the experiment but had free access to water.

2.4. Analysis of Serum Biochemical Indices. Serum levels of alanine aminotransferase (ALT), aspartate aminotransferase (AST), total cholesterol (TC), triglycerides (TGs), free fatty acids (FFAs), and iron were determined by commercial kits (Nanjing Jiancheng Bioengineering Institute, China) following the manufacturer's protocols.

2.5. Analysis of Liver Biochemical Indices. We removed the liver pieces that were frozen at -80°C and generated a liver homogenate (10%). The homogenate was centrifuged to obtain the supernatant, and the liver concentrations of TC, TG, FFA, iron, malondialdehyde (MDA), and glutathione (GSH) were assessed with commercial kits (Nanjing Jiancheng Bioengineering Institute, China) following the manufacturer's protocols. The data were then normalized to protein concentration.

2.6. Pathologic Examination of the Liver. Liver samples were fixed in 4% paraformaldehyde for 24 h, paraffin-embedded, sectioned at $5\ \mu\text{M}$, and stained with hematoxylin and eosin (H&E) (Baso, China) and Sirius red (Solarbio, China). Other portions of the samples were fixed in optimal cutting temperature compound (OCT) (SAKURA, Japan) and frozen immediately in liquid nitrogen. After cutting the samples at $10\ \mu\text{M}$, oil red O (Solarbio, China) staining was used to assess steatosis. All slices noted above were observed under an Olympus optical fluorescence microscope (Olympus Corporation, Japan).

2.7. Scoring of NAFLD Activity Score (NAS) and Fibrotic Stage. The NAS score (which ranged from 0 to 8) was calculated according to a previous study [31, 32] upon evaluation of H&E-stained sections; and the sum of the scores for steatosis (0-3), lobular inflammation (0-3), and hepatocyte ballooning (0-2) was considered the NAS score, with a score ≥ 5 strongly indicating NASH. The fibrotic stage was also evaluated according to a previous study and ranged from 0 to 4 [31].

2.8. RNA Sequencing. RNA-Seq experiments and data analysis were performed using fresh-frozen liver tissues from the FA+Veh and FA+Lip-1 mice ($n = 3$ per group) or Per2 $^{\Delta\text{hep}}$ and Per2 $^{\text{fl/fl}}$ mice ($n = 3 - 4$ per group). After total RNA was extracted and quantified, RNA sequencing was implemented using an Illumina Novaseq 6000 sequencer [33] to obtain the raw data.

To ensure the accuracy of subsequent biological information analysis, the raw sequenced data were filtered by removing the linker sequence, low-quality reads, and reads with N to obtain clean data for subsequent analysis. The clean data were mapped to the genotype of *Mus musculus* to obtain comprehensive transcript information using STRA software (version 2.5.3a) [34]. We employed FeatureCounts [35] to retrieve the reads that mapped to the exonic regions and calculated the reads per kilobase of transcript per million reads mapped (RPKM) [36] with the edgeR package

(version 3.12.1) [37] to obtain the expression levels of the differential genes (DEGs).

The DEGs were identified with an absolute value of $\log\text{FC} > 1$ and a P value < 0.05 . A gene expression heatmap was obtained by the hierarchical clustering method, and Kyoto Encyclopedia of Genes and Genomes (KEGG) enrichment analysis and Gene Ontology (GO) analysis were applied using KOBAS software (version: 2.1.1) [38] to attain the biological meaning and function of the genes. A P value < 0.05 indicated statistically significant enrichment. RNA-Seq experiments and data analyses were performed by the Wuhan Seqhealth Technology Co., Ltd.

2.9. Transmission Electron Microscopy (TEM). The examination of electron microscopic images was as previously reported [20]. Fresh liver sections were fixed in 2.5% glutaraldehyde (Servicebio, China) at 4°C for four hours, washed three times with phosphate-buffered saline (PBS, Servicebio, China) for 15 min each, and subsequently fixed with 1% OsO_4 in 0.1 mol/L PBS at room temperature for two hours. After dehydration and penetration, the liver sections were embedded in epoxy resin. Thin slices were cut on an ultramicrotome (Leica, Germany) and stained with lead citrate and 2% uranyl acetate, and TEM was used to procure images.

2.10. Fluorescence Staining. Frozen sections of liver sections were rewarmed and subsequently fixed in 4% paraformaldehyde. After washing in PBS, 0.2% Triton X-100 was used for 10 min, followed by 10 min of PBS washing. The sections were then incubated with C11-Bodipy ($5\ \mu\text{mol/L}$, Invitrogen, USA) at 37°C for 30 min and washed in PBS [20]. Finally, the cellular nuclei were stained with 4',6-diamidino-2'-phenylindole (DAPI, Servicebio, China) for 10 min, and images were observed with an Olympus optical fluorescence microscope (Olympus Corporation, Japan).

2.11. Real-Time Polymerase Chain Reaction (RT-qPCR) and Western Immunoblot Analysis. After total RNA was extracted and reverse-transcribed to cDNA, we performed RT-qPCR, and the fold change in mRNA expression was calculated with the $2^{-\Delta\Delta\text{Ct}}$ method [39] and compared using Student's t tests (the primers are depicted in Table 1). Total tissue proteins were extracted and denatured, and a PG-112 PAGE gel (10%, Epizyme Biomedical Technology Co., Ltd., China) was exploited separate the proteins. A PVDF membrane (Merck Millipore Ltd., USA) was adopted to transfer the proteins and was cut into pieces according to the molecular weights of the target proteins. We incubated membranes with the primary antibodies against Per2 rabbit mAb (ABclonal, China), Acsl4 rabbit mAb (ABclonal, China), Gpx4 mouse mAb (Proteintech, USA), Tfr1 rabbit pAb (ABclonal, China), PPAR α mouse mAb (ABclonal, China), and PPAR γ rabbit PAb (ABclonal, China) and utilized the secondary antibodies (AntGene, China) to detect the primary antibodies. The target proteins were ultimately visualized using a chemiluminescence kit (Vazyme, China).

TABLE 1: The primers used in this article.

Gene primers	Forward (5'-3')	Reverse (5'-3')
GAPDH	AACTTTGGCATTGTGGAAGG	ACACATTGGGGGTAGGAACA
Tnf- α	AGGGACCTCTCTAATCAG	TGGGAGTAGATGAGGTACAG
IL-6	GAAATGATGGATGCTACAAACTG	GACTCTGGCTTTGTCTTTCTTGT
IL-1 β	TTGTTGATGTGCTGCTGTGA	TGTGAAATGCCACCTTTTGA
Per1	GGTTCAGGATCCCACGAAG	AAGAGTCGATGCTGCCAAAG
Per2	CACACTTGCCTCCGAAATAACTC	AGCGCACGGCTGTCTGA
Bmal1	AACCTTCCCGCAGCTAACAG	AGTCCTCTTTGGGCCACCTT
Clock	GGCGTTGTTGATTGGACTAGG	GAATGGAGTCTCCAACACCCA
Rev-erba	TGGCCTCAGGCTTCCACTATG	CCGTTGCTTCTCTCTCTTGGG
Acs14	CTCACCATTATATTGCTGCCTGT	TCTCTTTGCCATAGCGTTTTTCT
Gpx4	GCCTGGATAAGTACAGGGGT	CATGCAGATCGACTAGCTGAG
Aifm2	TTACAAGCCAGAGACTGACCAA	ACAAGGCCTGTCACTGAAGAG
Ptgs2	TGAGCAACTATTCAAAACCAGC	GCACGTAGTCTTCGATCACTATC
Irp1	AGAACCATTGTCACACCTTG	AGCGTCCGTATCTTGAGTCT
Irp2	CTGCTATGAGGGAGGCAGTG	TGCAGGGAAGCTTCTTAGGC
Tfr1	TCCTGTCGCCCTATGTATCT	CGAAGCTTCAAGTTCTCCACTA
Tfr2	TTGGGGTCTACTTCGGAGAGT	GACAGGAGCCTAAGTGCTCAG
Slc40a1	ACCAAGGCAAGAGATCAAACC	AGACACTGCAAAGTGCCACAT

2.12. *Statistical Analysis.* All experimental data are presented as mean \pm standard error, and the data were analyzed with IBM SPSS 23. We adopted a one-way analysis of variance (ANOVA) and post hoc testing with least significant difference (LSD) or Dunnett's T3 tests (according to the homogeneity of variance observed) to identify differences among three or more independent groups [40, 41]. An independent sample *t* test was executed to determine the differences between the two independent groups. The figures in this experiment were created using GraphPad Prism 6.0 software. A *P* value < 0.05 indicated statistically significant differences.

3. Results

3.1. *TRF Alleviates HFHFD-Induced NASH.* We fed C57/BL6 J mice a HFHFD for 16 weeks to formulate a NASH model (the FA group), and a normal chow diet was used for the controls (NA group). To explore the effectiveness of TRF in the treatment of NASH, we fed TRF-treated mice with HFHFD for 10 h (from ZT13 to ZT23) per day (FT groups), with the FA group serving as a control. At last, we measured metabolic indices, liver injury markers, and liver pathologic findings of mice in the NA, NT, FA, and FT groups.

We found that mice in the FA group developed NASH with significant weight gain; high serum glucose; high concentrations of TG, TC, and FFA in their serum; and high concentrations of TG and TC in their livers (Figures 1(a)–1(d)). Regarding liver injury markers, the levels of ALT and AST were also increased in the FA group (Figure 1(e)). Compared with the FA group, the TRF strategy significantly lowered the body weight; reduced the serum levels of TG, TC, and FFA and liver concentrations of TG and TC; decreased

the ALT and AST levels; and improved the glucose tolerance without affecting food intake (Figures 1(a)–1(e) and S1A).

In addition to the improvement in liver enzymes and metabolic indices in the NASH mice, TRF also significantly alleviated the liver injury induced by HFHFD. Our results revealed that mice in the FA group developed significant steatosis, inflammation, and fibrosis with a higher NAS score and that these changes were significantly reduced in the FT group (Figures 1(f) and S1B–C). Furthermore, RT-qPCR showed that the expression of tumor necrosis factor- (Tnf-) α was elevated in the FA group and reduced in the FT group, confirming a reduction in overall inflammation (Figure S1D). These data showed that TRF effectively attenuated NASH with an improvement in pathologic findings, liver-injury markers, and metabolic indices.

3.2. *TRF Reverses the Overexpression of the Circadian Gene Per2 in NASH Mice.* Earlier studies reported that the effect of TRF in metabolic disorders might be achieved by restoring the expression of circadian genes [6]. To verify this hypothesis, we implemented RT-qPCR and measured the expression of circadian rhythm-related genes. Our results showed that the expression of circadian genes such as Bmal1, Clock, Rev-Erba, Per2, and Per1 increased in the FA group, and the strategy with TRF reduced the expression of the aforementioned circadian genes (Figure 2(a)).

Per2 is an indispensable gene in the modulation of circadian rhythm [13, 14] and participates in lipid and glucose metabolism [15, 16], thus attracting our attention. We therefore analyzed Per2 protein levels to identify the relationship between TRF and the Per2 gene. By applying western blotting, we ascertained that the protein levels of Per2 were

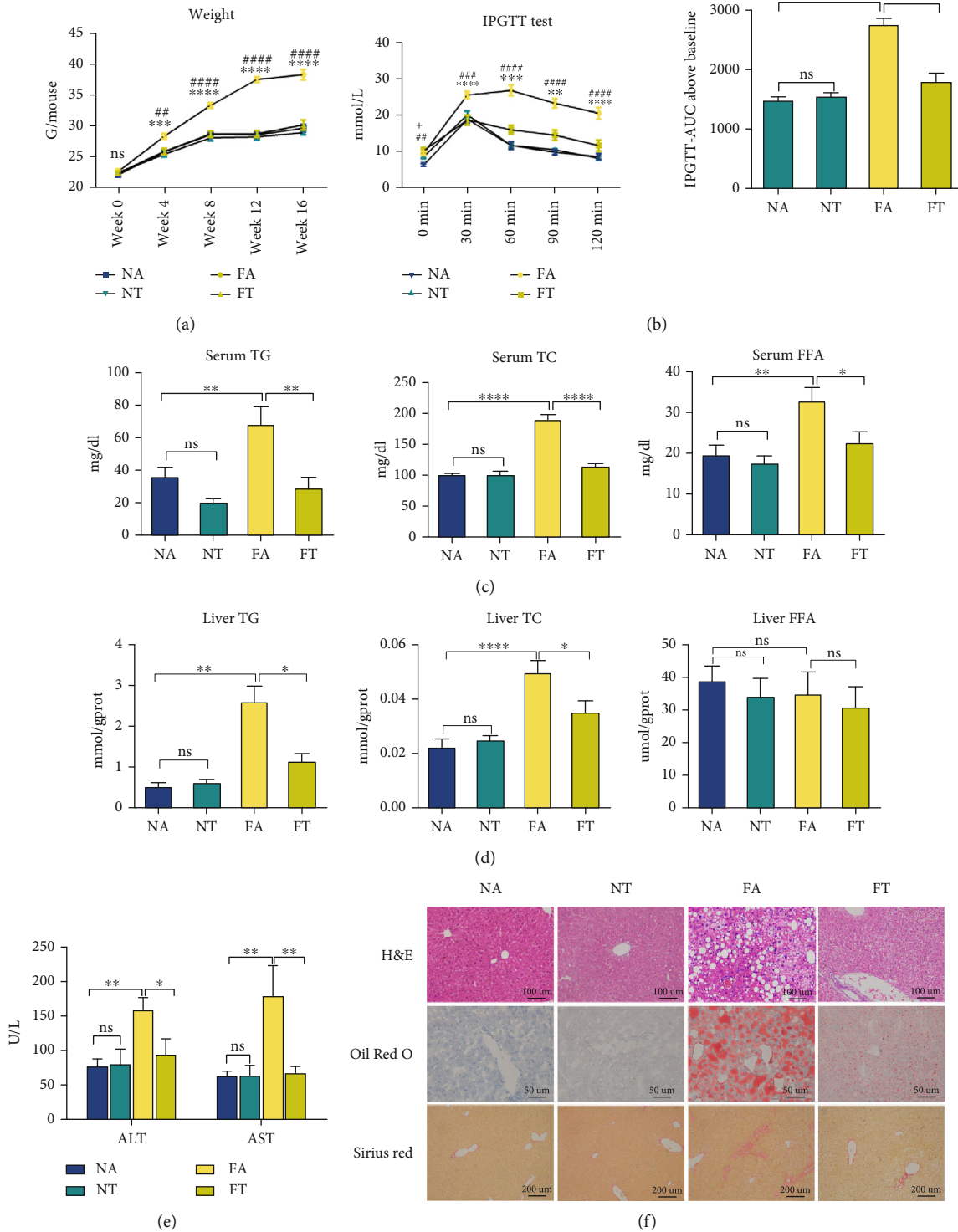


FIGURE 1: TRF alleviates HFHFD-induced NASH. (a) Body weights of mice measured at 0, 4, 8, 12, and 16 weeks in the present experiment; *FA vs. FT and #FA vs. NA. (b) An IPGTT test was performed at the end of 12 weeks, and the corresponding area under the curve was calculated to assess differences among the four groups; *FA vs. FT and #FA vs. NA. (c, d) Serum and liver TG, TC, and FFA levels are depicted to demonstrate lipid concentrations in the various groups. (e) Serum ALT and AST were measured to evaluate the levels of liver injury. (f) Pathologic findings in liver sections. Liver paraffin sections were stained with H&E (original magnification, 200x; scale bar, 100 μ m), oil red O (original magnification, 400x; scale bar, 50 μ m), and Sirius red (original magnification, 100x; scale bar, 200 μ m) to determine the levels of steatosis, inflammation, and fibrosis. Data are presented as mean \pm SEM. * $P < 0.05$, ** $P < 0.01$, *** $P < 0.001$, **** $P < 0.0001$, ## $P < 0.01$, ### $P < 0.001$, and #### $P < 0.0001$; ns: not significant (also refer to Figure S1).

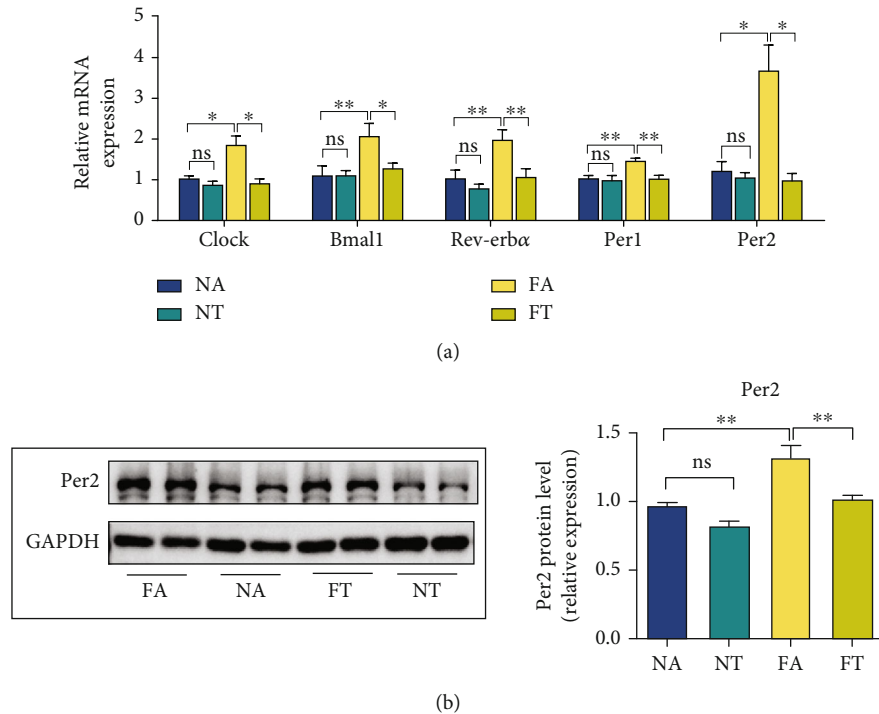


FIGURE 2: TRF reverses the overexpression of the circadian gene *Per2* in NASH mice. (a) Hepatic mRNA levels for *Bmal1*, *Clock*, *Per2*, *Per1*, and *Rev-Erb α* were measured by RT-qPCR with *GAPDH* used as a control. (b) The *Per2* protein level was measured by western blotting, and *GAPDH* was used as a control. Data are presented as mean \pm SEM. * $P < 0.05$ and ** $P < 0.01$; ns: not significant.

elevated in the FA group and that TRF effectively inhibited the expression of the *Per2* gene (Figure 2(b)).

3.3. TRF Suppresses the Ferroptosis in NASH Mice. Ferroptosis is reported to play an important role in the pathogenesis of NASH [20, 21]. Since TRF alleviated NASH, we intended to explore the role of TRF in ferroptosis. As we noted above, the ferroptosis is characterized by the accumulation of LPO and iron [17], alterations in mitochondrial morphology, and an elevated expression of some ferroptosis-related genes. We therefore examined the following components.

First, we measured the expression of ferroptosis-related genes. The mRNA levels for anti-acyl-CoA synthetase long-chain family member 4 (*Acsl4*), glutathione peroxidase 4 (*Gpx4*), apoptosis-inducing factor mitochondria-associated 2 (*Aifm2*), and prostaglandin-endoperoxide synthase 2 (*Ptgs2*); the protein levels of *Acsl4* and *Gpx4*; and the liver GSH concentrations were upregulated in the FA group but reduced by the TRF strategy (Figures 3(a)–3(c)). Second, the levels of LPO in the FA group that we measured by a combination of the specific fluorescent probe C11-Bodipy (581/591) with the concentration of MDA [42] were augmented, and electron microscopy revealed shrunken mitochondria and increased mitochondrial membrane density; TRF then subsequently relieved both of these indices (Figures 3(d)–3(f)). These results showed that ferroptosis occurred in NASH and that TRF inhibited ferroptosis.

3.4. TRF Reduces Iron Accumulation in Serum and Liver after Induction by HFHFD. Investigators have reported iron

overload in both animal and clinical studies [43, 44], promoting NASH and ferroptosis to a significant degree [45, 46]. Consistent with these studies, we discerned that the serum and liver iron concentrations rose in the FA group and that the TRF strategy significantly reduced these concentrations (Figure 4(a)). Furthermore, when we determined the expression of the iron metabolism-related genes iron regulatory protein (*Irp1*), *Irp2*, transferrin receptor (*Tfr1*), *Tfr2*, and ferroportin (*Slc40a1*), we noted that the expression of *Irp1*, *Irp2*, *Tfr1*, and *Tfr2* was enhanced in the FA group and attenuated in the FT group compared with the FA group (Figure 4(b)).

Tfr1 is a key receptor that transports iron to cells [47], and it is reported to contribute to ferroptosis [48, 49]. We thus analyzed *Tfr1* protein levels and demonstrated that its expression was upregulated in the FA group and restored by TRF, verifying iron overload in NASH and its mitigation by TRF (Figure 4(c)).

3.5. Hepatocyte-Specific Knockout of *Per2* Mitigates HFHFD-Induced NASH. The aforementioned information revealed that TRF not only ameliorated NASH but also suppressed ferroptosis, *Per2* expression, and iron overload. To investigate how *Per2* participated in NASH and whether *Per2* regulated the occurrence of ferroptosis, we deployed the use of *Per2* ^{Δ hep} mice (Figures 5(a) and S2A). In previous studies, *Per2* knockout or inhibition improved glucose and lipid metabolism [15, 16]. In our study, we fed both *Per2* ^{Δ hep} and *Per2*^{fl/fl} mice with an HFHFD to examine the effects of *Per2* on NASH and found that fasting blood glucose

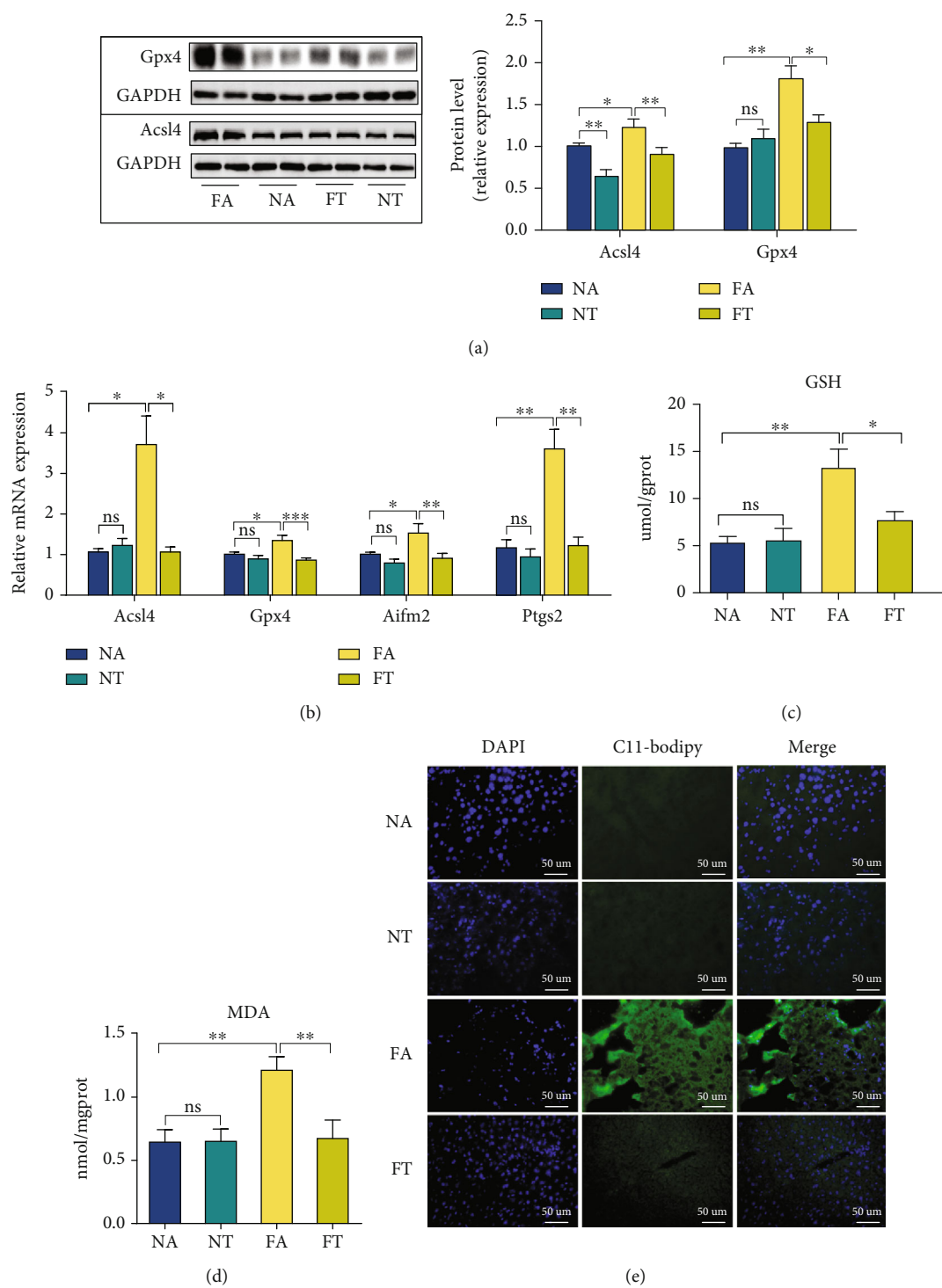


FIGURE 3: Continued.

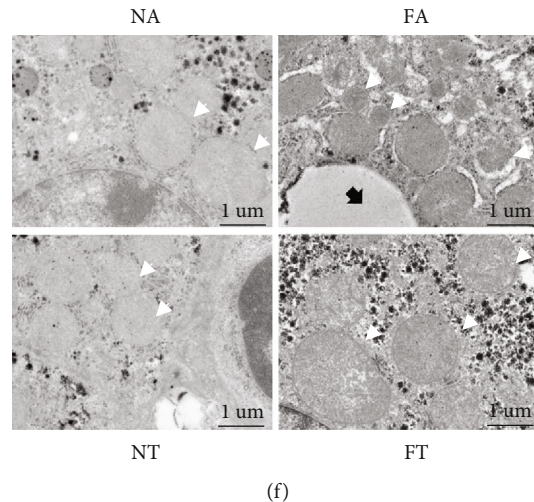


FIGURE 3: TRF suppresses the ferroptosis in NASH mice. (a) *Acsl4* and *Gpx4* protein levels were measured by western blotting, with *GAPDH* used as a control. (b) Hepatic mRNA levels for *Acsl4*, *Gpx4*, *Aifm2*, and *Ptgs2* were measured by RT-qPCR; and *GAPDH* was used as a control. (c, d) Liver GSH and MDA concentrations were quantified with commercial kits. (e) Fluorescence staining showing lipid peroxidation (LPO) levels in the FA, FT, NA, and NT groups. The nuclei were labeled with DAPI (left), and LPO (middle) was labeled with C11-Bodipy (original magnification, 400x; scale bar, 50 μm). (f) Electron microscopic analysis of the morphologic changes in mitochondria; the white arrow indicates lipid droplets, and the black arrow indicates mitochondria (original magnification, 5000x; scale bar, 1 μm) (NA and NT, $n = 2$; FA and FT, $n = 3$). * $P < 0.05$, ** $P < 0.01$, and *** $P < 0.001$; ns: not significant.

(Figure S2B), serum levels of TC and FFA, and liver TC levels (Figures 5(b) and 5(c)) were lower in $\text{Per2}^{\Delta\text{hep}}$ mice, while body weight, liver/body weight ratio, and IPGTT test (Figures S2B–C) were unchanged between the two groups.

In addition to the metabolic indices, we also evaluated the serum levels of hepatic enzymes and the degree of liver injury, and our data showed that both ALT and AST levels were lower in $\text{Per2}^{\Delta\text{hep}}$ mice than in $\text{Per2}^{\text{fl/fl}}$ mice (Figure 5(d)). Furthermore, our pathologic findings depicted $\text{Per2}^{\Delta\text{hep}}$ mice as exhibiting alleviated steatosis, inflammatory cell infiltration, and fibrosis with NASH (Figures 5(e) and S2D–E). RT-qPCR was used to assess inflammation in the liver, and these results characterized expression levels of interleukin- (IL-) 6 and IL-1 β as diminished in $\text{Per2}^{\Delta\text{hep}}$ mice (Figure S2F). These results indicated that *Per2* was not only elevated in HFHFD-induced NASH but that it also aggravated NASH.

3.6. Hepatocyte-Specific Knockout of *Per2* May Mitigate NASH by Inhibiting Ferroptosis. We conducted RNA-Seq to explore the possible mechanisms underlying the alleviation of NASH by hepatocyte-specific knockout of *Per2* and demonstrated that this knockout significantly promoted the expression of 71 genes and reduced the expression of 112 genes (Figures 6(a) and 6(b)). Furthermore, the KEGG analysis showed that the DEGs perturbed by *Per2* were principally enriched in the arachidonic acid metabolism pathway and glutathione metabolism pathway (Figure 6(c)). Ferroptosis can be induced by the peroxidation of polyunsaturated fatty acids (PUFAs) and can be inhibited by the GSH and GPX4 pathways [50, 51]. Arachidonic acid is a type of PUFAs, and its metabolic regulation has been suggested to influence ferroptotic sensitivity [52]. Therefore, the DEGs enriched in the arachidonic acid and glutathione metabolism

pathways implied that hepatocyte-specific knockout of *Per2* alleviated NASH by regulating ferroptosis.

To verify the hypothesis we mentioned above, we measured the expression of ferroptosis-related genes. Our results indicated that the expression of *Acsl4*, *Gpx4*, *Aifm2*, and *Ptgs2* was downregulated in $\text{Per2}^{\Delta\text{hep}}$ mice (Figure S2G) and that *Acsl4* and *Gpx4* protein levels and liver GSH levels were attenuated (Figures 6(d) and 6(e)). Furthermore, when we assessed LPO levels and mitochondrial morphologic changes in $\text{Per2}^{\Delta\text{hep}}$ and $\text{Per2}^{\text{fl/fl}}$ mice, we found that the levels of LPO as reflected by C11-Bodipy and MDA concentration were reduced in $\text{Per2}^{\Delta\text{hep}}$ mice and that mitochondrial morphology was restored (Figures 6(f)–6(h)), confirming that *Per2* promoted ferroptosis. Our results with regard to iron metabolism revealed that *Per2* did not influence either serum or liver iron levels and that the expression of *Tfr1* was also not altered by *Per2* (Figures 6(d) and 6(i) and S2H).

3.7. Ferroptosis Occurs in HFHFD-Induced NASH and Promotes Its Progression. To identify a role for ferroptosis in NASH, we applied liproxstatin-1 (Lip-1) to suppress ferroptosis in mice. Consistent with a previous study [20], the levels of LPO in the liver of Lip-1 treated mice (FA+Lip-1) as reflected by C11-Bodipy and MDA concentrations were reduced relative to those in the control mice (FA+Veh) (Figures 7(a) and 7(b)). Furthermore, RT-qPCR assay showed that the expression of *Acsl4* and *Ptgs2* was reduced, and that of *Gpx4* and *Aifm2* was increased in the FA+Lip-1 group (Figure S3A). Western blotting indicated that *Acsl4* protein levels as well as the liver GSH concentrations were reduced and that *Gpx4* protein levels were enhanced in the FA+Lip-1 group (Figures 7(c) and 7(d)). These results suggested the presence of ferroptosis in HFHFD-induced NASH.

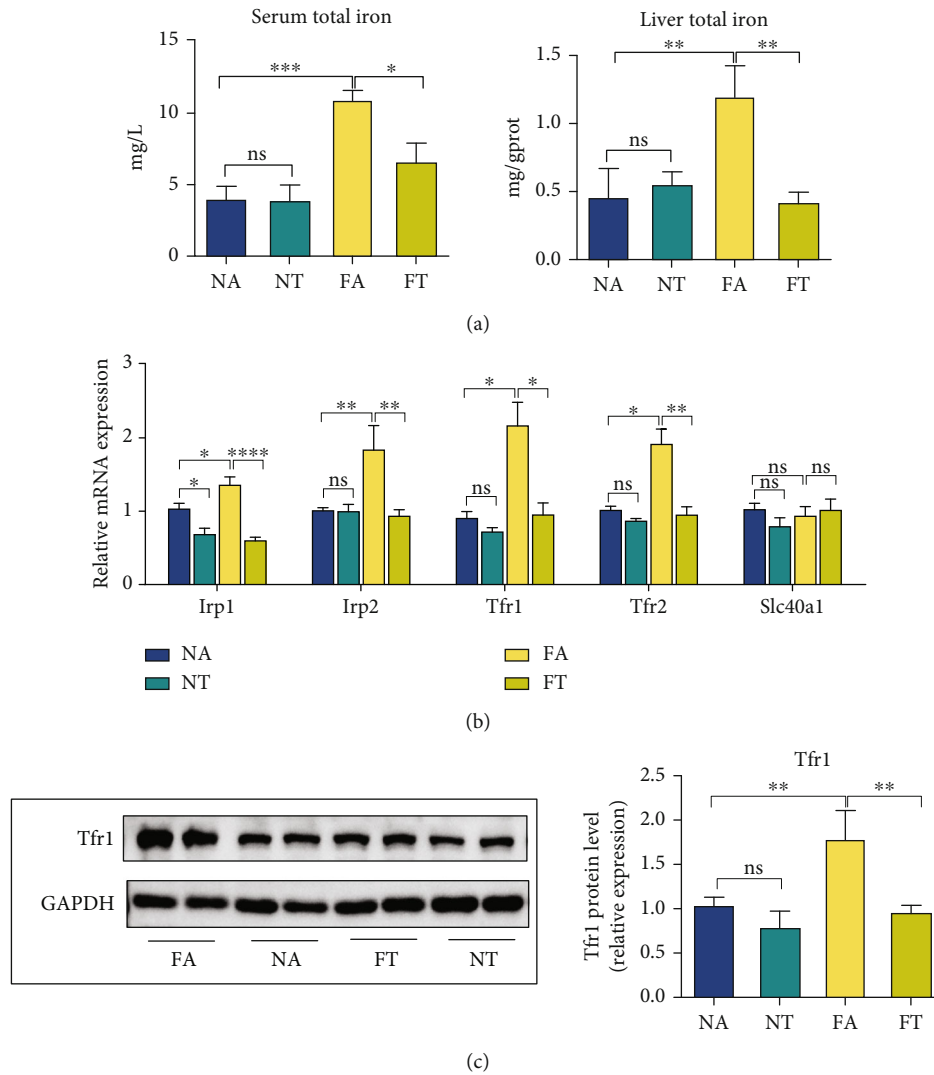


FIGURE 4: TRF reduces the iron accumulation in the serum and liver as induced by HFHFD. (a) Serum and liver iron concentrations were determined using a commercial kit to compare the iron overload levels among the four groups. (b) Hepatic mRNA levels for *Irp1*, *Irp2*, *Tfr1*, *Tfr2*, and *Slc40a1* were measured by RT-qPCR, and *GAPDH* was used as a control. (c) *Tfr1* protein levels were measured by western blotting, with *GAPDH* used as a control. Data are presented as mean \pm SEM. * $P < 0.05$, ** $P < 0.01$, *** $P < 0.001$, and **** $P < 0.0001$; ns: not significant.

In addition, body weights declined significantly, with a diminution in the liver/body weight ratio, but without a reduction in food intake in the group provided Lip-1 (Figures S3B–C). ALT and AST levels were also reduced as were serum concentrations of TG, TC, and FFA and liver concentrations of TG and TC with Lip-1 treatment (Figures 7(e)–7(g)). With respect to pathologic findings, Lip-1 treatment significantly reduced steatosis, inflammatory cell infiltration, and fibrosis (Figure 7(h)) and produced a lower NAS score (Figures S3D–E). These results indicate that ferroptosis is critical to the progression of NASH. However, Lip-1 exerts a limited influence on glucose metabolism (Figure S3F).

3.8. Ferroptotic Participation in NASH May Be Related to the Inhibition of PPAR α . When we executed RNA-Seq to determine the mechanism by which ferroptosis participated in NASH, we uncovered 132 upregulated and 199 downregu-

lated genes in the FA+Lip-1 group (Figures 8(a) and 8(b)). KEGG pathway enrichment analysis showed that the DEGs were mainly enriched in the fatty acid metabolism pathway between the FA+Veh and FA+Lip-1 groups (Figure 8(c)).

The family of peroxisome proliferator-activated receptors (PPARs) regulates energy metabolism, and PPAR α and PPAR γ are primarily expressed in the liver of NASH [24, 53–55]. We therefore measured PPAR α and PPAR γ mRNA and protein levels by RT-qPCR and western blotting and demonstrated that the expression of PPAR α was upregulated in the FA+Lip-1 group, but that protein levels of PPAR γ were unaltered (Figures 8(d) and 8(e)). These results suggested that ferroptosis participated in NASH by regulating the expression of PPAR α .

3.9. TRF and *Per2* Knockout Promote the Expression of PPAR α . We analyzed the mRNA and protein levels for

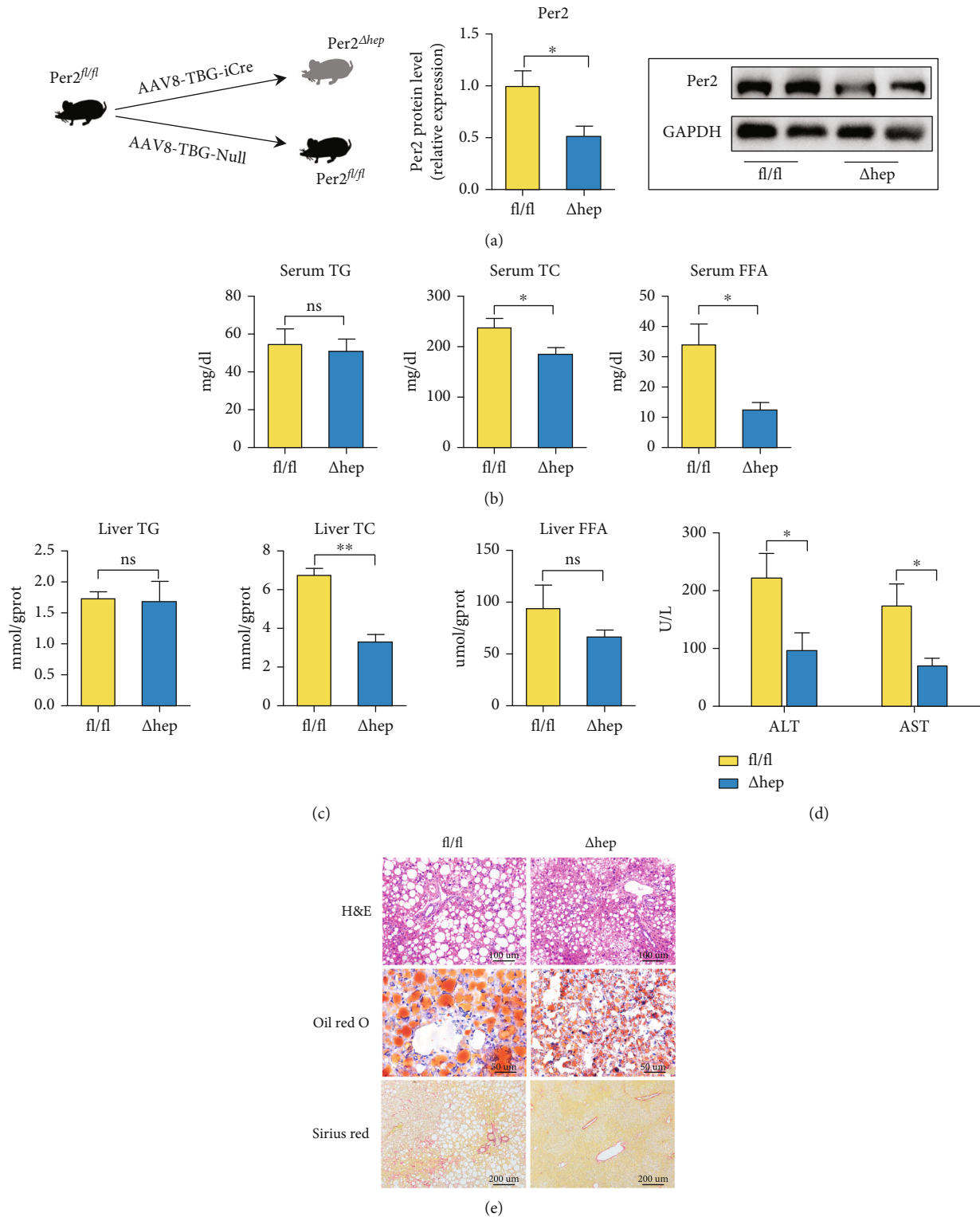
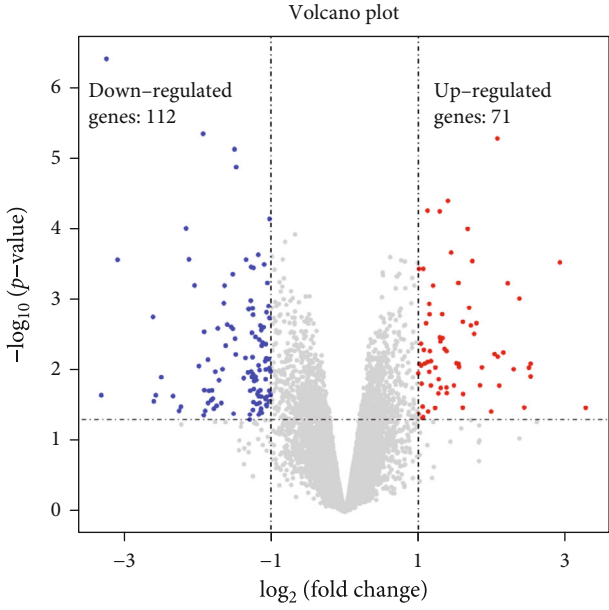
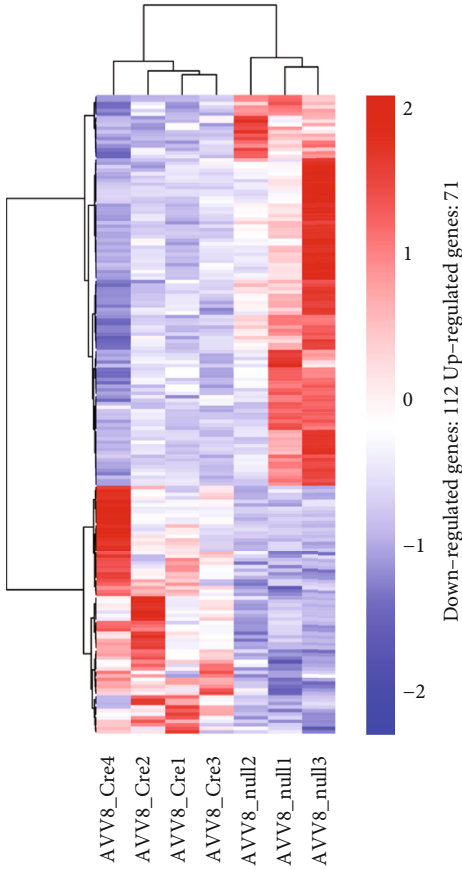


FIGURE 5: Hepatocyte-specific knockout of Per2 alleviates HFHFD-induced NASH. (a) Construction of the Per2 Δ hep mouse model and its verification by RT-qPCR and western blotting. (b, c) Serum and liver TG, TC, and FFA levels are depicted to demonstrate the lipid concentrations between the two groups. (d) ALT and AST levels were measured with a commercial kit to evaluate the levels of liver injury between the Per2 Δ hep and Per2^{fl/fl} mice. (e) Pathologic findings in the liver. Liver paraffin sections were stained with H&E (original magnification, 200x; scale bar, 100 μ m), oil red O (original magnification, 400x; scale bar, 50 μ m), and Sirius red (original magnification, 100x; scale bar, 200 μ m) to determine the levels of steatosis, inflammation, and fibrosis in Per2 Δ hep and Per2^{fl/fl} mice. Both Per2 Δ hep and Per2^{fl/fl} mice were fed with HFHFD to induce NASH. Data are presented as mean \pm SEM. * P < 0.05 and ** P < 0.01; ns: not significant (also refer to Figure S2).

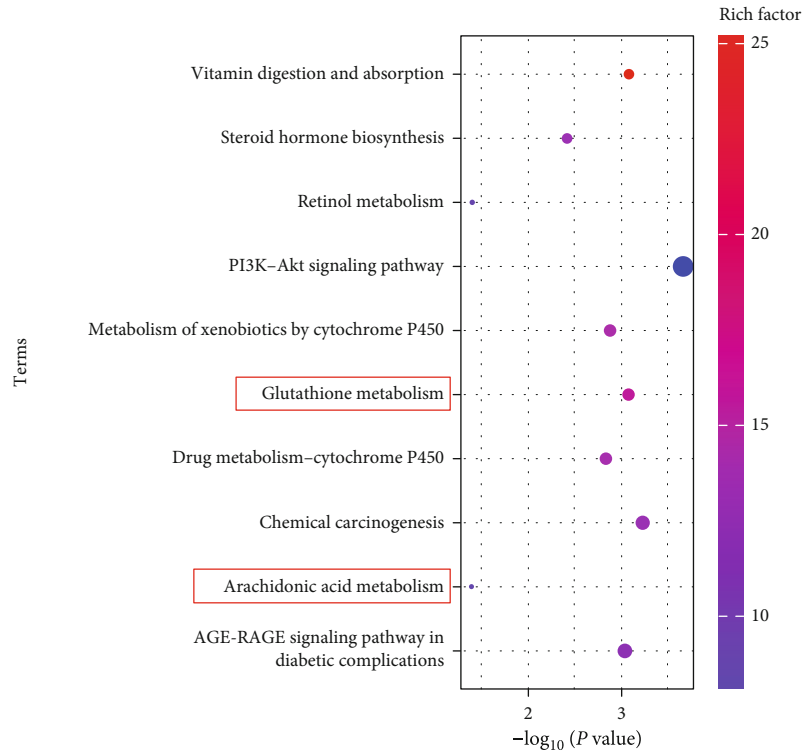


(a)

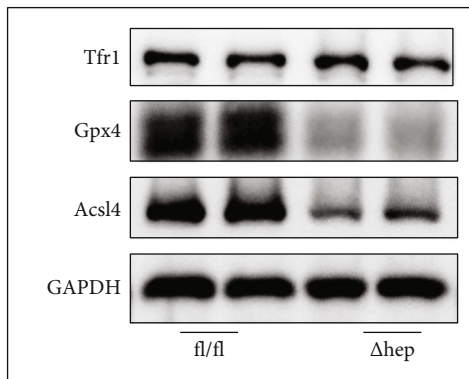


(b)

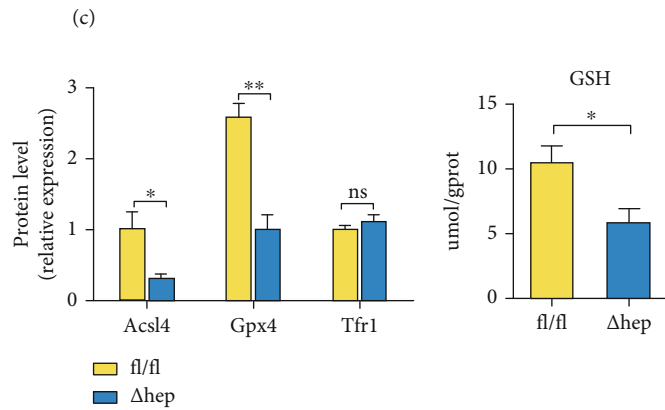
FIGURE 6: Continued.



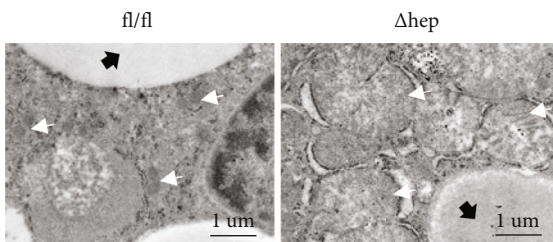
Input number



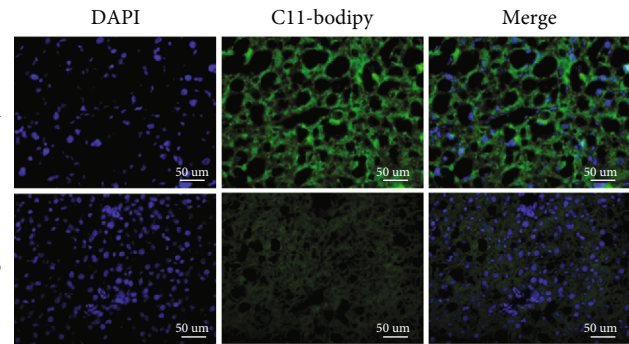
(d)



(e)



(f)



(g)

FIGURE 6: Continued.

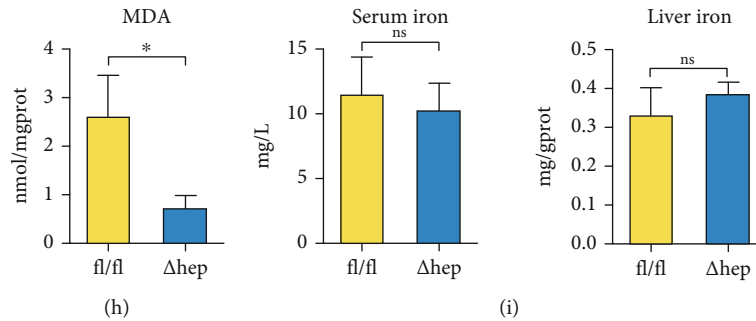


FIGURE 6: Hepatocyte-specific knockout of *Per2* might alleviate NASH by inhibiting ferroptosis. (a) Volcano plot showing upregulated and downregulated genes in *Per2*^{Δhep} and *Per2*^{fl/fl} mice. (b) Heatmap showing the differentially expressed genes (DEGs) between *Per2*^{Δhep} and *Per2*^{fl/fl} mice; blue indicates low expression and red indicates high expression. (c) The DEGs between *Per2*^{Δhep} and *Per2*^{fl/fl} mice were identified with the Kyoto Encyclopedia of Genes and Genomes (KEGG) pathway enrichment analysis. Rich factor (%) was the ratio of the number of DEGs annotated in a pathway (as indicated in the *y*-axis) to the number of all genes annotated in the pathway. (d) *Acs14*, *Gpx4*, and *Tfr1* protein levels were measured by western blotting, and *GAPDH* was used as a control. (e) Liver GSH concentrations were quantified by a commercial kit. (f) Electron microscopic evaluation of the morphologic changes in mitochondria; the white arrow indicates lipid droplets and the black arrow indicates mitochondria (original magnification, 5000x; scale bar, 1 μm) (*Per2*^{fl/fl}, *n* = 2; *Per2*^{Δhep}, *n* = 3). (g) Fluorescence staining represents lipid peroxidation (LPO) levels in the livers of *Per2*^{Δhep} and *Per2*^{fl/fl} mice. The nuclei were labeled with DAPI (left), and LPO (middle) was labeled by C11-Bodipy (original magnification, 400x; scale bar, 50 μm). (h) Liver MDA concentrations were quantified with a commercial kit. (i) Serum and liver iron concentrations were determined using a commercial kit to compare the iron-overload levels. Both *Per2*^{Δhep} and *Per2*^{fl/fl} mice were fed with HFHFD to induce NASH. Data are presented as mean ± SEM. **P* < 0.05 and ***P* < 0.01; ns: not significant (also refer to Figure S2).

PPARα in both TRF-treated and *Per2*^{Δhep} mice and demonstrated that hepatocyte-specific knockout of *Per2* significantly augmented the expression of PPARα (Figures 9(a) and 9(b)) and that TRF also elevated the expression of PPARα (Figures 9(c) and 9(d)). These data indicated that PPARα might constitute a target in the process by which TRF alleviated NASH.

4. Discussion

We herein examined the effectiveness and underlying mechanisms of action of TRF in the treatment of NASH, uncovering a pivotal role for the circadian gene *Per2* and ferroptosis in the pathogenesis and progression of NASH. We also hypothesized that *Per2* participated in NASH by promoting ferroptosis and inhibiting the expression of PPARα.

Authors of previous studies have reported a variety of modeling methods for NASH [56]. In this investigation, we chose an HFHFD to construct a NASH model in which corn starch and maltodextrin were replaced by fructose. As many foods rich in fructose are consumed in modern Western societies [57], the HFHFD-induced NASH model was thereby shown to be more similar to human NASH, and exhibiting more serious inflammation, fibrosis, and oxidative stress [56–58] relative to other dietary modeling methods. In a study in which the authors compared the animal models with human NAFLD, HFHFD-induced NAFLD exerted the greatest similarity to NAFLD in humans in both metabolic phenotype and histology; and HFHFD alone or combined with ip carbon tetrachloride (CCl₄) injection mimicked NAFLD in humans with respect to gene expression [59]. Although an HFHFD emulates human NAFLD, there remains some limitations. First of all, no model duplicates all the features of NAFLD in metabolic phenotype and

histology due to the complicated pathogenesis of human NAFLD, and the high proportion of HCC and lack of significant atherosclerosis in HFHFD-induced mouse models do not at all resemble human NAFLD [60, 61]. Second, as previous studies have revealed, an HFHFD necessitates an extensive period to induce cirrhosis and hepatocellular carcinoma (HCC) [59]. We herein thus aimed to explore novel underlying pathogenesis of human NASH, establishing a mouse model that is extremely similar in metabolic phenotype, histology, and gene expression, thereby increasing the reliability of our results to a considerable extent.

NASH is a type of progressive disease that occurs in both children and adults, and the characteristics of which are excessive fat accumulation and inflammatory cell infiltration in the liver [1, 2]. Fat accumulation is not only the basic characteristic of NASH but also promotes chronic inflammation and the progression of NASH through lipotoxicity [62]. In the present study, we ascertained that the TRF strategy, hepatocyte-specific knockout of *Per2*, and the application of a ferroptotic inhibitor not only improved metabolic indices and liver enzymes but also reduced liver steatosis, inflammation, and fibrosis induced by HFHFD. These results indicated that TRF effectively alleviated NASH and that both *Per2* and ferroptosis participated in the pathogenesis of NASH.

Per2 is an important circadian gene. Mice who lost *Per2* gene function suffered serious liver injury when exposed to CCl₄ [63], emphasizing the protective role of *Per2*. However, other authors reported that mice lacking the *Per2* gene or functional *Per2* protein manifested an improvement in some metabolic indices [15, 16], suggesting that *Per2* was an aggravating factor in metabolism-related disease. We herein first generated *Per2*^{Δhep} mice and found that *Per2* knockout significantly alleviated NASH, confirming that *Per2* was a

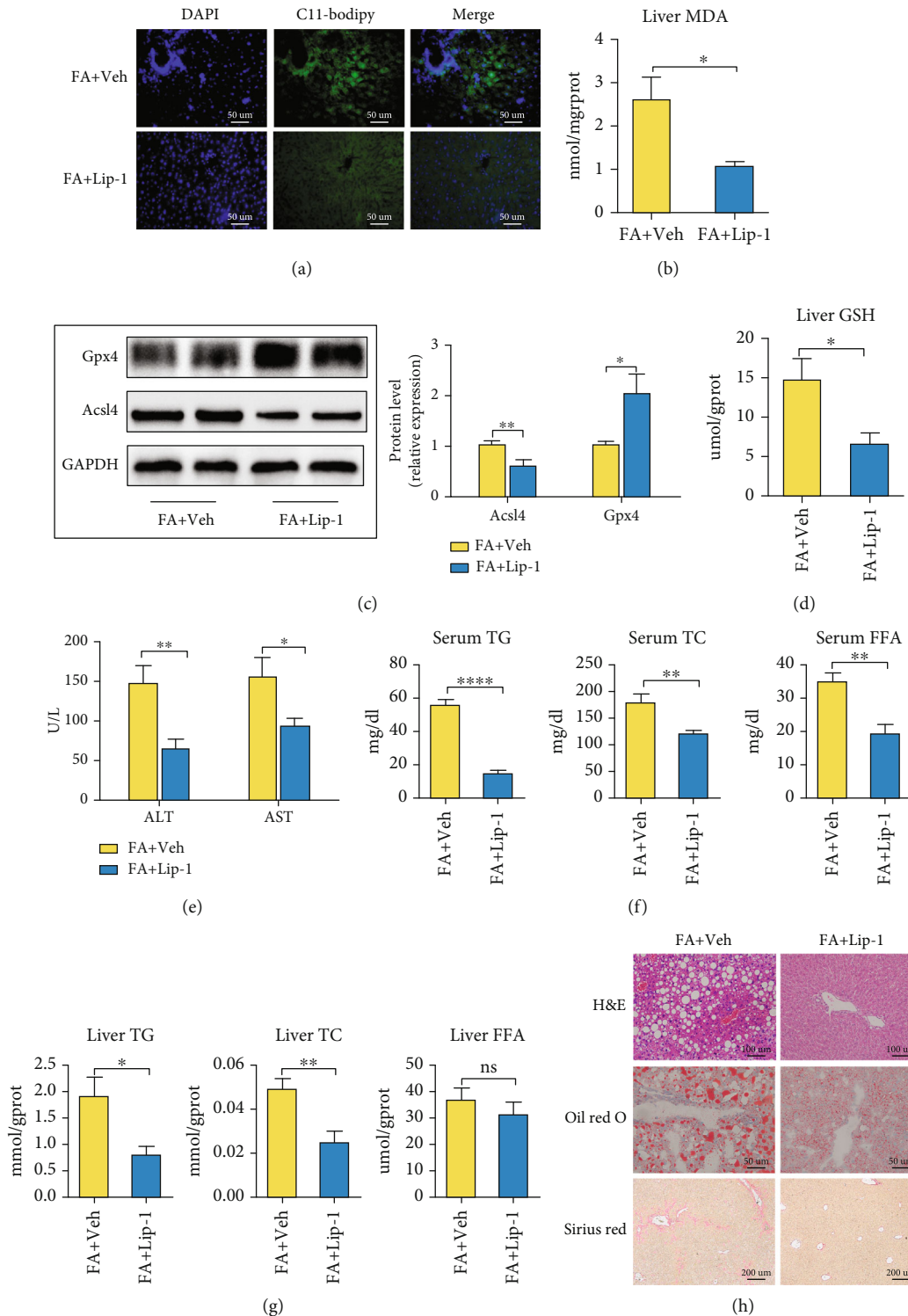


FIGURE 7: Ferroptosis occurs in HFHFD-induced NASH and promotes the progression of NASH. (a) Fluorescence staining showing lipid peroxidation (LPO) levels in the livers of the FA+Veh and FA+Lip-1 groups. The nuclei were labeled with DAPI (left) and LPO (middle) was labeled by C11-Bodipy (original magnification, 400x; scale bar, 50 μ m). (b) Liver MDA concentrations were measured with a commercial kit. (c) Acsl4 and Gpx4 protein levels were measured with western blotting, with GAPDH used as a control. (d) Liver GSH concentrations were measured by a commercial kit. (e) ALT and AST levels were determined by commercial kits to evaluate the levels of liver injury. (f, g) Serum and liver TG, TC, and FFA levels are depicted to demonstrate the lipid concentrations between the two groups. (h) Pathologic findings in liver sections. Liver paraffin sections were stained with H&E (original magnification, 200x; scale bar, 100 μ m), oil red O (original magnification, 400x; scale bar, 50 μ m), and Sirius red (original magnification, 100x; scale bar, 200 μ m) to determine the levels of steatosis, inflammation, and fibrosis in the FA+Veh and FA+Lip-1 groups. Data are presented as mean \pm SEM. * $P < 0.05$, ** $P < 0.01$, and **** $P < 0.0001$; ns: not significant (also refer to Figure S3).

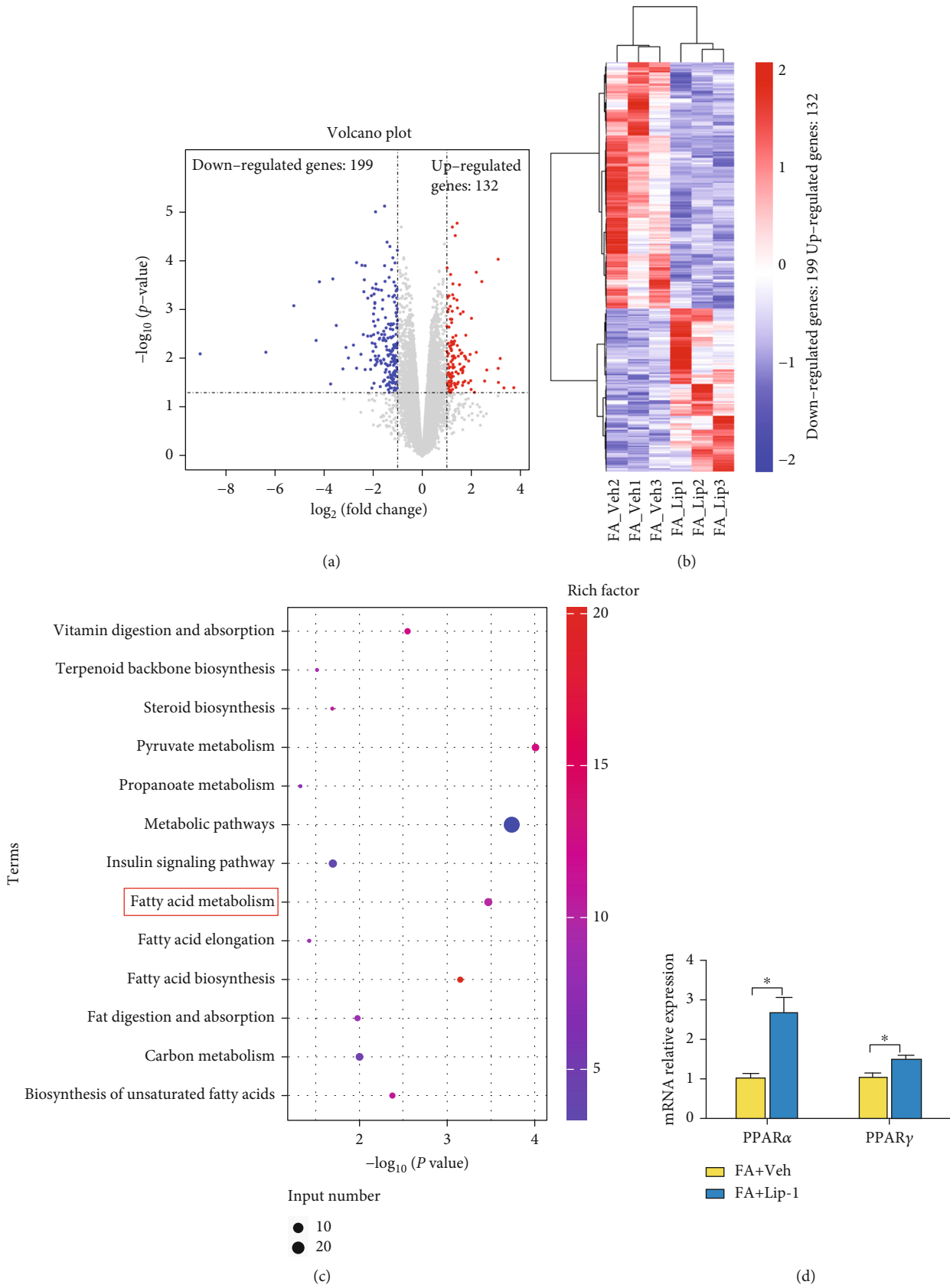
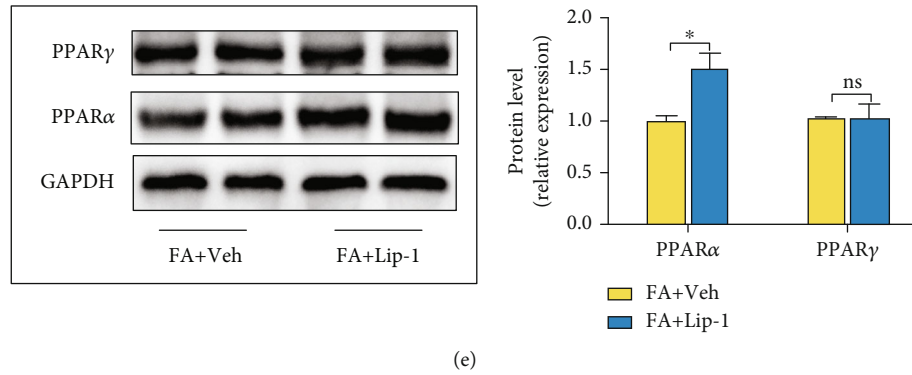


FIGURE 8: Continued.



(e)

FIGURE 8: Ferroptotic participation in NASH might be related to inhibition of PPAR α . (a) Volcano plot showing the upregulated and downregulated genes in the Lip-1 treatment group. (b) Heatmap shows the DEGs between the FA+Veh and FA+Lip-1 groups; blue indicates low expression and red indicates high expression. (c) The DEGs between the FA+Veh and FA+Lip-1 groups were identified with the Kyoto Encyclopedia of Genes and Genomes (KEGG) pathway enrichment analysis. Rich factor (%) was the ratio of the number of DEGs annotated in a pathway (as indicated in the y -axis) to the number of all genes annotated in the pathway. (d) Hepatic mRNA levels for PPAR α and PPAR γ were measured by RT-qPCR, and GAPDH was used as a control. (e) PPAR α and PPAR γ protein levels in the FA+Veh and FA+Lip-1 groups were assessed by western blotting and GAPDH was used as a control. Data are presented as mean \pm SEM. * $P < 0.05$; ns: not significant.

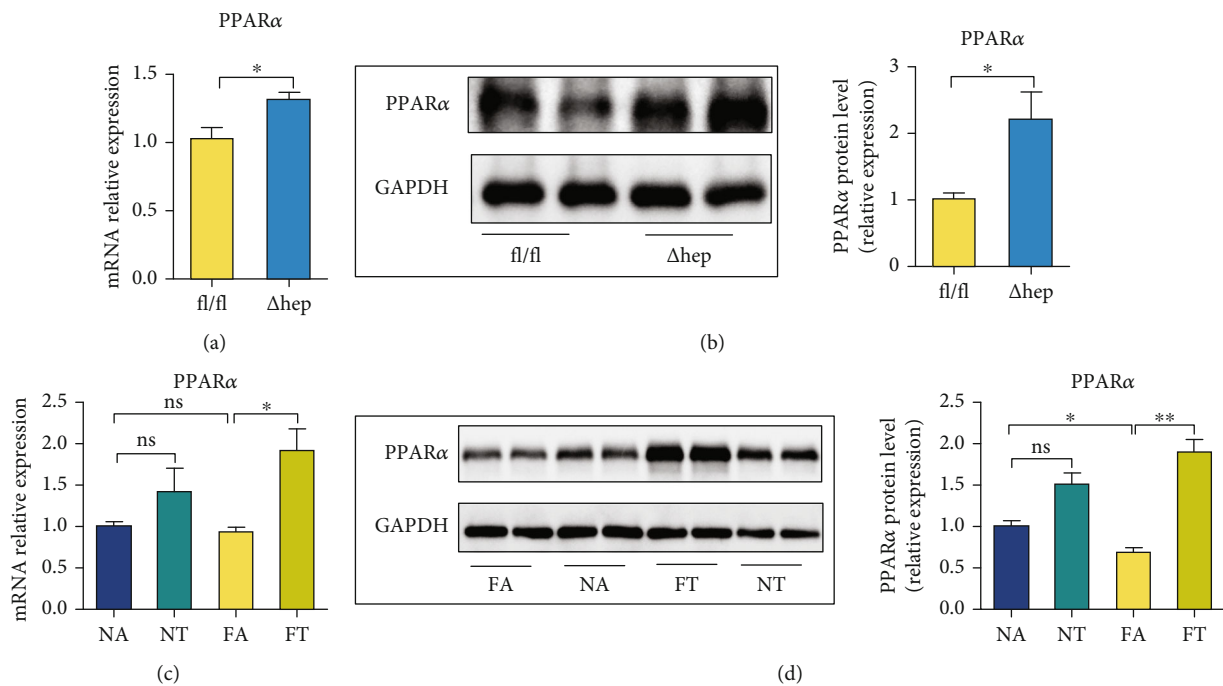


FIGURE 9: TRF and Per2 knockout promote the expression of PPAR α . (a) Hepatic mRNA levels for PPAR α in Per2 Δ hep and Per2 $^{fl/fl}$ mice were measured by RT-qPCR, and GAPDH was used as a control. (b) PPAR α protein levels in Per2 Δ hep and Per2 $^{fl/fl}$ mice were measured using western blotting, with GAPDH used as a control. (c) Hepatic mRNA levels for PPAR α in the NA, NT, FA, and FT groups were measured by RT-qPCR, and GAPDH was used as a control. (d) PPAR α protein levels in the NA, NT, FA, and FT groups were analyzed by western blotting, with GAPDH used as a control. Both Per2 Δ hep and Per2 $^{fl/fl}$ mice were fed with HFHFD to induce NASH. Data are presented as mean \pm SEM. * $P < 0.05$; ns: not significant.

factor that exacerbated NASH. It should be noted that this was the first-ever study designed to explore the role of Per2 in NASH by using Per2 Δ hep mice. Unlike the traditional knockout mice, the use of Per2 Δ hep mice principally focuses on the functional exploration of target genes in spe-

cific organs, thus enabling a more precise hepatic role for Per2.

While ferroptosis is a newly discovered type of cell death that has already been investigated in many diseases, its determination is difficult. The optimal detection methods

currently comprise the measurements of LPO accumulation, changes in mitochondrial morphology, overexpression of some ferroptosis-related genes, and the efficacy of ferroptotic inhibitors [20, 21]. By using the aforementioned methods, we thus initially confirmed that ferroptosis occurred in HFHFD-induced NASH.

To explore the mechanism by which TRF alleviated NASH, we discerned that TRF not only inhibited the expression of Per2 but also significantly inhibited ferroptosis—with reduced LPO levels, attenuated expression of ferroptosis-related genes, and the remission of morphologic changes in mitochondria. According to our RNA-Seq results, we found that Per2 is related to the occurrence of ferroptosis, and additional experiments indicated that ferroptosis was inhibited in Per2^{Δhep} mice. All of these results indicated that TRF inhibited the expression of the Per2 gene and that the amelioration of NASH by hepatocyte-specific knockout of Per2 might be related to the inhibition of ferroptosis. To our knowledge, this was the first study to examine a possible relationship between Per2 and ferroptosis.

GSH and Gpx4 are notable antioxidants in cells, and in the presence of GSH, Gpx4 plays a protective role in the process of ferroptosis by reducing the levels of LPO [64]; therefore, ferroptosis is caused by either GSH or Gpx4 depletion [65, 66]. However, in some cases, their expression increases, and GSH and Gpx4 then act as protective antioxidants in the process of ferroptosis [20, 28]; therefore, the elevated expression of Gpx4 and GSH also indicate the onset of ferroptosis. Consistent with previous reports [20, 28], this study showed that Gpx4 and GSH expression rates were elevated in HFHFD-induced NASH and that both TRF and hepatocyte-specific knockout of Per2 restored their expression. Congruent with a previous study, the expression of Gpx4 was elevated in a FA+Lip-1 group [67]; but in contradistinction, GSH concentration decreased in the FA+Lip-1 group, which was not consistent with Gpx4. Lip-1 is a lipid autoxidation inhibitor that effectively inhibits ferroptosis, but the other effects of Lip-1 are arcane and require further investigation.

Excessive fat accumulation in the liver promotes the progression of NASH [68], and the mechanisms generating hepatic steatosis constitutes the focal point of NASH pathogenesis. Among the PPAR subtypes, PPAR α is primarily expressed in the liver, and PPAR γ is highly expressed in the liver of individuals with NASH [24, 53–55]. According to our RNA-Seq results, the DEGs were primarily enriched in the fatty acid metabolism pathway between the FA+Veh and FA+Lip-1 groups. Therefore, we hypothesized a relationship between ferroptosis and PPAR α or PPAR γ , and our data revealed that Lip-1 promoted the expression of PPAR α without affecting PPAR γ , while TRF and hepatocyte-specific knockout of Per2 both enhanced the expression of PPAR α . These results suggest that PPAR α might be the downstream mechanism governing ferroptosis in its aggravation of NASH. Investigators previously reported that PPAR α activation alleviated ferroptosis by exploiting PPAR α knockout mice and a PPAR α ligand [69] and that activation of PPAR α exerted similar effects in protecting against ferroptosis-induced liver injury [69]; this indicated to these

authors that PPAR α might be the regulator of ferroptosis. In the current analysis, we found that the inhibition of ferroptosis promoted PPAR α expression, also implying that PPAR α was a component in the downstream mechanism underlying the process of ferroptosis in the exacerbation of NASH. Furthermore, although we are the first to raise this possibility, additional studies are needed to confirm this hypothesis.

In the present study, we found that TRF repressed the expression of Per2, that Per2 promoted ferroptosis, and that the expression of PPAR α was increased by TRF, hepatocyte-specific knockout of Per2, and the inhibition of ferroptosis. We therefore hypothesized that TRF likely alleviated NASH by regulating the circadian gene Per2 and ferroptosis and that this was ultimately related to the promotion of PPAR α expression. However, during our investigation we determined that hepatocyte-specific knockout of Per2 did not influence the body weight of mice, while TRF and Lip-1 did; and it is acknowledged that obesity itself is closely related to the prevalence and severity of NASH [70]. Therefore, in addition to the pathway we noted above, weight loss induced by TRF might constitute another means by which TRF alleviates NASH.

5. Limitations of the Study

For this study, we used an HFHFD to induce NASH, creating signs similar to those for human NASH; and we confirmed that TRF's alleviation of NASH was related to the regulation of the circadian gene Per2. Furthermore, we indicated an important role for ferroptosis in NASH and demonstrated that ferroptosis was regulated by Per2. The limitations to our study included the following. First, we did not examine the changes in the circadian rhythms for the various indicators—although this did not influence the conclusion that TRF and Per2 regulated the onset of ferroptosis. Second, as we used Per2^{Δhep} mice to examine the role of Per2 in NASH (implementing a model in which all mice were fed with an HFHFD), the results we generated from the Per2^{Δhep} mice did not modify the conclusions of this investigation; however, our conclusions may not apply to normal diets. Third, as the mechanism underlying NASH is complex and we only examined the effects of ferroptosis on the PPAR family, there might be additional pathways involved in the overall process. Finally, while we hypothesized that the PPAR α pathway was a downstream mechanism subserving ferroptosis in exacerbating NASH, we did not provide further verification. Although this should not affect the conclusions, additional studies are required to confirm these data. We posit that the conclusions of our study are reasonable, but also further elucidation is still needed.

6. Conclusions

In this study, we uncovered TRF as an effective therapeutic strategy for NASH. After further scrutiny, we also determined that the circadian gene Per2 might participate in NASH by promoting ferroptosis; moreover, ferroptosis likely promoted NASH by inhibiting the expression of PPAR α . Thus, these results fulfilled the pathophysiologic

underpinning mechanisms of NASH and provided some potentially novel treatment targets for this disorder.

Abbreviations

NASH:	Nonalcoholic steatohepatitis
TRF:	Time-restricted feeding
PPAR:	Peroxisome proliferator activated receptor
NAFLD:	Nonalcoholic fatty liver disease
LPO:	Lipid peroxidation
Per2 ^{Δhep} :	Hepatocyte-specific Per2-knockout
HFHFD:	High-fat and high-fructose diet
FA:	Ad libitum access to HFHFD
FT:	From ZT13 to ZT23 access to HFHFD
NA:	Ad libitum access to chow diet
NT:	From ZT13 to ZT23 access to chow diet
Lip-1:	Liproxstatin-1
Iv:	Injected intravenously
IPGTT:	Intraperitoneal glucose tolerance test
Ip:	Intraperitoneal
ALT:	Alanine aminotransferase
AST:	Aspartate aminotransferase
TC:	Total cholesterol
TG:	Triglyceride
FFA:	Free fatty acid
MDA:	Malondialdehyde
GSH:	Glutathione
H&E:	Hematoxylin and eosin
OCT:	Optimal cutting temperature compound
NAS:	NAFLD activity score
RPKMs:	Reads per kilobase of transcript per million reads mapped
DEGs:	Differential genes
KEGG:	Kyoto Encyclopedia of Genes and Genomes Enrichment
GO:	Gene Ontology
PBS:	Phosphate-buffered saline
TEM:	Transmission electron microscopy
DAPI:	4',6-Diamidino-2'-phenylindole
RT- qPCR:	Real-time polymerase chain reaction
ANOVA:	Analysis of variance
LSD:	Least significant difference
Tnf:	Tumor necrosis factor
Acs14:	Anti-acyl-CoA synthetase long-chain family member 4
Gpx4:	Glutathione peroxidase 4
Aifm2:	Apoptosis-inducing factor mitochondria-associated 2
Ptgs2:	Prostaglandin-endoperoxide synthase 2
Irp:	Iron regulatory protein
Tfr:	Transferrin receptor
Slc40a1:	Ferroportin
IL:	Interleukin
CCL4:	Carbon tetrachloride

Data Availability

All the data in this article are available from the corresponding author Xiaoli Pan. And the data of RNA-Seq are avail-

able in NCBI (BioProject: PRJNA836098 and PRJNA836019).

Conflicts of Interest

The authors declare no competing interests.

Authors' Contributions

X.-L.P and J.Y. conceptualized the study. Y.-Y.S. performed the methodology. Y.-Y.S and W.-K.G. investigated the study. X.-L.P and J.Y. supervised the study. H.-K.C. and L.Y. were responsible for the project administration. Y.-Y.S. wrote the original draft. Y.-Y.S., W.-K.G., H.-K.C., L.Y., X.-L.P, and J.Y. edited the manuscript and provided final approval.

Acknowledgments

This study was supported by the National Natural Science Foundation of China (grant no. 81770582).

Supplementary Materials

Some detected indices of mice in FA, FT, NA, and NT groups, Per2^{Δhep} and Per2^{fl/fl} mice, and FA+Veh and FA+Lip-1 groups. Figure S1: TRF alleviates HFHFD-induced NASH. Figure S2: hepatocyte-specific knockout of Per2 might alleviate NASH by inhibiting ferroptosis without influencing the iron concentration. Figure S3: ferroptosis occurs and participates in HFHFD-induced NASH. (*Supplementary Materials*)

References

- [1] L. A. Adams and V. Ratzliff, "Non-alcoholic fatty liver - perhaps not so benign," *Journal of Hepatology*, vol. 62, no. 5, pp. 1002–1004, 2015.
- [2] G. T. Brown and D. E. Kleiner, "Histopathology of nonalcoholic fatty liver disease and nonalcoholic steatohepatitis," *Metabolism*, vol. 65, no. 8, pp. 1080–1086, 2016.
- [3] B. J. Perumpail, M. A. Khan, E. R. Yoo, G. Cholankeril, D. Kim, and A. Ahmed, "Clinical epidemiology and disease burden of nonalcoholic fatty liver disease," *World Journal of Gastroenterology*, vol. 23, no. 47, pp. 8263–8276, 2017.
- [4] M. Povsic, O. Y. Wong, R. Perry, and J. Bottomley, "A structured literature review of the epidemiology and disease burden of non-alcoholic steatohepatitis (NASH)," *Advances in Therapy*, vol. 36, no. 7, pp. 1574–1594, 2019.
- [5] M. S. Mundi, S. Velapati, J. Patel, T. A. Kellogg, B. K. Abu Dayyeh, and R. T. Hurt, "Evolution of NAFLD and its management," *Nutrition in Clinical Practice*, vol. 35, no. 1, pp. 72–84, 2020.
- [6] M. Hatori, C. Vollmers, A. Zarrinpar et al., "Time-restricted feeding without reducing caloric intake prevents metabolic diseases in mice fed a high-fat diet," *Cell Metabolism*, vol. 15, no. 6, pp. 848–860, 2012.
- [7] E. Roeb and A. Geier, "Nonalcoholic steatohepatitis (NASH) - current treatment recommendations and future developments," *Zeitschrift für Gastroenterologie*, vol. 57, no. 4, pp. 508–517, 2019.

- [8] R. E. Patterson and D. D. Sears, "Metabolic effects of intermittent fasting," *Annual Review of Nutrition*, vol. 37, no. 1, pp. 371–393, 2017.
- [9] S. Welton, R. Minty, T. O'driscoll et al., "Intermittent fasting and weight loss: systematic review," *Canadian Family Physician*, vol. 66, no. 2, pp. 117–125, 2020.
- [10] A. Chaix, A. Zarrinpar, P. Miu, and S. Panda, "Time-restricted feeding is a preventative and therapeutic intervention against diverse nutritional challenges," *Cell Metabolism*, vol. 20, no. 6, pp. 991–1005, 2014.
- [11] G. Mazzoccoli, S. De Cosmo, and T. Mazza, "The biological clock: a pivotal hub in non-alcoholic fatty liver disease pathogenesis," *Frontiers in Physiology*, vol. 9, p. 193, 2018.
- [12] G. Mazzoccoli, M. Vinciguerra, J. Oben, R. Tarquini, and S. De Cosmo, "Non-alcoholic fatty liver disease: the role of nuclear receptors and circadian rhythmicity," *Liver International*, vol. 34, no. 8, pp. 1133–1152, 2014.
- [13] A. Arjona and D. K. Sarkar, "The circadian gene mPer2 regulates the daily rhythm of IFN- γ ," *Journal of Interferon & Cytokine Research*, vol. 26, no. 9, pp. 645–649, 2006.
- [14] M. Sujino, M. Nagano, A. Fujioka, Y. Shigeyoshi, and S. T. Inouye, "Temporal profile of circadian clock gene expression in a transplanted suprachiasmatic nucleus and peripheral tissues," *The European Journal of Neuroscience*, vol. 26, no. 10, pp. 2731–2738, 2007.
- [15] B. Grimaldi, M. M. Bellet, S. Katada et al., "PER2 controls lipid metabolism by direct regulation of PPAR γ ," *Cell Metabolism*, vol. 12, no. 5, pp. 509–520, 2010.
- [16] F. Zani, L. Breasson, B. Becattini et al., "PER2 promotes glucose storage to liver glycogen during feeding and acute fasting by inducing Gys2 PTG and G L expression," *Molecular Metabolism*, vol. 2, no. 3, pp. 292–305, 2013.
- [17] S. J. Dixon, K. M. Lemberg, M. R. Lamprecht et al., "Ferroptosis: an iron-dependent form of nonapoptotic cell death," *Cell*, vol. 149, no. 5, pp. 1060–1072, 2012.
- [18] I. Alim, J. T. Caulfield, Y. Chen et al., "Selenium drives a transcriptional adaptive program to block ferroptosis and treat stroke," *Cell*, vol. 177, no. 5, pp. 1262–1279, 2019.
- [19] M. J. Hangauer, V. S. Viswanathan, M. J. Ryan et al., "Drug-tolerant persister cancer cells are vulnerable to GPX4 inhibition," *Nature*, vol. 551, no. 7679, pp. 247–250, 2017.
- [20] X. Li, T. X. Wang, X. Huang et al., "Targeting ferroptosis alleviates methionine-choline deficient (MCD)-diet induced NASH by suppressing liver lipotoxicity," *Liver International*, vol. 40, no. 6, pp. 1378–1394, 2020.
- [21] S. Tsurusaki, Y. Tsuchiya, T. Koumura et al., "Hepatic ferroptosis plays an important role as the trigger for initiating inflammation in nonalcoholic steatohepatitis," *Cell Death & Disease*, vol. 10, no. 6, p. 449, 2019.
- [22] J. Liu, M. Yang, R. Kang, D. J. Klionsky, and D. Tang, "Autophagic degradation of the circadian clock regulator promotes ferroptosis," *Autophagy*, vol. 15, pp. 2033–2035, 2019.
- [23] J. Boeckmans, A. Natale, M. Rombaut et al., "Anti-NASH drug development hitches a lift on PPAR agonism," *Cell*, vol. 9, no. 1, 2019.
- [24] S. Francque, G. Szabo, M. F. Abdelmalek et al., "Nonalcoholic steatohepatitis: the role of peroxisome proliferator-activated receptors," *Nature Reviews Gastroenterology & Hepatology*, vol. 18, no. 1, pp. 24–39, 2021.
- [25] I. Schmutz, J. A. Ripperger, S. Baeriswyl-Aebischer, and U. Albrecht, "The mammalian clock component PERIOD2 coordinates circadian output by interaction with nuclear receptors," *Genes & Development*, vol. 24, no. 4, pp. 345–357, 2010.
- [26] D. Venkatesh, N. A. O'brien, F. Zandkarimi et al., "MDM2 and MDMX promote ferroptosis by PPAR α -mediated lipid remodeling," *Genes & Development*, vol. 34, no. 7-8, pp. 526–543, 2020.
- [27] X. Li, L. Duan, S. Yuan, X. Zhuang, T. Qiao, and J. He, "Ferroptosis inhibitor alleviates radiation-induced lung fibrosis (RILF) via down-regulation of TGF- β 1," *Journal of Inflammation*, vol. 16, no. 1, p. 11, 2019.
- [28] J. Qi, J. W. Kim, Z. Zhou, C. W. Lim, and B. Kim, "Ferroptosis affects the progression of nonalcoholic steatohepatitis via the modulation of lipid peroxidation-mediated cell death in mice," *The American Journal of Pathology*, vol. 190, no. 1, pp. 68–81, 2020.
- [29] S. Andrikopoulos, A. R. Blair, N. Deluca, B. C. Fam, and J. Proietto, "Evaluating the glucose tolerance test in mice," *American Journal of Physiology. Endocrinology and Metabolism*, vol. 295, no. 6, pp. E1323–E1332, 2008.
- [30] X. Zhu, H. Bian, L. Wang et al., "Berberine attenuates nonalcoholic hepatic steatosis through the AMPK-SREBP-1c-SCD1 pathway," *Free Radical Biology & Medicine*, vol. 141, pp. 192–204, 2019.
- [31] D. E. Kleiner and E. M. Brunt, "Nonalcoholic fatty liver disease: pathologic patterns and biopsy evaluation in clinical research," *Seminars in Liver Disease*, vol. 32, no. 1, pp. 3–13, 2012.
- [32] D. E. Kleiner, E. M. Brunt, M. Van Natta et al., "Design and validation of a histological scoring system for nonalcoholic fatty liver disease," *Hepatology*, vol. 41, no. 6, pp. 1313–1321, 2005.
- [33] S. Anslan, V. Mikryukov, K. Armolaitis et al., "Highly comparable metabarcoding results from MGI-Tech and Illumina sequencing platforms," *PeerJ*, vol. 9, article e12254, 2021.
- [34] A. Dobin, C. A. Davis, F. Schlesinger et al., "STAR: ultrafast universal RNA-seq aligner," *Bioinformatics*, vol. 29, no. 1, pp. 15–21, 2013.
- [35] Y. Liao, G. K. Smyth, and W. Shi, "featureCounts: an efficient general purpose program for assigning sequence reads to genomic features," *Bioinformatics*, vol. 30, no. 7, pp. 923–930, 2014.
- [36] A. Mortazavi, B. A. Williams, K. Mccue, L. Schaeffer, and B. Wold, "Mapping and quantifying mammalian transcriptomes by RNA-Seq," *Nature Methods*, vol. 5, no. 7, pp. 621–628, 2008.
- [37] M. D. Robinson, D. J. McCarthy, and G. K. Smyth, "edgeR: a bioconductor package for differential expression analysis of digital gene expression data," *Bioinformatics*, vol. 26, no. 1, pp. 139–140, 2010.
- [38] D. Bu, H. Luo, P. Huo et al., "KOBAS-i: intelligent prioritization and exploratory visualization of biological functions for gene enrichment analysis," *Nucleic Acids Research*, vol. 49, no. W1, pp. W317–w325, 2021.
- [39] A. H. Ali, E. J. Carey, and K. D. Lindor, "Diagnosis and management of primary biliary cirrhosis," *Expert Review of Clinical Immunology*, vol. 10, no. 12, pp. 1667–1678, 2014.
- [40] S. Lee and D. K. Lee, "What is the proper way to apply the multiple comparison test?," *Korean Journal of Anesthesiology*, vol. 73, no. 6, p. 572, 2020.
- [41] P. Mishra, U. Singh, C. M. Pandey, P. Mishra, and G. Pandey, "Application of Student's t-test, analysis of variance, and

- covariance," *Annals of Cardiac Anaesthesia*, vol. 22, no. 4, pp. 407–411, 2019.
- [42] D. Tsikas, "Assessment of lipid peroxidation by measuring malondialdehyde (MDA) and relatives in biological samples: analytical and biological challenges," *Analytical Biochemistry*, vol. 524, pp. 13–30, 2017.
- [43] R. Kirsch, H. P. Sijtsema, M. Tlali, A. D. Marais, and L. Hall Pde, "Effects of iron overload in a rat nutritional model of non-alcoholic fatty liver disease," *Liver International*, vol. 26, no. 10, pp. 1258–1267, 2006.
- [44] B. Turlin, M. H. Mendler, R. Moirand, D. Guyader, A. Guillygomarc'h, and Y. Deugnier, "Histologic features of the liver in insulin resistance-associated iron overload: A study of 139 patients," *American Journal of Clinical Pathology*, vol. 116, no. 2, pp. 263–270, 2001.
- [45] O. Protchenko, E. Baratz, S. Jadhav et al., "Iron chaperone polycystin 1 protects mouse liver from lipid peroxidation and steatosis," *Hepatology*, vol. 73, no. 3, pp. 1176–1193, 2021.
- [46] N. Sumneang, N. Siri-Angkul, S. Kumfu, S. C. Chattapakorn, and N. Chattapakorn, "The effects of iron overload on mitochondrial function, mitochondrial dynamics, and ferroptosis in cardiomyocytes," *Archives of Biochemistry and Biophysics*, vol. 680, article 108241, 2020.
- [47] R. Daher, H. Manceau, and Z. Karim, "Iron metabolism and the role of the iron-regulating hormone hepcidin in health and disease," *La Presse Médicale*, vol. 46, no. 12, pp. e272–e278, 2017.
- [48] W. S. Yang and B. R. Stockwell, "Synthetic lethal screening identifies compounds activating iron-dependent, nonapoptotic cell death in oncogenic-RAS-harboring cancer cells," *Chemistry & Biology*, vol. 15, no. 3, pp. 234–245, 2008.
- [49] F. Ye, W. Chai, M. Xie et al., "HMGB1 regulates erastin-induced ferroptosis via RAS-JNK/p38 signaling in HL-60/NRAS(Q61L) cells," *American Journal of Cancer Research*, vol. 9, no. 4, pp. 730–739, 2019.
- [50] G. C. Forcina and S. J. Dixon, "GPX4 at the crossroads of lipid homeostasis and ferroptosis," *Proteomics*, vol. 19, no. 18, article e1800311, 2019.
- [51] J. Y. Lee, M. Nam, H. Y. Son et al., "Polyunsaturated fatty acid biosynthesis pathway determines ferroptosis sensitivity in gastric cancer," *Proceedings of the National Academy of Sciences of the United States of America*, vol. 117, no. 51, pp. 32433–32442, 2020.
- [52] S. Doll, B. Proneth, Y. Y. Tyurina et al., "ACSL4 dictates ferroptosis sensitivity by shaping cellular lipid composition," *Nature Chemical Biology*, vol. 13, no. 1, pp. 91–98, 2017.
- [53] Z. Chen, Y. Yu, J. Cai, H. J. T. I. E. Li, and M. Tem, "Emerging molecular targets for treatment of nonalcoholic fatty liver disease," *Trends in Endocrinology & Metabolism*, vol. 30, pp. 903–914, 2019.
- [54] D. E. Moller and J. P. Berger, "Role of PPARs in the regulation of obesity-related insulin sensitivity and inflammation," *International Journal of Obesity and Related Metabolic Disorders*, vol. 27, Suppl 3, pp. S17–S21, 2003.
- [55] B. Staels, A. Rubenstunk, B. Noel et al., "Hepatoprotective effects of the dual peroxisome proliferator-activated receptor alpha/delta agonist, GFT505, in rodent models of nonalcoholic fatty liver disease/nonalcoholic steatohepatitis," *Hepatology*, vol. 58, no. 6, pp. 1941–1952, 2013.
- [56] P. K. Santhekadur, D. P. Kumar, and A. J. Sanyal, "Preclinical models of non-alcoholic fatty liver disease," *Journal of Hepatology*, vol. 68, no. 2, pp. 230–237, 2018.
- [57] R. Kohli, M. Kirby, S. A. Xanthakos et al., "High-fructose, medium chain trans fat diet induces liver fibrosis and elevates plasma coenzyme Q9 in a novel murine model of obesity and nonalcoholic steatohepatitis," *Hepatology*, vol. 52, no. 3, pp. 934–944, 2010.
- [58] M. F. Abdelmalek, A. Suzuki, C. Guy et al., "Increased fructose consumption is associated with fibrosis severity in patients with nonalcoholic fatty liver disease," *Hepatology*, vol. 51, no. 6, pp. 1961–1971, 2010.
- [59] Y. R. Im, H. Hunter, D. De Gracia Hahn et al., "A systematic review of animal models of NAFLD finds high-fat, high-fructose diets most closely resemble human NAFLD," *Hepatology*, vol. 74, no. 4, pp. 1884–1901, 2021.
- [60] A. Asgharpour, S. C. Cazanave, T. Pacana et al., "A diet-induced animal model of non-alcoholic fatty liver disease and hepatocellular cancer," *Journal of Hepatology*, vol. 65, no. 3, pp. 579–588, 2016.
- [61] K. Oda, H. Uto, S. Mawatari, and A. Ido, "Clinical features of hepatocellular carcinoma associated with nonalcoholic fatty liver disease: a review of human studies," *Clinical Journal of Gastroenterology*, vol. 8, no. 1, pp. 1–9, 2015.
- [62] M. E. Ertunc and G. S. Hotamisligil, "Lipid signaling and lipotoxicity in metaflammation: indications for metabolic disease pathogenesis and treatment," *Journal of Lipid Research*, vol. 57, no. 12, pp. 2099–2114, 2016.
- [63] P. Chen, C. Li, W. Pang et al., "The protective role of Per2 against carbon tetrachloride-induced hepatotoxicity," *The American Journal of Pathology*, vol. 174, no. 1, pp. 63–70, 2009.
- [64] F. Ursini and M. Maiorino, "Lipid peroxidation and ferroptosis: the role of GSH and GPx4," *Free Radical Biology & Medicine*, vol. 152, pp. 175–185, 2020.
- [65] W. S. Yang, R. Sriramaratnam, M. E. Welsch et al., "Regulation of ferroptotic cancer cell death by GPX4," *Cell*, vol. 156, no. 1–2, pp. 317–331, 2014.
- [66] W. S. Yang and B. R. Stockwell, "Ferroptosis: death by lipid peroxidation," *Trends in Cell Biology*, vol. 26, no. 3, pp. 165–176, 2016.
- [67] Y. Feng, N. B. Madungwe, A. D. Imam Aliagan, N. Tombo, and J. C. Bopassa, "Lipoxstatin-1 protects the mouse myocardium against ischemia/reperfusion injury by decreasing VDAC1 levels and restoring GPX4 levels," *Biochemical and Biophysical Research Communications*, vol. 520, no. 3, pp. 606–611, 2019.
- [68] S. Pittala, Y. Krelin, Y. Kuperman, and V. Shoshan-Barmatz, "A mitochondrial VDAC1-based peptide greatly suppresses steatosis and NASH-associated pathologies in a mouse model," *Molecular Therapy*, vol. 27, no. 10, pp. 1848–1862, 2019.
- [69] G. Xing, L. Meng, S. Cao et al., "PPAR α alleviates iron overload-induced ferroptosis in mouse liver," *EMBO Reports*, vol. 23, no. 8, p. e52280.10.15252/embr.202052280, 2022.
- [70] S. A. Polyzos, J. Kountouras, and C. S. Mantzoros, "Obesity and nonalcoholic fatty liver disease: from pathophysiology to therapeutics," *Metabolism*, vol. 92, pp. 82–97, 2019.

Research Article

Energy-Stress-Mediated AMPK Activation Promotes GPX4-Dependent Ferroptosis through the JAK2/STAT3/P53 Axis in Renal Cancer

Yanze Li , Ye Zhang , Qiangmin Qiu , Lei Wang , Hu Mao , Juncheng Hu , Zhiyuan Chen , Yang Du , and Xiuheng Liu 

Department of Urology, Renmin Hospital of Wuhan University, Wuhan, 430060 Hubei, China

Correspondence should be addressed to Zhiyuan Chen; chenzhiyuan163@163.com, Yang Du; phoenixneo@whu.edu.cn, and Xiuheng Liu; drliuxh@hotmail.com

Received 6 July 2022; Revised 15 August 2022; Accepted 7 September 2022; Published 4 October 2022

Academic Editor: Lianxiang Luo

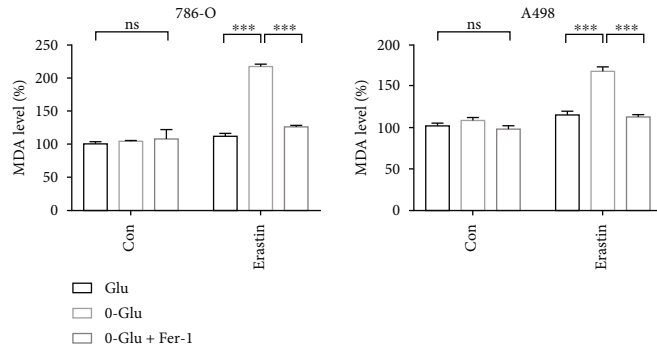
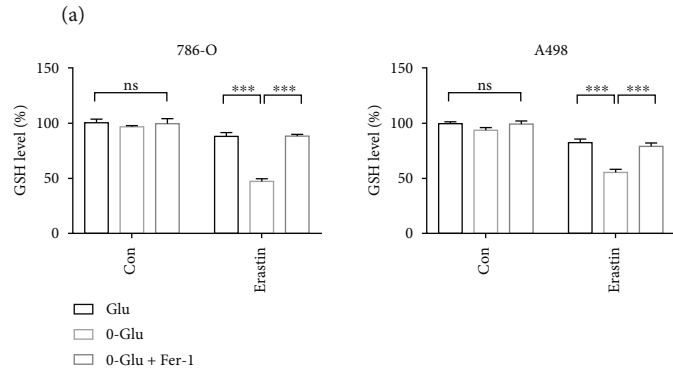
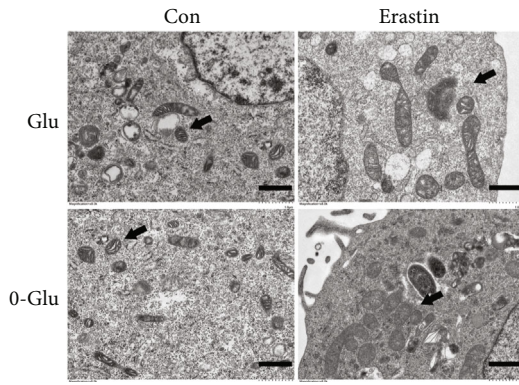
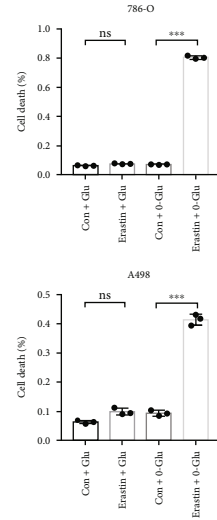
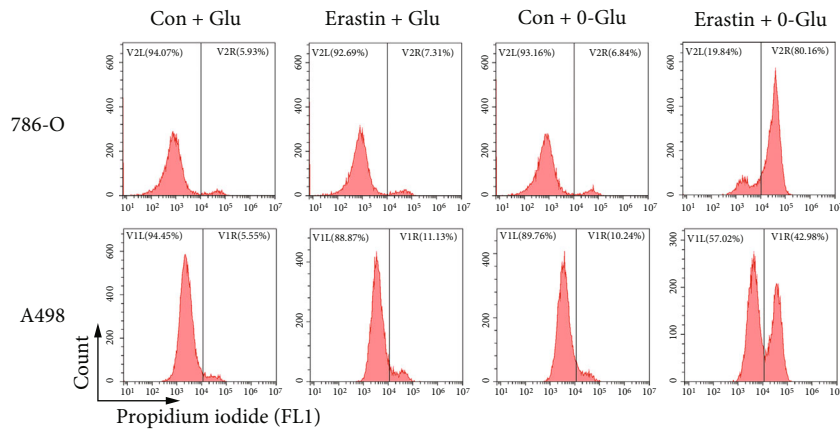
Copyright © 2022 Yanze Li et al. This is an open access article distributed under the Creative Commons Attribution License, which permits unrestricted use, distribution, and reproduction in any medium, provided the original work is properly cited.

Energy stress is an unfavorable condition that tumor cells are often exposed to. Ferroptosis is considered an emerging target for tumor therapy. However, the role of ferroptosis in energy stress in renal cancer is currently unknown. In this study, we found that glucose deprivation significantly enhanced GPX4-dependent ferroptosis through AMPK activation. Further, AMPK activation suppressed GPX4 expression at the transcriptional level through the upregulation of P53 expression. Additionally, the inactivation of JAK2/STAT3 transcriptionally promoted P53 expression, thereby promoting AMPK-mediated GPX4-dependent ferroptosis. In conclusion, energy stress promotes AMPK-mediated GPX4-dependent erastin-induced ferroptosis in renal cancer through the JAK2/STAT3/P53 signaling axis.

1. Introduction

Cancer cells often exhibit alternative pathways for energy metabolism for growth and proliferation. Findings from extensive reports have revealed that adaptive changes in energy metabolism play vital roles in cancer survival [1]. The upregulation of glycolysis is widely considered a major catabolic process alteration in cancer cells in response to energy stress, referred to as the Warburg effect [2]. Because of the Warburg effect, glucose acts as a primary metabolic fuel for several tumors [3]. Rapid growth and a relatively limited energy supply often expose tumors to energy stress. AMP-activated protein kinase (AMPK) is a critical energy sensor that can sense the cellular energy status [4]. Energy stress increases the AMP/ATP ratio in cells. In response, AMPK is activated to restore the energy balance, primarily through the inhibition of lipid and protein synthesis as well as the promotion of glucose uptake and glycolysis [4]. Thus, cancer cells can adapt to these harsh environmental conditions.

Ferroptosis is a novel form of regulated cell death. Unlike apoptosis, autophagy, or necrosis, ferroptosis is characterized by lethal iron-dependent lipid peroxidation accumulation. Emerging evidence has shown that ferroptosis is related to various human diseases and pathological conditions, such as degenerative diseases, stroke, ischemia-reperfusion injury, and cancer [5]. The sensitivity to ferroptosis is associated with many factors, and metabolic aberration is a major part of the same [6, 7]. Therefore, regulation of the expression of genes or kinases involved in these metabolic pathways can partially control ferroptosis sensitivity. System Xc- and glutathione peroxidase 4 (GPX4) are widely known to be required for ferroptosis prevention. For example, the inhibition of system Xc- can block cystine/glutamate transport, leading to cellular glutathione depletion. Glutathione is a major antioxidant and can be utilized by GPX4 to reduce lipid peroxidation. Thus, the depletion of glutathione eventually induces ferroptosis [8]. However, the relationship between ferroptosis and energy metabolism remains elusive. In particular, this has led to



(d)

FIGURE 1: Continued.

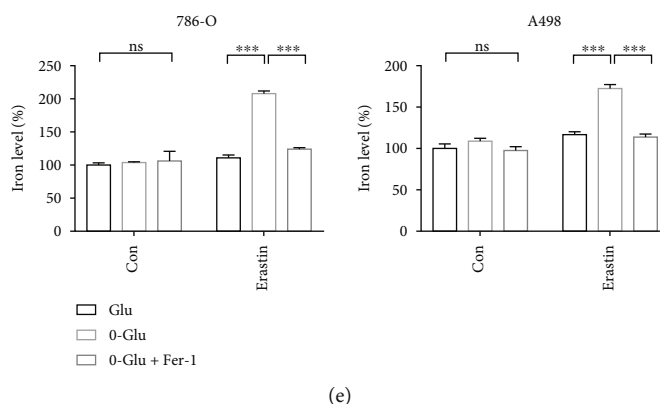


FIGURE 1: Energy stress promotes ferroptotic cell death in renal cancer cells. (a) Cell death measurement shows 0-Glu promotes erastin-induced cell death. (b) TEM was used to observe morphological changes of cellular ultrastructure. Cells in 0-Glu and erastin treatment group present aberrant mitochondria. Black arrows indicate mitochondria. Scale bars: $1\ \mu\text{m}$. Independent experiments were repeated three times and representative data were shown. (c–e) 0-Glu and erastin treatment-induced GSH deletion, MDA generation, and cellular iron elevation are rescued by Fer-1. Glu: glucose concentration of RPMI 1640 medium. 0-Glu: 0 mM glucose. Data shown represent mean \pm SD from at least three independent experiments. Comparisons were performed using Student's *t*-test. Fer-1: ferrostatin-1; ns: not significant. *** $p < 0.001$.

some controversies and discussions in previous reports [9, 10].

In recent years, Janus kinase (JAK)/signal transducer and activator of transcription (STAT) pathway has been discovered as an intracellular signal transduction pathway closely related to cytokines [11]. It was reported that JAK/STAT3 signaling pathway was involved in many biological processes such as cell proliferation, differentiation, apoptosis, and immune regulation [11]. JAK2/STAT3, an important isoform of JAK/STAT, is associated with proliferation, migration, metastasis, and cachexia in many cancers [12, 13]. Yet, the role of JAK2/STAT3 signaling pathway in energy stress condition is still unknown.

Renal cancer represents the sixth-most common diagnosed cancer in men and the eighth-most common cancer in women, accounting for 5% and 3% of all new cancer cases in 2020, respectively [14]. However, despite the application of various treatments, such as targeted therapy and immune therapy, the unfavorable outcomes in renal cancer suggest the urgency of the need for novel therapeutics [15]. Renal cancer cells are relatively susceptible to ferroptosis, suggesting a great potential for antitumor therapy [16]. Considering that the underlying mechanisms of energy stress-mediated ferroptosis in cancer remain ambiguous, we explore the effects of energy stress on ferroptosis in renal cancer.

2. Methods and Materials

2.1. Cell Culture. Renal cell cancer cell lines 786-O and A498 were purchased from ATCC (American Type Culture Collection, Manassas, VA, USA). The cells were cultured in RPMI 1640 medium supplemented with 10% fetal bovine serum (FBS, GIBCO, MA, USA) under 5% CO_2 at 37°C. For glucose starvation treatment, cells were cultured in normal medium for 24 h and washed twice with PBS, and the medium was replaced with a glucose-free medium supplemented with 10% FBS.

Cells were treated with the ferroptosis inducer erastin ($1.5\ \mu\text{M}$) (MedChemExpress, China) for 24 h, the ferroptosis inhibitor ferrostatin-1 ($2\ \mu\text{M}$) (Fer-1, MedChemExpress) for 24 h, the AMPK inhibitor Compound C (COM C) ($10\ \mu\text{M}$) (MedChemExpress) for 24 h, the AMPK activator AICAR ($2\ \text{mM}$) (MedChemExpress) for 24 h, Pifithrin- α ($5\ \mu\text{M}$) (PFT- α , MedChemExpress) for 24 h, the apoptosis inhibitor Z-VAD-FMK ($20\ \mu\text{M}$) (MedChemExpress), and the necroptosis inhibitor necrostatin-1 ($2\ \mu\text{M}$) (Nec-1, MedChemExpress).

2.2. siRNA Construction and Cell Transfection. siRNAs were constructed and purchased from Wuhan Viraltherapy Technologies Co. Ltd. Cells were transfected with the siRNAs using Lipofectamine 2000 (Invitrogen, China) for at least 48 h. If not specifically stated, siRNA negative control was transfected to the other groups as control.

2.3. Plasmid Construction and Cell Transfection. Plasmids were extracted using the Small Plasmid Extraction Kit (EM101, TransGen Biotech, China), and single colonies were then amplified. The bacterial culture fluid was subjected to sequencing. 293 T cells were cotransfected with pLVX-GPX4-ZsGreen-Puro and pLVX-JAK2-ZsGreen-Puro (recombinant plasmids) using the Lentivirus Packaging Kit (R003, Wuhan Viraltherapy Technologies Co., Ltd.) to obtain high-titer lentiviruses containing the target genes (rLV-GPX4, rLV-JAK2). Lentiviruses loaded with the recombinant plasmids were transfected into cells at an MOI of 20 for 48 h. Lentivirus-infected cells were selected using DMEM containing $10\ \mu\text{g}/\text{mL}$ puromycin.

2.4. Cell Death Assay. Cell death was measured by propidium iodide (PI) staining using a flow cytometer. After subjecting to different treatments, the cells, including floating cells, were collected and stained with $5\ \mu\text{g}/\text{mL}$ PI, following

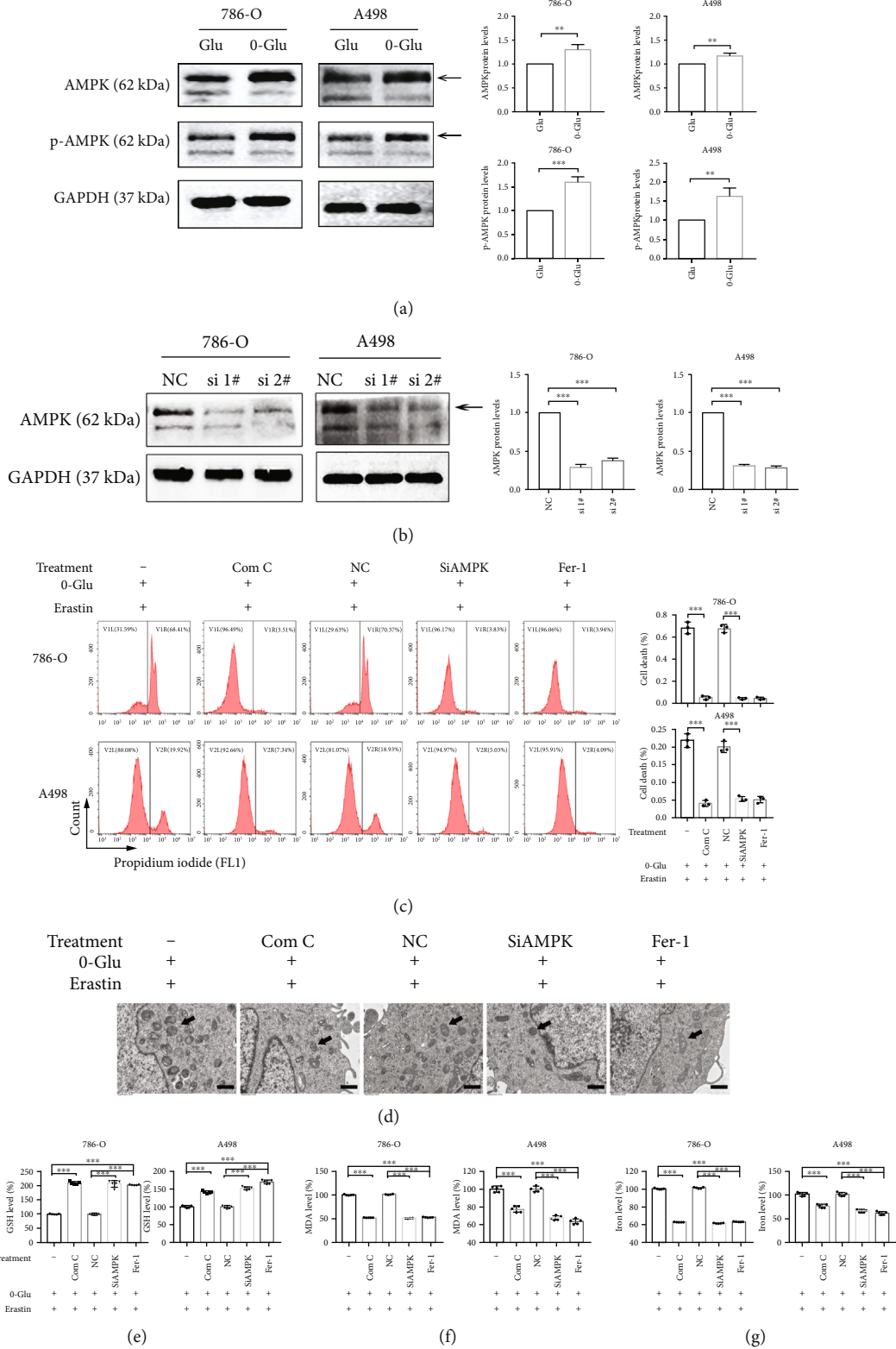


FIGURE 2: Energy stress promotes ferroptotic cell death through AMPK activation. (a and b) Western blotting assay verifies the activation of AMPK after 0-Glu treatment and the knockdown efficacy of two siAMPK. (c) Cell death measurement shows the alleviation of cell death by Com C, siAMPK, and Fer-1 after 0-Glu and erastin treatment. (d) TEM images shows that Com C, siAMPK, and Fer-1 treatments recover mitochondrial morphology. Black arrows indicate mitochondria. Scale bars: 1 μ m. Independent experiments were repeated three times, and representative data were shown. (e–g) Com C, siAMPK, and Fer-1 treatments reverse the changes of GSH, MDA, and cellular iron level caused by 0-Glu and erastin treatment. Data shown represent mean \pm SD from at least three independent experiments. Comparisons were performed using Student's *t*-test and one-way ANOVA. NC: negative control; Com C: Compound C; Fer-1: ferrostatin-1. ***p* < 0.01 and ****p* < 0.001.

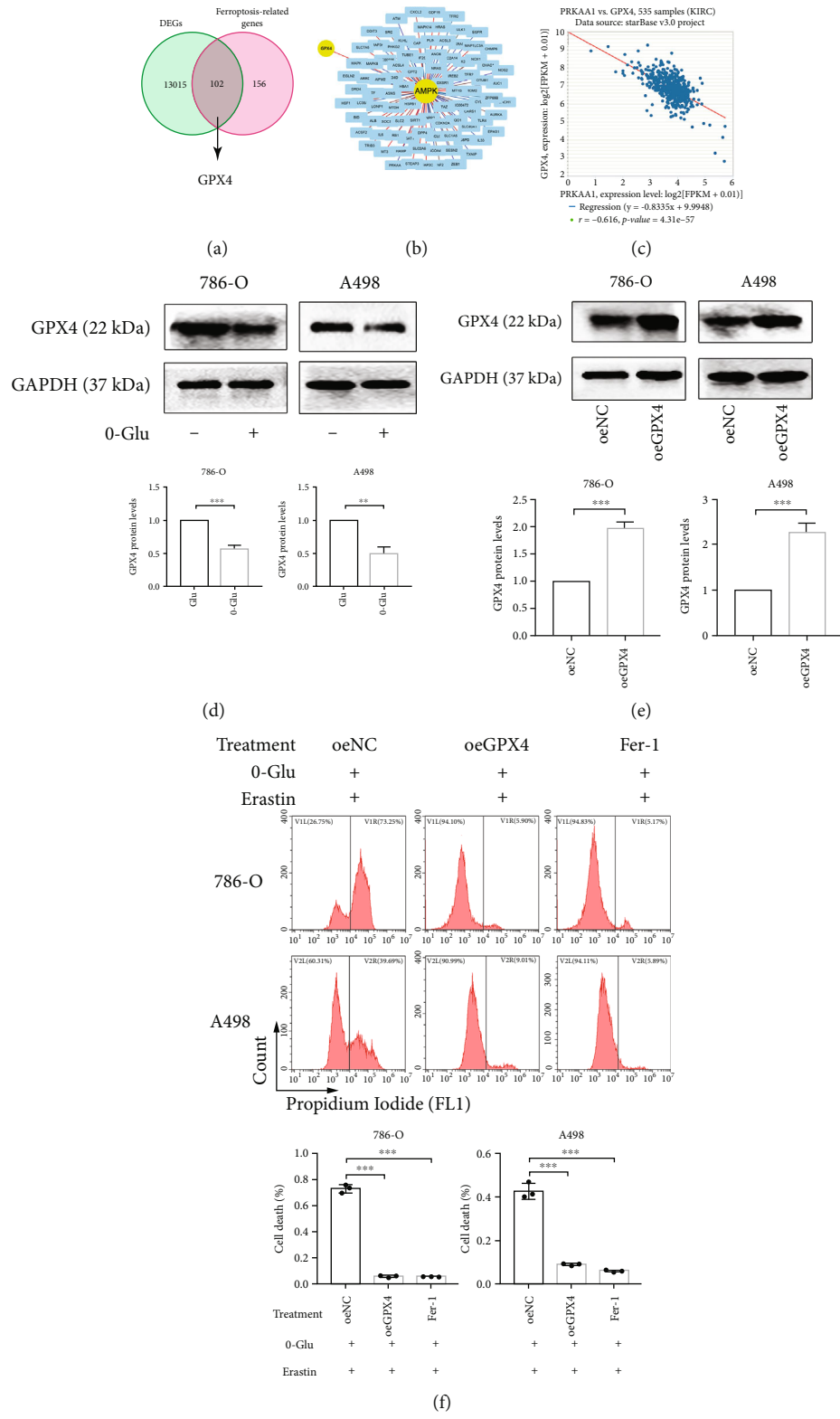


FIGURE 3: Continued.

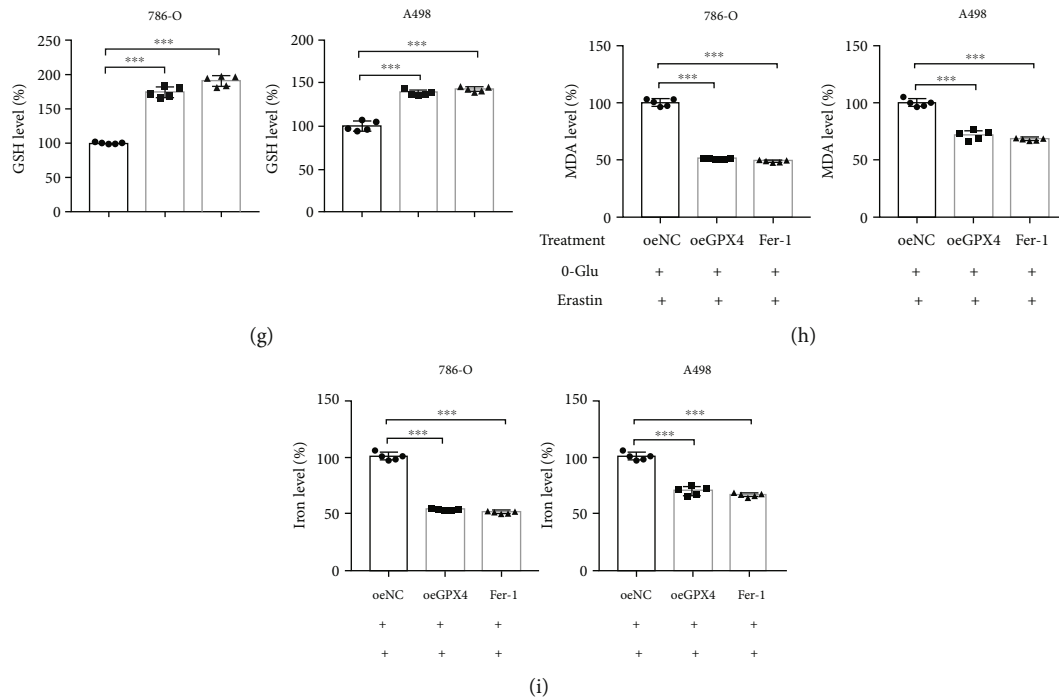


FIGURE 3: GPX4 overexpression alleviates energy-stress-mediated ferroptotic cell death. (a) VENN diagram shows *GPX4* as a ferroptosis-related differentially expressed genes. (b and c) PPI network and coexpression analysis shows the correlation between AMPK and GPX4. (d) Western blotting assay presents a decrease of GPX4 expression after glucose-starvation. (e) Western blotting assay verifies the effect of GPX4 overexpression. (f) Cell death measurement in cells treated with indicated treatments. Independent experiments were repeated three times, and representative data were shown. (g–i) The measurement of GSH, MDA, and cellular iron in cells treated with oeGPX4 or Fer-1 after o-Glu and erastin treatment. Data shown represent mean \pm SD from at least three independent experiments. Comparisons were performed using Student's *t*-test and one-way ANOVA. oeNC: overexpression negative control; Fer-1: ferrostatin-1. ** $p < 0.01$ and *** $p < 0.001$.

which the percentage of positive cells was counted and analyzed on a flow cytometer (BD Accuri C6).

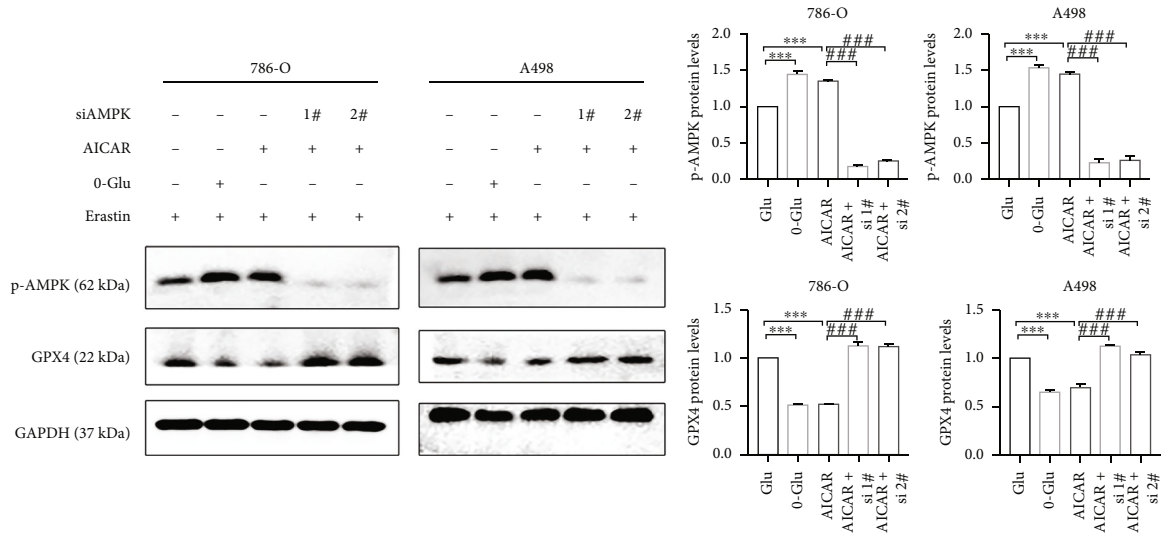
2.5. Lipid Peroxidation Assay. Malondialdehyde (MDA) is one of the end products of lipid peroxidation. The lipid peroxidation levels were evaluated using the MDA assay kit (Nanjing Jiancheng Bioengineering Institute, China). An assay was conducted according to the manufacturer's instructions. The absorbance was measured at 525 nm using a microplate reader (Bio-Rad Laboratories, Redmond, WA, USA) [17]. The MDA levels were presented as a ratio of the absorbance value of the control group.

2.6. Reduced Glutathione (GSH) Level Measurement. GSH levels were assayed using the GSH Assay Kit (Nanjing Jiancheng Bioengineering Institute, China) according to the manufacturer's instructions. Absorbance was measured at 405 nm using a microplate reader (Bio-Rad). The GSH levels were presented as a ratio to the absorbance value of the control group.

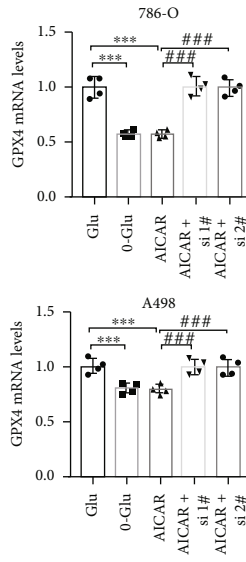
2.7. Cellular Iron Level Measurement. Cellular iron levels were detected by the Iron Assay kit (Nanjing Jiancheng Bioengineering Institute, China) according to the manufacturer's instructions. Absorbance was measured at 520 nm using a microplate reader (Bio-Rad). The cellular iron levels

were presented as a ratio of the absorbance value of the control group.

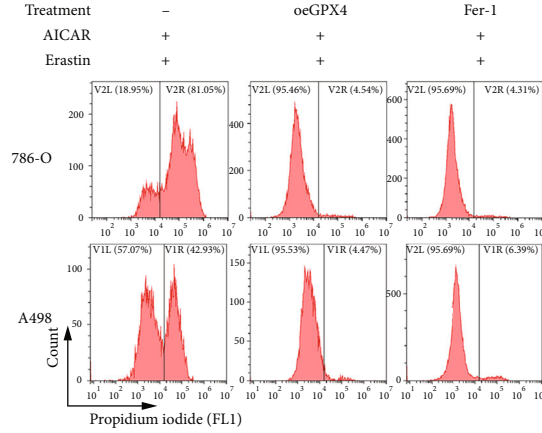
2.8. Western Blotting Analysis. Total proteins were collected by lysing the cells with the RIPA Lysis Buffer (Beyotime, China) and quantified using the BCA protein assay kit (Beyotime). The proteins were mixed with a loading buffer and denatured by heating in boiling water. The protein samples were separated on 10% SDS-PAGE gels and transferred to PVDF membranes. After blocking with 5% nonfat milk and washing with TBST buffer, the membranes were treated overnight with primary antibodies at 4°C. The primary antibodies used in our study were as follows: rabbit polyclonal anti-AMPK alpha antibody (AMPK α , 1: 1000, Affinity), rabbit polyclonal anti-phospho-AMPK alpha (Thr172) antibody (p-AMPK α , 1: 1000, Affinity), rabbit polyclonal anti-GPX4 antibody (1:1000, Affinity), rabbit polyclonal anti-P53 antibody (1:1000, Affinity), rabbit polyclonal anti-STAT3 antibody (1: 1000, Affinity), rabbit polyclonal anti-phospho-STAT3 (Tyr705) antibody (p-STAT3, 1: 1000, Affinity), rabbit polyclonal anti-JAK2 antibody (1: 1000, Affinity), rabbit polyclonal anti-phospho-JAK2 (Tyr931) antibody (p-JAK2, 1: 1000, Affinity), and rabbit polyclonal anti-GAPDH antibody (1: 4000, Affinity). After washing with TBST, the membranes were then treated with a



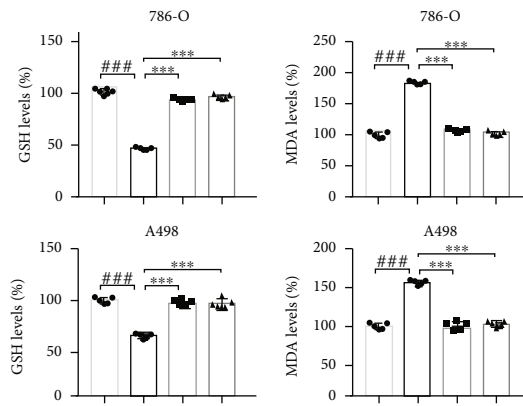
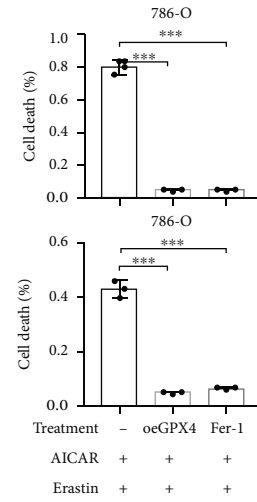
(a)



(b)



(c)



(d)

(e)

FIGURE 4: Continued.

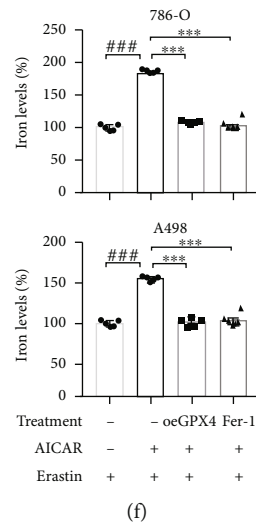


FIGURE 4: AMPK activation enhances GPX4-dependent ferroptosis. (a and b) Western blotting assay and qRT-PCR show the changes of p-AMPK and GPX4 protein levels and *GPX4* mRNA level in cells treated with AICAR and siAMPK. All groups were treated with erastin. (c) Cell death measurement presents the effect of AICAR and oeGPX4 on erastin-induced cell death. Independent experiments were repeated three times and representative data were shown. (d–f) The measurement of GSH, MDA, and cellular iron levels in cells treated with AICAR and oeGPX4. Data shown represent mean \pm SD from at least three independent experiments. Comparisons were performed using Student's *t*-test and one-way ANOVA. Fer-1: ferrostatin-1. ** $p < 0.01$, *** $p < 0.001$, ## $p < 0.01$, and ### $p < 0.001$.

secondary antibody (HRP-conjugated antirabbit secondary antibodies, 1:5000, Boster Biological Technology Co. Ltd) at room temperature for 2 h. Finally, the membranes were evaluated using a chemiluminescence system (Bio-Rad).

2.9. Quantitative Real-Time PCR. Total RNA was extracted by TRIzol, and the RNA concentration was measured using a spectrophotometer. cDNA was synthesized using the PrimeScript™ RT Reagent Kit (Takara) according to the manufacturer's instructions. qRT-PCR was conducted using a Bio-Rad real-time PCR system with the SYBR Green PCR Master Mix (Takara). The expression levels are presented as a ratio relative to the expression of GAPDH. Data analysis was performed using the $2^{-\Delta\Delta Ct}$ method. The primers used in the study are shown below.

GPX4 (Forward) 5'-GAGGCAAGACCGAAGTAAACTAC-3'
 (Reverse) 5'-CCGAAGTGGTTACACGGGAA-3'
TP53 (Forward) 5'-GAGATGTTCCGAGAGCTGA-3'
 (Reverse) 5'-TCAGCTCTCGGAACATCTC-3'
GAPDH (Forward) 5'-AACGGATTGGTCGTATTGG-3'
 (Reverse) 5'-CCTGGAAGATGGTGATGGGAT-3'

2.10. Transmission Electron Microscope (TEM). Cells were collected using trypsin. After centrifugation, the cells were fixed in 2.5% glutaraldehyde at 4°C for 24 h. Then, the cells were fixed in 2% osmium tetroxide at room temperature. After dehydration in increasing concentrations of ethanol, the samples were embedded in epoxy resin and cut into 60-nm ultrathin sections. Eventually, the sections were stained with 1% uranyl acetate and observed using a Hitachi TEM system (HT7800).

2.11. Bioinformatics Analysis. The mRNA expression profiles and corresponding clinical data of 537 patients with renal cancer were retrieved from TCGA (TCGA-KIRC, up to October 29, 2021), and data for 258 ferroptosis-related genes were retrieved from the FerrDb database. Differentially expressed genes (DEGs) between the AMPK high-expression and low-expression groups were screened using the “limma” R package with a false discovery rate < 0.05 , and following this, the intersecting genes between DEGs and ferroptosis-related genes were identified. Among the intersecting genes, the ones for which the expression had a correlation > 0.8 with the AMPK score were selected for visualization with a protein-protein interaction (PPI) network using STRING 11.5. Coexpression analysis was performed on ENCORI [18]. The “survival” and “survminer” R packages were used to perform univariate and multivariate COX analyses, and Kaplan-Meier (K-M) curves for overall survival were plotted using the “ggsurvplot2” R package. The variance in clinicopathological characteristics between subgroups was presented using the “ggpubr” R package.

2.12. Tissue Collection. Sixty-one pairs of renal cancer tissues and adjacent normal tissues were collected from patients undergoing ectomy of renal cancer carcinoma in Renmin Hospital of Wuhan University from January 2021 to December 2021. All research protocols were approved by the Ethics Committee of Renmin Hospital of Wuhan University.

2.13. Immunohistochemical Assay. Paraffinized blocks of tissues were cut into sections. The sections were deparaffinized and hydrated and then treated with a primary antibody and secondary antibody sequentially. Finally, the sections were stained with 3,3'-diaminobenzidine, a chromogenic agent (Dako Corp, Carpinteria, CA, USA). The primary antibodies

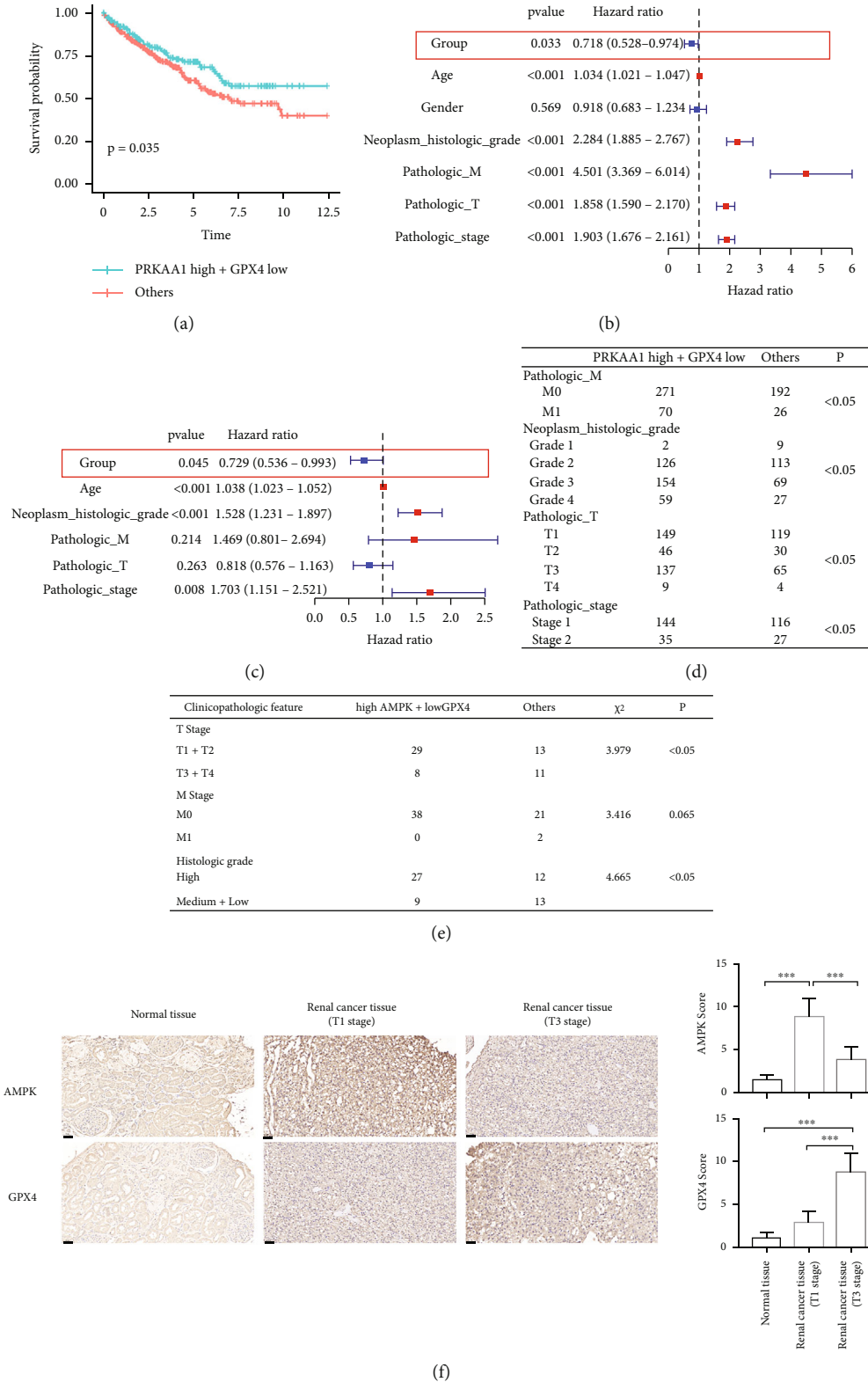
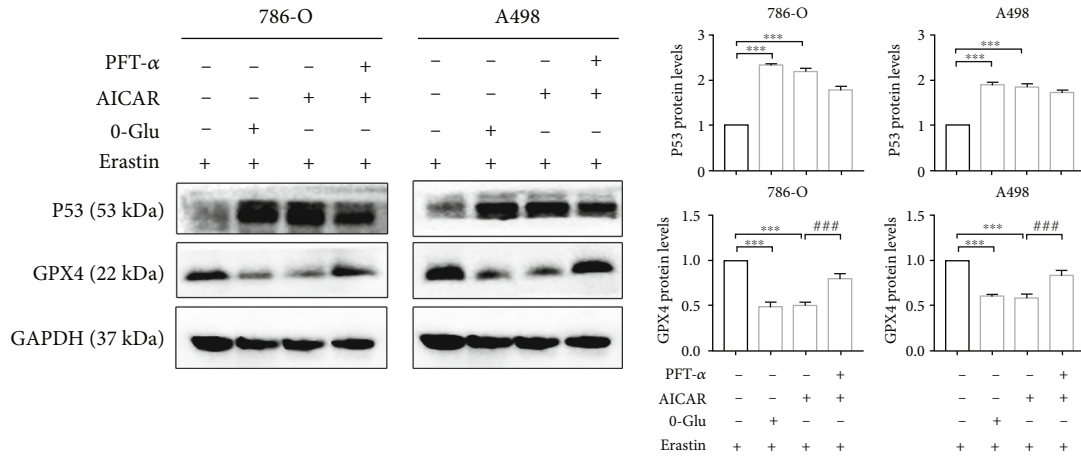
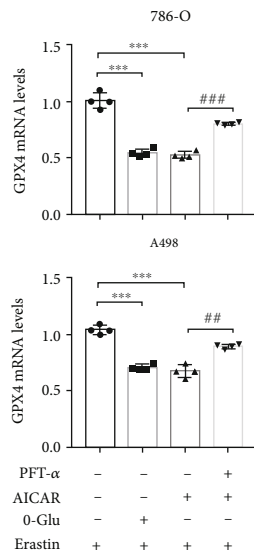


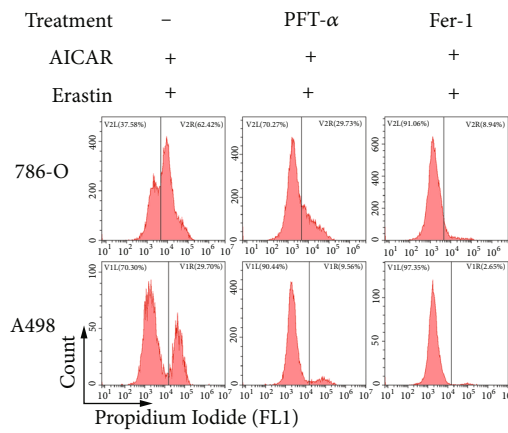
FIGURE 5: AMPK high+GPX4 low expression signature is a predictor of favorable prognosis of renal cancer. (a) K-M curves for the overall survival of patients in the AMPK high+GPX4 low expression group and others. (b and c) Forest map of univariate and multivariate COX regression analysis regarding overall survival. (d) The table shows the difference of clinicopathologic features between different group based on TCGA-KIRC dataset. (e) The table shows the information of 61 specimens we collected. Data shown represent mean \pm SD from at least three independent experiments. Comparisons were performed using chi-square test. (f) Representative images present AMPK and GPX4 expression in tissues of different stage of renal cancer (20 \times , scale bars: 50 μ m). Independent experiments were repeated three times, and representative data were shown.



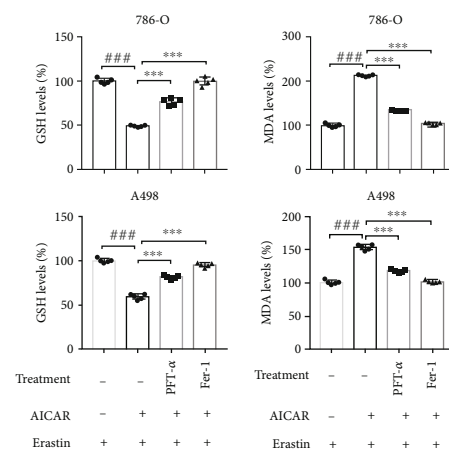
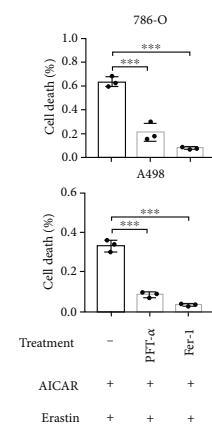
(a)



(b)



(c)



(d)

(e)

FIGURE 6: Continued.

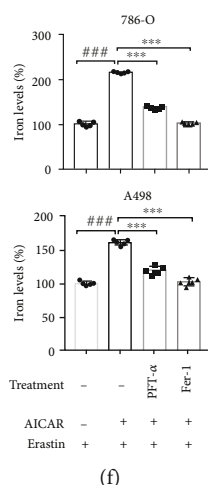


FIGURE 6: AMPK promotes GPX4-dependent ferroptosis partly through upregulation of p53. (a) Western blotting assay shows the expression of P53 and GPX4 after indicated treatments. (b) qRT-PCR presents the mRNA levels of *GPX4* after indicated treatments. (c–f) The measurements of cell death, GSH, MDA, and cellular iron in cells with indicated treatments. Independent experiments were repeated three times, and representative data were shown. Data shown represent mean \pm SD from at least three independent experiments. Comparisons were performed using Student's *t*-test and one-way ANOVA. Fer-1: ferrostatin-1; ns, not significant. *** $p < 0.001$ and ### $p < 0.001$.

used here were the same as those mentioned in the previous section, with a dilution of 1:50. The sections were scored independently by two experienced pathologists in a single-blind manner. The method of semiquantitative scoring has been described in a previous study [19]. A score ≤ 4 was considered to represent low expression, and a score > 4 was considered to represent high expression.

2.14. Statistical Analysis. All data are presented as mean \pm SD. Statistical analysis involved one-way ANOVA, chi-square test, and Student's *t*-test performed using GraphPad Prism 7. Unless specified otherwise, $p \geq 0.05$ was considered to represent a statistically significant difference.

3. Results

3.1. Energy Stress Promotes Ferroptotic Cell Death in Renal Cancer Cells. Glucose is the main source of energy for cancer cells. We simulated energy stress by glucose deprivation. Glucose deprivation significantly aggravated erastin-induced cell death (Figure 1(a)). To determine whether the increased cell death was ferroptotic cell death, we observed the cells via TEM and found that in response to treatment with erastin, the cells developed typical morphological features of ferroptosis, such as shrinkage of the mitochondria, increase in membrane density, and disappearance of mitochondrial cristae. Notably, these changes were more drastic after glucose deprivation (Figure 1(b)). GSH depletion and increase in lipid peroxidation were the key biochemical changes in ferroptosis. We demonstrated that glucose deprivation significantly decreased the intracellular GSH level while significantly increasing the MDA level and cellular iron level, and this trend could be reversed by Fer-1, a potent inhibitor of ferroptosis (Figures 1(c)–1(e)). The above results

suggest that energy stress promotes ferroptosis in renal cancer cells.

3.2. Energy Stress Promotes Ferroptotic Cell Death through AMPK Activation. AMPK, as an energy receptor, is known to be activated in response to energy stress. We next explored whether the activation of AMPK is involved in the promotion of ferroptosis by energy stress. The western blotting results confirmed that the activation of AMPK phosphorylation (p-AMPK) increased after glucose deprivation (Figure 2(a)). Next, we constructed two siAMPKs, of which 1#siAMPK was more effective and used in subsequent studies (Figure 2(b), Supplementary Figure 2). COM C is a potent selective AMPK inhibitor. After glucose deprivation, the inhibition of AMPK by COM C or siAMPK remarkably rescued erastin-induced ferroptosis, as observed with Fer-1 (Figure 2(c)). The TEM results also showed that the changes in mitochondrial size, membrane density, and mitochondrial cristae caused by glucose deprivation and erastin treatment were alleviated after the inhibition or knockdown of AMPK, and these changes were also identical to those observed after treatment with Fer-1 (Figure 2(d)). Similarly, GSH, MDA, and cellular iron levels reverted after AMPK inhibition or knockdown (Figures 2(e)–2(g)). Therefore, the inhibition or knockdown of AMPK reversed the erastin-induced ferroptosis enhanced by glucose deprivation. Collectively, energy stress promotes ferroptotic cell death through AMPK activation in renal cancer cells.

3.3. GPX4 Overexpression Alleviates Energy-Stress-Mediated Ferroptotic Cell Death. Next, we used bioinformatics analysis for identifying 102 differentially expressed ferroptosis-related genes between the AMPK (encoded by *PRKAA*) high- and low-expression groups using data from TCGA.

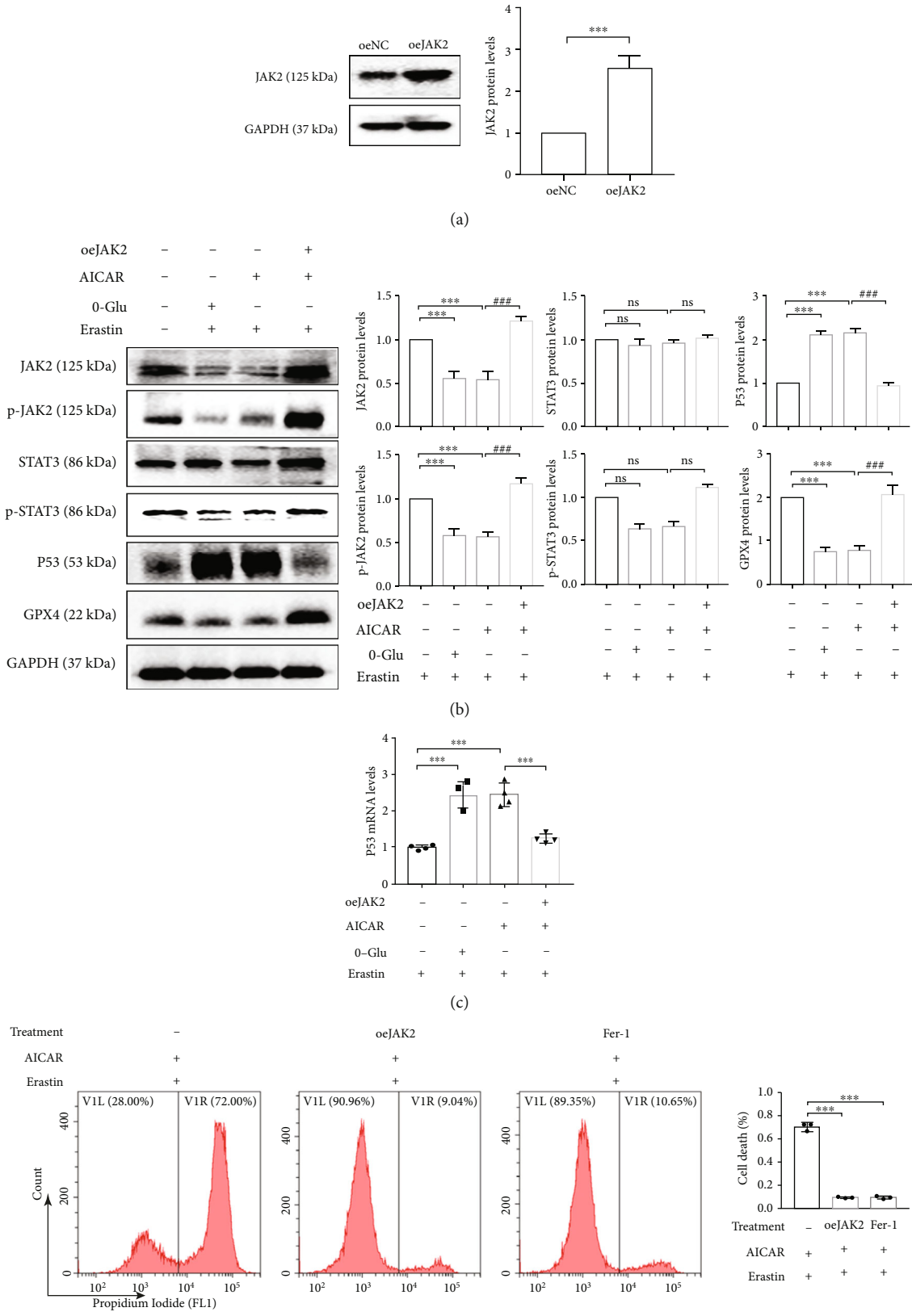


FIGURE 7: Continued.

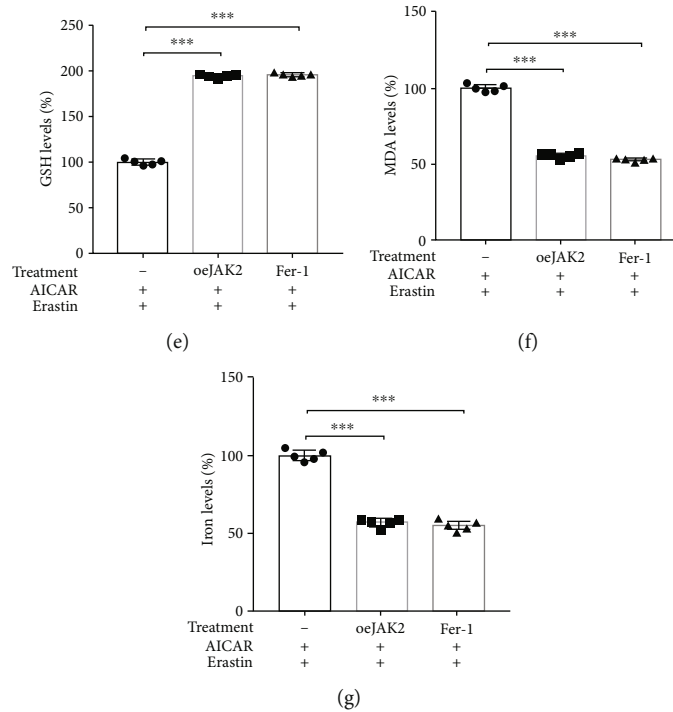


FIGURE 7: JAK2/STAT3 signaling pathway inactivation upregulates P53 expression participating AMPK-mediated GPX4-dependent ferroptosis. 786-O cells were transfected with a JAK2 overexpression plasmid. (a and b) Western blotting assay shows the effect of JAK2 overexpression and the expression of JAK2, p-JAK2, STAT3, p-STAT3, P53, and GPX4. (c) P53 mRNA levels were detected by qRT-PCR. (d–g) Overexpression of JAK2 reverses the changes in cell death, GSH, MDA, and cellular iron caused by AICAR and erastin. Independent experiments were repeated three times, and representative data were shown. Data shown represent mean \pm SD from at least three independent experiments. Comparisons were performed using Student’s *t*-test and one-way ANOVA. Fer-1: ferrostatin-1; ns: not significant. ****p* < 0.001 and ###*p* < 0.001.

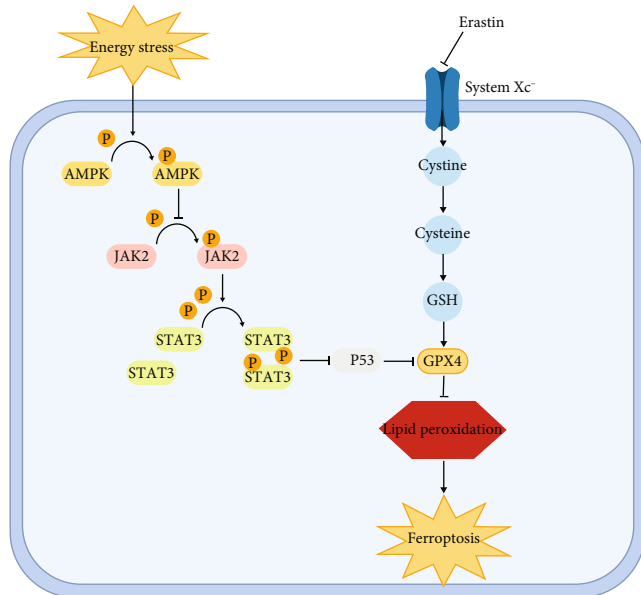


FIGURE 8: Schematic diagram displays potential mechanism of energy-stress-mediated promotion of erastin-induced ferroptosis.

Surprisingly, we found that GPX4, one of the most critical enzymes for ferroptosis, featured among these 102 genes (Figure 3(a)). Moreover, by PPI and coexpression analyses, we found that GPX4 expression showed high negative correlation with AMPK expression (Figures 3(b) and 3(c)).

Therefore, we further confirmed the role of GPX4 in energy-stress-mediated ferroptosis. Western blotting results showed a decrease in the GPX4 protein level after glucose deprivation (Figure 3(d)). Following this, we constructed GPX4 overexpression (oeGPX4) renal cancer cell lines (Figure 3(e)). Ferroptosis induced by glucose deprivation and erastin treatment decreased significantly after GPX4 overexpression, as observed after Fer-1 treatment as well (Figure 3(f)). In parallel, the GSH, MDA, and cellular iron levels were ameliorated by GPX4 overexpression (Figures 3(g)–3(i)). Hence, the results of bioinformatics analysis predicted that GPX4 may be involved in energy-stress-mediated ferroptosis, and findings from the rescue assays further confirmed that GPX4 overexpression alleviated energy-stress-mediated ferroptotic cell death.

3.4. AMPK Activation Enhances GPX4-Dependent Ferroptosis. The results indicate that the activation of AMPK may regulate ferroptosis through the regulation of GPX4. Next, we explored the relationship between AMPK

activation and GPX4-dependent ferroptosis via the pharmacological activation of AMPK. AICAR, an adenosine analog and AMPK activator, was used. The phosphorylation level of AMPK after treatment with AICAR was confirmed to be the same as that after glucose deprivation treatment, and likewise, the protein level of GPX4 declined significantly upon AICAR treatment. Nevertheless, this decline was reversed after AMPK knockdown (Figure 4(a)). To exclude off target effect of siRNA, two siAMPK was used. The same trend was also observed at the mRNA level (Figure 4(b)), suggesting that the phosphorylation-mediated activation of AMPK could reduce GPX4 expression at the transcriptional level. In terms of ferroptosis-related phenotypes, AICAR similarly increased erastin-induced ferroptosis, whereas cell survival was recovered in response to GPX4 overexpression (Figure 4(c)). Also, we demonstrated that the intracellular GSH levels had reduced significantly, and MDA and cellular iron levels had increased upon AICAR treatment, whereas these trends had reversed after GPX4 overexpression (Figures 4(d)–4(f)). The above results suggest that AMPK activation enhances GPX4-dependent ferroptosis.

3.5. AMPK High + GPX4 Low Expression Signature Is a Predictor of a Favorable Prognosis of Renal Cancer. Considering the previous results, we categorized patients into a high AMPK (encoded by *PRKAA*) + low GPX4 expression group and others group. K-M curve analysis showed that patients with high AMPK and low GPX4 expression had better overall survival (Figure 5(a)). Findings from the univariate and multivariate COX analyses suggested that high AMPK + low GPX4 expression was a low-risk prognostic factor (Figures 5(b) and 5(c)). In addition, patients with high AMPK and low GPX4 expression typically had lower pathological T and M grades as well as neoplasm histological grade and pathological stage (Figure 5(d), Supplementary Table 1). After statistical analysis of the data obtained from our specimens, we achieved a consistent result (Figure 5(e) and 5(f)). We showed representative images in adjacent normal tissue (Figure 5(f) left) and renal cancer tissue of T1 stage (Figure 5(f) middle) and T3 stage (Figure 5(f) right).

3.6. AMPK Promotes GPX4-Dependent Ferroptosis Partly through the Upregulation of P53. *TP53* is widely known as a critical oncogene. Recently, an increasing number of studies have focused on the role of P53 in ferroptosis [20]. In this study, we investigated whether P53 was involved in AMPK-mediated GPX4-dependent ferroptosis. We observed that after glucose deprivation and AICAR treatment, the P53 levels were significantly elevated, whereas the GPX4 levels were significantly lowered. In contrast, upon treatment with PFT- α (an inhibitor of P53), the protein levels of GPX4 were restored (Figure 6(a)). Similarly, the mRNA levels of GPX4 also showed the same trend (Figure 6(b)). Considering the previous results, AMPK activation was suggested to transcriptionally inhibit GPX4 expression, partly through P53 upregulation. Next, we focused on the role of P53 in ferroptosis. It was demonstrated that after treatment with PFT- α , the increase in ferroptosis caused by erastin and AICAR

was alleviated, intracellular GSH levels were elevated, MDA levels were lowered, and cellular iron levels were also reduced (Figures 6(c)–6(f)). Considering that AMPK and P53 are involved in the regulation of apoptosis in some cancers, we also performed experiments to exclude the potential of apoptosis. Firstly, the level of apoptosis hallmark cleaved caspase-3 was detected, and the results demonstrated that energy stress did not induce apoptosis in the context (Supplementary Figure 1A). Next, the cell death assay indicated that apoptosis inhibitor and necroptosis could not alleviate the cell death caused by AMPK activation and erastin (Supplementary Figure 1B). Moreover, the GSH, MDA, and cellular iron levels could not all be reversed by the inhibition of apoptosis and necroptosis either (Supplementary Figure 1C–1E). These results confirmed that the upregulation of P53 contributes to AMPK-mediated GPX4-dependent ferroptosis.

3.7. JAK2/STAT3 Signaling Pathway Inactivation Upregulates the Expression of P53, which Participates in AMPK-Mediated GPX4-Dependent Ferroptosis. STAT3 has been previously reported to negatively regulate ferroptosis [21], and the activation of the JAK2/STAT3 signaling pathway has been reported to inhibit P53 expression [22]. Thus, we explored the regulatory effect of the JAK2/STAT3 signaling pathway toward P53, which is involved in AMPK-mediated GPX4-dependent ferroptosis. We observed that after AMPK activation (in the glucose deprivation and AICAR groups), the phosphorylation levels of both JAK2 and STAT3 decreased significantly, whereas, after the overexpression of JAK2, the STAT3 phosphorylation level was restored, P53 expression reduced, and GPX4 expression increased significantly (Figures 7(a) and 7(b)), suggesting that AMPK activation regulates P53 expression via the JAK2/STAT3 signaling pathway. Moreover, the changes in the P53 mRNA levels suggest that the regulation of P53 by JAK2/STAT3 signaling occurred at the transcriptional level (Figure 7(c)). Findings from further experiments revealed that after the overexpression of JAK2, the enhancement of ferroptosis, reduction in GSH level, elevation in MDA level, and rise in cellular iron level in response to AMPK activation were ameliorated significantly (Figures 7(d)–7(g)). These results indicated that the regulation of the JAK2/STAT3 signaling pathway toward P53 contributes to AMPK-mediated GPX4-dependent ferroptosis (Figure 8).

4. Discussion

Glucose is a critical nutrient that is necessary for tumor cells to maintain normal metabolism and redox homeostasis. However, with rapid tumor growth, glucose deficiency-induced energy stress is a constant predicament for tumor cells. Glucose deficiency leads to redox system imbalance and energy metabolism deficiency in tumor cells, which further inhibits cell survival [23]. Ferroptosis is also primarily caused by lipid peroxidation owing to the dysregulation of the redox system in cells [5]. Therefore, we deduced that energy stress may promote ferroptosis in tumor cells. In the present study, we found that the simulation of energy

stress with glucose deprivation increased erastin-induced cell death, besides decreasing the intracellular GSH level and increasing the MDA level. Combined with findings from the TEM images, energy stress was found to promote ferroptosis in renal cancer cells. Next, we found that AMPK phosphorylation activation increased after energy stress, whereas the expression of GPX4, the core enzyme in the regulation of ferroptosis, decreased. After GPX4 overexpression was induced, the level of ferroptosis induced by erastin and AMPK activation decreased significantly, indicating that energy stress-induced ferroptosis is associated with an AMPK activation-mediated decrease in GPX4 expression. Mechanistically, we observed that energy stress-induced AMPK activation inhibits GPX4 expression at the transcriptional level via P53 through the suppression of the JAK2/STAT3 signaling pathway, which consequently promotes ferroptosis.

Owing to the rapid proliferation of tumor cells, their energy metabolism undergoes adaptive shifts, such as the Warburg effect and pentose phosphate pathway (PPP) upregulation, to fulfill the energy demands for survival and biosynthesis [24, 25]. Thus, tumor-specific energy metabolism is the central force regulating redox homeostasis in tumor cells and a key factor in the regulation of ferroptosis [5]. Excessive growth inevitably leads to a relative deficiency of energy supply in the tumor microenvironment [26]. This forces tumor cells into a condition of energy stress, which leads to the inhibition of metabolic pathways, such as glycolysis and PPP, and thus affects tumor cell survival [27]. As the most important energy sensor, AMPK has largely been the focus of existing studies on energy stress and ferroptosis. However, the role of AMPK in the regulation of ferroptosis is controversial, considering evidence from recent studies. Lee et al. reported that AMPK activation during energy stress could block ferroptosis induced by cystine deficiency and GPX4 inhibition [28]. Mechanistically, energy stress activates AMPK, leading to the inhibition of downstream ACC by phosphorylation. Acetyl-CoA carboxylase (ACC) is a rate-limiting enzyme for fatty acid biosynthesis, which increases fatty acid synthesis and inhibits fatty acid oxidation. The inhibition of ACC activity decreases the intracellular PUFA levels and thereby reduces cellular susceptibility to ferroptosis. In addition to the effect on lipid synthesis, the inhibition of ACC caused by AMPK activation also reduces NADPH consumption and enhances resistance to ferroptosis [28]. LKB1, a serine/threonine kinase, is also involved in the regulation of metabolism during energy stress in tumor cells [29]. Li et al. found that LKB1 enhanced downstream AMPK and ACC phosphorylation and inhibited PUFA production, thereby limiting the cellular susceptibility to ferroptosis [30]. These findings suggest that the activation of AMPK during energy stress can effectively enhance cellular resistance to ferroptosis and enable tumor cells to survive in an adverse environment. However, contrary to the findings, Song et al. showed that AMPK-mediated BECN1 phosphorylation promotes ferroptosis by directly binding to SLC7A11 to form a complex inhibiting the activity of system Xc- [31]. Consistently, our results also showed that energy stress-mediated AMPK activation transcriptionally inhibited

GPX4 to promote ferroptosis through the JAK2/STAT3/P53 axis. Taken together, we propose that the role of energy stress and AMPK on ferroptosis in cancer may be dependent on the context. Energy stress-mediated AMPK activation could either resist ferroptosis and promote tumor survival through the inhibition of unsaturated fatty acid synthesis or enhance ferroptosis and suppress tumor survival through the inhibition of protein biosynthesis or regulation of ferroptosis-related enzymes.

The JAK2/STAT3 signaling pathway is widely known to be involved in various biological processes, such as immunity, differentiation, cell death, and tumorigenesis [32]. In recent years, AMPK has been shown to inhibit the JAK/STAT signaling pathway through various mechanisms, participating in the regulation of inflammatory responses and tumor metabolism. He et al. found that the activation of AMPK inhibited STAT1-dependent inflammatory responses that protected against vascular inflammation and atherosclerosis [33]. In addition, the findings of this study suggested that AMPK inhibited STAT1 activation by inducing mitogen-activated protein kinase phosphatase-1. Nerstedt et al. successively confirmed that AMPK activation could inhibit liver inflammation and insulin resistance by suppressing the JAK/STAT signaling pathway [34, 35]. Besides, the inhibition of the mTOR pathway by AMPK was also reported to potentially contribute to the inhibition of the JAK/STAT signaling pathway [36]. In oncology research, Rutherford et al. identified that AMPK activation inhibited acute lymphoblastic leukemia by blocking the JAK/STAT signaling pathway through the inhibition of WT or JAK1^{V658F} [37]. Meanwhile, blockade of the JAK/STAT signaling pathway was also effective in limiting the inflammation-related side effects associated with current treatments. Studies on myeloproliferative neoplasms showed that AMPK activation could inhibit a series of JAK mutants, including JAK2^{V617F}, and could thus effectively control anti-proliferative effects and hemostatic dysfunction [38]. As evident, most current studies on the regulation of the JAK/STAT3 signaling pathway by AMPK focus on hematological tumors, probably because JAK mutations are relatively more prevalent in hematological tumors. Meanwhile, fewer studies have been conducted on solid tumors. In our study, AMPK activation could inhibit the phosphorylation of the JAK2/STAT3 signaling pathway and its functions in transcriptional regulation, which helped promote ferroptosis; however, the precise mechanism remains to be investigated further.

A growing body of evidence suggests that ferroptosis is a potential therapeutic target for tumor progression inhibition [20, 39, 40]. However, even though it has been established that tumor cells are often exposed to energy stress, the effect of energy stress on ferroptosis in renal cancer is yet to be reported. In the present study, we showed that energy stress-mediated AMPK activation could effectively promote ferroptosis in renal cancer via the JAK2/STAT3/P53 axis. We anticipate that the pharmacological activation of AMPK may exert a synergistic effect on chemotherapy with ferroptosis-inducing effects, facilitating a curative effect or reducing chemoresistance. Future studies will further

investigate the effects of the interaction between AMPK and ferroptosis in tumor development.

Data Availability

The datasets used and analyzed during the current study are available from the corresponding author on reasonable request.

Ethical Approval

The present study involving human participants were reviewed and approved by Renmin Hospital of Wuhan University Ethics Committee.

Consent

All patients signed consent for publication.

Conflicts of Interest

All authors have no conflicts of interest or financial ties to disclose.

Authors' Contributions

Yanze Li, Ye Zhang, and Qiangmin Qiu contributed equally to this work.

Acknowledgments

Our work was supported by the National Natural Science Foundation of China (nos. 82000639 and 81972408).

Supplementary Materials

Supplementary 1. Supplementary Figure 1: the effect of AMPK activation on apoptosis.

Supplementary 2. Supplementary Figure 2: another siAMPK was used to exclude off-target effect.

Supplementary 3. Supplementary Table 1: clinical characteristics of the TCGA-KIRC patients used in the study.

References

- [1] Z. D. Xiao, L. Han, H. Lee et al., "Energy stress-induced lncRNA_FILNC1 represses c-Myc-mediated energy metabolism and inhibits renal tumor development," *Nature Communications*, vol. 8, no. 1, p. 783, 2017.
- [2] D. Zhang, J. Li, F. Wang, J. Hu, S. Wang, and Y. Sun, "2-Deoxy-D-glucose targeting of glucose metabolism in cancer cells as a potential therapy," *Cancer Letters*, vol. 355, no. 2, pp. 176–183, 2014.
- [3] A. Poff, A. Kourtnik, K. M. Egan, S. Sahebjam, D. D'Agostino, and N. B. Kumar, "Targeting the Warburg effect for cancer treatment: ketogenic diets for management of glioma," *Seminars in Cancer Biology*, vol. 56, pp. 135–148, 2017.
- [4] Y. Zhao, X. Hu, Y. Liu et al., "ROS signaling under metabolic stress: cross-talk between AMPK and AKT pathway," *Molecular Cancer*, vol. 16, no. 1, p. 79, 2017.
- [5] B. R. Stockwell, J. P. Friedmann Angeli, H. Bayir et al., "Ferroptosis: a regulated cell death nexus linking metabolism, redox biology, and disease," *Cell*, vol. 171, no. 2, pp. 273–285, 2017.
- [6] W. S. Yang and B. R. Stockwell, "Ferroptosis: death by lipid peroxidation," *Trends in Cell Biology*, vol. 26, no. 3, pp. 165–176, 2016.
- [7] C. Han, Y. Liu, R. Dai, N. Ismail, W. Su, and B. Li, "Ferroptosis and its potential role in human diseases," *Frontiers in Pharmacology*, vol. 11, p. 239, 2020.
- [8] Y. H. Ma, F. Han, J. Min, and W. Lin, "Energy metabolism as a regulator of ferroptosis," *Cell Cycle*, vol. 19, no. 22, pp. 2960–2962, 2020.
- [9] M. M. Gaschler, F. Hu, H. Feng, A. Linkermann, W. Min, and B. R. Stockwell, "Determination of the subcellular localization and mechanism of action of ferrostatins in suppressing ferroptosis," *ACS Chemical Biology*, vol. 13, no. 4, pp. 1013–1020, 2018.
- [10] S. Cassim, M. Vučetić, M. Ždravčić, and J. Pouyssegur, "Warburg and beyond: the power of mitochondrial metabolism to collaborate or replace fermentative glycolysis in cancer," *Cancers (Basel)*, vol. 12, no. 5, p. 1119, 2020.
- [11] K. L. Owen, N. K. Brockwell, and B. S. Parker, "JAK-STAT signaling: a double-edged sword of immune regulation and cancer progression," *Cancers*, vol. 11, no. 12, p. 2002, 2019.
- [12] S. Hui, M. Guo, L. Wang, and X. Cui, "MUC16 facilitates cervical cancer progression via JAK2/STAT3 phosphorylation-mediated cyclooxygenase-2 expression," *Genes & Genomics*, vol. 42, no. 2, pp. 127–133, 2020.
- [13] D. Guo, C. Wang, Q. Wang, Z. Qiao, and H. Tan, "Pantoprazole blocks the JAK2/STAT3 pathway to alleviate skeletal muscle wasting in cancer cachexia by inhibiting inflammatory response," *Oncotarget*, vol. 8, no. 24, pp. 39640–39648, 2017.
- [14] R. L. Siegel, K. D. Miller, and A. Jemal, "cancer statistics, 2019," *CA: a Cancer Journal for Clinicians*, vol. 69, no. 1, pp. 7–34, 2019.
- [15] J. J. Hsieh, M. P. Purdue, S. Signoretti et al., "Renal cell carcinoma," *Nature Reviews. Disease Primers*, vol. 3, no. 1, p. 17009, 2017.
- [16] W. S. Yang, R. SriRamaratnam, M. E. Welsch et al., "Regulation of ferroptotic cancer cell death by GPX4," *Cell*, vol. 156, p. 15, 2014.
- [17] K. P. Loh, Q. Jia, B. Tan, X. H. Liu, B. G. Wei, and Y. Z. Zhu, "Leonurine protects middle cerebral artery occluded rats through antioxidant effect and regulation of mitochondrial function," *Stroke*, vol. 41, no. 11, pp. 2661–2668, 2010.
- [18] J. H. Li, S. Liu, H. Zhou, L. H. Qu, and J. H. Yang, "starBase v2.0: decoding miRNA-ceRNA, miRNA-ncRNA and protein-RNA interaction networks from large-scale CLIP-Seq data," *Nucleic Acids Res*, no. D92-7, 2014.
- [19] X. K. Qin, Y. Du, X. H. Liu, and L. Wang, "LSD1 promotes prostate cancer cell survival by destabilizing FBXW7 at post-translational level," *Frontiers in Oncology*, vol. 10, article 616185, 2021.
- [20] L. Jiang, N. Kon, T. Y. Li et al., "Ferroptosis as a p53-mediated activity during tumour suppression," *Nature*, vol. 520, no. 7545, pp. 57–62, 2015.
- [21] S. Ouyang, H. Li, L. Lou et al., "Inhibition of STAT3-ferroptosis negative regulatory axis suppresses tumor growth and alleviates chemoresistance in gastric cancer," *Redox Biology*, vol. 52, p. 102317, 2022.

- [22] T. H. Pham, H. M. Park, J. Kim, J. T. Hong, and D. Y. Yoon, "STAT3 and p53: dual target for cancer therapy," *Biomedicine*, vol. 8, no. 12, p. 637, 2020.
- [23] X. Yao, W. Li, D. Fang et al., "Emerging roles of energy metabolism in Ferroptosis regulation of tumor cells," *Advanced Science*, vol. 8, no. 22, article 2100997, 2021.
- [24] F. Chen, J. N. Chen, L. B. Yang et al., "Extracellular vesicle-packaged HIF-1 α -stabilizing lncRNA from tumour-associated macrophages regulates aerobic glycolysis of breast cancer cells," *Nature Cell Biology*, vol. 21, no. 4, pp. 498–510, 2019.
- [25] U. E. Martinez-Outschoorn, M. Peiris-Pagés, R. G. Pestell, F. Sotgia, and M. P. Lisanti, "Cancer metabolism: a therapeutic perspective," *Nature Reviews Clinical Oncology*, vol. 14, no. 1, pp. 11–31, 2017.
- [26] Y. Ren and H. M. Shen, "Critical role of AMPK in redox regulation under glucose starvation," *Redox Biology*, vol. 25, p. 101154, 2019.
- [27] S. C. Lin and D. G. Hardie, "AMPK: sensing glucose as well as cellular energy status," *Cell Metabolism*, vol. 27, no. 2, pp. 299–313, 2018.
- [28] H. Lee, F. Zandkarimi, Y. Zhang et al., "Energy-stress-mediated AMPK activation inhibits ferroptosis," *Nature Cell Biology*, vol. 22, no. 2, pp. 225–234, 2020.
- [29] R. R. Chhipa, W. Yue, J. L. Mohler, and C. Ip, "Survival advantage of AMPK activation to androgen-independent prostate cancer cells during energy stress," *Cellular Signalling*, vol. 22, no. 10, pp. 1554–1561, 2010.
- [30] C. Li, X. Dong, W. Du et al., "LKB1-AMPK axis negatively regulates ferroptosis by inhibiting fatty acid synthesis," *Signal Transduction and Targeted Therapy*, vol. 5, no. 1, p. 187, 2020.
- [31] X. Song, S. Zhu, P. Chen et al., "AMPK-mediated BECN1 phosphorylation promotes ferroptosis by directly blocking system Xc-activity," *Current Biology*, vol. 28, no. 15, pp. 2388–2399.e5, 2018.
- [32] C. Speirs, J. Williams, K. Riches, I. P. Salt, and T. M. Palmer, "Linking energy sensing to suppression of JAK-STAT signaling: a potential route for repurposing AMPK activators?," *Pharmacological Research*, vol. 128, pp. 88–100, 2018.
- [33] C. He, H. Li, B. Viollet, M. H. Zou, and Z. Xie, "AMPK suppresses vascular inflammation in vivo by inhibiting signal transducer and activator of transcription-1," *Diabetes*, vol. 64, no. 12, pp. 4285–4297, 2015.
- [34] A. Nerstedt, C. Cansby, M. Amrutkar, U. Smith, and M. Mahlapuu, "Pharmacological activation of AMPK suppresses inflammatory response evoked by IL-6 signalling in mouse liver and in human hepatocytes," *Molecular and Cellular Endocrinology*, vol. 375, no. 1-2, pp. 68–78, 2013.
- [35] A. Nerstedt, A. Johansson, C. X. Andersson, E. Cansby, U. Smith, and M. Mahlapuu, "AMP-activated protein kinase inhibits IL-6-stimulated inflammatory response in human liver cells by suppressing phosphorylation of signal transducer and activator of transcription 3 (STAT3)," *Diabetologia*, vol. 53, no. 11, pp. 2406–2416, 2010.
- [36] G. M. Delgoffe, T. P. Kole, Y. Zheng et al., "The mTOR kinase differentially regulates effector and regulatory T cell lineage commitment," *Immunity*, vol. 30, no. 6, pp. 832–844, 2009.
- [37] C. Rutherford, C. Speirs, and J. J. L. Williams, "Phosphorylation of Janus kinase 1 (JAK1) by AMP-activated protein kinase (AMPK) links energy sensing to anti-inflammatory signaling," *Science Signaling*, vol. 9, no. 453, article ra109, 2016.
- [38] I. Kawashima and K. Kirito, "Metformin inhibits JAK2V617F activity in MPN cells by activating AMPK and PP2A complexes containing the B56 α subunit," *Experimental Hematology*, vol. 44, no. 12, pp. 1156–1165.e4, 2016.
- [39] Y. Zhang, J. Shi, X. Liu et al., "BAP1 links metabolic regulation of ferroptosis to tumour suppression," *Nature Cell Biology*, vol. 20, no. 10, pp. 1181–1192, 2018.
- [40] Y. Luo, X. Gao, L. T. Zou, M. Lei, J. Feng, and Z. Hu, "Bavachin induces ferroptosis through the STAT3/P 53/SLC7A11 Axis in osteosarcoma cells," *Oxidative Medicine and Cellular Longevity*, vol. 2021, Article ID 1783485, 14 pages, 2021.

Research Article

Mesenchymal Stem Cell-Derived Exosomes Ameliorate Delayed Neurocognitive Recovery in Aged Mice by Inhibiting Hippocampus Ferroptosis via Activating SIRT1/Nrf2/HO-1 Signaling Pathway

Jie Liu ¹, Jingyao Huang,¹ Zhenjiang Zhang,² Rui Zhang ¹, Qijuan Sun,¹ Zhihao Zhang,¹ Yongxin Liu,¹ and Baoyu Ma ¹

¹Shandong Provincial Medicine and Health Key Laboratory of Clinical Anesthesia, School of Anesthesiology, Weifang Medical University, Weifang, China

²Department of Thoracic Surgery, Weifang People's Hospital, Weifang, China

Correspondence should be addressed to Rui Zhang; zhangrui@wfmcc.edu.cn

Received 14 June 2022; Revised 13 September 2022; Accepted 19 September 2022; Published 30 September 2022

Academic Editor: Xiang Xue

Copyright © 2022 Jie Liu et al. This is an open access article distributed under the Creative Commons Attribution License, which permits unrestricted use, distribution, and reproduction in any medium, provided the original work is properly cited.

Delayed neurocognitive recovery (dNCR) is a prevalent perioperative neurological complication in older patients and has common characteristics such as acute cognitive dysfunction, impaired memory, and inattention. Mesenchymal stem cell-derived exosomes (MSCs-Exo) are enclosed by a lipid bilayer contain proteins, DNA, miRNA, and other components, which are important mediators of intercellular communication. It has been reported that exosomes could play an important role in the treatment of neurodegenerative diseases, nerve injury, and other neurological diseases. In this study, we examined the effects of MSCs-Exo on dNCR aged mice after exploratory laparotomy and evaluated their potential regulatory mechanisms. We found that MSCs-Exo treatment ameliorated cognitive impairment in dNCR aged mice. MSCs-Exo inhibit hippocampus ferroptosis and increase the expression of silent information regulator 1 (SIRT1), factor nuclear factor-erythroid 2-related factor 2 (Nrf2), and heme oxygenase-1 (HO-1) in dNCR aged mice. Interestingly, the above effects of MSCs-Exo on dNCR aged mice were abolished by SIRT1 selective inhibitor EX-527. In conclusion, these findings indicated that MSCs-Exo can ameliorate cognitive impairment by inhibiting hippocampus ferroptosis in dNCR aged mice via activating SIRT1/Nrf2/HO-1 signaling pathway, providing a potential avenue for the treatment of dNCR.

1. Introduction

Delayed neurocognitive recovery (dNCR), which is described by cognitive impairment, is a prevalent perioperative neurological complication in patients within 30 days following surgery, especially in older patients [1]. dNCR is clinically characterized by a sharp decline in cognitive function, including learning, memory, information processing, and attention. And the development of dNCR can increase hospital costs, prolong hospitalization, and increase morbidity and mortality [2], affecting the life quality of patients and aggravating the economic burden of society. Despite significant advances in surgical techniques and anesthesia management, the incidence

of dNCR remains at 18-45% [3]. Many studies have attempted to explain the pathogenesis of dNCR from receptor changes, signaling pathways, cytokines, and other aspects, but no ideal therapeutic strategy has been found for the prevention and treatment of dNCR [4]. Therefore, to explore the prevention and treatment of dNCR has become an urgent and important issue in global medical research [5].

Growing evidence demonstrated that the overproduction of reactive oxygen species (ROS), mitochondrial damage, neuroinflammation, and abnormal homocysteine metabolism are crucial for the development of neurological diseases, such as ischemic stroke and cognitive impairment [6-10]. It was reported that ferroptosis could participate in oxidative

stress response, mitochondrial dysfunction, neuroinflammation, and abnormal homocysteine metabolism [11–13]. Ferroptosis, a new form of cell death, is characterized by the accumulation of a large amount of iron and lipid peroxidation in cells and mitochondrial shrinkage [14]. It is associated with various diseases, including cancer, acute kidney injury, intracerebral hemorrhage, traumatic brain injury, and various neurological diseases such as Parkinson's disease, Huntington's disease, and Alzheimer's disease [15–18]. Ferroptosis is mediated by glutathione peroxidase 4 (GPX4) [19], which can prevent cell death from oxidative damage [20]. Given the effect of oxidative damage in surgery-induced cognitive impairment [7, 21], we speculate that ferroptosis may participate in dNCR aged mice.

Exosomes are nanosized vesicles (30–150 nm diameter) released by different types of cells [22]. Exosomes contain proteins, DNA, miRNA, lncRNA, and other components, which play a significant role in the interaction between cells and extracellular microenvironment [23]. Numerous studies have found that exosomes could play an important role in the treatment of neurodegenerative diseases, nerve injury, and other neurological diseases [24]. And mesenchymal stem cell-derived exosomes (MSCs-Exo) can alleviate early brain injury and improve cognitive function after subarachnoid hemorrhage [25]. Exosomes have excellent antioxidant properties by stimulating some antioxidant enzymes, such as glutathione peroxidase (GPX) [20]. Moreover, exosomes were reported to inhibit ferroptosis and ameliorate ROS-mediated neuronal cell injury [26]. Hence, MSCs-Exo may inhibit ferroptosis to ameliorate cognitive function in dNCR mice.

Silent information regulator 1 (SIRT1) is a nicotinamide adenosine dinucleotide- (NAD-) dependent class III histone deacetylase [27]. It is widely expressed in various organs, and in the brain, the expression level of SIRT1 is higher in the hippocampus and hypothalamus [28]. SIRT1 in neural system plays an important role in regulating normal brain functions such as plasticity and memory [29]. Recently, SIRT1 was found to play an important role in Alzheimer's disease and Parkinson's disease [30, 31]. SIRT1 is regarded as a protector of the cells against oxidative stress injury and lipid peroxidation by mediating the expression of factor nuclear factor-erythroid 2-related factor 2 (Nrf2) and its downstream target heme oxygenase-1 (HO-1) [32]. Nrf2 can play a key role in neuronal resistance to oxidative stress by mediating HO-1 and alleviating diabetes-associated cognitive impairment [33]. In addition, Song and Long found that Nrf2 and HO-1 could participate in the synthesis of GPX4 [34]. And these two factors could play a critical role in the development of ferroptosis [35, 36]. It is reported that SIRT1 could protect against doxorubicin-induced ferroptosis in cardiomyopathy via the activation of Nrf2 [37]. Furthermore, exosomes can ameliorate ischemic brain injury and exert neuroprotective effects by activating SIRT1 [38].

Based on these promising findings, the present study is aimed at evaluating the effects of MSCs-Exo in model of dNCR and at determining if MSCs-Exo ameliorate cognitive impairment by inhibiting ferroptosis via activating SIRT1/Nrf2/HO-1 pathway, as well as provide potential theoretical

and experimental evidence for the treatments of dNCR patients, identifying potential therapeutic targets for clinical treatment.

2. Materials and Methods

2.1. MSCs-Exo Isolation and Characterization. Mouse bone marrow-derived MSCs were purchased from the Cyagen Biosciences Inc. (Santa Clara, CA, USA) and cultured with a Dulbecco's Modified Eagle's Medium (DMEM) (Solarbio, Beijing, China) containing 10% fetal bovine serum (FBS) (Gibco, Shanghai, China) and 1% penicillin-streptomycin solution (Solarbio, Beijing, China). For MSCs-Exo isolation, when the cells reached 70%–80% confluence, conventional culture medium was replaced by that containing 10% exosome-free FBS (Gibco, Shanghai, China). Following an additional 48 hours of culturing, MSCs-Exo were isolated from cell culture medium by differential centrifugation method using Exo Easy Maxi Kit (QIAGEN, Germantown, MD, USA). After centrifuging, the MSCs-Exo were carefully resuspended in PBS and used immediately or stored at -80°C .

The morphology of MSCs-Exo was observed using transmission electron microscope (TEM) (HT7700-SS, HITACHI, Japan). The characteristic surface marker protein CD63 of MSCs-Exo was analyzed by Western blot. The size distribution of MSCs-Exo was measured by Nanoparticle Tracking Analyzer (Malvern Instruments Ltd., Malvern, UK). The concentration of MSCs-Exo was determined by using bicinchoninic acid assay (BCA) Protein Assay Kit (CWBIO, Beijing, China).

2.2. MSCs-Exo Tracing and Immunofluorescence Assay. MSCs-Exo were dyed with PKH26 (Sigma-Aldrich, MO, USA) according to the manufacturer's protocol. In brief, MSCs-Exo were incubated with $4\ \mu\text{l}$ PKH26 diluted in 2 ml Diluent C at room temperature for 15 minutes; then, 2 ml of exosome-free medium was added to stop the labeling reaction. After centrifugation at $100,000 \times g$ for 1 hour, the labeled MSCs-Exo were resuspended with PBS before administration.

After the 24-hour MSCs-Exo treatment, the mice were perfused with saline followed by 4% ice-cold paraformaldehyde in PBS under deep anesthesia, and the hemispheres of the brain were dissected and washed with PBS and then fixed at 4°C for 24 hours. The tissues were dehydrated in 30% sucrose solution; when the tissue sank into the bottom, the brains were sliced into $8\ \mu\text{m}$ slices with a cryostat (Leica CM1860 UV, Germany) and placed on adhesive slides and washed with PBS for three times. Finally, the sections were stained with 4,6-diamidino-2-phenylindole (DAPI) at room temperature for 10 minutes and washed with PBS for three times and then captured under a fluorescence microscope (Olympus, Tokyo, Japan).

2.3. Animals. Eighteen-month-old specific pathogen-free male C57BL/6 mice (body weight 35–40 g) were purchased from the animal center of Weifang Medical University (Weifang, China). All mice were housed in a room under

controlled temperature and humidity conditions, with a 12-hour light/dark cycle, and had free access to food and water. The mice were acclimatized to the laboratory environment for 7 days before the studies. Animal handling and experimental procedures were approved by Committee on the Ethics of Animal Experiments of Weifang Medical University (Weifang, China).

2.4. Establishment of Animal Models. To establish the model of dNCR, an exploratory laparotomy was performed using aseptic procedures as previously described [39]. Briefly, the mice were deeply anesthetized with 2.5% isoflurane; their abdomen regions were shaved and sterilized with iodophor and ethanol. The abdomen was exposed by a 1-1.5 cm midline abdomen vertical incision and then softly to explore the viscera, including the liver, kidney, intestines, and musculature by the sterile swab soaked in saline. Next, 6 cm of intestine was exposed outside the abdominal cavity and rubbed for 30 seconds, and the operation lasted 30 minutes. Subsequently, the incision was closed from the peritoneal muscles to the skin using sterile 5-0 sutures and sterilized with iodophor for three times. After the operation, the mice were subcutaneous administered 1 ml saline for supplementation of liquid volume. Finally, they were placed on a heat blanket in a chamber until recovery, and lidocaine hydrochloride gel was applied to the incision to relieve the pain.

2.5. Experimental Design. All experimental mice were randomly divided into the following groups (5 mice/group).

Aged mice were used to evaluate the distribution of PKH26-labeled MSCs-Exo administered. Twenty-four hours after MSCs-Exo administration, all mice were decapitated under deep anesthesia and fixed with 4% paraformaldehyde before frozen sectioning.

To explore the effect of surgery on cognitive function in aged mice and whether ferroptosis was present in mice hippocampus, the mice were randomly divided into 3 groups. (1) Sham group: the mice were anesthetized, and their abdomen regions were shaved and sterilized with iodophor and ethanol, but not treated with exploratory laparotomy. And the mice were intraperitoneal injected with corresponding vehicle; (2) dNCR group: the mice were anesthetized and received exploratory laparotomy. And the mice were intraperitoneal injected with corresponding vehicle; (3) dNCR+Fer-1 (ferrostatin-1, a ferroptosis inhibitor) group: the mice were injected with Fer-1 1 hour before surgery through the tail vein (1.5 mg/kg, 1% DMSO diluted in sterile saline, Sigma-Aldrich, MO, USA). The doses of Fer-1 were administered, as described previously [40].

To explore the protective effect of MSCs-Exo in dNCR mice, the mice were randomly divided into 4 groups: (1) Sham group; (2) dNCR group; (3) dNCR+MSCs-Exo (50 μ g/mouse) group: the mice were injected with MSCs-Exo 1 hour before surgery through the tail vein; and (4) dNCR+Fer-1 group.

To explore the role of SIRT1 played on the protective effect of MSCs-Exo in dNCR mice, the mice were randomly divided into 5 groups: (1) Sham group; (2) dNCR group; (3)

dNCR+MSCs-Exo group; (4) dNCR+MSCs-Exo + EX-527 (a selective SIRT1 inhibitor [41, 42]) group: the mice were intraperitoneal injected with EX-527 daily for 3 days before surgery (5 mg/kg, 1% DMSO diluted in sterile saline, Selleck, Houston, TX, USA) and injected with MSCs-Exo 1 hour before surgery through the tail vein; and (5) dNCR+EX-527 group: the mice were intraperitoneal injected with EX-527 daily for 3 days before surgery. The doses of EX-527 were chosen based on earlier reports that EX-527 significantly inhibited the expression of SIRT1 [43]. The experimental timeline was shown in Figure 1; the EX-527 or corresponding vehicle was injected daily for 3 days before surgery; the MSCs-Exo, or Fer-1, or corresponding vehicle was administered 1 hour before surgery. Next, the behavioral tests were performed began at 24 hours after the surgery to verify the success of model and the influence of MSCs-Exo on cognitive function in dNCR aged mice. Eventually, after drug treatment and behavioral tests, the mice were killed for subsequent experiments.

2.6. Tail Vein Injection. One hour before surgery, the mouse was taken from the housing cage and introduced onto the tail vein injection device. The injection site of the tail was wiped with a 75% alcohol cotton ball. The needle of a 1 ml syringe was inserted into the skin in a 10-15° angle about 2-4 mm to penetrate the tail vein, and 50 μ g MSCs-Exo solution was slowly injected. Then, the needle was removed quickly, and the injection site was pressed firmly to prevent the backflow of the injected drugs and/or blood. Finally, the mouse was returned to its cage and monitored for at least 5 minutes to ensure the mouse has no further bleeding.

2.7. Morris Water Maze Test. Morris water maze (MWM), which is a hippocampus-dependent spatial learning and memory test for rodents, was performed as described previously with minor modifications [44]. The MWM consisted of a round steel pool that was 125 cm in diameter, 60 cm in height, and filled with white water maintained at $21 \pm 1^\circ\text{C}$. The pool was surrounded by a gray curtain and placed in a quiet room. The maze was divided into four quadrants with an escape platform (10 cm in diameter) immersed 1 cm below the water surface in one target quadrant, and marked objects are suspended from fixed positions in each quadrant. MWM testing began at the 24 hours after surgery and lasted for five days, with the first 4 days being a training period. The mice were released facing the pool rim from different quadrants and given 90 seconds to find the platform, and they were artificially guided to the platform and stayed there for 15 seconds if they failed to find the platform within 90 seconds. A video surveillance system was used to record and track the escape latency of mice (i.e., the time taken from being released in the water to finding the platform). On the 5th day, the mice were subjected to the space exploration experiment. The platform was removed, and the mice were released from the opposite quadrant of the platform and swam freely for 120 seconds and then recorded the number of crossings over the previously hidden platform and the time spent in the specific target quadrant.

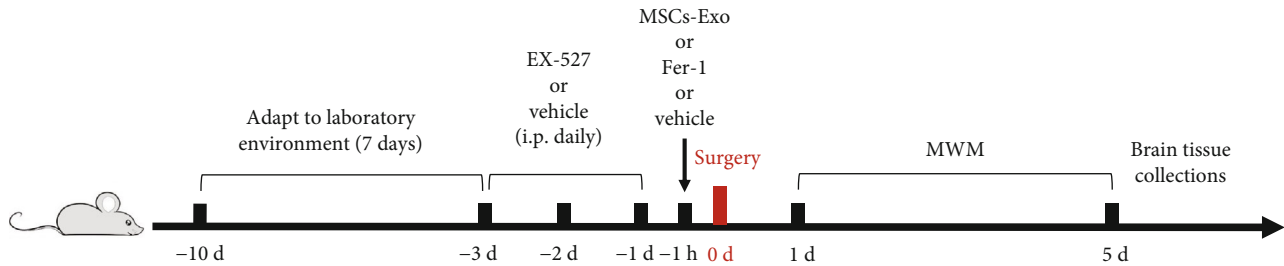


FIGURE 1: Schematic timeline of the experimental procedure. The mice were acclimatized to the laboratory environment for 7 days before the studies. The EX-527 or corresponding vehicle was injected daily for 3 days before surgery; the MSCs-Exo, or Fer-1, or corresponding vehicle was administered 1 hour before surgery. Next, the behavioral tests were performed began at the 24 hours after the surgery to verify the success of model and the influence of MSCs-Exo on cognitive function in dNCR aged mice. In the end, the mice were decapitated after the behavioral tests, and the brain tissues were collected for subsequent experiments.

2.8. Reactive Oxygen Species (ROS) Assays. The levels of ROS from hippocampus tissues were assessed using the dihydroethidium (DHE) fluorescent probe (Sigma-Aldrich, MO, USA), following the previously described protocols [45]. Briefly, frozen brain sections were incubated with 50 μ M DHE at room temperature for 1 hour in the dark; the sections were incubated for 10 minutes with DAPI. Then, the images were captured under a fluorescence microscope (Olympus, Tokyo, Japan).

2.9. Glutathione (GSH), Malondialdehyde (MDA), and Ferrous Ion (Fe^{2+}) Assays. Aged mice were decapitated under deep anesthesia, and the hippocampus was immediately collected. The fresh tissues of hippocampus were perfused with PBS containing heparin to remove blood and clots. After weighing the tissue, it was homogenized in slurry medium. The relative concentration of GSH was detected using GSH Colorimetric Assay Kit (Elabscience, Wuhan, China). The MDA content was detected using an MDA Colorimetric Assay Kit (TBA method) (Elabscience, Wuhan, China) and the determination of Fe^{2+} level using Ferrous Iron Colorimetric Assay Kit (Elabscience, Wuhan, China). All kits were used according to the manufacturer's instructions.

2.10. Western Blot Analysis. The hippocampus tissue was quickly collected under deep anesthesia and quickly bathed in a radioimmunoprecipitation assay (RIPA) lysis buffer combined with proteinase inhibitors. Subsequently, the tissue was ground into a suspension and lysed on ice for 30 minutes and then centrifuged at 12,000 rpm in a cold centrifuge at 4°C for 15 minutes. Afterward, the supernatant was carefully transferred into EP tube. Protein concentration was determined by BCA Protein Assay Kit (CWBIO, Beijing, China). The protein lysate was diluted to the same concentration with 5x loading buffer and denatured by boiling. Then, the proteins in each sample were loaded onto 10% sodium dodecyl sulfate-polyacrylamide gel electrophoresis (SDS-PAGE) gels. Electrophoresis was conducted at 80 V for 30 minutes first and, then, at 120 V for 60 minutes and subsequently transferred onto a 0.45 μ m polyvinylidene fluoride (PVDF) membrane. The membranes were blocked with 5% skim milk at room temperature for 3 hours and incubated overnight at 4°C with the following primary anti-

bodies: mouse anti-P53 (1:1,000 dilution, 60283-2-Ig; Proteintech), rabbit anti-solute carrier family 7 membrane 11 (SLC7A11) (1:1,000 dilution, ab175186; Abcam), rabbit anti-GPX4 (1:1,000 dilution, A11243; ABclonal), mouse anti-SIRT1 (1:1,000 dilution, 60303-1-Ig; Proteintech), rabbit anti-Nrf2 (1:1,000 dilution, ab92946; Abcam), rabbit anti-HO-1 (1:1,000 dilution, A19062; ABclonal), and β -actin (1:1,000 dilution, AC026; ABclonal). After that, the membranes were washed five times with 0.1 M TBST for 3 minutes each time and incubated with goat anti-rabbit immunoglobulin G (IgG) (H+L) horseradish peroxidase (HRP) (1:1,000 dilution, AS014; ABclonal) or goat anti-mouse IgG (H+L) HRP (1:5,000 dilution, AS003; ABclonal) at room temperature for 2 hours. The protein bands were visualized with enhanced chemiluminescence (ECL) detection reagents (CWBIO, Beijing, China) and a computerized image analysis system (Tanon 4600, Shanghai, China). The ImageJ software was used to quantify protein blot intensity.

2.11. Transmission Electron Microscope (TEM). In order to study the ultrastructure, the mice were decapitated while under anesthetized; the hippocampus were quickly separated and cut into 1 mm³ pieces with a sharp scalpel and soaked immediately in 2.5% cold glutaraldehyde. Next, these tissues were fixed, dehydrated, embedded, solidified, sectioned, and stained. Finally, the ultrastructural characteristics of hippocampus mitochondria were observed under the TEM (HT7700-SS, HITACHI, Japan).

2.12. Statistical Analysis. Data were analyzed using the GraphPad Prism software. All data were presented as mean \pm SEM. Group differences in the escape latency during the MWM test were analyzed using the two-way analysis of variance (ANOVA). Statistical significance between two groups was analyzed using a two-tailed Student's *t*-test, and statistical significance between multiple groups was analyzed using one-way ANOVA followed by Bonferroni post hoc test. $P < 0.05$ was considered to be statistically significant.

3. Results

3.1. Surgery Induced Cognitive Impairment and Hippocampus Ferroptosis in Aged Mice. Firstly, to verify

the reliability of the model, we evaluated the influence of exploratory laparotomy on cognitive function in aged mice using the MWM. When mice were trained for MWM, we found that the mice subjected to surgery showed longer escape latencies compared with the Sham group mice on days 3 and 4 of training (Figure 2(a)). Moreover, the mice in the dNCR group took longer swimming distance of finding the platform than those in the Sham group on days 4 of training (Figure 2(b)). Then, the space exploration experiment was performed on day 5 by removing the platform, releasing the mice from the opposite quadrant of the platform, and recording the number of crossings over the previously hidden platform and the time spent in the specific target quadrant within 120 seconds. We found that the platform-crossing times and the time spent in the target quadrant were significantly decreased in the dNCR group compared with the Sham group (Figures 2(c) and 2(d)). Hence, our results suggested that surgery induced cognitive impairment.

Next, the model of dNCR in aged mice was established. Fer-1 was used to determine whether ferroptosis was present in dNCR aged mice hippocampus. The hippocampus tissues of mice were collected to observe the morphology of mitochondria in hippocampus and explore the levels of ROS, GSH, MDA, Fe^{2+} , key ferroptosis-related protein GPX4 [46], P53 [47], and SLC7A11 [48]. As shown in Figure 3(a), we observed that compared with mitochondria in the Sham group, the mitochondria morphology in the hippocampus in the dNCR group showed the significant characteristic changes of ferroptosis, including the size of mitochondria became smaller, the density of double-layer membrane was increased, and the mitochondrial crest was decreased. In addition, compared with the Sham group, GSH level was lower, while ROS, MDA, and Fe^{2+} levels were higher in the dNCR group, and there was no significant difference in GSH, ROS, MDA, and Fe^{2+} levels between the Sham group and Sham+Fer-1 group (Figures 3(b)–3(f)). Meanwhile, the protein expression levels of GPX4 and SLC7A11 were decreased while the protein expression level of P53 was increased in the dNCR group, and there was no significant difference between the Sham group and Sham+Fer-1 group (Figures 3(g)–3(j)). These data suggested that ferroptosis may occur in dNCR aged mice hippocampus.

3.2. Phenotypic Identification of Collected MSCs-Exo. To investigate the role of MSCs-Exo in dNCR mice, the MSCs-Exo was isolated from culturing medium of MSCs. TEM analysis demonstrated that the particles obtained were round-shaped vesicles with a bilayer membrane structure and with a diameter of approximately 50–100 nm (Figure 4(a)). Western blot showed that the protein marker CD63 was remarkably higher in MSCs-Exo compared with MSC cytoplasm (Figure 4(b)). Nanoparticle tracking analysis demonstrated that the diameters of the most particles were within the range of 60–200 nm, and the peak diameter is 135.7 nm (Figure 4(c)). According to the quantification, the protein concentration of the MSCs-Exo was 0.7570 mg/ml. The above results indicated that the MSCs-Exo have been successfully isolated from MSCs.

To prove that the MSCs-Exo can change gene expression of the hippocampus, firstly, we have demonstrated that the MSCs-Exo could pass through the blood-brain barrier and was absorbed into neurons. We performed MSCs-Exo tracing assays using PKH26-dyed MSC-Exo. After the 24-hour MSCs-Exo treatment, brain sections were obtained. As shown in Figure 4(d), most neurons obtained the PKH26-labeled MSC-Exo.

3.3. MSCs-Exo Treatment Ameliorates Cognitive Impairment in dNCR Aged Mice. The hidden platform training and space exploration experiments were performed to test the cognitive function of mice. In Figures 5(a) and 5(b), compared with the dNCR group, the escape latencies on days 3 and 4 of training and the swimming distance of finding the platform on day 4 of training in the dNCR+MSCs-Exo group were significantly reduced. In the space exploration experiment (Figures 5(c) and 5(d)), the platform-crossing times and the time spent in the target quadrant were significantly longer in the dNCR+MSCs-Exo group compared with the dNCR group. Collectively, these findings indicated that MSCs-Exo treatment prevented spatial learning and memory impairments in dNCR aged mice.

3.4. MSCs-Exo Inhibit Hippocampus Ferroptosis in dNCR Aged Mice. We use Fer-1 to further determine whether the protective effect of MSCs-Exo on cognitive impairment is involved in inhibiting ferroptosis. As shown in Figure 6(a), compared with the dNCR group, the size of mitochondria was increased, the density of double-layer membrane was reduced, and the mitochondrial crest was increased in the dNCR+MSCs-Exo group and dNCR+Fer-1 group. Additionally, compared with increased ferroptosis in dNCR group, significantly reduced ROS, MDA, and Fe^{2+} levels combined with elevated GSH level was found in the dNCR+MSCs-Exo group and dNCR+Fer-1 group (Figures 6(b)–6(f)). Meanwhile, the results of Western blot showed that the protein expression levels of GPX4 and SLC7A11 were increased, while the protein expression level of P53 was reduced in the dNCR+MSCs-Exo group and dNCR+Fer-1 group compared with the dNCR group (Figures 6(g)–6(j)). These data suggested that MSCs-Exo inhibited hippocampus ferroptosis in dNCR aged mice.

3.5. The Effect of MSCs-Exo on Hippocampus Ferroptosis in dNCR Mice Is Mediated by the Nrf2/HO-1 Signaling Pathway. Ferroptosis is characterized by the massive accumulation of fatal intracellular lipid peroxide when the antioxidant capacity of cells decreases [34]. The transcription factor Nrf2 is a well-known transcription factor that plays a key role in against oxidative stress. A previous study demonstrated that Nrf2-regulated signaling pathway diminished anesthesia-induced memory impairment by inhibiting oxidative stress [49]. Thus, we determined whether the effect of MSCs-Exo on ferroptosis in dNCR aged mice is mediated by the Nrf2 and HO-1 pathways. According to Western blot analysis (Figures 7(a)–7(c)), the results suggested that MSCs-Exo and Fer-1 significantly increased the expression of Nrf2 compared with that in the dNCR group. Additionally, HO-

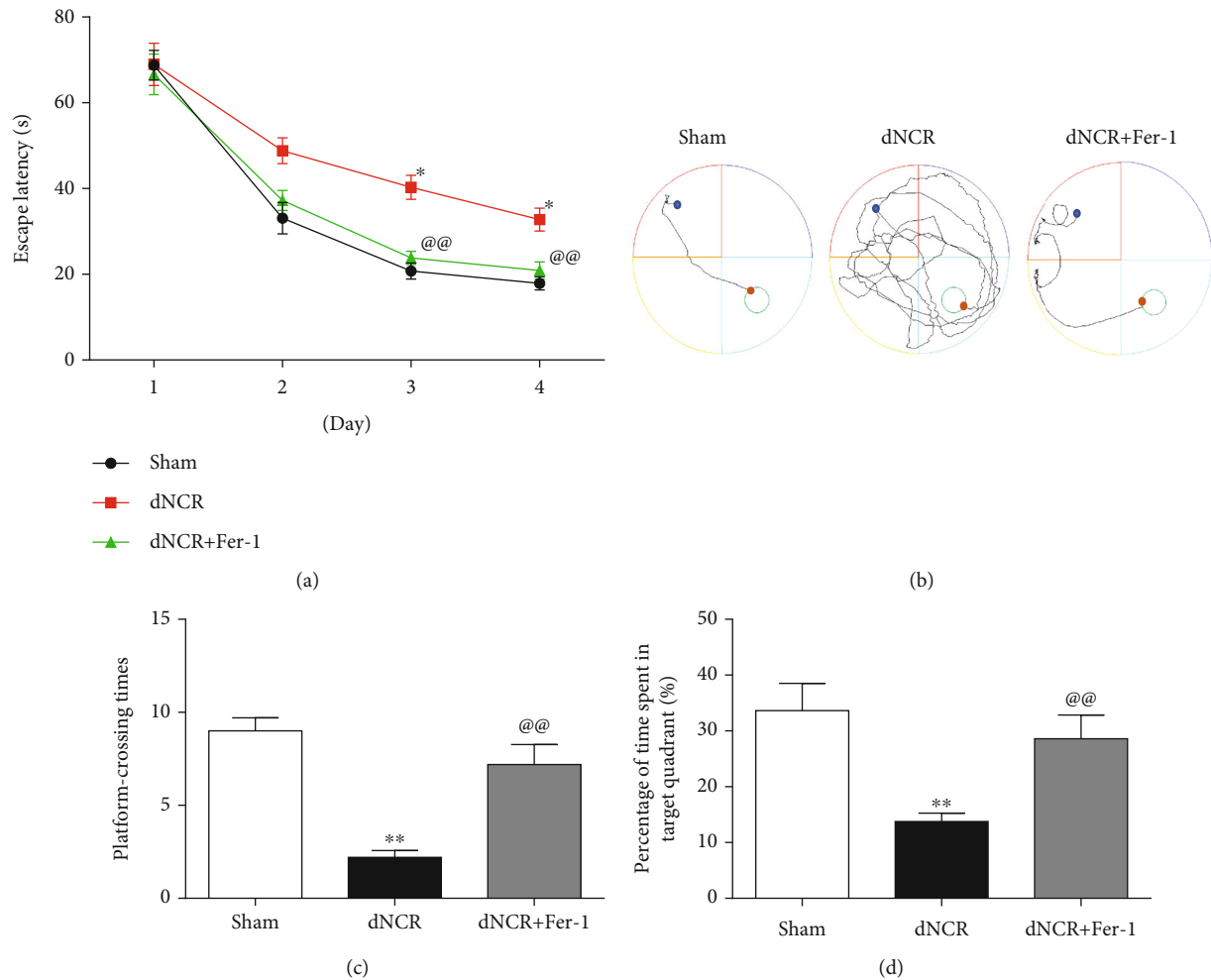
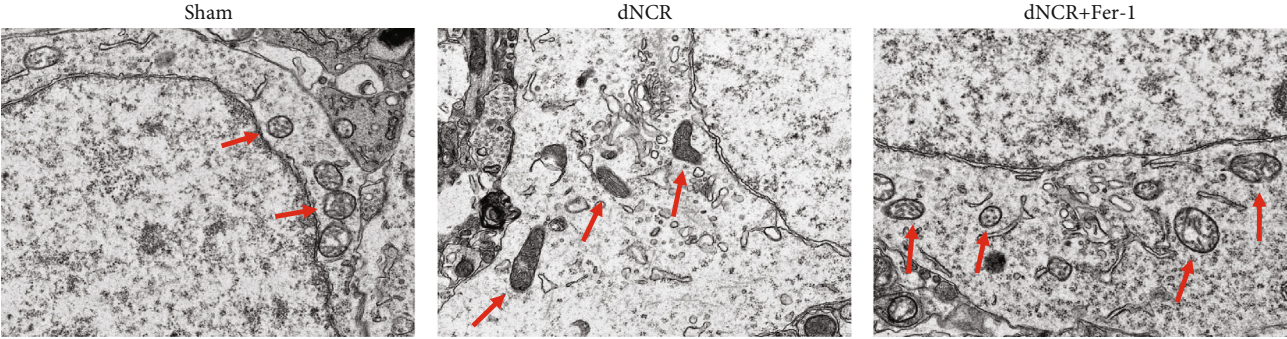


FIGURE 2: Surgery induced cognitive impairment in aged mice. The mice were randomly divided into 3 groups: Sham group, dNCR group, and dNCR+Fer-1 group. (a) Escape latency during the MWM navigation test. (b) The representative trajectory diagrams of the swimming distance to find the platform (blue dots: starting position; yellow dots: ending position). (c) The platform-crossing times in the MWM test. (d) The time spent in the target quadrant during the MWM test. Data are expressed as mean \pm SEM ($n = 5/\text{group}$). * $P < 0.05$ and ** $P < 0.01$, Sham vs. dNCR; @@ $P < 0.01$, dNCR vs. dNCR+Fer-1. Fer-1: ferrostatin-1, a ferroptosis inhibitor.

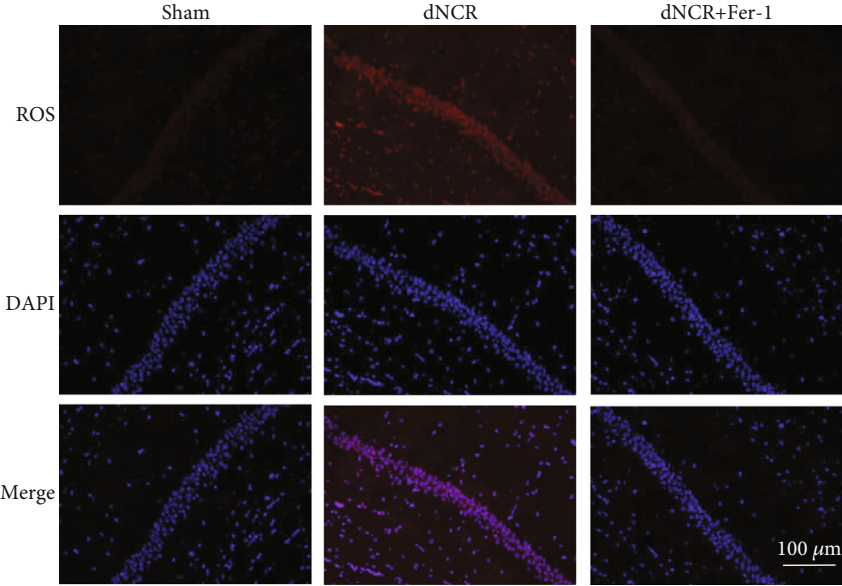
1, the downstream component of the Nrf2 pathway, was upregulated by treatment with MSCs-Exo and Fer-1. Thus, we suggested that MSCs-Exo mitigate the ferroptosis in dNCR mice via activating Nrf2/HO-1 pathway.

3.6. MSCs-Exo Alleviated Cognitive Impairment and Hippocampus Ferroptosis of dNCR Aged Mice in a SIRT1-Dependent Manner. SIRT1 is considered an effective protector of the cells against oxidative insult acting by targeting Nrf2 to regulate the expression of HO-1 [19]. The data of Figure 8(a) showed that surgery induced a decrease in the protein expression of SIRT1 compared with that in the Sham group. To explore whether the effect of MSCs-Exo is SIRT1 dependent, we pretreated mice with EX-527, a specific SIRT1 inhibitor. The data of Figure 8(b) showed that the protein expression level of SIRT1 was downregulated by surgery or EX-527 and restored by MSCs-Exo, which indicated that the effect of MSCs-Exo was mediated by regulation of SIRT1.

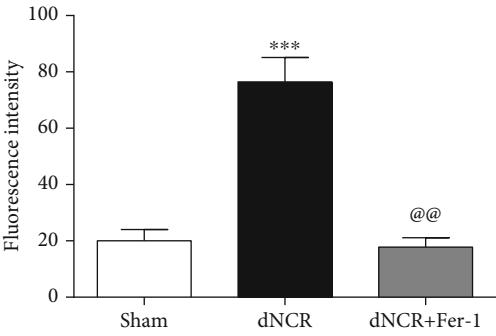
Additionally, the dNCR group and dNCR+EX-527 group exhibited longer escape latencies, longer swimming distance of finding the platform, fewer platform-crossing times, and shorter time spent in the target quadrant than the Sham group mice, and there was no difference between the dNCR group and the dNCR+EX-527 group (Figures 8(c)–8(f)). In contrast, in the dNCR+MSCs-Exo group, the escape latencies on days 3 and 4 of training were shorter, the swimming distance of finding the platform on day 4 of training was longer, the platform-crossing times and the time spent in the target quadrant were significantly increased (Figures 8(c)–8(f)). Interestingly, dNCR+MSCs-Exo + EX-527 treatment significantly affected the MSCs-Exo inhibitory effect on cognition impairment. Administration of EX-527 prior to dNCR+MSCs-Exo treatment abolished the protective effects of MSCs-Exo (Figures 8(c)–8(f)). Pretreated dNCR+MSCs-Exo mice with EX-527 extended their escape latencies and the swimming distance of finding the platform (Figures 8(c)



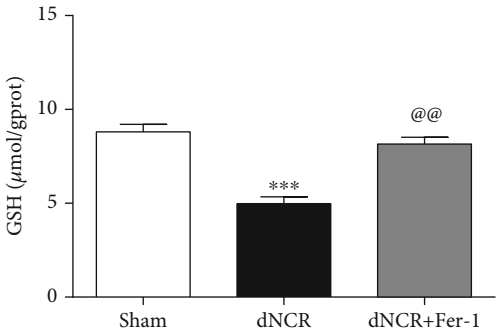
(a)



(b)



(c)



(d)

FIGURE 3: Continued.

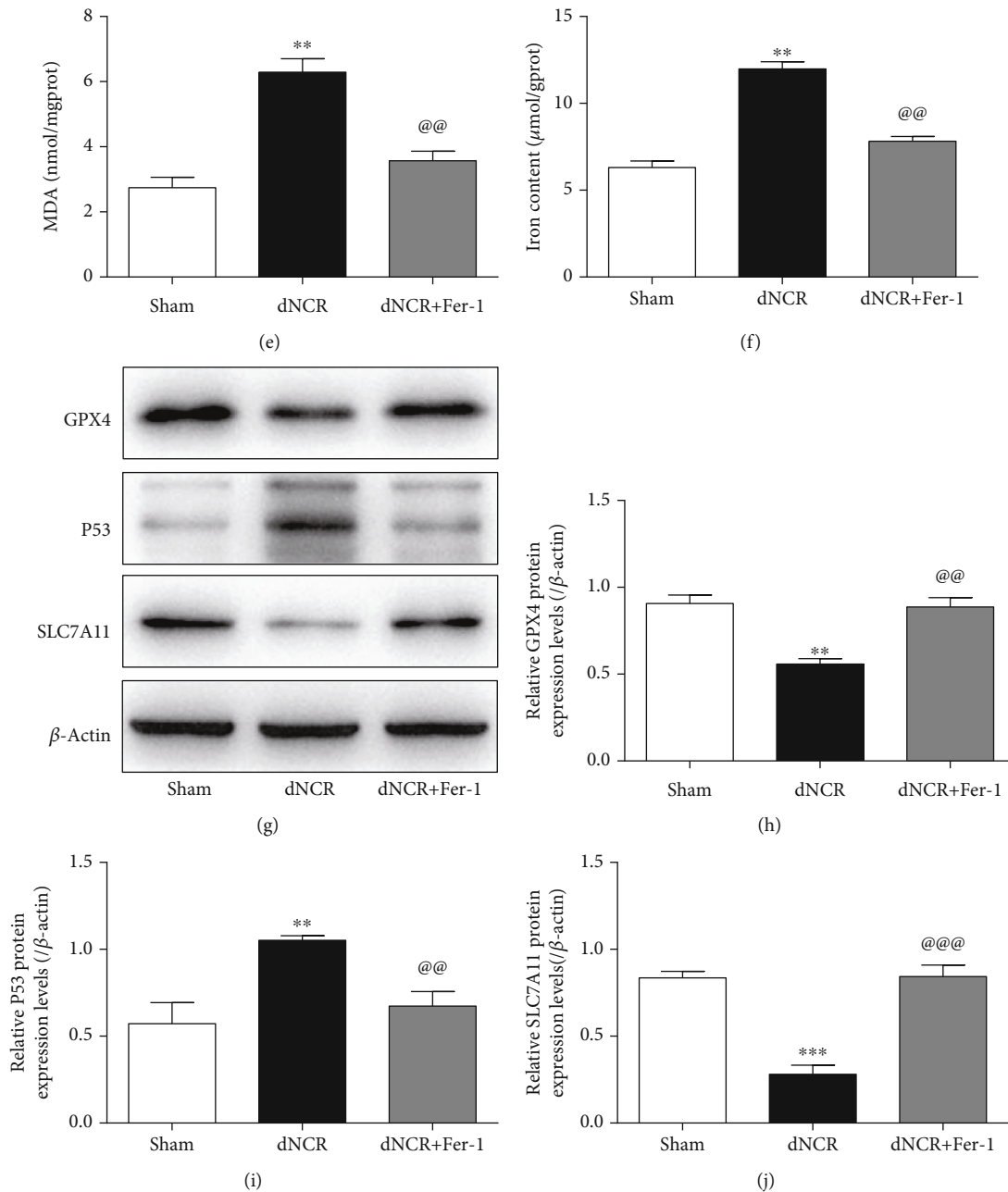


FIGURE 3: Surgery induced hippocampus ferroptosis in aged mice. The mice were randomly divided into 3 groups: Sham group, dNCR group, and dNCR+Fer-1 group. (a) TEM was employed to detect the ultrastructure of hippocampus in aged mice (bar = $1.0\ \mu\text{m}$). (b, c) ROS (red fluorescent signal) were detected using DHE staining (bar = $100\ \mu\text{m}$). (d) The GSH level by GSH Colorimetric Assay Kit. (e) The MDA level by MDA Colorimetric Assay Kit. (f) The Fe^{2+} level by Ferrous Iron Colorimetric Assay Kit. (g–j) GPX4, P53, and SLC7A11 expressions in each group were determined by Western blot. gprot: gram protein; mgprot: milligram protein. Data are expressed as mean \pm SEM ($n = 5/\text{group}$). ** $P < 0.01$ and *** $P < 0.001$, Sham vs. dNCR; @@ $P < 0.01$ and @@@ $P < 0.001$, dNCR vs. dNCR+Fer-1. Fer-1: ferrostatin-1, a ferroptosis inhibitor.

and 8(d)). In the space exploration experiment, the platform-crossing times and the time spent in the target quadrant were significantly shorter in the dNCR+MSCs-Exo + EX-527 group than in the dNCR+MSCs-Exo group (Figures 8(e) and 8(f)). These results indicated that MSCs-Exo treatment was effective in improving spatial learning and memory of dNCR aged mice in a SIRT1-dependent manner.

We then examined the effect of MSCs-Exo-mediated SIRT1 activation on hippocampus ferroptosis in dNCR mice. The results showed that the MSCs-Exo alleviated hippocampus ferroptosis of dNCR aged mice was abolished by EX-527 treatment. Compared with the Sham group, the dNCR group and dNCR+EX-527 group mitochondria observed via TEM had shrunk in size, the double-layer

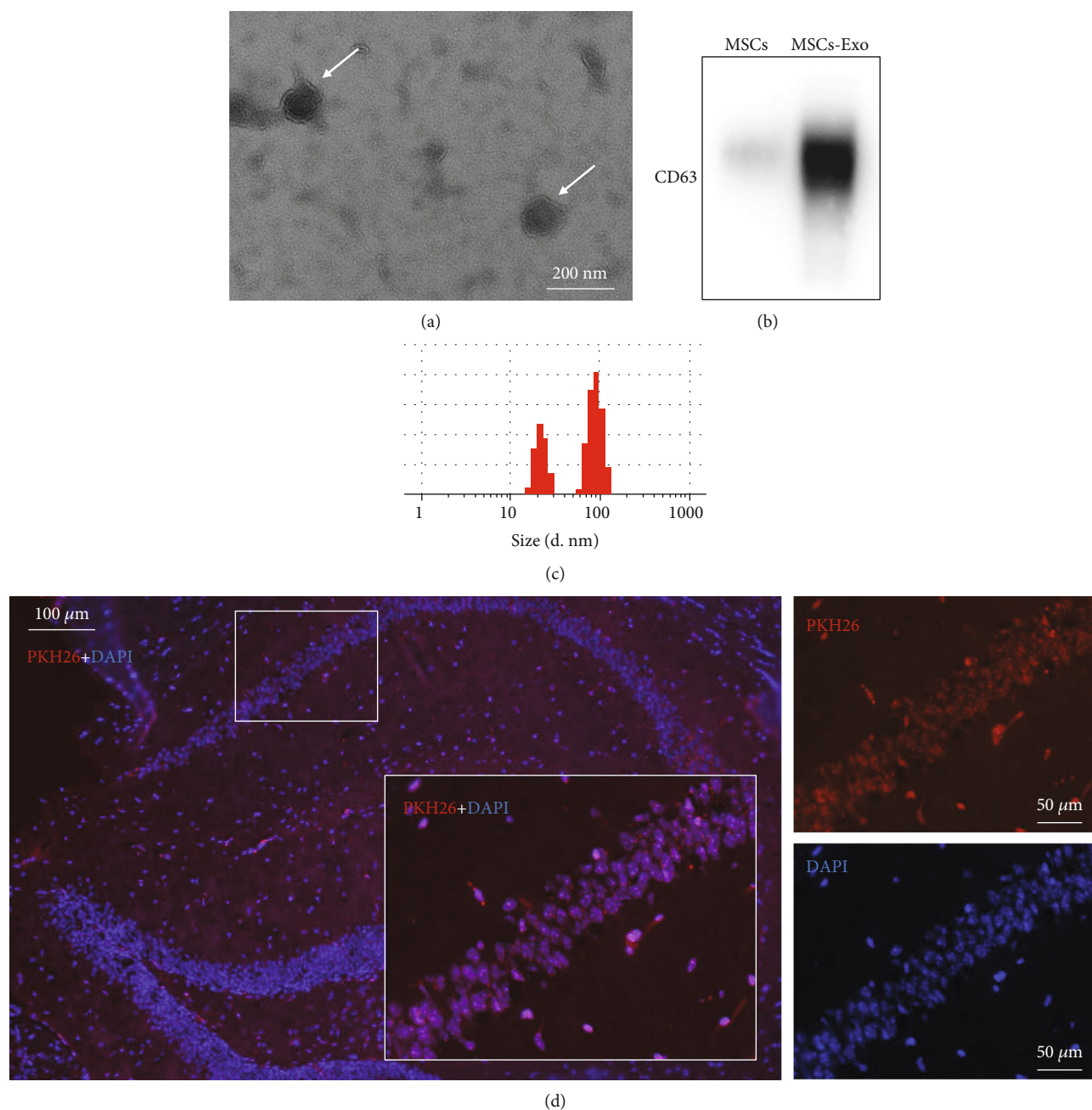


FIGURE 4: Phenotypic identification of collected MSCs-Exo. (a) Representative electron microscopy image of MSCs-Exo (bar = 200 nm). (b) Representative marker of isolated exosomes detected by Western blot. (c) Size distribution of exosomes determined by Nanoparticle Tracking Analyzer. (d) Representative fluorescence images of brain sections stained; PKH26-dyed exosomes were administered through tail vein into mice.

membrane density had reduced, and the mitochondrial crest had decreased or disappeared. In contrast, MSCs-Exo ameliorated ferroptosis-induced mitochondrial morphologic changes, and pretreating dNCR+MSCs-Exo mice with EX-527 the mitochondria morphology in hippocampus showed the characteristic changes of ferroptosis (Figure 9(a)). In addition, compared with the Sham group, the GSH level was lower, while ROS, MDA, and Fe^{2+} levels were higher in the dNCR group and dNCR+EX-527 group (Figures 9(b)–9(f)). Meanwhile, the protein expression levels

of GPX4 and SLC7A11 were decreased while the protein expression level of P53 was increased (Figures 9(g)–9(j)). There was no difference between the dNCR group and the dNCR+EX-527 group (Figures 9(b)–9(j)). In contrast, MSCs-Exo treatment increased the levels of GSH, GPX4, and SLC7A11 and decreased the levels of ROS, MDA, Fe^{2+} , and P53 which were reversed by EX-527 treatment (Figures 9(b)–9(j)). Furthermore, compared with the dNCR group, we observed that MSCs-Exo administration increased the expression of Nrf2 and HO-1 in the hippocampus, whereas pretreated mice with

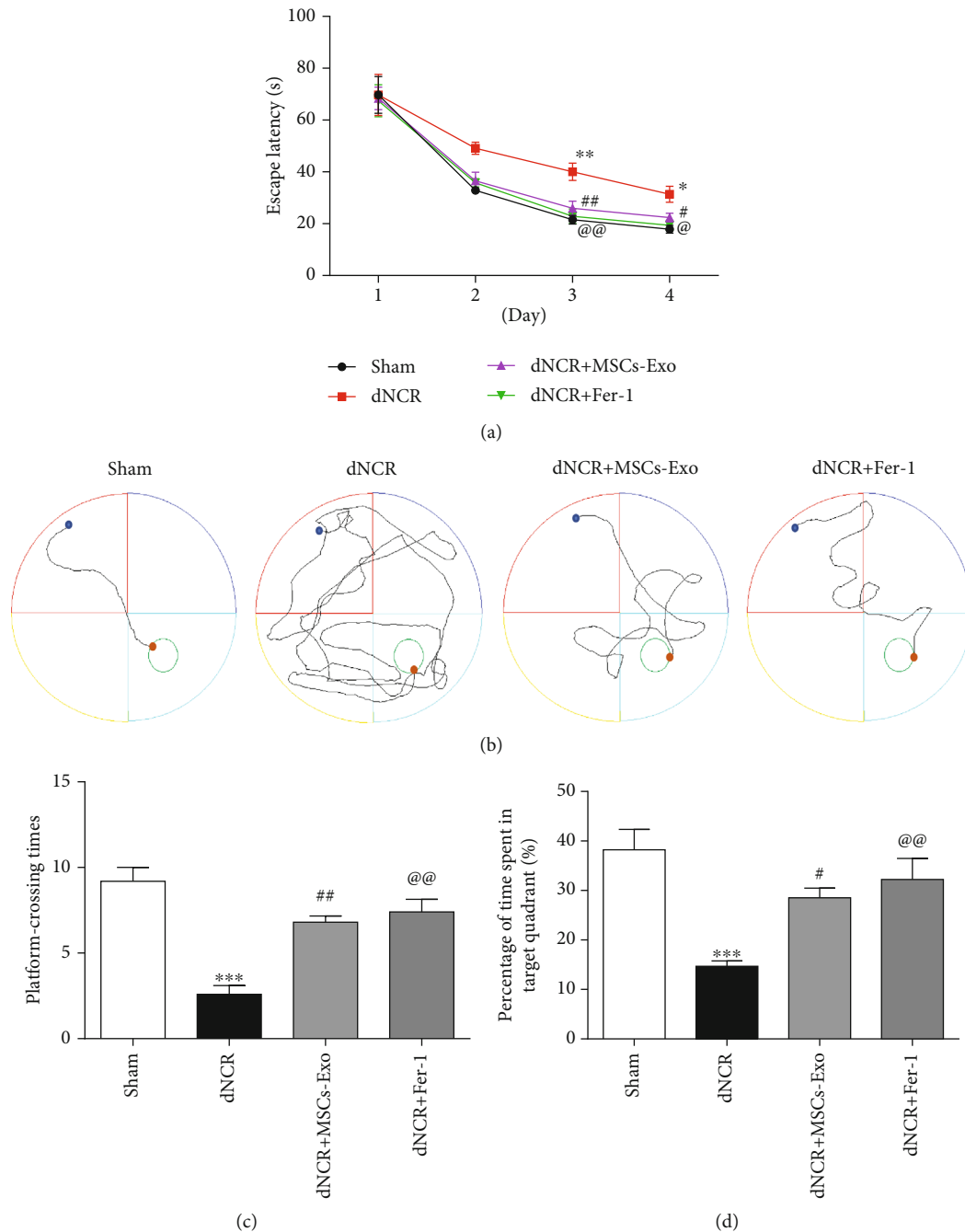


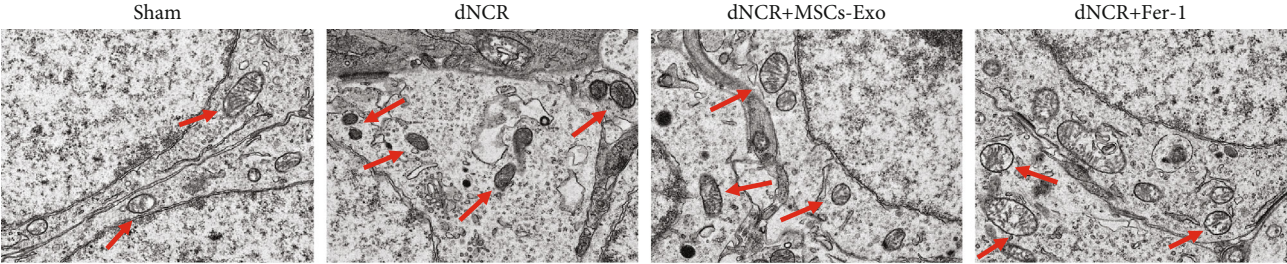
FIGURE 5: MSCs-Exo treatment ameliorates cognitive impairment in dNCR mice. The mice were randomly divided into 4 groups: Sham group, dNCR group, dNCR+MSCs-Exo group, and dNCR+Fer-1 group. (a) Escape latency during the MWM navigation test. (b) The representative trajectory diagrams of the swimming distance to find the platform (blue dots: starting position; yellow dots: ending position). (c) The platform-crossing times in the MWM test. (d) The time spent in the target quadrant during the MWM test. Data are expressed as mean \pm SEM ($n = 5/\text{group}$). * $P < 0.05$, ** $P < 0.01$, and *** $P < 0.001$, Sham vs. dNCR; # $P < 0.05$ and ## $P < 0.01$, dNCR vs. dNCR+MSCs-Exo; @ $P < 0.05$ and @@ $P < 0.01$, dNCR vs. dNCR+Fer-1. Fer-1: ferrostatin-1, a ferroptosis inhibitor.

EX-527 decreased their expression (Figures 9(k)–9(m)). These data suggested that the Nrf2/HO-1 pathway was regulated by SIRT1 to inhibit hippocampus ferroptosis.

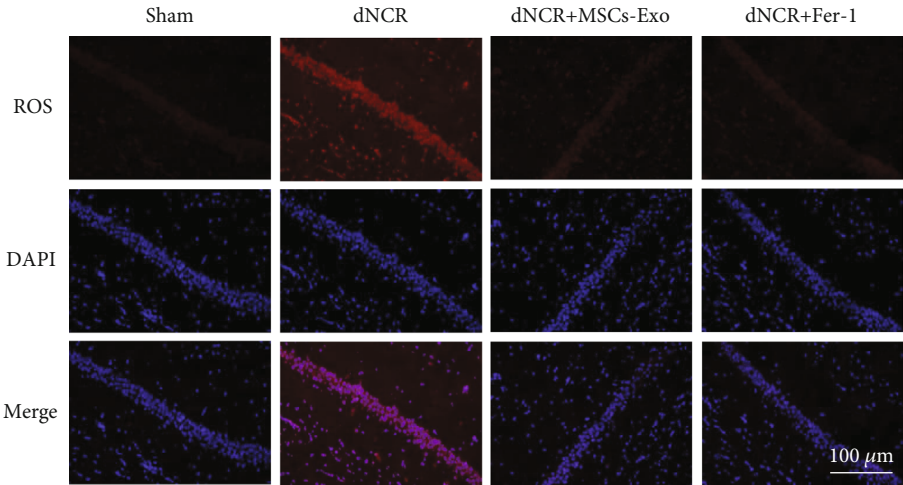
Taken together, our results suggested that MSCs-Exo effectively ameliorated the cognitive impairment and inhibited hippocampus ferroptosis in dNCR aged mice through a SIRT1-dependent mechanism.

4. Discussion

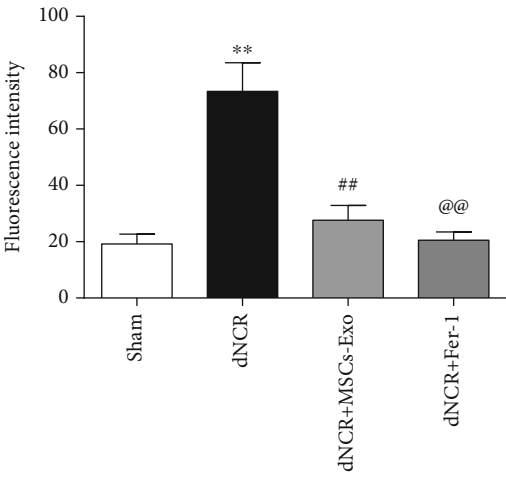
The current study was conducted to examine the effects and mechanisms of MSCs-Exo on cognitive dysfunction induced by surgery in aged mice. Here, we found that laparotomy surgery induced cognitive impairment and hippocampus ferroptosis. Exogenous MSCs-Exo could ameliorate cognitive



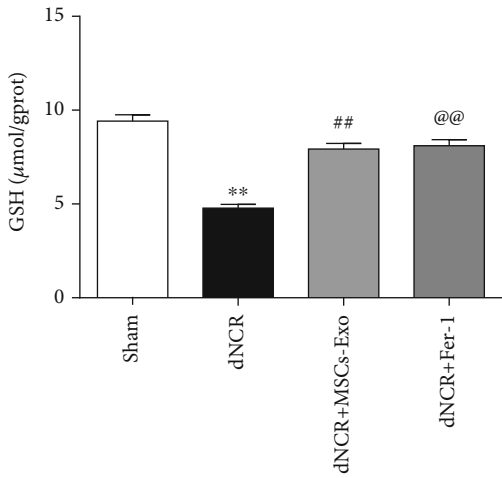
(a)



(b)



(c)



(d)

FIGURE 6: Continued.

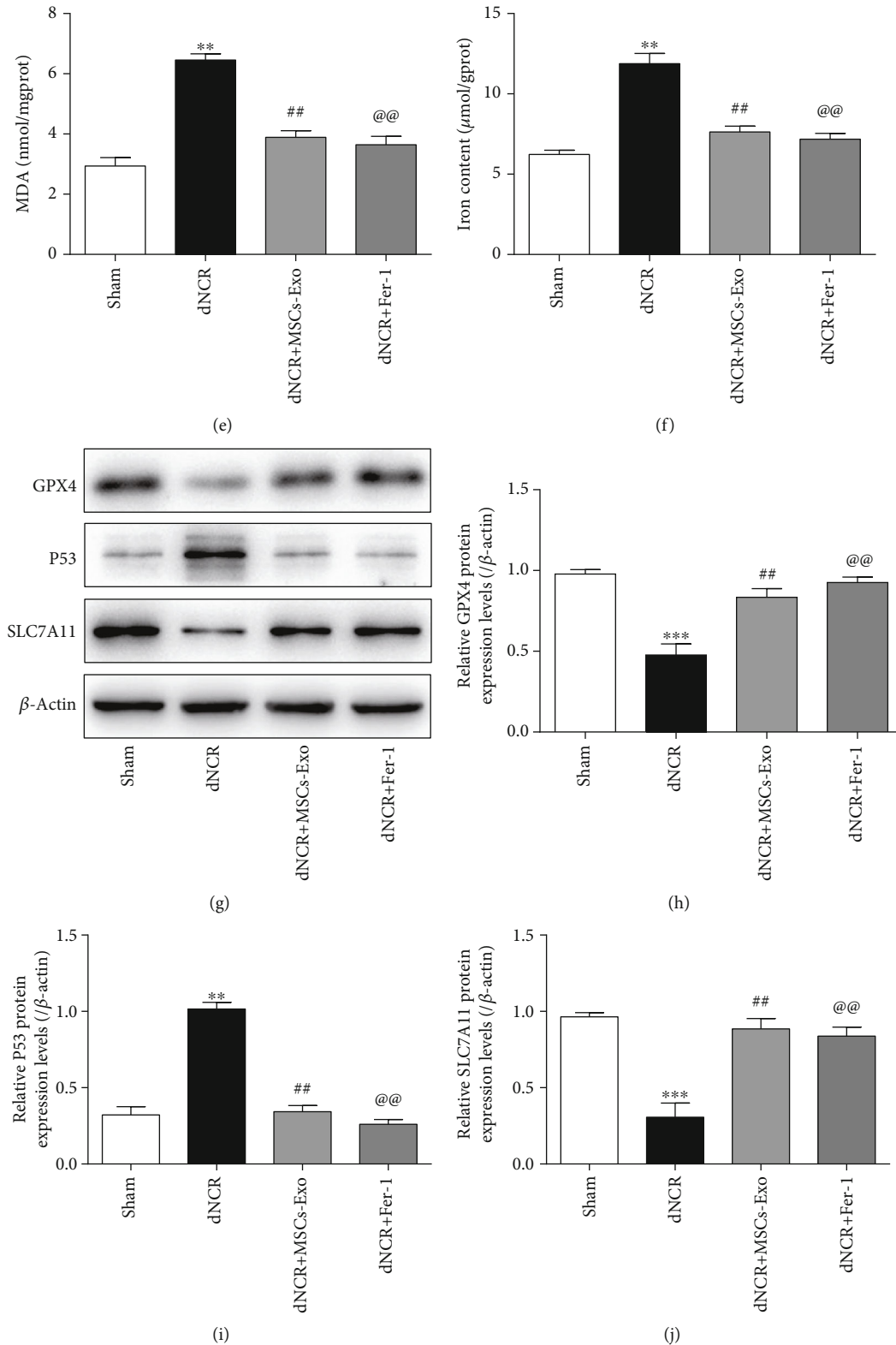


FIGURE 6: MSCs-Exo inhibit hippocampus ferroptosis in dNCR mice. The mice were randomly divided into 4 groups: Sham group, dNCR group, dNCR+MSCs-Exo group, and dNCR+Fer-1 group. (a) TEM was employed to detect the ultrastructure of hippocampus in aged mice (bar = $1.0 \mu\text{m}$). (b, c) ROS (red fluorescent signal) were detected using DHE staining (bar = $100 \mu\text{m}$). (d) The GSH level by GSH Colorimetric Assay Kit. (e) The MDA level by MDA Colorimetric Assay Kit. (f) The Fe^{2+} level by Ferrous Iron Colorimetric Assay Kit. (g–j) GPX4, P53, and SLC7A11 expressions in each group were determined by Western blot. gprot: gram protein; mgprot: milligram protein. Data are expressed as mean \pm SEM ($n = 5/\text{group}$). ** $P < 0.01$ and *** $P < 0.001$, Sham vs. dNCR; # $P < 0.01$, dNCR vs. dNCR+MSCs-Exo; @ $P < 0.01$, dNCR vs. dNCR+Fer-1. Fer-1: ferrostatin-1, a ferroptosis inhibitor.

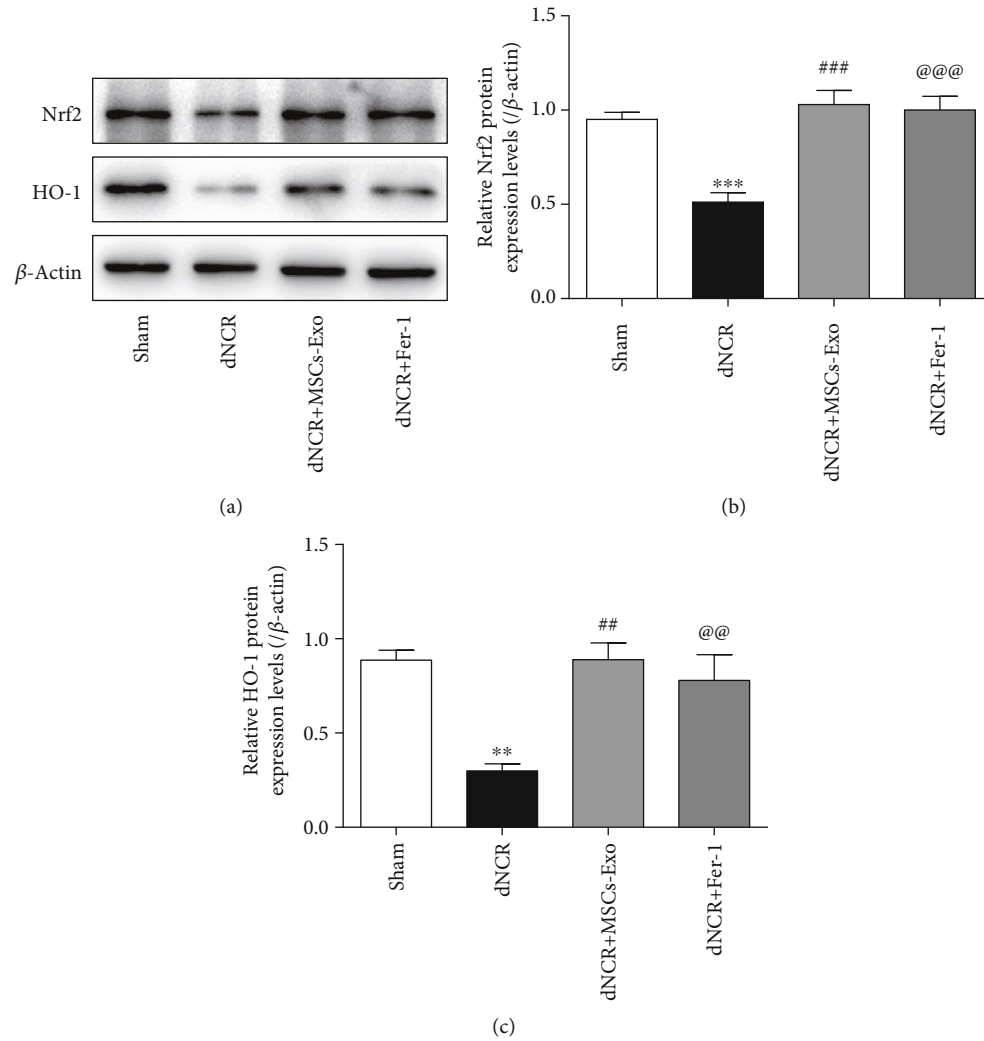


FIGURE 7: The effect of MSCs-Exo on hippocampus ferroptosis in dNCR mice is mediated by the Nrf2/HO-1 signaling pathway. The mice were randomly divided into 4 groups: Sham group, dNCR group, dNCR+MSCs-Exo group, and dNCR+Fer-1 group. (a–c) Nrf2 and HO-1 expressions in each group were determined by Western blot. Data are expressed as mean \pm SEM ($n = 5$ /group). ** $P < 0.01$ and *** $P < 0.001$, Sham vs. dNCR; ## $P < 0.01$ and ### $P < 0.001$, dNCR vs. dNCR+MSCs-Exo; @@ $P < 0.01$ and @@@ $P < 0.001$, dNCR vs. dNCR+Fer-1. Fer-1: ferrostatin-1, a ferroptosis inhibitor.

dysfunction by inhibiting ferroptosis. In addition, MSCs-Exo could reverse the expression level of SIRT1 reduced by surgery. And pretreatment specific SIRT1 inhibitor EX-527 abolished improving effects of MSCs-Exo in cognitive impairment and ferroptosis of aged mice after surgery. Moreover, using EX-527 could also block the Nrf2/HO-1 signaling pathway in MSCs-Exo-treated aged mice. The protective effects of MSCs-Exo on cognitive impairment in aged mice were related to its inhibited hippocampus ferroptosis by modulating the activity of SIRT1/Nrf2/HO-1 signaling pathway (Figure 10).

dNCR is a perioperative neurological complication, representing major health concerns for older surgical patients [50], especially experiencing hip-fracture repair and cardiac surgery [51]. dNCR is a main cause of functional impairment and increased morbidity and mortality [1]. Despite increasing investigation of dNCR mechanisms and therapeutic strategies, the current therapies for the management

of dNCR are still insufficient. Exosomes are rich in bioactive molecules, including DNA, proteins, mRNAs, and miRNAs, which make exosomes essential for intercellular communication [52]. MSCs-Exo plays an important role in oxidative stress response, neurodegenerative disease, and neurological diseases [53–55]. In our study, the dNCR model of aged mice was established to investigate the protective effect of MSC-Exo. Firstly, we found that an exploratory laparotomy was performed using aseptic procedures caused cognitive dysfunction in aged mice, which is consistent with previous studies [39]. And MWM tests showed that the mice in the dNCR+MSCs-Exo group spent less time to find the platform and more time in the target quadrant than that of the dNCR group. These results indicated that MSCs-Exo pretreatment could alleviate the cognitive impairment caused by surgery.

Iron is one of the most important minerals, which plays an indispensable role in many physiological and pathological

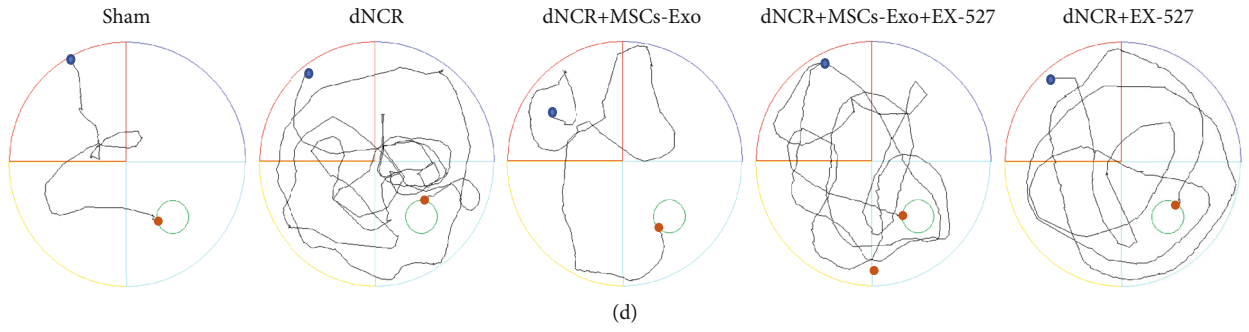
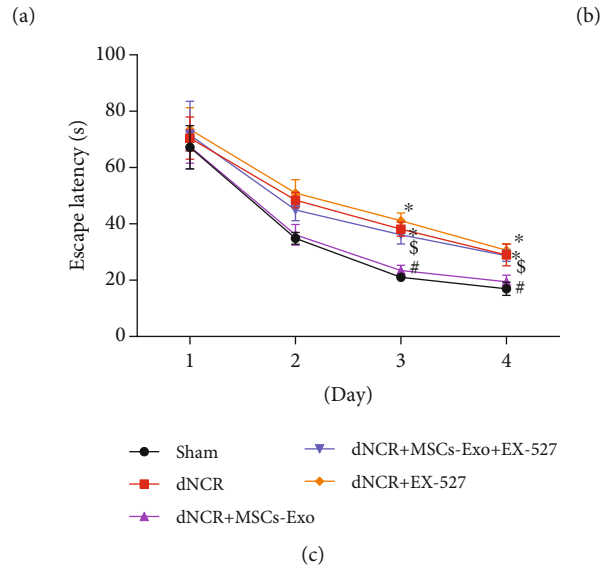
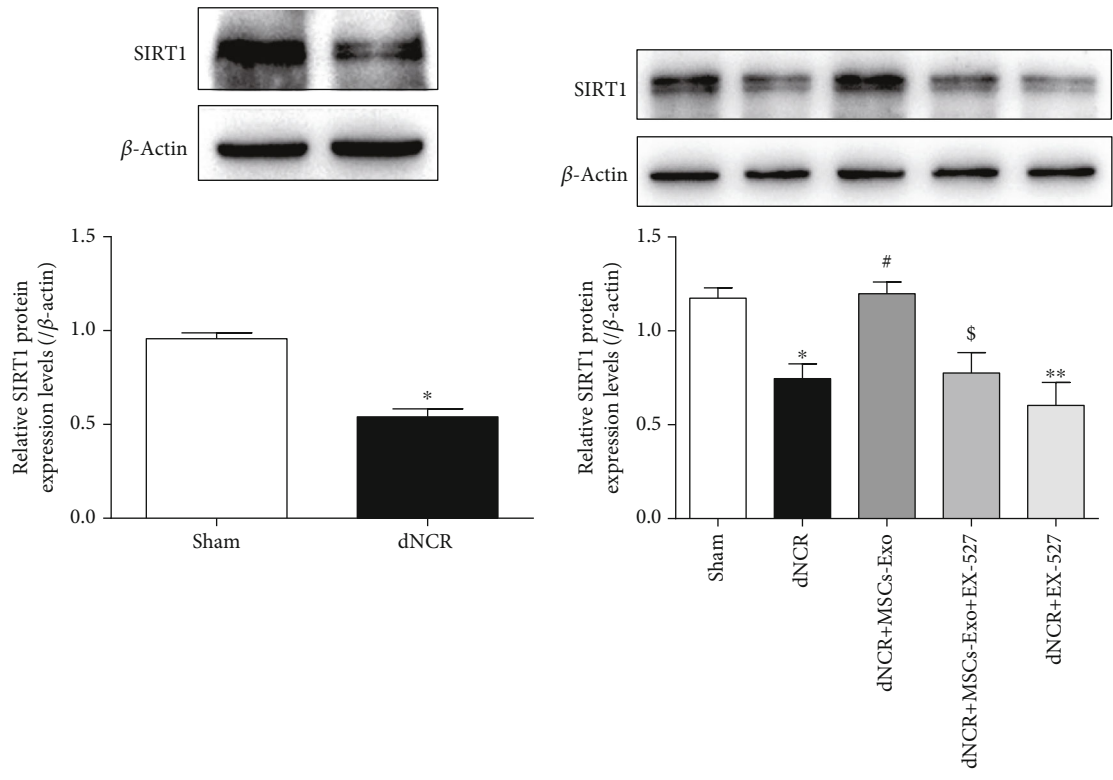


FIGURE 8: Continued.

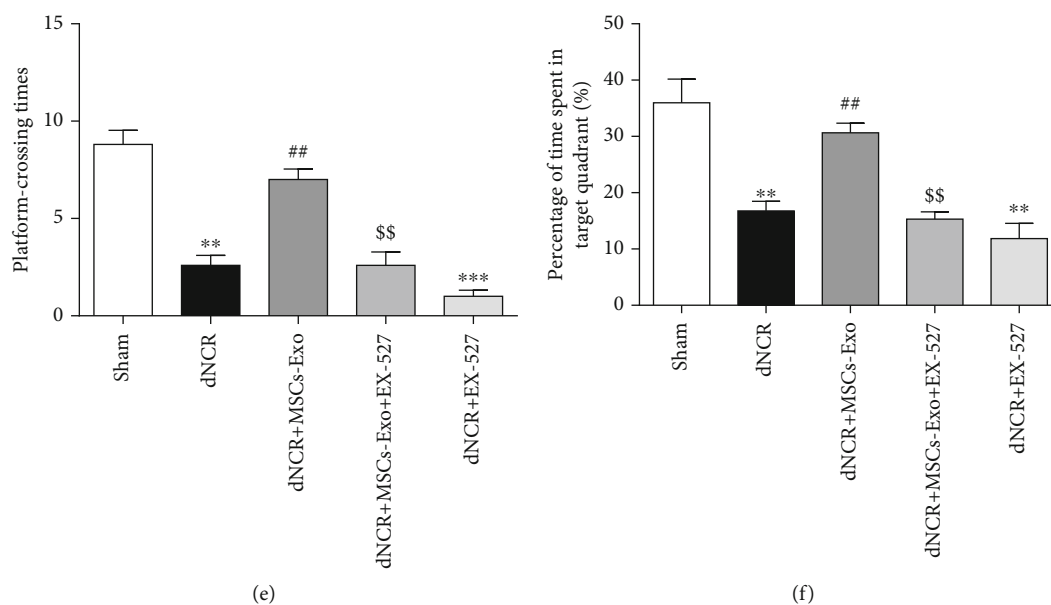


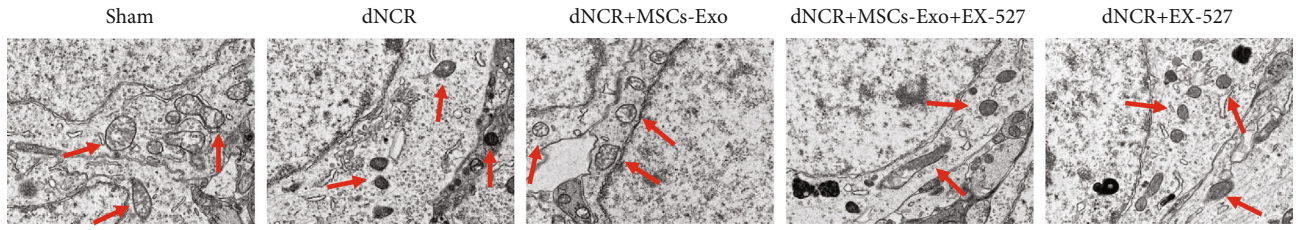
FIGURE 8: MSCs-Exo alleviated cognitive impairment of dNCR mice in a SIRT1-dependent manner. The mice were randomly divided into 5 groups: Sham group, dNCR group, dNCR+MSCs-Exo group, dNCR+MSCs-Exo + EX-527 group, and dNCR+EX-527 group. (a, b) SIRT1 expression in each group was determined by Western blot. (c) Escape latency during the MWM navigation test. (d) The representative trajectory diagrams of the swimming distance to find the platform (blue dots: starting position; yellow dots: ending position). (e) The platform-crossing times in the MWM test. (f) The time spent in the target quadrant during the MWM test. Data are expressed as mean \pm SEM ($n = 5/\text{group}$). * $P < 0.05$, ** $P < 0.01$, and *** $P < 0.001$, Sham vs. dNCR or Sham vs. dNCR+EX-527; # $P < 0.05$ and ## $P < 0.01$, dNCR vs. dNCR+MSCs-Exo; \$ $P < 0.05$ and \$\$ $P < 0.01$, dNCR+MSCs-Exo vs. dNCR+MSCs-Exo + EX-527. EX-527: a specific SIRT1 inhibitor.

processes of the body [34, 56, 57]. In neuronal system, iron homeostasis is important for brain function including enzyme catalysis, mitochondrial function, myelination, and synaptic plasticity. Dysregulation of iron homeostasis can cause oxidative stress and inflammation, leading to cell damage and ultimately neurological disease [58–60]. Ferroptosis is a programmed cell death process associated with dysregulation of iron homeostasis, which is characterized by iron-dependent lipid peroxidation [61]. Previous studies suggested that ferroptosis was present in intestinal I/R injury and lung I/R injury in mice [62, 63]. And ferroptosis was found an important role in cognitive deficits of neurodegenerative diseases [34, 64]. In our study, we found the increased Fe^{2+} level in hippocampus of dNCR mice. Meanwhile, the levels of ROS, MDA, and P53 were increased, while the levels of GSH, GPX4, and SLC7A11 were decreased in dNCR mice. In addition, we also found that the increased levels of ROS, MDA, Fe^{2+} , and P53 and decreased levels of GSH, GPX4, and SLC7A11 in dNCR mice were reversed by Fer-1, suggesting that ferroptosis can participate in the development of dNCR. Song et al. found that MSCs-Exo could attenuate myocardial injury by inhibiting ferroptosis [65]. In recent studies, exosomes could inhibit ferroptosis in neural system and play a protective role in intracerebral hemorrhage [66]. In this study, we found that MSCs-Exo treatment could downregulate the levels of ROS, MDA, Fe^{2+} , and P53, while increase the levels of GSH, GPX4, and SLC7A11 in dNCR mice. These results indicated that MSCs-Exo could alleviate the cognitive

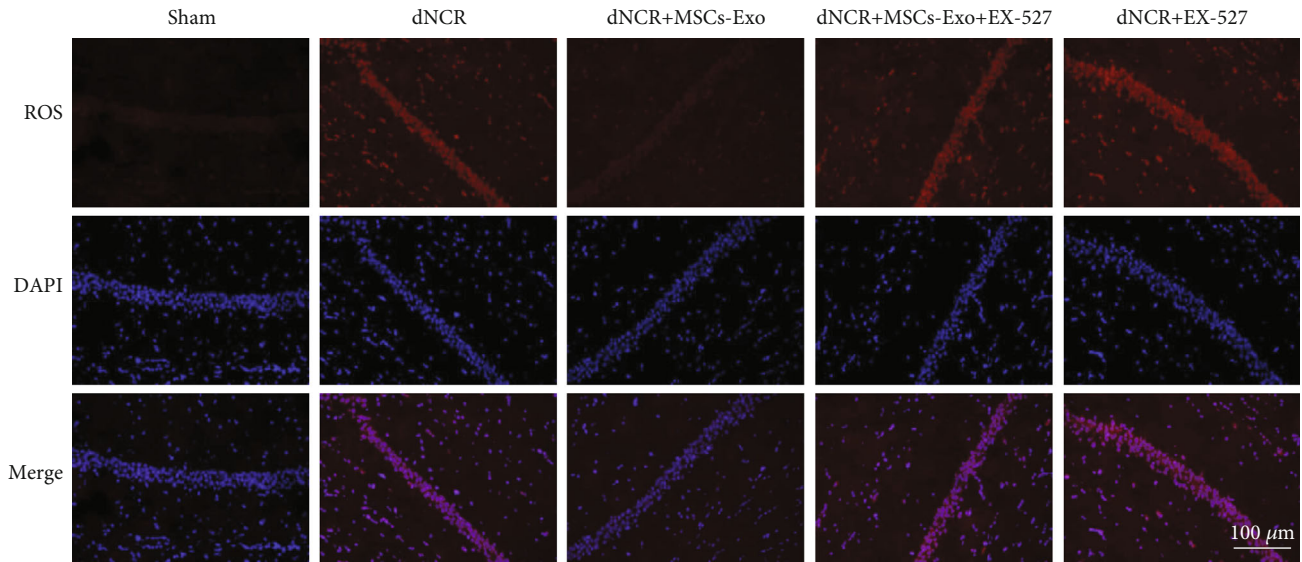
impairment by mediating hippocampus ferroptosis in dNCR aged mice.

SIRT1, a NAD-dependent deacetylase, plays a positive role in stress responses, cellular metabolism, and aging [67]. SIRT1 in the nervous system can participate in neuroprotection, oxidative stress, inflammatory response, autophagy, and other biological processes [68]. In our study, we found that SIRT1 expression was downregulated in the dNCR mice. Previous studies found that extracellular vesicles, which contain exosomes, could enhance SIRT1 activation, synaptic activity, and rescue cognitive deficits in AD model [69]. And another study suggested that SIRT1 was activated by exosomes to exert protective effect against radiation-induced brain injury [70]. Our results found that exogenous MSCs-Exo could restore the downregulation of SIRT1, suggesting the regulatory role of exosomes in SIRT1 function in dNCR. Furthermore, studies have shown that the bioactive molecules miRNA in exosomes can regulate SIRT1 [71, 72]. However, what component in MSCs-Exo regulate SIRT1 to ameliorate dNCR in aged mice needs to be further explored.

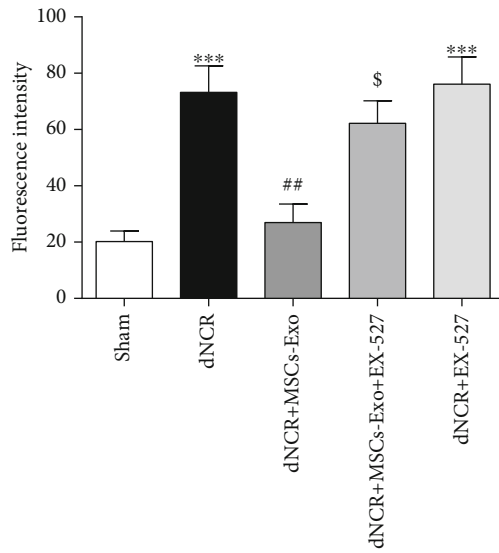
In addition, our results also found that inhibiting SIRT1 activation could result in ferroptosis in dNCR mice. SIRT1 plays an important role in neurodegenerative diseases and cognitive deficits via regulating the levels of Nrf2 and HO-1 [1, 73–76]. The activation of SIRT1 targeting Nrf2/HO-1 pathway activation can alleviate central nervous system inflammation-induced cognitive deficits [73]. Nrf2/HO-1 pathway can play a key role in suppressing ferroptosis in



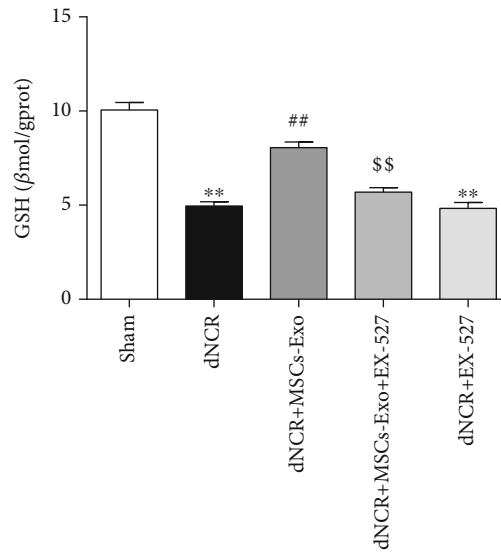
(a)



(b)



(c)



(d)

FIGURE 9: Continued.

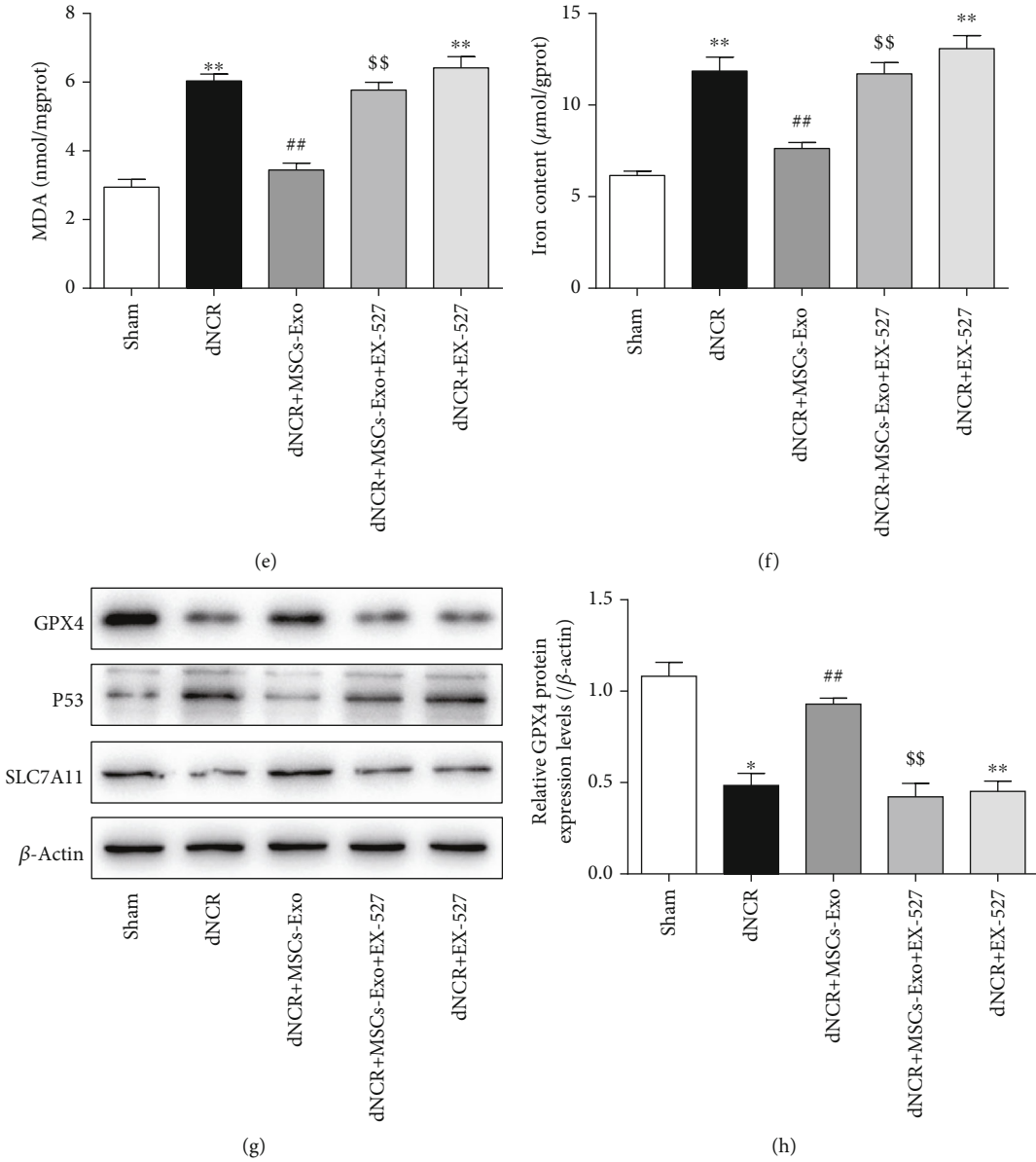


FIGURE 9: Continued.

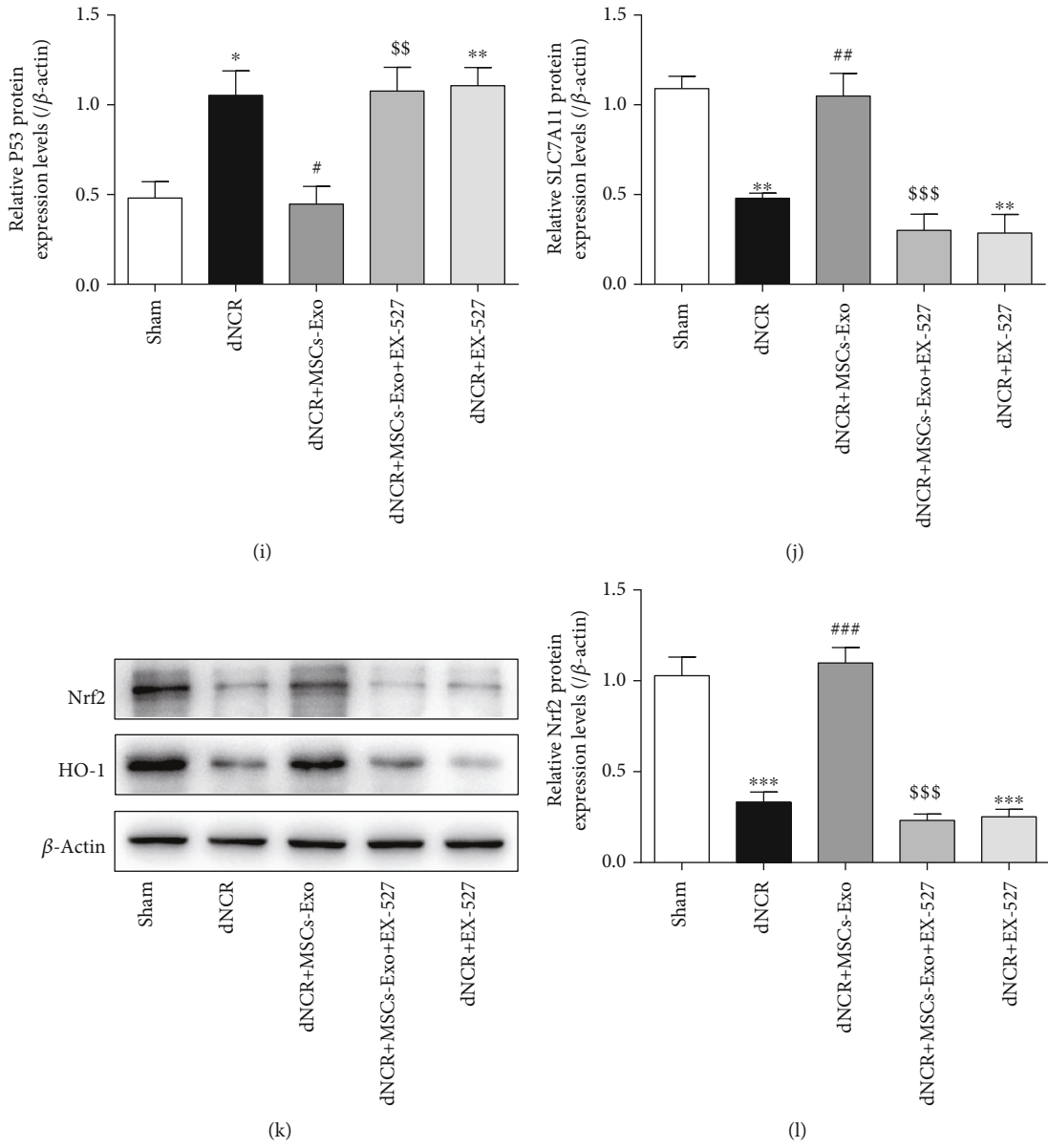


FIGURE 9: Continued.

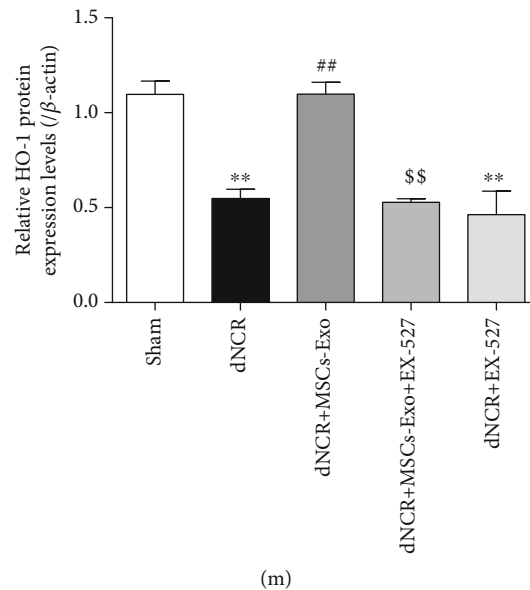


FIGURE 9: MSCs-Exo alleviated hippocampus ferroptosis of dNCR mice in a SIRT1-dependent manner. The mice were randomly divided into 5 groups: Sham group, dNCR group, dNCR+MSCs-Exo group, dNCR+MSCs-Exo + EX-527 group, and dNCR+EX-527 group. (a) TEM was employed to detect the ultrastructure of hippocampus in aged mice (bar = $1.0\ \mu\text{m}$). (b, c) ROS (red fluorescent signal) were detected using DHE staining (bar = $100\ \mu\text{m}$). (d) The GSH level by GSH Colorimetric Assay Kit. (e) The MDA level by MDA Colorimetric Assay Kit. (f) The Fe^{2+} level by Ferrous Iron Colorimetric Assay Kit. (g–j) GPX4, P53, and SLC7A11 expressions in each group were determined by Western blot. (k–m) Nrf2 and HO-1 expressions in each group were determined by Western blot. gprot: gram protein; mgprot: milligram protein. Data are expressed as mean \pm SEM ($n = 5/\text{group}$). * $P < 0.05$, ** $P < 0.01$, and *** $P < 0.001$, Sham vs. dNCR or Sham vs. dNCR+EX-527; # $P < 0.05$, ## $P < 0.01$, ### $P < 0.001$, dNCR vs. dNCR+MSCs-Exo; \$ $P < 0.05$, \$\$ $P < 0.01$, and \$\$\$ $P < 0.001$, dNCR+MSCs-Exo vs. dNCR+MSCs-Exo + EX-527. EX-527: a specific SIRT1 inhibitor.

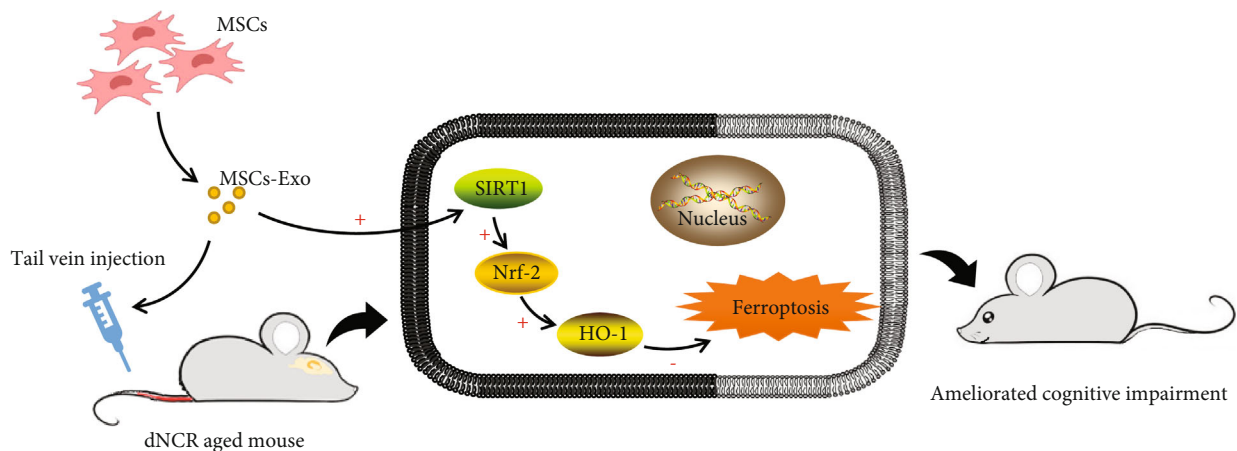


FIGURE 10: Diagrammatic presentation of the findings from this study. MSCs-Exo upregulates the expression level of SIRT1. SIRT1 restoration leads to an increase in Nrf2 and HO-1. Collectively, this mechanism inhibits ferroptosis induced by surgery so as to alleviate cognitive impairment. MSCs: mesenchymal stem cells; MSCs-Exo: mesenchymal stem cell-derived exosomes; dNCR: delayed neurocognitive recovery; SIRT1: silent information regulator 1; Nrf2: factor nuclear factor-erythroid 2-related factor 2; HO-1: heme oxygenase-1.

nervous system [34, 77]. Dang et al. revealed that edaravone abolished chronic social defeat stress-induced ferroptosis and ameliorated depressive and anxiety-like behaviors by regulating SIRT1/Nrf2/HO-1/GPX4 pathway [20]. Our study found that the expressions of Nrf2 and HO-1 were increased accompanied by ameliorated dNCR after MSCs-

Exo treatment, and SIRT1 inhibitor could inhibit this Nrf2/HO-1 pathway activation, suggesting that SIRT1 could mediate ferroptosis by activating Nrf2/HO-1 pathway. These results demonstrated that MSCs-Exo ameliorate surgery induced cognitive impairment by inhibiting hippocampus ferroptosis via activating SIRT1/Nrf2/HO-1 pathway.

5. Conclusion

In our study, we identified exosomes derived from MSCs and demonstrated that MSCs-Exo can ameliorate cognitive impairment by inhibiting hippocampus ferroptosis via activating SIRT1/Nrf2/HO-1 pathway in dNCR aged mice. These results confirmed that MSCs-Exo may have an efficient medicinal value and provide a novel insight of drug development for dNCR therapy.

Data Availability

All data generated and analyzed during this study are included in this published article; further inquiries can be directed to the corresponding authors.

Conflicts of Interest

The authors declare that the research was conducted in the absence of any commercial or financial relationships and there are no competing interests.

Authors' Contributions

Rui Zhang, Zhenjiang Zhang, and Jie Liu conceived and managed the study. Jie Liu performed the animal and molecular biology experiments and wrote the manuscript. Jingyao Huang, Qijuan Sun, Zhihao Zhang, Yongxin Liu, and Baoyu Ma performed the statistical analyses. Rui Zhang, Zhenjiang Zhang, and Jingyao Huang proofread the manuscript. All authors contributed to manuscript revision, read, and approved the submitted version.

Acknowledgments

We want to thank Shandong Provincial Medicine and Health Key Laboratory of Clinical Anesthesia, School of Anesthesiology, Weifang Medical University, for technical support. This work was supported by the Natural Science Foundation of Shandong Province (ZR2017MH066), the Weifang Science and Technology Development Program Project (No. 2019YX005), and the Shandong Medical and Health Technology Development Program (No. 202104020452).

References

- [1] Y. Li, T. Liu, Y. Li et al., "Baicalin ameliorates cognitive impairment and protects microglia from LPS-induced neuroinflammation via the SIRT1/HMGB1 pathway," *Oxidative Medicine and Cellular Longevity*, vol. 2020, Article ID 4751349, 16 pages, 2020.
- [2] L. Gong, C. Dong, Q. Cai, and W. Ouyang, "Interleukin 32: a novel player in perioperative neurocognitive disorders," *Medical Hypotheses*, vol. 144, article 110158, 2020.
- [3] C. Wen, T. Xie, K. Pan et al., "Acetate attenuates perioperative neurocognitive disorders in aged mice," *Aging (Albany NY)*, vol. 12, pp. 3862–3879, 2020.
- [4] Y. Cao, Z. Li, L. Ma et al., "Isoflurane-induced postoperative cognitive dysfunction is mediated by hypoxia-inducible factor-1 α -dependent neuroinflammation in aged rats," *Molecular Medicine Reports*, vol. 17, no. 6, pp. 7730–7736, 2018.
- [5] N. Terrando, M. Brzezinski, V. Degos et al., "Perioperative cognitive decline in the aging population," *Mayo Clinic Proceedings*, vol. 86, no. 9, pp. 885–893, 2011.
- [6] Q. Liu, Y. M. Sun, H. Huang et al., "Sirtuin 3 protects against anesthesia/surgery-induced cognitive decline in aged mice by suppressing hippocampal neuroinflammation," *Journal of Neuroinflammation*, vol. 18, no. 1, p. 41, 2021.
- [7] X. Lin, Y. Chen, P. Zhang, G. Chen, Y. Zhou, and X. Yu, "The potential mechanism of postoperative cognitive dysfunction in older people," *Experimental Gerontology*, vol. 130, article 110791, 2020.
- [8] J. Y. Wu and H. Prentice, "Potential new therapeutic intervention for ischemic stroke," *Journal of Translational Internal Medicine*, vol. 9, no. 1, pp. 1–3, 2021.
- [9] R. Li, H. Weng, Y. Pan et al., "Relationship between homocysteine levels and post-stroke cognitive impairment in female and male population: from a prospective multicenter study," *Journal of Translational Internal Medicine*, vol. 9, no. 4, pp. 264–272, 2021.
- [10] T. Kim, "Can gamma entrainment of the brain rhythms prevent or alleviate Alzheimer's disease," *Journal of Translational Internal Medicine*, vol. 9, no. 4, pp. 231–233, 2021.
- [11] X. Jiang, B. R. Stockwell, and M. Conrad, "Ferroptosis: mechanisms, biology and role in disease," *Nature Reviews. Molecular Cell Biology*, vol. 22, no. 4, pp. 266–282, 2021.
- [12] X. Chen, R. Kang, G. Kroemer, and D. Tang, "Ferroptosis in infection, inflammation, and immunity," *The Journal of Experimental Medicine*, vol. 218, no. 6, 2021.
- [13] X. Zhang, Z. Huang, Z. Xie et al., "Homocysteine induces oxidative stress and ferroptosis of nucleus pulposus via enhancing methylation of GPX4," *Free Radical Biology & Medicine*, vol. 160, pp. 552–565, 2020.
- [14] H. Ma, X. Wang, W. Zhang et al., "Melatonin suppresses ferroptosis induced by high glucose via activation of the Nrf2/HO-1 signaling pathway in type 2 diabetic osteoporosis," *Oxidative Medicine and Cellular Longevity*, vol. 2020, Article ID 9067610, 18 pages, 2020.
- [15] R. Hao, J. Ge, X. Song, F. Li, D. Sun-Waterhouse, and D. Li, "Cadmium induces ferroptosis and apoptosis by modulating miR-34a-5p/Sirt1axis in PC12 cells," *Environmental Toxicology*, vol. 37, no. 1, pp. 41–51, 2022.
- [16] Y. Su, B. Zhao, L. Zhou et al., "Ferroptosis, a novel pharmacological mechanism of anti-cancer drugs," *Cancer Letters*, vol. 483, pp. 127–136, 2020.
- [17] Y. Wang, F. Quan, Q. Cao et al., "Quercetin alleviates acute kidney injury by inhibiting ferroptosis," *Journal of Advanced Research*, vol. 28, pp. 231–243, 2021.
- [18] Q. Li, X. Han, X. Lan et al., "Inhibition of neuronal ferroptosis protects hemorrhagic brain," *JCI Insight*, vol. 2, no. 7, article e90777, 2017.
- [19] C. Wang, T. Liu, Y. Tong et al., "Ulinastatin protects against acetaminophen-induced liver injury by alleviating ferroptosis via the SIRT1/NRF2/HO-1 pathway," *American Journal of Translational Research*, vol. 13, no. 6, pp. 6031–6042, 2021.
- [20] R. Dang, M. Wang, X. Li et al., "Edaravone ameliorates depressive and anxiety-like behaviors via Sirt1/Nrf2/HO-1/Gpx4 pathway," *Journal of Neuroinflammation*, vol. 19, no. 1, p. 41, 2022.
- [21] Y. S. Ho, F. Y. Zhao, W. F. Yeung, G. T. Wong, H. Q. Zhang, and R. C. Chang, "Application of acupuncture to attenuate immune responses and oxidative stress in postoperative

- cognitive dysfunction: what do we know so far?," *Oxidative Medicine and Cellular Longevity*, vol. 2020, Article ID 9641904, 21 pages, 2020.
- [22] I. Wortzel, S. Dror, C. M. Kenific, and D. Lyden, "Exosome-mediated metastasis: communication from a distance," *Developmental Cell*, vol. 49, no. 3, pp. 347–360, 2019.
- [23] Q. Pan, X. Kuang, S. Cai et al., "miR-132-3p priming enhances the effects of mesenchymal stromal cell-derived exosomes on ameliorating brain ischemic injury," *Stem Cell Res Ther*, vol. 11, p. 260, 2020.
- [24] A. F. Hill, "Extracellular vesicles and neurodegenerative diseases," *The Journal of Neuroscience*, vol. 39, no. 47, pp. 9269–9273, 2019.
- [25] X. Gao, Y. Xiong, Q. Li et al., "Extracellular vesicle-mediated transfer of miR-21-5p from mesenchymal stromal cells to neurons alleviates early brain injury to improve cognitive function via the PTEN/Akt pathway after subarachnoid hemorrhage," *Cell Death & Disease*, vol. 11, no. 5, p. 363, 2020.
- [26] C. Shao, Y. Chen, T. Yang, H. Zhao, and D. Li, "Mesenchymal stem cell derived exosomes suppress neuronal cell ferroptosis via lncGm36569/miR-5627-5p/FSP1 Axis in acute spinal cord injury," *Stem Cell Reviews and Reports*, vol. 18, no. 3, pp. 1127–1142, 2022.
- [27] G. Ramadori, C. E. Lee, A. L. Bookout et al., "Brain SIRT1: anatomical distribution and regulation by energy availability," *The Journal of Neuroscience*, vol. 28, no. 40, pp. 9989–9996, 2008.
- [28] W. Cao, Y. Dou, and A. Li, "Resveratrol boosts cognitive function by targeting SIRT1," *Neurochemical Research*, vol. 43, no. 9, pp. 1705–1713, 2018.
- [29] H. Yu, F. Zhang, and X. Guan, "Baicalin reverse depressive-like behaviors through regulation SIRT1-NF- κ B signaling pathway in olfactory bulbectomized rats," *Phytotherapy Research*, vol. 33, no. 5, pp. 1480–1489, 2019.
- [30] F. Jiao and Z. Gong, "The beneficial roles of SIRT1 in neuroinflammation-related diseases," *Oxidative Medicine and Cellular Longevity*, vol. 2020, Article ID 6782872, 19 pages, 2020.
- [31] B. A. Q. Gomes, J. P. B. Silva, C. F. R. Romeiro et al., "Neuroprotective mechanisms of resveratrol in Alzheimer's disease: role of SIRT1," *Oxidative Medicine and Cellular Longevity*, vol. 2018, Article ID 8152373, 15 pages, 2018.
- [32] Y. Li, W. Xu, M. W. McBurney, and V. D. Longo, "SirT1 inhibition reduces IGF-I/IRS-2/Ras/ERK1/2 signaling and protects neurons," *Cell Metabolism*, vol. 8, no. 1, pp. 38–48, 2008.
- [33] L. Zhang, Q. Ma, and Y. Zhou, "Strawberry leaf extract treatment alleviates cognitive impairment by activating Nrf2/HO-1 signaling in rats with streptozotocin-induced diabetes," *Frontiers in Aging Neuroscience*, vol. 12, p. 201, 2020.
- [34] X. Song and D. Long, "Nrf2 and ferroptosis: a new research direction for neurodegenerative diseases," *Frontiers in Neuroscience*, vol. 14, p. 267, 2020.
- [35] H. F. Deng, L. X. Yue, N. N. Wang et al., "Mitochondrial iron overload-mediated inhibition of Nrf2-HO-1/GPX4 assisted ALI-induced nephrotoxicity," *Frontiers in Pharmacology*, vol. 11, article 624529, 2021.
- [36] M. Dodson, R. Castro-Portuguez, and D. D. Zhang, "NRF2 plays a critical role in mitigating lipid peroxidation and ferroptosis," *Redox Biology*, vol. 23, article 101107, 2019.
- [37] D. Li, X. Liu, W. Pi et al., "Fisetin attenuates doxorubicin-induced cardiomyopathy in vivo and in vitro by inhibiting ferroptosis through SIRT1/Nrf2 signaling pathway activation," *Frontiers in Pharmacology*, vol. 12, article 808480, 2022.
- [38] W. Chen, H. Wang, Z. Zhu, J. Feng, and L. Chen, "Exosome-shuttled circSHOC2 from IPAs regulates neuronal autophagy and ameliorates ischemic brain injury via the miR-7670-3p/SIRT1 axis," *Molecular Therapy-Nucleic Acids*, vol. 22, pp. 657–672, 2020.
- [39] J. He, T. Liu, Y. Li et al., "JNK inhibition alleviates delayed neurocognitive recovery after surgery by limiting microglia pyroptosis," *International Immunopharmacology*, vol. 99, article 107962, 2021.
- [40] Z. Qiang, H. Dong, Y. Xia, D. Chai, R. Hu, and H. Jiang, "Nrf2 and STAT3 alleviates ferroptosis-mediated IIR-ALI by regulating SLC7A11," *Oxidative Medicine and Cellular Longevity*, vol. 2020, Article ID 5146982, 16 pages, 2020.
- [41] A. D. Napper, J. Hixon, T. McDonagh et al., "Discovery of indoles as potent and selective inhibitors of the deacetylase SIRT1," *Journal of Medicinal Chemistry*, vol. 48, no. 25, pp. 8045–8054, 2005.
- [42] M. Gertz, F. Fischer, G. T. Nguyen et al., "Ex-527 inhibits sirtuins by exploiting their unique NAD⁺-dependent deacetylation mechanism," *Proceedings of the National Academy of Sciences of the United States of America*, vol. 110, no. 30, pp. E2772–E2781, 2013.
- [43] S. Shi, S. Lei, C. Tang, K. Wang, and Z. Xia, "Melatonin attenuates acute kidney ischemia/reperfusion injury in diabetic rats by activation of the SIRT1/Nrf2/HO-1 signaling pathway," *Bioscience Reports*, vol. 39, no. 1, 2019.
- [44] C. V. Vorhees and M. T. Williams, "Morris water maze: procedures for assessing spatial and related forms of learning and memory," *Nature Protocols*, vol. 1, no. 2, pp. 848–858, 2006.
- [45] Z. Qiongyue, Y. Xin, P. Meng et al., "Post-treatment with irisin attenuates acute kidney injury in sepsis mice through anti-ferroptosis via the SIRT1/Nrf2 pathway," *Frontiers in Pharmacology*, vol. 13, article 857067, 2022.
- [46] K. Bersuker, J. M. Hendricks, Z. Li et al., "The CoQ oxidoreductase FSP1 acts parallel to GPX4 to inhibit ferroptosis," *Nature*, vol. 575, no. 7784, pp. 688–692, 2019.
- [47] Y. Liu and W. Gu, "p53 in ferroptosis regulation: the new weapon for the old guardian," *Cell Death and Differentiation*, vol. 29, no. 5, pp. 895–910, 2022.
- [48] Y. Xie, W. Hou, X. Song et al., "Ferroptosis: process and function," *Cell Death & Differentiation*, vol. 23, no. 3, pp. 369–379, 2016.
- [49] H. Hong-Qiang, S. Mang-Qiao, X. Fen et al., "Sirt1 mediates improvement of isoflurane-induced memory impairment following hyperbaric oxygen preconditioning in middle-aged mice," *Physiology & Behavior*, vol. 195, pp. 1–8, 2018.
- [50] D. S. Wang, N. Terrando, and B. A. Orser, "Targeting microglia to mitigate perioperative neurocognitive disorders," *British Journal of Anaesthesia*, vol. 125, no. 3, pp. 229–232, 2020.
- [51] S. Saxena, I. K. Lai, R. Li, and M. Maze, "Neuroinflammation is a putative target for the prevention and treatment of perioperative neurocognitive disorders," *British Medical Bulletin*, vol. 130, no. 1, pp. 125–135, 2019.
- [52] G. Bellin, C. Gardin, L. Ferroni et al., "Exosome in cardiovascular diseases: a complex world full of hope," *Cell*, vol. 8, no. 2, p. 166, 2019.
- [53] C. Yang, S. Sun, Q. Zhang et al., "Exosomes of antler mesenchymal stem cells improve postoperative cognitive dysfunction in cardiopulmonary bypass rats through inhibiting the

- TLR2/TLR4 signaling pathway,” *Stem Cells International*, vol. 2020, Article ID 2134565, 13 pages, 2020.
- [54] M. Guo, Z. Yin, F. Chen, and P. Lei, “Mesenchymal stem cell-derived exosome: a promising alternative in the therapy of Alzheimer’s disease,” *Alzheimer’s Research & Therapy*, vol. 12, no. 1, p. 109, 2020.
- [55] A. Hervera, F. De Virgiliis, I. Palmisano et al., “Reactive oxygen species regulate axonal regeneration through the release of exosomal NADPH oxidase 2 complexes into injured axons,” *Nature Cell Biology*, vol. 20, no. 3, pp. 307–319, 2018.
- [56] N. Yan and J. Zhang, “Iron metabolism, ferroptosis, and the links with Alzheimer’s disease,” *Frontiers in Neuroscience*, vol. 13, p. 1443, 2020.
- [57] N. Yan and J. J. Zhang, “The emerging roles of ferroptosis in vascular cognitive impairment,” *Frontiers in Neuroscience*, vol. 13, p. 811, 2019.
- [58] Y. Li, Y. Zhou, D. Zhang et al., “Hypobaric hypoxia regulates iron metabolism in rats,” *Journal of Cellular Biochemistry*, vol. 120, no. 8, pp. 14076–14087, 2019.
- [59] C. Y. Wang and J. L. Babbitt, “Liver iron sensing and body iron homeostasis,” *Blood*, vol. 133, no. 1, pp. 18–29, 2019.
- [60] Y. Sun, P. Chen, B. Zhai et al., “The emerging role of ferroptosis in inflammation,” *Biomedicine & Pharmacotherapy*, vol. 127, article 110108, 2020.
- [61] S. Doll and M. Conrad, “Iron and ferroptosis: a still ill-defined liaison,” *IUBMB Life*, vol. 69, no. 6, pp. 423–434, 2017.
- [62] F. Deng, B. C. Zhao, X. Yang et al., “The gut microbiota metabolite capsiate promotes Gpx4 expression by activating TRPV1 to inhibit intestinal ischemia reperfusion-induced ferroptosis,” *Gut Microbes*, vol. 13, no. 1, pp. 1–21, 2021.
- [63] Y. Li, Y. Cao, J. Xiao et al., “Inhibitor of apoptosis-stimulating protein of p53 inhibits ferroptosis and alleviates intestinal ischemia/reperfusion-induced acute lung injury,” *Cell Death and Differentiation*, vol. 27, no. 9, pp. 2635–2650, 2020.
- [64] X. Wang, Z. Wang, J. Cao, Y. Dong, and Y. Chen, “Melatonin alleviates acute sleep deprivation-induced memory loss in mice by suppressing hippocampal ferroptosis,” *Frontiers in Pharmacology*, vol. 12, article 708645, 2021.
- [65] Y. Song, B. Wang, X. Zhu et al., “Human umbilical cord blood-derived MSCs exosome attenuate myocardial injury by inhibiting ferroptosis in acute myocardial infarction mice,” *Cell Biology and Toxicology*, vol. 37, no. 1, pp. 51–64, 2021.
- [66] X. Yi and X. Tang, “Exosomes from miR-19b-3p-modified ADSCs inhibit ferroptosis in intracerebral hemorrhage mice,” *Frontiers in Cell and Development Biology*, vol. 9, article 661317, 2021.
- [67] X. Yang, W. Zhang, H. Wu et al., “Downregulation of CDK5 restores sevoflurane-induced cognitive dysfunction by promoting SIRT1-mediated autophagy,” *Cellular and Molecular Neurobiology*, vol. 40, no. 6, pp. 955–965, 2020.
- [68] Y. Fujita and T. Yamashita, “Sirtuins in neuroendocrine regulation and neurological diseases,” *Frontiers in Neuroscience*, vol. 12, p. 778, 2018.
- [69] B. Li, J. Liu, G. Gu, X. Han, Q. Zhang, and W. Zhang, “Impact of neural stem cell-derived extracellular vesicles on mitochondrial dysfunction, sirtuin 1 level, and synaptic deficits in Alzheimer’s disease,” *Journal of Neurochemistry*, vol. 154, no. 5, pp. 502–518, 2020.
- [70] M. Liu, Y. Yang, B. Zhao et al., “Exosomes derived from adipose-derived mesenchymal stem cells ameliorate radiation-induced brain injury by activating the SIRT1 pathway,” *Frontiers in Cell and Development Biology*, vol. 9, article 693782, 2021.
- [71] M. M. Guo, K. Zhang, and J. H. Zhang, “Human breast Milk-derived exosomal miR-148a-3p protects against necrotizing enterocolitis by regulating p53 and sirtuin 1,” *Inflammation*, vol. 45, no. 3, pp. 1254–1268, 2022.
- [72] L. Zhang, H. H. Li, M. Yuan, D. Li, and G. Y. Wang, “Exosomal miR-22-3p derived from peritoneal macrophages enhances proliferation, migration, and invasion of ectopic endometrial stromal cells through regulation of the SIRT1/NF- κ B signaling pathway,” *European Review for Medical and Pharmacological Sciences*, vol. 24, no. 2, pp. 571–580, 2020.
- [73] N. Xu, F. Huang, C. Jian et al., “Neuroprotective effect of salidroside against central nervous system inflammation-induced cognitive deficits: a pivotal role of sirtuin 1-dependent Nrf2/HO-1/NF-kappaB pathway,” *Phytotherapy Research*, vol. 33, no. 5, pp. 1438–1447, 2019.
- [74] J. Han, X. Liu, Y. Li, J. Zhang, and H. Yu, “Sirt1/Nrf2 signalling pathway prevents cognitive impairment in diabetic rats through anti-oxidative stress induced by miRNA-23b-3p expression,” *Molecular Medicine Reports*, vol. 17, no. 6, pp. 8414–8422, 2018.
- [75] L. Zhu, F. Lu, X. Jia, Q. Yan, X. Zhang, and P. Mu, “Amyloid- β (25-35) regulates neuronal damage and memory loss via SIRT1/Nrf2 in the cortex of mice,” *Journal of Chemical Neuroanatomy*, vol. 114, article 101945, 2021.
- [76] Z. Mei, L. Du, X. Liu et al., “Diosmetin alleviated cerebral ischemia/reperfusion injury in vivo and in vitro by inhibiting oxidative stress via the SIRT1/Nrf2 signaling pathway,” *Food & Function*, vol. 13, no. 1, pp. 198–212, 2022.
- [77] T. Jiang, H. Cheng, J. Su et al., “Gastrodin protects against glutamate-induced ferroptosis in HT-22 cells through Nrf2/HO-1 signaling pathway,” *Toxicology In Vitro*, vol. 62, article 104715, 2020.

Review Article

The Regulatory Effects of Traditional Chinese Medicine on Ferroptosis

Qian Gao ^{1,2} **Xue-dong Yin**,^{1,2} **Fan Zhang**,³ **Yi-Zhun Zhu** ^{4,5} and **Zhi-ling Li** ¹

¹Department of Pharmacy, Shanghai Children's Hospital, School of Medicine, Shanghai Jiao Tong University, Shanghai 200062, China

²School of Medicine, Shanghai Jiao Tong University, Shanghai 200125, China

³Department of Pharmacy, Peking Union Medical College Hospital, Chinese Academy of Medical Sciences & Peking Union Medical College, Beijing 100730, China

⁴State Key Laboratory of Quality Research in Chinese Medicine & School of Pharmacy, Macau University of Science and Technology, Taipa, China

⁵Shanghai Key Laboratory of Bioactive Small Molecules & School of Pharmacy, Fudan University, Shanghai, China

Correspondence should be addressed to Yi-Zhun Zhu; yzzhu@must.edu.mo and Zhi-ling Li; lizl@shchildren.com.cn

Received 3 August 2022; Accepted 1 September 2022; Published 19 September 2022

Academic Editor: Lianxiang Luo

Copyright © 2022 Qian Gao et al. This is an open access article distributed under the Creative Commons Attribution License, which permits unrestricted use, distribution, and reproduction in any medium, provided the original work is properly cited.

Traditional Chinese medicine (TCM) has significantly contributed to protecting human health and promoting the progress of world civilization. A total of 2,711 TCMs are included in the 2020 version of the Chinese Pharmacopoeia, which is an integral part of the world's medical resources. Tu Youyou and her team discovered and purified artemisinin. And their contributions made the values and advantageous effects of TCM more and more recognized by the international community. There has been a lot of studies on TCM to treat diseases through antioxidant mechanisms, the reports on the new mechanisms beyond antioxidants of TCM has also increased year by year. Recently, many TCMs appear to have significant effects in regulating ferroptosis. Ferroptosis is an iron-dependent, non-apoptotic, regulated cell death characterized by intracellular lipid peroxide accumulation and oxidative membrane damage. Recently, accumulating studies have demonstrated that numerous organ injuries and pathophysiological process of many diseases are accompanied with ferroptosis, such as cancer, neurodegenerative disease, acute renal injury, arteriosclerosis, diabetes, and ischemia-reperfusion injury. This work mainly introduces dozens of TCMs that can regulate ferroptosis and their possible mechanisms and targets.

1. Introduction

The history of traditional Chinese medicine (TCM) has a long history, and written records of TCM have existed for more than 5,000 years. TCM reflects the wisdom of the Chinese people, which has evolved for thousands of years. It contains the precious experience of ancient Chinese people in fighting against diseases. TCM is one of the world's oldest medical systems, a healing approach based on the foundation of Chinese philosophy that utilizes the balance between mankind and nature. Its theories include the concept of yin and yang, the Five Elements, zang-fu, channels-collaterals, qi, blood, body fluid, methods of diagnosis, and the differentiation of symptom-complexes [1]. TCM is char-

acterized by two primary features: a holistic treatment strategy based on the differentiation of syndromes. The selection of TCM natural products is guided by their taste and Yin and Yang qualities [2]. TCM contributes greatly to the medical field by providing active pharmaceutical ingredient [3, 4]. TCM functions by individual adjustment of multiple components and targets and facilitates the transformation of the body from an abnormal to a normal state.

Ferroptosis is a novel form of programmed non-apoptotic cell death and is characterized by intracellular iron-dependent lipid peroxidation and accumulation of reactive oxygen species (ROS). The conception of ferroptosis was proposed by Dixon et al. in 2012, and the discovery of ferroptosis emerged from their identification in 2003 of

erastin that induced a non-apoptotic form of cell death [5]. Iron ions are not only importance trace elements in body but also are the triggered factor involved in the occurrence of ferroptosis [6]. Excessive Iron may directly generate plenty of ROS to induce oxidative damage and ferroptosis through the Fenton reaction [4]. Ferroptosis is involved in multiple diseases including cancer, arteriosclerosis, ischemia-reperfusion injury, neurodegenerative disease, and acute renal failure [7–12]. Glutathione peroxidase 4 (GPX4), ferroptosis suppressor protein 1 (FSP1), and dihydroorotate dehydrogenase (DHODH) constitute the three primary defense mechanisms against ferroptosis. They are as follows: 1) GPX4 specifically catalyzes lipid peroxidation to inactivate its oxidative activity in a GSH-dependent manner and protects the cells from ferroptosis [12–14]. 2) FSP1 is a GSH-independent ferroptosis inhibitor that acts as a redox catalyst, reducing coenzyme Q10 (CoQ10) to ubiquinol (CoQ10H2) at the cell membrane. CoQ10H2 acts as a lipophilic antioxidant by capturing free radicals and inhibiting lipid peroxides [15, 16]. 3) DHODH inhibits ferroptosis by inhibiting lipid peroxidation in mitochondria [17]. RSL3 and erastin are two experimental compounds that can induce ferroptosis. Dixon et al. found that erastin induced ferroptosis by blocking uptake of cystine through system Xc⁻, a cystine-glutamate anti-porter that transports extracellular cysteine into for the synthesis of GSH., resulting in depletion of GSH and cystine [18], and RSL3 inhibited GPX4 [13]. Lipid peroxidation is a free radical-driven reaction, which mainly affects metabolism of polyunsaturated fatty acids (PUFAs) in the cell membrane [19]. All mammalian cells have certain levels of PUFAs, and PUFAs is converted to phospholipid hydroperoxides (PLOOH). The products of lipid peroxidation include the PLOOH and malondialdehyde (MDA). During the ferroptosis process, ROS and phospholipid hydroperoxides (PLOOH) accumulate and cannot be neutralized efficiently. Excessive ROS may disrupt the integrity of the plasma membrane [20].

Ferroptosis is not only associated with several diseases but is also a key component of many signaling pathways. The process of ferroptosis can also be targeted by drugs. In this work, we mainly focused on regulating ferroptosis by TCMs and their active pharmaceutical ingredient. We reviewed the primary mechanisms of how TCMs affect ferroptosis. It is reported that dysregulation of ferroptosis is linked with numerous physiological conditions and pathological stress. However, ferroptosis is a two-edged sword. On the one hand, it induces the non-apoptotic destruction of cancer cells [21]. but on the other hand, it may lead to organ damage [12, 22, 23]. Among TCMs, some active pharmaceutical ingredients are ferroptosis inducers and have excellent anticancer efficacy, while some show organ-protective effects by acting as ferroptosis inhibitors.

2. The Main TCMs for Regulating Ferroptosis

2.1. Artemisinin. Artemisinin, as a natural sesquiterpene lactone compound, was isolated for the first time from the Asteraceae plant *Artemisia arbusus* in 1971 by the Chinese scientist Tu Youyou who won the Nobel Prize in Medicine. Artemisinin is now widely used in the treatment of malaria

[24, 25]. Dihydroartemisinin (DHA), a derivative of artemisinin, also has therapeutic effects on various cancers, including liver cancer [26], breast cancer [27], and lung cancer [28]. DHA functions by inhibiting the PRIM2/SLC7A11 axis and induces ferroptosis and inhibits cell proliferation. The peroxide bridge structure in the molecular structure of DHA may cause ferroptosis in tumor cells by disrupting the intracellular redox equilibrium [29–31]. Lin et al. found that DHA inhibits tumor progression in head and neck carcinoma by inducing ferroptosis in tumor cells [32]. Artemisinin and its derivatives, as the basic drugs for malaria treatment, save the lives of hundreds of thousands of patients around the world every year. Recently, discoveries in oncology studies have shown that artemisinin and its derivatives act as ferroptosis inducers by inducing tumor cells ferroptosis to exert anticancer effects. So far, artemisinin and its derivatives have no obvious serious adverse reactions using antimalarial treatment, and have very high safety. However, it has been reported that when artesunate suppositories are administered rectally, about 6% of patients experience tenesmus, but serious adverse reactions such as neutropenia are rare [33, 34].

2.2. Leonurine (Also Named as SCM-198). Leonurine is a primary active alkaloid compound extracted and purified from Motherwort, a traditional Chinese herbal medicine [35]. Motherwort has the effects of promoting blood circulation and regulating menstruation, diuresis and swelling, clearing heat and detoxification, and is often used for blood stagnation, amenorrhea and dysmenorrhea. In the past, motherwort was considered as a safe and non-toxic TCM. In recent years, accumulating studies have found that long-term and high-dose use of motherwort will cause some adverse reactions, mainly manifested as sudden feeling of general weakness, paralysis of the lower limbs, severe sweating, decreased blood pressure, and rapid breathing, and even cause uterine contractions and lead to miscarriage in pregnant women [36, 37].

Leonurine reduces renal podocyte injury, lipopolysaccharide-induced acute kidney injury, and renal fibrosis by inhibiting oxidative stress via reducing the production of ROS and protecting the kidneys [38, 39]. Ferroptosis is mediated by phospholipid peroxidation, a process that requires ROS and transition metal iron. Recently, Leonurine has been shown to inhibit ferroptosis by activating the antioxidant transcription factor Nrf2 and play a protective role against liver [40] and kidney [41] injuries. In addition, leonurine has also been confirmed to inhibit the expression of fibronectin by blocking the transforming growth factor- β (TGF- β)/NF- κ B signaling pathway and in chronic kidney disease rat model, leonurine can reduce tubulointerstitial fibrosis caused by unilateral ureteral obstruction [38].

2.3. Curculigoside, Astragalus Polysaccharide and Astragaloside IV. Astragalus membranaceus is sweet in taste and warm in nature. It has the functions of invigorating qi and raising yang, strengthening the surface and relieving sweat, and diuresis and swelling. It is a commonly used medicine in TCM for the

treatment of kidney disease. Clinical adverse reactions caused by it are rare, and the drug is relatively safe. Curculigoside (CUR) is a phenolic glycoside compound isolated and purified from *Astragalus membranaceus*. It shows various pharmacological activities, such as anti-inflammatory [42] and antioxidant [43], anti-osteoporotic effects [44]. Wang et al. found that CUR protects against hydrogen peroxide-induced osteoblast impairment by alleviating oxidative damage [45]. Another study has confirmed the efficacy of CUR in attenuating excess iron-induced bone loss and oxidative stress by inhibiting ROS production and increasing superoxide dismutase (SOD) and GPX4 [46]. The protective effect of CUR may be associated with the inhibition of ferroptosis. CUR inhibits intestinal epithelial cells ferroptosis by inducing GPX4 expression in ulcerative colitis (UC) [47].

Astragalus polysaccharide (APS), another bioactive compound extracted from *Astragalus membranaceus*, also possesses several potential pharmacological effects, including anti-inflammation [48], anti-infection [49], anti-tumor [50], and immune regulatory properties [51]. Similar to CUR, APS also protects intestinal epithelial cells (IECs) against ferroptosis by inhibiting Nrf2/HO-1 (Heme oxygenase 1) signaling pathways and reduces lesions in a murine model of experimental colitis [52].

Astragaloside IV, another compound isolated from *Astragalus membranaceus*, protects the endothelial cells by decreasing ROS production and oxidative stress [53]. Sheng et al. suggested that Astragaloside IV may prevent myocardial damage by protecting the Human Umbilical Vein Endothelial Cells (HUVECs) against ferroptosis [54].

2.4. Quercetin, QCT. Quercetin (3,3',4,5,7-pentahydroxyflavone) is a unique bioactive natural flavonoid widely distributed in nature and abundant in different vegetables. QCT has a wide range of pharmacological effects, including anticancer [55], antioxidant [56], and anti-inflammatory [57] effects. The antitumor activity of QCT may be associated with its pro-apoptotic effect [47]. However, in contrast, low-dose QCT (10 mg/kg) also protects against diabetic kidney injury by inhibiting apoptosis [58] in hypercholesterolemic mice, it also alleviates acute kidney injury (AKI) by inhibiting the expression of activating transcription factor 3 (ATF3) and blocking ferroptosis in renal proximal tubular epithelial cells [59]. QCT also impedes the accumulation of iron, attenuates lipid peroxide, and restores the expression of the voltage-dependent anion-selective channel protein 2 (VDAC2). It shows protective effects against type 2 diabetes by blocking ferroptosis in pancreatic β cells [60]. From these studies, we concluded that QCT might inhibit cancer progression by promoting apoptosis and exert a cytoprotective effect by inhibiting apoptosis and ferroptosis.

2.5. Erianin. Erianin, a natural product isolated from the herb *Dendrobium*, exerts many bioactive effects, including antitumor activity in several cancers. A study shows that erianin may be a promising medicine for osteosarcoma because it induces G2/M cell cycle arrest and triggers regulated cell death, such as apoptosis and autophagy [61]. Zhu et al. reported that erianin exhibits antitumor activity in

bladder cancer cells by inducing mitochondrial apoptosis and the JNK pathway [62]. Liu et al. showed that erianin may be used for treating human nasopharyngeal carcinoma since it induces cell apoptosis through the ERK signaling pathway [63]. Furthermore, it has been reported that erianin shows antitumor activity in lung cancer cells by inducing ferroptosis and G2/M-phase arrest to inhibit cell proliferation and migration. This study, for the first time, also found that erianin induces ferroptosis via the Ca^{2+} /CaM signaling pathway in lung cancer cells and inhibits the progression of the tumor [64]. We concluded that the antitumor effect of erianin is achieved by both pro-apoptotic and non-apoptotic pathways including ferroptosis.

2.6. Curcumin. Curcumin ([1,7-bis(4-hydroxy-3-methoxyphenyl)-1,6-heptadiene-3,5-dione]), discovered in *Curcuma longa* L., has been widely and safely consumed for hundreds of years. It is a natural food pigment and also shows potential applications in cancer treatment [65, 66]. Due to its rare adverse reactions [67], curcumin has been clinically used for the treatment of various diseases besides tumors, such as diabetes, obesity, cardiovascular disease, lung disease, neurological disease and autoimmune disease [68]. Previous studies have demonstrated that Curcumin inhibits the growth of cancer cells, including pancreatic cancer [69] and prostate cancer [70], by inhibiting cell proliferation and inducing cell apoptosis. Curcumin has been shown to be capable of eliminating ROS [71], once intracellular ROS accumulation significantly exceeds normal levels, it leads to significant damage to DNA, lipids, and proteins and finally induces cell death, including ferroptosis [4, 72]. A series of studies have shown that Curcumin inhibits cancer progression by inducing ferroptosis. Li et al. have found that Curcumin triggers ferroptosis in breast cancer cells by upregulating HO-1 expression [73]. Zhang et al. verified that curcumenol, another antitumor component extracted from turmeric rhizomes, induces ferroptosis in lung cancer cells through the lncRNA H19/miR-19b-3p/FTH1 axis [74]. Curcumin has the potential to be a broad-spectrum and safe anticancer drug.

2.7. Epigallocatechin-3-Gallate, EGCG. EGCG, an active polyphenol compound found in green tea, belongs to the same polyphenol family as curcumin [75] and shows multiple biological activities, including antitumor, anti-inflammatory, anti-bacterial, and cytoprotective activities [76, 77]. EGCG possesses powerful antioxidant activity due to its special stereochemical structure. It penetrates the blood-brain barrier and chelates Fe^{3+} to decrease ROS and α -synuclein, thereby preventing and treating neurodegeneration [78]. EGCG also regulates the expression of AMP-activated protein kinase (AMPK) and reduces lipid accumulation in canine hepatocytes [79]. Studies showed that EGCG protects cardiomyocytes against DOX-induced cardiotoxicity by inhibiting apoptosis and ferroptosis in Sarcoma 180 tumor-bearing mice [80, 81]. Furthermore, EGCG also ameliorates ionizing radiation-induced ferroptosis in mouse intestinal epithelial cells by deregulating ROS and activating Nrf2 and its downstream antioxidant proteins, including SLC7A11, HO-1, GPX4 [82]. It also alleviates erastin-induced ferroptosis

in pancreatic Beta-cells [75]. EGCG also inhibits ferroptosis in cerebellar granule neurons by promoting PKD1 phosphorylation after spinal injury [83].

2.8. Glycyrrhiza. The traditional herbal medicine licorice, the dried rhizome of *Glycyrrhiza* (GL), is used for spleen and stomach weakness, fatigue and fatigue, palpitations and shortness of breath, cough, and phlegm. Adverse reactions of GL and its derivatives includes increased blood pressure, edema, abdominal pain and so on. In addition, pregnant women should also use it with caution [84]. GL extracted from *Glycyrrhiza uralensis* Fisch is a natural glycosyl triterpenoid and is identified as an inhibitor of the high-mobility group box1 (HMGB1). GL has a neuroprotective effect on brain injury by inhibiting HMGB1 and its downstream inflammatory factors and reducing oxidative stress [85]. Recent studies have shown that cell ferroptosis induces HMGB1 release and inflammation in the acute pancreatitis model [86]. It has been shown that HMGB1 is released from injured cells and shows cytokine activity that has been linked with the pathogenesis of many central nervous system (CNS) diseases, including neonatal hypoxic-ischemic brain damage (HIBD) [87]. Therefore, as an HMGB1 inhibitor, GL provides a potential treatment for HIBD, and GL has been shown to reduce ferroptosis-mediated brain damage by modulating the GPX4 axis [88]. Echinatin, another active ingredient of licorice, effectively suppresses the activation of the NLRP3 inflammasome by targeting HSP90 and is used for treating a variety of human inflammatory diseases [89].

2.9. Honokiol, HNK. HNK is a biphenolic compound extracted from various parts of *Magnolia officinalis* [90]. HNK shows efficient and specific antitumor effects. HNK has been reported to suppress the growth of cancer cells by inducing apoptosis and autophagy. HNK promotes ROS generation and induces ROS-mediated cell death by regulating p53/PI3K/Akt/mTOR signaling pathway [91–93]. Recently, HNK also was shown to increase the intracellular ROS level by decreasing the activity of GPX4, thereby killing colon cancer cells (CCCs) [94]. Therefore, HNK shows potential in treating solid tumors. Lai et al. reported that HNK induces acute myeloid leukemia (AML) cells ferroptosis by upregulating HMOX1 [95].

2.10. Tanshinone IIA. *Salvia miltiorrhiza* Bunge. is a perennial upright herb of the genus Sage in the family Dicotyledonaceae; TCM salvia is a dried root and rhizome, which activates blood and dispels stasis and clears the heart [96]. With the increase in clinical application, reports of its toxic and side effects are also increasing, including allergic skin rash, liver damage, and gastrointestinal bleeding [97]. The main bioactive ingredients of salvia include liposoluble salvia ketone and water-soluble salvia phenolic acids [98]. Tanshinone IIA (Tan IIA) was isolated from *Salvia miltiorrhiza* Bunge. and found to exert an antineoplastic effect in gastric cancer cells MKN-45 by inducing apoptosis and cell cycle arrest [99] and in AGS cells by suppressing insulin-like growth factor receptor (IGFR), epidermal growth factor receptor (EGFR) expression and blocking PI3K/Akt/mTOR

pathways [100, 101]. A study showed that Tan IIA upregulates the expression of p53 and p53 is recruited to the SCL7A11 promotor to block the transcription of SLC7A11, which encodes system Xc⁻, a cystine-glutamate antiporter that transports extracellular cysteine into for the synthesis of GSH. Consequently, Tan IIA induces ROS-mediated ferroptosis [102, 103].

2.11. 1,6-O-O-Diacetyl-Britannilactone (OABL). Sesquiterpene lactones (STLs), are a lead bioactive component extracted from *Inula japonica* Thunb. They have been used for the treatment of multiple inflammatory diseases, including fever, migraine, arthritis, and atherosclerosis with few mild side effects [104, 105]. 1,6-o-o-diacetyl-britannilactone (OABL) is another STL mainly extracted from *Inula Britannica* L. OABL suppresses NO and PGE2 synthesis in RAW264.7 macrophages to exert an anti-inflammatory effect [106] and antineoplastic effect [107]. Oxidative stress and uncontrolled neuroinflammation induce neuronal damage in neurodegenerative diseases, such as Alzheimer's disease (AD) [108]. OABL may treat neurodegenerative disease by decreasing amyloid plaques (deposits of A β) and neurofibrillary tangles (hyperphosphorylated Tau). OABL increased the GSH level and reduced the MDA level in 5xFAD mice, showing that OABL protects neurons by inhibiting ferroptosis [109].

2.12. Beta-Elementene. Beta-elementene is a Class II anticancer drug extracted and purified from TCM *curcumae* rhizome. Beta-elementene has been used to treat various cancers, including colorectal cancer [110, 111]. Ferroptosis inhibitors prevented cell death mediated by beta-elementene treatment. This suggested that beta-elementene may inhibit tumor growth by inducing ferroptosis in KRAS mutant colorectal cancer cells. This study also has found that β -elementene also inhibits epithelial-mesenchymal transformation (EMT) by inhibiting metastasis of KRAS-mutant colon cancer tumor cells [112]. As a new ferroptosis inducer, beta-elementene is widely used in the treatment of various cancers, including lung, liver, brain, breast, ovary, gastric, and prostate cancers due to its low toxicity [113].

In addition to the above drugs, a variety of TCMs have also been found to be associated with cell ferroptosis.

2.13. Others. *Ajuga nipponensis* has abundant bioactivities, including hypoglycaemic [114] and antioxidant and hepatoprotective effects [115]. Recently, ajudecunoid C (ADC), a neoclerodane diterpenoid extracted from *Ajuga nipponensis*, has been shown to protect neurons from ferroptosis by activating the Nrf2 antioxidant pathway [116]. Cucurbitacins are a group of natural tetracyclic triterpenoids from oriental herbs, among which cucurbitacin B (CuB) is one of the most abundant and richly studied cucurbitacins extractive [117]. CuB mediates its potent antitumor activity not only by inducing cell apoptosis and related pathways [118] but also by the induction of a nonapoptotic pathway - CNE1 ferroptosis. CuB helps in the accumulation of iron and GSH depletion, resulting in the production of lipid peroxides. CuB also downregulates the expression of GPX4 [119]. Xie et al. have

TABLE 1: Representative TCMs as Ferroptosis Regulators.

TCMs or active pharmaceutical ingredients	Function	Possible mechanism of regulating Ferroptosis	Herb Chinese name
Artemisinin/Dihydro-artemisinin	Inducer	Inhibited the function of system x_c^-	Qinghao
Leonurine	Inhibitor	Upregulated the Nrf2/HO-1 signaling	Yimucao
Astragalus Membranaceus	Inducer	Down-regulated the expression GPX4	Huangqi
Quercetin	Inhibitor	Activated system x_c^- by inhibiting ATF3	Hupisu
Dendrobium/Erianin	Inducer	Upregulated the levels of intracellular ROS by Ca^{2+} /CaM signaling pathway	Shihu
Curcuma longa L/curcumin	Inducer	Inhibited system x_c^- by Nrf2/HO-1 signaling pathway	Jianghuang
Epigallocatechin-3-gallate,EGCG	Inhibitor	Activated system x_c^- by inducing Nrf2 nucleus translocation	Biaomeishizi
Glycyrrhiza	Inhibitor	Upregulated the expression of GPX4	Gancao
Magnolia officinalis/Honokiol, HNK	Inducer	Upregulated the levels of ROS	Guangyulan
Salvia miltiorrhiza Bge./Tanshinone IIA	Inducer	Inhibited the function of system x_c^-	Danshen
Inula japonica Thunb./1,6-o-o-diacetyl-britannilactone, OABL	Inhibitor	Upregulated the levels of GSH	Xuanfuhua
Curcumae rhizome/Beta-elemene	Inducer	Upregulated the levels of ROS	Ezhu

The English and Chinese name of these TCMs comes from the Pharmacopoeia of the People's Republic of China (version 2020).

found that *Selaginella* extractive induces ferroptosis in breast cancer cells (MCF7) by enhancing the expression of VDAC2 channels and inhibiting the expression of Nedd4 E3 ubiquitin ligase, leading to the accumulation of peroxidation and the production of ROS [120]. Gao et al. have reported that *Actinidia chinensis* plant prevents gastric cancer by inducing apoptosis and ferroptosis in gastric cells [121]. Zhang et al. showed that Bufotalin accelerates lipid peroxidation by inducing degradation of GPX4, and treats human non-small cell lung cancer (NSCLC) by targeting ferroptosis [122]. It has been indicated that brucine is a weakly alkaline compound isolated from the seeds of *Strychnos nux-vomica*, and induces the accumulation of H_2O_2 , causing ferroptosis in glioma cells by upregulating ATF3 [123]. Baicalein, a flavonoid compound mainly derived from the root of *Scutellaria baicalensis*, has recently been found as a ferroptosis inhibitor and functions through reducing iron accumulation, glutathione depletion, and lipid depletion peroxidation [124]. Brusatol, a natural product isolated from the *Brucea javanica* Merr., also regulates the ferroptosis process by blocking Nrf2 signaling [125]. So, as an inhibitor of Nrf2, brusatol showed therapeutic efficacy against human NSCLC by inducing ferroptosis through the FOCAD-FAK signaling pathway [126]. Ji et al. found that niujiao-dihuang detoxify decoction, as a ferroptosis inhibitor, could alleviate injury by promoting GSH synthesis and enhance GPX4 activity in acute liver failure models [127]. Another study showed that realgar could induce ferroptosis by downregulating expression of Slc7A11 and Gpx4 in HK-2 cells to play a nephrotoxic effect, and the toxicity of realgar on HK-2 was dose-dependent [128]. Huang et al. reported that *Hedyotis diffusa* injection could induce ferroptosis via the Bax/Bcl2/VDAC2/3 axis to inhibit the viability of lung adenocarcinoma cells [129].

Red ginseng polysaccharide, an active component of the herb *Panax ginseng* C. A. Meyer (Araliaceae), have an anticancer role in human lung cancer and breast cancer by inducing ferroptosis via targeting GPX4 [130].

In summary, tremendous endeavors have been made to explore the regulatory mechanisms of TCMs on ferroptosis over the past years. Table 1 lists the Chinese and English names of representative TCMs which act as ferroptosis regulators.

3. Discussion and Outlook

Here, we have summarized dozens of TCMs which regulate ferroptosis and have outlined their mechanisms and targets. DHA [28] and Tan IIA [102] induce ferroptosis by inhibiting System X_c^- , while QCT [59] activates System X_c^- and blocks ferroptosis through the ATF3 signaling pathway. Curcumin [73] promotes ferroptosis by inhibiting Nrf-2 nuclear translocation and its downstream signaling pathway and System X_c^- , while EGCG [82] and leonurine [40, 41] inhibits ferroptosis by promoting the Nrf-2/HO-1 signaling pathway. OABL [109] attenuates ferroptosis by upregulating GSH levels. *Astragalus membranaceus* [47, 53] promotes GPX4 activity to inhibit ferroptosis, while *Glycyrrhiza* [88] inhibits GPX4 to promote ferroptosis. EGCG [82] and β -elemene [113] inhibit ferroptosis by down-regulating intracellular ROS levels. HNK [94] promotes ferroptosis by upregulating intracellular ROS levels, and erianin promotes ferroptosis by upregulating ROS through the Ca^{2+} /CaM signaling pathway [64]. Additionally, in vivo and in vitro experiments have shown that CuB, *Selaginella*, *Actinidia chinensis* plant, bufotalin, brucine, brusatol, realgar, *Hedyotis diffusa* injection and Red ginseng polysaccharide may be used as ferroptosis inducers. In contrast, ADC, Baicalein, niujiaodihuang detoxify decoction may be used

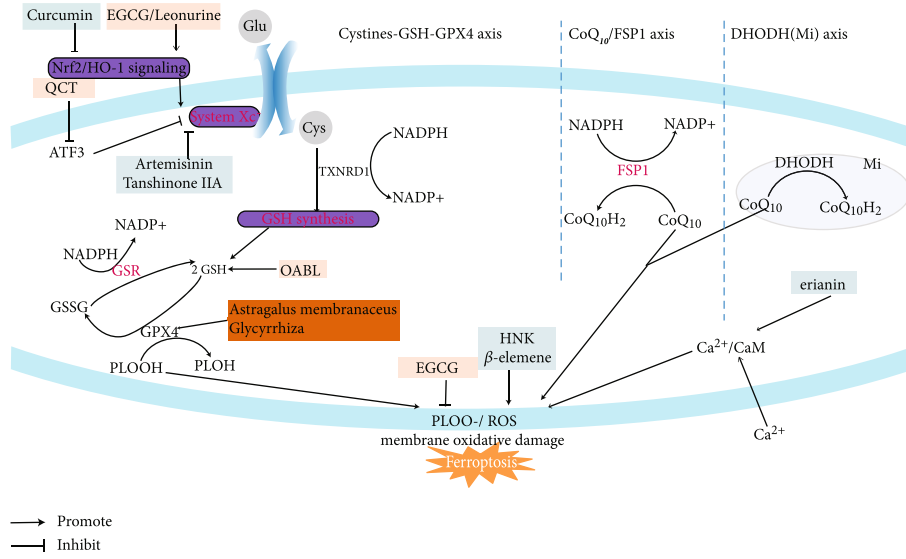


FIGURE 1: Significant TCMs involved in ferroptosis and their targets. There are three main iron death pathways, including the Cystine-GSH-GPX4 axis, CoQ10/FSP1, and DHODH axis. The frame of this color “peach” is filled with TCMs that are ferroptosis inhibitors; the frame of “light blue” is filled with ferroptosis inducers.

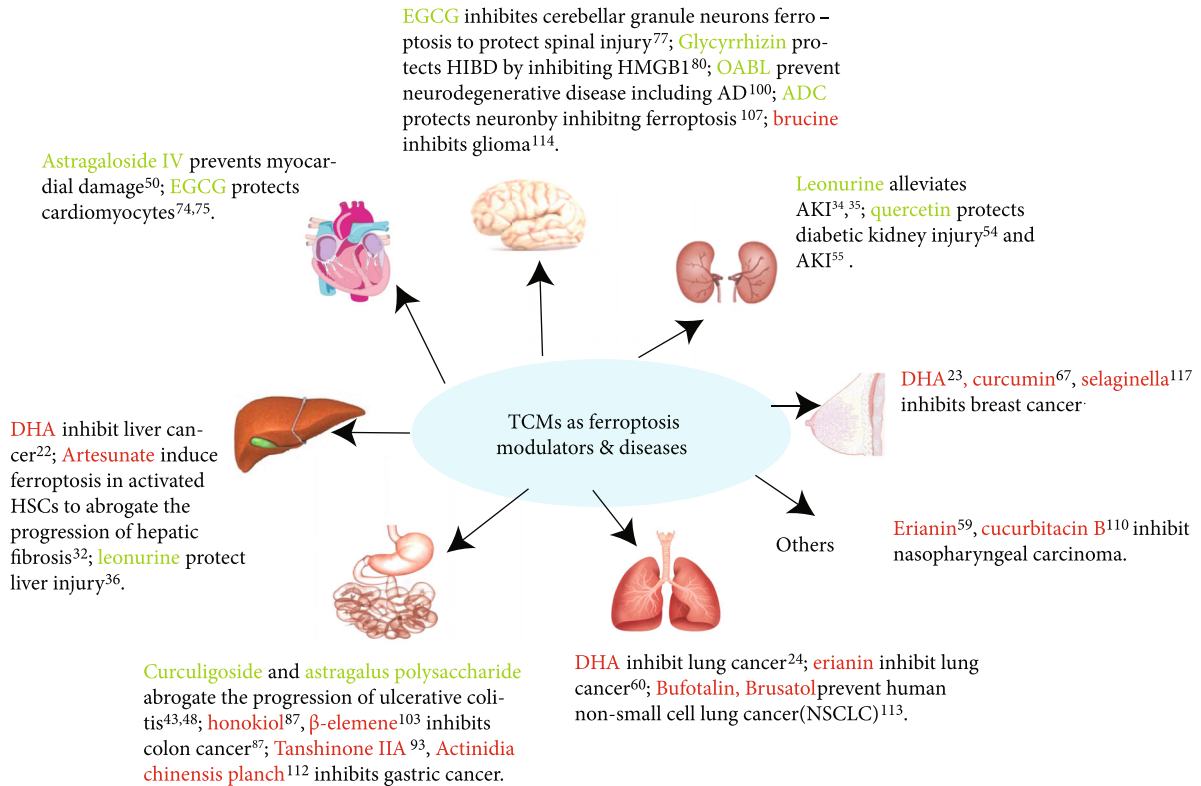


FIGURE 2: Ferroptosis has played an important role in multiple diseases, such as nervous system diseases, liver diseases, heart diseases, gastrointestinal diseases, lung diseases, kidney diseases, and breast diseases. TCM is engaged in the prevention and treatment of these diseases by regulating ferroptosis. Artemisinin derivatives: DHA, Artesunate; astragalus membranaceus derivatives: curculigoside, astragalus polysaccharide, astragaloside IV; glycyrrhiza derivatives: glycyrrhizin, echinatin; ajuga nipponensis: ajudecunoid C(ADC).

as ferroptosis inhibitors. The primary Chinese medicines that regulate ferroptosis and their possible targets are shown in Figure 1 [14, 17, 131, 132].

However, careful consideration should be given to the data obtained from cell experiments and animal experiments since cell and animal experiments are different from clinical

investigations; future studies, especially clinical trials, are essential for using TCMs in ferroptosis-related diseases. These research studies will be complicated and challenging due to the complexity of TCMs components and the interaction of various therapeutic drugs in regulating ferroptosis-related diseases including cancers, auto-immune diseases. Nevertheless, TCMs have tremendous potential in the treatment of ferroptosis-related diseases in the future due to their low toxicity and side effects compared with chemical medicine. Compared with the classical ferroptosis inducers including erastin and RAS-selective lethal 3 (RSL3) the reported TCMs and their active ingredients that have a regulatory effect on ferroptosis have the characteristics of more regulatory targets, stable structure, high safety, low cost and easy availability, but the accumulation of related researches is insufficient and needs to be further explored. This study reviews the functions and possible targets of TCMs in regulating ferroptosis and provides theoretical support for the subsequent clinical application of TCMs in preventing and treating ferroptosis-related diseases (Figure 2).

Abbreviations

TCM:	Traditional Chinese medicine
ROS:	Reactive oxygen species
GPX4:	Glutathione peroxidase 4
FSP1:	Ferroptosis suppressor protein 1
DHODH:	Dihydroorotate dehydrogenase
CoQ ₁₀ :	Coenzyme Q ₁₀
PLOOH:	Phospholipid hydroperoxides
PUFA:	Polyunsaturated fatty acyl
SOD:	Superoxide dismutase
DHA:	Dihydroartemisinin
TLR4:	Toll-like receptor 4
Nrf2:	Nuclear factor erythroid-related factor 2
HSCs:	Hepatic stellate cells
CUR:	Curcumin
APS:	Astragalus polysaccharide
IECs:	Intestinal epithelial cells
QCT:	Quercetin
AKI:	Acute kidney injury
HIBD:	Hypoxic-ischemic brain damage
ATF3:	Activating transcription factor 3
VDAC2:	Voltage-dependent anion-selective channel protein 2
HO-1:	Heme oxygenase 1
GL:	Glycyrrhizin
HMGB1:	High-mobility group box1
HNK:	Honokiol
OABL:	1,6-o-o-diacetyl-britannilactone
ADC:	Ajudecunoid C.

Conflicts of Interest

The authors declare no competing financial interest.

Authors' Contributions

Qian Gao and Xuedong Yin equally contributed to this work.

Acknowledgments

The present research was supported by the Shanghai Science and Technology Commission Grant Project (No. 21DZ2300700), Shanghai “Medical Rising Star” Youth Development Program “Excellent Young Medical Talents” (No. SHWSRS(2021)_099), Shanghai Talent Development Fund (No. 2020110), an Innovative research team of High-Level Local Universities in Shanghai (SHSMU-ZDCX20212200), and the Institute for Innovation in Clinical Pharmacy in the School of Medicine Shanghai Jiao Tong University (CX-YJY2019MS003). The authors appreciate the support of Dr. Hua-jun Sun from Shanghai Children’s Hospital.

References

- [1] C. Keji and X. Hao, “The integration of traditional Chinese medicine and Western medicine,” *European Review*, vol. 11, no. 2, pp. 225–235, 2003.
- [2] K. Chan, “Progress in traditional Chinese medicine,” *Trends in Pharmacological Sciences*, vol. 16, no. 6, pp. 182–187, 1995.
- [3] G. M. Cragg and D. J. Newman, “Natural products: a continuing source of novel drug leads,” *Biochimica et Biophysica Acta (BBA)-General Subjects*, vol. 1830, no. 6, pp. 3670–3695, 2013.
- [4] S. J. Dixon, K. M. Lemberg, M. R. Lamprecht et al., “Ferroptosis: an iron-dependent form of nonapoptotic cell death,” *Cell*, vol. 149, no. 5, pp. 1060–1072, 2012.
- [5] S. Dolma, S. L. Lessnick, W. C. Hahn, and B. R. Stockwell, “Identification of genotype-selective antitumor agents using synthetic lethal chemical screening in engineered human tumor cells,” *Cancer Cell*, vol. 3, no. 3, pp. 285–296, 2003.
- [6] M. Gao, P. Monian, N. Quadri, R. Ramasamy, and X. Jiang, “Glutaminolysis and transferrin regulate ferroptosis,” *Molecular Cell*, vol. 59, no. 2, pp. 298–308, 2015.
- [7] Y. Xie, W. Hou, X. Song et al., “Ferroptosis: process and function,” *Cell Death & Differentiation*, vol. 23, no. 3, pp. 369–379, 2016.
- [8] X. Sun, Z. Ou, R. Chen et al., “Activation of the p62-Keap1-NRF2 pathway protects against ferroptosis in hepatocellular carcinoma cells,” *Hepatology*, vol. 63, no. 1, pp. 173–184, 2016.
- [9] A. Linkermann, R. Skouta, N. Himmerkus et al., “Synchronized renal tubular cell death involves ferroptosis,” *Proceedings of the National Academy of Sciences*, vol. 111, no. 47, pp. 16836–16841, 2014.
- [10] X. Zhang, Y. Yu, H. Lei et al., “The Nrf-2/HO-1 signaling axis: a ray of hope in cardiovascular diseases,” *Cardiology Research and Practice*, vol. 2020, Article ID 5695723, 9 pages, 2020.
- [11] M. Abdalkader, R. Lampinen, K. M. Kanninen, T. M. Malm, and J. R. Liddell, “Targeting Nrf2 to suppress ferroptosis and mitochondrial dysfunction in neurodegeneration,” *Frontiers in Neuroscience*, vol. 12, p. 466, 2018.
- [12] J. P. Friedmann Angeli, M. Schneider, B. Proneth et al., “Inactivation of the ferroptosis regulator Gpx4 triggers acute renal failure in mice,” *Nature Cell Biology*, vol. 16, no. 12, pp. 1180–1191, 2014.
- [13] W. S. Yang, R. SriRamaratnam, M. E. Welsch et al., “Regulation of ferroptotic cancer cell death by GPX4,” *Cell*, vol. 156, no. 1–2, pp. 317–331, 2014.
- [14] X. Jiang, B. R. Stockwell, and M. Conrad, “Ferroptosis: mechanisms, biology and role in disease,” *Nature Reviews Molecular Cell Biology*, vol. 22, no. 4, pp. 266–282, 2021.

- [15] K. Bersuker, J. M. Hendricks, Z. Li et al., "The CoQ oxidoreductase FSP1 acts parallel to GPX4 to inhibit ferroptosis," *Nature*, vol. 575, no. 7784, pp. 688–692, 2019.
- [16] S. Doll, F. P. Freitas, R. Shah et al., "FSP1 is a glutathione-independent ferroptosis suppressor," *Nature*, vol. 575, no. 7784, pp. 693–698, 2019.
- [17] C. Mao, X. Liu, Y. Zhang et al., "DHODH-mediated ferroptosis defence is a targetable vulnerability in cancer," *Nature*, vol. 593, no. 7860, pp. 586–590, 2021.
- [18] S. J. Dixon, D. N. Patel, M. Welsch et al., "Pharmacological inhibition of cystine–glutamate exchange induces endoplasmic reticulum stress and ferroptosis," *elife*, vol. 3, p. e02523, 2014.
- [19] V. E. Kagan, G. Mao, F. Qu et al., "Oxidized arachidonic and adrenic PEs navigate cells to ferroptosis," *Nature Chemical Biology*, vol. 13, no. 1, pp. 81–90, 2017.
- [20] D. Liang, A. M. Minikes, and X. Jiang, "Ferroptosis at the intersection of lipid metabolism and cellular signaling," *Molecular Cell*, vol. 82, no. 12, pp. 2215–2227, 2022.
- [21] C. Liang, X. Zhang, M. Yang, and X. Dong, "Recent progress in ferroptosis inducers for cancer therapy," *Advanced Materials*, vol. 31, no. 51, p. 1904197, 2019.
- [22] Y. Li, D. Feng, Z. Wang et al., "Ischemia-induced ACSL4 activation contributes to ferroptosis-mediated tissue injury in intestinal ischemia/reperfusion," *Cell Death & Differentiation*, vol. 26, no. 11, pp. 2284–2299, 2019.
- [23] X. Song and D. Long, "Nrf2 and ferroptosis: a new research direction for neurodegenerative diseases," *Frontiers in Neuroscience*, vol. 14, p. 267, 2020.
- [24] S. Bhattacharjee, I. Coppens, A. Mbengue et al., "Remodeling of the malaria parasite and host human red cell by vesicle amplification that induces artemisinin resistance," *Blood, The Journal of the American Society of Hematology*, vol. 131, no. 11, pp. 1234–1247, 2018.
- [25] R. Varo, C. Chaccour, and Q. Bassat, "Actualizacion en malaria," *Medicina Clínica*, vol. 155, no. 9, pp. 395–402, 2020.
- [26] J. Zou, Q. Ma, R. Sun et al., "Dihydroartemisinin inhibits HepG2. 2.15 proliferation by inducing cellular senescence and autophagy," *BMB Reports*, vol. 52, no. 8, pp. 520–525, 2019.
- [27] Y. Yao, Q. Guo, Y. Cao et al., "Artemisinin derivatives inactivate cancer-associated fibroblasts through suppressing TGF- β signaling in breast cancer," *Journal of Experimental & Clinical Cancer Research*, vol. 37, no. 1, pp. 1–14, 2018.
- [28] B. Yuan, F. Liao, Z. Z. Shi et al., "Dihydroartemisinin inhibits the proliferation, colony formation and induces ferroptosis of lung cancer cells by inhibiting PRIM2/SLC7A11 axis," *Oncotargets and Therapy*, vol. 13, article 10829, 10840 pages, 2020.
- [29] S. Yang, D. Zhang, N. Shen, G. Wang, Z. Tang, and X. Chen, "Dihydroartemisinin increases gemcitabine therapeutic efficacy in ovarian cancer by inducing reactive oxygen species," *Journal of Cellular Biochemistry*, vol. 120, no. 1, pp. 634–644, 2019.
- [30] A. L. Greenshields, T. G. Shepherd, and D. W. Hoskin, "Contribution of reactive oxygen species to ovarian cancer cell growth arrest and killing by the anti-malarial drug artesunate," *Molecular Carcinogenesis*, vol. 56, no. 1, pp. 75–93, 2017.
- [31] Y. Su, D. Zhao, C. Jin et al., "Dihydroartemisinin induces Ferroptosis in HCC by promoting the formation of PEBP1/15-LO," *Oxidative Medicine and Cellular Longevity*, vol. 2021, Article ID 3456725, 22 pages, 2021.
- [32] R. Lin, Z. Zhang, L. Chen et al., "Dihydroartemisinin (DHA) induces ferroptosis and causes cell cycle arrest in head and neck carcinoma cells," *Cancer Letters*, vol. 381, no. 1, pp. 165–175, 2016.
- [33] H. B. Ndagije, V. Nambasa, L. Manirakiza et al., "The burden of adverse drug reactions due to artemisinin-based antimalarial treatment in selected Ugandan health facilities: an active follow-up study," *Drug Safety*, vol. 41, no. 8, pp. 753–765, 2018.
- [34] B. Zani, M. Gathu, S. Donegan, P. L. Olliaro, D. Sinclair, and Cochrane Infectious Diseases Group, "Dihydroartemisinin-piperazine for treating uncomplicated plasmodium falciparum malaria," *Cochrane Database of Systematic Reviews*, vol. 1, 2014.
- [35] Y. Li, Y. K. Lin, X. H. Liu et al., "Leonurine: from gynecologic medicine to pleiotropic agent," *Chinese Journal of Integrative Medicine*, vol. 26, no. 2, pp. 152–160, 2020.
- [36] W. Meng, R. Li, and N. Zha, "Efficacy and safety of motherwort injection add-on therapy to carboprost tromethamine for prevention of post-partum blood loss: a meta-analysis of randomized controlled trials," *Journal of Obstetrics and Gynaecology Research*, vol. 45, no. 1, pp. 47–56, 2019.
- [37] W.-T. Xia, H. Zhou, Y. Wang et al., "Motherwort injection in preventing post-abortion hemorrhage after induced abortion: a multi-center, prospective, randomized controlled trial," *Explore*, vol. 16, no. 2, pp. 110–115, 2020.
- [38] H. Cheng, Y. Bo, W. Shen et al., "Leonurine ameliorates kidney fibrosis via suppressing TGF- β and NF- κ B signaling pathway in UUO mice," *International Immunopharmacology*, vol. 25, no. 2, pp. 406–415, 2015.
- [39] X. Liu, W. Cao, J. Qi et al., "Leonurine ameliorates adriamycin-induced podocyte injury via suppression of oxidative stress," *Free Radical Research*, vol. 52, no. 9, pp. 952–960, 2018.
- [40] S. A. Salama, M. S. Abdel-Bakky, and A. A. Mohamed, "Upregulation of Nrf2 signaling and suppression of ferroptosis and NF- κ B pathway by leonurine attenuate iron overload-induced hepatotoxicity," *Chemico-Biological Interactions*, vol. 356, article 109875, 2022.
- [41] J. Hu, W. Gu, N. Ma, X. Fan, and X. Ci, "Leonurine alleviates ferroptosis in cisplatin-induced acute kidney injury by activating the Nrf2 signalling pathway," *British Journal of Pharmacology*, vol. 179, no. 15, 2022.
- [42] H. Ding, G. Gao, L. Zhang et al., "The protective effects of curculigoside a on adjuvant-induced arthritis by inhibiting NF- κ B/NLRP3 activation in rats," *International Immunopharmacology*, vol. 30, pp. 43–49, 2016.
- [43] Q. Wu, D. X. Fu, A. J. Hou et al., "Antioxidative phenols and phenolic glycosides from *Curculigo orchoides*," *Chemical and Pharmaceutical Bulletin*, vol. 53, no. 8, pp. 1065–1067, 2005.
- [44] L. Wang, Y. J. He, T. Han et al., "Metabolites of curculigoside in rats and their antiosteoporotic activities in osteoblastic MC3T3-E1 cells," *Fitoterapia*, vol. 117, pp. 109–117, 2017.
- [45] Y. Wang, L. Zhao, Y. Wang et al., "Curculigoside isolated from *Curculigo orchoides* prevents hydrogen peroxide-induced dysfunction and oxidative damage in calvarial osteoblasts," *Acta Biochimica et Biophysica Sinica*, vol. 44, no. 5, pp. 431–441, 2012.
- [46] Q. Zhang, L. Zhao, Y. Shen et al., "Curculigoside protects against excess-iron-induced bone loss by attenuating Akt-FoxO1-dependent oxidative damage to mice and osteoblastic MC3T3-E1 cells," *Oxidative Medicine and Cellular Longevity*, vol. 2019, Article ID 9281481, 14 pages, 2019.

- [47] S. Wang, W. Liu, J. Wang, and X. Bai, "Curculigoside inhibits ferroptosis in ulcerative colitis through the induction of GPX4," *Life Sciences*, vol. 259, article 118356, 2020.
- [48] T. Liu, M. Zhang, H. Niu et al., "Astragalus polysaccharide from Astragalus Melittin ameliorates inflammation via suppressing the activation of TLR-4/NF- κ B p65 signal pathway and protects mice from CVB3-induced virus myocarditis," *International Journal of Biological Macromolecules*, vol. 126, pp. 179–186, 2019.
- [49] H. Xue, F. Gan, G. Qian et al., "Astragalus polysaccharides attenuate PCV2 infection by inhibiting endoplasmic reticulum stress in vivo and in vitro," *Scientific Reports*, vol. 7, pp. 1–12, 2017.
- [50] W. Li, X. Hu, S. Wang et al., "Characterization and anti-tumor bioactivity of astragalus polysaccharides by immunomodulation," *International Journal of Biological Macromolecules*, vol. 145, pp. 985–997, 2020.
- [51] O. A. Bamodu, K. T. Kuo, C. H. Wang et al., "Astragalus polysaccharides (PG2) enhances the M1 polarization of macrophages, functional maturation of dendritic cells, and T cell-mediated anticancer immune responses in patients with lung cancer," *Nutrients*, vol. 11, no. 10, p. 2264, 2019.
- [52] Y. Chen, J. Wang, J. Li et al., "Astragalus polysaccharide prevents ferroptosis in a murine model of experimental colitis and human Caco-2 cells via inhibiting NRF2/HO-1 pathway," *European Journal of Pharmacology*, vol. 911, article 174518, 2021.
- [53] Q. Nie, L. Zhu, L. Zhang, B. Leng, and H. Wang, "Astragaloside IV protects against hyperglycemia-induced vascular endothelial dysfunction by inhibiting oxidative stress and Calpain-1 activation," *Life Sciences*, vol. 232, article 116662, 2019.
- [54] S. Sheng, J. Xu, Q. Liang, L. Hong, and L. Zhang, "Astragaloside IV inhibits bleomycin-induced Ferroptosis in human umbilical vein endothelial cells by mediating LPC," *Oxidative Medicine and Cellular Longevity*, vol. 2021, Article ID 6241242, 15 pages, 2021.
- [55] A. Rauf, M. Imran, I. A. Khan et al., "Anticancer potential of quercetin: a comprehensive review," *Phytotherapy Research*, vol. 32, no. 11, pp. 2109–2130, 2018.
- [56] R. V. Patel, B. M. Mistry, S. K. Shinde, R. Syed, V. Singh, and H. S. Shin, "Therapeutic potential of quercetin as a cardiovascular agent," *European Journal of Medicinal Chemistry*, vol. 155, pp. 889–904, 2018.
- [57] S. Cui, Q. Wu, J. Wang, M. Li, J. Qian, and S. Li, "Quercetin inhibits LPS-induced macrophage migration by suppressing the iNOS/FAK/paxillin pathway and modulating the cytoskeleton," *Cell Adhesion & Migration*, vol. 13, no. 1, pp. 1–12, 2019.
- [58] I. B. S. Gomes, M. L. Porto, M. C. L. F. S. Santos et al., "The protective effects of oral low-dose quercetin on diabetic nephropathy in hypercholesterolemic mice," *Frontiers in Physiology*, vol. 6, p. 247, 2015.
- [59] Y. Wang, F. Quan, Q. Cao et al., "Quercetin alleviates acute kidney injury by inhibiting ferroptosis," *Journal of Advanced Research*, vol. 28, pp. 231–243, 2021.
- [60] D. Li, C. Jiang, G. Mei et al., "Quercetin alleviates ferroptosis of pancreatic β cells in type 2 diabetes," *Nutrients*, vol. 12, no. 10, p. 2954, 2020.
- [61] H. Wang, T. Zhang, W. Sun et al., "Erianin induces G2/M-phase arrest, apoptosis, and autophagy via the ROS/JNK signaling pathway in human osteosarcoma cells *in vitro* and *in vivo*," *Cell Death & Disease*, vol. 7, no. 6, pp. e2247–e2247, 2016.
- [62] Q. Zhu, Y. Sheng, W. Li et al., "Erianin, a novel dibenzyl compound in Dendrobium extract, inhibits bladder cancer cell growth via the mitochondrial apoptosis and JNK pathways," *Toxicology and Applied Pharmacology*, vol. 371, pp. 41–54, 2019.
- [63] Y.-T. Liu, M. J. Hsieh, J. T. Lin et al., "Erianin induces cell apoptosis through ERK pathway in human nasopharyngeal carcinoma," *Biomedicine & Pharmacotherapy*, vol. 111, pp. 262–269, 2019.
- [64] P. Chen, Q. Wu, J. Feng et al., "Erianin, a novel dibenzyl compound in dendrobium extract, inhibits lung cancer cell growth and migration via calcium/calmodulin-dependent ferroptosis," *Signal Transduction and Targeted Therapy*, vol. 5, no. 1, pp. 1–11, 2020.
- [65] S. Prasad, S. C. Gupta, A. K. Tyagi, and B. B. Aggarwal, "Curcumin, a component of golden spice: from bedside to bench and back," *Biotechnology Advances*, vol. 32, no. 6, pp. 1053–1064, 2014.
- [66] S. Prasad, A. K. Tyagi, and B. B. Aggarwal, "Recent developments in delivery, bioavailability, absorption and metabolism of curcumin: the golden pigment from golden spice," *Cancer Research and Treatment: Official Journal of Korean Cancer Association*, vol. 46, no. 1, pp. 2–18, 2014.
- [67] E. Pagano, B. Romano, A. A. Izzo, and F. Borrelli, "The clinical efficacy of curcumin-containing nutraceuticals: an overview of systematic reviews," *Pharmacological Research*, vol. 134, pp. 79–91, 2018.
- [68] A. B. Kunnumakkara, D. Bordoloi, G. Padmavathi et al., "Curcumin, the golden nutraceutical: multitargeting for multiple chronic diseases," *British Journal of Pharmacology*, vol. 174, no. 11, pp. 1325–1348, 2017.
- [69] R. Sahu, S. Batra, and S. Srivastava, "Activation of ATM/Chk1 by curcumin causes cell cycle arrest and apoptosis in human pancreatic cancer cells," *British Journal of Cancer*, vol. 100, no. 9, pp. 1425–1433, 2009.
- [70] T. Dorai, Y. C. Cao, B. Dorai, R. Buttyan, and A. E. Katz, "Therapeutic potential of curcumin in human prostate cancer. III. Curcumin inhibits proliferation, induces apoptosis, and inhibits angiogenesis of LNCaP prostate cancer cells *in vivo*," *The Prostate*, vol. 47, no. 4, pp. 293–303, 2001.
- [71] Y.-J. Surh, J. K. Kundu, and H.-K. Na, "Nrf2 as a master redox switch in turning on the cellular signaling involved in the induction of cytoprotective genes by some chemopreventive phytochemicals," *Planta Medica*, vol. 74, no. 13, pp. 1526–1539, 2008.
- [72] B. D'Autr aux and M. B. Toledano, "ROS as signalling molecules: mechanisms that generate specificity in ROS homeostasis," *Nature Reviews Molecular Cell Biology*, vol. 8, no. 10, pp. 813–824, 2007.
- [73] R. Li, J. Zhang, Y. Zhou et al., "Transcriptome investigation and *in vitro* verification of curcumin-induced HO-1 as a feature of ferroptosis in breast cancer cells," *Oxidative Medicine and Cellular Longevity*, vol. 2020, Article ID 3469840, 18 pages, 2020.
- [74] R. Zhang, T. Pan, Y. Xiang et al., "Curcumenol triggered ferroptosis in lung cancer cells via lncRNA H19/miR-19b-3p/FTH1 axis," *Bioactive materials*, vol. 13, pp. 23–36, 2022.
- [75] T. Kose, M. Vera-Aviles, P. A. Sharp, and G. O. Latundeda, "Curcumin and (–)-epigallocatechin-3-gallate protect murine MIN6 pancreatic beta-cells against iron toxicity and erastin-induced ferroptosis," *Pharmaceuticals*, vol. 12, no. 1, p. 26, 2019.

- [76] Q. Y. Eng, P. V. Thanikachalam, and S. Ramamurthy, "Molecular understanding of epigallocatechin gallate (EGCG) in cardiovascular and metabolic diseases," *Journal of Ethnopharmacology*, vol. 210, pp. 296–310, 2018.
- [77] L. Xing, H. Zhang, R. Qi, R. Tsao, and Y. Mine, "Recent advances in the understanding of the health benefits and molecular mechanisms associated with green tea polyphenols," *Journal of Agricultural and Food Chemistry*, vol. 67, no. 4, pp. 1029–1043, 2019.
- [78] J. Zhao, L. Xu, Q. Liang et al., "Metal chelator EGCG attenuates Fe(III)-induced conformational transition of α -synuclein and protects AS-PC12 cells against Fe(III)-induced death," *Journal of Neurochemistry*, vol. 143, no. 1, pp. 136–146, 2017.
- [79] H. Ding, Y. Li, W. Li et al., "Epigallocatechin-3-gallate activates the AMP-activated protein kinase signaling pathway to reduce lipid accumulation in canine hepatocytes," *Journal of Cellular Physiology*, vol. 236, no. 1, pp. 405–416, 2021.
- [80] Y.-F. Yao, X. Liu, W. J. Li et al., "(–)-Epigallocatechin-3-gallate alleviates doxorubicin-induced cardiotoxicity in sarcoma 180 tumor-bearing mice," *Life Sciences*, vol. 180, pp. 151–159, 2017.
- [81] H. He, L. Wang, Y. Qiao, B. Yang, D. Yin, and M. He, "Epigallocatechin-3-gallate pretreatment alleviates doxorubicin-induced ferroptosis and cardiotoxicity by upregulating AMPK α 2 and activating adaptive autophagy," *Redox Biology*, vol. 48, article 102185, 2021.
- [82] L.-W. Xie, S. Cai, T.-S. Zhao, M. Li, and Y. Tian, "Green tea derivative (–)-epigallocatechin-3-gallate (EGCG) confers protection against ionizing radiation-induced intestinal epithelial cell death both *in vitro* and *in vivo*," *Free Radical Biology and Medicine*, vol. 161, pp. 175–186, 2020.
- [83] J. Wang, Y. Chen, L. Chen et al., "EGCG modulates PKD1 and ferroptosis to promote recovery in ST rats," *Translational Neuroscience*, vol. 11, no. 1, pp. 173–181, 2020.
- [84] S. Nazari, M. Rameshrad, and H. Hosseinzadeh, "Toxicological effects of *Glycyrrhiza glabra* (licorice): a review," *Phytotherapy Research*, vol. 31, no. 11, pp. 1635–1650, 2017.
- [85] S. W. Mu, Y. Dang, Y. C. Fan et al., "Effect of HMGB1 and RAGE on brain injury and the protective mechanism of glycyrrhizin in intracranial-sinus occlusion followed by mechanical thrombectomy recanalization," *International Journal of Molecular Medicine*, vol. 44, no. 3, pp. 813–822, 2019.
- [86] Y. Liu, Y. Wang, J. Liu, R. Kang, and D. Tang, "The circadian clock protects against ferroptosis-induced sterile inflammation," *Biochemical and Biophysical Research Communications*, vol. 525, no. 3, pp. 620–625, 2020.
- [87] X. Chen, J. Zhang, B. Kim et al., "High-mobility group box-1 translocation and release after hypoxic ischemic brain injury in neonatal rats," *Experimental Neurology*, vol. 311, pp. 1–14, 2019.
- [88] K. Zhu, X. Zhu, S. Liu, J. Yu, S. Wu, and M. Hei, "Glycyrrhizin attenuates hypoxic-ischemic brain damage by inhibiting Ferroptosis and Neuroinflammation in neonatal rats via the HMGB1/GPX4 pathway," *Oxidative Medicine and Cellular Longevity*, vol. 2022, Article ID 8438528, 18 pages, 2022.
- [89] G. Xu, S. Fu, X. Zhan et al., "Echinatin effectively protects against NLRP3 inflammasome-driven diseases by targeting HSP90," *JCI insight*, vol. 6, no. 2, 2021.
- [90] R. Prasad and S. K. Katiyar, "Honokiol, an active compound of magnolia plant, inhibits growth, and progression of cancers of different organs," *Anti-inflammatory Nutraceuticals and Chronic Diseases*, vol. 928, 2016.
- [91] J. Pan, Y. Lee, Y. Wang, and M. You, "Honokiol targets mitochondria to halt cancer progression and metastasis," *Molecular Nutrition & Food Research*, vol. 60, no. 6, pp. 1383–1395, 2016.
- [92] C.-J. Lin, T. L. Chen, Y. Y. Tseng et al., "Honokiol induces autophagic cell death in malignant glioma through reactive oxygen species-mediated regulation of the p53/PI3K/Akt/mTOR signaling pathway," *Toxicology and Applied Pharmacology*, vol. 304, pp. 59–69, 2016.
- [93] C.-H. Lu, S. H. Chen, Y. S. Chang et al., "Honokiol, a potential therapeutic agent, induces cell cycle arrest and program cell death *in vitro* and *in vivo* in human thyroid cancer cells," *Pharmacological Research*, vol. 115, pp. 288–298, 2017.
- [94] C. Guo, P. Liu, G. Deng et al., "Honokiol induces ferroptosis in colon cancer cells by regulating GPX4 activity," *American Journal of Cancer Research*, vol. 11, no. 6, pp. 3039–3054, 2021.
- [95] X. Lai, Y. Sun, X. Zhang et al., "Honokiol induces Ferroptosis by upregulating HMOX1 in acute myeloid leukemia cells," *Frontiers in Pharmacology*, vol. 13, 2022.
- [96] J.-Y. Song, H. M. Luo, C. F. Li, C. Sun, J. Xu, and S. L. Chen, "Salvia miltiorrhiza as medicinal model plant," *Acta Pharmaceutica Sinica*, vol. 48, no. 7, pp. 1099–1106, 2013.
- [97] J. Xu, C. Zhang, X. Shi et al., "Efficacy and safety of sodium tanshinone IIA sulfonate injection on hypertensive nephropathy: a systematic review and meta-analysis," *Frontiers in Pharmacology*, vol. 10, p. 1542, 2019.
- [98] X. Wang, S. L. Morris-Natschke, and K. H. Lee, "New developments in the chemistry and biology of the bioactive constituents of Tanshen," *Medicinal Research Reviews*, vol. 27, no. 1, pp. 133–148, 2007.
- [99] X. Dong, J. Dong, G. Peng, X. Hou, and G. Wu, "Growth-inhibiting and apoptosis-inducing effects of Tanshinone II a on human gastric carcinoma cells," *Journal of Huazhong University of Science and Technology [Medical Sciences]*, vol. 27, no. 6, pp. 706–709, 2007.
- [100] C.-C. Su and T.-L. Chiu, "Tanshinone IIA decreases the protein expression of EGFR, and IGFR blocking the PI3K/Akt/mTOR pathway in gastric carcinoma AGS cells both *in vitro* and *in vivo*," *Oncology Reports*, vol. 36, no. 2, pp. 1173–1179, 2016.
- [101] C.-C. Su, "Tanshinone IIA inhibits gastric carcinoma AGS cells by decreasing the protein expression of VEGFR and blocking Ras/Raf/MEK/ERK pathway," *International Journal of Molecular Medicine*, vol. 41, pp. 2389–2396, 2018.
- [102] Z. Guan, J. Chen, X. Li, and N. Dong, "Tanshinone IIA induces ferroptosis in gastric cancer cells through p53-mediated SLC7A11 down-regulation," *Bioscience Reports*, vol. 40, no. 8, 2020.
- [103] L. Jiang, N. Kon, T. Li et al., "Ferroptosis as a p53-mediated activity during tumour suppression," *Nature*, vol. 520, no. 7545, pp. 57–62, 2015.
- [104] S. B. Erel, S. Demir, A. Nalbantsoy et al., "Bioactivity screening of five *Centaurea* species and *in vivo* anti-inflammatory activity of *C. aethoa*," *Pharmaceutical Biology*, vol. 52, no. 6, pp. 775–781, 2014.
- [105] L. M. Bedoya, M. J. Abad, and P. Bermejo, "The role of parthenolide in intracellular signalling processes: review of current knowledge," *Current Signal Transduction Therapy*, vol. 3, no. 2, pp. 82–87, 2008.

- [106] M. Han, B. Zheng, and D.-Q. Zhang, "Acetylbritannilactone suppresses NO and PGE₂ synthesis in RAW 264.7 macrophages through the inhibition of iNOS and COX-2 gene expression," *Life Sciences*, vol. 75, no. 6, pp. 675–684, 2004.
- [107] S. Dong, J. J. Tang, C. C. Zhang et al., "Semisynthesis and *in vitro* cytotoxic evaluation of new analogues of 1-*O*-acetylbritannilactone, a sesquiterpene from *Inula britannica*," *European Journal of Medicinal Chemistry*, vol. 80, pp. 71–82, 2014.
- [108] M. T. Heneka, M. J. Carson, J. E. Khoury et al., "Neuroinflammation in Alzheimer's disease," *The Lancet Neurology*, vol. 14, no. 4, pp. 388–405, 2015.
- [109] J.-J. Tang, L. F. Huang, J. L. Deng et al., "Cognitive enhancement and neuroprotective effects of OABL, a sesquiterpene lactone in 5xFAD Alzheimer's disease mice model," *Redox Biology*, vol. 50, p. 102229, 2022.
- [110] B. Zhai, N. Zhang, X. Han et al., "Molecular targets of β -elemene, a herbal extract used in traditional Chinese medicine, and its potential role in cancer therapy: a review," *Biomedicine & Pharmacotherapy*, vol. 114, article 108812, 2019.
- [111] Y. Pan, W. Wang, S. Huang et al., "Beta-elemene inhibits breast cancer metastasis through blocking pyruvate kinase M2 dimerization and nuclear translocation," *Journal of Cellular and Molecular Medicine*, vol. 23, no. 10, pp. 6846–6858, 2019.
- [112] P. Chen, X. Li, R. Zhang et al., "Combinative treatment of β -elemene and cetuximab is sensitive to KRAS mutant colorectal cancer cells by inducing ferroptosis and inhibiting epithelial-mesenchymal transformation," *Theranostics*, vol. 10, no. 11, pp. 5107–5119, 2020.
- [113] B. Zhai, Y. Zeng, Z. Zeng et al., "Drug delivery systems for elemene, its main active ingredient β -elemene, and its derivatives in cancer therapy," *International Journal of Nanomedicine*, vol. 13, pp. 6279–6296, 2018.
- [114] C.-W. Hsieh, J.-Y. Cheng, T.-H. Wang, H.-J. Wang, and W.-J. Ho, "Hypoglycaemic effects of *Ajuga* extract *in vitro* and *in vivo*," *Journal of Functional Foods*, vol. 6, pp. 224–230, 2014.
- [115] C.-W. Hsieh, W. C. Ko, W. J. Ho, C. K. Chang, G. J. Chen, and J. C. Tsai, "Antioxidant and hepatoprotective effects of *Ajuga nipponensis* extract by ultrasonic-assisted extraction," *Asian Pacific Journal of Tropical Medicine*, vol. 9, no. 5, pp. 420–425, 2016.
- [116] Q. Tan, Y. Fang, X. Peng, H. Zhou, J. Xu, and Q. Gu, "A new ferroptosis inhibitor, isolated from *Ajuga nipponensis*, protects neuronal cells via activating NRF2-antioxidant response elements (AREs) pathway," *Bioorganic Chemistry*, vol. 115, article 105177, 2021.
- [117] N. H. Thoenissen, G. B. Iwanski, N. B. Doan et al., "Cucurbitacin B induces apoptosis by inhibition of the JAK/STAT pathway and potentiates antiproliferative effects of gemcitabine on pancreatic cancer cells," *Cancer Research*, vol. 69, no. 14, pp. 5876–5884, 2009.
- [118] K. T. Chan, F. Y. Meng, Q. Li et al., "Cucurbitacin B induces apoptosis and S phase cell cycle arrest in BEL-7402 human hepatocellular carcinoma cells and is effective via oral administration," *Cancer Letters*, vol. 294, no. 1, pp. 118–124, 2010.
- [119] S. Huang, B. Cao, J. Zhang et al., "Induction of ferroptosis in human nasopharyngeal cancer cells by cucurbitacin B: molecular mechanism and therapeutic potential," *Cell Death & Disease*, vol. 12, no. 3, pp. 1–13, 2021.
- [120] Y. Xie, X. Zhou, J. Li et al., "Identification of a new natural biflavonoids against breast cancer cells induced ferroptosis via the mitochondrial pathway," *Bioorganic Chemistry*, vol. 109, article 104744, 2021.
- [121] Z. Gao, G. Deng, Y. Li et al., "Actinidia chinensis planch prevents proliferation and migration of gastric cancer associated with apoptosis, ferroptosis activation and mesenchymal phenotype suppression," *Biomedicine & Pharmacotherapy*, vol. 126, article 110092, 2020.
- [122] W. Zhang, B. Jiang, Y. Liu, L. Xu, and M. Wan, "Bufotalin induces ferroptosis in non-small cell lung cancer cells by facilitating the ubiquitination and degradation of GPX4," *Free Radical Biology and Medicine*, vol. 180, pp. 75–84, 2022.
- [123] S. Lu, X. Z. Wang, C. He et al., "ATF3 contributes to brucine-triggered glioma cell ferroptosis via promotion of hydrogen peroxide and iron," *Acta Pharmacologica Sinica*, vol. 42, no. 10, pp. 1690–1702, 2021.
- [124] Y. Xie, X. Song, X. Sun et al., "Identification of baicalein as a ferroptosis inhibitor by natural product library screening," *Biochemical and Biophysical Research Communications*, vol. 473, no. 4, pp. 775–780, 2016.
- [125] M. H. Ge, H. Tian, L. Mao et al., "Zinc attenuates ferroptosis and promotes functional recovery in contusion spinal cord injury by activating Nrf2/GPX4 defense pathway," *CNS Neuroscience & Therapeutics*, vol. 27, no. 9, pp. 1023–1040, 2021.
- [126] P. Liu, D. Wu, J. Duan et al., "NRF2 regulates the sensitivity of human NSCLC cells to cystine deprivation-induced ferroptosis via FOCAD-FAK signaling pathway," *Redox Biology*, vol. 37, article 101702, 2020.
- [127] Y. Ji, W. Si, J. Zeng et al., "Niujiadihuang detoxify decoction inhibits ferroptosis by enhancing glutathione synthesis in acute liver failure models," *Journal of Ethnopharmacology*, vol. 279, article 114305, 2021.
- [128] S. Zhang, S. Cao, H. Zhou et al., "Realgar induced nephrotoxicity via ferroptosis in mice," *Journal of Applied Toxicology*, 2022.
- [129] F. Huang, J. Pang, L. Xu et al., "Hedyotis diffusa injection induces ferroptosis via the Bax/Bcl2/VDAC2/3 axis in lung adenocarcinoma," *Phytomedicine*, vol. 104, article 154319, 2022.
- [130] F. Zhai, Q. C. Liang, Y. Y. Wu, J. Q. Liu, and J. W. Liu, "Red ginseng polysaccharide exhibits anticancer activity through GPX4 downregulation-induced ferroptosis," *Pharmaceutical Biology*, vol. 60, no. 1, pp. 909–914, 2022.
- [131] E. Habib, K. Linher-Melville, H.-X. Lin, and G. Singh, "Expression of xCT and activity of system x_c⁻ are regulated by NRF2 in human breast cancer cells in response to oxidative stress," *Redox Biology*, vol. 5, pp. 33–42, 2015.
- [132] P. Maher, K. van Leyen, P. N. Dey, B. Honrath, A. Dolga, and A. Methner, "The role of Ca²⁺ in cell death caused by oxidative glutamate toxicity and ferroptosis," *Cell Calcium*, vol. 70, pp. 47–55, 2018.

Research Article

lncRNA ZFAS1 Positively Facilitates Endothelial Ferroptosis via miR-7-5p/ACSL4 Axis in Diabetic Retinopathy

Yu Liu ^{1,2}, Zhengyu Zhang ¹, Jing Yang ³, Jingfan Wang ¹, Yan Wu ¹,
Rongrong Zhu ², Qinghuai Liu ¹ and Ping Xie ¹

¹Department of Ophthalmology, The First Affiliated Hospital of Nanjing Medical University, Nanjing 210029, China

²Department of Ophthalmology, The Affiliated Hospital of Nantong University, Nanjing 226000, China

³Nanjing University, Nanjing 210029, China

Correspondence should be addressed to Rongrong Zhu; zrrey@126.com, Qinghuai Liu; liuqh@njmu.edu.cn, and Ping Xie; xieping9@126.com

Received 6 July 2022; Revised 5 August 2022; Accepted 12 August 2022; Published 31 August 2022

Academic Editor: Yanqing Liu

Copyright © 2022 Yu Liu et al. This is an open access article distributed under the Creative Commons Attribution License, which permits unrestricted use, distribution, and reproduction in any medium, provided the original work is properly cited.

Accumulating evidence has suggested the significant role of long noncoding RNAs (lncRNA) in regulating ferroptosis, while its regulatory mechanism in diabetic retinopathy (DR) remains unelucidated. In this work, we first demonstrated that lncRNA zinc finger antisense 1 (ZFAS1) is upregulated in high glucose-cultured human retinal endothelial cells (hRECs) and ZFAS1 inhibition attenuated high glucose- (HG-) induced ferroptosis, which was evidenced by cell viability, total iron and ferrous iron levels, reactive oxygen species (ROS) level, and Glutathione Peroxidase 4 (GP_x4) expression detection. Mechanistically, we validated that ZFAS1 may act as a competing endogenous RNA by competitively binding with microRNA-7-5p (miR-7-5p) and modulating the expression of its downstream molecule acyl-CoA synthetase long-chain family member 4 (ACSL4), which is now identified as a classic driver gene of ferroptosis process. In conclusion, our results demonstrate that HG-induced ZFAS1 elevation activates ferroptosis in hRECs and the ZFAS1/miR-7-5p/ACSL4 axis may serve as a therapeutic target for endothelial dysfunction in DR.

1. Introduction

Diabetic retinopathy (DR) is a complication of diabetes mellitus which seriously affects visual health. The number of diabetes mellitus patients was estimated to be 9.3% (463 million people) globally in 2019 [1]. Approximately 30% of patients with diabetes mellitus deteriorate into DR, and the mechanism and treatment of DR have always been the focus of medical research [2–4]. It has been well documented that microvascular endothelial cells are sensitive targets of hyperglycemia [5, 6]. In nonproliferative stage of DR, excess microvascular cell death was observed to be involved in the subsequent diabetic neuropathy by cutting down blood supplies to nervous system [7–10]. Given the initial role of microvascular cell death in diabetic retinopathy progression, efforts should be made to prevent or slow down the retinal microvascular cell loss process.

Apoptosis is known to be a major contributor to endothelial cell death [11, 12]. However, several studies have pointed out that apoptosis itself cannot explain all the endothelial loss processes, making exploring new forms of cell death urgently needed [13–15]. Ferroptosis is a newly identified nonapoptosis cell death, characterized by lethal accumulation of intracellular iron and iron-induced lipid reactive oxygen species (ROS) [16, 17]. The overaccumulation of ROS production leads to an oxidative stress response in cells that causes unfold or misfold proteins and cytoplasmic swelling and eventually to cell death [18–20]. Accumulating evidence reported that ferroptosis is involved in diverse biological processes and diseases, including immune disease, cancer, and neurodegenerative diseases [21–24]. Intriguingly, ferroptosis processes share many similar features with diabetes-induced endothelial dysfunction, both characterized by reactive oxygen species (ROS) accumulation

and enhanced oxidative stress [25, 26]. Recently, Luo et al. reported that HG and interleukin-1 beta can induce human umbilical vein endothelial cells ferroptosis, which indicates that ferroptosis is involved in endothelial dysfunction [27]. However, the regulatory mechanism underlying the ferroptosis-mediated endothelial dysfunction has yet been elucidated.

A growing number of evidences have suggested that lncRNAs are involved in multiple biological processes through a number of different signaling pathways [28, 29]. lncRNA ZFAS1 is a lncRNA on chromosome 20 and has been reported to play either oncogenic or tumor suppressor role in different cancers [30–33], while its role in endothelial dysfunction requires further study. In our current study, we discovered that the expression level of lncRNA ZFAS1 was upregulated under hyperglycemia in both RNA sequencing dataset and in cultured hRECs. Further, our results revealed that ZFAS1 exerts its efforts by acting as a miR-7-5p sponge to regulate the ACSL4 expression. Recently, Zhuang et al. reported that upregulation of miR-7-5p promotes ferroptosis by regulating levels of transferrin receptor, uptake of iron, and production of lipid reactive oxygen species in cardiomyocyte [34]. Another group of researchers found that knockdown of miR-7-5p in malignant cells results in the downregulation of the iron storage gene expression such as ferritin as well as the upregulation of the ferroptosis marker gene expression [35]. ACSL4, a lipid metabolizing enzyme required for ferroptosis and a driver gene of ferroptosis process, catalyzes the linkage of long-chain poly-unsaturated fatty acids to coenzyme A and preferentially utilizes long PUFAs for functions in phospholipid biosynthesis [36, 37]. In this work, we provide new insights into the molecular function of ZFAS1 in DR, supporting the notion that ZFAS1 may serve as a therapeutic target for DR treatment. Moreover, we proved the potential diagnostic and therapeutic application of ZFAS1/miR-7-5p/ACSL4 axis in DR treatment.

2. Methods

2.1. Data Collection and Bioinformatics Analysis. GEO dataset was downloaded from GEO database (<http://www.ncbi.nlm.nih.gov/geo>). The GSE94019 dataset contained CD31⁺ endothelial cells isolated from nine fibrovascular membrane samples from patients with proliferative DR and four control retinal samples without diabetes diagnosis. The “limma” package in R was employed ($|\log_2(\text{FC})| = 0.5$ and $P < 0.05$) to process and identify the differentially expressed lncRNA.

2.2. Cell Culture. Primary hRECs were purchased from PromoCell (C-12200, Heidelberg, Germany), and all of the experiments were performed using 2–5 passages of hRECs. hRECs were grown in complete endothelial culture medium ECM (ScienCell, 1001) containing 1% endothelial cell growth supplement (ScienCell, 1052), 5% fetal bovine serum (Gibco, A3160802), and 1% penicillin/streptomycin solution (Gibco, 15140-122) at 37°C in a humidified atmosphere of 5% carbon dioxide. Cell culture plates and centrifuge tubes were purchased from NEST Biotechnology Co. Ltd. (Wuxi,

China). For high glucose cells, experiments indicated that the amount of D-glucose (MCE, HY-B0389) was added directly in ECM media to obtain a final concentration of 10, 15, 20, or 30 mM, and a hypertonic group (24.5 mM mannitol and 5.5 mM glucose) was added to exclude hyperosmolarity effects. To detect the role of ferroptotic signals in HG-induced endothelial dysfunction, hRECs were treated with 10 μM apoptosis inhibitor tauroursodeoxycholic acid (TUDCA) (MCE, 35807-85-3), 10 μM necrosis inhibitor necrostatin-1 (MCE, 4311-88-0), 10 μM ferroptosis inhibitor ferrostatin-1 (Fer-1) (MCE, HY-100579), and 10 μM pyroptosis inhibitor tetraethylthiuram disulfide (TETD) (MCE, 97-77-8) for 48 h.

2.3. Plasmid and shRNA Transfection. hRECs were plated in a 6-well plate with the density of 10^5 cells per well. The ZFAS1 shRNA (Sh-ZFAS1), miR-7-5p mimics/inhibitor, and blank plasmids were purchased from GenePharma (Shanghai, China). Transfection of miRNA mimics/inhibitor and shRNAs was conducted using Lipo 3000 transfection agent (Invitrogen) according to the manufacturer’s instruction. The shRNA sequences used in this study were presented in Supplementary Table 1. The pCDNA3.1-ZFAS1 plasmids were generated by inserting the ZFAS1 coding sequences into pCDNA3.1 empty vector (Invitrogen). After 18 h of starvation, the cells were transfected, and 72 hours later, the efficacies of this shRNA were validated by RT-qPCR before being used in subsequent experiments.

2.4. Cell Viability. Cell viability was performed using trypan blue staining method as previously described [38]. Briefly, cells were seeded in a 6-well plate at densities of 10^5 per well with 2 ml medium. After attachment, hRECs were transfected or treated with various plasmids and cultured for 48 h. $10 \mu\text{l}$ cell suspension was mixed up with $10 \mu\text{l}$ 0.1% trypan blue solution (Keygen, KGY015) and pipetted into a blood cell counting plate. To assess the cell viability in each experimental group, three randomly selected fields were counted manually by two experienced evaluators under a stereomicroscope.

2.5. Measurement of Lipid Peroxidation Levels. C11-BOD-IPY assay was used to assess lipid peroxidation according to the manufacturer’s instruction. Cells were seeded into 6-well dishes at a concentration of 10^6 cells per well. After treatment, cells were stained with BODIPY 581/591 C11 (Thermo Fisher Scientific, D3861) for 30 min at 37°C in the dark and then washed twice using PBS and then detected at an emission wavelength of 510 nm and an excitation wavelength of 488 nm.

2.6. Measurement of Total and Ferrous Iron. The measurement of total and ferrous iron level in cell samples was conducted using Iron Assay Kit (Sigma, Cat. # MAK025) [39]. Cells were plated at 1×10^5 cells/well in a six-well plate. 48 h later, cell samples were collected using $12,000 \times g$ centrifugation for 10 min at 4°C. In each group, $5 \mu\text{l}$ of assay buffer was first added in $50 \mu\text{l}$ sedimentation to measure total iron, and $5 \mu\text{l}$ of iron reducer buffer was then added to convert Fe^{3+} to Fe^{2+} , before being adjusted to a final

volume of 100 μ l per well in a 96-well plate with assay buffer. The plate was gently shaken for 30 min at room temperature. After, 100 μ l iron probe buffer was added in each well, and the system was shaken for another 60 min at room temperature. The plate was protected from light during the whole procedure, and the absorbance was measured at 593 nm on fluorescence microplate reader.

2.7. Dual-Luciferase Reporter Assay. The dual-luciferase reporter assay was performed to validate the interaction between lncRNA ZFAS1 and miR-7-5p, or between miR-7-5p and ACSL4. Briefly, wild-type and mutated 3'-untranslated region (3'-UTR) regions of ZFAS1 luciferase reporter gene vectors (named ZFAS1-WT and ZFAS1-MUT, respectively) were designed and synthesized by Guangzhou RiboBio Co., Ltd., China. The cells were transfected with miR-7-5p mimic or NC-mimic and the ZFAS1-WT or ZFAS1-MUT for 48 h. Cells were then lysed to detect luciferase activity using the dual-luciferase reporter assay system (Promega, Madison, MI, USA) according the manufacturer's instruction. Likewise, cells were transfected with miR-7-5p mimic or miR-NC and the ACSL4-WT or ACSL4-MUT for 48 h, before subsequent luciferase activity was detected.

2.8. Cellular Fractionation. To determine the subcellular localization of ZFAS1, hRECs were lysed on ice and fractionated using the Cell Fractionation Kit (Abcam, ab109719) following the manufacturer's instructions. Nuclear and cytoplasmic fractions were then analyzed by western blotting. GAPDH and U6 were utilized as cytoplasmic and nuclear markers, respectively.

2.9. RNA Fluorescence In Situ Hybridization. Specific fluorescence-conjugated probes for ZFAS1 were designed and synthesized by Life Technologies (Shanghai). The signals of the probe were detected by FISH Kit (GenePharma, Shanghai) according to the manufacturer's instructions. Nuclei were stained with DAPI. The images were monitored and captured using a Leica confocal microscopy (Leica Microsystems, Mannheim, Germany).

2.10. Western Blotting. Western blotting was performed as previously described [40]. After 72 hours of shRNA transfection, hRECs were washed once with ice-cold PBS and then resuspended in RIPA buffer (HY-K1001, MCE, USA) with protease and phosphatase inhibitors. The samples were then lysed by a constant vortex for 30 min at 4°C, after which the protein concentration of the supernatant was determined by the Pierce BCA protein assay kit (#23225, Thermo Fisher, USA). A total of 30 μ g protein samples were loaded on 10% sodium dodecyl sulfate-polyacrylamide gel electrophoresis gels, transferred to PVDF membrane (Merck-Millipore, USA), and blocked with 5% skim milk in TBST. The target proteins were immunodetected using GP_x4 (1:1000, ab125066, Abcam) and GAPDH (1:1000, A2228, Sigma) antibodies following overnight incubation at 4°C. The protein bands were detected by Chemistar substrate (Tanon, Nanjing). Bio-Rad Quantity One software was employed to quantify the intensity of the protein bands.

2.11. Quantitative Real-Time PCR. Total RNA from the cells was extracted using the TRIzol method (Invitrogen, 10296010) following the manufacturer's instructions. Total RNA (1.5 μ g) was reverse transcribed to cDNA by random hexamers and SuperScript IV (Invitrogen). Power SYBR-Green Mix (Thermo Fisher, 4367659) and StepOnePlus real-time PCR system (Applied Biosystems) were then used to quantify relative RNA ratio. Samples were biologically triplicated for mean \pm SEM. The primer sequences for RT-qPCR are listed in Supplementary Table 1, and GAPDH and U6 were used as internal references.

2.12. Diabetic Retinopathy Model. A total of 48 C57BL/6J male mice at six weeks old were purchased and randomly assigned to four groups: controls, diabetic, diabetic with sh-ZFAS1 transfection, and diabetic with sh-ZFAS1 transfection and miR-7-5p inhibitor ($n = 12$ in each group). Streptozotocin (STZ) (Sigma-Aldrich, 55 mg/kg) was injected intraperitoneally for 5 consecutive days to induce hyperglycemia, and controls were injected intraperitoneally with an equivalent volume of sodium citrate buffer [41–43]. All mice accepted intravitreal injection of plasmids (Sh-ZFAS1 or miR-7-5p inhibitor) or vehicles six weeks post the first STZ injection.

2.13. Isolation of CD31⁺ RECs Using Flow Sorting. RECs were isolated from the retinæ in four experimental groups using the flow sorting method as described before [44, 45]. In each experimental group, mice were euthanized, and their retinas were carefully enucleated for subsequent analysis. Retinæ were dissociated using 1 mg/ml type II collagenase (Worthington, cat. #LS004176), washed with DPBS three times, and then decanted through the 40- μ m strainer. After that, cells were labeled with isotype control or anti-CD31 antibody (Cat. No. 563607, BD Bioscience), kept in the dark, and incubated on ice for 30 min. After positive selection for CD31, cells were washed three times and subsequently sorted on a FACS Aria (BD Biosciences), and the CD31⁺ RECs were finally obtained.

2.14. Immunostaining Assay. To characterize the primary hRECs as shown in Supplementary Figure 1, cells were fixed in 4% paraformaldehyde (PFA) for 15 min and permeabilized with 0.5% Triton X-100 and 1% BSA for 15 min at room temperature. Cells were blocked with 5% BSA for 1 h and incubated overnight at 4°C with the anti-CD31 primary antibodies (1 μ g/ml, ab281583, Abcam). Cells were counterstained with DAPI (Southern Bio, 0100-20), mounted using LSM-880 confocal fluorescence microscope (Carl Zeiss, Jena, Germany). For in vivo experiments, the eyes in each group ($n = 6$) were enucleated carefully and processed for indirect immunofluorescence in whole-mount or cross-section as previously described [46]. For cryosections, the eyes ($n = 3$ retinæ from 3 mice) were fixed in 4% PFA at room temperature for 15 min. The frozen samples were then sliced transversely (6 μ m) at -20°C. For retinal flat-mounts, the eyes ($n = 3$ eyes from 3 mice) were fixed in 4% PFA at room temperature for 15 min, and the retinæ were dissected out as cups. Both cryosections and

retinal cups were blocked with PBS containing 0.5% Triton-X100 and 5% BSA at 4°C overnight and included with the anti-CD31 and anti-GP_x4 (1:100, ab125066, Abcam) primary antibodies.

2.15. Statistical Analysis. The data presented are representative of at least three independent experiments and are presented as mean ± SEM. Statistical analysis was performed in GraphPad. *P* values were determined by ANOVA with Tukey HSD post hoc test, and *P* value less than 0.05 was considered statistically significant. Pearson's correlation analysis analyzed the correlation between the ZFAS1 and miR-7-5p level in hRECs. Significance between samples is denoted as **P* < 0.05 and ***P* < 0.01.

3. Results

3.1. ZFAS1 Is Upregulated in hRECs under High Glucose. A total of 108 dysregulated lncRNAs were identified between the CD31⁺ endothelial cells isolated from nine fibrovascular membrane (FVM) samples and four control retinal samples without diabetes diagnosis using a differential gene expression analysis (Figure 1(a) and Supplementary Table 2). Among the significantly upregulated lncRNAs, ZFAS1 was chosen for further investigation for its previously reported role in promoting ferroptosis [47]. Given that hyperglycemia is now regarded as the primary cause of DR by activating subsequent interconnecting biochemical pathways, the expression levels of ZFAS1 were detected in low and high glucose-cultured hRECs. In consistent with RNA sequencing result from GSE94019 dataset (Figure 1(b)), RT-qPCR results validated that HG (25 mM and 30 mM) stimulation for 48 h generated high level of ZFAS1 expression compared with that under low glucose (LG) (5.5 mM) (Figure 1(c)).

3.2. ZFAS1 Knockdown Alleviates High Glucose-Induced Ferroptosis. It has been reported that lncRNA ZFAS1 can promote ferroptosis and finally accelerates the progression of pulmonary fibrosis; one can expect that ZFAS1 may be associated with hyperglycemia-induced endothelial dysfunction, which is also associated with ferroptosis processes according to previous studies [27]. In line with Luo et al.'s study, cell viability of hRECs was compromised, and the iron accumulation was aggravated under HG for 48 h (Figures 2(a)–2(c)). C11-BODIPY probe was employed to assess the lipid peroxidation level as described before [48]. An increase of oxidated to unoxidated C11 ratio was observed after HG treatment, suggesting the ability of HG condition to induce lipid peroxidation-related ferroptosis (Figures 2(d) and 2(e)). As the sole enzyme in mammalian cells to eliminate lipid ROS, the expression level of GP_x4 determines cell fate upon ferroptotic signals [49]. As shown in Figure 2(f), HG treatment dramatically downregulated the protein abundance of ferroptosis-associated gene GP_x4. Moreover, all the above changes could be reversed by ferroptosis inhibitor ferrostatin-1 but not by TUDCA, necrostatin-1, and TETD (inhibitors of apoptosis, necrosis, and pyroptosis, respectively), except for the cell viability downregulation was rescued by ferrostatin-1 and TUDCA treatment, indicat-

ing the crucial role of ferroptosis process in HG-induced endothelial dysfunction. In addition, quantification of the GP_x4 intensity showed that the GP_x4 protein level was higher in HG+shZFAS1 group compared to HG+Fer-1 group, while the lipid peroxidation level in these two groups showed no significant difference. This asynchronism indicated that there may exist other mechanisms involved in the Fer-1 preventing the accumulation of lipid peroxidation products, apart from its reported role in maintaining GP_x4 expression [50, 51]. It is worth noting that both quantifications of lipid ROS and GP_x4 expression here cannot be used as the determinants to assess ferroptosis activity separately. The precise mechanism under this asynchronism requires further investigations.

To further determine whether the upregulation of ZFAS1 is involved in HG-induced ferroptosis, Sh-ZFAS1 as well as its scramble control (Sh-NC) was transfected into hRECs. Cell viability assay revealed that depletion of ZFAS1 significantly restored the cell viability repressed by HG. Moreover, ZFAS1 silencing resulted in the deactivation of ferroptosis, as reflected by significantly diminished lipid peroxidation level and relatively high levels of GP_x4 expression. Altogether, our results demonstrate that ZFAS1 knockdown alleviates high glucose-induced ferroptosis in hRECs.

3.3. ZFAS1 Served as miR-7-5p Sponge. Evidence has confirmed that lncRNAs act as competing endogenous RNAs (ceRNAs) by competing for binding to microRNAs. To obtain insight into the regulatory mechanism for the observed ferroptosis promoting phenotypes of ZFAS1, we further tested the downstream signal. A total of 69 miRNAs were identified to interact with ZFAS1 using starBase database (Supplementary Table 3), among which miR-7-5p was chosen for further evaluation for its reported role in regulating ferroptosis in various cell types, including cardiomyocyte, malignant HeLa cells, and clinically relevant radioresistant cancer cells [34, 35, 52]. Dual-luciferase reports assay was performed to verify the potential combination between ZFAS1 and miR-7-5p (Figures 3(a) and 3(b)). Subsequently, the subcellular distribution of ZFAS1 in hRECs was validated using subcellular fractionation and fluorescence in situ hybridization (FISH) assays. As shown in Figures 3(c) and 3(d), subcellular fractionation and FISH results both revealed that ZFAS1 was mainly localized in the cytoplasm of hRECs. Moreover, we also observed that the expression of miR-7-5p in hRECs was significantly repressed after ZFAS1 overexpression, indicating the negative regulation of ZFAS1 on miR-7-5p (Figure 3(e)).

Further, the potential target genes of miR-7-5p were predicted using predictive datasets miRDB, DIANA, miRmap, and PicTar (<http://mirdb.org/>; http://carolina.imis.athena-innovation.gr/diana_tools/web/index.php; <https://mirmap.ezlab.org/>; <https://pictar.mdc-berlin.de/>) (Figures 3(f) and 3(g) and Supplementary Table 4). ACSL4 was chosen for subsequent experiments for its previously reported roles in inducing ferroptosis in retinal pigmented epithelial cells in DR. Luciferase activity assay showed that the luciferase

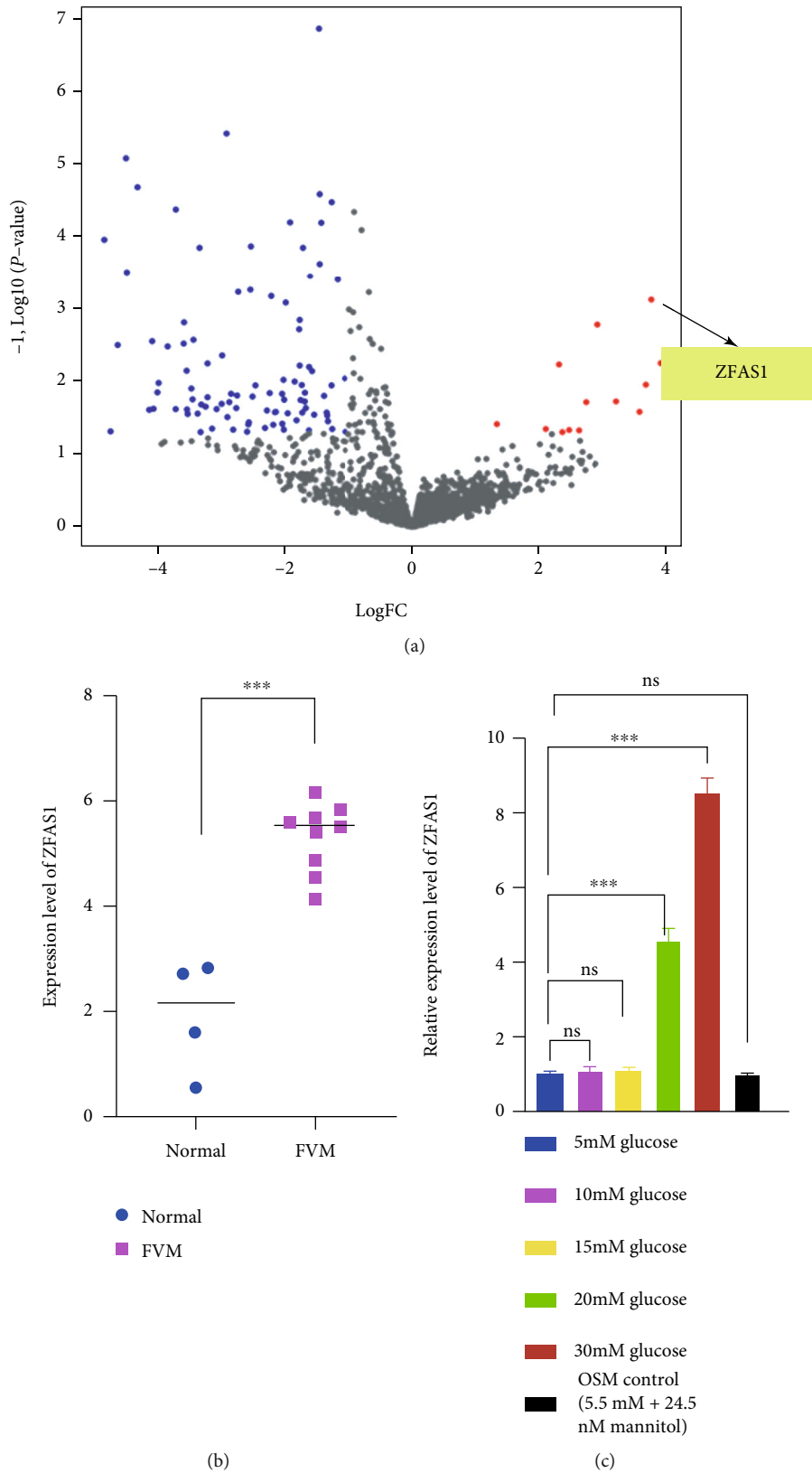


FIGURE 1: ZFAS1 is upregulated in hRECs under HG and in FVM tissues. (a) The volcano map of differentially expressed lncRNAs in GEO: GSE94019. (b) The expression level of lncRNA ZFAS1 in endothelial cells isolated from FVM samples and healthy control retinal samples. (c) RT-PCR was performed to detect the ZFAS1 expression cultured in LG (5.5 mM), HG (10, 15, 20, and 30 mM), or hypertonic control group (5.5 mM glucose and 24.5 mM mannitol) medium for 48 h. $n = 5$ replicates. Data are presented as \pm SEM. *** $P < 0.001$.

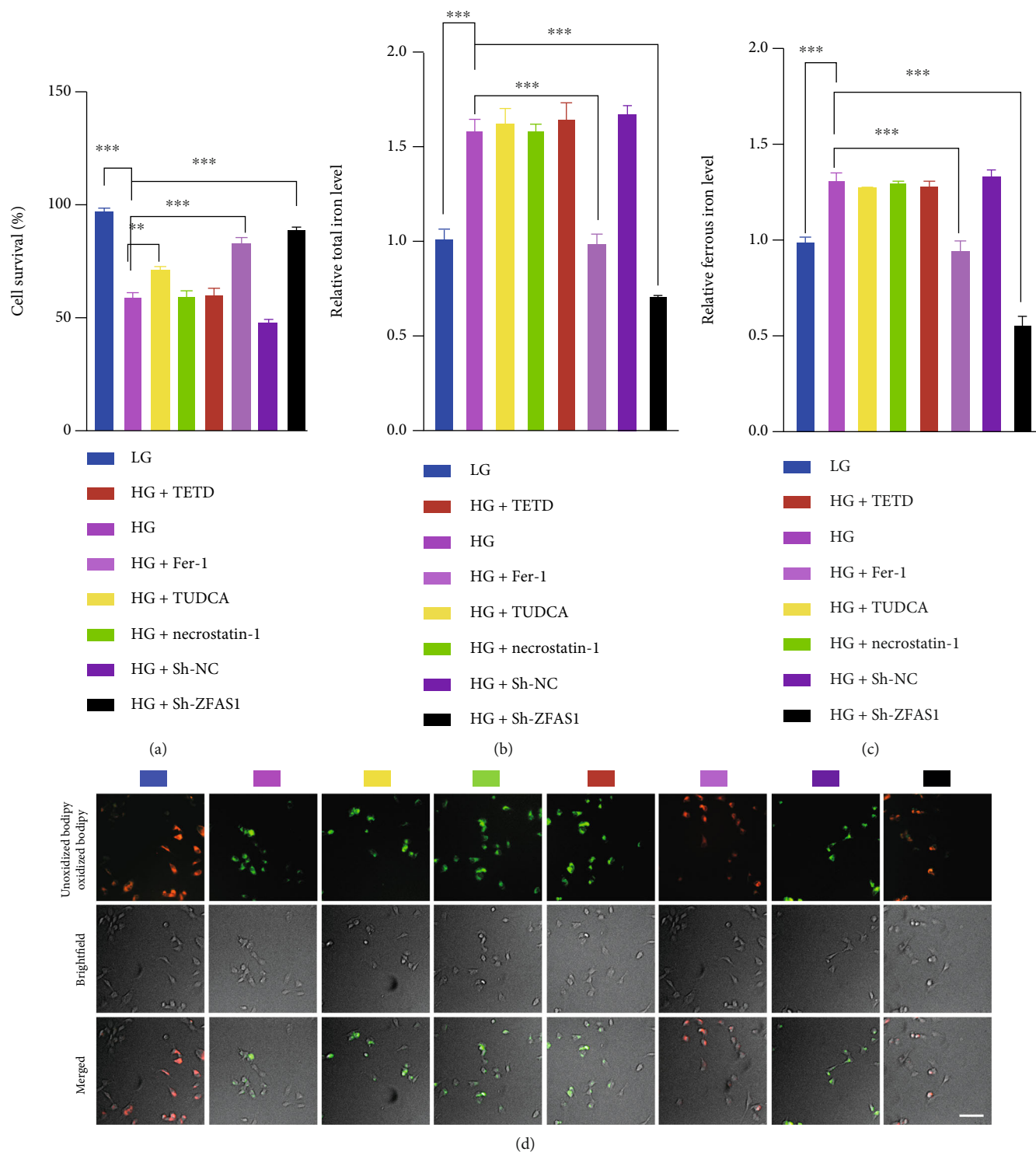


FIGURE 2: Continued.

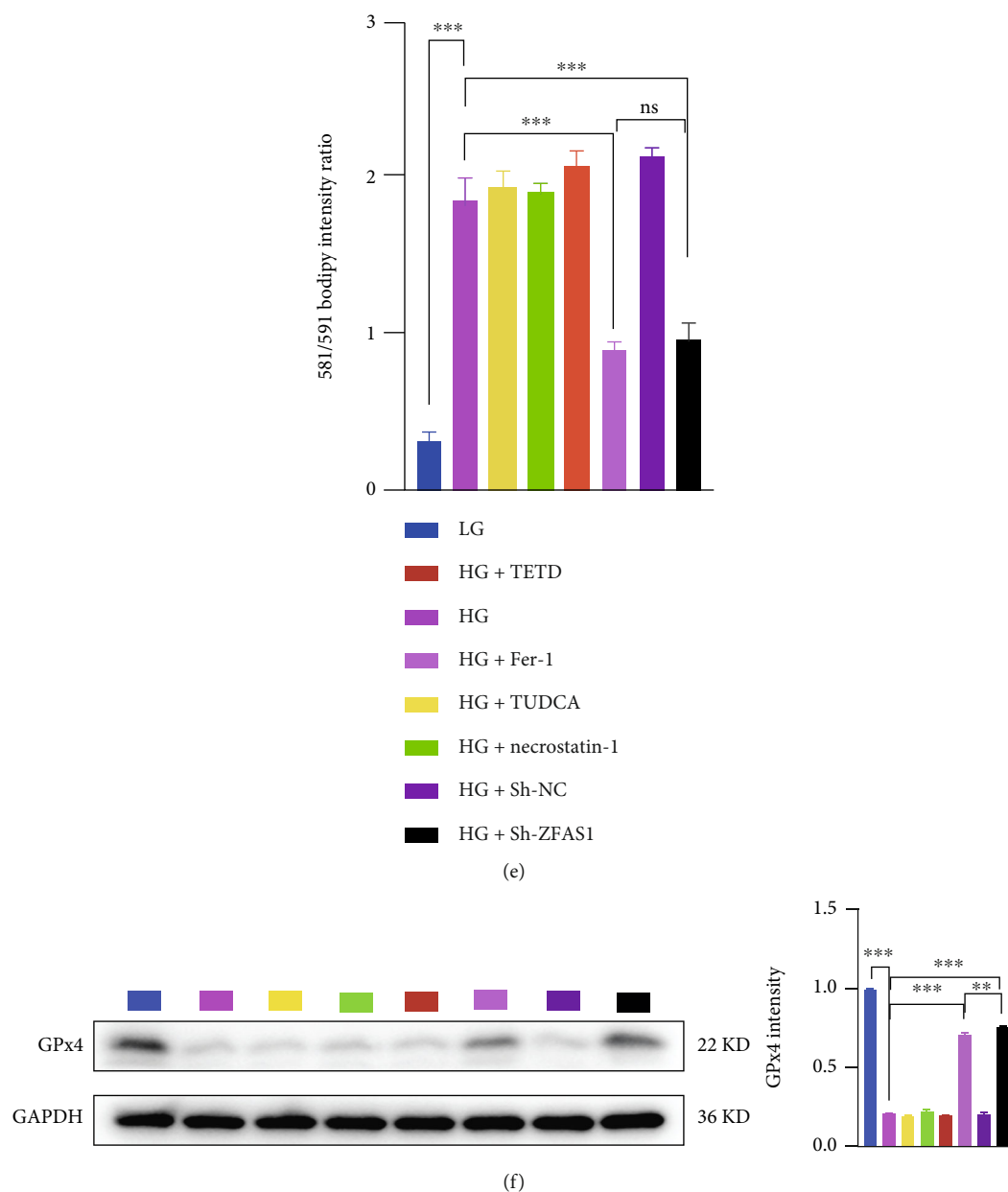


FIGURE 2: Inhibition of ZFAS1 rescued HG-induced ferroptosis in hRECs. (a) Both apoptosis inhibitor TUDCA and ferroptosis inhibitor Fer-1 administration rescued the downregulated cell viability in HG group. Compared to HG control, there is no difference in total (b) or ferrous iron level (c), lipid hydroperoxide accumulation (d and e), nor GPx4 expression level (f) after 10 μ M apoptosis inhibitor TUDCA, necrosis inhibitor necrostatin-1, pyroptosis inhibitor TETD treatment for 48 h, while transfection of Sh-ZFAS1 remarkably lightened the above ferroptosis phenotypes. $n = 5$ replicates. $P > 0.05$. 10 μ M Fer-1 treatment for 48 h notably ameliorated the HG-induced ferroptosis-related phenotypes indicated above. $n = 5$ replicates. Data are presented as \pm SEM. Ns: no significant; ** $P < 0.01$ and *** $P < 0.001$. Scale bar, 50 μ m.

activity of ACSL4-WT was inhibited by miR-7-5p mimics, while ACSL4-MUT not affected (Figure 3(h)).

3.4. ZFAS1 Promoted Ferroptosis through miR-7-5p/ACSL4 Axis. To investigate whether ZFAS1 exerts its role through miR-7-5p/ACSL4 axis, hRECs were transfected with Sh-ZFAS1 or together with miR-7-5p inhibition (Inhi-miR-7-5p). As shown in Figures 4(a) and 4(b), RT-qPCR showed that Sh-ZFAS1 transfection restored the repressed expression level of ACSL4 under HG, whereas the Inhi-miR-7-5p

downregulated its expression by approximately six times. We further compared the ferroptosis-related phenotypes in the above experimental groups. Transfection of Sh-ZFAS1 resulted in a relatively higher cell viability and less total and ferrous iron level in hRECs compared with their negative controls, while miR-7-5p depletion brought them all to a basal level (Figures 4(c)–4(e)). Collectively, C11-BODIPY assay showed that lipid peroxidation level was significantly elevated, and the GPx4 expression was downregulated following knockdown of the miR-7-5p, both indicating the

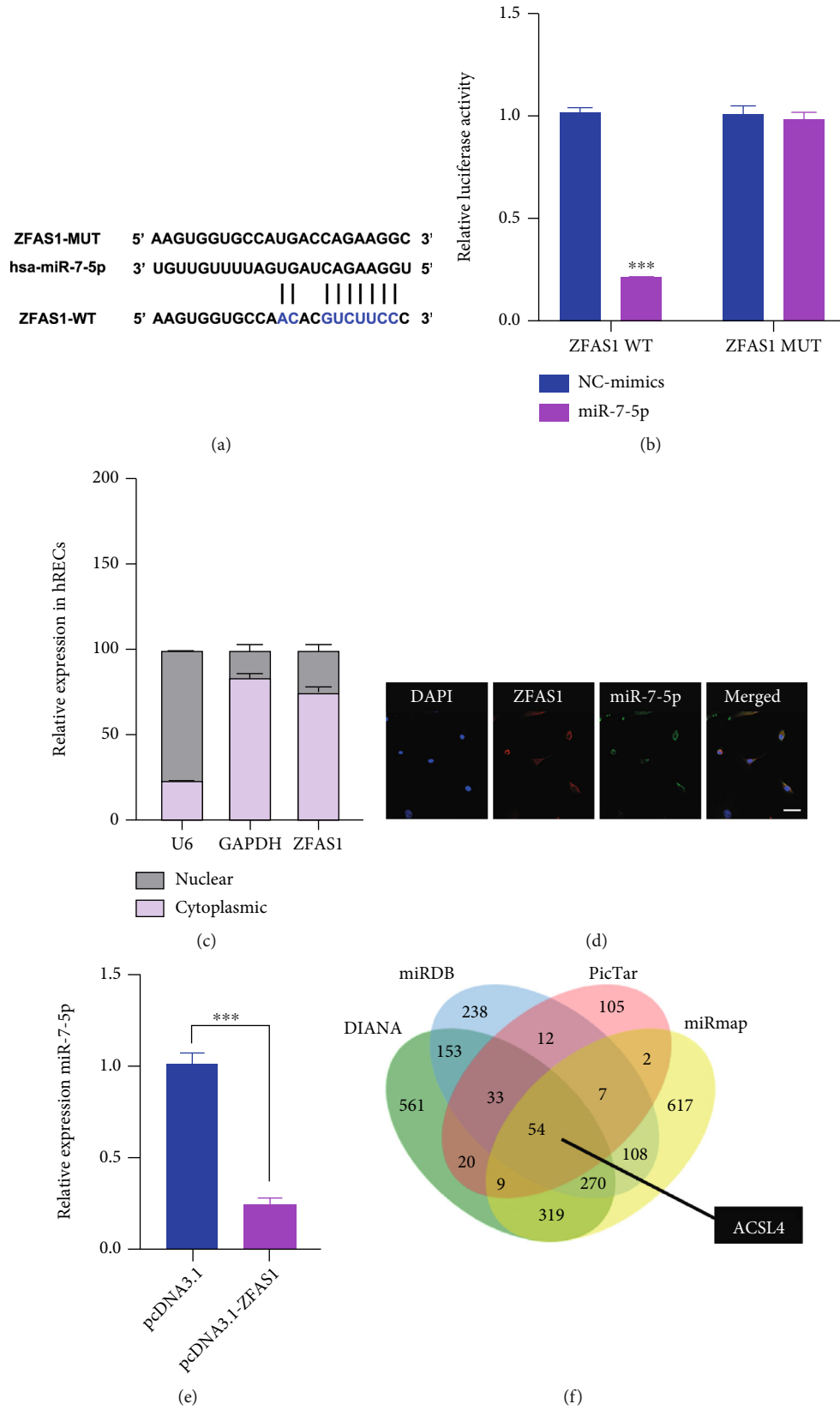


FIGURE 3: Continued.

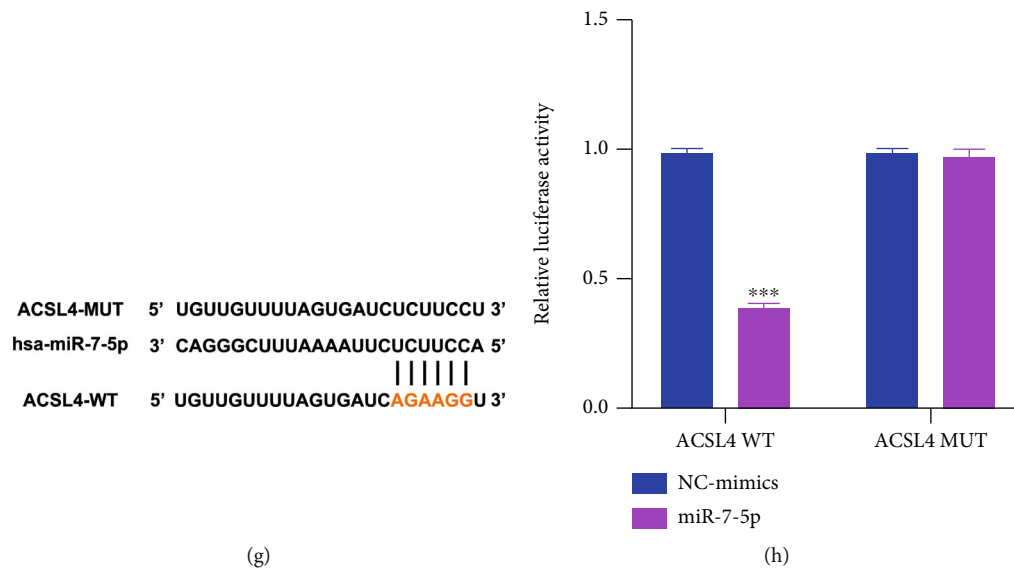


FIGURE 3: ZFAS1 regulates ACSL4 expression by directly interacting with miR-7-5p. (a) The binding sites of ZFAS1 with miR-7-5p as predicted by starBase. (b) Transfection of miR-7-5p mimics remarkably attenuated the luciferase activity of ZFAS1-WT compared with negative control groups. (c) RT-qPCR was employed to detect the expression of lncRNA ZFAS1 in the cytoplasm and nucleus of hRECs. GAPDH and U6 served as cytoplasmic and nuclear markers, respectively. $n = 5$ in each group. (d) Colocalization between ZFAS1 (labeled in red) and miR-7-5p (labeled in green) was observed by RNA FISH in hRECs. Scale bar, $25 \mu\text{m}$. (e) hRECs were transfected with empty vector pcDNA3.1 or pcDNA3.1-ZFAS1 for 48 h, and the expression level of miR-7-5p was validated using RT-qPCR. miR-39-3p served as an exogenous normalization. $n = 5$ in each group. (f) Five different datasets were utilized to predict the downstream molecule of miR-7-5p. (g) The binding sites of miR-7-5p with ACSL4 as predicted by starBase. All data are presented as \pm SEM. *** $P < 0.001$. (h) miR-7-5p mimics remarkably attenuated the luciferase activity of ACSL4-WT compared with negative control groups.

activation of ferroptosis processes (Figures 4(f)–4(g)). Western blotting result revealed that the HG-brought ACSL4 overexpression was restrained by ZFAS1 silencing, and this effect was largely reversed by miR-7-5p inhibition (Figure 4(h)). Of note, we overexpress GP_x4 to further detect whether it can influence the miR-7-5p/ACSL4 axis. As validated in Supplementary Figure 2, the expression level of miR-7-5p as well as ACSL4 was not detectably altered after GP_x4 overexpression, indicating that GP_x4 is more likely a downstream molecule of ZFAS1/miR-7-5p/ACSL4 axis. Taken together, these results imply that ZFAS1 may modulate ferroptosis-mediated endothelial dysfunction through ACSL4, a well-recognized promoter of ferroptosis, by sponging miR-7-5p [53–55].

3.5. ZFAS1/miR-7-5p/ACSL4 Axis Modulates Endothelial Ferroptosis in Diabetic Mice Retinae. Considering that STZ-induced diabetic mouse is a well-recognized animal model of diabetic retinopathy, we next investigated the effects of ZFAS1/miR-7-5p/ACSL4 axis on endothelial ferroptosis using the STZ mouse model as described before (Figure 5(a)). A total of 48 male mice were assigned to four treatment groups: WT, STZ, Sh-ZFAS1+STZ, and Sh-ZFAS1+Inhi-miR-7-5p+STZ ($n = 12$ in each group). After being isolated from the retinae in four experimental groups using the flow sorting, RECs in each group were subjected to RT-qPCR analysis to have transfection efficiency of Sh-ZFAS1 and Inhi-miR-7-5p evaluated (Figures 5(b) and 5(c)). In line with what we observed *in vitro*, the restraining

effect of Sh-ZFAS1 on ACSL4 expression was dramatically abolished after inhi-miR-7-5p treatment, as demonstrated by RT-qPCR and western blotting analysis (Figures 5(d) and 5(e)). Next, retinal flat mounts as well as the cross section revealed that five consecutive days of STZ injection produced classical retinal vascular leakage in six-week-old mice when their retinae were collected at D70 [56]. The downregulation of GP_x4 expression were observed in all STZ groups, and intravitreally injection of Sh-ZFAS1 markedly rescued the GP_x4 expression loss, which was further blocked by miR-7-5p inhibition (Figures 5(f) and 5(g)). Taken together, our data indicates that elevated ZFAS1 expression level in STZ mice is responsible for excess oxidative environment in RECs and implies the important modulatory roles played by ZFAS1/miR-7-5p/ACSL4 axis in ferroptosis process.

4. Discussion

Among the current treatments of DR, the first and foremost is controlling blood sugar. Multiple evidence has pointed out that changing lifestyle, ameliorating insulin resistance, and repairing damaged β islet cell function can effectively delay the occurrence of DR [57–59]. DR is now recognized as a neuro- and vaso-degenerative rather than a microvascular disease, even in early stage when neuron loss is not evident [60, 61]. Recently, the crucial role of ferroptotic cell death has been noted in various neurodegenerative diseases, especially in Alzheimer's disease and Parkinson's disease, while its role in DR is largely unknown [62–65]. Here, we provide

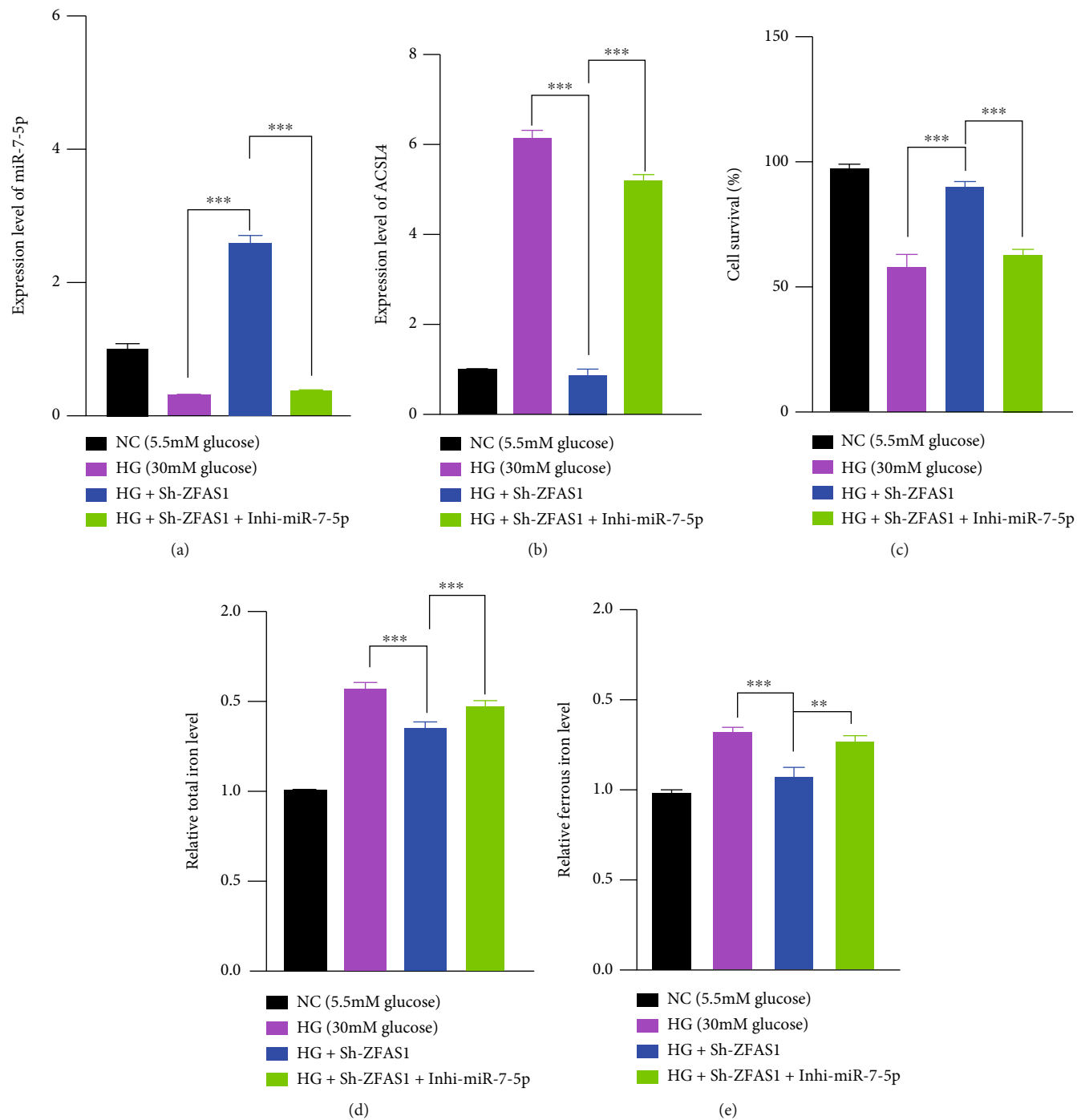


FIGURE 4: Continued.

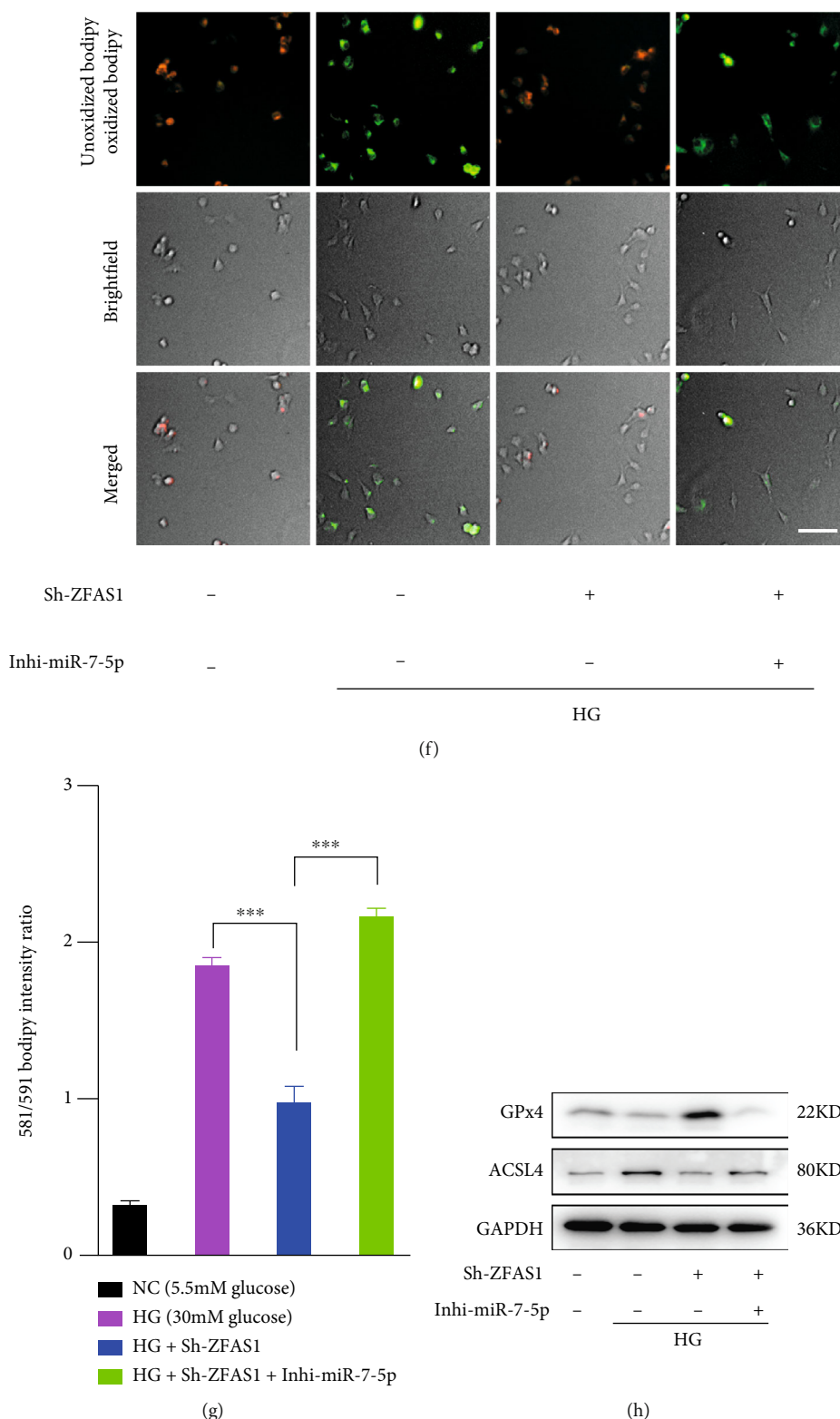


FIGURE 4: The effect of ZFAS1 silencing on preventing ferroptosis was abolished by dual knockdown of ZFAS1 and miR-7-5p. RT-qPCR results demonstrated the miR-7-5p (a) and ACSL4 expression level (b). GAPDH and miR-39-3p served as endogenous and exogenous normalization for ACSL4 and miR-7-5p detection, respectively. $n = 5$ replicates. Data are presented as \pm SEM. *** $P < 0.001$. (c–g) hRECs were transfected with $50 \mu\text{M}$ Sh-ZFAS1 or together with $50 \mu\text{M}$ miR-7-5p inhibition, and the cell viability (c), total (d), ferrous iron level (e), and lipid hydroperoxide accumulation (f and g) were assessed 72 hours after the transfection. $n = 5$ replicates. Data are presented as \pm SEM. *** $P < 0.001$. Scale bar, $50 \mu\text{m}$. (h) Analysis of GPx4 and ACSL4 expression level.

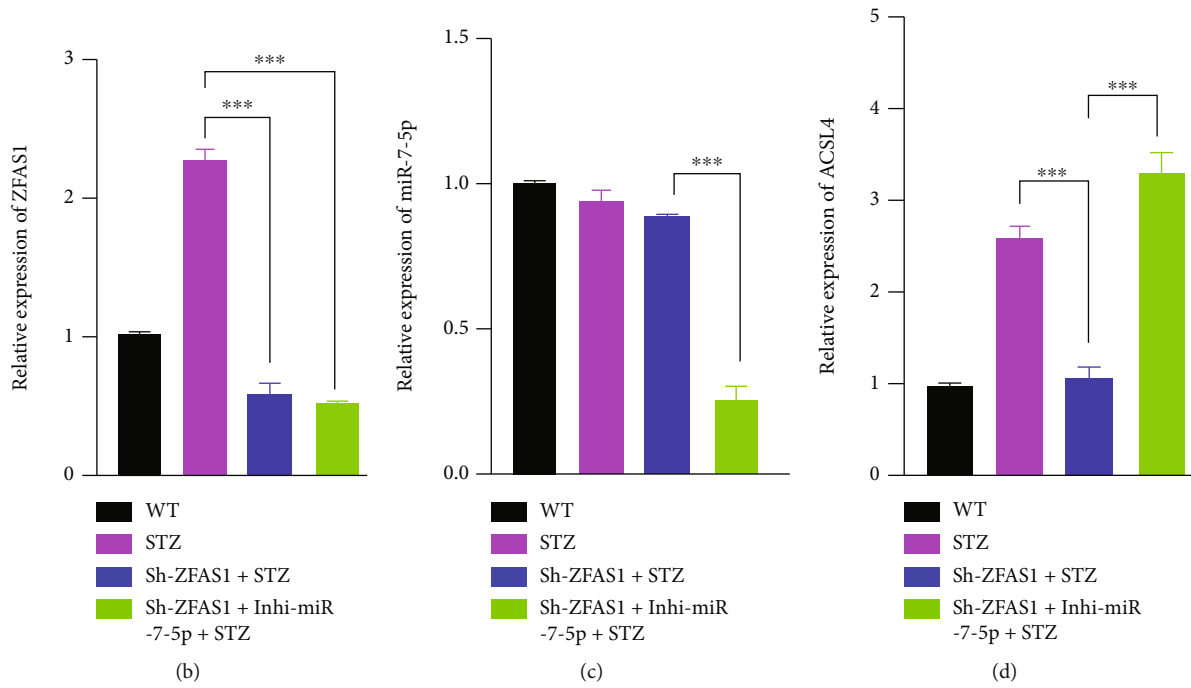
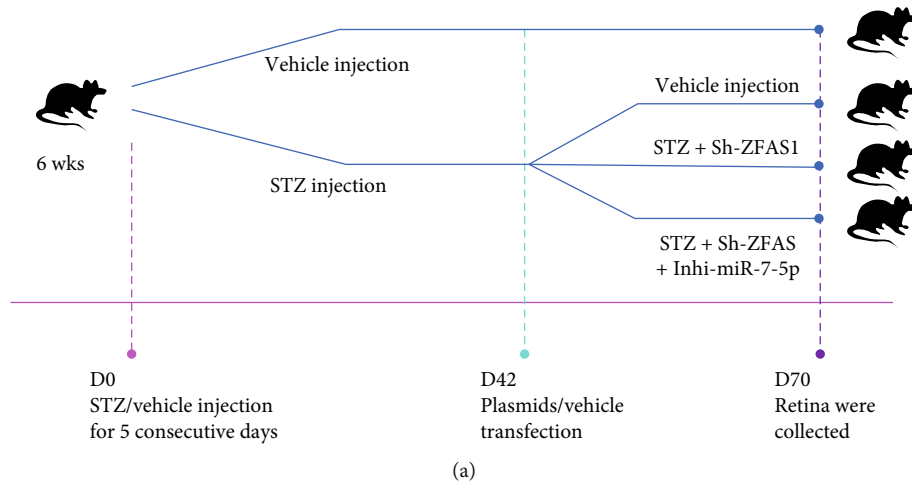


FIGURE 5: Continued.

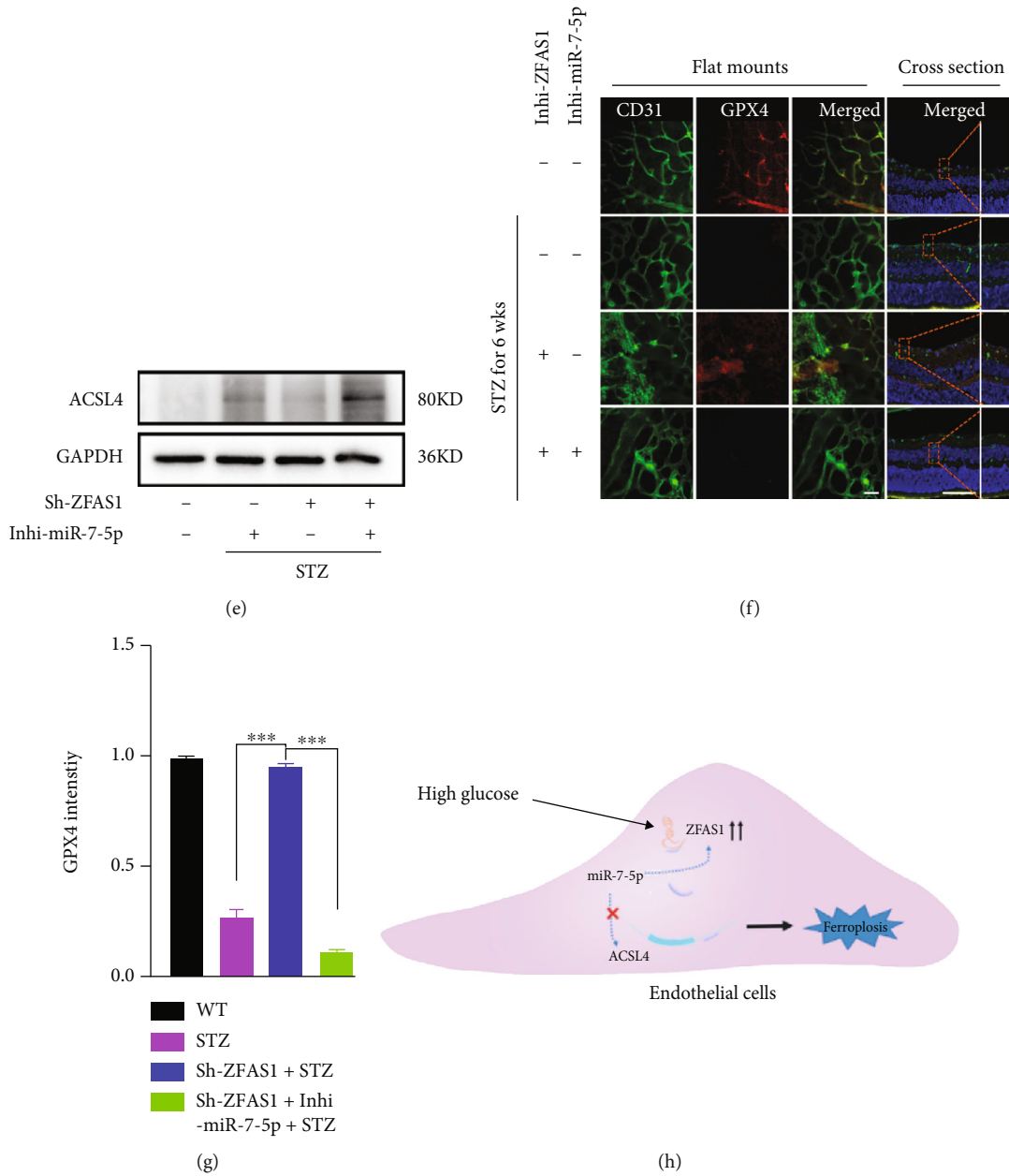


FIGURE 5: miR-7-5p knockdown partially reverses the functional effect of ZFAS1 knockdown on endothelial ferroptosis in DR mice. (a) Schematic representation of STZ administration. C57BL/6J male mice at 6 weeks old were randomly separated into four experimental groups. Streptozotocin was injected intraperitoneally at a final concentration of 55 mg/kg for 5 consecutive days to induce diabetes, and all diabetic mice were fed with high-fat diet subsequently. Six weeks after the final injection, indicated plasmids (including 100 nM Sh-ZFAS1 and 50 nM Inhi-miR-7-5p) or vehicles were intravitreally injected once a week for four weeks. RT-qPCR validated the expression level of ZFAS1 (b), miR-7-5p (c), and ACSL4 (d). (e) Western blotting analysis validated the ACSL4 protein level. (f) Immunofluorescence assay for GPx4 (labelled red) expression in mouse retinal endothelial cell (labelled green). Scale bar for retinal flat mounts, 50 μ m. Scale bar for retinal cross section, 50 μ m. (g) Quantification of GPx4 intensity. Data are presented as \pm SEM. *** $P < 0.001$. (h) The summary diagram. ZFAS1 was induced under HG condition. It functioned as a “ceRNA” by sponging miR-7-5p, thus upregulating ACSL4 expression and accelerating ferroptosis-related endothelial dysfunction in DR. All data are presented as \pm SEM. *** $P < 0.001$.

the first evidence that in DR, hyperglycemia causes endothelial dysfunction via activating ferroptosis and ZFAS1/miR-7-5p/ACSL4 axis may serve as a key signaling in ferroptosis process.

Reactive oxygen species (ROS) are mainly produced during mitochondrial oxidative metabolism and decisively

contribute to multiple cellular signaling pathways, affecting almost all aspects of cellular function including gene expression, proliferation, migration, and cell death [66, 67]. Normally, retinal cells maintain a balance between pro- and antioxidative signaling [68–70]. In diabetes, ROS production in the retina is significantly increased and further

exacerbated by the collapse of antioxidant defensive system, including superoxide dismutase (SOD2) and glutathione peroxidase (GP_x4) [71–74]. In our current work, both total and intercellular ROS in hRECs were elevated, and the expression of GP_x4 was significantly compromised under hyperglycemia, indicating the highly oxidative environment in endothelial cells under HG. Besides, the ROS level acts as an important promotor of lipid peroxidation-induced ferroptosis [75, 76]. It has been suggested that oxidants may participate in ferroptosis by altering the physical properties of lipid bilayers or increasing membrane curvature and membrane damage through micelle formation [77–79]. In the present study, hyperglycemia-induced ROS accumulation was alleviated by Fer-1 administration. Combined, our data reveals that ferroptosis plays a crucial role in ROS-induced endothelial damage in DR.

ZFAS1 partakes in the pathogenesis of diverse human disorders, including in neurodegenerative disorders, immune responses, and cancer [80–82]. Given that it is mainly localized in cytoplasm, ZFAS1 exerts its effect mostly as a molecular sponge for many miRNAs and ultimately alters the stability and translation of cytoplasmic mRNAs [83, 84]. For instance, it was previously proposed that ZFAS1 acts as an oncogene via sponging miR-329 to facilitate bladder cancer tumorigenesis [85]. Although the targeting site of miR-7-5p on ZFAS1 was validated in nasopharyngeal carcinoma cells [86], very limited efforts have been made in reporting the role, nor the molecular mechanism of ZFAS1 in ocular diseases. Here, we report for the first time that in DR, ZFAS1 expression was upregulated in hRECs. More importantly, our data reveals that high ZFAS1 level induces ROS accumulation and ferroptosis, in agreement with the previous work [47].

Of note, ACSL4, a key positive regulator and biomarker in ferroptosis, was found to be a target gene of ZFAS1/miR-7-5p axis [87]. ACSL4 is required for the production of poly-unsaturated fatty acids required for the execution of ferroptosis. Yuan et al. once reported that ACSL4 depletion by specific shRNA enhances resistance to erastin-induced ferroptosis in cancer cells [88]. By contrast, increase of ACSL4 promotes ferroptosis via activating NF2-YAP signaling [89]. More recently, researchers have indicated the key role of ACSL4 in the onset of DR. The expression level of ACSL4 was found upregulated in retinal pigmental epithelial cells in the early stage of DR, and cells transfected with ACSL4-siRNA were much more resistant to high glucose-induced ferroptosis [90]. In line with the previous report, we noticed that ZFAS1 silencing as well as the miR-7-5p overexpression ameliorated the glucose-induced endothelial ferroptosis phenotypes via downregulating the ACSL4 expression, indicating that the ZFAS1/miR-7-5p/ACSL4 signaling may serve as a promising therapeutic target for DR.

Altogether, we found that the lncRNA ZFAS1 was induced by hyperglycemia in hRECs and proposed that ZFAS1 may exerts its role by competitively binding with miR-7-5p and modulating the expression of its downstream mRNA ACSL4 expression (Figure 5(h)). Our data indicates that ZFAS1 is a major regulator of endothelial dysfunction and could be a new therapeutic target for the DR treatment. Moreover, molecules targeting ZFAS1/miR-7-5p/ACSL4

axis may play an important role in preventing the loss of endothelial cells, capillary occlusion, and the subsequent hypervascularization, which provides a future direction for early intervention of DR.

5. Conclusion

In conclusion, we demonstrated that lncRNA ZFAS1 has a ferroptotic effect on the retinal vascular endothelial cells which function as a sponge RNA to miR-7-5p and ultimately regulate ACSL4 expression. Our data strongly suggests that lncRNA ZFAS1 is a key contributor to the development of DR.

Data Availability

The original contributions presented in the study are included in the article material; further inquiries can be directed to the corresponding author.

Conflicts of Interest

All authors declare no competing interests.

Authors' Contributions

Y.L. and J.Y. conceived and designed the experiments. Y.L., J.Y., and Z.Z. performed cell culture. Z.Z. wrote the manuscript. All authors contributed to data analysis and gave final approval of the version to be published. Y.L. and J.Y. together performed the animal experiments. J.W. and Y.W. analyzed the data. P.X., Q.L., and R.Z. provided resources and funds. Yu Liu, Zhengyu Zhang, and Jing Yang contributed equally to this work.

Acknowledgments

This study was supported by the National Natural Science Foundation of China (81970821 to Q.L. and 8207097 to P.X.)

Supplementary Materials

Supplementary Figure 1: identification of primarily cultured hRECs. Supplementary Figure 2: the effects of GP_x4 overexpression on ZFAS1/miR-7-5p/ACSL4 axis. Supplementary Table 1: RNA sequences and the primer sequences for RT-qPCR. Supplementary Table 2: a total of 108 dysregulated lncRNAs were identified between the endothelial cells isolated from nine fibrovascular membrane (FVM) samples and four control retinal samples without diabetes diagnosis. Supplementary Table 3: a total of 69 miRNAs were identified to interact with ZFAS1 using starBase database. Supplementary Table 4: a total of 54 potential target genes of miR-7-5p were predicted using predictive datasets miRDB, DIANA, miRmap, and PicTar. (*Supplementary Materials*)

References

- [1] P. Saedi, I. Petersohn, P. Salpea et al., “Global and regional diabetes prevalence estimates for 2019 and projections for

- 2030 and 2045: results from the International Diabetes Federation Diabetes Atlas, 9th edition,” *Diabetes Research and Clinical Practice*, vol. 157, article 107843, 2019.
- [2] D. S. Fong, L. Aiello, T. W. Gardner et al., “Retinopathy in diabetes,” *Diabetes Care*, vol. 27, supplement 1, pp. S84–S87, 2004.
 - [3] Diabetes Control and Complications Trial Research Group, “Effect of intensive diabetes treatment on the development and progression of long-term complications in adolescents with insulin-dependent diabetes mellitus: diabetes control and complications trial,” *The Journal of Pediatrics*, vol. 125, no. 2, pp. 177–188, 1994.
 - [4] X. F. Zhou, W. E. Zhou, W. J. Liu et al., “A network pharmacology approach to explore the mechanism of HuangZhi YiShen capsule for treatment of diabetic kidney disease,” *Journal of Translational Internal Medicine*, vol. 9, no. 2, pp. 98–113, 2021.
 - [5] S. T. Keating and A. El-Osta, “Glycemic memories and the epigenetic component of diabetic nephropathy,” *Current Diabetes Reports*, vol. 13, no. 4, pp. 574–581, 2013.
 - [6] M. Mizutani, T. S. Kern, and M. Lorenzi, “Accelerated death of retinal microvascular cells in human and experimental diabetic retinopathy,” *The Journal of Clinical Investigation*, vol. 97, no. 12, pp. 2883–2890, 1996.
 - [7] G. Siasos, N. Gouliopoulos, M. M. Moschos et al., “Role of endothelial dysfunction and arterial stiffness in the development of diabetic retinopathy,” *Diabetes Care*, vol. 38, no. 1, pp. e9–e10, 2015.
 - [8] S. Roy, T. S. Kern, B. Song, and C. Stuebe, “Mechanistic insights into pathological changes in the diabetic retina: implications for targeting diabetic retinopathy,” *The American Journal of Pathology*, vol. 187, no. 1, pp. 9–19, 2017.
 - [9] A. M. Spijkerman, M. A. Gall, L. Tarnow et al., “Endothelial dysfunction and low-grade inflammation and the progression of retinopathy in type 2 diabetes,” *Diabetic Medicine*, vol. 24, no. 9, pp. 969–976, 2007.
 - [10] E. S. Shin, C. M. Sorenson, and N. Sheibani, “Diabetes and retinal vascular dysfunction,” *Journal of Ophthalmic and Vision Research*, vol. 9, no. 3, pp. 362–373, 2014.
 - [11] S. L. Elshaer, T. Lemtalsi, and A. B. El-Remessy, “High glucose-mediated tyrosine nitration of PI3-kinase: a molecular switch of survival and apoptosis in endothelial cells,” *Antioxidants*, vol. 7, no. 4, p. 47, 2018.
 - [12] P. Geraldes, J. Hiraoka-Yamamoto, M. Matsumoto et al., “Activation of PKC- δ and SHP-1 by hyperglycemia causes vascular cell apoptosis and diabetic retinopathy,” *Nature Medicine*, vol. 15, no. 11, pp. 1298–1306, 2009.
 - [13] W. Yuan, H. Xia, Y. Xu et al., “The role of ferroptosis in endothelial cell dysfunction,” *Cell Cycle*, vol. 14, pp. 1–18, 2022.
 - [14] Y. D. Feng, W. Ye, W. Tian et al., “Old targets, new strategy: apigenin-7-O- β -d-(-6"-p-coumaroyl)-glucopyranoside prevents endothelial ferroptosis and alleviates intestinal ischemia-reperfusion injury through HO-1 and MAO-B inhibition,” *Free Radical Biology & Medicine*, vol. 184, pp. 74–88, 2022.
 - [15] H. Kong, H. Zhao, T. Chen, Y. Song, and Y. Cui, “Targeted P2X7/NLRP3 signaling pathway against inflammation, apoptosis, and pyroptosis of retinal endothelial cells in diabetic retinopathy,” *Cell Death & Disease*, vol. 13, no. 4, p. 336, 2022.
 - [16] S. J. Dixon, K. M. Lemberg, M. R. Lamprecht et al., “Ferroptosis: an iron-dependent form of nonapoptotic cell death,” *Cell*, vol. 149, no. 5, pp. 1060–1072, 2012.
 - [17] J. Y. Cao and S. J. Dixon, “Mechanisms of ferroptosis,” *Cellular and Molecular Life Sciences*, vol. 73, no. 11–12, pp. 2195–2209, 2016.
 - [18] D. Tang, X. Chen, R. Kang, and G. Kroemer, “Ferroptosis: molecular mechanisms and health implications,” *Cell Research*, vol. 31, no. 2, pp. 107–125, 2021.
 - [19] X. Jiang, B. R. Stockwell, and M. Conrad, “Ferroptosis: mechanisms, biology and role in disease,” *Nature Reviews. Molecular Cell Biology*, vol. 22, no. 4, pp. 266–282, 2021.
 - [20] M. Riegman, L. Sagie, C. Galed et al., “Ferroptosis occurs through an osmotic mechanism and propagates independently of cell rupture,” *Nature Cell Biology*, vol. 22, no. 9, pp. 1042–1048, 2020.
 - [21] Y. Sun, P. Chen, B. Zhai et al., “The emerging role of ferroptosis in inflammation,” *Biomedicine & Pharmacotherapy*, vol. 127, article 110108, 2020.
 - [22] C. Liang, X. Zhang, M. Yang, and X. Dong, “Recent progress in ferroptosis inducers for cancer therapy,” *Advanced Materials*, vol. 31, no. 51, article e1904197, 2019.
 - [23] A. Weiland, Y. Wang, W. Wu et al., “Ferroptosis and its role in diverse brain diseases,” *Molecular Neurobiology*, vol. 56, no. 7, pp. 4880–4893, 2019.
 - [24] B. R. Stockwell, X. Jiang, and W. Gu, “Emerging mechanisms and disease relevance of ferroptosis,” *Trends in Cell Biology*, vol. 30, no. 6, pp. 478–490, 2020.
 - [25] D. Kim, R. P. Mecham, P. C. Trackman, and S. Roy, “Down-regulation of lysyl oxidase protects retinal endothelial cells from high glucose-induced apoptosis,” *Investigative Ophthalmology & Visual Science*, vol. 58, no. 5, pp. 2725–2731, 2017.
 - [26] R. A. Kowluru, “Effect of reinstatement of good glycemic control on retinal oxidative stress and nitrate stress in diabetic rats,” *Diabetes*, vol. 52, no. 3, pp. 818–823, 2003.
 - [27] E. F. Luo, H. X. Li, Y. H. Qin et al., “Role of ferroptosis in the process of diabetes-induced endothelial dysfunction,” *World Journal of Diabetes*, vol. 12, no. 2, pp. 124–137, 2021.
 - [28] J. Sun, W. Su, X. Zhao et al., “LncRNA PFAR contributes to fibrogenesis in lung fibroblasts through competitively binding to miR-15a,” *Bioscience Reports*, vol. 39, no. 7, 2019.
 - [29] X. Wang, Z. Cheng, L. Dai et al., “Knockdown of long noncoding RNA H19 represses the progress of pulmonary fibrosis through the transforming growth factor β /Smad3 pathway by regulating microRNA 140,” *Molecular and Cellular Biology*, vol. 39, no. 12, 2019.
 - [30] H. Wu, W. Qin, S. Lu et al., “Long noncoding RNA ZFAS1 promoting small nucleolar RNA-mediated 2'-O-methylation via NOP58 recruitment in colorectal cancer,” *Molecular Cancer*, vol. 19, no. 1, p. 95, 2020.
 - [31] X. Chen, K. Zeng, M. Xu et al., “SP1-induced lncRNA-ZFAS1 contributes to colorectal cancer progression via the miR-150-5p/VEGFA axis,” *Cell Death & Disease*, vol. 9, no. 10, p. 982, 2018.
 - [32] Z. Li, X. Jiang, Z. Su et al., “Current insight into a cancer-implicated long noncoding RNA ZFAS1 and correlative functional mechanisms involved,” *Pathology, Research and Practice*, vol. 214, no. 10, pp. 1517–1523, 2018.
 - [33] Z. Li, X. Qin, W. Bian et al., “Exosomal lncRNA ZFAS1 regulates esophageal squamous cell carcinoma cell proliferation, invasion, migration and apoptosis via microRNA-124/STAT3 axis,” *Journal of Experimental & Clinical Cancer Research*, vol. 38, no. 1, p. 477, 2019.

- [34] S. Zhuang, Y. Ma, Y. Zeng et al., "METTL14 promotes doxorubicin-induced cardiomyocyte ferroptosis by regulating the KCNQ1OT1-miR-7-5p-TFRC axis," *Cell Biology and Toxicology*, vol. 37, 2021.
- [35] K. Tomita, T. Nagasawa, Y. Kuwahara et al., "MiR-7-5p is involved in ferroptosis signaling and radioresistance thru the generation of ROS in radioresistant HeLa and SAS cell lines," *International Journal of Molecular Sciences*, vol. 22, no. 15, p. 8300, 2021.
- [36] X. Chen, J. Li, R. Kang, D. J. Klionsky, and D. Tang, "Ferroptosis: machinery and regulation," *Autophagy*, vol. 17, no. 9, pp. 2054–2081, 2021.
- [37] S. Doll, B. Proneth, Y. Y. Tyurina et al., "ACSL4 dictates ferroptosis sensitivity by shaping cellular lipid composition," *Nature Chemical Biology*, vol. 13, no. 1, pp. 91–98, 2017.
- [38] D. H. Lopez, M. A. Fiol-deRoque, M. A. Noguera-Salva et al., "2-Hydroxy arachidonic acid: a new non-steroidal anti-inflammatory drug," *PLoS One*, vol. 8, no. 8, article e72052, 2013.
- [39] J. Riemer, H. H. Hoepken, H. Czerwinska, S. R. Robinson, and R. Dringen, "Colorimetric ferrozine-based assay for the quantitation of iron in cultured cells," *Analytical Biochemistry*, vol. 331, no. 2, pp. 370–375, 2004.
- [40] Y. Liu, H. Shen, S. T. Yuan, and Q. H. Liu, "Role of microRNA-25 in high glucose cultured Müller glia," *International Journal of Ophthalmology*, vol. 14, no. 5, pp. 643–648, 2021.
- [41] Y. Zhong, J. Li, Y. Chen, J. J. Wang, R. Ratan, and S. X. Zhang, "Activation of endoplasmic reticulum stress by hyperglycemia is essential for Müller cell-derived inflammatory cytokine production in diabetes," *Diabetes*, vol. 61, no. 2, pp. 492–504, 2012.
- [42] L. Zhu, J. Xu, Y. Liu et al., "Prion protein is essential for diabetic retinopathy-associated neovascularization," *Angiogenesis*, vol. 21, no. 4, pp. 767–775, 2018.
- [43] R. Sachdeva, A. Schlotterer, D. Schumacher et al., "TRPC proteins contribute to development of diabetic retinopathy and regulate glyoxalase 1 activity and methylglyoxal accumulation," *Molecular Metabolism*, vol. 9, pp. 156–167, 2018.
- [44] K. Allan, R. DiCicco, M. Ramos, K. Asosingh, and A. Yuan, "Preparing a single cell suspension from zebrafish retinal tissue for flow cytometric cell sorting of Müller glia," *Cytometry. Part A*, vol. 97, no. 6, pp. 638–646, 2020.
- [45] T. Wakabayashi, H. Naito, T. Iba, K. Nishida, and N. Takakura, "Identification of CD157-positive vascular endothelial stem cells in mouse retinal and choroidal vessels: fluorescence-activated cell sorting analysis," *Investigative Ophthalmology & Visual Science*, vol. 63, no. 4, p. 5, 2022.
- [46] Y. Liu, Z. Yang, P. Lai et al., "Bcl-6-directed follicular helper T cells promote vascular inflammatory injury in diabetic retinopathy," *Theranostics*, vol. 10, no. 9, pp. 4250–4264, 2020.
- [47] Y. Yang, W. Tai, N. Lu et al., "lncRNA ZFAS1 promotes lung fibroblast-to-myofibroblast transition and ferroptosis via functioning as a ceRNA through miR-150-5p/SLC38A1 axis," *Aging (Albany NY)*, vol. 12, no. 10, pp. 9085–9102, 2020.
- [48] G. P. Drummen, L. C. van Liebergen, J. A. Op den Kamp, and J. A. Post, "C11-BODIPY^{581/591}, an oxidation-sensitive fluorescent lipid peroxidation probe: (micro)spectroscopic characterization and validation of methodology," *Free Radical Biology & Medicine*, vol. 33, no. 4, pp. 473–490, 2002.
- [49] W. S. Yang, R. SriRamaratnam, M. E. Welsch et al., "Regulation of ferroptotic cancer cell death by GPX4," *Cell*, vol. 156, no. 1–2, pp. 317–331, 2014.
- [50] V. E. Kagan, G. Mao, F. Qu et al., "Oxidized arachidonic and adrenic PEs navigate cells to ferroptosis," *Nature Chemical Biology*, vol. 13, no. 1, pp. 81–90, 2017.
- [51] Y. Zhang, M. Xia, Z. Zhou et al., "p53 promoted ferroptosis in ovarian cancer cells treated with human serum incubated-superparamagnetic iron oxides," *International Journal of Nanomedicine*, vol. 16, pp. 283–296, 2021.
- [52] K. Tomita, M. Fukumoto, K. Itoh et al., "MiR-7-5p is a key factor that controls radioresistance via intracellular Fe²⁺ content in clinically relevant radioresistant cells," *Biochemical and Biophysical Research Communications*, vol. 518, no. 4, pp. 712–718, 2019.
- [53] Z. Pei, Y. Liu, S. Liu et al., "FUNDC1 insufficiency sensitizes high fat diet intake-induced cardiac remodeling and contractile anomaly through ACSL4-mediated ferroptosis," *Metabolism*, vol. 122, article 154840, 2021.
- [54] S. Shui, Z. Zhao, H. Wang, M. Conrad, and G. Liu, "Non-enzymatic lipid peroxidation initiated by photodynamic therapy drives a distinct ferroptosis-like cell death pathway," *Redox Biology*, vol. 45, article 102056, 2021.
- [55] Y. Li, D. Feng, Z. Wang et al., "Ischemia-induced ACSL4 activation contributes to ferroptosis-mediated tissue injury in intestinal ischemia/reperfusion," *Cell Death and Differentiation*, vol. 26, no. 11, pp. 2284–2299, 2019.
- [56] K. Miyamoto, S. Khosrof, S. E. Bursell et al., "Prevention of leukostasis and vascular leakage in streptozotocin-induced diabetic retinopathy via intercellular adhesion molecule-1 inhibition," *Proceedings of the National Academy of Sciences of the United States of America*, vol. 96, no. 19, pp. 10836–10841, 1999.
- [57] Q. Huang, Q. Fang, and Z. Hu, "A P4 medicine perspective of gut microbiota and prediabetes: systems analysis and personalized intervention," *Journal of Translational Internal Medicine*, vol. 8, no. 3, pp. 119–130, 2020.
- [58] F. Yuan, Q. Zhang, H. Dong et al., "Effects of des-acyl ghrelin on insulin sensitivity and macrophage polarization in adipose tissue," *Journal of Translational Internal Medicine*, vol. 9, no. 2, pp. 84–97, 2021.
- [59] Z. Wang, H. Xiong, and T. Y. S. Ren, "Repair of damaged pancreatic β cells: new hope for a type 2 diabetes reversal?," *Journal of Translational Internal Medicine*, vol. 9, no. 3, pp. 150–151, 2021.
- [60] S. Zafar, M. Sachdeva, B. J. Frankfort, and R. Channa, "Retinal neurodegeneration as an early manifestation of diabetic eye disease and potential neuroprotective therapies," *Current Diabetes Reports*, vol. 19, no. 4, p. 17, 2019.
- [61] M. A. Mohammed, M. M. Lolah, M. F. Doheim, and A. AbouSamra, "Functional assessment of early retinal changes in diabetic patients without clinical retinopathy using multifocal electroretinogram," *BMC Ophthalmology*, vol. 20, no. 1, p. 411, 2020.
- [62] M. Buijs, N. T. Doan, S. van Rooden et al., "In vivo assessment of iron content of the cerebral cortex in healthy aging using 7-Tesla T2*-weighted phase imaging," *Neurobiology of Aging*, vol. 53, pp. 20–26, 2017.
- [63] S. Masaldan, A. A. Belaidi, S. Ayton, and A. I. Bush, "Cellular senescence and iron dyshomeostasis in Alzheimer's disease," *Pharmaceuticals (Basel)*, vol. 12, no. 2, 2019.
- [64] A. A. Belaidi and A. I. Bush, "Iron neurochemistry in Alzheimer's disease and Parkinson's disease: targets for therapeutics," *Journal of Neurochemistry*, vol. 139, Supplement 1, pp. 179–197, 2016.

- [65] P. A. Dionisio, J. D. Amaral, and C. M. P. Rodrigues, "Oxidative stress and regulated cell death in Parkinson's disease," *Ageing Research Reviews*, vol. 67, article 101263, 2021.
- [66] V. Suryadevara, L. Huang, S. J. Kim et al., "Role of phospholipase D in bleomycin-induced mitochondrial reactive oxygen species generation, mitochondrial DNA damage, and pulmonary fibrosis," *American Journal of Physiology. Lung Cellular and Molecular Physiology*, vol. 317, no. 2, pp. L175–L187, 2019.
- [67] R. M. Liu and L. P. Desai, "Reciprocal regulation of TGF- β and reactive oxygen species: a perverse cycle for fibrosis," *Redox Biology*, vol. 6, pp. 565–577, 2015.
- [68] M. Polak and Z. Zagorski, "Lipid peroxidation in diabetic retinopathy," *Annales Universitatis Mariae Curie-Skłodowska. Sectio D: Medicina*, vol. 59, no. 1, pp. 434–437, 2004.
- [69] D. Armstrong and F. Al-Awadi, "Lipid peroxidation and retinopathy in streptozotocin-induced diabetes," *Free Radical Biology & Medicine*, vol. 11, no. 4, pp. 433–436, 1991.
- [70] R. P. Brandes and J. Kreuzer, "Vascular NADPH oxidases: molecular mechanisms of activation," *Cardiovascular Research*, vol. 65, no. 1, pp. 16–27, 2005.
- [71] R. X. Santos, S. C. Correia, X. Zhu et al., "Mitochondrial DNA oxidative damage and repair in aging and Alzheimer's disease," *Antioxidants & Redox Signaling*, vol. 18, no. 18, pp. 2444–2457, 2013.
- [72] R. N. Jadeja and P. M. Martin, "Oxidative stress and inflammation in retinal degeneration," *Antioxidants*, vol. 10, no. 5, p. 790, 2021.
- [73] M. D. Evans, M. Dizdaroglu, and M. S. Cooke, "Oxidative DNA damage and disease: induction, repair and significance," *Mutation Research*, vol. 567, no. 1, pp. 1–61, 2004.
- [74] H. Li, S. Horke, and U. Forstermann, "Oxidative stress in vascular disease and its pharmacological prevention," *Trends in Pharmacological Sciences*, vol. 34, no. 6, pp. 313–319, 2013.
- [75] W. Sha, F. Hu, Y. Xi, Y. Chu, and S. Bu, "Mechanism of ferroptosis and its role in type 2 diabetes mellitus," *Journal Diabetes Research*, vol. 2021, article 9999612, 10 pages, 2021.
- [76] A. Sharma and S. J. S. Flora, "Positive and negative regulation of ferroptosis and its role in maintaining metabolic and redox homeostasis," *Oxidative Medicine and Cellular Longevity*, vol. 2021, Article ID 9074206, 13 pages, 2021.
- [77] J. W. Borst, N. V. Visser, O. Kouptsova, and A. J. Visser, "Oxidation of unsaturated phospholipids in membrane bilayer mixtures is accompanied by membrane fluidity changes," *Biochimica et Biophysica Acta*, vol. 1487, no. 1, pp. 61–73, 2000.
- [78] X. M. Li, R. G. Salomon, J. Qin, and S. L. Hazen, "Conformation of an endogenous ligand in a membrane bilayer for the macrophage scavenger receptor CD36," *Biochemistry*, vol. 46, no. 17, pp. 5009–5017, 2007.
- [79] E. Agmon, J. Solon, P. Bassereau, and B. R. Stockwell, "Modeling the effects of lipid peroxidation during ferroptosis on membrane properties," *Scientific Reports*, vol. 8, no. 1, p. 5155, 2018.
- [80] G. Wang, Y. Le, L. Wei, and L. Cheng, "CREB3 transactivates lncRNA ZFAS1 to promote papillary thyroid carcinoma metastasis by modulating miR-373-3p/MMP3 regulatory axis," *International Journal of Endocrinology*, vol. 2021, Article ID 9981683, 9 pages, 2021.
- [81] J. C. Lin, P. M. Yang, and T. P. Liu, "PERK/ATF4-dependent ZFAS1 upregulation is associated with sorafenib resistance in hepatocellular carcinoma cells," *International Journal of Molecular Sciences*, vol. 22, no. 11, p. 5848, 2021.
- [82] H. Deng, M. Wang, Q. Xu, and H. Yao, "ZFAS1 promotes colorectal cancer metastasis through modulating miR-34b/SOX4 targeting," *Cell Biochemistry and Biophysics*, vol. 79, no. 2, pp. 387–396, 2021.
- [83] S. J. O'Brien, C. Fiechter, J. Burton et al., "Long non-coding RNA ZFAS1 is a major regulator of epithelial-mesenchymal transition through miR-200/ZEB1/E-cadherin, vimentin signaling in colon adenocarcinoma," *Cell Death Discovery*, vol. 7, no. 1, p. 61, 2021.
- [84] L. Jiao, M. Li, Y. Shao et al., "lncRNA-ZFAS1 induces mitochondria-mediated apoptosis by causing cytosolic Ca(2+) overload in myocardial infarction mice model," *Cell Death & Disease*, vol. 10, no. 12, p. 942, 2019.
- [85] J. S. Wang, Q. H. Liu, X. H. Cheng, W. Y. Zhang, and Y. C. Jin, "The long noncoding RNA ZFAS1 facilitates bladder cancer tumorigenesis by sponging miR-329," *Biomedicine & Pharmacotherapy*, vol. 103, pp. 174–181, 2018.
- [86] J. Peng, F. Liu, H. Zheng, Q. Wu, and S. Liu, "lncRNA ZFAS1 contributes to the radioresistance of nasopharyngeal carcinoma cells by sponging hsa-miR-7-5p to upregulate ENO2," *Cell Cycle*, vol. 20, no. 1, pp. 126–141, 2021.
- [87] O. Zilka, R. Shah, B. Li et al., "On the mechanism of cytoprotection by ferrostatin-1 and liproxstatin-1 and the role of lipid peroxidation in ferroptotic cell death," *ACS Central Science*, vol. 3, no. 3, pp. 232–243, 2017.
- [88] H. Yuan, X. Li, X. Zhang, R. Kang, and D. Tang, "Identification of ACSL4 as a biomarker and contributor of ferroptosis," *Biochemical and Biophysical Research Communications*, vol. 478, no. 3, pp. 1338–1343, 2016.
- [89] J. Wu, A. M. Minikes, M. Gao et al., "Intercellular interaction dictates cancer cell ferroptosis via NF2-YAP signalling," *Nature*, vol. 572, no. 7769, pp. 402–406, 2019.
- [90] C. Liu, W. Sun, T. Zhu et al., "Glia maturation factor- β induces ferroptosis by impairing chaperone-mediated autophagic degradation of ACSL4 in early diabetic retinopathy," *Redox Biology*, vol. 52, article 102292, 2022.

Research Article

Ferroptosis-Related Long Noncoding RNAs Have Excellent Predictive Ability for Multiomic Characteristics of Bladder Cancer

Jingchao Liu ^{1,2}, Jingyi Cui ^{2,3}, Shuangyi Zhao ¹, Meng Wu ¹, Jiawen Wang,^{1,2}
Yaoguang Zhang ^{1,2}, Bin Jin ^{1,2} and Jianye Wang ^{1,2}

¹Department of Urology, Beijing Hospital, National Center of Gerontology, Institute of Geriatric Medicine, Chinese Academy of Medical Sciences, No. 1 DaHua Road, Dong Dan, Beijing 100730, China

²Graduate School of Peking Union Medical College, Chinese Academy of Medical Sciences, 9 DongDan SanTiao, Beijing 100730, China

³The Key Laboratory of Geriatrics, Beijing Institute of Geriatrics, Institute of Geriatric Medicine, Chinese Academy of Medical Sciences, Beijing Hospital, National Center of Gerontology of National Health Commission, Beijing 100730, China

Correspondence should be addressed to Yaoguang Zhang; zygbjhospital@126.com, Bin Jin; jin_bin2001@163.com, and Jianye Wang; wjy08pro@126.com

Received 9 June 2022; Revised 30 July 2022; Accepted 10 August 2022; Published 29 August 2022

Academic Editor: Lianxiang Luo

Copyright © 2022 Jingchao Liu et al. This is an open access article distributed under the Creative Commons Attribution License, which permits unrestricted use, distribution, and reproduction in any medium, provided the original work is properly cited.

Background. The role of ferroptosis-related long non-coding RNAs (lncRNAs) in bladder cancer remains elusive. This study is aimed at examining the prognostic role of ferroptosis-related lncRNAs in bladder cancer. **Materials and Methods.** The transcriptomic matrix and clinical information of patients with bladder cancer were obtained from The Cancer Genome Atlas (TCGA) database. A ferroptosis-related lncRNA signature was developed via the least absolute shrinkage and selection operator (LASSO) analysis using data from the training cohort, and the signature was further validated using data from the test cohort. The role of AC006160.1, the most significant lncRNA in the risk signature, was examined in various cell lines including SV-HUC-1, BIU-87, HT-1376, T24, RT4, RT-112, 5637, and UMUC3. The pcDNA3.1-AC006160.1 plasmid was constructed and transfected into the bladder cancer cell lines T24 and BIU-87. In addition, cell proliferation, colony formation, transwell, and wound healing assays were performed to examine the biological function of AC006160.1 in T24 and BIU-87 cell lines. **Results.** Two clusters were identified through consensus clustering based on prognostic ferroptosis-related lncRNAs. A 5-lncRNA risk signature was successfully constructed using data from the training cohort and validated using data from the test cohort. The risk signature had excellent ability to predict survival outcomes, clinical stages, pathological grades, expression of immune checkpoints, and immunotherapeutic responses in bladder cancer samples. Furthermore, AC006160.1 expression was found to be lower in the cancer cell lines BIU-87, T24, RT4, RT-112, and 5637 than in the normal control cell line SV-HUC-1. Cell proliferation, colony formation, transwell migration, and wound healing assays validated that overexpression of AC006160.1 significantly inhibited the proliferation and invasion abilities of both T24 and BIU-87 cells. Drug sensitivity analysis revealed that patients with high expression of AC006160.1 were sensitive to metformin and methotrexate, and the results were further validated via in vitro drug experiments. **Conclusions.** Ferroptosis-related lncRNAs play a vital role in predicting the multiomic characteristics of bladder cancer. The lncRNA AC006160.1 serves as a protective factor for the development of bladder cancer.

1. Introduction

Bladder cancer, one of the most malignant tumours, originates from the transitional epithelium of the urinary tract and leads

to >2,00,000 deaths annually worldwide [1]. Non-muscle-invasive bladder cancer accounts for 50% of bladder cancer cases, whereas muscle-invasive bladder cancer accounts for 30% of cases [1, 2]. Although bladder cancer can be treated

via transurethral tumour resection or radical cystectomy, a considerable proportion of patients develops tumour recurrence or metastasis [3]. During the past decade, limited progress has been made in the development of relative treatment modalities for bladder cancer owing to unclear mechanisms underlying cancer development. At present, cisplatin-based chemotherapy is recommended as the first-line treatment for advanced bladder cancer, and immunotherapy is recommended as the second-line treatment [4, 5]. However, only a limited number of patients can benefit from chemotherapy and immunotherapy. Moreover, patients with the same clinical stage or grade often have distinct survival outcomes after receiving similar treatment strategies. These discrepancies indicate that other biological mechanisms may be involved in the development of bladder cancer, which remain elusive at present. Recent developments in large-scale gene expression and sequencing technology have helped clinicians to explore valuable tools for improving the diagnosis and treatment of bladder cancer [6].

Ferroptosis is a novel cell death mechanism, which is different from previously known programmed cell death mechanisms including autophagy and apoptosis [7, 8]. It is typically characterised by iron dependence and accumulation of reactive oxygen species in cells [8, 9]. The unique morphological characteristics of ferroptosis include the loss of mitochondrial cristae, shrinkage of cell mitochondria, and enhanced density of the mitochondrial membrane [10]. These characteristics confirm that ferroptosis is a novel cell death mechanism, which may offer promising directions for research into cell death and cancer treatment. Several studies have demonstrated that ferroptosis plays a vital regulatory role in various malignant cancers including colorectal cancer, non-small-cell lung cancer, hepatocellular carcinoma, breast cancer, and acute myeloid leukaemia [9, 11, 12]. Identification of drugs interfering with ferroptosis in cancer cells may help to develop novel treatment strategies for cancer in the future, especially for patients who are resistant to chemotherapy or immunotherapy [13–15]. Eling et al. reported that pancreatic cancer cells can be inhibited by inducing ferroptosis using the combination of cotylenin A and phenylethyl isothiocyanate [16]. A recent study reported that sorafenib plays a therapeutic role by inducing ferroptosis in hepatocellular carcinoma [17]. Previous high-quality studies have validated that several mRNAs participate in the regulation of ferroptosis in various malignancies, and their results have been experimentally validated and widely recognised in recent studies [15, 18–20]. In addition, studies employing cutting-edge technology have reported a vital role of lncRNAs in various biological activities including differentiation, apoptosis, metastasis, cell cycle, and proliferation in multiple cancers [21, 22]. Coexpression analysis can help to screen for lncRNAs that are coexpressed with known ferroptosis mRNAs and further identify ferroptosis-related lncRNAs in malignancies [23, 24]. Studies have shown that lncRNAs participate in multiple ferroptosis-related regulatory activities in various cancers. The competing endogenous RNA LINC00336 inhibits ferroptosis in cancer cells, thereby promoting the development and deterioration of lung cancer [25]. In addition, LINC00618 enhances vincristine-induced ferroptosis and is a potential prognostic factor for predicting the survival of patients with

leukaemia [26]. Furthermore, studies have also discovered that lncRNAs regulate tumour progression by affecting the immune microenvironment [22, 27]. However, the role of ferroptosis-related lncRNAs in the development of bladder cancer remains elusive. This study is aimed at examining the prognostic role of ferroptosis-related lncRNAs in bladder cancer; in addition, a risk signature based on prognostic lncRNAs was established to guide the currently available diagnostic and treatment strategies of bladder cancer from a genetic perspective.

2. Materials and Methods

2.1. Extraction and Processing of Sequencing Data. The mRNA and lncRNA sequencing data of 411 bladder cancer samples were extracted from The Cancer Genome Atlas (TCGA) database (<https://portal.gdc.cancer.gov>). Samples without clinical information were excluded, and a total of 403 bladder cancer samples with both transcriptomic and clinical information were eventually included for further analysis. The 403 bladder cancer samples were randomly divided into the training (203 samples) and validation (200 samples) cohorts for the construction and validation of an lncRNA signature, respectively.

2.2. Identification of Ferroptosis-Related lncRNAs and Prognostic lncRNAs. High-quality studies concerning ferroptosis (impact factor of >10 points in the last 4 years) were comprehensively reviewed, and a total of 60 ferroptosis-related mRNAs were identified, which were listed in Supplementary Table 1 [18–20, 28]. Pearson's correlation analysis ($|R| > 0.5$ and $p < 0.001$) of ferroptosis-related mRNAs and lncRNAs was performed to identify ferroptosis-related lncRNAs. Subsequently, univariate Cox regression analysis was performed to identify ferroptosis-related lncRNAs associated with prognosis (overall survival) ($p < 0.01$).

2.3. Distinct Ferroptosis Mediation Patterns in Bladder Cancer. Based on the expression of prognostic ferroptosis-related lncRNAs, distinct ferroptosis mediation patterns were identified via consensus clustering using the “ConsensusClusterPlus” package of R software. The Euclidean distance was calculated to assess similarity between samples, and the *K*-means algorithm was used for clustering. Differences in survival between distinct patterns were evaluated via Kaplan–Meier survival analysis using the “survival” and “survminer” packages. The potential relationship between distinct ferroptosis mediation patterns and various clinical parameters including age, sex, clinical stage, and tumour grade were investigated using the “pheatmap” package.

2.4. Construction and Validation of Ferroptosis-Related lncRNA Signature. Based on the prognostic ferroptosis-related lncRNAs identified via univariate Cox regression analysis, an lncRNA risk signature was developed in the training cohort via the least absolute shrinkage and selection operator (LASSO) analysis using the “glmnet” package. Each ferroptosis mediation pattern was quantified using the following formula: risk score = \sum (ferroptosis-related lncRNA expression * corresponding regression coefficient). All cancer samples in both training and validation cohorts were divided into the high- or low-risk groups based on the corresponding median risk score.

Kaplan–Meier analysis was performed to compare the survival of patients in the high- and low-risk groups in both training and validation cohorts. In addition, receiver operating characteristic (ROC) analysis was performed to examine the performance of risk scores in predicting survival outcomes at 1–5 years in both training and validation cohorts.

2.5. Independent Prognostic Analysis and Stratified Survival Analysis of the Ferroptosis-Related lncRNA Risk Signature. Univariate and multivariate Cox regression analyses were performed to examine the independent prognostic role of the ferroptosis-related lncRNA risk signature in the training cohort and verify its role in the validation cohort. Furthermore, stratified survival analysis was performed to investigate the predictive value of the risk signature in different subgroups, including old (age, >65 years) or young (age, ≤65 years) group, male or female group, stage I–II or stage III–IV group, T1–T2 or T3–T4 group, and N0 or N1–3 stage group. Differences in risk scores between these groups were analysed using Student's t-test.

2.6. Expression of Immune Checkpoints, Infiltration Analysis of Immune Cells, and Gene Set Enrichment Analysis between Distinct Ferroptosis Mediation Patterns. Differences in the expression of classic immune checkpoints including PD-1, PD-L1 and CTLA-4 between distinct ferroptosis mediation patterns were investigated using the “limma,” “ggplot2” and “ggpubr” packages in R. The CIBERSORT algorithm (<https://cibersort.stanford.edu/>) was used to analyse the infiltration levels of 22 types of immune cells in bladder cancer [29]. The ESTIMATE algorithm was used to evaluate the immune cell microenvironment scores of each bladder cancer sample [30]. Differences in the immune infiltration levels of 22 immune cell types between distinct ferroptosis mediation patterns were further examined. Gene set enrichment analysis (GSEA) (version 4.0.4) was performed based on the whole transcriptomic profiles of bladder cancer samples to investigate potential biological activities of distinct ferroptosis mediation patterns.

2.7. Guidance of the lncRNA Risk Signature for Immunotherapy. Differences in the expression of immune checkpoints between the high- and low-risk groups were examined using the “limma” and “ggpubr” packages in R. The standard symbol names of PD-L1, PD-1 and CTLA-4 were derived from the NCBI website (<https://www.ncbi.nlm.nih.gov/gene>), which were CD274, PDCD1, and CTLA-4, respectively. Additionally, correlation analysis was performed to examine the relationship between risk scores and infiltration levels of immune cells, and the Tumour Immune Dysfunction and Exclusion (TIDE) algorithm was used to evaluate the response of patients to immunotherapy [31].

2.8. Cell Lines and Cell Culture. The biological functions of the most significant lncRNA, AC006160.1, were examined via in vitro experiments. Human cell lines SV-HUC-1 (CL-0222), BIU-87 (CL-0035), HT-1376 (CL-0672), T24 (CL-0227), RT4 (CL-0431), RT-112 (CL-0682), 5637 (CL-0002), and UMUC3 (CL-0463) were purchased from Procell Life Science & Technology Co., Ltd. (Wuhan, China). BIU-87, T24, RT4, RT-112, and 5637 cells were cultured in the Roswell Park Memorial

Institute (RPMI)-1640 (Macgene, China) medium supplemented with 10% foetal bovine serum (FBS) (Gibco, MA, USA). HT-1376 and UMUC3 cells were cultured in MEM (Macgene, China) supplemented with 10% FBS (Gibco, MA, USA). SV-HUC-1 cells were cultured in Ham's F-12K medium (Macgene, China) supplemented with 10% FBS (Gibco, MA, USA). All cell lines were cultured at 37°C in a humidified incubator containing 5% CO₂.

2.9. Vector Construction. The lncRNA AC006160.1 was cloned into the pcDNA3.1 vector at the NheI and KpnI sites to produce the pcDNA3.1-AC006160.1 plasmid. The primers used for plasmid construction were as follows: forward, 5'-CTAG CTAGCCACGTGACAGGACCGAGC-3'; reverse, 5'-GGGG TACCTCATCTTCCGATTTAAAATTTTTTCCC-3'. Empty pcDNA3.1 vector was used as the negative control. The pcDNA3.1-AC006160.1 and negative control plasmids were transfected into bladder cancer cells using the Lipo8000 Transfection Reagent (Beyotime Biotechnology, China) according to the manufacturer's instructions and cultured in 6-well plates.

2.10. RNA Extraction and Reverse Transcription Polymerase Chain Reaction. The TRIzol reagent (Invitrogen, USA) was used to isolate total RNA from bladder cancer cells, and first-strand complementary deoxyribonucleic acid (cDNA) was synthesised using the Evo M-MLV RT Premix (Accurate Biology, China). Quantitative polymerase chain reaction (qPCR) was performed using the Taq Pro Universal SYBR qPCR Master Mix (Vazyme, China). All reactions were performed on the iQ5 Real-Time PCR Thermal Cycler (Bio-Rad, USA). The specific qPCR primers used for detecting lncRNA AC006160.1 were as follows: forward, 5'-ATGCCTGGAGAGACTTTGG C-3'; reverse, 5'-GCCTGTCTTGTTCCTCCGCTAT-3'; GAPDH forward, 5'-GGTATCGTGGAAGGACTCATGAC-3'; reverse, 5'-ATGCCAGTGAGCTTCCCGTTCAG-3'.

2.11. Cell Proliferation Assay. Cell viability was measured using the CCK-8 kit (Meilunbio, China). According to bioinformatic analysis and experimental results, AC006160.1 was found to be significantly downregulated in bladder cancer and served as a protective factor for cancer development. Therefore, cell lines with low expression of AC006160.1 were randomly selected to validate the biological functions of AC006160.1. BIU-87 and T24 cells were selected as ideal experimental cells. Briefly, BIU-87 or T24 cells were transfected with the pcDNA3.1-AC006160.1 or negative control plasmid for 24 h, and the transfected cells were seeded in a 96-well plate at a density of 3×10^3 cells/well. The cells were cultured for 1, 2, 3, 4, or 5 days, and 10 μL of the CCK-8 reagent was added to each well. After 2 h of incubation, absorbance was measured at 450 nm using a multimode microplate reader (BioTek, USA). For drug sensitivity analysis, BIU-87 cells were transfected with the pcDNA3.1-AC006160.1 or negative control plasmid for 24 h, and the transfected cells were seeded in a 96-well plate at a density of 3×10^3 cells/well and incubated for 24 h. Thereafter, the cells were cultured with or

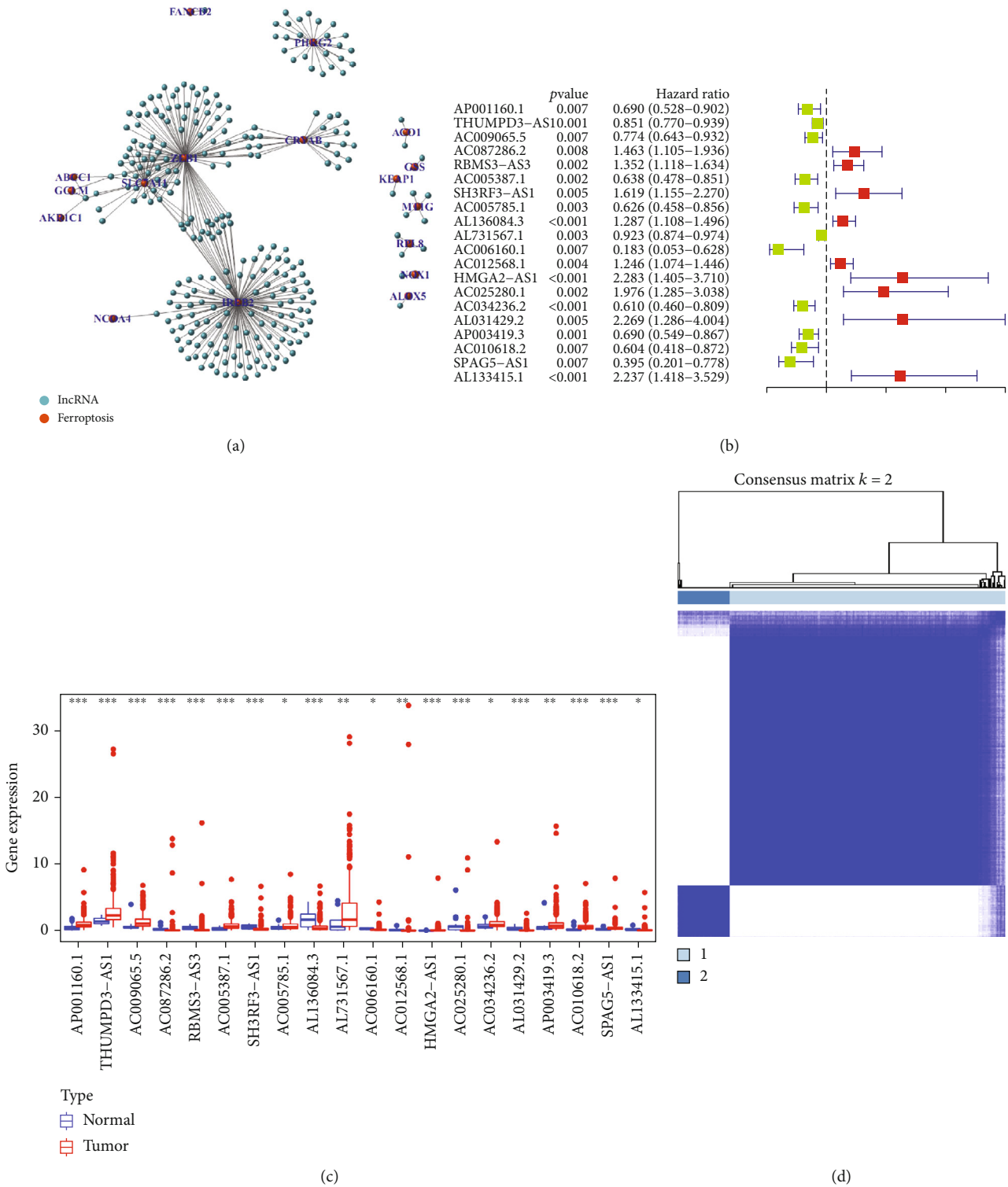
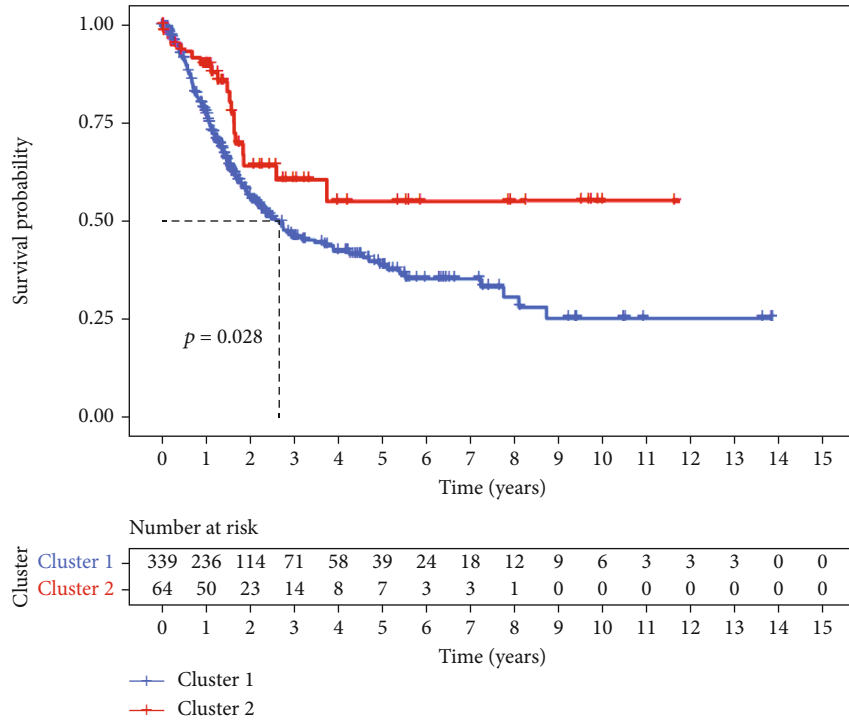
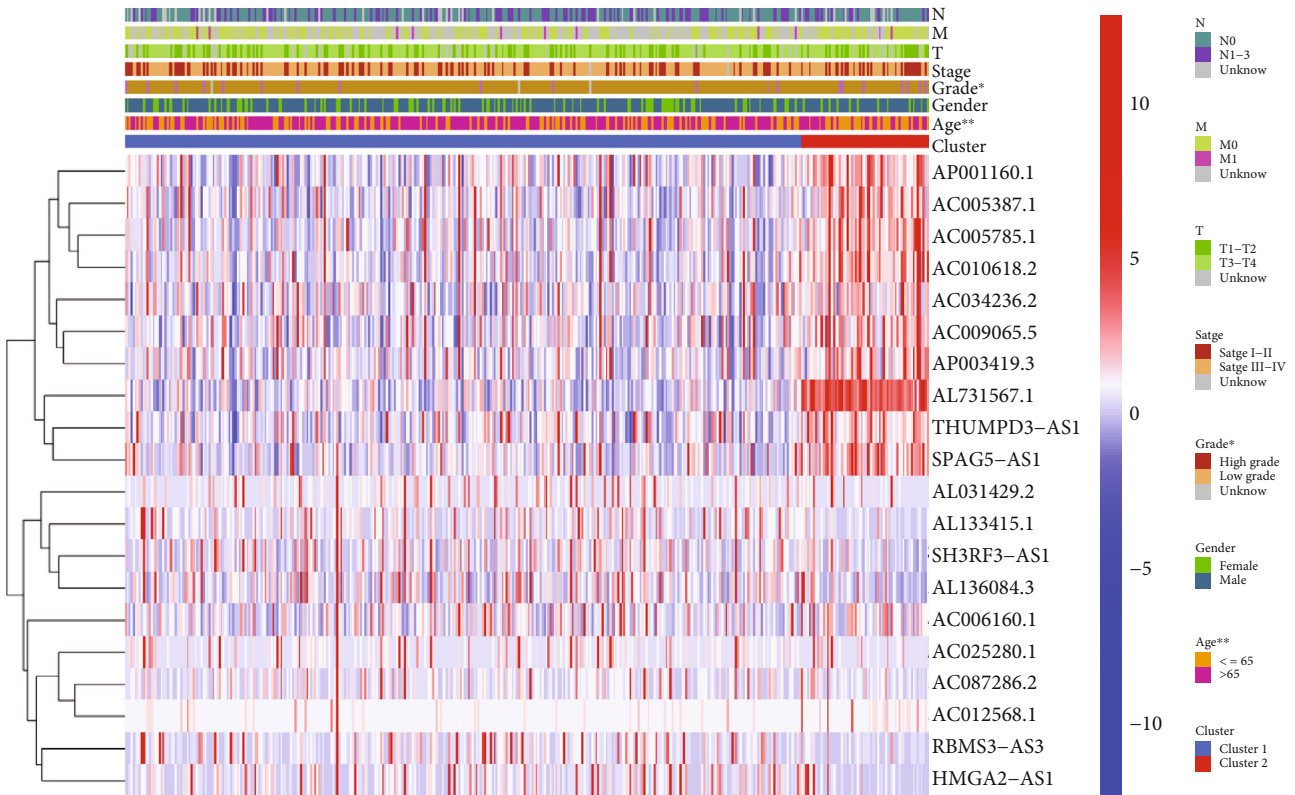


FIGURE 1: Continued.



(e)



(f)

FIGURE 1: Ferroptosis-related lncRNAs associated with the prognosis of bladder cancer. (a) Coexpression network of ferroptosis-related mRNAs and lncRNAs. (b) The 20 prognostic ferroptosis-related lncRNAs identified via univariate Cox regression analysis. (c) The 20 prognostic ferroptosis-related lncRNAs were differentially expressed between tumour and healthy tissues. (d) Consensus clustering when k was 2. (e) Cluster 1 had significantly poorer survival outcomes than cluster 2. (f) Heatmap demonstrating the relationship between the two clusters and various clinical parameters including the age, sex, clinical stage, and tumour grade of patients with bladder cancer.

without 1-mM metformin (MET) for 72 h, and absorbance was measured as mentioned above.

2.12. Colony Formation Assay. BIU-87 or T24 cells were transfected with the pcDNA3.1-AC006160.1 or negative control plasmid for 24 h, and approximately 2.0×10^3 transfected cells were seeded in 6-well plates and incubated at 37°C in RPMI-1640 medium supplemented with 10% FBS. After 14 days, cell colonies were washed with phosphate-buffered saline (PBS), fixed in methanol for 15 min and stained with crystal violet for 30 min. Subsequently, photographs were captured for evaluating colony formation. For drug sensitivity analysis, BIU-87 cells were transfected with the pcDNA3.1-AC006160.1 or negative control plasmid for 24 h, and approximately 2.0×10^3 transfected cells were seeded in 6-well plates and incubated for 24 h at 37°C in RPMI-1640 medium supplemented with 10% FBS. Thereafter, the cells were cultured with or without 1-mM MET, and subsequent analysis was performed as mentioned above. The number of colonies formed was evaluated using the ImageJ software.

2.13. Wound Healing Assay. Transfected BIU-87 and T24 cells were seeded in a 12-well plate and cultured to complete confluence. A clear wound was created by scratching the cell monolayer with a 200 μ L pipette tip. Thereafter, the cells were cultured in a serum-free medium. At 0 h and 48 h, images were captured with the aid of an optical microscope, and the wound area was measured using the ImagePro software.

2.14. Transwell Migration Assay. Transfected BIU-87 and T24 cells in 200 μ L of serum-free medium were added to the upper transwell chamber, whereas 600 μ L of the medium containing 10% FBS was added to the lower chamber. After 48 h of incubation, cells in the upper chamber were removed with a cotton swab, whereas those in the bottom chamber were fixed with ethanol, stained with 0.1% crystal violet for 30 min, and photographed. Thereafter, the number of migrated cells was evaluated using the ImageJ software.

2.15. Drug Sensitivity Analysis. All bladder cancer samples were divided into the high- and low-expression groups based on the median expression of the target lncRNA AC006160.1. Data from the Genomics of Drug Sensitivity in Cancer (GDSC) database were used to perform drug sensitivity analysis in both groups [32]. To validate the results of drug sensitivity analysis, BIU-87 cells were transfected with the pcDNA3.1-AC006160.1 or negative control plasmid for 24 h, and the transfected cells were seeded in a 96-well plate at a density of 3×10^3 cells/per well and incubated for 24 h. Subsequently, the cells were cultured with or without 1-mM MET for 72 h, and absorbance was measured as mentioned in the section Cell proliferation assay. Furthermore, colony formation assay was performed as mentioned earlier to validate the results of drug sensitivity analysis. BIU-87 cells were transfected with the pcDNA3.1-AC006160.1 or negative control plasmid for 24 h, and approximately 2.0×10^3 transfected cells were seeded in 6-well plates and incubated at 37°C in RPMI-1640 medium supplemented with 10% FBS for 24 h. Thereafter, the cells

TABLE 1: The five ferroptosis-related lncRNAs included in the risk signature.

lncRNA	Coefficient
AL136084.3	0.12
AL731567.1	-0.05
AC006160.1	-0.98
AC012568.1	0.25
AC034236.2	-0.35

were cultured with or without 1-mM MET, and subsequent analysis was performed as mentioned above.

2.16. Statistical Analysis. The chi-squared test was used to compare categorical variables, whereas the Student's *t*-test or Mann-Whitney *U* test was used to compare continuous variables. One-way ANOVA was used to compare data among ≥ 3 groups, and Kaplan-Meier analysis with the log-rank test was used to compare survival. All statistical analyses were performed using either the R or the SPSS Statistics software.

3. Results

3.1. Identification of Ferroptosis-Related lncRNAs in Bladder Cancer Samples. The transcriptomic data of 411 bladder cancer samples and 19 normal bladder samples were used to screen for ferroptosis-related lncRNAs. The mRNAs and lncRNAs were separated based on annotations in the GENCODE database [33]. Pearson's correlation analysis ($|R| > 0.5$ and $p < 0.001$) were conducted between these ferroptosis-related mRNAs and lncRNAs to identify ferroptosis-related lncRNAs. A total of 263 ferroptosis-related lncRNAs were identified via Pearson's correlation analysis (Supplementary Tables 2 and 3). The coexpression network of ferroptosis-related mRNAs and lncRNAs is demonstrated in Figure 1(a). Only 403 samples with available clinical information were selected for analysing the relationship between the ferroptosis-related lncRNAs and prognosis via univariate Cox regression analysis (Supplementary Table 4). A total of 20 ferroptosis-related lncRNAs were identified to be significantly associated with the prognosis of bladder cancer, including AP001160.1, THUMP3-AS1, AC009065.5, AC087286.2, RBMS3-AS3, AC005387.1, SH3RF3-AS1, AC005785.1, AL136084.3, AL731567.1, AC006160.1, AC012568.1, HMG2-AS1, AC025280.1, AC034236.2, AL031429.2, AP003419.3, AC010618.2, SPAG5-AS1, and AL133415.1 (Figure 1(b)). The expression of these 20 prognostic lncRNAs was found to be different between tumour and healthy bladder tissues ($p < 0.05$) (Figure 1(c)). These results verified the important role of ferroptosis-related lncRNAs in the development of bladder cancer.

3.2. Distinct Ferroptosis Mediation Patterns Based on Prognostic Ferroptosis-Related lncRNAs in Bladder Cancer. Based on the 20 prognostic ferroptosis-related lncRNAs, two ferroptosis mediation patterns were identified via consensus clustering using the "ConsensusClusterPlus" package in R (Figure 1(d)). The results of cluster analysis for all bladder cancer samples

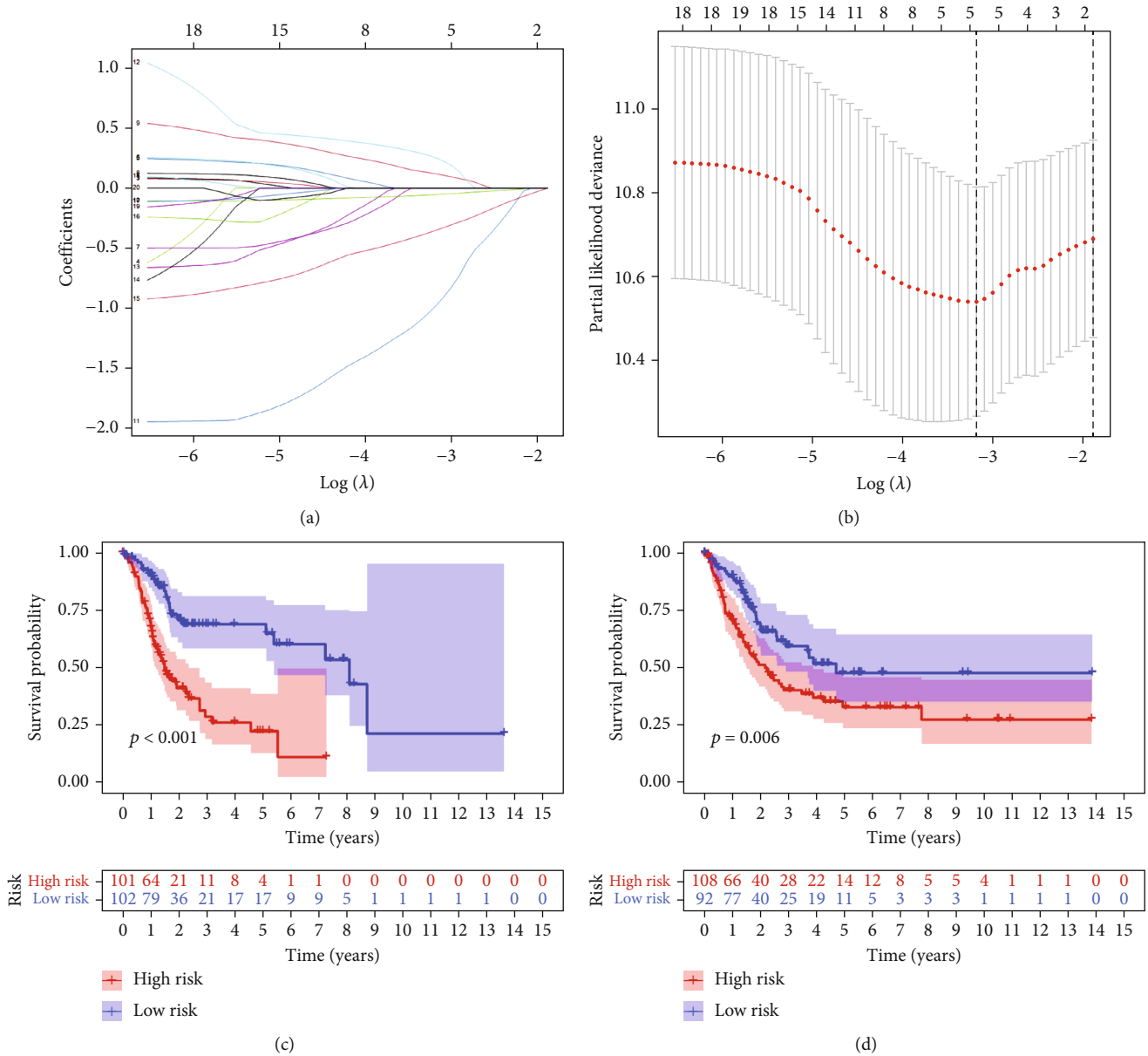


FIGURE 2: Construction and validation of the ferroptosis-related lncRNA signature for predicting prognosis in the training and validation cohorts. (a) LASSO coefficients of the five ferroptosis-related lncRNAs used to construct the signature. (b) Ten-fold cross-validation for tuning parameter selection in the LASSO model. (c) Kaplan–Meier survival curves of the high- and low-risk groups in the training cohort. (d) Kaplan–Meier survival curves of the high- and low-risk groups in the validation cohort.

are shown in Supplementary Table 5. Kaplan–Meier survival analysis (Figure 1(e)) revealed that survival outcomes were significantly poorer in cluster 1 than in cluster 2 ($p < 0.05$). Detailed clinical characteristics of bladder cancer samples are mentioned in Supplementary Table 6, and the relationship between the two ferroptosis mediation patterns and various clinical parameters including age, sex, grade, and tumour stage is demonstrated in Figure 1(f). Significant differences in the tumour grade and age of patients were observed between clusters 1 and 2.

3.3. Construction and Validation of a Ferroptosis-Related-lncRNA Risk Signature. The 403 bladder cancer samples were

randomly divided into the training (203 samples) and validation (200 samples) cohorts to investigate the prognostic role of ferroptosis-related lncRNAs. LASSO regression analysis was performed to examine the 20 ferroptosis-related lncRNAs associated with prognosis, and a risk signature including 5 lncRNAs was successfully constructed in the training cohort. The five targeted lncRNAs are listed in Table 1. Figure 2(a) demonstrates the LASSO coefficients of the five lncRNAs, and Figure 2(b) demonstrates the 10-fold cross-validation of the LASSO model, indicating that the selection of these five lncRNAs is optimal for constructing the signature. All samples were further divided into the high- and low-risk groups according to the median risk score. The risk scores and grouping of the

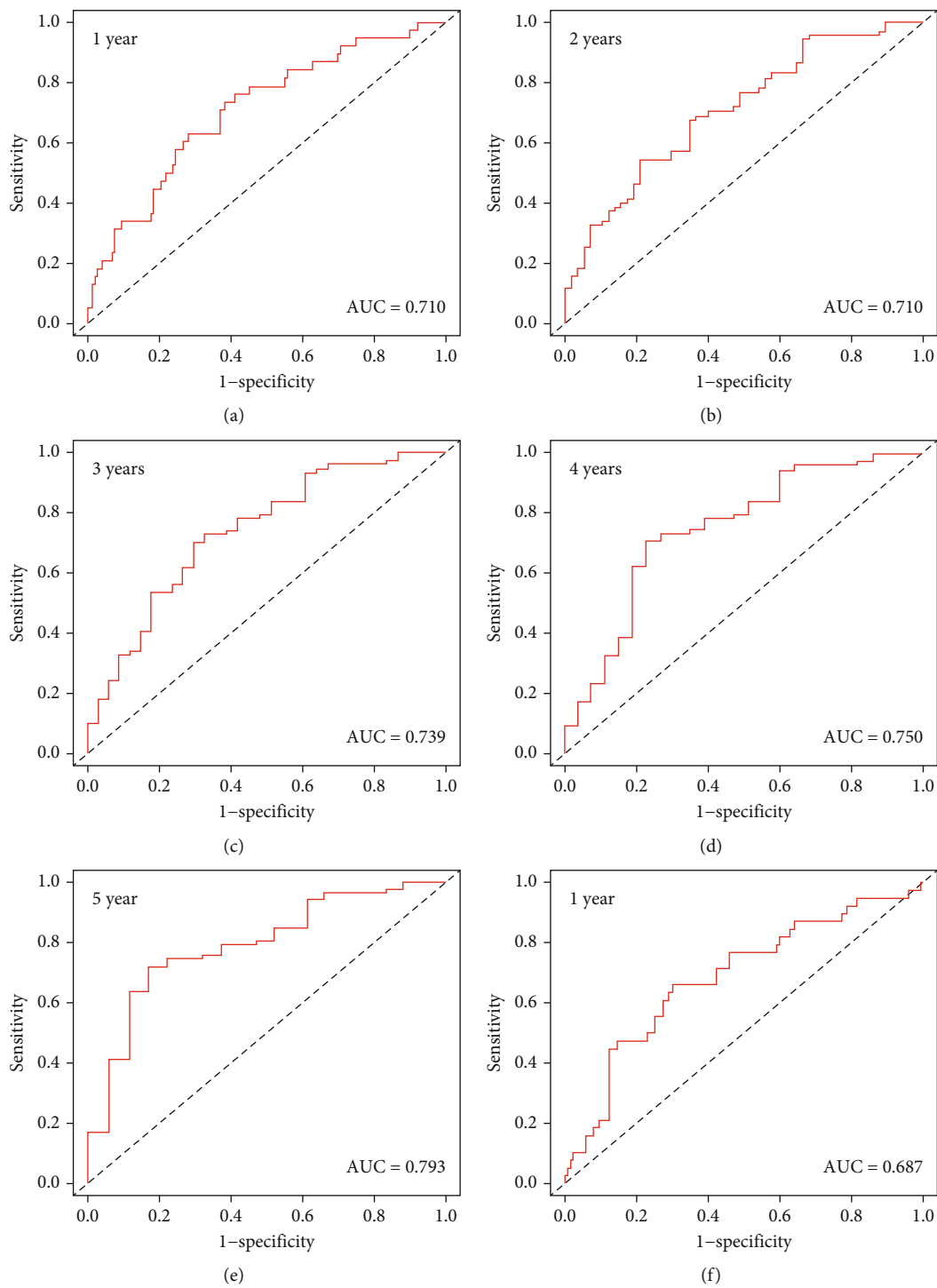


FIGURE 3: Continued.

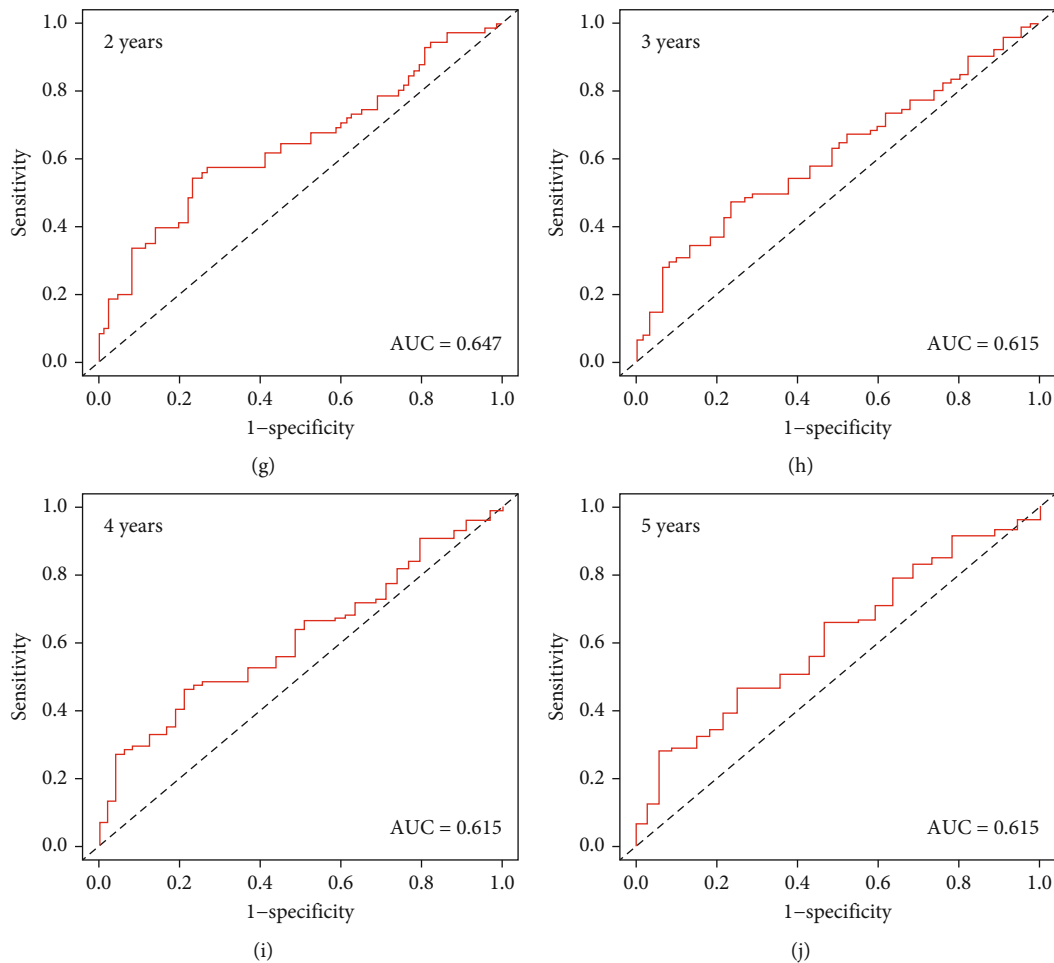


FIGURE 3: ROC curve analysis of the relationship between the ferroptosis-related lncRNA signature and survival in both training and validation cohorts. (a–e) ROC curves for predicting survival at 1–5 years in the training cohort. (f–j) ROC curves for predicting survival at 1–5 years in the validation cohort.

training and validation cohorts are shown in Supplementary Tables 7 and 8, respectively. Survival outcomes were significantly poorer in the high-risk group than in the low-risk group in both training ($p < 0.001$) (Figure 2(c)) and validation ($p = 0.006$) (Figure 2(d)) cohorts. To verify the predictive role of the risk signature, ROC analysis was performed to compare survival outcomes at 1–5 years in the training and validation cohorts. The area under the ROC curve (AUC) for predicting 1-, 2-, 3-, 4-, and 5-year survival in the training cohort was 0.710, 0.710, 0.739, 0.750, and 0.793, respectively. These results demonstrated promising performance of the risk signature in predicting the survival of patients with bladder cancer (Figures 3(a)–3(e)). As shown in Figures 3(f)–3(j), the risk signature showed excellent predictive performance in the validation cohort. These results indicate that the identified ferroptosis-related lncRNAs can be used to predict survival outcomes in bladder cancer.

3.4. Independent Predictive Role of the Ferroptosis-Related lncRNA Signature. The distribution of risk scores in the training cohort is demonstrated in Figure 4(a), and the cor-

responding survival status is demonstrated in Figure 4(c). In both training and validation cohorts, the death rate is significantly higher in the high-risk group than in the low-risk group (Figures 4(b) and 4(d)). Heatmaps (Figures 4(e) and 4(f)) are plotted to demonstrate the expression of the five target lncRNAs in the high- and low-risk groups. Univariate and multivariate cox regression analyses are performed in both training and validation cohorts to investigate the independent predictive role of the lncRNA signature. As shown in Figures 5(a) and 5(b), the risk score ($p < 0.001$), stage ($p < 0.001$), and age ($p < 0.001$) are identified as independent risk factors for survival in the validation cohort. As shown in Figures 5(c) and 5(d), the risk score ($p < 0.001$) and stage ($p < 0.001$) are identified as independent risk factors for overall survival in the training cohort. These results demonstrate that the lncRNA risk signature established in this study can independently predict survival outcomes.

3.5. Prognostic Role of the lncRNA Signature in Different Subgroups. An excellent prognostic tool in clinical practice should have consistent predictive performance in different

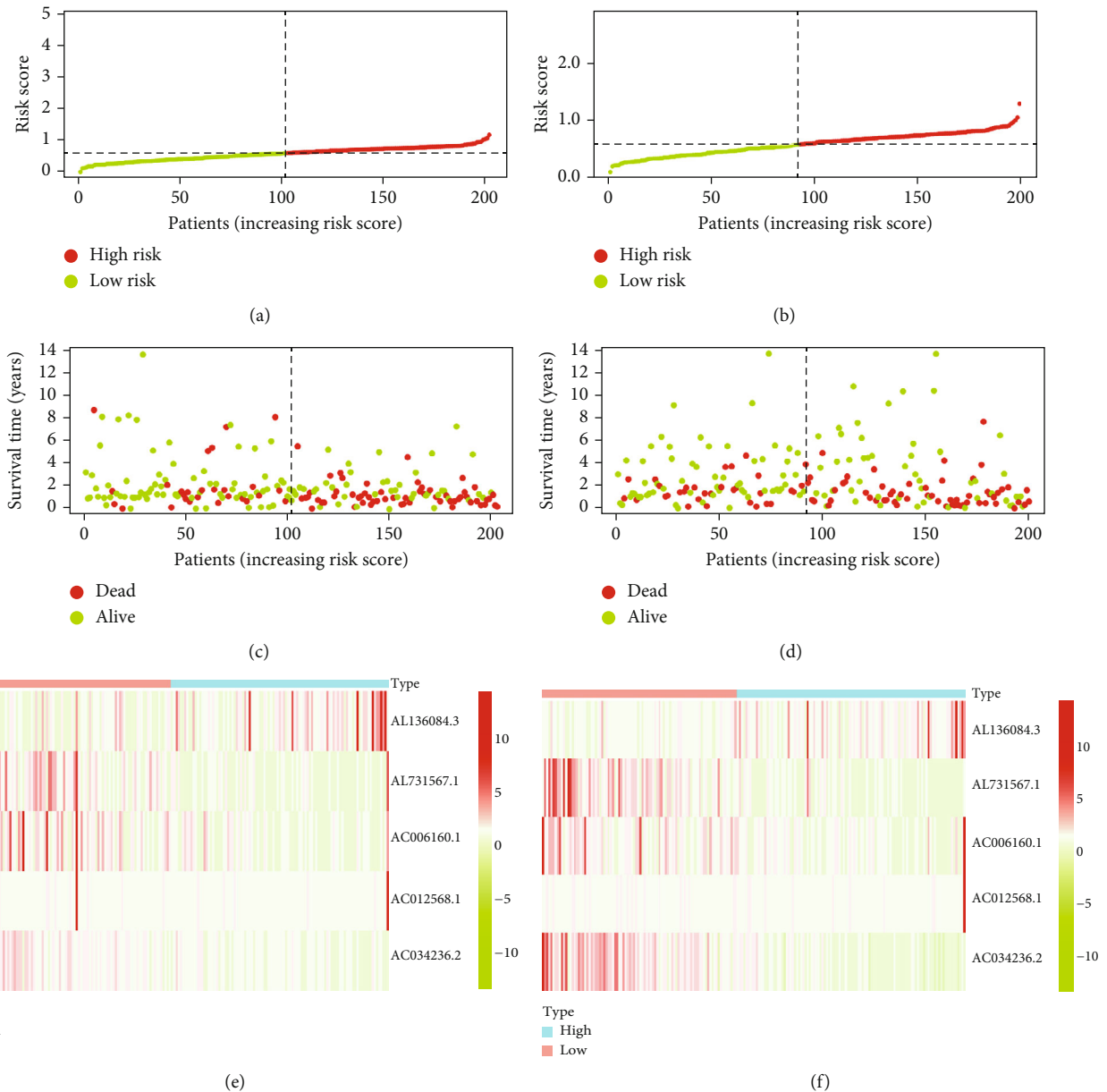
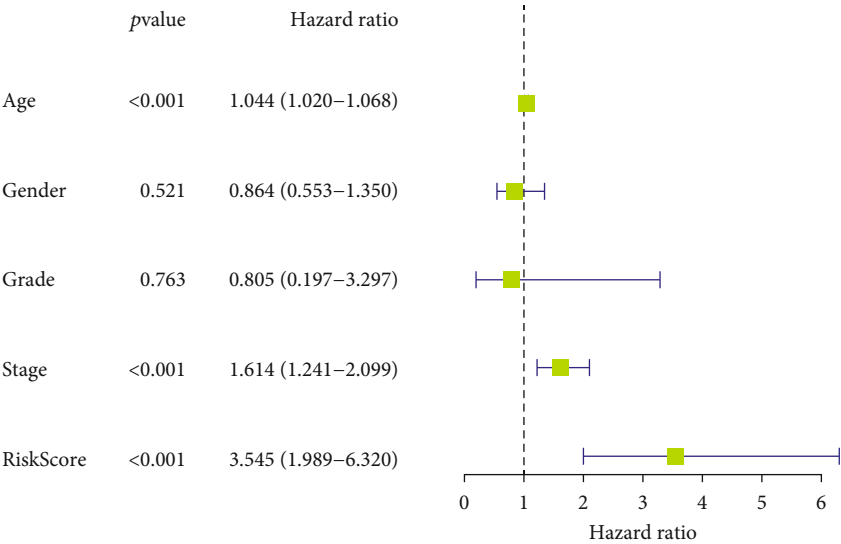


FIGURE 4: Distribution of risk scores and survival outcomes in both training and validation cohorts. (a) Distribution of risk scores in the training cohort. (b) Distribution of risk scores in the validation cohort. (c) Survival outcomes in the training cohort. (d) Survival outcomes in the validation cohort. (e) Heatmap demonstrating the expression of the five target lncRNAs in the training cohort. (f) Heatmap demonstrating the expression of the five target lncRNAs in the validation cohort.

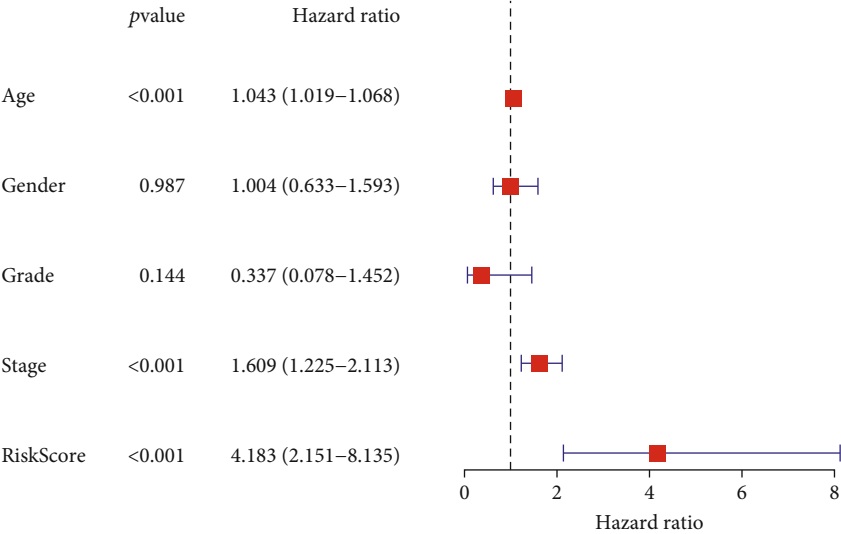
subgroups. As shown in Figure 6, the 5-lncRNA risk signature was significantly associated with prognosis in the old (age > 65 years) ($p < 0.001$), male ($p < 0.001$), female ($p = 0.014$), stage I–II ($p = 0.007$), stage III–IV ($p < 0.001$), T1–T2 ($p = 0.022$), T3–T4 ($p < 0.001$), and N0 stage ($p < 0.001$) groups. However, the lncRNA risk signature was not associated with prognosis among patients aged ≤ 65 years, suggesting that the prognosis of younger patients may be influenced by various other mechanisms underlying the development of bladder cancer. Furthermore, the subgroup analysis verified that the lncRNA risk signature can serve as a biomarker to predict survival outcomes in bladder cancer. As shown in Figure 7(a), the

risk signature was significantly correlated with the ferroptosis mediation patterns ($p < 0.001$), immune scores ($p < 0.001$), clinical stages ($p < 0.001$), and tumour grades ($p < 0.01$). In addition, elderly patients, patients with advanced-stage disease, and those with advanced T- or N-grade disease had higher risk scores (Figures 7(b)–7(f)). These results indicate that the lncRNA risk signature reflects various clinical characteristics from a genetic or molecular perspective, which should be further investigated in future studies.

3.6. Infiltration Abundance of Immune Checkpoints and Immune Cells in Clusters 1 and 2. The expression of PD-1



(a)



(b)

FIGURE 5: Continued.

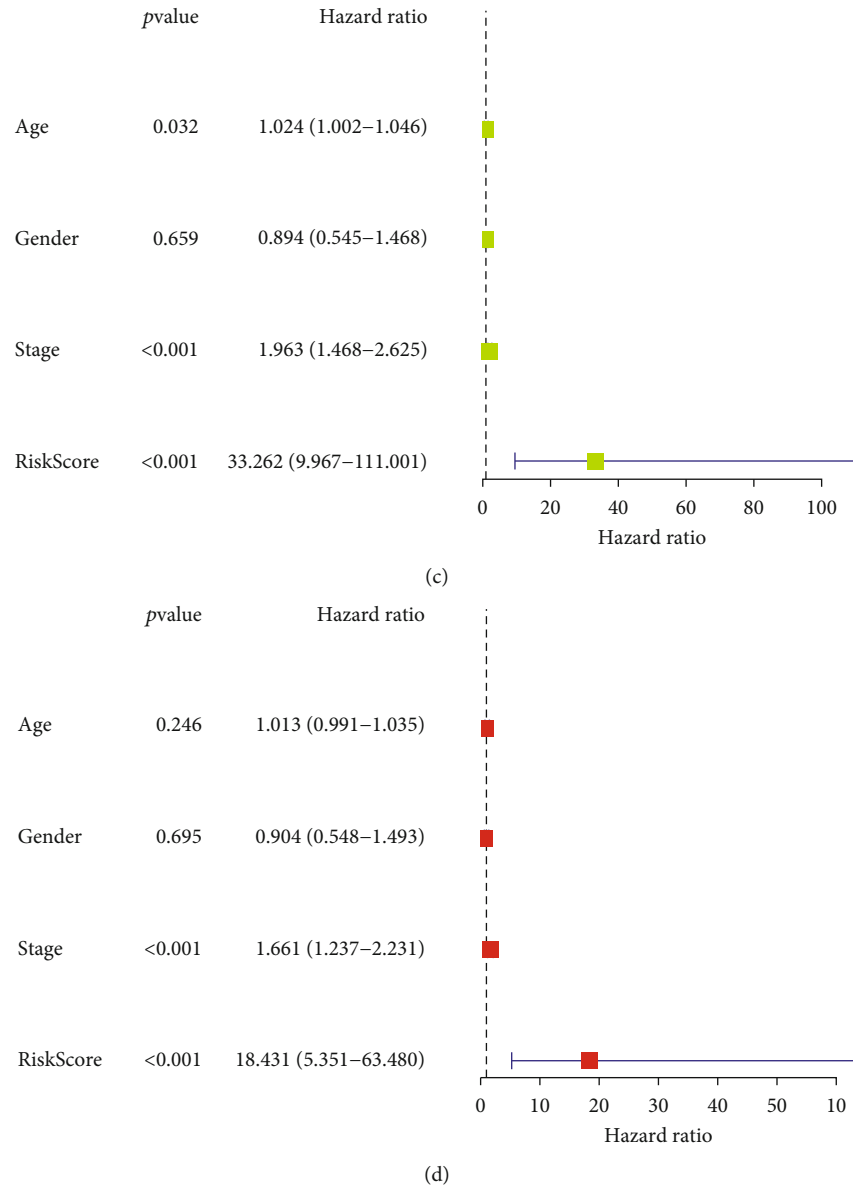


FIGURE 5: The lncRNA risk signature was identified as an independent prognostic factor in both training and validation cohorts. (a) Univariate Cox regression analysis in the validation cohort. (b) Multivariate Cox regression analysis in the validation cohort. (c) Univariate Cox regression analysis in the training cohort. (d) Multivariate Cox regression analysis in the training cohort.

($p < 0.001$), PD-L1 ($p < 0.001$), and CTLA-4 ($p < 0.001$) was significantly higher in cluster 1 than in cluster 2 (Figures 8(a)–8(c)). Higher expression of these immune checkpoints was associated with poorer survival outcomes in cluster 1. As shown in Figure 8(d), PD-1 expression was positively correlated with AL136084.3 and negatively correlated with AC005785.1, AL731567.1 and AC010618.2. As shown in Figure 8(e), PD-L1 expression was positively correlated with AC006160.1 and negatively correlated with AC009065.5, AC005387.1, AL731567.1, AC034236.2, AP003419.3, and AC010618.2. As shown in Figure 8(f), CTLA-4 expression was significantly correlated with various ferroptosis-related lncRNAs. Furthermore, based on the cellular biomarkers of immune cells shown in Supplementary Table 9, the infiltration levels of 22 types of immune cells were

calculated using the CIBERSORT algorithm (Supplementary Table 10). The ESTIMATE scores of each sample are shown in Supplementary Table 11, and the relationship between the infiltration of 22 types of immune cells and ferroptosis mediation patterns is demonstrated in Figure 8(g). As shown in box plots in Figures 8(h)–8(l), cluster 1 had lower infiltration levels of naive B cells ($p = 0.006$), activated dendritic cells ($p = 0.015$), follicular helper T cells ($p = 0.015$), and Tregs ($p = 0.003$) and higher infiltration levels of M2 macrophages. These results indicate that poorer survival outcomes observed in cluster 1 may be associated with the tumour immune microenvironment of bladder cancer. Furthermore, GSEA was performed to investigate mechanisms underlying poorer survival outcomes in cluster 1. The results

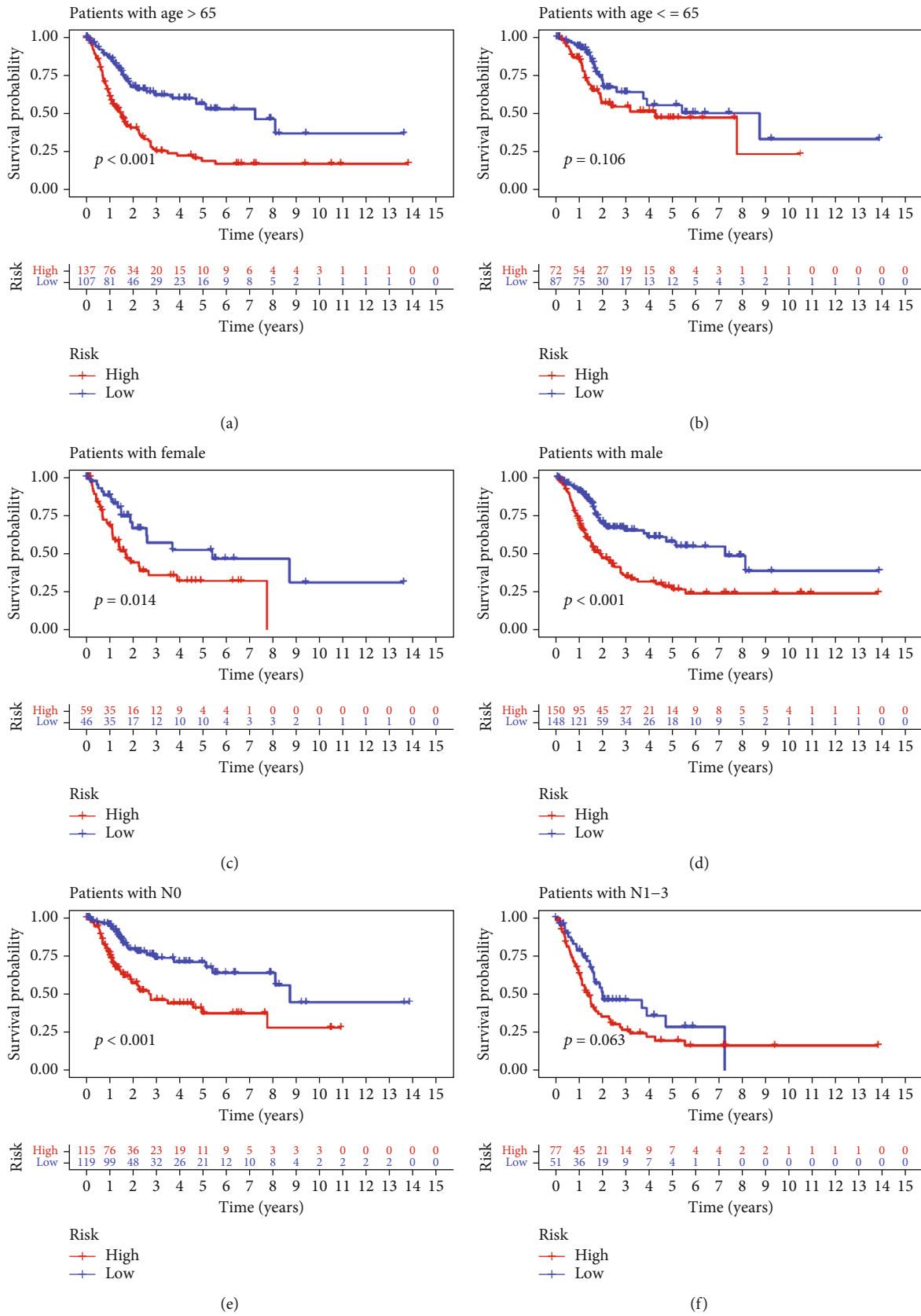


FIGURE 6: Continued.

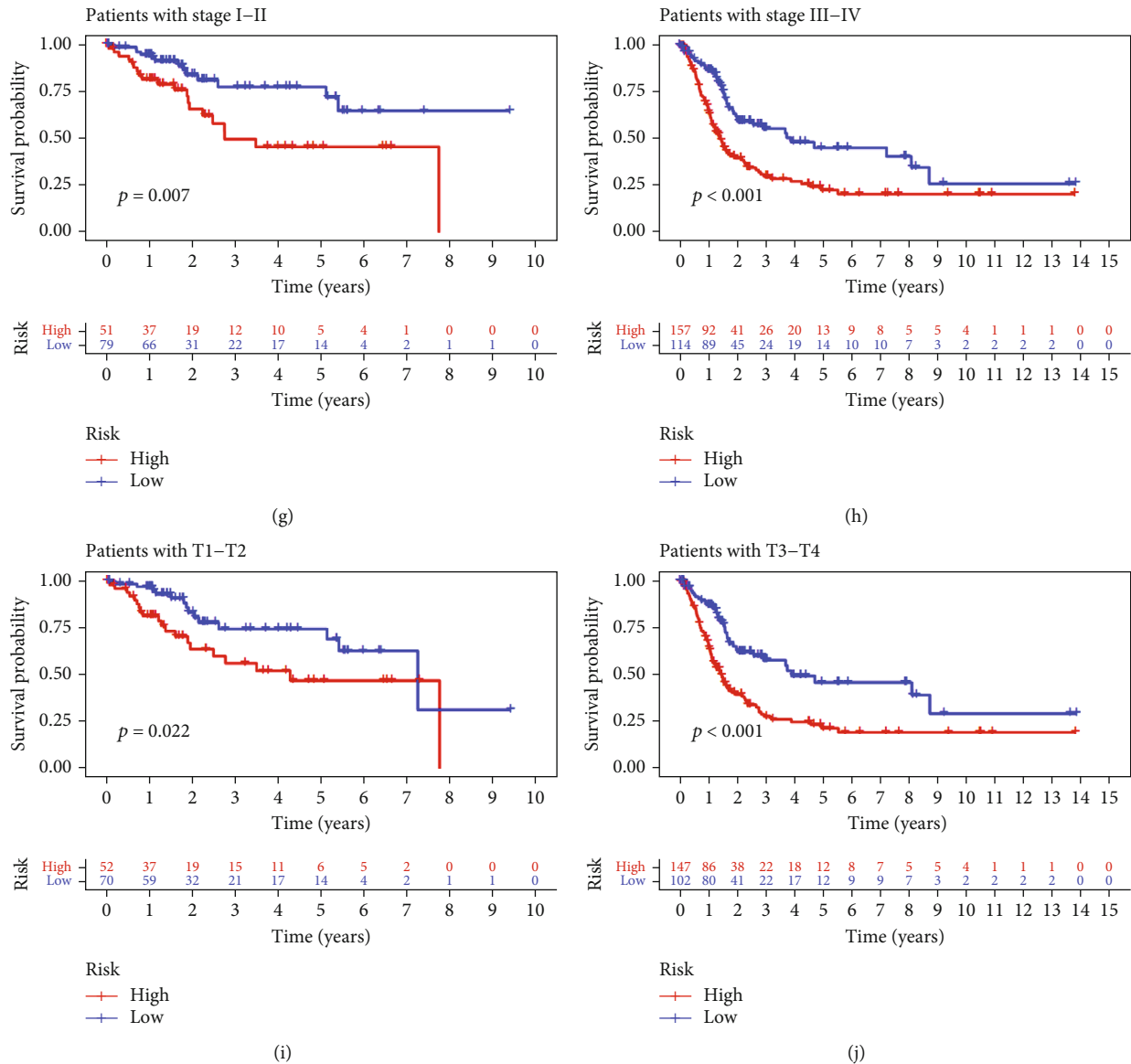


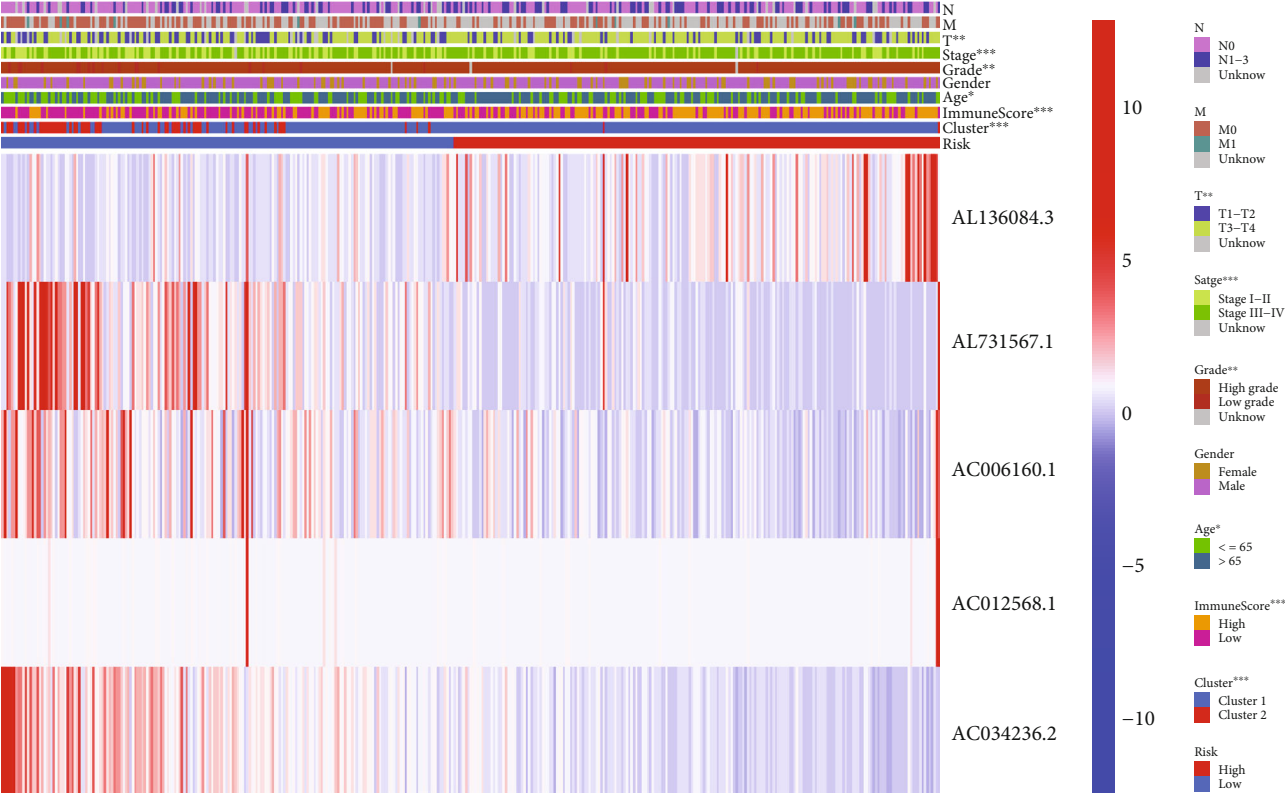
FIGURE 6: The lncRNA signature showed excellent performance in predicting survival in different subgroups. (a, b) Age (age, >65 or ≤ 65 years). (c, d) Sex (female or male). (e, f) Lymphatic invasion (no or yes). (g, h) Tumour stage (I–II or III–IV). (i, j) Clinical T stage (T1–T2 or T3–T4).

revealed that the toll-like receptor signalling pathway, T-cell receptor signalling pathway, regulation of the actin cytoskeleton, cytokine and cytokine–receptor interaction, and chemokine signalling pathway were significantly enriched in cluster 1 ($p < 0.01$) (Supplementary Figure 1). These results indicate that ferroptosis-related lncRNAs play a regulatory role through these pathways during the development of bladder cancer.

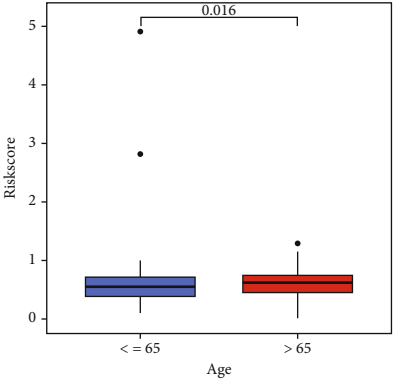
3.7. Guidance of Immunotherapy for Bladder Cancer Based on the lncRNA Signature. The expression of PD-1 ($p < 0.001$), PD-L1 ($p < 0.001$), and CTLA-4 ($p < 0.001$) (Figures 9(a)–9(c)) was higher in the high-risk group, which indicated the potential role of the lncRNA signature in immunotherapy. Therefore, the correlation between risk scores and immune cell infiltration was further investigated. As shown in Figures 9(d)–9(n), risk scores were significantly correlated

with the infiltration levels of naive B cells, eosinophils, M0 macrophages, M2 macrophages, CD4 memory resting T cells, CD8 T cells, follicular helper T cells, Tregs, activated mast cells, neutrophils, and plasma cells. Furthermore, the response of patients to immunotherapy was evaluated using the TIDE algorithm (Supplementary Table 12). As shown in Figures 9(o) and 9(p), patients with high risk scores posed a better response to immunotherapy ($p < 0.001$). With the rapid development of sequencing technology, the lncRNA risk signature established in this study can be used to guide immunotherapy for bladder cancer in the future.

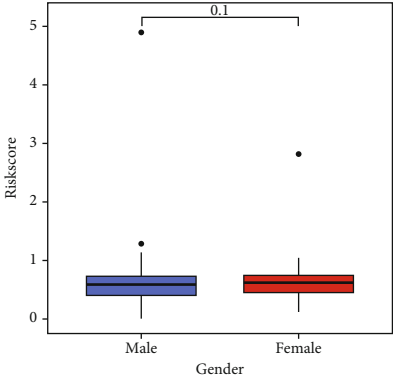
3.8. lncRNA AC006160.1 Inhibited the Proliferation and Migration of Bladder Cancer Cells. Because the lncRNA AC006160.1 had the highest correlation with the risk signature, it was selected for further analysis. The qRT-PCR indicated that AC006160.1 expression was lower in the bladder



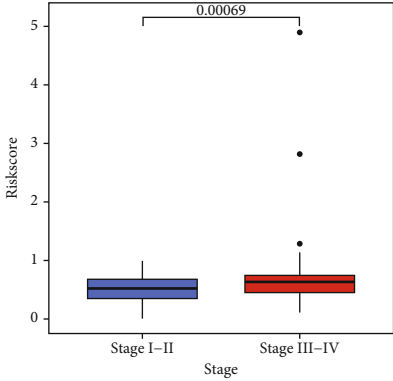
(a)



(b)



(c)



(d)

FIGURE 7: Continued.

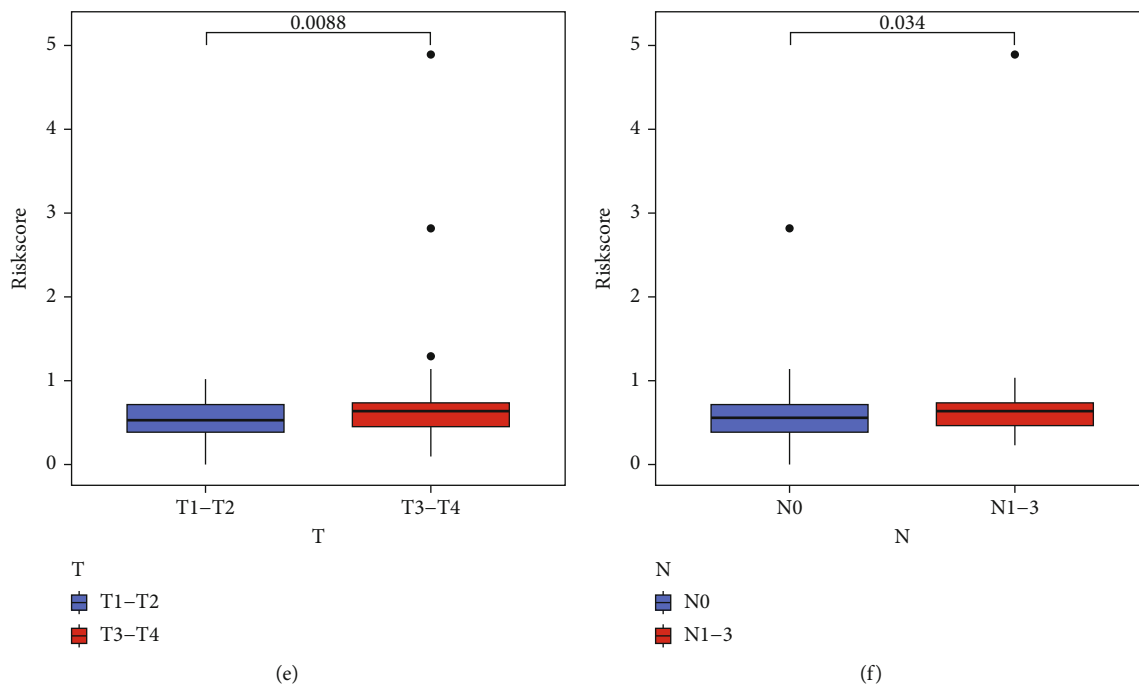


FIGURE 7: Correlation between the lncRNA risk signature and clinicopathological features. (a) Heatmap demonstrating the correlation between risk scores and clinicopathological features. (b) Differences in risk scores between patients aged >65 years and those aged ≤65 years. (c) Differences in risk scores between female and male patients. (d) Differences in risk scores between patients with stage I–II disease and those with stage III–IV disease. (e) Differences in risk scores between patients with T1–T2-stage disease and those with T3–T4-stage disease. (f) Differences in risk scores between patients with and without lymphatic invasion (* $p < 0.05$; ** $p < 0.01$; *** $p < 0.001$).

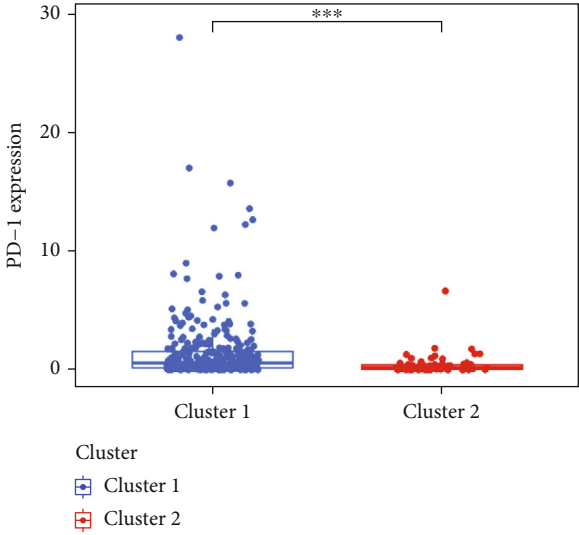
cancer cell lines BIU-87, T24, RT4, RT-112, and 5637 than in the normal human uroepithelial cell line SV-HUC-1 (Figure 10(a)). Furthermore, CCK-8 assay was performed to examine the influence of AC006160.1 on the viability of bladder cancer cells. AC006160.1 expression was lower in T24 and BIU-87 cells than in the other bladder cancer cell lines; therefore, these two cell lines were used for examining the biological functions of AC006160.1. A plasmid overexpressing AC006160.1 was constructed, and the results of qPCR verified that transfection with this plasmid increased AC006160.1 expression by approximately 15- and 5-fold in T24 and BIU-87 cells, respectively (Figure 10(b)). CCK8 assay revealed that AC006160.1 overexpression significantly suppressed the proliferation of T24 and BIU-87 cells (Figure 10(c)). Furthermore, the influence of AC006160.1 on colony formation was examined. As shown in Figure 10(d), AC006160.1 overexpression decreased the number of colonies of both T24 and BIU-87 cells compared with the control group (Figure 10(e)). Transwell (Figures 10(f) and 10(g)) and wound healing (Figures 10(h) and 10(i)) assays revealed that AC006160.1 overexpression significantly inhibited the migration of T24 and BIU-87 cells. Altogether, these results indicate that the ferroptosis-related lncRNA AC006160.1 suppresses the viability of bladder cancer cells, which is consistent with the results of bioinformatic analysis.

3.9. Drug Sensitivity Analysis. As shown in Figure 11(a), drug sensitivity analysis based on IC50 values revealed that patients with low expression of AC006160.1 were sensitive to most anticancer drugs. However, compared with patients with low

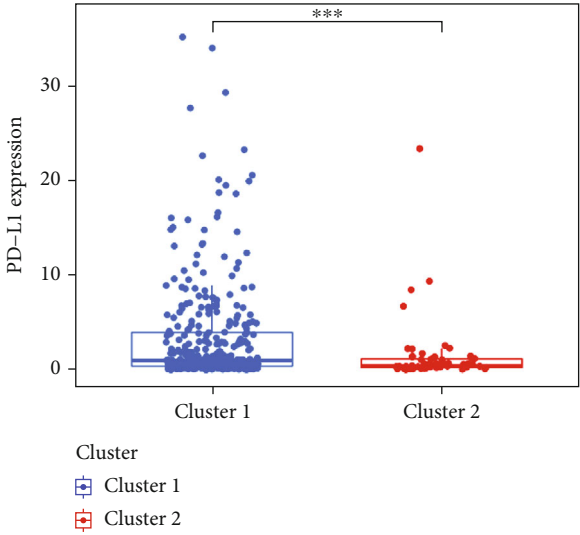
expression of AC006160.1, those with high expression of AC006160.1 were more sensitive to MET and methotrexate ($p < 0.01$) (Figure 11(b)). Furthermore, in vitro drug sensitivity analysis was performed to examine whether AC006160.1 could enhance MET sensitivity in BIU-87 cells. AC006160.1 overexpression combined with MET treatment decreased the number of BIU-87 colonies (Figure 11(c)). In addition, CCK8 assay revealed that AC006160.1 overexpression combined with MET treatment significantly suppressed the proliferation of BIU-87 cells (Figure 11(d)). These results indicate that AC006160.1 may enhance drug sensitivity in the treatment of bladder cancer.

4. Discussion

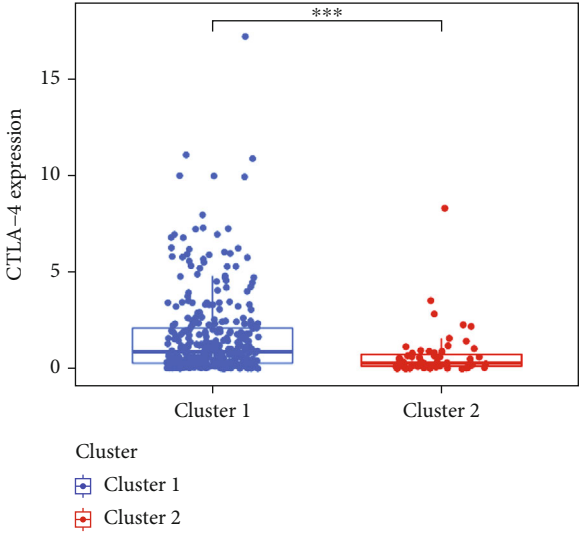
Bladder cancer is one of the most malignant tumours. According to recent statistical data, >500,000 new cases of bladder cancer are reported annually worldwide [34]. Bladder cancer is classified as non-muscle-invasive and muscle-invasive bladder cancer, and its metastasis depends on its clinical characteristics. The currently available diagnostic strategies for bladder cancer include urine cytology and cystoscopy, which are invasive and can lead to many complications in patients [35]. Transurethral resection of tumours combined with intravesical perfusion therapy is recommended for non-muscle-invasive cancer, whereas radical cystectomy is recommended for muscle-invasive cancer. In addition, cisplatin-based chemotherapy is recommended for patients with advanced cancer with metastasis [36]. For chemotherapy-resistant tumours, immune checkpoint inhibitor (ICI) therapy is recommended in clinical settings [37].



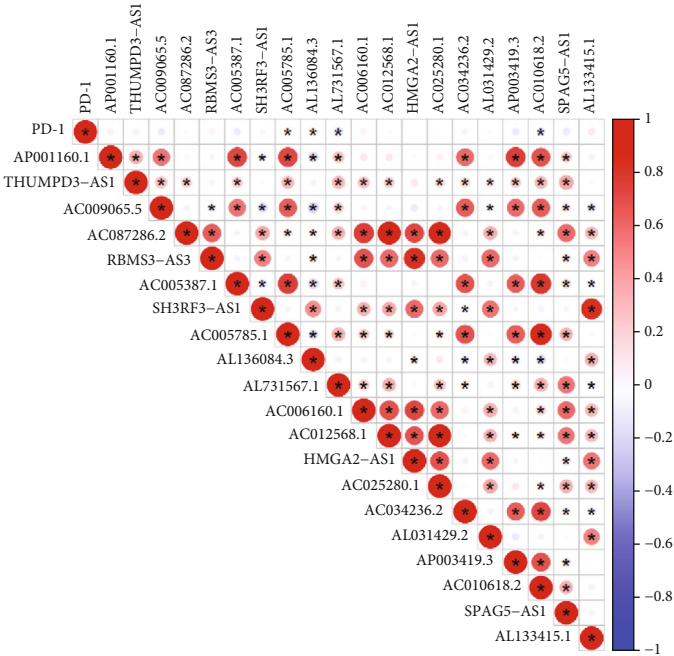
(a)



(b)



(c)



(d)

FIGURE 8: Continued.

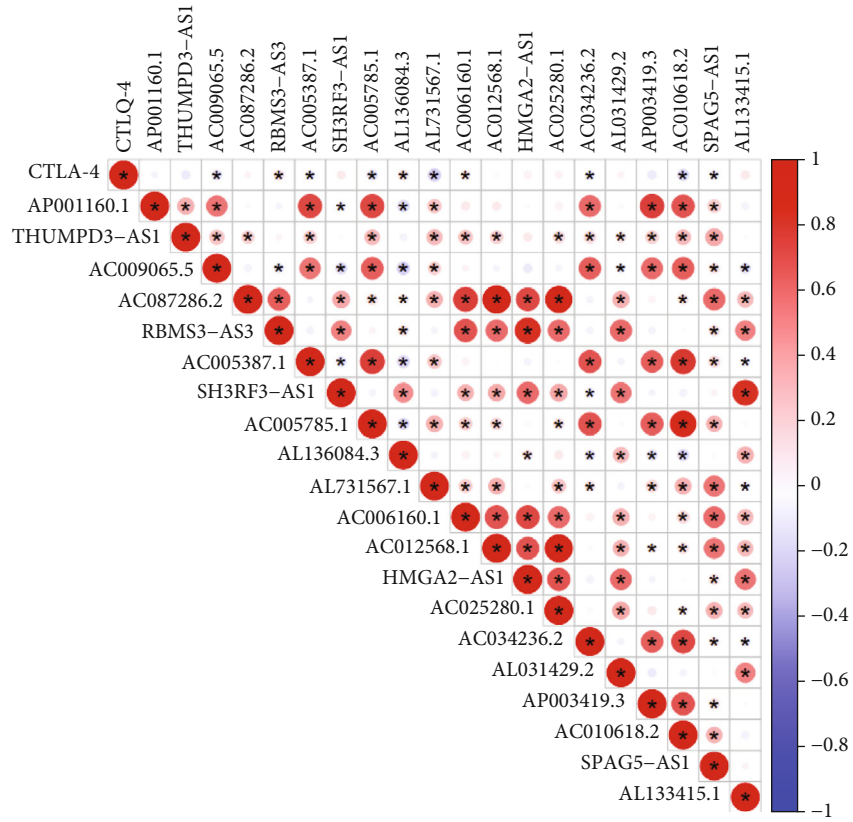
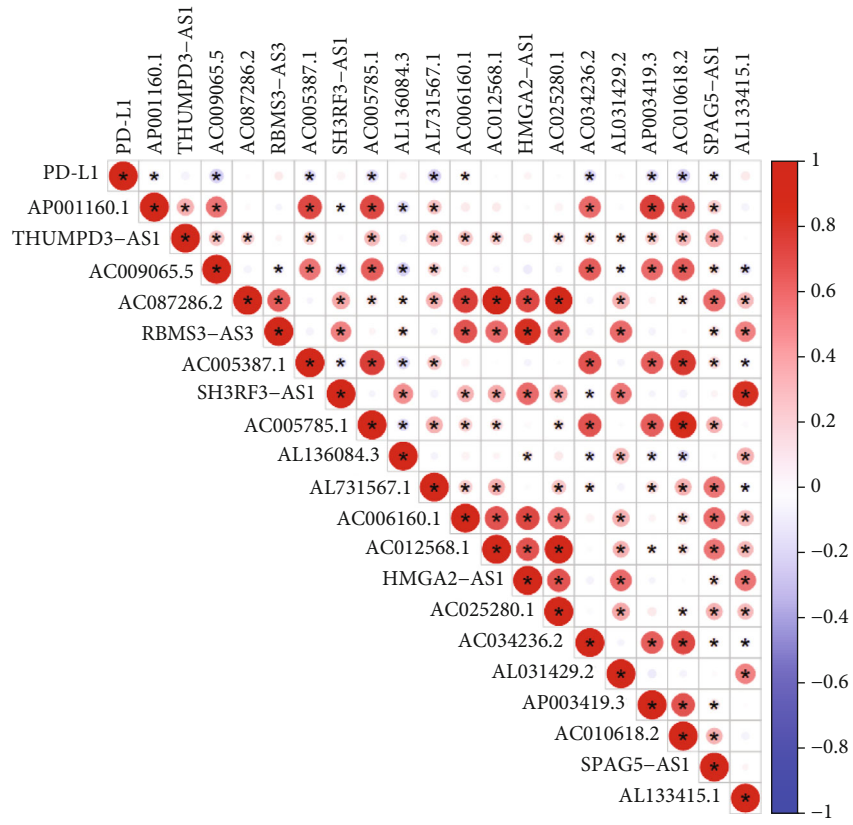
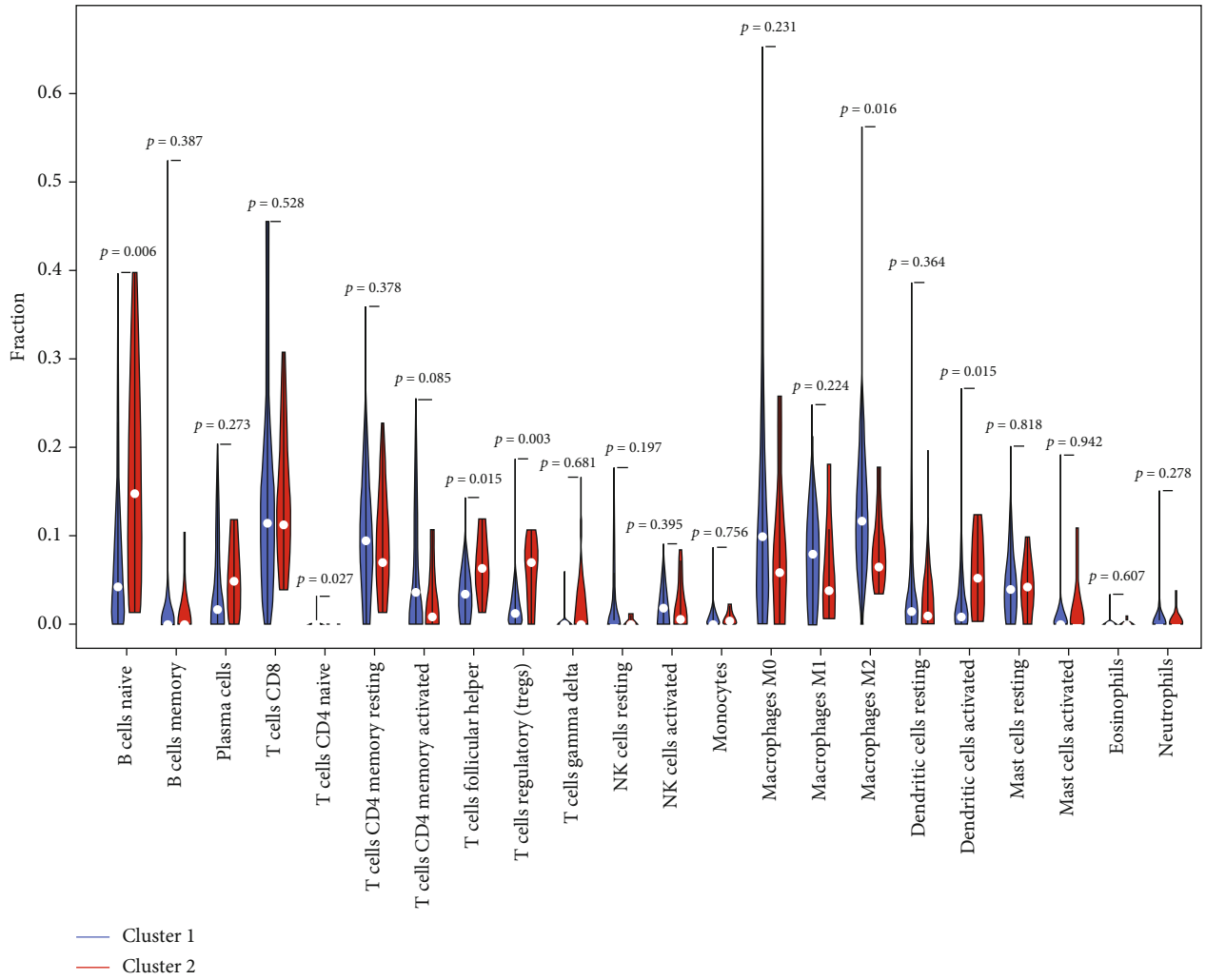
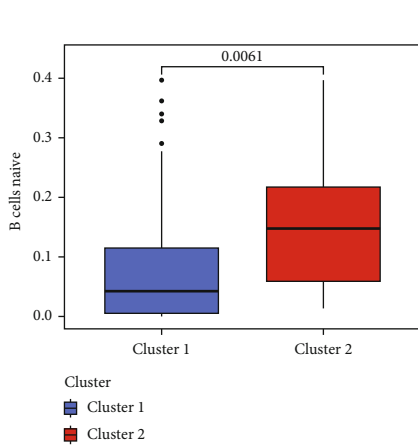


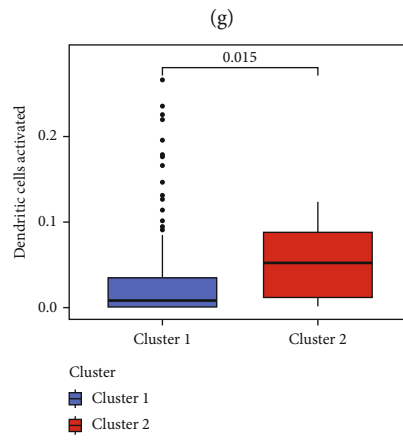
FIGURE 8: Continued.



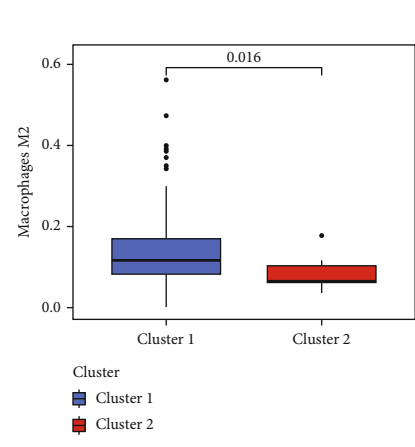
Cluster 1
Cluster 2



(h)



(i)



(j)

FIGURE 8: Continued.

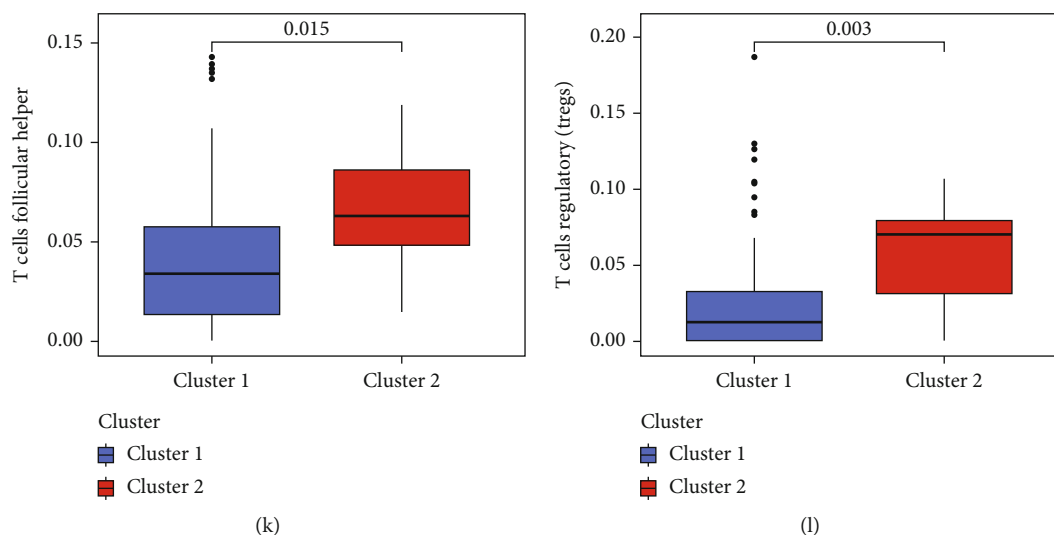


FIGURE 8: Correlation of ferroptosis-related lncRNAs with immune checkpoints and immune microenvironment in bladder cancer. (a–c) Differences in the expression of PD-1, PD-L1, and CTLA-4 between clusters 1 and 2. (d–f) Correlation between the expression of PD-1, PD-L1, and CTLA-4 and the 20 prognostic lncRNAs. (g) Infiltration of 22 types of immune cells in clusters 1 and 2. (h–l) The two clusters had significantly different infiltration levels of various immune cells including naive B cells, activated dendritic cells, M2 macrophages, follicular helper T cells, and Tregs ($*p < 0.05$; $**p < 0.01$; $***p < 0.001$).

However, owing to the irregular expression of various immune checkpoints and heterogeneity of genetic mutations, chemotherapy or ICI therapy has limited benefits in only a small number of patients. Moreover, because mechanisms underlying the development of bladder cancer remain unclear, limited progress has been achieved in the development of relative treatment strategies for bladder cancer during the past decade. Furthermore, bladder cancer has a high genetic mutation burden, and cancers with a high mutation burden such as lung cancer and melanoma may benefit the most from ICI therapy if robust biomarkers are discovered for clinical application [38–40]. However, the rapid development of next-generation sequencing and large-scale gene expression tools may help to improve the treatment of cancer in the future. The next-generation sequencing can provide vital genetic information for improving the diagnosis of bladder cancer and distinguishing treatment responses. Whole-transcriptome matrix information can also help to discover distinct molecular subtypes of bladder cancer with different mechanisms and molecular characteristics [6, 41]. In addition, establishing valuable risk signatures for predicting survival outcomes and response to ICI therapy can greatly improve therapeutic efficacy among patients with bladder cancer. Identifying patients who are sensitive to ICIs or chemotherapeutic agents can significantly improve the guidance of targeted therapy and increase the therapeutic benefits, especially among patients with advanced cancer. In addition, it can help to avoid unnecessary ICI or chemotherapy toxicity and potential delay in radical cystectomy for patients with treatment resistance. In a previous study, we reported that ferroptosis-related genes identified using sequencing data played a vital role in predicting the clinical information of bladder cancer samples [42]. In this study, we investigated the potential role of ferroptosis-related lncRNAs in bladder cancer and successfully constructed a risk signature based on five ferroptosis-related lncRNAs to

predict survival outcomes, the tumour microenvironment, and the response of patients with bladder cancer to ICI therapy. In addition, the lncRNA AC006160.1 was identified as a protective factor for the development of bladder cancer.

Univariate cox regression analysis was used to construct a risk signature based on 20 prognostic ferroptosis-related lncRNAs, which were differentially expressed between tumour and healthy bladder tissues (Figure 1(c)). Significant differences in expression indicated the potential role of these lncRNAs in the development of bladder cancer. These prognostic lncRNAs were further used to divide samples into two groups with different survival outcomes. However, differences in only the tumour grade and age of patients were observed between clusters 1 and 2, which indicated that more accurate scoring methods are required for prognostic analysis. Therefore, a prognostic risk signature was constructed based on LASSO regression analysis, and the risk scores were found to have a significant relationship with various clinical parameters, including survival outcomes, immune microenvironment, ferroptosis clusters, age, clinical stages and tumour grades (Figure 7). The predictive ability of the lncRNA-based risk signature was validated in different clinical groups via subgroup analysis. The risk signature can be used as a novel tool for the treatment of bladder cancer in the future, especially considering the wide development and popularisation of whole-transcriptome sequencing technology.

The risk signature comprised five ferroptosis-related lncRNAs, namely, AC006160.1, AL136084.3, AL731567.1, AC012568.1, and AC034236.2. AL136084.3, has been identified as a risk factor for tumour invasiveness and resistance [43, 44]. To the best of our knowledge, no study has reported on the other four lncRNAs to date. In this study, AC006160.1 was found to have the highest coefficient in the risk signature and was hence analysed as the most important lncRNA. AC006160.1 overexpression significantly suppressed the viability of bladder cancer cells, indicating that AC006160.1 plays a

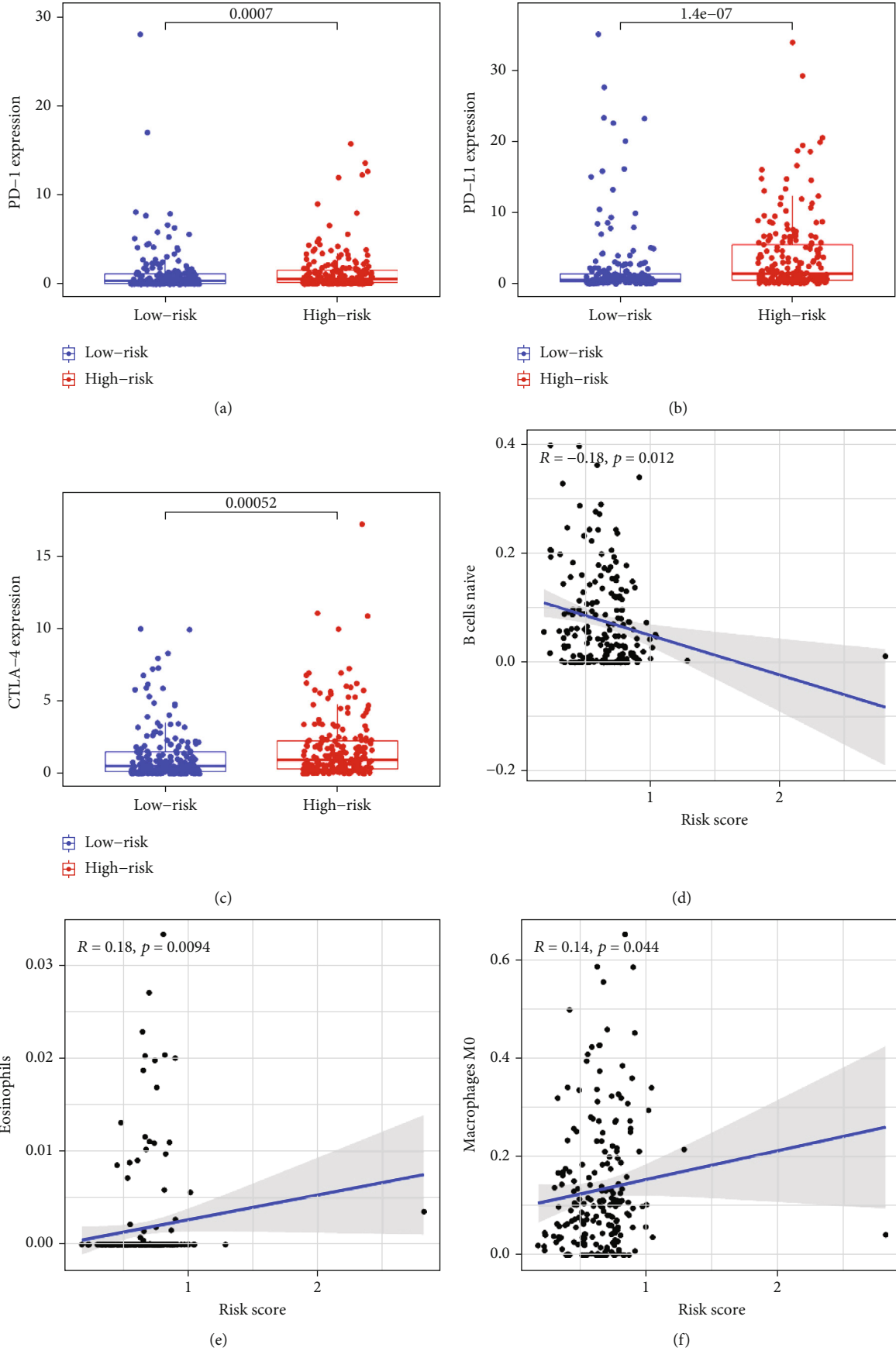


FIGURE 9: Continued.

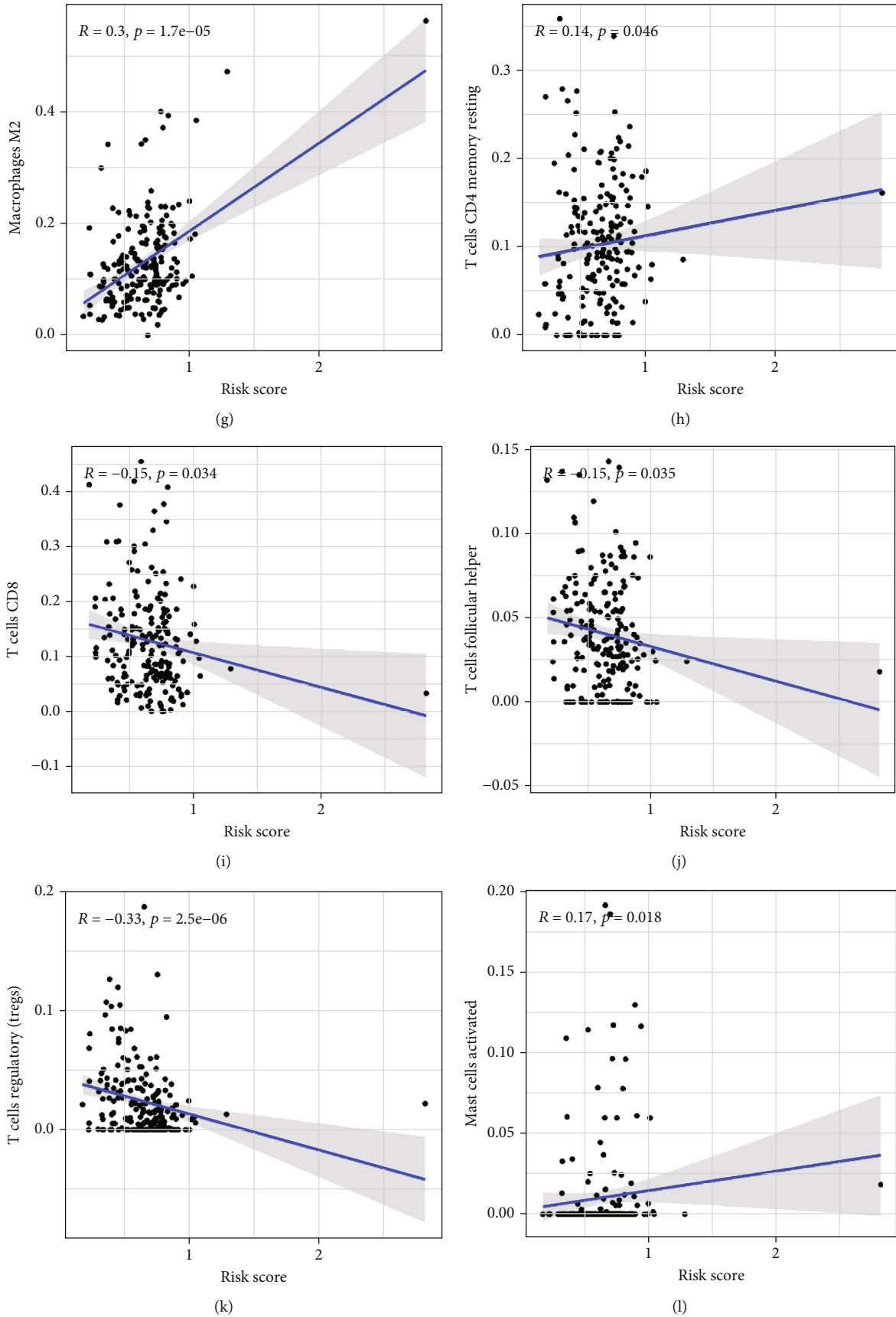


FIGURE 9: Continued.

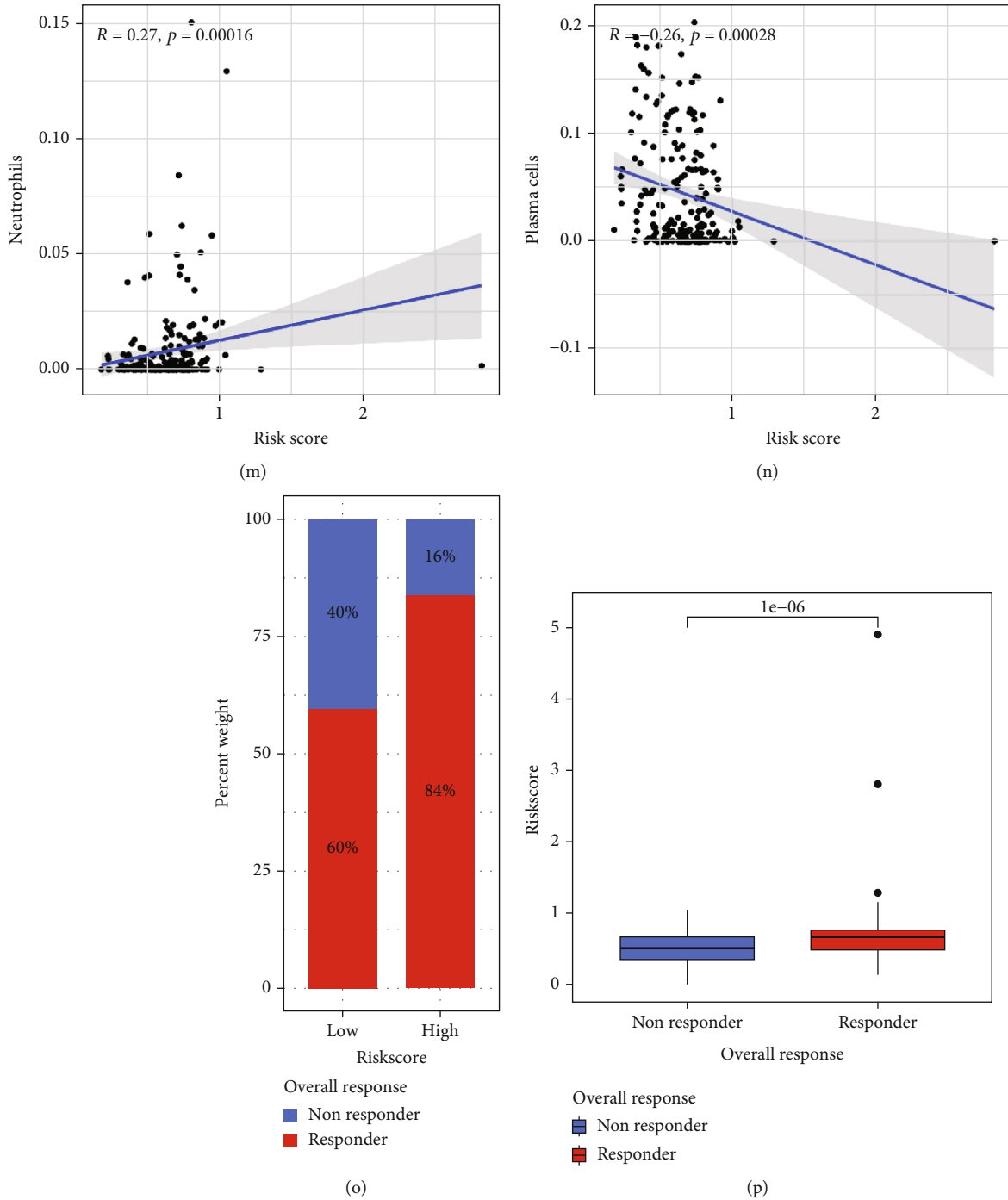


FIGURE 9: The lncRNA risk signature plays a vital role in predicting the response of patients to immunotherapy. (a–c) The high-risk group had significantly higher expression of various immune checkpoints including PD-1, PD-L1, and CTLA-4. (d–n) Risk scores were significantly correlated with the infiltration of 11 types of immune cells, including naive B cells, eosinophils, M0 macrophages, M2 macrophages, CD4 memory resting T cells, CD8 T cells, follicular helper T cells, Tregs, activated mast cells, neutrophils, and plasma cells. (o, p) As evaluated using the TIDE algorithm, high risk scores indicated a response to immunotherapy.

protective role by inhibiting the proliferation and invasion abilities of tumour cells. Therefore, examining the underlying regulatory mechanisms of AC006160.1 may help to identify novel therapeutic targets for bladder cancer. Previous studies have demonstrated the vital role of lncRNAs in tumour develop-

ment and treatment. For example, lncRNAs can influence tumour invasiveness and resistance through the miR-302a-3p/AKT axis, miR-124-3p/MCP-1 pathway, or miR-132-3p/USP22 pathway [45, 46]. In addition, studies have reported the involvement of the WNT signalling pathway and CeRNAs

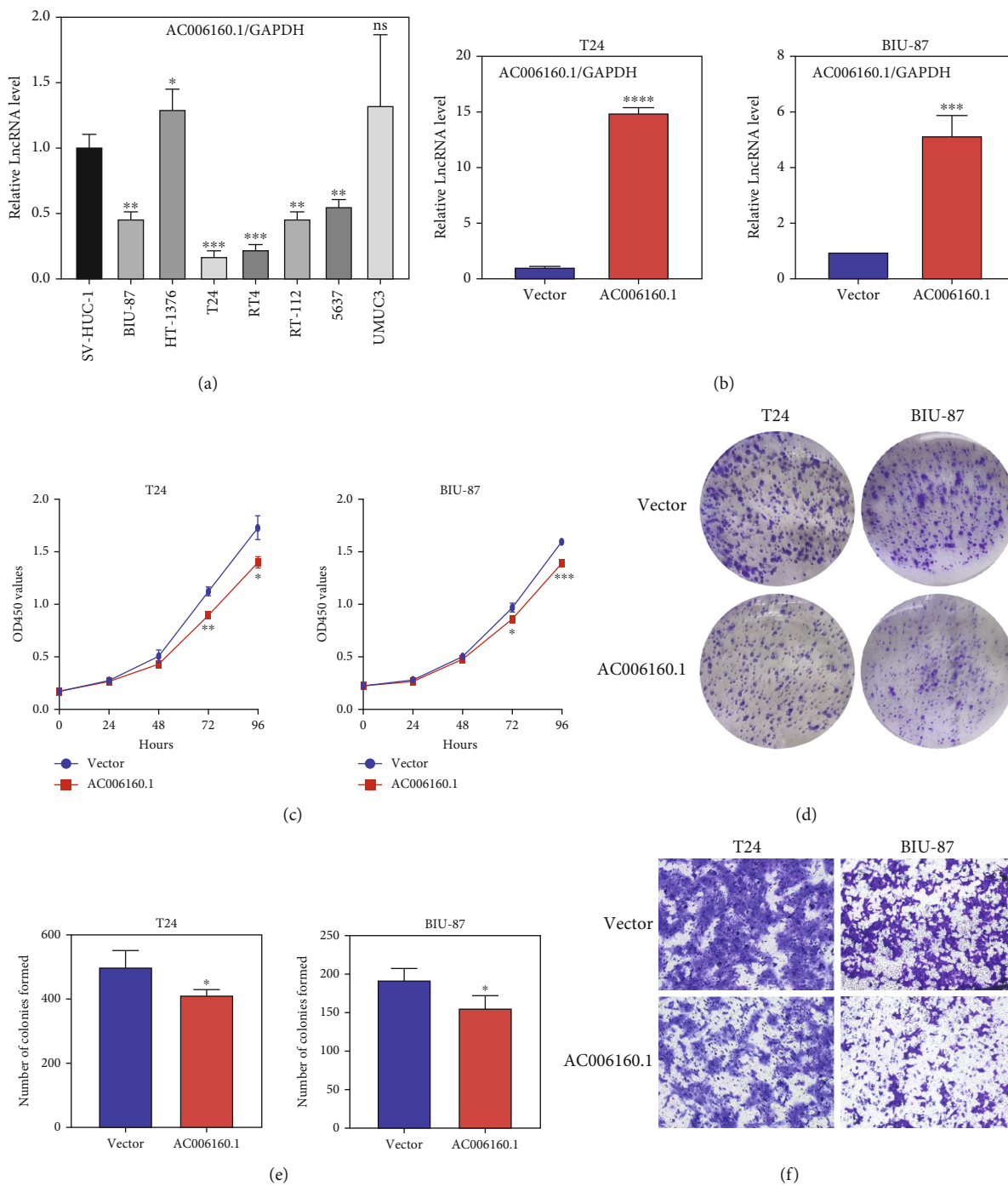


FIGURE 10: Continued.

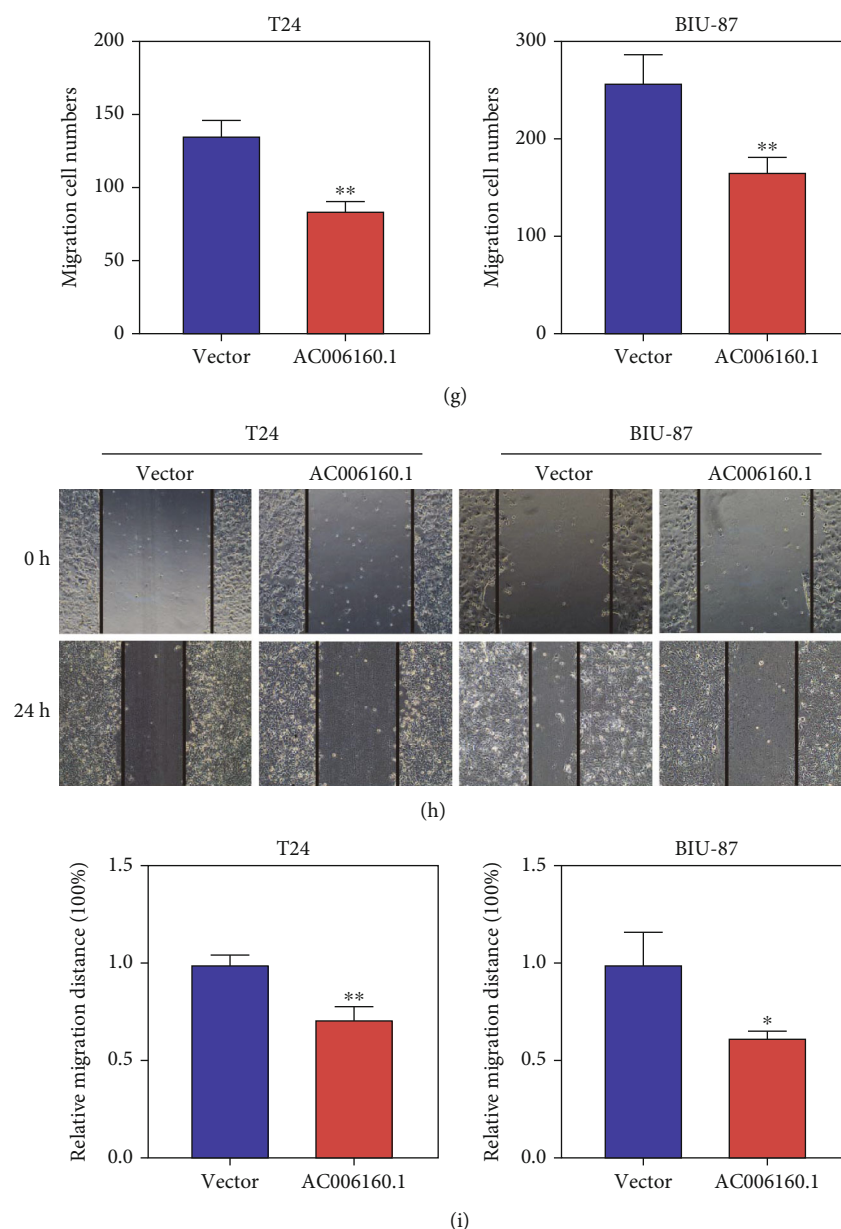
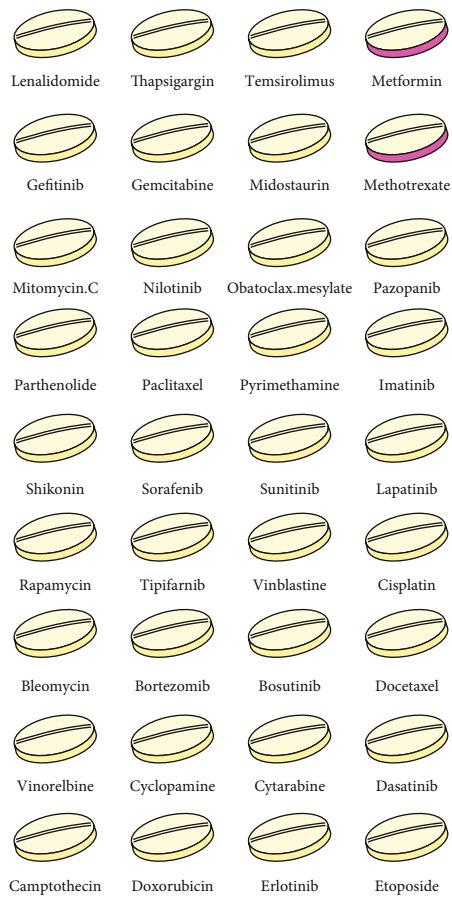


FIGURE 10: The lncRNA AC006160.1 suppresses the viability of bladder cancer cells. (a) Expression of AC006160.1 in bladder cancer cell lines and SV-HUC-1 cells was measured via qRT-PCR and normalised to GAPDH expression. (b) T24 and BIU-87 cells were transfected with the pcDNA3.1-AC006160.1 or negative control plasmid for 24 h, and the relative expression of AC006160.1 was measured via qRT-PCR and normalised to GAPDH expression. (c) T24 and BIU-87 cells were transfected with the pcDNA3.1-AC006160.1 or negative control plasmid, and cell proliferation was examined via the CCK8 assay. (d, e) Colony formation assay was performed to detect the proliferation of cells transfected with the indicated vectors. (f, g) The migration ability of T24 and BIU-87 cells transfected with the pcDNA3.1-AC006160.1 or negative control plasmid was measured via transwell assay. (h, i) The migration ability of cells transfected with the pcDNA3.1-AC006160.1 or negative control plasmid was detected via wound healing assay. All experiments were performed in triplicate. All data are expressed as the mean \pm standard deviation (SD) (* $p < 0.05$, ** $p < 0.01$, and *** $p < 0.001$ versus the control group).

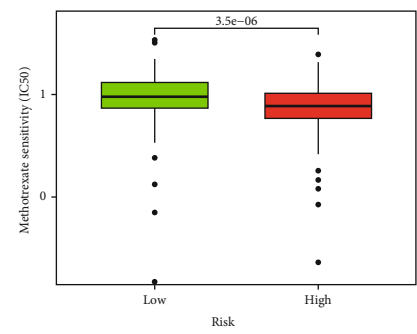
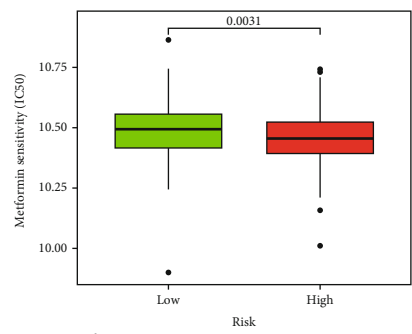
in regulatory mechanisms of lncRNAs in malignant tumours [47, 48]. Moreover, studies employing whole-transcriptome sequencing have broadened the horizon for cancer treatment.

In this study, the independent prognostic role of the ferroptosis-related-lncRNA risk signature was validated in both training and validation cohorts. The ability of the risk signature to predict survival outcomes was better than that of various clinicopathological parameters including age,

sex, tumour stages, and grades. However, in the training cohort, 6 samples had a low grade, of which 5 were included in the low-risk group. Therefore, “grade” was excluded from multivariate Cox regression analysis to avoid statistical bias. The risk scores were used to evaluate bladder cancer samples at the transcriptomic (lncRNA) level and were theoretically more accurate than the currently used clinical parameters. Elderly patients, patients with advanced-stage disease, and

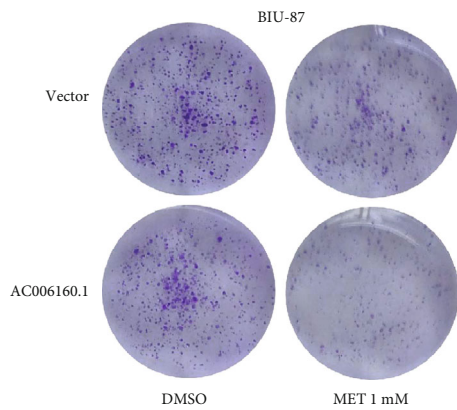


(a)



Risk
■ Low
■ High

(b)



(c)

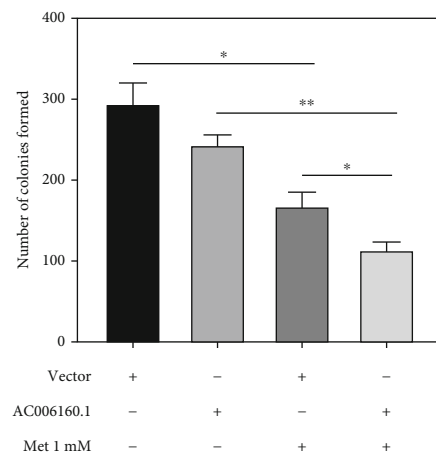


FIGURE 11: Continued.

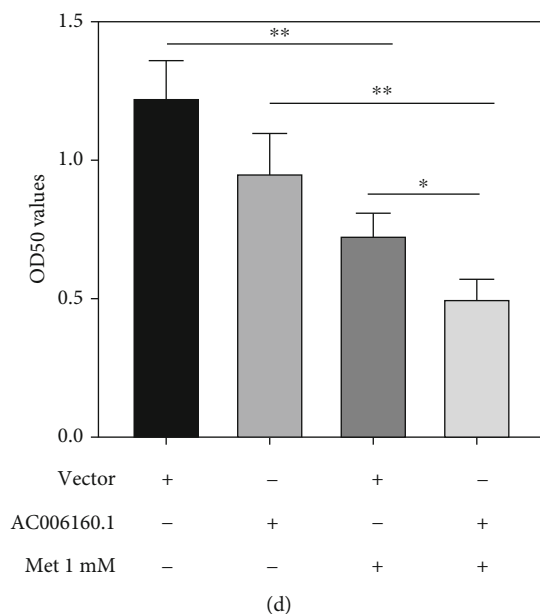


FIGURE 11: Drug sensitivity analysis based on IC₅₀ values. (a) Drug sensitivity analysis of patients with bladder cancer with high or low AC006160.1 expression. The red colour indicates sensitive drugs for samples with high AC006160.1 expression. (b) Compared with patients with low AC006160.1 expression, those with high AC006160.1 expression were more sensitive metformin and methotrexate ($p < 0.01$). (c) Crystal violet staining of BIU-87 cells transfected with the pcDNA3.1-AC006160.1 or negative control plasmid and subsequently treated with 1-mM metformin for 14 days. (d) CCK-8 assay was performed to examine the proliferation of BIU-87 cells transfected with the pcDNA3.1-AC006160.1 or negative control plasmid and subsequently treated with 1-mM metformin for 72 h. All experiments were performed in triplicate. All data are expressed as the mean \pm standard deviation (SD) ($*p < 0.05$, $**p < 0.01$, $***p < 0.001$ versus the control group).

those with higher T or N grades had higher risk scores, indicating that the risk signature can reflect various clinical characteristics from a genetic or molecular perspective. Therefore, the lncRNA risk signature has valuable application prospects for the treatment of bladder cancer.

Furthermore, the relationship between the immune microenvironment and the two ferroptosis mediation patterns was examined. Cluster 1 had lower infiltration of naive B cells, activated dendritic cells, and follicular helper T cells, which are responsible for activation of the immune system [5]. However, cluster 1 had higher infiltration of M2 macrophages, which are responsible for immune suppression [49]. These results were consistent with the significantly poorer survival outcomes of cluster 1. Bladder, skin and lung cancers are classical malignancies with a high mutation burden [50, 51]. Patients with such malignancies can potentially benefit from immunotherapy, which is closely associated with the tumour immune microenvironment. Therefore, this study mainly focused on the relationship among the risk signature, expression of immune checkpoints, and immune microenvironment of bladder cancer. Both cluster 1 (Figure 8) and high-risk group (Figure 9) had significantly higher expression of PD-1, PD-L1, and CTLA-4. Higher expression of these immune checkpoints in cluster 1 or the high-risk group might have led to poorer survival outcomes. Furthermore, PD-1 expression was positively correlated with AL136084.3 and negatively correlated with AC005785.1, AL731567.1, and AC010618.2. Similarly, various ferroptosis-related lncRNAs were significantly correlated with the expression of PD-L1

and CTLA-4. Cluster analysis revealed that the prognostic lncRNAs were significantly associated with the infiltration of various immune cells. These results indicate that ferroptosis-related lncRNAs not only regulate the malignant phenotype of bladder cancer through genetic alterations but also play a vital role in remodelling the tumour immune microenvironment of bladder cancer. Furthermore, the toll-like receptor signalling pathway, T-cell receptor signalling pathway, regulation of the actin cytoskeleton, cytokine and cytokine-receptor interaction, and chemokine signalling pathway were significantly enriched in cluster 1, indicating that ferroptosis-related lncRNAs may play a regulatory role in the development of bladder cancer through these biological pathways. Investigating the role of lncRNAs in these biological pathways may provide novel insights into the treatment of bladder cancer. The risk signature established in this study can be used to examine ferroptosis mediation patterns. The risk scores were significantly correlated with the infiltration of naive B cells, eosinophils, M0 macrophages, M2 macrophages, CD4 memory resting T cells, CD8 T cells, follicular helper T cells, Tregs, activated mast cells, neutrophils, and plasma cells, which indicated that the risk signature can be used to guide immunotherapy. In addition, the risk signature can be used to predict the response of patients to immunotherapy. Previous studies have demonstrated that malignant and immune cells coexist in the tumour microenvironment and react with each other to promote tumour growth and progression [52, 53]. However, the role of immune cells in tumour development remains elusive. The ferroptosis-related lncRNAs identified in this study may

help to examine the relationship between immune cells and tumour progression. In conclusion, a novel lncRNA-based risk signature was constructed to predict survival outcomes, clinical stages, tumour grades, immune cell infiltration, immune checkpoint expression, and immunotherapeutic responses in bladder cancer samples. In addition, the lncRNA AC006160.1 was identified as a protective factor for the progression of bladder cancer *in vitro*.

However, this study has several limitations. First, all analysed lncRNA-sequencing data were extracted from public databases; therefore, large-scale sequencing studies in multi-centre institutions are required to validate the lncRNA-based risk signature established in this study. Second, the TIDE algorithm was used to evaluate the potential response to immunotherapy; however, prospective clinical trials concerning different immunotherapeutic strategies should be conducted for bladder cancer with varying risk factors. In addition, the regulatory role of AC006160.1 in the progression of bladder cancer and the underlying mechanisms should be investigated in future studies.

5. Conclusion

Ferroptosis-related lncRNAs can accurately predict survival outcomes, clinical stages, tumour grades, immune cell infiltration, immune checkpoint expression, and immunotherapeutic responses in bladder cancer. The lncRNA AC006160.1 may serve as a protective factor for the progression of bladder cancer.

Abbreviations

TCGA:	The Cancer Genome Atlas
lncRNA:	Long noncoding RNA
PD-1:	Programmed cell death 1
ssGSEA:	Single-sample gene set enrichment analysis
PD-L1:	Programmed cell death-ligand 1
DEGs:	Differentially expressed genes
CTLA-4:	Cytotoxic T lymphocyte antigen 4
LASSO:	Least absolute shrinkage and selection operator
ROC:	Receiver operating characteristic
GSVA:	Gene set variation analysis
TMB:	Tumour mutation burden
TIDE:	Tumour Immune Dysfunction and Exclusion
GDSC:	Genomics of Drug Sensitivity in Cancer
MET:	Metformin
qPCR:	Quantitative polymerase chain reaction
cDNA:	Complementary deoxyribonucleic acid.

Data Availability

The data used to support the findings of this study are included within the article and the supplementary information files.

Conflicts of Interest

The authors declare no competing interests.

Authors' Contributions

JCL is assigned to the data collection and experimental validation. JYC and SYZ collected the data. MW and JWW revised the figures and manuscript. YGZ, BJ, and JYW are responsible for the study design. All authors have approved the final version of this manuscript. Jingchao Liu and Jingyi Cui contributed equally to this study.

Acknowledgments

This study was funded by the National Key Research and Development Plan (No. 2018YFC2002200).

Supplementary Materials

Supplementary Table 1: expression matrix of 60 ferroptosis-related genes. Supplementary Table 2: results for coexpression analysis of ferroptosis-related lncRNAs and mRNAs. Supplementary Table 3: expression of 263 ferroptosis-related lncRNAs. Supplementary Table 4: expression of lncRNAs and clinical information of 403 bladder cancer samples. Supplementary Table 5: cluster analysis based on 20 prognostic lncRNAs. Supplementary Table 6: detailed clinical information of bladder cancer samples. Supplementary Table 7: data of the high- and low-risk groups of the training cohort. Supplementary Table 8: data of the high- and low-risk groups of the validation cohort. Supplementary Table 9: markers of different immune cells. Supplementary Table 10: infiltration of 22 types of immune cells analysed using the CIBERSORT algorithm. Supplementary Table 11: immune scores evaluated using the ESTIMATE algorithm. Supplementary Table 12: immunotherapeutic response evaluated using the Tumour Immune Dysfunction and Exclusion (TIDE) algorithm. Supplementary Figure 1: gene set enrichment analysis. (A–F) Most significantly enriched biological pathways in cluster 1. (G–I) Most significantly enriched biological pathways in cluster 2. (*Supplementary Materials*)

References

- [1] A. Richters, K. K. H. Aben, and L. Kiemeny, "The global burden of urinary bladder cancer: an update," *World Journal of Urology*, vol. 38, no. 8, pp. 1895–1904, 2020.
- [2] D. S. Kaufman, W. U. Shipley, and A. S. Feldman, "Bladder cancer," *Lancet*, vol. 374, no. 9685, pp. 239–249, 2009.
- [3] M. Grayson, "Bladder cancer," *Nature*, vol. 551, no. 7679, p. S33, 2017.
- [4] M. Rouanne, M. Roumiguié, N. Houédé et al., "Development of immunotherapy in bladder cancer: present and future on targeting PD(L)1 and CTLA-4 pathways," *World Journal of Urology*, vol. 36, no. 11, pp. 1727–1740, 2018.
- [5] L. Tran, J. F. Xiao, N. Agarwal, J. E. Duex, and D. Theodorescu, "Advances in bladder cancer biology and therapy," *Nature Reviews. Cancer*, vol. 21, no. 2, pp. 104–121, 2021.
- [6] A. G. Robertson, J. Kim, H. al-Ahmadie et al., "Comprehensive molecular characterization of muscle-invasive bladder cancer," *Cell*, vol. 171, no. 3, pp. 540–556.e25, 2017.

- [7] J. Y. Cao and S. J. Dixon, "Mechanisms of ferroptosis," *Cellular and Molecular Life Sciences*, vol. 73, no. 11-12, pp. 2195–2209, 2016.
- [8] S. J. Dixon, K. M. Lemberg, M. R. Lamprecht et al., "Ferroptosis: an iron-dependent form of nonapoptotic cell death," *Cell*, vol. 149, no. 5, pp. 1060–1072, 2012.
- [9] J. Guo, B. Xu, Q. Han et al., "Ferroptosis: a novel anti-tumor action for cisplatin," *Cancer Research and Treatment*, vol. 50, no. 2, pp. 445–460, 2018.
- [10] Y. Xie, W. Hou, X. Song et al., "Ferroptosis: process and function," *Cell Death and Differentiation*, vol. 23, no. 3, pp. 369–379, 2016.
- [11] S. Y. Ryu, W. M. Lee, K. Kim et al., "Randomized clinical trial of weekly vs. triweekly cisplatin-based chemotherapy concurrent with radiotherapy in the treatment of locally advanced cervical cancer," *International Journal of Radiation Oncology • Biology • Physics*, vol. 81, no. 4, pp. e577–e581, 2011.
- [12] C. Louandre, Z. Ezzoukhy, C. Godin et al., "Iron-dependent cell death of hepatocellular carcinoma cells exposed to sorafenib," *International Journal of Cancer*, vol. 133, no. 7, pp. 1732–1742, 2013.
- [13] A. Belavgeni, S. R. Bornstein, A. von Mässenhausen et al., "Exquisite sensitivity of adrenocortical carcinomas to induction of ferroptosis," *Proceedings of the National Academy of Sciences of the United States of America*, vol. 116, no. 44, pp. 22269–22274, 2019.
- [14] D. Basuli, L. Tesfay, Z. Deng et al., "Iron addiction: a novel therapeutic target in ovarian cancer," *Oncogene*, vol. 36, no. 29, pp. 4089–4099, 2017.
- [15] V. S. Viswanathan, M. J. Ryan, H. D. Dhruv et al., "Dependency of a therapy-resistant state of cancer cells on a lipid peroxidase pathway," *Nature*, vol. 547, no. 7664, pp. 453–457, 2017.
- [16] N. Eling, L. Reuter, J. Hazin, A. Hamacher-Brady, and N. R. Brady, "Identification of artesunate as a specific activator of ferroptosis in pancreatic cancer cells," *Oncoscience*, vol. 2, no. 5, pp. 517–532, 2015.
- [17] C. Louandre, I. Marcq, H. Bouhhal et al., "The retinoblastoma (Rb) protein regulates ferroptosis induced by sorafenib in human hepatocellular carcinoma cells," *Cancer Letters*, vol. 356, no. 2, pp. 971–977, 2015.
- [18] K. Bersuker, J. M. Hendricks, Z. Li et al., "The CoQ oxidoreductase FSP1 acts parallel to GPX4 to inhibit ferroptosis," *Nature*, vol. 575, no. 7784, pp. 688–692, 2019.
- [19] S. Doll, F. P. Freitas, R. Shah et al., "FSP1 is a glutathione-independent ferroptosis suppressor," *Nature*, vol. 575, no. 7784, pp. 693–698, 2019.
- [20] B. Hassannia, P. Vandenabeele, and T. Vanden Berghe, "Targeting ferroptosis to iron out cancer," *Cancer Cell*, vol. 35, no. 6, pp. 830–849, 2019.
- [21] A. Sanchez Calle, Y. Kawamura, Y. Yamamoto, F. Takeshita, and T. Ochiya, "Emerging roles of long non-coding RNA in cancer," *Cancer Science*, vol. 109, no. 7, pp. 2093–2100, 2018.
- [22] M. Xu, X. Xu, B. Pan et al., "LncRNA SATB2-AS1 inhibits tumor metastasis and affects the tumor immune cell microenvironment in colorectal cancer by regulating SATB2," *Molecular Cancer*, vol. 18, no. 1, p. 135, 2019.
- [23] S. van Dam, U. Vösa, A. van der Graaf, L. Franke, and J. P. de Magalhães, "Gene co-expression analysis for functional classification and gene-disease predictions," *Briefings in Bioinformatics*, vol. 19, no. 4, pp. 575–592, 2018.
- [24] S. Mukherjee, B. Banerjee, D. Karasik, and M. Frenkel-Morgenstern, "mRNA-lncRNA co-expression network analysis reveals the role of lncRNAs in immune dysfunction during severe SARS-CoV-2 infection," *Viruses*, vol. 13, no. 3, p. 402, 2021.
- [25] M. Wang, C. Mao, L. Ouyang et al., "Correction to: long non-coding RNA LINC00336 inhibits ferroptosis in lung cancer by functioning as a competing endogenous RNA," *Cell Death and Differentiation*, vol. 27, no. 4, p. 1447, 2020.
- [26] Z. Wang, X. Chen, N. Liu et al., "A nuclear long non-coding RNA LINC00618 accelerates Ferroptosis in a manner dependent upon apoptosis," *Molecular Therapy*, vol. 29, no. 1, pp. 263–274, 2021.
- [27] C. C. Sun, W. Zhu, S. J. Li et al., "FOXC1-mediated LINC00301 facilitates tumor progression and triggers an immune-suppressing microenvironment in non-small cell lung cancer by regulating the HIF1 α pathway," *Genome Medicine*, vol. 12, no. 1, p. 77, 2020.
- [28] B. R. Stockwell, J. P. Friedmann Angeli, H. Bayir et al., "Ferroptosis: a regulated cell death nexus linking metabolism, redox biology, and disease," *Cell*, vol. 171, no. 2, pp. 273–285, 2017.
- [29] A. M. Newman, C. L. Liu, M. R. Green et al., "Robust enumeration of cell subsets from tissue expression profiles," *Nature Methods*, vol. 12, no. 5, pp. 453–457, 2015.
- [30] K. Yoshihara, M. Shahmoradgoli, E. Martínez et al., "Inferring tumour purity and stromal and immune cell admixture from expression data," *Nature Communications*, vol. 4, no. 1, p. 2612, 2013.
- [31] P. Jiang, S. Gu, D. Pan et al., "Signatures of T cell dysfunction and exclusion predict cancer immunotherapy response," *Nature Medicine*, vol. 24, no. 10, pp. 1550–1558, 2018.
- [32] W. Yang, J. Soares, P. Greninger et al., "Genomics of Drug Sensitivity in Cancer (GDSC): a resource for therapeutic biomarker discovery in cancer cells," *Nucleic Acids Research*, vol. 41, no. Database issue, pp. D955–D961, 2013.
- [33] J. Harrow, A. Frankish, J. M. Gonzalez et al., "GENCODE: the reference human genome annotation for the ENCODE project," *Genome Research*, vol. 22, no. 9, pp. 1760–1774, 2012.
- [34] F. Bray, J. Ferlay, I. Soerjomataram, R. L. Siegel, L. A. Torre, and A. Jemal, "Global cancer statistics 2018: GLOBOCAN estimates of incidence and mortality worldwide for 36 cancers in 185 countries," *CA: a Cancer Journal for Clinicians*, vol. 68, no. 6, pp. 394–424, 2018.
- [35] R. Batista, N. Vinagre, S. Meireles et al., "Biomarkers for bladder cancer diagnosis and surveillance: a comprehensive review," vol. 10, Tech. Rep. 1, Diagnostics (Basel), 2020.
- [36] J. Tse, R. Ghandour, N. Singla, and Y. Lotan, "Molecular predictors of complete response following neoadjuvant chemotherapy in urothelial carcinoma of the bladder and upper tracts," *International Journal of Molecular Sciences*, vol. 20, no. 4, p. 793, 2019.
- [37] R. Nadal and J. Bellmunt, "Management of metastatic bladder cancer," *Cancer Treatment Reviews*, vol. 76, pp. 10–21, 2019.
- [38] R. M. Samstein, C. H. Lee, A. N. Shoushtari et al., "Tumor mutational load predicts survival after immunotherapy across multiple cancer types," *Nature Genetics*, vol. 51, no. 2, pp. 202–206, 2019.
- [39] L. Fehrenbacher, A. Spira, M. Ballinger et al., "Atezolizumab versus docetaxel for patients with previously treated non-small-cell lung cancer (POPLAR): a multicentre, open-label,

- phase 2 randomised controlled trial,” *Lancet*, vol. 387, no. 10030, pp. 1837–1846, 2016.
- [40] A. M. Goodman, S. Kato, L. Bazhenova et al., “Tumor mutational burden as an independent predictor of response to immunotherapy in diverse cancers,” *Molecular Cancer Therapeutics*, vol. 16, no. 11, pp. 2598–2608, 2017.
- [41] W. Choi, S. Porten, S. Kim et al., “Identification of distinct basal and luminal subtypes of muscle-invasive bladder cancer with different sensitivities to frontline chemotherapy,” *Cancer Cell*, vol. 25, no. 2, pp. 152–165, 2014.
- [42] J. Liu, H. Ma, L. Meng et al., “Construction and external validation of a ferroptosis-related gene signature of predictive value for the overall survival in bladder cancer,” *Frontiers in Molecular Biosciences*, vol. 8, article 675651, 2021.
- [43] G. Tan, A. Wu, Z. Li et al., “Bioinformatics analysis based on immune-autophagy-related lncRNAs combined with immune infiltration in bladder cancer,” *Translational Andrology and Urology*, vol. 10, no. 8, pp. 3440–3455, 2021.
- [44] Y. Cui, Z. Zhou, Y. Chai, X. Che, and Y. Zhang, “Identification of a nomogram from ferroptosis-related long noncoding RNAs signature to analyze overall survival in patients with bladder cancer,” *Journal of Oncology*, vol. 2021, Article ID 8533464, 18 pages, 2021.
- [45] D. Ke, Q. Wang, S. Ke, L. Zou, and Q. Wang, “Long-non coding RNA SNHG16 supports colon cancer cell growth by modulating miR-302a-3p/AKT axis,” *Pathology Oncology Research*, vol. 26, no. 3, pp. 1605–1613, 2020.
- [46] T. Ghasemi, M. Khalaj-Kondori, M. A. Hosseinpour feizi, and P. Asadi, “lncRNA-miRNA-mRNA interaction network for colorectal cancer; an in silico analysis,” *Computational Biology and Chemistry*, vol. 89, article 107370, 2020.
- [47] R. Chang, X. Xiao, Y. Fu, C. Zhang, X. Zhu, and Y. Gao, “ITGB1-DT facilitates lung adenocarcinoma progression via forming a positive feedback loop with ITGB1/Wnt/ β -catenin/MYC,” *Frontiers in Cell and Development Biology*, vol. 9, article 631259, 2021.
- [48] Q. R. Huang and X. B. Pan, “Prognostic lncRNAs, miRNAs, and mRNAs form a competing endogenous RNA network in colon cancer,” *Frontiers in Oncology*, vol. 9, p. 712, 2019.
- [49] A. Mantovani, A. Sica, and M. Locati, “Macrophage polarization comes of age,” *Immunity*, vol. 23, no. 4, pp. 344–346, 2005.
- [50] M. S. Lawrence, P. Stojanov, P. Polak et al., “Mutational heterogeneity in cancer and the search for new cancer-associated genes,” *Nature*, vol. 499, no. 7457, pp. 214–218, 2013.
- [51] L. B. Alexandrov, S. Nik-Zainal, D. C. Wedge et al., “Signatures of mutational processes in human cancer,” *Nature*, vol. 500, no. 7463, pp. 415–421, 2013.
- [52] S. H. Lee, W. Hu, J. T. Matulay et al., “Tumor evolution and drug response in patient-derived organoid models of bladder cancer,” *Cell*, vol. 173, no. 2, pp. 515–528.e17, 2018.
- [53] J. L. Sottnik, V. Mallareddy, A. Chauca-Diaz et al., “Elucidating the role of Agl in bladder carcinogenesis by generation and characterization of genetically engineered mice,” *Carcinogenesis*, vol. 40, no. 1, pp. 194–201, 2019.

Research Article

MITD1 Deficiency Suppresses Clear Cell Renal Cell Carcinoma Growth and Migration by Inducing Ferroptosis through the TAZ/SLC7A11 Pathway

Ye Zhang , Yanze Li , Qiangmin Qiu , Zhiyuan Chen , Yang Du , and Xiuheng Liu 

Department of Urology, Renmin Hospital of Wuhan University, Wuhan, 430060 Hubei, China

Correspondence should be addressed to Zhiyuan Chen; chenzhiyuan163@163.com, Yang Du; phoenixneo@whu.edu.cn, and Xiuheng Liu; drliuxh@hotmail.com

Received 10 June 2022; Revised 20 July 2022; Accepted 25 July 2022; Published 22 August 2022

Academic Editor: Lianxiang Luo

Copyright © 2022 Ye Zhang et al. This is an open access article distributed under the Creative Commons Attribution License, which permits unrestricted use, distribution, and reproduction in any medium, provided the original work is properly cited.

Clear cell renal cell carcinoma (ccRCC), the major histopathological subtype of renal cancer, is sensitive to ferroptosis. MIT-domain containing protein 1 (MITD1) has been reported to play an important role in hepatocellular carcinoma, while it remains unclear whether MITD1 is involved in ccRCC. Based on available data in The Cancer Genome Atlas, we found the expression of MITD1 increased through bioinformatics analysis and high MITD1 expression suggests a poor prognosis. And we validated that MITD1 expressed significantly in ccRCC through Western blot analysis. Then, we further compared the proliferation and migration capacity of ccRCC before and after MITD1 knockdown and further explored the effect of MITD1 knockdown on ferroptosis. The results indicated that MITD1 knockdown inhibited ccRCC cell proliferation and migration and induced ferroptosis in ccRCC. Furthermore, we found and analyzed the key molecule TAZ which was involved in ferroptosis caused by MITD1 knockdown. Subsequent overexpression experiments demonstrated that MITD1 knockdown induced ferroptosis and suppressed tumor growth and migration through the TAZ/SLC7A11 pathway. In summary, our study revealed the role of MITD1 in the ferroptosis of ccRCC and provided a novel target for ccRCC treatment.

1. Introduction

Renal cell carcinoma (RCC) originates from renal tubular epithelial cells and is one of the most common malignant tumors of the urinary system, of which the incidence is still increasing year by year [1]. Clear cell renal cell carcinoma (ccRCC) is the most common and aggressive type of RCC, which accounts for approximately more than 85% of RCC [2]. For the lack of clinical symptoms in the early stage of ccRCC, a considerable number of patients are diagnosed with locally advanced and even have distant metastases at the first-time consultancy. Localized ccRCC is generally cured by surgery, whereas patients with advanced ccRCC still have a poor prognosis due to the inability to undergo radical surgery [3]. Despite a variety of treatments including radiotherapy, chemotherapy, vascular endothelial growth factor (VEGF) receptor tyrosine kinase inhibitors, and immune-checkpoint inhibitors to delay the progress of the

disease, it is hard to select treatment strategies for patients with advanced cancer due to the frequently occurring severe side effects and intrinsic or acquired drug resistance of each treatment [4, 5]. Therefore, it is necessary to further explore the mechanism of occurrence and development of ccRCC and to find more novel diagnostic markers and therapeutic targets.

MITD1 encodes MIT-domain containing protein 1 and participates in the process of cell division in the form of ESCRT-III dependence. MITD1 is able to be recruited to the midbody through the intermediate of MIT-domain of the N-terminus and ESCRT-III and coordinates abscission with earlier stages of cytokinesis [6, 7]. A study [8] found that MITD1 was able to serve as a predictor for human hepatocellular carcinoma prognosis and correlated with immune infiltrating cells around the carcinoma. In another research [9], the researchers identified MITD1 as one of the most important survival-related genes in bladder cancer,

which was able to influence the migration ability of tumor cells by knocking down or overexpressing it. Despite some studies having found an abnormal expression of MITD1 in ccRCC, the role of MITD1 in the progression of ccRCC remains largely unknown.

Ferroptosis is a novel nonapoptotic form of death characterized by accumulation of intracellular reactive oxygen species (ROS), depletion of reduced glutathione (GSH), resulting in iron dependent accumulation of lipid hydroperoxides reaching cell-lethal levels [10]. It is generally accepted that ferroptosis is involved in a variety of physiological and pathological processes, including cancer, ischemia reperfusion injury, and neurodegeneration [11]. At present, ferroptosis has been considered to be closely related to tumor progression, indicating a potential means of cancer therapy [12]. Solute carrier family 7 membrane 11 (SLC7A11) is the major subunit of the cystine/glutamate antiporter (System Xc⁻), which is the key enzyme in the synthesis of GSH and resistance to ferroptosis [13]. Li et al. [14] found that inhibition of SLC7A11 induced ferroptosis in renal cancer. Therefore, ferroptosis may be a novel strategy for the treatment of RCC, and SLC7A11 is likely to be an extremely vital target.

In this study, we conducted a systematic bioinformatics analysis and found that MITD1 expression was significantly increased in ccRCC, of which the difference suggested different clinical prognoses. Further studies have shown that MITD1 knockdown of RCC cell lines with high expression of MITD1 decreased cell proliferation and migration ability. Notably, it was first observed that knockdown of MITD1 induced ferroptosis in ccRCC. Moreover, we confirmed that knockdown of MITD1 was able to regulate TAZ and reduce the expression of SLC7A11 to induce ferroptosis and decrease cell proliferation and migration ability. Our study provides a detailed analysis of the relationship between MITD1 and ferroptosis in ccRCC, which will aid in the treatment of ccRCC.

2. Materials and Methods

2.1. Bioinformatics Analysis. The expression of the target gene MITD1 in various malignant tumors was analyzed in the GEPIA (<http://gepia.cancer-pku.cn/>), a web-based tool to deliver fast and customizable functionalities based on TCGA and GTEx data. We utilized the TCGA (<https://cancergenome.nih.gov/>) database to obtain RCC data, containing all data of 611 ccRCC samples. We retained both primary RNA sequencing (RNA-seq) data and corresponding clinical information, which we used for comprehensive analysis of MITD1.

2.2. Cell Lines and Cell Culture. All cell lines were acquired from ATCC. HK-2 cell line was cultured with Dulbecco's modified eagle medium/10% fetal bovine serum (A3160901, Gibco) media while RCC cell lines (786-O, ACHN, A498, 769-P, Caki-1) were cultured with RPMI 1640/10% fetal bovine serum media. All cells were cultured in an incubator with 5% CO₂ at 37°C.

2.3. Transfection. MITD1 siRNA, negative control siRNA, SLC7A11 plasmid, TAZ plasmid, and vector plasmid were synthesized by Sangon Biotech (Shanghai). RCC cells were seeded in 6-well plates at an appropriate density. After 12 h, transfection was then carried out using Lipofectamine 3000 (L3000001, Thermo Fisher Scientific) according to the manufacturer's instructions.

2.4. Cell Counting Kit-8-Based Cell Viability Assay. RCC cells were first seeded into 96-well plates at the density of 2×10^3 cells/well. 10 μ L of CCK-8 solution (C0037, Beyotime Biotechnology) was added to each well and incubated for 1 h; the absorbance measurements at 450 nm were determined at 24 h, 48 h, 72 h, and 96 h.

2.5. Tumor Cell Colony Formation Assay. RCC cells were seeded into 6-well plates at approximately 200 cells per well and cultured for 14 days. Before counting, cells were fixed with 3.7% paraformaldehyde for 15 min and then stained with 0.1% crystal violet for 30 min. Colonies with >0.05 mm diameter were recorded and analyzed.

2.6. Wound Healing Assay. RCC cells were inoculated into 6-well plates at an appropriate density. When the cell density reached 90% to 95%, the surface of cells was scratched with a straight gap. Washed 3 times with phosphate buffer saline (PBS), the width of the gap was recorded 24 h later.

2.7. Western Blot Analysis. HK-2 cells and RCC cells were homogenized in RIPA lysis buffer containing protease inhibitors. We measured the protein concentration of each sample by bicinchoninic acid (BCA) assay and then were separated by SDS-PAGE. Transferred onto a piece of polyvinylidene difluoride transfer membrane, proteins of each sample were blocked with 5% nonfat milk for 1 h. The membranes were incubated with antibodies against MITD1 (PA5-116854, Cell Signaling Technology), SLC7A11 (ab37185, Abcam), glutathione peroxidase 4 (GPX4; ab125066, Abcam), cyclooxygenase 2 (COX2; ab62331, Abcam), acyl-CoA synthetase long-chain family member 4 (ACSL4; ab155282, Abcam), and glyceraldehyde 3-phosphate dehydrogenase (GAPDH; ab8245, Abcam). After incubation with primary antibodies for one night, the membranes were washed and incubated with secondary antibodies. The protein bands were visualized using enhanced chemiluminescence reagents (WP20005, Thermo Fisher Scientific). Finally, using ImageJ software performed the densitometric analysis to quantify differences in protein levels.

2.8. Measurement of ROS Level. After different treatments, RCC cells were incubated with 10 μ M dichlorodihydrofluorescein diacetate (DCFH-DA, S0033S-1, Beyotime Biotechnology) at 37°C for 20 min in the dark. Then, cell nuclei were labeled by using DAPI dihydrochloride (C1002, Beyotime Biotechnology) for 5 min. Finally, the cells were observed and photographed under a fluorescence microscope after washing with PBS three times.

2.9. Lipid Peroxidation Measurements. Malondialdehyde (MDA) is one of the end products of lipid peroxidation,

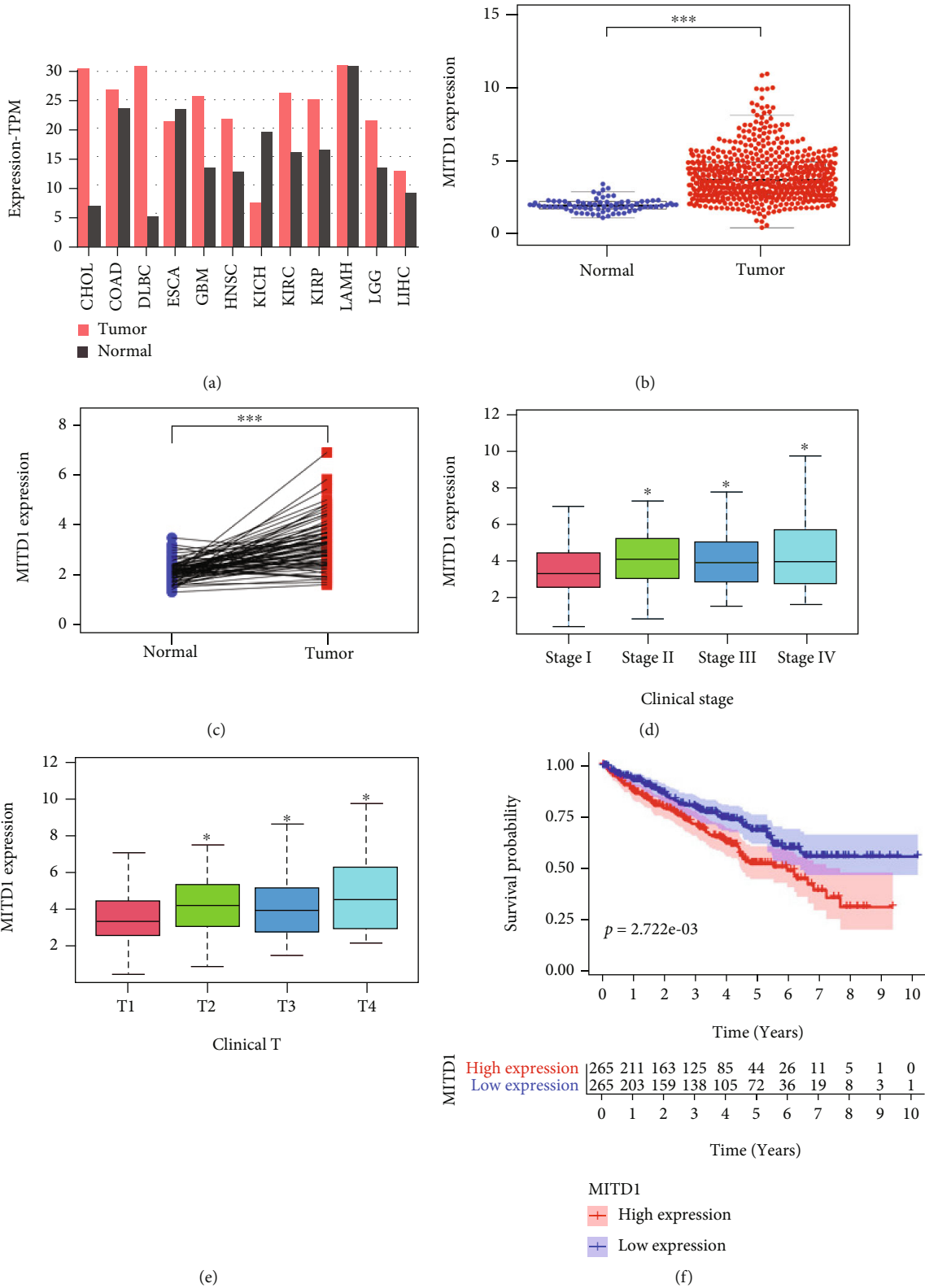


FIGURE 1: Continued.

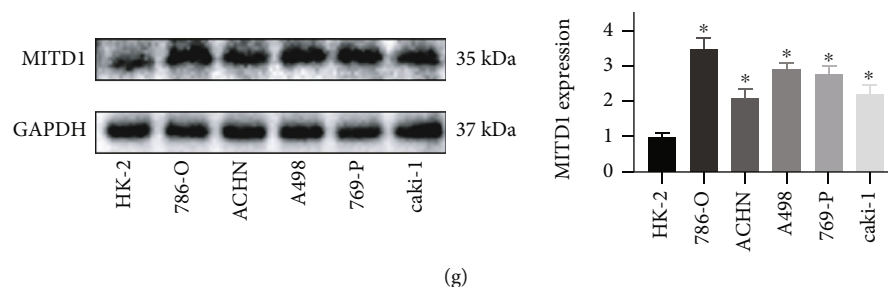


FIGURE 1: MITD1 was generally highly expressed in ccRCC. (a) Analysis from the GEPIA showing the expression of MITD1 in common malignant tumors. (b) The expression of MITD1 in ccRCC tissues was higher compared to the normal tissues through TCGA dataset analysis. (c) The expression of MITD1 in paired ccRCC tissues was also higher compared to the paracancerous tissues. (d, e) Relationship between MITD1 expression and tumor stage as well as that between MITD1 expression and T stage. (f) Based on the median values of MITD1 expression, patients were divided into the low-expression or high-expression group. Kaplan-Meier's survival curve of two groups through the analysis of clinical information of ccRCC in TCGA. (g) Representative blotting of MITD1 in different cell lines, and quantification of MITD1 proteins levels relative to HK-2 cells. Values are expressed as the mean \pm SEM, $n = 3$. * $P < 0.05$ and *** $P < 0.001$.

which is widely accepted as a biomarker of lipid peroxidation. The level of MDA was detected by MDA assay kit (S0131S, Beyotime Biotechnology). After different treatments, the supernatant was collected and added to the assay kit. Then, the absorbance measurements at 450 nm were determined by a microplate reader.

2.10. Reduced Glutathione and Superoxide Dismutase. Reduced glutathione (GSH) and superoxide dismutase (SOD) were detected using Glutathione Detection Kit (S0053, Beyotime Biotechnology) and SOD assay kit (S0109, Beyotime Biotechnology) according to the manufacturer's instruction.

2.11. Statistical Analysis. All the data was expressed by mean value \pm standard error and analyzed by SPSS 25.0. The differences between groups were analyzed through one-way analysis of variance (ANOVA) and the Student–Newman–Keuls test. $P < 0.05$ was considered to be statistically significant.

3. Results

3.1. MITD1 Expression Is Upregulated in ccRCC Tumors and Correlated with the Progression and Prognosis. To assess the role of MITD1 in malignant tumors, we first investigated the expression of MITD1 in various malignant tumors in the GEPIA. As shown in Figure 1(a), MITD1 was generally highly expressed in tumors. Then, we further analyzed publicly available data of ccRCC from TCGA and found that the expression of MITD1 was significantly higher in tumor cases compared with normal cases in paired or unpaired ccRCC tissues (Figures 1(b) and 1(c)). What is more, the expression of MITD1 gradually increased with the increase of stage and depth of invasion (Figures 1(d) and 1(e)). And patients with high MITD1 expression had a lower overall survival rate than those with low expression (Figure 1(f)), suggesting that MITD1 was associated with the progression and prognosis. Finally, we verified that the expression of MITD1 in RCC cell lines was generally higher than that of HK2 cell lines and selected 786-O and A498 cell lines in subsequent experiments (Figure 1(g)).

3.2. MITD1 Knockdown Inhibits ccRCC Cell Proliferation and Migration. To explore the functional role of MITD1 in ccRCC, MITD1 siRNA was used to knock down the expression of MITD1. As shown in Figures 2(a) and 2(b), the expression of MITD1 in 786-O and A498 cells significantly reduced after MITD1 transient knockdown. CCK-8 and clone formation experiments indicated that MITD1 knockdown inhibited the proliferation (Figures 2(c) and 2(d)) and clonogenic capacity (Figure 2(e) and Supplementary Figure 1A) of ccRCC cells compared to the NC group. And the results of wound healing assays demonstrated that silencing of MITD1 prolonged the wound healing time, indicating that MITD1 knockdown was able to reduce the migration ability of ccRCC (Figure 2(f) and Supplementary Figure 1B).

3.3. MITD1 Deficiency Induces Ferroptosis in ccRCC. In order to determine how MITD1 depletion inhibits the proliferation and migration of ccRCC, KEGG pathway enrichment analyses were used to explore the potential pathway of MITD1. GSEA was used to reveal the significantly enriched (FDR < 0.05 , P value < 0.05) KEGG pathways with high or low MITD1 expression. As shown in Figure 3(a), the top 3 KEGG pathways significantly correlated with MITD1 high expression were alpha-linolenic acid metabolism, arachidonic acid metabolism, and linoleic acid metabolism. And the top 3 pathways significantly correlated with MITD1 low expression were as follows: citrate cycle TCA cycle, pentose phosphate pathway, and steroid-biosynthesis (Figure 3(b)). In addition, we found that the remaining pathway significantly correlated with MITD1 low expression was not directly related to proliferation and migration. These results suggested that MITD1 might be associated with lipid and energy metabolism to regulate cell proliferation and migration. Therefore, we further explored whether MITD1 was involved in ferroptosis and found that MITD1 low expression was significantly associated with ferroptosis through the GSEA platform with the WikiPathways (c2.cp.wikipathways.v7.5.1.symbols.gmt) (Figure 3(c)). Subsequently, ROS levels of 786-O cells were detected by ROS assay kit. Figure 3(d) showed that ROS levels obviously

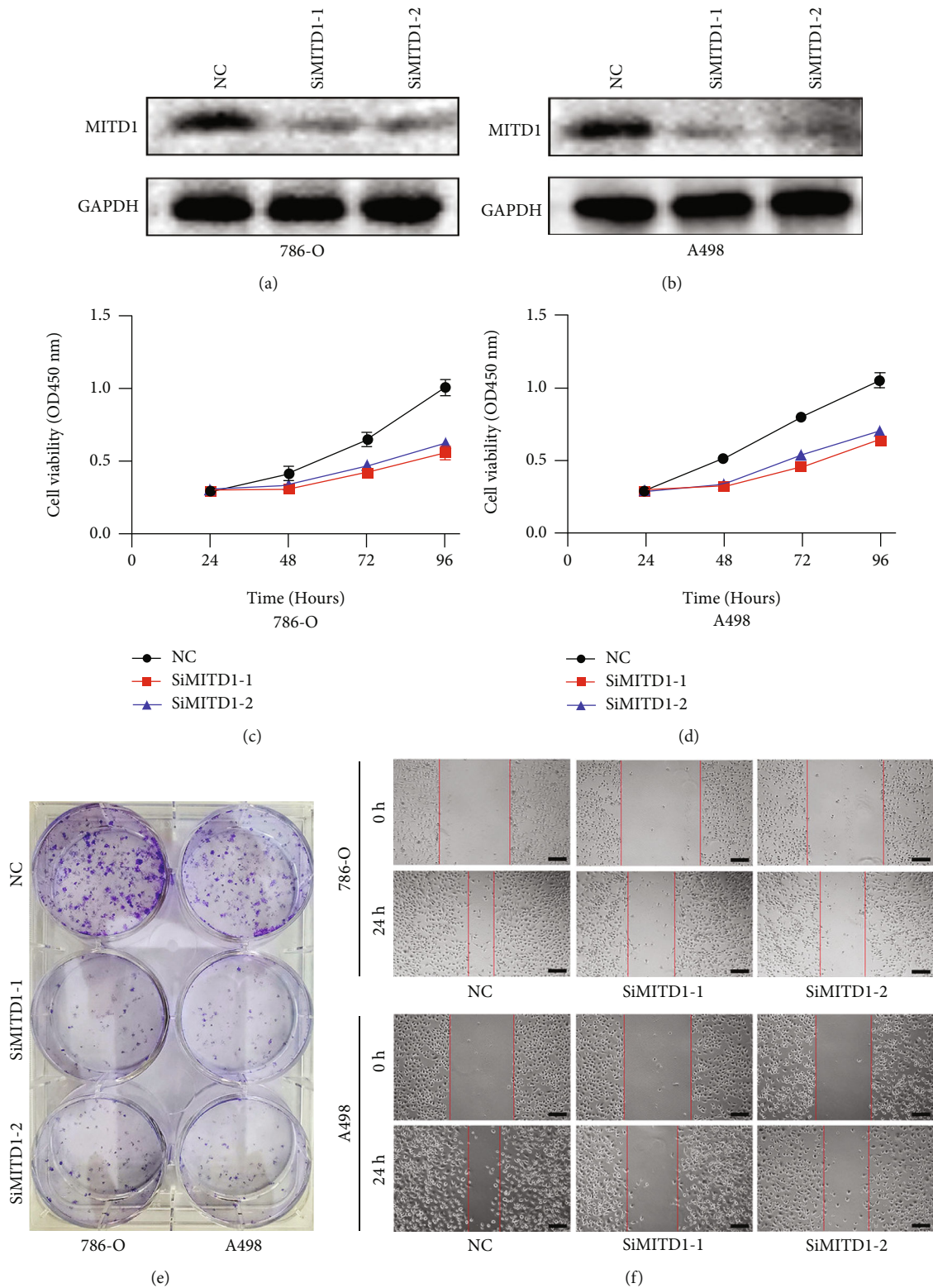


FIGURE 2: MITD1 knockdown inhibits ccRCC cell proliferation and migration. (a, b) 786-O cells or A498 cells were transfected with negative control or different si-RNA (SiMITD1-1 or SiMITD1-2). Western blot of MITD1 to test the effect of si-RNA transfection. (c, d) Knockdown of MITD1 suppressed cell growth ability in ccRCC cells (786-O and A498). (e) Proliferation of 786-O and A498 cells was suppressed by MITD1 knockdown. (f) When 786-O and A498 cells with different treatments grew to 90%-95% density, the surface of cells was scratched with a straight gap. Scratches at 0 and 24 hours were photographed and recorded under the microscope (magnification $\times 40$; scale bars = 200 μm). Values are expressed as the mean \pm SEM, $n = 3$.

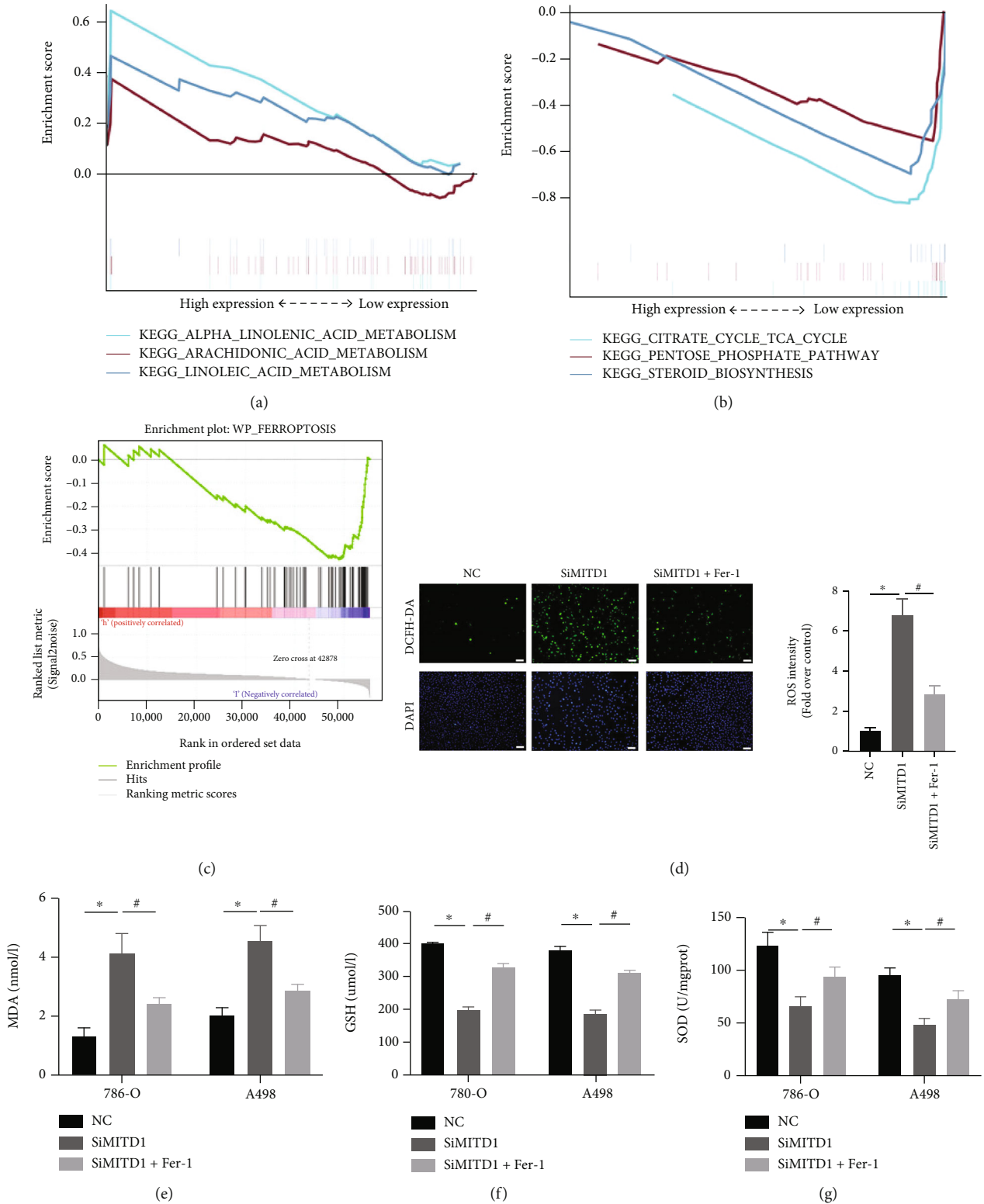


FIGURE 3: MITD1 knockdown induces ferroptosis in ccRCC. (a) KEGG pathway showed top three positively correlated groups. (b) KEGG pathway showed top three negatively correlated groups. (c) Results of MITD1 enriching to the ferroptosis pathway through GSEA platform with the WikiPathways. (d) Representative images of 786-O with DCFH-DA staining (magnification $\times 100$; scale bars = $100 \mu\text{m}$) and their quantitative analysis. (d-f) Levels of MDA, GSH, and SOD in ccRCC cells with different treatments. Values are expressed as the mean \pm SEM, $n = 3$. * $P < 0.05$, relative to the control group; # $P < 0.05$, relative to the SiMITD1.

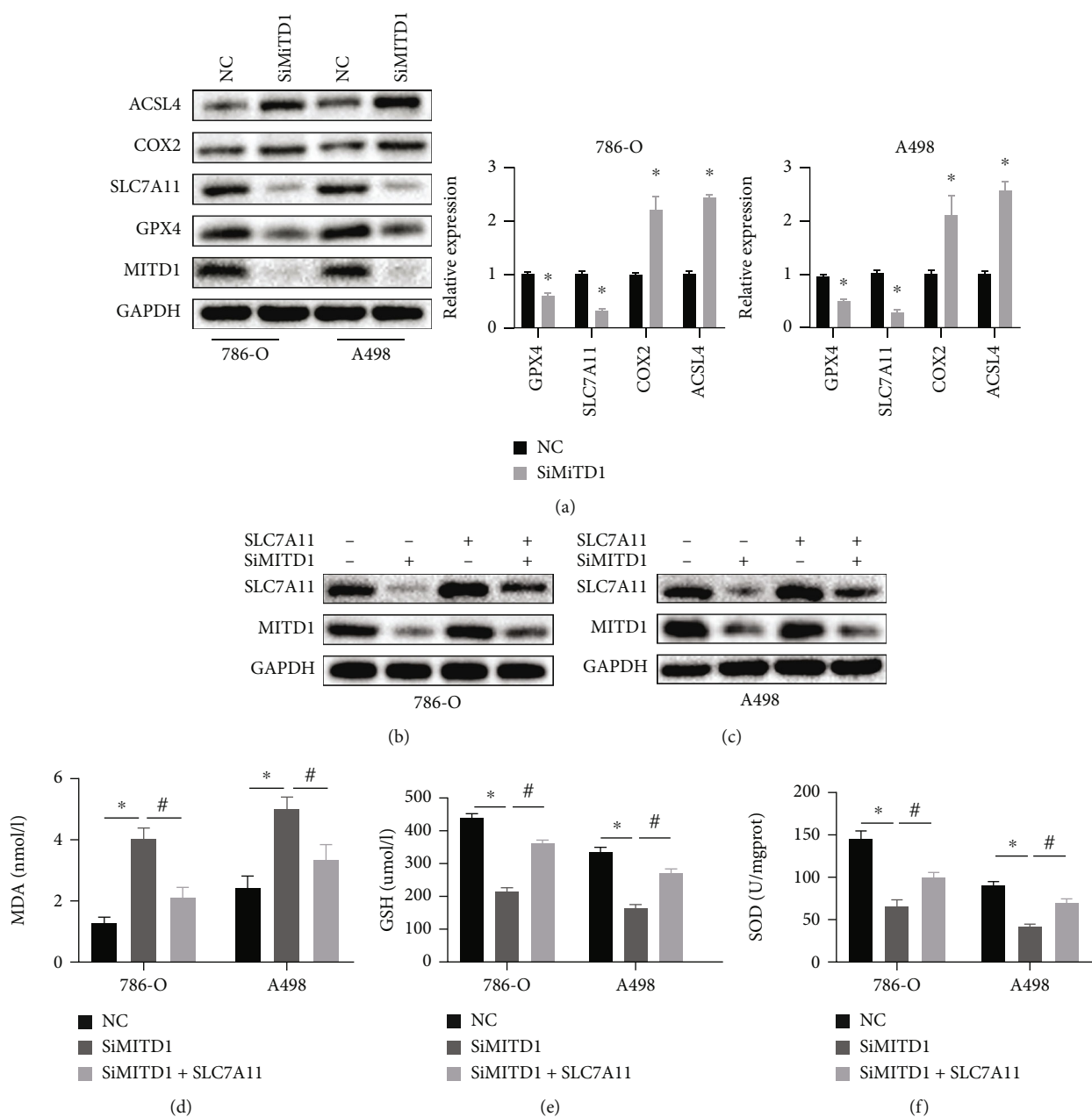


FIGURE 4: MITD1 knockdown induces ferroptosis through downregulating SLC7A11. (a) Western blot of MITD1 and ferroptosis-related proteins (GPX4, SLC7A11, COX2, and ACSL4) in ccRCC cells after silencing MITD1 (SiMITD1). (b, c) 786-O cells or A498 cells were transfected with TAZ plasmid after silencing MITD1. Western blot of MITD1 and SLC7A11. (d–f) Levels of MDA, GSH, and SOD in ccRCC cells with different treatments. Values are expressed as the mean \pm SEM, $n = 3$. * $P < 0.05$, relative to the control group; # $P < 0.05$, relative to the SiMITD1.

increased after knockdown of MITD1 while ROS levels of MITD1 knockdown ccRCC cells recovered to some extent after Ferrostatin-1 (Fer-1, a potent ferroptosis inhibitor) treatment [15]. In addition, we assessed MDA, GSH, and SOD levels in ccRCC cells. As expected, MITD1 knockdown increased the level of MDA and reduced the level of antioxidant GSH and SOD in ccRCC cells; these changes were partially reversed by Fer-1 treatment (Figures 3(e)–3(g)). Moreover, we treated ccRCC cells with another potent inhibitor of ferroptosis (lipoxystatin-1, Lip-1), and the results were consistent with Fer-1 treatment (Supplementary

Figure 2), indicating that MITD1 was involved in ferroptosis.

3.4. MITD1 Deficiency Induces Ferroptosis through Downregulating SLC7A11. To further confirm the impact of MITD1 on ferroptosis in ccRCC, ferroptosis-related proteins were detected in 786-O and A498 cells after MITD1 knockdown. As revealed in Figure 4(a), the expression of GPX4 and SLC7A11 was decreased and COX2 and ACSL4 were upregulated, further suggesting that silencing MITD1 induced ferroptosis. More specifically, the downregulation

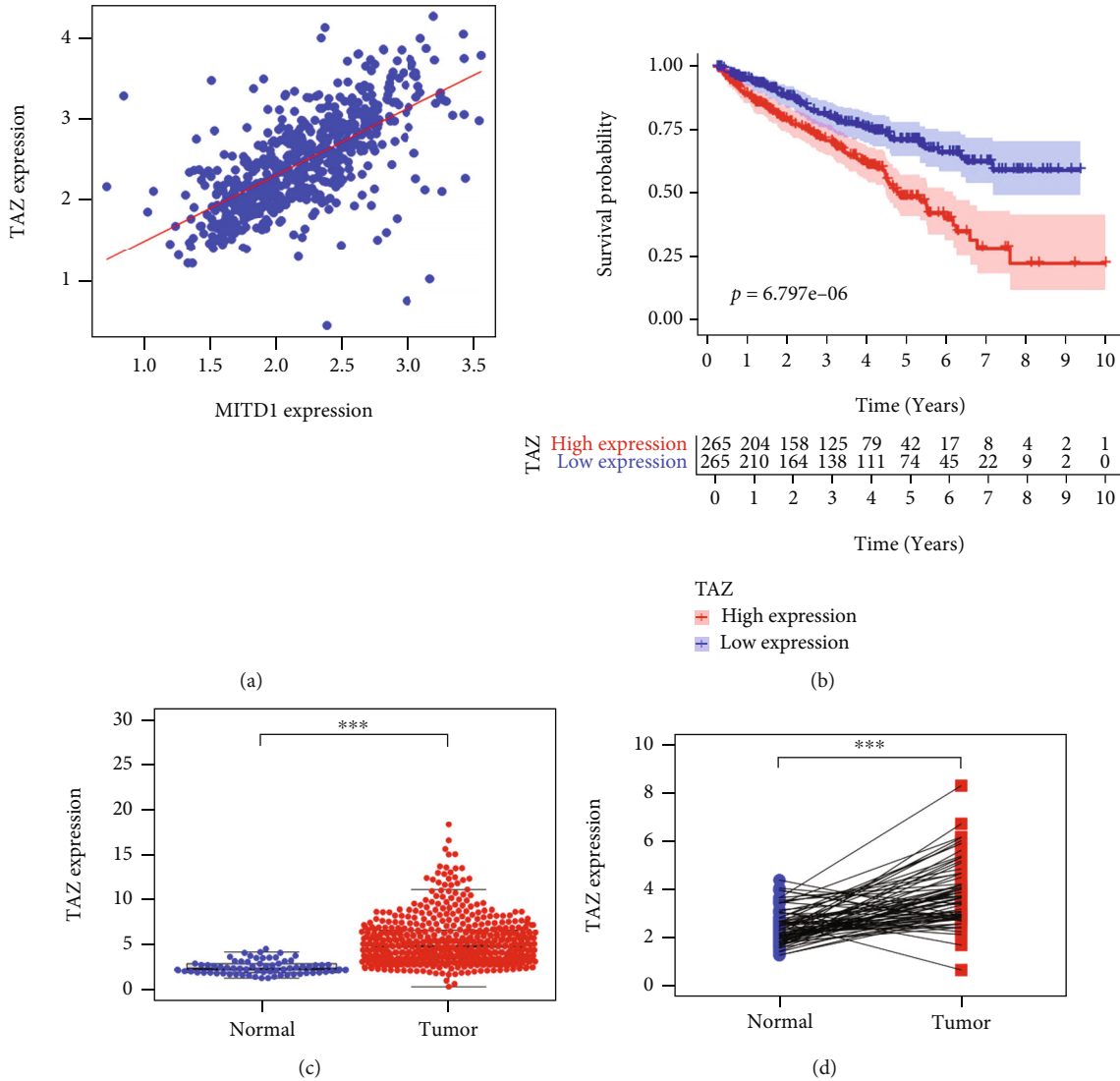


FIGURE 5: TAZ was highly correlated with MITD1 and high expressed in ccRCC. (a) A positive correlation between the MITD1 and TAZ expressions through bioinformatics analysis. (b) Based on the median values of TAZ expression, patients were divided into the low-expression or high-expression group. Kaplan-Meier's survival curve of two groups through the analysis of clinical information of ccRCC in TCGA. (c) The expression of TAZ in ccRCC tissues was higher compared to the normal tissues through TCGA dataset analysis. (d) The expression of TAZ in paired ccRCC tissues was also higher compared to the paracancerous tissues. Values are expressed as the mean \pm SEM, $n = 3$. * $P < 0.05$ and *** $P < 0.001$, relative to the control group.

of SLC7A11 was the most significant, indicating that MITD1 deficiency might induce ferroptosis through SLC7A11. Subsequently, ccRCC cells were transfected with SLC7A11 plasmid or vector control after MITD1 knockdown or not. Figures 4(b) and 4(c) showed the expression level of MITD1 and SLC7A11 to demonstrate the effect of silence and overexpression in different ccRCC cells. We then examined the levels of MDA, GSH, and SOD in ccRCC with different treatments, which could reflect the degree of ferroptosis. Similarly, it was found that MDA increased significantly and GSH and SOD decreased significantly in ccRCC cells after MITD1 silencing. Furthermore, overexpression of SLC7A11 restored the levels of MDA, GSH, and SOD changed by MITD1 silencing (Figures 4(d)–4(f)), which demonstrated that MITD1 deficiency induced ferroptosis through SLC7A11.

3.5. MITD1 Knockdown Induces Ferroptosis through TAZ/SLC7A11 Pathway. To further investigate how MITD1 knockdown regulates ferroptosis in ccRCC, we screened coexpressed genes of MITD1 and discovered that the correlation between MITD1 and TAZ was extraordinarily strong (Figure 5(a)). And we further found that TAZ showed high expression in ccRCC and patients with high TAZ expression had a lower overall survival rate (Figures 5(b)–5(d)), which was consistent with MITD1. Furthermore, a recent study [16] found that YAP/TAZ induced the expression of SLC7A11 to enable HCC cells to overcome sorafenib-induced ferroptosis. Therefore, we proposed the idea that whether MITD1 knockdown promoted ferroptosis through regulating the TAZ/SLC7A11 pathway in ccRCC cells.

In order to explore whether TAZ participated in the ferroptosis process induced by MITD1 knockdown, we carried

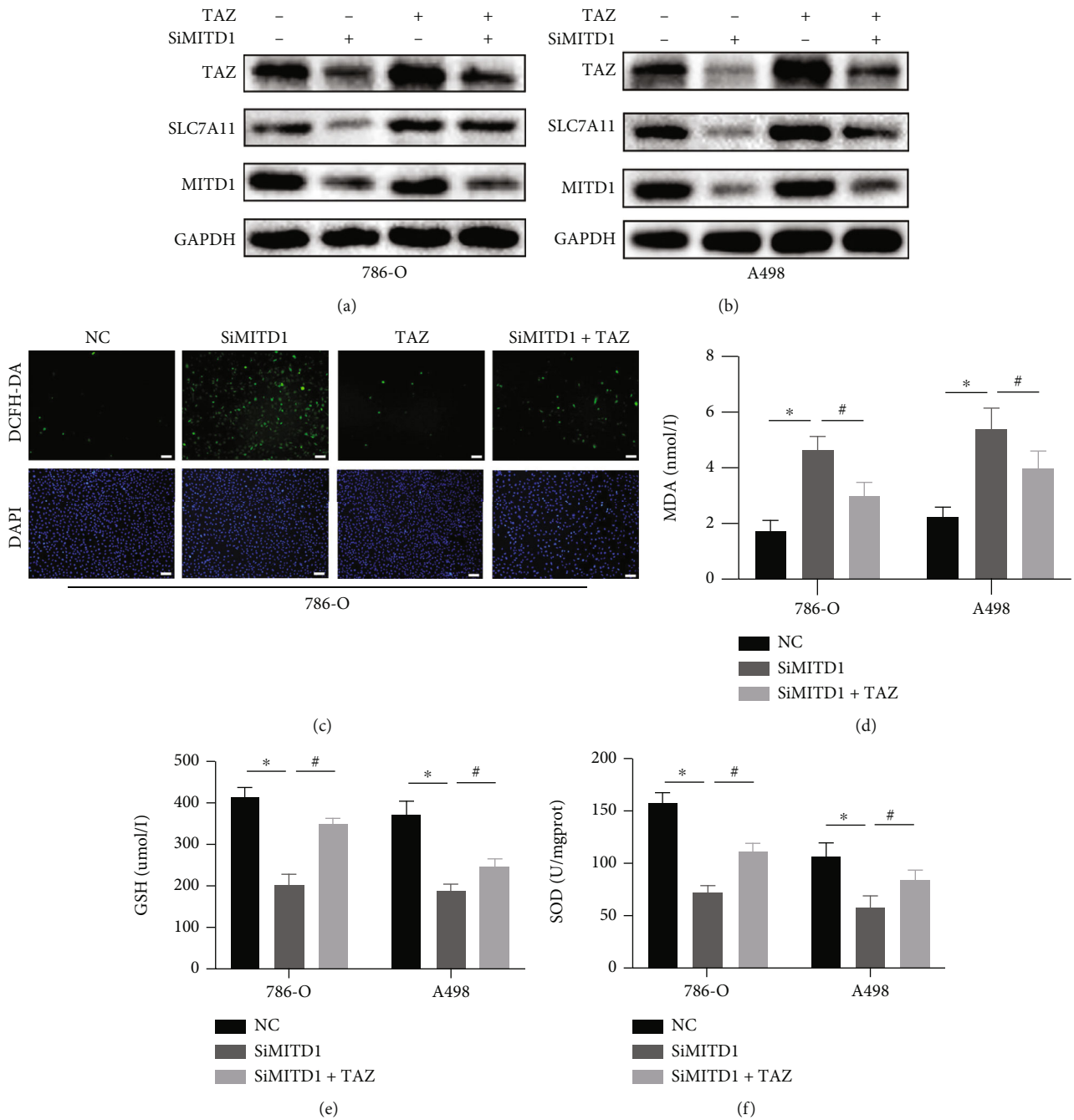


FIGURE 6: MITD1 knockdown induces ferroptosis through the TAZ/SLC7A11 pathway. (a, b) 786-O cells or A498 cells were transfected with negative control or si-RNA for MITD1 (SiMITD1) and then were transfected with TAZ plasmid. Western blot of MITD1, SLC7A11, and TAZ. (c) Representative images of 786-O cells with DCFH-DA staining (magnification $\times 100$; scale bars = $100 \mu\text{m}$) after different treatments. (d–f) Levels of MDA, GSH, and SOD in ccRCC cells with different treatments. Values are expressed as the mean \pm SEM, $n = 3$. * $P < 0.05$, relative to the control group; # $P < 0.05$, relative to the SiMITD1.

out a series of experiments. In subsequent experiments, we found that the expression of TAZ was significantly reduced with downregulation of SLC7A11 after MITD1 knockdown in 786-O and A498 cells. What is more, overexpression of TAZ markedly increased the expression of SLC7A11 and also partially restored the down-regulation of SLC7A11 caused by MITD1 knockdown in different ccRCC cells (Figures 6(a) and 6(b)). Moreover, overexpression of TAZ reduced the levels of ROS which were obviously increased by MITD1 knockdown in

ccRCC cells (Figure 6(c) and Supplementary Figure 1C). In addition, we also measured the level of MDA, GSH, and SOD. As shown in Figures 6(d)–6(f), MITD1 knockdown aggravated oxidative stress and ferroptosis which could be rescued by TAZ overexpression treatment.

3.6. MITD1 Knockdown Suppresses Growth and Migration through TAZ/SLC7A11 Pathway. To explore the role of SLC7A11 and TAZ expression changes caused by MITD1

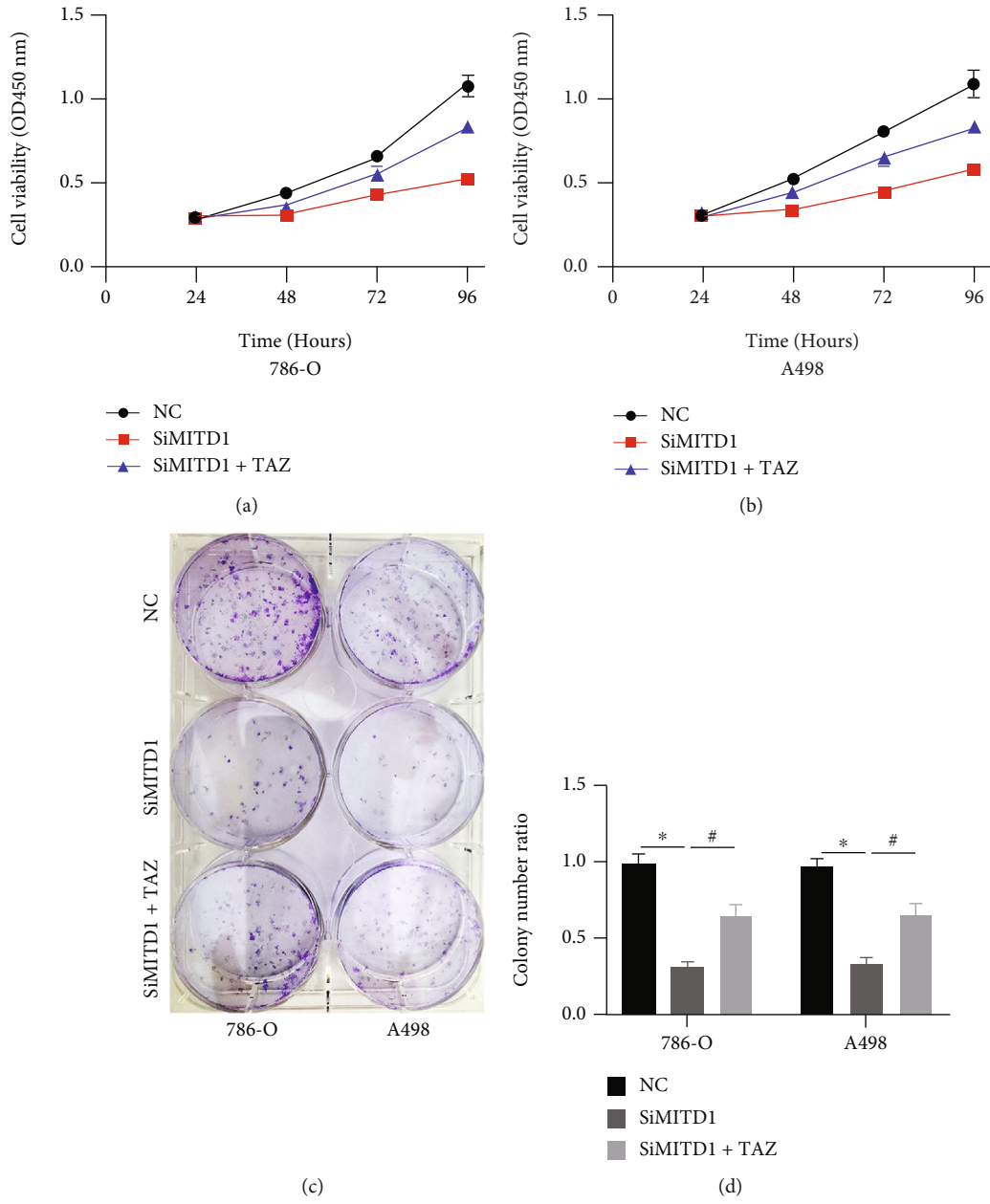


FIGURE 7: Continued.

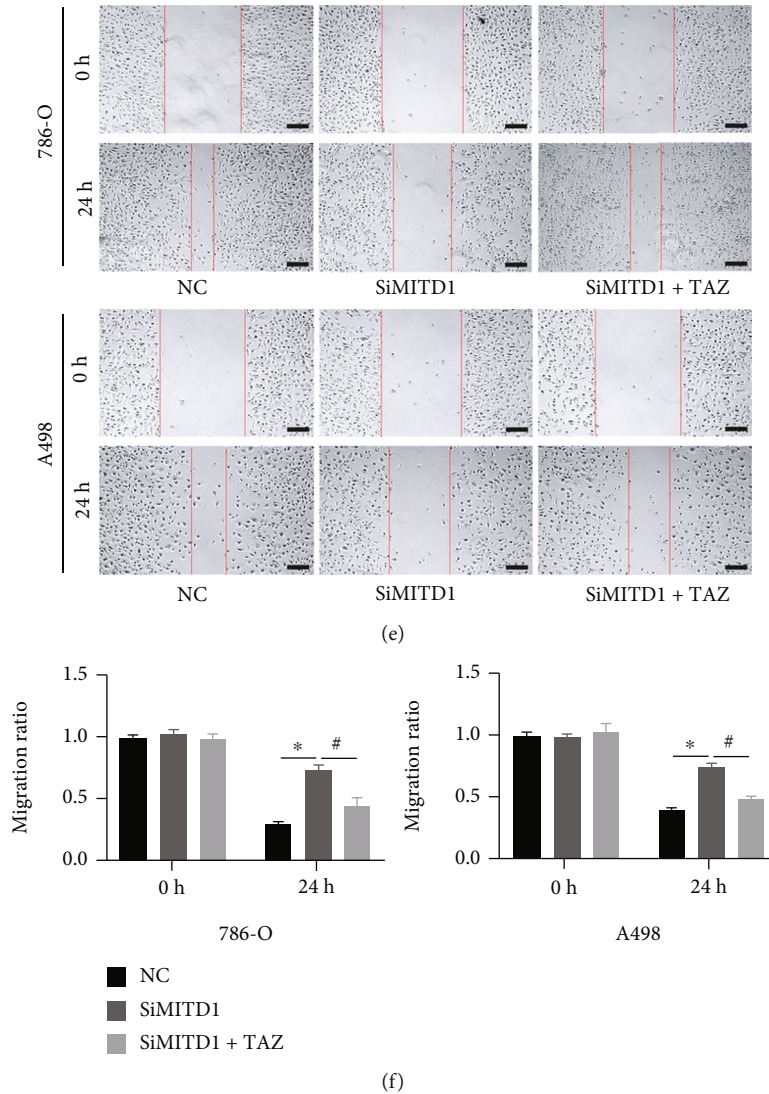


FIGURE 7: MITD1 knockdown suppresses growth and migration through the TAZ/SLC7A11 pathway. (a, b) 786-O cells or A498 cells were transfected with negative control or si-RNA for MITD1 (SiMITD1) and then were transfected with TAZ plasmid. Cell viability of each group was detected at 24 h, 48 h, 72 h, and 96 h, respectively. (c, d) Colony formation assay was performed on ccRCC cells with different treatments. The quantification data are also indicated. (e, f) When ccRCC cells with different treatments grew to 90%-95% density, the surface of cells was scratched with a straight gap. Scratches at 0 and 24 hours were photographed and recorded under the microscope (magnification $\times 40$; scale bars = $200 \mu\text{m}$). The quantification data are also indicated. Values are expressed as the mean \pm SEM, $n = 3$. * $P < 0.05$, relative to the control group; # $P < 0.05$, relative to the SiMITD1.

knockdown in cell proliferation and migration, we performed a further series of experiments. The CCK-8 assay showed that the cell viability of the MITD1 knockdown group was significantly lower than that of the control group. After treatment with TAZ overexpression, the expression of TAZ and SLC7A11 increased and cell viability was partially restored (Figures 7(a) and 7(b)). Cell colony formation assay also demonstrated that TAZ overexpression rescued the reduction of cell proliferation caused by MITD1 knockdown (Figures 7(c) and 7(d)). Moreover, the wound-healing assay (Figures 7(e) and 7(f)) showed that the change of cell migration ability caused by MITD1 knockdown could be rescued after TAZ overexpression treatment. These results indicated that MITD1 knockdown induced ferroptosis through down-

regulating SLC7A11 and TAZ and inhibited the proliferation and migration ability of ccRCC. Therefore, MITD1 deficiency suppresses ccRCC growth and migration by inducing ferroptosis through the TAZ/SLC7A11 pathway.

4. Discussion

MITD1, an MIT-domain containing protein 1, recognizes subunits of ESCRT-III through a typical MIT-MIM1 read-out in the dimer of MITD1. And the interaction of each other made the MITD1 recruit to the midbody during cell division [6]. Depletion of MITD1 is able to cause cytokinesis failure, which affects cell proliferation [17]. Previous studies [8, 9] revealed that MITD1 was abnormally expressed in

patients with liver cancer and bladder cancer and had a significant correlation with prognosis. In addition, MITD1 regulated proliferation and invasion of tumor cells and was able to alter the tumor microenvironment by recruiting and regulating immune infiltrating cells [8, 18]. In our study, we analyzed public databases and found that MITD1 was highly expressed in ccRCC and the expression level was related to tumor stage and clinical T stage. In the subsequent survival analysis, patients in the MITD1 high expression group had a lower survival rate. In vitro experiment, it was verified that MITD1 was highly expressed in ccRCC through Western blot analysis of MITD1 expression in common RCC cell lines and HK2 cell lines. Furthermore, it was found that the growth, proliferation, and migration of ccRCC cells were inhibited after MITD1 knockdown treatment.

Ferroptosis has been identified as a nonapoptotic form of cell death, of which the two most important features are iron accumulation and lipid peroxidation. And lipid peroxidation has many manifestations, including an increase in ROS and a decrease in antioxidants [19]. Ferroptosis is involved in the development of many diseases, especially cancer [11, 20]. Therefore, inducing ferroptosis by destroying the redox balance in tumor cells may be an effective means of cancer treatment [21]. Although scholars have searched for key molecules that induce ferroptosis in ccRCC, related research is still rare. Wang et al. [22] found that SUV39H1 expression is frequently upregulated in ccRCC tumors and SUV39H1 knockdown induced iron accumulation and lipid peroxidation, leading to ferroptosis that disrupted ccRCC cell growth. Another study [23] showed that KLF2 inhibited the migration and invasion abilities of ccRCC cells by regulating ferroptosis through the GPX4 pathway. In this study, we found that MITD1 was mainly related to the pathways of energy metabolism and lipid metabolism and could be enriched to the ferroptosis-related pathways through pathway enrichment analysis. We subsequently found that MITD1 deficiency increased ROS and MDA in ccRCC cells and decreased cellular GSH and SOD levels. However, the effects of MITD1 knockdown on these indicators were partially abolished by Fer-1 treatment. The above results demonstrated that MITD1 knockdown could induce ferroptosis in ccRCC.

The regulation of ferroptosis is a complex process that is affected by many factors, the two most important of which are transporter-dependent and enzyme-dependent [24]. System Xc⁻ is an amino acid transporter widely distributed on phospholipid bilayer membranes, mainly containing 2 subunits SLC7A11 and SLC3A2, which plays a key role in a transporter-dependent pathway [25]. System Xc⁻ is responsible for the transport of cystine into the cell and the transport of glutamate out of the cell. Cystine is reduced to cysteine after being transported into cells, which is the raw material for the synthesis of GSH. GSH is able to reduce intracellular ROS and lipid peroxidation through glutathione peroxidase (GPXs), the most typical of which is glutathione peroxidase 4 (GPX4) [25]. Inhibition of SLC7A11 reduces cystine absorption and glutathione synthesis, ultimately leading to oxidative damage and ferroptosis [26]. Therefore, targeting SLC7A11 is an important means to induce ferroptosis for

cancer therapy. Inhibition of PARP downregulated the expression of SLC7A11 in a p53-dependent manner to promote ferroptosis in ovarian cancer cells, revealing a previously unrecognized mechanism of PARP inhibitor therapy for ovarian cancer [27]. Another study [14] in ccRCC found that SLC16A1-AS1 served as a sponge of miR-143-3p and knockdown of SLC16A1-AS1 could induce ferroptosis through the miR-143-3p/SLC7A11 pathway. In the present study, MITD1 deficiency could significantly affect the expression levels of ferroptosis proteins, such as GPX4, SLC7A11, ACSL4, and COX2. The downregulation of SLC7A11 was the most significant, indicating that MITD1 deficiency was most likely to induce ferroptosis by regulating SLC7A11. In addition, ROS, MDA, GSH, and SOD affected by MITD1 knockdown could be restored by overexpression of SLC7A11, further confirming the regulatory effect of MITD1 deficiency on SLC7A11.

Transcriptional coactivator with PDZ-binding motif (TAZ), which is also named as WW domain-containing transcriptional coregulatory 1 (WWTR1), is a key downstream effector of the Hippo signaling pathway [28]. Hippo signaling pathway is a potent tumor-suppressing mechanism and has been established as a novel determinant of ferroptosis [29]. Previous research [30] indicated that the expression of TAZ generally increased in kidney cancer tissue and cells and TAZ knockdown inhibited the proliferation, migration, and invasion of ccRCC in vitro and in vivo. Another study [31] found that the changes in cell density affect the expression of TAZ, which could regulate the sensitivity of renal cell carcinoma to ferroptosis through the EMP1-NOX4 pathway. Nevertheless, a latest study [16] demonstrated that YAP/TAZ could induce the expression of SLC7A11 to inhibit ferroptosis and maintain the resistance of liver cell carcinoma to sorafenin. Based on correlation analysis, we found that MITD1 was highly correlated with TAZ. In addition, TAZ was highly expressed in ccRCC and TAZ high expression indicated a lower survival rate, same as MITD1. In the subsequent experiments, we found that MITD1 knockdown downregulated TAZ expression and a corresponding downregulation of SLC7A11 expression. In addition, overexpression of TAZ partially restored cellular ROS, MDA, GSH, and SOD changes caused by MITD1 knockdown. Moreover, overexpression of TAZ also restored the proliferation and migration of ccRCC which were inhibited by MITD1 knockdown. These results suggested that MITD1 knockdown suppressed ccRCC growth and migration by inducing ferroptosis through the TAZ/SLC7A11 pathway.

5. Conclusion

In conclusion, our study firstly proposed that MITD1 could change the proliferative and migratory capacity of ccRCC and affect prognosis by regulating ferroptosis. What is more, we further explored that MITD1 deficiency could increase the ferroptosis of ccRCC through the TAZ/SLC7A11 pathway. Therefore, MITD1 is expected to be a prognostic biomarker of ccRCC and a new therapeutic target for tumor ferroptosis.

Data Availability

Data supporting the findings of this study are included in the manuscript and the supplementary materials.

Conflicts of Interest

All authors have no conflicts of interest or financial ties to disclose.

Authors' Contributions

Ye Zhang, Yanze Li, and Qiangmin Qiu conceived and designed the study. Ye Zhang, Yanze Li, Qiangmin Qiu, and Zhiyuan Chen performed the experiments. Ye Zhang, Yanze Li, and Qiangmin Qiu wrote the manuscript. Zhiyuan Chen, Yang Du, and Xiuheng Liu reviewed and revised the manuscript. Ye Zhang, Yanze Li, and Qiangmin Qiu contributed equally to this work.

Acknowledgments

This work was supported by the National Natural Science Foundation of China (No. 81972408) and Application and Basic Research Project of Wuhan City (No. 2018060401011321).

Supplementary Materials

Supplemental Figure 1: quantified results for Figures 2(e) and 2(f) and DCFH-DA staining results of A498 cell line. Supplemental Figure 2: the results of DCFH-DA staining, SOD, GSH, and MDA treated with Lip-1 in ccRCC cells. (*Supplementary Materials*)

References

- [1] R. L. Siegel, K. D. Miller, H. E. Fuchs, and A. Jemal, "Cancer statistics, 2021," *CA: a Cancer Journal for Clinicians*, vol. 71, no. 1, pp. 7–33, 2021.
- [2] B. Ljungberg, K. Bensalah, S. Canfield et al., "EAU guidelines on renal cell carcinoma: 2014 update," *European Urology*, vol. 67, no. 5, pp. 913–924, 2015.
- [3] U. Capitanio, K. Bensalah, A. Bex et al., "Epidemiology of renal cell carcinoma," *European Urology*, vol. 75, no. 1, pp. 74–84, 2019.
- [4] R. R. Kotecha, R. J. Motzer, and M. H. Voss, "Towards individualized therapy for metastatic renal cell carcinoma," *Nature Reviews Clinical Oncology*, vol. 16, no. 10, pp. 621–633, 2019.
- [5] E. M. Posadas, S. Limvorasak, and R. A. Figlin, "Targeted therapies for renal cell carcinoma," *Nature Reviews Nephrology*, vol. 13, no. 8, pp. 496–511, 2017.
- [6] M. A. Hadders, M. Agromayor, T. Obita et al., "ESCRT-III binding protein MITD1 is involved in cytokinesis and has an unanticipated PLD fold that binds membranes," *Proceedings of the National Academy of Sciences of the United States of America*, vol. 109, no. 43, pp. 17424–17429, 2012.
- [7] S. Lee, J. Chang, B. Renvoise, A. Tipirneni, S. Yang, and C. Blackstone, "MITD1 is recruited to midbodies by ESCRT-III and participates in cytokinesis," *Molecular Biology of the Cell*, vol. 23, no. 22, pp. 4347–4361, 2012.
- [8] H. Shen, Z. Wang, S. Ren et al., "Prognostic biomarker MITD1 and its correlation with immune infiltrates in hepatocellular carcinoma (HCC)," *International Immunopharmacology*, vol. 81, article 106222, 2020.
- [9] Y. Chen, T. Xu, F. Xie et al., "Evaluating the biological functions of the prognostic genes identified by the Pathology Atlas in bladder cancer," *Oncology Reports*, vol. 45, no. 1, pp. 191–201, 2021.
- [10] J. Li, F. Cao, H. L. Yin et al., "Ferroptosis: past, present and future," *Cell Death & Disease*, vol. 11, no. 2, p. 88, 2020.
- [11] X. Jiang, B. R. Stockwell, and M. Conrad, "Ferroptosis: mechanisms, biology and role in disease," *Nature Reviews. Molecular Cell Biology*, vol. 22, no. 4, pp. 266–282, 2021.
- [12] S. J. Dixon, "Ferroptosis: bug or feature?," *Immunological Reviews*, vol. 277, no. 1, pp. 150–157, 2017.
- [13] P. Koppula, Y. Zhang, L. Zhuang, and B. Gan, "Amino acid transporter SLC7A11/xCT at the crossroads of regulating redox homeostasis and nutrient dependency of cancer," *Cancer Communications*, vol. 38, no. 1, p. 12, 2018.
- [14] Y. Z. Li, H. C. Zhu, Y. Du, H. C. Zhao, and L. Wang, "Silencing lncRNA SLC16A1-AS1 induced ferroptosis in renal cell carcinoma through miR-143-3p/SLC7A11 signaling," *Technology in Cancer Research & Treatment*, vol. 21, p. 2081147605, 2022.
- [15] O. Zilka, R. Shah, B. Li et al., "On the mechanism of cytoprotection by ferrostatin-1 and liproxstatin-1 and the role of lipid peroxidation in ferroptotic cell death," *ACS Central Science*, vol. 3, no. 3, pp. 232–243, 2017.
- [16] R. Gao, R. Kalathur, M. Coto-Llerena et al., "YAP/TAZ and ATF4 drive resistance to sorafenib in hepatocellular carcinoma by preventing ferroptosis," *EMBO Molecular Medicine*, vol. 13, no. 12, article e14351, 2021.
- [17] M. Agromayor and J. Martin-Serrano, "Knowing when to cut and run: mechanisms that control cytokinetic abscission," *Trends in Cell Biology*, vol. 23, no. 9, pp. 433–441, 2013.
- [18] C. Duan, "LncRNA SLC16A1-AS1 contributes to the progression of hepatocellular carcinoma cells by modulating miR-411/MITD1 axis," *Journal of Clinical Laboratory Analysis*, vol. 36, no. 4, article e24344, 2022.
- [19] D. Li and Y. Li, "The interaction between ferroptosis and lipid metabolism in cancer," *Signal Transduction and Targeted Therapy*, vol. 5, no. 1, p. 108, 2020.
- [20] D. Tang and G. Kroemer, "Ferroptosis," *Current Biology*, vol. 30, no. 21, pp. R1292–R1297, 2020.
- [21] B. Hassannia, P. Vandenabeele, and B. T. Vanden, "Targeting ferroptosis to iron out cancer," *Cancer Cell*, vol. 35, no. 6, pp. 830–849, 2019.
- [22] J. Wang, X. Yin, W. He, W. Xue, J. Zhang, and Y. Huang, "SUV39H1 deficiency suppresses clear cell renal cell carcinoma growth by inducing ferroptosis," *Acta Pharmaceutica Sinica B*, vol. 11, no. 2, pp. 406–419, 2021.
- [23] Y. Lu, H. Qin, B. Jiang et al., "KLF2 inhibits cancer cell migration and invasion by regulating ferroptosis through GPX4 in clear cell renal cell carcinoma," *Cancer Letters*, vol. 522, pp. 1–13, 2021.
- [24] W. S. Yang and B. R. Stockwell, "Ferroptosis: death by lipid peroxidation," *Trends in Cell Biology*, vol. 26, no. 3, pp. 165–176, 2016.
- [25] M. R. Liu, W. T. Zhu, and D. S. Pei, "System Xc(-): a key regulatory target of ferroptosis in cancer," *Investigational New Drugs*, vol. 39, no. 4, pp. 1123–1131, 2021.

- [26] X. Lang, M. D. Green, W. Wang et al., “Radiotherapy and immunotherapy promote tumoral lipid oxidation and ferroptosis via synergistic repression of SLC7A11,” *Cancer Discovery*, vol. 9, no. 12, pp. 1673–1685, 2019.
- [27] T. Hong, G. Lei, X. Chen et al., “PARP inhibition promotes ferroptosis via repressing SLC7A11 and synergizes with ferroptosis inducers in BRCA-proficient ovarian cancer,” *Redox Biology*, vol. 42, article 101928, 2021.
- [28] S. Piccolo, S. Dupont, and M. Cordenonsi, “The biology of YAP/TAZ: hippo signaling and beyond,” *Physiological Reviews*, vol. 94, no. 4, pp. 1287–1312, 2014.
- [29] T. Sun and J. T. Chi, “Regulation of ferroptosis in cancer cells by YAP/TAZ and Hippo pathways: the therapeutic implications,” *Genes & Diseases*, vol. 8, no. 3, pp. 241–249, 2021.
- [30] H. Ruan, L. Bao, Z. Song et al., “High expression of TAZ serves as a novel prognostic biomarker and drives cancer progression in renal cancer,” *Experimental Cell Research*, vol. 376, no. 2, pp. 181–191, 2019.
- [31] W. H. Yang, C. C. Ding, T. Sun et al., “The Hippo pathway effector TAZ regulates ferroptosis in renal cell carcinoma,” *Cell Reports*, vol. 28, no. 10, pp. 2501–2508.e4, 2019.

Research Article

Dapagliflozin Ameliorates Renal Tubular Ferroptosis in Diabetes via SLC40A1 Stabilization

Bin Huang ¹, Wenjie Wen,^{1,2} and Shandong Ye ¹

¹Department of Endocrinology, The First Affiliated Hospital of USTC, Division of Life Science and Medicine, University of Science and Technology of China, Hefei, Anhui 230001, China

²Division of Life Sciences, University of Science and Technology of China, Hefei, Anhui 230001, China

Correspondence should be addressed to Shandong Ye; 981257013@qq.com

Received 18 June 2022; Revised 23 July 2022; Accepted 26 July 2022; Published 10 August 2022

Academic Editor: Yanqing Liu

Copyright © 2022 Bin Huang et al. This is an open access article distributed under the Creative Commons Attribution License, which permits unrestricted use, distribution, and reproduction in any medium, provided the original work is properly cited.

Tubular injury has been shown to play a critical role in the morbidity of diabetic kidney disease (DKD); ferroptosis often occurs in tubules during renal disease development. This study was aimed at evaluating the inhibitory effects and potential mechanism of dapagliflozin (DAPA) against diabetic-related ferroptosis in the kidney. C57BL/6 mice were fed a high-fat diet (HFD) for 12 weeks, administered a small dose of streptozocin (STZ) for three consecutive days by intraperitoneal injection, and then orally administered dapagliflozin (10 mg/kg/day) for 8 weeks. Mouse blood and urine samples were collected, and their renal cortices were harvested for subsequent investigations. The effects of DAPA were also evaluated in HK-2 cells subjected to simulated diabetic conditions through excess glucose or palmitic acid (PA) administration. DAPA significantly ameliorated tubular injury independently of glycemic control in diabetic model mice. In vivo and in vitro investigations showed that dapagliflozin ameliorated tubular injury by inhibiting ferroptosis. Docking experiments demonstrated that dapagliflozin and SLC40A1 could bind with each other and may consequently reduce ubiquitination degradation. In conclusion, in this study, the tubular protective effects of DAPA, irrespective of glycemic control, were observed in a diabetic mouse model. DAPA ameliorated ferroptosis during diabetic tubular injury via SLC40A1 stabilization, and this may be the mechanism underlying its action. To the best of our knowledge, this is the first study to investigate the ferroptosis inhibitory effects of DAPA in the treatment of DKD.

1. Introduction

Diabetic kidney disease (DKD) is a common and morbid chronic diabetic complication. Approximately 30–40% of patients with type 2 diabetes mellitus (T2DM) develop DKD, and in approximately 50% of them, the disease progresses to end-stage renal disease (ESRD) [1]. Hyperglycemia is considered to drive the development of DKD. However, existing intensive glycemic control has not reduced the prevalence of DKD, and inhibitors of the renin-angiotensin-aldosterone system (RAAS) have been proven to have renal protective function on DKD patients, but the clinical effect is not always satisfactory [2, 3]. As a whole, despite the advancements made in diabetic renal pathologies over the years, DKD still causes significant mortality and morbidity [4]. Therefore, there is an urgent need for the discovery of novel therapeutic targets or drugs for the management of DKD.

Ferroptosis, which is a novel type of programmed cell death, is involved in the processes of inflammation and oxidation in various human disease states, including DKD [5, 6]. Intracellular iron homeostasis is essential for cell survival, while iron overload contributes to ROS overproduction through the Fenton reaction, thereby facilitating ferroptosis [7]. Of note, solute carrier family 40 member 1 (SLC40A1, also known as FPN1) is the only discovered iron export protein in mammals, and inhibiting SLC40A1 induces ferroptosis [8]. The study of Hao et al. shows that diabetes decreased the expression of SLC40A1 mediating ferroptosis, which induced diabetic cognitive dysfunction [9]. Due to the special reabsorption function of renal tubular tissue (including glucose and iron), which contains numerous mitochondria, its metabolic activity and energy demand are high; diabetes induces impairments in mitochondrial energy metabolism, which results in significant intrarenal

oxidative stress and cell damage [10]. Tubular injury has been shown to play a critical role in DKD progression, which correlates with renal functional deterioration, a primary change associated with the disease [11]. Ferroptosis often occurs in renal tubules during the development of renal diseases because of the sensitivity of renal tubular tissue to oxidative stress and lipid peroxidation [12]. Zhu et al. recently demonstrated that miR-4735-3p facilitates ferroptosis and tumor suppression in clear cell renal cell carcinoma by targeting SLC40A1 [13]. However, it has not been reported whether SLC40A1 is involved in renal tubular ferroptosis in the diabetic conditions.

Dapagliflozin (DAPA), one of the clinically employed hypoglycemic agents for diabetes treatment, functions primarily by decreasing glucose reabsorption in the proximal tubule via sodium-glucose cotransporter 2 (SGLT2) [14]. The cardioprotective and renoprotective function beyond their hypoglycemic effect of SGLT2 inhibitors (SGLT2i) has recently been reported and recognized [15–17]. Quagliarillo et al. reported that empagliflozin reduced ferroptosis in doxorubicin-treated mice through the NLRP3 and MyD88-related pathways, which resulted in significant improvements in cardiac function [18]. However, the DKD-improving effects of SGLT2i through the inhibition of tubular ferroptosis have not been evaluated. In this study, we sought to determine whether diabetes-related ferroptosis could be inhibited by DAPA, thereby delaying the progression of DKD. This study is expected to provide a new perspective on the therapeutic mechanism of DAPA in DKD.

2. Materials and Methods

2.1. Animal Experiments. Eight-week-old specific pathogen-free C57BL/6 mice weighing 20–23 g were purchased from Shandong Kesibei Biotechnology Co., Ltd., China. All mice were maintained in a $48 \pm 10\%$ humid environment at room temperature ($20 \pm 1^\circ\text{C}$), under a 12 h light/dark cycle, with free access to food. All animal experiments were strictly carried out following the guidelines stated by the Ethics Committee of the First Affiliated Hospital of the University of Science and Technology of China (Anhui Provincial Hospital). Every effort was made to minimize the number of animals used and their suffering. Eight mice were randomly selected to constitute the normal control (NC) group ($n = 8$) and were fed a normal chow diet; the rest of the mice were fed a high-fat diet (HFD). With small-dose streptozocin (STZ) administration by intraperitoneal injection (50 mg/kg, dissolved in 0.1 mol/L citrate buffer, pH = 4.2, for three consecutive days) after 4 months of HFD feeding, mice in the NC group were injected an equal amount of citrate buffer. After one week, tail vein blood glucose levels were measured using a glucometer. Mice with random blood glucose levels > 16.7 mmol/L for 3 days were used for subsequent investigations. These mice were randomly divided into three groups; the T2DM group ($n = 7$), in which mice were administered sterile saline daily by gavage for 8 weeks; the DAPA group ($n = 8$), in which mice were administered DAPA (10 mg/kg/day) daily by gavage for 8 weeks; and the glibenclamide (GLIB, a clinically employed antidia-

betic molecule, which has no protective effect on the kidney beyond glycemic control) group ($n = 7$), in which mice were administered GLIB (2.5 mg/kg/day) daily by gavage for 8 weeks. At the 8th week, mouse urine was collected and weighed. Then, the mice were fasted overnight, anesthetized by intraperitoneal injection of sodium pentobarbital (30 mg/kg), and sacrificed by cervical dislocation, and blood samples were collected. Mouse kidneys were also collected; one part of each kidney was fixed in 4% polyoxymethylene-phosphate buffer for histological analysis, and the other part was snap-frozen for subsequent molecular analyses.

2.2. Detection of Blood and Urine Indicators. When the treatment was over, blood was collected from the tail vein of the mice. Hemoglobin A1C (HbA1C) and fasting blood glucose (FBG) levels were determined using a commercial ELISA kit (Meimian, Jiangsu, China). Urine creatinine (UCR) levels were measured using the picrate method (Jiancheng, Nanjing, China). Urine albumin (ALB), Retinol-Binding Protein (RBP), Tamm Horsfall protein (THP), α -Microglobulin (a1MG), 8-hydroxy-2 deoxyguanosine (8OHdG), and 8-iso prostaglandin (8iso-PG) levels were measured using an ELISA kit (Meimian, Jiangsu, China). Urine ALB/UCR (UACR), PCX/UCR, RBP/UCR, THP/UCR, a1MG/UCR, 8OHdG/UCR, and 8iso-PG/UCR ratios were subsequently calculated to exclude the effect of urine concentration.

2.3. Electron Microscopic Observation. Mouse renal cortices were harvested and fixed using a fixing solution for the preparation of ultra-thin sections. After postfixation with 1% OsO₄ and gradient dehydration, they were dehydrated in a series of ethanol (50–100%) and embedded in resin, sliced, and placed on a formvar carrier grid, followed by uranyl acetate and lead citrate treatments. Then, the sections were examined under a 20,000x transmission electron microscope (JEM1400, JEDL, Japan). Ultrastructural damage to mitochondria was assessed.

2.4. Quantitative PCR Analysis. Total RNA was extracted from mouse kidney tissues using the TRIzol reagent and reverse-transcribed to cDNA. Quantitative PCR was performed using SYBR Green PCR technology on a Bio-Rad CFX96 Touch Real-Time PCR System. The sequences of the primers used for real-time PCR are listed in Supplement Table S1. The PCR cycling conditions were as follows: predenaturation at 95°C for 5 min, 40 cycles of 95°C for 10 s and 60°C for 30 s, and one cycle of 95°C for 15 s, 60°C for 60 s, and 95°C for 15 s. Cycle threshold (Ct) values were determined by the comparative Ct method and normalized to β -actin levels.

2.5. Cell Culture and Treatment. Human kidney proximal tubular cells (HK-2 cells) were maintained in DMEM supplemented with 5.5 mmol/L glucose, 10% fetal bovine serum (FBS), 100 U/mL penicillin, and 100 mg/mL streptomycin and were cultured at 37°C in a 95% humid and 5% CO₂-containing environment. BSA-conjugated PA (Sigma-Aldrich, St. Louis, MO, USA) was prepared as previously described [19]. HK2 cells were then divided into 6 groups: (1) group HG: the cells were treated with 50 mM glucose; (2) group

HG+DAPA: after the cells were treated with HG for 48 h, they were treated with DAPA for 24 h; (3) group PA: the cells were treated with 300 μ M PA; (4) group PA+DAPA: after the cells were treated with PA for 48 h, they were treated with DAPA for 24 h; (5) group erastin: the cells were treated with erastin; and (6) group erastin +DAPA: after the cells were treated with erastin for 48 h, they were treated with DAPA for 24 h.

2.6. RNA Interference Analysis. HK2 cells were transfected with specific or scrambled small interfering RNAs (siRNAs) using a Lipofectamine 2000 device (Invitrogen, Grand Island, NY, USA) following the manufacturer's protocol. siRNAs were purchased from General Biol (Chuzhou, China). The sequences of the siRNAs were as follows: si-SLC40A1: 5'-CAAGAAUGCUAGACUAAAATT-3', scramble: 5'-UUUAAGUCUAGCAUUCUUGTT-3', si-SGLT2: 5'-GUAUGACAACAGCCUCAAGTT-3', and scramble: 5'-UUCUCCGAA CGUGUCACGUTT-3'. Unless otherwise specified, DAPA was added to the cells 24 h posttransfection.

2.7. Western Blot and Immunoprecipitation. For western blot, total proteins in renal tissues and cells were extracted by grinding the tissues in the RIPA buffer; protein concentrations were measured through the BCA assay. After centrifugation at 13000 g at 4°C for 10 min, the same quantity of protein was extracted with 10% sodium dodecyl sulfate-polyacrylamide gel electrophoresis (SDS-PAGE) gels and then transferred to nitrocellulose filter (NC) membranes. Then, the membranes were blocked in 5% skim milk. The proteins were detected using specific primary anti- β -actin (1:5000, Enogene, Nanjing, China), anti-SLC40A1 (1:1000, Bioss, Beijing, China), anti-GPX4 (1:1000, Bioss) and anti-SLC7A11 (1:1000, Bioss) antibodies, anti-TFR1 (1:1000, Affinity, Jiangsu, China) antibodies, anti-NCOA4 (1:1000, Affinity) antibodies, anti-FTH1 (1:1000, Bioss) antibodies, anti-SLC39A8 (1:1000, ABclonal, Wuhan, China) antibodies, and anti-ubiquitination (1:1000, PTM, Hangzhou, China). Protein bands were visualized using a Super ECL kit (Uelandy, Suzhou, China) and analyzed using the ImageJ software. For immunoprecipitation, cells were lysed in MCBL buffer (50 mM Tris-HCl, 150 mM NaCl, 5 mM EDTA, and 0.5% NP-40), supplemented with protease inhibitors (Topscience, Shanghai, China). Protein A/G magnetic beads (Bimake, USA) were incubated with antibody for 1 hour. Then, cell lysates were added and incubated overnight at 4°C. The next day, immunocomplexes were washed three times using lysis buffer, resolved by SDS/PAGE, and detected by western blot.

2.8. Determination of ROS Generation. Intracellular ROS levels were evaluated using 2',7'-dichlorofluorescein diacetate (DCFH-DA) (Solarbio, Beijing, China). In brief, the cells were incubated with 10 μ mol/L DCFH-DA at 37°C for 20 min and then washed with PBS. Fluorescence was evaluated using a fluorescence microscope at excitation and emission wavelengths of 488 and 525 nm, respectively.

2.9. GSH, MDA, and Iron Assays. Kidney tissue and cell samples were homogenized on ice using a homogenizer and then centrifuged for supernatant collection. Glutathione (GSH) levels were measured using a reduced GSH assay kit (Jiancheng, Nanjing, China), and optical density was measured at 405 nm. Malondialdehyde (MDA) levels were measured using a lipid peroxidation MDA assay kit (Biosharp, Hefei, China), and optical density was measured at 535 nm. Tissue iron levels were measured using a tissue iron assay kit (Jiancheng, Nanjing, China), and optical density was measured at 520 nm. Fe^{2+} concentrations were measured using a ferrous ion colorimetric assay kit (Elabscience, Wuhan, China), and optical density was measured at 590 nm. The kits were used following the manufacturers' instructions.

2.10. Cell Viability Assay. Cell viability was evaluated using the Cell Counting Kit-8 (Topscience, Shanghai, China), according to the manufacturer's instructions. In brief, cells were seeded in 96-well plates at a density of 3000 cells per well and exposed to various concentrations of the compounds for specified durations. Ten microliters of the working reagent was added to each well and incubated for 2 h at 37°C. Absorbance was measured at 450 nm using a microplate reader (Thermo Fisher Scientific, USA). Optical density was taken to be proportional to the number of living cells in the plate.

2.11. Lipid Reactive Oxygen Species Measurement. Cells were treated as indicated; then, 50 μ M BODIPY™ 665/676 (Thermo Fisher Scientific, USA) was added to the cells, which were incubated for 1 h. Excess BODIPY™ 665/676 was removed by washing the cells twice with PBS. Representative images were obtained using a confocal microscope.

2.12. Molecular Docking. The binding mode between dapagliflozin and SLC40A1 was determined using AutoDock 4.2. The three-dimensional (3D) structure of SLC40A1 was downloaded from the RCSB Protein Data Bank (PDB ID: 6W4S), and that of dapagliflozin was obtained from the NCBI PubChem Compound (CID: 9887712) database. The AutoDockTools 1.5.6 software package was used to generate the docking input files.

2.13. Statistical Analysis. Statistical analyses were performed using SPSS 26.0 (IBM, Inc., Armonk, NY, USA). Data are presented as mean \pm standard deviation (mean \pm SD). Comparisons between two groups were performed using Student's *t*-test. One-way ANOVA with post hoc analysis of variance was used to compare data between multiple groups. For normally distributed data, pairwise comparisons were conducted using the LSD test. Otherwise, pairwise comparisons were conducted using Dunnett's T3 test. Values of *P* < 0.05 were considered statistically significant.

3. Results

3.1. The Additional Renal Protective Effect of Dapagliflozin in T2DM Mice. An animal T2DM model was established by feeding male C57BL/6 mice high-fat diet (HFD)/low-dose

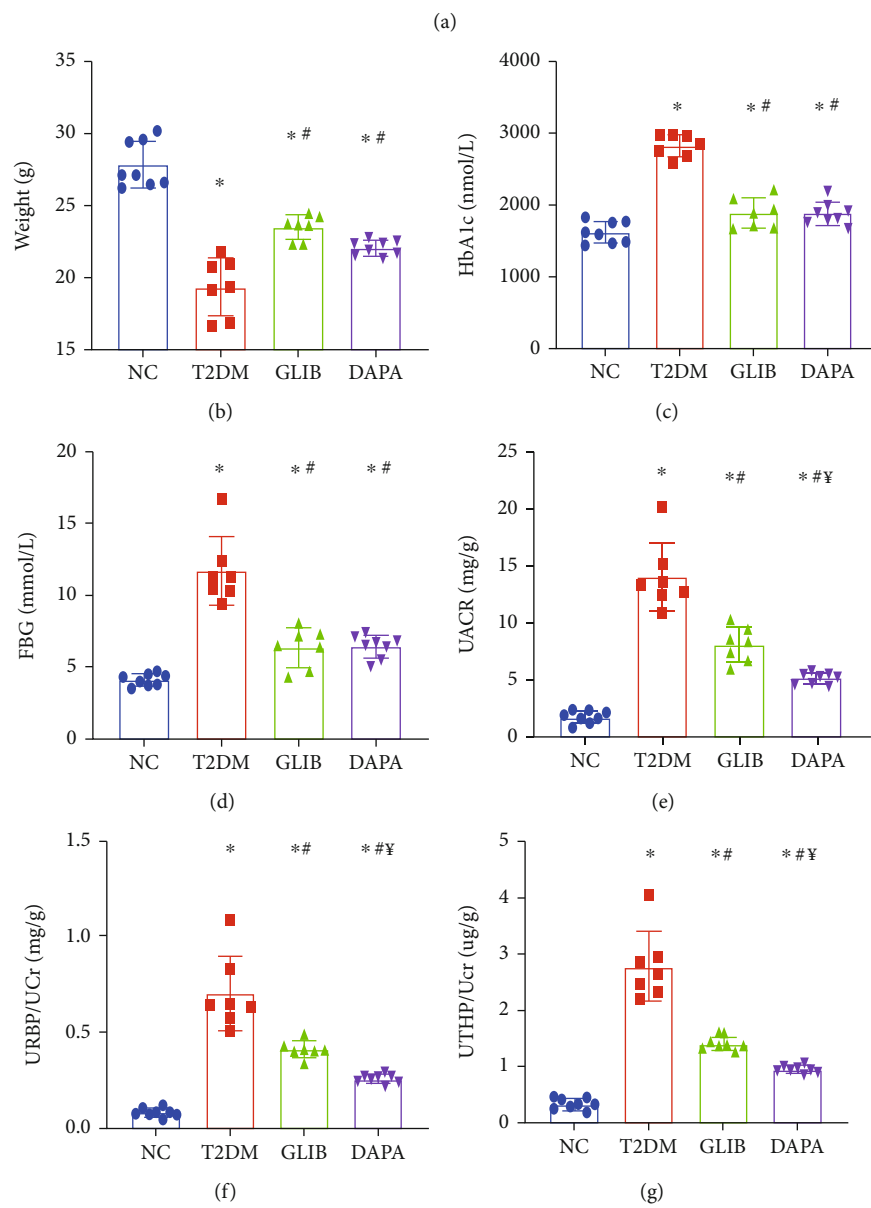
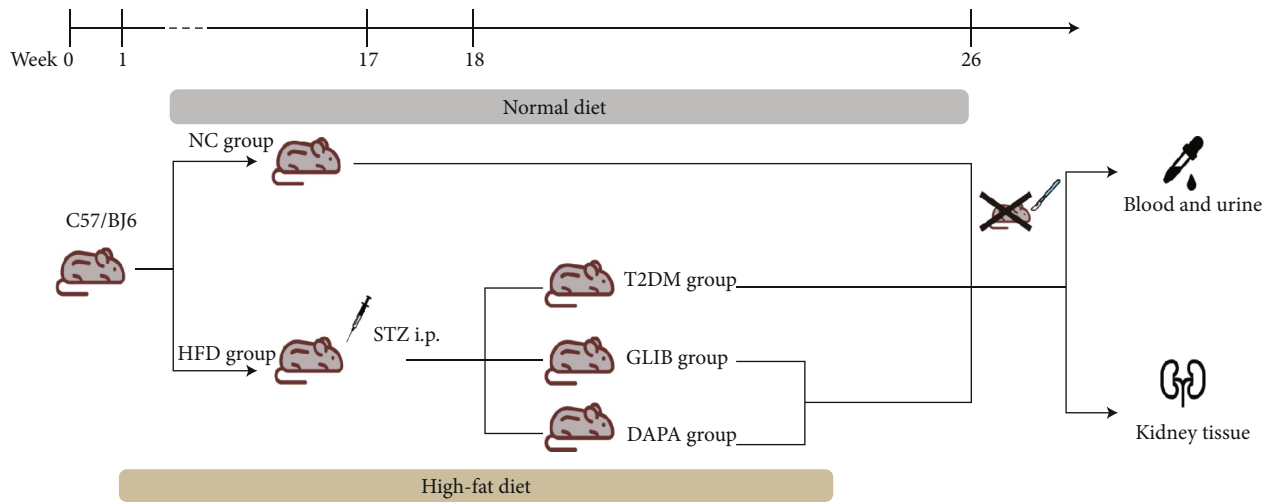


FIGURE 1: Continued.

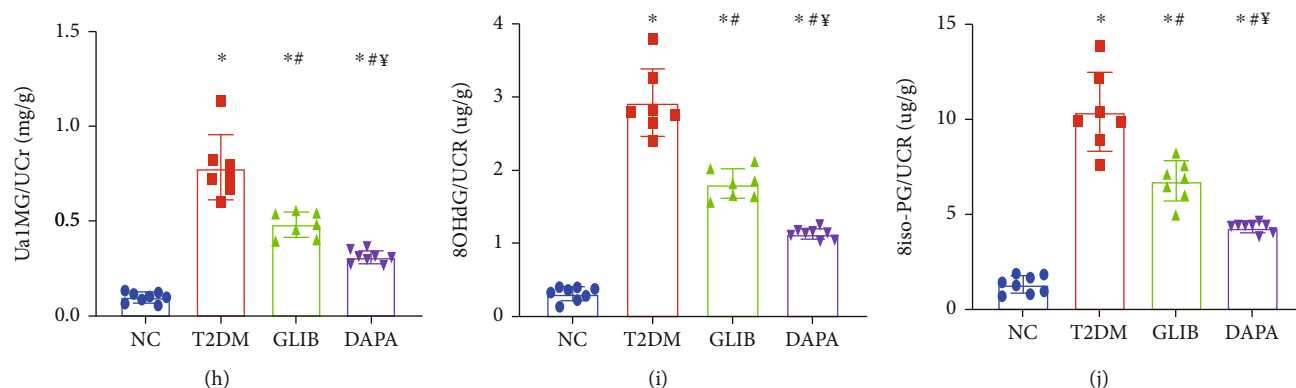


FIGURE 1: The additional renal protective effect of dapagliflozin in T2DM mice: (a) workflow of the experiment; (b) body weights in each group; (c) HbA1c concentrations in each group; (d) FBG concentrations in each group; (e) urinary ACRs; (f) urinary RBP/creatinine ratio; (g) urinary THP/creatinine ratio; (h) urinary a1MG/creatinine ratio; (i) urinary 8-OHdG/creatinine ratio; (j) urinary 8iso-PG/creatinine ratio. Values are the mean \pm SD. $n = 7$ mice in the T2DM group and GLIB group, respectively; $n = 8$ mice in the NC group and DAPA group, respectively. * $P < 0.05$ vs. NC; # $P < 0.05$ vs. T2DM; ¥ $P < 0.05$ vs. GLIB.

STZ. In our experiment, we used a clinically employed anti-diabetic drug (GLIB) as a hypoglycemic control, which has no protective effect on the kidney beyond glycemic control; the workflow for this experiment is shown in Figure 1(a). These mice were used to evaluate the therapeutic effects of DAPA against DKD. As shown in Figures 1(b)–1(d), there was a significant increase in HbA1c and FBG levels and a decrease in body mass in mice in the T2DM group; however, these changes were reversed when treated with DAPA or GLIB, indicating similar hypoglycemic effect was produced by those two drugs. At the end of the study, the levels of different urine proteins were evaluated (Figures 1(e)–1(j)). We found that DAPA and GLIB significantly ameliorated the increased urine protein excretion levels in T2DM mice. Furthermore, as compared to GLIB, DAPA significantly decreased UACR levels and URBP/UCR, Ua1MG/UCR, UTHP/UCR, 8OHdG/UCR, and 8iso-PG/UCR ratios, indicating that its additional renal protective effects were independent of glycemic control.

3.2. Dapagliflozin Ameliorates Tubular Injury in T2DM Mice Independently of Glycemic Control. Considering those urine biomarkers were reflecting tubular injury, we evaluated the renal mRNA levels of Kim, Ngal, and PAI-1, all of which were typical markers of tubular damage [20]. We found that Kim, Ngal, and PAI-1 expression was higher in the kidneys of T2DM mice than in those of mice in the NC group; however, as shown in Figures 2(a)–2(c), their expression was significantly reduced following dapagliflozin administration when compared to the GLIB group. The protein level had also validated those phenomena (Figure 2(d)). Collectively, these findings indicate that dapagliflozin treatment might significantly ameliorate tubular injury in T2DM mice independently of glycemic control.

3.3. Dapagliflozin Ameliorated Ferroptosis in T2DM Mice. Ferroptosis is an iron-dependent and regulated type of necrosis characterized by increased lipid peroxidation [21]. Thus, to determine the involvement of ferroptosis in DKD,

the levels of glutathione, iron ions, lipid peroxidation, and massive reactive oxygen species (ROS), as well as the expression levels of some ferroptosis markers, were determined in kidney tissues. GSH, iron ion, and MDA levels in mouse kidney tissues were found to be significantly higher in the T2DM group than in the control group; however, these abnormal levels were significantly restored after 8 weeks of dapagliflozin administration (Figures 3(a)–3(c)). Furthermore, the kidney tissues were stained with 2',7'-dichlorofluorescein diacetate to evaluate ROS generation. Minimal background fluorescence was observed in the kidney tissues of mice in the NC group; the kidney tissues of mice in the diabetic group showed the highest fluorescence intensities, and these significantly decreased following dapagliflozin administration (Figure 3(d)). In line with this finding, transmission electron microscopy also revealed ruptured mitochondrial membranes and the disappearance of mitochondrial cristae in the kidney cells of mice in the T2DM and glibenclamide groups; these changes were significantly ameliorated by treatment with dapagliflozin (Figure 3(e)). GPX4 and SLC7A11 are considered to be the primary proteins for ferroptosis prevention, and the deletion or inhibition of GPX4/SLC7A11 could induce ferroptosis. In this study, there was a significant decrease in GPX4 and SLC7A11 levels in mice in the T2DM and GLIB groups; however, their expression levels were upregulated in mice in the DAPA treatment group (Figure 3(f)). Collectively, these findings suggested that dapagliflozin may ameliorate tubular injury in the T2DM mouse model by inhibiting ferroptosis.

3.4. Dapagliflozin Ameliorates Ferroptosis in HK-2 Cell Injury Models In Vitro. To describe cell death via ferroptosis in kidney cells, we analyzed HK-2 cells treated with various concentrations of erastin. The CCK-8 assay revealed a significant dose-dependent increase cell death in erastin-stimulated cells as compared to control cells ($P < 0.05$ for $2 \mu\text{M}$; $P < 0.01$ for 4 and $6 \mu\text{M}$; and $P < 0.001$ for 8 and $10 \mu\text{M}$; Figure 4(a)), suggesting that HK-2 cells were

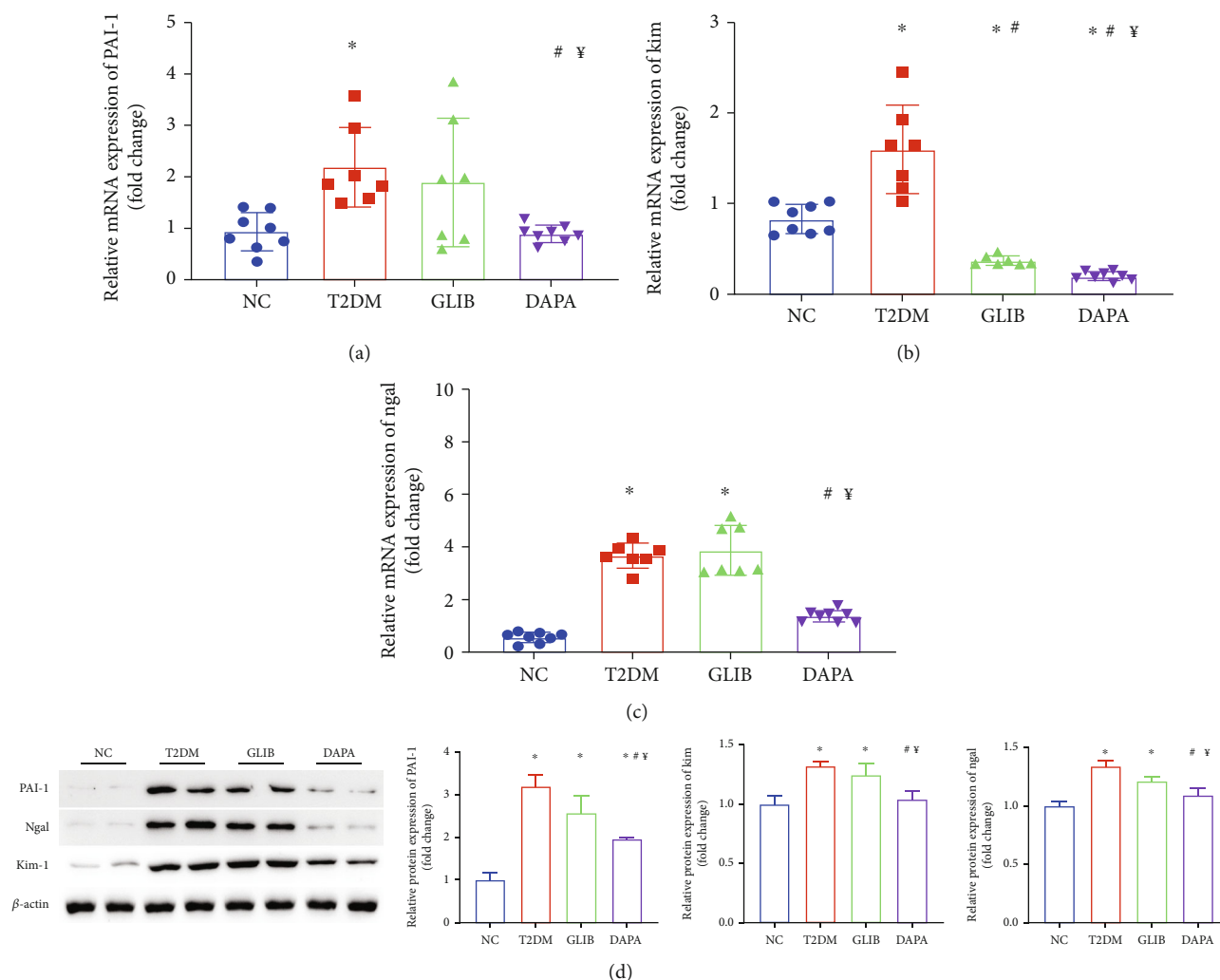
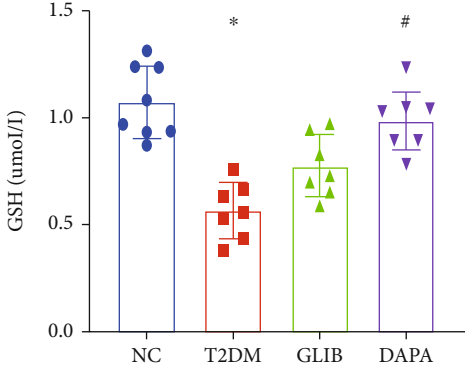


FIGURE 2: Dapagliflozin ameliorates tubular injury in T2DM mice independently of glycemic control. RT-PCR results of PAI-1 (a), KIM1 (b), and Ngal (c) in the kidney. (d) Quantification of the average band densities calculated from different western blots and the protein levels of PAI-1, KIM1, and Ngal in the kidney tissue in these groups. $n = 7$ mice in the T2DM group and GLIB group, respectively; $n = 8$ mice in the NC group and DAPA group, respectively. * $P < 0.05$ vs. NC; # $P < 0.05$ vs. T2DM; ¥ $P < 0.05$ vs. GLIB.

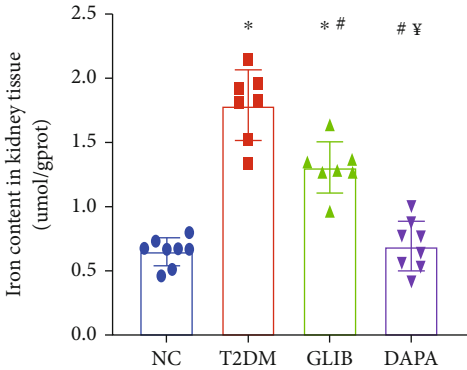
sensitive to ferroptosis. Diabetes has a complex pathophysiological mechanism, which involves changes in glucose and lipid metabolism. To verify the previously obtained findings, we pretreated HK-2 cells with different concentrations of high glucose (HG) and palmitic acid (PA) for 48 h to model the metabolic disorder environment observed during diabetes. The cell viability assay showed that as compared to the NC group, cell death significantly increased when glucose concentrations exceeded 50 mM or at a PA concentration of 300 μ M (Figures 4(b) and 4(c)). Next, we assessed, in vitro, whether the tubular injury-ameliorating effects of dapagliflozin were dependent on ferroptosis signaling. The CCK-8 assay showed that dapagliflozin inhibited high glucose- (50 mM) or PA- (300 μ M) induced cell death in HK-2 cells, and this effect was reversed by erastin (2 μ M) (Figure 4(d)). We further evaluated ferroptosis-related markers in these groups. After treatment with 50 mM glucose or 300 μ M PA, iron ion (Figure 4(e)) and glutathione levels (Figure 4(f)), as well as MDA content (Figure 4(g)), increased; however, their levels significantly decreased following dapagliflozin administra-

tion. The expression changes of GPX4 and SLC7A11 levels in vitro were also consistent with the mouse model (Figure 4(h)). Collectively, these findings suggested that dapagliflozin ameliorates ferroptosis in HK-2 cell injury models. The hypoglycemic function of dapagliflozin is primarily by decreasing glucose reabsorption in the proximal tubule via SGLT2 inhibition [22]. In order to explore whether its therapeutic effect of ferroptosis also depends on SGLT2 suppression, we knocked out SGLT2 in HK-2 cells, and this was validated by western blot. There was no significant improvement in GPX4 and SLC7A11 expression when compared to the HG/PA group, indicating that the ferroptosis improvement effect of dapagliflozin was independent of inhibition of SGLT2 (Figure 4(i)).

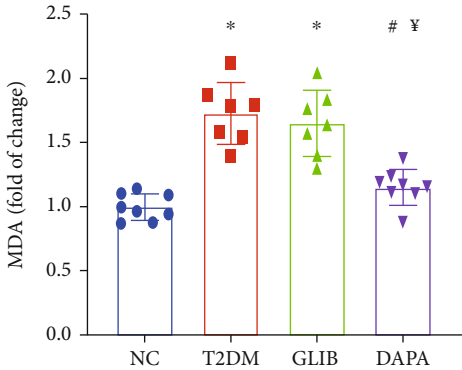
3.5. Dapagliflozin Ameliorates Ferroptosis in HK-2 Cells via SLC40A1. Given the important role played by iron overload in ferroptosis, a disruption in cellular iron homeostasis can contribute to tubular injury [23]. To examine the underlying mechanism governing the aberrant elevation of Fe^{2+} in HK-



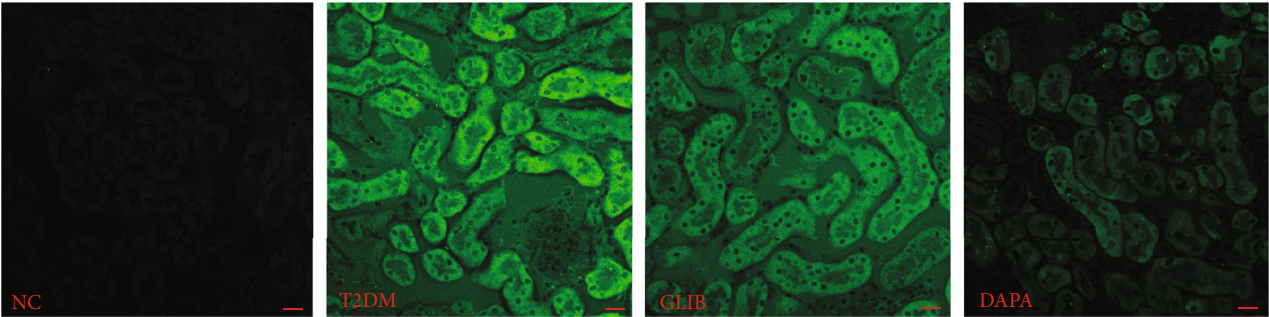
(a)



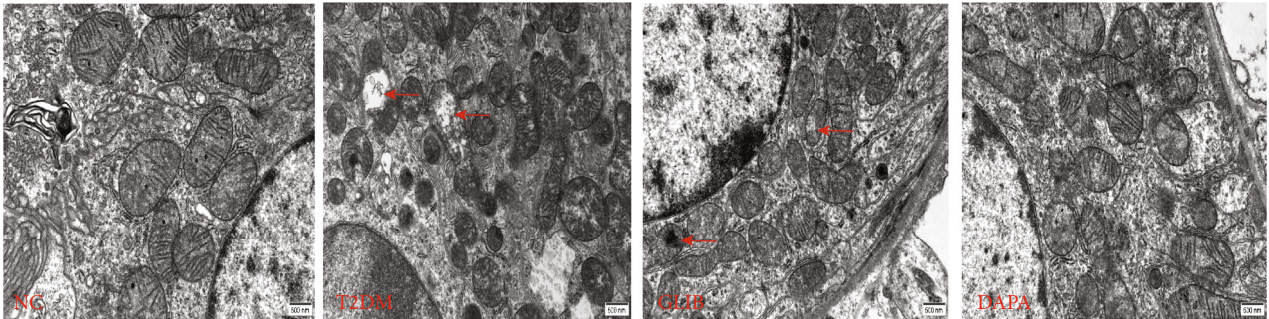
(b)



(c)



(d)



(e)

FIGURE 3: Continued.

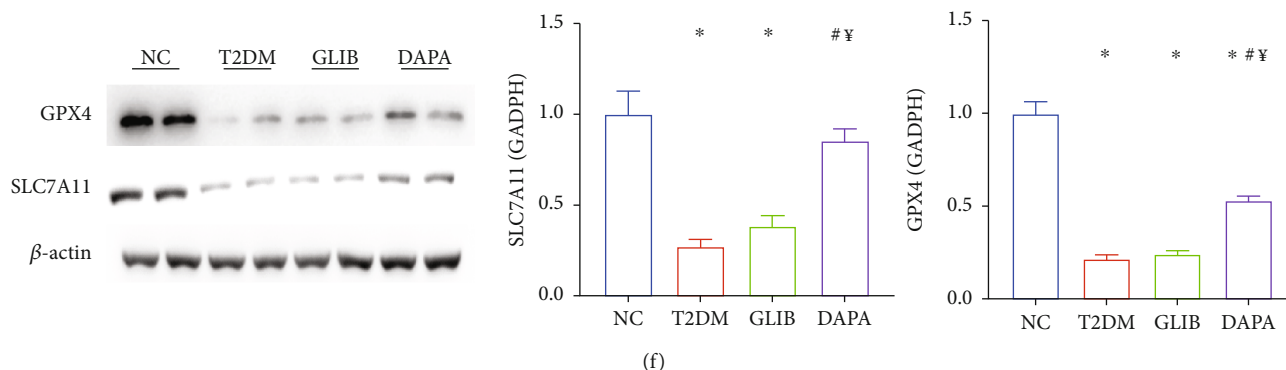


FIGURE 3: Dapagliflozin ameliorated ferroptosis in T2DM mice. (a) GSH, (b) iron, and (c) MDA contents in the kidneys of mice in these groups. (d) The production of ROS (green) in each group. (e) Transmission electron microscopy was used to detect the mitochondrial morphology of renal tubular epithelial cells in each group. The red arrow indicates the damaged mitochondria (ruptured mitochondrial membranes and the disappearance of mitochondrial cristae). (f) Quantification of the average band densities calculated from different western blots and the protein levels of GPX4 and SLC7A11 in the kidney tissue in these groups. Values are the mean \pm SD. $n = 7$ mice in the T2DM group and GLIB group, respectively; $n = 8$ mice in the NC group and DAPA group, respectively. * $P < 0.05$ vs. NC; # $P < 0.05$ vs. T2DM; ¥ $P < 0.05$ vs. GLIB.

2 cells, the Fe^{2+} transport-related proteins were detected firstly. The protein level of SLC40A1, which is responsible for Fe^{2+} export from the cytoplasm to extracellular space, was significantly inhibited by HG or PA exposure, while DAPA administration can recover the expression of SLC40A1. However, the expression of iron metabolism-related proteins [24], including FTH1, TFR1, SLC39A8, and NCOA4, which transport cytoplasm Fe^{2+} into the lysosome for storage or mediate iron import into cells were not affected by HG or PA incubation. That is, HG/PA could inhibit intracellular iron efflux but did not affect iron influx, storage, and metabolism (Figure 5(a)). To determine the role played by SLC40A1 in diabetic tubular ferroptosis, we modified SLC40A1 levels in HK-2 cells by transfecting them with SLA40A1-siRNA, and this was validated by western blot (Figure 5(b)). Following si-SLC40A1 pretreatment, the CCK-8 assay showed that the dapagliflozin inhibited HG- or PA-induced cell death in HK-2 cells, and this effect was reversed by SLC40A1 knockout (Figure 5(c)). Similarly, there was a reversal in the therapeutic effects of dapagliflozin in the HK-2 cell injury models on GPX4 and SLC7A11 expression levels (Figure 5(d)). Those findings indicate that DAPA ameliorates ferroptosis in HK-2 cells dependent on SLC40A1 expression.

3.6. The Potential Mechanism of Dapagliflozin Stabilizes SLC40A1 of the Renal Tubule in Diabetes. The main function of ubiquitination is the control of protein degradation [25]. In our study, we found that HG or PA administration in HK-2 cells significantly increased ubiquitination of SLC40A1 but reduced upon DAPA treatment (Figure 6(a)). Those findings indicate that dapagliflozin ameliorates ferroptosis in HK-2 cells by SLC40A1 stabilization. To explore the interaction between dapagliflozin and SLC40A1, a molecular docking experiment was performed using AutoDock4.2. The structure of human SLC40A1 was obtained from the Protein Data Bank (PDB 6W4S). The binding affinity score for dapagliflozin to SLC40A1 was -4.31 kcal/mol.

Three-dimensional ribbon models for the DAPA-SLC40A1 complex is depicted in Figure 6(b). We found that dapagliflozin has multiple hydroxyl groups and forms eight hydrogen bonds with the Gly55, Ser57, and Leu58 residues in SLC40A1. The donor-acceptor distance was in the 2.0 to 2.4 Å range (Figures 6(c) and 6(d)). Moreover, the dapagliflozin displayed hydrophobic interactions with amino acid residues Asn56, Thr61, and Cys326 of SLC40A1. The above results showed a strong and most favorable binding interaction between protein SLC40A1 and DAPA and may induce conformational changes in SLC40A1, which stabilizes SLC7A11 by reducing its ubiquitination levels.

4. Discussion

Previous studies have shown that dapagliflozin exerts protective effects against DKD development [26]. In this study, we observed the in vivo tubular protective effects of dapagliflozin irrespective of glycemic control. Furthermore, through animal experiments and using tubular injury cell models induced by high glucose and palmitic acid concentrations, it was confirmed that dapagliflozin and SLC40A1 could bind with each other; this may induce conformational changes in SLC40A1, which subsequently causes a reduction in ubiquitination degradation and consequently ameliorates tubular ferroptosis in diabetes (Figure 6(e)). To the best of our knowledge, this is the first study to investigate the ferroptosis inhibitory effect of dapagliflozin against DKD.

DKD, which is a major microvascular diabetic complication, is a public health problem that affects millions of people worldwide. As the disease progresses, significant proteinuria occurs in most patients and it eventually develops into chronic renal failure with uremia [27]. Despite the implementation of strict measures aimed at improving glucose and lipid metabolism and normalizing blood pressure, the risk of developing DKD has remained steady over the years [28]. As opposed to other diabetic complications, the prevalence of DKD has not significantly changed over the last 30

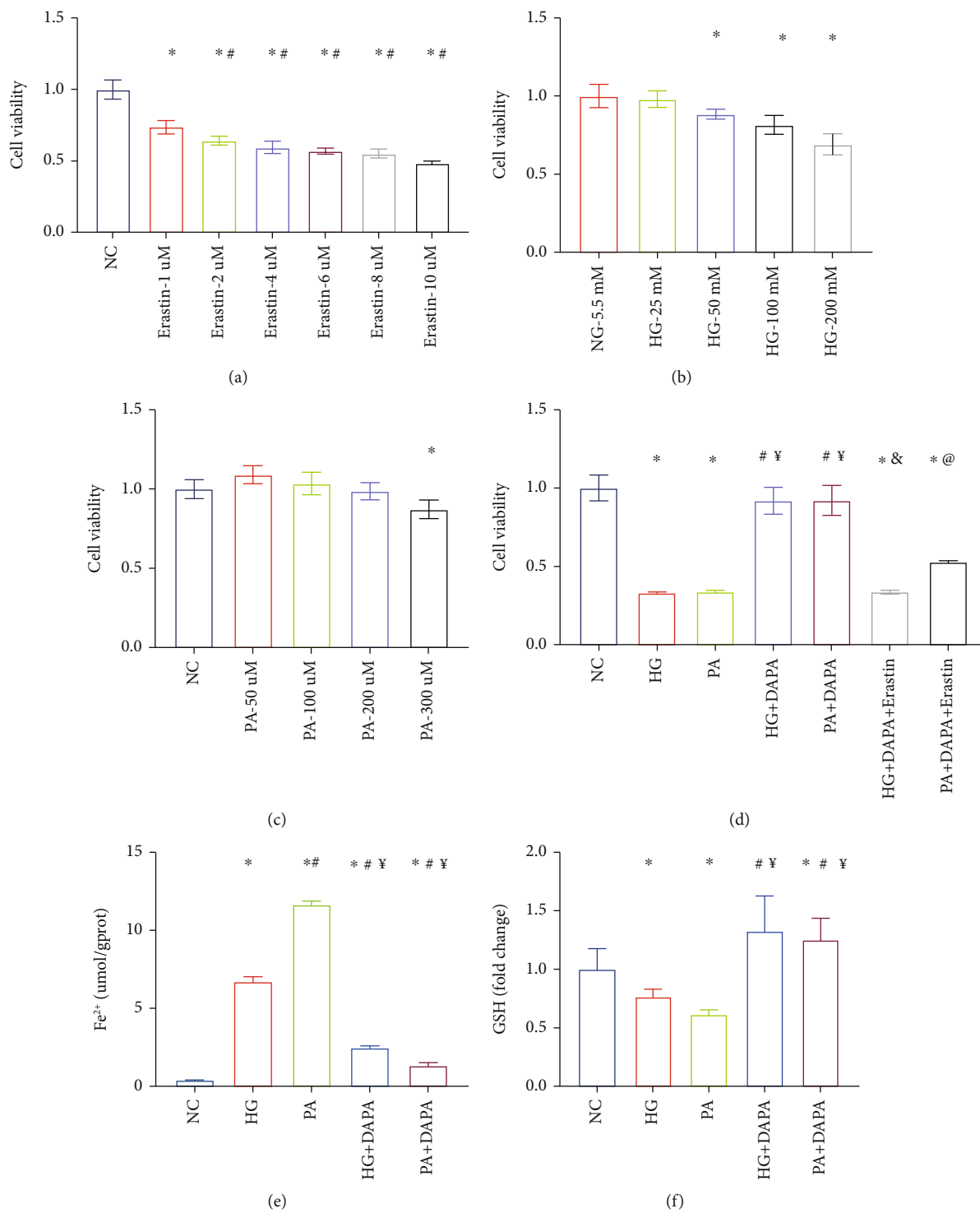


FIGURE 4: Continued.

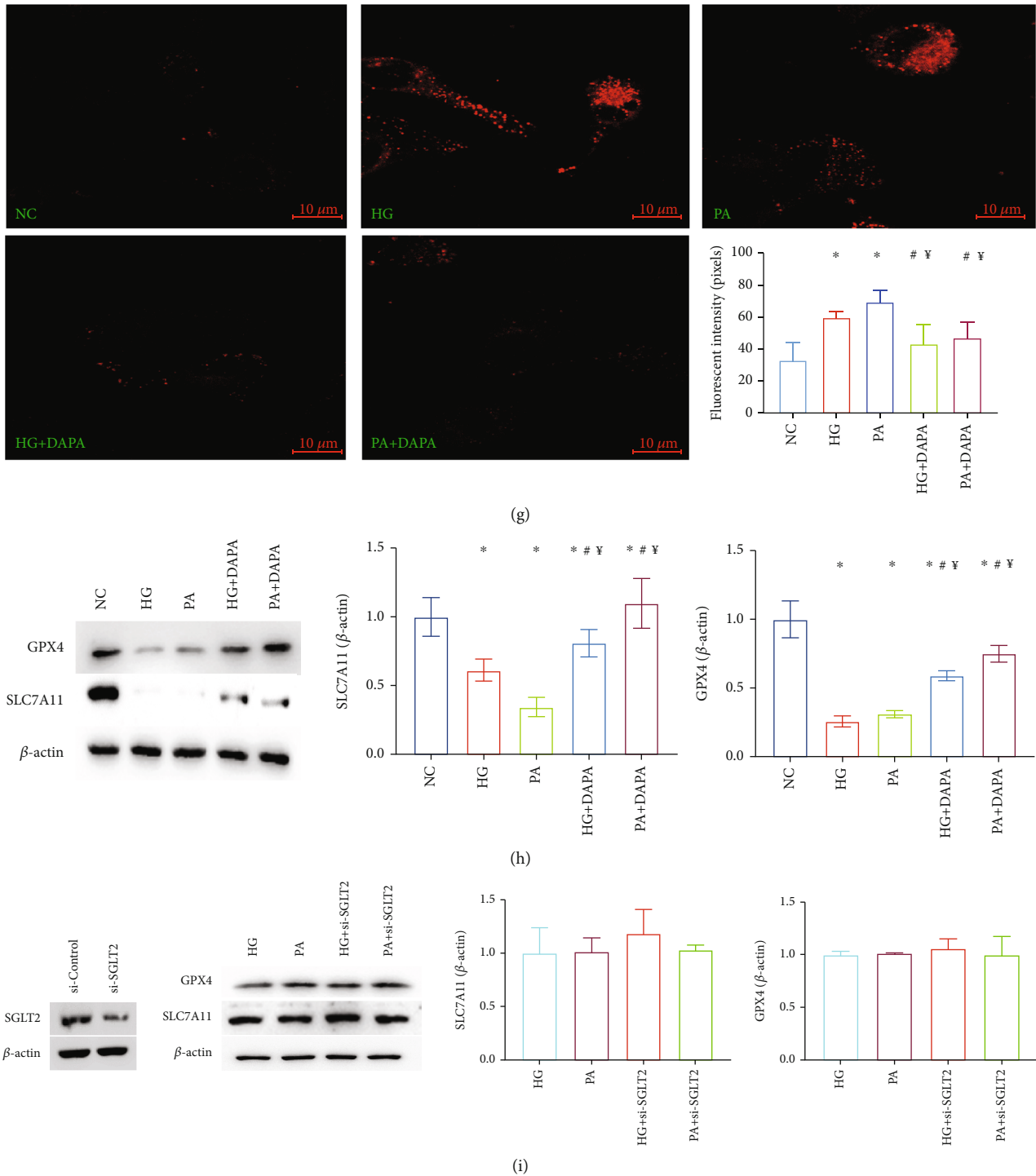


FIGURE 4: Dapagliflozin ameliorates ferroptosis in HK-2 cell injury models in vitro. (a) The cell viability assay revealed a significant dose-dependent increase cell death in erastin-stimulated cells as compared to control cells; CCK-8 assays with different stimulating glucose (b) or PA (c) concentrations in HK-2 cells. (d) Dapagliflozin inhibited HG- or PA-induced cell death in HK-2 cells, and this effect was reversed by erastin; (e) iron ion, (f) GSH, and (g) MDA contents in these groups. (h) Quantification of the average band densities calculated from different western blots and the protein levels of GPX4 and SLC7A11 in HK-2 cells in these groups. (i) SGLT2-siRNA was validated by western blot and the expression of SLC7A11 and GPX4 in those groups. Values are the mean \pm SD. $n = 3$ independent experiments. * $P < 0.05$ vs. NC; # $P < 0.05$ vs. HG or erastin $1 \mu\text{M}$ group; $^{\ddagger}P < 0.05$ vs. PA; $^{\&}P < 0.05$ vs. HG+DAPA; $^{\textcircled{P}}P < 0.05$ vs. PA+DAPA.

years [29]. At present, the renoprotective effects of a new class of antidiabetic agents known as sodium-glucose cotransporter 2 inhibitors have been demonstrated. SGLT2 inhibi-

tors reduce the risk of dialysis, transplantation, and death due to kidney disease in individuals with type 2 diabetes and provide protection against acute kidney injury [30]. A

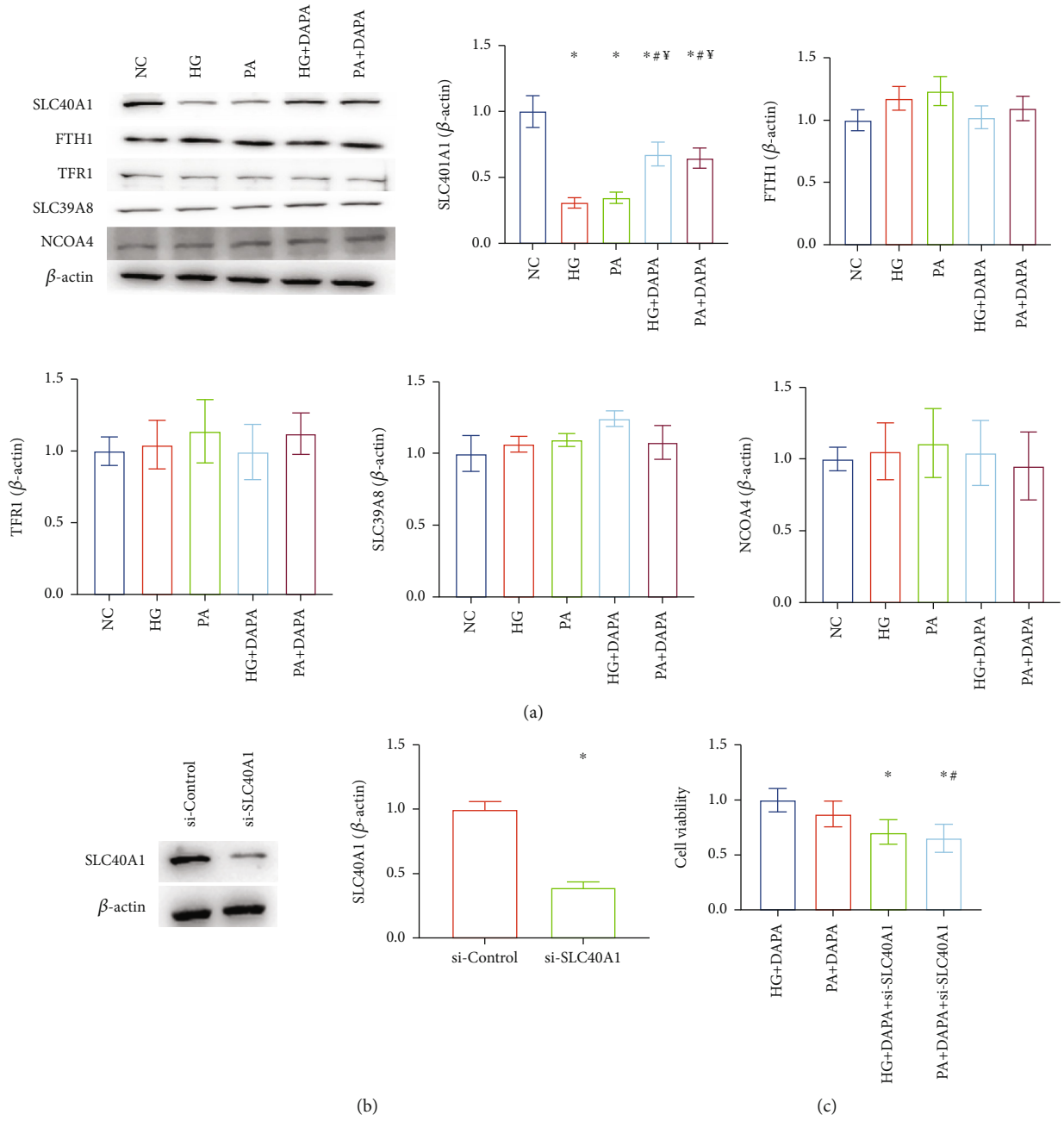


FIGURE 5: Continued.

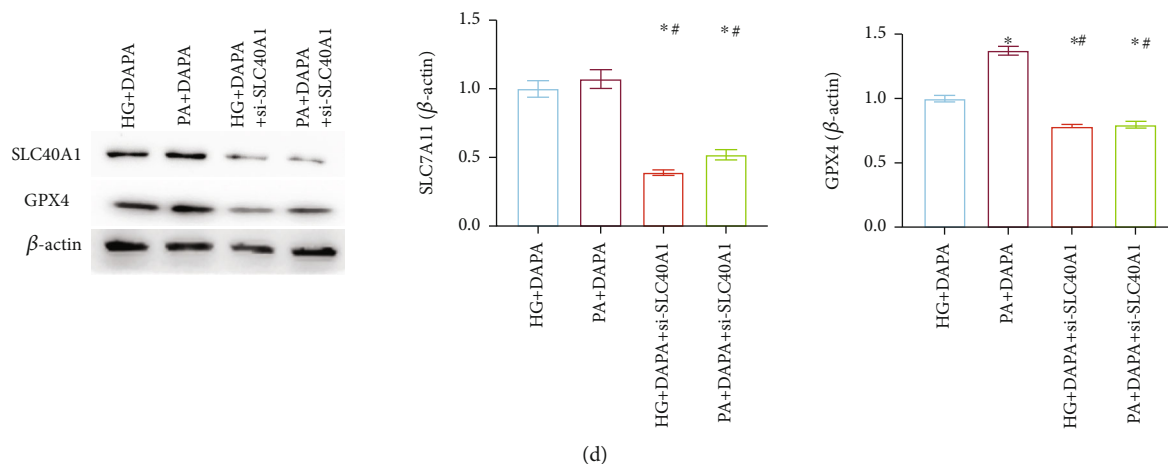


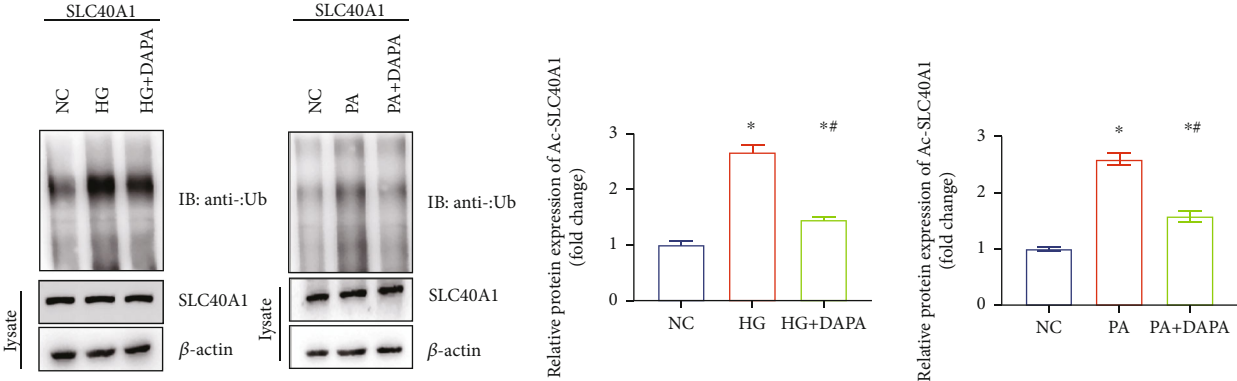
FIGURE 5: Dapagliflozin ameliorates ferroptosis in HK-2 cells via SLC40A1. (a) Fe^{2+} transport-related proteins were detected. (b) SLC40A1-siRNA was validated by western blot. (c) CCK-8 assays with these groups. (d) The expression of GPX4 and SLC7A11 in these groups. Values are the mean \pm SD. $n = 3$ independent experiments. * $P < 0.05$ vs. NC; ** $P < 0.05$ vs. HG; † $P < 0.05$ vs. PA.

systematic review and meta-analysis that included a total of 38 723 participants demonstrated the renoprotective effects of an SGLT2 inhibitor in T2DM patients with eGFRs ranging from 30 to 45 mL/min/1.73 m² [31]. Aside from decreasing blood glucose levels, SGLT2 inhibitors also affect several other pathogenic pathways that underlie DKD [32]. In our experiment, we used a clinically employed antidiabetic drug (glibenclamide) as a hypoglycemic control, which has no protective effect on the kidney beyond its hypoglycemic effect. We observed that as compared to the glibenclamide group, dapagliflozin significantly decreased a series of typical markers of tubular injury, implying that treatment with dapagliflozin may significantly ameliorate tubular damage independently of glycemic control.

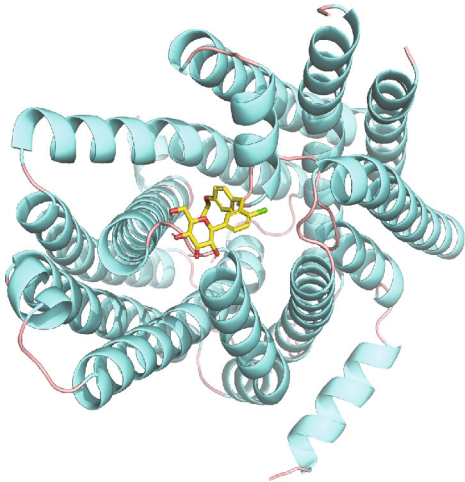
Under diabetic conditions, high glucose concentrations, advanced glycation end products (AGEs), protein oxidation products, urinary proteins, and other endogenous nephrotoxins can induce the activation, transdifferentiation, hypertrophy, and apoptosis of renal tubular epithelial cells (TECs) [33]. Recent studies have shown that TEC injury may be a primary pivotal trigger for DKD development [34]. To perform their reabsorption functions, TECs require large amounts of energy; diabetes induces impaired mitochondrial energy metabolism, which results in significant intrarenal oxidative stress and TEC damage [35]. Decreased antioxidant capacity, iron overload, and lipid peroxidation product accumulation are characteristic indicators of ferroptosis, and these were observed in the DKD models, especially in the diabetic tubular injury models [36]. Li et al. showed that ferroptosis is involved in the development of DKD and that fenofibrate-induced Nrf2 upregulation inhibits diabetes-related ferroptosis, thereby delaying DKD progression [37]. As compared to the control group, SLC7A11 and GPX4 expression was found to be significantly lower in cultured tubular epithelial cells exposed to TGF- β 1, as well as in the kidney tissues of diabetic mice; these changes were alleviated by Fer-1 treatment, indicating that ferroptosis is involved in kidney tubular cell death under diabetic conditions [38]. Feng et al. reported that ferroptosis may promote DKD

and renal tubular damage in diabetic models through the HIF-1 α /HO-1 pathway [39]. A recent study by Quagliariello et al. showed that empagliflozin reduces ferroptosis in doxorubicin-treated mice through the NLRP3 and MyD88-related pathways, thereby significantly improving cardiac function [12]. However, the involvement of the ferroptosis signaling pathway in the tubular injury-ameliorating mechanism of dapagliflozin under diabetic conditions has not been determined. Thus, to determine the involvement of ferroptosis in DKD, the levels of glutathione, iron ions, lipid peroxidation, massive ROS, and ECM and the expression of some ferroptosis markers were further evaluated. Our findings suggested that dapagliflozin ameliorated tubular injury in vivo and in vitro through ferroptosis inhibition. The hypoglycemic function of DAPA is primarily by decreasing glucose reabsorption in the proximal tubule via SGLT2 inhibition. In order to explore whether its therapeutic effect of ferroptosis also depends on SGLT2 suppression, we knocked out SGLT2 in HK-2 cells; surprisingly, the inhibition effect of DAPA on ferroptosis was not simulated when compared to the HG/PA group, indicating that the ferroptosis improvement effect of dapagliflozin was independent of inhibition of SGLT2.

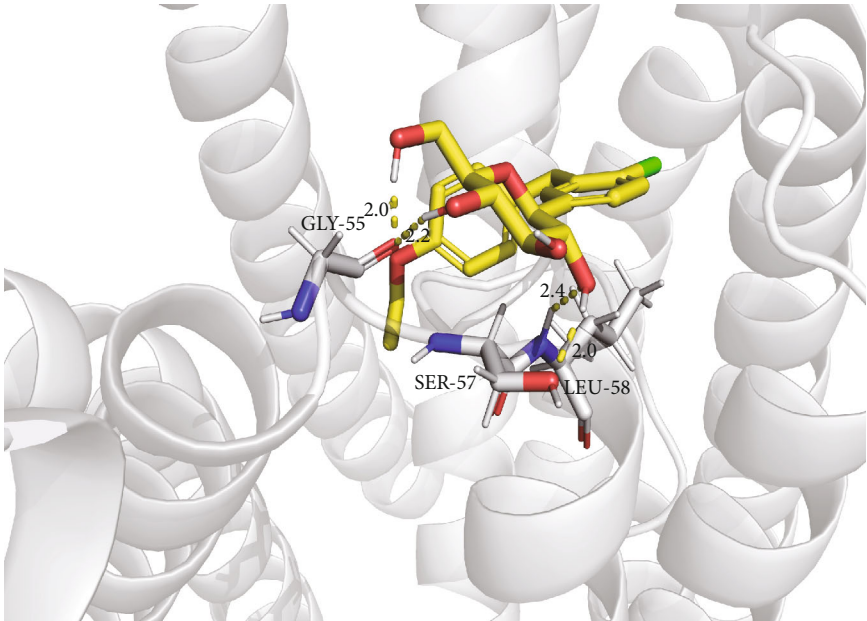
Iron is an essential mineral that is required for various metabolic and physiological functions in living organisms [40]. Iron-dependent cell death, generally known as ferroptosis, is an iron metabolic disorder [41]. Thus, an imbalance in iron homeostasis is associated with several pathological processes [42]. Over the last three decades, iron homeostatic disorders and iron-mediated cell toxicity have been recognized as causes and consequences of kidney injury [43]. Under diabetic conditions, extensive inflammation and/or oxidative stress may occur; these mechanisms among others may cause excessive iron retention in the kidney tubules and consequently cause iron-induced kidney injury [44]. Mitigating iron overload is a primary focus for potential therapeutic interventions for DKD management [45]. SLC40A1 (also known as ferroportin) can export iron into interstitial fluid and the general circulation through the basolateral



(a)



(b)



(c)

FIGURE 6: Continued.

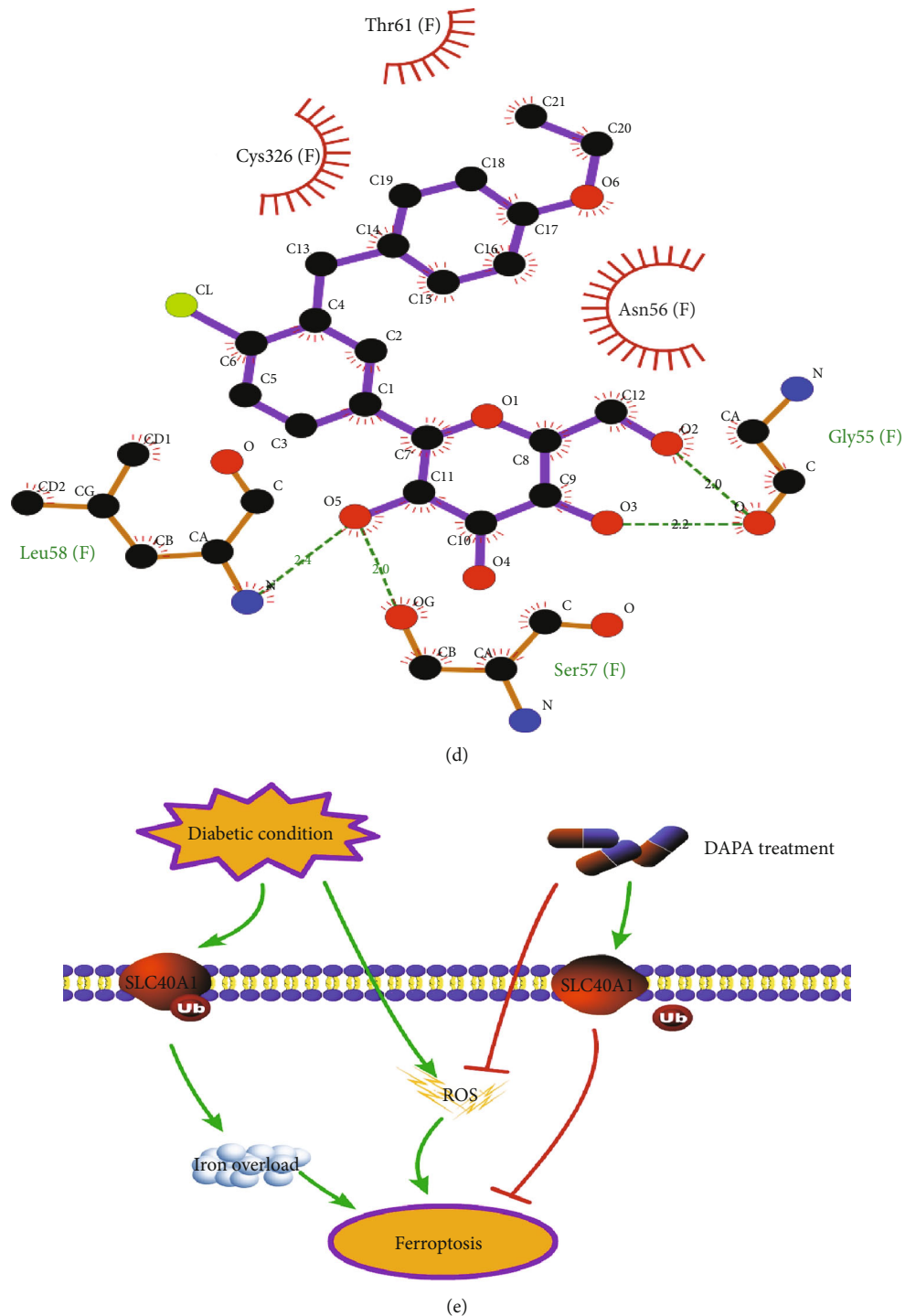


FIGURE 6: The potential mechanism of dapagliflozin stabilizes SLC40A1 of the renal tubule in diabetes. (a) The ubiquitination of SLC40A1, assessed by western blot analysis following immunoprecipitation. (b) Frontal view of the 3D model of the binding of dapagliflozin to the SLC40A1 complex. (c) Stereoview of the binding mode of dapagliflozin in its complex with SLC40A1, in which the H-bonds are depicted as yellow dotted lines. (d) Specific view of the 2D ligand interaction of dapagliflozin with SLC40A1. (e) Schematic representation of the pathways involved in DKD through the dapagliflozin-regulated SLC40A1/ferroptosis pathway.

membrane of renal tubular epithelial cells [46]. SLC40A1 downregulation compromises intracellular iron output, causing iron overload and accelerating cellular ferroptosis [47]. In this study, we observed that the HG- or PA-induced decrease in HK-2 cell SLC40A1 levels was reversed

following dapagliflozin administration. Moreover, after pre-treatment with si-SLC40A1, the in vitro therapeutic effects of dapagliflozin in HK-2 cell injury models were reversed. Those findings indicate that DAPA ameliorates ferroptosis in HK-2 cells dependent on SLC40A1. The main function

of ubiquitination is the control of protein degradation. Many studies have shown that the ubiquitin system is involved in SLC40A1 degradation, resulting in cellular iron overload [48–50]. In this study, we found that HG or PA administration in HK-2 cells significantly increased ubiquitination of SLC40A1 but reduced upon DAPA treatment, which demonstrated that DAPA ameliorates tubular ferroptosis by SLC40A1 stabilization. To explain the potential mechanism of dapagliflozin stabilizing SLC40A1 of the renal tubule in diabetes, a molecular docking experiment was performed. The analyses showed that dapagliflozin and SLC40A1 could bind with each other; this may cause a conformational change in SLC40A1, consequently leading to a decrease in ubiquitination degradation.

Our study has some limitations. First, considering the involvement of multiple organs in iron metabolism and the complexity of the diabetic environment, a lack of tubular-targeted knockout mice constituted a limitation to this study. Second, we verified decreased ubiquitination SLC40A1 levels following treatment with dapagliflozin but did not explore the specific mechanism underlying this regulatory process. Hence, further investigations are needed to improve our understanding of how conformational changes occur in SLC40A1 and which ubiquitin enzymes are involved in the mechanism of action of dapagliflozin.

5. Conclusions

This study concludes that the ferroptosis pathway was involved in the tubule protective effect of dapagliflozin in diabetes, and the decrease in ubiquitination degradation of SLC40A1 after binding with dapagliflozin may be the mechanism underlying its action. To the best of our knowledge, this is the first study to investigate the ferroptosis inhibitory effects of dapagliflozin in the treatment of DKD.

Data Availability

The datasets analyzed during the current study are available from the corresponding author.

Ethical Approval

The study protocol was approved by the ethics committee of the First Affiliated Hospital of USTC, Division of Life Science and Medicine, University of Science and Technology of China.

Conflicts of Interest

The authors declare that they have no competing interests.

Authors' Contributions

Huang Bin and Wen Wenjie performed the data acquisition and the analysis job and drafted the work. Ye Shandong substantively revised it. All authors read and approved the final manuscript. Bin Huang and Wenjie Wen contributed equally to this work.

Acknowledgments

This study was supported by the National Natural Science Foundation of China (81800713) and the Local Scientific and Technological Development Project Guided by the Central Government of China (no. 2017070802D147).

Supplementary Materials

The sequences of the primers used for real-time PCR are listed in Supplement Table S1. (*Supplementary Materials*)

References

- [1] W. Hua, Z. Shu, and G. Jia, "Lipotoxic proximal tubular injury: a primary event in diabetic kidney disease," *Frontiers in Medicine*, vol. 8, p. 751529, 2021.
- [2] S. Da, W. Jiaojiao, S. Wansong et al., "Pathogenesis and damage targets of hypertensive kidney injury," *Journal of Translational Internal Medicine*, vol. 8, no. 4, pp. 205–209, 2020.
- [3] L. Yuliya, B. Petter, J. A. Lovshin et al., "Renal hemodynamic function and RAAS activation over the natural history of type 1 diabetes," *American Journal of Kidney Diseases*, vol. 73, no. 6, pp. 786–796, 2019.
- [4] H. Bin, W. Wenjie, and Y. Shandong, "Correlation between serum 25-hydroxyvitamin D levels in albuminuria progression of diabetic kidney disease and underlying mechanisms by bioinformatics analysis," *Frontiers in Endocrinology*, vol. 13, no. - undefined, p. 880930, 2022.
- [5] A. M. F. Martines, R. Masereeuw, H. Tjalsma, J. G. Hoenderop, J. F. M. Wetzels, and D. W. Swinkels, "Iron metabolism in the pathogenesis of iron-induced kidney injury," *Nature Reviews. Nephrology*, vol. 9, no. 7, pp. 385–398, 2013.
- [6] H. Keiko, H. Tanisorn, and C. Susama, "Ferroptosis: a potential therapeutic target in acute kidney injury," *International Journal of Molecular Sciences*, vol. 23, no. 12, 2022.
- [7] L. Long-Xia, G. Fang-Fang, L. Hong, and Z. Tao, "Iron overload in alcoholic liver disease: underlying mechanisms, detrimental effects, and potential therapeutic targets," *Cellular and Molecular Life Sciences*, vol. 79, no. 4, p. 201, 2022.
- [8] R. P. L. van Swelm, F. M. Wetzels Jack, and D. W. Swinkels, "The multifaceted role of iron in renal health and disease," *Nature Reviews. Nephrology*, vol. 16, no. 2, pp. 77–98, 2020.
- [9] L. Hao, J. Mi, L. Song et al., "SLC40A1 mediates ferroptosis and cognitive dysfunction in type 1 diabetes," *Neuroscience*, vol. 463, pp. 216–226, 2021.
- [10] H. Ya-Chun, T. Shi-Qi, L. Yu-Ting et al., "AMPK agonist alleviate renal tubulointerstitial fibrosis via activating mitophagy in high fat and streptozotocin induced diabetic mice," *Cell Death & Disease*, vol. 12, no. 10, p. 925, 2021.
- [11] Y. Mori, A. K. Ajay, J. H. Chang et al., "KIM-1 mediates fatty acid uptake by renal tubular cells to promote progressive diabetic kidney disease," *Cell metabolism*, vol. 33, no. 5, pp. 1042–1061, 2021.
- [12] Y. Wang, M. Zhang, R. Bi et al., "ACSL4 deficiency confers protection against ferroptosis-mediated acute kidney injury," *Redox biology*, vol. 51, p. 102262, 2022.
- [13] C. Zhu, Z. Song, Z. Chen et al., "MicroRNA-4735-3p Facilitates Ferroptosis in Clear Cell Renal Cell Carcinoma by Targeting SLC40A1," *Analytical Cellular Pathology*, C. Amantini, Ed., vol. 2022, 12 pages, 2022.

- [14] V. Volker and S. C. Thomson, "Targeting renal glucose reabsorption to treat hyperglycaemia: the pleiotropic effects of SGLT2 inhibition," *Diabetologia*, vol. 60, no. 2, pp. 215–225, 2017.
- [15] R. Sreenithya and M. Shankar, "Renoprotective mechanisms of sodium-glucose co-transporter 2 (SGLT2) inhibitors against the progression of diabetic kidney disease," *Journal of Cellular Physiology*, vol. 237, pp. 1182–1205, 2022.
- [16] Z. Yutong, L. Fang, M. E. Cooper, and C. Zhonglin, "Advances in clinical research in chronic kidney disease," *Journal of Translational Internal Medicine*, vol. 9, no. 3, pp. 146–149, 2021.
- [17] M. R. Cowie and F. Miles, "SGLT2 inhibitors: mechanisms of cardiovascular benefit beyond glycaemic control," *Nature Reviews. Cardiology*, vol. 17, no. 12, pp. 761–772, 2020.
- [18] Q. Vincenzo, D. L. Michelino, R. Domenica et al., "The SGLT-2 inhibitor empagliflozin improves myocardial strain, reduces cardiac fibrosis and pro-inflammatory cytokines in non-diabetic mice treated with doxorubicin," *Cardiovascular Diabetology*, vol. 20, no. 1, p. 150, 2021.
- [19] B. Feng, R. Meng, B. Huang, Y. Bi, S. Shen, and D. Zhu, "Silymarin protects against renal injury through normalization of lipid metabolism and mitochondrial biogenesis in high fat-fed mice," *Free Radical Biology and Medicine*, vol. 110, pp. 240–249, 2017.
- [20] F. T. Hammad and L. Loay, "The effect of thymoquinone on the renal functions following ischemia-reperfusion injury in the rat," *International Journal of Physiology, Pathophysiology and Pharmacology*, vol. 8, no. 4, pp. 152–159, 2016.
- [21] M. Eikan and C. Marcus, "Nutritional and metabolic control of ferroptosis," *Annual Review of Nutrition*, vol. 42, no. 1, 2022.
- [22] C. Ting, K. Qingqing, F. Yi et al., "Sodium-glucose cotransporter 2 inhibition suppresses HIF-1 α -mediated metabolic switch from lipid oxidation to glycolysis in kidney tubule cells of diabetic mice," *Cell Death & Disease*, vol. 11, no. 5, p. 390, 2020.
- [23] H. F. Deng, L. X. Yue, N. N. Wang et al., "Mitochondrial iron overload-mediated inhibition of Nrf2-HO-1/GPX4 assisted ALI-induced nephrotoxicity," *Frontiers in Pharmacology*, vol. 11, p. 624529, 2021.
- [24] B. Bartłomiej and M. Jolanta, "Iron, ferroptosis, and new insights for prevention in acute kidney injury," *Advances in Medical Sciences*, vol. 65, no. 2, pp. 361–370, 2020.
- [25] X. Chen, L. Jiang, Z. Zhou et al., "The Role of Membrane-Associated E3 Ubiquitin Ligases in Cancer," *Frontiers in Pharmacology*, vol. 13, p. 928794, 2022.
- [26] J. Niels, G. Tom, G. M. Chertow et al., "Effect of dapagliflozin on urinary albumin excretion in patients with chronic kidney disease with and without type 2 diabetes: a prespecified analysis from the DAPA-CKD trial," *The Lancet Diabetes and Endocrinology*, vol. 9, no. 11, pp. 755–766, 2021.
- [27] H. J. Anders, T. B. Huber, B. Isermann, and M. Schiffer, "CKD in diabetes: diabetic kidney disease versus nondiabetic kidney disease," *Nature Reviews. Nephrology*, vol. 14, no. 6, pp. 361–377, 2018.
- [28] H. J. Sun, S. P. Xiong, X. Cao et al., "Polysulfide-mediated sulfhydration of SIRT1 prevents diabetic nephropathy by suppressing phosphorylation and acetylation of p65 NF- κ B and STAT3," *Redox biology*, vol. 38, p. 101813, 2021.
- [29] F. Annelie, M. Annika, P. Isolde et al., "Reducing VEGF-B signaling ameliorates renal lipotoxicity and protects against diabetic kidney disease," *Cell Metabolism*, vol. 25, no. 3, pp. 713–726, 2017.
- [30] A. DeFronzo Ralph, R. W. Brian, and A. S. Awad, "Pathophysiology of diabetic kidney disease: impact of SGLT2 inhibitors," *Nature Reviews. Nephrology*, vol. 17, no. 5, pp. 319–334, 2021.
- [31] B. L. Neuen, Y. Tamara, J. L. Heerspink Hiddo et al., "SGLT2 inhibitors for the prevention of kidney failure in patients with type 2 diabetes: a systematic review and meta-analysis," *The Lancet Diabetes and Endocrinology*, vol. 7, no. 11, pp. 845–854, 2019.
- [32] P. Usha and P. Carol, "Organ protection beyond glycaemic control with SGLT2 inhibitors," *Nature Reviews. Nephrology*, vol. 17, no. 4, pp. 223–224, 2021.
- [33] L. I. Xiao, X. Xu, F. Zhang et al., "The mitochondria-targeted antioxidant MitoQ ameliorated tubular injury mediated by mitophagy in diabetic kidney disease via Nrf2/PINK1," *Redox biology*, vol. 11, pp. 297–311, 2017.
- [34] J. Wen-Juan, X. Chuan-Ting, D. Chang-Lin et al., "Tubular epithelial cell-to-macrophage communication forms a negative feedback loop via extracellular vesicle transfer to promote renal inflammation and apoptosis in diabetic nephropathy," *Theranostics*, vol. 12, no. 1, pp. 324–339, 2022.
- [35] H. Yanjuan, W. Qian, H. Baosheng, C. Yiliang, Q. Xi, and W. Lihua, "CD36 promotes NLRP3 inflammasome activation via the mtROS pathway in renal tubular epithelial cells of diabetic kidneys," *Cell Death & Disease*, vol. 12, no. 6, p. 523, 2021.
- [36] Y. Wang, R. Bi, F. Quan et al., "Ferroptosis involves in renal tubular cell death in diabetic nephropathy," *European journal of pharmacology*, vol. 888, p. 173574, 2020.
- [37] S. Li, L. Zheng, J. Zhang, X. Liu, and Z. Wu, "Inhibition of ferroptosis by up-regulating Nrf2 delayed the progression of diabetic nephropathy," *Free Radical Biology & Medicine*, vol. 162, pp. 435–449, 2021.
- [38] K. Seonghun, K. Shin-Wook, J. Jeongho et al., "Characterization of ferroptosis in kidney tubular cell death under diabetic conditions," *Cell Death & Disease*, vol. 12, no. 2, p. 160, 2021.
- [39] X. Feng, S. Wang, Z. Sun et al., "Ferroptosis enhanced diabetic renal tubular injury via HIF-1 α /HO-1 pathway in db/db mice," *Frontiers in endocrinology*, vol. 12, p. 626390, 2021.
- [40] G. Tomas, "Hepcidin and iron regulation, 10 years later," *Blood*, vol. 117, no. 17, pp. 4425–4433, 2011.
- [41] J. Xuejun, B. R. Stockwell, and C. Marcus, "Ferroptosis: mechanisms, biology and role in disease," *Nature Reviews. Molecular Cell Biology*, vol. 22, no. 4, pp. 266–282, 2021.
- [42] M. Jung, J. C. Drapier, H. Weidenbach et al., "Effects of hepatocellular iron imbalance on nitric oxide and reactive oxygen intermediates production in a model of sepsis," *Journal of Hepatology*, vol. 33, no. 3, pp. 387–394, 2000.
- [43] R. Agoro and K. E. White, "Anemia and fibroblast growth factor 23 elevation in chronic kidney disease: homeostatic interactions and emerging therapeutics," *Current Opinion in Nephrology & Hypertension*, vol. 31, no. 4, pp. 320–325, 2022.
- [44] K. A. Nath, "Heme oxygenase-1: a provenance for cytoprotective pathways in the kidney and other tissues," *Kidney International*, vol. 70, no. 3, pp. 432–443, 2006.
- [45] S. Sundararaman, V. A. Fonseca, M. G. Alam, and S. V. Shah, "The role of iron in diabetes and its complications," *Diabetes Care*, vol. 30, no. 7, pp. 1926–1933, 2007.
- [46] W. Ewa, M. Borna, M. Laurence, and S. Yogesh, "Iron metabolism: an under investigated driver of renal pathology in lupus nephritis," *Frontiers in Medicine*, vol. 8, p. 643686, 2021.

- [47] R. Dissanayake, N. Samarasinghe, S. Waidyanatha et al., "Assessment of iron overload in a cohort of sri lankan patients with transfusion dependent beta thalassaemia and its correlation with pathogenic variants in hbb, hfe, slc40a1, and tfr2 genes," *BMC Pediatrics*, vol. 2, no. 1, p. 344, 2022.
- [48] A. Sharraya, Q. Bo, S. Deborah et al., "Structure-function analysis of ferroportin defines the binding site and an alternative mechanism of action of hepcidin," *Blood*, vol. 131, no. 8, pp. 899–910, 2018.
- [49] P. Sagar, S. Angmo, R. Sandhir, V. Rishi, H. Yadav, and N. K. Singhal, "Effect of hepcidin antagonists on anemia during inflammatory disorders," *Pharmacology & Therapeutics*, vol. 226, p. 107877, 2021.
- [50] T. Lisa, S. B. Wiegand, A. J. Sauer et al., "UBA6 and NDFIP1 regulate the degradation of ferroportin," *Haematologica*, vol. 107, no. 2, pp. 478–488, 2022.

Review Article

From Iron Metabolism to Ferroptosis: Pathologic Changes in Coronary Heart Disease

Xinbiao Fan ^{1,2}, Aolin Li ¹, Zhipeng Yan ¹, Xiaofei Geng ¹, Lu Lian ¹, Hao Lv ¹,
Dongjie Gao ¹ and Junping Zhang ¹

¹First Teaching Hospital of Tianjin University of Traditional Chinese Medicine, Tianjin 300183, China

²National Clinical Research Center for Chinese Medicine Acupuncture and Moxibustion, Tianjin 300193, China

Correspondence should be addressed to Junping Zhang; tjzhtcm@163.com

Received 26 June 2022; Accepted 25 July 2022; Published 10 August 2022

Academic Editor: Lianxiang Luo

Copyright © 2022 Xinbiao Fan et al. This is an open access article distributed under the Creative Commons Attribution License, which permits unrestricted use, distribution, and reproduction in any medium, provided the original work is properly cited.

Coronary heart disease (CHD) is closely related to oxidative stress and inflammatory response and is the most common cardiovascular disease (CVD). Iron is an essential mineral that participates in many physiological and biochemical reactions in the human body. Meanwhile, on the negative side, iron has an active redox capacity, which leads to the accumulation of reactive oxygen species (ROS) and lipid peroxidation. There is growing evidence that disordered iron metabolism is involved in CHD's pathological progression. And the result of disordered iron metabolism is associated with iron overload-induced programmed cell death, often called ferroptosis. That features iron-dependent lipid peroxidation. Ferroptosis may play a crucial role in the development of CHD, and targeting ferroptosis may be a promising option for treating CHD. Here, we review the mechanisms of iron metabolism in cardiomyocytes (CMs) and explain the correlation between iron metabolism and ferroptosis. Meanwhile, we highlight the specific roles of iron metabolism and ferroptosis in the main pathological progression of CHD.

1. Introduction

Coronary atherosclerotic heart disease, also known as CHD, refers to localized myocardial ischemia, hypoxia, and even necrosis due to atherosclerosis (AS) [1]. As the population ages and people's lifestyles change, the morbidity and mortality of CHD are also increasing yearly. CHD is not only the most common CVD but also one of the leading causes of death worldwide [2]. And AS is the pathological basis of CHD, which involves inflammation, lipid deposition, plaque formation, and calcification. In addition, pathological changes such as vascular endothelial damage, arterial wall plaque stability damage, CM death, myocardial fibrosis (MF), and myocardial hypertrophy (MH) are also involved in the progress of CHD [3, 4].

Iron is an essential metal for the body and is the primary raw material for manufacturing hemoglobin and myoglobin. In addition, iron is critical for cellular viability and partici-

pates in a wide range of biochemical and physiological processes, including oxygen storage and transportation, mitochondrial respiration, DNA synthesis and repair, and enzymatic reactions in cells. However, excessive iron has toxic effects on the body. Iron has an active redox capacity, making it easy for free iron to receive and contribute electrons. The most important mechanism of iron biotoxicity is the involvement of excess intracellular ferrous iron (Fe^{2+}) in the Fenton or Haber-Weiss reaction [5]. The interaction of Fe^{2+} with oxygen or hydrogen peroxide catalyzes the production of large amounts of ROS, leading to lipid peroxidation and further severe organ damage [6]. At the same time, Fe^{2+} is oxidized to ferric iron (Fe^{3+}). Iron is also associated with the pathological mechanisms of various diseases such as hemochromatosis, cancer, and CVD [7, 8].

Recent studies have shown that dysregulation of iron metabolism is associated with CHD [9, 10]. Severe iron overload is involved in vascular injury and CM death, promoting

the development of AS, myocardial infarction (MI), and heart failure (HF) [11]. And these results are related to iron overload-induced programmed cell death, or ferroptosis, a new form of programmed cell death discovered in recent years. Ferroptosis is featured by iron-dependent lipid peroxidation, unlike autophagy, apoptosis, and pyroptosis [12]. Some studies have directly or indirectly proved that ferroptosis exists in ischemic heart disease and plays an essential role in the process of CM death [13–15]. However, the effect of ferroptosis on CHD remains unclear. Here, we review the mechanisms of iron metabolism and regulation in CMs and explain the correlation between iron metabolism and ferroptosis. Moreover, we focus on the specific role of ferroptosis in the pathological progression of CHD.

2. Iron Homeostasis in CMs

Iron-mediated injury plays an essential role in many CVD, and studies on iron metabolism in the heart have attracted many scientists (Figure 1).

2.1. Iron Import in CMs. Systemic iron can form transferrin-bound iron (TBI) in the blood by binding to the transferrin (Tf), but binding sites in Tf have a limited high affinity for Fe^{3+} . Studies have shown that the Tf saturation level is about 30% [16]. When high plasma iron concentration exceeds Tf iron binding capacity, iron mainly binds to serum albumin and citric acid to produce non-transferrin-bound iron (NTBI). TBI and NTBI both have access to CMs, but the pathways and regulatory mechanisms are different. CMs accumulate TBI through Tf receptors (TfRs), whereas accumulation of NTBI is via the divalent metal transporter 1 (DMT1), calcium channels, and zinc transporters.

2.1.1. TBI-Dependent Pathways. Under physiological conditions, iron mainly combines with Tf and enters CMs through TfR1 on the cell membrane [17, 18]. Fe^{3+} is released in endosomes and then reduced to Fe^{2+} by the six-transmembrane epithelial antigen of prostate 3 (STEAP3). Subsequently, Fe^{2+} is transferred to the cytoplasm by DMT1. TfR1 gene has a conserved stem-loop structure in the 3' untranslated region (UTR) called the iron response element (IRE). Iron regulatory protein (IRP) is the main protein that controls the balance of iron metabolism in CMs. IRP1 and IRP2, two forms of IRPs, have been found to act by binding to IRE [19]. The binding of IRP1 and IRP2 to IRE protected TfR1 mRNA from intranuclear degradation when CMs were iron deficient. That ensures the stability of TfR1 mRNA, increases its expression, and promotes iron absorption. Downregulation of TfR1 expression and a significant decrease in iron concentration occurred in mice with IRP gene knockout in CMs [20]. When iron overload occurs in CMs, IRP1 is converted to functional cytoplasmic aconitase via iron-sulfur clusters (Fe-S). At the same time, IRP1 loses its IRE-binding activity and the degradation of IRP2 increases. DMT mRNA with IRE in its 3' UTRs has also been identified. IRE binding to IRP inhibits DMT mRNA degrada-

tion and facilitates iron uptake, which is consistent with the regulation of TfR1 [21].

2.1.2. NTBI-Dependent Pathways. When iron overload occurs, plasma NTBI levels are elevated. There is a consensus that NTBI is potentially toxic and can cause tissue damage by increasing oxidative stress and inducing tissue iron overload. NTBI cannot enter cells through TfR1 but DMT1, L-type calcium channel (LTCC), T-type calcium channel (TTCC), zinc transporters, and other non-transferrin receptor-dependent pathways [22]. Studies have shown that LTCC and TTCC are the main pathways for NTBI to enter CMs. Efonidipine is a dual TTCC and LTCC blocker. In thalassemic mice, efonidipine reduced cardiac iron accumulation and improved cardiac function. However, it did not affect the expression of cardiac ferroportin (FPN) [23]. In addition, ZRT/IRT-like protein 14 (ZIP14) and DMT1 may be involved in the uptake of NTBI in CMs [20]. A vivo study found that ZIP14 is consistently expressed in iron overloaded hearts but is not upregulated in response to increased iron deposition. It is speculated that ZIP14 is involved in the uptake of NTBI by CMs, but there may be other pathways involved in the uptake of NTBI [24]. And the control of NTBI import by DMT1 is regulated by the IRP/IRE system. It should be noted that the entry of NTBI into CMs through calcium channels and zinc transporters is not affected by IRP/IRE, but the specific regulatory mechanism remains unclear.

2.2. Iron Export from CMs. Once iron enters CMs, it becomes part of the labile iron pool (LIP). Iron enters the mitochondria as a feedstock for heme and Fe-S. In addition, ferritin (FT) stores some of the iron, and FPN exports the excess iron. Iron can enter CMs through multiple pathways, but only FPN is the export pathway, suggesting that CMs are particularly sensitive to iron overload. One study specifically knocked out FPN in the hearts of mice and found that their cardiac function was severely impaired, which was associated with cardiac iron overload [9]. However, there was no significant change in systemic iron status, suggesting that CMs have their unique regulation mechanism of iron metabolism. Notably, IREs are also present in the 5' UTR of FPN mRNA and FT mRNA. The combination of IRE and IRP inhibits the translation of FPN and FT and prevents intracellular iron export and storage. Another more critical mechanism of iron export regulation is the role of the hepcidin (HEP)-FPN axis in the heart. The HEP-FPN axis in the heart is not affected by systemic HEP. Myocardial iron deficiency or hypoxia promotes local HEP expression and limits iron export by degrading FPN [10, 25]. A study prepared mouse models of HEP-resistant FPN knockout and cardiomyocyte-specific deletion of HEP. Both models showed severe cardiac dysfunction and iron deficiency in CMs rather than systemic iron deficiency [26]. A recent study found that knock-in HEP-resistant FPN in mouse pulmonary arterial smooth muscle cells (SMCs) leads to pulmonary hypertension and HF, suggesting that the HEP-FPN axis also plays a crucial role in regulating vascular homeostasis [26].

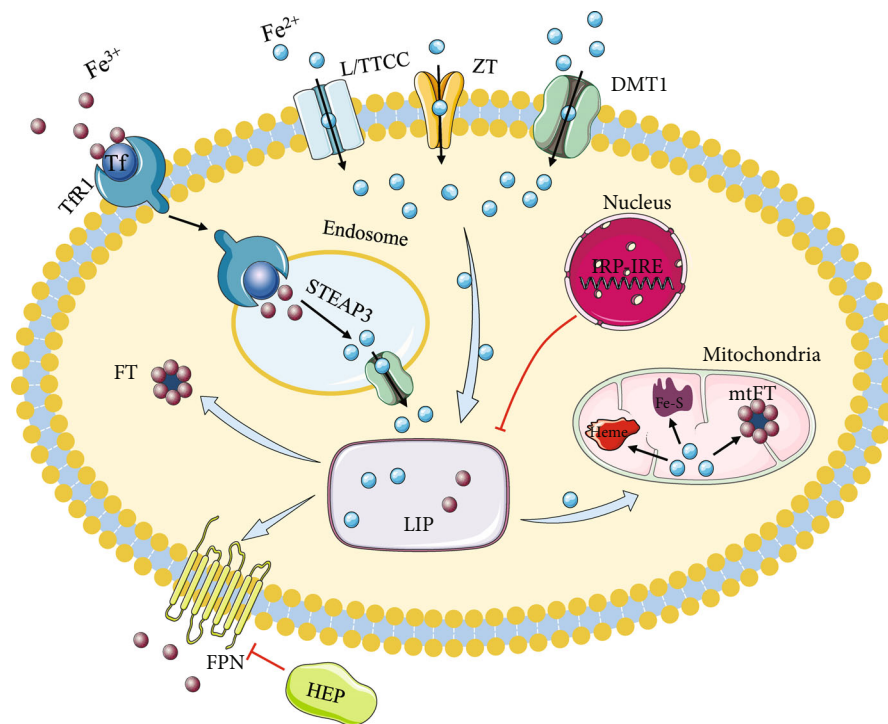


FIGURE 1: Iron homeostasis in cardiomyocytes. TBI enters cardiomyocytes via TfR1. TBI is reduced to Fe^{2+} by STEAP3 after release in the endosome, and Fe^{2+} is transferred to the cytoplasm by DMT1. NTBI enters via DMT1, LTCC, TTCC, and ZT. After entering the CMs, iron becomes part of the LIP and works through different pathways. A portion of iron is used by mitochondria to produce heme and Fe-S, and a portion is stored in FT. Furthermore, another part of iron is exported through the FPN and regulated by HEP. And cardiac iron homeostasis is regulated by IRP-IRE. TBI: Tf-bound iron; NTBI: non-Tf-bound iron; TfR1: transferrin receptor 1; STEAP3: six-transmembrane epithelial antigen of prostate 3; DMT1: divalent metal transporter 1; LTCC: L-type calcium channel; TTCC: T-type calcium channel; ZT: zinc transporters; LIP: labile iron pool; FT: ferritin; FPN: ferroportin; Fe-S: iron-sulfur cluster; mtFT: mitochondrial ferritin; HEP: hepcidin; IRP: iron regulatory protein; IRE: iron-responsive elements.

3. Effect of Iron Accumulation on Cardiac Ischemic and Hypoxic Injuries

During the development of CHD, we can observe abnormalities in multiple cell death signaling cascades. These include apoptosis, autophagy, pyroptosis, and ferroptosis (Table 1). Disordered iron metabolism runs through the whole pathological progression of CHD, and iron overload is considered an essential pathological factor of cardiovascular injury [9]. The data suggested that nearly 1/3 of the iron in CMs is distributed in mitochondria, catalyzing electron transport through the reversible oxidation state of iron and providing the energy required for normal cardiac function. Mitochondrial function is associated with disordered iron metabolism in the development of CVD [27]. When myocardial ischemia and hypoxia occur, LIP is imbalanced. Iron overload leads to the peroxidation of oxygen radicals in the cytoplasm and mitochondria. And it then will damage DNA, proteins, and lipids, resulting in cardiotoxicity [27]. In addition, AS was shown to be exacerbated significantly in FPN knockout mice, suggesting that iron overload has a promotive effect on AS. This effect is associated with iron overload-induced pathological changes, including dyslipidemia, altered vascular permeability, sustained endothelial activation, and elevated proinflammatory mediators. However, iron clearance

mediated by transferrin or iron chelators and a low-iron diet may rescue NTBI-mediated toxicity [28].

Iron metabolism and oxidative stress in CMs are closely related to autophagy. Autophagy is a process of cellular self-feeding that relies primarily on lysosomes for intracellular degradation and recycling, promoting cellular repair or accelerating cell death. Thus, autophagy plays a dual role in maintaining cellular homeostasis and promoting cell renewal and metabolism [29]. Autophagy is activated by various environmental stressors, such as energy depletion, nutrient deficiency, and endoplasmic reticulum stress [30]. Appropriate autophagy can protect CMs by reducing oxidative stress and weakening myocardial inflammation, but excessive autophagy can lead to CM death and thus aggravate cardiac functional impairment. In the early stage of myocardial ischemia and hypoxia, appropriate autophagy facilitates the removal of mitochondria from damaged tissues, reduces the production of ROS, and maintains CM homeostasis to protect the heart from ischemic injury. However, in the late phase of myocardial ischemia and hypoxia, disordered iron metabolism induces CM autophagy to release iron stored in FT [31]. In addition, ferritinophagy is mediated by NCOA4 and exacerbates myocardial injury by increasing cellular unstable iron levels through degradation of cellular FT and induction of TfR1 expression, which

TABLE 1: Comparison of different forms of programmed cell death.

Cell death mode	Morphological characteristics	Biochemical features	Characteristic molecules	References
Apoptosis	Chromatin condensation, nuclear fixation, cell shrinkage, membrane blistering, and formation of apoptotic bodies	DNA fragmentation, no leakage of cell contents, no inflammatory reaction	Caspase 3, caspase 7, caspase 8, BCL-2, Bax, P53, Fas	[34, 35]
Autophagy	Accumulation of double-membraned autophagic vesicles	Increased lysosomal activity	Beclin 1, mTOR, ATG5, ATG7, LC3, TFE3, DRAM-3	[35]
Pyroptosis	Nuclear consolidation, plasma membrane pore formation, cell swelling and rupture	DNA fragmentation and inflammatory cascade response	NLRP3, ASC, pro-caspase 1, IL-1 β , IL-18	[4, 36]
Ferroptosis	Mitochondrial shrinkage, increased membrane density, decreased mitochondrial cristae, and outer membrane rupture	Iron overload, lipid peroxidation, mitochondrial membrane potential changes	ACSL4, LPCAT3, xCT, GPX4, Fer-1, OxPLs, TfR1, SLC7A11, Nrf2, NCOA4	[37, 38]

subsequently sensitizes cells to ferroptosis [32]. Erastin is a classical ferroptosis inducer that acts on multiple molecular structures to induce ferroptosis. According to published reports, NCOA4 can prevent erastin-induced ferroptosis [33]. Therefore, timely regulation of autophagy by maintaining iron homeostasis during myocardial ischemia and hypoxia can reduce autophagy-induced myocardial injury.

4. Effect of Iron and ROS on Ferroptosis in the Heart

Ferroptosis is a newly discovered form of regulated cell death driven by iron-dependent lipid peroxidation. A growing number of studies have demonstrated that lipid peroxidation is a key trigger and landmark event in ferroptosis [39]. And high levels of intracellular NTBI are a prerequisite for triggering ferroptosis [40]. Extensive ROS generated by intracellular iron via the Fenton reaction and the Haber-Weiss reaction can directly produce a chain reaction with polyunsaturated fatty acids (PUFAs) in membrane phospholipids [38]. Further analysis has shown that AA and AdA are essential phospholipids to facilitate the peroxidation reaction [41]. PUFAs are highly sensitive to lipid peroxidation due to their unstable double bonds. With the help of ACSL4 and LPCAT3, PUFAs in cell membranes undergo synthesis, activation, and incorporation into phospholipids to produce PUFA-phosphatidyl ethanolamine (PUFA-PE) [42]. That makes the cell membrane easier to be attacked by ROS and produces more lipid peroxides. Also closely associated with ferroptosis is lipoxygenase (LOX). It can catalyze the peroxidation reaction of PUFA-PE [42]. Harmful lipid peroxides are scavenged by the intracellular antioxidant system when they accumulate. However, when the antioxidant system is weakened, lipid peroxides will not be scavenged in time, leading to an attack on the cytoplasmic membrane and morphological changes associated with ferroptosis [43]. Notably, ferroptosis inhibitors has been proven to inhibit the occurrence of ferroptosis [15, 44]. Research has shown that MI can lead to high levels of ROS production in the myocardium and that ferrostatin-1 (Fer-1) can significantly reduce the area of MI [45].

5. Regulatory Pathways of Ferroptosis

Under physiological conditions, the antioxidant response in the body is in a relative balance. When this balance is disrupted, it causes the accumulation of free radicals and triggers ferroptosis [46]. The System Xc- glutathione (GSH)-glutathione peroxidase 4 (GPX4) axis is the central redox mechanism inhibiting ferroptosis [47]. GSH is an essential antioxidant in the oxidative stress response, and cystine is one of the basic raw materials for GSH synthesis. GPX4 is an antioxidant enzyme that scavenges lipid peroxides and prevents the conversion of iron-dependent conversion of lipid peroxides to more reactive lipid radicals [48]. The reduction of toxic lipid peroxides to nontoxic lipid alcohols by GPX4 depends on the electrons provided by GSH [43]. System Xc- is a cystine/glutamate antiporter composed of SLC7A11 and SLC3A2, which mediates the exchange of extracellular cystine with intracellular glutamate and is responsible for the transport of cystine into the cell [49]. When selectively inhibiting System Xc-, cystine uptake will be reduced, and GSH synthesis in the organism will also be reduced [50]. Notably, erastin causes GSH depletion and GPX4 inactivation by inhibiting System Xc-, inducing ferroptosis [51]. The expression of SLC7A11 and GPX4 was significantly decreased in H/R-induced H9C2 cells. In addition, the naringin ameliorated cardiomyocyte ferroptosis via the System Xc-/GPX4 axis. However, the protective effect could be counteracted by erastin [52]. The data confirmed that the System Xc-GSH-GPX4 axis plays an essential role in the process of myocardial injury.

In addition to the System Xc-GSH-GPX4 axis, several pathways of ferroptosis regulation have been identified (Figure 2). Among them, the GCH1-BH4 pathway and the FSP1-CoQ-NADPH pathway are the other two independent mechanisms unaffected by GPX4 [47]. BH4 is a potent antioxidant. The expression of GCH1 triggers the production of BH4, thus exerting an antioxidant effect to inhibit ferroptosis [53, 54]. CoQ10 is another strong oxidant, and its fully reduced state, CoQH2, can trap lipid peroxide radicals and prevent peroxidative damage to the plasma membrane. FSP1 is a novel oxygen reductase that inhibits ferroptosis. It can catalyze CoQ10 regeneration dependent

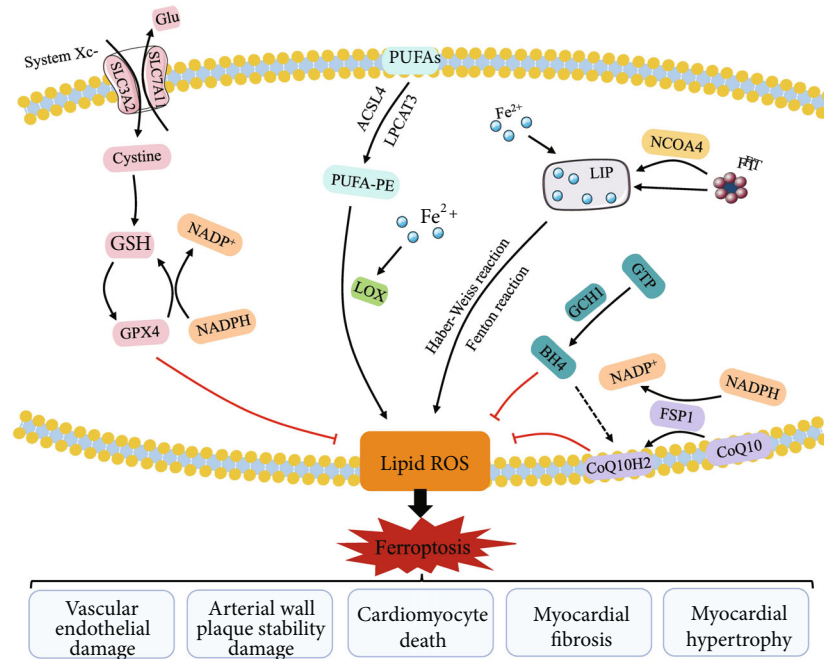


FIGURE 2: The regulatory mechanisms of ferroptosis in the pathological progression of CHD. There are three major independent regulatory pathways of ferroptosis: the System Xc-GSH-GPX4 axis, the GCH1-BH4 pathway, and the FSP1-CoQ-NADPH pathway. In addition, iron metabolism and lipid peroxidation are the main mechanisms. Abbreviations: PUFAs: polyunsaturated fatty acids; PUFA-PE: polyunsaturated fatty acid-phosphatidyl ethanolamine; ACSL4: acyl-CoA synthetase long-chain family member 4; LPCAT3: lysophosphatidylcholine acyltransferase 3; LOX: lipoxygenase; SLC7A11: subunit solute carrier family 7 member 11; SLC3A2: solute carrier family 3 member 2; Glu: glutamate; GSH: glutathione; GPX4: glutathione peroxidase 4; GTP: guanosine triphosphate; BH4: tetrahydrobiopterin; GCH1: guanosine triphosphate cyclohydrolase 1; FSP1: ferroptosis suppressor protein 1; NCOA4: nuclear receptor coactivator 4; NADPH: nicotinamide adenine dinucleotide phosphate; ROS: reactive oxygen species; FT: ferritin; LIP: labile iron pool; CoQ10: coenzyme Q10.

on NADPH and inhibit GPX4 deficiency-induced ferroptosis [55, 56].

6. Ferroptosis Involvement in the Pathological Progression of CHD

The primary pathological mechanism of CHD lies in the formation, growth, and even rupture of atherosclerotic plaques, resulting in luminal narrowing or blockage. Reduced myocardial perfusion induces MI and eventually leads to the progression of HF [3]. Several studies have shown that iron metabolism and ferroptosis are involved throughout the development of CHD and influence the key pathological changes of CHD. These include vascular endothelial damage, arterial wall plaque stability damage, CM death, MF, and MH [11, 37] (Table 2).

6.1. Vascular Endothelial Damage. Vascular endothelial cells (VECs) are border cells between blood and the vascular wall. They have highly selective permeability and are biological barriers to the interchange of material and protection of the inner surface of blood vessels [74]. Normal VECs have the effects of regulating vascular tone, procoagulation, anti-thrombosis, and anti-inflammatory, which are critical for maintaining vascular homeostasis [75]. VEC dysfunction and morphological damage are the beginning of AS and participate in the occurrence and development of CHD. In the

early stages of AS, risk factors lead to increased adhesion molecule expression and dysregulation of antioxidant effects [76, 77]. All these alterations lead to the adhesion of leukocytes (especially monocytes) to VECs. Monocytes adhering to the vascular intima gradually migrate to the intima and differentiate into macrophages in response to inflammatory factors and the expression of receptors that facilitate lipid uptake [78]. As a result, lipid components of the blood, especially low-density lipoprotein (LDL), are absorbed and gradually deposited in the intima. LDL is oxidatively modified to oxidize LDL (ox-LDL) in the subintima. The oxidative process and toxic effects of ox-LDL can lead to or aggravate vascular endothelial damage and dysfunction, thereby significantly promoting lipid deposition [79]. Subsequently, scavenger receptors on the surface of macrophages can rapidly recognize ox-LDL and phagocytose it to form foam cells. Foam cells and lipids accumulate massively under the intima, producing an early lesion of AS known as fatty streaks [80, 81].

Although the pathological mechanism of AS is complex, current studies emphasize that oxidative stress is a key factor in the occurrence and development of AS. ROS generated during oxidative stress can oxidize lipids and proteins, induce inflammatory responses, and directly damage vascular cells, leading to endothelial dysfunction [82, 83]. Iron is considered potentially toxic because of its intense oxidative activity. When iron is overloaded, the body can produce

TABLE 2: Ferroptosis involvement in the pathological progression of CHD.

Histological type	Interventions	Features or changes	Pathways or signals	References
Vascular endothelial damage	Knock out FPN genes	Increase NTBI, induce chronic iron overload, increase vascular oxidative stress levels, promote AS		[28]
	High sugar and high lipid diet	Iron overload, elevated ROS level, downregulation of GPX4 and lipid peroxidation	HMOX1 increase	[57]
	PDSS2	Inhibit VEC ferroptosis and AS progression	Nrf2 activation	[58]
	miR-17-92 overexpression	Reduce erastin-induced growth inhibition and ROS generation of HUVEC	A20-ACSL4 axis	[59]
	Fluvastatin	Reverse ox-LDL-induced decreases in GPX4 and xCT levels	Regulate GPX4 and xCT	[60]
	PM2.5	Increase ROS production and iron content, decrease GSH, GSH-Px, and NADPH levels, promote lipid peroxidation		[40]
Arterial wall plaque stability damage	High-iron diet	Iron overload, accelerate inflammation and the formation of macrophage-derived foam cells		[61]
	Macrophage-specific FPN1 deficiency	Iron overload, increase oxidative stress and systemic inflammation levels, inhibit ABC transporter protein expression, increase numbers of macrophages, decrease collagen	Downregulate LXR α expression	[62]
	High levels of uric acid	Induce the formation of macrophage-derived foam cells and lipid peroxidation	Nrf2/SLC7A11/GPX4 signaling pathway	[63]
	Cigarette smoke extract	Increase PTGS2 expression, GSH depletion, and lipid peroxidation, SMC ferroptosis		[64]
CM death	Models of HF after MI	Downregulate FTH levels, increase oxidative stress and free iron levels, decrease CM viability		[14]
	Erastin, isoprenaline	Increase free iron levels, promote lipid peroxidation, and decrease CM viability		[65]
	Fer-1, puerarin	Inhibit ferroptosis, reduce the loss of CMs	Upregulate the expression of GPX4 and FTH1	[65]
	MI models	Downregulate the levels of GPX4 protein and GPX4 mRNA expression, increase CM death	Reduce GPX4 level	[66]
	HUCB-MSC exosomes	Inhibit H/R-induced CM ferroptosis, attenuate myocardial injury	miR-23a-3p/DMT1 axis	[13]
	Dexmedetomidine	Inhibit ROS production, maintain the structural integrity of mitochondria, inhibit ferroptosis, attenuate myocardial I/R injury	SLC7A11/GPX4 axis	[67]
	Propofol	Reduce SOD and iron accumulation, decrease lipid peroxidation levels, and increase the expression of antioxidant enzymes	AKT/P53 signaling pathway	[68]
	HF models	Downregulate GPX4 and FTH1 protein levels	TLR4-NOX4 pathway	[69]
MF	Inject iron dextran	Increase MDA levels, decrease glutathione peroxidase levels, leading to the occurrence of MF		[70]
	miR-375-3p	Promote MF due to CM ferroptosis	Downregulate GPX4	[71]
	Dexmedetomidine	Inhibit CM ferroptosis after myocardial I/R, reduce the area of MF	SLC7A11/GPX4 signaling pathway	[67]
MH	Apelin-13	Increase iron and ROS levels in mitochondria of CM, induce mitochondrial damage	Induce the expression of SFXN1 and NCOA4	[72]
	Knock out xCT	Increase PTGS2, MDA, and ROS levels, exacerbate Ang II-induced MH	Downregulate xCT	[50]
	Beclin 1 haploinsufficient	Elevate levels of SLC7A11, GPX4, and NCOA4, promote autophagy and ferroptosis, and exacerbate low ambient temperature-induced MH		[73]

large amounts of oxygen free radicals that injure VECs and other target cells [6, 84]. FPN is the only pathway of iron export in cells. If FPN is lost, intracellular and systemic iron overload will occur [9]. In one study, deletion of apoE and FPN genes in mice led to increased NTBI and induced chronic iron overload, subsequently increasing vascular oxidative stress levels and promoting AS [28]. These results may result from iron overload-induced endothelial activation and dysfunction. In contrast, restricting dietary iron intake or treating with iron chelators inhibited the progression of AS in mice [28].

The imbalance of redox reactions and iron overload as the main characteristics of ferroptosis provide indirect evidence to explore the role of ferroptosis in vascular endothelial damage in AS [85]. Direct evidence suggested that VEC ferroptosis was observed in diabetic AS mouse models [57]. The mice showed iron overload, downregulation of GPX4, and lipid peroxidation following upregulation of HMOX1. In addition, the study also found that Fer-1 alleviated the increase in ROS and endothelial dysfunction induced by a high-fat-high-sugar diet [57]. Ox-LDL is commonly used to prepare animal models of AS, and multiple studies have found that AS induced by ox-LDL is associated with ferroptosis [60, 63]. The prenyldiphosphate synthase subunit 2 (PDSS2) is a primary regulator of AS [86]. In ox-LDL-induced human coronary AS models, PDSS2 inhibited VEC ferroptosis and AS progression by promoting Nrf2 activation, thereby inducing the proliferation of human coronary endothelial cells [58]. Research has shown that miR-17-92 protected VECs from erastin-induced ferroptosis by targeting the A20-ACSL4 axis [59]. As a classical lipid-lowering drug, fluvastatin reversed the reduction of GPX4 and xCT levels induced by ox-LDL, thus achieving inhibition of VEC ferroptosis and vascular protection [60]. The discovery provides scientific evidence for the new role of statins in the prevention and treatment of AS. In terms of environment and health, studies have shown that PM2.5 accelerates the progression of CVD in numerous ways [87]. A recent study showed that PM2.5-induced vascular endothelial damage is also associated with ferroptosis [40]. The data showed that PM2.5 increases ROS production and iron content in VECs. In addition, the study provided the primary evidence for ferroptosis induced by iron uptake and storage dysfunction (disordered iron metabolism) by monitoring transferrin receptor, ferritin light chain (FTL), and ferritin heavy chain (FTH1) expression. This study further found that PM2.5 decreased the levels of GSH, glutathione peroxidase (GSH-Px), and NADPH. It was concluded here that PM2.5 induces VEC ferroptosis [40]. Although the mechanism of vascular endothelial damage is still unclear, the role of ferroptosis in triggering endothelial dysfunction has been widely proved. And Fer-1 and iron chelators can reverse the toxicity to a certain extent. Therefore, exploring the relationship between ferroptosis and endothelial damage is relevant to the mechanism research and prevention of CHD.

6.2. Arterial Wall Plaque Stability Damage. With the development of coronary AS, macrophages constantly phagocytose

lipids and transform them into foam cells. At the same time, macrophages secrete inflammatory cytokines, which aggravate the local inflammatory response and further promote macrophage death [88]. That will further accelerate the formation of plaques and destabilize them. Under the stimulation of inflammation, SMCs in the middle membrane of the coronary artery migrate to the intima. Subsequently, they fuse with SMCs in the intima, proliferate, and secrete extracellular matrices (ECMs), such as elastin and interstitial collagen. SMCs and ECMs are the main components of the fibrous cap. They cover the foam cells and lipids accumulated under the intima. Then, the lipid core of the plaque gradually forms [89]. Under the stimulation of long-term hypoxia and inflammation, foam cells in the lipid core die in various ways and release lipids and cell debris. Significant amounts of cell components accumulate in the central area of plaques, forming a lipid-rich pool called the necrotic core [90]. As the pathological basis of coronary atherosclerotic plaque formation, necrotic core and fibrous cap are closely related to the unstable progress of the plaque. Angina pectoris occurs when the coronary arteries gradually narrow with plaque growth and block the blood supply to the heart muscle. When acute thrombosis obstructs large coronary vessels, blood flow is rapidly interrupted, leading to MI and unstable angina [91]. The foremost common cause of thrombosis is the rupture of vulnerable plaques. It has been established that the characteristics of vulnerable plaques include massive monocyte/macrophage infiltration, bulky lipid-rich necrotic cores, thin fibrous caps, and fewer SMCs [92]. Macrophages under the fibrous cap can reduce ECMs by their phagocytic function. The macrophages also can secrete plenty of matrix metalloproteinases to hydrolyze ECMs within the fibrous cap. As a result, the fibrous cap becomes thin and brittle, causing the plaque to become unstable and rupture to form a thrombus [80, 93]. In contrast, SMCs can secrete ECMs, which are the main ingredient of the fibrous cap, thus improving plaque stability [89]. Therefore, understanding further the role of macrophages and SMCs in plaque stability may provide new ideas for treating CHD.

Recent studies have shown that increased free iron can promote pathological processes such as oxidative stress and lipid peroxidation, accelerating inflammation and the formation of macrophage-derived foam cells, thus affecting plaque stability [61]. There are two primary sources of reactive iron in atherosclerotic plaques. One is plaque rupture and bleeding, and the other is the phagocytosis and rapid lysis of red blood cells by macrophages [94]. Considering the significant role of macrophages in systemic iron metabolism and the formation and progression of atherosclerotic plaques, Apoe^{-/-} mouse models of macrophage-specific FPN1 deficiency were prepared in a study to investigate the effects and mechanisms of iron overload in macrophages on the progression of CHD [62]. The results indicated that iron overload in macrophages inhibited ATP-binding cassette (ABC) transporter protein expression by downregulating the liver X receptor α (LXR α) expression. This progression increased oxidative stress and systemic inflammation levels, promoted foam cell formation, and restricted lipid efflux,

ultimately contributing to AS progression. In addition, iron overload also causes several changes in the composition of atherosclerotic plaques, with an increase in the number of macrophages and a decrease in collagen within the plaques, which make the plaques more prone to rupture [62]. However, iron chelation therapy increased ABC transporter protein expression, reversed lipid deposition, and reduced the surface volume of atherosclerotic plaques, ultimately slowing the progression of AS [62]. In another study, high levels of uric acid inhibited the Nrf2/PTGS2/GPX4 signaling pathway, induced the formation of macrophage-derived foam cells, and lipid peroxidation, thereby promoting the progression of AS. However, all these changes were reversed by Fer-1 [63]. There are no systematic studies to explore the mechanism between macrophage ferroptosis and CHD. Even so, several studies have shown that ROS accumulation, lipid oxidation, and iron deposition in macrophages are critical features of advanced atherosclerotic plaques [95]. Thus, macrophage ferroptosis may play an essential role in coronary AS and vulnerable plaque formation. And regulation of macrophage ferroptosis may be a promising approach to enhance plaque stability and delay the progression of CHD.

Unlike macrophages, SMCs impair the stability of atherosclerotic plaques mainly by affecting fibrous cap components [89]. A study found that iron overload stimulated SMCs to migrate, proliferate abnormally, and calcify, causing them to acquire a macrophage-like phenotype. In addition, iron overload increased ROS production to create a prooxidant microenvironment, which promoted foam cell formation and plaque instability progression. Moreover, researches demonstrated that removing excess iron and reducing the production of ROS can reverse these results mentioned above [96–98]. Notably, cigarettes are a major risk factor for AS. A study found that cigarette smoke extract (CSE) induced ferroptosis in vascular SMCs but not VECs [64]. The data showed increased PTGS2 expression, GSH depletion, and lipid peroxidation in vascular SMCs. However, GPX4 overexpression had no significant effect on CSE-induced ferroptosis [64]. The triggering mechanisms of ferroptosis in SMCs and VECs may be different. Therefore, inhibiting ferroptosis in SMCs may also be a new research direction for plaque stabilization.

6.3. Cardiomyocyte Death. The main pathological change of CHD is the formation and development of atherosclerotic plaques. The plaques gradually increase in size or even fall off, narrowing or blocking the lumen of the arterial blood vessels, resulting in insufficient blood supply to the coronary arteries. And the lack of perfusion causes local damage and mass death of CMs [99]. CMs are terminally differentiated cells with extremely limited regenerative capacity [100]. The mass death of CMs will result in structural and functional defects in the heart and cause HF [101]. The best way to prevent ischemic damage to the heart is to restore blood flow to the myocardial tissue, also known as reperfusion. However, reperfusion itself can also cause damage to the myocardium, called myocardial ischemia/reperfusion (I/R) injury. The mechanisms involved are oxidative stress, calcium overload, and mitochondrial damage, all of which

can cause CM death [102]. Therefore, how to prevent CM death is key to improving and restoring cardiac function after MI and myocardial I/R injury. New insights into how cells are programmed to die have provided new ideas for salvaging myocardial injury in recent years. A study showed increased iron deposition and ROS in CMs around the MI region during ischemia and early reperfusion, suggesting that ferroptosis is a prominent form of CM death [103].

In HF mouse and rat models after MI, FTH levels were significantly downregulated, and oxidative stress and free iron levels were significantly increased. And then, desferrioxamine, an iron chelator, reversed these results and improved the viability of CMs [14]. Iron overload as a crucial mechanism for ferroptosis occurrence has attracted scientists to explore the underlying mechanisms of ferroptosis involvement in CM death. Either erastin or isoproterenol-treated H9C2 cells significantly increased free iron levels and promoted lipid peroxidation, thereby decreasing the viability of CMs. This result suggested that ferroptosis is associated with CM death. Both Fer-1 and puerarin upregulated the expression of GPX4 and FTH1 and inhibited ferroptosis [65]. In another study, the levels of GPX4 protein and GPX4 mRNA expression were downregulated in mice during early and midstage MI. To further determine the role of GPX4 in CM ferroptosis, a study transfected H9C2 cells with GPX4 siRNA. The results showed a significant increase in malondialdehyde (MDA) and superoxide dismutase (SOD) levels. And Fer-1 reduced CM death induced by GPX4 downregulation and inhibited lipid peroxide production, which suggested that ferroptosis is involved in CM death and myocardial injury after MI and is partially associated with reduced GPX4 levels [66]. In addition, studies have demonstrated that NADPH oxidase (NOX), a key enzyme for ROS production, is highly expressed in CMs [104]. In the descending aortic banding procedure-induced HF models, ferroptosis and autophagy were associated with massive CM death, and they were regulated by the TLR4-NOX4 pathway. It mainly showed downregulation of TLR4 and NOX4 expression, decreased LC3B-II and Belcin1, and upregulation of p62, GPX4, and FTH1 protein expression. It also significantly reduced CM death and improved cardiac function [69]. Drugs targeting the associated pathways of autophagy and ferroptosis in CMs may also be new therapeutic strategies for CHD, but others in both need to be studied in depth. Currently, CM ferroptosis during MI and HF has not been well studied. Are these mechanisms still applicable to clinical practice? Is blocking the process of ferroptosis in CMs effective? Addressing these questions may lead to new treatments to protect CMs from ferroptosis and delay the progression of MI to HF.

The exosome of MSCs derived from HUCB-MSC is known to alleviate myocardial injury caused by MI in mice. In the CM H/R models, investigators found that overexpression of DMT1 promoted CM ferroptosis. However, HUCB-MSC exosomes could inhibit H/R-induced CM ferroptosis through the miR-23a-3p/DMT1 axis and attenuate myocardial injury [13]. In addition, dexmedetomidine was demonstrated to inhibit myocardial I/R-induced ferroptosis via the SLC7A11/GPX4 axis [67]. Iron overload and ferroptosis

have also been found in myocardial I/R. In one study, propofol inhibited ferroptosis via the AKT/P53 signaling pathway, thereby protecting CM from I/R injury. Specifically, it reduced SOD and iron accumulation, decreased lipid peroxidation levels, thereby increasing the expression of antioxidant enzymes [68]. Ferroptosis as one of the mechanisms of CM death after myocardial I/R has been widely demonstrated, and inhibiting ferroptosis may be an effective way to attenuate myocardial I/R injury.

6.4. Myocardial Fibrosis. MF after MI is a process of self-repair and inflammatory response of the myocardium [105]. The pathology is characterized by the proliferation of myofibroblasts in the myocardial tissue, secretion and excessive deposition of ECMs, and disorders in the ratio and arrangement of various types of collagen [106, 107]. After MI, local ischemia and hypoxia lead to the mass death of CMs. The body then produces a repair response that includes cardiac fibroblast activation, proliferation, and phenotypic transformation to form myofibroblasts. The above pathological changes lead to a replacement fibrotic process, in which fibroblasts and myofibroblasts produce fibrous scars to replace the damaged tissue [108]. Furthermore, the process of replacement fibrosis will reduce further dilatation of the infarcted area and maintain the structural integrity of the ventricles, thus preventing cardiac rupture. In addition, increased intraventricular mechanical pressure and inflammatory response after MI can induce expansion of connective tissue in the noninfarcted region and cause reactive fibrosis in the noninfarcted area. Reactive fibrosis can alter ventricular compliance and increase ventricular wall stiffness, thus affecting cardiac systolic and diastolic function and synchronicity, eventually leading to HF, worsening arrhythmias, and even sudden death [106, 109]. MF is a significant manifestation of cardiac remodeling and an essential factor influencing the prognosis of MI. Therefore, inhibition of the progression of reactive fibrosis in the peripheral myocardium of the infarct area would be an ideal treatment after MI.

In one study, iron overload increased oxidative stress levels and led to MF in gerbil hearts, as evidenced by increased MDA levels and decreased GPX4 levels [70]. It is suggested that iron overload may foster MF development by inducing lipid peroxidation damage. In addition, GPX4 participates in various pathological processes such as inflammation, cellular repair, oxidative stress, and ferroptosis. And GPX4 is closely associated with the development of fibrotic diseases [48]. Recent studies on ferroptosis intervention in MF have focused on GPX4. In myocardial I/R injury mouse models, miR-375-3p was found to promote MF development by downregulating GPX4 expression. However, both miR-375-3p inhibitors and Fer-1 significantly attenuated MF in these mice and enhanced the antioxidant capacity of cardiac fibroblasts *in vitro* [71]. In another study, dexmedetomidine activated the SLC7A11/GPX4 signaling pathway, inhibited CM ferroptosis after myocardial I/R in mice, and significantly reduced the area of MF. Predictably, the extent of myocardial injury and fibrosis area markedly increased following erastin treatment [67]. All these studies have con-

firmed the role of ferroptosis in MF. However, the current studies on its pathogenesis are relatively homogeneous, without distinguishing the location and type of MF occurrence. Future studies should delve into the effects of ferroptosis on reactive fibrosis and its mechanisms.

6.5. Myocardial Hypertrophy. CHD, especially MI, leads to CM damage or death due to ischemia and hypoxia, resulting in a localized cardiac function deficit. Under prolonged stimulation, peripheral CMs gradually hypertrophy to compensate for partial cardiac function [110, 111]. The early stage of MH is a beneficial compensatory response for the organism, but its compensatory capacity is limited. The late-stage shows increased myocardial oxygen consumption and reduced cardiac compliance and contractility, leading to loss of compensatory effect of pathological MH, further increasing the risk of HF and malignant arrhythmias [112, 113]. Studies have shown that MH is an independent risk factor for increased morbidity and mortality from various CVD during clinical practice [114, 115].

Apelin-13 can accelerate the progression of MH. In a study, apelin-13 induced hypertrophy and elevated free iron levels in H9C2 cells. It was further observed that apelin-13 increased iron and ROS levels in mitochondria of CM and triggered mitochondrial damage. This experiment showed that apelin-13-stimulated MH was closely related to NCOA4-mediated ferritinophagy and sideroflexin 1 (a mitochondria iron transporting protein) mediated mitochondrial iron overload [72, 116]. The initial relationship between ferroptosis and MH has also been established. In addition, one study used angiotensin II to induce MH in mice and found that oxidative stress and ferroptosis occurred [50]. Knock-down of xCT increased PTGS2, MDA, and ROS levels and exacerbated Ang II-induced MH in mice [50]. In addition, Beclin 1 is a homolog of the yeast autophagy gene Atg6/Vps30, an essential molecule in the autophagic process. A study found elevated levels of SLC7A11, GPX4, and NCOA4 in Beclin 1 haploinsufficient mice. They promoted autophagy and ferroptosis and exacerbated low-temperature-induced MH [73]. Currently, there is no direct evidence that post-MI ferroptosis is associated with MH. However, MH induced by other methods is strongly associated with iron overload and ferroptosis. These studies further imply the potential of ferroptosis as a therapeutic target for MH after MI.

7. Ferroptosis as a Novel Therapeutic Target for CHD

As discussed above, ferroptosis has been found to play a significant role in the pathological progression of CHD [11, 37]. Accordingly, targeting ferroptosis will become a new therapeutic strategy for treating CHD. With intensive studies on the mechanisms and regulatory pathways of ferroptosis, three main methods of ferroptosis inhibition have been identified.

First, iron chelators can bind to iron in the body to effectively increase iron excretion, thus blocking the redox reaction caused by iron overload. Currently, the main iron chelators used in clinical practice are deferoxamine,

deferiprone, and deferasirox [117]. Several studies have shown that iron chelators have cardiovascular protective effects, such as improving vascular endothelial function, inhibiting SMC proliferation, and protecting CMs [64, 118]. Second, genetic manipulation of ferroptosis has been shown to inhibit ferroptosis and reduce myocardial injury [119]. These include upregulation of GPX4 and overexpression of SLC7A11 [66, 120]. However, this approach is currently not clinically applicable. Last, the cardioprotective effects of antioxidants have also been widely demonstrated [121]. Fer-1 is one of the most common antioxidants. It can upregulate the expression of GPX4 and FTH1, thus inhibiting lipid peroxidation [65]. And Fer-1 can slow down the progression of AS and reduce the area of MI [45, 57, 63]. Vitamin E is a common clinical antioxidant that can inhibit ferroptosis by inhibiting LOX [41]. Therefore, antioxidants may be the most promising ferroptosis inhibitors for widespread use. Excavating drugs with inhibiting ferroptosis from clinically available drugs may provide new options for treating CHD more quickly, such as vitamin E, fluvastatin, puerarin, dexmedetomidine, and propofol [41, 60, 65, 67, 68].

8. Conclusions

This article reviews the mechanisms of iron metabolism in CMs. It also focuses on the role of iron metabolism and ferroptosis in the crucial pathological changes of CHD. In contrast, the current research on the mechanisms of ferroptosis is still at an early stage, and most findings are obtained from animal and cellular experiments. We cannot conclude whether inhibition of ferroptosis is totally beneficial at different stages of human CHD. Inhibition of vascular and cardiac ferroptosis may bring new benefits to patients with CHD. Therefore, exploring the mechanisms and clinical feasibility is necessary for future studies. At this point, we have some unanswered questions that need to be concerned. (1) What are the roles and mechanisms of iron overload and ferroptosis in intraplaque angiogenesis? (2) Is ferroptosis involved in cardiomyocyte proliferation a target for cardiac regeneration? (3) How do we select methods to regulate ferroptosis in the pathological progression of CHD? With ongoing research, the mystery of ferroptosis will be further uncovered. Maintaining iron homeostasis and targeting ferroptosis will be promising strategies for the staged treatment of CHD.

Abbreviations

DNA:	Deoxyribonucleic acid
Bcl-2:	B cell lymphoma 2
Bax:	Bcl-2-associated X protein
mTOR:	Mammalian target of rapamycin
ATG:	Autophagy-related protein
LC3:	Light chain 3
TFEB:	Transcription factor EB
DRAM-3:	Damage-regulated autophagy modulator 3
NLRP3:	NOD-like receptor protein 3
ASC:	Apoptosis-associated speck-like protein
IL-1 β :	Interleukin-1beta

IL-18:	Interleukin-18
ACSL4:	Acyl-CoA synthetase long-chain family member 4
LPCAT3:	Lysophosphatidylcholine acyltransferase 3
xCT:	Cystine-glutamate antiporter
OxPLs:	Oxidized phospholipids
SLC7A11:	Subunit solute carrier family 7 member 11
SLC3A2:	Subunit solute carrier family 3 member 2
Nrf2:	Nuclear factor E2-related factor 2
NCOA4:	Nuclear receptor coactivator 4
AA:	Arachidonic acid
AdA:	Adrenic acid
GCH1:	Guanosine triphosphate cyclohydrolase 1
BH4:	Tetrahydrobiopterin
CoQ10:	Coenzyme Q10
CoQH2:	Dihydroubiquione
FSP1:	Ferroptosis suppressor protein 1
NADPH:	Nicotinamide adenine dinucleotide phosphate
PTGS2:	Prostaglandin synthase 2
TLR4:	Toll-like receptor 4
AKT:	Protein kinase B
HMOX1:	Heme oxygenase-1
HUVEC:	Human umbilical vein endothelial cells
H/R:	Hypoxia/reoxygenation
PTGS2:	Prostaglandin-endoperoxide synthase 2.

Conflicts of Interest

The authors declare that there is no conflict of interest regarding the publication of this article.

Authors' Contributions

X.F. was responsible for conceptualization; X.F. and J.Z. were responsible for methodology; X.F. and A.L. were responsible for formal analysis; X.F. and H.L. were responsible for writing—original draft preparation; X.F., A.L., Z.Y., L.L., and J.Z. were responsible for writing—review and editing; H.L. and D.G. were responsible for visualization; Z.Y. and X.G. were responsible for supervision; J.Z. was responsible for funding acquisition. All authors have read and agreed to the published version of the manuscript.

Acknowledgments

The present study was supported by the National Natural Science Foundation of China (grant number 81774232) and QI HUANG Scholars (Junping Zhang) Special Funding (National Traditional Chinese Medicine People's Education Letter [2021] grant number 203).

References

- [1] P. Libby and P. Theroux, "Pathophysiology of coronary artery disease," *Circulation*, vol. 111, pp. 3481–3488, 2005.
- [2] D. P. Leong, P. G. Joseph, M. McKee et al., "Reducing the global burden of cardiovascular disease, part 2: prevention and treatment of cardiovascular disease," *Circulation Research*, vol. 121, no. 6, pp. 695–710, 2017.

- [3] N. Narula, J. W. Olin, and N. Narula, "Pathologic disparities between peripheral artery disease and coronary artery disease," *Arteriosclerosis, Thrombosis, and Vascular Biology*, vol. 40, no. 9, pp. 1982–1989, 2020.
- [4] N. Ji, Z. Qi, Y. Wang et al., "Pyroptosis: a new regulating mechanism in cardiovascular disease," *Journal of Inflammation Research*, vol. 14, pp. 2647–2666, 2021.
- [5] P. Wardman and L. P. Candeias, "Fenton Chemistry: An Introduction," *Radiation Research*, vol. 145, no. 5, pp. 523–531, 1996.
- [6] D. Galaris, A. Barbouti, and K. Pantopoulos, "Iron homeostasis and oxidative stress: an intimate relationship," *Biochimica et Biophysica Acta (BBA)-Molecular Cell Research*, vol. 2019, article 118535, 2019.
- [7] R. Gozzelino and P. Arosio, "Iron homeostasis in health and disease," *International Journal of Molecular Sciences*, vol. 17, no. 1, 2016.
- [8] C. Fischer, C. Volani, T. Komlódi et al., "Dietary Iron Overload and *Hfe*^{-/-} Related Hemochromatosis Alter Hepatic Mitochondrial Function," *Antioxidants*, vol. 10, no. 11, p. 1818, 2021.
- [9] S. Lakhal-Littleton, M. Wolna, C. A. Carr et al., "Cardiac ferroportin regulates cellular iron homeostasis and is important for cardiac function," *Proceedings of the National Academy of Sciences of the United States of America*, vol. 112, no. 10, pp. 3164–3169, 2015.
- [10] S. Lakhal-Littleton, "Mechanisms of cardiac iron homeostasis and their importance to heart function," *Free Radical Biology & Medicine*, vol. 133, pp. 234–237, 2019.
- [11] S. Li and X. Zhang, "Iron in cardiovascular disease: challenges and potentials," *Frontiers in Cardiovascular Medicine*, vol. 8, article 707138, 2021.
- [12] Y. Guo, W. Zhang, X. Zhou et al., "Roles of ferroptosis in cardiovascular diseases," *Front Cardiovasc Med*, vol. 9, p. 911564, 2022.
- [13] Y. Song, B. Wang, X. Zhu et al., "Human umbilical cord blood-derived MSCs exosome attenuate myocardial injury by inhibiting ferroptosis in acute myocardial infarction mice," *Cell Biology and Toxicology*, vol. 37, no. 1, pp. 51–64, 2021.
- [14] S. Omiya, S. Hikoso, Y. Imanishi et al., "Downregulation of ferritin heavy chain increases labile iron pool, oxidative stress and cell death in cardiomyocytes," *Journal of Molecular and Cellular Cardiology*, vol. 46, no. 1, pp. 59–66, 2009.
- [15] B. Zhou, J. Zhang, Y. Chen et al., "Puerarin protects against sepsis-induced myocardial injury through AMPK-mediated ferroptosis signaling," *Aging*, vol. 14, no. 8, pp. 3617–3632, 2022.
- [16] M. Cazzola, H. A. Huebers, M. H. Sayers, A. P. MacPhail, M. Eng, and C. A. Finch, "Transferrin saturation, plasma iron turnover, and transferrin uptake in normal humans," *Blood*, vol. 66, no. 4, pp. 935–939, 1985.
- [17] A. Paterek, U. Mackiewicz, and M. Mączewski, "Iron and the heart: a paradigm shift from systemic to cardiomyocyte abnormalities," *Journal of Cellular Physiology*, vol. 234, no. 12, pp. 21613–21629, 2019.
- [18] W. Xu, T. Barrientos, L. Mao, H. A. Rockman, A. A. Sauve, and N. C. Andrews, "Lethal cardiomyopathy in mice lacking transferrin receptor in the heart," *Cell Reports*, vol. 13, no. 3, pp. 533–545, 2015.
- [19] T. A. Rouault, "The role of iron regulatory proteins in mammalian iron homeostasis and disease," *Nature Chemical Biology*, vol. 2, no. 8, pp. 406–414, 2006.
- [20] S. Haddad, Y. Wang, B. Galy et al., "Iron-regulatory proteins secure iron availability in cardiomyocytes to prevent heart failure," *European Heart Journal*, vol. 38, no. 5, pp. ehw333–ehw372, 2016.
- [21] L. C. Kühn, "Iron regulatory proteins and their role in controlling iron metabolism," *Metallomics*, vol. 7, no. 2, pp. 232–243, 2015.
- [22] A. M. N. Silva and M. Rangel, "The (bio)chemistry of non-transferrin-bound iron," *Molecules*, vol. 27, no. 6, p. 1784, 2022.
- [23] S. Kumfu, S. C. Chattipakorn, S. Fucharoen, and N. Chattipakorn, "Dual T-type and L-type calcium channel blocker exerts beneficial effects in attenuating cardiovascular dysfunction in iron-overloaded thalassaemic mice," *Experimental Physiology*, vol. 101, no. 4, pp. 521–539, 2016.
- [24] H. Nam, C.-Y. Wang, L. Zhang et al., "ZIP14 and DMT1 in the liver, pancreas, and heart are differentially regulated by iron deficiency and overload: implications for tissue iron uptake in iron-related disorders," *Haematologica*, vol. 98, no. 7, pp. 1049–1057, 2013.
- [25] Z. M. Qian, Y. Z. Chang, G. Leung et al., "Expression of ferroportin1, hephaestin and ceruloplasmin in rat heart," *Biochimica et Biophysica Acta (BBA) - Molecular Basis of Disease*, vol. 1772, no. 5, pp. 527–532, 2007.
- [26] S. Lakhal-Littleton, M. Wolna, Y. J. Chung et al., "An essential cell-autonomous role for hepcidin in cardiac iron homeostasis," *eLife*, vol. 5, article e19804, 2016.
- [27] M. F. Hoes, N. Grote Beverborg, J. D. Kijlstra et al., "Iron deficiency impairs contractility of human cardiomyocytes through decreased mitochondrial function," *European Journal of Heart Failure*, vol. 20, no. 5, pp. 910–919, 2018.
- [28] F. Vinchi, G. Porto, A. Simmelbauer et al., "Atherosclerosis is aggravated by iron overload and ameliorated by dietary and pharmacological iron restriction," *European Heart Journal*, vol. 41, no. 28, pp. 2681–2695, 2020.
- [29] Y. Liu and B. Levine, "Autosis and autophagic cell death: the dark side of autophagy," *Cell Death and Differentiation*, vol. 22, no. 3, pp. 367–376, 2015.
- [30] G. Kroemer, G. Mariño, and B. Levine, "Autophagy and the integrated stress response," *Molecular Cell*, vol. 40, no. 2, pp. 280–293, 2010.
- [31] J. Ito, S. Omiya, M.-C. Rusu et al., "Iron derived from autophagy-mediated ferritin degradation induces cardiomyocyte death and heart failure in mice," *eLife*, vol. 10, article e62174, 2021.
- [32] E. Park and S. W. Chung, "ROS-mediated autophagy increases intracellular iron levels and ferroptosis by ferritin and transferrin receptor regulation," *Cell Death & Disease*, vol. 10, no. 11, p. 822, 2019.
- [33] W. Hou, Y. Xie, X. Song et al., "Autophagy promotes ferroptosis by degradation of ferritin," *Autophagy*, vol. 12, no. 8, pp. 1425–1428, 2016.
- [34] S. Elmore, "Apoptosis: a review of programmed cell death," *Toxicologic Pathology*, vol. 35, no. 4, pp. 495–516, 2007.
- [35] Y. Dong, H. Chen, J. Gao, Y. Liu, J. Li, and J. Wang, "Molecular machinery and interplay of apoptosis and autophagy in coronary heart disease," *Journal of Molecular and Cellular Cardiology*, vol. 136, pp. 27–41, 2019.
- [36] C. Jia, H. Chen, J. Zhang et al., "Role of pyroptosis in cardiovascular diseases," *International Immunopharmacology*, vol. 67, pp. 311–318, 2019.

- [37] Y. Leng, X. Luo, J. Yu, H. Jia, and B. Yu, "Ferroptosis: a potential target in cardiovascular disease," *Frontiers in Cell and Development Biology*, vol. 9, p. 813668, 2021.
- [38] J. Li, F. Cao, H.-L. Yin et al., "Ferroptosis: past, present and future," *Cell Death & Disease*, vol. 11, no. 2, p. 88, 2020.
- [39] Y. Shen, X. Wang, X. Shen et al., "Geniposide possesses the protective effect on myocardial injury by inhibiting oxidative stress and ferroptosis via activation of the Grsf1/GPx4 axis," *Frontiers in Pharmacology*, vol. 13, article 879870, 2022.
- [40] Y. Wang and Tang, "PM2.5 Induces Ferroptosis in Human Endothelial Cells through Iron Overload and Redox Imbalance," *Environmental Pollution*, vol. 254, p. 112937, 2019.
- [41] V. E. Kagan, G. Mao, F. Qu et al., "Oxidized arachidonic and adrenic PEs navigate cells to ferroptosis," *Nature Chemical Biology*, vol. 13, no. 1, pp. 81–90, 2017.
- [42] W. S. Yang, K. J. Kim, M. M. Gaschler, M. Patel, M. S. Shchepinov, and B. R. Stockwell, "Peroxidation of polyunsaturated fatty acids by lipoxygenases drives ferroptosis," *Proceedings of the National Academy of Sciences*, vol. 113, no. 34, pp. E4966–E4975, 2016.
- [43] F. Ursini and M. Maiorino, "Lipid peroxidation and ferroptosis: the role of GSH and GPX4," *Free Radical Biology and Medicine*, vol. 152, pp. 175–185, 2020.
- [44] A. Stamenkovic, G. N. Pierce, and A. Ravandi, "Phospholipid oxidation products in ferroptotic myocardial cell death," *American Journal of Physiology. Heart and Circulatory Physiology*, vol. 317, no. 1, pp. H156–H163, 2019.
- [45] X. Fang, H. Wang, D. Han et al., "Ferroptosis as a target for protection against cardiomyopathy," *Proceedings of the National Academy of Sciences of the United States of America*, vol. 116, no. 7, pp. 2672–2680, 2019.
- [46] R. Sun, M. Liu, K. Xu et al., "Ferroptosis is involved in the benzene-induced hematotoxicity in mice via iron metabolism, oxidative stress and NRF2 signaling pathway," *Chemico-Biological Interactions*, vol. 362, 2022.
- [47] M. Liu, X. Y. Kong, Y. Yao et al., "The critical role and molecular mechanisms of ferroptosis in antioxidant systems: a narrative review," *Annals of translational medicine*, vol. 10, no. 6, p. 368, 2022.
- [48] Z. Li, Z. Zhu, Y. Liu, Y. Liu, and H. Zhao, "Function and regulation of GPX4 in the development and progression of fibrotic disease," *Journal of Cellular Physiology*, vol. 237, no. 7, pp. 2808–2824, 2022.
- [49] H. Sato, M. Tamba, K. Kuriyama-Matsumura, S. Okuno, and S. Bannai, "Molecular cloning and expression of human XCT, the light chain of amino acid transport system Xc," *Antioxidants & Redox Signaling*, vol. 2, no. 4, pp. 665–671, 2000.
- [50] X. Zhang, C. Zheng, Z. Gao et al., "SLC7A11/XCT prevents cardiac hypertrophy by inhibiting ferroptosis," *Cardiovascular Drugs and Therapy*, vol. 36, no. 3, pp. 437–447, 2022.
- [51] P. Hu, Y. Xu, Y. Jiang et al., "The mechanism of the imbalance between proliferation and ferroptosis in pulmonary artery smooth muscle cells based on the activation of SLC7A11," *European Journal of Pharmacology*, vol. 928, 2022.
- [52] S. Xu, B. Wu, B. Zhong et al., "Naringenin alleviates myocardial ischemia/reperfusion injury by regulating the nuclear factor-erythroid factor 2-related factor 2 (Nrf2) /system Xc-/glutathione peroxidase 4 (GPX4) axis to inhibit ferroptosis," *Bioengineered*, vol. 12, no. 2, pp. 10924–10934, 2021.
- [53] V. A. N. Kraft, C. T. Bezjian, S. Pfeiffer et al., "GTP cyclohydrolase 1/tetrahydrobiopterin counteract ferroptosis through lipid remodeling," *ACS Central Science*, vol. 6, no. 1, pp. 41–53, 2020.
- [54] A. Latremoliere and M. Costigan, "GCH1, BH4 and pain," *Current Pharmaceutical Biotechnology*, vol. 12, no. 10, pp. 1728–1741, 2011.
- [55] K. Bersuker, J. M. Hendricks, Z. Li et al., "The CoQ oxidoreductase FSP1 acts parallel to GPX4 to inhibit ferroptosis," *Nature*, vol. 575, no. 7784, pp. 688–692, 2019.
- [56] J. Zhu, Y. Xiong, Y. Zhang et al., "The molecular mechanisms of regulating oxidative stress-induced ferroptosis and therapeutic strategy in tumors," *Oxidative Medicine and Cellular Longevity*, vol. 2020, Article ID 8810785, 14 pages, 2020.
- [57] Z. Meng, H. Liang, J. Zhao et al., "HMOX1 upregulation promotes ferroptosis in diabetic atherosclerosis," *Life Sciences*, vol. 284, article 119935, 2021.
- [58] K. Yang, H. Song, and D. Yin, "PDSS2 inhibits the ferroptosis of vascular endothelial cells in atherosclerosis by activating Nrf2," *Journal of Cardiovascular Pharmacology*, vol. 77, no. 6, pp. 767–776, 2021.
- [59] F.-J. Xiao, D. Zhang, Y. Wu et al., "MiRNA-17-92 protects endothelial cells from erastin-induced ferroptosis through targeting the A20-ACSL4 axis," *Biochemical and Biophysical Research Communications*, vol. 515, no. 3, pp. 448–454, 2019.
- [60] Q. Li, C. Liu, L. Deng et al., "Novel function of fluvastatin in attenuating oxidized low-density lipoprotein-induced endothelial cell ferroptosis in a glutathione peroxidase-4- and cystine-glutamate antiporter-dependent manner," *Experimental and Therapeutic Medicine*, vol. 22, no. 5, p. 1275, 2021.
- [61] X. Hu, X. Cai, R. Ma, W. Fu, C. Zhang, and X. Du, "Iron-load exacerbates the severity of atherosclerosis via inducing inflammation and enhancing the glycolysis in macrophages," *Journal of Cellular Physiology*, vol. 234, pp. 18792–18800, 2019.
- [62] J. Cai, M. Zhang, Y. Liu et al., "Iron accumulation in macrophages promotes the formation of foam cells and development of atherosclerosis," *Cell & Bioscience*, vol. 10, no. 1, p. 137, 2020.
- [63] W. Yu, W. Liu, D. Xie et al., "High level of uric acid promotes atherosclerosis by targeting NRF2-mediated autophagy dysfunction and ferroptosis," *Oxidative Medicine and Cellular Longevity*, vol. 2022, Article ID 9304383, 2022.
- [64] A. Sampilvanjil, T. Karasawa, N. Yamada et al., "Cigarette smoke extract induces ferroptosis in vascular smooth muscle cells," *American Journal of Physiology. Heart and Circulatory Physiology*, vol. 318, no. 3, pp. H508–H518, 2020.
- [65] B. Liu, C. Zhao, H. Li, X. Chen, Y. Ding, and S. Xu, "Puerarin protects against heart failure induced by pressure overload through mitigation of ferroptosis," *Biochemical and Biophysical Research Communications*, vol. 497, no. 1, pp. 233–240, 2018.
- [66] T.-J. Park, J. H. Park, G. S. Lee et al., "Quantitative proteomic analyses reveal that GPX4 downregulation during myocardial infarction contributes to ferroptosis in cardiomyocytes," *Cell Death & Disease*, vol. 10, no. 11, p. 835, 2019.
- [67] P. Yu, J. Zhang, Y. Ding et al., "Dexmedetomidine post-conditioning alleviates myocardial ischemia-reperfusion injury in rats by ferroptosis inhibition via SLC7A11/GPX4 axis activation," *Human Cell*, vol. 35, no. 3, pp. 836–848, 2022.

- [68] S. Li, Z. Lei, X. Yang et al., "Propofol protects myocardium from ischemia/reperfusion injury by inhibiting ferroptosis through the AKT/P53 signaling pathway," *Frontiers in Pharmacology*, vol. 13, article 841410, 2022.
- [69] X. Chen, S. Xu, C. Zhao, and B. Liu, "Role of TLR4/NADPH oxidase 4 pathway in promoting cell death through autophagy and ferroptosis during heart failure," *Biochemical and Biophysical Research Communications*, vol. 516, no. 1, pp. 37–43, 2019.
- [70] M. Wang, R.-R. Liu, C.-J. Wang et al., "Combined histological and hematological assessment of iron-induced organ damage in a gerbil model of iron overload," *American Journal of Translational Research*, vol. 7, no. 2, pp. 385–392, 2015.
- [71] Y. Zhuang, D. Yang, S. Shi et al., "MiR-375-3p promotes cardiac fibrosis by regulating the ferroptosis mediated by GPX4," *Computational Intelligence and Neuroscience*, vol. 2022, Article ID 9629158, 2022.
- [72] M. Tang, Z. Huang, X. Luo et al., "Ferritinophagy activation and sideroflexin1-dependent mitochondria iron overload is involved in apelin-13-induced cardiomyocytes hypertrophy," *Free Radical Biology & Medicine*, vol. 134, pp. 445–457, 2019.
- [73] Z. Yin, G. Ding, X. Chen et al., "Beclin1 haploinsufficiency rescues low ambient temperature-induced cardiac remodeling and contractile dysfunction through inhibition of ferroptosis and mitochondrial injury," *Metabolism*, vol. 113, article 154397, 2020.
- [74] E. Gutiérrez, A. J. Flammer, L. O. Lerman, J. Elízaga, A. Lerman, and F. Fernández-Avilés, "Endothelial dysfunction over the course of coronary artery disease," *European Heart Journal*, vol. 34, no. 41, pp. 3175–3181, 2013.
- [75] D. Tousoulis, C. Simopoulou, N. Papageorgiou et al., "Endothelial dysfunction in conduit arteries and in microcirculation. Novel therapeutic approaches," *Pharmacology & Therapeutics*, vol. 144, no. 3, pp. 253–267, 2014.
- [76] P. Poredos, A. V. Poredos, and I. Gregoric, "Endothelial dysfunction and its clinical implications," *Angiology*, vol. 72, no. 7, pp. 604–615, 2021.
- [77] S. Xu, I. Ilyas, P. J. Little et al., "Endothelial dysfunction in atherosclerotic cardiovascular diseases and beyond: from mechanism to pharmacotherapies," *Pharmacological Reviews*, vol. 73, no. 3, pp. 924–967, 2021.
- [78] P. Libby, P. M. Ridker, and G. K. Hansson, "Progress and challenges in translating the biology of atherosclerosis," *Nature*, vol. 473, no. 7347, pp. 317–325, 2011.
- [79] S. Ryoo, A. Bhunia, F. Chang, A. Shoukas, D. E. Berkowitz, and L. H. Romer, "OxLDL-dependent activation of arginase II is dependent on the LOX-1 receptor and downstream RhoA signaling," *Atherosclerosis*, vol. 214, no. 2, pp. 279–287, 2011.
- [80] E. M. Maguire, S. W. A. Pearce, and Q. Xiao, "Foam cell formation: a new target for fighting atherosclerosis and cardiovascular disease," *Vascular Pharmacology*, vol. 112, pp. 54–71, 2019.
- [81] D. A. Chistiakov, A. A. Melnichenko, V. A. Myasoedova, A. V. Grechko, and A. N. Orekhov, "Mechanisms of foam cell formation in atherosclerosis," *Journal of Molecular Medicine (Berlin, Germany)*, vol. 95, no. 11, pp. 1153–1165, 2017.
- [82] M. Ardiana, B. Susetyo Pikir, A. Santoso, H. Oky Hermawan, and M. Jibril Al-Farabi, "The effect of subchronic cigarette smoke exposure on oxidative stress parameters and endothelial nitric oxide synthase in a rat aorta," *ARYA Atherosclerosis*, vol. 17, pp. 1–7, 2021.
- [83] M. A. Incalza, R. D’Oria, A. Natalicchio, S. Perrini, L. Laviola, and F. Giorgino, "Oxidative stress and reactive oxygen species in endothelial dysfunction associated with cardiovascular and metabolic diseases," *Vascular Pharmacology*, vol. 100, pp. 1–19, 2018.
- [84] V. B. Marques, M. A. S. Leal, J. G. A. Mageski et al., "Chronic iron overload intensifies atherosclerosis in apolipoprotein E deficient mice: role of oxidative stress and endothelial dysfunction," *Life Sciences*, vol. 233, p. 116702, 2019.
- [85] S. Zhang, W. Xin, G. J. Anderson et al., "Double-edge sword roles of iron in driving energy production versus instigating ferroptosis," *Cell Death & Disease*, vol. 13, no. 1, p. 40, 2022.
- [86] C. R. Bain, M. Ziemann, A. Kaspi et al., "DNA methylation patterns from peripheral blood separate coronary artery disease patients with and without heart failure," *ESC Heart Failure*, vol. 7, no. 5, pp. 2468–2478, 2020.
- [87] E. Cho, Y. Kang, and Y. Cho, "Effects of fine particulate matter on cardiovascular disease morbidity: a study on seven metropolitan cities in South Korea," *International Journal of Public Health*, vol. 67, 2022.
- [88] A. Chawla, K. D. Nguyen, and Y. P. S. Goh, "Macrophage-mediated inflammation in metabolic disease," *Nature Reviews. Immunology*, vol. 11, no. 11, pp. 738–749, 2011.
- [89] M. R. Bennett, S. Sinha, and G. K. Owens, "Vascular smooth muscle cells in atherosclerosis," *Circulation Research*, vol. 118, no. 4, pp. 692–702, 2016.
- [90] I. Tabas, "Macrophage death and defective inflammation resolution in atherosclerosis," *Nature Reviews. Immunology*, vol. 10, no. 1, pp. 36–46, 2010.
- [91] B. A. Bergmark, N. Mathenge, P. A. Merlini, M. B. Lawrence-Wright, and R. P. Giugliano, "Acute coronary syndromes," *Lancet*, vol. 399, no. 10332, pp. 1347–1358, 2022.
- [92] G. Cimmino, L. Di Serafino, and P. Cirillo, "Pathophysiology and mechanisms of acute coronary syndromes: atherothrombosis, immune-inflammation, and beyond," *Expert Review of Cardiovascular Therapy*, vol. 20, no. 5, pp. 351–362, 2022.
- [93] P. K. Shah, E. Falk, J. J. Badimon et al., "Human monocyte-derived macrophages induce collagen breakdown in fibrous caps of atherosclerotic plaques. Potential role of matrix-degrading metalloproteinases and implications for plaque rupture," *Circulation*, vol. 92, no. 6, pp. 1565–1569, 1995.
- [94] D. A. Chistiakov, A. N. Orekhov, and Y. V. Bobryshev, "Contribution of neovascularization and intraplaque haemorrhage to atherosclerotic plaque progression and instability," *Acta Physiologica (Oxford, England)*, vol. 213, no. 3, pp. 539–553, 2015.
- [95] W. Martinet, I. Coornaert, P. Puylaert, and G. R. Y. De Meyer, "Macrophage death as a pharmacological target in atherosclerosis," *Frontiers in Pharmacology*, vol. 10, p. 306, 2019.
- [96] Z. Yang, T. Song, L. Truong et al., "Important role of sarcoplasmic reticulum Ca²⁺ release-activated calcium receptor-2 channel in hypoxia-induced rielke iron-sulfur protein-mediated mitochondrial reactive oxygen species generation in pulmonary artery smooth muscle cells," *Antioxidants & Redox Signaling*, vol. 32, no. 7, pp. 447–462, 2020.
- [97] L. Ramakrishnan, S. L. Pedersen, Q. K. Toe et al., "The hepcidin/ferroportin axis modulates proliferation of pulmonary

- artery smooth muscle cells," *Scientific Reports*, vol. 8, no. 1, p. 12972, 2018.
- [98] R. Malhotra, F. Wunderer, H. J. Barnes et al., "Hepcidin deficiency protects against atherosclerosis," *Arteriosclerosis, Thrombosis, and Vascular Biology*, vol. 39, no. 2, pp. 178–187, 2019.
- [99] A. Arbab-Zadeh, "Does "vulnerable" atherosclerotic plaque modify coronary blood flow?: how myths perpetuate," *JACC: Cardiovascular Imaging*, vol. 13, no. 3, pp. 757–759, 2020.
- [100] R. F. P. Castellán and M. Meloni, "Mechanisms and therapeutic targets of cardiac regeneration: closing the age gap," *Front Cardiovasc Med*, vol. 5, p. 7, 2018.
- [101] T. Marunouchi and K. Tanonaka, "Cell death in the cardiac myocyte," *Biological & Pharmaceutical Bulletin*, vol. 38, no. 8, pp. 1094–1097, 2015.
- [102] D. J. Hausenloy and D. M. Yellon, "Myocardial ischemia-reperfusion injury: a neglected therapeutic target," *The Journal of Clinical Investigation*, vol. 123, no. 1, pp. 92–100, 2013.
- [103] W. H. Tang, S. Wu, T. M. Wong, S. K. Chung, and S. S. M. Chung, "Polyol pathway mediates iron-induced oxidative injury in ischemic-reperfused rat heart," *Free Radical Biology & Medicine*, vol. 45, no. 5, pp. 602–610, 2008.
- [104] M. Zhang, A. Perino, A. Ghigo, E. Hirsch, and A. M. Shah, "NADPH oxidases in heart failure: poachers or gamekeepers?," *Antioxidants & Redox Signaling*, vol. 18, no. 9, pp. 1024–1041, 2013.
- [105] P. Zuo, Y. Zhu, Y. Li et al., "Protease-activated receptor 2 deficiency in hematopoietic lineage protects against myocardial infarction through attenuated inflammatory response and fibrosis," *Biochemical and Biophysical Research Communications*, vol. 526, no. 1, pp. 253–260, 2020.
- [106] M. Gyöngyösi, J. Winkler, I. Ramos et al., "Myocardial fibrosis: biomedical research from bench to bedside," *European Journal of Heart Failure*, vol. 19, no. 2, pp. 177–191, 2017.
- [107] H. Venugopal, A. Hanna, C. Humeres, and N. G. Frangogiannis, "Properties and functions of fibroblasts and myofibroblasts in myocardial infarction," *Cell*, vol. 11, no. 9, p. 1386, 2022.
- [108] F. A. van Nieuwenhoven and N. A. Turner, "The role of cardiac fibroblasts in the transition from inflammation to fibrosis following myocardial infarction," *Vascular Pharmacology*, vol. 58, no. 3, pp. 182–188, 2013.
- [109] V. Talman and H. Ruskoaho, "Cardiac fibrosis in myocardial infarction—from repair and remodeling to regeneration," *Cell and Tissue Research*, vol. 365, no. 3, pp. 563–581, 2016.
- [110] C. N. Toepfer, M. B. Sikkell, V. Caorsi et al., "A post-MI power struggle: adaptations in cardiac power occur at the sarcomere level alongside MyBP-C and RLC phosphorylation," *American Journal of Physiology. Heart and Circulatory Physiology*, vol. 311, no. 2, pp. H465–H475, 2016.
- [111] K. Khalid, J. Padda, D. Ismail et al., "Correlation of coronary artery disease and left ventricular hypertrophy," *Cureus*, vol. 13, no. 8, article e17550, 2021.
- [112] R. Pawlinski, M. Tencati, C. R. Hampton et al., "Protease-activated receptor-1 contributes to cardiac remodeling and hypertrophy," *Circulation*, vol. 116, no. 20, pp. 2298–2306, 2007.
- [113] B. C. Bernardo, K. L. Weeks, L. Pretorius, and J. R. McMullen, "Molecular distinction between physiological and pathological cardiac hypertrophy: experimental findings and therapeutic strategies," *Pharmacology & Therapeutics*, vol. 128, no. 1, pp. 191–227, 2010.
- [114] R. Kabir, P. Sinha, S. Mishra et al., "Inorganic arsenic induces sex-dependent pathological hypertrophy in the heart," *American Journal of Physiology. Heart and Circulatory Physiology*, vol. 320, no. 4, pp. H1321–H1336, 2021.
- [115] N. Frey and E. N. Olson, "Cardiac hypertrophy: the good, the bad, and the ugly," *Annual Review of Physiology*, vol. 65, no. 1, pp. 45–79, 2003.
- [116] R. Bellelli, G. Federico, A. Matte' et al., "NCOA4 deficiency impairs systemic iron homeostasis," *Cell Reports*, vol. 14, no. 3, pp. 411–421, 2016.
- [117] S. Entezari, S. M. Haghi, N. Norouzkhani et al., "Iron chelators in treatment of iron overload," *Journal of Toxicology*, vol. 2022, Article ID 4911205, 2022.
- [118] H. Jansová, M. Macháček, Q. Wang et al., "Comparison of various iron chelators and prochelators as protective agents against cardiomyocyte oxidative injury," *Free Radical Biology & Medicine*, vol. 74, pp. 210–221, 2014.
- [119] F. Huang, R. Yang, Z. Xiao et al., "Targeting ferroptosis to treat cardiovascular diseases: a new continent to be explored," *Frontiers in Cell and Development Biology*, vol. 9, article 737971, 2021.
- [120] X. Fang, Z. Cai, H. Wang et al., "Loss of cardiac ferritin H facilitates cardiomyopathy via Slc7a11-mediated ferroptosis," *Circulation Research*, vol. 127, no. 4, pp. 486–501, 2020.
- [121] C. Sun, F. Peng, J. Li, X. Cui, X. Qiao, and W. Zhu, "Ferroptosis-specific inhibitor ferrostatin-1 relieves H₂O₂-induced redox imbalance in primary cardiomyocytes through the Nrf2/ARE pathway," *Disease Markers*, vol. 2022, Article ID 4539932, 2022.

Research Article

Lysionotin Induces Ferroptosis to Suppress Development of Colorectal Cancer via Promoting Nrf2 Degradation

Zhuo Gao ¹, Junnan Jiang ², Lijian Hou ³, and Fujian Ji ²

¹Department of Gastroenterology and Endoscopy Center, China-Japan Union Hospital of Jilin University, Changchun 130033, Jilin Province, China

²Department of Gastrointestinal Colorectal Surgery, China-Japan Union Hospital of Jilin University, Changchun, 130033 Jilin Province, China

³Department of Pathology, China-Japan Union Hospital of Jilin University, Changchun, 130033 Jilin Province, China

Correspondence should be addressed to Fujian Ji; jifj@jlu.edu.cn

Received 5 July 2022; Accepted 28 July 2022; Published 10 August 2022

Academic Editor: Yanqing Liu

Copyright © 2022 Zhuo Gao et al. This is an open access article distributed under the Creative Commons Attribution License, which permits unrestricted use, distribution, and reproduction in any medium, provided the original work is properly cited.

Extensive use of substances derived from natural sources has been documented in the treatment of colorectal cancer (CRC). Lysionotin (Lys) is a flavonoid present in the flowers and leaves of Gesneriaceae family plants. Despite its various pharmacological properties, which include neuroprotective, pro, antimalarial, and anticancer effects, the therapeutic advantages of Lys for CRC remain uncertain. In this present study, we demonstrated that Lys treatment successfully inhibited cell proliferation, migration, and invasion in HCT116 and SW480 CRC cells *in vitro*. Intriguingly, significant ferroptosis and reactive oxygen species (ROS) accumulation in CRC cells were induced by Lys treatment, whereas antagonism of ferroptosis by Liproxstatin-1 (Lip1) pretreatment retarded the anti-CRC effects of Lys. In addition, Lys reduced the amount of Nrf2 protein in CRC cells by increasing the rate at which it is degraded. Overexpression of Nrf2 rescued Lys reduced ferroptosis, suggesting the Nrf2 signaling is a crucial determinant of whether Lys induces ferroptosis in CRC cells. We also revealed that Lys suppressed tumor growth *in vivo* without obvious adverse effects on the main organs of mice. In conclusion, our results discovered that Lys treatment induced ferroptosis to exert antitumor effects in HCT116 and SW480 CRC cells by modulating Nrf2 signaling, providing a potential therapeutic approach for the prevention of colorectal cancer.

1. Introduction

In the year 2021, it was estimated that colorectal cancer (CRC) causes 52,980 deaths and is responsible for 11 percent of all new cancer diagnoses [1]. As a result, colorectal cancer is one of the kinds of cancerous tumors that has the highest mortality rate across the whole globe [2]. Adenocarcinomas, signet ring cell carcinomas, squamous cell carcinomas, and a few other less frequent types of colorectal cancer may be distinguished from one another by their histological features. Colorectal cancer is sometimes referred to by its medical abbreviation, CRC. Adenocarcinoma accounts for more than 90 percent of all CRC diagnoses, and many individuals are found to have advanced disease at the time of diagnosis [3]. In recent years, targeted therapy and immunotherapy have made significant strides towards becoming viable ther-

apeutic options for CRC, complementing more traditional therapies such as chemotherapy, radiation therapy, and surgery [4]. Due to treatment resistance and evident systemic side effects, only 63 percent of CRC patients will live for five years or more after diagnosis. Consequently, there is an urgent need for innovative medicines that might prevent the course of the disease and save lives.

A rising amount of evidence demonstrates that phytochemical substances produced from natural sources are very efficient against cancer and other disorders [5–13]. Paclitaxel, a diterpenoid discovered in the bark of *Taxus brevifolia* in 1971, is the most prominent example of a drug that has been commercially successful [14]. It is often used in the treatment of malignant tumors such as cancer of the lung, esophagus cancer, breast cancer, and cancer of the pancreas. Produced by the soil fungus *Streptomyces peucetius*,

doxorubicin is often used to treat a broad variety of solid cancers [15]. Camptothecin, podophyllotoxin, anhydrovinblastine, and vinorelbine are well-known anticancer medications derived from natural products [16]. Contrarily, there is evidence that colorectal cancer is resistant to a variety of chemotherapies [17]. Rising research has shown that phytochemicals including curcumin, resveratrol, bixin, and Ginkgo biloba offer great therapeutic potential for patients with CRC. The research and development of innovative drugs derived from natural chemicals is still required [16].

In contrast to apoptosis, necrosis, and autophagy, iron death is a unique kind of controlled cell death [18, 19]. The process is called ferroptosis because it is dependent on ferric ions. Dr. Brent R. Stockwell of Columbia University presented this theory for the first time in 2012 [20]. Iron death is caused by several factors, including glutathione depletion, decreased glutathione peroxidase (GPx4) activity, and the inability of lipid oxides to be metabolized by the GPx4-catalyzed glutathione reductase reaction [21]. This is then followed by iron oxidizing lipids via the Fenton reaction, which generates reactive oxygen species (ROS). Iron toxicity is the outcome of having an excessive amount of iron in the body, and circulating iron binds to transferrin as Fe^{3+} , and excess iron is deposited in ferritin without taking part in ROS generation activities through transferrin receptor 1 [22]. Intriguingly, ferroptosis is also deeply involved in p53-mediated tumor suppression [23, 24]. Due to its important role in cell fate determination, ferroptosis is expected to be a valuable drug target in the treatment of cancers [21].

Mounting studies demonstrated that natural compounds targeting ferroptosis can be used for treatment of solid tumors such as lung cancer [25], bladder cancer [26], and pancreatic cancer [27]. However, evidence regarding the anti-CRC activities of ferroptosis-targeted natural compounds is still deficient. In this study, we reported lysionotin (Lys), a flavonoid isolated from *Lysionotus pauciflorus* Maxim (Gesneriaceae), exerts tumor-suppressing characteristics in CRC cell line HCT116 and SW480 cells. Intriguingly, Lys treatment induced potent ferroptosis in CRC cells, and inhibition of ferroptosis retarded the anti-CRC activities *in vitro* and *in vivo*. We further demonstrated that Lys-induced ferroptosis is dependent on the promotion of nuclear factor erythroid 2-related factor 2 (Nrf2) degradation. These results suggest that Lys induced ferroptosis to suppress the progression of CRC via regulating Nrf2 signaling, which paves the way for a new potential strategy for CRC therapy.

2. Materials and Methods

2.1. Regents. Selleck Chemicals Co., Ltd. (TX, USA) provided MG132, Lys (>97% pure), and Liproxstatin-1 (Lip1). For treating cells, Lip1 and MG132 were diluted using dimethyl sulfoxide (DMSO). Lys and Lip1 were diluted in dilution buffer (5 percent DMSO, 40 percent PEG 300, 5 percent Tween 80, and 50 percent H_2O) for animal studies. Abcam (Cambridge, United Kingdom) provided antibodies for cystine/glutamate transporter (xCT, catalog number: ab175186), glutaminase (catalog number: ab93424), and glutathione peroxidase 4 (GPX4, catalog number: ab125066). Cell Signaling

Technology (CST, Danvers, United States) provided antibodies for Ubiquitin (Ub, catalog number 3936S), Ferritin Heavy Chain 1 (FTH1, catalog number 4393S), Nrf2 (catalog number 12721), and glyceraldehyde 3-phosphate dehydrogenase (GAPDH, catalog number 5174S).

2.2. Cell Cultures. We obtained human CRC HCT116 and SW480 cell lines, as well as HIEC and NCM460 cell lines from normal human colon epithelial tissue, from the American Type Culture Collection (ATCC). Cells were cultured in DMEM with 10 percent fetal bovine serum (Sigma-Aldrich, St. Louis, MO, USA) at a temperature of 37 degrees Celsius in an environment containing 5 percent carbon dioxide.

2.3. Assay of Cell Viability. To determine the toxicity of Lys in CRC cells, a CCK-8 kit purchased from Sigma-Aldrich was used. In an effort to maintain clarity, each well of the 96-well plates was populated with 2,000 cells. Following a Lys-containing or Lys-free incubation period of 24 hours, CCK-8 reagent was added to each well, and the cells were allowed to continue growing at 37 degrees Celsius for an additional 2 hours. In order to determine the 450 nm absorbance of each well, a microplate reader (BioTek, Winooski, VT, USA) was used.

2.4. Colony Formation Assay. Colony formation assay was performed in HCT116 and SW480 cells according to a previous report [28]. Briefly, cells were seeded into 6-well plates (400 cells each well). Immediately upon seeing the formation of colonies on the Petri plate, the culture was terminated. PBS was used to wash the cells for a total of 3 times. After that, the cells were fixed for a further 15 minutes using a 1:3 solution of acetic acid and methanol. To stain the cells, the fixation solution was removed, and a staining solution containing 0.1 percent crystal violet was applied to them at room temperature for a period of 30 minutes. Following the final wash with PBS, an inverted microscope (Olympus, Tokyo, Japan) was used to achieve the cell images, and the number of colonies that had more than 60 cells in each well was counted.

2.5. Measurement of Ferrous Ion. FerroOrange, manufactured in Japan by Dojindo, was applied to cells in order to ascertain the quantity of cellular iron. Briefly, cells were subjected to a treatment with 1 mM of FerroOrange in serum-free media for a period of 30 minutes at 37 degrees Celsius. A fluorescence microscope (Olympus) was used for the detection of fluorescence of the CRC cells.

2.6. Transduction. The gene coding Nrf2 was inserted into pAPH vectors [29] for overexpressing Nrf2 in CRC cells. We temporarily transfected an empty vector or a vector that expresses Nrf2 into HCT116 and SW480 cells using Lip3000 (Invitrogen) as directed by the company's protocol.

2.7. Wound Healing Analysis. Wound healing analysis was performed in HCT116 and SW480 cells according to a previous study [30]. Briefly, either HCT116 or SW480 cells was cultured in 6-well plates until they achieved a confluency level of about 90 percent. After that, a p200 pipette

TABLE 1: The information of primers used in qPCR.

Gene	Forward primer (5'-3')	Reverse primer (5'-3')
Nrf2	CACATCCAGTCAGAAACCAGTGG	GGAATGTCTGCGCCAAAAGCTG
Keap1	CAACTTCGCTGAGCAGATTGGC	TGATGAGGGTCACCAGTTGGCA
GAPDH	GTCTCCTCTGACTTCAACAGCG	ACCACCCTGTTGCTGTAGCCAA

tip was used to scrape the cell monolayer in a linear fashion. Before placing the cells back into the incubator at 37 degrees Celsius for a further 24 hours, the cell debris was removed with PBS. Immediate photographs of the damage were taken using a microscope (Olympus).

2.8. Quantitative Polymerase Chain Reaction (qPCR). Using the RNA isolation solution TRIzol (Invitrogen, USA), total RNA was extracted from cells or homogenized tissue samples, and then, it was used as a template for the synthesis of cDNA using the MonScript™ RTIII All-in-One Mix with dsDNase (Monad biotech, China). qRT-PCR was carried out with the MonAmp™Fast SYBR® Green qPCR Mix (manufactured by Monad biotech) on a CFX connect system (Bio-Rad, USA). The primer sequence information is listed in Table 1. The relative gene expression was calculated using the $2^{-\Delta\Delta Ct}$ method.

2.9. Transwell Assay. *In vitro* cell migration and invasion were investigated via the use of a Transwell experiment, as was mentioned before [31]. 2×10^4 cells in DMEM devoid of serum were plated into the top chamber of Corning Transwell Inserts. After that, the top chambers were placed on a 24-well plate, and the bottom chamber was filled with DMEM containing 10 percent FBS. After spending 24 hours in an incubator set to 37 degrees Celsius, the membrane was removed and colored using a crystal violet solution. The images were captured with an Olympus microscope. The number of migratory cells was determined by counting the cells in six random areas. The migration test and the invasion test were both carried out in the same manner, with the exception that Matrigel was utilized to cover the membrane of the top chamber.

2.10. Measurement of Glutathione (GSH) and Malondialdehyde (MDA) Levels. Cells with or without treatment were lysed using the RIPA buffer (CST). The BCA assay kit (Beyotime Biotechnology, Shanghai, China) was used to measure the amount of total protein. The intracellular GSH and MDA levels were determined using a GSH assay kit and an MDA kit (Beyotime), respectively, according to the manufacturer's instructions.

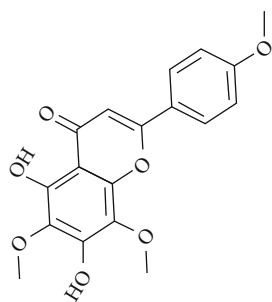
2.11. Western Blot. The Western blot analysis was performed as described before [32, 33]. Briefly, after boiling the samples in $5\times$ loading buffer, an appropriate quantity of each sample was loaded onto a discontinuous sodium dodecylsulfate-polyacrylamide gel (SDS-PAGE), and the proteins were transferred to PVDF membranes (Millipore, Bedford, MA, USA). It took one hour of using nonfat dry milk dissolved in PBS-Tween-20 (PBST) at a concentration of 5% for the

membrane blocking procedure. After this, three washes with PBST were performed, and then either primary (1:2000) or monoclonal (1:5000) anti-GAPDH antibodies were incubated overnight at 4 degrees Celsius with the samples. Following washing with PBST, the membranes were incubated at room temperature with the secondary antibody that was coupled to horseradish peroxidase for a period of two hours (1:5000). With the assistance of the BioRad ChemiDoc MP Image System, the chemical signals were at long last discovered.

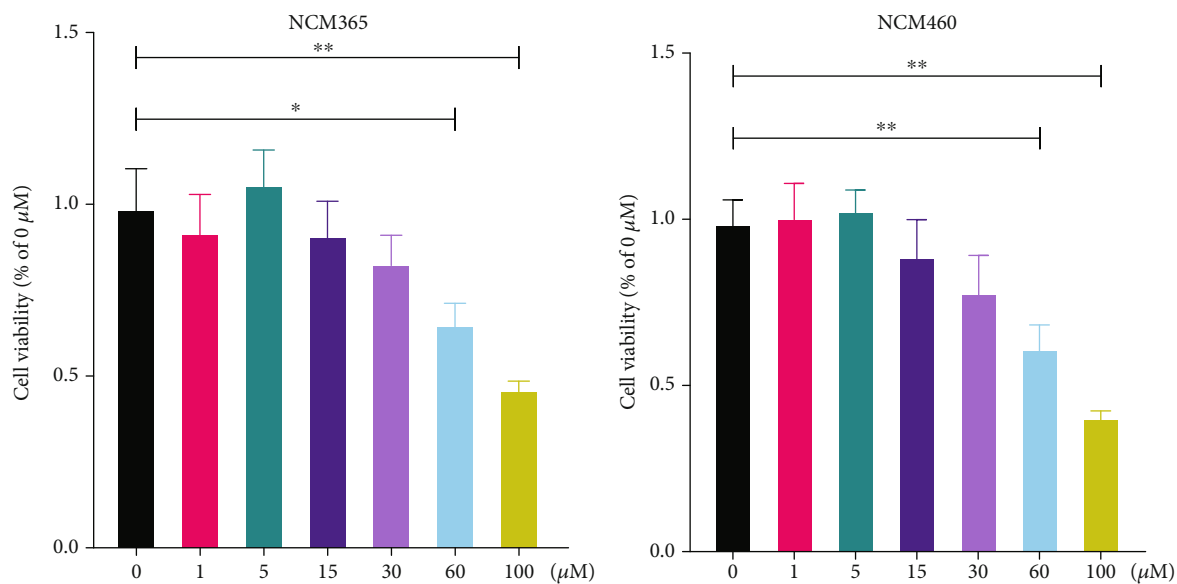
2.12. Determination of Reactive Oxygen Species (ROS) Generation. With the use of the fluorescent probe 2', 7'-dichlorofluorescein diacetate (DCFH, Beyotime), levels of ROS were determined in CRC cells as previously described [34]. At a temperature of 37 degrees Celsius, the cells were treated with 5 M DCFH for an hour. After washes with PBS, cells were observed under a fluorescence microscope and the cell images were taken for quantitative analysis of the fluorescence using ImageJ.

2.13. Xenograft Mouse Models. Charles River Laboratories provided male athymic nude mice that were four weeks old weighing 18-22 g and housed in animal facilities at temperatures between 20 and 25 degrees Celsius, with humidity between 50 and 60 percent and a light/dark cycle of 12 hours on and 12 hours off. The mice had unrestricted access to clean food and water, and the Animal Care and Use Committee of the China-Japan Union Hospital of Jilin University granted approval for the animal trials (Changchun, China). Under the skin of each mouse's left flank, 0.2 milliliters of HCT116 cells suspended in PBS and Matrigel were injected. The cells were kept alive by suspending them in PBS containing Matrigel. At 6 days post the xenograft, the mice received intraperitoneal (i.p.) injections of Lys (20 mg/kg) with or without Lip1 (10 mg/kg) every three days for five times. The size of the tumor was measured using a Vernier caliper every three days. The following formula was used to calculate the size of the tumor: tumor volume (mm^3) = maximum length (mm) \times perpendicular width (mm) $2/2$. On day 24, after the administration of the injection, the tumors were surgically opened up and photographs were obtained of their interiors.

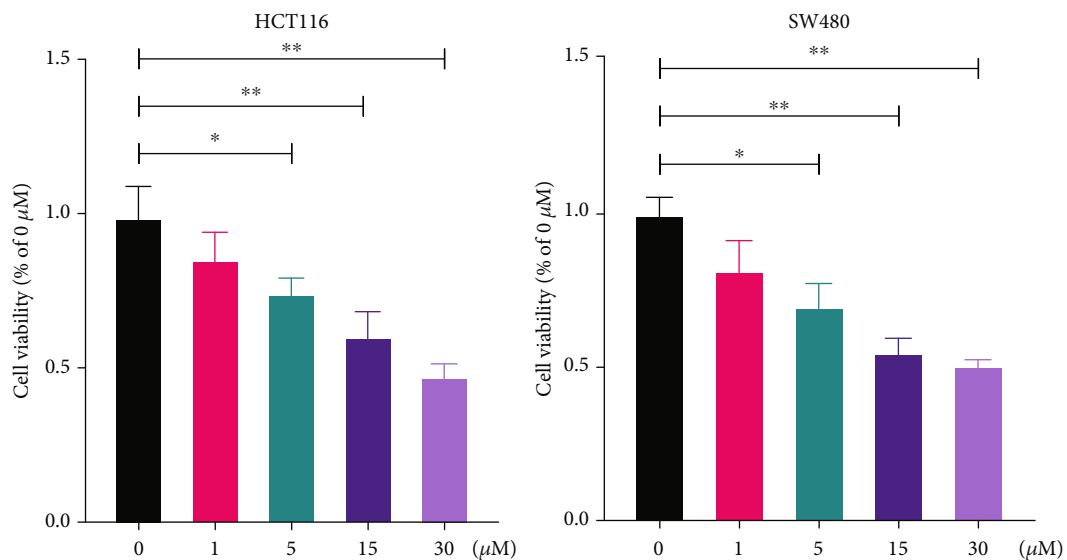
2.14. Hematoxylin and Eosin (HE) Staining. Histology analysis was used in a standard way to measure organ damage. In short, hematoxylin was put on the piece of tissue, which was then put in an incubator for 5 minutes. The slides were then cleaned twice with water that had been distilled. After that, a bluing reagent was put on the tissue slice for 10 seconds. After being washed, the slides were left in eosin Y



(a)



(b)



(c)

FIGURE 1: Continued.

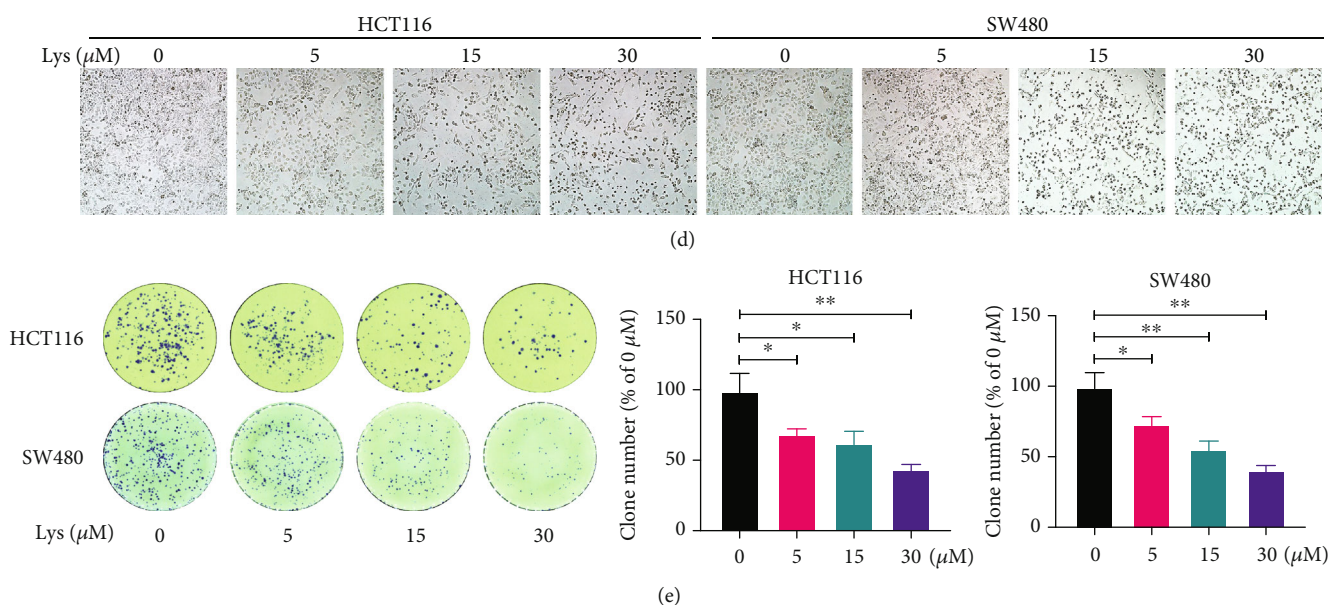


FIGURE 1: Lys inhibits cell viability in HCT116 and SW480 cells. (a) Chemistry formula of Lys. After treatment with the relevant dosages of Lys *in vitro* for a period of 24 hours, the CCK-8 assay was used to determine the level of cell viability of HIEC and NCM460 cells (b), as well as HCT116 and SW480 Cells (c). (d) A microscope was used to evaluate the morphology of the cells. (e) Crystal violet staining was used in order to investigate the cell colony development. *P* values: **P* ≤ 0.05 and ***P* ≤ 0.01.

reagent for 2 minutes. The slides were then put in pure alcohol to dry them out. After sealed with resin, the slides were photographed with a microscope.

2.15. Statistical Analysis. GraphPad Prism 8, a tool developed by GraphPad Software, was used for statistical analysis, and all of the data were presented as means and standard deviations (SD). When looking at the data, the one-way analysis of variance (ANOVA) test with post hoc multiple comparisons was employed, and the Student *t*-test was used when comparing the two groups. It was deemed statistically significant to use a *P* value of 0.05, thus, that is what was utilized.

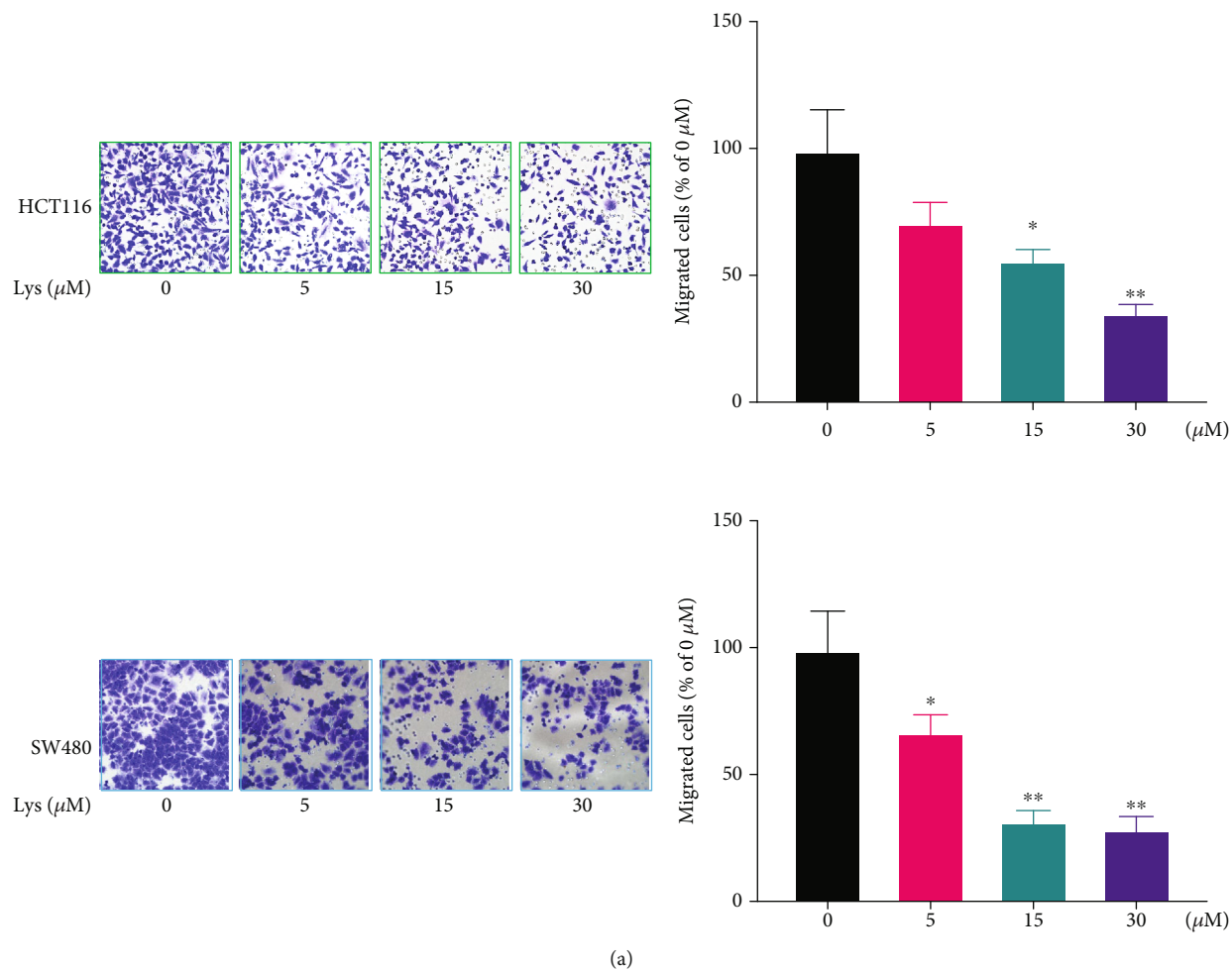
3. Results

3.1. Lys Restrained the Proliferation of HCT116 and SW480 Cells *In Vitro*. The chemistry formula of Lys is shown in Figure 1(a). The CCK-8 assay was used to measure the cytotoxicity of Lys in normal colon epithelial cells and CRC cell line cells. The results revealed that the cell viability was not decreased in the HIEC and NCM460 cells that were treated with Lys at dosages that were lower than 60 μM. (Figure 1(b)). However, 5 μM, 15 μM, or 30 μM concentrations of Lys effectively inhibited the proliferation of HCT116 and SW480 cell lines *in vitro* (Figure 1(c)). In line with this finding, morphological analysis showed that CRC cells were sensitive to Lys treatment at a dosage more than 5 μM (Figure 1(d)). Furthermore, Lys significantly decreased the growth of HCT116 and SW480 cell colonies by a lot (Figure 1(e)). So, our results showed that Lys therapy effectively stopped CRC cells from growing *in vitro*.

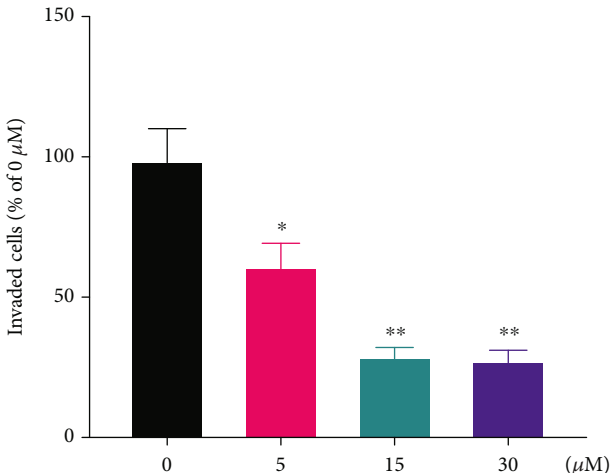
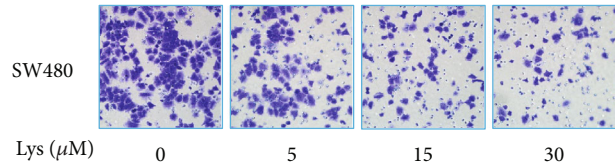
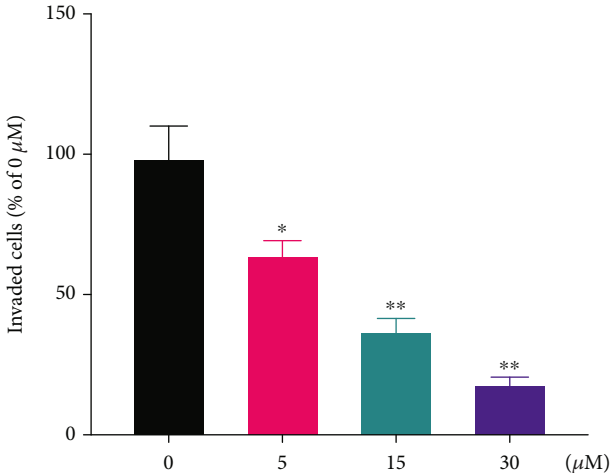
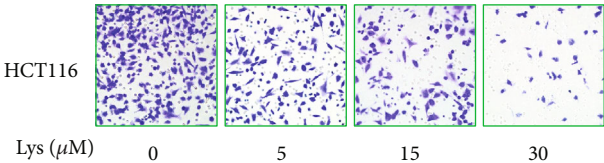
3.2. Lys Treatment Suppresses the Motility of HCT116 and SW480 Cells. Using wound healing, Transwell migration,

and invasion experiments with HCT116 and SW480 cells, the effects of Lys treatment on CRC cells motility were investigated. When HCT116 and SW480 cells were treated with Lys, the wounds that were caused by scratches took much longer to heal in comparison to when the cells were treated with a vehicle (Figure 2(a)). A dose-dependent reduction in the number of migrating (Figure 2(b)) and invading (Figure 2(c)) cells was seen in response to treatment with Lys, as shown by the findings of the Transwell test (see above). According to the findings, Lys significantly reduced the ability of CRC cells to migrate and disseminate *in vitro*.

3.3. Lys Induced Ferroptosis in CRC Cells. In ferroptosis, it is well known that lipid peroxidation and GSH depletion are important processes. After Lys was added to HCT116 and SW480 cells, the amount of ROS, GSH, and MDA inside the cells was measured. The results showed that after treatment with Lys, ROS went up (Figures 3(a) and 3(b)) and GSH went down (Figure 3(c)). Lys treatment, on the other hand, clearly raised the intracellular MDA levels (Figure 3(d)). Western blotting was used to determine the effects of Lys on ferroptosis makers. As shown in Figure 3(e), after treatment with Lys, the protein levels of FTH1, GPX4, glutaminase, and solute carrier family 7 member 11 (xCT/SLC7A11) in HCT116 and SW480 cells were significantly lower than in the control group. Ferroptosis is a buildup of cells that depends on iron. So, an iron probe, FerroOrange was used to measure the amount of iron inside HCT116 and SW480 cells. Lys-treated cells gave off a lot more orange light than cells that had not been treated (Figure 3(f)). In conclusion, the results of our studies demonstrated that Lys induced CRC cells to transition towards ferroptosis.

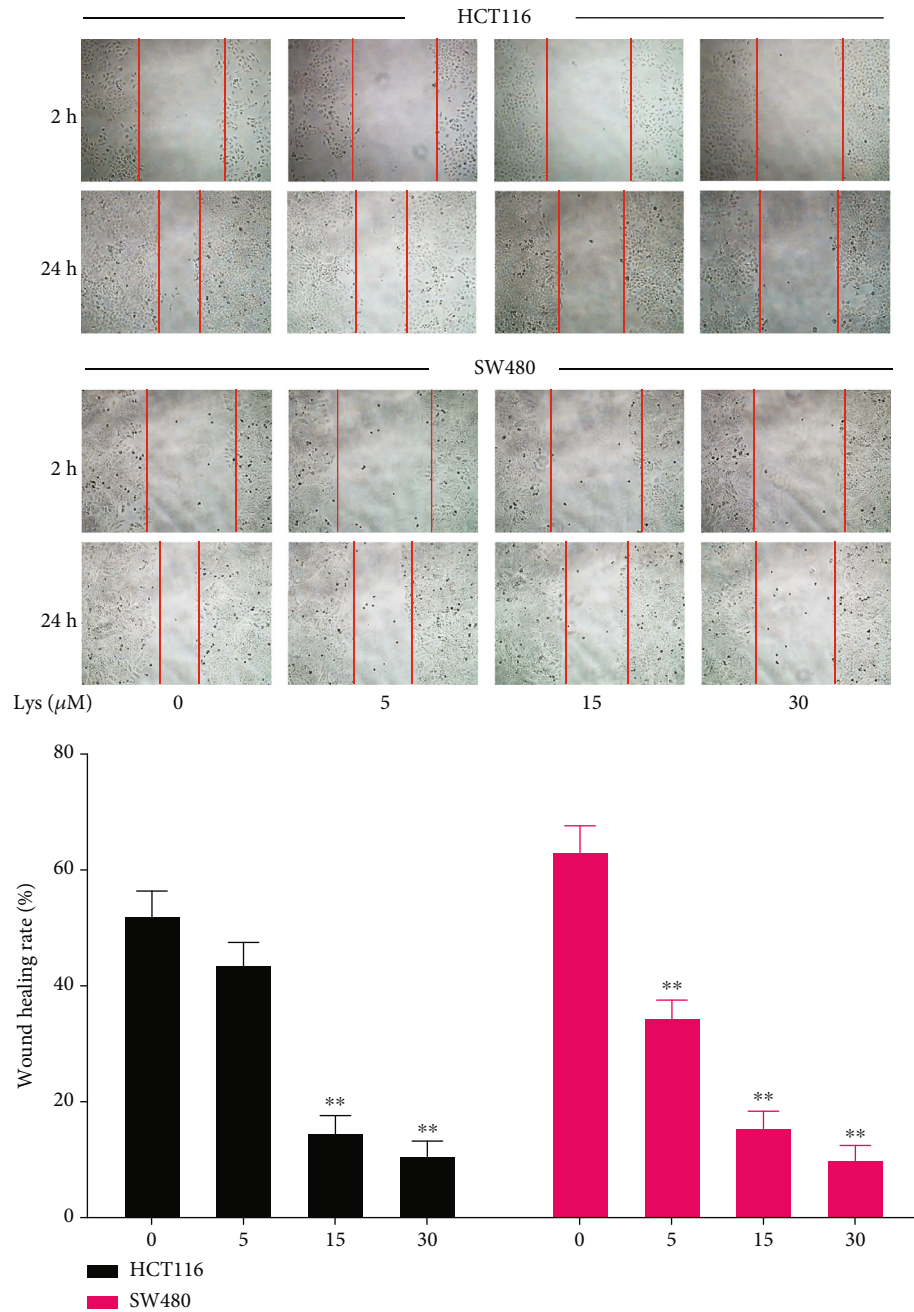


(a)
FIGURE 2: Continued.



(b)

FIGURE 2: Continued.



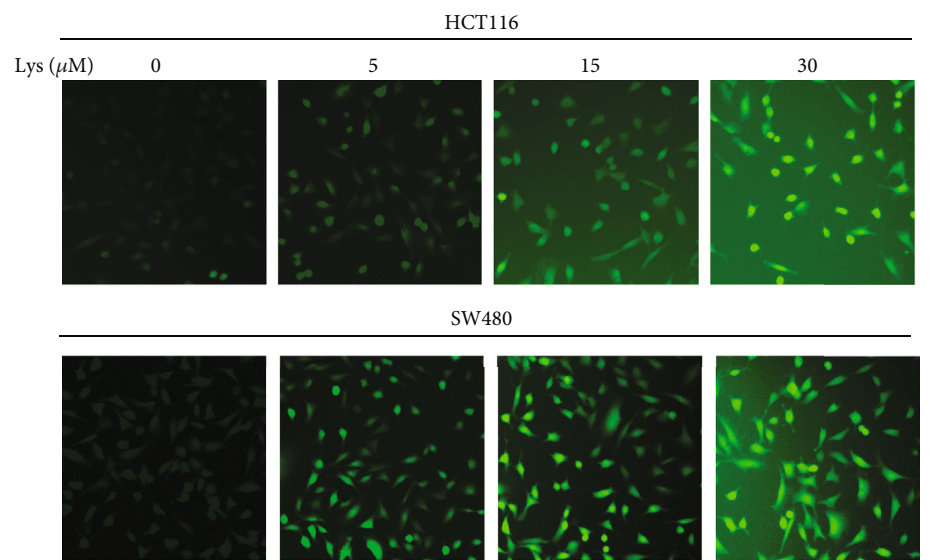
(c)

FIGURE 2: Lys treatment suppresses the migration and invasion of CRC cells. At 24 hours after incubating HCT116 and SW480 cells with Lys at concentrations ranging from 0-30 μ M, wound healing analysis (a) was used to analyze the effects of a therapy called Lys on the migration of CRC cells. The use of Transwell assays allowed for the investigation of the effects of Lys on the migration (b) and invasion (c) of CRC cells. *P* values: **P* \leq 0.05 and ***P* \leq 0.01.

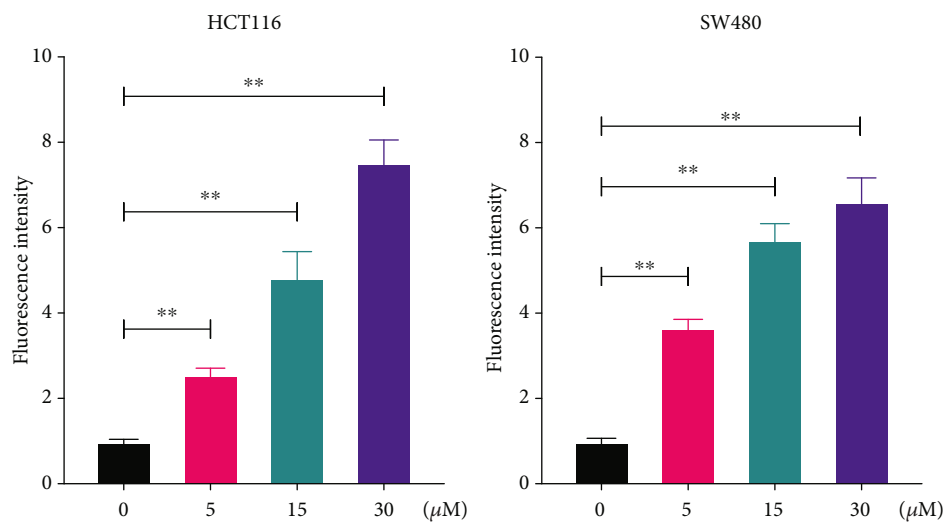
3.4. Inhibition of Ferroptosis Abrogates the Anti-CRC Effects of Lys *In Vitro*. To confirm the involvement of ferroptosis in the inhibitory effects of Lys in CRC, we pretreated the cells with Lip1, a ferroptosis inhibitor, before administering Lys. Lip1 pretreatment, as demonstrated in Figures 4(a) and 4(b), reversed the Lys-induced deficiency in proliferation and clonogenic ability of HCT116 and SW480 cells *in vitro*. Furthermore, Lip1 pretreatment reduced Lys' inhib-

itory effects on CRC cell migration (Figure 4(c)) and invasion (Figure 4(d)).

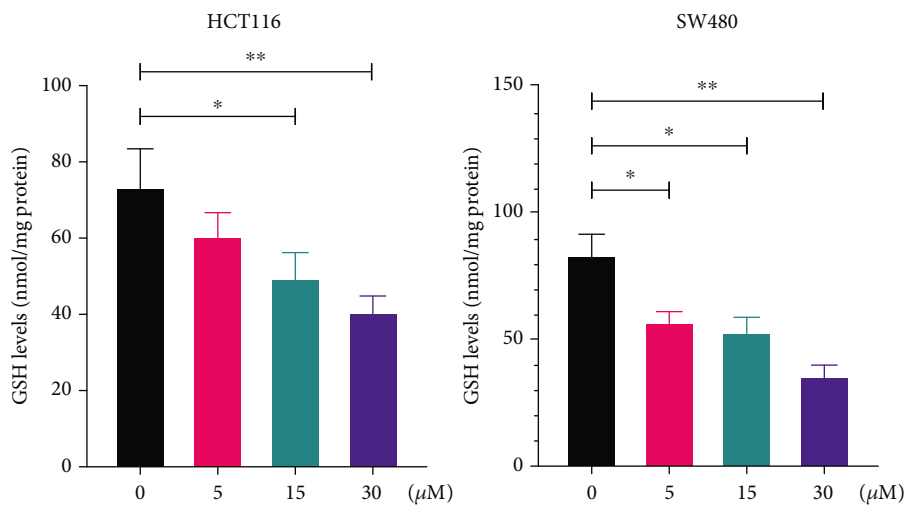
3.5. Lys Reduces Nrf2 Protein Levels by Promoting Nrf2 Protein Degradation. Nrf2 is a key regulator in cell redox and ferroptosis. The effects of Lys on the expression of the Nrf2 protein were then seen in HCT116 and SW480 cells. As shown in Figure 5(a), at concentrations of 5, 15, and



(a)

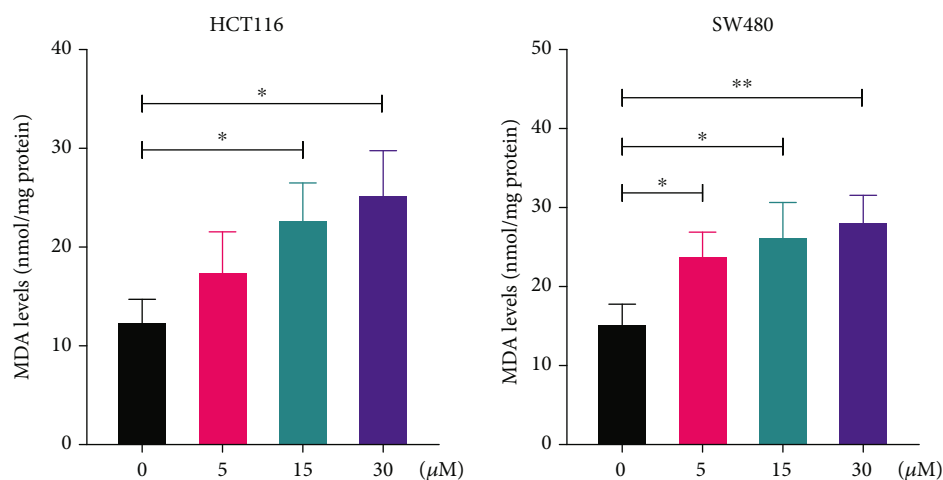


(b)

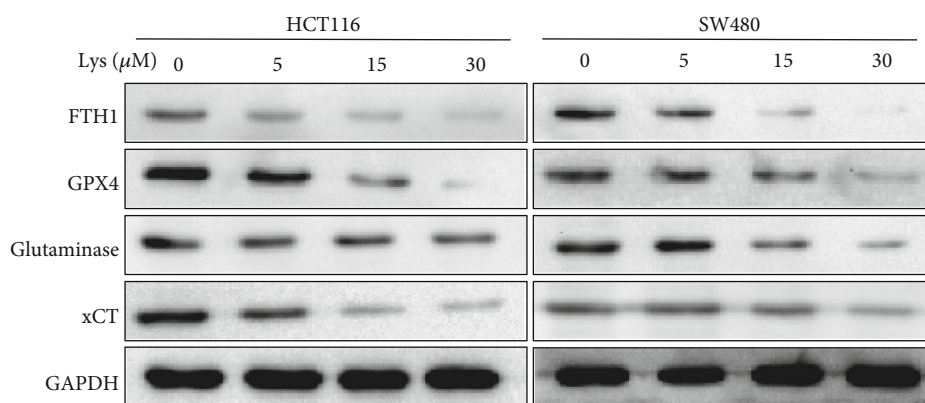


(c)

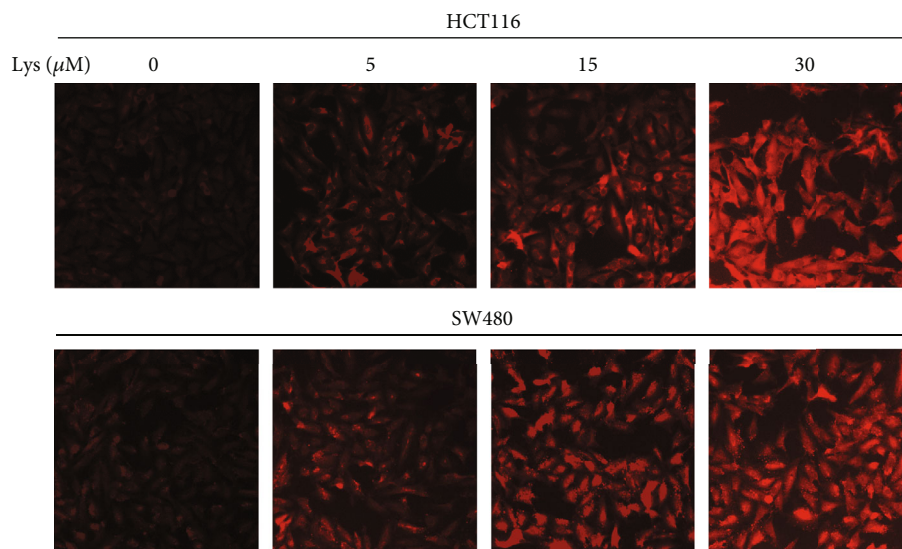
FIGURE 3: Continued.



(d)



(e)



(f)

FIGURE 3: Lys triggered ferroptosis in CRC cells. (a, b) ROS levels were measured by DCFH-DA staining after HCT116 and SW480 cells had been treated with Lys for 24 hours. The results are shown as the mean standard deviation. (c) The GSH level in HCT116 and SW480 cells was determined after the treatment with Lys for 24 hours, and the results showed that there was a significant difference between the groups. (d) The MDA level in HCT116 and SW480 cells was measured following the treatment with Lys for 24 hours. (e) Following a treatment with Lys for 24 hours, the iron content of HCT116 and SW480 cells was evaluated using the ferroOrange staining method. (f) Western blotting was used in order to identify a number of proteins connected to ferroptosis. * $P < 0.05$ and ** $P < 0.01$.

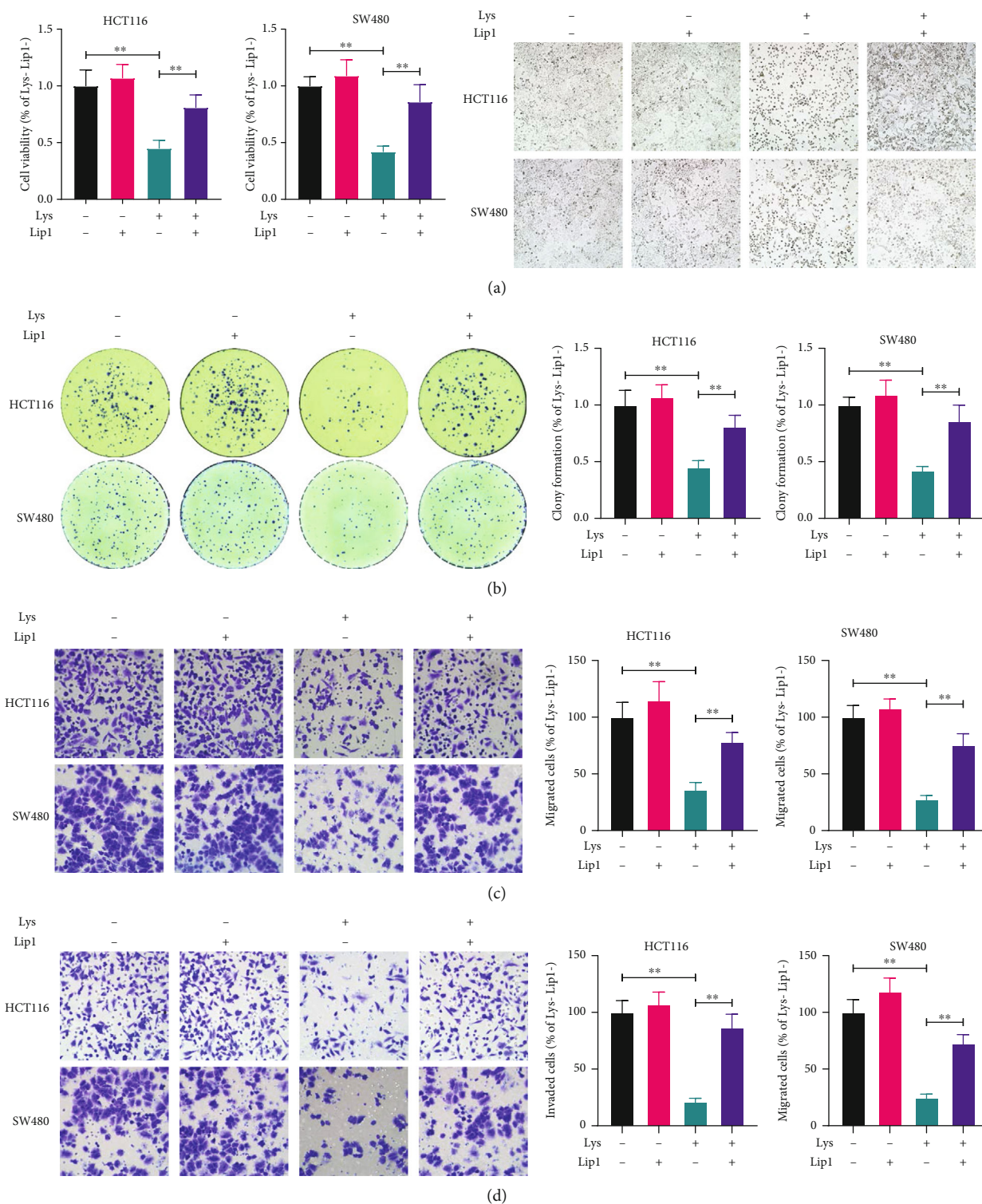


FIGURE 4: Lip1 pretreatment abolished Lys-mediated suppression of CRC cells. Prior to the addition of 30 M of Lys, HCT116 and SW480 cells were pretreated with Lip1 at a concentration of 200 nM for six hours. The CCK-8 test and the clonogenic assay were used to determine the level of cell viability (b) and survival (c), respectively, 24 hours after Lys was administered. The Transwell test was used to ascertain the level of motility present in CRC cells (c, d). The data are either pictures that are typical of the whole or are given as the mean plus the standard deviation. * $P < 0.05$, ** $P < 0.01$.

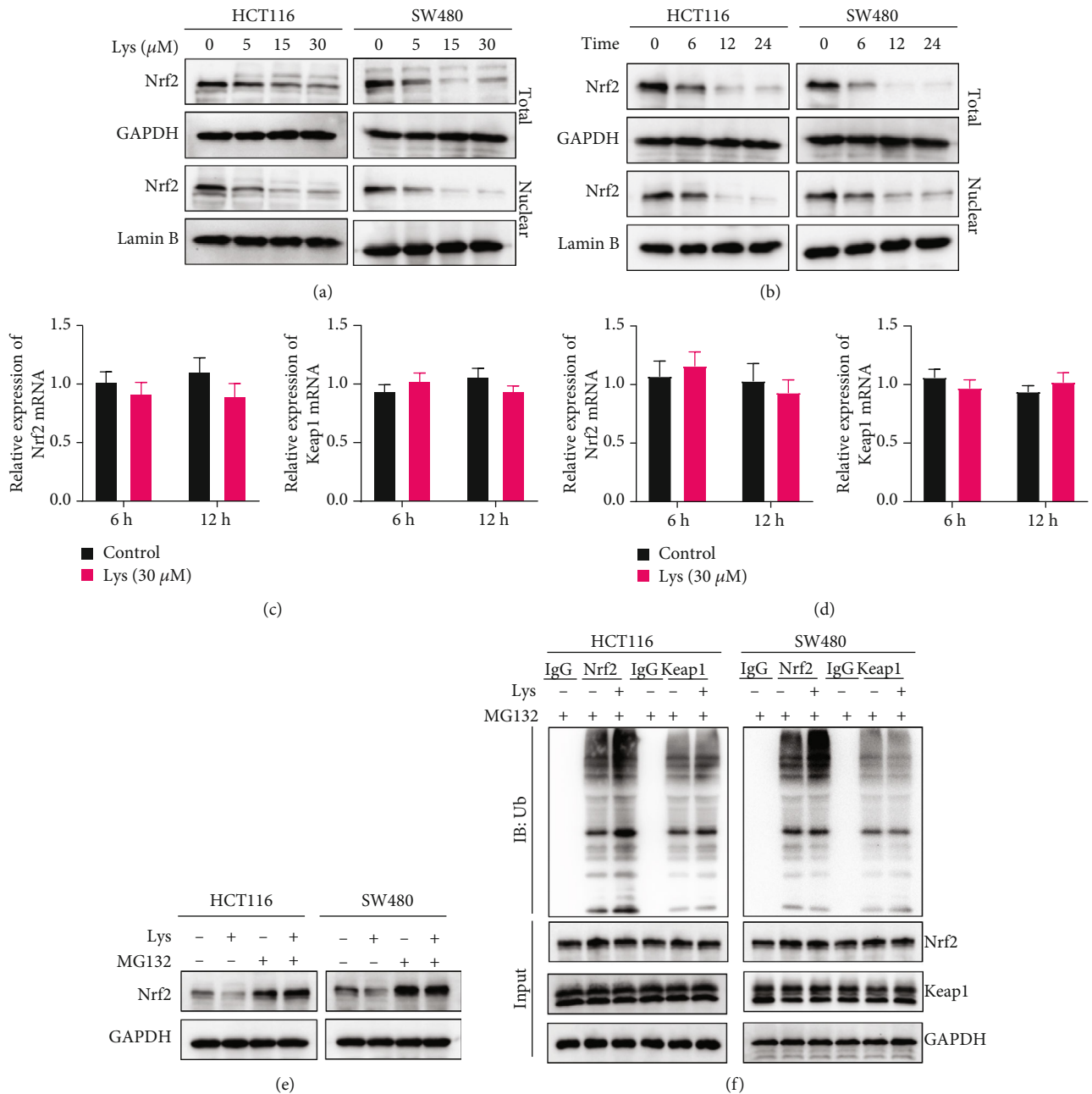


FIGURE 5: Lys inhibits Nrf2 protein levels in HCT116 and SW480 cells. (a) HCT116 and SW480 cells were treated with varying doses of Lys (ranging from 0 to 30 μM) over a period of 24 hours, and western blot analysis was done to determine the amount of the Nrf2 protein produced. (b) HCT116 and SW480 cells were treated with 30 μM of Lys for 6 hours, 12 hours, and 24 hours, and western blot analysis was done to determine how much Nrf2 protein was produced. qRT-PCR was performed to quantify the mRNA levels of Nrf2 and Keap1 in CRC cells after HCT116 and SW480 cells were treated with 30 μM of Lys for a duration of 6 hours and 12 hours (c, d). (e) HCT116 and SW480 cells were treated with 30 μM of Lys, 10 μM of MG132, or a combination of Lys and MG132 for a period of 12 hours, and then, the protein levels of Nrf2 were analyzed by western blotting. (f) The ubiquitination test was used to determine the levels of ubiquitination of Nrf2 in HCT116 and SW480 cells after they were treated with or without 30 μM of Lys for a period of 12 hours. The data are presented as the mean standard deviation, with a sample size of three.

30 μM , Lys drastically downregulated the amount of Nrf2 protein in cells. Also, the amount of Nrf2 protein in cells was much lower at 6, 12, and 24 h after being treated with 30 μM Lys (Figure 5(b)). Additionally, quantitative reverse transcription-PCR was used to determine the mRNA levels of Nrf2 and Keap1 in Lys-treated HCT116 and SW480 cell

cultures. Because the findings revealed that there was no significant difference between the mRNA levels of Nrf2 and Keap1 in Lys-treated cells and control cells (Figures 5(c) and 5(d)), indicating that Lys does not inhibit the transcription of Nrf2. In light of this, we investigated whether or not Lys decreases the quantity of Nrf2 protein by affecting its

protein stability. As shown in Figure 5(e), the proteasomal inhibitor MG132 protected the levels of Nrf2 in CRC cells from Lys treatment. Also, research on ubiquitination showed that the levels of ubiquitination of Nrf2 in cells were much higher after Lys treatment (Figure 5(f)). Also, when cells were treated with Lys, the level of ubiquitination of Keap1 did not change much (Figure 5(f)). These results suggest that Lys downregulated the amount of Nrf2 protein in CRC cells by speeding up the degradation of Nrf2 protein.

3.6. Overexpression of Nrf2 Retarded Lys Induced Ferroptosis. Recent studies have demonstrated that inhibiting the activity of the Nrf2 signaling pathway is essential to preventing cancer from expanding and halting the process of ferroptosis. We employed a Nrf2 expressing vector to specifically boost the activation of Nrf2 in order to get a better understanding of the relationship that exists between the Lys-induced ferroptosis and the Nrf2 signaling. We discovered that increasing the amount of Nrf2 in the cell led to an increase in the expression of GPX4, ferritin, xCT, and glutaminase, while Lys treatment made the expression of all of these genes go down (Figure 6(a)). By overexpressing Nrf2, both Lys-induced increases in intracellular iron (Figure 6(b)) and ROS (Figure 6(c)) were reversed. Also, Nrf2 overexpression helped a lot to fix the lower GSH levels and higher MDA levels that Lys treatment caused (Figures 6(d) and 6(e)). Based on these results, it seems likely that Lys-induced ferroptosis in CRC cells is mostly controlled by modulating Nrf2 signals.

3.7. Lys Inhibits Tumor Growth In Vivo by Activating Ferroptosis. The antitumor properties of Lys were studied further *in vivo*. The results showed that administration of Lys to mice with SW480 tumor xenografts greatly reduced tumor growth, whereas Lip1 treatment decreased Lys' antitumor potential (Figures 7(a) and 7(b)). The weight of the mice did not change when Lys and/or Lip1 were used (Figure 7(c)). Also, the results of histopathology studies showed that treatment with Lys and/or Lip1 showed no obvious toxicities to the main organs of mice, including the lung, heart, liver, and kidney (Figure 7(e)), suggesting that Lys treatment with efficient dosage does not exert side effects *in vivo*.

4. Discussion

Therapeutic reagents derived from phytomedicine have been used in China for thousands of years [35, 36]. The fact that Lys is a trimethoxyflavone denotes that it has methoxy groups at positions 6, 8, and 4' in addition to hydroxy groups at positions 5 and 7 in the chemical structure [37]. It functions as a phytometabolite and consists of both trimethoxyflavone and dihydroxyflavone. Lys naturally exists as a free chemical or a glycoside in the leaves and flowers of the Gesneriaceae family [38]. Clearly, Lys suppresses *Staphylococcus aureus* [38], and the activity of cytochrome P450 enzymes *in vitro* [37]. Lys also mediated mitochondrial apoptosis in hepatocellular carcinoma cells via activating caspase-3 [39]. Despite these various effects, the therapeutic

benefits of Lys for CRC remain undetermined. *In vitro* cell viability experiments utilizing cell cultures demonstrated that Lys treatment may inhibit the development and survival of CRC cells without harming normal colon epithelial cells. In contrast, wound healing, Transwell migration, and invasion experiments were performed on HCT116 and SW480 cells to determine the effects of Lys treatment on CRC cell movement and invasion. Results surface Lys-treated HCT116 and SW480 cells displayed a slower rate of wound healing than vehicle-treated cells. In addition, the Transwell test results revealed that Lys treatment dose dependently decreased the number of migrating and invading cells. We made the discovery that Lys has the potential to inhibit the formation of tumors and the invasion of CRC cells *in vivo*.

Recent research has revealed that triggering ferroptosis dramatically reduces the risk of developing a tumor, as well as increases the efficiency of both targeted treatment and chemotherapy [40]. It has been shown, for example, that vitamin C may trigger ferroptosis and that treating RAS/BRAF wild-type CRC patients with a combination therapy consisting of vitamin C and cetuximab may prevent the development of acquired resistance to cetuximab in such patients [41]. Upregulation of MT-1G expression results in a reduction in ferroptosis, which in turn protects hepatocellular carcinoma cells from the action of sorafenib and contributes to the progression of cancer [42]. The use of erastin, even for a short period of time, amplifies the cytotoxic effects of cisplatin to a significant degree [43]. Ferroptosis is induced in p53 mutant hypopharyngeal squamous cell carcinoma cells by treatment with paclitaxel and RSL3 at low doses [44]. When compared to the control group, the Lys treatment led to a decrease in the amount of protein that was found in FTH1, GPX4, glutaminase, and solute carrier family 7 member 11 (xCT/SLC7A11) in HCT116 and SW480 cells. In addition, the iron probe FerroOrange was used to examine the quantities of intracellular iron present in HCT116 and SW480 cells. When compared to untreated cells, cells that had been treated with Lys produced a much higher amount of orange fluorescence. The inhibitory effects of Lys on the migration and invasion of CRC cells were reduced when the cells were pretreated with Lip1. This provides more evidence that ferroptosis occurred in CRC cells that had been treated with Lys.

External stimuli (e.g., drugs, UV, and ionizing radiation) and endogenous free radicals and reactive oxygen species (ROS) can directly or indirectly damage cellular components such as proteins, lipids, and DNA [45]. To defend against these adverse effects, the body has developed a complex set of oxidative stress response systems to mitigate cell damage. In addition, Nrf2, which is a crucial transcription factor in the regulation of antioxidant stress, plays a crucial role in the induction of the body's antioxidant response [46, 47]. This includes the regulation of redox balance, drug metabolism and excretion, energy metabolism, iron metabolism, amino acid metabolism, survival, proliferation, autophagy, proteasomal degradation, DNA repair, and mitochondrial physiology, among other processes [48]. In addition, the Keap1-Nrf2 system has recently emerged as an important therapeutic target in the treatment of a variety of diseases,

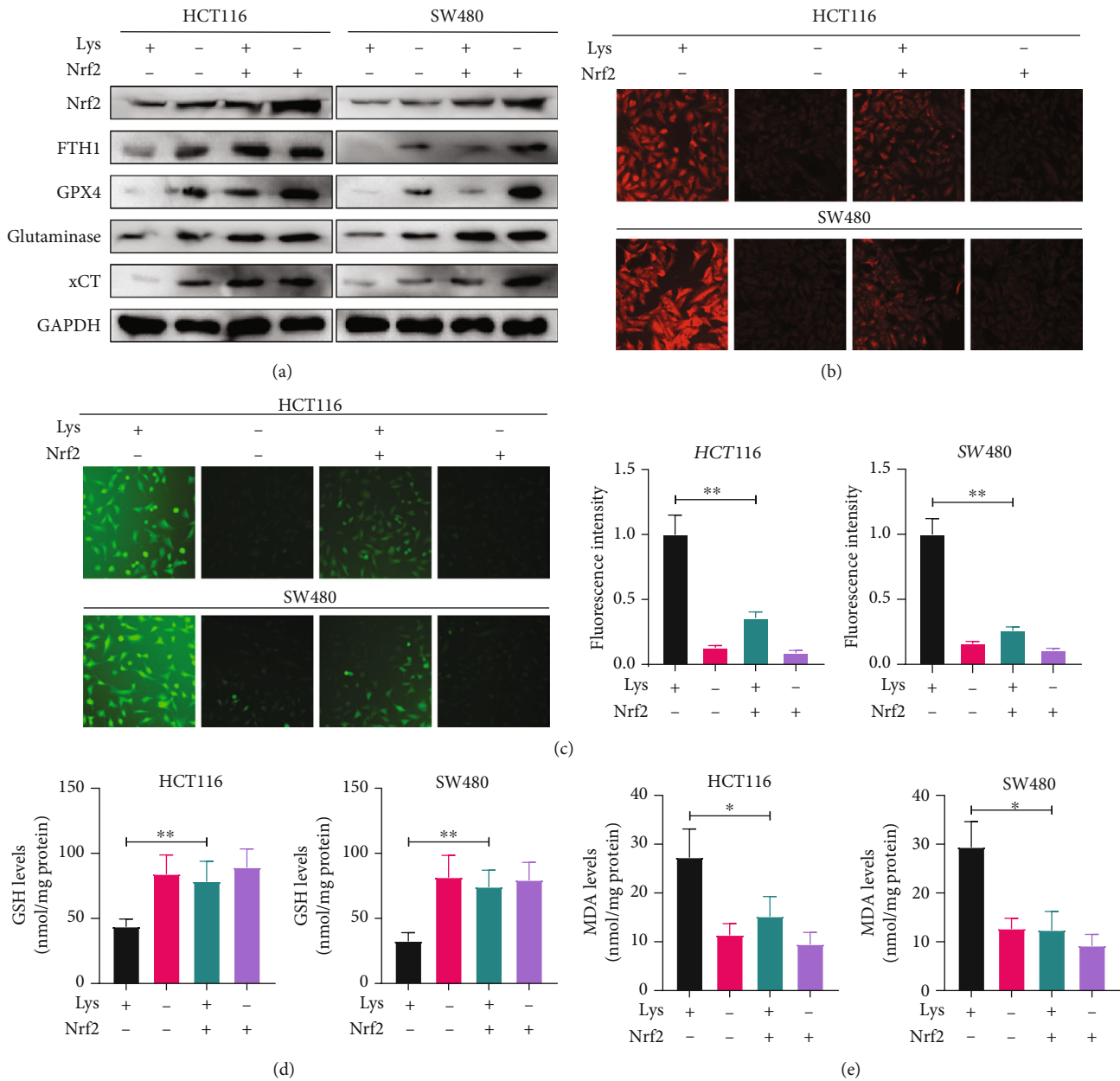


FIGURE 6: Lys triggered ferroptosis via the Nrf2 pathway. After transfecting the HCT116 and SW480 cells with an empty vector or Nrf2 for 18 hours, the cells were treated with Lys for an additional 24 hours. (a) Using immunoblotting, we examined the levels of Nrf2, GPX4, ferritin, and glutaminase expression in HCT116 and SW480 cells. (b) FerroOrange staining was used to determine the amount of iron present in HCT116 and SW480 cells. (c) A flow cytometer was used to determine the ROS level; the mean and standard deviation are shown here, * $P < 0.05$. (d, e) Commercial kits were used to determine the GSH levels and MDA levels in HCT116 and SW480 cells, respectively. After being treated with Lys for 24 hours, the results were as follows: * $P < 0.05$, ** $P < 0.01$.

including cancer, neurological disorders, autoimmune diseases, and inflammatory conditions [49]. Activation of the Keap1-Nrf2 pathway is one of the most essential antitumorigenesis pathways [49]. Not only synthetic drugs, such as oltipraz, but also plant-derived substances, such as sulforaphane, curcumin, resveratrol, etc., regulate genes and have chemopreventive effects by targeting the Nrf2 pathway [50]. Enhancing the activity of Nrf2 is a tried-and-true method for preventing chronic illnesses and cancer originating from oxidative and inflammatory stress [48]. However, constitu-

tive activation of Nrf2 in diverse tumors will boost cancer cell proliferation and result in chemoresistance and radioreistance of cancer cells. In our work, we discovered that Lys reduces Nrf2 protein levels in CRC cells by promoting their degradation. Lys at doses of 5, 15, and 30 μM significantly decreased cellular Nrf2 protein levels. At 6, 12, and 24 hours after a 30 μM Lys treatment, the Nrf2 protein level in cells was seen to be significantly reduced. In addition, quantitative real-time polymerase chain reaction (qRT-PCR) was used to detect the mRNA levels of Nrf2 and Keap1 in

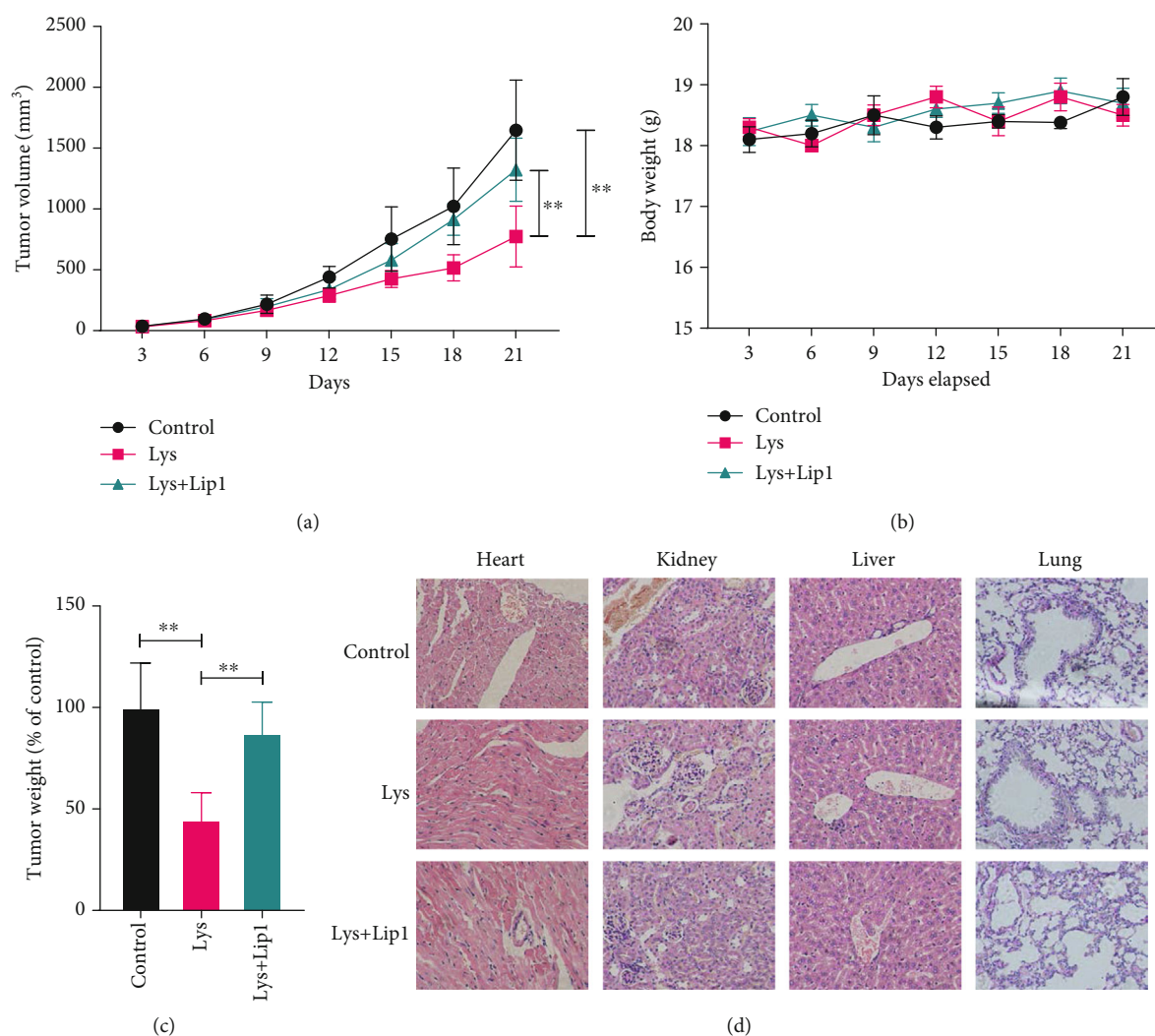


FIGURE 7: Lys suppresses CRC development *in vivo* through priming ferroptosis. Seven days following the xenograft, the patient received an intraperitoneal (i.p.) injection of Lys containing 20 mg/kg once every three days for a total of four doses. In order to suppress ferroptosis, Lip1 (10 milligrams per kilogram) was injected intraperitoneally (i.p.) once day after the administration of Lys up to the time of sacrifice. At the end of the 24th day following the xenograft, all of the mice were put to sleep, and the weight and volume of the tumor were measured. (c) The total number of treatments continued till the body weight of the mice was recorded. (d) Histological data of H&E staining performed on samples taken from various experimental groups' hearts, kidneys, and livers; P values: $*P \leq 0.05$, $**P \leq 0.01$.

HCT116 and SW480 cells after treatment with Lys. The results showed that there was no significant difference in the mRNA levels of Nrf2 and Keap1 between Lys treated cells and control cells, which suggests that Lys does not inhibit the transcription of Nrf2. Determining if activation of Nrf2 causes cancer, how to target Nrf2 (direct or indirect suppression of upstream protein kinases), and elucidating the structure of Keap1 have therefore been the focus of academic research. Following Lys therapy, Nrf2 ubiquitination levels were significantly raised, according to study on ubiquitination. Keap1 ubiquitination levels did not change significantly after Lys treatment, indicating that Keap1 is not required for Lys-induced degradation of the Nrf2 protein.

Nrf2 served as a key regulator in ferroptosis, due to its functions in maintaining the redox homeostasis and directly regulating the ferroptosis related genes such as GPX4, xCT,

ferritin, and glutaminase [51, 52]. In order to get a deeper understanding of the connection between Lys-induced ferroptosis and Nrf2 signaling, we transfected a Nrf2 expressing vector into the cells in order to selectively stimulate Nrf2 activity. We found that Nrf2 overexpression boosted the expression of Nrf2, GPX4, ferritin, xCT, and glutaminase, which were all reduced by Lys treatment. The buildup of intracellular iron and reactive oxygen species produced by Lys was reduced by Nrf2 overexpression. In addition, Nrf2 overexpression dramatically reversed the Lys-induced decrease in GSH levels and rise in MDA levels. According to these findings, the Nrf2 signaling pathway is a crucial regulator of the Lys-induced ferroptosis that occurs in CRC cells. *In vivo* examination of Lys' antitumor capabilities revealed that injection of Lys significantly reduced tumor formation in mice harboring SW480 tumor xenografts, but

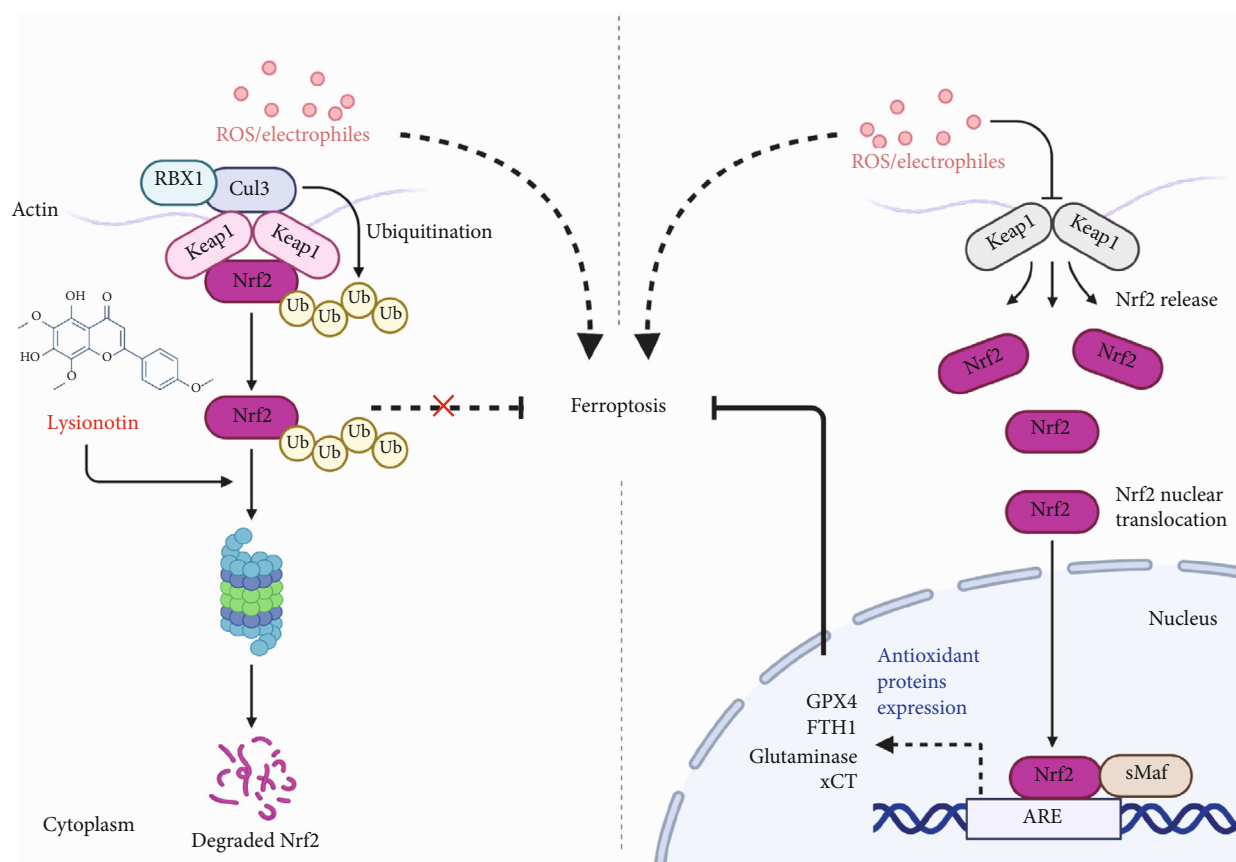


FIGURE 8: Schematic diagram of the pharmacology effects of Lys.

Lip1 therapy lowered Lys' antitumor capability. The use of Lys and/or Lip1 had no impact on the mice's weight. In addition, histological evidence showed that treatments with Lys and/or lip1 did not result in toxicity in the main organs of mice. These organs include the lung, the heart, the liver, and the kidneys.

Here are the limitations of our study: First, we exclusively evaluated the impact of Lys on HCT116 and SW480 CRC cells using *in vitro* cell culture procedures, despite the fact that the human environment and *in vitro* conditions are quite different. Consequently, the findings of this investigation cannot alone inform therapeutic practice. We delivered just three doses of Lys, namely, 5, 15, and 30 mg, and observed only six, twelve, and 24 hours for three time points. This is incongruous with the biological rhythm and timing of therapy in CRC. We feel that repeated usage of Lys (4-6 h dosage interval) may one day be used as an adjuvant therapy for CRC. We cannot rule out the possibility that Lys is a predictor of intestinal damage in patients with colorectal cancer due to the fact that Lys experiments were conducted on the body of mice, whereas the rectal region is the primary site of CRC onset in humans, where the cell types and arrangement structure are quite different from mice.

In summary, the findings of our study revealed that Lys inhibited the progression of colorectal cancer via induction of ferroptosis. We also provide evidence that Lys promotes the degradation of Nrf2 in proteasome, which contributes

to its pharmacology effects in regulating ROS accumulation and ferroptosis (Figure 8), suggesting it can be used as a chemotherapeutic agent for the treatment of CRC.

Data Availability

The data used to support the findings of this study are included within the article.

Conflicts of Interest

The authors declare that they have no conflicts of interest.

Acknowledgments

This study is funded by the Jilin University (2019932240).

References

- [1] F. Bray, J. Ferlay, I. Soerjomataram, R. L. Siegel, L. A. Torre, and A. Jemal, "Global cancer statistics 2018: GLOBOCAN estimates of incidence and mortality worldwide for 36 cancers in 185 countries," *CA: a Cancer Journal for Clinicians*, vol. 68, no. 6, pp. 394-424, 2018.
- [2] R. L. Siegel, K. D. Miller, H. E. Fuchs, and A. Jemal, "Cancer statistics, 2021," *CA: A Cancer Journal for Clinicians*, vol. 71, no. 1, pp. 7-33, 2021.

- [3] C. Li, H. Zheng, H. Jia et al., "Prognosis of three histological subtypes of colorectal adenocarcinoma: a retrospective analysis of 8005 Chinese patients," *Cancer Medicine*, vol. 8, no. 7, pp. 3411–3419, 2019.
- [4] Y. H. Xie, Y. X. Chen, and J. Y. Fang, "Comprehensive review of targeted therapy for colorectal cancer," *Signal Transduction and Targeted Therapy*, vol. 5, no. 1, p. 22, 2020.
- [5] Z. Wen, W. Hou, W. Wu et al., "6'-O-Galloylpaeoniflorin attenuates cerebral ischemia reperfusion-induced neuroinflammation and oxidative stress via PI3K/Akt/Nrf2 activation," *Oxidative Medicine and Cellular Longevity*, vol. 2018, 2018.
- [6] J. Gao, L. Song, H. Xia, L. Peng, and Z. Wen, "6'-O-galloylpaeoniflorin regulates proliferation and metastasis of non-small cell lung cancer through AMPK/miR-299-5p/ATF2 axis," *Respiratory Research*, vol. 21, no. 1, p. 39, 2020.
- [7] Y. Zhu, D. Sun, H. Liu et al., "Bixin protects mice against bronchial asthma through modulating PI3K/Akt pathway," *International Immunopharmacology*, vol. 101, p. 108266, 2021.
- [8] C. Wang, J. Luo, X. Bai et al., "Calycosin alleviates injury in airway epithelial cells caused by PM 2.5 exposure via activation of AMPK signalling," *Evidence-based Complementary and Alternative Medicine*, vol. 2021, Article ID 8885716, 2021.
- [9] L. Song, X. Li, X. X. Bai, J. Gao, and C. Y. Wang, "Calycosin improves cognitive function in a transgenic mouse model of Alzheimer's disease by activating the protein kinase C pathway," *Neural Regeneration Research*, vol. 12, no. 11, pp. 1870–1876, 2017.
- [10] Y. Zhang, Y. Liu, J. Luo, J. Jie, X. Deng, and L. Song, "The herbal compound thymol targets multiple Salmonella typhimurium virulence factors for Lon protease degradation," *Frontiers in Pharmacology*, vol. 12, p. 674955, 2021.
- [11] X. Bai, Y. Zhu, J. Jie, D. Li, L. Song, and J. Luo, "Maackiain protects against sepsis via activating AMPK/Nrf2/HO-1 pathway," *International Immunopharmacology*, vol. 108, p. 108710, 2022.
- [12] Y. Zhu, C. Wang, J. Luo et al., "The protective role of Zingerone in a murine asthma model via activation of the AMPK/Nrf2/HO-1 pathway," *Food & Function*, vol. 12, no. 7, pp. 3120–3131, 2021.
- [13] J. Xu, J. Zhang, and J. Wang, "The application of traditional Chinese medicine against the tumor immune escape," *Journal of Translational Internal Medicine*, vol. 8, no. 4, pp. 203–204, 2020.
- [14] M. E. Wall and M. C. Wani, "Camptothecin and taxol: discovery to clinic - thirteenth Bruce F. Cain Memorial Award lecture," *Cancer Research*, vol. 55, no. 4, pp. 753–760, 1995.
- [15] O. Tacar, P. Sriamornsak, and C. R. Dass, "Doxorubicin: an update on anticancer molecular action, toxicity and novel drug delivery systems," *The Journal of Pharmacy and Pharmacology*, vol. 65, pp. 157–170, 2012.
- [16] A. Lichota and K. Gwozdziński, "Anticancer activity of natural compounds from plant and marine environment," *International journal of molecular sciences*, vol. 19, no. 11, p. 3533, 2018.
- [17] S. Rivankar, "An overview of doxorubicin formulations in cancer therapy," *Journal of Cancer Research & Therapeutics*, vol. 10, no. 4, pp. 853–858, 2014.
- [18] M. Zhu, Q. Ding, Z. Lin, X. Chen, S. Chen, and Y. Zhu, "New insights of epigenetics in vascular and cellular senescence," *Journal of Translational Internal Medicine*, vol. 9, no. 4, pp. 239–248, 2021.
- [19] E. P. McGrath, F. G. Centonze, E. Chevet, T. Avril, and E. Lafont, "Death sentence: the tale of a fallen endoplasmic reticulum," *Biochimica et Biophysica Acta (BBA) - Molecular Cell Research*, vol. 2021, p. 119001, 2021.
- [20] J. Li, F. Cao, H. L. Yin, Z. J. Huang, and G. Wang, "Ferroptosis: past, present and future," *Cell Death & Disease*, vol. 11, no. 2, p. 88, 2020.
- [21] Y. Liu and W. Gu, "p53 in ferroptosis regulation: the new weapon for the old guardian," *Cell Death and Differentiation*, vol. 29, no. 5, pp. 895–910, 2022.
- [22] N. Bresgen and P. M. Eckl, "Oxidative stress and the homeodynamics of iron metabolism," *Biomolecules*, vol. 5, no. 2, pp. 808–847, 2015.
- [23] Y. Liu, O. Tavana, and W. Gu, "p53 modifications: exquisite decorations of the powerful guardian," *Journal of Molecular Cell Biology*, vol. 11, no. 7, pp. 564–577, 2019.
- [24] Y. Liu and W. Gu, "The complexity of p53-mediated metabolic regulation in tumor suppression," in *Seminars in Cancer Biology*, Academic Press, 2021.
- [25] J. S. Lou, L. P. Zhao, Z. H. Huang et al., "Ginkgetin derived from Ginkgo biloba leaves enhances the therapeutic effect of cisplatin via ferroptosis-mediated disruption of the Nrf2/HO-1 axis in EGFR wild-type non-small-cell lung cancer," *Phytomedicine*, vol. 80, p. 153370, 2021.
- [26] Y. Xiang, X. Chen, W. Wang et al., "Natural product erianin inhibits bladder cancer cell growth by inducing ferroptosis via NRF2 inactivation," *Frontiers in Pharmacology*, vol. 12, p. 775506, 2021.
- [27] Z. Song, X. Xiang, J. Li et al., "Ruscogenin induces ferroptosis in pancreatic cancer cells," *Oncology Reports*, vol. 43, pp. 516–524, 2019.
- [28] L. Song, L. Peng, S. Hua et al., "miR-144-5p enhances the radiosensitivity of non-small-cell lung cancer cells via targeting ATF2," *BioMed research international*, vol. 2018, Article ID 5109497, 2018.
- [29] L. Song, Y. Xie, C. Li et al., "The Legionella effector SdjA is a bifunctional enzyme that distinctly regulates phosphoribosyl ubiquitination," *mBio*, vol. 12, no. 5, article e0231621, 2021.
- [30] L. Song, J. Luo, H. Wang et al., "Legionella pneumophila regulates host cell motility by targeting Phldb2 with a 14-3-3zeta-dependent protease effector," *Elife*, vol. 11, 2022.
- [31] L. Song, D. Li, Y. Gu et al., "MicroRNA-126 targeting PIK3R2 inhibits NSCLC A549 cell proliferation, migration, and invasion by regulation of PTEN/PI3K/AKT pathway," *Clinical Lung Cancer*, vol. 17, no. 5, pp. e65–e75, 2016.
- [32] J. Fu, M. Zhou, M. A. Gritsenko, E. S. Nakayasu, L. Song, and Z. Q. Luo, "Legionella pneumophila modulates host energy metabolism by ADP-ribosylation of ADP/ATP translocases," *Elife*, vol. 11, 2022.
- [33] Y. Zhang, J. Fu, S. Liu et al., "Coxiella burnetii inhibits host immunity by a protein phosphatase adapted from glycolysis," *Proceedings of the National Academy of Sciences*, vol. 119, article e2110877119, 2022.
- [34] L. Song, D. Li, Y. Gu, X. Li, and L. Peng, "let-7a modulates particulate matter ($\leq 2.5 \mu\text{m}$)-induced oxidative stress and injury in human airway epithelial cells by targeting arginase 2," *Journal of Applied Toxicology*, vol. 36, no. 10, pp. 1302–1310, 2016.
- [35] X. H. Wang, R. Lang, Y. Liang, Q. Zeng, N. Chen, and R. H. Yu, "Traditional Chinese medicine in treating IgA nephropathy: from basic science to clinical research," *Journal of Translational Internal Medicine*, vol. 9, no. 3, pp. 161–167, 2021.

- [36] X. F. Zhou, W. E. Zhou, W. J. Liu et al., "A network pharmacology approach to explore the mechanism of HuangZhi YiShen capsule for treatment of diabetic kidney disease," *Journal of Translational Internal Medicine*, vol. 9, no. 2, pp. 98–113, 2021.
- [37] Y. Li, J. Qin, H. Wu, Y. Xu, and H. Wang, "In vitro inhibitory effect of lysionotin on the activity of cytochrome P450 enzymes," *Pharmaceutical Biology*, vol. 58, no. 1, pp. 695–700, 2020.
- [38] Z. Teng, D. Shi, H. Liu et al., "Lysionotin attenuates Staphylococcus aureus pathogenicity by inhibiting α -toxin expression," *Applied Microbiology & Biotechnology*, vol. 101, no. 17, pp. 6697–6703, 2017.
- [39] A. Yang, P. Zhang, Z. Sun et al., "Lysionotin induces apoptosis of hepatocellular carcinoma cells via caspase-3 mediated mitochondrial pathway," *Chemico-Biological Interactions*, vol. 344, p. 109500, 2021.
- [40] M. J. Kim, G. J. Yun, and S. E. Kim, "Metabolic regulation of ferroptosis in cancer," *Biology*, vol. 10, no. 2, p. 83, 2021.
- [41] X. Wang, S. Xu, L. Zhang et al., "Vitamin C induces ferroptosis in anaplastic thyroid cancer cells by ferritinophagy activation," *Biochemical and Biophysical Research Communications*, vol. 551, pp. 46–53, 2021.
- [42] X. Sun, X. Niu, R. Chen et al., "Metallothionein-1G facilitates sorafenib resistance through inhibition of ferroptosis," *Hepatology*, vol. 64, no. 2, pp. 488–500, 2016.
- [43] Y. Zhao, Y. Li, R. Zhang, F. Wang, T. Wang, and Y. Jiao, "The role of erastin in ferroptosis and its prospects in cancer therapy," *OncoTargets and therapy*, vol. 13, pp. 5429–5441, 2020.
- [44] J. Ye, X. Jiang, Z. Dong, S. Hu, and M. Xiao, "Low-concentration PTX and RSL3 inhibits tumor cell growth synergistically by inducing ferroptosis in mutant p53 hypopharyngeal squamous carcinoma," *Cancer Management and Research*, vol. 11, pp. 9783–9792, 2019.
- [45] G. Pizzino, N. Irrera, M. Cucinotta et al., "Oxidative stress: harms and benefits for human health," *Oxidative Medicine and Cellular Longevity*, vol. 2017, 2017.
- [46] I. Bellezza, I. Giambanco, A. Minelli, and R. Donato, "Nrf2-Keap1 signaling in oxidative and reductive stress," *Biochimica et Biophysica Acta (BBA)-Molecular Cell Research*, vol. 1865, no. 5, pp. 721–733, 2018.
- [47] H. Qian, Y. Zhang, B. Wu et al., "Structure and function of HECT E3 ubiquitin ligases and their role in oxidative stress," *Journal of Translational Internal Medicine*, vol. 8, no. 2, pp. 71–79, 2020.
- [48] A. V. Ulasov, A. A. Rosenkranz, G. P. Georgiev, and A. S. Sobolev, "Nrf2/Keap1/ARE signaling: towards specific regulation," *Life Sciences*, vol. 291, article 120111, 2022.
- [49] M.-Y. Song, D.-Y. Lee, K.-S. Chun, and E.-H. Kim, "The role of NRF2/KEAP1 signaling pathway in cancer metabolism," *International Journal of Molecular Sciences*, vol. 22, no. 9, p. 4376, 2021.
- [50] D. D. Zhang and E. Chapman, "The role of natural products in revealing NRF2 function," *Natural Product Reports*, vol. 37, no. 6, pp. 797–826, 2020.
- [51] M. Dodson, R. Castro-Portuguez, and D. D. Zhang, "NRF2 plays a critical role in mitigating lipid peroxidation and ferroptosis," *Redox Biology*, vol. 23, p. 101107, 2019.
- [52] J. Lu, Y. Zhao, M. Liu, J. Lu, and S. Guan, "Toward improved human health: Nrf2 plays a critical role in regulating ferroptosis," *Food & Function*, vol. 12, no. 20, pp. 9583–9606, 2021.

Review Article

Emerging Potential Therapeutic Targets of Ferroptosis in Skeletal Diseases

Xin Liu ¹, Tianhao Wang ¹, Wei Wang ¹, Xiaolong Liang ¹, Yating Mu ², Yaozeng Xu ^{1,3}, Jiaxiang Bai ^{1,3,4} and Dechun Geng ^{1,3,4}

¹Department of Orthopedics, The First Affiliated Hospital of Soochow University, 188 Shizi Street, Suzhou, Jiangsu 215006, China

²School of Chemical Engineering and Technology, Tianjin University, Yaguan Road 135, Tianjin 300350, China

³Orthopedics Institute, Medical College, Soochow University, Suzhou 215000, China

⁴State and Local Joint Engineering Laboratory for Novel Functional Polymeric Materials, Soochow University, Suzhou, 215123, China

Correspondence should be addressed to Jiaxiang Bai; jxbai1995@163.com and Dechun Geng; szgengdc@suda.edu.cn

Received 8 June 2022; Accepted 12 July 2022; Published 30 July 2022

Academic Editor: Lianxiang Luo

Copyright © 2022 Xin Liu et al. This is an open access article distributed under the Creative Commons Attribution License, which permits unrestricted use, distribution, and reproduction in any medium, provided the original work is properly cited.

Ferroptosis is a new programmed cell death characterized by the accumulation of lipid peroxidation mediated by iron and inflammation. Since the transcurency realization of ferroptosis as an iron-dependent modality of nonapoptotic cell death in 2012, there has been growing interest in the function of ferroptosis and its relationship to clinical diseases. Recent studies have shown that ferroptosis is associated with multiple diseases, including degenerative diseases, ischemia reperfusion injury, cardiovascular disease, and cancer. Cell death induced by ferroptosis has also been related to several skeletal diseases, such as inflammatory arthritis, osteoporosis, and osteoarthritis. Research on ferroptosis can clarify the pathogenesis of skeletal diseases and provide a novel therapeutic target for its treatment. In this review, we summarize current information about the molecular mechanism of ferroptosis and describe its emerging role and therapeutic potential in skeletal diseases.

1. Introduction

Ferroptosis is a new cell death mode characterized by the accumulation of lipid peroxidation mediated by iron. In 2012, Dixon et al. first proposed the definition of ferroptosis, an iron-dependent nonapoptotic mode of cell death characterized by the accumulation of lipid reactive oxygen species (ROS) [1, 2]. Recent studies have shown that ferroptosis is obviously distinct from previous cell death patterns, such as autophagy, necrosis, and necrotic apoptosis, at genetic and characterized levels (Table 1) [1–3]. Unlike the morphological features of necrosis, it does not have membranolytic properties or swelling of the cytomembrane and cytoplasm. Furthermore, in contrast with autophagy, ferroptosis is characterized by rupture of the cell membrane. Specifically, ferroptosis is morphologically shown by reduced mitochondrial cristae and rupture of the mitochondrial outer membrane, which leads to mitochondrial dysfunction [1, 4, 5].

Iron homeostasis and lipid peroxidation are committed steps in the process of ferroptosis (Figure 1) [2, 6]. Superfluous iron induces ferroptosis by producing ROS, while suppressing GPX4 can inhibit ferroptosis through the accumulation of intracellular lipid peroxide [1, 6, 7]. In addition, upon exposure to some compounds used in experiments and clinics, such as erastin, sorafenib, lanperisone, and Ras-selective lethal small molecule 3 (RSL3), ferroptosis was promoted, while ferrostatin-1 (Fer-1), liproxstatin-1 (Lip-1), and zileuton inhibited ferroptosis [8–10]. Current studies have indicated that the relationship between ferroptosis and orthopedic diseases has also attracted extensive attention [1, 6, 11–16]. Ferroptosis has been reported in osteosarcoma cells, promoting their sensitivity to cisplatin with the application of erastin or RSL3, thus attenuating resistance of osteosarcoma to cisplatin *in vitro* [17]. Another report showed that iron overload induced by erythrocyte rupture and the increasing excitatory toxicity of glutamate induced by

TABLE 1: Comparison of cell death in ferroptosis, autophagy, and apoptosis.

Comparison of characteristics of cell death in ferroptosis, autophagy, and apoptosis			
Cell death types	Ferroptosis	Autophagy	Apoptosis
Morphological characteristics	Smaller mitochondria, decreased mitochondrial ridge	Autolysosome	Cells became round, chromatin is condensed and fragmented, and cytoplasm shrunk
Other features	Iron ion aggregation, cell membrane rupture	No obvious changes in the nucleus and membrane	Cell shrinks, cytoplasm flows out, and membrane vacuoles
Detection index	ROS, PTGS \uparrow ; NADPH \downarrow	LC3-I \rightarrow LC3II	Caspase \uparrow ; intracellular Ca ²⁺ \uparrow
Positive regulatory factor	Erastin, RSL3, RAS, Sorafenib, p53	ATG family, Beclin1	P53, Bax, Bak, TGF- β , radiation, dexamethasone
Negative regulatory factor	GPX4, FSP1, SLC7A11, Nrf2, ferrostatin-1, lipoxstatin-1, DFO	mTOR, 3-methyladenine, wortmannin, Spautin1	Bcl-2, Bcd-XL, Z-VAD-FMK, IL-4

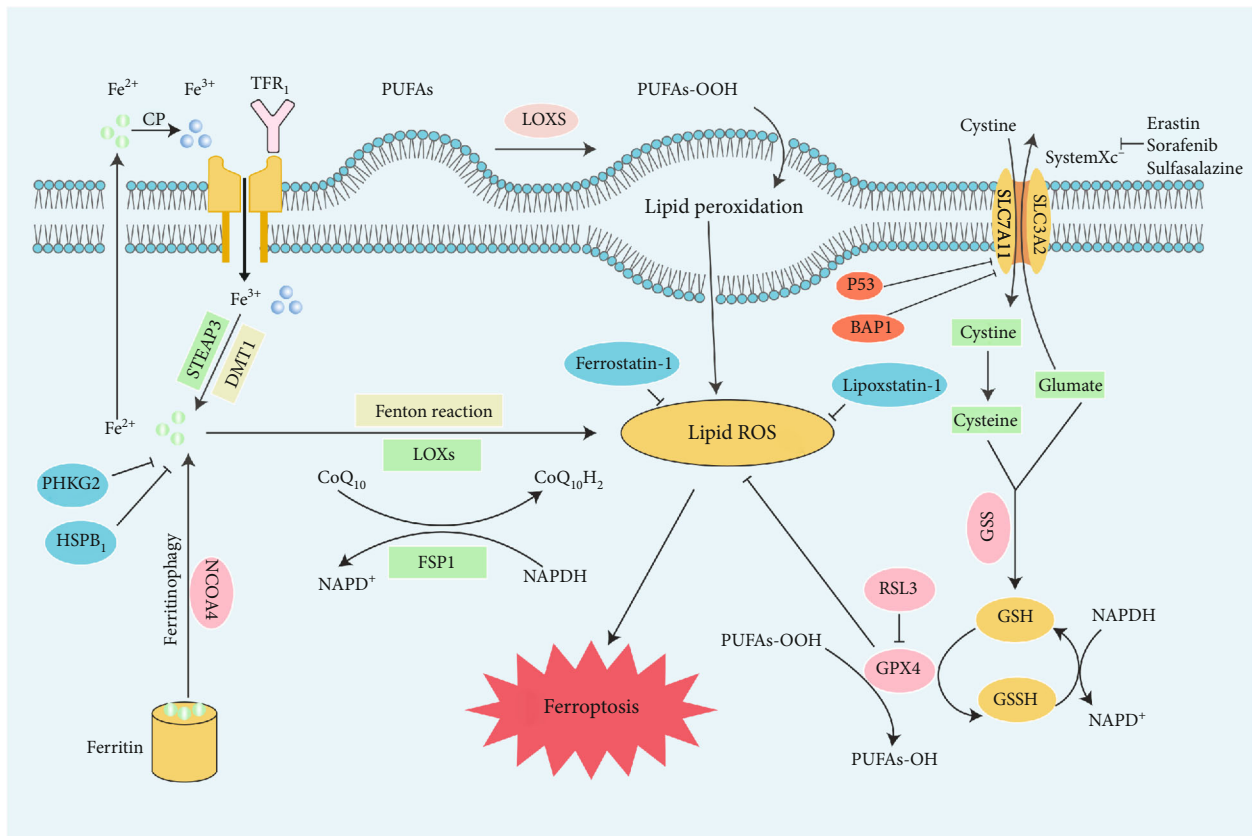


FIGURE 1: Mechanisms of ferroptosis. Ferroptosis is characterized by iron accumulation, excessive production of ROS, and lipid peroxidation. This illustration shows the process of ferroptosis, summarizing the key molecules and targets regulating iron and lipid peroxidation. TFR1: transferrin receptor 1; PUFA: polyunsaturated fatty acid; LOX: lipoxygenase; STEAP3: six-transmembrane epithelial antigen of prostate 3 metalloredutase; SLC7A11: solute carrier family 7 member 11; DMT1: divalent metal transporter 1; SLC3A2: solute carrier family 3 member 2; BAP1: BRCA1-associated protein 1; ROS: reactive oxygen species; FSP1: ferroptosis suppressor protein 1; FPN1: ferroportin 1; GPX4: glutathione peroxidase 4; GSH; glutathione; GSSG: oxidized glutathione; GSS: glutathione synthetase; PHKG2: phosphorylase kinase G2; HSPB1: heat shock protein beta-1; NCOA4: nuclear receptor coactivator 4; RSL3: Ras-selective lethal 3.

stress in acute spinal cord injury (SCI) lead to ferroptosis, while desferrioxamine (DFO), an inhibitor dampening ferroptosis, can improve SCI [18]. In view of these findings, this review summarizes recent research progress on ferroptosis to supply references for further understanding of its mechanism and describe its emerging role in skeletal diseases.

2. Origin and Development

The concept of programmed cell death first emerged in the 1960s, before ferroptosis was defined [19, 20]. Previous studies on cell death indicated that GPX4, the fourth member of the selenium containing GPX family, but not GPX1, reduces

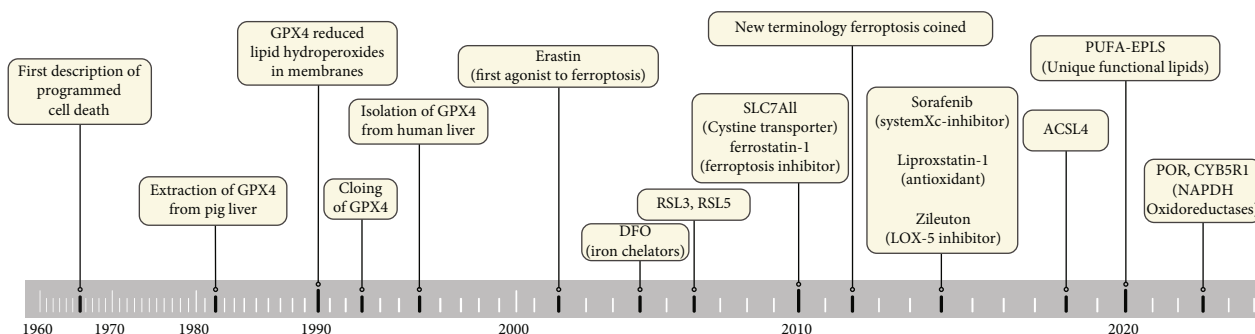


FIGURE 2: The timeline of ferroptosis.

lipid hydroperoxides in membranes, and cloning GPX4 reveals its distinct nature such as the scavenging capacity of membrane lipid hydrogen peroxide products compared to other GPXs, thus suppressing cell death [21, 22]. It was thought that this phenomenon was caused by the inhibition of apoptosis or autophagy. Meanwhile, the presence of GPX4 has been further observed in animals and humans [23, 24]. This further confirms the important role of GPX4 in cell death patterns. Before long, Dolma et al. found that erastin had selective lethality in Ras-expressing cancer cells, and the cell death pattern was different from what we previously knew until the 2000s [25]. In addition, RSL3 and RSL5, which can directly bind to GPX4 protein to inactivate it and induce the production of lipid ROS, selectively killed Ras-transformed (BJeLR) BJ fibroblasts in a new way different from apoptosis [1]. It is interesting that the mode of cell death induced by this composition is nonapoptotic, as cell death is induced by erastin and RSL3 in the absence of apoptotic markers [4, 5, 25]. Ushered in a major breakthrough in 2012, the new terminology ferroptosis was coined from nutrient consumption-induced cancer cell death and oxidation, the death of neurons yielding to the glutamate excitotoxin and inhibiting the amino acid antiporter solute carrier family 7 member 11 (SLC7A11/x CT/system Xc⁻) [26–29]. With the discovery of this concept, subsequent studies confirmed the phenomenon that GPX4 inhibited iron-mediated death by inhibiting ROS production rather than autophagy or apoptosis, as previously thought. Recent studies have identified lipophilic antioxidants as powerful inhibitors of erastin-induced cell death, suggesting that ROS are involved in this cell death process (Figure 1) [5, 30]. Moreover, iron chelating agents were identified as suppressors of cell death induction after RSL3 treatment, suggesting the requirement for cellular iron [4].

In 2014, Skouta et al. found that Fer-1, a chemical compound inhibiting the peroxidation induced by iron and trace lipid hydroperoxide in liposomes, suppressed cell death in some disease “models,” such as Huntington’s disease (HD), periventricular white matter (PVL), and renal insufficiency. This discovery provides the basis for the use of ferrostatin in models of diseases, and it is the first to stress the importance of ferroptosis beyond the cellular level [31]. In 2015, new results revealed that the retinoblastoma- (Rb-) negative status of hepatocellular carcinoma cells promotes iron oxidation disease (a type of oxidative necrosis) after exposure

to sorafenib. These findings highlight the role of retinoblastoma in the response of HCC cells to sorafenib and the regulation of iron disease [32]. Subsequent studies showed that the iron chelating agent deferoxamine (DFO) significantly inhibited RSL3/BV6-induced cell death, but it did not protect erastin/BV6 cells from death, suggesting that RSL3/BV6- and not erastin/BV6-mediated cell death depended on iron in 2017 [33]. In addition, activation of the Nrf2-ARE pathway contributed to HNV cell resistance to GPX4 inhibition, and inhibition of the Nrf2-ARE pathway reversed resistance to iron transformation in HNC cells in 2018 [34]. In 2020, glutamine deprivation increased vorinostat-mediated cell death and ROS accumulation, and genetic elimination of xCT improved the efficacy of vorinostat by inducing ferroptosis (Figure 2) [35]. In summary, the discovery and development of a new death mode named ferroptosis may provide a research approach to learn and treat multidisciplinary diseases.

3. The Relationship between Bone Metabolism and Iron

Iron is an important trace element in nature. In recent years, people have gradually realized that iron deficiency and iron overload are important inducers of the occurrence and development of ferroptosis. For the sake of a deeper understanding of bone metabolism and ferroptosis, researchers have begun to explore the relationship between iron and bone metabolism. Medeiros et al. found that bone volume fraction (BV/TV) and bone trabecular thickness decreased with the increment of bone trabecular separation analyzed by micro-CT in a female rat model fed an iron-deficient diet [36]. With the exception of the effects of iron deficiency on bone structure, markers of bone transformation were also affected, which may provide ideas into the detailed mechanism of how iron deficiency affects bone. In contrast, the expression levels of parathyroid hormone (PTH) and tartrate-resistant acid phosphatase 5B (TRAP) were upregulated in iron-deficient rats, suggesting that severe iron deficiency leads to increased bone resorption as bone formation decreases. In addition, previous studies have shown that the mineralization function of osteoblasts is damaged through a lack of iron [37]. A population study also reported that iron deficiency anemia (IDA) played a significant role in some bone health indicators. In a population-

TABLE 2: Overview of inducers of ferroptosis.

Target	Inducer	Mechanisms associated with ferroptosis
System Xc ⁻	Erastin	Inhibit system Xc ⁻ activity
	Erastin2	Inhibition of system Xc ⁻ cystine/glutamate transporter
	Imidazole ketone Erastin	Metabolic stabilization inhibitor of system Xc ⁻
	Glutamate	Inhibit system Xc ⁻ activity
GPX4	RSL3	GPX4 bound to selenocysteine sites
	DPI7 (ML162)	Covalently bind GPX4 (same binding site as RSL3)
	DPI10 (ML210)	Indirectly inhibit GPX4 activity or bind to sites different from RSL3
	Altretamine	Inhibit GPX4 activity
GSH	Buthionine sulfoximine	Reduce GSH synthesis
	N-Acetyl-4-benzoquinone imine	Toxic doses deplete glutathione reserves in the liver
	Cisplatin	Binding to GSH inactivates GXP4
	DPI2	Excessive consumption of GSH
ROS and iron ions	Piperlongumine	Consume GSH and inhibit GPX4 activity
	Heme	Increase of intracellular unstable iron
	Withaferin A	Medium dose upregulated HMOX1 expression and increased intracellular unstable iron. High dose inhibited GPX4 activity
	BAY 11-7085	Upregulation of HMOX1 expression and increase of intracellular unstable iron
	FINO ₂	Oxidation of Fe ²⁺ promotes ROS accumulation in cells
	Artesunate	Induce ferritin autophagy and release unstable iron
	Dihydroartemisinin	Induce ferritin autophagy and release unstable iron; binding to free iron inhibits ferritin translation
	Siramesine	Decrease the expression of FPN, increased the expression of transferrin, increased the intracellular unstable iron
	BAY 87-2243	Inhibit mitochondrial respiratory chain complex 1 and increase ROS
	iFSP1	Inhibition of FSP1 inhibits ferroptosis unrelated to glutathione activity
ROS	Auranofin	Inhibit thioredoxin reductase activity
	Statins	Inhibits HMG-COA reductase, which catalyzes rate-limiting steps of the MVA pathway
ROS and GSH	QD-394	Induce lipid peroxidation and decrease GSH/GSSH ratio
ROS and SQS	FIN56	Induce GPX4 degradation. Bind and activate SQS to reduce CoQ10

based study from Taiwan, the risk ratio of IDA to osteoporosis was 1.74 higher than that of individuals with normal iron status [38]. Contrary to common sense, the more iron there is, the better. High levels of iron in menopausal female and some genetic diseases are correlated with a decrease in bone quality and activity. These processes eventually lead to loss of bone mass, increased risk of bone fracture, and formation of osteoporotic bone phenotypes, as stated elsewhere [39]. Although the effects of menopause were excluded, Kim et al. also found that an increase in ferritin resulted in bone loss [40]. Subsequent studies have shown that there is a relationship between iron overload and a high incidence rate of osteoporosis in hereditary hemochromatosis (HH) [41, 42]. As described above, bone metabolism is disordered in an environment of iron deficiency, which leads to the occurrence of orthopedic diseases.

4. Inducers

To date, there are many inducers of ferroptosis (Table 2). We briefly describe the following compounds.

4.1. Erastin. Cell death induced by erastin is efficiently suppressed by antioxidants such as α -tocopherol, β -carotene, butylated hydroxytoluene, and iron chelators, indicating that ferroptosis induced by erastin requires ROS- and iron-dependent signaling [1, 43]. Upregulation of RAF/MEK/ERK signaling can be significant for ferroptosis induced by erastin in tumor cells carrying oncogenic Ras [43]. *In vivo*, the adaptation and water solubility of piperazine erastin are better than those of erastin in suppressing cancer growth [44].

The mitochondrial voltage-dependent anion channel (VDAC) is one of the direct molecular targets of erastin, which can be directly attached to VDAC2/3 in BjeLR cells [43]. Reducing the expression of VDAC2 and VDAC3, instead of VDAC1, brings about erastin resistance [43]. In addition, erastin is able to decrease glutathione (GSH) levels by directly suppressing system Xc⁻ activity to affect the cystine/glutamate antiporter, activating the stress response in the ER in bone marrow-derived mesenchymal stem cells [1, 45, 46]. This response will accelerate ROS accumulation in ferroptosis.

TABLE 3: Overview of inhibitors of ferroptosis.

Target	Inhibitor	Mechanisms associated with ferroptosis
ROS and iron ions	Minocycline	Minocycline reduces iron overload after ICH and iron induced brain injury
	Ferrostain-1	Scavenge ROS, inhibit lipid peroxidation, and reduce unstable iron in cells
	Liproxstatin-1	Scavenge ROS, inhibit lipid peroxidation, and activate the Nrf2 signaling pathway
	Curcumin	Chelate iron, reduce iron accumulation, and activate the Nrf2 signaling pathway
	Alpha tocopherol analogs	Remove ROS and inhibit lipid peroxidation
GSH and GPX4	Nitrogen oxides	Inhibit Fenton reaction and hydroxyl radical production
	Baicalein	Inhibit GSH depletion, GPX4 degradation, and lipid peroxidation and activate the Nrf2 signaling pathway
	Gastrodin	Inhibit glutamate-induced iron death in HT-22 cells
ACSL4	Rezulin	Prevention of ferroptosis and lipid peroxidation in Pfa1 cells induced by RSL3
5-LOx	Zileuton	Protect ACSL4 overexpressed LNCaP and K562 cells from erastin-induced ferroptosis
TFR1 and FTH1	HSPB1	Inhibit ferroptosis induced by erastin
Lipid peroxidation	XJB-5-131	Suppress lipid peroxidation
Iron	Deferoxamine	Deplete iron and prevent iron-dependent lipid peroxidation

4.2. *RSL3 and RSL5*. In tumor cells, ROS, iron, and MEK are essential in ferroptosis induced by RSL3 and RSL5 [4]. VDAC2/3 is necessary for RSL5 to realize ferroptosis but not for RSL3 [4]. RSL3 can directly inhibit GPX4 [7]. After integrating into GPX4, RSL3 suppresses GPX4 to promote lipid peroxidation to increase ROS production [7]. Therefore, recent studies have shown that at least two types of RSLs exist. Type I RSLs, such as erastin and RSL5, can trigger ferroptosis by targeting upstream regulators. Type II RSLs suppress downstream regulators such as GPX4 to induce ferroptosis. RSL5-induced ferroptosis can be inhibited by a protein synthesis inhibitor but not RSL3-induced ferroptosis, indicating that type I RSL-induced ferroptosis requires protein synthesis.

4.3. *Lanperisone*. Lanperisone, an improved version of tolperisone, has been developed as a skeletal muscular relaxant [45]. Lanperisone can selectively kill K-Ras-mutant mouse embryonic fibroblasts through the induction of ROS mediated through iron and Ras/RAF/MEK/ERK signaling. In addition, lanperisone may inhibit the function of system Xc^- or other targets in ferroptotic pathways [1]. LP appears to be similar to erastin in terms of potential mechanisms. By binding to mitochondrial voltage-dependent anion channels (VDACs), erastin alters VDAC gating, leading to mitochondrial dysfunction and ROS production and ultimately inducing ferroptosis. Lanperisone also suppresses tumor growth in a K-Ras-driven mouse model of lung cancer *in vivo* [47]. The specific mechanism of ROS generation induced by lanperisone is not clear, but a study suggests that the interference of voltage-gated ion channels is important [45].

4.4. *Sorafenib*. Sorafenib can induce ferroptosis in some cancer cells, such as colorectal cancer cells, hepatoma cells, and osteosarcoma cell [32, 48, 49]. Ferroptosis induced by sorafenib occurs free from the carcinogenic state [50]. However,

the expression of Nrf2 and Rb can suppress ferroptosis induced by sorafenib in HCC [32, 51]. The function of sorafenib in ferroptosis may be associated with the inhibition of system Xc^- instead of GPX4 expression. This process is linked to the upregulation of ER stress [52]. Further research on sorafenib analogs shows that sorafenib suppresses system Xc^- via a nonkinase target [52].

5. Inhibitors

In addition to the above, we also summarized the inhibitors of ferroptosis classified by some targets (Table 3).

5.1. *Ferrostatin*. Initial ferrostatin is known as ferrostatin-1 (Fer-1) and acts as an inhibitor of ferroptosis induced by RSL3 and erastin in fibrosarcoma HT-1080 [1]. The activity of Fer-1 is determined by the primary aromatic amine, which particularly suppresses lipid oxidation and decreases the accumulation of ROS [1]. In addition, Fer-1 can inhibit osteoblast ferroptosis by regulating the Nrf2-ARE signaling pathway, thereby alleviating nanoparticle-induced peri-implant osteolysis [53]. In comparison with Fer-1, new-generation ferrostatins (SRS 11–92 and SRS 16–86) have the advantages of improving the stability of metabolism and tremendously preventing diseases such as acute kidney injury and ischemia-reperfusion injury [54, 55].

5.2. *Liproxstatin-1*. Liproxstatin-1 (Lip-1), a potent spiroquinoxalinamine derivative, is known to inhibit the accumulation of ROS from lipid oxidation and cell death in GPX4 knockout cells [43]. Lip-1 may function as a lipophilic antioxidant, although the mechanism of action of this inhibitor has yet to be reported. Previous studies have proven the close relationship between Lip-1 and ferroptosis. *In vitro*, Lip-1 inhibits ferroptosis induced by ferroptosis inducers such as erastin, RSL3, and buthionine sulfoximine. Recent studies have also found that Lip-1 suppresses ferroptosis in

osteosarcoma cells induced by bavachin through the stat3/p53/slc7a11 axis [56]. Intraperitoneal injection of Lip-1 in GPX4 knockout mice prolongs animal life in response to renal injury [43]. Lip-1 can also prevent other organ ischemia reperfusion injuries in mice, such as hepatic and cerebral injury by evaluating proferroptotic changes after ischemia and the levels of protein and lipid peroxidation [57].

5.3. Prominin-2. Ferroptosis causes clinically extensive necrosis during heart attack and acute kidney injury. Belavgeni et al. described the terpenoid membrane glycoprotein prominin-2 as a novel endogenous ferroptosis inhibitor [58]. Subsequent studies found that iron-promoting stimulants (including inhibition of GPX4 and its withdrawal from the extracellular matrix) induce the expression of prominin2, a pentapeptide involved in the dynamic regulation of the vitamin. Prominin2 promotes iron-resistant death of breast epithelial and breast cancer cells [59]. Mechanistically, prominin2 promotes the formation of ferritin-containing polyvesicles (MVBs) and exosomes that transport iron out of the cell, thereby inhibiting ferroptosis. These findings suggest that resistance to iron death can be driven by the prominin2-MVB-exosome-ferritin pathway and has broad implications for iron homeostasis, intracellular transport, and cancer [59, 60].

6. Important Mechanisms Associated with Ferroptosis

6.1. Inducing Ferroptosis by Suppressing System Xc⁻. System Xc⁻ is a plasma membrane cystine/glutamate antiporter made up of a twelve-pass transmembrane transporter protein linked to the transmembrane regulatory protein SLC3A2 through a disulfide bridge that is often present in phospholipid bilayers. It is also an integral part of the cell antioxidant system. Cystine and glutamate are intercellularly and extracellularly exchanged by system Xc⁻ at equal proportions [1]. Cysteine is degraded into cysteine in cells and is closely related to the production of glutathione (GSH). GSH suppressed ROS in the presence of glutathione peroxidases (GPXs). Suppressing the viability of system Xc⁻ influences the production of GSH by decreasing the absorption of cystine, which results in downregulating GPX activity and greatly weakening cell antioxidant capacity. Due to the influence described above, the eventual occurrence of oxidative damage and ferroptosis is inevitable. In addition, by downregulating the expression of SLC7A11, p53 can also inhibit cystine uptake by system Xc⁻, thus reducing the activity of GPX4, leading to decreased cell antioxidant capacity and ferroptosis [61, 62].

6.2. Inducing Ferroptosis by Suppressing GPX4 through the MVA Pathway. In the case of the GPX family, recent studies have shown that GPX4 plays a considerable role in the occurrence of ferroptosis mainly by suppressing the formation of lipid peroxides. GPX4 is a unique selenium-utilizing form of glutathione peroxidase that can specifically protect lipids in cell membranes from oxidative damage. GPX4 acts as a phospholipid hydroperoxidase and plays a

role in the conversion of glutathione to oxidized glutathione (GSSG) and decreases phospholipid hydroperoxide production (AA/ADA-PE-OOH) to the corresponding phospholipid alcohol (PLOH) [63]. The accumulation of lipid peroxides induced by the downregulation of GPX4 activity can result in the emergence of ferroptosis. In contrast, cells overexpressing GPX4 suppress ferroptosis by decreasing the production of lipid peroxides [43]. RSL3, which induces ferroptosis, has a direct function on GPX4 and suppresses its activity to reduce the generation of the antioxidant capacity of cells and accumulate ROS, thus resulting in the occurrence of ferroptosis [7]. Selenocysteine is one of the essential amino acids in the activation of GPX4, and its tRNA, which plays a crucial role in efficient translational decoding of UGA and synthesis of selenoproteins through isopentenylation, links selenocysteine to GPX4 [64]. The mevalonate (MVA) pathway is a metabolic pathway for the synthesis of isoprene pyrophosphate and dimethyl allyl pyrophosphate from acetyl coenzyme A. In addition, when GPX4 is inactivated, it will inhibit the conversion of lipid peroxide to lipid alcohol. Lipid peroxide (LPO) can be used as an important indicator of ferroptosis. For example, nanoplat-form could inhibit the expression of HMGCR to downregulate the mevalonate (MVA) pathway and glutathione peroxidase 4 (GPX4), thereby producing more LPO to induce cancer cell ferroptosis. Apart from these, IPP and CoQ₁₀ play vital roles in the mevalonate (MVA) pathway [64–66]. Consequently, suppressing the MVA pathway can reduce the synthesis of selenocysteine tRNA, thus influencing GPX4 expression and leading to ferroptosis.

6.3. Inducing Ferroptosis by Injuring Mitochondrial VDACS. VDAC is involved in energy metabolism mainly by affecting the transport of ATP/ADP in and out of mitochondria. Meanwhile, VDACS, as transmembrane channels, can transport ions and metabolites and play a key role in regulating ferroptosis [67]. Tarangelo et al. found that erastin exerts effects on VDACS, leading to mitochondrial structural injury and dysfunction and bringing about a large amount of released reactive oxygen species (ROS), ultimately leading to ferroptosis [68]. By blocking the oligomerization of VDAC1 but not VDAC2 or VDAC3, they found that liproxtatin-1 short-circuited the ferroptosis pathway [69].

6.4. Ferroptosis Mediated by p53. p53 is a pivotal tumor suppressor gene, which regulates cell growth and senility by promoting apoptosis and repairing DNA under stressful conditions and plays a vitally important role in the occurrence and development of tumors [70]. Researchers have accidentally found that p53 is also closely related to ferroptosis. A study has shown that acetylation-deficient p53 mutants can boost ferroptosis. Jiang et al. found that the activity of p53-silenced H1299 cells was not different when induced by ROS [61]. However, almost all of the cells died induced by reactive oxygen species after activating p53. The cell death rate decreased significantly when cells were treated with Fer-1, a ferroptosis inhibitor. Recent studies have reported that p53 can suppress cystine uptake by system Xc⁻ through downregulation of SLC7A11 expression,

thus regulating GPX4 expression and reducing antioxidant capacity and ultimately ferroptosis [61]. In addition, the p53-SAT1-ALOX15 pathway is also associated with the process [67]. In addition, the expression of p53 can also have an opposite effect on ferroptosis. Tarangelo et al. found that p53 suppressed the competence of system Xc⁻ but also decreased the sensitivity of many cells, such as human HT-1080 fibroblasts, to ferroptosis [68]. He et al. found that these cells, called human HT-1080 fibroblasts, were not sensitive to ferroptosis induced by erastin-2 when treated with the p53 inducer nutlin3. Subsequent research demonstrated that nutlin-3 increases the expression of wild-type p53 in wild-type U-2OS, Caki-1, and A549 cells, which could lead to ferroptosis [71]. In addition, inhibition of ferroptosis sensitivity requires the help of CDKN1A (encoding p21), which regulates glutathione synthesis and metabolism. Previous outcomes clearly state that the p53-p21 axis can negatively regulate ferroptosis in cancer cells [68]. Apart from what was mentioned before, Xie et al. found that p53 played an important role in suppressing ferroptosis in colorectal cancer [72]. Consequently, p53 regulation of ferroptosis may be bidirectional and the detailed mechanism needs to be further studied.

6.5. Relationship between Iron Metabolism and Ferroptosis. Iron is a necessary trace element for humans. Abnormal iron metabolism in the body can affect the occurrence and development of normal physiological processes. In the blood, iron mainly exists in the form of Fe²⁺, which originates from erythrocyte degradation or intestinal absorption [73]. Six transmembrane epithelial antigen of the prostate 3 (STEAP3) can resolve Fe³⁺ into Fe²⁺, and unstable iron pool (LIP) and ferritin will finally be storage places for Fe²⁺ with mediation of zinc-iron regulatory protein family 8/14 (ZIP8/14) or divalent metal transporter 1 (DMT1). Superfluous Fe²⁺ is oxidized to Fe³⁺ by ferroportin (FPN) [74]. The recyclability of internal iron, as mentioned above, strictly regulates iron homeostasis in cells. Silencing TFR1 (the gene encoding TFR1) can suppress ferroptosis induced by erastin [11], but heme oxygenase-1 (HO-1) can expedite ferroptosis induced by erastin by replenishing iron [75]. Recent studies have found that ferroptosis is related to heat shock protein beta-1 (HSPB1). This protein can suppress TFR1 expression to decrease intracellular iron content, and the overexpression of HSPB1 can effectively inhibit ferroptosis [76]. Iron response element binding protein 2 (IREB2) plays a key role in iron metabolism, and inhibiting it can significantly inhibit ferroptosis by increasing the expression of ferritin heavy chain 1 (FTH1), which is an important component of ferritin [77].

6.6. Regulating Ferroptosis through the Lipid Metabolism Pathway. The accumulation of ROS is one of the important characteristics of ferroptosis. Lipid metabolism and ferroptosis are closely related. The lipid peroxidation of polyunsaturated fatty acids (PUFAs) is susceptible and closely related to the occurrence of ferroptosis [78]. The process of esterification and oxidation is necessary to transmit signals to cause ferroptosis. Recent research shows that phosphatidyletha-

nolamine (PE), containing arachidonic acid (AA) or its derivative adrenaline, plays a pivotal role in ferroptosis [79]. Lysophosphatidylcholine acyltransferase 3 (LPCAT3) and acyl-CoA synthetase long-chain family member 4 (ACSL4) are related to the synthesis and reconstruction of PE, activating PUFAs and influencing the transmembrane function of PUFAs [80]. Therefore, downregulating the expression of the above two products can reduce the accumulation of intracellular lipid peroxide substrates and inhibit ferroptosis. Ultimately, with the catalysis of lipoxygenase (LOX), PUFA-PE can play a further oxidative role and eventually induce ferroptosis.

7. Ferroptosis in Bone-Related Diseases

7.1. Osteoporosis. Osteoporosis is a systemic bone disease that is prone to fracture due to the decrease in bone density and quality, destruction of bone microstructure, and increase in bone fragility [81]. In addition, pain caused by osteoporosis can reduce the quality of life of patients; spinal deformation and fracture can be disabled, limiting patients' activities and increasing the incidence of pulmonary infection and bedsores, not only increasing the quality of life and mortality of patients but also imposing a heavy economic burden on individuals, families, and society [82]. Current treatments for osteoporosis are limited, and calcium is only supplemented when appropriate, but calcium alone cannot be used as an osteoporosis treatment, only as a basic adjunct, and an increasing number of people are experiencing the problem, so addressing this aspect is imminent [83]. In addition, previous studies on autophagy, apoptosis and osteoporosis have some shortcomings [84, 85]. The discovery of ferroptosis may provide a new direction for the treatment of osteoporosis.

Along with the further comprehension of ferroptosis, ferroptosis is recognized as a new factor for osteoporosis. Tian et al. observed that the death of osteoblasts *in vitro* induced by ferroptosis is involved in the mitochondrial apoptotic pathway through the analysis of intracellular labile iron levels by flow cytometry and fluorescence microscopy and mitochondrial membrane potential (MMP) [86]. Iron overload could induce apoptosis in osteoblasts and osteoporosis *in vivo*. Mitochondrial apoptosis and ROS-mediated necroptosis are closely related to ferroptosis, leading to the death of osteoblasts and thus causing bone rarefaction [87, 88]. In addition, some experts found that the characteristics of ferroptosis such as the function of osteoblasts and osteoclasts in osteoporotic mice are reflected in bone mineral density, trabecular number, and trabecular bone mass measured by micro-CT in the femur [89]. The above studies suggest that ferroptosis has a great influence on osteoporosis (Figure 3).

Recently, Ni et al. observed that ferroptosis affected osteoclasts in the process of differentiation induced by RANKL. The overexpression of TFR1 and the amount of significantly decreased ferritin induced by downregulating aconitase activity can lead to ferroptosis during RANKL stimulation without oxygen deficiency. However, these phenomena regarding changes in intracellular iron homeostasis and the

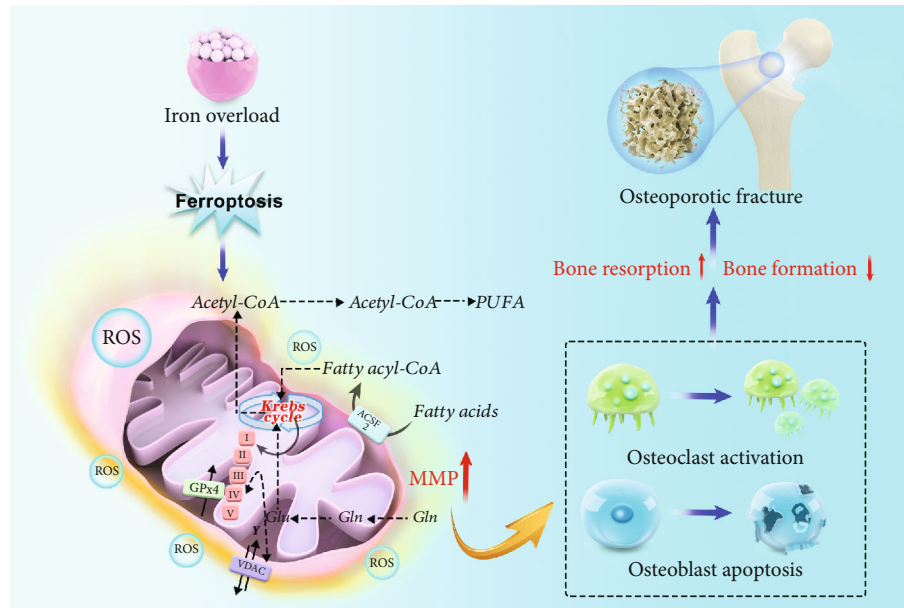
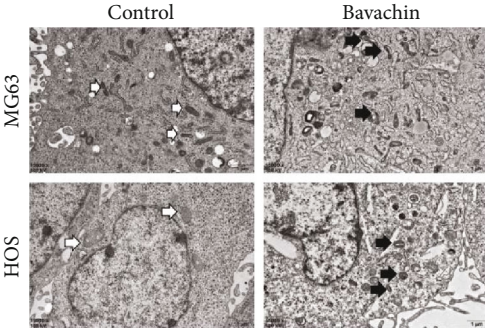


FIGURE 3: The mechanism of ferroptosis induced by iron overload in osteoporosis. Ferroptosis induced by iron overload leads to an increase in mitochondrial membrane potential and the accumulation of lipid peroxide by affecting glutathione and fatty acid cycle. It further promotes the activation of osteoclasts and the apoptosis of osteoblasts, leading to the increase of bone resorption and the decrease in bone formation, resulting in osteoporosis and finally osteoporotic fracture.

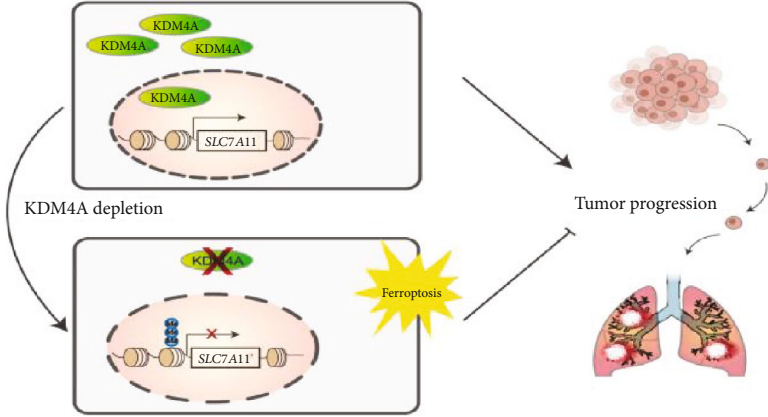
activation of ferritinophagy could not be observed under hypoxia. In addition, they also found that HIF-1 α impaired autophagic flux under hypoxia *in vitro*. 2ME2, a HIF-1 α -specific inhibitor, prevents OVX-induced osteoporosis in rats *in vivo*, probably due to the increase in ferroptosis markers such as PTGS2 and MDA [90]. In addition, other scholars found interesting phenomena about the occurrence of ferroptosis in skeletal muscle related to changes in iron metabolism and lipid peroxidation and different expression of TFR1 by comparing different age groups of mice. With intramuscular injection of lentivirus expressing TFR1, skeletal muscle regeneration is enhanced and suppresses ferroptosis in different age groups of mice, thus preventing osteoporosis [91]. Liu et al. further clarified the relationship between ferroptosis and osteoporosis through animal models of osteoporosis *in vivo* and cell models *in vitro* [92]. From the above research content, we have a better understanding of ferroptosis orchestrated with osteoporosis than before and can treat and prevent osteoporosis according to some targets. However, due to some technical limitations, many detailed mechanisms in ferroptosis involved in osteoporosis remain unclear.

7.2. Acute Spinal Cord Injury. SCI is usually caused by fractures and/or dislocations of the spine as a result of direct or indirect violence. It leads to severe dysfunction of the lower limb and thus causes serious physical and psychological damage to patients themselves and causes a huge economic burden on society. SCI has high mortality and disability rates [93]. Due to previous research on SCI, the prevention, treatment, and rehabilitation of SCI have become major topics in today's medical community.

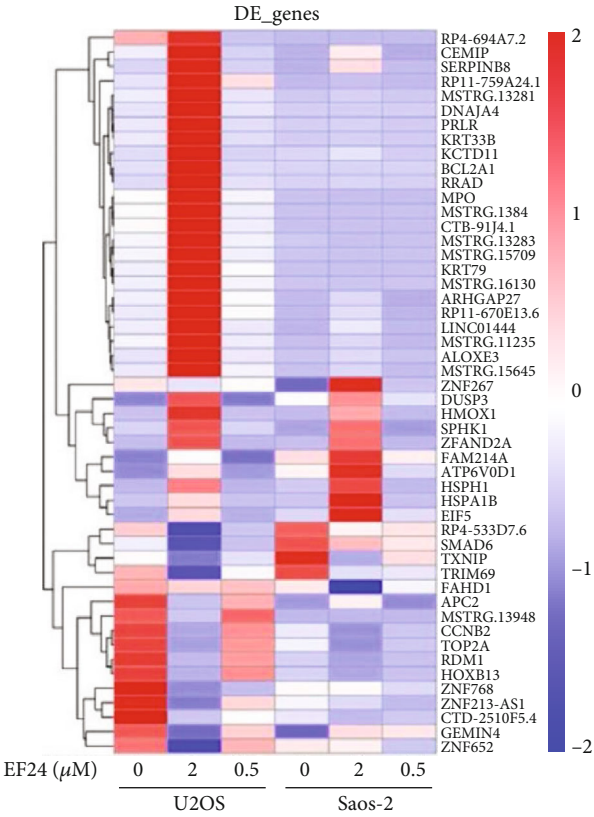
Previous studies have mostly studied the mechanisms of acute spinal cord injury from the aspects of apoptosis and autophagy. For example, the AMPK/mTOR signaling pathway is activated after spinal cord injury. This inactivates the intracellular AMPK-activated mTOR, which catalyzes the phosphorylation of ULK1 to promote autophagy. After spinal cord injury, the mitochondria of neurons produce excessive reactive oxygen species through the processes of protein decomposition, lipid peroxidation, and DNA damage, which leads to the aggravation of spinal cord injury and apoptosis [94, 95]. In addition, potential roles of phenolic compounds as key phytochemicals have also been revealed in preclinical and clinical studies in regulating upstream dysregulated oxidative stress/inflammatory signaling mediators and extrinsic mechanisms of axon regeneration after SCI [96, 97]. Meanwhile, polyphenols were also identified as a potent inhibitor of ferroptosis, which was confirmed in *in vitro* and *in vivo* studies in different disease models [98–101]. However, whether polyphenols can improve acute SCI by interfering with ferroptosis and whether they interact with apoptosis and autophagy still need further study. Fortunately, recent studies have shown that variances in mitochondrial function and structure in ferroptosis can be observed by transmission electron microscopy, and ferroptosis markers in SCI rats exhibit several changes in spinal cord tissue, which are different from autophagy and apoptosis. As mentioned above, ferroptosis plays an important role in SCI [18]. After SCI, spinal cord hemorrhage, degeneration, red blood cell rupture, and hemolysis occurred in the injured spinal cord and thus caused iron overload. Stress also activated ROS accumulation and lipid peroxidation [102].



(a)



(b)



(c)

FIGURE 4: Continued.

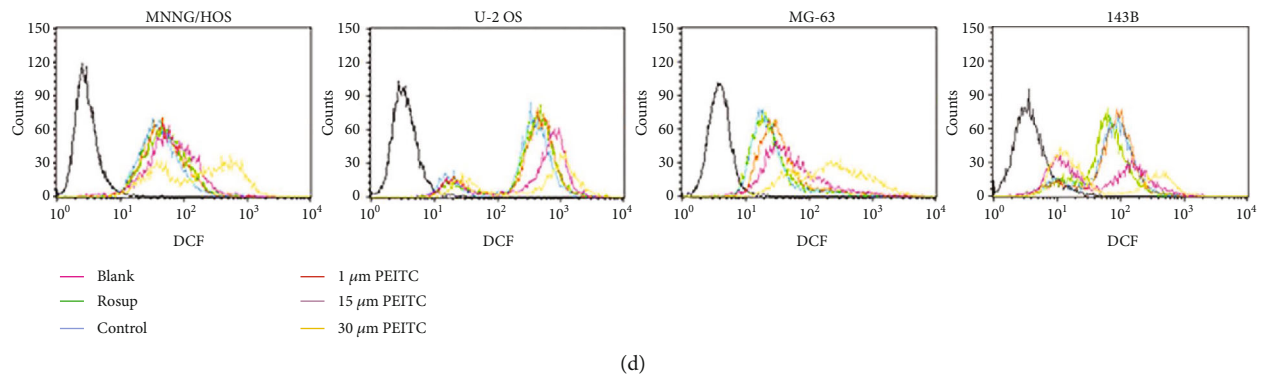


FIGURE 4: (a) The ultrastructure of MG63 and HOS cells (reproduced from ref. [56] with permission from 2021 Hindawi Publishing Corporation); (b) KDM4A regulation of ferroptosis and tumor progression in OS (reproduced from ref. [107] with permission from 2021 Elsevier B.V.); (c) RNA sequencing analysis of gene transcriptional profiles changes of U2os cells and Saos2 cells after treating with indicated dose of EF24 (reproduced from ref. [108] with permission from 2021 Elsevier B.V.); (d) ROS levels in MNNG/HOS, U-2 OS, MG-63, and 143B cells treated with PEITC for 24 h (reproduced from ref. [110] with permission from 2020 Hindawi Publishing Corporation).

Some scholars have found that ferroptosis can lead to serious consequences of secondary injury after spinal cord injury and that DFO can suppress ferroptosis to promote functional recovery in SCI rats [18]. Galluzzi *et al.* experimented on spinal nerve cells with ferrous ions and found that with the increase in iron in cells, the degree and metabolites of lipid peroxidation related to neuronal inactivation also increased [103]. Zhang *et al.* observed that a ferroptosis inhibitor called SRS16-86 can reduce ferroptosis markers and upregulate the levels of GPX4, xCT, and GSH in SCI rats, thus preventing more complications after SCI [104]. In addition, the morphology of mitochondria was similar to normal, and more mitochondrial cristae appeared after SRS16-86 intervention. Subsequent studies have shown that the extracellular regulated protein kinase (ERK) pathway has a certain connection with ferroptosis, and downregulating the RAS/RAF/ERK pathway by the ferroptosis inhibitor U0126 could inhibit neuroinflammation and protect neurons, thus recovering from SCI and reducing local redox damage [105]. As will be readily seen from what we mentioned above, acute SCI is closely related to ferroptosis. However, the current research is still insufficient, and the detailed mechanism of SCI related to ferroptosis is unclear.

7.3. Osteosarcoma. Osteosarcoma is one of the most common bone malignancies. The typical osteosarcoma originates from the bone; another completely different type is osteosarcoma juxtaposed with the bone cortex, which originates from the periosteum and adjacent connective tissue [106]. The mortality and disability rate of osteosarcoma is high in children and adolescents. Some patients suffer from both physical and psychological damage. Although early diagnosis and timely medication or surgery have greatly improved patient quality of life, subsequent physical and mental rehabilitation treatment is limited, and its curative effect is not satisfactory.

Gratifyingly, bavachin, a bioactive compound extracted from the fruit of *Psoralea corylifolia*, induces ferroptosis through the STAT3/p53/SLC7A11 axis in osteosarcoma

cells, such as MG63 and HOS cells, thus inhibiting the further development of osteosarcoma (Figure 4(a)) [56]. Meanwhile, Chen *et al.* found that ferroptosis can lead to lipid peroxidation and dysfunction after osteosarcoma and that Fer-1 could suppress ferroptosis to promote functional recovery in osteosarcoma mice (Figure 4(b)) [107]. Recent studies have shown that osteosarcoma cells, such as U2os and Saos-2 cells, have a high level of ROS and more lipid peroxidation metabolites than normal cells. Coincidentally, they observed ferroptosis marker changes in osteosarcoma cells. Lin *et al.* confirmed that a ferroptosis inhibitor named ferrostatin-1 could reduce ferroptosis-related genes such as HMOX1 and upregulate GPX4 expression in osteosarcoma cells after intervention with EF24 (a synthetic analog of curcumin), thus promoting the recovery of cell function and morphology (Figure 4(c)) [108]. In addition, subsequent studies have shown that NF- κ B signaling and the mitogen-activated protein kinase (MAPK) pathway have a certain connection with ferroptosis, and downregulating the MAPK pathway by the ferroptosis inhibitor Fer-1 could promote osteosarcoma cell death, thus recovering from osteosarcoma and reducing ROS production (Figure 4(d)) [17, 108–110]. Lv *et al.* also found that β -phenethyl isothiocyanate, a valid medicine against cancers such as lung cancer and breast cancer, could lead to human osteosarcoma cell death by interfering with iron metabolism through upregulating the MAPK signaling pathway [111–113]. As time goes by, people may pay much more attention to osteosarcoma in children and adolescents, and we also have a profound understanding of this disease. However, as far as we know, the role of ferroptosis in the regulation of osteosarcoma is unclear. Further research is needed to elucidate the detailed mechanism of osteosarcoma correlated with ferroptosis.

7.4. Osteoarthritis. Osteoarthritis is a degenerative disease that involves the degeneration and injury of articular cartilage and reactive hyperplasia of articular edge and subchondral bone caused by many factors, such as aging, trauma, congenital joint abnormalities, and joint deformities [114].

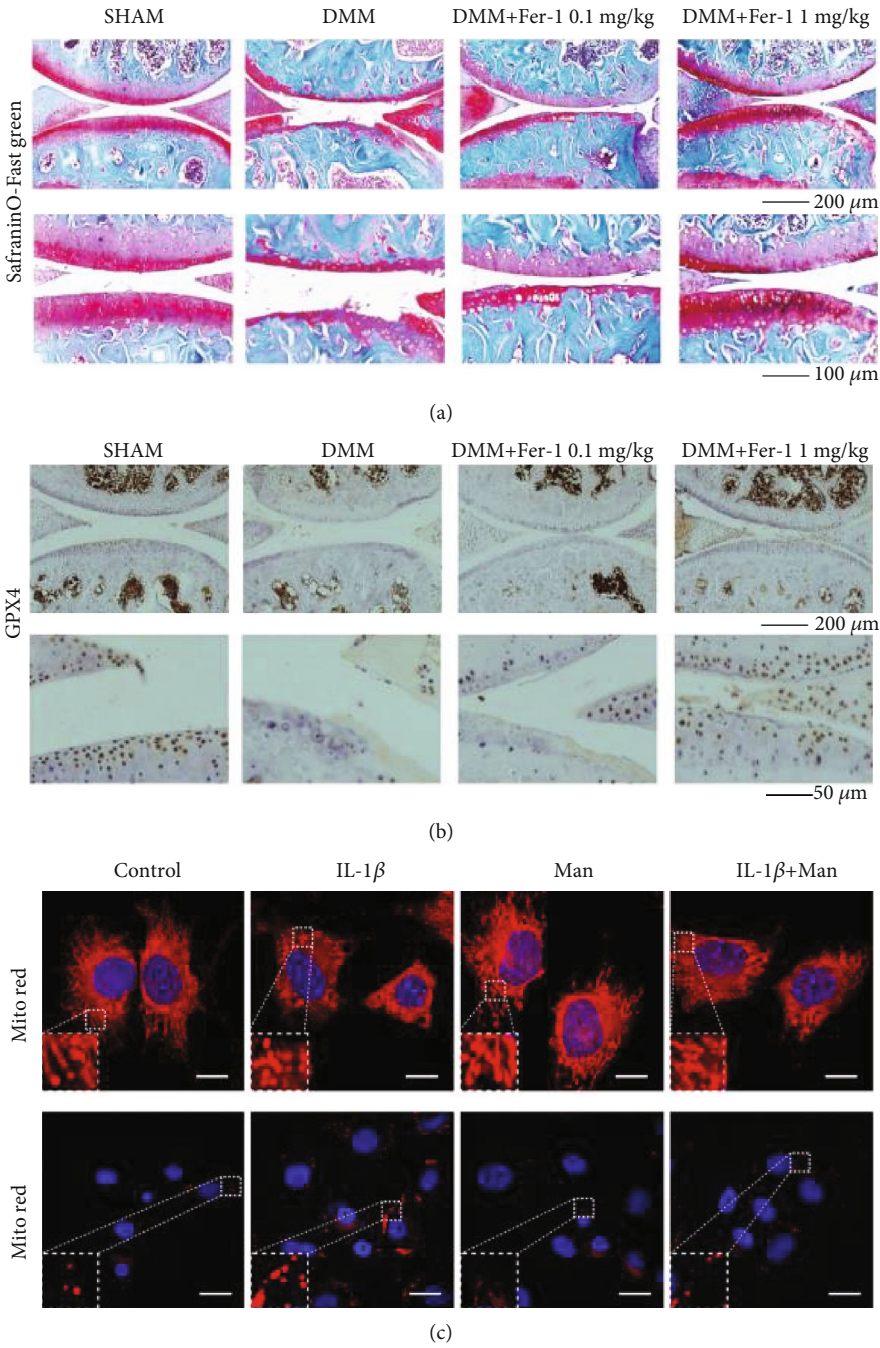


FIGURE 5: Continued.

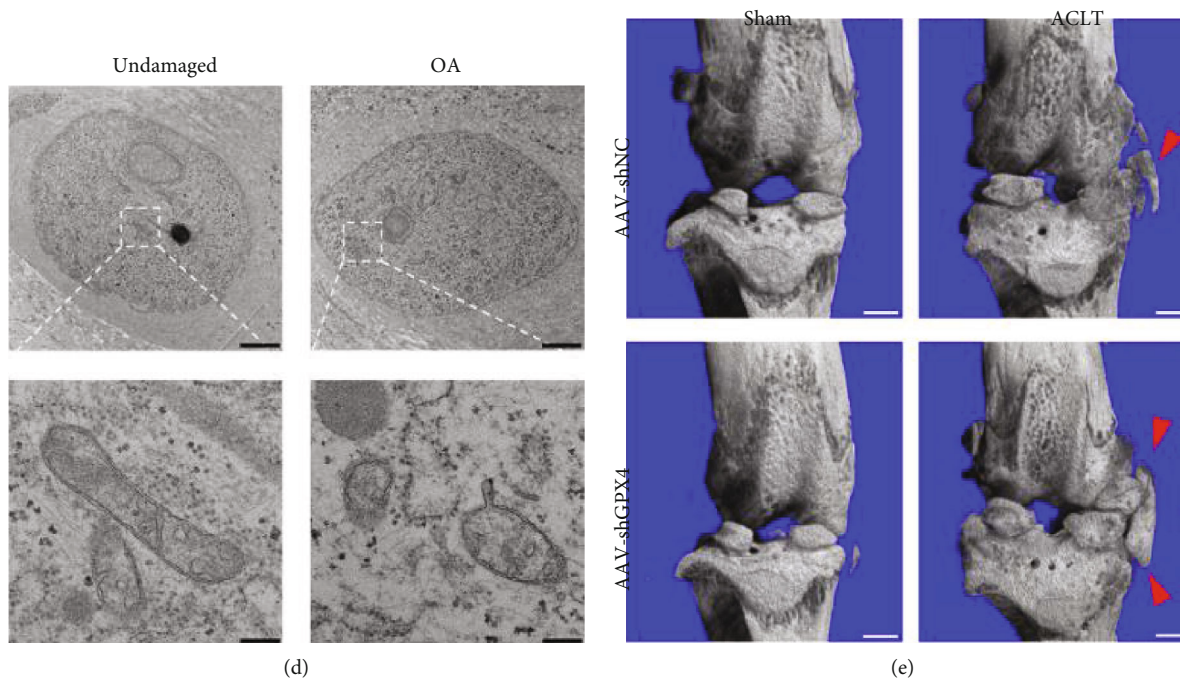


FIGURE 5: (a) Cartilage degradation was assessed by safranin O/fast green about collagen II and GPX4 expression in an OA model (reproduced from ref. [119] with permission from 2020 Elsevier B.V.); (b) immunohistochemistry staining of GPX4 (reproduced from ref. [119] with permission from 2020 Elsevier B.V.); (c) chondrocytes 24 h postindicated treatments by MitoTracker Red staining (reproduced from ref. [121] with permission from 2021 Ovid Technologies, Inc.); (d) mitochondrial membrane rupture in OA cartilage tissues by a transmission electron microscope (reproduced from ref. [122] with permission from 2022 Elsevier B.V.); (e) three-dimensional models of mouse knee joints. Red arrow shows osteophyte formation (reproduced from ref. [122] with permission from 2022 Elsevier B.V.).

According to statistics, approximately 300 million people suffer from osteoarthritis worldwide [115]. While surgery and medication have greatly improved the motor functions of patients, subsequent rehabilitation treatment requires further perfection [116].

Recent studies have shown that OA, which is closely related to inflammation, is a complex process associated with ferroptosis in terms of iron homeostasis [117, 118]. Yao et al. found that erastin, a specific ferroptosis inducer, downregulated type II collagen (collagen II) expression orchestrated with OA in chondrocytes, while ferrostatin-1 could ameliorate this phenomenon by eliminating lipid ROS (Figures 5(a) and 5(b)) [119]. Ferrostatin-1 attenuated OA progression, as detected by immunohistochemistry and the OARSI score, by suppressing ferroptosis and upregulating GPX4 expression in the OA mouse model. In addition, the Nrf2 antioxidant system and ferroptosis regulate each other under inflammatory and iron overload conditions, although the detailed mechanism is still unclear [120]. A subsequent study also found that D-mannose, a compound involved in immune regulation, exerted a chondroprotective effect by attenuating the sensitivity of chondrocytes to ferroptosis and alleviating OA progression (Figure 5(c)) [121]. Through further research, GPx4 was shown to play an important role in the relationship between osteoarthritis and ferroptosis. GPx4 regulates ferroptosis or oxidative stress and ECM degradation through the MAPK/NF- κ B signaling pathway to alleviate the progression of osteoarthritis

(Figures 5(d) and 5(e)) [122]. Bin et al. also found that inflammation induced by suppressing miR-10a-5p regulated by IL-6 can promote ferroptosis in cartilage cells through cellular oxidative stress and iron homeostasis imbalance [105]. In addition, subsequent results suggest that IL-6 in IVD exacerbates its degeneration by inducing cartilage cell ferroptosis, thus causing lumbar instability, fracture, and intervertebral disc degeneration [123]. They may make the IL-6/miR-10a-5p/IL-6R axis a potential therapeutic target for IDD intervention in the future. To date, we realize that ferroptosis plays an important role in osteoarthritis, but the detailed mechanisms require further study.

7.5. Rheumatoid Arthritis. Rheumatoid arthritis (RA), a chronic systemic disease with a sophisticated etiology, is considered a common disease that affects 0.5–1% of the global population [124]. RA is a chronic autoimmune disease that is characterized by multijoint, symmetrical, and invasive joint inflammation and is often accompanied by the involvement of extraarticular organs and positive serum rheumatoid factor, which can lead to joint deformity and loss of function [125, 126]. However, current medical strategies only alleviate symptoms and delay the process instead of healing it completely, and later rehabilitation exercise is not very satisfactory [127, 128].

Recent studies have shown that ferroptosis plays an important regulatory role in autoimmune and inflammatory diseases [129, 130]. For example, treatment with the Gpx4

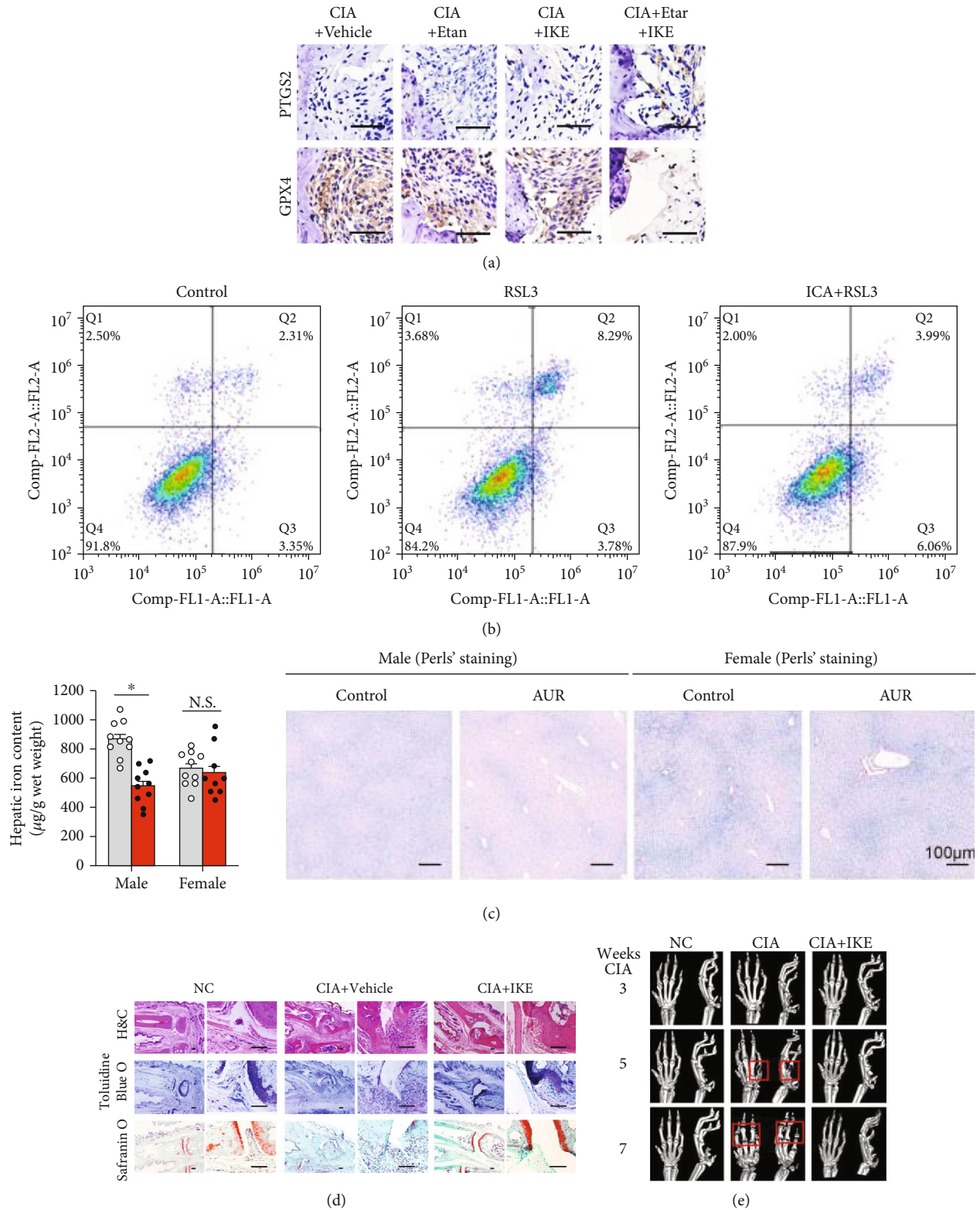


FIGURE 6: (a) Immunohistochemical staining about PTGS2 and GPX4 expression in the joints of CIA mice (reproduced from ref. [131] with permission from 2022 Nature Publishing Group); (b) cell death in the different study groups by flow cytometry (reproduced from ref. [136] with permission from 2021 Ingenta PLC); (c) Perls' Prussian blue-stained liver sections (reproduced from ref. [138] with permission from 2020 Nature Publishing Group); (d) images of hematoxylin and eosin (H&E), toluidine blue O, and safranin O staining of representative joints in control and CIA mice with or without IKE treatment at day 22 after treatment initiation (reproduced from ref. [131] with permission from 2022 Nature Publishing Group); (e) representative microcomputed tomography (micro-CT) images of control and CIA model mice with or without IKE treatment (reproduced from ref. [131] with permission from 2022 Nature Publishing Group).

inhibitor RSL3 specifically increased cell death in fibroblast activation protein- α (FAP α +) fibroblasts, but not macrophages, endothelial cells, T cells, or B cells of cell death. In addition, the number of surviving FAP α fibroblasts in the synovial area was higher, close to that of macrophages, suggesting that macrophages may protect FAP α fibroblasts from IKE treatment-induced lipid peroxidation and ferroptosis in CIA mice [131]. Of course, how immune cells induce ferroptosis in RA requires further study. Besides, a previous study revealed that in an RA model, metalloproteinases (MMPs) are activated by excessive ROS, thus suppressing the synthesis of cartilage protein and leading to cartilage injury and bone destruction. In short, excessive ROS is closely related to RA [132]. Simultaneously, excessive ROS also have a hand in ferroptosis of synovial cell death. In ferroptosis, ROS are transformed into hydrogen peroxide through the Fenton reaction, which produces hydroxyl ($\cdot\text{OH}$) or alkoxy ($\text{RO}\cdot$) radicals with the help of superoxide dismutase in the presence of reduced Fe^{2+} . Afterwards, Fe^{3+} can be converted into Fe^{2+} by the Haber-Weiss reaction [133]. Meanwhile, FSP1 improves lipid peroxidation and blocks iron sagging by combining with CoQ_{10} [134, 135]. It could be calculated that FSP1, which acts parallel to GPX4, is likely to abolish the TNF- α /ROS feedback loop and prevent ferroptosis of cell death in RA. Moreover, low-dose imidazole ketone erastin (IKE) together with etanercept, a TNF antagonist, induced ferroptosis in fibroblasts and attenuated arthritis progression in a collagen-induced arthritis (CIA) mouse model (Figures 6(a), 6(d), and 6(e)) [131]. Luo and Zhang and Zu et al. also observed the same phenomenon as ICA, an important role in both rheumatoid arthritis and osteoarthritis and associated with gene expression and cellular functions in the synoviocytes of osteoarthritis, inhibiting ferroptosis through the Xc⁻/GPX4 axis, thus attenuating cell death in the RA model (Figure 6(b)) [136, 137]. On the basis of previous research, Yang *et al.* observed lipid peroxidation and iron metabolism disorders in LPS-induced synovial cells (Figure 6(c)) [138]. At present, many scholars have invested much time and energy in the study of ferroptosis in RA and have developed related drugs, such as curcumin and baicalein, to intervene in RA due to lipid peroxidation and iron metabolism disorders in RA [139, 140]. However, we still know little about the detailed mechanisms. We hope that subsequent research can overcome these bottlenecks.

8. Questions and Perspectives

In recent years, our understanding of ferroptosis has gradually deepened in biomedicine, and thousands of articles have been published. On the whole, ferroptosis is considered to be a programmed regulation of cell death, which is strictly regulated at multiple layers and multiple levels [141, 142]. Many pharmacological and genetic operations have been used to regulate changes induced by ferroptosis in multidisciplinary diseases such as cardiovascular diseases, renal injury, and skeletal muscle diseases and attenuate disease mortality and disability rates [43, 138, 143, 144]. However, research on ferroptosis is in an immature stage, and an array

of doubts remain unanswered, especially in skeletal diseases. For example, cell death patterns have many similarities in skeletal diseases, such as ferroptosis, autophagy, and apoptosis. What is the association between these cell death patterns? Is it mutual promotion or antagonism? How these different cell death patterns can be integrated into a system still needs further study [6]. According to previous research, iron plays an indispensable role in the development of ferroptosis [1]. With the exception of iron ions, ferroptosis occurs under the regulation of some metal ions in some instances [145, 146]. This makes us doubt the traditional definition of ferroptosis. Is iron vital to promote lipid peroxidation, or can other fungi induce ferroptosis? This view requires further discussion. Subsequent studies have shown that FPN, as an upstream iron metabolism gene, can regulate ferroptosis, but how the downstream pathway is regulated is still not very clear [11, 75–77]. Ferroptosis accompanies inflammation in some diseases such as RA and acute kidney injury and modulates the immune system, causing inflammatory damage and inhibiting cell growth [147–150]. Under what circumstances will it promote ferroptosis-induced inflammation? In addition, no clinical trials have been conducted on ferroptosis activators in skeletal diseases. How can we integrate basic research results and thus promote the recovery of skeletal diseases to reduce disability and mortality? As stated above, even if we invest more time and enthusiasm than before in conducting research on ferroptosis, a series of detailed problems about ferroptosis urgently need to be solved.

9. Conclusion

In this review, we summarize the mechanism of ferroptosis, such as suppressing GPX4 expression and activating the lipid metabolism pathway; briefly list several inducers and inhibitors; and expound on the manifestations of iron death in skeletal diseases. As will be readily seen from this article, our research on ferroptosis is still superficial at present. It is of great significance to explore the mystery of ferroptosis and its specific role in multiple distinct diseases, especially skeletal diseases, and to develop targeted therapeutic regimens. This will be the general trend of future research.

Abbreviations

TFR1:	Transferrin receptor 1
PUFA:	Polyunsaturated fatty acid
LOXs:	Lipoxygenase
STEAP3:	Six-transmembrane epithelial antigen of prostate 3 metalloreductase
SLC7A11:	Solute carrier family 7 member 11
DMT1:	Divalent metal transporter 1
SLC3A2:	Solute carrier family 3 member 2
BAP1:	BRCA1-associated protein 1
ROS:	Reactive oxygen species
FSP1:	Ferroptosis suppressor protein 1
FPN1:	Ferroportin 1
GPX4:	Glutathione peroxidase 4
GSH:	Glutathione

GSSG: Oxidized glutathione
 GSS: Glutathione synthetase
 PHKG2: Phosphorylase kinase G2
 HSPB1: Heat shock protein beta-1
 NCOA4: Nuclear receptor coactivator 4
 RSL3: Ras-selective lethal 3
 RSL5: Ras-selective lethal 5.

Data Availability

The authors confirm that the data supporting the findings of this study are available within the article.

Conflicts of Interest

The authors have declared that no competing interest exists.

Authors' Contributions

LX and WT wrote the manuscript. GD and BJ designed the manuscript. WW, LX, MY, GD, and XY revised the manuscript. LX and LX designed the figures. All authors read and approved the final paper. Xin Liu, Tianhao Wang, and Wei Wang contributed equally to this work.

Acknowledgments

This work is supported by grants from the National Natural Science Foundation of China (82072425, 82072498, and 82074473), the Young Medical Talents of Jiangsu Province (QNRC2016751), the Natural Science Foundation of Jiangsu Province (BK20200198, BE2021650), Special Project of Diagnosis and Treatment Technology for Key Clinical Diseases in Suzhou (LCZX202003, LCZX201824), and the Priority Academic Program Development of Jiangsu Higher Education Institutions (PAPD).

References

- [1] S. J. Dixon, K. M. Lemberg, M. R. Lamprecht et al., "Ferrop-tosis: an iron-dependent form of nonapoptotic cell death," *Cell*, vol. 149, no. 5, pp. 1060–1072, 2012.
- [2] S. J. Dixon and B. R. Stockwell, "The role of iron and reactive oxygen species in cell death," *Nature Chemical Biology*, vol. 10, no. 1, pp. 9–17, 2014.
- [3] B. R. Stockwell, J. P. Friedmann Angeli, H. Bayir et al., "Fer-roptosis: a regulated cell death nexus linking metabolism, redox biology, and disease," *Cell*, vol. 171, no. 2, pp. 273–285, 2017.
- [4] W. S. Yang and B. R. Stockwell, "Synthetic lethal screening identifies compounds activating iron-dependent, nonapopto-tic cell death in oncogenic-RAS-harboring cancer cells," *Chemistry & Biology*, vol. 15, no. 3, pp. 234–245, 2008.
- [5] N. Yagoda, M. von Rechenberg, E. Zaganjor et al., "RAS-RAF-MEK-dependent oxidative cell death involving voltage-dependent anion channels," *Nature*, vol. 447, no. 7146, pp. 864–868, 2007.
- [6] Y. Xie, W. Hou, X. Song et al., "Ferroptosis: process and func-tion," *Cell Death and Differentiation*, vol. 23, no. 3, pp. 369–379, 2016.
- [7] W. S. Yang, R. SriRamaratnam, M. E. Welsch et al., "Regula-tion of ferroptotic cancer cell death by GPX4," *Cell*, vol. 156, no. 1–2, pp. 317–331, 2014.
- [8] H. Imai, M. Matsuoka, T. Kumagai, T. Sakamoto, and T. Koumura, "Lipid peroxidation-dependent cell death regu-lated by GPx4 and ferroptosis," *Current Topics in Microbiol-ogy and Immunology*, vol. 403, pp. 143–170, 2017.
- [9] J. P. F. Angeli, R. Shah, D. A. Pratt, and M. Conrad, "Ferroptosis inhibition: mechanisms and opportunities," *Trends in Pharmacological Sciences*, vol. 38, no. 5, pp. 489–498, 2017.
- [10] Y. Su, B. Zhao, L. Zhou et al., "Ferroptosis, a novel pharmaco-logical mechanism of anti-cancer drugs," *Cancer Letters*, vol. 483, pp. 127–136, 2020.
- [11] M. Gao, P. Monian, N. Quadri, R. Ramasamy, and X. Jiang, "Glutaminolysis and transferrin regulate ferroptosis," *Molec-ular Cell*, vol. 59, no. 2, pp. 298–308, 2015.
- [12] Z. Hu, H. Zhang, S. K. Yang et al., "Emerging role of ferroptosis in acute kidney injury," *Oxidative Medicine and Cellular Lon-gevity*, vol. 2019, Article ID 8010614, 8 pages, 2019.
- [13] D. P. Del Re, D. Amgalan, A. Linkermann, Q. Liu, and R. N. Kitsis, "Fundamental mechanisms of regulated cell death and implications for heart disease," *Physiological Reviews*, vol. 99, no. 4, pp. 1765–1817, 2019.
- [14] S. Xu, Y. He, L. Lin, P. Chen, M. Chen, and S. Zhang, "The emerging role of ferroptosis in intestinal disease," *Cell Death & Disease*, vol. 12, no. 4, p. 289, 2021.
- [15] M. Hong, J. Rong, X. Tao, and Y. Xu, "The emerging role of ferroptosis in cardiovascular diseases," *Frontiers in Pharma-cology*, vol. 13, p. 822083, 2022.
- [16] C. Zhang, X. Liu, S. Jin, Y. Chen, and R. Guo, "Ferroptosis in cancer therapy: a novel approach to reversing drug resis-tance," *Molecular Cancer*, vol. 21, no. 1, p. 47, 2022.
- [17] Q. Liu and K. Wang, "The induction of ferroptosis by impair-ing STAT3/Nrf2/GPx4 signaling enhances the sensitivity of osteosarcoma cells to cisplatin," *Cell Biology International*, vol. 43, no. 11, pp. 1245–1256, 2019.
- [18] X. Yao, Y. Zhang, J. Hao et al., "Deferoxamine promotes recovery of traumatic spinal cord injury by inhibiting ferroptosis," *Neural Regeneration Research*, vol. 14, no. 3, pp. 532–541, 2019.
- [19] J. F. Kerr, "A histochemical study of hypertrophy and ischaem-ic injury of rat liver with special reference to changes in lysosomes," *The Journal of Pathology and Bacteriology*, vol. 90, no. 2, pp. 419–435, 1965.
- [20] R. A. Lockshin and C. M. Williams, "Programmed cell death—I. cytology of degeneration in the intersegmental muscles of the Pernyi silkworm," *Journal of Insect Physiology*, vol. 11, no. 2, pp. 123–133, 1965.
- [21] R. Schuckelt, R. Brigelius-Flohe, M. Maiorino et al., "Phospho-lipid hydroperoxide glutathione peroxidase is a selenoenzyme distinct from the classical glutathione peroxidase as evident from cDNA and amino acid sequencing," *Free Radical Research Communications*, vol. 14, no. 5–6, pp. 343–361, 1991.
- [22] J. P. Thomas, M. Maiorino, F. Ursini, and A. W. Girotti, "Pro-protective action of phospholipid hydroperoxide glutathione peroxidase against membrane-damaging lipid peroxidation. In situ reduction of phospholipid and cholesterol hydroper-oxides," *Journal of Biological Chemistry*, vol. 265, no. 1, pp. 454–461, 1990.
- [23] F. Ursini, M. Maiorino, M. Valente, L. Ferri, and C. Gregolin, "Purification from pig liver of a protein which protects

- liposomes and biomembranes from peroxidative degradation and exhibits glutathione peroxidase activity on phosphatidylcholine hydroperoxides," *Biochimica et Biophysica Acta*, vol. 710, no. 2, pp. 197–211, 1982.
- [24] S. J. Chambers, N. Lambert, and G. Williamson, "Purification of a cytosolic enzyme from human liver with phospholipid hydroperoxide glutathione peroxidase activity," *The International Journal of Biochemistry*, vol. 26, no. 10-11, pp. 1279–1286, 1994.
- [25] S. Dolma, S. L. Lessnick, W. C. Hahn, and B. R. Stockwell, "Identification of genotype-selective antitumor agents using synthetic lethal chemical screening in engineered human tumor cells," *Cancer Cell*, vol. 3, no. 3, pp. 285–296, 2003.
- [26] S. Tan, D. Schubert, and P. Maher, "Oxytosis: a novel form of programmed cell death," *Current Topics in Medicinal Chemistry*, vol. 1, no. 6, pp. 497–506, 2001.
- [27] J. B. Davis and P. Maher, "Protein kinase C activation inhibits glutamate-induced cytotoxicity in a neuronal cell line," *Brain Research*, vol. 652, no. 1, pp. 169–173, 1994.
- [28] H. Sato, M. Tamba, K. Kuriyama-Matsumura, S. Okuno, and S. Bannai, "Molecular cloning and expression of human xCT, the light chain of amino acid transport system xc," *Antioxidants & Redox Signaling*, vol. 2, no. 4, pp. 665–671, 2000.
- [29] H. Eagle, "Nutrition needs of mammalian cells in tissue culture," *Science*, vol. 122, no. 3168, pp. 501–504, 1955.
- [30] D. E. Root, S. P. Flaherty, B. P. Kelley, and B. R. Stockwell, "Biological mechanism profiling using an annotated compound library," *Chemistry & Biology*, vol. 10, no. 9, pp. 881–892, 2003.
- [31] R. Skouta, S. J. Dixon, J. Wang et al., "Ferostatins inhibit oxidative lipid damage and cell death in diverse disease models," *Journal of the American Chemical Society*, vol. 136, no. 12, pp. 4551–4556, 2014.
- [32] C. Louandre, I. Marcq, H. Bouhlal et al., "The retinoblastoma (Rb) protein regulates ferroptosis induced by sorafenib in human hepatocellular carcinoma cells," *Cancer Letters*, vol. 356, no. 2, pp. 971–977, 2015.
- [33] J. Dachert, H. Schoeneberger, K. Rohde, and S. Fulda, "RSL3 and Erastin differentially regulate redox signaling to promote Smac mimetic-induced cell death," *Oncotarget*, vol. 7, no. 39, pp. 63779–63792, 2016.
- [34] D. Shin, E. H. Kim, J. Lee, and J. L. Roh, "Nrf2 inhibition reverses resistance to GPX4 inhibitor-induced ferroptosis in head and neck cancer," *Free Radical Biology & Medicine*, vol. 129, pp. 454–462, 2018.
- [35] K. Miyamoto, M. Watanabe, S. Boku et al., "xCT inhibition increases sensitivity to vorinostat in a ROS-dependent manner," *Cancers (Basel)*, vol. 12, no. 4, p. 827, 2020.
- [36] D. M. Medeiros, B. Stoecker, A. Plattner, D. Jennings, and M. Haub, "Iron deficiency negatively affects vertebrae and femurs of rats independently of energy intake and body weight," *The Journal of Nutrition*, vol. 134, no. 11, pp. 3061–3067, 2004.
- [37] M. Parelman, B. Stoecker, A. Baker, and D. Medeiros, "Iron restriction negatively affects bone in female rats and mineralization of hFOB osteoblast cells," *Experimental Biology and Medicine*, vol. 231, no. 4, pp. 378–386, 2006.
- [38] I. Wright, R. Blanco-Rojo, M. C. Fernandez et al., "Bone remodelling is reduced by recovery from iron-deficiency anaemia in premenopausal women," *Journal of Physiology and Biochemistry*, vol. 69, no. 4, pp. 889–896, 2013.
- [39] V. Jeney, "Clinical impact and cellular mechanisms of iron overload-associated bone loss," *Frontiers in Pharmacology*, vol. 8, p. 77, 2017.
- [40] B. J. Kim, S. H. Ahn, S. J. Bae et al., "Iron overload accelerates bone loss in healthy postmenopausal women and middle-aged men: a 3-year retrospective longitudinal study," *Journal of Bone and Mineral Research*, vol. 27, no. 11, pp. 2279–2290, 2012.
- [41] P. Richette, S. Ottaviani, E. Vicaut, and T. Bardin, "Musculoskeletal complications of hereditary hemochromatosis: a case-control study," *The Journal of Rheumatology*, vol. 37, no. 10, pp. 2145–2150, 2010.
- [42] T. Diamond, D. Stiel, and S. Posen, "Osteoporosis in hemochromatosis: iron excess, gonadal deficiency, or other factors," *Annals of Internal Medicine*, vol. 110, no. 6, pp. 430–436, 1989.
- [43] J. P. Friedmann Angeli, M. Schneider, B. Proneth et al., "Inactivation of the ferroptosis regulator Gpx4 triggers acute renal failure in mice," *Nature Cell Biology*, vol. 16, no. 12, pp. 1180–1191, 2014.
- [44] M. Yu, C. Gai, Z. Li et al., "Targeted exosome-encapsulated erastin induced ferroptosis in triple negative breast cancer cells," *Cancer Science*, vol. 110, no. 10, pp. 3173–3182, 2019.
- [45] K. Sakitama, Y. Ozawa, N. Aoto, H. Tomita, and M. Ishikawa, "Effects of a new centrally acting muscle relaxant, NK433 (lanperisone hydrochloride) on spinal reflexes," *European Journal of Pharmacology*, vol. 337, no. 2-3, pp. 175–187, 1997.
- [46] X. Li, J. Zeng, Y. Liu et al., "Inhibitory effect and mechanism of action of quercetin and quercetin Diels-Alder anti-dimer on erastin-induced ferroptosis in bone marrow-derived mesenchymal stem cells," *Antioxidants (Basel)*, vol. 9, no. 3, p. 205, 2020.
- [47] A. T. Shaw, M. M. Winslow, M. Magendantz et al., "Selective killing of K-ras mutant cancer cells by small molecule inducers of oxidative stress," *Proceedings of the National Academy of Sciences of the United States of America*, vol. 108, no. 21, pp. 8773–8778, 2011.
- [48] C. Louandre, Z. Ezzoukhry, C. Godin et al., "Iron-dependent cell death of hepatocellular carcinoma cells exposed to sorafenib," *International Journal of Cancer*, vol. 133, no. 7, pp. 1732–1742, 2013.
- [49] R. Belayneh, M. S. Fourman, S. Bhogal, and K. R. Weiss, "Update on osteosarcoma," *Current Oncology Reports*, vol. 23, no. 6, p. 71, 2021.
- [50] E. Lachaier, C. Louandre, C. Godin et al., "Sorafenib induces ferroptosis in human cancer cell lines originating from different solid tumors," *Anticancer Research*, vol. 34, no. 11, pp. 6417–6422, 2014.
- [51] X. Sun, Z. Ou, R. Chen et al., "Activation of the p62-Keap1-NRF2 pathway protects against ferroptosis in hepatocellular carcinoma cells," *Hepatology*, vol. 63, no. 1, pp. 173–184, 2016.
- [52] S. J. Dixon, D. N. Patel, M. Welsch et al., "Pharmacological inhibition of cystine-glutamate exchange induces endoplasmic reticulum stress and ferroptosis," *eLife*, vol. 3, p. e02523, 2014.
- [53] Y. Xu, W. Sang, Y. Zhong et al., "CoCrMo-nanoparticles induced peri-implant osteolysis by promoting osteoblast ferroptosis via regulating Nrf2-ARE signalling pathway," *Cell Proliferation*, vol. 54, no. 12, article e13142, 2021.
- [54] H. Dong, Z. Qiang, D. Chai et al., "Nrf2 inhibits ferroptosis and protects against acute lung injury due to intestinal

- ischemia reperfusion via regulating SLC7A11 and HO-1," *Aging (Albany NY)*, vol. 12, no. 13, pp. 12943–12959, 2020.
- [55] L. Martín-Saiz, J. Guerrero-Mauvecin, D. Martín-Sánchez et al., "Ferrosstatin-1 modulates dysregulated kidney lipids in acute kidney injury," *The Journal of Pathology*, vol. 257, no. 3, pp. 285–299, 2022.
- [56] Y. Luo, X. Gao, L. Zou, M. Lei, J. Feng, and Z. Hu, "Bavachin induces ferroptosis through the STAT3/P53/SLC7A11 axis in osteosarcoma cells," *Oxidative Medicine and Cellular Longevity*, vol. 2021, Article ID 1783485, 14 pages, 2021.
- [57] Y. Feng, N. B. Madungwe, A. D. Imam Aliagan, N. Tombo, and J. C. Bopassa, "Liproxstatin-1 protects the mouse myocardium against ischemia/reperfusion injury by decreasing VDAC1 levels and restoring GPX4 levels," *Biochemical and Biophysical Research Communications*, vol. 520, no. 3, pp. 606–611, 2019.
- [58] A. Belavgeni, S. R. Bornstein, and A. Linkermann, "Prominin-2 suppresses ferroptosis sensitivity," *Developmental Cell*, vol. 51, no. 5, pp. 548–549, 2019.
- [59] C. W. Brown, J. J. Amante, P. Chhoy et al., "Prominin2 drives ferroptosis resistance by stimulating iron export," *Developmental Cell*, vol. 51, no. 5, pp. 575–586.e4, 2019.
- [60] C. W. Brown, P. Chhoy, D. Mukhopadhyay, E. R. Karner, and A. M. Mercurio, "Targeting prominin2 transcription to overcome ferroptosis resistance in cancer," *EMBO Molecular Medicine*, vol. 13, no. 8, p. e13792, 2021.
- [61] L. Jiang, J. H. Hickman, S. J. Wang, and W. Gu, "Dynamic roles of p53-mediated metabolic activities in ROS-induced stress responses," *Cell Cycle*, vol. 14, no. 18, pp. 2881–2885, 2015.
- [62] L. Jiang, N. Kon, T. Li et al., "Ferroptosis as a p53-mediated activity during tumour suppression," *Nature*, vol. 520, no. 7545, pp. 57–62, 2015.
- [63] M. Maiorino, M. Conrad, and F. Ursini, "GPx4, lipid peroxidation, and cell death: discoveries, rediscoveries, and open issues," *Rediscoveries, and Open Issues, Antioxid Redox Signal*, vol. 29, no. 1, pp. 61–74, 2018.
- [64] G. J. Warner, M. J. Berry, M. E. Moustafa, B. A. Carlson, D. L. Hatfield, and J. R. Faust, "Inhibition of selenoprotein synthesis by selenocysteine tRNA Ser Sec lacking isopentenyladenosine," *The Journal of Biological Chemistry*, vol. 275, no. 36, pp. 28110–28119, 2000.
- [65] X. Yao, R. Xie, Y. Cao et al., "Simvastatin induced ferroptosis for triple-negative breast cancer therapy," *Journal of Nanobiotechnology*, vol. 19, no. 1, p. 311, 2021.
- [66] H. Yu, P. Guo, X. Xie, Y. Wang, and G. Chen, "Ferroptosis, a new form of cell death, and its relationships with tumorous diseases," *Journal of Cellular and Molecular Medicine*, vol. 21, no. 4, pp. 648–657, 2017.
- [67] Y. Ou, S. J. Wang, D. Li, B. Chu, and W. Gu, "Activation of SAT1 engages polyamine metabolism with p53-mediated ferroptotic responses," *Proceedings of the National Academy of Sciences of the United States of America*, vol. 113, no. 44, pp. E6806–E6812, 2016.
- [68] A. Tarangelo, L. Magtanong, K. T. Bieging-Rolett et al., "p53 suppresses metabolic stress-induced Ferroptosis in cancer cells," *Cell Reports*, vol. 22, no. 3, pp. 569–575, 2018.
- [69] B. Niu, X. Lei, Q. Xu et al., "Protecting mitochondria via inhibiting VDAC1 oligomerization alleviates ferroptosis in acetaminophen-induced acute liver injury," *Cell Biology and Toxicology*, vol. 38, no. 3, pp. 505–530, 2022.
- [70] M. Kanapathipillai, "Treating p53 mutant aggregation-associated cancer," *Cancers (Basel)*, vol. 10, no. 6, p. 154, 2018.
- [71] W. He, W. Shu, L. Xue et al., "Synergistic effect of erastin combined with Nutlin-3 on vestibular schwannoma cells as p53 modulates erastin-induced ferroptosis response," *Journal of Oncology*, vol. 2022, Article ID 7507857, 18 pages, 2022.
- [72] Y. Xie, S. Zhu, X. Song et al., "The tumor suppressor p53 limits ferroptosis by blocking DPP4 activity," *Cell Reports*, vol. 20, no. 7, pp. 1692–1704, 2017.
- [73] D. M. Frazer and G. J. Anderson, "The regulation of iron transport," *BioFactors*, vol. 40, no. 2, pp. 206–214, 2014.
- [74] A. R. Bogdan, M. Miyazawa, K. Hashimoto, and Y. Tsuji, "Regulators of iron homeostasis: new players in metabolism, cell death, and disease," *Trends in Biochemical Sciences*, vol. 41, no. 3, pp. 274–286, 2016.
- [75] M. Y. Kwon, E. Park, S. J. Lee, and S. W. Chung, "Heme oxygenase-1 accelerates erastin-induced ferroptotic cell death," *Oncotarget*, vol. 6, no. 27, pp. 24393–24403, 2015.
- [76] X. Sun, Z. Ou, M. Xie et al., "HSPB1 as a novel regulator of ferroptotic cancer cell death," *Oncogene*, vol. 34, no. 45, pp. 5617–5625, 2015.
- [77] E. Gammella, S. Recalcati, I. Rybinska, P. Buratti, and G. Cairo, "Iron-induced damage in cardiomyopathy: oxidative-dependent and independent mechanisms," *Oxidative Medicine and Cellular Longevity*, vol. 2015, Article ID 230182, 10 pages, 2015.
- [78] W. S. Yang and B. R. Stockwell, "Ferroptosis: death by lipid peroxidation," *Trends in Cell Biology*, vol. 26, no. 3, pp. 165–176, 2016.
- [79] J. Y. Lee, W. K. Kim, K. H. Bae, S. C. Lee, and E. W. Lee, "Lipid metabolism and ferroptosis," *Biology (Basel)*, vol. 10, no. 3, p. 184, 2021.
- [80] J. Liu, R. Kang, and D. Tang, "Signaling pathways and defense mechanisms of ferroptosis," *The FEBS Journal*, 2021.
- [81] N. E. Lane, "Epidemiology, etiology, and diagnosis of osteoporosis," *American Journal of Obstetrics and Gynecology*, vol. 194, no. 2, pp. S3–11, 2006.
- [82] J. L. Kelsey, "Risk factors for osteoporosis and associated fractures," *Public Health Reports*, vol. 104, pp. 14–20, 1989.
- [83] K. M. Prestwood, C. C. Pilbeam, and L. G. Raisz, "Treatment of osteoporosis," *Annual Review of Medicine*, vol. 46, no. 1, pp. 249–256, 1995.
- [84] R. S. Weinstein and S. C. Manolagas, "Apoptosis and osteoporosis," *The American Journal of Medicine*, vol. 108, no. 2, pp. 153–164, 2000.
- [85] K. H. Kim and M. S. Lee, "Autophagy—a key player in cellular and body metabolism," *Nature Reviews. Endocrinology*, vol. 10, no. 6, pp. 322–337, 2014.
- [86] Q. Tian, S. Wu, Z. Dai et al., "Iron overload induced death of osteoblasts in vitro: involvement of the mitochondrial apoptotic pathway," *PeerJ*, vol. 4, p. e2611, 2016.
- [87] Q. Tian, B. Qin, Y. Gu et al., "ROS-mediated necroptosis is involved in iron overload-induced osteoblastic cell death," *Oxidative Medicine and Cellular Longevity*, vol. 2020, Article ID 1295382, 22 pages, 2020.
- [88] W. Ge, J. Jie, J. Yao, W. Li, Y. Cheng, and W. Lu, "Advanced glycation end products promote osteoporosis by inducing ferroptosis in osteoblasts," *Molecular Medicine Reports*, vol. 25, no. 4, 2022.

- [89] H. Ma, X. Wang, W. Zhang et al., "Melatonin suppresses ferroptosis induced by high glucose via activation of the Nrf2/HO-1 signaling pathway in type 2 diabetic osteoporosis," *Oxidative Medicine and Cellular Longevity*, vol. 2020, Article ID 9067610, 18 pages, 2020.
- [90] S. Ni, Y. Yuan, Z. Qian et al., "Hypoxia inhibits RANKL-induced ferritinophagy and protects osteoclasts from ferroptosis," *Free Radical Biology & Medicine*, vol. 169, pp. 271–282, 2021.
- [91] H. Ding, S. Chen, X. Pan et al., "Transferrin receptor 1 ablation in satellite cells impedes skeletal muscle regeneration through activation of ferroptosis," *Journal of Cachexia, Sarcopenia and Muscle*, vol. 12, no. 3, pp. 746–768, 2021.
- [92] P. Liu, W. Wang, Z. Li et al., "Ferroptosis: a new regulatory mechanism in osteoporosis," *Oxidative Medicine and Cellular Longevity*, vol. 2022, Article ID 2634431, 10 pages, 2022.
- [93] R. Galeiras Vazquez, M. E. Ferreira Velasco, M. Mourelo Farina, A. Montoto Marques, and S. Salvador de la Barrera, "Actualización en lesión medular aguda postraumática. Parte 1," *Medicina Intensiva (English Edition)*, vol. 41, no. 4, pp. 237–247, 2017.
- [94] N. Chen, P. Zhou, X. Liu et al., "Overexpression of Rictor in the injured spinal cord promotes functional recovery in a rat model of spinal cord injury," *The FASEB Journal*, vol. 34, no. 5, pp. 6984–6998, 2020.
- [95] W. R. Yu and M. G. Fehlings, "Fas/FasL-mediated apoptosis and inflammation are key features of acute human spinal cord injury: implications for translational, clinical application," *Acta Neuropathologica*, vol. 122, no. 6, pp. 747–761, 2011.
- [96] F. Abbaszadeh, S. Fakhri, and H. Khan, "Targeting apoptosis and autophagy following spinal cord injury: therapeutic approaches to polyphenols and candidate phytochemicals," *Pharmacological Research*, vol. 160, p. 105069, 2020.
- [97] S. Fakhri, F. Abbaszadeh, S. Z. Moradi, H. Cao, H. Khan, and J. Xiao, "Effects of polyphenols on oxidative stress, inflammation, and interconnected pathways during spinal cord injury," *Oxidative Medicine and Cellular Longevity*, vol. 2022, Article ID 8100195, 34 pages, 2022.
- [98] M. Takashima, K. Ichihara, and Y. Hirata, "Neuroprotective effects of Brazilian green propolis on oxytosis/ferroptosis in mouse hippocampal HT22 cells," *Food and Chemical Toxicology*, vol. 132, p. 110669, 2019.
- [99] E. M. Kenny, E. Fidan, Q. Yang et al., "Ferroptosis contributes to neuronal death and functional outcome after traumatic brain injury," *Critical Care Medicine*, vol. 47, no. 3, pp. 410–418, 2019.
- [100] H. He, L. Wang, Y. Qiao, B. Yang, D. Yin, and M. He, "Epigallocatechin-3-gallate pretreatment alleviates doxorubicin-induced ferroptosis and cardiotoxicity by upregulating AMPK α 2 and activating adaptive autophagy," *Redox Biology*, vol. 48, p. 102185, 2021.
- [101] M. Lesjak, N. Simin, and S. K. S. Srail, "Can polyphenols inhibit ferroptosis," *Antioxidants (Basel)*, vol. 11, no. 1, p. 150, 2022.
- [102] K. Venkatesh, S. K. Ghosh, M. Mullick, G. Manivasagam, and D. Sen, "Spinal cord injury: pathophysiology, treatment strategies, associated challenges, and future implications," *Cell and Tissue Research*, vol. 377, no. 2, pp. 125–151, 2019.
- [103] L. Galluzzi, I. Vitale, J. M. Abrams et al., "Molecular definitions of cell death subroutines: recommendations of the Nomenclature Committee on Cell Death," *Cell Death & Differentiation*, vol. 19, no. 1, pp. 107–120, 2012.
- [104] Y. Zhang, C. Sun, C. Zhao et al., "Ferroptosis inhibitor SRS 16-86 attenuates ferroptosis and promotes functional recovery in contusion spinal cord injury," *Brain Research*, vol. 1706, pp. 48–57, 2019.
- [105] S. Bin, L. Xin, Z. Lin, Z. Jinhua, G. Rui, and Z. Xiang, "Targeting miR-10a-5p/IL-6R axis for reducing IL-6-induced cartilage cell ferroptosis," *Experimental and Molecular Pathology*, vol. 118, p. 104570, 2021.
- [106] J. Ritter and S. S. Bielack, "Osteosarcoma," *Annals of Oncology*, vol. 21, no. 7, pp. vii320–vii325, 2010.
- [107] M. Chen, Y. Jiang, and Y. Sun, "KDM4A-mediated histone demethylation of SLC7A11 inhibits cell ferroptosis in osteosarcoma," *Biochemical and Biophysical Research Communications*, vol. 550, pp. 77–83, 2021.
- [108] H. Lin, X. Chen, C. Zhang et al., "EF24 induces ferroptosis in osteosarcoma cells through HMOX1," *Biomedicine & Pharmacotherapy*, vol. 136, p. 111202, 2021.
- [109] H. H. Lv, C. X. Zhen, J. Y. Liu, and P. Shang, "PEITC triggers multiple forms of cell death by GSH-iron-ROS regulation in K7M2 murine osteosarcoma cells," *Acta Pharmacologica Sinica*, vol. 41, no. 8, pp. 1119–1132, 2020.
- [110] H. Lv, C. Zhen, J. Liu, and P. Shang, " β -Phenethyl isothiocyanate induces cell death in human osteosarcoma through altering iron metabolism, disturbing the redox balance, and activating the MAPK signaling pathway," *Oxidative Medicine and Cellular Longevity*, vol. 2020, Article ID 5021983, 23 pages, 2020.
- [111] H. Lv, C. Zhen, J. Liu, and P. Shang, "Beta-Phenethyl isothiocyanate induces cell death in human osteosarcoma through altering iron metabolism, disturbing the redox balance, and activating the MAPK signaling pathway," *Oxidative Medicine and Cellular Longevity*, vol. 2020, Article ID 5021983, 23 pages, 2020.
- [112] J. M. Yuan, I. Stepanov, S. E. Murphy et al., "Clinical trial of 2-phenethyl isothiocyanate as an inhibitor of metabolic activation of a tobacco-specific lung carcinogen in cigarette smokers," *Cancer Prevention Research*, vol. 9, no. 5, pp. 396–405, 2016.
- [113] E. Tseng, E. A. Scott-Ramsay, and M. E. Morris, "Dietary organic isothiocyanates are cytotoxic in human breast cancer MCF-7 and mammary epithelial MCF-12A cell lines," *Experimental Biology and Medicine*, vol. 229, no. 8, pp. 835–842, 2004.
- [114] S. Glyn-Jones, A. J. Palmer, R. Agricola et al., "Osteoarthritis," *Lancet*, vol. 386, no. 9991, pp. 376–387, 2015.
- [115] G. B. D. Disease, I. Injury, and C. Prevalence, "Global, regional, and national incidence, prevalence, and years lived with disability for 354 diseases and injuries for 195 countries and territories, 1990-2017: a systematic analysis for the Global Burden of Disease Study 2017," *Lancet*, vol. 392, no. 10159, pp. 1789–1858, 2018.
- [116] B. Abramoff and F. E. Caldera, "Osteoarthritis: pathology, diagnosis, and treatment options," *Medical Clinics*, vol. 104, no. 2, pp. 293–311, 2020.
- [117] G. Musumeci, F. C. Aiello, M. A. Szychlinska, M. Di Rosa, P. Castrogiovanni, and A. Mobasher, "Osteoarthritis in the XXIst century: risk factors and behaviours that influence disease onset and progression," *International Journal of Molecular Sciences*, vol. 16, no. 12, pp. 6093–6112, 2015.
- [118] R. Gozzelino and P. Arosio, "Iron homeostasis in health and disease," *International Journal of Molecular Sciences*, vol. 17, no. 1, p. 130, 2016.

- [119] X. Yao, K. Sun, S. Yu et al., "Chondrocyte ferroptosis contribute to the progression of osteoarthritis," *Journal of Orthopaedic Translation*, vol. 27, pp. 33–43, 2021.
- [120] M. Dodson, R. Castro-Portuguez, and D. D. Zhang, "NRF2 plays a critical role in mitigating lipid peroxidation and ferroptosis," *Redox Biology*, vol. 23, p. 101107, 2019.
- [121] X. Zhou, Y. Zheng, W. Sun et al., "D-mannose alleviates osteoarthritis progression by inhibiting chondrocyte ferroptosis in a HIF-2 α -dependent manner," *Cell Proliferation*, vol. 54, no. 11, p. e13134, 2021.
- [122] Y. Miao, Y. Chen, F. Xue et al., "Contribution of ferroptosis and GPX4's dual functions to osteoarthritis progression," *eBioMedicine*, vol. 76, p. 103847, 2022.
- [123] M. Molinos, C. R. Almeida, J. Caldeira, C. Cunha, R. M. Gonçalves, and M. A. Barbosa, "Inflammation in intervertebral disc degeneration and regeneration," *Journal of the Royal Society Interface*, vol. 12, no. 108, p. 20150429, 2015.
- [124] J. S. Smolen, D. Aletaha, and I. B. McInnes, "Rheumatoid arthritis," *Lancet*, vol. 388, no. 10055, pp. 2023–2038, 2016.
- [125] W. Tang, Y. Lu, Q. Y. Tian et al., "The growth factor progranulin binds to TNF receptors and is therapeutic against inflammatory arthritis in mice," *Science*, vol. 332, no. 6028, pp. 478–484, 2011.
- [126] Y. Zhao, A. Zhang, H. Du, S. Guo, B. Ning, and S. Yang, "Tolerogenic dendritic cells and rheumatoid arthritis: current status and perspectives," *Rheumatology International*, vol. 32, no. 4, pp. 837–844, 2012.
- [127] P. C. Taylor, E. C. Keystone, D. van der Heijde et al., "Baricitinib versus placebo or adalimumab in rheumatoid arthritis," *The New England Journal of Medicine*, vol. 376, no. 7, pp. 652–662, 2017.
- [128] J. S. Smolen, D. Aletaha, J. W. Bijlsma et al., "Treating rheumatoid arthritis to target: recommendations of an international task force," *Annals of the Rheumatic Diseases*, vol. 69, no. 4, pp. 631–637, 2010.
- [129] P. Li, M. Jiang, K. Li et al., "Glutathione peroxidase 4-regulated neutrophil ferroptosis induces systemic autoimmunity," *Nature Immunology*, vol. 22, no. 9, pp. 1107–1117, 2021.
- [130] H. Mao, Y. Zhao, H. Li, and L. Lei, "Ferroptosis as an emerging target in inflammatory diseases," *Progress in Biophysics and Molecular Biology*, vol. 155, pp. 20–28, 2020.
- [131] J. Wu, Z. Feng, L. Chen et al., "TNF antagonist sensitizes synovial fibroblasts to ferroptotic cell death in collagen-induced arthritis mouse models," *Nature Communications*, vol. 13, no. 1, p. 676, 2022.
- [132] R. Ni, G. Song, X. Fu et al., "Reactive oxygen species-responsive dexamethasone-loaded nanoparticles for targeted treatment of rheumatoid arthritis via suppressing the iRhom2/TNF- α /BAFF signaling pathway," *Biomaterials*, vol. 232, article ???, 2020.
- [133] L. J. Su, J. H. Zhang, H. Gomez et al., "Reactive oxygen species-induced lipid peroxidation in apoptosis, autophagy, and ferroptosis," *Oxidative Medicine and Cellular Longevity*, vol. 2019, Article ID 5080843, 13 pages, 2019.
- [134] S. Doll, F. P. Freitas, R. Shah et al., "FSP1 is a glutathione-independent ferroptosis suppressor," *Nature*, vol. 575, no. 7784, pp. 693–698, 2019.
- [135] K. Bersuker, J. M. Hendricks, Z. Li et al., "The CoQ oxidoreductase FSP1 acts parallel to GPX4 to inhibit ferroptosis," *Nature*, vol. 575, no. 7784, pp. 688–692, 2019.
- [136] H. Luo and R. Zhang, "Icariin enhances cell survival in lipopolysaccharide-induced synoviocytes by suppressing ferroptosis via the Xc-/GPX4 axis," *Experimental and Therapeutic Medicine*, vol. 21, no. 1, p. 72, 2021.
- [137] Y. Zu, Y. Mu, Q. Li, S. T. Zhang, and H. J. Yan, "Icariin alleviates osteoarthritis by inhibiting NLRP3-mediated pyroptosis," *Journal of Orthopaedic Surgery and Research*, vol. 14, no. 1, p. 307, 2019.
- [138] L. Yang, H. Wang, X. Yang et al., "Auranofin mitigates systemic iron overload and induces ferroptosis via distinct mechanisms," *Signal Transduction and Targeted Therapy*, vol. 5, no. 1, p. 138, 2020.
- [139] J. Xu, J. Liu, G. Yue et al., "Therapeutic effect of the natural compounds baicalein and baicalin on autoimmune diseases," *Molecular Medicine Reports*, vol. 18, no. 1, pp. 1149–1154, 2018.
- [140] Q. Dai, D. Zhou, L. Xu, and X. Song, "Curcumin alleviates rheumatoid arthritis-induced inflammation and synovial hyperplasia by targeting mTOR pathway in rats," *Drug Design, Development and Therapy*, vol. 12, pp. 4095–4105, 2018.
- [141] X. Chen, J. Li, R. Kang, D. J. Klionsky, and D. Tang, "Ferroptosis: machinery and regulation," *Autophagy*, vol. 17, pp. 2054–2081, 2021.
- [142] B. R. Stockwell, X. Jiang, and W. Gu, "Emerging mechanisms and disease relevance of ferroptosis," *Trends in Cell Biology*, vol. 30, no. 6, pp. 478–490, 2020.
- [143] Y. Yang, Y. Lin, M. Wang et al., "Targeting ferroptosis suppresses osteocyte glucolipotoxicity and alleviates diabetic osteoporosis," *Bone Research*, vol. 10, no. 1, p. 26, 2022.
- [144] I. Alim, J. T. Caulfield, Y. Chen et al., "Selenium drives a transcriptional adaptive program to block ferroptosis and treat stroke," *Cell*, vol. 177, no. 5, pp. 1262–1279.e25, 2019.
- [145] P. Maher, "Potentiation of glutathione loss and nerve cell death by the transition metals iron and copper: implications for age-related neurodegenerative diseases," *Free Radical Biology & Medicine*, vol. 115, pp. 92–104, 2018.
- [146] J. Lewerenz, G. Ates, A. Methner, M. Conrad, and P. Maher, "Oxytosis/ferroptosis-(Re-) emerging roles for oxidative stress-dependent non-apoptotic cell death in diseases of the central nervous system," *Frontiers in Neuroscience*, vol. 12, p. 214, 2018.
- [147] A. von Massenhausen, W. Tonnus, and A. Linkermann, "Cell death pathways drive necroinflammation during acute kidney injury," *Nephron*, vol. 140, no. 2, pp. 144–147, 2018.
- [148] C. Li, X. Deng, X. Xie, Y. Liu, J. P. Friedmann Angeli, and L. Lai, "Activation of glutathione peroxidase 4 as a novel anti-inflammatory strategy," *Frontiers in Pharmacology*, vol. 9, p. 1120, 2018.
- [149] X. Chen, R. Kang, G. Kroemer, and D. Tang, "Ferroptosis in infection, inflammation, and immunity," *The Journal of Experimental Medicine*, vol. 218, no. 6, 2021.
- [150] T. Zhao, Q. Yang, Y. Xi et al., "Ferroptosis in rheumatoid arthritis: a potential therapeutic strategy," *Frontiers in Immunology*, vol. 13, article 779585, 2022.